

FOOD PRESERVATION TECHNOLOGY SERIES



Water Properties of Food, Pharmaceutical, and Biological Materials



EDITED BY

Maria del Pilar Buera

Jorge Welte-Chanes

Peter J. Lillford

Horacio R. Corti



Taylor & Francis
Taylor & Francis Group

Water Properties of Food, Pharmaceutical, and Biological Materials

FOOD PRESERVATION TECHNOLOGY SERIES

Series Editor

Gustavo V. Barbosa-Cánovas

Engineering and Food for the 21st Century

Editors: Jorge Welti-Chanes, Gustavo V. Barbosa-Cánovas,
and José Miguel Aguilera

Food Science and Food Biotechnology

Editors: Gustavo F. Gutiérrez-López
and Gustavo V. Barbosa-Cánovas

Innovations in Food Processing

Editors: Gustavo V. Barbosa-Cánovas and Grahame W. Gould

Osmotic Dehydration and Vacuum Impregnation: Applications in Food Industries

Editors: Pedro Fito, Amparo Chiralt, Jose M. Barat, Walter E. L. Spiess,
and Diana Behnslian

Pulsed Electric Fields in Food Processing: Fundamental Aspects and Applications

Editors: Gustavo V. Barbosa-Cánovas and Q. Howard Zhang

Transport Phenomena in Food Processing

Editors: Jorge Welti-Chanes, Jorge F. Vélez-Ruiz,
and Gustavo V. Barbosa-Cánovas

Trends in Food Engineering

Editors: Jorge E. Lozano, Cristina Añón, Efrén Parada-Arias,
and Gustavo V. Barbosa-Cánovas

Unit Operations in Food Engineering

Albert Ibarz and Gustavo V. Barbosa-Cánovas

Water Properties of Food, Pharmaceutical, and Biological Materials

María del Pilar Buera, Jorge Welti-Chanes, Peter J. Lillford,
and Horacio R. Corti

Water Properties of Food, Pharmaceutical, and Biological Materials

EDITED BY

Maria del Pilar Buera

Universidad de Buenos Aires
Argentina

Jorge Welte-Chanes

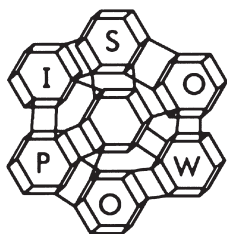
Universidad de las Americas-Puebla
Mexico

Peter J. Lillford

University of York
Bedfordshire, England

Horacio R. Corti

Universidad de Buenos Aires
CNEA, Centro Atómico Constituyentes
Argentina



Taylor & Francis

Taylor & Francis Group
Boca Raton London New York

A CRC title, part of the Taylor & Francis imprint, a member of the
Taylor & Francis Group, the academic division of T&F Informa plc.

Published in 2006 by
CRC Press
Taylor & Francis Group
6000 Broken Sound Parkway NW, Suite 300
Boca Raton, FL 33487-2742

© 2006 by Taylor & Francis Group, LLC
CRC Press is an imprint of Taylor & Francis Group

No claim to original U.S. Government works
Printed in the United States of America on acid-free paper
10 9 8 7 6 5 4 3 2 1

International Standard Book Number-10: 0-8493-2993-0 (Hardcover)
International Standard Book Number-13: 978-0-8493-2993-7 (Hardcover)
Library of Congress Card Number 2005052881

This book contains information obtained from authentic and highly regarded sources. Reprinted material is quoted with permission, and sources are indicated. A wide variety of references are listed. Reasonable efforts have been made to publish reliable data and information, but the author and the publisher cannot assume responsibility for the validity of all materials or for the consequences of their use.

No part of this book may be reprinted, reproduced, transmitted, or utilized in any form by any electronic, mechanical, or other means, now known or hereafter invented, including photocopying, microfilming, and recording, or in any information storage or retrieval system, without written permission from the publishers.

For permission to photocopy or use material electronically from this work, please access www.copyright.com (<http://www.copyright.com/>) or contact the Copyright Clearance Center, Inc. (CCC) 222 Rosewood Drive, Danvers, MA 01923, 978-750-8400. CCC is a not-for-profit organization that provides licenses and registration for a variety of users. For organizations that have been granted a photocopy license by the CCC, a separate system of payment has been arranged.

Trademark Notice: Product or corporate names may be trademarks or registered trademarks, and are used only for identification and explanation without intent to infringe.

Library of Congress Cataloging-in-Publication Data

Water properties of food, pharmaceutical, and biological materials / edited by María del Pilar Buera
... [et al.].

p. cm. -- (Food preservation technology ; 9)

Includes bibliographical references and index.

ISBN 0-8493-2993-0

1. Food--Water activity--Congresses. 2. Food--Moisture--Congresses. I. Pilar Buera, María del. II. Food preservation technology series ; 9.

TX553.W3W3685 2005
664'.07--dc22

2005052881



Taylor & Francis Group
is the Academic Division of T&F Informa plc.

Visit the Taylor & Francis Web site at
<http://www.taylorandfrancis.com>

and the CRC Press Web site at
<http://www.crcpress.com>

Dedication

This book is dedicated to the memory of Dr. Martine Le Meste who, until her death on February 6, 2004, was a professor at ENSBANA, Université de Bourgogne, France and a member of the ISOPOW Central Committee. We recognize, with regret, the passing of Professor Le Meste, and the “ISOPOW family” will remember her for her many contributions to our present understanding of the behavior of water in foods and biological systems.

Contents

Preface	xv
---------------	----

SECTION 1 Invited Lectures

Part 1: Dynamics and Relaxation in Amorphous Aqueous Systems

1. Thermodynamics of Supercooled and Glassy Water	5
<i>Pablo G. Debenedetti</i>	
2. Water Dynamics at the Surface of Proteins and Micelles: Understanding the Fast and the Slow Components	11
<i>Subrata Pal, Sudip Chakraborty, Sarika Maitra Bhattacharyya, Sanjoy Bandyopadhyay, Sundaram Balasubramanian, and Biman Bagchi</i>	
3. How Does Water Diffuse in Glasses of Carbohydrates?.....	39
<i>Valeria Molinero and William A. Goddard III</i>	
4. Manifestation of Molecular Mobilities in Amorphous Aqueous Systems: The View from Different Experimental Techniques	59
<i>David S. Reid</i>	

Part 2: Role of Water in Structural and Functional Properties: From Microscopic to Macroscopic Properties

5. The Effect of Microstructure on Solvent and Solute Diffusion on the Micro- and Nanolength Scales	79
<i>Anne-Marie Hermansson, Niklas Lorén, and Magnus Nydén</i>	
6. Probing Water–Solid Interactions in Crystalline and Amorphous Systems Using Vibrational Spectroscopy	101
<i>Lynne S. Taylor</i>	
7. Structure–Property Relationships in Low Moisture Products	115
<i>José Miguel Aguilera</i>	

8. Ice Nucleation in Bulk and Dispersed Water: Application to Freezing of Foods	133
<i>Danièle Clausse, Jean-Louis Lanoisellé, and Saïd Touni</i>	
9. Molecular-Level Characterization of Lipid Bilayers in Disaccharide Matrices and Its Consequences for Cell Lyophilization	151
<i>Juan J. de Pablo, Carolina Schebor, Satoshi Ohtake, and Amadeu Sum</i>	

Part 3: Responses to Water Stress in Living Organisms: Related New Potential Technologies

10. Water Stress of Bacteria and Molds from an NMR Water Mobility Standpoint	167
<i>Pavinee Chinachoti and Elena Vittadini</i>	
11. Water Properties and Cell Longevity	191
<i>Christina Walters</i>	
12. Water and Biological Structures at High Pressure.....	205
<i>Jorge Weltri-Chanes, Fernanda San Martín-González, José A. Guerrero-Beltrán, and Gustavo V. Barbosa-Cánovas</i>	
13. Viability of Probiotic Bacteria as Affected by Drying.....	233
<i>Barry Corcoran, Catherine Stanton, Song Miao, Gerald F. Fitzgerald, and R. Paul Ross</i>	

Part 4: Water and the Structure and Stability of Microdisperse Systems

14. Proteins and Lipids Can Alter the Thermodynamic and Dynamic Characteristics of Water at Fluid Interfaces	251
<i>Juan Miguel Rodríguez-Patino, María Rosario Rodríguez-Niño, Cecilio Carrera-Sánchez, and Ana Lucero-Caro</i>	
15. Studies on Molecular Organization at the Water Interface	273
<i>Victor J. Morris</i>	
16. Stability of Cloudy Apple Juice Colloidal Particles Modeled with the Extended DLVO Theory	289
<i>Diego B. Genovese and Jorge E. Lozano</i>	

Part 5: Overlapping Water Relations and Material Sciences for the Improvement of Quality Products

- 17. The Hydration Limit of Amorphous Solids and Long-Term Stability.....** 303
David Lechuga-Ballesteros and Danforth P. Miller
- 18. Physicochemical Changes in Frozen Products: Glass Transition and Rheological Behavior in Frozen Starch–Sucrose Hydrocolloid Systems.....** 309
Noemí Zaritzky and Cristina Ferrero
- 19. The Mystery of Marshmallow Hardening.....** 325
Miang Hoong Lim, Yin Jia, and Samuel Heenan
- 20. Beyond Water Activity and Glass Transition: A Broad Perspective on the Manner by which Water Can Influence Reaction Rates in Foods** 343
Craig P. Sherwin and Theodore P. Labuza

SECTION 2 Oral and Poster Presentations

Part 6: Functional and Mechanical Properties of Biomolecules

- 21. Glass-Transition Temperature and Self-Detaching of Maltodextrin Films: Effect of Molecular Weight and Sucrose Addition.....** 377
Fernanda P. Collares, José R.D. Finzer, and Theo G. Kieckbusch
- 22. The Polyproline II Conformation: How Protein Hydration Influences Conformation in Solution.....** 387
Patricio A. Carvajal and Tyre C. Lanier
- 23. Rheology and Microstructure of Interfaces Stabilized by Mixed Proteins and Surfactants: A Computer Simulation Study** 401
Luis A. Pagnaloni, Rammile Ettelaie, and Eric Dickinson
- 24. Effects of Content and Type of Binary Polyol Mixtures on Physical and Mechanical Properties of Starch-Based Edible Films** 413
Riku A. Talja, Harry Helén, Yrjö H. Roos, and Kirsi Jouppila

25. **The Dynamics of Formation and Structure of the Air–Water Interface in the Presence of Protein–Polysaccharide Mixtures.....** 421
Rosa Baeza, Cecilio Carrera-Sánchez, Juan Miguel Rodríguez-Patino, and Ana M.R. Pilosof

26. **Mechanical and Water Vapor Properties of Gelatin-Based Films as Function of Relative Humidity, Temperature, and Film Thickness** 431
Rosemary A. Carvalho, Paulo José do Amaral Sobral, and Florencia C. Menegalli

27. **Thermal Analysis and Textural Properties of Frozen French Bread Dough with Different Quantities of Ascorbic Acid.....** 439
Tatiana G. Matuda, Clarissa C. Romeu, Denise T. Tavares, Duclerc Fernandes Parra, Ademar Benévolo Lugão, and Carmen Cecília Tadini

28. **Effect of Nutraceuticals on Physico-Chemical Properties of Sodium Caseinate Films Plasticized with Glycerol** 445
Elizabeth Lima-Lima, Susana Altamirano-Romo, Rocío Rivas-Araiza, Gabriel Luna-Bárcenas, and Cristina Pérez-Pérez

29. **Behavior of Hydroxypropylmethylcelluloses of Different Molecular Structure and Water Affinity at the Air–Water Interface.....** 455
Oscar E. Pérez, Cecilio Carrera-Sánchez, Juan Miguel Rodríguez-Patino, and Ana M.R. Pilosof

30. **Drying of *Lactobacillus bulgaricus* Grown at High Osmolarity in the Presence of Disaccharides** 463
Emma Tymczyszyn and E. Aníbal Disalvo

Part 7: Structure, Microstructure, and the Stability of Biomolecules and Biological Systems

31. **The Effect of High Pressure and Temperature on the Macroscopic, Microscopic, Structural, and Molecular Properties of Tapioca Starch Gels** 471
Elena Vittadini, Eleonora Carini, and Davide Barbanti

32. **Characterization of Food Product Surfaces during Drying Using Fractal Geometry.....** 483
Gustavo F. Gutiérrez-López, José Jorge Chanona-Pérez, Liliana Alamilla-Beltrán, Roberto Campos-Mendiola, and Reynold Ramón Farrera-Rebollo

33. Effect of Vacuum Impregnation and Microwave Application on Structural Changes during Air Drying of Apple.....	495
<i>Carolina Contreras, María Eugenia Martín, Nuria Martínez-Navarrete, and Amparo Chiralt</i>	
34. Modulation of the Hydration of Lipid Membrane Phosphates by Choline, Glycerol, and Ethanolamine Groups.....	503
<i>Fabiana Lairion, Florencia Martíni, Sonia Díaz, Silvia Brandan, Aída Ben Altabef, and E. Aníbal Disalvo</i>	
35. Morphology and Size of Particles during Spray Drying	513
<i>Liliana Alamilla-Beltrán, José Jorge Chanona-Pérez, Antonio R. Jiménez-Aparicio, and Gustavo F. Gutiérrez-López</i>	
36. Evaluation of Morphological and Microstructural Changes during Air Drying of Spheres Using Fractal Analysis and Relationships with Spray Drying	519
<i>José Jorge Chanona-Pérez, Liliana Alamilla-Beltrán, Reynold Ramón Farrera-Rebollo, and Gustavo F. Gutiérrez-López</i>	
37. Heat Transfer Units and Morphology of Particles in Spray Drying.....	525
<i>Liliana Alamilla-Beltrán, José Jorge Chanona-Pérez, Antonio R. Jiménez-Aparicio, and Gustavo F. Gutiérrez-López</i>	
38. Convective Drying with Tempering of Mushrooms (<i>Pleurotus ostreatus</i>) and Color Changes of Final Product	531
<i>Santiago S. Ocegüera, José Jorge Chanona-Pérez, Liliana Alamilla-Beltrán, Jorge Mendoza-Pérez, Ramón Arana-Erassquín, and Gustavo F. Gutiérrez-López</i>	
39. Modeling of Structural and Quality Changes during Drying of Vegetables: Application to Red Sweet Pepper (<i>Capsicum annuum</i> L.)	537
<i>Karina C. di Scala, Sara I. Roura, and Guillermo H. Crapiste</i>	
40. The Role of Residual Water for the Stability of Protein Freeze-Dried with Trehalose.....	543
<i>Kiyoshi Kawai, Tomoaki Hagiwara, Rikuo Takai, and Toru Suzuki</i>	
41. Effects of Trehalose on the Stability and Phase Transition Behavior of Freeze-Dried Liposomes Containing Cholesterol	551
<i>Satoshi Ohtake, Carolina Schebor, Sean P. Palecek, and Juan J. de Pablo</i>	

42. **Storage Changes and Subcellular Freezing Injuries in Recalcitrant *Araucaria angustifolia* Embryos** 557
Víctor H. Panza, Verónica R. Láinez, Sara B. Maldonado, Horacio L. Maroder, and María del Pilar Buera

43. **Thermal Transitions of Quinoa Embryos and Seeds as Affected by Water Content**..... 565
Silvia B. Matiacevich, Martina L. Castellión, Sara B. Maldonado, and María del Pilar Buera

Part 8: Molecular Mobility, State Diagrams, and Chemical Reactions

44. **Physical Structure, Water Plasticization, and Crystallization of Spray-Dried and Freeze-Dried Lactose** 573
Md. Kamrul Haque and Yrjö H. Roos

45. **FT-IR Study of the Hydration of Caffeine, Sucrose, and Their Mixtures in Water** 583
Barbara Rogé, Vincent Aroulmoji, and Mohamed Mathlouthi

46. **Solute Diffusion in Biopolymers as a Function of Water Activity Using a Modified Free Volume Theory** 593
Mustafa E. Yildiz and Jozef L. Kokini

47. **Molecular Mobility in Glassy Starch: Influence of Hydration and Sucrose** 603
Fabienne Poirier, Marie Tanguy, Dominique Champion, and Gaëlle Roudaut

48. **High-Speed Observations of the Nucleation of Ice by Power Ultrasound** 613
Rachel C. Chow, Derek Atkins, Scott Singleton, Robert Mettin, Bernhard Lindinger, Thomas Kurz, Werner Lauterborn, Malcolm Povey, and Robert Chivers

49. **Relationships between the Maximum Rate of Nonenzymatic Browning, Relative Humidity, and Structural Changes**..... 623
Nuria Acevedo, Carolina Schebor, and María del Pilar Buera

50. **Water Determination in Dried Milk Products: Is the International Standard Method Reasonable?** 631
Heinz-Dieter Isengard, Andrea Felgner, Renate Kling, and Christoph T. Reh

51. The Impact of Water Adsorption on the Energetics of Surface Interactions of Powders of Different Crystal Forms	639
<i>M. Teresa Carvajal</i>	
52. Water-Sorption Behavior of Glycinebetaine and the State Diagram of Its Aqueous System.....	647
<i>Kenta Komai and Norio Murase</i>	
53. Effects of Sugar Crystallization on Nonenzymatic Browning Kinetics in Low-Moisture Food Systems	655
<i>Song Miao and Yrjö H. Roos</i>	
54. Chemical and Physical Stability of Disaccharides as Affected by the Presence of $MgCl_2$	663
<i>Patricio Román Santagapita and María del Pilar Buera</i>	
55. Evolution of Some Physical Properties of “Aceto Balsamico Tradizionale Di Reggio Emilia” during Long-Term Aging	671
<i>Paola Pittia, Dino Mastrocola, and Enrico Maltini</i>	
56. Incorporation of Solute in the Ice Phase during Freezing.....	677
<i>Julia Telford and Peter Lillford</i>	
57. Enthalpy Relaxation in Freeze-Concentrated Sucrose–Water Glasses	683
<i>Chiharu Inoue and Toru Suzuki</i>	
58. State Diagram for Freeze-Dried Plum and Glass Transitions of Plum Skin and Pulp	689
<i>Vânia Regina Nicoletti Telis, Paulo José do Amaral Sobral, and Javier Telis-Romero</i>	
59. Effect of Type of Amorphous Sugar Excipients on the Preservation of Lactate Dehydrogenase Activity as a Function of Storage Conditions	697
<i>Kazuhito Kajiwara and Tomoko Imai</i>	
60. The Water Content Effect on the Glass-Transition Temperature of Low Calory Candy Formulations	703
<i>Adelina G. Celeghein and Amelia C. Rubiolo</i>	
61. Release of Encapsulated Aroma Compounds from Amorphous Maltodextrin Matrices.....	709
<i>Kirsi Jouppila, Susanna Sundberg, Sanna-Maija Miettinen, and Lea Hyvönen</i>	

62. Relationship between Glass-Transition Curves and Sorption Isotherms for the Evaluation of Storage Conditions of Freeze-Dried Camu-Camu (*Myrciaria dubia* (Hbk) Mcvaugh) Pulp with and without Maltodextrin Addition 715
Mariana Altenhofen da Silva, Paulo José do Amaral Sobral, and Theo G. Kieckbusch

63. Water-Sorption Isotherms and Water-Plasticization Effect in Dried Pear 723
King Xue, Consuelo González-Martínez, M. Teresa Cháfer, and Amparo Chiralt

Index 731

Preface

Water Properties of Food, Pharmaceutical, and Biological Materials is based on lectures and papers presented by leading international researchers in the field at the Ninth International Symposium on the Properties of Water in Foods (ISOPOW, 2004) held at Mar del Plata, Argentina, from September 25 to 30, 2004.

Food materials, biological, and pharmaceutical scientists have recognized that water plays an important role in the structure, functionality and stability of biomaterials. The ubiquitous water molecules are small and simple, but they develop complex interactions and present unusual properties for unprepared observers. We thus aimed to overlap areas of different fields of research having in common problems faced by how and why water behaves as it does. The theme chosen for the ISOPOW 9 meeting was "Water properties related to the technology and stability of food, pharmaceutical, and biological materials." The understanding of the properties of water in foods, enriched by approaches from polymer and materials sciences and by the advances of analytical techniques, enabled us to detect unsolved questions and the need to go deeply into them.

About 90 participants from 19 different countries attended ISOPOW 9, whose programme embraced areas of contemporary interest. In each of the seven sessions there were three or four oral presentations by invited speakers giving a total of 24 invited lectures. There was ample time provided for discussions. From the 89 submitted abstracts, 74 were accepted, and the members of the scientific committee recommended 20 of them to be presented orally.

ISOPOW 9 also made possible the organization of a workshop on "Dynamics and relaxation in supercooled fluids and glassy systems." This activity was organized with the objective of bringing together post-graduate students and researchers in the area to generate an environment for discussion of the theoretical and experimental aspects of nonequilibrium processes in supercooled fluids and glasses. The workshop was attended by 20 young researchers and Ph.D. students of different universities and national laboratories of Argentina. Lectures were performed by C.A. Angell (Arizona State University), G. Appignanesi (National South University, Argentina), B. Bagchi (Indian Institute of Science, Bangalore, India), H. Corti (Comisión Nacional de Energía Atómica, Argentina), J. de Pablo (University of Wisconsin), P. Debenedetti, (Princeton University), R. Grigera (University of La Plata, Argentina), T. Grigera, (University of La Plata, Argentina) and V. Molinero (California Institute of Technology).

Section 1: Invited Lectures

Roberto Fernández Prini presented “Water: A Simple Molecule and a Fascinating Liquid” at the opening conference. Dr. Fernández Prini is an honorary fellow of The International Association for the Properties of Water and Steam (IAPWS), and he gave a general picture from an interesting point of view on some features that are not yet satisfactorily explained to understand aqueous systems at ambient temperature, the role of length scale to explain features of the behavior of hydrophobic solutes, and the need to use theories for inhomogeneous fluids to deal with confined aqueous systems.

Section 1 of this book is based on presentations from invited speakers.

The first four chapters cover several basic aspects discussed in Session I, “Dynamics and relaxation in amorphous aqueous systems,” chaired by Dr. Raúl Grigera. This session served as a starting point for the Symposium, before moving to more applied aspects in the following parts.

Several phenomena occurring at different length scales, from macroscopic to molecular dimensions, are covered in Chapters 5 to 9, “Role of Water in Structural and Functional Properties: From Microscopic to Macroscopic Properties.” These topics were discussed in Session II (chaired by Dr. David Reid) and III (chaired by Dr. Anne Marie Hermansson), remarking on the usefulness of new tools both for instrumental and computer calculations to solve questions on the behavior of water in its relation to solutes.

The subject of “Responses to Water Stress in Living Organisms: Related New Potential Technologies” was discussed in Session IV, in which Dr. Yrjö Roos acted as chairman. The corresponding conferences were included in Chapters 10 to 13.

It is interesting to note that the different contributors to this session covered several aspects of living organisms from innovative viewpoints on the basis of new experimental and theoretical tools for understanding the response of stressed organisms under extreme conditions.

Special aspects of suspensions and emulsions with particular emphasis on the characteristics of the interfaces were covered in Session V, “Water and the Structure and Stability of Microdisperse Systems.” Dr. Ana Pilosof chaired this session, and the conferences were included in Chapters 14 to 16.

Some of the subjects discussed in Sessions VI (chaired by Dr. Pilar Buera) and VII (chaired by Dr. Peter Lillford) were included in Chapters 17 to 20 of this book, under a general title “Overlapping Water Relations and Material Sciences for the Improvement of Quality Products: Past, Present, and Future.” Researchers from pharmaceutical and food sciences were gathered to provide a clear picture of recent advances in understanding the preservation of biomolecule functionality in restricted water environments and how to manage the adverse effects of water on sensitive components. In the last session, Dr. Theodore Labuza dedicated a space to the subject “Material Science in Food Technology and Pharmaceuticals” inspired by Dr. Marcus Karel. Those who were his former students (Theodore Labuza,

Jorge Chirife, Yrjo Roos, and Pilar Buera) made a combined presentation on that subject.

In this last session it was made evident first, how the main areas of water relations of foods had evolved through the years and second, how several phenomena which could not be explained some years ago can now be interpreted with new tools from polymer and materials sciences.

Section 2: Oral and Poster Presentations

Four special sessions were dedicated to oral presentations and discussion of 20 selected posters. Drs. Jorge Welti-Chanes, Miang Hoong Lim, Norio Murase, and Peter Lillford were the chairmen of the oral sessions, which are included in Section 2. Short papers from poster presentations are also included. Regarding these presentations, in his report to the Central Committee, Dr. Lillford pointed out that "of particular note was the quality of short presentations and posters. The benefit of screening this material by the local organizers was evident, and Central Committee recommends that this practice be adopted in future meetings."

It was interesting to see how different fields of knowledge (food, pharmaceutical, and biological sciences) are affected by common phenomena and share analytical tools to solve different problems, and how water is the conducting wire among them.

It was made clear in the whole symposium that food science has broadened its spectrum of subjects and points of view, from basic to applied aspects, from macroscopic to microscopic and molecular phenomena. The combination of efforts from several disciplines has also advantageously enriched the knowledge on water and its relationships with food components.

Editors

María del Pilar Buera received her licenciate degree in chemical sciences from the Facultad de Ciencias Exactas y Naturales, University of Buenos Aires, Argentina (UBA); she later earned a master's degree in food science and technology from the Universidad Nacional de Mar del Plata, Argentina and her doctorate in chemical sciences from the UBA. She received a grant from the Argentine Council of Science and Technology (CONICET) and performed postdoctoral work at Professor Marcus Karel's laboratory at Rutgers University, New Jersey, U.S.A. during 1990–1992. She received research grants from the International Foundation for Science, the UBA and CONICET. Professor Buera is a member of CONICET and an associate professor in food chemistry at the Organic Chemistry Department; she also performs research activities at the Departamento de Industrias, Facultad de Ciencias Exactas y Naturales, UBA. She has participated in international cooperative activities in CYTED and CONICET projects and acted as an evaluator of research projects and scientific papers in food, chemistry, and engineering areas. Her research interests are kinetic aspects related to state transitions in the conservation of foods and food ingredients. She has published over 70 papers in international refereed journals, participated as an author at more than 50 scientific meetings, and is advisor to several postgraduate students. Professor Buera has been a member of ISOPOW since 2000 and was scientific program chair of the ninth ISOPOW meeting held in Mar del Plata, Argentina in 2004.

Jorge Welte-Chanes was born in Puebla City, México. He obtained his bachelor of science in biochemical engineering (1976) and master of science in food engineering (1979) at the Instituto Tecnológico y de Estudios Superiores de Monterrey (ITESM). In 1979 he moved to Spain to obtain a Ph.D. in chemical sciences, with a major in food technology, from the Universidad de Valencia. He has been a professor at the ITESM and since 1977 at the University of the Américas-Puebla (UDLA), where he has taught in the Departments of Chemical and Food Engineering and of Chemistry and Biology. He was head of the department for one year, then dean of the Engineering School (1986–1988), and academic vice-president (1988–2002). He is currently professor and researcher at UDLA and a visiting research scholar in Texas Christian University. His research areas are focused mainly on food and biological polymers, candy technology, food drying, water activity, minimal processing of foods and biological materials, process simulation, and emerging technologies. He has been the coordinator of diverse international research projects and an advisor to different industries within the mentioned research areas. He was the world president of the

International Association of Food and Engineering (1997–2000). Dr. Welti-Chanes is the author of more than 140 scientific publications in refereed journals and books and more than 150 presentations in international meetings. He is the author or coeditor of several books on food preservation and food engineering, a member of the editorial boards of different journals and book series, and an evaluator of research projects in Latin America and the United States. He is an advisor for different food enterprises in areas such as processing, quality assurance, and processes optimization. Also, he has advised many different universities in Mexico and Latin America in strategic planning of educational processes.

Peter Lillford was educated in chemistry at King's College, London, where he received his Ph.D. in physical organic chemistry, and at Cornell University, Ithaca, New York, U.S.A. where he did his postdoctoral research in ultra-fast reaction kinetics. Professor Lillford worked at the Colworth Laboratory of Unilever Research from 1971 to 2001. He retired from the post of chief scientist (foods) in November 2001. From 1993 until 1997 he was chairman of the food and drink panel of the Office of Science and Technology's Technology Foresight Programme. From 1998 until 2000, he was chairman of the BBSRC Agri-Food Committee and a member of the BBSRC Strategy Board. He currently holds a visiting chair in public awareness of science at the University of York in the Centre for Novel Applications of Plants (CNAP). He was president of the Institute of Food Science and Technology (IFST). From 2000 to 2004 (at the time of the ninth symposium), he was president of the International Symposium on the Properties of Water in Foods (ISOPOW). He is currently chairman, LINK Advanced Manufacturing for U.K. Government (DEFRA); chairman, National Centre for Non-Food Crops (U.K.); member, Management Advisory Committee, Biochemical Engineering, UC London; and a member, Strategic Advisory Team, EPSRC, Life Sciences Programme. In 1991 he was awarded the senior medal by the Foods Group of the Royal Society of Chemistry, and in 1998 he was awarded a CBE for services to the food industry and science in the Queen's Birthday Honours. He was also awarded a DEng (Hon) in recognition of services to food engineering by Birmingham University.

Horacio R. Corti received his Ph.D. at the University of Buenos Aires (UBA), Argentina in 1980. He became a postdoctoral fellow at the Central Electricity Research Laboratories, CEGB, Leatherhead, U.K. in 1981. Since 1977, he has been a scientific staff member at the National Atomic Energy Commission (CNEA) in Argentina. Since 1984, he has been professor of chemistry at the Facultad de Ciencias Exactas y Naturales, UBA, where he became full professor of physical chemistry in 1996. He has been a member of the National Research Council (CONICET) since 1987 and is the coordinator of the Argentine–Brazilian Committee of the International Association for the Properties of Water and Steam. He participates in international cooperative

projects in SECyT, Fundación Antorchas, and IUPAC and has been responsible for the project evaluation system in chemistry at the Agencia de Promoción Científica y Tecnológica (ANPCyT) of Argentina. His main interests are thermodynamic and transport properties of aqueous systems, including supercooled and vitrified aqueous systems of interest in cryopreservation of foods and biomolecules. He has published over 60 papers in international journals and is the author of several books and book chapters in his research field area.

Acknowledgments

ISOPOW 9 has been made possible through the efforts of a number of individuals and organizations.

The International Union of Food Science and Technology (IUFoST) and two research organizations, the National Agency of Scientific and Technological Promotion (ANPCYT) and National Research Council (CONICET) from Argentina co-sponsored the meeting. The participation of several Ph.D. students and young researchers was made possible by financial support provided by the Fundación Antorchas. ISOPOW 9 also received financial support from Decagon Devices, Mettler-Toledo, Bruker, and the local Universidad Católica Argentina, D'Amico Sistemas, Microanalítica and Tec Instrumental. The organizing Committee acknowledges the auspices of the Universidad de Buenos Aires, the Universidad Nacional de Luján and the Municipalidad de General Pueyrredón.

The symposium programme was prepared by the members of central and local committees. The editors wish to recognize members of all ISOPOW 9 committees and session chairmen for their considerable efforts in the evaluation of papers and for their help in the organization. All local arrangements were the responsibility of the local committee.

ISOPOW 9 Committees

ISOPOW Central Committee at the time of the event

Dr. Peter Lillford University of York, U.K., President
Dr. María del Pilar Buera Universidad de Buenos Aires, Argentina
Dr. Miang Hoong Lim University of Otago, New Zealand
Dr. Jim Leslie Consultant, U.K.
Dr. Norio Murase Tokyo Denki University, Japan
Dr. David S. Reid University of California, U.S.A.
Dr. Louis B. Rockland Foodtech Research and Development, U.S.A.
Dr. Yrjö H. Roos University College, Cork, Ireland
Dr. Denise Simatos Université de Bourgogne, France
Dr. Jorge Weltri-Chanes Universidad de las Américas, Puebla, México

Local Committee

- Dr. María del Pilar Buera* Departamento de Industrias, FCEyN, Universidad de Buenos Aires
Dr. Horacio Corti* Comisión Nacional de Energía Atómica, Buenos Aires
Dr. Beatriz Elizalde FCEyN, Universidad de Buenos Aires
Dr. Sara Maldonado* Departamento de Biología, FCEyN, Universidad de Buenos Aires
Dr. Florencia Mazzobre* Comisión Nacional de Energía Atómica, Buenos Aires
Dr. Ana Pilosof* Departamento de Industrias, FCEyN, Universidad de Buenos Aires
Dr. Carolina Schebor* Departamento de Industrias, FCEyN, Universidad de Buenos Aires

The following Ph.D. students have collaborated in the organization: Nuria Acevedo, Martina Catellón, Alicia Gallo, Silvia Matiacevich, Patricio Santagapita, Rosa Baeza, and Oscar Pérez.

Scientific Committee

- Dr. José Miguel Aguilera Pontificia Universidad Católica de Chile
Dr. María del Pilar Buera FCEy N, Universidad de Buenos Aires, Argentina
Dr. Jorge Chirife FCEyN, Universidad de Buenos Aires, Argentina
Dr. Horacio Corti Comisión Nacional de Energía Atómica, Argentina
Dr. Theodore Labuza University of Minnesota, U.S.A.
Dr. Peter Lillford University of York, U.K.
Dr. Ana Pilosof FCEyN, Universidad de Buenos Aires, Argentina
Dr. David Reid University of California, Davis, U.S.A.
Dr. Yrjö H. Roos University College, Cork, Ireland
Dr. Denise Simatos Université de Bourgogne, France
Dr. Jorge Welte-Chanes Universidad de las Américas, Puebla, México
Dr. Noemi Zaritzky CIDCA, Universidad Nacional de La Plata, Argentina

International Advisory Committee

- Dr. Amparo Chiralt Universidad de Valencia, Spain
Dr. Gustavo Gutiérrez Instituto Politécnico Nacional, México
Dr. Martine Le Meste Université de Bourgogne, France (*deceased February 6, 2004*).
Dr. Jim Leslie Consultant, U.K.
Dr. Harry Levine Kraft Foods, U.S.A.

*Members of CONICET, Argentina

Dr. Miang Hoong Lim University of Otago, New Zealand
Dr. Norio Murase Tokyo Denki University, Japan
Dr. Louis Rockland Foodtech Research and Development, U.S.A.
Dr. Louise Slade Kraft Foods, U.S.A.
Dr. Paulo José do Amaral Sobral FZEA, USP, Brazil

The editors would also like to record their thanks, especially to Drs. Carolina Schebor and Florencia Mazzobre, who collaborated in the preparation of manuscripts for this volume, and to Drs. E. Aníbal Disalvo, Richard Hartel, Victor Morris, and David Lechuga-Ballesteros for their help given to ISOPOW 9 committees in the reviewing process.

The Organizers would like to thank Aerolíneas Argentinas for the provision of discounted flights and Nestlé Argentina for the kind donation of candies.

Contributors

Acevedo, Nuria Departamento de Industrias, Facultad de Ciencias Exactas y Naturales, Universidad de Buenos Aires, Buenos Aires, Argentina

Aguilera, José Miguel Department of Chemical and Bioprocess Engineering, Pontificia Universidad Católica, Santiago, Chile

Alamilla-Beltrán, Liliana Departamento de Graduados e Investigación en Alimentos, Escuela Nacional de Ciencias Biológicas, Instituto Politécnico Nacional, México City, México

Altamirano-Romo, Susana Instituto Tecnológico de Celaya, Departamento Ingeniería Bioquímica, Celaya, México

Altenhofen da Silva, Mariana Faculdade de Engenharia Química, Universidade Estadual de Campinas, São Paulo, Brazil

Arana-Errasquín, Ramón Escuela Nacional de Ciencias Biológicas, Instituto Politécnico Nacional, México City, México

Aroulmoji, Vincent Laboratoire de Chimie Physique Industrielle, Faculté des Sciences, Université de Reims Champagne Ardenne, Reims, France

Atkins, Derek Unilever Research and Development, Bedfordshire, U.K.

Baeza, Rosa Departamento de Industrias, Facultad de Ciencias Exactas y Naturales, Universidad de Buenos Aires, Buenos Aires, Argentina

Bagchi, Biman Solid State and Structural Chemistry Unit, Indian Institute of Science, Bangalore, India

Balasubramanian, Sundaram Chemistry and Physics of Materials Unit, Jawaharlal Nehru Centre for Advanced Scientific Research, Jakkur, Bangalore, India

Bandyopadhyay, Sanjoy Molecular Modeling Laboratory, Department of Chemistry, Indian Institute of Technology, Kharagpur, India

Barbanti, Davide Dipartimento di Ingegneria Industriale, Area di Scienze e Tecnologie Alimentari, Università degli Studi, Parma, Italy

Barbosa-Cánovas, Gustavo V. Washington State University, Pullman, Washington, U.S.A.

Ben Altabef, Aída Instituto de Química Física, Facultad de Bioquímica, Química y Farmacia, Universidad Nacional de Tucumán, Tucumán, Argentina

Bhattacharyya, Sarika Maitra Solid State and Structural Chemistry Unit, Indian Institute of Science, Bangalore, India

Brandan, Silvia Instituto de Química Física, Facultad de Bioquímica, Química y Farmacia, Universidad Nacional de Tucumán, Tucumán, Argentina

Buera, María del Pilar Departamento de Industrias, Facultad de Ciencias Exactas y Naturales, Universidad de Buenos Aires, Buenos Aires, Argentina

Campos-Mendiola, Roberto Escuela Nacional de Ciencias Biológicas, Instituto Politécnico Nacional, México City, México

Carini, Eleonora Dipartimento di Ingegneria Industriale, Area di Scienze e Tecnologie Alimentari, Università degli Studi, Parma, Italy

Carrera-Sánchez, Cecilio Departamento de Ingeniería Química, Facultad de Química, Universidad de Sevilla, Sevilla, Spain

Carvajal, M. Teresa Department of Industrial and Physical Pharmacy, Purdue University, West Lafayette, Indiana, U.S.A.

Carvajal, Patricio A. Department of Food Science, North Carolina State University, Raleigh, North Carolina, U.S.A.

Carvalho, Rosemary A. Department of Food Engineering, University of São Paulo, São Paulo, Brazil

Castellión, Martina L. Departamento de Biodiversidad y Biología Experimental, Facultad de Ciencias Exactas y Naturales, Universidad de Buenos Aires, Buenos Aires, Argentina

Celeghin, Adelina G. Facultad de Bioquímica y Ciencias Biológicas, Santa Fe, Argentina

Cháfer, M. Teresa Departamento de Tecnología de Alimentos, Universidad Politécnica de Valencia, Valencia, Spain

Chakraborty, Sudip Molecular Modeling Laboratory, Department of Chemistry, Indian Institute of Technology, Kharagpur, India

Champion, Dominique Department of Molecular and Sensory Engineering of Foods and Pharmaceuticals, Dijon, France

Chanona-Pérez, José Jorge Departamento de Graduados e Investigación en Alimentos, Escuela Nacional de Ciencias Biológicas, Instituto Politécnico Nacional, México City, México

Chinachoti, Pavinee Product Science Fellow, Hill's Pet Nutrition, Inc., Science and Technology Center, Topeka, Kansas, U.S.A.

Chiralt, Amparo Departamento de Tecnología de Alimentos, Universidad Politécnica de Valencia, Valencia, Spain

Chivers, Robert (deceased) University of Cambridge, Cambridge, U.K.

Chow, Rachel C. Unilever Research and Development, Colworth, Sharnbrook, Bedfordshire, U.K. and Department of Food Science, University of Leeds, Leeds, U.K.

Clausse, Danièle Université de Technologie de Compiègne, Département de Génie Chimique, Compiègne, France

Collares, Fernanda P. Departamento de Tecnologia de Alimento, Faculdade de Engenharia de Alimentos, Cidade Universitária, São Paulo, Brazil

Contreras, Carolina Food Technology Department, Universidad Politécnica de Valencia, Valencia, Spain

Corcoran, Barry Biotechnology Centre, Teagasc, Moorepark, Fermoy, County Cork and Department of Microbiology, University College, Cork, Ireland

Crapiste, Guillermo H. PLAPIQUI (UNS-CONICET), La Carrindanga, Bahía Blanca, Argentina

Debenedetti, Pablo G. Department of Chemical Engineering, Princeton University, New Jersey, U.S.A.

de Pablo, Juan J. Chemical and Biological Engineering Department, University of Wisconsin, Madison, Wisconsin, U.S.A.

Disalvo, E. Aníbal Laboratorio de Fisicoquímica de Membranas Lipídicas, Facultad de Farmacia y Bioquímica, Buenos Aires, Argentina

Díaz, Sonia Instituto de Química Física, Facultad de Bioquímica, Química y Farmacia, Universidad Nacional de Tucumán, Tucumán, Argentina

Dickinson, Eric Department of Food Science, University of Leeds, Leeds, U.K.

Ettelaie, Rammile Department of Food Science, University of Leeds, Leeds, U.K.

Farrera-Rebollo, Reynold Ramón Escuela Nacional de Ciencias Biológicas, Instituto Politécnico Nacional, México City, México

Felgner, Andrea University of Hohenheim, Institute of Food Technology, Stuttgart, Germany

Fernandes Parra, Duclerc Instituto de Pesquisas Energéticas e Nucleares, Chemical Engineering and Environment Department, São Paulo, Brazil

Ferrero, Cristina Centro de Investigación y Desarrollo en Criotecnología de Alimentos, Facultad Ciencias Exactas, and Departamento de Ingeniería Química, Facultad Ingeniería, Universidad Nacional de La Plata, La Plata, Argentina

Finzer, José R.D. Departamento de Engenharia Química, Campus Santa Mônica, Uberlândia, Brazil

Fitzgerald, Gerald F. Biotechnology Centre, Teagasc, Moorepark, Fermoy, County Cork and Department of Microbiology, University College, Cork, Ireland

Genovese, Diego B. PLAPIQUI (UNS-CONICET), La Carrindanga, Bahía Blanca, Argentina

Goddard III, William A. Materials and Process Simulation Center, California Institute of Technology, Pasadena, California, U.S.A.

González-Martínez, Consuelo Departamento de Tecnología de Alimentos, Universidad Politécnica de Valencia, Valencia, Spain

Guerrero-Beltrán, José A. Departamento de Ingeniería Química y Alimentos, Universidad de las Américas, Puebla, México

Gutiérrez-López, Gustavo F. Escuela Nacional de Ciencias Biológicas,
Instituto Politécnico Nacional, México City, México

Hagiwara, Tomoaki Department of Food Science and Technology, Tokyo
University of Marine Science and Technology, Tokyo, Japan

Haque, Md. Kamrul Department of Food and Nutritional Sciences,
University College Cork, Cork, Ireland

Heenan, Samuel Department of Food Science, University of Otago,
Dunedin, New Zealand

Helén, Harry Department of Food Technology, University of Helsinki,
Helsinki, Finland

Hermansson, Anne-Marie SIK, The Swedish Institute for Food and
Biotechnology, Göteborg, Sweden

Hyvönen, Lea Department of Food Technology, University of Helsinki,
Helsinki, Finland

Imai, Tomoko Katayanagi Institute, Tokyo University of Technology,
Tokyo, Japan

Inoue, Chiharu Unilever Research and Development, Colworth,
Sharnbrook, Bedfordshire, U.K.

Isengard, Heinz-Dieter University of Hohenheim, Institute of Food
Technology, Stuttgart, Germany

Jia, Yin Department of Food Science, University of Otago, Dunedin,
New Zealand

Jiménez-Aparicio, Antonio R. Centro de Desarrollo de Productos Bióticos
del Instituto Politécnico Nacional, México City, México

Jouppila, Kirsi Department of Food Technology, University of Helsinki,
Helsinki, Finland

Kajiwara, Kazuhito School of Bionics, Tokyo University of Technology,
Tokyo, Japan

Kawai, Kiyoshi Department of Food Science and Technology, Tokyo
University of Marine Science and Technology, Tokyo, Japan

Kieckbusch, Theo G. DTF/Faculdade de Engenharia Química, São Paulo,
Brazil

Kling, Renate University of Hohenheim, Institute of Food Technology,
Stuttgart, Germany

Kokini, Jozef L. Department of Food Science and Center for Advanced
Food Technology, Rutgers University, New Brunswick, New Jersey, U.S.A.

Komai, Kenta Tokyo Denki University, Department of Biotechnology,
School of Science and Engineering, Ishizaka, Saitama, Japan

Kurz, Thomas Drittes Physikalisches Institut, Universität Göttingen,
Göttingen, Germany

Labuza, Theodore P. University of Minnesota, Saint Paul, Minnesota, U.S.A.

Láinez, Verónica R. Departamento de Biodiversidad y Biología Experi-
mental, Facultad de Ciencias Exactas y Naturales, Buenos Aires, Argentina

Lairion, Fabiana Laboratorio de Fisicoquímica de Membranas Lipídicas,
Facultad de Farmacia y Bioquímica, Buenos Aires, Argentina

Lanier, Tyre C. Department of Food Science, North Carolina State
University, Raleigh, North Carolina, U.S.A.

Lanoisellé, Jean-Louis Université de Technologie de Compiègne, Dépar-
tement de Génie Chimique, Compiègne, France

Lauterborn, Werner Drittes Physikalisches Institut, Universität Göttingen,
Göttingen, Germany

Lechuga-Ballesteros, David Nektar Therapeutics, San Carlos, California,
U.S.A.

Lillford, Peter Department of Biology, University of York, York, U.K.

Lim, Miang Hoong Department of Food Science, University of Otago,
Dunedin, New Zealand

Lima-Lima, Elizabeth Instituto Tecnológico de Celaya, Departamento de
Ingeniería Bioquímica, Celaya, México

Lindinger, Bernhard Drittes Physikalisches Institut, Universität Göttingen,
Göttingen, Germany

Lorén, Niklas SIK, The Swedish Institute for Food and Biotechnology,
Göteborg, Sweden

Lozano, Jorge E. PLAPIQUI (UNS-CONICET), Camino La Carrindanga
Bahía Blanca, Argentina

Lucero-Caro, Ana Departamento de Ingeniería Química, Facultad de
Química, Universidad de Sevilla, Sevilla, Spain

Lugão, Ademar Benévolo Instituto de Pesquisas Energéticas e Nucleares,
Chemical Engineering and Environment Department, São Paulo, Brazil

Luna-Bárceñas, Gabriel CINVESTAV-Querétaro Libramiento Norpo-
niente 2000, Querétaro, México

Maldonado, Sara B. Departamento de Biodiversidad y Biología Experi-
mental, Facultad de Ciencias Exactas y Naturales, Buenos Aires, Argentina

Maltini, Enrico Dipartimento di Scienze degli Alimenti, University of
Udine, Udine, Italy

Maroder, Horacio L. Departamento de Ciencias Básicas, Universidad
Nacional de Luján, Argentina

Martín, María Eugenia Departamento de Tecnología de Alimentos,
Universidad Politécnica de Valencia, Valencia, Spain

Martínez-Navarrete, Nuria Departamento de Tecnología de Alimentos,
Universidad Politécnica de Valencia, Valencia, Spain

Martíni, Florencia Laboratorio de Fisicoquímica de Membranas Lipídicas,
Facultad de Farmacia y Bioquímica, Buenos Aires, Argentina

Mastrocola, Dino Dipartimento di Scienze degli Alimenti, University of
Teramo, Mosciano Stazione (Teramo), Italy

Mathlouthi, Mohamed Laboratoire de Chimie Physique Industrielle,
Faculté des Sciences, Université de Reims Champagne Ardenne, Reims,
France

Matiacevich, Silvia B. Departamento de Industrias, Facultad de Ciencias
Exactas y Naturales, Universidad de Buenos Aires, Buenos Aires,
Argentina

Matuda, Tatiana G. São Paulo University, Escola Politécnica, Chemical
Engineering Department, Food Engineering Laboratory, São Paulo, Brazil

Mendoza-Pérez, Jorge Escuela Nacional de Ciencias Biológicas, Instituto Politécnico Nacional, Mexico City, México

Menegalli, Florencia C. Department of Food Engineering, São Paulo, Brazil

Mettin, Robert Drittes Physikalisches Institut, Universität Göttingen, Göttingen, Germany

Miao, Song Department of Food and Nutritional Sciences, University College Cork, Cork, Ireland

Miettinen, Sanna-Maija Department of Food Technology, University of Helsinki, Helsinki, Finland

Miller, Danforth P. Nektar Therapeutics, San Carlos, California, U.S.A.

Molinero, Valeria Materials and Process Simulation Center, California Institute of Technology, Pasadena, California, U.S.A.

Morris, Victor J. Institute of Food Research, Norwich Research Park, Colney, Norwich, U.K.

Murase, Norio Tokyo Denki University, Department of Biotechnology, School of Science and Engineering, Ishizaka, Saitama, Japan

Nydén, Magnus Department of Applied Surface Chemistry, Chalmers University of Technology, Göteborg, Sweden

Oceguera, Santiago S. Escuela Nacional de Ciencias Biológicas, Instituto Politécnico Nacional, México City, México

Ohtake, Satoshi Chemical and Biological Engineering Department, University of Wisconsin, Madison, Wisconsin, U.S.A.

Pal, Subrata Solid State and Structural Chemistry Unit, Indian Institute of Science, Bangalore, India

Palecek, Sean P. Chemical and Biological Engineering Department, University of Wisconsin, Madison, Wisconsin, U.S.A.

Panza, Víctor H. Departamento de Biodiversidad y Biología Experimental, Facultad de Ciencias Exactas y Naturales, Buenos Aires, Argentina

Pérez, Oscar E. Departamento de Industrias, Facultad de Ciencias Exactas y Naturales, Universidad de Buenos Aires, Buenos Aires, Argentina

Pérez-Pérez, Cristina Instituto Tecnológico de Celaya, Departamento de Ingeniería Bioquímica, Celaya, México

Pilosof, Ana M.R. Departamento de Industrias, Facultad de Ciencias Exactas y Naturales, Universidad de Buenos Aires, Buenos Aires, Argentina

Pittia, Paola Dipartimento di Scienze degli Alimenti, University of Udine, Udine, Italy

Poirier, Fabienne Department of Molecular and Sensory Engineering of Foods and Pharmaceuticals, Dijon, France

Povey, Malcolm Department of Food Science, University of Leeds, Leeds, U.K.

Pugnalon, Luis A. Procter Department of Food Science, University of Leeds, Leeds, U.K.

Reh, Christoph T. Nestlé Research Center, Nestec Ltd, Vers-chez-les-Blanc, Lausanne, Switzerland

Reid, David S. Food Science and Technology, University of California, Davis, California, U.S.A.

Rivas-Araiza, Rocío CINVESTAV-Querétaro Libramiento Norponiente 2000, Querétaro, México

Rodríguez-Niño, María Rosario Departamento de Ingeniería Química, Facultad de Química, Universidad de Sevilla, Sevilla, Spain

Rodriguez-Patino, Juan Miguel Departamento de Ingeniería Química, Universidad de Sevilla, Sevilla, Spain

Rogé, Barbara Laboratoire de Chimie Physique Industrielle, Faculté des Sciences, Université de Reims Champagne Ardenne, Reims, France

Romeu, Clarissa C. São Paulo University, Escola Politécnica, Chemical Engineering Department, Food Engineering Laboratory, São Paulo, Brazil

Roos, Yrjö H. Department of Food and Nutritional Sciences, University College, Cork, Ireland

Ross, R. Paul Biotechnology Centre, Teagasc, Moorepark, Fermoy, County Cork and Alimentary Pharmabiotic Centre, Cork, Ireland

Roudaut, Gaëlle Department of Molecular and Sensory Engineering of Foods and Pharmaceuticals, Dijon, France

Roura, Sara I. Facultad de Ingeniería, UNMdP-CONICET, Mar del Plata, Argentina

Rubiolo, Amelia C. Instituto de Desarrollo Tecnológico para la Industria Química, Santa Fe, Argentina

San Martín-González, Fernanda Departamento de Ingeniería Química y Alimentos, Universidad de las Américas, Puebla, México

Santagapita, Patricio Román Departamento de Industrias, Facultad de Ciencias Exactas y Naturales, Universidad de Buenos Aires, Buenos Aires, Argentina

Scala, Karina C. di Facultad de Ingeniería, Mar del Plata, Argentina

Schebor, Carolina Departamento de Industrias, Facultad de Ciencias Exactas y Naturales, Universidad de Buenos Aires, Buenos Aires, Argentina

Sherwin, Craig P. University of Wisconsin, Madison, Wisconsin, U.S.A.

Singleton, Scott Unilever Research and Development, Colworth, Sharnbrook, Bedfordshire, U.K.

Sobral, Paulo José do Amaral Department of Food Engineering, University of São Paulo, São Paulo, Brazil

Stanton, Catherine Biotechnology Centre, Teagasc, Moorepark, Fermoy, County Cork and Alimentary Pharmabiotic Centre, Cork, Ireland

Sum, Amadeu Chemical and Biological Engineering Department, University of Wisconsin, Madison, Wisconsin, U.S.A.

Sundberg, Susanna Department of Food Technology, University of Helsinki, Helsinki, Finland

Suzuki, Toru Department of Food Science and Technology, Tokyo University of Marine Science and Technology, Tokyo, Japan

Tadini, Carmen Cecília São Paulo University, Escola Politécnica, Chemical Engineering Department, Food Engineering Laboratory, São Paulo, Brazil

Takai, Rikuo Department of Food Science and Technology, Tokyo University of Marine Science and Technology, Tokyo, Japan

Talja, Riku A. Department of Food Technology, University of Helsinki, Helsinki, Finland

Tanguy, Marie Department of Molecular and Sensory Engineering of Foods and Pharmaceuticals, Dijon, France

Tavares, Denise T. São Paulo University, Escola Politécnica, Chemical Engineering Department, Food Engineering Laboratory, São Paulo, Brazil

Taylor, Lynne S. Industrial and Physical Pharmacy, Purdue University, West Lafayette, Indiana, U.S.A.

Telford, Julia Unilever Corporate Research, Colworth House, Sharnbrook, Bedfordshire, U.K.

Telis, Vânia Regina Nicoletti DETA/UNESP, São José do Rio Preto, São Paulo, Brazil

Telis-Romero, Javier DETA/UNESP, São José do Rio Preto, São Paulo, Brazil

Toumi, Saïd Université de Technologie de Compiègne Département de Génie Chimique Compiègne, France

Tymczyszyn, Emma Laboratorio de Fisicoquímica de Membranas Lipídicas, Facultad de Farmacia y Bioquímica, Buenos Aires, Argentina

Vittadini, Elena Università degli Studi di Parma, Dipartimento di Chimica Ingegneria Industriale, Parma, Italy

Walters, Christina National Center for Genetic Resources Preservation, Fort Collins, Colorado, U.S.A.

Welti-Chanes, Jorge Departamento de Ingeniería Química y Alimentos, Universidad de las Américas, Puebla, México

Xue, King Departamento de Tecnología de Alimentos, Universidad Politécnica, Valencia, Spain

Yildiz, Mustafa E. PRISM, Princeton University, Princeton, New Jersey, U.S.A.

Zaritzky, Noemí Centro de Investigación y Desarrollo en Criotecnología de Alimentos, Facultad de Ciencias Exactas, Universidad Nacional de La Plata, and Departamento de Ingeniería Química, La Plata, Argentina

Other Participants at ISOPOW 9

Angell, C. Austen Department of Chemistry and Biochemistry, Arizona State University, Tempe, Arizona, U.S.A.

Appignanesi, Gustavo Departamento de Química, Universidad Nacional del Sur, Bahía Blanca, Argentina

Auffret, Tony Pfizer Global Research and Development, Sandwich, U.K.

Charoenrein, Sanguansri Department of Food Science and Technology, Faculty of Agro-Industry, Kasetsart University, Bangkok, Thailand

Chirife, Jorge Universidad Católica Argentina and Universidad de Buenos Aires, Buenos Aires, Argentina

Corti, Horacio Unidad de Actividad Química, Comisión Nacional de Energía Atómica, Buenos Aires and FCEyN Universidad de Buenos Aires, Buenos Aires, Argentina

de Bry, Luc G.C.T.A. bvba, Sint-Katelijne-Waver, Belgium

Fernández Prini, Roberto Unidad de Actividad Química, Comisión Nacional de Energía Atómica, Buenos Aires and Facultad de Ciencias Exactas y Naturales, Universidad de Buenos Aires, Buenos Aires, Argentina

Fontana, Anthony Decagon Devices, Pullman, Washington, U.S.A.

Grigera, Raúl IFLYSIB and Universidad de La Plata, La Plata, Argentina

Grigera, Tomás Universidad de La Plata, La Plata, Argentina and Kellogg Company, Battle Creek, Michigan, U.S.A.

Longinotti, M. Paula Unidad de Actividad Química, Comisión Nacional de Energía Atómica, Buenos Aires, Argentina

Mazzobre, M. Florencia Unidad de Actividad Química, Comisión Nacional de Energía Atómica, Buenos Aires, Argentina

Meunier, Vincent Nestlé Research Center, Lausanne, Switzerland

Morgan, François Nestle Research Center, Lausanne, Switzerland

Müller, Daniel Biotechnological Center, University of Technology and Max Planck Institute of Molecular Cell Biology and Genetics, Dresden, Germany

Spiess, Walter Institute of Food Process Engineering, Universitat Karlsruhe, Karlsruhe, Germany

SECTION 1

Invited Lectures

Part 1: Dynamics and Relaxation in Amorphous Aqueous Systems

1

Thermodynamics of Supercooled and Glassy Water

Pablo G. Debenedetti

CONTENTS

Introduction	5
Stability Limit Conjecture.....	6
Liquid–Liquid Phase Transition	6
Singularity-Free Scenario.....	7
Conclusion	7
References	8

Introduction

Water has long been a source of fascination on account of its peculiar physical properties. It is the only chemical compound that occurs naturally in the solid, liquid and vapor phases. If sufficiently cold, it becomes more compressible and less dense when cooled, and less viscous when compressed. Its dielectric constant in the normal liquid range is unusually large, and its melting and boiling temperatures are uncommonly high for a non-metallic hydride. Liquid water's anomalies become more pronounced when it is cooled below the freezing point without crystallizing (supercooled) (Debenedetti, 2003). Speedy and Angell, (1976) showed that a variety of thermodynamic and transport properties of water in the supercooled state appear to diverge upon power-law extrapolation to -45°C , that is to say a few degrees below the homogeneous nucleation temperature. Since then, an important and uninterrupted body of experimental, theoretical and computational work has sought to understand the physical properties of cold, non-crystalline, metastable forms of water, and in particular to provide a unifying theoretical framework within which both the microscopic origin

and the phase behavior implications of the apparent divergencies can be understood. Although such a definitive interpretation is not yet available, important progress has been made, and the number of thermodynamically consistent interpretations that can explain experimental observations is very small.

Stability Limit Conjecture

Speedy (1982) proposed what has come to be known as the stability limit conjecture. In this scenario, the spinodal curve along which the superheated liquid becomes unstable with respect to the vapor phase retraces at low temperatures towards positive pressures. This curve would then provide a continuous boundary to superheated, stretched and supercooled states of water. The isothermal compressibility, isobaric heat capacity and magnitude of the thermal expansion coefficient diverge at the spinodal curve. Speedy's picture would then explain the experimentally observed increase in these quantities upon supercooling at atmospheric pressure as the inevitable consequence of the approach to the underlying retracing spinodal. Speedy's conjecture played an important role as an organizing principle for thinking about supercooled water's anomalies. However, computer simulations show no evidence of a retracing spinodal (Poole et al., 1993), and the thermodynamic consistency of the stability limit conjecture has been questioned recently (Debenedetti, 2003, 2004; Speedy, 2004).

Liquid–Liquid Phase Transition

In 1985, Mishima showed that there exists an apparently first-order transition between two forms of amorphous solid water (glassy water) (Mishima et al., 1985), and nine years later he showed that this transition is reversible (Mishima, 1994). Poole et al. (1992) in Gene Stanley's group at Boston University, using molecular dynamics computer simulation, proposed the liquid–liquid transition (or second critical point) interpretation of supercooled water's thermodynamic behavior. According to this viewpoint, at low temperature and high pressure a first-order transition occurs between two distinct phases of liquid water, high-density liquid (HDL) and low-density liquid (LDL). HDL is also the higher-entropy phase, and hence the transition locus has a negative slope in the pressure–temperature plane, and terminates at a critical point. At temperatures higher than (and pressures lower than) this critical point, supercooled water exists as a single-phase fluid. Mishima's observed transition between low- and high-density glasses (low-density amorphous ice (LDA) and high-density amorphous ice (HDA)), would then simply be, according to this interpretation, the

kinetically arrested manifestation of the liquid–liquid transition. Moreover, water’s thermodynamic anomalies are seen as a natural consequence of the approach to a critical point. The best estimates of water’s metastable critical point (Mishima and Stanley, 1998a) place it at conditions where liquid water is too cold not to crystallize when cooled, and too hot not to crystallize when warmed across its glass transition. Thus, direct experimental proof of the existence of a second critical point has been elusive. Nevertheless, decompression-induced melting experiments by Mishima and Stanley (Mishima and Stanley, 1998b; Mishima, 2000), computer simulations (Harrington et al., 1997), and theoretical calculations (Poole et al., 1994; Truskett et al., 1999) all point to the soundness of the underlying picture. The preponderance of evidence thus supports the liquid–liquid transition (or second critical point) hypothesis.

Singularity-Free Scenario

In the singularity-free interpretation of supercooled water’s thermodynamics (Sastry et al., 1996; Rebelo et al., 1998), the increase in water’s response functions upon cooling is linked through thermodynamic arguments to the line of temperatures of maximum density (TMD). From the fact that this locus has a negative slope in the (P , T) plane there follow certain consequences, such as the increase in water’s compressibility upon cooling. Thus, one can explain water’s thermodynamic anomalies without invoking low-temperature singularities or phase transitions. Earlier theoretical work by Stanley and Teixeira (Stanley, 1979; Blumberg et al., 1980; Stanley and Teixeira, 1980) had in fact predicted singularity-free behavior for a schematic water model, although the general thermodynamic formulation of this scenario is accorded to Sastry et al. (1996).

It has been reported recently that upon annealing at high pressure a denser form of amorphous water, very high-density amorphous ice (VHDA), is formed (Loerting et al., 2001). Whether this is indeed a new form of glassy water, or whether, as suggested by molecular simulations (Moaronak et al., 2004), it is simply the more stable form to which HDA relaxes is a question that is currently under investigation. Similarly, the possibility, also suggested by molecular simulation, that there may be multiple liquid–liquid transitions (Brovchenko et al., 2003) at low temperatures is also a subject of ongoing interest.

Conclusion

The last 20 years have seen explosive growth in interest and knowledge on supercooled and glassy water. The most important development has been

the discovery of apparently distinct amorphous forms of this substance (polyamorphism). The sharpness and apparent reversibility of the transition between LDA and HDA inspired an important body of work aimed at exploring, theoretically and computationally, the notion of a first-order transition between distinct liquid phases of a pure substance. There has resulted a vastly expanded perspective on the liquid state of matter (Katayama et al., 2000; Kurita and Tanaka, 2004; Katayama et al., 2004). The experimental study of glassy water has added significantly to the body of experimental and factual knowledge on this most important of substances. Nevertheless, and in spite of impressive progress in measuring, modeling and simulation, important gaps in our understanding of the global phase behavior of cold, non-crystalline, metastable water remain.

This lecture has focused on thermodynamic properties. A discussion of experimental observations, theoretical interpretations and open questions on supercooled water's dynamical properties can be found in a recent comprehensive review (Debenedetti, 2003).

References

- Blumberg, R.L., Shlifer, G., and Stanley, H.E. Monte Carlo tests of universality in a correlated-site percolation problem, *J. Phys. A: Math. Gen.*, 13, L147, 1980.
- Brovchenko, I., Geiger, A., and Oleinikova, A. Multiple liquid–liquid transitions in supercooled water, *J. Chem. Phys.*, 118, 9473, 2003.
- Debenedetti, P.G. Supercooled and glassy water, *J. Phys.: Condens. Matter*, 15, R1669, 2003.
- Debenedetti, P.G. Reply to comment on ‘Supercooled and glassy water’, *J. Phys.: Condens. Matter*, 16, 6815, 2004.
- Harrington, S., Zhang, R., Poole, P.H., Sciortino, F., and Stanley, H.E. Liquid–liquid phase transition: evidence from simulations, *Phys. Rev. Lett.*, 78, 2409, 1997.
- Katayama, Y., Inamura, Y., Mizutani, T., Yamakata, M., Utsumi, W., and Shimomura, O. Macroscopic separation of dense fluid phase and liquid phase of phosphorus, *Science*, 306, 848, 2004.
- Katayama, Y., Mizutani, T., Utsumi, W., Shimomura, O., Yamakata, M., and Funakoshi, K.-i. A first-order liquid–liquid phase transition in phosphorus, *Nature*, 403, 170, 2000.
- Kurita, R. and Tanaka, H. Critical-like phenomena associated with liquid–liquid transition in a molecular liquid, *Science*, 306, 845, 2004.
- Loerting, T., Salzmann, C., Kohl, I., Mayer, E., and Hallbrucker, A. A second distinct structural “state” of high-density amorphous ice at 77 K and 1 bar, *Phys. Chem. Chem. Phys.*, 3, 5355, 2001.
- Mishima, O. Reversible first-order transition between two H₂O amorphs at ca 0.2 GPa and ca. 135 K, *J. Chem. Phys.*, 100, 5910, 1994.
- Mishima, O. Liquid–liquid critical point in heavy water, *Phys. Rev. Lett.*, 85, 334, 2000.
- Mishima, O., Calvert, L.D., and Whalley, E. An apparently first-order transition between two amorphous phases of ice induced by pressure, *Nature*, 314, 76, 1985.

- Mishima, O. and Stanley, H.E. The relationship between liquid, supercooled and glassy water, *Nature*, 396, 329, 1998a.
- Mishima, O. and Stanley, H.E. Decompression-induced melting of ice IV and the liquid-liquid transition in water, *Nature*, 392, 164, 1998b.
- Moaronak, R., Donadio, D., and Parrinello, M. Polyamorphism of ice at low temperatures from constant-pressure simulations, *Phys. Rev. Lett.*, 92, 225702, 2004.
- Poole, P.H., Sciortino, F., Essmann, U., and Stanley, H.E. Phase behavior of metastable water, *Nature*, 360, 324, 1992.
- Poole, P.H., Sciortino, F., Essmann, U., and Stanley, H.E. Spinodal of liquid water, *Phys. Rev. E*, 48, 3799, 1993.
- Poole, P.H., Sciortino, F., Grande, T., Stanley, H.E., and Angell, C.A. Effect of hydrogen bonds on the thermodynamic behavior of liquid water, *Phys. Rev. Lett.*, 73, 1632, 1994.
- Rebelo, L.P., Debenedetti, P.G., and Sastry, S. Singularity-free interpretation of the thermodynamics of supercooled water. II. Thermal and volumetric behavior, *J. Chem. Phys.*, 109, 626, 1998.
- Sastry, S., Debenedetti, P.G., Sciortino, F., and Stanley, H.E. Singularity-free interpretation of the thermodynamics of supercooled water, *Phys. Rev. E*, 53, 6144, 1996.
- Speedy, R.J. Stability-limit conjecture. An interpretation of the properties of water, *J. Phys. Chem.*, 86, 982, 1982.
- Speedy, R.J. Comment on 'Supercooled and glassy water', *J. Phys.: Condens. Matter*, 16, 6811, 2004.
- Speedy, R.J. and Angell, C.A. Isothermal compressibility of supercooled water and evidence for a thermodynamic singularity at -45°C , *J. Chem. Phys.*, 65, 851, 1976.
- Stanley, H.E. A polychromatic correlated-site percolation problem with possible relevance to the unusual behavior of supercooled H_2O and D_2O , *J. Phys. A: Math. Gen.*, 12, L329, 1979.
- Stanley, H.E. and Teixeira, J. Interpretation of the unusual behavior of H_2O and D_2O at low temperatures: test of a percolation model, *J. Chem. Phys.*, 73, 3404, 1980.
- Truskett, T.M., Debenedetti, P.G., Sastry, S., and Torquato, S. A single-bond approach to orientation-dependent interactions and its implications for liquid water, *J. Chem. Phys.*, 111, 2647, 1999.

2

Water Dynamics at the Surface of Proteins and Micelles: Understanding the Fast and the Slow Components

**Subrata Pal, Sudip Chakraborty, Sarika Maitra Bhattacharyya,
Sanjoy Bandyopadhyay, Sundaram Balasubramanian,
and Biman Bagchi**

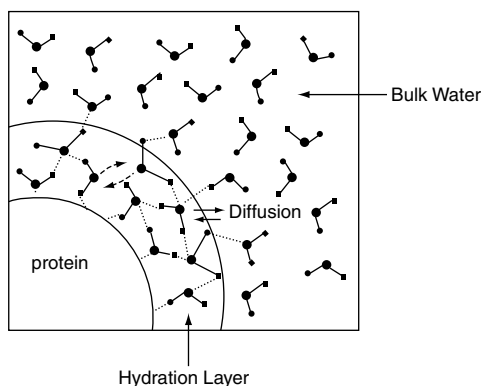
CONTENTS

Introduction	12
Qualitative Predictions of the Dynamic Exchange Model.....	13
Solvation Dynamics.....	15
Solvation Dynamics in Aqueous Protein Solutions	16
Solvation Dynamics in Aqueous Micellar Solutions.....	18
Dielectric Relaxation.....	19
Dielectric Relaxation of Aqueous Protein Solutions	19
Dielectric Relaxation of Aqueous Micellar Solutions	20
Single Water Molecule Reorientational Dynamics	22
Water Reorientation in Aqueous Protein Solutions	22
Water Reorientation in Aqueous Micellar Solution	25
Hydrogen Bond Lifetime Dynamics.....	25
Protein–Water Hydrogen Bond.....	26
Micelle–Water Hydrogen Bond.....	28
Protein–Glass Transition	28
Concluding Remarks.....	33
Acknowledgments	34
Appendix A	34
System and Simulation Details of CsPFO Micelle.....	34
System and Simulation Details of DTAB Micelle	34
System and Simulation Details of 1ETN Protein.....	34
System and Simulation Details of HP-36 Protein.....	35
References	36

Introduction

A molecular level understanding of the biological activity of a given protein is a goal that is hard to achieve but highly sought after. To perform this biological activity, such as ligand binding, the protein must undergo certain critical motions or fluctuations. The timescales of these motions may determine the reaction pathways and also the rate. Since biological activity is connected to the hydration level of a protein (Rupley and Careri, 1991), it is natural to enquire how these water molecules also participate in the dynamical events that lead to activity. Thus a microscopic level understanding of the dynamical coupling between the protein and the interfacial water molecules (hydration layer) is crucial to understand microscopic aspects of biological processes. Because of the importance of the issues involved, this area is currently a subject of intense research. Ultrafast laser spectroscopic techniques and computer simulation studies have played a crucial role in answering many of the detailed questions regarding the timescale and the nature of the dynamics near a protein surface. Experiments and simulation studies have shown that the protein side chain motions that are essential for its functionality require the breaking and making of protein–water hydrogen bonds (Gu and Schoenborn, 1995; Doster and Settles, 1998). The bond dynamics, however, is determined by the protein–water coupling and the hydration layer dynamics. The water molecules in the hydration layer experiences a surface that is heterogeneous, even on a molecular length scale, and the interaction with the surface is often quite strong, leading to a disruption of the regular hydrogen bond network of bulk water. Studies have shown that the hydration layer exhibits rich dynamical properties that are quite distinct from those of the bulk (Nandi et al., 2000; Balasubramanian et al., 2002, 2003; Bizzarri and Cannistraro, 2002; Pal et al., 2002, 2004; Bagchi, 2003; Bandyopadhyay et al., 2004). The dynamics involves multiple timescales, ranging from the bulk-like timescale to at least an order of magnitude slower than that of the bulk. As a prototype for simple globular proteins, the study of micelle is important because it is considered a biomimetic system. This article deals with the slow dynamics of water molecules at the surface of self-assemblies and proteins in aqueous solution. Considering these systems together, we obtain a broader view of water dynamics at an interacting surface. A schematic representation of the hydration layer around a protein is given in Figure 2.1.

In order to gain an in-depth understanding of hydration dynamics, we have carried out an analytical study of a model, the dynamic exchange model (DEM), describing the protein–water system. We have also performed detailed atomistic molecular dynamics (MD) simulations of water dynamics at the surface of an anionic micelle of cesium perfluorooctanoate (CsPFO), a cationic micelle of decyl trimethyl ammonium bromide (DTAB), the surface of two proteins, toxic domain of enterotoxin (1ETN) and

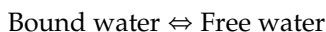
**FIGURE 2.1**

A schematic representation of the hydration shell around a protein. The shapes in the real systems are seldom perfectly spherical. The shell is not rigid or static. The big filled circle (●) represents the oxygen atom and the small filled circle (•) represents the hydrogen atom of a water molecule. The dotted lines are the hydrogen bonds and dashed arrows represent the transition between the bound and free water. The solid arrows represent the diffusion in and outside the hydration layer.

chicken villin headpiece sub-domain (HP-36) using classical, non-polarizable force fields. The system and simulation details are provided in Appendix A.

Qualitative Predictions of the Dynamic Exchange Model

The DEM (Nandi and Bagchi, 1997; Pal et al., 2002; Bhattacharyya et al., 2003) envisages the emergence of multiple (especially slow) timescales because of the existence of a dynamic equilibrium between the bound and free water molecules in the surface of biomolecules or self-assembly. At the center of this model lies the assumption that some of the water molecules at the surface of proteins can be considered as distinct species because of their strong hydrogen bonding to the biomolecular surface, and they are called “bound water.” The bound water molecules are also not permanently bound but remain bound longer than the average residence time of a quasi-free water molecule. The water not directly bonded to the protein surface but still in the hydration layer is called “free water.” Simulations have shown that there is constant exchange between these bound and free water molecules (Gu and Schoenborn, 1995). This equilibrium can be symbolically written as



Bound water is not a unique species because there is a distribution of the water protein binding energies (ϵ_{wp}), which according to simulation studies

is an exponential with a very sharp fall at low values of ε_{wp} . Low values of ε_{wp} correspond to quasi-free water molecules near the hydrophobic surface whereas the bound water molecules are expected to have a broad distribution centered around a relatively large binding energy.

An expression for the slow relaxation in the hydration layer has been derived where we model the protein surface as an infinite wall in the x - y plane. The starting point is coupled reaction-diffusion equations that describe the time evolution of bound and free water densities (Nandi and Bagchi, 1997; Pal et al., 2002; Bhattacharyya et al., 2003),

$$\begin{aligned} \frac{\partial}{\partial t} \rho_f(r, \Omega, t) = & D \nabla^2 \rho_f(r, \Omega, t) + D_R \nabla_\Omega^2 \rho_f(r, \Omega, t) - [\rho_f(r, \Omega, t) \int d\Omega_1 k_1(\Omega, \Omega_1) \\ & - \int d\Omega_1 \rho_b(r, \Omega_1, t) k_2(\Omega_1, \Omega)] h(z_L - z) \end{aligned} \quad (2.1)$$

$$\begin{aligned} \frac{\partial}{\partial t} \rho_b(r, \Omega, t) = & -\rho_b(r, \Omega, t) \int d\Omega_1 k_2(\Omega, \Omega_1) \\ & + \int d\Omega_1 \rho_f(r, \Omega_1, t) k_1(\Omega_1, \Omega) \text{ at } 0 < z < z_L \end{aligned} \quad (2.2)$$

where $\rho_f(r, \Omega, t)$ and $\rho_b(r, \Omega, t)$ are the densities of free and bound water, respectively. The first two terms on the right-hand-side of Equation 2.1 describe the change in free water density caused by rotational and translational motion (D and D_R are the translational and rotational diffusion coefficients, respectively), which is valid in the entire semi-infinite space $0 < z < \infty$. The third term represents the loss of free water from free to bound conversion where $k_1(\Omega, \Omega_1)$ is the transition rate from free water with orientation Ω to bound water with orientation Ω_1 . The last term accounts for the creation of free water from bound water where $k_2(\Omega, \Omega_1)$ is the transition rate from bound water with orientation Ω_1 to free water with orientation Ω . Because the bound water exists only in the surface layer, the last two terms are defined only in this layer, which is taken into account by the presence of the Heaviside step function, $h(z_L - z)$, where z_L is the width of the surface layer. In the case of bound water, because it cannot translate or rotate by itself, its density can change only because of transition between bound and free water. All terms in Equation 2.2 are defined only in the surface layer. After some simplifications, the timescales of collective reorientational dynamics in the asymptotic limit are given by (Bhattacharyya et al., 2003),

$$\tau_{\text{fast}}(q_{\parallel}) = (2D_R + Dq_{\parallel}^2)^{-1} \quad (2.3)$$

where q_{\parallel} is the wave number parallel to the surface. The fast timescale is found to be similar to the timescale of the bulk dynamics. However, because of the breakdown of the translational symmetry of the system by the presence of the protein surface, the wave number is conjugate only to the x - y plane.

The slow timescale is given by,

$$\tau_{\text{slow}}(q_{\parallel}) = \frac{1}{k_2} + \frac{k_1 z_L}{D k_2 \left(\frac{2D_R + D q_{\parallel}^2}{D} \right)^{1/2}} \propto \frac{1}{k_2} \quad (2.4)$$

Thus, while one time constant remains fast, of the order of 4–5 ps, the other is predicted to slow down appreciably, even to the extent of hundreds of picoseconds (ps). The model predicts that the slow timescale is proportional to the inverse of k_2 , which is of course determined by the binding energy, and for the majority of sites, the time constant may range between approximately 20 and 500 ps. Note that the slow timescale is slower than the inverse of the bound to free conversion rate because the free to bound conversion further slows down the relaxation of a free water molecule. Only a few water molecules may be so slow as to have a residence time of 500 ps or above.

Solvation Dynamics

Solvation dynamics refers to the energy stabilization of a probe solute caused by reorganization of the polar solvent dipoles around the charged probe when the charge is created suddenly in the solvent.

The solvation dynamics is monitored by the decay of solvation time correlation function (TCF), $S(t)$, defined as,

$$S(t) = \frac{E(t) - E(\infty)}{E(0) - E(\infty)} \quad (2.5)$$

where $E(t)$ and $E(\infty)$ are the energies of the probe at time t and equilibrium energy, respectively.

The solvation TCF can be related by linear response theory to auto TCF of energy fluctuation. This is usually termed $C(t)$ and defined as,

$$C(t) = \frac{\langle \delta E(0) \delta E(t) \rangle}{\langle \delta E(0) \delta E(0) \rangle} \quad (2.6)$$

where $\delta E = E - \langle E \rangle$ denotes a fluctuation in the solvation energy difference between the excited and the ground state of the solute and $\langle \cdots \rangle$ indicates an equilibrium ensemble average.

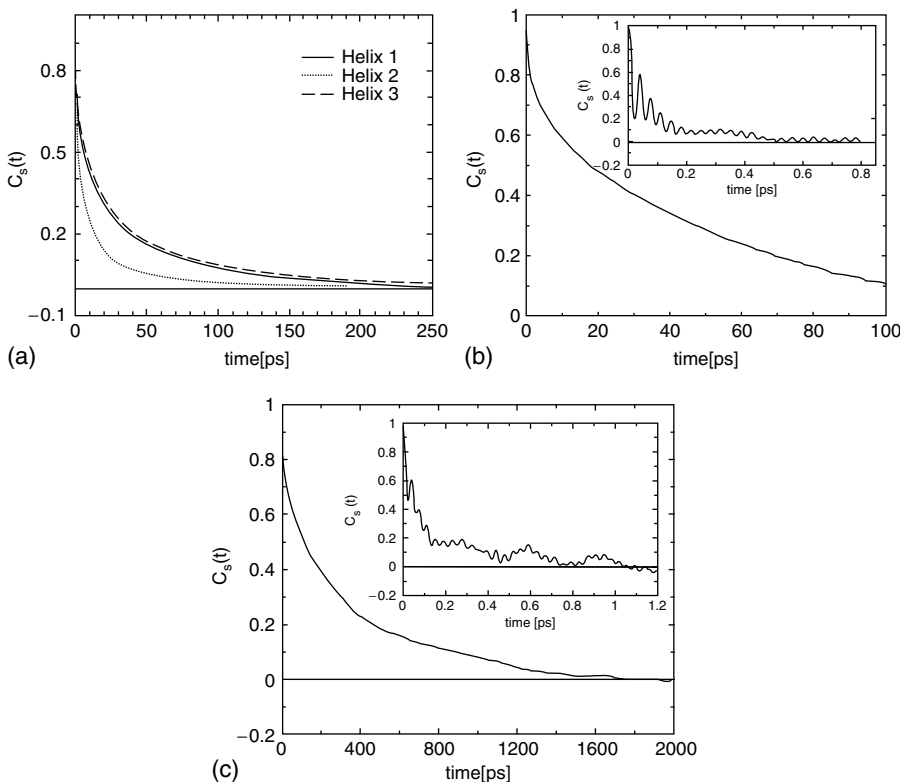
For solvation dynamics of dipoles in pure water, experimental studies find a sub-50 fs Gaussian component, followed by a slow bi-exponential decay with time constants 126 and 880 fs, respectively (Jimenez et al., 1994). It is believed that the initial ultra-fast response comes from the intermolecular O···O vibrational modes of water while the slowest one comes from the reorientational dynamics of water (Roy and Bagchi, 1993; Nandi et al., 1995). The success in the investigation of solvation dynamics in bulk water motivated many additional studies on complex systems where water is an

important ingredient. The organized assemblies include self-assembled molecular aggregates in polar liquids (e.g., micelles or vesicles in water) or nonpolar liquids (e.g., reverse micelles or microemulsions in hydrocarbons), cage-like hosts soluble in many liquids (cyclodextrins or calixarenes) and semi-rigid materials (e.g., polymers). Such studies revealed that water dynamics gets modified at such surfaces.

Solvation Dynamics in Aqueous Protein Solutions

Several important experiments have been carried out to study the solvation dynamics of hydrated proteins where the probe is on the surface or buried in the core, thus studying the hydration layer or buried water dynamics, respectively. These experiments have repeatedly found a significant slow component that is at least an order of magnitude slower than the solvation time in the bulk. Jordanides et al. (1999) used the three-pulse photon echo peak shift technique to examine the solvation dynamics of Eosin at the surface of aqueous lysozyme. They found a slow component of 500 ps, which made an 8% contribution to the total dynamics. Analysis of the experimental data via a generalized continuum model led to the conclusion that the slow component originates from the motion of the side-chains of the protein. In a series of experiments, Pal et al. (2002) have examined solvation dynamics of newly excited tryptophan in several proteins by using time dependent fluorescent Stokes shift. They have found a slow component in the solvation TCF that was in the range of 20–40 ps, more than an order of magnitude slower than the bulk response. Usually in these experiments the tryptophan is exposed to the surface water, thus the slow component is expected to reflect the hydration layer dynamics. Recently Sen et al. (2003) have studied the solvation dynamics in the molten globule state of a protein, glutaminyl-tRNA synthetase (GlnRs) using both a non-covalent probe (bis-ANS) and a covalent probe 4-(*N*-thioacetyl-amino)-phthalimide. They found that, in the native state of the protein, where the non-covalent probe resides deep inside the core, the average solvation time is 1400 ps, whereas for the covalent probe, which is close to the protein surface, it is 120 ps, 12 times faster than the non-covalent probe (Sen et al., 2003). The average solvation time of the probe in the molten globule state is much slower than the longest component of solvation dynamics of the probe in bulk water (~ 1 ps).

The above experimental studies motivated us to carry out atomistic computer simulation studies of hydration layer dynamics of globular protein HP-36 (details of the system are given in Appendix A). In Figure 2.2(a), we show solvation TCF $C_S(t)$ for the polar amino acid residues of the three α -helices of the HP-36 protein. We have calculated $C_S(t)$ by measuring the polar part of the interaction energy between the polar amino acid residues of each of the three helices of the protein and the rest of the system. The decay of solvation TCFs clearly shows the presence of a significantly slow component for all three helices, which is in good agreement with femtosecond (fs) time-resolved fluorescence studies

**FIGURE 2.2**

(a) The solvation time correlation function $C_S(t)$ for the polar amino acid residues of the three α -helices of the HP-36 protein. (b) Decay of the solvation time correlation function, $C_S(t)$, for the surface cesium ions (CsPFO micellar solution) at 300 K. For comparison, the solvation time correlation function of a cesium ion in bulk water at 300 K is shown in the inset. (c) Solvation time correlation function, $C_S(t)$, for bromine ions in the DTAB micellar solution at 300 K. Inset shows the same for a bromine ion in pure water.

(Pal et al., 2002). To understand the different solvation timescales, we have fitted the decay curves to multiexponentials. Four different solvation timescales are identified, from ultrafast to slow components. An ultrafast component with a time constant of 40–50 fs, followed by a fast component at 0.7–1.2 ps was observed. Two slower components with time constants in the range of 6–17 and 42–88 ps were also noticed. Such different solvation timescales arise from the presence of different types of water molecules within the hydration layer (Bandyopadhyay et al., 2005). The initial ultrafast relaxation arises from the high frequency librational (hindered rotation) and intermolecular vibrational (hindered translation) motions of the “free” or bulk-like water molecules. The moderately damped rotational motions of these water molecules contribute to the fast relaxation (~ 1 ps). The slowest component observed (42–88 ps) arises from those water molecules which

are “quasi-bound” to the amino acid residues of the protein molecule by strong hydrogen bonds.

Interestingly, we notice that the $C_S(t)$ curve decays much faster for helix-2, compared with the other two helices. There could be several factors responsible for this, such as the relative hydrophilicity of the polar amino acid residues present in the three helices and their relative exposure to the solvent, the life-time of the hydrogen bonds between the “bound” water molecules and the protein residues, the side chain motion of the residues, etc. Further investigation is necessary to obtain a microscopic level understanding of such solvation behavior.

The slow component in the solvation TCF should have contributions both from the protein surface and from the hydration water. The DEM has been successful in quantifying the contribution of the hydration water to this slow dynamics. According to this model, dynamical equilibrium between the bound and free water introduces a slow timescale in the collective reorientational of the hydration water, which in turns slows down the solvation dynamics (Nandi and Bagchi, 1997; Pal et al., 2002; Bhattacharyya et al., 2003).

Solvation Dynamics in Aqueous Micellar Solutions

Micelles have some characteristics that are similar to protein surfaces in certain respects, whilst being different in many other ways. Micelles have a dense hydrophobic core while the polar head groups are on the surface. The surface is homogeneous on a length scale of somewhat larger than the diameter of water molecules. It is expected that water molecules on the surface are constrained by hydrogen bonding with the polar head groups. However, the extent of this effect is not clear. An additional complexity in this case is that there are three possible locations of the probe, namely the bulk water, the micellar core, and the Stern layer. Solvation dynamics in micelles have been studied using Coumarin 480 (C480) and 4-aminophthalimide (4-AP) as probes. Emission properties of these probes in the micelles are very different from those in bulk water, indicating that the probes reside neither in the bulk nor in the core of the micelle and, hence, are located in the stern layer. Sarkar et al. (1996) and Datta et al. (1998) studied solvation dynamics of C480 and 4-AP, respectively, in neutral (TX-100), cationic (CTAB), and anionic (SDS) micelles. It is observed that for SDS, CTAB, and TX-100, the average solvation times are, respectively, 180, 470, and 1450 ps for C480 (Sarkar et al., 1996) and 80, 270, and 720 ps (Datta et al., 1998) for 4-AP. Thus, the solvation dynamics in the Stern layer of micelles is two orders of magnitude slower than that in the bulk water. Because of limited time resolution, these experiments have missed all the fast time scales (with time constants less than 40 ps).

These experiments have motivated us to carry out fully atomistic simulation of micelle water systems (details are provided in Appendix A). In Figure 2.2(b) and (c), we show the solvation dynamics of cesium ions near

the micellar surface of CsPFO and the bromine ions in DTAB micellar solution at 300 K. The insets show for both cases the same function for counter ions in neat water at 300 K. The decay of the solvation TCF is highly nonexponential and one needs a sum of at least three exponentials to fit the solvation TCF. The average solvation time is slower by about a factor of 20 than the corresponding value in the bulk for both cases. However, the long time decay is slower by more than two orders of magnitude in agreement with the experimental results (Sarkar et al., 1996; Datta et al., 1998; Bhattacharyya, 2003). The analysis of the partial solvation TCF (not shown here) for the CsPFO and DTAB micellar systems show that the contribution from the polar interaction of the cesium and bromine ions with the micelle head groups is the most dominant. This partial TCF also exhibits a very slow component, which is the leading cause for the slow decay of the total solvation TCF.

Dielectric Relaxation

Dielectric relaxation (DR) experiments measure the collective polarization response of all the polar molecules present in a given system. The DR time provides a measure of the time taken by a system to reach the final (equilibrium) polarization after an external field is suddenly switched on (or off). DR measures the complex dielectric function, $\varepsilon(\omega)$, that can be decomposed into real and imaginary parts as $\varepsilon(\omega) = \varepsilon'(\omega) - i\varepsilon''(\omega)$ where $\varepsilon'(\omega)$ and $\varepsilon''(\omega)$ are the real (permittivity factor) and imaginary (dielectric loss) parts, respectively. The total dipole moment of the system, at any given time t , $M(t) = \sum_{i=1}^N \mu_i(t)$ where N is the total number of dipolar molecules and μ_i is the dipole moment vector of the i th molecule. The complex dielectric function $\varepsilon(\omega)$ is given by the following relation,

$$\frac{\varepsilon(\omega) - \varepsilon(\infty)}{\varepsilon(0) - \varepsilon(\infty)} = \int_0^\infty dt e^{-i\omega t} \left[-\frac{d\Phi_M(t)}{dt} \right] = 1 - i\omega \int_0^\infty dt e^{-i\omega t} \Phi_M(t) \quad (2.7)$$

where $\varepsilon(0)$ and $\varepsilon(\infty)$ are the limiting low- and high-frequency permittivities, respectively. $\Phi_M(t)$ is the normalized time auto correlation function of the system's total dipole, \mathbf{M} , and is defined as, $\Phi_M(t) = \langle \mathbf{M}(t) \cdot \mathbf{M}(0) \rangle / \langle \mathbf{M}(0) \cdot \mathbf{M}(0) \rangle$. The total moment of the system can be split into contributions from the water, the micelle, and the ions. Thus, $\Phi_M(t)$ will contain terms that are self-correlation functions, such as water–water, and cross-correlations, such as water–micelle/protein.

Dielectric Relaxation of Aqueous Protein Solutions

Aqueous solutions of proteins exhibit a number of interesting properties. In contrast to solutions of many other polar compounds, their static dielectric constants are noticeably higher than that of water. Several relaxation

processes are noticed in the DR of aqueous protein solutions; they are (a) a very slow motion corresponding to the overall tumbling of the protein, called the β -relaxation, (b) the fast relaxation of unperturbed water, called γ -relaxation, and (c) an intermediate timescale, called δ -relaxation. The δ -relaxation originates from the interaction between the protein and the solvent, as well as from water molecules bound to the protein. Boresch et al. (2000) recently studied the static and frequency-dependent dielectric properties of an aqueous solution of ubiquitin through a 5-ns-long MD simulation. They decomposed the total dielectric function into self and cross terms. Their analysis shows that the most significant contribution to the dielectric function arises from the two self-terms, approximately 65% from water and 21% from the protein. These two components determine the bimodal shape of the dielectric loss. Here we present DR of micellar solution.

Dielectric Relaxation of Aqueous Micellar Solutions

We focus here on the contribution from water alone to the DR of the micellar system, i.e., we calculate, $\Phi_M^W(t) = \langle \mathbf{M}_W(t) \cdot \mathbf{M}_W(0) \rangle / \langle \mathbf{M}_W(0) \cdot \mathbf{M}_W(0) \rangle$ where $\mathbf{M}_W(t)$ is the total moment of all water molecules in the system. Figure 2.3 shows the total moment–moment TCF, $\Phi_M^W(t)$, of water (only), both in the presence (solid line) and absence of the CsPFO micelle in the simulation box, i.e., in bulk or neat water. The TCF, $\Phi_M^W(t)$, was fitted to a form containing a sum of three exponential terms ($\Phi_M^W(t) = C_1 e^{-t/\tau_1} + C_2 e^{-t/\tau_2} + C_3 e^{-t/\tau_3}$) to get the time constants and amplitudes that can be used to calculate the frequency dependent dielectric constant. The fitting parameters and the amplitudes can be found elsewhere (Pal et al., 2004). The simulations

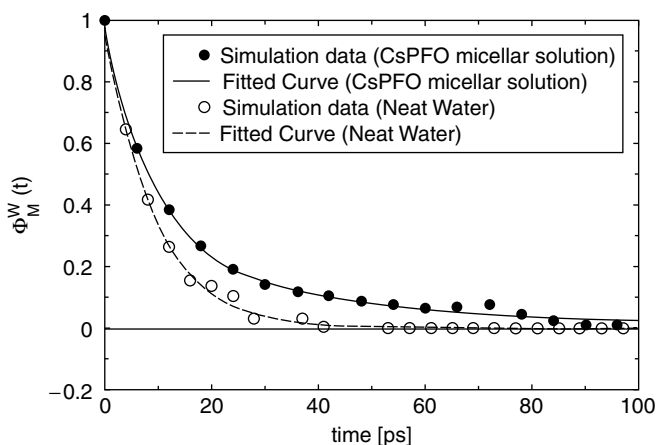


FIGURE 2.3

Time dependence of the normalized total moment–moment time correlation function [$\Phi_M^W(t)$] for the water molecules, both in the CsPFO micellar solution (solid line) and in neat water. Circles are the simulation data and the continuous line is a multiexponential fit.

show the presence of a slow component in $\Phi_M^W(t)$, with a time constant of 41 ps, in contrast to a value of only 9 ps for bulk water. The presence of the 41 ps component in the DR of the micellar water can be traced back to the dynamic exchange of water molecules between its bound and free states at the interface (Pal et al., 2004).

Using the fitted parameters we calculated the frequency dependent dielectric function of the water molecules in the CsPFO micellar solution. In Figure 2.4(a) we show the frequency dependence of the real part, ϵ' of the dielectric function. In Figure 2.4(b), we show the same for the imaginary part. When compared with the water, a clear shift of population to the slow frequency range is observed. The Cole–Cole plot shown in Figure 2.4(c) shows a considerable degree of nonexponentiality in the dielectric spectrum.

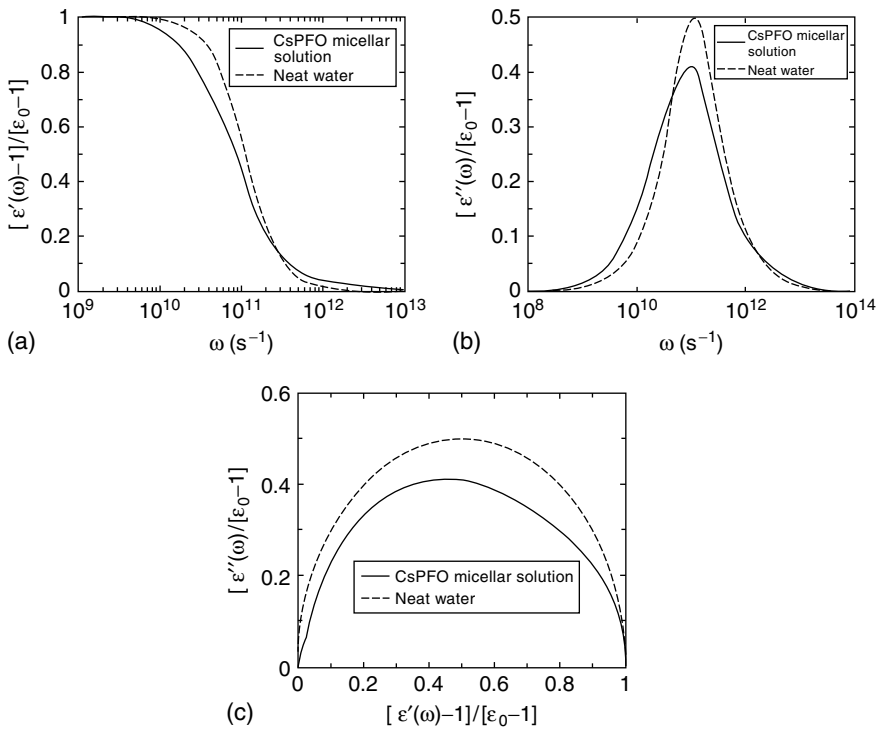


FIGURE 2.4

(a) Real part of the frequency dependent dielectric function, $\{[\epsilon'(\omega) - 1]/[\epsilon_0 - 1]\}$, for the water molecules in the CsPFO micellar solution (solid line) and in neat water (dashed line). (b) Frequency dependence of the imaginary part of the dielectric function, $\{[\epsilon''(\omega)]/[\epsilon_0 - 1]\}$, for the water molecules, both in the CsPFO micellar solution (solid line) and in neat water (dashed line). (c) Cole–Cole plot of the frequency dependent dielectric function, where the imaginary part, $\{[\epsilon''(\omega)]/[\epsilon_0 - 1]\}$, is plotted against the real part, $\{[\epsilon'(\omega) - 1]/[\epsilon_0 - 1]\}$, for the water molecules, both in CsPFO micellar solution (solid line) and in neat water (dashed line).

The well-known continuum models and also the microscopic theories of solvation dynamics suggest a close relation between solvation dynamics and DR. This is expressed as $\tau_L = (\epsilon_\infty/\epsilon_0)\tau_D$ where τ_L is the longitudinal relaxation time and τ_D is the Debye relaxation time. However, the solvation dynamics of an ion at the protein surface is difficult to understand because of the heterogeneous environment of the protein surface. Therefore, a straightforward application of the continuum model with a multi-exponential description of DR is not possible. The continuum theory suggests that at short length scales, the relaxation time is essentially given by the DR time. Therefore, we certainly expect a slow component in the solvation dynamics.

Single Water Molecule Reorientational Dynamics

An important determinant of the dynamics of water molecule is the reorientation of its dipole vector that can be probed with NMR measurements. This reorientational motion is severely affected near a macromolecular interface. In this heterogeneous system, total dielectric response will have contribution from the macromolecule, the solvent, and from the cross correlations. Here we focus our attention on the contribution from the water molecules in specific regions around the micelle/proteins. Within the framework of linear response theory, the reorientational motion of water at an interface can also be studied by DR experiments. The rotational motion of water can be investigated by measuring the reorientational dynamics of its electrical dipole μ , defined as the vector connecting the oxygen atom of the water molecule to the center of the line connecting the two hydrogen atoms.

The time evolution of μ can be estimated by measuring the dipole–dipole TCF, defined as:

$$C_\mu(t) = \frac{\langle \mu_i(t) \mu_i(0) \rangle}{\langle \mu_i(0) \mu_i(0) \rangle} \quad (2.8)$$

where $\mu_i(t)$ is the dipole moment vector of the i th water molecule at time t , and the angular brackets denote time averaging over the trajectory of the water molecules, as well as over the initial configurations, $\mu_i(0)$.

Here we report the studied reorientational water dynamics through atomistic molecular dynamics simulations at the surface of two proteins (HP-36 and 1ETN) and two micelles (CsPFO and DTAB).

Water Reorientation in Aqueous Protein Solutions

We have studied the reorientational motion of water molecules that are in the proximity of the three α -helices of HP-36 protein. To be specific, we have performed the calculations for those water molecules that reside within 5 Å from any atom of the helices. The correlation functions were calculated by

averaging over these water molecules only. In Figure 2.5(a) we show the variation of $C_\mu(t)$ against time for the water molecules near the three helices of HP-36 protein. For comparison, we have also shown the relaxation for bulk water. It is evident that the water molecules around helix-3 reorient noticeably faster than those around helix-1 or helix-2. The exhibition of faster dipolar reorientational motion of water near helix-3 correlates nicely with the presence of active sites taking part in the actin binding process. The extraordinary slow decay for the helix-2 (manifested in a nearly flat decay curve) is found to be caused by the presence of a small fraction of “bound” water molecules near the surface of the helix. However, much more work is necessary to understand the correlation between the biological activity of a protein and the faster dynamics of water around the active sites.

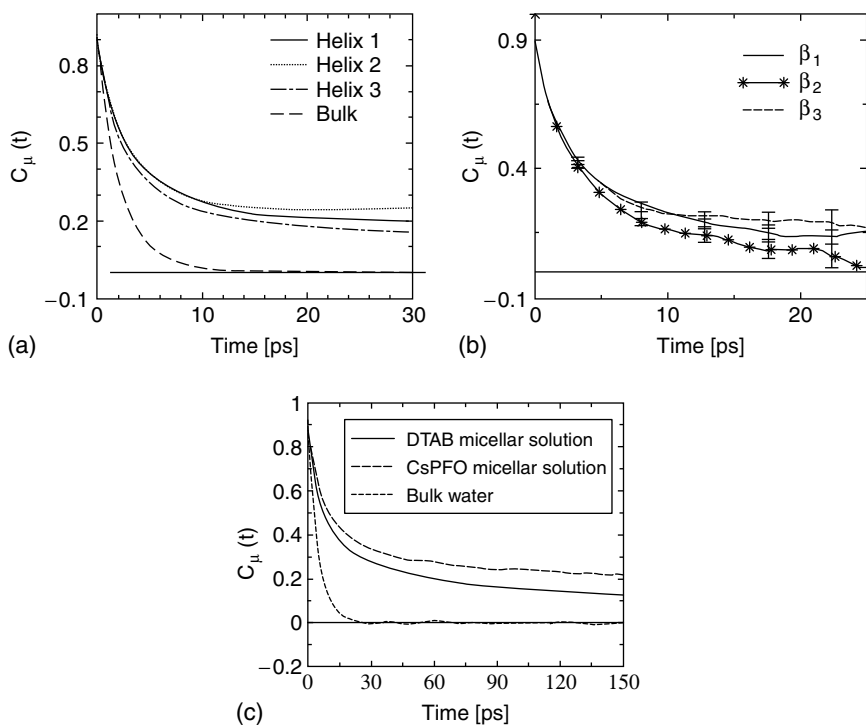


FIGURE 2.5

(a) Dipolar time correlation function of the water molecules, $C_\mu(t)$, for the water molecules in proximity to three α -helices of the HP-36 protein. The TCF for the bulk water is shown for comparison. (b) Reorientational time correlation function of the water dipole, $C_\parallel(t)$, for water molecules in the three segments of 1ETN protein. The vertical bars are error on the mean value of the TCF at specified times, and are displayed infrequently for clarity. (c) Dipole–dipole time correlation function $[C_\mu(t)]$ for the interfacial water molecules both in the CsPFO micellar solution (long dashed line) and DTAB micellar solution (continuous line). TCF for the bulk water is shown for comparison (short dashed line).

We notice that even though the water molecules around helix-3 reorient faster compared with those around the other two helices, all the curves show slower decay at long times. Such long-time decay cannot be described by a single exponential law. We have used a sum of three exponentials to obtain the timescales associated with the three TCFs. The parameters for best fit are shown in Table 2.1. Water molecules around helix-2 exhibit significantly slower dynamics with a long time component (> 500 ps), which we could not determine because of the limitation of the timescale of our simulation. As discussed above, the existence of such a long time component arises because of particular water molecules which are “bound” to specific residues in helix-2. However, we need to investigate this aspect further. One can note that the average reorientational motion of water molecules around helix-3 is almost twice as fast compared with that for the water around helix-1. This is because of the presence of a long time component of about 126 ps for water around helix-1, which is more than twice as long as the corresponding long time component for helix-3. It can also be noted that the reorientation of water molecules in bulk ($= 2$ ps) is much faster than the water molecules near any of the three helices. From our results it is clear that even though the rotational motion of water at the interface of a protein is much slower compared with bulk water, distinct differences might arise in different regions of the interface, containing almost identical secondary structures, such as the three α -helices in HP-36 (Bandyopadhyay et al., 2004).

Bandyopadhyay et al. (2005) observed that the residues in the second β turn are proximal to the receptor in the binding of 1ETN protein. This ties in

TABLE 2.1
Multiexponential Fitting Parameters for the Dipolar Time Correlation Functions of Water Molecules around the Three α -Helices of the Protein. Corresponding Parameters for Bulk Water is also Listed for Comparison

Segment	Time Constant (ps)	Amplitude (%)	$\langle \tau \rangle$ (ps)
Helix-1	0.4	25.0	33.1
	4.1	50.5	
	126.4	24.5	
Helix-2	0.5	22.0	> 125
	3.7	53.7	
	> 500	24.3	
Helix-3	0.31	20.4	17.1
	3.03	54.4	
	61.0	25.2	
Bulk water	0.4	21.3	2.1
	2.5	78.7	

Note: $\langle \tau \rangle$ = the average time constant.

with the observation that the toxicity of the protein is unaffected by changing specific residues in the first and the third β turns. In Figure 2.5(b), we present the reorientation TCF of the water dipole for water molecules near (within 5 Å from any atoms of the segments) the three segments of the 1ETN protein. Water molecules near the second β turn exhibit a considerably faster ability to reorient than those molecules near the other segments of the protein. The faster water dynamics around this segment can be correlated with the biological activity of the protein since it is the active site of this protein. To obtain a microscopic understanding of such differential dynamics and its likely influence on the binding activity of the protein, it is necessary to study the properties of the hydrogen bonds formed between the interfacial water molecules and the protein.

Water Reorientation in Aqueous Micellar Solution

In Figure 2.4(c), we show the single particle dipolar orientational relaxation [$C_\mu(t)$] of interfacial water molecule in the micellar solution (CsPFO and DTAB), comparing it with its relaxation in bulk. Interfacial water molecules are those that are within the first coordination shell of head group carbon (for CsPFO micelle) or head group nitrogen (for DTAB micelle). Note the pronounced slower decay of the interfacial water molecules. The interfacial water molecules in the CsPFO micellar solution have slower orientational relaxation than those in DTAB micellar solution. This is caused by the hydrogen bonding of the water molecules with the PHG of the CsPFO micelle, which is not possible for the DTAB micelle. This slow decay can be correlated with the slow decay observed in the total moment–moment TCF by using the well-known micro–macro relation of statistical mechanics (Nandi et al., 2000).

The decay of the orientational correlation function is highly non-exponential and one needs at least four exponentials to fit it. The average orientational correlation time, τ_μ , is slower by about a factor of 20 than that of its bulk value. The orientational correlation function for the interfacial water molecules will, of course, decay in the very long time (of the order of tens of nanoseconds), either because of “evaporation” of the interfacial water molecules or rotation of the micelle.

Hydrogen Bond Lifetime Dynamics

The study of hydrogen bond (HB) dynamics has proven to be a very useful tool for understanding the origin of many fascinating dynamical properties of water that arise because of its ability to form extended networks of hydrogen bonds. However, such properties exhibit drastic changes for water molecules at the surfaces of self-organized assemblies and biological macromolecules. The structural organization and dynamics of the interfacial

water molecules are coupled with the protein residues by a network of hydrogen bonds formed between them (Bizzarri and Cannistraro, 2002). The formation and breaking of these hydrogen bonds play an important role in determining the functionality of the protein. One can use either a geometric or an energetic criterion to define a hydrogen bond. Here we have employed a purely geometric criterion to define protein–water as well as micelle–water hydrogen bonds.

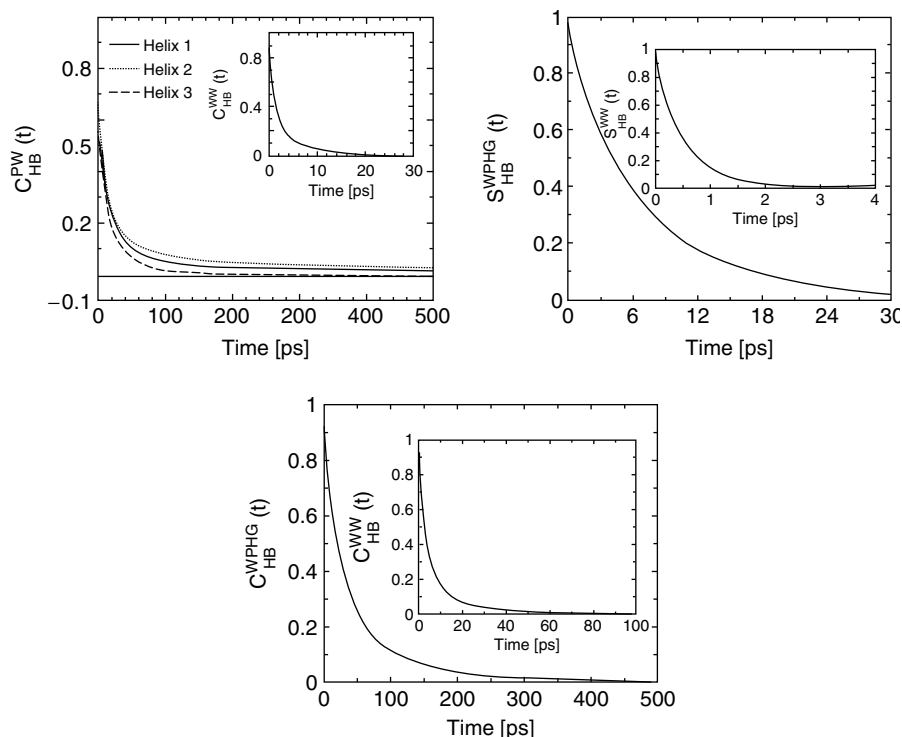
The structural relaxation of hydrogen bonds can be characterized by the TCFs,

$$S_{\text{HB}}(t) = \frac{\langle h(\tau)H(t + \tau) \rangle}{\langle h \rangle} \quad \text{and} \quad C_{\text{HB}}(t) = \frac{\langle h(\tau)h(t + \tau) \rangle}{\langle h \rangle} \quad (2.9)$$

where the hydrogen bond population variables $h(t)$ is unity when a particular site is hydrogen bonded at time t , and zero otherwise. On the other hand, $H(t) = 1$ if the site remains continuously hydrogen bonded during the time duration t , and zero otherwise. The angular brackets denote averaging over all the hydrogen bonds and different initial times τ . Thus $S_{\text{HB}}(t)$ describes the lifetime of a tagged pair. The correlation function $C_{\text{HB}}(t)$ describes the probability that a particular hydrogen bond is intact at time $t + \tau$, given that it was intact at time τ . Thus, $C_{\text{HB}}(t)$ allows the reformation of a bond that is broken at some intermediate time. In other words, it allows recrossing of the barrier separating the bonded and non-bonded states. Therefore, the relaxation of $S_{\text{HB}}(t)$ provides information about the structural relaxation of a particular hydrogen bond. In the next two sections, we present the lifetime dynamics of protein–water and micelle–water hydrogen bonds obtained from fully atomistic molecular dynamics simulations.

Protein–Water Hydrogen Bond

In Figure 2.6(a), we display the TCF $C_{\text{HB}}^{\text{PW}}(t)$ for the hydrogen bonds formed between the amino acid residues of the three helices of HP-36 protein and the water molecules. The inset of the figure shows the corresponding function $C_{\text{HB}}^{\text{WW}}(t)$ for bulk water. It is apparent from the figure that the structural relaxation of the protein–water hydrogen bonds is much slower than that of the water–water hydrogen bonds. However, the most interesting observation from this figure is the differences in the relaxation behavior of $C_{\text{HB}}^{\text{WW}}(t)$ for the three helices. The structural relaxation of the hydrogen bonds formed between the residues in helix-3 and the interfacial water molecules is faster than that for the other two helices. We have fitted the $C_{\text{HB}}^{\text{PW}}(t)$ curves with a sum of multi-exponentials to obtain the average relaxation time (τ) of the network of protein–water hydrogen bonds for the three helices. The calculated values are 28.7, 45.5, and 14.1 ps for the helices 1, 2, and 3, respectively. The corresponding value for the bulk water molecules has been found to be 2.6 ps. One can note that the average relaxation of the hydrogen bonds between the amino acid residues of helix-3 and water molecules is about 2–3 times faster than those for the helices 1 and 2. It can also be noted

**FIGURE 2.6**

(a) The time correlation function ($C_{HB}^{PW}(t)$) for the hydrogen bonds formed between the amino acid residues of the three α -helices of the protein and the interfacial water molecules. The inset shows the same for the hydrogen bonds formed between water molecules present in the bulk. (b) $S_{HB}^{WPHG}(t)$ function for the hydrogen bond between the polar head group of the CsPFO micelle and water molecules. Inset shows the same between pairs of water molecules in bulk water. (c) $C_{HB}^{WPHG}(t)$ function for the hydrogen bond between the polar head group of the CsPFO micelle and water molecules. Inset shows the same between pairs of water molecules in the bulk.

that the structural relaxation of the network of water–water hydrogen bonds in bulk water is much faster compared with the protein–water hydrogen bonds.

Thus, we have clearly shown that the hydrogen bond dynamics can vary significantly near different secondary structures of a protein. In this case it is found that the hydrogen bonds between the residues in helix-3 of HP-36 and water relax much faster than those involving similar secondary structures, namely helices 1 and 2. This is an important result and agrees nicely with the faster orientation relaxation of water molecules around helix-3, as discussed before. It also correlates pretty well with the biological functionality of the protein. This is because most of the active site residues in HP-36 are located in helix-3, and it is expected that for successful binding activities, the water molecules around the active sites should exhibit faster dynamics.

Micelle–Water Hydrogen Bond

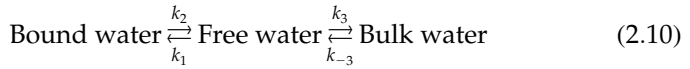
In Figure 2.6(b) we show the time dependence of the water–surfactant hydrogen bond TCF $S_{\text{HB}}^{\text{WPHG}}(t)$ of the CsPFO micellar solution. The inset shows the same between pairs of water molecules in pure water ($S_{\text{HB}}^{\text{WW}}(t)$). Note the lengthening of the timescale in the hydrogen bonding with the PHG of the micelle. The $S_{\text{HB}}^{\text{WPHG}}(t)$ function can be fitted to a sum of three exponentials with the longest time component being equal to 9 ps, which is to be compared with 0.97 ps of bulk water. The parameters of the multi-exponential fit to the $S_{\text{HB}}^{\text{WPHG}}(t)$ function can be found elsewhere (Balasubramanian et al., 2002). Figure 2.5(c) shows the hydrogen bond time correlation $C_{\text{HB}}^{\text{WPHG}}(t)$ in the CsPFO micellar solution. The inset shows the same ($C_{\text{HB}}^{\text{WW}}(t)$) between pairs of water molecules in pure water. Note again the lengthening of the long time component. In this case, the long time constant is more than 100 ps. The reason for the unusually long decay time can be traced back to those trajectories that leave the micellar surface to go to the bulk but return after a long time to get bounded to the same PHG at the surface. Thus, the $S(t)$ function is a more accurate representation of the lifetime dynamics of the hydrogen bond than the $C(t)$ function. We found that the lifetime of the hydrogen bond between the PHG and water molecules is almost 13 times larger than that in the bulk between two tagged water molecules.

Protein–Glass Transition

Many experiments have demonstrated the existence of a dynamical transition in hydrated proteins at ~ 180 – 220 K and this transition is characterized by the deviation of the temperature dependence of the mean square displacement $\langle u^2 \rangle$ from linearity (Knapp et al., 1982). As in glass-forming liquids, proteins exhibit diffusive motions above the transition temperature and are trapped in harmonic potential well below. This transition is often associated with the loss of biological functionality of the protein (Tarek and Tobias, 2002). There can be two factors contributing to this transition and also the loss of functionality. First, it is the proteins internal kinetic energy that reduces because of lowering of the temperature and then the hydration layer also becomes more rigid at lower temperatures. As mentioned earlier, the onset of biological activity of a protein is already connected to the formation of a spanning hydrogen bonded water network on the protein surface (Rupley and Careri, 1991). Empirical energy function calculations have shown that rigid protein poses a high energy barrier for ligand binding (Case and Karplus, 1979), thus ligand binding must involve structural fluctuations that eventually lowers the energy barrier. Experiments (Doster and Settles, 1998) and simulations (Gu and Schoenborn, 1995) have shown that structural fluctuation of a protein or the side chain motions

is closely associated with the breaking and making of hydrogen bonds with the water molecules. Thus all these studies indicate that it is water that plays an important role in the protein–glass transition. But since the protein–water system is strongly coupled, it was not possible to make such a definite statement from the experimental results. However, recent computer simulation studies of the protein–water system using a dual heat bath mode has been able to decouple the effect of the protein and the water and have shown that it is the translational hydration water dynamics that drives the protein–glass transition (Tournier et al., 2003). Thus, to understand the protein–glass transition it is important to study the hydration layer dynamics and the changes it undergoes with lowering of the temperature.

In order to understand the effect of temperature on the water dynamics and how it leads to the glass transition of the protein, we have performed a study of a model protein–water system. The model is quite similar to the DEM, which deals with the collective dynamics within and outside the hydration layer. However, since we want to calculate the mean square displacement and diffusion coefficients, we are primarily interested in the single particle properties. The single particle dynamics is essentially the motion of a particle in an effective potential described by its neighbors and thus coupled to the collective dynamics. A schematic representation of the dynamics of a water molecule within the hydration layer can be given by:



Although the bound to free transition is a uni-molecular process, the free to bound transition is a bi-molecular process and depends on the availability of the binding site. Thus k_2 is calculated using the famous transition state theory but k_1 is given by $k_1 = (\rho_{bs} - \rho_b) \frac{k_B T}{h} e^{-\Delta E_1/k_B T}$, where ρ_{bs} and ρ_b are the densities of the total and occupied bound sites, respectively. Thus $(\rho_{bs} - \rho_b)$ is the density of the available bound sites. ΔE_1 is the water–water interaction energy. k_3 and k_{-3} are the free to bulk and bulk to free transition rates, respectively. Because these conversions happen only through diffusion, thus $k_3 = k_{-3} = Dq^2$, where q is the wavenumber.

The dynamics of the bound water when bound to the protein surface is represented by the motion of a particle in a harmonic well and can be given by a Smoluchowski equation. The frequency of the harmonic well is calculated from the following expression, $\omega_R = (8E_2/m\sigma^2)^{1/2} = 11.8 \times 10^{12} \text{ sec}^{-1}$ where E_2 is the protein–water interaction energy, which is generally site specific but we consider an average value of $4140 \times 10^{-16} \text{ erg}$. m and σ are the mass and diameter of the water molecule, respectively. The calculated frequency is quite close to the peak value of the density of state of hydration water of a dendrimer (Lin et al., 2005). The mean square displacement in the bound state is given by $\langle \Delta r^2(t) \rangle_b = \int_0^\infty dr r^2 P(r, t)$, where $P(r, t)$ is the time and position dependent probability calculated from the Smoluchowski equation.

The dynamics of the free water in the hydration layer is coupled to the slow structural relaxation of the hydration layer and can be calculated using standard, well-known mode coupling theory (MCT) prescription (Bagchi and Bhattacharyya, 2001) where the structural relaxation is now obtained from the DEM (Bhattacharyya et al., in preparation). Similarly the dynamics of a water molecule in bulk water can also be calculated using the same MCT technique. The mean square displacement of the free ($i = f$) and bulk ($i = w$) water can be written as $\langle \Delta r^2(t) \rangle_i = 2 \int_0^t ds C_{vi}(s)(t - s)$. Here, $C_{vi}(z) = k_B T / m(z + \zeta_i(z))$, where $\zeta_i(z)$ is the friction calculated from MCT. To calculate the friction we need the water–water interaction potential, which is modeled by a Lennard–Jones 6–12 potential where the well depth is calculated from water–water hydrogen bond energy, and the diameter, from the first peak in the radial distribution function, $\epsilon = 1656 \times 10^{-16}$ erg and $\sigma = 2.49$ Å. The time dependent diffusion of the water molecule when bound ($i = b$), free ($i = f$) and in the bulk ($i = w$) are given by, $D_i(t) = (1/6)(\partial \langle \Delta r^2(t) \rangle_i / \partial t)$. The bulk diffusion coefficient calculated using this potential at $T = 300$ K is $D_{\text{theory}} = 2.7 \times 10^{-5} \text{ cm}^2 \text{ sec}^{-1}$, whereas the experimental value is $D_{\text{expt}} = 2.5 \times 10^{-5} \text{ cm}^2 \text{ sec}^{-1}$ (Pal et al., 2002). Similar approximations for the water potential have been used earlier by other groups, which are known to give good results (Molinero and Goddard, 2004).

Now that we know the individual dynamics of bound, free and bulk water, our aim is to find the dynamics of a water molecule that was initially bound and later is still bound, free, or escaped to the bulk. Towards this goal we use a linear superposition approximation to express the mean square displacement of such a water molecule as:

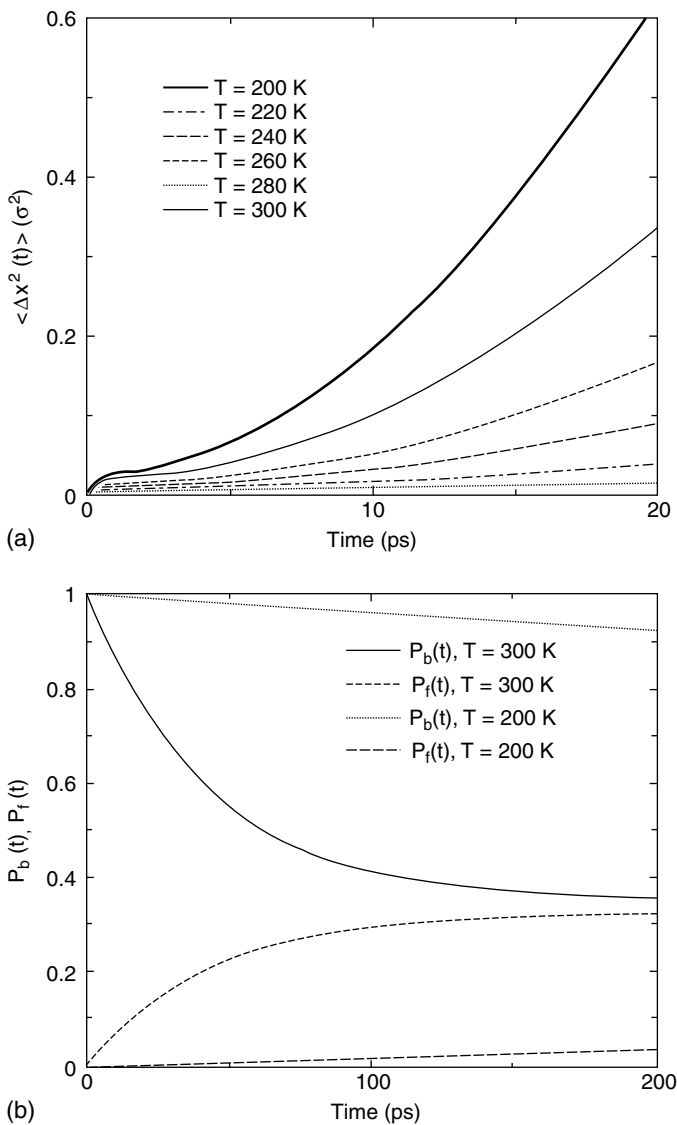
$$\Delta x^2(t) = \int_0^t D_b(s)P_b(s)ds + \int_0^t D_f(s)P_f(s)ds + \int_0^t D_w(s)P_w(s)ds \quad (2.11)$$

Where $P_b(t)$, $P_f(t)$ and $P_w(t)$ are the probabilities that the water molecule which was initially bound will remain bound, will be free or will go to bulk at time t , respectively. The three probabilities are calculated by using statistical mechanics.

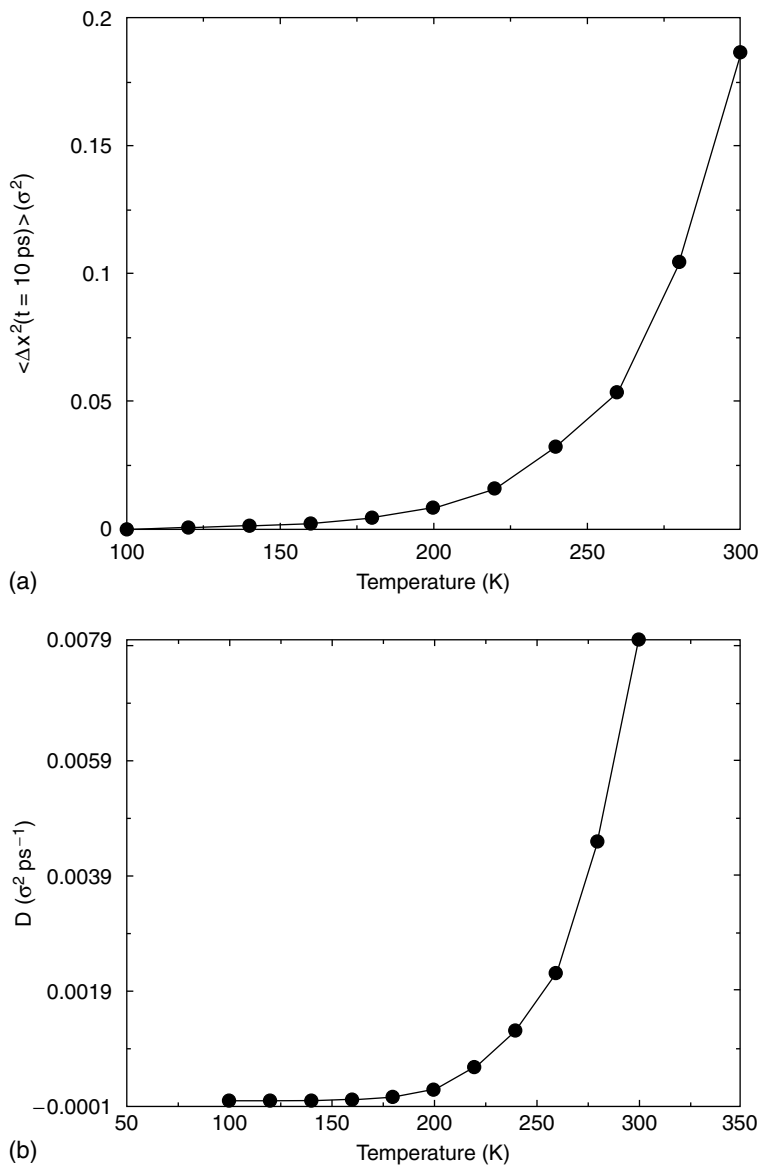
The calculated MSDs at different temperatures are plotted in Figure 2.7(a). These figures show that although at high temperature the motion is diffusive, at low temperature (due to a drastic decrease in the probability of the bound to free transition [shown in Figure 2.7(b)]), the motion becomes largely non-diffusive.

In Figure 2.8(a) we have plotted the MSD of a water molecule (bound at time $t = 0$) after $t = 10$ ps over the whole temperature range. It shows a non-monotonic temperature dependence. Because the protein motion is coupled to the water dynamics it is expected that the MSD of the protein will also show similar behavior, which would lead to a protein–glass transition and eventually to the loss of protein functionality.

The diffusion coefficient of water when plotted against temperature shows similar behavior (shown in Figure 2.8(b)). In the log plot (not shown here) we find a small break at $T = 160$ K with two regimes of linear behavior, which

**FIGURE 2.7**

(a) The temperature dependence of the time evolution of the mean square displacement (MSD) of a water molecule that was initially bound to the protein surface (calculated from Equation 2.11). The MSD is diffusive at high temperature but at low temperatures become non-diffusive. (b) The time evolution of the probabilities of a bound water to remain bound, $P_b(t)$, and to become free, $P_f(t)$, are plotted at two different temperatures. At low temperature, the bound water has a low probability of becoming a free water and thus remains bound to the protein surface for a longer time.

**FIGURE 2.8**

(a) The mean square displacements after 10 ps (solid circles), obtained from Equation 2.11 or Figure 2.7(a) are plotted against temperature. The MSD at $t = 10$ ps, shows a nonmonotonic temperature dependence. (b) The diffusion coefficients (D) (solid circles) of an initially bound water, calculated from the MSDs', and plotted against temperature. The solid line is a guide to the eye. The diffusion coefficients also show a nonmonotonic temperature dependence.

implies that diffusion behaves as an activated process, $D = \exp(-a/T)$ with a change in activation energy at 160 K. Although, similar transition has been obtained in the simulation studies, the transition is stronger and takes place at a higher temperature. The possible reasons behind such discrepancies are the following. In the DEM, the protein surface is considered to be static, thus the change in the protein dynamics with the temperature is not taken into account. Simulation studies have shown that if the protein is kept fixed at a constant temperature, then a weaker transition happens at a lower temperature (Boresch et al., 2000). The second reason for a weaker transition predicted by the model is that the water is known to undergo a liquid–liquid transition from fragile to strong liquid at around 220 K (Angell, 2002), which would effectively mean a change in the water–water interaction energy and thus the water dynamics. This, when taken into consideration, might lead to a stronger dynamical transition. Finally, we show that the model qualitatively predicts the hydration water dynamics and its change with temperature and how this can lead to a protein–glass transition.

Concluding Remarks

We have investigated the microscopic nature of water molecules in the hydration shell. The experimental, theoretical, and computer simulation studies clearly demonstrate that the dynamics of hydration water molecules are significantly different from those of bulk water.

According to the DEM, the dynamics in the hydration layer has multiple timescales. The fast one is bulk-like and the slow ones are at least an order of magnitude slower and depend on the transition rates between bound and free water molecules.

The solvation dynamics study shows the presence of a slow component in the ion solvation TCF, with a relaxation time 2–3 orders of magnitude slower than that in the corresponding bulk solvent, in agreement with the experimental results. The presence of a 40 ps component in the DR of the micellar water can be traced back to dynamic exchange of water molecules between its bound and free states at the interface. We find the rather surprising result that the hydrogen bond between the polar head group of the micelle and the water molecule has a longer lifetime — almost 13 times — than that in the bulk between two tagged water molecules.

In order to understand the role of water in the glass transition of the protein and its subsequent loss of functionality, we have performed a temperature dependent study of the hydration layer dynamics. The study shows that at low temperatures the bound to free conversion rates reduce drastically and this leads to a non-diffusive motion of the bound water. The mean square displacement obtained after 10 ps and the diffusion coefficient

shows nonmonotonic temperature dependence. The diffusion is found to be an activated process with a change in the activation energy at $T = 160$ K.

Acknowledgments

We thank Mr. Arnab Mukherjee for valuable discussions. The work presented here is supported by grants from Department of Science and Technology (DST), Department of Biotechnology (DBT), and Council of Scientific and Industrial Research (CSIR), Government of India.

Appendix A

System and Simulation Details of CsPFO Micelle

In this simulation the surfactant is perfluorooctanoate, with cesium being the counter ion. The MD simulations were performed in the NVT ensemble for an aggregate of 62 CsPFO molecules in 10562 water molecules at 300 K. The potential for water molecules is the extended simple point charge (SPC/E) model. The counter ions carry a unit positive charge that is compensated by a $+0.4e$ charge on the carbonyl carbon and a $-0.7e$ charge on each of the oxygen atoms of the polar head group of the PFO surfactant (Balasubramanian et al., 2002; Pal et al., 2004). The equations of motion were integrated with the reversible reference system propagator algorithm (RESPA) scheme using the PINY_MD MD package.

System and Simulation Details of DTAB Micelle

For this micelle bromine is the counter ion. Here we have used the united atom model to represent the methyl groups that surround the central nitrogen atom in the head group of the DTA surfactant. The MD simulations were performed in the NVT ensemble for an aggregate of 47 DTAB molecules in 5834 water molecules at 300 K. The carbon atom that is adjacent to the nitrogen in the surfactant tail is denoted as CT. CT and the methyl groups in the head group carry a $+0.25e$ charge, while the central nitrogen atom is neutral. Thus, the whole DTAB molecule is neutral. The potential for water molecules for this micellar system is SPC/E. The equations of motion were integrated with the reversible reference system propagator algorithm scheme using the PINY_MD MD package.

System and Simulation Details of 1ETN Protein

Heat stable enterotoxins are produced by *Eschericia coli* bacteria in the intestine and are responsible for acute diarrhea in humans and animals. They display a remarkable ability to retain their activity even at 100°C .

This class of peptides typically contains 18 or 19 amino acid residues and share a common 13 amino acid sequence, which is Cys⁵-Cys-Glu-Leu-Cys-Cys¹⁰-Asn-Pro-Ala-Cys-Ala¹⁵-Gly-Cys (full peptide position) and Cys¹-Cys-Glu-Leu-Cys-Cys⁶-Asn-Pro-Ala-Cys-Ala¹¹-Gly-Cys (toxic domain). Since the domain is conserved in several enterotoxins, one expects this 13 residue domain to be the primary reason for the toxicity. The six Cys residues form three disulphide bridges, and provide stability to the structure of the protein. 1ETN has a simple structure: it has got three beta (β) turns. In addition, the crystal structure contains five intramolecular hydrogen bonds that also add to the stability of the protein. Another interesting aspect of this protein is the presence of 13 water molecules in the crystal structure (Sato et al., 1986). Overall, this protein has a hydrophobic character, as the side chains of all residues are oriented to the outside of the molecule (Balasubramanian et al., 2003).

The MD simulations of 1ETN protein in water were performed in the NVT ensemble at 300 K. Cys⁵ is the N-terminus carrying a +1.0e charge and is capped with two hydrogen atoms. Cys¹⁷ is the C-terminus with a -1.0e charge, and is capped with an oxygen atom. The final system contains one 1ETN protein (152 atoms) and 2962 water molecules. The equations of motion were integrated with the reversible reference system propagator algorithm scheme using the PINY_MD MD package. The CHARM22 all-atom force fields and potential parameters were used for the interaction between atoms of the protein, while the TIP3P interaction model was used for water molecules.

System and Simulation Details of HP-36 Protein

HP-36 is a small 36-residue globular protein, which is the thermo-stable sub-domain present at the extreme C-terminus of the 76-residue chicken villin headpiece domain. Villin is a unique protein that can both assemble and disassemble actin structures. In the absence of calcium ions it can act as an actin-bundling protein, while in the presence of calcium it becomes an actin-severing protein. HP-36 contains one of the two F-actin binding sites in villin necessary for F-actin bundling activity. For HP-36 protein we number the residues from 1 to 36. Thus, residue numbers 1–36 correspond to residues 41–76 in the NMR structure (McKnight et al., 1997). The secondary structure of the protein contains three short α -helices. These helices are connected and held together by a few turns and loops and a hydrophobic core. We denote the three α -helices as, helix-1 (Asp-4 to Lys-8), helix-2 (Arg-15 to Phe-18), and helix-3 (Leu-23 to Glu-32). The remaining segments of the protein are defined as, coil-1 (Met-1 to Ser-3), coil-2 (Ala-9 to Thr-14), coil-3 (Ala-19 to Pro-22), and coil-4 (Lys-33 to Phe-36). The biological activity is believed to be centered around helix-3, which contains ten amino acid residues (McKnight et al., 1997).

The final system contained the protein molecule (596 atoms) in a cubic box containing 6842 water molecules. The MD simulations were performed in

the NVT ensemble. The equations of motion were integrated with the reversible reference system propagator algorithm scheme using the PINY_MD MD package. The CHARM22 all-atom force fields and potential parameters were used for the interaction between atoms of the protein, while the TIP3P interaction model was used for water molecules.

References

- Angell, C.A. Liquid fragility and the glass transition in water and aqueous solutions, *Chem. Rev.*, 102, 2627, 2002.
- Bagchi, B. Water solvation dynamics in the bulk and in the hydration layer of proteins and self-assemblies, *Ann. Rep. Prog. Chem., Sect. C*, 99, 127, 2003.
- Bagchi, B. and Bhattacharyya, S. Mode coupling theory approach to liquid-state dynamics, *Adv. Chem. Phys.*, 116, 67, 2001.
- Balasubramanian, S., Pal, S., and Bagchi, B. Hydrogen-bond dynamics near a micellar surface: origin of the universal slow relaxation at complex aqueous interface, *Phys. Rev. Lett.*, 89, 115505, 2002.
- Balasubramanian, S., Bandyopadhyay, S., Pal, S., and Bagchi, B. Dynamics of water at the interface of a small protein, enterotoxin, *Curr. Sci.*, 85, 1571, 2003.
- Bandyopadhyay, S., Chakraborty, S., Balasubramanian, S., and Bagchi, B. Sensitivity of polar solvation dynamics to the secondary structures of aqueous proteins and the role of surface exposure of the probe, *J. Am. Chem. Soc.*, 127, 4071, 2005.
- Bandyopadhyay, S., Chakraborty, S., Balasubramanian, S., Pal, S., and Bagchi, B. Atomistic simulation study of the coupled motion of amino acid residues and water molecules around protein HP-36: fluctuations at and around the active sites, *J. Phys. Chem. B*, 108, 12608, 2004.
- Bhattacharyya, K. Solvation dynamics and proton transfer in supramolecular assemblies, *Acc. Chem. Res.*, 36, 95, 2003.
- Bhattacharyya, S.M., Mukherjee, A., and Bagchi, B. (to be published).
- Bhattacharyya, S.M., Wang, Z.-G., and Zewail, A.H. Dynamics of water near a protein surface, *J. Phys. Chem. B*, 107, 13218, 2003.
- Bizzarri, A.R. and Cannistraro, S. Molecular dynamics of water at the protein-solvent interface, *J. Phys. Chem. B*, 106, 6617, 2002.
- Boresch, S., Hochtl, P., and Steinhauser, O. Studying the dielectric properties of a protein solution by computer simulation, *J. Phys. Chem. B*, 104, 8743, 2000.
- Case, D. and Karplus, M. Dynamics of ligand binding to heme proteins, *J. Mol. Biol.*, 132, 343, 1979.
- Datta, A., Mandal, D., Pal, S. K., Das, S., and Bhattacharyya, K., Solvation dynamics in organized assemblies. 4-Aminophthalimide in micelles, *J. Mol. Liq.*, 77, 121, 1998.
- Doster, W. and Settles, M. *The Dynamical Transition in Proteins: The Role of Hydrogen Bond*, *Workshop on Hydration Process in Biology: Theoretical and Experimental Approaches*, M.C. Bellissent-Funel and J. Teixeira, eds, IOS Press, Amsterdam, 177, 1998.
- Gu, W. and Schoenborn, B.P. Molecular dynamics simulation of hydration in myoglobin, *Proteins: Struct. Funct. Genet.*, 22, 20, 1995.

- Jimenez, R., Fleming, G. R., Kumar, P. V., and Maroncelli, M. Femtosecond solvation dynamics of water, *Nature*, 369, 471, 1994.
- Jordanides, X. J., Lang, M. J., Song, X., and Fleming, G. R. Solvation dynamics in protein environment studied by photon echo spectroscopy, *J. Phys. Chem. B*, 103, 7995, 1999.
- Knapp, E.W., Fischer, S.F., and Parak, F. Protein dynamics from Mossbauer spectra. The temperature dependence, *J. Am. Chem. Soc.*, 86, 5042, 1982.
- Lin, S.M., Maiti, P.K., and Goddard III, W.A. Dynamics and thermodynamics of water in PAMAM dendrimers at subnanosecond time scale, *J. Phys. Chem. B*, 109, 8663, 2005.
- McKnight, C.J., Matsudaira, P.T., and Kim, P.S. NMR structure of the 35-residue villin headpiece subdomain, *Nat. Struct. Biol.*, 4, 180, 1997.
- Molinero, V. and Goddard, W.A. III M3B: a coarse grain simulations of malto-oligosaccharides and their water mixtures, *J. Phys. Chem. B*, 108, 1414, 2004.
- Nandi, N. and Bagchi, B. Dielectric relaxation of biological water, *J. Phys. Chem. B*, 101, 10954, 1997.
- Nandi, N., Bhattacharyya, K., and Bagchi, B. Dielectric relaxation and solvation dynamics of water in complex chemical and biological systems, *Chem. Rev.*, 100, 2013, 2000.
- Nandi, N., Roy, S., and Bagchi, B. Ultrafast solvation dynamics in water: Isotope effects and comparison with experimental results, *J. Chem. Phys.*, 102, 1390, 1995.
- Pal, S. K., Peon, J., Bagchi, B., and Zewail, A. H. Biological water: femtosecond dynamics of macromolecular hydration, *J. Phys. Chem. B*, 106, 12376, 2002.
- Pal, S., Balasubramanian, S., and Bagchi, B. Anomalous dielectric relaxation of water molecules at the surface of an aqueous micelle, *J. Chem. Phys.*, 120, 1912, 2004.
- Roy, S. and Bagchi, B. Solvation dynamics in liquid water. A novel interplay between librational and diffusive modes, *J. Chem. Phys.*, 99, 9938, 1993.
- Rupley, J.A. and Careri, G. Protein hydration of function, *Adv. Protein Chem.*, 41, 37, 1991.
- Sarkar, N., Datta, A., Das, S., and Bhattacharyya, K. Solvation dynamics of coumarin 480 in micelles, *J. Phys. Chem.*, 100, 15483, 1996.
- Sato, T., Gariépy, J., Lane, A., Frayman, F., Wilbur, D., Robien, W., Schoolnik, G. K., and Jardetzky, O. Structural characteristics for biological activity of heat-stable enterotoxin ST I, *Biochemistry*, 25, 7854, 1986.
- Sen, P., Mukherjee, S., Dutta, P., Halder, A., Mandal, D., Banerjee, R., Roy, S., and Bhattacharyya, K. Solvation dynamics in the molten globule state of a protein, *J. Phys. Chem. B*, 107, 14563, 2003.
- Tarek, M. and Tobias, D.J. Role of protein–water hydrogen bond dynamics in the protein dynamical transition, *Phys. Rev. Lett.*, 88, 138101, 2002.
- Tournier, A.L., Xu, J., and Smith, J.C. Translational hydration water dynamics drives the protein glass transition, *Biophys. J.*, 85, 1871, 2003.

3

How Does Water Diffuse in Glasses of Carbohydrates?

Valeria Molinero and William A. Goddard III

CONTENTS

Introduction	39
Results and Discussion	41
Conclusions.....	54
Acknowledgments.....	56
References	56

Introduction

Understanding and predicting water diffusivity in supercooled and glassy carbohydrates is of great importance in the practical applications of these mixtures, in particular to the preservation of foods and pharmaceuticals. Since the discovery more than a decade ago that water retained liquid-like heat capacity in glassy starch (Noel and Ring, 1992) several studies have shown that water is mobile in glasses of carbohydrates (van den Dries et al., 1998; van den Dries et al., 2000; Tromp et al., 1997; Hills et al., 2001; Chatakanonda et al., 2003; Kou et al., 2000; Vodovotz et al., 2000; Aldous et al., 1997) and foods (Roudaut et al., 1999).

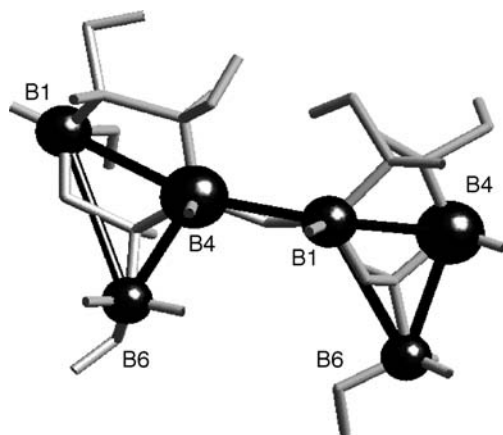
Nevertheless, the microscopic mechanism that allows water diffusion in these glasses has remained an unsolved puzzle. We present here a computer simulation study of the microscopic mechanisms of water diffusion in carbohydrate from the viscous liquid state up to the glass. To understand the nature of water diffusion in glassy food-like systems, we employed molecular dynamics (MD) simulations techniques to study in detail the structure and dynamics of a concentrated glucose solution, a simple binary

glass-former that is considered to be a model for food systems (Levine and Slade, 1988). In this work, we extend a previous study for the supercooled mixture (Molinero et al., 2004), present results that unravel the mechanism of water diffusion in the glassy state (Molinero and Goddard, 2004), and compare the relaxation in supercooled glucose and a malto-oligomer ($\alpha(1 \rightarrow 4)$ glucose oligomer) to assess the effect of the carbohydrate local modes on the dynamics of water.

In previous atomistic and coarse grain simulations of water–glucose solutions (Molinero et al., 2004), and atomistic simulations of water–sucrose solutions (Molinero et al., 2003), we found that water has a locally heterogeneous structure with a percolation threshold around $\sim 18\%$ wt water content. We showed that the free volume in water–sucrose mixtures is nonmonotonic with increasing water content and that the percolation of the free volume pathways occurs for a probe radius much smaller than the water size. These results reinforce the idea that water diffusion in supercooled and frozen matrices does not occur through free-volume channels but rather it might be strongly coupled to the water structure. In a frozen matrix with low water content, we expect water pathways to facilitate water diffusion, especially at temperatures close to and below the glass transition where the matrix mobility is expected to be very low.

MD simulations provide an optimum level of detail for elucidating microscopic mechanisms. Nevertheless, the study of glassy molecular mixtures by MD simulations has been hampered by the computational cost of atomistic simulations. To overcome this problem, we have developed the M3B coarse grain model for malto-oligosaccharides and their water mixtures (Molinero and Goddard, 2004), which is ~ 7000 times faster than atomistic MD (Molinero and Goddard, 2004), extending the accessible simulation times to the order of a microsecond. The M3B force field was derived from atomistic simulations of glucose, maltose and higher malto-oligosaccharides, and can represent any $\alpha(1 \rightarrow 4)$ glucose oligomer of arbitrary chain length. In the M3B model, each glucose residue (AGU) is represented by three particles (beads) located on the positions of carbons 1, 4 and 6 of the atomistic model. An oligosaccharide is made linking together those AGU, as shown in Figure 3.1 for the disaccharide, α -maltose. The water molecule is represented by a single particle. The M3B model does not consider charges, hydrogen bonds or directional nonbond interactions, yet is able to reproduce the helical structure of polysaccharides (Molinero and Goddard, 2004) and the distribution of water in glucose (Molinero et al., 2004).

We present here coarse grain simulation results of two simple binary water–carbohydrate mixtures that shed light on the mechanism of water diffusion in the supercooled and glassy state, the coupling of water mobility in the glass to the sub- T_g dynamics of the matrix, and the effect of the internal modes of the saccharide on the decoupling of water motion from carbohydrate translation.

**FIGURE 3.1**

Coarse grain M3B model (black) and atomistic model (gray) of the simplest $\alpha(1 \rightarrow 4)$ glucose oligomer, the dimer α -maltose. The coarse grain particles B1, B4 and B6 representing each monomer are mapped from the positions of the carbons C1, C4, and C6 of the atomistic model, respectively.

Results and Discussion

We selected to study two water–carbohydrate binary systems with the same water content and different degree of polymerization (DP) of the sugar, to analyze the effect of the saccharide internal degrees of freedom on the mobility of water: (i) a concentrated glucose solution with 12.2%wt water in a range of temperatures from the glass to the supercooled regime $T = 220\text{--}365\text{ K}$ ($T/T_g = 0.92, 1.05, 1.2, 1.3, 1.4$, and 1.5), and (ii) a mixture of the dodecamalto-oligomer (DP12) with the same water content, 12%wt, at $T = 475\text{ K}$ ($T/T_g = 1.4$).

The M3B model predicts a glass transition temperature $T_g^{\text{M3B}} = 239 \pm 25\text{ K}$ (Molinero and Goddard, 2004) for the 12% water–glucose mixture. The experimental value is $T_g^{\text{exp}} = 240\text{ K}$ (Roos, 1993). The periodic simulation cell consisted of 90 glucose and 125 water molecules. The simulations were performed in the NPT ensemble, with $p = 1\text{ bar}$ and $T = 365, 335, 310, 280, 250$, and 220 K for simulation times ranging from $0.1\text{ }\mu\text{s}$ at the highest T to $0.85\text{ }\mu\text{s}$ at the lowest. Details of the preparation of the initial conditions and simulation methods are given elsewhere (Molinero et al., 2004). The 12%wt water–DP12 (W–DP12) periodic cell consisted of 37 DP12 and 600 water molecules, and the NPT simulations were carried out at 475 K . The glass transition temperature for the W–DP12 mixture was estimated to be $T_g^{\text{M3B}} = 341 \pm 17\text{ K}$ using the procedure of Molinero and Goddard (2004). The experimental value $T_g^{\text{exp}} = 325 \pm 4\text{ K}$ (Orford et al., 1989) is within the

error of the M3B estimation. In what follows, we examine closely the mechanism of water diffusion in the glucose solution across the entire temperature range from $0.92T_g$ to $1.5T_g$, and compare with the same concentration of water in the DP12 oligomer, both at $1.4T_g$. To further examine the effect of the internal degrees of freedom of the matrix on the water dynamics, we compare simulations of the 12%wt water–DP12 solution at 475 K, where the oligomer torsional barriers that control the segmental motion (Molinero and Goddard, 2004) are turned off from the force field.

We computed three quantities for the examination of water mobility in the solutions, which provide an increasing level of detail on the mobility mechanism: (i) the mean square displacement $\langle r^2(t) \rangle = \langle |\vec{r}(t) - \vec{r}(0)|^2 \rangle$, where the average $\langle \dots \rangle$ is over the trajectory and all water molecules, (ii) the van Hove self-correlation function, $G_s(r, t)$, which indicates the probability for each component to travel a distance r in a time interval t , $4\pi r^2 G_s^\alpha(r, t) = \frac{1}{N_\alpha} \langle \sum_{i=1}^{N_\alpha} \delta(r - |\vec{r}_i(t) - \vec{r}_i(0)|) \rangle$, and (iii) the examination of the distance traveled by individual water molecules, $d_i(t) = |\vec{r}_i(t) - \vec{r}_i(0)|$.

Figure 3.2 shows the mean square displacement (MSD) for water in the glassy and supercooled glucose solutions in a log–log scale. The most remarkable result is that water diffuses at 220 K, in the glass, as observed in the experiments. The diffusion at 220 K, however, occurs in a scale comparable with the μ s of the simulation and cannot be quantified from the data in Figure 3.2. For the five supercooled solutions, $T = 250$ to 365 K, we computed the diffusion coefficient from the long time dependence of

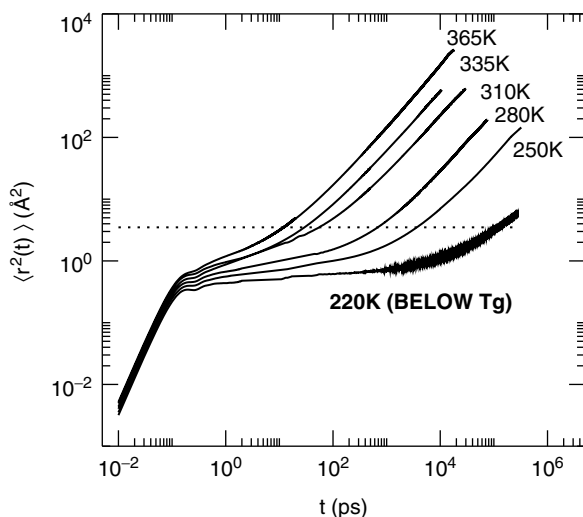


FIGURE 3.2

Mean square displacement of water in 12%wt water–glucose in the supercooled and glass regime. The dotted line corresponds to 3.5 Å, comparable with the diameter of a water molecule.

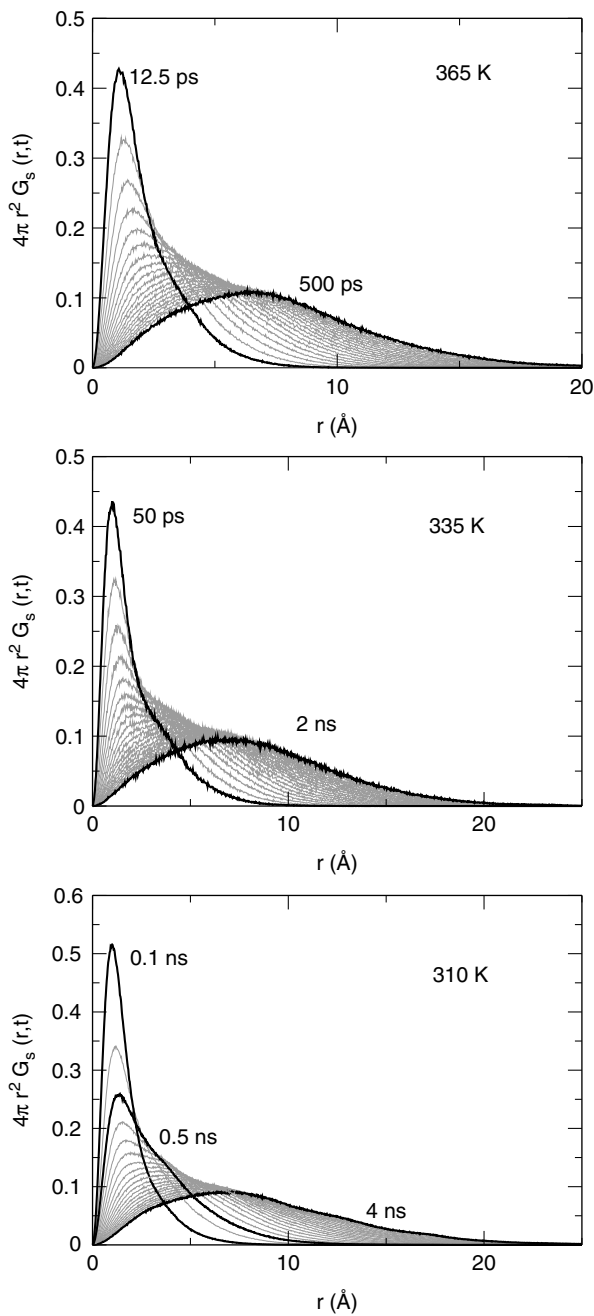
$\text{MSD} \langle r^2(t) \rangle = 6Dt$. Water diffusion coefficients show an Arrhenius temperature dependence in the range $T = 250$ to 365 K (Molinero et al., 2004), with a preexponential factor $D_0 = 8.8 \times 10^{-5} \text{ m}^2/\text{sec}$ and activation energy $E_a = 38.3 \pm 2.3 \text{ kJ/mol}$. These results compare well with the activation parameters obtained experimentally for a 25%wt water–glucose solution $D_0 = 1.7 \pm 0.8 \times 10^{-5} \text{ m}^2/\text{sec}$ and $E_a = 31.1 \pm 1.0 \text{ kJ/mol}$ (Moran and Jeffrey, 1999), and indicate that the M3B model is able to reproduce the energetics of water in glucose.

The plateau observed in Figure 3.2 between the subpicosecond ballistic regime and the diffusional regime at long times, increases with supercooling and becomes well defined for $T = 280$ K and below. The plateau is indicative of the time during which the molecule remains caged by its neighbors. However, it provides no clue on the actual mechanism of water diffusion. Some insight on this mechanism can be obtained through the analysis of the van Hove self-correlation function (VHSCF) at different times. Figure 3.3 and Figure 3.4 show the VHSCF for water translation at the six temperatures studied. Two temperature ranges can be distinguished from the time evolution of this function: (i) for $T = 310$ K ($T/T_g = 1.3$) and above, $4\pi r^2 G_s(r, t)$ displays only one peak for each time t , and the peak's position advances in time towards longer distances r . (ii) For $T = 280$ K and lower, $4\pi r^2 G_s(r, t)$ displays multiple peaks whose positions do not evolve with time. These secondary peaks are already prefigured at $T = 365$ to 310 K as humps at $r \sim 3.5 \text{ \AA}$, and indicate the existence of preferential distance for water translation. For $T \leq 280$ K, the VHSCF suggests that the prevailing mechanism involves water rattling in the cage formed by its neighbors and then jumping into a new position approximately one water diameter away. This mechanism is confirmed by the analysis of individual water trajectories, shown in Figure 3.5 for $T = 250$ K.

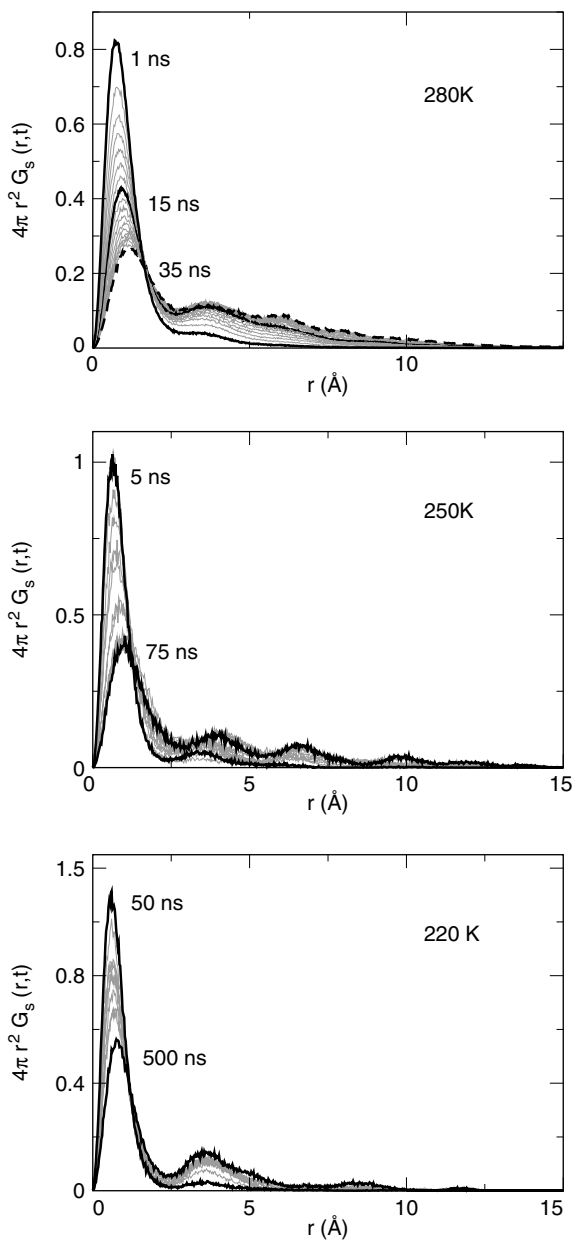
A quantification of the time scales of water diffusion requires the computation of the incoherent scattering function $F_s(k, t)$, the space Fourier transform of $G_s(r, t)$. To extract the characteristic time for water diffusion, we approximated the relaxation of $F_s(k, t)$ by a stretched exponential function, $F_s(k, t) = A \exp(-(t/\tau)^\beta)$ where $\beta \leq 1$ quantifies the departure from purely exponential relaxation and is a measure of the heterogeneity of the dynamics. The relaxation of water is clearly nonexponential already in the range $T = 310$ to 365 K (Figure 3.6), and it can be seen that β decreases with supercooling. The nonexponential character of the relaxation is more pronounced at shorter distances, comparable with the molecular size ($k > 1 \text{ \AA}^{-1}$), stressing the importance of first neighbors in the heterogeneity of water dynamics in supercooled glucose.

More revealing is the analysis of the variation of the characteristic times $\bar{\tau} = \Gamma(1/\beta)\tau/\beta$ with the reciprocal distance k . For a continuous diffusion mechanism,

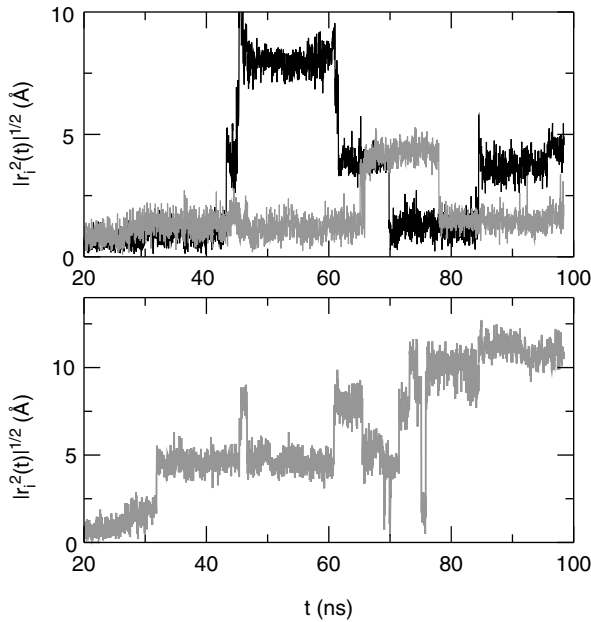
$$\bar{\tau}^{-1} = Dk^2 \quad (3.1)$$

**FIGURE 3.3**

van Hove self-correlation function for water translation in 12%wt water-glucose. At the three temperatures shown in this graph, water shows a diffusive behavior, although the presence of an additional jump mechanism for water translation is also evident in the appearance of a hump at ~ 3.5 Å, which becomes more pronounced with supercooling.

**FIGURE 3.4**

van Hove self-correlation function for water translation in 12%wt water-glucose in the deep supercooled and glassy regime. Below $1.2T_g$ the continuous diffusion contribution to water diffusion becomes negligible, and the translation occurs mainly through jumps of a size comparable with water diameter. These preferential jumping positions are evidenced by the existence of (multiple) secondary peaks in the VHSCF of water. Note that at 220 K, below the glass transition, water remains translationally mobile.

**FIGURE 3.5**

Displacements of four randomly selected water molecules in 12%wt water–glucose just above the glass transition temperature, at $T = 250$ K. Water motion proceeds essentially through jumps. The jumps are not instantaneous, but are rather a drift that can take as much as 100 ps to complete at this temperature.

while for a purely jump-diffusion mechanism in which the molecule jumps over distances l_o waiting in average for a time $\bar{\tau}_o$ between jumps,

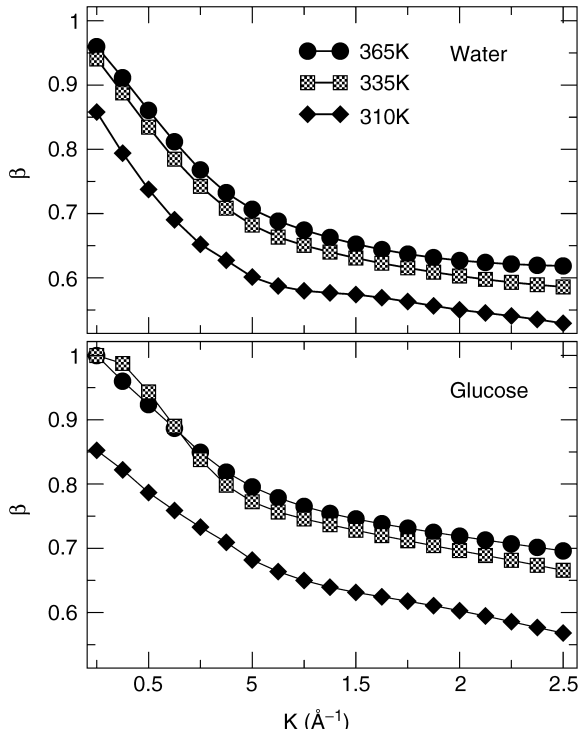
$$\frac{1}{\bar{\tau}} = \frac{1}{\bar{\tau}_o} \left(\frac{k^2 l_o^2}{6 + k^2 l_o^2} \right) \quad (3.2)$$

We find that water in glucose translate through the two relaxation channels — translation through small steps and through big jumps,

$$\frac{1}{\bar{\tau}} = \frac{1}{\bar{\tau}_o} \left(\frac{k^2 l_o^2}{6 + k^2 l_o^2} \right) + D^c k^2 \quad (3.3)$$

Equation 3.3 (Figure 3.7, lines) represents very well the simulation data obtained for water relaxation in glucose (Figure 3.7, symbols), and is in agreement with the shape of $\bar{\tau}^{-1}$ vs. k^2 of neutron scattering data measured for concentrated water–carbohydrate solutions (Feeney et al., 2001; Magazu et al., 2001).

Our results indicate that the two contributions to water relaxation slow down with supercooling (Table 3.1), but the continuous one decreases faster,

**FIGURE 3.6**

Nonexponential parameter β of the translational relaxation of water (upper panel) and glucose (lower panel) in the viscous supercooled liquid at temperatures from $1.5T_g$ (365 K), through $1.4T_g$ (335 K), to $1.3T_g$ (310 K). Note that for each temperature, water relaxation is more nonexponential (lower β) than for glucose. The β parameters were obtained from the stretched exponential fit of the intermediate scattering function $F_s(k, t)$ for each component.

and, as seen in Figure 3.4, is irrelevant below 280 K. In the deep supercooled regime the only mechanism for water translation is through jumps of length l_o comparable with the water size.

Figure 3.2 and Figure 3.4 (lowest panel) show evidence that *water remains mobile in the glass*, and diffuses exclusively through jumps. From a stretched exponential fit of the incomplete decay of $F_s(k, t)$ at 220 K, we estimated the characteristic time for water to move one water diameter ($k = 2\pi/3.5 \text{ \AA}$) to be $\tau_W \sim 1.3 \mu\text{s}$. This renders an estimated water diffusion coefficient $D = l^2/6\tau = 1.6 \times 10^{-14} \text{ m}^2/\text{sec}$, in excellent agreement with the $D \sim 10^{-14} \text{ m}^2/\text{sec}$ measured for water in 10 and 6%wt water–maltose mixtures at their respective glass transition temperatures (Tromp et al., 1997; Parker and Ring, 1995). Note that the diffusion coefficient of water is nine orders of magnitude higher than predicted by assuming it follows the viscosity through the Stokes–Einstein equation at T_g , $D \sim 10^{-23} \text{ m}^2/\text{sec}$, assuming that for T_g the viscosity is 10^{12} Pa s .

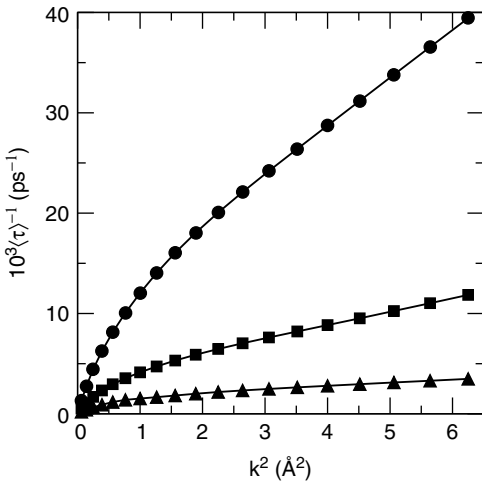


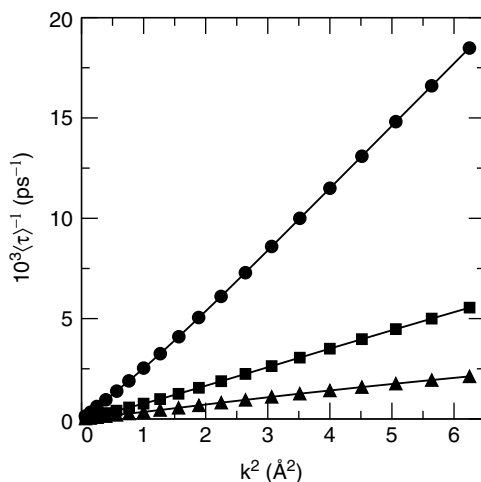
FIGURE 3.7
The k^2 dependence of the inverse of the characteristic times $\langle\tau\rangle^{-1}$ for water translation does not show exclusively the linear behavior of continuous diffusion (Equation 3.1) or exclusively the shape of a simple jump diffusion model (Equation 3.2), but is very well represented (lines) by considering that *both* mechanisms contribute to the relaxation (Equation 3.3). The symbols correspond to the simulation data at different temperatures: 365 K (circles), 335 K (squares), and 310 K (triangles).

TABLE 3.1
Translational Diffusion of Water in Supercooled 12%wt Water Glucose

T (K)	$\bar{\tau}_o$ (ps)	l_o (Å)	D^{jump} (Å ² /ps)	D^c (Å ² /ps)
365	72.6	2.77	1.8×10^{-2}	4.3×10^{-3}
335	211.6	3.16	7.9×10^{-3}	1.2×10^{-3}
310	514.6	3.28	3.5×10^{-3}	2.7×10^{-4}
E_a (kJ/mol)	—	—	26.8 ± 0.6	45.4 ± 1.2

$D^{\text{jump}} = l_o^2/6\bar{\tau}_o$ is the low k -vector contribution to the diffusion coefficient due to water jumps, shown for comparison with the continuous component D^c . The activation energy E_a shown in the last row corresponds to an Arrhenius analysis of the respective time constants and diffusion coefficients.

While water dynamics in the sugar have two components, jumps plus continuous diffusion, with the latter diminishing faster while approaching the glass transition, the translation of the glucose occurs only through continuous diffusion even in the deep supercooled regime (see Figure 3.8). Though the mechanism of translation of glucose and water are different, both relaxations are nonexponential, as shown in Figure 3.6. Contrary to

**FIGURE 3.8**

The k^2 dependence of the inverse of the characteristic times $\langle \tau \rangle^{-1}$ for glucose translation shows the linear behavior characteristic of continuous diffusion (Equation 3.1, lines in the figure). The symbols correspond to the simulation data at different temperatures: 365 K (circles), 335 K (squares), and 310 K (triangles).

water that diffuses below T_g ; glucose translation is arrested in the glass. In what follows, we analyze the factors that allow such decoupling of water diffusion from the carbohydrate translation.

It was suggested (Tromp et al., 1997; Hills and Pardoe, 1995) that water may diffuse in carbohydrate glasses through free volume (FV) channels formed by the packing of the sugars. To examine this hypothesis for the water–glucose glass, we computed the FV available to spherical probes with radius ranging from $R_p = 0$ to 1.5 \AA , using the method described in Molinero et al. (2003). The FV was computed for the glassy water–glucose mixture on configurations selected every 50 ns. To facilitate the comparisons with the results for water–sucrose mixtures (Molinero et al., 2003), the atomistic coordinates of the water and glucose molecules were reconstructed (Molinero and Goddard, 2004) from the M3B model for each of the studied configurations. Our results indicate that the FV network in 12.2% W–G percolates for a probe radius $R_{\text{perc}} \sim 0.5 \text{ \AA}$, much smaller than the water size. We found no free volume channels that facilitate water diffusion in the glass, and we conclude that water motion must imply the displacement of other water molecules or glucose beads. At 220 K, we observe that 68% of the water jumps correspond to water jumping into a neighbor water position, 22% into the position of the bead B6 that represents the exocyclic group of glucose, and 4 and 6% into the position of “backbone” beads B4 and B1. The existence of jumps for the individual glucose beads, along with the lack of jumps in the center of mass translation of the sugar, indicates that it is the *rotation* of the molecule that proceeds through jumps in the glass.

To obtain an insight into the mechanism of glucose rotation in the glass, we studied the reorientation of glucose by computing the time autocorrelation function for the angles defined by two unit vectors: the “backbone vector” \mathbf{r}_B in the direction that connects the beads B1 and B4, and the “side vector” \mathbf{r}_S that connects the middle of \mathbf{r}_B to the position of B6, which represents the exocyclic, or side group, of the atomistic glucose molecule (see Figure 3.1). The autocorrelation of the corresponding angles $\theta^m(t) = \mathbf{r}_m(t) \cdot \mathbf{r}_m(0)$ is defined by Equation 3.4:

$$4\pi \sin(\theta) P^m(\theta, t) = \frac{1}{N_G} \left\langle \sum_{i=1}^{N_G} \delta(\theta - [\theta_i^m(t) - \theta_i^m(0)]) \right\rangle \quad (3.4)$$

Figure 3.9 shows that both the backbone and side rotation of glucose in the glass proceed through jumps that appear as secondary peaks in the autocorrelation function. Our observation of glucose rotation through jumps in the glass transition region is in agreement with 2D NMR-experiments on

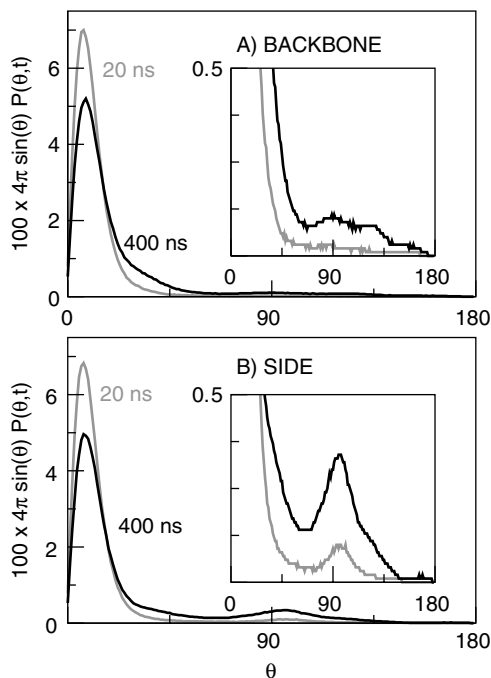


FIGURE 3.9

The orientational van Hove self-correlation function corresponding to the relaxation of the backbone (top panel) and side (lower panel) vectors of glucose (see text for definition) at 220 K show that glucose rotation in the glass proceed by big jumps and does not have a continuous diffusion component. The side rotation, which involves the jump of the smaller glucose bead, the “exocyclic” B6, relaxes faster ($\tau_S \sim 3 \mu s$) than the rotation involving the jumps of the big “backbone” beads B4 and B1 ($\tau_B \sim 15 \mu s$).

15%wt water–glucose (Wachner and Jeffrey, 1999). At $T/T_g = 0.92$, a rough estimation of the characteristic rotational times computed from the partial decay of first order time autocorrelation function for the *side* and *backbone* vectors of glucose up to $0.5 \mu\text{s}$ renders $\tau_S \sim 3 \mu\text{s}$ and $\tau_B \sim 15 \mu\text{s}$, respectively. These times are longer, yet comparable with, the estimated relaxation time for water, $\tau_W \sim 1.8 \mu\text{s}$. Our results indicate that the most relevant mechanism for the rotation of glucose in the glass is through big jumps. The contribution of continuous diffusion (small jumps) to the rotational relaxation in the glass is not significant, as can be seen from the invariant position of the first peak of $P(\theta, t)$ in Figure 3.9. It should be noted that the magnitude of the jumps obtained in the M3B coarse grain may be bigger than the ones corresponding to the actual atomistic model, because the rotation of the coarse grain glucose probably occurs on a smoother potential energy surface, because of the lack of “sticky points” represented by the atoms and their hydrogen bonds in the atomistic model.

The existence of jumps in the rotation of the glucose mirrors the appearance of jumps in the translation of the water, showing the intimate relationship between the local motion of matrix (sugar) and solute (water). Figure 3.10 shows the rotational VHSCF, $4\pi\sin(\theta)P(\theta, t)$, for the “side” vector of glucose in the mixture at different temperatures. For each temperature, we selected the time t for which the angle has relaxed on average to $\langle\theta_S(t)\rangle = 40^\circ$. The shape of $4\pi\sin(\theta)P(\theta, t)$ changes from a single peaked one at high T , to present also a well defined secondary one at $T \leq 280 \text{ K}$, the same

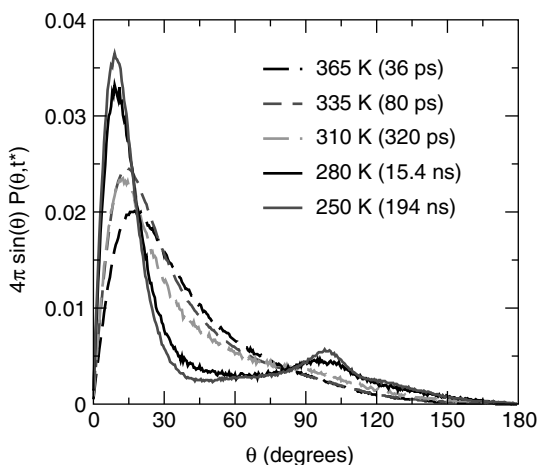


FIGURE 3.10

The orientational van Hove self-correlation function for the side vector of glucose (see definition in text) develops well-defined secondary peaks corresponding to rotational jumps at the same temperatures that these peaks develop in the translational VHSCF of water (see Figure 3.3 and Figure 3.4). The curves correspond to times (indicated in the figure) for which the side vector has rotated an average of 40° .

temperatures for which water translational VHSCF presents multiple peaks (Figure 3.4).

Water in the supercooled (Molinero et al., 2004) and glassy 12.2% W-G mixture has a locally heterogeneous structure that we characterized by their number of first neighbor waters. This neighbor distribution of the M3B model is in excellent agreement with the one obtained by atomistic simulations of the same systems (Molinero et al., 2004). We computed the *water facilitation*, defined (Molinero et al., 2004) as the ratio between the fraction of total jumps for a given number of water neighbors and the fraction of waters having this coordination number irrespective of whether they are jumping or not. The resulting facilitation for water in glucose from $T = 220$ to 365 K (Figure 3.11) shows that the presence of water neighbors notoriously increases the probability of jumping for water. This effect is more important the lower the temperature, when the route of water–water exchange is privileged because of the decrease of the alternative relaxation channel involving the displacement of the glucose molecules.

Finally, we examine the effect of the timescale of the local degrees of freedom of the carbohydrate on the dynamics of water by comparing the mechanism of water diffusion in the solutions of the supercooled monomer DP1 and the oligomer DP12. We have studied the two mixtures of identical

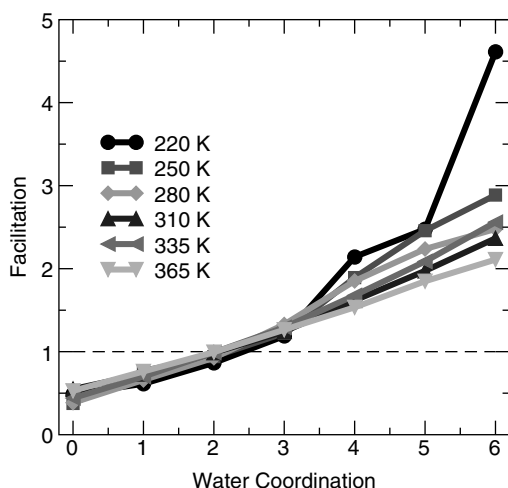
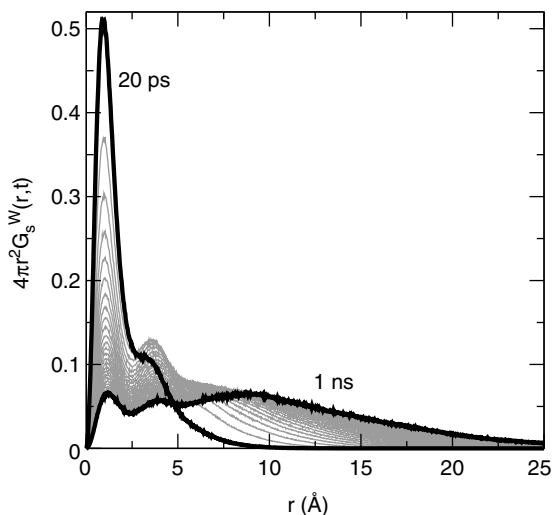


FIGURE 3.11

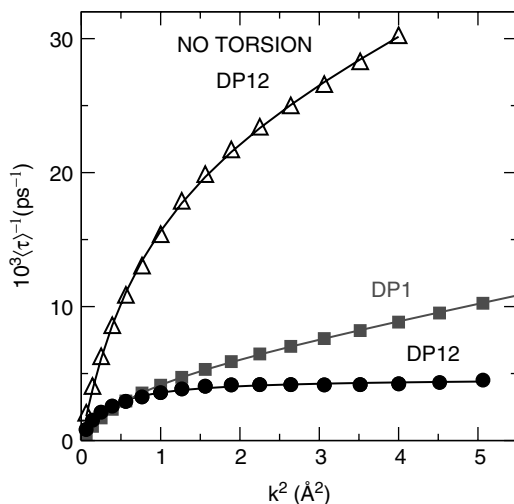
The existence of water neighbors facilitates the jumping of water. The water coordination (WC) is the number of first water neighbors, and the facilitation for each WC is defined as the ratio between the fraction of the total jumps made by water molecules with that WC and the fraction of water molecules with that WC, irrespective of whether they are jumping or not. The lower the temperature, the more relevant is the water coordination for the mobility of water. Water molecules completely surrounded by glucose ($WC = 0$) have a lower but non-zero probability of jumping, even in the glass, because glucose helps to the translation of water through its rotation, which persists below T_g .

**FIGURE 3.12**

van Hove self-correlation function for water translation in DP12 at 475 K ($1.4T_g$). At this temperature, the relaxation of water in the oligomer occurs mainly through jumps in an already translationally frozen matrix, and there is no noticeable contribution from continuous diffusion (contrary to what is observed for water in glucose at $1.4T_g$; see medium panel of Figure 3.3). The relaxation times of water in the monomer and oligomer at $1.4T_g$ are nevertheless comparable, although higher for water in DP12.

water content at the same “reduced temperature” with respect to the glass transition, $T/T_g = 1.4$. Figure 3.12 shows the VHSCF of water in 12%W–DP12 at $T = 475$ K. The existence of multiple peaks, and the non-diffusive behavior of them resemble that of water in the 12%W–G at $T/T_g = 1.2$. The timescales of water relaxation, however, are comparable with 12%wt W–G at $T/T_g = 1.4$, although the diffusion of water in DP12 does not present the continuous diffusion component. This is evident in Figure 3.13, where τ^{-1} vs. k^2 was perfectly fitted considering only the jump-diffusion mechanism (Equation 3.2). The absence of a continuous diffusion component for water diffusion in DP12 is associated with the lack of the continuous diffusion mode for the saccharide: at $T/T_g = 1.4$ the only relevant motion in the submicrosecond scale is the segmental motion of the glucose residues around the glycosidic bonds; and this motion occurs through jumps between different conformational states. We estimated the characteristic time of this segmental motion from the autocorrelation of the torsional angles, and found that it is on the order of several tens of nanoseconds for DP12 at 475 K. This time is ~ 500 times slower than that observed for water in the same system, indicating an extensive decoupling of the two motions.

A further indication that it is the coupling to the dynamics of saccharide, in this case the torsional one, that determines the existence of a continuous diffusion mode for the water is obtained from the analysis of the 12%wt

**FIGURE 3.13**

The k^2 dependence of the inverse of the characteristic times $\langle\tau\rangle^{-1}$ for water translation in 12% water–DP12 at $T = 1.4T_g = 475$ K (circles) shows the characteristic shape of jump-diffusion mechanism (Equation 3.2) without any contribution from a continuous diffusion mechanism. When the segmental mobility of the oligomer is increased by eliminating the torsional barriers between the monomeric residues, water mobility acquires a continuous diffusion component (squares). The data for water in the monomer at the same reduced temperature $T = 1.4T_g = 335$ K and water content is also shown for comparison (triangles). The existence of a continuous component in water diffusion in these low water content mixtures requires a continuous component in the mobility of the sugar.

water–DP12* system, where DP12* is modeled at 475 K with the M3B force field turning off the explicit torsions that control the segmental motion of the oligomer. It should be pointed out that this change in intramolecular potential does not affect the water distribution on the mixture that remains the same for the two DP12 models considered. The diffusion of water, however, is noticeably enhanced (Figure 3.13), and the relaxation recovers the continuous diffusion contribution.

Conclusions

The results presented here on the relaxation of water–glucose glass indicate that the translation of water and the rotation of the sugar both contribute to the relaxation in the glass, and that the microscopic mechanisms of mobility observed in the glass manifest already in the deep supercooled regime: the existence of jumps in the translation of water and the rotation of glucose. A continuous diffusion mechanism for the translation of water is observed in glucose in the viscous liquid, but its contribution to the relaxation decreases

with temperature and below $1.2T_g$ the jumps dominate the dynamics of water in glucose. A different scenario is observed for the relaxation of water in the oligomer, where the diffusion is already exclusively through jumps at a temperature of $1.4T_g$. This coincides with an increased decoupling of water translation from the translation of the carbohydrate.

In the water–glucose glass, both water translation and glucose rotation occur through big jumps with comparable characteristic times: $t_W \sim 1.8 \mu\text{s}$, $t_S \sim 3 \mu\text{s}$ and $t_B \sim 15 \mu\text{s}$. We have observed diffusive and non-diffusive contributions to the relaxation: while the water translates in the glass, the glucose mobility involves only rotation. We consider that these motions, plus the rotational motion of water (meaningless in the M3B coarse grain model) should be responsible for the existence of the pronounced secondary β relaxation observed in dielectric spectroscopy of water–glucose glasses (Chan et al., 1986). The relaxation times are close enough to account for the existence of a single broad β peak in the dielectric relaxation of water–glucose mixtures (Chan et al., 1986). It should be noted that the mobile glucose molecules are mobile only with respect to their rotation. We observe no sign of translational diffusion of the glucose molecules in the binary glass, even for the ones that display high rotational mobility.

With respect to the microscopic mechanism of water diffusion in the glass, we conclude that water mobility decouples from the translation of the sugar, though it is still coupled to the local dynamics of the carbohydrate, also persistent below T_g . We find that water diffusion in the glass occurs through two relaxation pathways: (a) water jumping into a neighbor water position, and (b) water jumping into a neighbor glucose bead position. The former couples the water dynamics to its local structure, and the latter couples to the rotational dynamics of the carbohydrate, in particular to the rotation that involves the exchange of water with the smaller, “side group” B6 of the glucose. The mechanism for water diffusion unraveled in this predicts that water mobility in carbohydrate mixtures will be more sensitive to the glass transition for lower water content mixtures, where the water facilitation mechanism is less relevant and water mobility relies on its coupling to the dynamics of the sugar matrix. An NMR study of water mobility in maltose for water contents in the range 5 to 20%wt confirms this prediction (van den Dries et al., 1998). On the other hand, the existence of facilitated diffusion of water because of glucose rotation explains why water diffusion is observed, albeit very slow, in carbohydrate glasses even at very low water contents (Tromp et al., 1997), below the percolation threshold for water in these systems (Molinero et al., 2004).

We did not find any evidence of free volume channels in the mixtures of water and glucose, consistent with previous results of a study for water–sucrose in a broader range of water content (Molinero et al., 2003). The existence of such channels, and the role of free volume in the dynamics of mixtures of oligosaccharides with a high degree of polymerization deserve further study. The results presented here for water relaxation in supercooled DP12 allows us to generalize the observed mechanism for water diffusion in

glasses of oligosaccharides. In these glassy mixtures, we expect the local mobility of the sugar corresponding to the rotation of the side groups and the torsional dynamics around the glycosidic bonds (corresponding to torsional modes between monomers in the M3B model) to be the ones that couple with the dynamics of water. We have shown here that the release of the rigidity on the segmental mobility of the carbohydrate has drastic effects on the mobility of water, and we expect that an increase of the rigidity of the carbohydrate molecule will decrease the mobility of water in the glass. In this respect, the lower water diffusivity in the disaccharide trehalose than in sucrose (Ekdawi-Sever et al., 2003) may be related to the higher conformational rigidity of the former. The design of preservation mixtures should consider decreasing the water content and the carbohydrate segmental mobility as ways to minimize water mobility.

Acknowledgments

The facilities of the Materials and Process Simulation Center are supported by ONR-DURIP, ARO-DURIP. In addition, the MSC is supported by MURI-ARO, MURI-ONR, DOE (ASC, FETL), NSF (CHE). NIH, Aventis Pharma, ChevronTexaco, Nissan Corp., Berlix Biopharma, and Beckman Institute.

References

- Aldous, B.J., Franks, F., and Greer, A.L. Diffusion of water within an amorphous carbohydrate, *J. Mater. Sci.*, 32, 301, 1997.
- Chan, R.K., Pathmanathan, K., and Johari, G.P. Dielectric relaxations in the liquid and glassy states of glucose and its water mixtures, *J. Phys. Chem.*, 90, 6358, 1986.
- Chatakanonda, P., Dickinson, L.C., and Chinachoti, P. Mobility and distribution of water in cassava and potato starches by H-1 and H-2 NMR, *J. Agric. Food Chem.*, 51, 7445, 2003.
- Ekdawi-Sever, N., de Pablo, J.J., Feick, E., and Von Meerwall, E. Diffusion of sucrose and alpha, alpha-trehalose in aqueous solutions, *J. Phys. Chem. A*, 107, 936, 2003.
- Feeney, M., Brown, C., Tsai, A., Neumann, D., and Deberedetti, P.G. Incoherent quasi-elastic neutron scattering from fructose-water solutions, *J. Phys. Chem. B*, 105, 7799, 2001.
- Hills, B.P. and Pardoe, K. Proton and deuterium NMR-studies of the glass transition in a 10-percent water-maltose solution, *J. Mol. Liq.*, 63, 229, 1995.
- Hills, B.P., Wang, Y.L., and Tang, H.R. Molecular dynamics in concentrated sugar solutions and glasses: an NMR field cycling study, *Mol. Phys.*, 99, 1679, 2001.
- Kou, Y., Dickinson, L.C., and Chinachoti, P. Mobility characterization of waxy corn starch using wide-line H-1 nuclear magnetic resonance, *J. Agric. Food Chem.*, 48, 5489, 2000.

- Levine, H. and Slade, L. Principles of cryostabilization technology from structure property relationships of carbohydrate water-systems — a review, *Cryo-Lett.*, 9: 1, 21, 1988.
- Magazu, S., Villari, V., Migliando, P., Maisano, G., Telling, M.T.F., and Middendorf, H.D. Quasielastic neutron scattering study on disaccharide aqueous solutions, *Physica B*, 301, 130, 2001.
- Molinero, V., Cagin, T., and Goddard III, W.A. The mechanisms of nonexponential relaxation in supercooled glucose solutions: The role of water facilitation, *J. Phys. Chem.*, 108, 3699, 2004.
- Molinero, V., Cagin, T., and Goddard III, W.A. Sugar, water and free volume networks in concentrated sucrose solutions, *Chem. Phys. Lett.*, 377, 469, 2003.
- Molinero, V. and Goddard III, W.A. Microscopic mechanism of water diffusion in glucose glasses, *Phys. Rev. Lett.*, 95 045701, 2005.
- Molinero, V. and Goddard III, W.A. M3B: A coarse grain model for the simulation of malto-oligosaccharides and their water mixtures, *J. Phys. Chem. B*, 108, 1414, 2004.
- Moran, G.R. and Jeffrey, K.R. A study of the molecular motion in glucose/water mixtures using deuterium nuclear magnetic resonance, *J. Chem. Phys.*, 110, 3472, 1999.
- Noel, T.R. and Ring, S.G. A study of the heat-capacity of starch water mixtures, *Carbohydr. Res.*, 227, 203, 1992.
- Orford, P.D., Parker, R., Ring, S.G., and Smith, A.C. Effect of water as a diluent on the glass-transition behavior of malto-oligosaccharides, amylose and amylopectin, *Int. J. Biol. Macromol.*, 11, 91, 1989.
- Parker, R. and Ring, S.G. Diffusion in maltose–water mixtures at temperatures close to the glass transition, *Carbohydr. Res.*, 273, 147, 1995.
- Roos, Y. Melting and glass transitions of low-molecular-weight carbohydrates, *Carbohydr. Res.*, 238, 39, 1993.
- Roudaut, G.L., Maglione, M., van Dusschoten, D., and Le Meste, M. Molecular mobility in glassy bread: a multispectroscopy approach, *Cereal Chem.*, 76, 70, 1999.
- Tromp, R.H., Parker, R., and Ring, S.G. Water diffusion in glasses of carbohydrates, *Carbohydr. Res.*, 303, 199, 1997.
- van den Dries, I.J., van Dusschoten, D., and Hemminga, M.A. Mobility in maltose–water glasses studied with H-1 NMR, *J. Phys. Chem. B*, 102, 10483, 1998.
- van den Dries, I.J., van Dusschoten, D., and Hemminga, M.A. Effects of water content and molecular weight on spin probe and water mobility in malto-oligomer glasses, *J. Phys. Chem. B*, 104, 10126, 2000.
- Vodovotz, Y., Dickinson, L.C., and Chinachoti, P. Molecular characterization around a glassy transition of starch using H-1 cross-relaxation nuclear magnetic resonance, *J. Agric. Food Chem.*, 48, 4948, 2000.
- Wachner, A.M. and Jeffrey, K.R. A two-dimensional deuterium nuclear magnetic resonance study of molecular reorientation in sugar/water glasses, *J. Chem. Phys.*, 111, 10611, 1999.

4

Manifestation of Molecular Mobilities in Amorphous Aqueous Systems: The View from Different Experimental Techniques

David S. Reid

CONTENTS

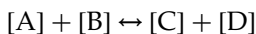
Introduction	59
Phase and State Diagrams.....	61
The Ideal.....	61
The Reality	63
Determining the Diagram.....	65
Limitations to Measurement.....	66
Calorimetric Techniques	67
Mechanical Measurements	71
Electrical Measurements	73
Relaxational Spectroscopy	74
Conclusion	75
References	75

Introduction

While the title for this presentation is quite clear, it is appropriate to provide an alternative title, which more clearly indicates the general direction that I propose to take in addressing the issues. This alternative title is “How do we locate the boundaries within our state diagrams, and what might they represent?” This alternative title is particularly appropriate for this meeting, because the utility of state diagrams in understanding the behavior of aqueous systems has been a continuing theme over many ISOPOW conferences. In order to address the topic, we must first recognize that there are two distinct scenarios that have to be considered. These are the

scenario appropriate to a system at thermodynamic equilibrium, and the scenario appropriate to a system under kinetic constraint.

Thermodynamic/equilibrium parameters describe the end point of a process, and are always the same for a given system, regardless of the route taken to arrive at the end point. Kinetic parameters describe a point in time and space, are valid only for that instant in time, and vary with conditions, history, and the many factors that have interacted to produce the system as it is at the instant of its description. At this point, it is appropriate to provide a simple example. Consider the reaction:



The thermodynamic functions that describe this equilibrium include the equilibrium constant, the enthalpy, the free energy, and the heat capacity. These are all predictable, and can be derived by a variety of routes, each route yielding the same values for the functions. The equation describing the reaction is sufficient to allow for the initiation of all appropriate calculations. In contrast, the rate of the reaction, and the temperature dependence of the rate of the reaction are inherently unpredictable, and require empirical measurement. In particular, the equation describing the reaction stoichiometry cannot, *a priori*, enable the kinetic equations to be predicted. Detailed knowledge of the reaction mechanism would be required. This distinction between the inherent predictability of equilibrium conditions, and the empirical nature of kinetic conditions, must be borne in mind when considering the phase behavior of aqueous systems.

Considering both phase diagrams and state diagrams, it must be remembered that the phase diagram describes a thermodynamic system, and as such requires a demonstration of equilibrium. It defines the “final resting points” of the system under a range of applied conditions. Each resting point is route independent. A typical phase diagram shows the phase relationships as a function of temperature and composition, and enables the description of the phases that exist, or coexist, under different conditions. The state diagram, too, describes the phases in a system. However, the state diagram does not imply equilibrium, but rather describes the phases present under different conditions after following some particular protocol. In this case, kinetic factors are involved, and the state of the system under a specified set of conditions may be route dependent. While the diagram still illustrates the phase relationships as a function of temperature and composition, now the locations of the boundaries may be both route and time dependent.

As a consequence of the kinetic nature of the state diagram, we can reach an important conclusion. While the phase diagram for a system should be independent of the techniques used to determine it (which provides an important validation mechanism), the state diagram must be expected to be dependent upon the probe technique, because the condition of the system is dependent on the sample history, and may also change with time after

establishing the final holding condition. Given this insight, the key question becomes "How do we arrive at a meaningful and useful state diagram, and how should it be interpreted?" A useful analogy for this situation is to consider traffic in a major urban area. At first, traffic may flow freely, but after a while congestion develops, followed by a traffic jam. However, the dynamics of a traffic jam depend upon the size of the vehicle. Large trucks and busses are soon stationary, while small cycles easily thread through, and pedestrians can weave their way across, should they be so inclined. Continuing with this analogy, consider how different the picture of unit motion would be for transponders located on different sizes of unit. Clearly the information obtained from phase and state diagrams differs, and the techniques required to obtain representative diagrams also differs. I propose to discuss the phase behavior of amorphous aqueous systems by first considering traditional phase diagrams, and then expanding the discussion to state diagrams.

Phase and State Diagrams

The Ideal

Consider a simple binary aqueous system. The schematic temperature–composition phase diagram appears as that in Figure 4.1a. The region above the curves AEF represents the solution phase. Curve AE delineates the temperature–composition relationship of the melting point curve. Curve EF represents the solubility curve. The line BED is the boundary below which the system is totally solid. Region ABE represents a mixture of ice and solution. Region FED represents a mixture of crystalline solute and solution. Below BED we have a mixture of ice and crystalline solute. Point E represents the eutectic point, the temperature at which, in a mixture of composition C_{E_r} , both ice and solute will co-crystallize in a ratio that is the same as their ratio in the solution phase. One might ask how such a diagram is determined. The answer is that we can do so either by maintaining a concentration, varying temperature, and plotting the temperatures at which "events" are detected. If this procedure is performed for different overall concentrations, a diagram such as Figure 4.1b is obtained. Here, experimental results from temperature scans of samples of eight separate overall concentrations (points 1 to 8 in Figure 4.1b) have allowed for the identification of a series of points at which the monitored behavior clearly shows a change in trend. The lines of the phase diagram are constructed by connecting these points. The line diagram is as in Figure 4.1a, which would indicate to the researcher that the system studied produced a standard binary phase diagram, with a eutectic point. Clearly, at least conceptually, a similar diagram could be obtained by maintaining a range of constant temperatures, and somehow varying sample concentrations at each

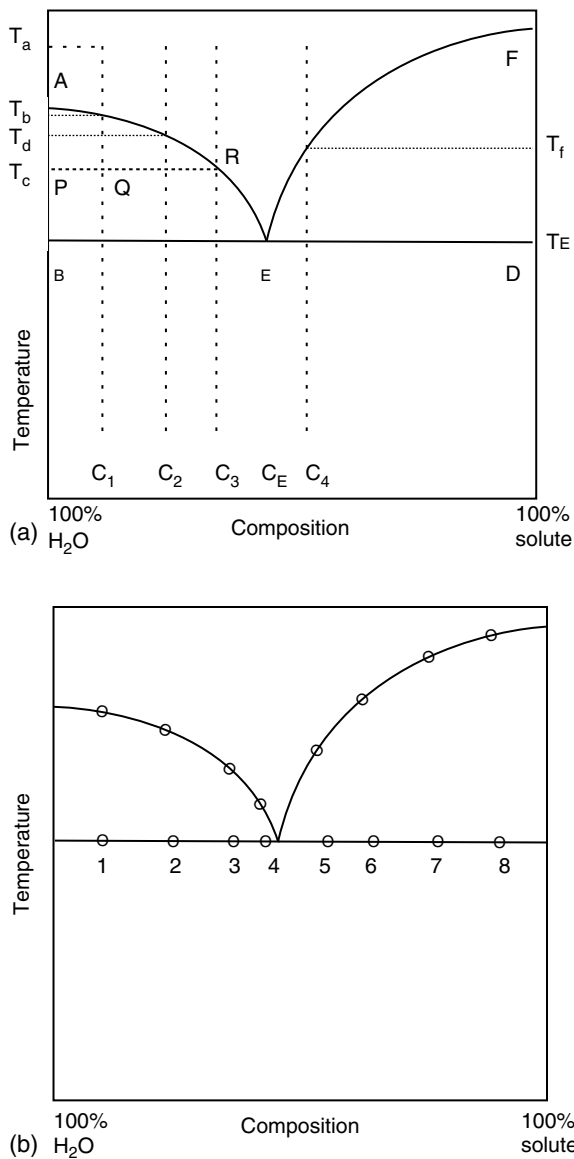


FIGURE 4.1
(a) Schematic phase diagram showing crystallization behavior of a binary aqueous system. Labels as discussed in text. (b) Binary phase diagram showing data points used to construct curves.

individual temperature to look for events. The first procedure is usually chosen because of the greater ease of experiment. Continuous scanning through a monitored range of temperatures is easier to perform than continuous scanning through a monitored range of concentrations. Observable events can be changes in heat flow, changes in mobility, or

changes in some other readily monitored parameter. These events are plotted as the temperature of their occurrence. For the phase diagram, a convenient check is that, regardless of method, the same diagram should be obtained. Consider what information can be obtained from this diagram. Assume a solution of composition C_1 (Figure 4.1a). Starting at temperature T_A , we have a homogeneous solution. On cooling to T_B , a point on the melting point curve, ice should begin to separate. While in a real system there might be undercooling, we will assume crystallization does indeed initiate (we are discussing an equilibrium diagram at this point, and undercooling is a nonequilibrium, kinetic event). As cooling continues, ice separates, and the system becomes two phase. The phases are ice (represented by a line along the Y-axis, and an aqueous solution, with concentration represented by the melting point curve. At temperature T_C , for example, the mixture is of ice and a solution of composition C_3 . The ratio of the amount of ice to the amount of solution can be calculated using the tie-line, in this case, PQR. As cooling continues, and we reach T_E , in addition to ice separating, solute will now co-crystallize, and with removal of sufficient heat, the system will completely solidify, remaining at T_E during this process. Cooling a solution of composition C_2 results in a similar process, with ice crystallization commencing at T_D . Cooling a solution of composition C_4 , greater than C_E , results in similar behavior, except that, at T_F on the solubility curve, solute will begin to crystallize, and cooling continues the solution concentration will decrease until we reach T_E , at which point ice will also crystallize.

The Reality

So much for the equilibrium process, but what happens in reality? There are many different possibilities to discuss, but first it is appropriate to consider what happens should the solute prove difficult to crystallize. Following the above scenario for ice separation, we arrive at T_E , and an unfrozen solution concentration of C_E . If solute fails to crystallize, continued cooling will result in further ice separation, and the locus of solute concentration will follow an extension of AE, as shown in Figure 4.2a. Here we are assuming that the amount of ice formed is the maximal amount of ice possible under these conditions, with inhibited solute crystallization. At some point, we reach a temperature, and solute concentration, where any further ice formation is kinetically constrained. This point would be expected to be where the melting point curve intersects the glass curve. The glass curve we define as the locus of the temperatures at which homogeneous systems of the complete range of concentrations from pure water to pure solute change from being in the homogeneous liquid state to being in the homogeneous amorphous solid state. At this intersection, in the liquid phase, viscosities and mobilities would be such that any further separation of water in a pure crystalline phase, with consequent increase in unfrozen matrix concentration, would take "eons" where the definition of the time unit "eon" is

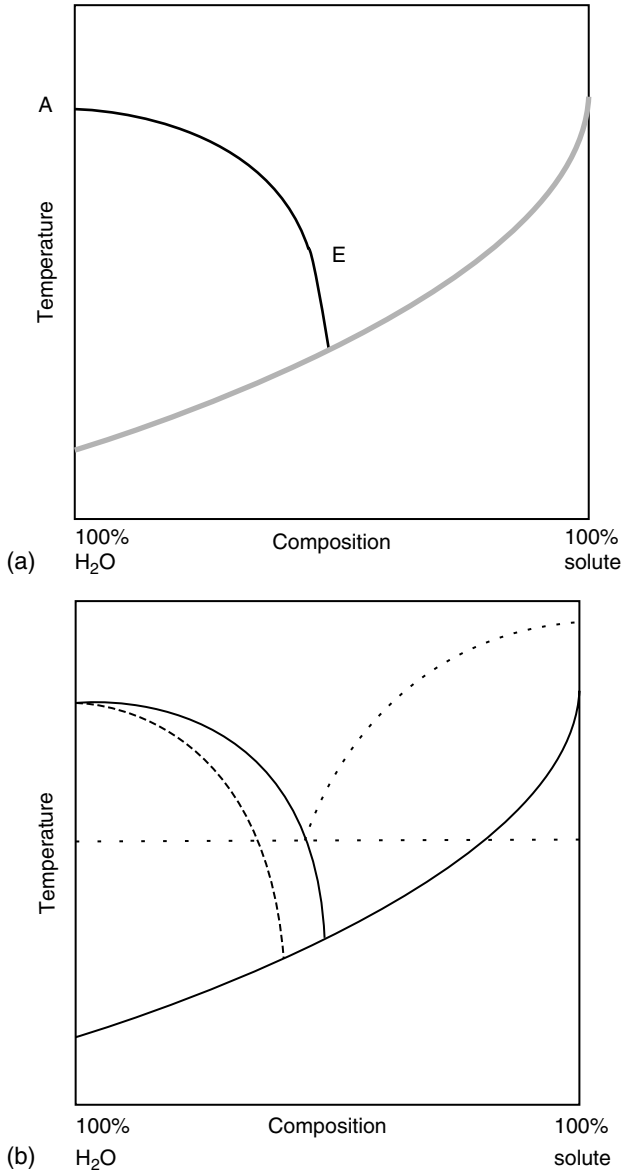


FIGURE 4.2

(a) Partial state diagram for a binary system, with solute crystallization inhibited, showing freezing curve in solid black, and the glass curve in grey. The glass curve represents the temperature of the glass transition for a homogeneous glass of the indicated concentration. (b) State diagram for a binary aqueous system. Dotted lines show the inhibited part of the binary phase diagram, and also a freezing curve, tracking at lower concentration, typical of a situation where ice formation is less than that maximally possible, indicated by the solid curve of maximal freezing.

dependent on the individual investigator. This point of intersection would define the “maximally freeze concentrated matrix” from which no more ice can be separated (unless solute crystallization becomes enabled). It is appropriate to consider this limiting system in detail, as it represents the boundary of potential ice separation in the absence of solute crystallization, and as such is a metastable state, constrained only by the failure of the solute to crystallize. Kinetic constraints may reduce the amount of ice formed within a system, but this curve of “maximum freeze concentration” represents a limiting case, and as such is the most appropriate for reporting when describing the properties of a system. Once again, location of the curve is achieved by monitoring system properties at constant composition as temperature is varied, preferably for several separate concentrations, with an alternative being compositional variation at constant temperature. Once again, temperature variation is the simpler approach. A typical limiting state diagram, as just described, is shown in Figure 4.2b. If the rate of cooling exceeds the maximum achievable rate of ice crystallization, then the unfrozen phase will be more dilute than would be the maximally freeze-concentrated phase. Here the limiting factor is the time required for solute to diffuse away from the location at which the water molecule will add to the crystalline ice phase, in contrast to the control of the location of the maximally freeze concentrated line, which is the inability of the solute to orient and form a crystalline phase. Two kinetic factors enter into the location of the more dilute unfrozen phase. The first is the rate of cooling, which can be faster than that which allows for maximal ice crystallization. The result is a more dilute phase than the maximally freeze concentrated phase at each temperature during the cooling process. The second factor involves both the temperature of storage, and time. Depending upon the temperature, solute diffusion may occur and allow for additional ice formation during storage. A dotted line in the diagram of Figure 4.2b represents just one possible pattern of unfrozen phase/temperature relationship of an infinite set, controlled by the kinetics and time–temperature history of the sample. Only the maximally freeze-concentrated state represents a metastable state that can be unambiguously defined.

Determining the Diagram

To this point, methods of determining phase and state diagrams have been only vaguely identified. It is, however, an unfortunate fact that the measuring system is an imperfect monitor of the condition of the sample. It is therefore necessary to consider the means of measurement, and to try to identify which best characterize both the state diagram and the limiting state diagram. It is also necessary to consider the effectiveness of the coupling between sample and measuring sensor, and any distortions likely to emanate from the choice of instrumental technique, or the choice of sample size. In other words, it is necessary to consider the relationship between the ideal conceptual measurement, and the real, practical measurement. Some of the

TABLE 4.1
Typical Techniques Used to Probe Phase Relationships

Technique	Measured Property
Differential scanning calorimetry (DSC)	Heat content and heat flow
Modulated or stepwise DSC	Heat content and heat flow
Dielectric thermal analysis (DETA)	Dielectric properties
Dynamic mechanical thermal analysis (DMTA)	Mechanical relaxation
Dilatometer	Volume expansion
Thermally stimulated current (TSC)	Electrical properties
Nuclear magnetic resonance (NMR)	Molecular relaxations
Electron spin resonance spectroscopy (ESR)	Molecular mobility

techniques that have been used in determining phase/state diagrams in aqueous systems are listed in Table 4.1.

Limitations to Measurement

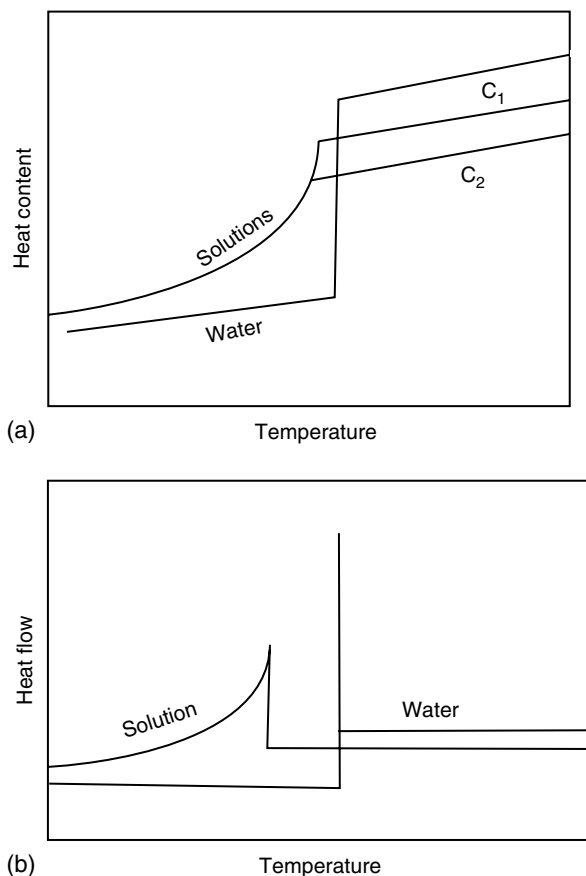
One problem that is immediately apparent on examining the literature is that, for essentially the same system, different techniques yield different results for the location of the transitions (Levine and Slade, 1991; Blanshard and Lillford, 1993; Roos, 1995; Champion et al., 2000; Levine, 2002). It is, therefore, important to have some appreciation of the reasons for these differences. There needs to be some understanding of the relationships that exist between techniques, and also some understanding of the relationship between the instrumental indicators and the actual properties and interactions within the test system. In order to compare results, it is helpful to pose a series of questions, which questions may influence the design of the experimental investigation. The first critical questions involve the apparent effects of sample concentration. A key question asks if the location of significant events appears to depend upon the overall concentration of the system. It is particularly important to identify events whose location seems independent of overall concentration. A note should be made of the temperature and time dependence of observed properties, and in particular how these properties appear to change with the rate of change of the experimentally applied conditions.

Since we are attempting to reconcile measurements made by different techniques, the artifacts, limits and constraints that accompany each technique must be identified. These include the challenges inherent in the methods of sample-sensor coupling. For example, thermal temperature or heat flow sensors are influenced by factors such as the thermal conductivity of the cell-sensor construct, the thermal resistance of the sample-cell interface, and the internal thermal properties of the sample. The geometry of the heat flow pathways is also important. Mechanical sensors (force or

displacement) may be difficult to couple to fluid samples, or the effectiveness of coupling may change with the mechanical condition of the sample. The coupling may also be a source of thermal distortion, changing the temperature profile within the sample. Remote, spectroscopic sensors may be influenced by the environment, or may influence the environment. Electrical sensors may be influenced by sample conductivity. In addition to the complex effects of coupling between sample and sensor, account must be taken of the existence of thermal inhomogeneity within the sample, and how this affects the spatial distribution of sample properties, which will influence both the overall sample average property and the bandwidth of the sample response and may also influence the potential sensor response. Given that the conditions around the sample are likely to be under dynamic change, the response rate of the sensors and of the instrument as a whole must also be considered. For these reasons, it is often appropriate to utilize several samples of significantly different size, as in so doing, manifestations of instrumental limitations and sample constraints often become obvious. The use of different temperature scanning rates, when appropriate, often provides further indications of potential artifacts linked to the rate of temperature equilibration within the sample, and to thermal lags within the instrument itself. For instruments requiring large samples, rapid change of the internal environmental temperature often produces artifacts resulting from extreme thermal inhomogeneity within the sample. It is important here to distinguish between those effects resulting from the thermal inhomogeneity, and those effects resulting from continued change in the sample because of slow kinetics of change, which would be evidenced even at a constantly maintained temperature in a sample at uniform temperature. These are better identified by either holding samples for extended periods of time, or by cycling samples through the region of the glass transformation multiple times in order to maximize potential crystallization, and approach the maximally freeze-concentrated glass. Needless to say, the separation of the effects of internal temperature inhomogeneity from the effects of time is a significant challenge of experimental design.

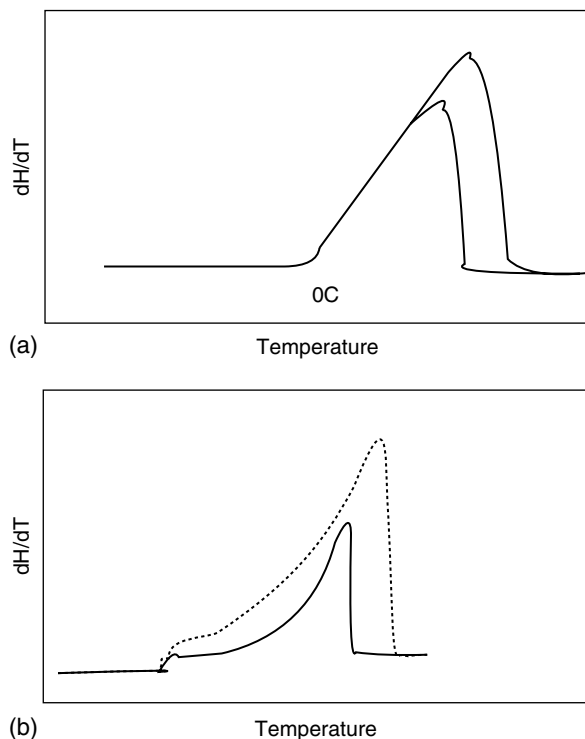
Calorimetric Techniques

Calorimetric techniques have been used most frequently to investigate the behavior of amorphous aqueous systems (Levine and Slade, 1991; Blanshard and Lillford, 1993). Based on the general state diagrams of Figure 4.2b, what might we expect the response of a calorimetric instrument to be? Figure 4.3a shows schematically the change in heat content to be expected of systems of pure water and of compositions C_1 and C_2 . The location of the glass transition is clearly visible, seen as a change in the heat capacity, or slope, as the temperature rises. The curve representing the increasing extent of ice melting as temperature increases is also clear, as is the final melting point, beyond which the heat content increases according to the heat capacity of the final solution. Based on these heat content curves, the heat capacity curves

**FIGURE 4.3**

(a) The dependence of heat content of pure water, and of solutions of concentration C_1 and C_2 , as a function of temperature (schematic). (b) Relative heat flow (proportional to heat capacity) of the pure water, and C_1 systems of figure 3a. This represents the ideal calorimetric behavior.

would be as in Figure 4.3b. These figures show what one would expect to see from an instantaneously reactive differential scanning calorimetry (DSC). However, the typical results from a DSC are shown in Figure 4.4a and b, showing the effects of sample coupling, thermal resistance and thermal lag. While in the hypothetical system, the effect of sample size would be just to change the enthalpy scale in Figure 4.3a and b, in the real instrument, there is a change in the shape of the curves, and the characteristic temperatures, as located by the instrument display, are influenced by sample size. This effect is most obvious looking at pure water. While the true behavior for samples of different size is represented in Figure 4.3b merely by changing the heat flow scale, a typical set of DSC scans for ice/water appears as in Figure 4.4a. Knowing that the melting point of pure ice is constant,

**FIGURE 4.4**

(a) Schematic illustration of the real DSC behavior to be expected for two water samples of different weight. Note that the melting process initiates at the same program temperature, and that, until melting of the smaller sample is complete, the two curves superpose. (b) Schematic illustration of the real DSC response for heating a binary system with ice. The dotted curve represents a larger sample of the same system. Note that, in this case, the melting curves do not superpose.

correction is not difficult. Extrapolating the rising slope back to the baseline yields the correct temperature. However, this correction procedure is not valid for solutions, since in these, ice does not melt at a constant temperature. Figure 4.4b illustrates the result to be expected from two samples of the same solution of different size. It is important to note here that, for a typical, real DSC scan, the total enthalpy of melting measured from the peak area above the baseline will be correct, it is the profile of the curve that is distorted. Hence, estimating the change of enthalpy with temperature by summing partial area measurements to intermediate temperatures will not yield the correct enthalpy temperature relationship describing the melting process.

Comparing the different calorimetric techniques available, conventional DSC, by its very nature, is prone to thermal lags, and hence care has to be taken in interpreting temperature information. Instrumental calibration with

known reference samples clearly overcomes some problems, but the effect of sample size remains, as do the effects of the large heat flows that accompany ice melting. A stepwise technique, where total heat flow is measured for each of a series of steps from one isothermal hold temperature to another, can yield results more closely corresponding to the true enthalpy–temperature diagram (Kerr and Reid, 1994). With this technique, the effect of sample size, and internal temperature gradients is minimized, because the initial and final states for each measurement are close to uniform temperature. Modulated DSC, (Lammert et al., 1999) in which the uniform scan has a superimposed temperature–time modulation of known frequency, allows for deconvolution into what are referred to as reversing and nonreversing heat flows. This procedure serves to make clearer features such as the glass transition. However, caution is required in the application. Because, as can be seen, the DSC response does not correspond to a linear response to the actual sample behavior, especially true for the melting process, application of linear response theories to deconvolution of DSC curves may not always be appropriate, particularly where ice melting is taking place. While data collected in a region where melting is not significant are probably robust, any melting, given the extent of heat flow, and the increase in internal thermal gradients, is likely to distort the final result. Care must therefore be taken in interpreting apparent changes in heat capacity, to ensure that the operational theory of modulated DSC is not compromised by the occurrence of melting induced thermal disequilibrium. A good test is to compare samples of significantly different size, and also to use significantly different scanning rates. If results remain consistent, they are likely to be reliable. A variety of calorimetric studies have been performed on a wide range of aqueous glass forming systems (Levine and Slade, 1986; Roos and Karel, 1991; Ablett et al., 1992; Goff, 1995; 1997). The general results show overall agreement as to the appearance of the thermal curves. Two key events have been the subject of controversy. First has been the actual location of the glass transition. After extensive debate, it is likely that the transition labeled T'_g by Levine and Slade is actually the beginning of ice melting, and is the temperature at which solute mobility first becomes great enough to allow for dilution of the amorphous aqueous phase by addition water, which is a catastrophic event indicating a transfer from kinetic constraint to thermodynamic control. The glass temperature is indeed lower, as suggested by Ablett et al. (1992) and by Roos and Karel (1991), but the temperature of significant change in molecular mobility is that identified by Levine and Slade (1986). By labeling this temperature T'_m , meaning either “incipient melting” or “the mobility temperature”, its significance can be confirmed and some of the controversy ended. The other issue is the exact location of the transformation. Different instruments, and different investigators, yield different results for nominally the same system. This may be a reflection of different inherent errors associated with different instrumental characteristics. Or it may be an indication of insufficient time taken in sample handling, such that the sample has not yet reached the limiting, maximally freeze concentrated state,

and is, therefore, reflecting an ice melting curve such as those represented by a dotted line in Figure 4.2b, with a correspondingly more dilute glass, with a lower glass transition temperature. That achieving the maximally freeze concentrated state is a nontrivial exercise is attested to by the results of many studies that have used different temperature-cycling and annealing protocols to try to achieve maximal freeze concentration. That maximal freeze concentration is a difficult state to achieve even for a small sample with the ability to be rapidly cycled in temperature (i.e. the typical DSC sample) should be borne in mind when considering experimental data obtained from other techniques that use much larger samples and that are in less effective contact with the temperature programming device.

Mechanical Measurements

A variety of mechanical measurements can also be used to locate the glass transition (MacInnes, 1993; Blond, 1994; Sahagian and Goff, 1995; Goff, 1997; Braga da Cruz et al., 2002). There are expected to be significant changes in mechanical properties as a sample transits through this zone. Note that the generic diagrams often used to illustrate the volumetric changes to be expected through both a glass transition and crystal melting (Figure 4.5a) are misleading for aqueous systems, because ice has a greater specific volume than water, and also water has a temperature of maximum density. The true position for crystalline ice is shown in Figure 4.5b. Whilst for a homogeneous aqueous glass the volumetric behavior is probably similar to that of the generic diagram of Figure 4.5a with a discontinuous increase in volume

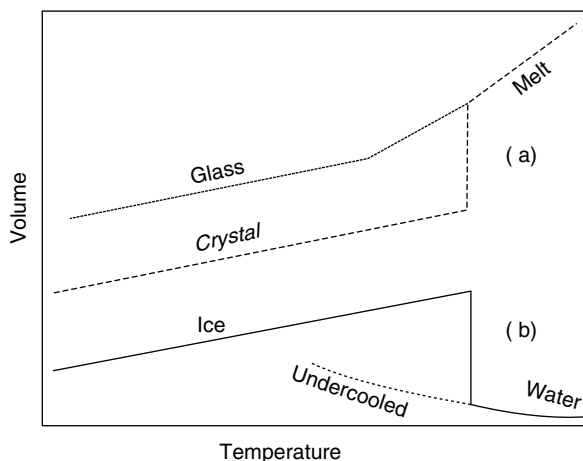
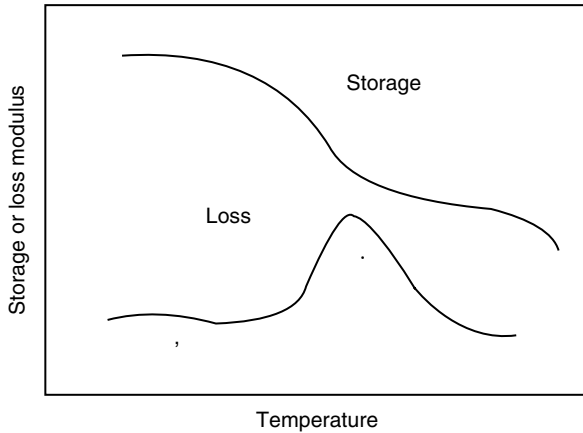


FIGURE 4.5

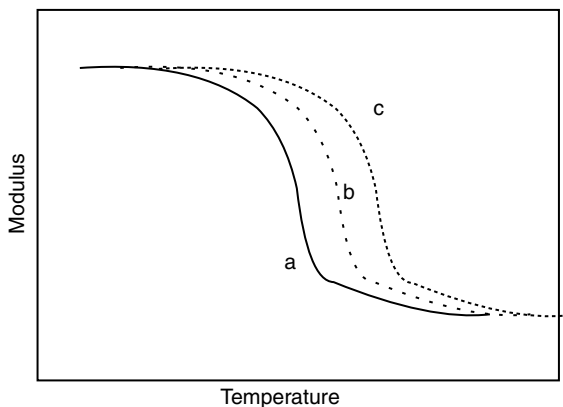
(a) Comparison of the volumetric behavior of crystallization/melting process, and a melt quench to glass. The melt quench is represented by the upper line. (b) Volumetric behavior of ice heated through melting. The dotted line tracks the behavior of undercooled liquid water.

**FIGURE 4.6**

Change of storage and loss moduli with temperature through the region of a glass transition.

expansibility at the glass transition, in an aqueous system containing ice as the temperature rises, and ice melts the volume reduction that accompanies the melting will tend to reduce expansibility. Given that the rate of increase of the fraction of ice melted as a function of temperature increases as the temperature increases, we would expect an overall volumetric behavior along the lines shown in Figure 4.5b. Figure 4.6 illustrates the expected relaxational behavior, with the loss curve showing two processes, an α process reflecting an event linked to a larger mobile species or segment, and a β process associated with a smaller, more mobile species or segment. In Figure 4.7, the effect of frequency on the storage curve is illustrated, with the temperature of the detected transition increasing with increasing frequency.

The changes in properties as a system becomes more fluid comprise a significant challenge for coupling. For expansion, the sensor must not change its location on the sample surface. For torsion type measurements, the grip must not begin to slip. Since the change is from “rigid” solid to “mobile” fluid this can be a major challenge. A common solution is to use a porous, inert substrate impregnated with the sample as to material for study (MacInnes, 1993; Braga da Cruz et al., 2002). While change in sample properties is readily seen, quantification can be a challenge, because the subtraction of the substrate contribution is not a trivial exercise. Also, the method of temperature control is challenging. Given that the mechanical sensors are physically coupled to the sample, the thermal system must not have a physical coupling to the sample, because such a coupling could distort the mechanical behavior. The thermal system tends, therefore, to be a control of the temperature of the sample chamber. This, in conjunction with the sample size, leads to a relatively slow responding system, and also significant thermal gradients within the sample. Also, there is an additional

**FIGURE 4.7**

Effect of frequency on temperature dependence of storage modulus. A is the low frequency, b is an intermediate frequency and c is a higher frequency.

challenge of preventing moisture exchange between sample and environmental chamber. Note that similar challenges related to sample size, temperature uniformity, and potential moisture redistribution may exist for some of the electrical and spectroscopic techniques used to monitor molecular mobility.

Sahagian and Goff (1995) have illustrated the use of volume and expansibility to locate the glass transition. The decrease in volume that occurs as ice begins to melt (indicative of T'_m) is quite clearly visible. Typical DMTA results, e.g. in studies by MacInnes and coworkers (MacInnes, 1993; Braga da Cruz et al., 2002), show a clear frequency dependence of the position of the glass transition, as is to be expected. A good discussion of the role of frequency in the detection of glass transitions is contained in Appendix 1 of the proceedings of the RSC conference on amorphous food and pharmaceutical systems (Roos, 1995). The challenge in comparing DMTA results with DSC results is in ascribing a characteristic frequency to the DSC measurement.

Electrical Measurements

Dielectric properties (Chan et al., 1986; Noel et al., 1996; Lourdin et al., 1998) also alter through the glass transition in a manner similar to mechanical relaxations. The behavior of the complex dielectric modulus can also be separated into a storage (capacitive) and loss (conductive) component. Figure 4.6, employed to explain mechanical relaxations, can also illustrate the ideal behavior to be expected for the dielectric properties. Note that there may be two separate events, represented by the α - and β -transitions, once again linked to the characteristics of the relaxing entity. Here we have to consider another complicating factor in the relationship between glass transitions and molecular mobility, the characteristics of the mobile species.

It has to be borne in mind that several different types of molecular mobility exist, each with its own characteristics. First we have translational mobility, then rotational mobility, vibrational mobility, and, as an additional complication, segmental mobility. When studying molecular relaxations, it can often be a challenge to unambiguously assign the appropriate relaxational process, though clearly large domains will have lower mobility than do small domains, and rotation is easier to achieve than translation. An additional instrumental challenge relates to identifying the true sample temperature, and also to distinguishing between the effects of thermal inhomogeneity and the effects of time. Given the geometry of a typical dielectric cell, there are opportunities to use sample thickness and sample diameter as variables to help sort out these two effects. In scanning instruments, characterization of the true sample temperature can be a difficult problem, and often the available scanning rates are limited. Also, data collection can be a slow process, which tends to limit kinetic studies. As with mechanical relaxation, the position of the temperature zone in which the dielectric relaxation transforms from that typical of a solid system to that typical of a mobile system is dependent upon the frequency of the applied field. Water molecules relax at very high (GHz) frequencies, and to study water relaxation in the region of the glass transformation requires very specialized equipment. Fourier transform (time domain) methods are the most promising, as data can be collected rapidly, enabling kinetic change to be monitored. However, electrical conductivity in a sample limits the effectiveness of time domain methods.

Relaxational Spectroscopy

Spectroscopic relaxation techniques such as ESR and NMR are powerful probes of molecular mobility, and can provide useful information (Hemminga et al., 1999; Le Meste et al., 1999). As noninvasive techniques, there is little problem in the coupling of the sensor to the sample, because, unlike the techniques discussed up to this point, there is no requirement for direct contact between the sample and the sensor system. The challenges of producing temperature uniformity within the sample still exist. Measuring sample temperature can also be a problem, as in some cases the thermal probe can interfere with the spectroscopic measurement. Once more there is a challenge in the identification of the species whose relaxation is being monitored, and also in identifying the exact nature of the relaxation process. The size of the molecular species, or the molecular segment that is being monitored will influence the temperature at which a mobility increase is seen, since the temperature of restricted motion is in part a function of molecular weight, with small species retaining mobility at temperatures much lower than that for large species, and side chain motions being retained at temperatures below those at which the main chain exhibits significant mobility.

Conclusion

The location of the position of the glass transition, and the estimation of changes in molecular mobility, remains a challenge. It is difficult to distinguish between the effects of instrumental limitations, and real kinetic effects within the sample. The best approach is to use a wide range of sample sizes, sample concentrations, and test conditions, and also to compare results from a variety of techniques, and from a variety of instruments. While the properties of the maximally freeze-concentrated matrix are expected to be reproducible, proof that this state has actually been produced is difficult to achieve. There is material for argument and discussion sufficient for many future ISOPOW meetings.

References

- Ablett, S., Izzard, M.J., and Lillford, P.J. Differential scanning calorimetric study of frozen sucrose and glycerol solutions, *J. Chem. Soc. Faraday Trans.*, 88, 789, 1992.
- J.M.V. Blanshard and P.J. Lillford, eds., *The Glassy State in Foods*, Nottingham University Press, Loughborough, UK, 1993.
- Blond, G. Mechanical properties of frozen model solutions, *J. Food Eng.*, 22, 253, 1994.
- Braga da Cruz, I., MacInnes, W.M., Oliveira, J.C., and Malcata, F.X. Supplemented state diagram for sucrose from dynamic mechanical thermal analysis, *Amorphous Food and Pharmaceutical Systems*, H. Levine, ed., Royal Society of Chemistry, Cambridge, UK, pp. 59, 2002.
- Champion, D., Le Meste, M., and Simatos, D. Towards an improved understanding of glass transition and relaxations in foods: molecular mobility in the glass transition range, *Trends Food Sci. Technol.*, 11, 41, 2000.
- Chan, R.K., Pathmanathan, K., and Johari, G.P. Dielectric relaxations in the liquid and glassy states of glucose and its water mixtures, *J. Phys. Chem.*, 90, 6358, 1986.
- Goff, H.D. The use of thermal analysis in the development of a better understanding of frozen food stability, *Pure Appl. Chem.*, 67, 1801, 1995.
- Goff, H.D. Measurement and interpretation of the glass transition in frozen foods, *Quality in Frozen Food*, M.C. Erickson and Y.-C. Hung, eds., Chapman Hall, New York, 1997, Chap. 3.
- Hemminga, M.A., Van den Dries, J., Magusin, P.C.M.M., van Dusschoten, D., and van den Berg, C. Molecular mobility in food components as studied by magnetic resonance spectroscopy, *Water Management in the Design and Distribution of Quality Foods*, Y.H. Roos, R.B. Leslie and P.J. Lillford, eds., Technomic, Lancaster, PA, pp. 255, 1999.
- Kerr, W.L. and Reid, D.S. The use of stepwise DSC for thermal analysis of foods, *Thermochim. Acta*, 246, 299, 1994.
- Lammert, A.M., Lammert, R.M., and Schmidt, S.J. Physical aging of maltose glasses as measured by standard and modulated DSC, *J. Therm. Anal. Calorim.*, 55, 949, 1999.
- Le Meste, M., Champion, D., Roudaut, G., Contreras-Lopez, E., Blond, G., and Simatos, D. Mobility and reactivity in low moisture and frozen foods, *Water*

- Management in the Design and Distribution of Quality Foods (Isopow 7)*, Y.H. Roos, R.B. Leslie and P.J. Lillford, eds., Technomic, Lancaster, PA, pp. 267, 1999.
- H. Levine, ed., *Amorphous Food and Pharmaceutical Systems*, Royal Society of Chemistry, Cambridge, UK, 2002.
- Levine, H. and Slade, L. A polymer physico-chemical approach to the study of commercial starch hydrolysis products, *Carbohydr. Polym.*, 6, 213, 1986.
- Levine, H. and Slade, L. *Water Relationships in Foods*, Plenum Press, New York, 1991.
- Lourdin, D., Ring, S.G., and Colonna, P. Study of plasticizer-oligomer and plasticizer-polymer interactions by dielectric analysis: maltose-glycerol and amylose-glycerol-water systems, *Carbohydr. Res.*, 306, 551, 1998.
- MacInnes, W.M. Dynamic mechanical thermal analysis of sucrose solutions, Chap. 11, *The Glassy State in Foods*, J.M.V. Blanshard and P.J. Lillford, eds., Nottingham University Press, Loughborough UK, 1993.
- Noel, T.R., Parker, R., and Ring, S.G. A comparative study of the dielectric relaxation behavior of glucose, maltose, and their mixtures with water in the liquid and glassy states, *Carbohydr. Res.*, 282, 193, 1996.
- Roos, Y.H. *Phase Transitions in Foods*, Academic Press, San Diego, CA, 1995.
- Roos, Y. and Karel, M. Amorphous state and delayed ice formation in sucrose solutions, *Int. J. Food Sci. Technol.*, 26, 553, 1991.
- Sahagian, M.E. and Goff, H.D. Thermal, mechanical, and molecular relaxation properties of stabilized sucrose solutions at sub-zero temperatures, *Food Res. Int.*, 28, 1, 1995.

Part 2: Role of Water in Structural and Functional Properties: From Microscopic to Macroscopic Properties

5

The Effect of Microstructure on Solvent and Solute Diffusion on the Micro- and Nanolength Scales

Anne-Marie Hermansson, Niklas Lorén, and Magnus Nydén

CONTENTS

Introduction	79
Length Scales of Gels and Emulsions.....	81
Emulsions	82
Gels.....	83
Mass Transport Studies Using a Combination of Microscopy and	
NMR Diffusometry.....	85
Diffusion in Heterogeneous Materials.....	86
General Features of Emulsions and Gels.....	89
Microstructure-Based Modeling of Water Diffusion.....	91
Microstructure	91
Calculation of the Propagator.....	92
Comparisons between Microstructure-Based Diffusion	
Calculations and NMR Diffusometry	93
Probe Diffusion.....	95
Acknowledgments	97
References	98

Introduction

Many products are composed of heterogeneous structures of vital importance to properties such as the diffusion of water and soluble compounds, release of active compounds, behavior of molecules in complex structures, consistency, microbial growth, water binding, etc. Yet there is a lack of knowledge about how to use microstructure design to tailor-make

TABLE 5.1
The Importance of Structure-Related Diffusion Properties

Properties	Applications
Release of compounds	Biological tissues
Drug adsorption	Drugs
Flavor release	Foods
Water management	Packaging material
Microbial growth	Rocks and soil
Barrier properties	Diaper and hygiene tissues
Consistency	Biofilms
Stability	Chromatographic separation
Separation	Paints

properties related to water management. One reason is that we know too little about how a certain complex structure affects the mass transport in relation to heterogeneity or connectivity over a wide range of length scales. We also lack techniques for approaching time-dependent structural changes and interactions between the material and the solvents or solutes.

A number of important properties that have a strong influence on a variety of industrial applications are listed in Table 5.1. There are many aspects to consider when it comes to the desired properties in the different applications, and an understanding of several of the listed properties is needed for each application. The typical length scales present in the structure determine both rapid water uptake and release, and water holding, diffusion and molecular mobility of soluble compounds. Because most structures are heterogeneous we need to know how the different parts of the aqueous domains contribute to the overall property over a wide range of length scales. In many structured products water management includes several mass transport mechanisms such as hydrodynamic flow, capillary flow, and molecular self-diffusion depending on the length scale. Hydrodynamic flow is active in large and open structures and it is ultimately driven by differences in the chemical potential, i.e., differences in concentrations at different locations in the structure. Fick’s Law describes the flux induced by the concentration differences (Cussler, 2003). Moreover, hydrodynamic flow can also be driven by external forces such as gravity or flow induced during the manufacturing process. Capillary flow occurs in channels and pores mainly on shorter length scales than hydrodynamic flow and it is driven by the surface tension. Molecular self-diffusion is a random-walk process that is governed by Brownian motion because of the thermal fluctuations that always exist in the solution.

The kinetics of water transport has a major impact on many applications. Very rapid kinetics of fluid uptake is vital for products such as diapers and hygiene tissues, whereas controlled swelling and subsequent dissolution are

more important for drugs for oral intake. Here we need to develop new measuring techniques for fast kinetics to follow structural changes from the dry state to the functional structure in the wet state. When considering mass transport in a heterogeneous structure we need to take the time-dependent structural changes, i.e., the structure dynamics into account. A structure consisting of a supramolecular matrix in which water diffusion takes place is not likely to be static, even if most microscopy has until now visualized static situations. Moreover, interactions with the surrounding matrix will also influence the kinetics of mass transport.

The combination of advanced new technologies opens up new avenues for determining the structural distribution of water and its effect on product properties. In this paper we will present a new approach to combining microscopy, nuclear magnetic resonance (NMR) diffusometry, and finite element calculation in order to elucidate the effect of the microstructure on solvent and solute diffusion over a range of length scales (Hagslätt et al., 2003; Lorén et al., 2005). This makes it possible to determine how heterogeneity, connectivity and shape, etc. affect mass transport rates of probes of different size, shape and interaction potential with the material. We also want to illustrate the relevance of length scales to the morphology of heterogeneous gels and emulsions and some useful methods for their characterization.

Length Scales of Gels and Emulsions

It is necessary to use a combination of microscopy techniques to cover the relevant length scales of a heterogeneous structured product. A number of microscopy techniques are listed in Table 5.2. Even if the focus is on the micro- and nanoscales, it is wise to start a structure characterization on

TABLE 5.2
Microstructure Characterization on Different Length Scales

Microscopy Technique	Length Scale
<i>Macroscopy</i> : bulk specimen	2×10^{-2} to 1×10^{-4} m
<i>NMR microscopy</i> : micro- and macroimaging	$\sim 5 \times 10^{-6}$ m
<i>Light microscopy</i> : smears, cryosections, plastic sections	2×10^{-3} to 5×10^{-7} m
<i>CLSM</i> : bulk specimen, cryosections, dynamic structures	2×10^{-3} to 5×10^{-7} m
<i>Scanning electron microscopy</i> — <i>SCEM</i> , <i>LVSEM</i> , <i>ESEM</i> : critical point drying, cryo-SEM uncoated wet samples, dynamic structures	2×10^{-3} to 5×10^{-9} m
<i>Transmission electron microscopy</i> : thin-sectioning, negative staining, freeze etching, mica-technique, cryo-TEM	2×10^{-5} to 5×10^{-9} m
<i>Atomic force microscopy</i>	$\sim 2 \times 10^{-5}$ to 3×10^{-9} m

the macroscale. Macro pores and cracks are often present, and they will have a significant effect on mass transport properties. They can be an incidental effect of processing, but they may also be deliberately introduced to enhance hydrodynamic flow and water uptake or as defects to enhance fracture properties.

Emulsions

Both the light microscope (LM) and the confocal scanning laser microscopy (CLSM) operate in the micron range. The advantage of the CLSM is that it allows for measurements of dynamic events such as crack propagation and three-dimensional reconstructions. Moreover, the optical resolution in the CLSM is about 40% better than in the LM. The CLSM also makes it possible to study bulk samples with a minimum of preparation, which is quite important when handling multiphase colloidal structures such as emulsions.

Many emulsions have droplets and structural features such as interfacial arrangements on the nanoscale that require electron microscopy, but the examples given here will only deal with structures of emulsions in the micron range. Figure 5.1 shows two-dimensional CLSM images of commercial spreads, where the fat phase is stained to make it fluorescent. The fat phase, therefore, appears bright in the images and the water phase appears dark.

The emulsions are quite different in character. The spread to the left has a very open structure that appears bicontinuous, whereas the spread to the right is fat continuous with spherical or elongated pores of varying pore size distribution. The structure in the middle is also fat continuous, but the structure is very heterogeneous. The bigger aqueous domains have irregular shapes and one can suspect that there is some degree of connectivity between the aqueous domains that cannot be revealed in the two-dimensional image. The smaller pores cannot be clearly seen at this magnification, but they appear spherical and enclosed in the bright fat phase. This structure shows many of the features of interest such as heterogeneity, connectivity and pore sizes of various shapes, and a large size distribution. It has, therefore, been used as a

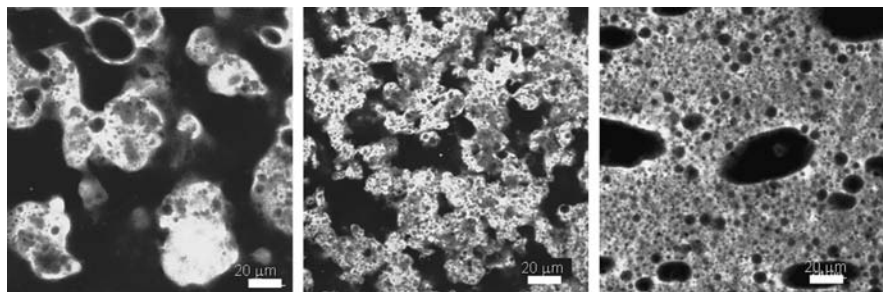


FIGURE 5.1

CLSM images of three different commercial spreads.

model system for the combined microscopy–NMR diffusometry approach and will be discussed in more detail later.

Gels

Gel networks cover a very wide range of length scales from the micron to the nanometer scale. Particulate gels, as for example the milk protein network in yoghurt or whey protein gels in the isoelectric pH region, are composed of clusters of aggregated protein particles that can easily be seen in an LM or a CLSM. These clusters often have an internal aggregated protein structure that requires electron microscopy for more detailed information (Langton and Hermansson, 2001; Olsson et al., 2002a). Figure 5.2 gives examples of the distribution of phases in mixed biopolymer gels on the micron scale. Figure 5.2a,b shows phase-separated gelatin/maltodextrin gels, where the structure in Figure 5.2a is bicontinuous and Figure 5.2b shows a discontinuous, so-called water-in-water emulsion of the same mixture but of a different composition (Lorén et al., 2001). Figure 5.2c,d shows particulate β -lactoglobulin gels. The change in aggregation of the whey protein network after addition of nongelling amylopectin is shown in Figure 5.2d (Olsson et al., 2002b). Figure 5.2 illustrates how the morphology of mixed biopolymer gels can be tailor-made.

Transparent gels, on the other hand have a network structure within the nano range. Proteins outside the isoelectric region and most polysaccharide gels have nanoscale networks that require electron microscopy. Even so, there are large variations in length scales, as illustrated in Figure 5.3. The superabsorbent is used in diapers, where the requirements for rapid water uptake and water holding are very high. This gel has a very dense network structure with pores in the range of 10 nm. The Sepharose gel is based on agarose and used as gel beads in gel chromatography, where controlled diffusion of molecules is desired in order to differentiate between molecules of different sizes and charges. This gel has a heterogeneous structure and pore sizes a factor of 10 bigger than in the superabsorbent gel. Amylose, together with amylopectin, forms the structure of starch. Amylose gels have a very open gel structure with pore sizes of several hundreds of nanometers. The amylose superstrands are probably composed of helical structures

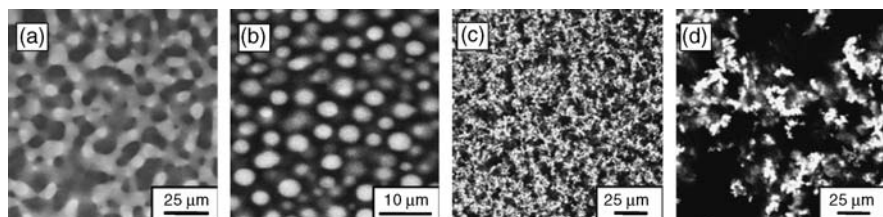
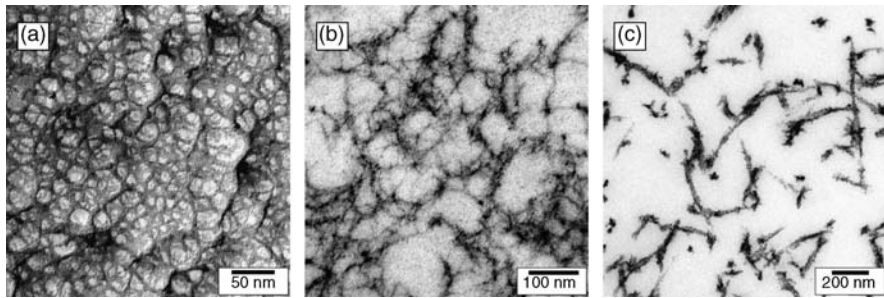


FIGURE 5.2

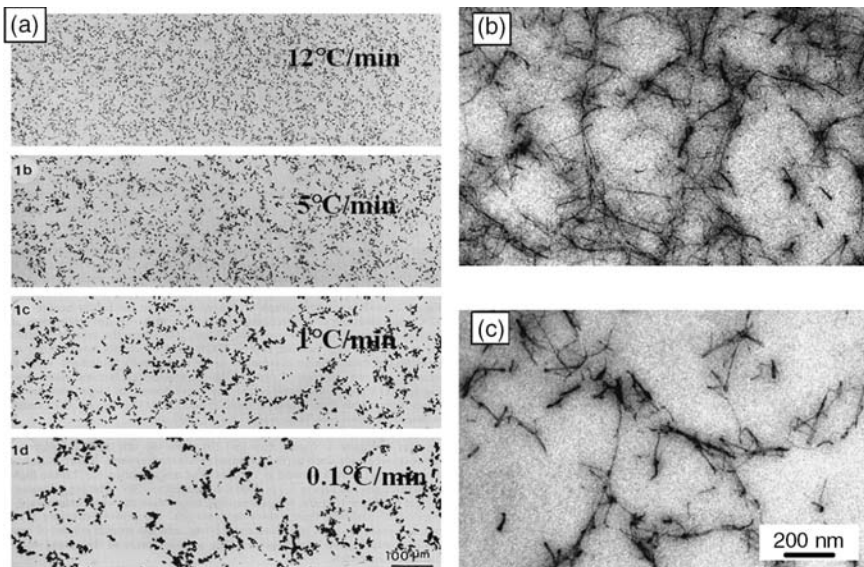
CLSM images of mixed biopolymer gels.

**FIGURE 5.3**

Transmission electron microscope (TEM) images of (a) a freeze etched replica of a superabsorbent, (b) a thin section of a Sepharose gel, and (c) a thin section of an amylose gel.

aggregated into a stiff, rod-like network structure (Leloup et al., 1992; Hermansson, 1995).

As illustrated in Figure 5.2, a gel structure can be modified by changing its composition. It is also possible to tune the structure and thereby the diffusion as well as other properties just by changing the kinetics without altering the composition of the system. This can be illustrated both on the nano- and the microscale of biopolymer gels. β -Lactoglobulin form aggregated gels on heating, and the heating rate will strongly affect the state of aggregation and the final gel structure (Stading et al., 1993). Figure 5.4a shows β -lactoglobulin

**FIGURE 5.4**

(a) Light micrographs of 10% β -lactoglobulin gel at pH 5.3 heated to 90° at different heating rates. (b) TEM micrographs of 1% κ -carrageenan, 100 mM KCl, 200 mM NaCl fast cooling. (c) TEM micrographs of 1% κ -carrageenan, 100 mM KCl, 200 mM NaCl slow cooling.

gels at pH 5.3 formed under exactly the same conditions but at different heating rates. These are light micrographs, and there are very big differences in the particle and pore size distribution depending on the heating rate. The scale bar is 100 μm , and pore sizes above that size are formed at very low heating rates. These differences induced by the heating rate have pronounced effects on the rheological behavior of the gels (Stading et al., 1993).

Kinetic effects can also affect gel formation on the nanoscale. κ -Carrageenan form gels on cooling. Potassium promotes coil-helix transitions and aggregation of κ -carrageenan, and synergistic effects can be achieved by a mixture of cations (Rochas and Rinaudo, 1984; Hermansson, 1989; Hermansson et al., 1991). Figure 5.4b,c shows a clear example where a slow cooling rate gives rise to a more aggregated and open network structure on the nanoscale of a 1% κ -carrageenan gel in a mixture of potassium and sodium ions.

These results illustrate the possibilities for tuning the network structure and thereby its properties relating to mass transport of solvents or solutes. Differences in the microstructure have been qualitatively related to water-holding properties mainly under hydrodynamic flow conditions. Studies of coarse aggregated protein gels have shown that an increase in the coarseness and pore size in the range of 0.2 to 2 μm resulted in a pronounced loss of water-holding capacity (Hermansson, 1986). For large pore sizes in the micron range, permeability studies give information on the hydrodynamic flow and diffusion in gel networks (Bremer, 1992; Mellema et al., 2000). However, we still lack information on how the heterogeneity over length scales from the nano- to the micrometer regime comes into play when it comes to mass transport of solvents or solutes. This information is important for a complete understanding of the relationships between the microstructure and mass transport.

Mass Transport Studies Using a Combination of Microscopy and NMR Diffusometry

A new approach combining microscopy, image analysis, mathematical modeling, and NMR diffusometry has been recently presented to explain how the microstructure of supramolecular structures products governs mass transport and diffusion (Hagslätt et al., 2003; Lorén et al., 2005). In particular, we have for the first time performed diffusion calculations on microscopy images obtained from very complex and heterogeneous materials. By combining techniques it will be possible to predict and control diffusion properties in supramolecular structured gels and complex emulsions. An important task is to determine the effects of complex structural parameters such as heterogeneity, connectivity and shape of pores over several length scales on diffusion properties of probe molecules of different sizes and

shapes and interactions with the material. In this paper we will demonstrate the technique on a heterogeneous emulsion structure and discuss diffusion in gels and emulsions on micro- and nanoscales.

Diffusion in Heterogeneous Materials

The time series in Figure 5.5 illustrates how the heterogeneity of the emulsion affects water diffusion. The aqueous phase is black, and an area of artificially labeled water molecules is monitored over time as they diffuse in the structure. With no restrictions there will be a Gaussian concentration distribution as in the domain at the bottom of the figure, at least when considering diffusion along a horizontal line. If the pores are closed and small, as demonstrated in the middle small water domain, diffusion is restricted and steady state is reached. Bottlenecks, connectivity and the shape of the aqueous domain will also have an effect on the diffusion, as shown in the upper part of the figure where diffusion is restricted in one direction and strongly influenced by a bottleneck in the opposite direction. Consequently, it is hardly surprising that structure entities such as connectivity, dimensionality, heterogeneity, shape, and pore size distribution are important for the diffusion process.

Diffusion can be conveniently divided into free and restricted diffusion as schematically illustrated in Figure 5.6. Free diffusion is described by a random-walk process where all directions have the same probability of occurring. The probability of finding a molecule at a certain position after being released at $t = 0$ is then Gaussian distributed around the starting position, and the probability of finding a molecule at a certain position depends on how long the molecules have diffused and how fast they diffuse. If we perform a NMR diffusometry experiment on molecules in a solution with free diffusion, then the experiment gives the diffusion coefficients as a result.

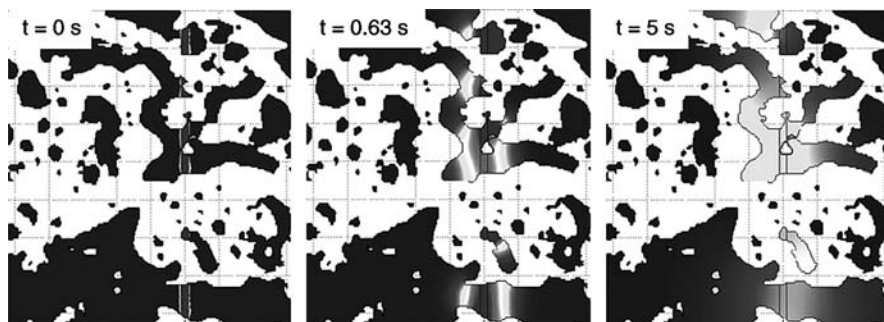
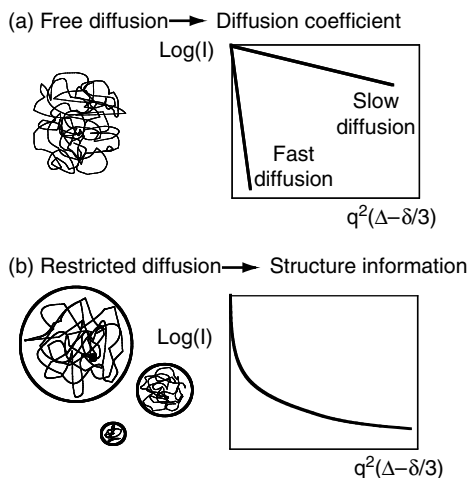


FIGURE 5.5

Simulation of artificially labeled water molecules diffusing into a heterogeneous spread as a function of time.

**FIGURE 5.6**

Free and restricted diffusion and its effect on the echo attenuation.

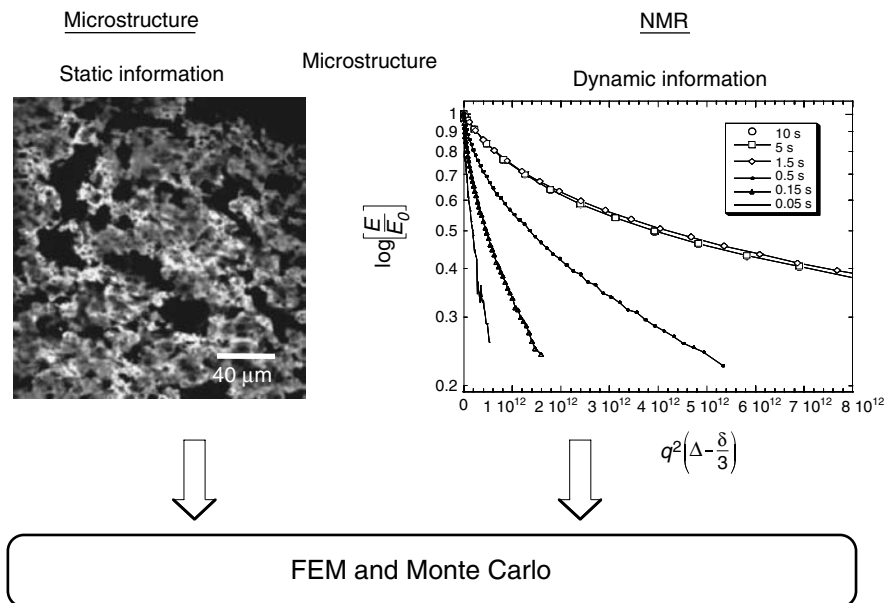
For this NMR diffusometry experiment the echo intensities for free diffusion is given by (Balinov et al., 1993):

$$\ln \left[\frac{E}{E_0} \right] = -q^2 D \left(\Delta - \frac{\delta}{3} \right) \quad (5.1)$$

where E and E_0 are the echo intensities at the time of the echo maximum in the presence and absence of gradient pulses, respectively. Furthermore, $q = \gamma g \delta$ where γ is the nuclear gyromagnetic ratio, g , the strength of field gradient and δ , the length of the gradient pulse. D is the self-diffusion coefficient and Δ is the time between the gradient pulses. It is assumed that the relaxation term is constant, and it is therefore included in E_0 . Consequently, by plotting the intensity as a function of $q^2(\Delta - \delta/3)$, we obtain the slope as the diffusion coefficient.

In contrast, when diffusion is restricted, the probability of finding a molecule at a certain position in the sample is strongly dependent on the geometry of the material. Furthermore, intermolecular interactions and the dynamics of the surrounding material can influence the rate of diffusion. NMR diffusometry experiments performed on systems showing restricted diffusion produce a large amount of structural information, although in an averaged and convoluted form.

Microscopy generally gives static information about the microstructure in which molecules diffuse for a wide range of length scales in both two- and three-dimensional and for nearly all kinds of materials. NMR diffusometry gives dynamic information about diffusion rates of molecules. When these techniques are brought together, synergistic effects are obtained, and the combination allows a much deeper understanding of the diffusion mechanisms of molecules in complex structures (see Figure 5.7).

**FIGURE 5.7**

The main concept of a combination of microscopy and NMR techniques.

The fact that the microstructure is heterogeneous is very important, because it means that the diffusion behavior varies from one part of the microstructure to another. For instance, in dense parts, the diffusion is slower than in open parts. Diffusion simulations by finite element methods (FEMLAB[®]) and Monte Carlo methods make it possible to combine microscopy and NMR diffusometry in a qualitative and quantitative manner.

NMR diffusometry is a suitable tool for measuring self-diffusion in restricted and unrestricted geometries (Callaghan, 1991). The basic theory and practical aspects have been thoroughly reviewed (Price, 1997, 1998). It is well established that the time-dependent diffusion coefficient and mean square displacement of a fluid imbibed in a porous matrix contain information about surface-to-volume ratio, pore size, and tortuosity (Callaghan et al., 1991; Mitra et al., 1992; Latour et al., 1993, 1995; Hürlimann et al., 1994). Physical models of the diffusion of molecules in polymer solutions, gels and solids have been reviewed previously (Masaro and Zhu, 1999). Early NMR studies of emulsions include work in which the apparent water diffusion coefficient was related to the permeability of water through the oil and surfactant film (Balinov et al., 1996). Pulse-train techniques have been used to investigate the frequency-dependent diffusion coefficient (Topgaard et al., 2002). Furthermore, compartment size has been determined by q -space diffusion diffractograms (Håkansson, 1999). It has been found that local

diffusion rates, restrictions due to interfaces and diffusion of the droplets themselves must be considered when determining the correct size distribution of the emulsion droplets (Garasanin et al., 2002). Regularization methods have also been used to determine the emulsion droplet size distribution (Hollingsworth and Johns, 2003). Although they are very powerful methods for structure determination, it should be emphasized that it is impossible to obtain structural information from NMR diffusometry data alone — this always requires a structural model, e.g., the assumption of spherical emulsion droplets.

The properties of food products such as margarine or low-fat spreads are extremely dependent on the droplet size distribution. Water and fat diffusion in cheese have been studied in this context (Callaghan et al., 1983) and the size distribution of water droplets in margarine products has been measured (Van den Enden et al., 1990). The Gaussian phase distribution (GPD) approximation has been used to determine the size distribution of water droplets in margarine and low-fat spreads (Balinov et al., 1994). NMR diffusometry studies have been compared in some cases with results from image analysis (Fourel et al., 1995). However, up to now, most studies assume that the emulsion droplets are more or less spherical.

General Features of Emulsions and Gels

One objective has been to choose model systems that have a close connection with materials of interest for a variety of applications. Heterogeneous emulsions and gels have been used as our two model systems, as shown in Figure 5.8. The heterogeneous emulsion was a commercially available spread from Arla Foods with a wide pore size distribution with water domains of about 0.5 μm up to 200 μm in diameter, and irregularly shaped water domains that are connected through different kinds of bottlenecks in three dimensions.

A number of gels of varying length scales and heterogeneities such as amylose, β -lactoglobulin, superabsorbents and κ -carrageenan were characterized (see Figure 5.3 and Figure 5.4). Most of the initial work was performed on commercially available sepharose gels (from Amersham Biosciences) and κ -carrageenan, both having a wide pore size distribution with pores ranging from about 10 nm up to 300 nm in diameter, and an irregular gel strand network.

The aim was to develop a general concept that could be applied to most materials of varying length scales and heterogeneity. Binary systems can be generally discussed in terms of a two-phase model, which is illustrated on two different length scales by the emulsions and gels shown in Figure 5.9. This is a simplified two-phase system that can serve as a basis for discussion. Imagine a molecule that starts at a random position inside one of the phases, Ω_A in Figure 5.9. Note that the molecule is only allowed to move horizontally in Figure 5.9 in order to make the discussion simple. Then the molecule moves in a certain random horizontal direction. After a while, the molecule

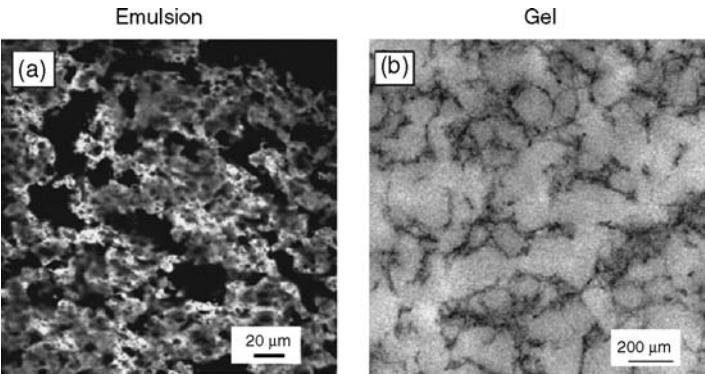


FIGURE 5.8
Model systems: (a) CLSM micrograph of a heterogeneous emulsion. The bright phase is the fat phase; (b) TEM micrograph of a heterogeneous sepharose gel.

will pass a phase boundary, S , and continue into the other phase, Ω_B . Subsequently, the molecule will remain for a while in phase Ω_B moving in random horizontal directions and occasionally it will pass the phase boundary, S , and continue into phase Ω_A , either on the same side or on the opposite side. This model is valid for all kinds of two-phase systems. In emulsions there are oil and water phases, and in gels there are liquid and “solid” phases containing the gel strands. Therefore, this simple model serves as a discussion basis for a comparison between the emulsion and gel model systems.

As previously pointed out, the length scales in emulsions and gels differ considerably. The length scale is in most cases much shorter in gels than in emulsions. This means that the contact area or the interfacial area between the phases and the probability of a molecule coming close to a phase boundary are much larger in gels than in emulsions. Therefore, the effect of

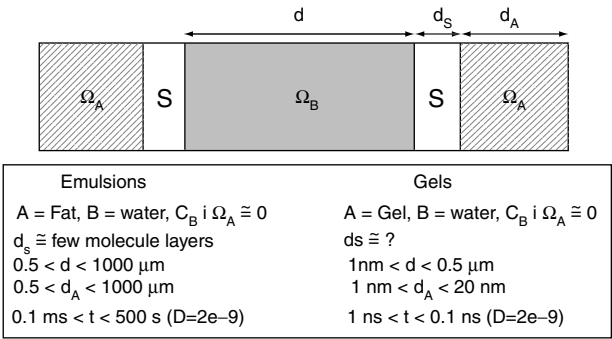


FIGURE 5.9
Simple model for comparisons between emulsions and gels.

interactions at phase boundaries becomes more pronounced in gels than in emulsions and interactions should be taken into account in the modeling of the diffusion behavior in gels. Furthermore, interactions constitute another effect that can be used to control diffusion properties in applications based on gels. The average time, t , for a diffusing molecule to encounter the boundary is indicated in Figure 5.9. It can be seen that the diffusing molecules hit the surrounding gel strands nearly instantaneously given the length scales presented in Figure 5.9 and the diffusion coefficient of water. Thus molecules will hit a large number of gel strands in a very short time by diffusing in between, over and under the gel strands. The NMR diffusometry response to such a situation is a diffusion coefficient given by the rate of free diffusion and the obstructing effect from the gel. In such systems where diffusion in one dimension depends on the three-dimensional structure, diffusion simulations must also be performed in three dimensions to enable quantitative comparison between NMR results and simulations based on microscopy images.

In contrast, in emulsions it can be seen that the molecules encounter the boundaries after parts of seconds given the length scales presented in Figure 5.9 and the diffusion coefficient of water. This means that the effect of dimensionality and connectivity is not so pronounced for emulsion systems as for gel systems on a short time scale. However, the effects of dimensionality and connectivity increase over longer time scales.

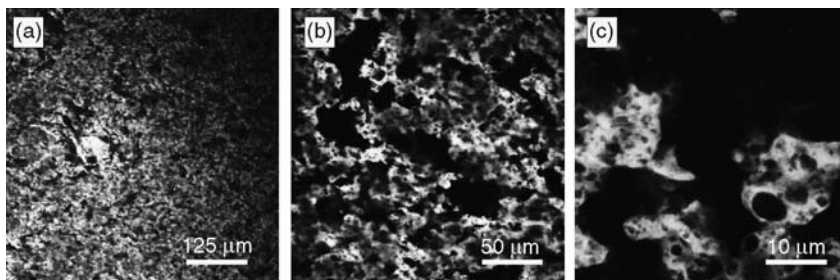
By changing the diffusion time it is possible to find an experimental window that allows for calculations of structure-related diffusion. During shorter diffusion times, the effect of dimensionality and connectivity is small and it is possible to perform calculations in two dimensions without losing too much information. However, during long diffusion times, the effect of dimensionality and connectivity increases and a three-dimensional description of the microstructure is needed.

Microstructure-Based Modeling of Water Diffusion

In this section we will demonstrate calculations made from two-dimensional images of the emulsions and how they relate to experimental NMR measurements on short time scales. The new methodology has recently been described in detail by Lorén et al. (Lorén et al., 2005).

Microstructure

The microstructure of the emulsion is shown at three different magnifications in Figure 5.10. It can be seen that the pore size distribution of the water domains ranges from hundreds of micrometers down to half microns, and that the water domains have irregular shapes and a connected structure. It was necessary to use at least three different magnifications to describe the morphology appropriately. A collection of 15 CLSM micrographs was acquired at low magnification ($16\times$) and put together in order to display the

**FIGURE 5.10**

CLSM micrographs that show the microstructure of the heterogeneous emulsion used in this work at three different magnifications. Magnification (a) 16 \times ; (b) 40 \times ; and (c) 200 \times . The bright phase is the oil phase and the dark phase is the water phase.

largest water domains in the emulsion. The shape of the water domains changes considerably with size. Basically, small water domains have a rather spherical shape and large water domains have a very irregular shape. Another feature of this emulsion is the presence of bottlenecks. An example of a connected water domain that contains a bottleneck is shown in the upper left corner in Figure 5.10b. It is important to note that many of the larger water domains are connected, forming a percolating network of water domains. This means that a considerable number of the water molecules diffuse in large, interconnected and irregularly shaped volumes connected through bottlenecks. However, Figure 5.10c shows that the small water domains inside the oil phase are closed. This was confirmed by CLSM by simply moving the confocal plane up and down in the sample. Figure 5.10b,c also shows that there are small oil domains in some of the larger water domains. Consequently, this emulsion is also a double emulsion that possesses a very intriguing morphology well suited for testing our simulation methodology.

Calculation of the Propagator

In NMR diffusometry, a spatially dependent magnetic field gradient is added to the static magnetic field so that the Larmor frequency becomes spatially dependent. Thus, if a linear gradient of known magnitude is imposed throughout the sample, the Larmor frequency becomes a spatial label with respect to the direction of the gradient. Diffusion was measured in the present work with the gradient oriented along the z -axis. For diffusion perturbed by restricting boundaries, the echo decay is given by complicated expressions and it is necessary to use different levels of approximation or limits (Balinov et al., 1993). We assume that the restricting boundary in this work is the interface between the fat phase and the water phase that the water molecule experiences during its molecular motion in the emulsion. If the length of the gradient pulse is allowed to go to zero ($\delta \rightarrow 0$) while keeping

the product δg constant, the short-gradient-pulse approximation (SGP) is applied and the echo decay is given by (Stejskal, 1965; Tanner and Stejskal, 1968):

$$E_{\Delta}(q) = \int \rho(z_0) \int P(z_0|z, \Delta) e^{i2\pi q(z-z_0)} dz dz_0 \quad (5.2)$$

where $\rho(z_0)$ is the initial density of spin bearing molecules and propagator $P(z_0|z, \Delta)$ is the conditional probability that a molecule originally at z_0 has moved to z after time Δ . The validity of the SGP approximation has been thoroughly discussed (Linse and Söderman, 1995; Callaghan, 1997; Barzykin, 1999). The approach can be applied to an arbitrary geometry. Basically, the SGP approximation implies that the length of the gradient pulse, δ , is much shorter than the diffusion time, Δ , and that the effective diffusion of the molecules of interest during the gradient is small. In the present work, the SGP approximation is used to calculate the echo attenuation from an average propagator of the system. The average propagator is the link between the microstructure of the heterogeneous emulsion and the water mobility measured by NMR diffusometry.

Comparisons between Microstructure-Based Diffusion Calculations and NMR Diffusometry

One of our main tasks has been to calculate the average propagator from the microstructure of the heterogeneous emulsions and gels. This has been achieved by directly inserting the “true” microstructure into the simulations, as shown in Figure 5.11. Figure 5.11a shows a magnified part of a heterogeneous emulsion. The CLSM image has been enhanced in order to emphasize the water phase in the microstructure and subsequently divided into fat and water phases using binarization. The binarized image is then vectorized and imported into FEMLAB[®].

At $t_0 \cong 0$, millions of “marked” water molecules having similar properties to the rest of the water molecules are located inside the black vertical lines in Figure 5.11b. Figure 5.11b shows the spatial distribution of the marked water molecules, i.e., the concentration at $t > t_0$ in the microstructure. This has been achieved by solving the diffusion equation directly into the microstructure. It is possible to calculate the propagator by locating many different starting bands of marked water molecules at different locations and directions in the micrographs, by solving the diffusion equation for the all starting bands and subsequently summarizing and weighing the results together. However, this method of computation is very time-consuming and you do not know the result before your calculations are fully complete (it can take weeks). Instead, we have isolated single water domains of different sizes and shapes in two dimensions. This allowed us to use several magnifications during the image acquisition, and it was also possible to cover the whole size distribution of the heterogeneous emulsion

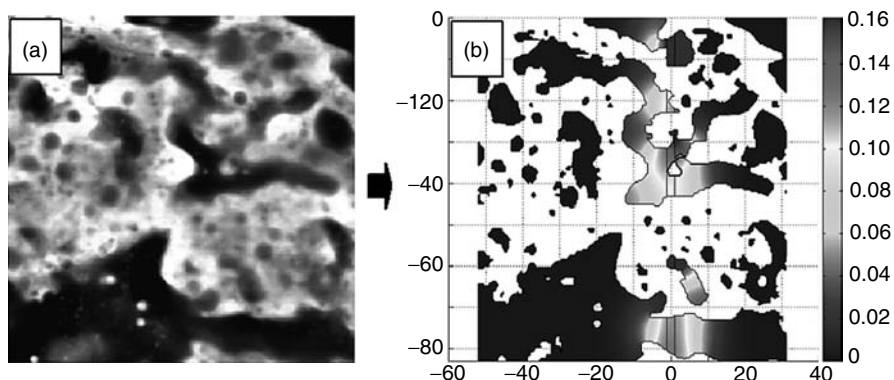


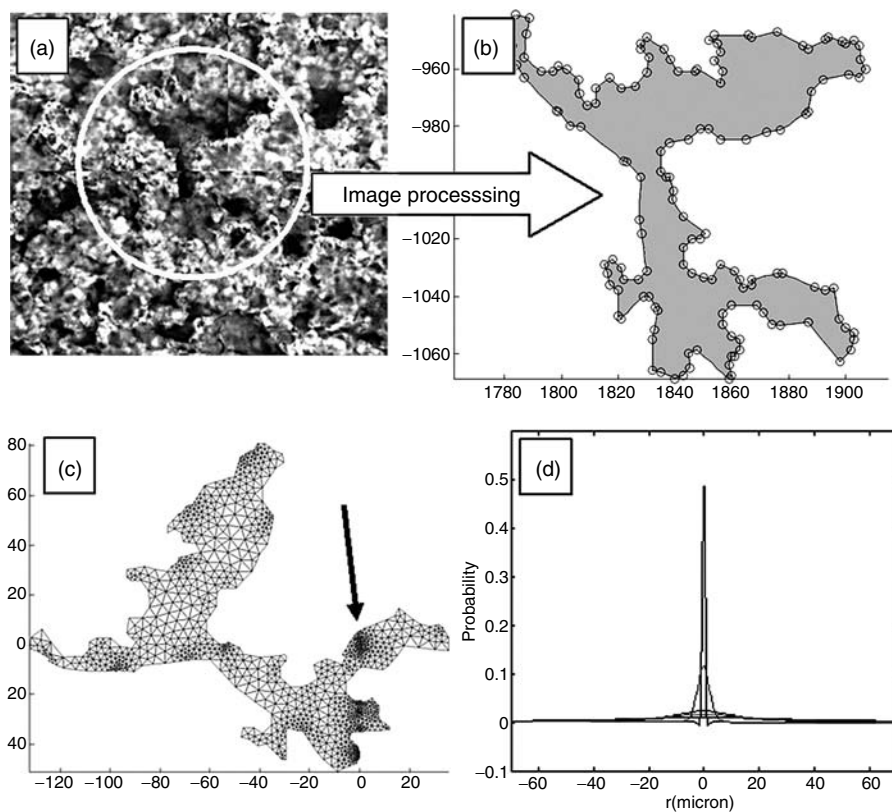
FIGURE 5.11

CLSM micrograph of a heterogeneous emulsion that is used directly in the simulations of the average propagator. (a) The bright phase is the fat phase; (b) The gray phase is the water phase.

with high spatial resolution in an easy way. Moreover, it is easy to adapt the method to different kinds of materials and the simulations can be stopped as soon as enough accuracy has been achieved.

The main simulation procedure (Lorén et al., 2005) used for the heterogeneous emulsions is shown in Figure 5.12. First, several hundred water domains of different sizes and forms are isolated, binarized, converted to vector format and imported into FEMLAB[®]. The CLSM micrographs used in this example were acquired at the three different magnifications shown in Figure 5.12. Then, the diffusion equation is solved in two dimensions directly into each single water domain with different starting positions and different rotations of the water domain using finite element methods to obtain the propagator for each single water domain. Subsequently, these propagators are weighted together by their individual area to form the average propagator for the spread sample. Finally, the echo decay $E(q)$ is calculated using Equation 5.2, which corresponds to the SGP approximation. The calculated echo decay is then compared with experimental NMR diffusometry data for different diffusion times (Δ).

Figure 5.13 shows a comparison between the echo decay calculated directly from the microstructure as described in the previous section and the measured echo decay using NMR diffusometry at $\Delta = 100, 200$ and 500 msec. It was found that the calculated echo decay fitted reasonably well with the experimental echo decay, especially at intermediate and high q -values. There is an inverse relation between the q -values and the length scales in the microstructure, i.e., low q -values correspond to long distances in the microstructure and vice versa. Another way to look at it is to say that low q -values correspond to large details in the microstructure, and high q -values correspond to fine details in the microstructure. Three CLSM micrographs showing different length scales in the structure are inserted in Figure 5.13. They are inserted in order to show which type of structure affects different

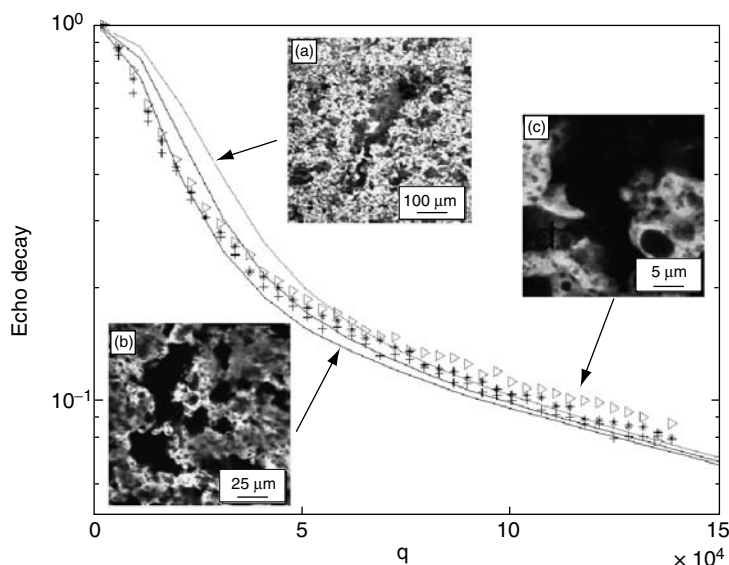
**FIGURE 5.12**

The main simulation procedure for the heterogeneous emulsions. (a) The original CLSM micrographs with the white ring that show the processed water domain. (b) Imported geometry in FEMLAB®. (c) An example of a rotated meshed water domain with a band of starting “marked” molecules. (d) The propagator for the single water domain.

parts of the echo decay. It can be seen that the large water domains with a complicated shape mostly influence the echo decay at low q -values. At low q -values the calculation underestimated the volumes available for the molecules to diffuse into. This is probably an effect of connectivity between the water domains in the third invisible dimension. Figure 5.13 shows that the small water domains mainly influence the echo decay at high q -values. They also act as an offset for the echo decay. It is also believed that the effect of shape is more pronounced at high q -values.

Probe Diffusion

So far the discussion about using diffusion properties of molecules in certain materials has been limited to water diffusion. Water is, however, not a

**FIGURE 5.13**

Comparison between the calculated echo decay (full lines) and the measured echo decay using NMR diffusometry (discrete symbols), and the pertinent microstructure on different length scales. (a) 16 \times . The bright fluorescent phase is fat. (b) 40 \times . (c) 200 \times . Triangles, dashed line = 100 msec; Stars, dotted line = 200 msec; Plus, full line = 500 msec.

suitable probe in structures with a low volume fraction of material. A gel, for instance, sometimes has very little gelling matter. In those circumstances the probe should be much larger than water so that the obstruction can be clearly observed in the NMR diffusometry experiment. Thus, small molecules that diffuse in a material with small amounts of obstructing matter having an open structure, i.e., with connectivity in three dimensions, will not be significantly slowed down. However, the diffusion rate of a much larger molecule can be greatly affected. The degree of obstruction depends on the size of the pores in the material compared with the size of the probe molecule.

Polymers have been used as probes in NMR diffusometry (Hagel et al., 1996; Nydén et al., 1999), and solid particles are common probes in light scattering (Phillies and Clomenil, 1993) investigations. Because of the relatively high internal dynamics of polymers, the NMR relaxation times, T_1 and T_2 , are often quite long. This offers the possibility not only of using a very small amount of the probe but also of performing time-dependent diffusion experiments with a wide range of diffusion observation times, typically from a few milliseconds up to several seconds. Depending on the pore size and degree of heterogeneity, the outcome of an NMR diffusometry experiment then depends on several factors, such as the size and shape of the probe, the size and shape of the pores in the material, and also the

intermolecular interaction between the probe and the material. With regard to measuring the effect of intermolecular interactions, polymers with different chemical structures may be used. For instance, if the aim is to measure the effect of charges on a gel, polymers with similar or opposite charges may be used as probes. Similarly, the structure of the material, disregarding the effects of intermolecular interactions, may be investigated by using polymers with a similar chemical structure but with different geometries. Important examples of these are linear polymers and dendrimers with a similar chemical structure but different geometry. In a crowded gel, a linear polymer can always reptate and move in a wormlike fashion (de Gennes, 1979) when the pores are small compared with the size of the hydrodynamic radius of the polymer. However, a dendrimer cannot change its structure and can only diffuse with the same diffusion mechanism independent of its surroundings. For that reason a dendrimer is most likely a better probe for gels with small pores and/or gels with a large range of pore size distribution.

Informative probe diffusion alone cannot reveal structural and intermolecular interaction details because the echo decay from a probe in a heterogeneous matrix is not unique and a large number of different structures and/or interaction possibilities may give rise to the same echo decay. One way to attack this problem is to use a similar approach to the one mentioned previously, regarding water diffusion in emulsions. In order to succeed with this, however, we believe that a three-dimensional gel structure must be used for diffusion simulations. For this reason work is in progress to develop a new combination of methods, NMR diffusometry, microscopy, mathematical reconstruction, image analysis and diffusion calculations/simulations by Monte Carlo and finite element methods (to be published shortly).

Using a combination of NMR diffusometry and microscopy techniques it is possible to master inherent structural properties giving rise to functionality with regard to mass transport, water management and molecular mobilities. The results illustrate how new information over several length scales can be used for structure design of supramolecular materials as well as insights into how probes carrying active compounds should be chosen for the desired mass transport and release properties in a wide range of applications.

Acknowledgments

The financial support from VINNOVA (The Swedish Agency for Innovation Systems) and SSF (The Foundation for Strategic Research) is gratefully acknowledged. Thanks are due to the Swedish NMR centre, where all NMR experiments were performed. Jan-Erik Löfroth, AstraZeneca R&D, is warmly thanked for fruitful discussions during this work.

References

- Balinov, B., Jönsson, B., Linse, P., and Söderman, O. The NMR self-diffusion method applied to restricted diffusion. Simulation of echo attenuation from molecules in spheres and between planes, *J. Magn. Reson. A*, 104, 17, 1993.
- Balinov, B., Söderman, O., and Warnheim, T. Determination of water droplet sizes in margarines and low-calorie spreads by means of the NMR self-diffusion experiment, *J. Am. Oil Chem. Soc.*, 71, 513, 1994.
- Balinov, B., Linse, P., and Söderman, O. Diffusion of the dispersed phase in a highly concentrated emulsion: emulsion structure and film permeation, *J. Colloid Interface Sci.*, 182, 539, 1996.
- Barzykin, A.V. Theory of spin echo in restricted geometries under a step-wise gradient pulse sequence, *J. Magn. Reson.*, 139, 342, 1999.
- Bremer, L. Fractal aggregation in relation to formation and properties of particle gels. PhD Thesis, Wageningen Agricultural University, 1992.
- Callaghan, P.T. *Principles of Nuclear Magnetic Resonance Microscopy*, Clarendon Press, Oxford, 1991.
- Callaghan, P.T. A simple matrix formalism for spin echo analysis of restricted diffusion under generalised gradient waveforms, *J. Magn. Reson.*, 129, 74, 1997.
- Callaghan, P.T., Coy, A., MacGowan, D., Packer, K.J., and Zelaya, F.O. Diffraction-like effects in NMR diffusion studies of fluids in porous solids, *Nature*, 351, 467, 1991.
- Callaghan, P.T., Jolley, K.W., and Humphrey, R.S. The diffusion of fat and water in cheese as studied by pulsed field gradient nuclear magnetic resonance, *J. Colloid Interface Sci.*, 93, 521, 1983.
- Cussler, E.L. *Diffusion—Mass Transfer in Fluid Systems*, 2nd Ed., Cambridge University Press, Cambridge, 2003.
- de Gennes, P.G. *Scaling Concepts in Polymer Physics*, Cornell University Press, Ithaca, NY, 1979.
- Fourel, I., Guillement, J.P., and Le Botlan, D. Determination of water droplet size distributions by low resolution PFG-NMR, *J. Colloid Interface Sci.*, 169, 119, 1995.
- Garasanin, T., Cosgrove, T., Marteaux, L., and Zick, K. NMR self-diffusion studies on PDMS oil-in-water emulsions, *Langmuir*, 18, 10298, 2002.
- Hagel, L., Östberg, M., and Andersson, T. Apparent pore size distributions of chromatography media, *J. Chromatogr.*, 743, 33, 1996.
- Hagslätt, H., Jönsson, B., Nydén, M., and Söderman, O. Predictions of pulsed field gradient NMR echo-decays for molecules diffusing in various restrictive geometries. Simulations of diffusion propagators based on a finite element method, *J. Magn. Reson.*, 161, 138, 2003.
- Håkansson, B., Pons, and Söderman, O. Structure determination of a highly concentrated W/O emulsion using pulsed-field-gradient spin-echo nuclear magnetic resonance diffusion diffractograms, *Langmuir*, 15, 988, 1999.
- Hermansson, A.M. and Svegmark, K., Starch—a phase separated biopolymer system, *Biopolymer Mixtures*, S.E.Harding, S.E.Hill and J.R.Mitchell, eds., Nottingham University Press, Nottingham, pp. 225–246, 1995.
- Hermansson, A.M. Rheological and microstructural evidence for transient states during gelation of kappa-carrageenan gels in the presence of potassium, *Carbohydr. Polym.*, 10, 163, 1989.

- Hermansson, A.M. Water- and fat holding, *Functional Properties of Food Macromolecules*, J.R.Mitchell and D.A.Ledward, eds., Elsevier, Amsterdam, pp. 273–314, 1986.
- Hermansson, A.-M., Eriksson, E., and Jordansson, E. Effects of potassium, sodium and calcium on the microstructure and the rheological behaviour of kappa-karrageenan gels, *Carbohydr. Polym.*, 16, 297, 1991.
- Hollingsworth, K.G. and Johns, M.L. Measurement of emulsion droplet sizes using PFG NMR and regularization methods, *J. Colloid Interface Sci.*, 258, 383, 2003.
- Hürlimann, M.D., Helmer, K.G., Latour, L.L. and Sotak, C.H. Restricted diffusion in sedimentary rocks: determination of surface-area to volume ratio and surface relaxivity, *J. Magn. Reson. A*, 111, 169, 1994.
- Langton, M. and Hermansson, A.M. Effect of emulsifiers on the aggregation of β -lactoglobulin. *Food Colloids, Fundamentals of Formulation*, E.Dickinson and E.Miller, eds., Royal Society of Chemistry, London, pp. 369–375, 2001.
- Latour, L.L., Mitra, P.P., Kleinberg, R.L. and Sotak, C.H. Time-dependent diffusion-coefficient of fluids in porous media as a probe of surface-to-volume ratio, *J. Magn. Reson. A*, 101, 342, 1993.
- Latour, L.L., Kleinberg, R.L., Mitra, P.P., and Sotak, C.H. Pore-size distributions and tortuosity in heterogeneous porous-media, *J. Magn. Reson. A*, 112, 83, 1995.
- Leloup, V.M., Colonna, P., Ring, S.G., Roberts, K., and Wells, B. Microstructure of amylose gels, *Carbohydr. Polym.*, 18, 189, 1992.
- Linse, P. and Söderman, O. The validity of the short-gradient-pulse approximation in NMR studies of restricted diffusion. Simulations of molecules diffusing between planes, in cylinders and spheres, *J. Magn. Reson. Ser. A*, 116, 77, 1995.
- Lorén, N., Altskär, A., and Hermansson, A.-M. Structure evolution during gelation at later stages of spinodal decomposition in gelatin/maltodextrin mixtures, *Macromolecules*, 34, 8117, 2001.
- Lorén, N., Hagslätt, H., Nydén, M., and Hermansson, A.-M. Water mobility in heterogeneous emulsions determined by a new combination of confocal laser scanning microscopy, image analysis, NMR diffusometry and finite element method simulations, *J. Chem. Phys.*, 122, 024716/5, 2005.
- Masaro, L. and Zhu, X.X. Physical models of diffusion in polymer solutions, gels and solids, *Prog. Polym. Sci.*, 24, 731, 1999.
- Mellema, M., van Opheusden, J.H.J., and van Vliet, T. Structure and scaling behaviour of aging rennet-induced casein gels examined by confocal microscopy and permeametry, *Langmuir*, 16, 6847, 2000.
- Mitra, P.P., Sen, P.N., Schwartz, L.M., and Le Doussal, P. Diffusion propagator as a probe of the structure of porous media, *Phys. Rev. Lett.*, 68, 3555, 1992.
- Nydén, M., Karlström, G., and Söderman, O. A PFG NMR self-diffusion investigation of probe diffusion in an ethyl(hydroxyethyl)cellulose matrix, *Macromolecules*, 32, 127, 1999.
- Olsson, C., Langton, M., and Hermansson, A.M. Microstructures of β -lactoglobulin/amylopectin gels on different length scales and their significance for rheological properties, *Food Hydrocolloids*, 16, 111, 2002a.
- Olsson, C., Langton, M. and Hermansson, A.M. Dynamic measurements of β -lactoglobulin structures during aggregation, gel formation and gel break-up in mixed biopolymer systems, *Food Hydrocolloids*, 16, 477, 2002b.
- Phillies, G.D.J. and Clomenil, D. Probe diffusion in polymer solutions under Q and good conditions, *Macromolecules*, 26, 167, 1993.

- Price, W.S. Pulsed-field gradient nuclear magnetic resonance as a tool for studying translational diffusion: Part I. Basic theory, *Concepts Magn. Reson.*, 9, 299, 1997.
- Price, W.S. Pulsed-field gradient nuclear magnetic resonance as a tool for studying translational diffusion: Part II. Experimental aspects, *Concepts Magn. Reson.*, 10, 197, 1998.
- Rochas, C. and Rinaudo, M. Mechanism of gel formation in kappa-carrageenan, *Biopolymers*, 23, 735, 1984.
- Stading, M., Langton, M. and Hermansson, A.-M. Microstructure and rheological behaviour of particulate β -lactoglobulin gels, *Food Hydrocolloids*, 7, 195, 1993.
- Stejskal, E.O. Use of spin echoes in a pulsed magnetic-field gradient to study anisotropic restricted diffusion and flow, *J. Chem. Phys.*, 43, 3597, 1965.
- Tanner, J.E. and Stejskal, E.O. Restricted self-diffusion of protons in colloidal systems by the pulsed-gradient, spin-echo method, *J. Chem. Phys.*, 49, 4938, 1968.
- Topgaard, D., Malmborg, C. and Söderman, O. Restricted self-diffusion of water in a highly concentrated W/O emulsion studied using modulated gradient spin-echo NMR, *J. Magn. Reson.*, 156, 195, 2002.
- Van den Enden, J.C., Waddington, D., Van Aalst, H., Van Kralingen, C.G. and Packer, K.J. Rapid determination of water droplet size distribution by PFG-NMR, *J. Colloid Interface Sci.*, 140, 105, 1990.

6

Probing Water–Solid Interactions in Crystalline and Amorphous Systems Using Vibrational Spectroscopy

Lynne S. Taylor

CONTENTS

Introduction	101
Fourier Transform Raman Spectroscopic Study of the Interaction of Water Vapor with Amorphous Polymers	102
Water Diffusion in Hydrated Crystalline and Amorphous Sugars Monitored Using H/D Exchange	107
Acknowledgments	112
References	112

Introduction

Vibrational spectroscopy has a long history of use for the investigation of water structure and the interaction of water with other materials (Kusanagi and Yukawa, 1994; Maeda and Kitano, 1995; Walrafen, 1971). In the gas state, the peaks arise from combinations of three vibrations: symmetric and asymmetric OH stretch and OH deformation. In the condensed state, the vibrational spectra are far more complex because of vibrational overtones and combinations with librations (restricted rotations; i.e., rocking motions) resulting from hydrogen bonds. Thus, there is a wealth of information contained in the spectrum of water. There are at least three ways in which water–solid interactions can be investigated using vibrational spectroscopy. First, the change in the water peaks upon interaction with the solid can be assessed and interpreted to provide information about the structure of water in the system. For example, the OH stretching peak position of the water molecule has been correlated to the strength of the hydrogen bonding

between water and solid in crystalline hydrates (Falk and Knop, 1973). Second, the change in the vibrational spectrum of the solid can be investigated in the presence of water to extract information about structural changes. Third, the dynamics of water–solid interactions can be probed by monitoring spectral changes as a function of time under carefully controlled environmental conditions. Dynamics have been investigated in a number of systems including monitoring of the phenomenon of deliquescence (Cantrell et al., 2002) and the exchange of D₂O with water and hydroxyl groups in cyclodextrins (Steiner et al., 1995; Dasilva et al., 1997).

In this presentation, two examples of the use of vibrational spectroscopy to probe water–solid interactions in materials of interest to the food and pharmaceutical sciences are described. First, the interaction of water vapor with hydrophilic amorphous polymers has been investigated. Second, water accessibility in hydrated crystalline versus amorphous sugars has been probed using deuterium exchange. In both of these studies, Raman spectroscopy was used as the method of choice. Raman spectroscopy is especially useful of these types of studies as it is possible to control the environment of the sample more easily than with infrared spectroscopy.

Fourier Transform Raman Spectroscopic Study of the Interaction of Water Vapor with Amorphous Polymers

Many of the polymers used for ingestible products such as food and pharmaceuticals are hygroscopic. Such polymers are often partially or totally amorphous and thus absorb water vapor into the bulk structure as well as adsorbing water at the surface. The amount of water sorbed is dependent on the chemistry and structure of the polymer, the relative humidity and the temperature. Because the absorbed moisture can greatly influence the chemical and physical properties, it is of importance to understand more about the water–solid interactions in such systems. For example, water is a well-known plasticizer, reducing the glass transition temperature (T_g) and completely altering the viscoelastic properties of the system. In fact, some polymers can absorb sufficient water so that they are plasticized to such an extent that they change from being in the low mobility glassy state at room temperature to the more mobile rubbery state.

Because of the important role of water in influencing both the properties of the polymer and the chemical stability of the system, there has been a great deal of interest in trying to better understand the nature of water–solid interactions. The purpose of our study was to investigate intermolecular interactions between various solid polymers and the water molecules sorbed in these materials with the aim of gaining a better understanding of the water structure in the polymers (Taylor et al., 2001). Vibrational spectroscopy is an excellent method for probing solid-state hydrogen bonding interactions and Raman spectroscopy was chosen for these studies because of the ease

with which the sample environment could be controlled during the experiment. Four polymers were investigated, two molecular weight grades of poly(vinylpyrrolidone) (PVP), K90 and K12, the copolymer poly(vinyl pyrrolidone-co-vinyl acetate) (PVP/VA), and poly(vinyl acetate) (PVAc).

Samples of each polymer were equilibrated at different relative humidities by storage over saturated salt solutions in desiccators. The equilibrated samples were then examined using FT Raman spectroscopy and differential scanning calorimetry (DSC). Gravimetry was used to assess the water vapor sorption profile. Chemometric analysis of spectroscopic data was performed using a commercial software package, Unscrambler (Camo.).

The order of hygroscopicity was found to be $\text{PVP K90} \geq \text{PVP K30} > \text{PVP/VA} > \text{PVAc}$ as shown in Figure 6.1. The hydrogen bonding of water to hydrophilic groups can easily be interrogated by examining the carbonyl stretching peaks of the polymers. In the dry state, none of the polymers can undergo hydrogen bonding as they lack acidic protons; however, the sorbed water can hydrogen bond to the carbonyl functions. Figure 6.2 shows Raman spectra obtained from the co-polymer, PVP/VA, which was stored at different relative humidities. There are two carbonyl peaks, one from the vinyl acetate portion of the polymer and one from the vinyl pyrrolidone group. As the water content of the polymer increases, each peak shifts to a lower wavenumber, indicating that hydrogen bonding with water is occurring. The acetate carbonyl, however, doesn't shift as much as the pyrrolidone carbonyl, particularly at low moisture contents, indicating that more water hydrogen bonds to the latter group. The extent of hydrogen bonding with water for each polymer can be compared qualitatively by plotting the shift in carbonyl peak position as a function of water content. Such a plot is shown in Figure 6.3. In the case of PVP/VA, the shift of

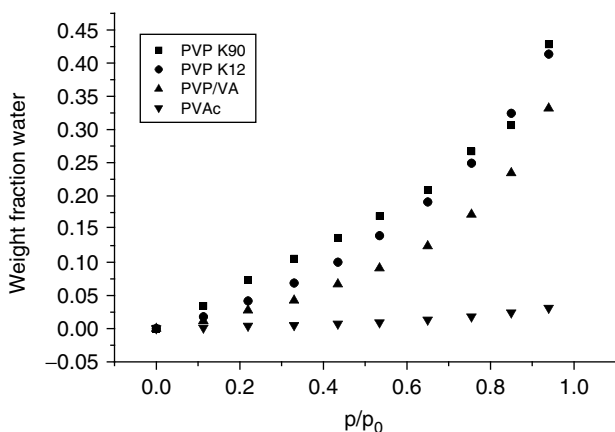
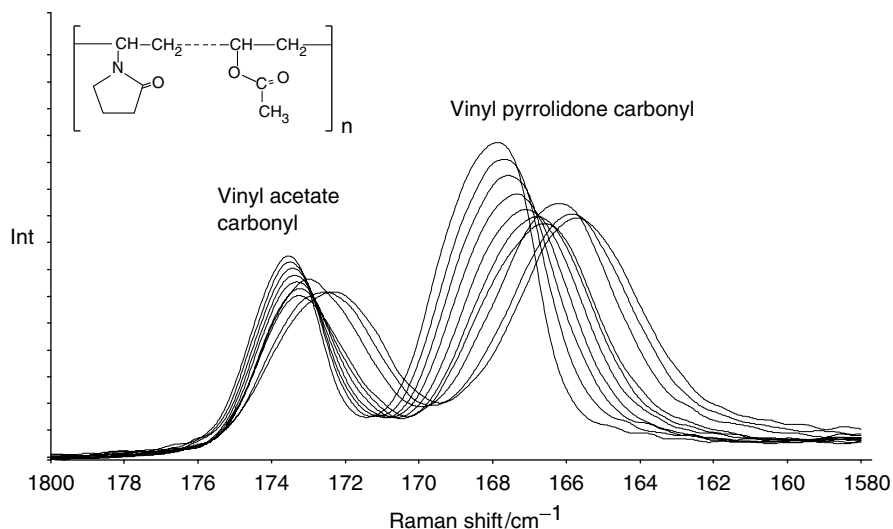


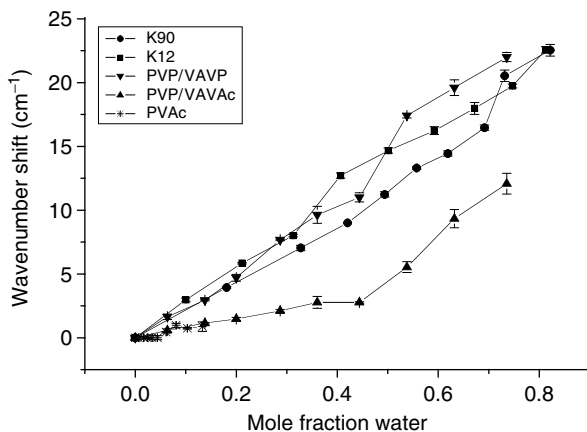
FIGURE 6.1

Water vapor absorption as a function of partial pressure at 22°C for the various polymers investigated.

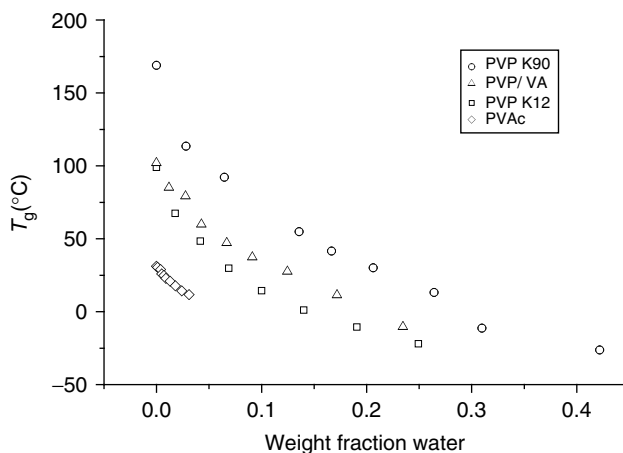
**FIGURE 6.2**

Shift in carbonyl peak positions with increasing water content for PVP/VA. As the water content increases, a downward shift in peak position for both the vinyl acetate carbonyl and the vinyl pyrrolidone carbonyl is observed. The magnitude of this shift is greater for the vinyl pyrrolidone carbonyl, particularly at low water contents. The spectra shown in this figure were obtained after storage at relative humidities ranging from 0 to 94%.

both carbonyls can be included on the plot. The water content has been expressed as the mole fraction of water calculated using the molecular weight of the monomer unit. All of the polymers show an increase in shift with increasing moisture content with no sign of leveling off over the range

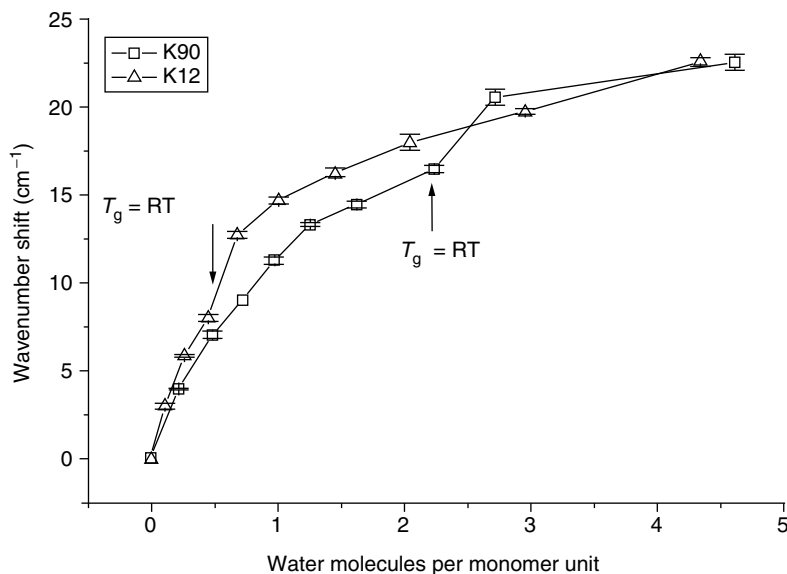
**FIGURE 6.3**

Shift in carbonyl peak position for each polymer as a function of water content. A larger shift indicates more hydrogen bonding. For PVP/VA, shifts for both carbonyl groups are shown. The mole fraction water has been calculated using the molecular weight of the monomer unit of each polymer.

**FIGURE 6.4**

Glass transition temperatures of each polymer as a function of water content as determined using differential scanning calorimetry.

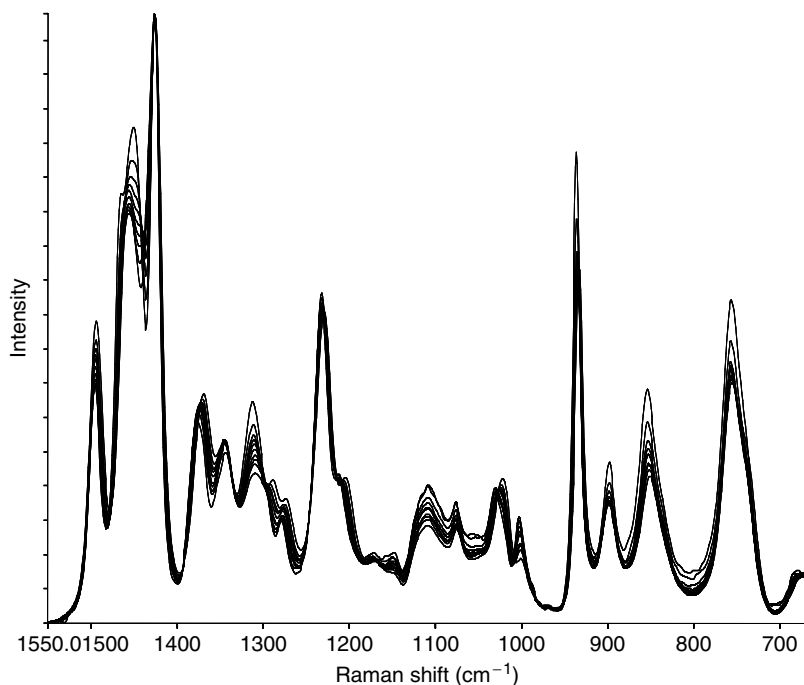
of water contents studied. Careful inspection of the plots for all the pyrrolidone carbonyls and the acetate carbonyl of PVP/VA indicates that there is a break in the trend at some water content that varies for each polymer, although it is the same for both the carbonyls in PVP/VA. These breaks occur at approximately 0.7, 0.35 and 0.5 mole fraction water for PVP K90, PVP K12 and PVP/VA, respectively. PVAc interacts very little with water and no trends can be discerned. To interpret these results, we need to examine how each polymer is plasticized as a function of moisture content. Figure 6.4 shows a plot of the glass transition temperatures for each polymer as a function of moisture content, measured using DSC. Each of the polymers in the dry state has a glass transition temperature higher than room temperature. As the weight fraction of water increases, T_g is depressed and at some water content the polymer is sufficiently plasticized so that the operating temperature (room temperature) exceeds the glass transition temperature. Thus, for each polymer, some of the spectra represent the glassy state while others have been obtained from the rubbery state. The breaks in the hydrogen bonding trends shown in Figure 6.3 occur around the point when T_g is depressed to room temperature. This can be seen in more detail if the carbonyl positions are compared as a function of water content for PVP K12 and K90; such a plot is shown in Figure 6.5. As the chemistry of these polymers is very similar, the ability to hydrogen bond with water should also be very similar. PVP K12, however, has a lower initial T_g and is plasticized to room temperature at a much lower water content than K90 (Figure 6.4). From Figure 6.5 it can be observed that at low moisture contents, when both polymers are in the glassy state, that the water interacts to a similar extent in both systems. As K12 becomes plasticized to a rubber, it

**FIGURE 6.5**

Shift in carbonyl peak position as a function of number of water molecules associated with each monomer unit in PVP K90 as compared with PVP K12. The arrows indicate the point where the polymer is plasticized to the operating temperature, which was room temperature (RT).

appears as if water can interact to a greater extent than in the still glassy K90 and an enhanced shift in carbonyl peak occurs for K12 compared with K90. This enhancement, although small, persists until high moisture contents where K90 becomes sufficiently plasticized to be rubbery at room temperature, and again the carbonyl groups have a similar interaction with water in both polymers. It can be postulated that in the more mobile rubbery state that the carbonyl group is better able to interact with the absorbed moisture, perhaps because of increased accessibility of bonding sites as a consequence of the increased free volume and mobility of the polymer chains.

Although water clearly has an effect on the spectra of the polymers through hydrogen bonding to the carbonyl groups, there are also some more subtle effects, as shown in Figure 6.6. Many of the peaks in this region arise from vibrations such as C–C and C–H groups in the polymer, which would not be expected to interact directly with water (note water has no discernable peaks in this region of the spectrum). To analyze these variations, a principle components analysis was performed on the spectral data. Results are shown in Figure 6.7. The data indicate that for each polymer (with the exception of PVAc), the vibrational changes progress in a gradual manner until the polymer passes into the T_g region, and the score plots exhibit a discontinuity. Because there is no sudden change in the amount of water absorbed, it can be hypothesized that the spectra are most influenced by conformational

**FIGURE 6.6**

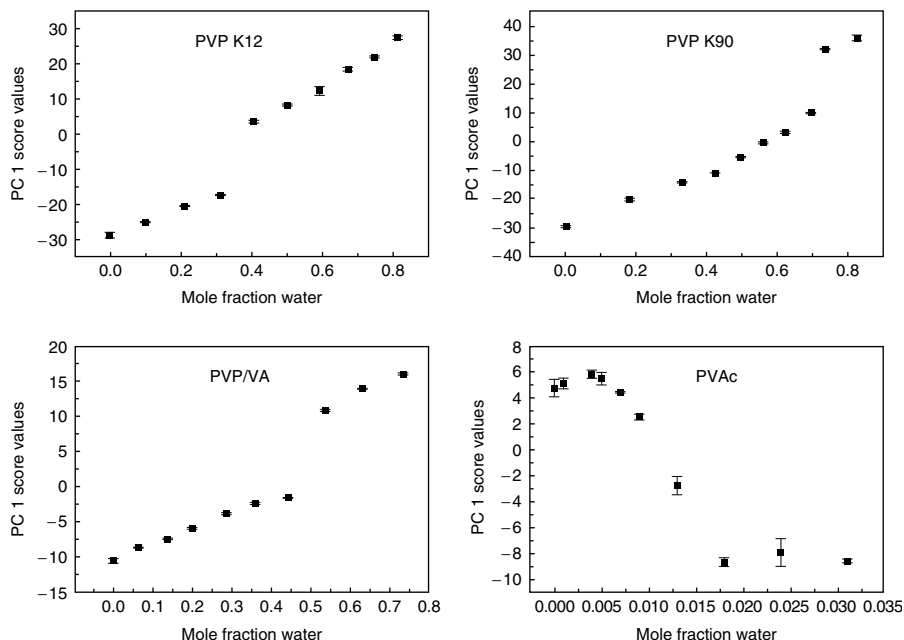
Spectral changes occurring in the 1150 to 700 cm^{-1} spectral region of PVP K90 stored at different relative humidities. The spectra were normalized against the peak at 1425 cm^{-1} .

changes that occur in the region of T_g . Thus the change in molecular mobility results in changes in the molecular vibrations presumably reflecting conformational variation.

In summary, it has been observed that the hydrogen bonding interaction of water with amorphous polymers depends both on the chemistry of the polymer and to a lesser extent, on the changes in structural relaxation accompanying plasticization by water. In addition, the plasticizing effect of moisture produces other subtle effects on the polymer spectrum.

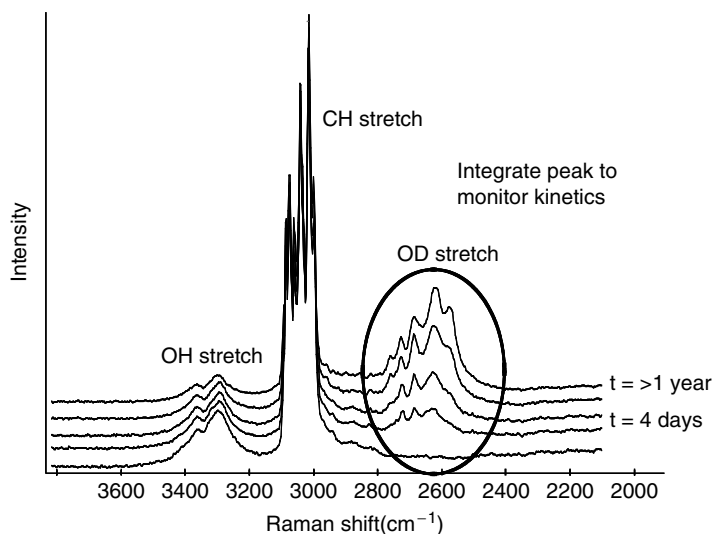
Water Diffusion in Hydrated Crystalline and Amorphous Sugars Monitored Using H/D Exchange

Water can interact with both amorphous and crystalline materials. In both amorphous phases and crystal hydrates, the water molecules are present in the bulk structure; however, in the latter they are considered to occupy specific sites (for stoichiometric isolated lattice site hydrates) and often contribute to the structure, while for the former the water molecules would be expected to exhibit significant mobility.

**FIGURE 6.7**

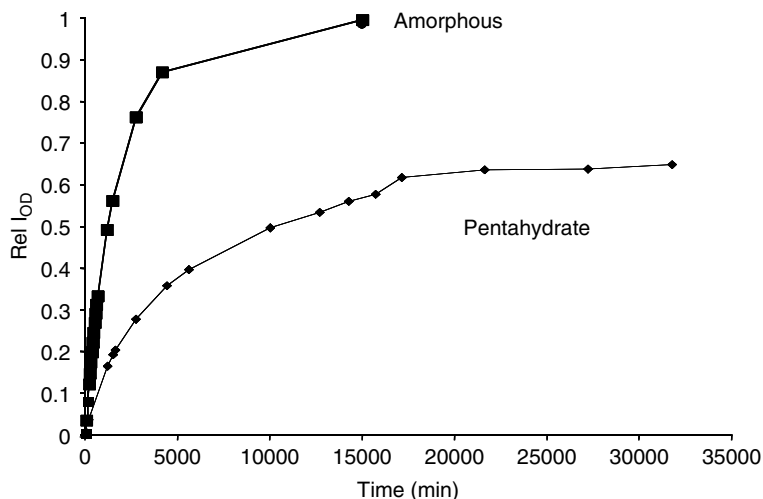
Score values of the first principal component following analysis of the 1550 to 600 cm^{-1} spectral region plotted against the mole fraction water. (Source: Reproduced from Taylor, L.S., Langkilde, F.W., and Zografi, G. Fourier transform Raman spectroscopic study of the interaction of water vapor with amorphous polymers, *J. Pharm. Sci.*, 90, 888–901, 2001. With permission of the copyright owner.)

An innovative approach for exploring hydrate structure has been developed by Saenger and co-workers who studied cyclodextrin–water interactions using deuterium oxide exchange (Dasilva et al., 1996, 1997). Essentially, different cyclodextrins were exposed to deuterium oxide (D_2O) vapor and the exchange of hydrate water with D_2O and the sugar hydroxyl hydrogens with deuterium was monitored. Through monitoring of the kinetics of the exchange process and the extent of the process, they were able to draw conclusions about the mobility and accessibility of water in various cyclodextrins. We were interested in applying this technique to probe water interactions in different types of hydrated materials, namely in crystalline hydrate in which water contributes to the structural integrity and in their amorphous counterparts (Ahlqvist and Taylor, 2002). The model compounds employed were raffinose pentahydrate and trehalose dehydrate, while sucrose (which does not form a hydrate) was used as a control. Amorphous samples were prepared by freeze drying. All samples were exposed to D_2O vapor (the vapor pressure was controlled by using saturated salt solutions) and the kinetics of exchange was monitored using Raman spectroscopy.

**FIGURE 6.8**

Raman spectra of raffinose pentahydrate following exposure to an atmosphere of D_2O vapor (approximately 75% RH). The OD stretching peak increases with time and can be integrated to monitor the kinetics of the exchange process.

An example is shown in Figure 6.8. Following exposure to D_2O vapor, the OH peak in raffinose pentahydrate observed between 3500 and 3100 cm^{-1} diminishes in intensity while an OD peak appears between 2700 and 2200 cm^{-1} . This indicates the water molecules and/or the hydroxyl groups in raffinose are capable of exchange. By integrating the peak intensities for the OD peak, the exchange process can be monitored as a function of time, as shown in Figure 6.9. It can be observed that, for raffinose pentahydrate, the exchange process is not complete over the experimental time scale ($>1 \text{ year}$). In contrast, amorphous raffinose undergoes complete exchange. Moreover, it can be seen that the timescale for exchange is much faster for amorphous raffinose compared with the pentahydrate. It thus appears that raffinose pentahydrate contains unexchangeable OH groups, although whether these arise from water or hydroxyl groups is unknown. This issue was further investigated by drying the partially exchanged sample and analyzing the dried material. Drying resulted in an amorphous phase in which the OH intensity decreased suggesting that at least part of the unexchangeable OH oscillators in raffinose pentahydrate were caused by water molecules that were removed on drying. However, the dried sample had a small OH peak remaining, which suggests that some hydroxyl groups are also not exchangeable. By making some assumptions, from a comparison of peak intensities in the pentahydrate with those in the exchanged sample, it can be estimated that six OH oscillators do not exchange. By then comparing peak intensities in the exchanged dehydrated sample with those in a dehydrated sample prepared from the pure pentahydrate, we can further estimate that

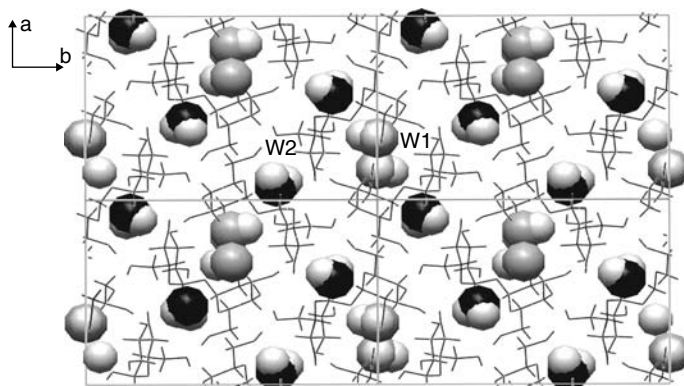
**FIGURE 6.9**

Plot of integrated relative Raman intensity of the OD peak ($\text{Rel } I_{OD}$) as a function of time of exposure to a D_2O atmosphere.

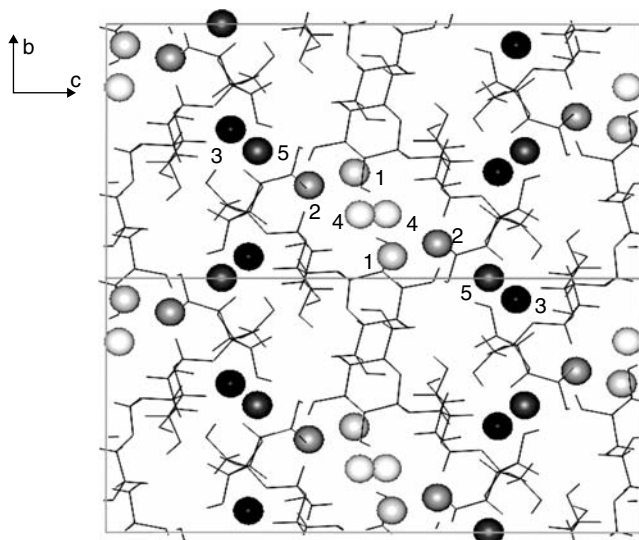
two hydroxyl groups do not exchange and from a simple mass balance this suggests that two water molecules cannot be exchanged.

In the case of trehalose, partial exchange was also observed for the dihydrate and complete exchange for the amorphous sample. Similar calculations to those described above suggested that one water molecule and two of the eight hydroxyls are exchanged. The control sample, crystalline anhydrous sucrose showed no detectable exchange, although the amorphous counterpart again showed complete exchange.

The observation that the crystalline hydrates can exchange some of the water of hydration with D_2O molecules on exposure to D_2O vapor indicates that some of the water of hydration is dynamic and in constant exchange with the atmosphere. Such results have been observed before with the cyclodextrins. However, it was also observed that not all of the water molecules are exchangeable, suggesting that a barrier to diffusion exists and these water molecules are more isolated in the crystal structure than those that exchange. The crystal structures of our model compounds have been published and can be used to aid in data interpretation. For trehalose dihydrate, the two water molecules are isolated from each other in the crystal lattice, as shown in Figure 6.10. Both of the waters hydrogen bonds with trehalose molecules are integral to the structure and it has been shown that removal of the water molecules results in either a collapse of structure or rearrangement to a new crystalline form. From Figure 6.10, it is also evident that the crystallographically unique water molecule W2 would be able to diffuse along the c -axis with less hindrance from the surrounding trehalose molecules than the other crystallographic water, W1, which is more caged in.

**FIGURE 6.10**

Crystal packing diagram for trehalose dihydrate showing the two crystallographically independent waters, W1 and W2. It is believed that W2 can diffuse through the framework of trehalose molecules in the *c*-crystallographic direction and can exchange with D₂O molecules. (Source: Reproduced from Ahlqvist, M.U.A. and Taylor, L.S. Water diffusion in hydrated crystalline and amorphous sugars monitored using H/D exchange, *J. Pharm. Sci.*, 91, 690–698, 2002. With permission of the copyright owner.)

**FIGURE 6.11**

Crystal packing diagram for raffinose pentahydrate. Three of the water molecules are located in a channel (W1, W2, and W4) and two are located outside of the channel (W3 and W5). For clarity, only the oxygen molecules of the water are shown at 50% of the van der Waals radii. (Source: Reproduced from Ahlqvist, M.U.A. and Taylor, L.S. Water diffusion in hydrated crystalline and amorphous sugars monitored using H/D exchange, *J. Pharm. Sci.*, 91, 690–698, 2002. With permission of the copyright owner.)

Given that only one of the water molecules exchanges, we can speculate that it is W2 that does so. The hydroxyl groups that exchange are most likely those that hydrogen bond to this water molecule.

Raffinose pentahydrate is more complex, because it contains five water molecules. A crystallographic packing diagram is shown in Figure 6.11. Three of the water molecules are found in a channel (W1, W2, and W4) and the remaining two waters are outside of this channel (W3 and W5), although associated with each other. There is hydrogen bonding within the two groups of water molecules. Our results suggest that three water molecules exchange and it would seem logical to speculate that these are the three waters found in the channel. The hydroxyl exchange can be explained by groups that come into contact with the exchanged D₂O molecules.

Thus it appears that the structure of crystal hydrates most influences the extent of exchange with D₂O molecules rather than the number or strength of the hydrogen bonds. In contrast, for the amorphous sugars studied, all hydroxyl groups were found to be exchangeable. This would tend to imply that water has access to most parts of the molecule in the amorphous state, particularly hydrophilic groups able to interact with water molecules through hydrogen bonding. In addition, any hydrogen bonding network that exists between the sugar molecules is not able to inhibit the exchange. Presumably, these results reflect the lack of long range order in amorphous materials and nicely highlight how water can directly influence reactivity in such systems. In summary, we believe that exchange experiments using D₂O vapor provides a useful method to probe water–solid interactions in crystalline and amorphous materials.

Acknowledgments

I would like to acknowledge Matti Ahlqvist, Frans Langkilde and George Zografi for their contributions to this work.

References

- Ahlqvist, M.U.A. and Taylor, L.S. Water diffusion in hydrated crystalline and amorphous sugars monitored using H/D exchange, *J. Pharm. Sci.*, 91, 690, 2002.
- Cantrell, W., McCrory, C., and Ewing, G.E. Nucleated deliquescence of salt, *J. Chem. Phys.*, 116, 2116, 2002.
- Dasilva, A., Steiner, T., Saenger, W., Empis, J.M.A., and Teixeira, J.J.C. Hydration and dehydration processes of beta-cyclodextrin — a Raman spectroscopic study, *J. Inclusion Phenom. Mol. Recognit. Chem.*, 25, 21, 1996.

- Dasilva, A.M., Steiner, T., Saenger, W., Empis, J., and Teixeiradias, J.J.C. Dynamics of H/D and D/H exchanges in beta-cyclodextrin dodecahydrate observed in real time — effects from zero-point vibrational energy, *Chem. Commun.*, 465, 1997.
- Falk, M. and Knop, O. Water in stoichiometric hydrates, *Water, A Comprehensive Treatise*, F. Franks, ed., Plenum Press, New York, pp. 55–113, 1973.
- Kusanagi, H. and Yukawa, S. Fourier transform infra-red spectroscopic studies of water molecules sorbed in solid polymers, *Polymer*, 35, 5637, 1994.
- Maeda, Y. and Kitano, H. The structure of water in polymer systems as revealed by Raman spectroscopy, *Spectrochim. Acta Part A-Mol. Biomol. Spectrosc.*, 51, 2433, 1995.
- Steiner, T., Moreira da Silva, A.M., Teixeira-Dias, J.J.C., Muller, J., and Saenger, W. Rapid water diffusion in a cage-type crystal lattice: beta cyclodextrin dodecahydrate, *Angew. Chem. Int. Ed. Engl.*, 34, 1452, 1995.
- Taylor, L.S., Langkilde, F.W., and Zografi, G. Fourier transform Raman spectroscopic study of the interaction of water vapor with amorphous polymers, *J. Pharm. Sci.*, 90, 888, 2001.
- Walrafen, G.E. *Water — A Comprehensive Treatise*, Plenum Press, New York, 1971, chap. 5.

7

Structure–Property Relationships in Low Moisture Products

José Miguel Aguilera

CONTENTS

Introduction	116
Food Structure	116
Definition and Importance	116
The Structure of Low-Moisture Foods	117
Microheterogeneity	118
Viewing the Microstructure of LMF	118
Quantifying Structure.....	119
Properties	119
Properties Relevant to Foods	119
Structure–Property Relationships.....	120
Texture	121
An Example: Hardening of Legumes	122
Effect of Moisture Content on Mechanical Properties of LMF.....	122
Crispness of LMF.....	122
Effect of Moisture Content.....	123
Crispness and the Glass Transition.....	124
Fracture of Polymers	126
Fracture and the Glass Transition in LMF.....	126
Structure–Property Relationships in a Low-Moisture Starch Model System	127
Microstructure and Auditory Sensations.....	129
Concluding Remarks and Future Trends.....	130
Acknowledgment.....	130
References	130

Introduction

Although food technologists have been dealing with functional structures made from natural molecules since ancestral times, their impact in biomaterials science has been limited. The problem has been an insufficient basic understanding of how structures are formed and relate to desirable properties. In their favor, it can be argued that foods are complex, multicomponent systems where key structural components are beyond the resolution of the naked eye and that some properties are quite subjective. Only in the last 20 years with the development of food materials science, which is application of concepts from polymer science, colloidal chemistry and modern microscopy techniques, is a basic understanding emerging of how food structures are created and how they perform. This trend will be illustrated in this paper for the case of low-moisture foods (LMF). Although LMF were originally produced to increase storage stability and safety (i.e., minimize microbial growth and reduce the rate of deleterious chemical reactions) there are many other desirable physical properties of foods associated with low water content.

Food Structure

Definition and Importance

The structure of foods comes from nature or it is imparted through processing, storage, or during preparation. The structure of processed foods evolved throughout the centuries, mostly by trial-and-error, based on a few raw materials and simple transformations induced by mankind. Structure is important in foods because it can be related to physical properties and, by extension, to their quality and acceptability.

The appearance of foods may be perceived with the naked eye but their microstructure has to be studied using microscopes or other imaging techniques. There are many definitions of food microstructure but all of them refer to *structural elements* discerned at different length scales that are known to contribute to the properties of foods. In natural foods these may be cells, cell walls, pores, intercellular cement, tissue fibers, and so on, down to the macromolecular level. Natural structures show an organizational *hierarchy* from macromolecules to the tissue level that is required to achieve biological functionality. In processed foods the structure is mostly that of a *dispersed system* and elements take the form of gas cells, crystals (ice, sugar, or fat), swollen starch granules, or fat droplets, usually embedded in a polymer network or amorphous matrix. In this case, functionality stems from the organization of elements (architecture) and their *interactions*. Nowadays structures can be resolved to the atomic level but the challenge is to identify

the relevant scale(s) responsible for the desired functionality, which may vary from molecules at interfaces to visible particles.

This relevance of food structure has been confirmed at the recent International Congress of Engineering and Food (ICEF 9) where the subject of *Processing and Characterization of Polyphasic Structured Systems* had the largest number of papers presented, surpassing classical subjects such as methods of food engineering and emerging technologies.

The Structure of Low-Moisture Foods

In the context of this article, LMF are those having a moisture content below 20%. As shown in Figure 7.1, LMF come in many structures that depend not only on the original material from where moisture has been removed (e.g., tissue, colloidal dispersion) but on the type of process and the level of variables leading to the low moisture condition. Drying and baking are classical technologies giving origin to traditional LMF. Frying, extrusion, crystallization, and mixing/forming operations may also result in products that are low in water content. For example, boiled sweets, chocolate, and

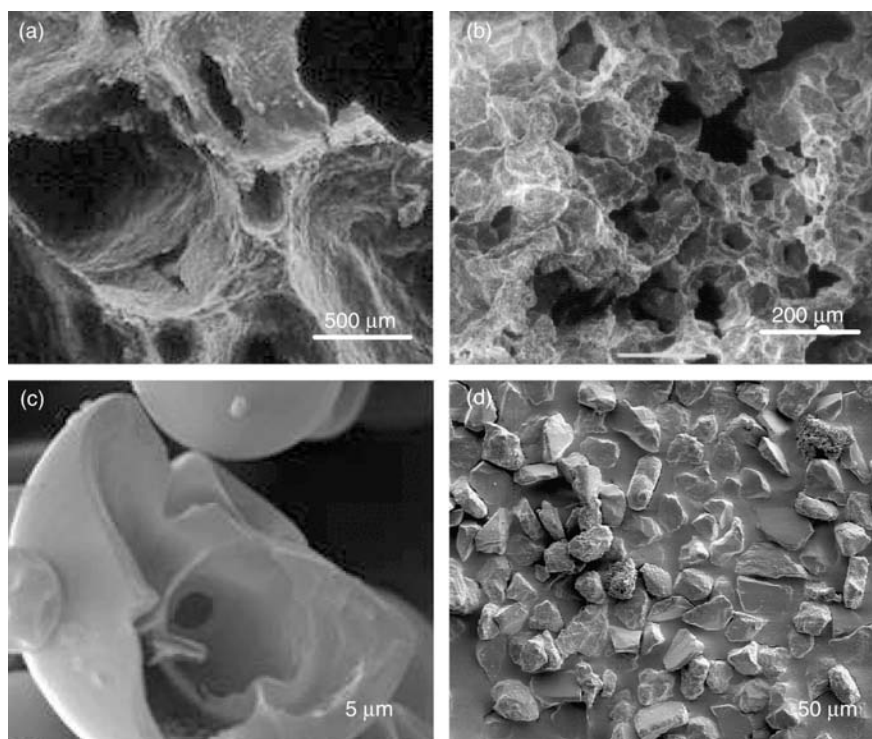


FIGURE 7.1

The many structures of low moisture foods viewed by scanning electron microscopy: (a) bread; (b) chocolate biscuit; (c) whey protein powder; (d) milk chocolate.

toffees have less than 4% moisture, so they are also LMF. Moreover, although composites such as French fries have a high overall moisture content, their quality and acceptability depends on the dryness of the outer crust (*ca* 3% moisture content), so in a sense they may be considered LMF.

Microheterogeneity

Microheterogeneity is ubiquitous in dry multicomponent food systems. The physical states of major components of LMF (e.g., proteins, polysaccharides, sugars) could be amorphous, rubbery, or crystalline. For example, wheat starch in baked products may be in its native semicrystalline form (sugar cookies) or gelatinized forming a glass (white bread), depending on formulation and process conditions (Blanshard, 1988). Moreover, processing produces domains of different moisture content, which are not in thermodynamic equilibrium, hence, states and product morphology may change with time if there is enough mobility in the system. Amorphous sugars may be slowly converted into their crystalline form at low moisture content or rapidly (i.e., within minutes) if enough water is present in the system (Roos, 1995). Similarly, gelatinized starch may retrograde into a semicrystalline form after storage. Morphologies of multicomponent systems are controlled by a fine balance between thermodynamics (equilibrium) and kinetics. Examples are phase segregation in freeze-dried materials produced during freezing as ice separates from a concentrated solution, and thermodynamic incompatibility of proteins and polysaccharides in concentrated mixtures (Tolstoguzov, 2000).

Viewing the Microstructure of LMF

A review of current techniques to probe the microstructure of LMF is beyond the scope of this chapter. Readers are referred to specific references for details and applications of microscopy and image technology to foods (Kalab et al., 1995; Aguilera and Stanley, 1999; Russ, 2005). Relevant to the present discussion is that a plethora of new instrumentation has become available to study the microstructure of foods with minimal preparation and nonintrusively. Confocal laser scanning microscopy (CLSM) is most advantageous in its ability to provide high-resolution optical sections through a thick specimen that can remain hydrated during examination. Environmental scanning electron microscopy (ESEM) allows the study of food samples, even liquid systems, in their natural state without the risk of artifacts during drying or freezing the specimen as is the case of traditional SEM or cryo-SEM. There are many applications of magnetic resonance imaging (MRI) to localize water within foods and to assess moisture transfer between phases, although the level of resolution of the technique is still low (McCarthy, 1994). A very interesting approach for engineering analysis is that images can now be obtained in real time by video-microscopy or with high-speed cameras while foods are subjected to manipulation

(e.g., mechanical or thermal, probing, heating, cooling, etc.) under the lens of a microscope and in conditions mimicking those of processing or storage (Aguilera and Lillford, 1996). Ultrasound, acoustic and x-ray tomography are slowly finding their ways into the assessment of food microstructure as nonintrusive techniques to reveal internal defects and structure in 3D.

Quantifying Structure

It would be an oversimplification to assume that the use of more powerful and sophisticated microscopes automatically leads to a better knowledge of the microstructure of foods. Unfortunately human vision is not very well suited to make objective and quantitative determinations of the image features we see under the lens of a microscope. Physical models and mathematical relationships demand as input quantitative information and numerical data of structure. Image analysis relies heavily on mathematical algorithms and computer technology to recognize, differentiate and quantify images. At a first level of image analysis is commercial software that performs basic tasks, e.g., image editing, segmentation, object selection, and measurement of geometrical features. The second level has algorithms that perform fractal analysis that convert complex geometry or topography into numbers. A third level of image analysis is the description of the whole image. Image texture means the spatial arrangement of features in an image and it is commonly used to find out specific patterns, i.e., the distribution of pixels in the image is not totally random. Texture (not to be confused with food texture) measures intuitive smoothness, coarseness, and regularity. In reference to Figure 7.1, one may be interested not only in the size of air cells but in how they are distributed in bread. The three principal approaches in image analysis to describe texture are statistical, structural, and spectral. Statistical approaches characterize textures into smooth, coarse, grainy, and so on. Structural techniques deal with the arrangement of “image primitives.” Spectral techniques (e.g., Fourier spectrum) are used primarily to detect global periodicity represented by high and narrow peaks in the spectrum. Three features of the Fourier spectrum are useful for texture description: (i) prominent peaks in the spectrum give the principal direction of texture patterns; (ii) the location of peaks in the frequency plane gives the fundamental spatial period of the patterns; and (iii) the nonperiodic image elements can be described by statistical techniques (Gonzalez and Woods, 2001).

Properties

Properties Relevant to Foods

Material scientists try to find relationships between the microstructure and physical properties so product functionality can be predicted and controlled.

They are quite successful because engineering properties of materials (e.g., strength, electrical conductance, etc.) are measured by precise instruments and data generated is directly linked to applications. Foods also exhibit engineering properties that can be measured and important efforts were made worldwide in the 1980s and 1990s to adapt experimental techniques to foods, generating massive amounts of data. The problem is that the chemical and structural complexity of foods make interpretation of results more difficult. An example is moisture diffusivity in LMF where data spans eight orders of magnitude in a narrow moisture range (0 to 0.3 g/g dry basis), a result that is still waiting for a fundamental interpretation (Saravacos and Maroulis, 2001). Most physical properties relevant to foods — including mechanical, rheological, thermal, optical, and transport properties — depend on the moisture content. As moisture content increases, the system becomes more mobile, continuously changing in structure and, thus, in properties. Other desirable properties of foods are more difficult to define and measure, for example, texture, taste, and flavor, yet they are critical to product performance and consumer acceptability. Hence, the major challenge today is not to measure “food properties” but to understand what they mean in the realm of the experimental conditions and how do they translate into higher quality products and consumer acceptance.

Structure–Property Relationships

Structure–property relationships imply a causal connection between structure and the way the product behaves. So far most structure–property relationships in foods are of an empirical or subjective nature, yet they provide evidence that structure does play a key role in transport phenomena, physical properties, texture, chemical stability, and bioavailability of nutrients (Aguilera, 2005). Nutrient data for foods determined by laboratory analyses means little if availability of those nutrients for absorption in the gut depends on mastication and release of nutrients during digestion from the food matrices formed by processing. Air drying of carrot severely restricts availability of carotene, which becomes entrapped within cell walls of dried cells and is hardly liberated by gastric juices. Enzyme action on starch in the gut depends on the porosity and permeability of the starch matrix formed during processing. The effect of food structure on nutrient availability deserves more attention because consumers are increasingly concerned about the effects of foods on health and well being. As mentioned before, the relation between structure and transport properties has also received marginal attention, the problem being circumvented by food engineers through the use of “apparent” transport coefficients that are process- and product-specific. Unless efforts are directed to quantify the microstructure and the properties of microstructural elements intervening in the architecture of foods, modeling the relation between structure and transport phenomena will remain largely empirical and qualitative.

According to Bailey (1998) modeling relationships should bring order to experience, clarify which components and interactions are important, generate new working hypotheses, and lead to proper interpretation of qualitative observations. Fundamental models are based on physical and engineering laws and generally represent ideal situations rarely achieved in practice. However, they are valuable in that critical parameters relating the intervening variables can be identified. Kinetic models are frequently used by food engineers because they provide a way of describing how a property varies with time and temperature using well-known mathematical expressions derived from chemical kinetics. Temperature effects are taken into account through the use of the Arrhenius equation for the glassy and fluid states or, for example, by the WLF equation for the rubbery state. Structural models, however, are preferred by engineers because they are based on the architecture and structural properties of the intervening elements and materials. Last, but not least, many relationships are the result of empirical curve fitting. This is the case of many equations that describe nonNewtonian behavior of foods, although it is accepted by rheologists that they represent structural changes induced by the rate of deformation.

Texture

An extremely important property of foods is texture. The term texture refers to an elusive but important quality attribute of foods that is difficult to measure or analyze. It is clear that whether testing is performed in our mouth or by an engineering probe, what is being measured is the manifestation of the structural organization of the food material. Food scientists define texture as “the sensory and functional manifestation of the structural and mechanical properties of foods, detected through the senses of vision, hearing, touch and kinesthetics” (Szczeniak, 1998). Most textural attributes of foods are perceived through mastication, a process by which a solid food is torn, ripped, crushed, and ground, mixed with saliva so that a bolus is formed that can be swallowed and digested. Considering that food texture is sensed through the response of nerve endings throughout the mouth and that these signals are integrated in the brain, it is easy to understand that texture may mean different things to different people (e.g., toughness of meat). To circumvent this complication (and limitation), food technologists have developed imitative tests and/or make use of engineering testing conditions using appropriate instruments. The so-called materials science approach states that the physical properties of a food are a reflection of the structural arrangements of elements in the microstructure. With this *caveat*, the term texture as used in this chapter refers also to a value determined instrumentally under controlled conditions.

What is the relationship between microstructure and texture in the realm of foods, both being such elusive terms? It would be ideal for the food processor to have a quantitative relationship (preferably a mathematical equation) that predicts texture from structure. A simple mechanical example

is a spring or coil. In a structural element like this the force will be linearly correlated with the deformation, with the spring constant taken care for structural variables (type of coil, material, etc.). Evidently almost no food exhibits such simple behavior, instead its response to a force would more likely be nonlinear or time-dependant.

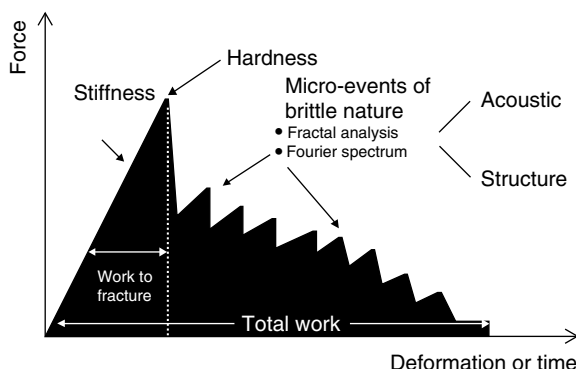
An Example: Hardening of Legumes

An interesting case of a qualitative structure–property relationship in LMF is hardening of dry legumes during storage. Legumes and other pulses stored at high temperature and humidity are susceptible to the hard-to-cook phenomenon. Beans with this defect do not soften sufficiently during cooking because they do not imbibe sufficient quantities of water. Structural factors that have been shown to influence water absorption are seed coat thickness, hilum size, seed volume, and color (Aguilera and Stanley, 1999). Observation of the cotyledons of cooked soft and hard beans using several microscopy techniques demonstrates a major structural difference. Legume hardening leads to a failure of cotyledon cells to separate during cooking. The middle lamellae between cells is largely dissolved in soft beans while it remains, cementing the cells together, in hard beans. A low fracture force (indicative of softness) is mechanically related to the sliding of individual cells one past another (much like the collapse of a wall of Lego cubes) while fracture in hard beans occurs across the cellular material and requires a much higher force.

Effect of Moisture Content on Mechanical Properties of LMF

Crispness of LMF

Crispness is an important textural property of LMF and has been studied both by instrumental and sensory techniques (Roudaut et al., 2002). The interpretation of crispness from a force–deformation curve proposed by Vincent (1998) will be adopted here (Figure 7.2). The initial rising part of the curve is a function of the *stiffness* of the sample. Stiffness depends on mechanical properties of the material and structural effects (e.g., air cells, microheterogeneities, geometrical parameters of the sample). The maximum force achieved before fracture is called *hardness*. An object may appear harder simply because it is denser (structure) or it has less cracks and not necessarily because the material is different. A *brittle* object will exhibit a large hardness, low work to fracture, and a sudden drop in force as the crack propagates fast. As deformation increases the phenomena repeat as a series of smaller events of rise and sudden drop of the force giving a jagged appearance to the diagram. This behavior is known in textural terms as *crispness*. As the events become larger with less crispness, this transforms

**FIGURE 7.2**

Typical force–deformation curve for mechanical testing of a brittle food.

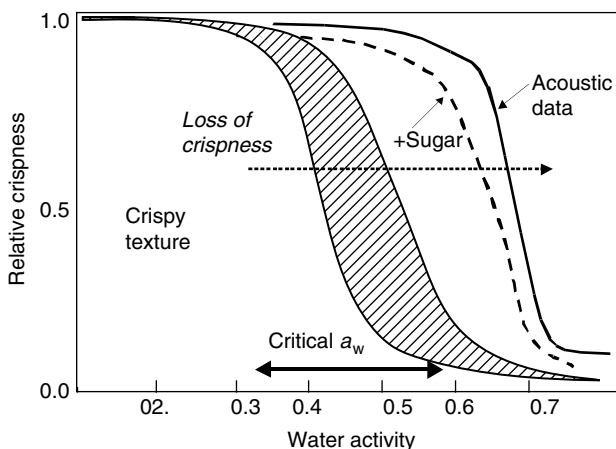
into *textural hardness*, while if they are smaller and more frequent, the texture becomes *crumbly*. The area under the force–displacement curve is defined as work (or as work per unit volume if measured under the area in the stress–strain curve) and known in engineering as *toughness* (Suwonsichon and Peleg, 1998).

The jagged portion of the force–deformation curve and of acoustic emission data has been assessed by fractal analysis and Fourier transform analysis (Barrett et al., 1992) and by the weighted distribution spectrum of the individual peaks (Vincent, 1998).

Effect of Moisture Content

In the range of moisture content of LMF (e.g., 3 to 20%) water acts as an effective plasticizer because of its low molecular weight, low density, high dielectric constant and ability to form H-bonds (Tolstoguzov, 2000). This role of water comes from its affinity with macromolecules and the interactions with charged and polar groups, shielding intra- and intermolecular interactions. A second factor is the increase in the distance between macromolecules by dilution. The net effect is a drop in the viscosity or modulus of the system and increased mobility of macromolecules (motion of chains, chain segments, torsion of end segments and side groups, etc.). The plasticizing effect of water has been related to structure related phenomena in LMF such as stickiness, collapse, and caking of amorphous powders (Roos, 1995).

Most low-moisture cereal-based foods (e.g., biscuits, extruded products, potato chips, etc.) have a crunchy or crisp texture that is lost as the moisture content increases either by redistribution within the product or moisture pick-up from the environment. The loss of crispness of cereal products and

**FIGURE 7.3**

Schematic diagram of the dependence of crispness on water activity (data of many authors). A sudden loss of crispness occurs in low-moisture cereal products within a relatively narrow range of moisture contents (critical a_w).

their main components is detected in instrumental testing as a change in the pattern and in the value of parameters derived from the force–deformation curve (Nicholls et al., 1985; Li et al., 1998; Norton et al., 1998; Suwonsichon and Peleg, 1998; Chang et al., 2000). At low water activities the force–deformation curve exhibits a jagged pattern that becomes smoother as this parameter exceeds some intermediate value (lets say 0.4 to 0.5). The loss of crunchiness as moisture content increases results in an increase in fracture force and toughness, a decrease in the fractal dimension and the disappearance of the high-frequency harmonics from the power spectrum of the jagged portion of the curve (Seymour and Hamann, 1988; Rohde et al., 1993). In particular, when any parameter characterizing crispness (e.g., stiffness, sensory crispness, or sensory crunchiness, a measure of jaggedness of the force deformation curve, or of acoustic emission) is plotted against moisture content or water activity, a sudden drop in value occurs at some intermediate value (Figure 7.3). The sigmoidal shape of this curve has been adequately fitted by a Fermi distribution function, where one parameter represents the steepness of the decay and defines the range where the change occurs (Rohde et al., 1993). Recently, European researchers have presented instrumental and sensory data showing that crispness of extruded starch can be preserved at higher water activities in the presence of added sucrose (Valles Pamies et al., 2000).

Crispness and the Glass Transition

The temperature at which a polymer changes from a glass to a rubber is known as the glass transition temperature, T_g . In the glassy condition,

molecules stay in an isoconfigurational state and the cooperativity effect is highly restricted; however, some molecular relaxation processes continue to take place below T_g . There is a dramatic change in the properties of a polymer at the glass transition temperature, for instance, a glassy polymer will lose its stiffness and start to flow above T_g . Unlike synthetic polymers that do not interact with water, in hydrophilic food polymers T_g decreases as the moisture content increases. This change may be quite dramatic, for example, 1% of water may lower the T_g of an anhydrous food polymer by 10°C or more. Textural properties of low-moisture cereal products are described as *crisp* or *brittle* when they are in the glassy state (i.e., their T_g is above the ambient temperature). Hence, it is not surprising that many authors have attempted to correlate the loss of crispness to the glass transition phenomenon. Figure 7.4 clusters many data for T_g of cereal products and their components as a function of water activity (Nikolaidis and Labuza, 1996; Vodovotz and Chinachioti, 1996).

There are several techniques available to determine T_g which are not equivalent in their way of probing the sample (e.g., DSC and DMTA). T_g depends on experimental conditions (e.g., scanning rate or loading) and its calculation from scans or curves is not always easy. This fact and the presence of multiple chemical components in LMF result in the wide range of T_g s observed in Figure 7.4. Sugars are known to plasticize starch but a single T_g is observed at low sugar:starch ratios, while two transitions are observed at higher ratios, suggesting phase separation (Tolstoguzov, 2000).

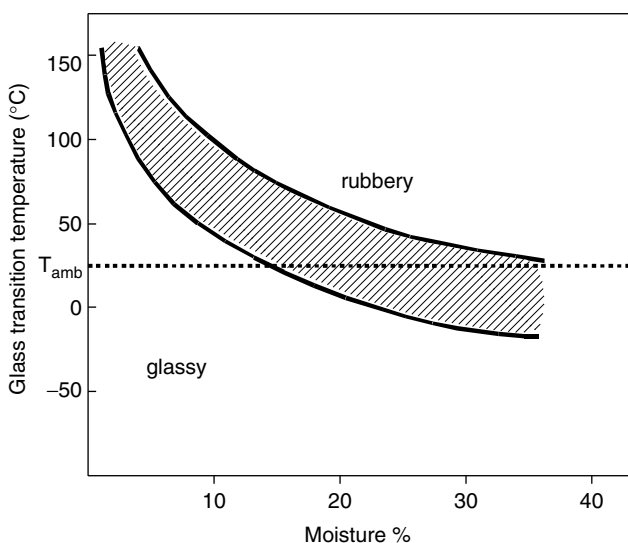


FIGURE 7.4

Schematic of range of glass transition data for low moisture cereal foods and their major components (starch, amylopectin, gluten).

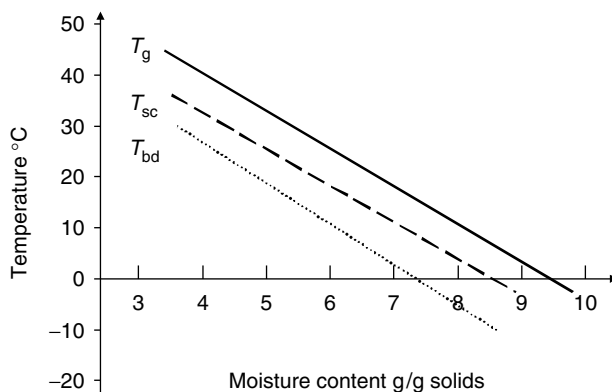
To summarize, finding a single T_g value that characterizes the glass–rubber transition in multicomponent foods may be difficult to accomplish.

Fracture of Polymers

Since crispness of LMF is manifested when a product is fractured, either experimentally or by mastication, it may be analyzed from the viewpoint of polymer fracture. If temperature is reduced sufficiently, polymers fail in a brittle manner, this is, at low strains and with almost no plastic deformation. Materials contain flaws and cracks that act as stress concentrators lowering their theoretical ultimate strength predicted from interatomic forces. In brittle materials, the stress is concentrated locally around the crack tip and the energy supplied makes it easy for the crack to propagate. Besides having a clean fracture surface, most brittle materials have lines and ridges beginning at the origin of the crack and spreading out across the crack surface. Ductile materials dissipate energy through plastic deformation around the crack tip, preventing crack propagation. Plastic flow, hence ductile fracture, depends on the rate of deformation, whereas brittle fracture is almost independent of the rate (Dobraszczyk and Vincent, 1999). The brittle stress of a polymer material decreases linearly as the temperature increases, while the yield stress drops dramatically at high temperatures. It is assumed that the fracture process is that which can take place at the lowest stress. At low temperature (low moisture content) the brittle stress is reached before the yield stress and brittle fracture takes place. At a critical temperature the brittle stress becomes higher than the yield stress required to cause brittle fracture and ductile fracture prevails. Glassy polymers may display a considerable amount of ductility below T_g when deformed under compression. The temperature crossover of the brittle and yield stress curves of a material (T_{bd}) marks the so-called *brittle-to-ductile* transition (Young and Lovell, 1991).

Fracture and the Glass Transition in LMF

It is understandable that efforts have been made to relate data for crispness with the glass transition temperature and at least in the case of a simple extruded maltodextrin/wheat flour model system loss of crispness started as T_g was depressed below ambient temperature (Roos et al., 1998). In general, evidence of such relationship is quite ambiguous. Li et al. (1998) reported major changes in the pattern of the force–deformation curves of corn cakes as water activity increased, suggesting a shift from brittle to ductile fracture; however, according to measured T_g values (DSC), all samples were in the glassy state. The preservation of crispness into higher water activities by sucrose referred to before (Valles Pamies et al., 2000) did not include T_g data, but it is known that addition of sucrose lowers the T_g of starch. Labuza et al. (2004) defined a brittle–ductile transition (T_{bd}) for chocolate wafers from data of force (N) vs. temperature (-20 to *ca* 40°C) at

**FIGURE 7.5**

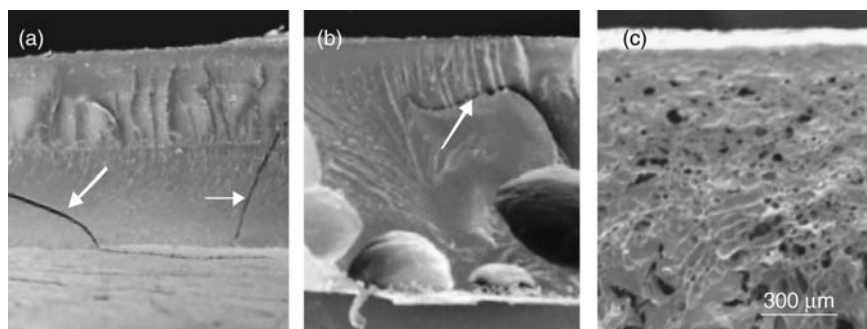
Effect of moisture content of chocolate cookies on the transition temperature: the glass transition, T_g , the critical sensorial transition, T_{sc} , and the brittle–ductile transition, T_{bd} .

constant moisture content (*ca* 5%). At temperatures below 20°C the “crispness intensity” remained high and constant while a dramatic decrease started to occur at around 28°C (the T_{bd}) and crispness dropped to zero at 40°C. They also performed sensorial analysis at different temperatures and by fitting data to a Fermi model defined a critical or transition temperature (T_{sc}) for the perceived crispness intensity. A plot of these transition temperatures and T_g (derived from the E' onset measured by DMTA) as a function of moisture content are shown in Figure 7.5. All three lines run almost parallel and separated by about 7°C from each other in the order $T_g > T_{sc} > T_{bd}$. The authors concluded that loss of crispness correlated well with the plasticizing effect of water in the system.

As discussed in Young and Lovell (1991) it is hard to believe that general correlations can be derived between the brittle–ductile transition and molecular relaxations (e.g., T_g data obtained by DSC). Molecular relaxations are detected at low strains, whereas T_{bd} is measured at high strains and depends on factors such as the presence of notches, which do not affect molecular relaxations.

Structure–Property Relationships in a Low-Moisture Starch Model System

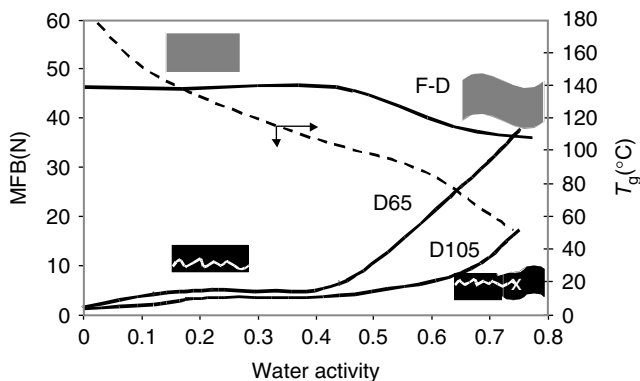
Different microstructures and product properties may be achieved for the same material by varying the processing conditions. In a recent study, the effect of type of drying (air vs. freeze-drying) and temperature of the drying air was assessed with respect to the microstructure and mechanical properties of a starch model system (Aguilera et al., 2004). Equal volumes of a 20% (w/w) suspension of pregelatinized potato starch were poured into molds and dried at 65°C (D65) and 105°C (D105) in a laboratory oven or freeze-dried (FD).

**FIGURE 7.6**

Low-vacuum SEM photomicrographs of fracture surfaces of dried starch samples. (a) Air dried at 65°C; (b) air dried at 105°C; (c) Freeze-dried. Arrows in (a) point at cracks that may extend into the outer surface (bottom). In (b) arrows show possible sites of cracks at which fracture occurred.

Photomicrographs of dried products are shown in Figure 7.6. Specimen D65 exhibited a very dense structure as it shrunk during drying to almost one third of the original volume. Sample D105 also presented a dense microstructure caused by shrinkage but contained a few large air bubbles as inclusions. FD maintained almost exactly the original volume and presented a porous structure because of water sublimation from ice crystals.

Of several physical parameters derived from the force–deformation curve (three-point bending assay) only the relation of the maximum force at breakage (MFB) of the dried products with water activity will be discussed here (Figure 7.7). At low moisture content, air dried samples showed a lower MFB than the FD sample. This may be because during drying in hot air,

**FIGURE 7.7**

Dependence of the maximum force at breakage (MFB) with water activity for a dry starch model. D65 and D105: air dried at 65 and 105°C, respectively; FD: freeze-dried. Dotted line represents the glass transition temperature.

moisture gradients set in, inducing tensile stresses in the surface (dry) and compressive stresses in the interior (wet) of the slab. This stress gradient is likely to produce cracks in the material (a well known problem in the pasta industry) that propagate readily upon application of a force causing brittle fracture. During freeze drying, on the other hand, water sublimates as a receding sharp front formed by the interface of dry and frozen material. Because of this peculiar moisture gradient almost no shrinkage occurs, internal stresses are low and the formation of extended cracks is severely limited by the presence of multiple pores, which also act to arrest any crack propagation later during testing. At a water activity of 0.4 to 0.5, the MFB of air dried samples started to increase sharply, as also observed for corn cakes (Li et al., 1998). This trend can also be interpreted from the microstructure. Increased moisture results in plasticization of the zone surrounding the tips of cracks, causing yield and deformation before fracture to occur at a higher force (Figure 7.7). The FD sample responds as a typical polymeric material undergoing a glass–rubber transition; this is, the force drops as moisture content increases. The fact that the change in force occurs at the same water activity in both cases supports this interpretation. It should be noted that the glass transition temperature determined by DSC is similar for all three materials (as it should be). As shown in Figure 7.7 from the value of T_g it is impossible to predict the type of fracture or the force necessary for breaking a material. The challenge now is to acquire microstructural information (e.g., by video-microscopy) and physical data simultaneously to correlate actual structural events with the mechanical response of the material.

Microstructure and Auditory Sensations

The sound released by foods as they are broken or bitten into is part of the perceived texture. Crisp foods are expected to emit sounds upon biting and the lack of acoustic emission is a sign of staleness and poor quality (Duizer, 2001). The microstructure of LMF, in particular, the size and arrangement of air cells, cell wall thickness and brittleness, density and presence of cracks, affect noise production. Sound waves in cellular LMF are generated during breakage of cell walls as broken lamellas vibrate, generating sound waves. In noncellular LMF it is the repeated fracture that produces the sound. Amplitude–time curves (acoustic signatures) obtained during mechanical testing have been studied by fractal analysis and fast Fourier transform, much in the same way as force jaggedness. The relationship between acoustic emission data and water activity follows the sigmoidal shape already reported for mechanical and sensorial parameters related to crispness. Acoustic emission of starch and gluten shows a sharp downward concavity at 10 to 13% moisture content (Attenburrow, 1992) while acoustic parameters for pasta exhibit a sharp drop between water activities of 0.48 and 0.75 (Alchakra et al., 1997). The contribution of sound to crispness perception seems to be very product-dependant. Nevertheless, samples from different brands of crispbread could not be classified correctly using noise data alone but when

this variable was combined with information of the crushing force all samples but one could be correctly classified (Winqvist et al., 1999). It appears that the use of more complex classification schemes such as neural networks would allow grouping of samples of a product into crispness categories as a function of their moisture content and the frequency domain spectra of acoustic signals, as reported for selected snack foods (Srisawas and Jindal, 2003). To conclude, the sentence by Duizer (2001), who has recently reviewed the subject of crispness and crunchiness, seems appropriate: "... the next stage for acoustic research should be to relate structure of the products to the sounds produced during mechanical breakdown."

Concluding Remarks and Future Trends

Ample agreement exists within the food science community that control of food microstructure is critical in food product quality. Linking structure to physical properties of foods is still an open task for food scientists and food technologists. New microscopy and imaging techniques spanning many decades of length scale, applied noninvasively to actual food samples and providing quantitative microstructural data promise spectacular developments in years ahead. The next step will be to develop models that correlate microstructural information with the appropriate physical data. Ultimately, these models and relationships need to be validated by sensorial analysis so true structure–property relationships are available for practical use. This approach constitutes a paradigmatic shift in food product development and food product design.

Acknowledgment

Research on structure–property relationships in amorphous systems has been supported by a grant from the FONDECYT project 1030339.

References

- Aguilera, J.M. Why microstructure?, *J. Food Eng.*, 62, 3, 2005.
- Aguilera, J.M., Castro, L., and Cadoche, L. Structure relationships in a starch amorphous model, *Drying — Proceedings of the 14th International Drying Symposium*, Sao Paulo, Brazil, Vol. B, p. 1468, 2004.
- Aguilera, J.M. and Lillford, P. Microstructural and image analysis as related to food engineering, *Food Engineering 2000*, P. Fito, E. Ortega, and G. Barbosa-Canovas, eds., Chapman & Hall, London, pp. 23, 1996.

- Aguilera, J.M. and Stanley, D.W. *Microstructural Principles of Food Processing and Engineering*, 2nd ed., Aspen Publishers Inc., Gaithersburg, 1999.
- Alchakra, W., Allaf, K., and Ville, J.M. Acoustical emission technique applied to the characterization of brittle materials, *Appl. Acoust.*, 52, 53, 1997.
- Attenburrow, G.E. The fracture behavior of starch and gluten in the glassy state, *J. Cereal Sci.*, 16, 1, 1992.
- Bailey, J.E. Mathematical modeling and analysis in chemical engineering: past accomplishments and future opportunities, *Biotechnol. Prog.*, 14, 8, 1998.
- Barrett, A.H., Normand, M.D., Peleg, M., and Ross, E. Characterization of the jagged stress–strain relationships of puffed extrudates using the fast Fourier transform and fractal analysis, *J. Food Sci.*, 57, 227, 1992.
- Blanshard, J.M.V. Elements of cereal product structure, *Food Structure — Its Creation and Evaluation*, J.M.V. Blanshard and J.R. Mitchell, eds., Butterworths, London, pp. 313, 1988.
- Chang, Y.P., Cheah, P.B., and Seow, C.C. Variations in flexural and compressive fracture behavior of a brittle cellular food (bread) in response to moisture sorption, *J. Texture Stud.*, 31, 525, 2000.
- Dobraszczyk, B.J. and Vincent, J.F.V. Measurement of mechanical properties of food materials in relation to texture: the materials approach, *Food Texture: Measurement and Perception*, A.J. Rosenthal, ed., Aspen Publishers Inc., Gaithersburg, 1999, chap. 5.
- Duizer, L. A review of acoustic research for studying the acoustic perception of crisp, crunchy and crackly textures, *Trends Food Sci. Technol.*, 12, 17, 2001.
- Gonzalez, R.C. and Woods, R.E. *Digital Image Processing*, 2nd ed., Prentice-Hall, New Jersey, 2001.
- Kalab, M., Allan Wojtas, P., and Miller, S.S. Microscopy and other imaging techniques in food structure analysis, *Trends Food Sci. Technol.*, 6, 177, 1995.
- Labuza, T., Roe, K., Payne, C., Panda, F., Labuza, T.J., Labuza, P.S., and Krush, L. Storage stability of dry food systems: influence of state changes during drying and storage, *Drying — Proceedings of the 14th International Drying Symposium*, Sao Paulo, Brazil, Vol. A, 2004.
- Li, Y., Kloeppel, K.M., and Hsieh, F. Texture of glassy corn cakes as a function of moisture content, *J. Food Sci.*, 63, 869, 1998.
- McCarthy, M.J. *Magnetic Resonance Imaging in Foods*, Chapman & Hall, New York, 1994.
- Nicholls, R.J., Appelqvist, I.A.M., Davies, A.P., Ingman, S.J., and Lillford, P.J. Glass transitions and the fracture behaviour of gluten and starches within the glassy state, *J. Cereal Sci.*, 21, 25, 1985.
- Nikolaïdis, A. and Labuza, T.P. Glass transition state diagram of a baked cracker and its relationship to gluten, *J. Food Sci.*, 61, 803, 1996.
- Norton, C.R.T., Mitchell, J.R., and Blanshard, J.M.V. Fractal determination of crisp and crackly textures, *J. Texture Stud.*, 29, 239, 1998.
- Rohde, F., Normand, M.D., and Peleg, M. Effect of relative humidity on the mechanical signatures of brittle food materials, *Biotechnol. Prog.*, 9, 497, 1993.
- Roos, Y.H. *Phase Transitions in Foods*, Academic Press, San Diego, CA, 1995.
- Roos, Y.H., Roininen, K., Jouppila, K., and Tuorila, H. Glass transition and water plasticization effects on crispness of a snack food extrudate, *Int. J. Food Prop.*, 1, 163, 1998.

- Roudaut, G., Dacremont, C., Valles Pamies, B., Collas, B., and Le Meste, M. Crispness: a critical review on sensory and material science approaches, *Trends Food Sci. Technol.*, 13, 217, 2002.
- Russ, J.C. *Image Analysis of Food Microstructure*, CRC Press, Boca Raton, FL, 2005.
- Saravacos, G.D. and Maroulis, Z.B. *Transport Properties of Foods*, Marcel Dekker, New York, 2001.
- Seymour, S.K. and Hamann, D.D. Crispness and crunchiness of selected low moisture foods, *J. Texture Stud.*, 19, 79, 1988.
- Srisawas, W. and Jindal, V.K. Acoustic testing of snack food crispness using neural networks, *J. Texture Stud.*, 34, 401, 2003.
- Suwonsichon, T. and Peleg, M. Instrumental and sensory detection of simultaneous brittleness loss and moisture toughening in three puffed cereals, *J. Texture Stud.*, 29, 255, 1998.
- Szczesniak, A.S. Sensory texture profiling: historical and scientific perspectives, *Food Technol.*, 52, 54, 1998.
- Tolstoguzov, V.B. The importance of glassy biopolymer components in foods, *Nahrung*, 44, 76, 2000.
- Valles Pamies, B., Roudaut, G., Dacremont, C., Le Meste, M., and Mitchell, J.R. Understanding the texture of low moisture cereal products: mechanical and sensory measurements of crispness, *J. Sci. Food Agric.*, 80, 1679, 2000.
- Vincent, J.F.V. The quantification of crispness, *J. Sci. Food Agric.*, 78, 162, 1998.
- Vodovotz, Y. and Chinachioti, P. Thermal transitions in gelatinized wheat starch at different contents by dynamic mechanical analysis, *J. Food Sci.*, 61, 932, 1996.
- Winqvist, F., Wide, P., Eklov, T., Hjort, C., and Lundstrom, I. Crispbread quality evaluation based on fusion of information from the sensor analogies to human olfactory, auditory and tactile senses, *J. Food Process Eng.*, 22, 337, 1999.
- Young, R.J. and Lovell, P.A. *Introduction to Polymers*, 2nd ed., Chapman & Hall, London, 1991.

8

Ice Nucleation in Bulk and Dispersed Water: Application to Freezing of Foods

Danièle Clause, Jean-Louis Lanoisellé, and Saïd Toumi

CONTENTS

Introduction	133
Ice Nucleation in Bulk Water.....	134
Experimental Determination of the Sample Freezing	137
Calorimetry	137
Microscopy	139
Experimental Results.....	139
Bulk Water.....	139
Bulk Water + NaCl	140
Dispersed Water	143
Raw Bean.....	144
Blanched Bean	146
Blanched Bean + Immersion + Freezing.....	147
Extracted Juice.....	148
Solid Residue	148
Conclusions.....	149
Acknowledgments	150
References	150

Introduction

A way to preserve vegetables vs. time is first to blanch them and afterwards to cool them in order to transform available liquid water into ice. This process is called “freezing” and has been established as an excellent method for preserving high quality in foods (Reid, 1983). Nucleation (formation of ice crystals) and crystal growth are the two major thermal events of the

freezing process. Crystal growth depends on three factors: rate of reaction at the crystal surface, diffusion rate of water, and rate of heat removal (George, 1997). Freezing food materials rapidly leads to a large number of nucleation sites and to small ice crystals. Then after a freeze/thaw cycle, the food product characteristic changes tend to be less than those obtained at slow freezing rates. In the aim of setting up an ameliorated process, we have studied the conditions of ice nucleation and ice melting in order to define and determine the parameters needed for the process such as temperature and energy freezing. Because water is the predominant constituent in most foods, water content significantly influences the thermophysical properties of food and their behavior during the freezing process. For fruits and vegetables, the average value of moisture content (percent by mass) is around 85% varying from 59% for garlic to 96% for cucumbers (ASHRAE, 2002). For these products, water contents vary with the cultivar as well as with the stage of development or maturity. Although it is not yet clearly understood how water is distributed within vegetables, it is known that water could appear as bulk water like a continuous medium outside the cells and as dispersed within the cells. Water is not pure and the influence of solute has also to be taken into account.

Therefore, it is the theoretical basis of ice nucleation in bulk and dispersed water that will be first recalled. Numerous articles are available on the subject and not only on water. Nevertheless, the main points will be given in this article in order to be able to stress the points needed to interpret the results obtained. Afterwards the techniques used to detect the freezing and melting of water will be presented. From numerous works dealing with ice nucleation in bulk and dispersed materials it appears that differential scanning calorimetry (currently named DSC) is suitable and allows the collection of numerous data such as: freezing and melting temperatures and energies, quantity of water dispersed, water transfer (Clause et al., 1999a, 1999b, 2002; Fouconnier et al., 2000; Dalmazzone and Clause, 2001) and presence of solutes. Moreover, the test being performed is very simple to set up and does not need any previous treatment. For comparison, the DSC signals dealing with bulk water, dispersed water, and vegetable, information about the amount of water in the vegetable, the way it is distributed within the vegetable, the presence of solutes, and the effect of freezing/melting cycles can be also deduced. Microscopy of the samples under study has been also undertaken to get more information for interpreting the results obtained by DSC. Studies of the microstructure of frozen plant products indicate clearly how freezing causes disruption of the internal cell structures (Reid, 1987).

Ice Nucleation in Bulk Water

Let us consider a sample of water volume V that is submitted to a regular cooling. To initiate the freezing it is necessary to get an ice embryo that is

very small so that it can form in the liquid without any supplementary external energy. Thermodynamics of such a system tell us that because of capillary effects giving rise to excess pressure inside the embryo, the metastable equilibrium of this embryo with the surroundings is reached at a temperature T , which is lower than the solid–liquid equilibrium one for water ($T_m = 0^\circ\text{C}$, under atmospheric pressure). Moreover, according to Equation 8.1, the smaller the embryo, the lower this temperature

$$\ln \frac{T}{T_m} = -\frac{2\gamma V_i}{RL_C} \quad (8.1)$$

where γ is the interfacial ice — under cooled water energy, L_C is the freezing molar energy at temperature T , V_i is the ice molar volume, and R is the radius of the germ.

The embryo radius R has a critical size that means that all the embryos formed having a smaller size will dissolve and those having a higher size will grow and induce the freezing of the whole sample as far as pure water is concerned. As it will be shown later on, the situation is different when solutes are dissolved within the water.

Some of the internal energy, $\Delta\Phi$, which comes from local fluctuations is needed to get the embryo to critical size R . This energy is given by Equation 8.2

$$\Delta\Phi = \frac{4}{3}\pi R^2 \gamma \quad (8.2)$$

The embryos appear by chance within water and the kinetic aspect of their formation has to be taken into account. This point is achieved by introducing what is called the nucleation rate, J , which gives the number of embryos formed by time and the volume unit. It appears also that the probability of freezing by volume and time unit requires only one embryo to induce the whole freezing of the sample. The nucleation rate J is given by

$$J = A e^{-\Delta\Phi/kT} \quad (8.3)$$

with A depending essentially upon the viscosity of the medium.

Considering now the total volume V of the sample and what is going on during the lapse of time dt , the corresponding freezing probability dP is given by Equation 8.4

$$dP = JVdt \quad (8.4)$$

It follows that between time 0 corresponding to $T = T_m$ and a given temperature less than T_m and reached at time t , the sample may freeze with a probability given by Equation 8.5

$$P = \int_0^t JVdt \quad (8.5)$$

From Equation 8.1 to Equation 8.3, it appears that the lower the temperature, the smaller the embryos radius, and the lower the energy, the greater the

value of J . Therefore, it is very difficult to freeze a sample when its temperature is close to T_m . Moreover, from Equation 8.4 and Equation 8.5, it can be deduced that the smaller the volume sample, the lower the freezing probability at any temperature. It becomes obvious that the freezing temperature of a sample is not an invariant and can change from one experiment to another, even if nothing has been changed. Studying the freezing of identical samples of the same volume V , the number of samples that are expected to freeze during time dt is given by Equation 8.6

$$dN = JV(N - N(t))dt \quad (8.6)$$

where $N(t)$ is the number of frozen samples at time t .

It can be deduced from Equation 8.6 that dN is passing through a maximum because it is null above T_m with $J = 0$ and it is again null when all the samples are frozen because $N(t) = N$. The corresponding schematic histogram is given in Figure 8.1. When all the freezing events are cumulated, the probability defined by Equation 8.7 can be deduced at any time and therefore at any temperature reached during the regular cooling:

$$P = \frac{N(t)}{N} \quad (8.7)$$

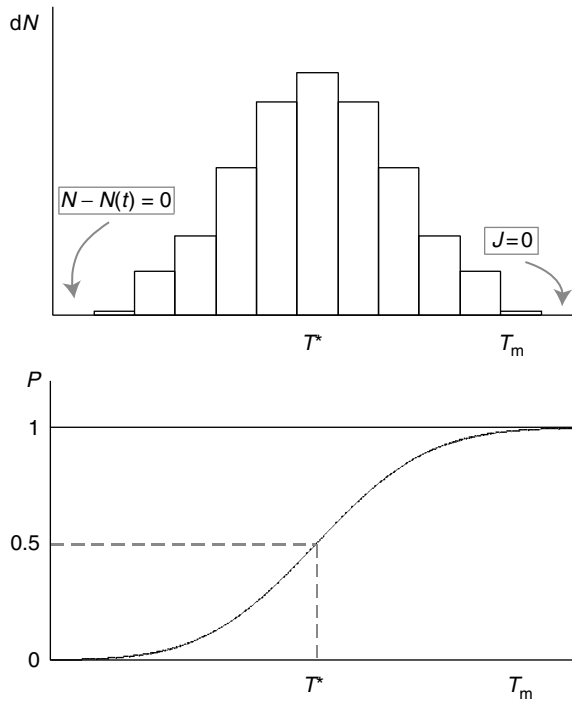


FIGURE 8.1

Freezing temperatures distribution.

To characterize the freezing of one sample, a most probable freezing temperature T^* has been defined by Equation 8.8

$$P(T^*) = 0.5 \quad (8.8)$$

From these considerations it appears that freezing is a stochastic event considering a single sample and only a probability of freezing can be defined. Therefore, the freezing temperatures of identical samples are expected to be scattered around a mean value given by T^* , which becomes lower as the samples get smaller. For example for identical water samples of a few cm^3 , this temperature is found to be around -15°C , for a few mm^3 they are around -20°C and for a few μm^3 around -40°C .

Experimental Determination of the Sample Freezing

Two complementary techniques have been used: calorimetry and microscopy. The results obtained are described in the following sections.

Calorimetry

One technique for pointing out the freezing of a sample is to do it through the energy released and therefore to use a calorimeter. This has been achieved by testing the sample in a differential scanning calorimeter: DSC 111 — SETARAM. The mm^3 water sample is put directly in a sealed cell, which is introduced into the head of a calorimeter and submitted to a regular cooling (at 2 K/min) from $+20^\circ\text{C}$ down to -60°C .

The heat generated by the freezing of the sample, dh/dt , is given by Equation 8.9

$$\frac{dh}{dt} = \frac{dq}{dt} + (C_s - C_r) \frac{dT}{dt} - RC_s \frac{d^2q}{dt^2} \quad (8.9)$$

where dq/dt is the difference of energy exchanged between the sample at temperature T_s and the reference at temperature T_r . It is given by $(T_s - T_r)/R$, R being the thermal resistance through which the thermal energy flows from the sample; dT/dt is the cooling rate of the sample holder; C_s and C_r are the total heat capacities of the sample plus container and the reference (container empty), respectively; R is the thermal resistance through which the thermal energy flows from the sample.

According to Equation 8.9, dh/dt appears as the sum of three contributions:

- the signal from the zero signal line and given directly by the calorimeter
- the baseline displacement from the difference in heat capacity between the sample and the reference and
- the slope of the recorded curve multiplied by the quantity RC_s .

When no freezing occurs, $dh/dt = 0$ and it can be shown that Equation 8.9 can be written as:

$$\frac{dq}{dt} = (C_s - C_r) \frac{dT}{dt} \quad \text{for } t \gg RC_s \quad (8.10)$$

Therefore, by following the displacement of the baseline, it can be possible to determine the changes of C_s vs. temperature. It can be expected that the baseline is not continuous between before and after freezing; C_s for ice (0.5 cal/g/°C) is half the value of C_s for liquid water.

During freezing, the corresponding value of dh/dt can be deduced from Equation 8.9 graphically when RC_s is known. It has been shown that RC_s can be deduced from the melting signal of pure water and the cooling rate is less than around 2 K/min and the sample volume small enough less than a few mm³. T can be considered as uniform within the sample and $dh/dt \approx dq/dt$.

The total energy released is obtained from Equation 8.11

$$\Delta H = Q = \int_{t_1}^{t_s} \frac{dh}{dt} dt \quad (8.11)$$

t_1 and t_s being the times before and after freezing. The corresponding energy is deduced from the area of the signal correctly delimited. Generally a simple straight line is drawn between the beginning and the end of the signal. This method should be considered as an approximation that is reliable if the signal is well defined and if the baseline is correctly defined before and after the freezing signal.

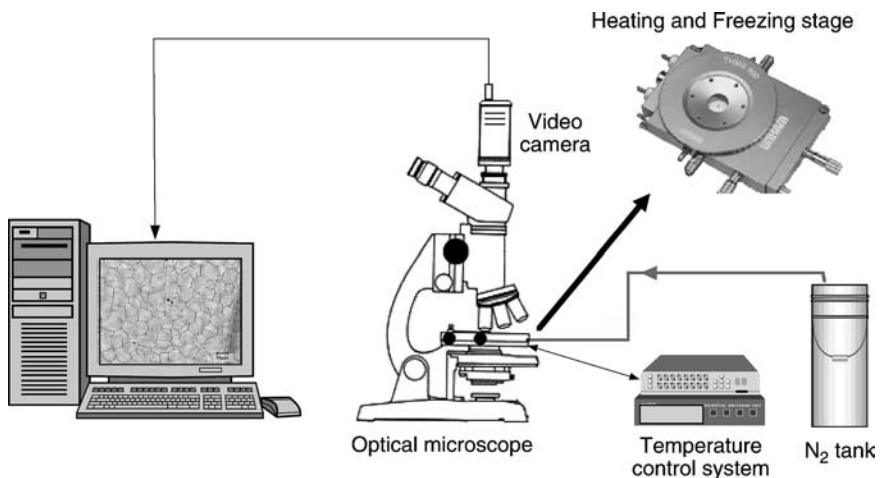


FIGURE 8.2
Cryomicroscopy experimental setup.

Microscopy

To observe the freezing of a sample it is necessary to cool it below 0°C and it could be as low as -60°C if solutes are present. The problem is to reach this temperature range without moist and frost. That was achieved by using a special device (Figure 8.2): Linkam THMS600 heating and freezing stage (temperature can be controlled within 0.1°C for the range of -192 to +600°C). Freezing of a sample was observed using an optical microscope (Nikon, Japan). The images from the microscope were converted to digital images through a SSC-DC58AP color video camera (Sony, Japan), and captured and processed with image analysis software.

Experimental Results

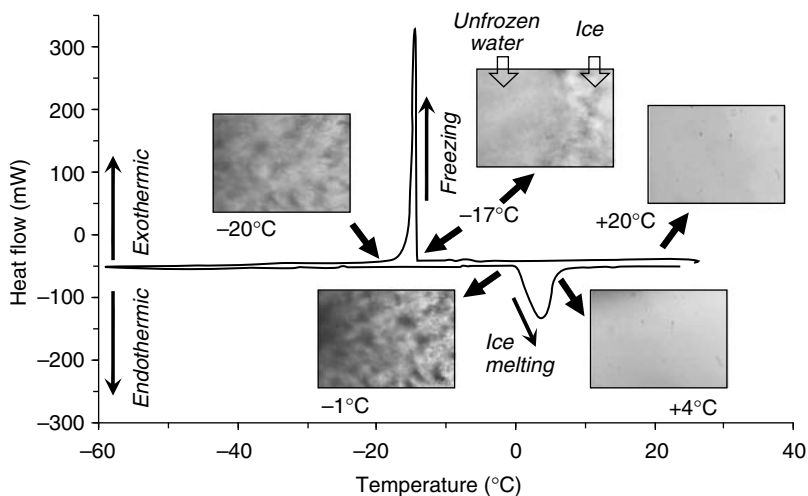
The results obtained by studying:

- bulk water (mm³) with and without solute
- dispersed water (μm³) with and without solute
- raw bean
- blanched bean
- blanched bean that has been submitted to an immersion + freezing process and
- extracted bean juice

are given. The thermograms obtained by DSC of these materials submitted to a regular cooling and heating between +20 and -60°C are compared in order to point out the mechanisms of ice formation and melting in beans that have been submitted to various thermal treatments. As it was indicated in the introduction, the aim of this study is to find the best process of bean preservation that will avoid structural damage of the bean. Therefore, before studying the beans themselves, it is important to have in mind what is the response of bulk water and dispersed water submitted to a regular cooling and heating as nucleation phenomena depending upon the volume have to be considered and these results will be given first. For some samples, microscopy pictures will be also given.

Bulk Water

Figure 8.3 represents the freezing thermogram obtained during the regular cooling of 28 mg of pure water. For comparison, the thermogram obtained during the regular heating from -60°C is also given. Despite the fact that during the cooling some energy is released (exothermic signal) and that during heating some energy is adsorbed (endothermic signal), very different behaviors are found. Freezing begins very sharply

**FIGURE 8.3**

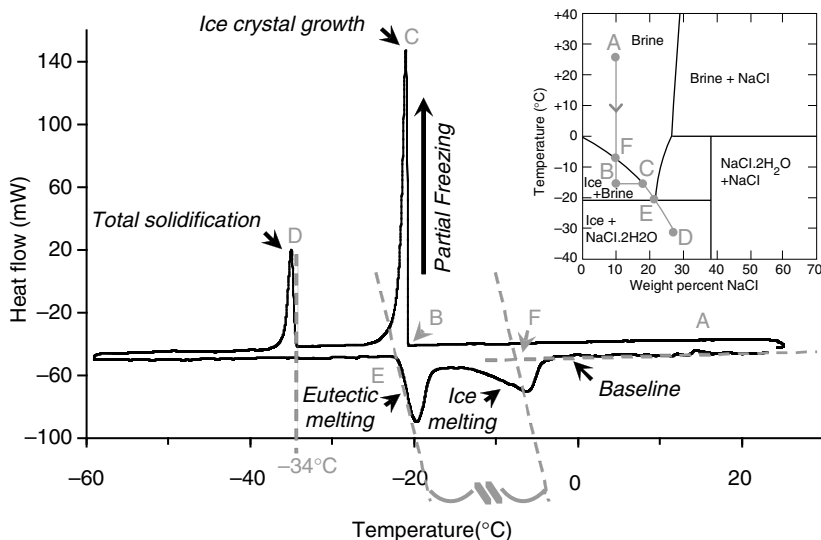
DSC thermogram of bulk water ($M_{\text{water}} = 28 \text{ mg}$). Freezing energy: 66.06 cal/g; melting energy: 78.45 cal/g.

at -17°C , whereas melting begins smoothly at 0°C . For this sample it appears that it is necessary to cool it down to -17°C to get at least one embryo that will then sharply induce the transformation into ice of the bulk under cooled liquid water. The freezing temperature may be found to be different for some samples because of the stochastic aspect of the freezing phenomenon, as has been described in the previous section. Melting is found to occur differently, with no nucleation phenomenon having to be considered and the extension of the signal is caused by heat transfer and the response of the calorimeter exclusively. From the signal areas, the corresponding energies have been found to be different, a result that is not surprising as the heat capacities of ice and water are quite different.

The microscopic photographs taken at different stages of the cooling and heating of a water drop put directly onto the microscope plate confirm what has been obtained by DSC (Figure 8.3).

Bulk Water + NaCl

The corresponding thermograms obtained for a 30.9 mg solution containing 10% wt/wt NaCl is reported in Figure 8.4. A sharp freezing is found to occur at around -20°C (point B) but, as expected, the ice nucleation does not induce the total solidification of the available water. This one occurs at a lower temperature, namely at -34°C (point D). The behavior can be followed on the phases diagram at atmospheric pressure of the binary NaCl + H_2O between $+40$ and -40°C (Figure 8.4). Point A represents the state of the solution under

**FIGURE 8.4**

DSC thermogram of bulk aqueous NaCl solution (10%) ($M_{\text{water}} = 30.9 \text{ mg}$).

study at +25°C. During cooling, the sample remains liquid until the ice nucleation occurs (point B). A certain amount of ice formed instantaneously and therefore a sharp release of energy is observed. The amount of ice formed at the end is such that the system is made of a solution that is in equilibrium with pure ice, given by point C. During further cooling, more and more ice is formed and the remaining solution is more and more concentrated according to the liquidus curve and its extension below the eutectic point E. When the remaining supersaturated solution is concentrated enough with respect to salt, NaCl precipitates and the remaining water transforms instantaneously into ice (point D). It is this last energy from the formation of ice that is significant, the energy from the salt precipitation being rather small in comparison.

During melting, as for pure water, there are no nucleation phenomena and the thermal events that show the thermogram is the eutectic melting (point E) followed by the progressive ice melting, which ends when the temperature reaches the equilibrium of ice with the solution under study (point F). This point is obtained by drawing a parallel straight line to the eutectic signal, as indicated on the thermogram. This is a way of obtaining the corresponding slope given by dT/dt divided by the thermal resistance R defined previously. More details of this determination may be found in Clausse et al. (1999a).

The microscopic photographs taken at different stages of the cooling and heating of a water + NaCl drop put directly onto the microscope plate confirm that some ice was formed before -20°C and that melting started at -21°C to be nearly achieved at -6°C (Figure 8.5).

TABLE 8.1
Comparison of Expected Proportion of Ice Formed and Height of the DSC Signal

Freezing Temperature (°C)	Percentage of Ice Formed	Height of DSC Signal (mW/g)
- 11.2	80.4	5731
- 13.0	82.4	6353
- 15.2	84.2	6936

proportion of ice formed can be obtained using the ratio of the lengths of the segments B_i and $(A_i + B_i)$. Therefore, when the ice nucleation occurs by breakdown of the undercooling of the solution, a sharp release of energy is expected, as the DSC curve points out. For comparison, the values of this ratio and the height H_i of the DSC signals have been determined for the three temperatures found. The results obtained are given in Table 8.1.

As described previously, the second signal observed during the cooling is dealing with the total solidification of the sample. The corresponding temperature is given at point D. The stochastic aspect appears clearly also but the amount of ice formed is rather small because of the low salt concentration, so this effect is less noticeable.

Dispersed Water

The thermogram dealing with pure water (30% wt/wt) dispersed within mineral oil (70% wt/wt paraffin oil + span 80) is given in Figure 8.7.

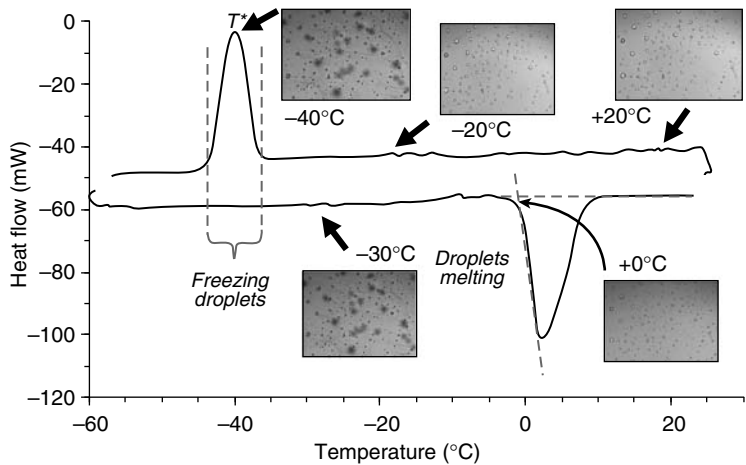


FIGURE 8.7
DSC thermogram of W/O emulsion (water 30% wt/wt, mineral oil 70% wt/wt) ($M_{\text{emulsion}} = 82 \text{ mg}$).

The scattering of the freezing temperatures are observed around -40°C as expected and the melting without delay at 0°C . Compared with the freezing signal of one bulk water sample (Figure 8.3), the shapes are quite different, one showing a sharp slope and the other one a rather symmetrical shape. These differences in shape and in the corresponding temperatures are a way of obtaining some information about the distribution of water within a material.

If some ice nucleators are present in the droplets such as AgI or bacteria (Clausse et al., 1988), the freezing signal is moved to the highest temperatures, suggesting a smaller undercooling as expected with the energy barrier being smaller (Figure 8.8).

Raw Bean

An extra-fine green bean (*Phaseolus vulgaris*) variety from Kenya was used in our experiments. A piece of green bean was cut with a scalpel, weighed (approximately 40 mg) and put in an aluminum cell, the volume of which was approximately 250 mm^{-3} . The cell was closed and placed in the head of the calorimeter at 20°C . After this, the piece of green bean went through

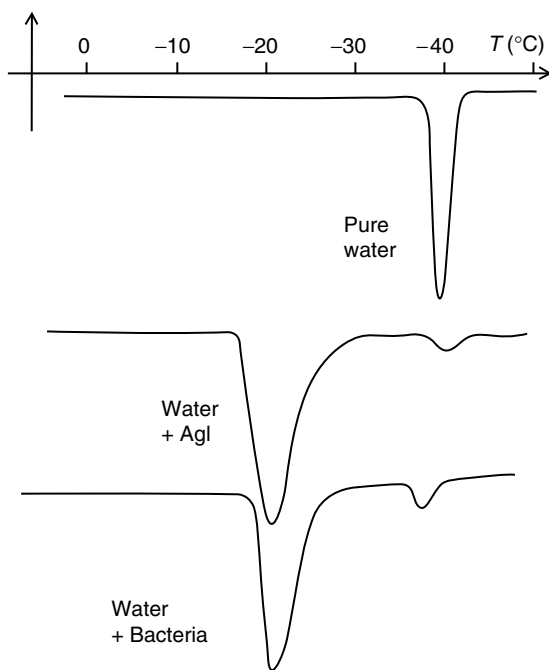


FIGURE 8.8

DSC thermograms of pure water and water with nucleators (AgI or bacteria). Adapted from Clausse et al. (1988).

seven regular cycles of cooling and heating between $+20$ and -40°C at a nominal scanning rate of $2^{\circ}\text{C}/\text{min}$.

The thermograms obtained from DSC tests performed on a 37.8 mg sample are given in Figure 8.9. In the first cycle, the signal obtained during cooling is exothermic and is attributed to ice formation, which begins at -9.6°C . The sharp release of energy (nearly infinite slope) shows that some bulk water has an effect, as was found in Figure 8.3. This sharp release is followed by a signal that is similar to the signal obtained for the freezing of dispersed water (Figure 8.7). Nevertheless, the freezing temperatures are quite different, as if some ice nucleators are present (Figure 8.8). Some scattering of the ice crystal formation could be suspected given birth to ice crystals smaller than the ones formed in bulk. The observation of the freezing of a sample cooled in the cryomicroscopy experimental device displays effectively a sharp freezing that propagates rapidly through the whole sample, followed by freezing events in different points of the sample (Figure 8.10; cooling at -12.5 , -13 , and -13.5°C). This phenomenon tends to disappear during the later cycles as can be seen from the signals obtained during the second, third, and seventh cycles. The melting endothermic signals that show the ice melting in the presence of solutes as the starting point have to be compared with the ones obtained for a solution (Figure 8.6). It shows also an evolution with the number of cycles performed. The widths are diminishing and a slight outgrowth is observed at 0°C that disappears with the cycles. These kinds of thermograms have been obtained with materials that show some similarities (Li and Lee, 1998) but a reliable interpretation requires more experiments dealing with more samples, because of the stochastic aspect of the phenomena observed, and more

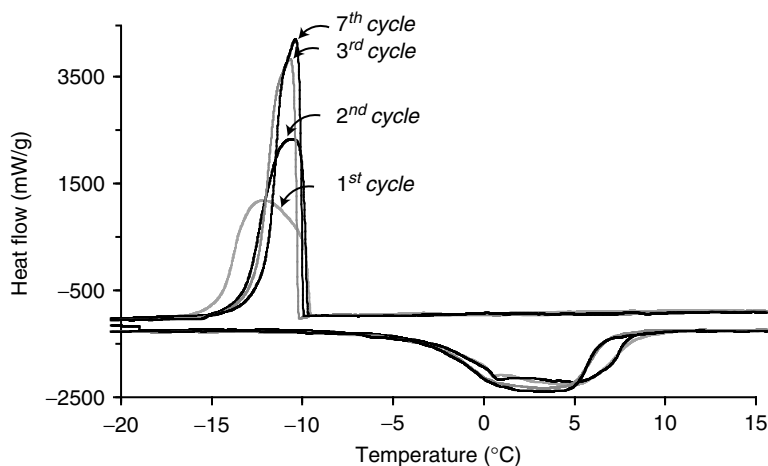


FIGURE 8.9

DSC thermograms of raw bean ($M_{\text{bean}} = 34$ mg).

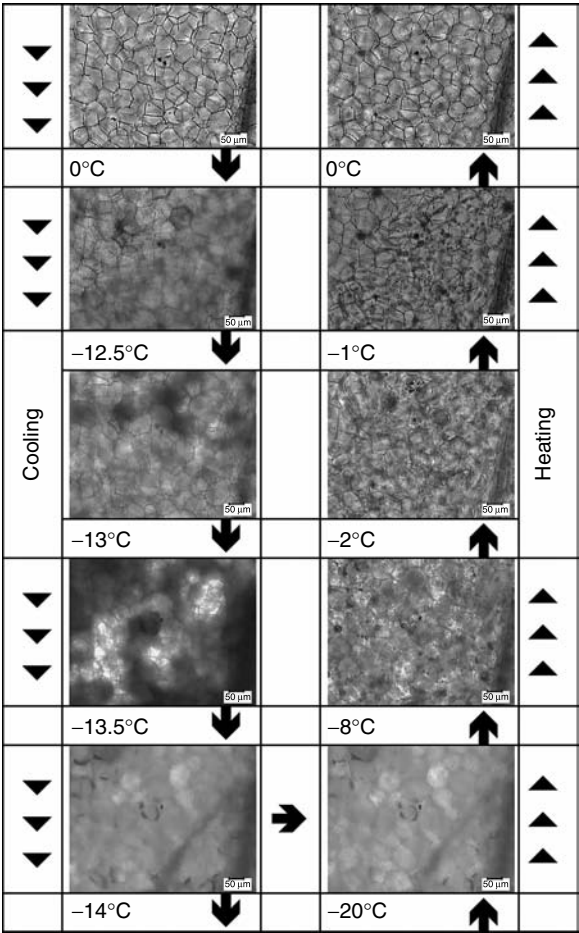
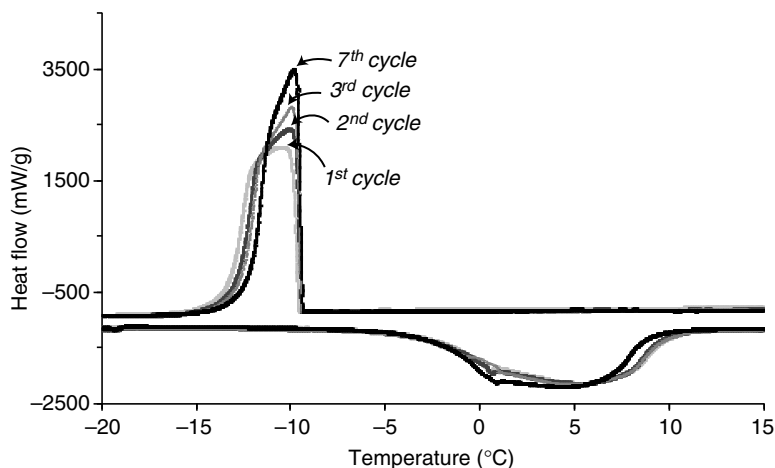


FIGURE 8.10
Raw bean freezing and melting micrographs (magnification 180x).

samples that are different in composition and which have been submitted to various thermal treatments. In the following sections, results obtained for some of these conditions are reported.

Blanched Bean

The raw beans, with their extremities cut, were immersed for 3 min in a water bath, at a temperature of 96°C. Afterwards, they were submitted to a DSC test and an example of the thermograms obtained for successive cycles performed on the same sample is given in Figure 8.11. The thermograms obtained are very similar to the ones obtained for raw beans. Nevertheless, some slight differences can be observed. First, the shoulder is less

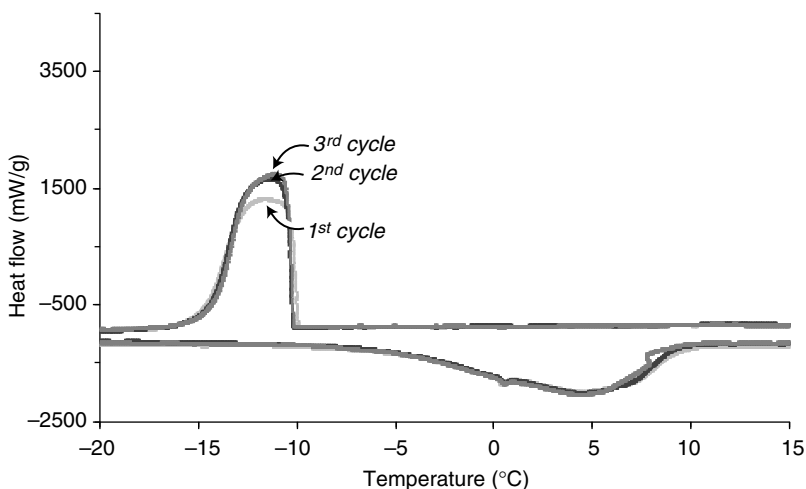
**FIGURE 8.11**

DSC thermograms of 3 min blanched bean ($M_{\text{bean}} = 37.8$ mg).

pronounced and polynucleation of ice is less important. In these conditions of study, the ice melting seems to occur nearly always in the same manner. The conclusion of these studies, which has to be confirmed, suggest that blanching could induce the probability of having bigger ice crystals and this has to be taken into account when explaining the resulting texture of the beans.

Blanched Bean + Immersion + Freezing

After having been blanched as described before, the beans are immersed in a salt solution maintained to a subzero temperature (-16°C). Immersion contact chilling and freezing in aqueous refrigerating media consists of soaking food stuffs in a cooled aqueous solution. Binary brine solutions (sodium chloride or calcium chloride) are usually used. The advantages claimed for such a process include shorter processing times, consequent energy savings and better food quality (Lucas and Raoult-Wack, 1998). After immersion, beans are directly frozen in a cold chamber maintained at a suitable temperature. The suitable temperatures are now under study and cannot be given because of confidential constraints with the company involved in the project. Nevertheless, the DSC tests give information about this kind of treatment, as can be seen on the corresponding thermograms given in Figure 8.12. At this stage of the study, it can be deduced that this treatment has the advantage of preserving the polynucleation of ice and therefore the formation of small crystals, as seen on the thermogram obtained from the first cycle. This is shown by the quite symmetrical extension of the signal after the part

**FIGURE 8.12**

DSC thermograms of blanching bean that have been submitted to an immersion + freezing process ($M_{\text{bean}} = 36.5 \text{ mg}$).

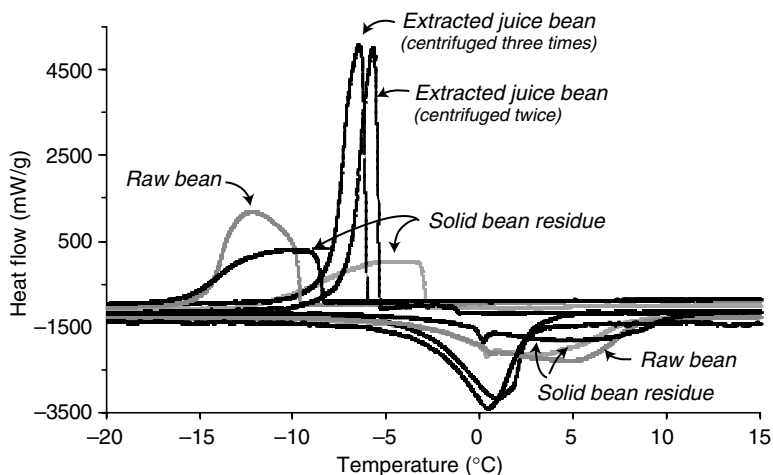
dealing with the sharp ice nucleation of the bulk water, as previously described.

Extracted Juice

In order to obtain the juice of the beans and to find out how this part of the bean freezes, the beans were crushed using an electric mixer. Afterwards, the resulting mixture was filtered using a sieve with $80 \mu\text{m}$ pores to achieve separation of the liquid and a solid residue (cake). A 10 ml sample of the suspension was introduced into a test tube and submitted to centrifugation at a rate of 4000 rpm/min for 6 min in order to obtain the extracted juice (floating part). The thermogram obtained from a DSC test performed on the resulting extracted juice is given in Figure 8.13 and compared with raw bean and solid residue thermograms. By comparison with the one obtained from the raw bean it can be seen that only the sharp ice nucleation is observed and the melting shows the presence of solutes as expected. These thermograms are very similar to the ones obtained for the bulk solution. The amount of solute is not high enough to detect the complete solidification and more details about the composition are needed to completely interpret the results.

Solid Residue

From the DSC test performed on the solid residue on the sieve (Figure 8.13) and taking into account the scale for the energy released, it can be deduced

**FIGURE 8.13**

DSC thermograms of extracted bean juice and solid bean residue.

that it is this part of the bean that is responsible for the section of signal showing a quasi symmetrical part and attributed to polynucleation. Some bulk liquid is still present and gives the sharp release of energy.

Conclusions

The aim of this study was first to precisely find the way that ice nucleation occurs within water samples, which can be either in the bulk or dispersed. Because of nucleation phenomena, the results shown for the freezing temperatures present in the stochastic character and for bulk samples cannot be reliable unless a sufficient number of samples are studied. When water is dispersed, each fragmented part can be considered as a sample and a statistic response is given. Therefore, by submitting the material to a very simple DSC correctly done it is possible to distinguish, on the one hand, what is relevant to bulk water, which needs only one ice embryo to freeze and, on the other hand, what is relevant to the dispersed matter, which needs numerous ice embryos. These results have been taken into account for interpreting the ones obtained from DSC tests performed on vegetables submitted to various thermal treatments involving ice nucleation for preservation purposes. When the thermograms obtained are gathered and compared, the conclusion is that bulk water is responsible for the sharp ice nucleation because of the restraining number of ice embryos that will give rather big crystals and it is the dispersed water that is responsible for the scattered freezing temperatures that induce smaller ice crystals.

Acknowledgments

The authors gratefully acknowledge the Regional Council of Picardie for its financial support (Grant No. 2002.02, Pôle Génie des Procédés).

References

- ASHRAE, Thermal properties of foods, *ASHRAE Handbook: Refrigeration*, Atlanta, 2002, chap. 8.
- Clausse, D., Cochet, N., Bouzabaa, M., and Aguerd, M. Heterogeneous ice nucleation within emulsions, *Lecture Notes in Physics, Atmospheric Aerosols and Nucleation, Proceedings of the Twelfth International Conference on Atmospheric Aerosols and Nucleation, Vienna, Austria, August 22–27, 1988*, Vol. 309, P.E. Wagner and G. Vali, eds., Springer, Berlin, pp. 721, 1988.
- Clausse, D., Fouconnier, B., and Avendano, J. Ripening phenomena in emulsions. A calorimetry investigation, *J. Dispersion Sci. Technol.*, 23, 379, 2002, Special issue devoted to P. Becher.
- Clausse, D., Pezron, I., and Behaegel, A. Water transfer between water and water + NaCl droplets in emulsions, *J. Dispersion Sci. Technol.*, 20, 315, 1999a.
- Clausse, D., Pezron, I., and Komunjer, L. Stability of W/O and W/O/W emulsions as a result of partial solidification, *Colloids Surf. A: Phys. Eng. Aspects*, 152, 23, 1999b.
- Dalmazzone, C. and Clausse, D. Microcalorimetry, *Encyclopedic Handbook of Emulsion Technology*, J. Sjöblom, ed., Marcel Dekker, New York, 2001, chap. 4.
- Fouconnier, B., Avendano-Gomez, J., Ballerat, K., and Clausse, D. Effects of cooling–heating cycles on emulsions, *Thermal Behavior of Dispersed Systems*, Surfactant Science Series, Vol. 93, N. Garti, ed., Marcel Dekker, New York, 2000, chap. 5.
- George, R.M. Freezing systems, *Quality in Frozen Foods*, M.C. Erickson and Y.C. Hung, eds., Chapman & Hall, New York, 1997, chap. 1.
- Li, J. and Lee, T.C. Bacterial extracellular ice nucleator effects on freezing of foods, *J. Food Sci.*, 63, 375, 1998.
- Lucas, T. and Raoult-Wack, A.L. Immersion chilling and freezing in aqueous refrigerating media: review and future trends, *Int. J. Refrig.*, 21, 419, 1998.
- Reid, D.S. Fundamental physicochemical aspects of freezing, *Food Technol.*, 37, 110, 1983.
- Reid, D.S. The freezing of food tissues, *The Effects of Low Temperatures on Biological Systems*, B.W.W. Grout and G.J. Morris, eds., Edward Arnold, London, 1987, chap. 15.

9

Molecular-Level Characterization of Lipid Bilayers in Disaccharide Matrices and Its Consequences for Cell Lyophilization

Juan J. de Pablo, Carolina Schebor, Satoshi Ohtake, and Amadeu Sum

CONTENTS

Introduction	151
Cryoprotectants and Lyoprotectants	153
Preservation of Proteins	153
Cryopreservation	153
Lyophilization.....	154
Preservation of Cells and Tissue	155
Molecular Models of Cryo- and Lyoprotectants.....	158
Conclusions.....	160
Acknowledgment.....	161
References	161

Introduction

Biological systems such as proteins, vaccines (viruses), or cells must often be stored for extended periods of time by resorting to freezing in solutions of cryoprotectants. In some cases, it is also possible to freeze-dry (or lyophilize) such systems in solutions of lyoprotectants, thereby leading to products that are stable at ambient conditions (Science News, 1995; Wang, 2000; Arakawa et al., 2001; Brumfiel, 2004). Achieving long-term stability in biological systems has been a long-standing goal of the food, pharmaceutical, and biomedical industries. Avoiding the need for refrigeration would reduce production and storage costs drastically. Development of suitable storage formulations could increase the availability of labile pharmaceutical products (e.g., recombinant proteins) in rural areas or third-world countries,

and could facilitate the storage of cells or tissue for subsequent therapeutic or transplant applications.

Cryoprotectant and lyoprotectant molecules are added to biological solutions or suspensions to prevent damage during freezing and freeze-drying, respectively. These molecules are believed to play a number of important roles, including the stabilization of bilayer-membrane or protein structures, the inhibition of ice formation, and the enhancement of glass formation at ambient temperatures (Carpenter et al., 1997; Craig et al., 1999; Wang, 2000; Arakawa et al., 2001).

Naturally occurring disaccharides have been found to be particularly effective cryo- and lyoprotectants. Trehalose (see Figure 9.1), a naturally occurring disaccharide of glucose, has been found in organisms (such as arthropods) that can survive severe cold and drought in a state of suspended animation, and recover all of their functions upon rehydration (Clegg, 2001; Duman et al., 1991; Westh and Ramlov, 1991). These findings have helped fuel the more general belief that disaccharides provide an effective class of molecules for cryopreservation and lyophilization of biological systems. A number of reports have suggested that trehalose is superior to other disaccharides in its ability to prevent freeze and desiccation damage (Leslie et al., 1995; Rossi et al., 1997; Librizzi et al., 1999), but the general validity of such findings is a matter of debate (Oliver et al., 2001). Currently, the pharmaceutical industry relies extensively on sucrose, a different disaccharide, for the lyophilization of drug formulations (Wang, 2000).

In spite of their practical importance, the precise mechanisms by which cryo- and lyoprotectants work are not well understood. Protectant formulations are often conceived through a trial-and-error process. Moreover, the thermophysical property data required to formulate protectant solutions rationally and to design cryopreservation and lyophilization protocols are rarely available. As discussed in this proposal, it is of particular interest to understand how protectants interact with cell membranes. Over the last several years we have conducted a systematic study of the structure, thermodynamic and transport properties of model cell membranes in liquid and glassy solutions of protectant molecules. Our two-pronged theoretical and experimental approach comprises the development of novel and powerful methods for molecular simulation of complex fluids near the

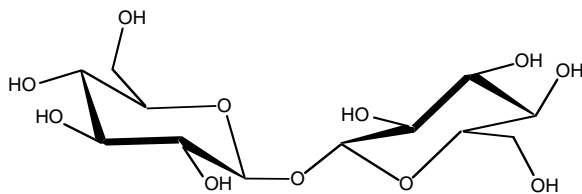


FIGURE 9.1

Molecular structure of trehalose.

glass transition, and the experimental characterization of lyophilized phospholipid vesicles.

Cryoprotectants and Lyoprotectants

The main role of a *cryoprotectant* is that of avoiding the damage to a biological system that can be caused by sub-zero temperatures and the concomitant formation of ice crystals (Wang, 2000; Arakawa et al., 2001). The role of a *lyoprotectant* is to avoid the damage that can be caused by the subsequent removal of water through freeze-drying (or lyophilization) (Arakawa et al., 2001; Wang, 2000). In this section we provide a brief overview of current views regarding the preservation of proteins, the preservation of cells, and available molecular models of cryo- and lyoprotectants.

Preservation of Proteins

Cryopreservation

When a biological system is frozen, a number of physical processes can induce damage. Perhaps the more apparent of these is the formation of ice; as crystals form, the remaining liquid becomes increasingly concentrated in solutes, thereby altering considerably its composition and chemical potential. The resulting “osmotic” stresses that arise in this unfrozen, highly concentrated remaining solution can cause cells to lyse and proteins to denature. Cryoprotectants for protein solutions have been proposed to act in a number of different ways. Their efficacy has been attributed to their ability to form amorphous solids, or glasses, to their ability to inhibit the formation of ice crystals, to their tendency to be excluded from the immediate vicinity of a biological molecule. It has been argued, for example, that the order of efficacy of several widely used cryoprotectants is correlated with their respective glass transition temperatures (Green and Angell, 1989; Franks et al., 1991). This correlation, however, is not general or absolute and it is not well understood; in fact, many solutes that exhibit a high glass transition temperature (e.g., Dextran) can be poor cryoprotectants (Pikal et al., 1991). As discussed below, a high glass transition temperature is more relevant in the context of lyophilization. Solute that are excluded from the immediate vicinity of a protein have also been shown to confer stability in solution, and be better cryoprotectants than solutes that interact strongly with the protein (Xie and Timasheff, 1997). As discussed below, this so-called “preferential-exclusion principle” has been cast using thermodynamic arguments, and is supported by available experimental data (Arakawa et al., 2001). It is relevant to our work in that it provides a basis for using molecular models to establish a relation between cryoprotectant molecular structure and cryoprotection efficacy (Baynes and Trout, 2003).

Lyophilization

Lyoprotectants, which are used to minimize damage during the removal of water (desiccation) from a frozen sample, have been proposed to be effective substitutes for water in anhydrous environments. Good lyoprotectants should be capable of self-organizing in a solid matrix that allows a protein to maintain its native structure. The so-called “water-replacement” hypothesis states that, in a dry system, effective protectants can replace water in the immediate vicinity of biological molecules, thereby providing a structural environment that is not too different from that encountered in aqueous solution (Carpenter and Crowe, 1988; Carpenter and Crowe, 1989). Recent experiments suggest that effective lyoprotectants interact with dry proteins through hydrogen bonding, and lead to conformations analogous to those encountered in the native state; in contrast, poor lyoprotectants lead to protein structures in the dry matrix that differ considerably from the corresponding native states (Carpenter and Crowe, 1989; Tanaka et al., 1991; Datta et al., 2001). Unfortunately, the precise nature and magnitude of lyoprotectant-protein interactions are not known, and the mechanism by which these interactions preserve protein structure and enzyme activity are not well understood. Moreover, the extent to which residual water is necessary to mediate such interactions is unknown. At this point, it is also important to emphasize that a high glass transition temperature (T_g) is generally desirable, as it facilitates long-term storage of a lyophilized formulation at elevated temperatures (Miller et al., 1997; Allison et al., 2000) (by slowing down degradative processes). Note, however, that solutes that result in high- T_g lyophilized products are not necessarily good lyoprotectants (Pikal et al., 1991; Tanaka et al., 1991).

The “preferential-exclusion principle,” which states that good cryoprotectants are excluded from the vicinity of a protein, has been invoked in the context of protein stability in solution or protein freezing in aqueous environments. The “water-replacement” hypothesis, which states that effective lyoprotectants replace water in the vicinity of a protein, has been used in the context of largely anhydrous environments. These two mechanisms of action are orthogonal (Crowe et al., 1990). However, it is important to recognize that a lyophilized product must be frozen before it is dried. If a single protectant is envisaged for a given application, it should act as both a good cryoprotectant and a good lyoprotectant. These two functions constitute a dilemma and present an interesting challenge, as the stresses that arise during freezing and drying are fundamentally different. It is also important to note that many of the arguments described above have been proposed in the context of proteins. The extent to which those arguments can be extended to the lyophilization of bilayer structures and cells is unclear. A systematic study of molecular structure of proteins and membrane bilayers during the cross-over from an aqueous, “exclusion” dominated regime, to a more anhydrous, “replacement” dominated regime, would generate much-needed insights regarding the

function and role of each species during cryopreservation and lyophilization of biological systems.

Disaccharides are unique in that they have been shown to be effective for both cryo- and lyoprotection. They therefore represent an ideal system in which to explore at the molecular level the specific interactions that arise between an effective protectant and a biological system.

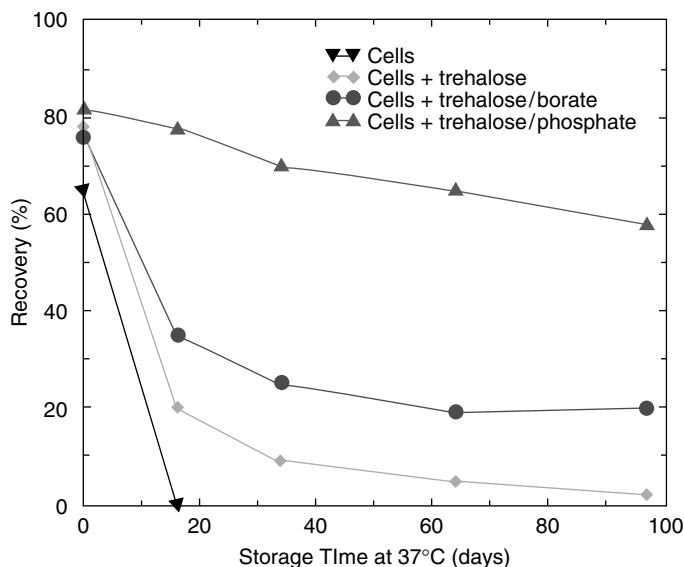
Preservation of Cells and Tissue

So far, our description of preservation has focused mostly on proteins or enzymes in solution. Less is known about the cryopreservation and lyophilization of entire cells or tissues, which is one of the ultimate objectives of our work. While many of the ideas or hypotheses described above in the context of proteins are also applicable to cells or tissue, the inherent complexity of such systems poses important, additional challenges. In particular, the role played by cell membranes must be taken into consideration.

A number of reports, mostly in the medical literature, have proposed protocols for freezing cells. Most of these are variations around a central theme, namely the use of a 10% solution of dimethyl sulfoxide (DMSO) in culture media and fetal bovine serum (Freshney, 2000). Available freezing protocols often lead to a serious loss of viability after freezing and thawing (in the case of human embryonic stem cells, for example, 99.9% of the cells are irreversibly damaged during freezing (de Pablo et al., 2004)); such low recoveries, however, are accepted by the medical community as a fact of life. More concerning is the fact that DMSO is considerably toxic and has negative side effects. It has recently become apparent, however, that cell viability after freezing and thawing can be improved considerably by resorting to carefully designed formulations and freezing procedures (Beattie et al., 1997; Conrad et al., 2000; Oliver et al., 2001; Wolkers et al., 2001; de Pablo et al., 2004). Interestingly, it appears that the use of disaccharides such as trehalose in cryoprotectant formulations offers distinct benefits.

In some of our own work, we have developed formulations to lyophilize and preserve bacteria for extended periods of time at relatively high temperatures (Conrad et al., 2000; Ekdawi-Sever and de Pablo, 2003). Some of our data are shown in Figure 9.2, where it can be seen that freeze-dried samples of *Lactobacillus acidophilus* in trehalose-phosphate mixtures retain more than 60% of their viability after 3 months of storage at relatively high temperatures. In contrast, commercial processes and formulations lead to complete loss of viability after a few days of storage.

For a cell preservation protocol to be effective, it is necessary to introduce cryo- or lyoprotectants into the interior of the cell. Two general approaches have been followed with that end in mind. In the first, cells have been genetically modified to produce their own cryo- or lyoprotectants (Billi et al., 2000; Guo et al., 2000). In the second, the cell membrane has been

**FIGURE 9.2**

Viability of *Lactobacillus acidophilus* during storage at 37°C as a function of storage time. The cells were lyophilized in a solution of trehalose and phosphate ions. The symbols show results for cells lyophilized without additives (inverted triangles), with trehalose only (diamonds), with a trehalose-borate mixture (bullets), and with a trehalose-phosphate mixture (triangles).

manipulated in various ways (e.g., by changing temperature or by creating artificial pores) to increase the transport of protectants from extracellular media (Beattie et al., 1997; Eroglu et al., 2000). The latter approach is attractive in that it can be carried out without the need to alter a cell's genetic machinery, and it offers considerable promise for practical applications.

Lipid bilayers undergo distinct phase transitions as a function of temperature. Cell membranes undergo similar transitions, and researchers have argued that these can be manipulated to introduce cryoprotectants into the interior of mammalian cells, thereby providing a method to prevent intracellular damage during freezing (Beattie et al., 1997). These ideas have been used to freeze and thaw pancreatic islets in mixtures of DMSO and trehalose with minimal damage to the cells (Beattie et al., 1997). More recently, approaches based on trehalose uptake by endocytosis have been used to freeze-dry mammalian cells (Wolkers et al., 2001). The results of these efforts, however, have been a matter of debate. Some authors have shown that mammalian cells can be successfully freeze-dried (Eroglu et al., 2000; Guo et al., 2000; Wolkers et al., 2001), while others have had limited success (de Castro and Tunnacliffe, 2000).

Membrane phase transitions are particularly relevant to lyophilization (Oliver et al., 2001). For concreteness (but without loss of generality), we discuss this issue in the context of dipalmitoylphosphocholine (DPPC)

bilayers (DPPC is one of the major components of cell membranes). Aqueous DPPC bilayers exhibit a gel to liquid crystal transition at 42°C (Oliver et al., 2001; Oliver et al., 2004) (see Figure 9.3). In dry DPPC bilayers the transition occurs at 105°C. This implies that as a dry bilayer is rehydrated with warm water at room temperature, the transition drops from 105 to 42°C. In doing so, the membrane undergoes a phase transition from a gel to a liquid, and becomes leaky in the process. In contrast, when DPPC bilayers are freeze-dried with trehalose or sucrose, the transition actually *drops* to 23°C (Oliver et al., 2001; Oliver et al., 2004). The membrane therefore remains in a liquid crystal state throughout the drying and rehydration process, thereby preventing leakage as a result of any underlying phase transitions. These data suggest that one of the roles of cell lyoprotectants is that of lowering phase transition temperatures when the system is freeze dried.

In this context, it is of interest to discuss the behavior of hibernating animals (Andrews et al., 2003). Ground squirrels, for example, are able to enter long hibernating periods of a month during which their body temperature falls abruptly to about 4°C. The melting temperature for most pure phospholipid bilayers is in the range of 10 to 40°C. As squirrels drop their body temperature to 4°C, one would expect most cell membranes to enter a gel state and become leaky. A collaboration with Prof. Hannah Carey from the University of Wisconsin's School of Veterinary Science, suggests that this phase transition is preempted by a sudden production of cholesterol and by a sudden change in the phospholipid composition of cell membranes. Liver cells from ground squirrels harvested during normal activities indicate that the main phospholipids in the membrane

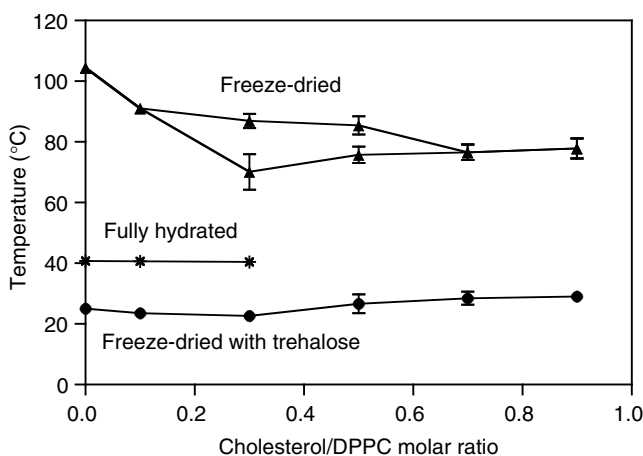


FIGURE 9.3

Gel to liquid-crystal melting transition for DPPC liposomes as a function of cholesterol content. Results are shown for aqueous liposomes (stars), liposomes freeze-dried without trehalose (triangles), and liposomes freeze-dried in the presence of trehalose (circles).

have PC, PE (phosphatidylethanolamine) and PS (phosphatidylserine) head groups. The ratio of cholesterol to phospholipid is approximately 17% by weight during the torpid state, but during arousal from hibernation, within just 2 h that ratio increases to 21%. These data lead to our proposition that an understanding of the interplay between cholesterol content and lyophilization would be valuable for design of optimal lyophilization strategies for mammalian cells.

We note here that systematic studies of the melting transition of dry or nearly dry phospholipids bilayers (e.g., vesicles) have been scarce. While there is an abundant experimental and theoretical literature concerning the structure and properties of bilayers in water, less is known about their behavior when water is removed. We have therefore initiated a systematic experimental study of the gel-liquid crystal transition of pure DPPC and DPPC-cholesterol vesicles freeze-dried with and without disaccharides and oxanion-disaccharide complexes. Some of our results to date are shown in Figure 9.3.

Molecular Models of Cryo- and Lyoprotectants

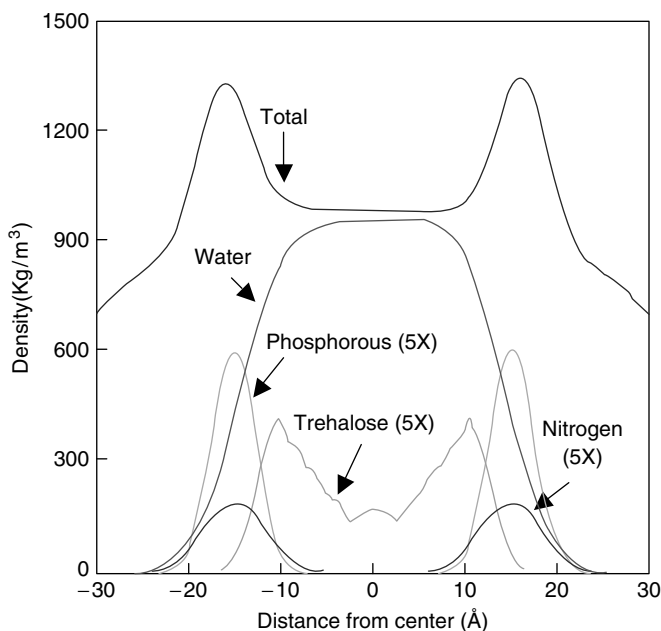
As mentioned earlier, for proteins in solution Timasheff and co-workers have proposed a classical-thermodynamics framework that explains stability in terms of a “preferential-exclusion” principle (Xie and Timasheff, 1997). The basic tenet of this principle is that effective protectants are expelled from the immediate vicinity of the protein, thereby causing it to be preferentially hydrated. Furthermore, it postulates that native structures are stabilized because denaturation would lead to entropically unfavorable states. This framework has been used successfully in a number of experimental studies of protein stability and, more importantly, it appears to be applicable to the case of stability during freezing (Crowe et al., 1990; Arakawa et al., 2001). It has also been substantiated by recent theoretical, atomic-level calculations (Baynes and Trout, 2003). While there are systems for which the principle appears to fail (e.g., polyethylene glycol) (Arakawa et al., 1990), it is attractive in that it provides a means for relating measurable thermodynamic properties to cryopreservation ability. If such quantities could in turn be related to molecular structure (e.g., via molecular simulations), it would be possible to devise a strategy to design or identify highly effective cryoprotectant molecules from first principles. It is therefore of interest to ask whether the preferential-exclusion encountered in protein stabilization also applies to cell bilayer membranes.

Molecular simulations of cryo- and lyoprotectants could provide valuable insights into the behavior and effectiveness of these molecules. Unfortunately, studies of that nature have been scarce; only recently have some reports begun to appear in the literature (Donnamaria et al., 1994; Liu et al., 1997; Conrad and de Pablo, 1999; Roberts and Debenedetti, 1999). In previous work, we have conducted molecular simulations of pure, amorphous trehalose, sucrose, and their aqueous solutions (Conrad and de Pablo, 1999; Ekdawi et al., 2001).

We have found that trehalose is generally more hydrated than sucrose. We have shown that, in dilute solution, trehalose does not exhibit intramolecular hydrogen bonds, whereas sucrose has two. In concentrated solutions, however, these disaccharides “fold” onto themselves to adopt a more compact structure, which includes the formation of additional intramolecular hydrogen bonds. These findings were subsequently confirmed experimentally (Branca et al., 2001a; Branca et al., 2001b). Our simulations have also shown that the mobility of water in trehalose solutions is lower than in sucrose solutions. Moreover, we have found that water undergoes a jump-like motion in concentrated trehalose or sucrose solutions (Conrad and de Pablo, 1999; Ekdawi et al., 2001), analogous to that observed for small penetrants in glassy polymers (Gusev and Suter, 1993). This jump-like motion is accompanied by a pronounced decay of the diffusion coefficient of water, and a decoupling of the motion of water and trehalose (Ekdawi-Sever et al., 2003). These findings have been confirmed by our NMR measurements, which are in good agreement with the results of our simulations (Ekdawi-Sever et al., 2003). Recent neutron scattering studies of fructose/water solutions have revealed a similar behavior (Feeney et al., 2001), consistent with the monosaccharide simulations of Roberts and Debenedetti (Roberts and Debenedetti, 1999).

Our results to date have established that the atomistic models and force fields employed in our simulations give rise to thermodynamic-property and transport-coefficient predictions that are in quantitative agreement with experiment (Conrad et al., 1999; Ekdawi et al., 2001; Ekdawi-Sever et al., 2003). On the basis of these results, we propose that these models can be relied upon to generate insights regarding the order of efficacy of various protectants. In the particular case of trehalose and sucrose, our findings suggest that part of the alleged superior performance of trehalose over sucrose for preservation of proteins is related to its ability to hydrogen bond with water (Ekdawi et al., 2001).

We have conducted a detailed study of the interactions of trehalose and sucrose with phospholipids bilayers (Faller et al., 2003). For pure DPPC bilayers, the results of our simulations are in good agreement with available numerical results and experimental data. We have found that, even in relatively dilute solutions, these two disaccharide molecules interact strongly with the phospholipid head groups. Figure 9.4 shows the density profile for water, trehalose, and phospholipid molecules across a fully hydrated DPPC bilayer. One can see that the concentration of trehalose is greater in the immediate vicinity of the phosphate groups than in the bulk of the aqueous region. We have found that trehalose can form a relatively stable complex with two or even three phospholipid molecules, thereby conferring stability to the membrane even in low-moisture environments. This finding should be contrasted with the preferential-exclusion principle observed in protein solutions, which would predict just the opposite behavior (i.e., an exclusion of trehalose from the vicinity of the membrane). This observation further illustrates that the mechanisms by which cells are stabilized can be different from those by which proteins are stabilized.

**FIGURE 9.4**

Density profile for water, trehalose, and phospholipid headgroups (nitrogen and phosphorous) for a fully hydrated DPPC bilayer. Simulations at 50°C indicate that trehalose concentration is higher near phospholipid head groups than in the bulk (Faller et al., 2003). The concentration of trehalose in the aqueous phase is 4% by weight.

We have also conducted a detailed study of the interactions of DMSO with DPPC bilayers (Faller et al., 2003). We have found that DMSO is able to swell the bilayers considerably and that it diffuses almost unhindered across the membrane. The nature of the swelling and the diffusion, however, are strongly temperature dependent; at low temperatures, DMSO exhibits a hydrophilic nature and it is excluded from the interior of the bilayer. At intermediate to high temperatures (e.g., 50°C), it exhibits a hydrophobic character and it penetrates the bilayers much more readily. This finding helps explain why DMSO is more toxic at intermediate-to-high temperatures than at low temperatures, and why many empirical cell-freezing protocols advocate adding DMSO only after the cells have been cooled to sub-ambient temperatures.

Conclusions

Our work to date has focused on the interactions of cryoprotectants with DPPC phospholipid bilayers in solution. The range of concentrations that we

have investigated is comparable with that encountered in experimental protocols before samples are frozen or freeze-dried. This work has revealed that disaccharides exhibit intimate interactions with phospholipid bilayers, thereby influencing phase behavior and dynamic properties. The results of simulations and experiments are fully consistent with each other.

This work, however, represents only a beginning. It is of considerable interest, for example, to examine how protectants interact with cell membranes in the absence of water, or in the presence of minute amounts of "residual" water. It is also important to consider how bilayers consisting of mixtures of phospholipids, which provide a better representation of actual cell membranes, respond to cryo and lyoprotectants. Along the same lines, it is important to consider how additional components of cell membranes, such as cholesterol, influence the behavior of anhydrous or nearly anhydrous bilayers. Our current research efforts are aimed at answering some of these questions, so that more effective methods of cell preservation can be devised.

Acknowledgment

The authors are grateful to the National Science Foundation for financial support.

References

- Allison, S.D., Manning, M.C., Randolph, T.W., Middleton, K., Davis, A., and Carpenter, J.F. Optimization of storage stability of lyophilized actin using combinations of disaccharides and dextran, *J. Pharm. Sci.*, 89, 199, 2000.
- Andrews, M.T., Carey, H.V., and Martin, S.L. Mammalian hibernation: Cellular and molecular responses to depressed metabolism and low temperature, *Physiol. Rev.*, 83, 2003.
- Arakawa, T., Bhat, R., and Timasheff, S.N. Preferential hydration does not always stabilize the native structure of globular proteins, *Biochemistry*, 29, 1924, 1990.
- Arakawa, T., Prestrelski, S.J., Kenney, W.C., and Carpenter, J.F. Factors affecting short-term and long-term stabilities of proteins, *Adv. Drug Deliv. Rev.*, 46, 307, 2001.
- Baynes, B.M. and Trout, B.L. Proteins in mixed solvents: a molecular-level perspective, *J. Phys. Chem. B*, 50, 14058, 2003.
- Beattie, G.M., Crowe, J.H., Lopez, A.D., Cirulli, V., Ricordi, C., and Hayek, A. Trehalose: a cryoprotectant that enhances recovery and preserves function of human pancreatic islets after long-term storage, *Diabetes*, 46, 519, 1997.
- Billi, D., Wright, D.J., Helm, R.F., Prickett, T., Potts, M., and Crowe, J.H. Engineering desiccation tolerance in *Escherichia coli*, *Appl. Env. Microbiol.*, 66, 1680, 2000.
- Branca, C., Magazu, S., and Maisano, G. Vibrational and relaxational contributions in disaccharide/H₂O glass formers, *Phys. Rev. B*, 6422, 4202, 2001a.

- Branca, C., Magazu, S., and Maisano, G. α,α -trehalose/water solutions. 5. Hydration and viscosity in dilute and semidilute disaccharide solutions, *J. Phys. Chem. B*, 105, 10140, 2001b.
- Brumfiel, G. Just add water, *Nature*, 428, 14, 2004.
- Carpenter, J.F. and Crowe, J.H. Modes of stabilization of a protein by organic solutes during desiccation, *Cryobiology*, 25, 459, 1988.
- Carpenter, J.F. and Crowe, J.H. An infrared spectroscopic study of the interactions of carbohydrates with dried protein, *Biochemistry*, 28, 3916, 1989.
- Carpenter, J.F., Pikal, M.J., Chang, B.S., and Randolph, T.W. Rational design of stable lyophilized protein formulations: some practical advice, *Pharm. Res.*, 14, 969, 1997.
- Clegg, J.S. Cryptobiosis — a peculiar state of biological organization, *Comp. Biochem. Phys. B*, 128, 613, 2001.
- Conrad, P.B. and de Pablo, J.J. Molecular simulation of the cryoprotectant α,α -trehalose in aqueous solution, *J. Chem. Phys. A*, 103, 4049, 1999.
- Conrad, P.B., Miller, D.P., Ciesleski, P.R., and de Pablo, J.J. Stabilization and preservation of *Lactobacillus acidophilus* in saccharide matrices, *Cryobiology*, 41, 17, 2000.
- Conrad, P.B., Miller, D.P., Fucito, S., Corti, H.R., and de Pablo, J.J. Electrical conductivity of supercooled aqueous mixtures of trehalose with sodium chloride, *J. Chem. Phys. B*, 104, 10419, 1999.
- Craig, D.Q.M., Royall, P.G., Kett, V.L., and Hopton, M.L. The relevance of the amorphous state to pharmaceutical dosage forms: glassy drugs and freeze-dried systems, *Int. J. Pharm.*, 179, 179, 1999.
- Crowe, J.H., Carpenter, J.F., and Crowe, T.J. Are freezing and dehydration similar stress vectors? A comparison of modes of interaction of stabilizing solutes, *Cryobiology*, 27, 219, 1990.
- Datta, S., Biswal, B.K., and Vijayan, M. The effect of stabilizing additives on the structure and hydration of proteins: a study involving tetragonal lysozyme, *Crystallogr. D Biol. Crystallogr.*, 57, 1614, 2001.
- de Castro, A.G. and Tunnacliffe, A. Intracellular trehalose improves osmotolerance but not desiccation tolerance in mammalian cells, *FEBS Letters*, 487, 199, 2000.
- de Pablo, J.J., Yi, L., and Palecek, S. Erective cryopreservation of human embryonic stem cells, *Bioeng. Biotech.*, 2004.
- Donnamaria, M.C., Howard, E.I., and Grigera, J.R. Interaction of water with α,α -trehalose in solution — molecular dynamics simulation approach, *J. Chem. Soc. Faraday Trans.*, 90, 2731, 1994.
- Duman, J.G., Wu, D.W., Tursman, D., and Olsen, T.M. Adaptations of insects to subzero temperatures, *Q. Rev. Biol.*, 66, 387, 1991.
- Ekdawi, N., Conrad, P.B., and de Pablo, J.J. Molecular simulation of sucrose solutions near the glass-transition temperature, *J. Phys. Chem. A*, 105, 734, 2001.
- Ekdawi-Sever, N. and de Pablo, J.J. Effect of annealing on the stability and morphology of lyophilized *L. acidophilus* disaccharide matrices, *J. Food Sci.*, 68, 2504, 2003.
- Ekdawi-Sever, N., de Pablo, J.J., Feick, E., and von Meerwall, E. Diffusion of sucrose and α,α -trehalose in aqueous solutions, *J. Phys. Chem. A*, 107, 936, 2003.
- Eroglu, A., Russo, M.J., Bieganski, R., Fowler, A., Cheley, S., Bayley, H., and Toner, M. Intra-cellular trehalose improves the survival of cryopreserved mammalian cells, *Nature Biotechnol.*, 18, 163, 2000.

- Faller, R., Sum, A., and de Pablo, J.J. Molecular simulation study of phospholipid bilayers and insights of the interactions with disaccharides, *Biophys. J.*, 85, 2830, 2003.
- Faller, R., Sum, A., and de Pablo, J.J. Molecular simulation study on the influence of dimethyl-sulfoxide on the structure of phospholipid bilayers, *Biophys. J.*, 85, 3636, 2003.
- Feeney, M., Brown, C., and Tsai, A. Incoherent quasi-elastic neutron scattering from fructose-water solutions, *J. Phys. Chem. B*, 105, 7799, 2001.
- Franks, F., Hatley, R.H.M., and Mathias, S.F. Materials science and production of shelf-stable biologicals, *Biopharmaceutics*, 4, 38, 1991.
- Freshney, R.I. Culture of Animal Cells: A Manual of Basic Technique, Wiley-Liss, Inc., pp. 297–308, 2000, chap. 19.
- Green, J.L. and Angell, C.A. Phase-relations and vitrification in saccharide–water solutions and the trehalose anomaly, *J. Phys. Chem.*, 93, 2880, 1989.
- Guo, N., Puhlev, I., Brown, D.R., Mansbridge, J., and Levine, F. Trehalose expression converse desiccation tolerance on human cells, *Nature Biotechnol.*, 18, 168, 2000.
- Gusev, A.A. and Suter, U.W. Dynamics of small molecules in polymers subject to thermal motion, *J. Chem. Phys.*, 99, 2228, 1993.
- Leslie, S.B., Israeli, E., Lighthart, B., Crowe, J.H., and Crowe, L.M. Trehalose and sucrose protect both membranes and proteins in intact bacteria during drying, *Appl. Environ. Microbiol.*, 61, 3592, 1995.
- Librizzi, F., Vitrano, E., and Cordone, L. Dehydration and crystallization of trehalose and sucrose glasses containing carbonmonoxy-myoglobin, *Biophys. Chem.*, 76, 2727, 1999.
- Liu, Q., Schmidt, R.K., Teo, B., Karplus, P.A., and Brady, J.W. Molecular dynamics studies of the hydration of α,α -trehalose, *J. Am. Chem. Soc.*, 119, 7851, 1997.
- Miller, D.P., Corti, H.R., and de Pablo, J.J. Thermophysical properties of trehalose and its concentrated aqueous solutions, *Pharm. Res.*, 14, 578, 1997.
- Ohtake, S., Schebor, C., Palecek, S.P., and de Pablo, J.J. Effect of sugar-phosphate mixtures on the stability of dppc membranes in dehydrated systems, *Cryobiology*, 48, 81, 2004.
- Oliver, A., Crowe, J., and Crowe, L. The trehalose myth revisited: introduction to a symposium on stabilization of cells in the dry state, *Cryobiology*, 43, 89, 2001.
- Oliver, A., Crowe, J., and Crowe, L. Lipid phase behavior and stabilization of domains in membranes of platelets, *Cell Biochem. Biophys.*, 40, 123, 2004.
- Pikal, M., Dellerman, K.M., Roy, M.L., and Riggin, R.M. The effects of formulation variables on the stability of freeze-dried human growth hormone, *Pharm. Res.*, 8, 427, 1991.
- Roberts, C.J. and Debenedetti, P.G. Structure and dynamics in concentrated, amorphous carbohydrate-water systems by molecular dynamics simulation, *J. Phys. Chem. B*, 103, 7308, 1999.
- Rossi, S., Buera, M.P., Moreno, S., and Chirife, J. Stabilization of the restriction enzyme EcoRI dried with trehalose and other selected glass-forming solutes, *Biotechnol. Prog.*, 13, 609, 1997.
- Science News, Biopreservation, *Science*, 267, 1922, 1995.
- Tanaka, R., Takeda, T., and Miyajima, R. Cryoprotective effect of saccharides on denaturation of catalase during freeze-drying, *Chem. Pharm. Biol.*, 39, 1091, 1991.
- Wang, W. Lyophilization and development of solid protein formulations, *Int. J. Pharm.*, 203, 1, 2000.

- Westh, R. and Ramlov, H. Trehalose accumulation in the tardigrade *Adorybiotus coronifer* during anhydrobiosis, *J. Exp. Zool.*, 258, 303, 1991.
- Wolkers, W.F., Walker, N.J., and Tablin, F. Human platelets loaded with trehalose survive freeze-drying, *Cryobiology*, 42, 79, 2001.
- Xie, G.F. and Timasheff, S.N. The thermodynamic mechanism of protein stabilization by trehalose, *Biophys. Chem.*, 64, 25, 1997.

**Part 3: Responses to Water
Stress in Living Organisms:
Related New Potential
Technologies**

10

Water Stress of Bacteria and Molds from an NMR Water Mobility Standpoint

Pavinee Chinachoti and Elena Vittadini

CONTENTS

Introduction	167
Historic Perspective	168
Theory on NMR Water Mobility	169
Why Water Mobility?	169
Liquid Systems (<i>S. aureus</i> Growth)	170
Semi-Solid Heterogeneous Systems (Mold Spore Germination)	177
¹⁷ O NMR Signal Intensity (Liquid Water) in <i>Aspergillus niger</i> Study	177
H and ¹⁷ O NMR in <i>Aspergillus nidulans</i> Germination Study	181
Solid System (Survivability)	184
Concluding Remarks	187
Acknowledgments	188
References	188

Introduction

The existence of living organisms on Earth relies heavily on water. Living cells require water as a solvent that brings important nutrients and other solutes to and from the surrounding environment in order to maintain survival and sustain growth. In addition, the properties of water partially contribute to shape the ability of some cells to survive several harsh environments such as high temperature, high salt, and freezing. For instance, the ability to form spores and relative resistance to thermal damage is an evolutionary adaptation over millions of years in which cells developed cellular rearrangement that, we think, manipulates the properties

of water and cellular contents to cope with environmentally severe conditions. There is no doubt that, in general, water is life. But that is not always the case. For example, in an extremely dry condition, exposure of a dehydrated cell to water from such a dry state can also lead to cell death. In this chapter we will explore some situations where the presence of water can also lead to death. To understand the involvement of water in microbial survival and death, we turn to an investigation on water mobility using nuclear magnetic resonance (NMR). The objective of this work is to further understand the multifaceted roles of water and neighboring solutes that impact cell growth as well as death.

Historic Perspective

Controlling water availability for microbial growth has been one of the oldest food preservation technologies. Over the last several decades, food scientists have attempted to define the true meaning of water “availability.” Parameters such as water activity (a_w), “bound” water, glass transition, and molecular water mobility, are among most discussed but yet, the true understanding of such terms remain to be realized. The historical report by Scott (1953), implied that the relative water vapor pressure (later known as a_w) is a key parameter for *Staphylococcus aureus* growth activity. The reported experiment involved titrating various amounts of humectants to reduce the a_w and hence the observed phenomenon was masked by the change in solid composition. Many of the later scientific reports were similar in approach, leading to a great development in the 1960s and 1970s in the area of intermediate moisture foods (IMF) which was (and still is) one of the most economical food preservation technologies for several ready-to-eat food products. a_w undoubtedly is a powerful empirical parameter used to monitor water “availability” in commercial food products.

The limitation of a_w is apparent in lieu of solute-specific effects. Low molecular weight solutes influence a_w very differently and in part lead to some deviation in the minimum a_w value for a microbial growth (Christian, 1981; Ballesteros et al., 1993).

In the original theory, water availability was theorized to be closely related to a_w , with an assumption that the ratio of fugacities (or vapor pressure) referred to pure water, depending on the degree of water binding to the solid interface. Hence, for years, a_w was used to measure the degree of “bound” and “free” water, and water with different thermodynamic states and with different degrees of binding to various substrates was supposed to determine the “availability” for mold spore germination and bacterial growth (Lang, 1980; Gilbert, 1985). Franks (1991) later emphasized the fact that availability may be more related to the dynamic properties of water such as diffusional (translational) mobility. The glass transition proposal would then follow using the argument that to measure diffusional dynamics of

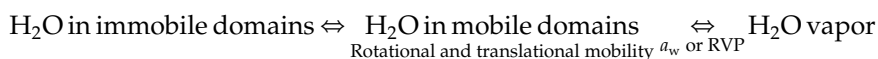
water, glass transition temperature (T_g) could be used to measure the availability of water (Slade and Levine, 1988). In addition, van den Berg and Bruin (1981), and Gilbert (1985) emphasized that availability is driven by the kinetic nature of most multi-component systems.

It has been noted that although non-equilibrium situations exist in semi-moist food products, observed a_w values may predict microbial and biochemical activities fairly well (Chirife and Buera, 1994; Chirife and Buera, 1995; Chirife and Buera, 1996; Chirife et al., 1996; Cardona, 1997). The glass transition theory, on the other hand, remains inconclusive as more counter challenging data have been published (Chirife et al., 1996; Cardona, 1997; Buera et al., 1998). In this report, the investigation into water mobility has provided additional insights on the molecular dynamics of water (mobility) since water is the key solvent carrying nutrients and oxygen to cells.

Theory on NMR Water Mobility

Why Water Mobility?

Dynamic properties of water determine several important kinetic processes that determine key deteriorative quality changes and hence commercial food shelf-lives. Foods are mostly in a state of thermodynamic instability and kinetic barriers do exist as water molecules are transferred from phase to phase and state to state. Molecular mobility of water in different domains can be measured by methods such as NMR which, as with a_w , involves the ability to become vapor and requires a thermodynamic equilibrium. In a non-equilibrium situation, the use of relative vapor pressure (RVP) has been proposed (Slade and Levine, 1988).



However, measurement of water mobility in multicomponent, multi-domained systems is not so simple. In food systems, water may be associated with different domains that control its local molecular motions. Within a specific timeframe, water molecules may migrate between two domains (of two different local mobilities). If the migration rate is slow (due to kinetic barriers) with respect to the experimental observable time frame, then the system experimental data would report multiple components in terms of water mobility. If another system has a reduced kinetic barrier, translational exchange between domains is rapid within the timeframe of the experiment. In this case, the data obtained would only report seemingly one water population (with one average mobility) leading to a misleading conclusion. Because most dynamic experiments are limited by the instrumental timeframe, it is important to select the appropriate instrument for the

intended dynamic rate(s) for the specific event(s) of interest. For instance, to observe molecular mobility of water, NMR or dielectric relaxometry would offer the needed benefit of detecting the mobility of a short range (molecular) motion (picosecond or ps and microsecond or μ s timeframe) whereas supra-structural relaxatometry (e.g., differential scanning calorimetry (DSC) and dynamic mechanical analysis (DMA)) offer a longer range of relaxation events in seconds or longer. Because some water molecules move at rapid rates (in ps), selecting the appropriate methodology with experimental timeframe and frequency matching the very event of interest is one of the key approaches. Hence, to observe water mobility, using a slower methodology (such as DSC and DMA in structural or phase transition) would not be appropriate and would lead to misleading conclusions. There is one exception. That is when the system is simple and homogeneous, such as a simple sugar solution; in this case, molecular mobility of water is closely related to the local viscosity and structural glassy–rubbery transition. In complex food systems, investigation of water molecules in multiple domains poses an experimental challenge. Today, field-cycling NMR has offered an opportunity to investigate molecular dynamics at a range of frequencies so that multi-domain systems with multiple relaxation rates can be properly evaluated. Unfortunately, it is not widely available and much work is needed in the food science area.

In this investigation, three main focus areas are reported; (1) *S. aureus* growth in homogeneous liquid media system, (2) mold spore germination in heterogeneous semi-solid starch–sugars and cellulose–sorbitol systems with, and (3) survival of organisms in freeze-dried locust bean and xanthan gum systems.

Liquid Systems (*S. aureus* Growth)

Two types of rich media (brain heart infusion (BHI) and homogenized chicken meat media (CMM)) containing various concentrations of NaCl, glycerol, or raffinose and various water contents to obtain a_w values 0.86 to 0.99 at 25°C have been considered related to *S. aureus* growth. The CMM media was more viscous than the BHI media at given moisture content, probably because of the presence of unhydrolyzed proteins. The presence of raffinose also led to a higher viscosity than the presence of NaCl or glycerol. ^{17}O (oxygen-17) NMR was applied to these media according to a method described previously (Chinachoti and Stengle, 1990; Lavoie et al., 1997). Spectral line-width showed similarities for all media when plotted against water content, regardless of solute type present. However, *S. aureus* growth patterns vastly differed among the three solutes suggesting a strong solute specificity. Although marked viscosity changes were observed, within the range of composition studied, NMR line-width changed only from 62 to 200 Hz (within an order of magnitude) in an isotropic region (low viscosity).

The differences in lag time and in growth rate were therefore contributed by other physical factors such as solute specificity and the difference in osmotic pressure. a_w was found to be a strong factor influencing the organism growth.

Preservation of IMF benefits from the osmotic effect of added solutes on the microorganisms. Titration of the same three solutes to BHI media from 0 to 20 g solute/g BHI (BHI:water ratio 26:1) resulted in a_w decreasing from 0.98 to 0.845 (for NaCl), 0.86 (glycerol) and 0.964 (raffinose) but the minimum a_w values for growth were different among solutes (closed symbols in Figure 10.1). The ^{17}O NMR line-width increased slightly with added solutes from 70 to 150 Hz, depending on the type of solutes. Figure 10.2 depicts the shift in ^{17}O NMR line-width with added solutes indicating a similar pattern with solute content. The small impact on line-width (and viscosity) means that the effect of solutes is likely related to osmotic and other physiological effects. Lag times were found to increase with decreasing a_w values (from 0.99 to 0.85) independently of the solute type (Figure 10.3). Inversely, the cell density at a given incubation time (24 h) increased with increasing a_w values

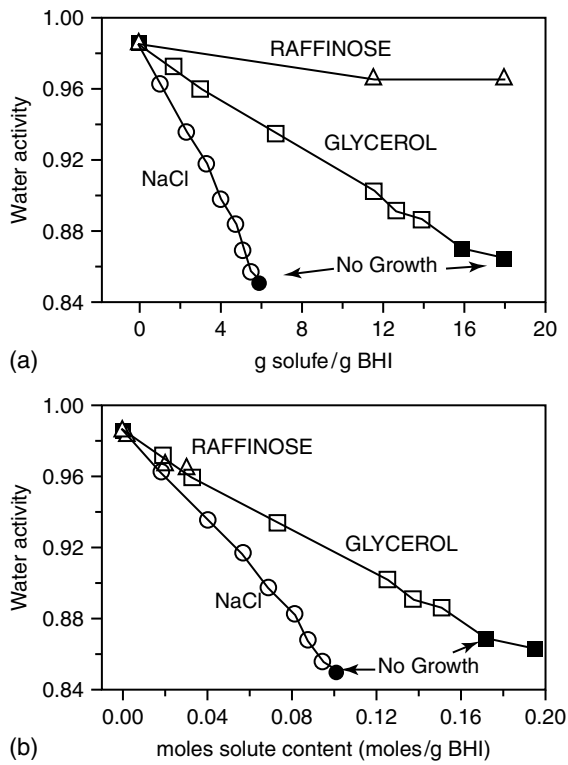
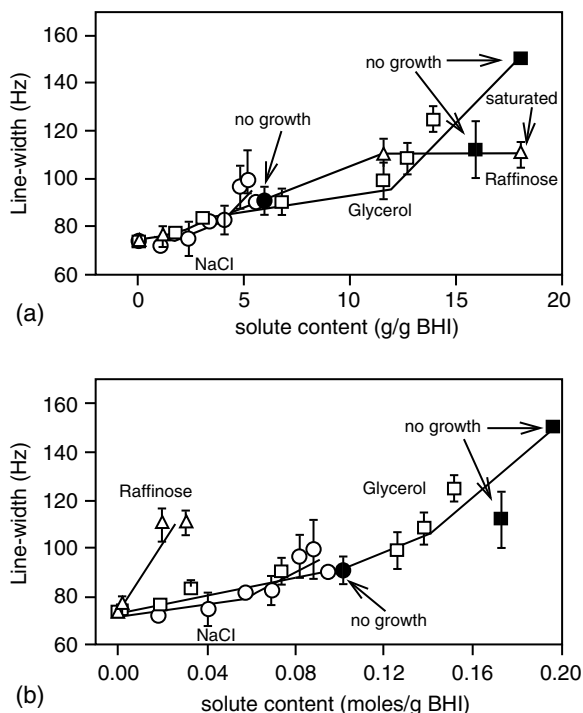


FIGURE 10.1
Effect of addition of small solutes on BHI media a_w (systems in which microbial growth was not detected are indicated).

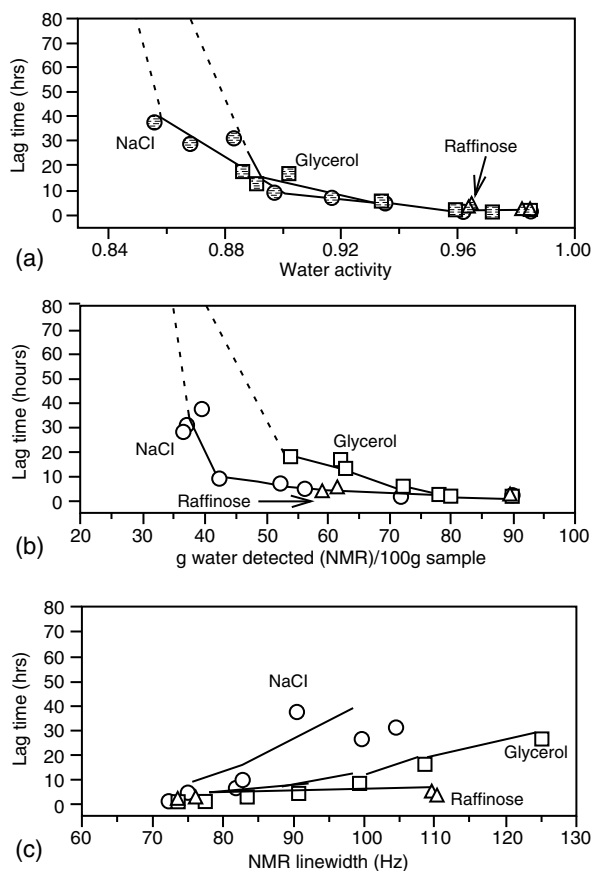
**FIGURE 10.2**

Effect of addition of small solutes on BHI ^{17}O NMR mobility as observed from line-width increase (Lavoie, 1998).

independently but universally for all three solutes (Figure 10.4). More details can be found elsewhere (Vittadini et al., 2001).

Therefore, in a liquid system when water is isotropically oriented (almost all water is free, with ^{17}O NMR line-width in the same magnitude as pure water) the effects of NaCl, glycerol and raffinose were highly correlated with the degree of a_w depression. It is interesting to note that for the case of raffinose, as a_w was reduced to 0.96 (25°C) a super-saturated solution occurred and NMR line-width remained unchanged because of saturation. Beyond this point, microbial growth was still observed (but with a longer lag time). During the time period when no raffinose crystals were observed, *S. aureus* continued to grow (a_w and ^{17}O NMR line-width remained relatively unchanged compared with the same system at saturation).

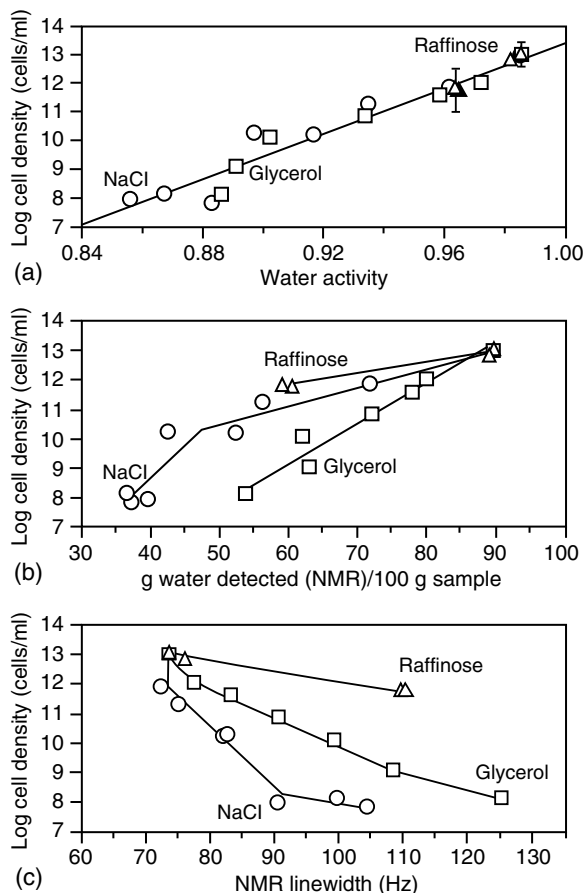
Vittadini et al., (2001) investigated the media systems further with the proton decoupled ^{17}O NMR relaxation rate measurement using a 300 MHz NMR spectrometer (Bruker MSL 300) with a WALTZ pulse sequence. Acquisition parameters were 41 ms acquisition time, 9 μs 90° pulse width, 100 ms recycle delay and 32°C sample temperature. Transverse relaxation rate (R_2) was analyzed from line shape analysis after the system was

**FIGURE 10.3**

Effect of added solutes on lag time. Lag times correlated more closely with a_w than with water mobility (NMR parameters) (Lavoie, 1998).

experimentally verified that the extreme narrowing limit condition was satisfied ($T_1 \sim T_2$). The molecular dynamics behavior of water molecules was analyzed according to the "anisotropic, two correlation time model" for bound water (Halle et al., 1982; Hills and Multinuclear, 1991).

In a simple system, when a solute is placed in water, it perturbs the water molecules creating anisotropic conditions on a long time scale compared with the reorientation time of bulk water. Traditionally, this was attributed to fast exchange between the "free" and "bound" water. Unfortunately, such a simple model has been shown to fail at fitting a number of experimental data. Further consideration is needed according to the following observations. In the slow process, some of the water molecules are strictly related to the concentration of solute and modulated by the solution viscosity (Halle et al., 1982; Hills and Multinuclear, 1991). The water molecules in the fast

**FIGURE 10.4**

Correlation between a_w and *Staphylococcus aureus* cell density at 24 h. The NMR parameters show a strong solute dependence (Lavoie, 1998).

reorienting water fraction will instead be independent of solute concentration. Hence, the two-site, fast-exchange model can be modified in such a way that the fraction of “bound” water includes fast and slow motions as follows (Halle et al., 1982; Halle and Winnerstrom, 1928; Belton et al., 1991; Hills and Multinuclear, 1991; Colquhoun and Goodfellow, 1994):

$$R = P_{bw}(R_{bw}^f + R_{bw}^s) - (1 - P_{bw})R_w$$

where R = transverse relaxation rate of the sample; R_{bw}^f = relaxation rate of the fast component of perturbed water; R_{bw}^s = relaxation rate of the slow component of perturbed water; R_w = relaxation rate in bulk water of same temperature; and P_{bw} = mole fraction of water molecules detectable interacting with the solute (or population of “bound” water).

The following equations are used to describe the correlation times of the fast (τ_{bw}^f) and slow (τ_{bw}^s) components of the bound water fractions:

$$\begin{aligned}\tau_{bw}^f &= [(1 + \eta^2/3)/(1 + \eta^2/3 - S^2)](R_{bw}^f/R_{bw}^s)\tau_w \\ &= \tau_{bw}^s = \tau_w B_{bw}(1 + \eta^2/3)(n/\rho)S^2 R_w\end{aligned}$$

where η = asymmetry parameter of the quadrupolar interaction; S = order parameter (it is a measure of the degree of orientation of bound water molecules with respect to the solute surface, value of 0 indicates no effect of solute and 1 indicates rigid binding (Halle and Winnerstrom, 1928)); τ_w = bulk water correlation time, 2.4 ps; τ_{bw}^f = correlation time for the fast component of bound water, found to be about eight times longer than that of pure water and it is concentration independent; and τ_{bw}^s = correlation time for the slow component of bound water, found to become longer with an increase in solute concentration as it is related to increased viscosity of the solution (see Figure 10.5, a representation of “the anisotropic, two correlation time model for bound water”, model.18).

A more detailed description of the method is described elsewhere (Halle et al., 1982; Hills and Multinuclear, 1991; Vittadini, 1998; Vittadini et al., 2001).

From this model, τ_{bw}^f for BHI (50 to 100% water), NaCl (60 to 100% water), and BHI:NaCl mixture (75 to 100% water) were 12.8, 10.4, and 6.1 ps, respectively (compared with 2.4 ps for τ_w). τ_{bw}^s for each system was approximately 1 to 2.5 orders of magnitude higher than the respective τ_{bw}^f and it increased with decreasing water content accordingly with kinematic viscosity increase. The population of “bound” water (slow + fast), or P_{bw} , was found to match the unfreezable water values obtained from DSC, whereas P_{bw} obtained from a two-site, fast exchange model overestimated the amount of “bound” water, particularly in NaCl containing systems.

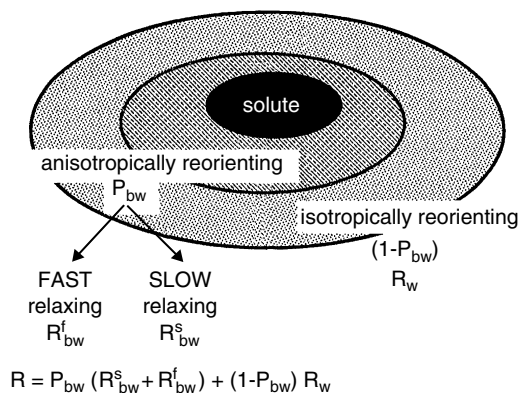


FIGURE 10.5

Model describing the interpretation for the anisotropic, two correlation time model for bound water (Vittadini et al., 2001).

S. aureus growth in the BHI and BHI-NaCl (1:1) media was investigated. It was found that the lag time increased with decreasing a_w and similarly between the two media and cell density after 24 h incubation increased almost linearly with increasing a_w (Figure 10.6). Containing >70% of free water, the media P_{bw} increased with increasing solid content primarily because of the change in the slow component of “bound” water that decreased in its mobility (τ_{bw}^s) according to the kinematic viscosity increase. ^{17}O NMR data showed that when plotted against P_{bw} growth parameters for *S. aureus* (lag time and cell density at 24 h) changed but in a way depending on the media composition (presence of NaCl in this case).

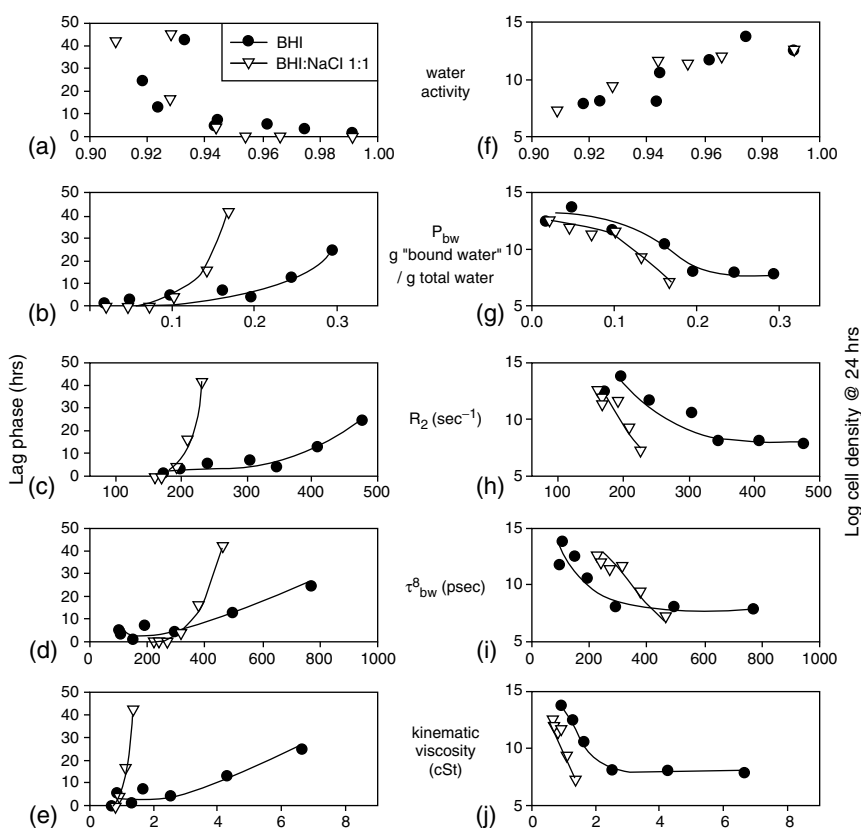


FIGURE 10.6

Correlation between lag phase (hours) and cell growth at 24 h (log) for *Staphylococcus aureus* and physico-chemical parameters measured for BHI (black circles) and BHI:NaCl 1:1 mixture (white triangles): water activity, population of bound water (P_{bw}), ^{17}O NMR relaxation rate (R_2), correlation time of the slow component of the anisotropically reorienting water population (τ_{bw}^s) and kinematic viscosity. (Source: Reprinted from Vittadini, E. and Chinachoti, P. Correlation of microbial response in model food systems with physico-chemical and mobility (NMR descriptors) of the media, *Int. J. Food Sci. Technol.*, 38, 841, 2003. With permission.)

The data suggest that in this diluted system (liquid 0.90 to $0.99a_w$), the growth response for *S. aureus* is governed by the osmotic pressure of the media (as shown from the data when plotted against a_w ; Figure 10.6). The dynamic molecular mobility of water indicates that the perturbation of water in the presence of BHI solids was greater than in the presence of NaCl but growth was more inhibited when NaCl was present, possibly because of the physiological effect of NaCl. Since there is limited data of this kind available it is difficult to explicitly attribute the extent of the different contributing factors. Nevertheless, it is very clear that the effect of a_w is related to osmotic pressure rather than to the increase in the amount of “bound” water (although a_w reduction was accompanied by the experimentally observed increase in the population of “bound” water and the increase in the correlation time of the slow component of the bound water fraction, τ_{bw}^s). As a_w is depressed further below ~ 0.85 , it is expected that the perturbation of water will highly impact the cell mechanisms to sustain life but physiological effects of a_w and solute would remain primary factors (see also data in Figure 10.1 to Figure 10.4).

Semi-Solid Heterogeneous Systems (Mold Spore Germination)

Mold spore germination as influenced by the presence of water has been a subject for debate for quite some time. One of the highly debated issues involves an earlier report in systems containing starch and sucrose and other fermentable solutes. It was earlier proposed that the “states” of water and the energy of binding might play a role on spore germination (Lang, 1980; Gilbert, 1985; Paik, 1985). Later the glass transition concept was proposed to be used to describe mold germination since local viscosity was the kinetic barrier to spore germination and hence could better describe water availability (Slade and Levine, 1991). However, there have been experimental reports that did not seem to support the glass transition theory (Chirife and Buera, 1994; Chirife and Buera, 1995; Chirife and Buera, 1996; Chirife et al., 1996; Buera et al., 1998). In this work, NMR was applied to determine water mobility and offers a means to probe if the dynamic properties of water are closely related to key parameters that allow dormant spores to germinate. Both ^{17}O and ^2H (deuterium) NMR are applied to semi-solid systems as follows:

^{17}O NMR Signal Intensity (Liquid Water) in *Aspergillus niger* Study

In some of our earlier preliminary study, *Aspergillus niger* spore germination was studied in a sucrose–starch system (a repeat of Lang’s report, (Lang, 1980)). The ^{17}O NMR signal was highly susceptible to quadrupolar line broadening at the solid–liquid interface (i.e., starch) because of its strong quadrupole moment. In addition, in the NMR timeframe, local water

molecules that are in regions or domains within the starch entity ineffectively exchange with bulk water on the outside of granules or domains. Hence, it was found that the ^{17}O NMR signal highly corresponded with the fraction of water associated with sugar solutions in the system. As shown in Figure 10.7, the NMR signal intensity gave a good correlation with the amount of water associated with sucrose (based on the mass balance calculation from starch–sucrose water sorption isotherms; see method of calculation in Chinachoti and Steinberg, (1984). In other words, the ^{17}O NMR signal was mainly determined by the water involved in solubilizing the sugar (the majority of which remains on the outside of the starch granules because of steric exclusion).

Spore germination time was monitored by microscopic observation. It was found that germination time was long at a lower a_w and it decreased with increasing a_w , as expected, but this was highly dependent on the sucrose:starch ratio in these systems (Figure 10.8). However, the germination time was found to be highly correlated with the ^{17}O NMR signal intensity independently of the ratios between starch and sucrose (Figure 10.8) (Lavoie and Chinachoti, 1995; Kou et al., 2000). Because the ^{17}O NMR signal in this case was related primarily to the water molecules associated with soluble sugar molecules (based on the intensity evaluation above), mold spore

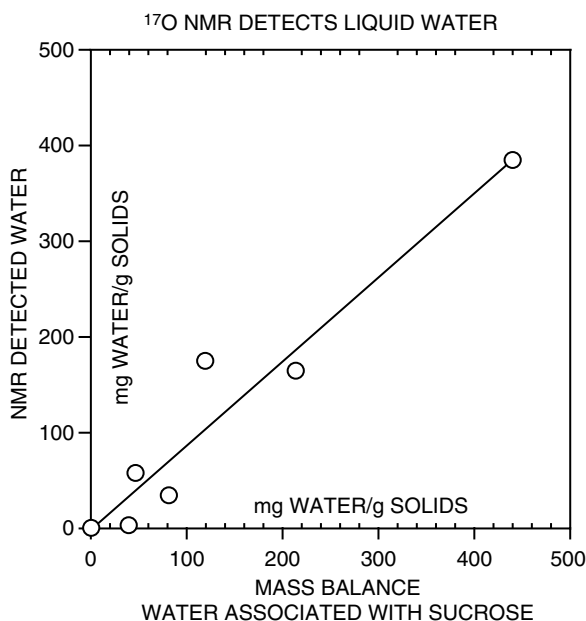


FIGURE 10.7

^{17}O NMR signal intensity (NMR detected water) as obtained from the spectral signal integration in sucrose–starch water systems at 0.86 to 0.97 a_w as a function of the mass of water associated with solids. (Source: Data obtained from Chinachoti, P. and Stengle, T.R. Water mobility in starch/sucrose systems: An oxygen-17 NMR study, *J. Food Sci.*, 55, 1732, 1990. With permission.)

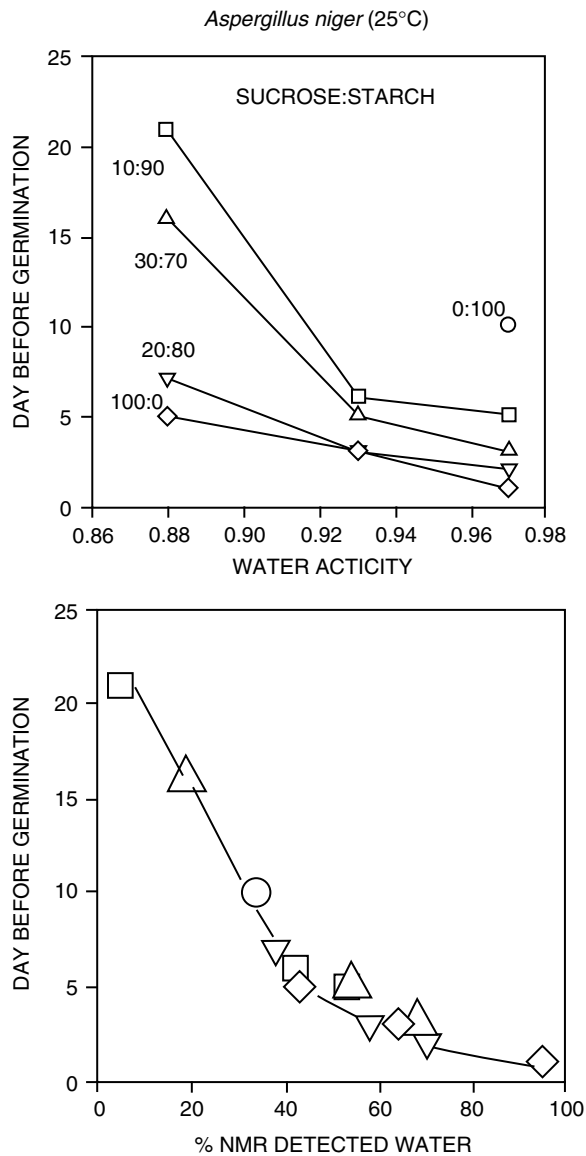


FIGURE 10.8
Aspergillus niger spore germination time as a function of a_w and ^{17}O NMR in sucrose:starch systems at various a_w . Relative intensity expressed as NMR active (detected) water. (Source: Obtained from Lavoie, J.P. and Chinachoti, P. The role of water mobility in promoting *Staphylococcus aureus* and *Aspergillus niger* activities, *Magnetic Resonance in Food Science*, Belton, P., et al., The Royal Society of Chemistry, Cambridge, U.K, pp. 33, 1995. With permission.)

germination is concluded to be highly dependent on such populations of water and on the amount of soluble sugar present. Because sucrose also serves as a nutrient to the mold, in such an experiment, one cannot clearly separate the contributions of water and sugar.

To address these issues, additional sets of experiments were performed.

The experiments were replicated using other small molecular carbohydrates (in order to vary the carbon source availability, such as sucrose, lactose, glucose, maltose and maltotriose, xylose and ribose (all at 1:9 solute:starch ratio)). Data in Figure 10.9 show a similar dependence on ^{17}O NMR detected water. When all data were compiled into one graph (Figure 10.10), it was clear that germination time for mold spores was more dependent on the ^{17}O NMR intensity (and thus was associated with soluble sugars) than on a_w . The work done on *A. niger* germination in nutritive sugars and starch suggest that there is a correlation between germination time and ^{17}O NMR signal intensity but the degree of scatter of the data in Figure 10.10 indicates a considerable deviation because of specific solutes.

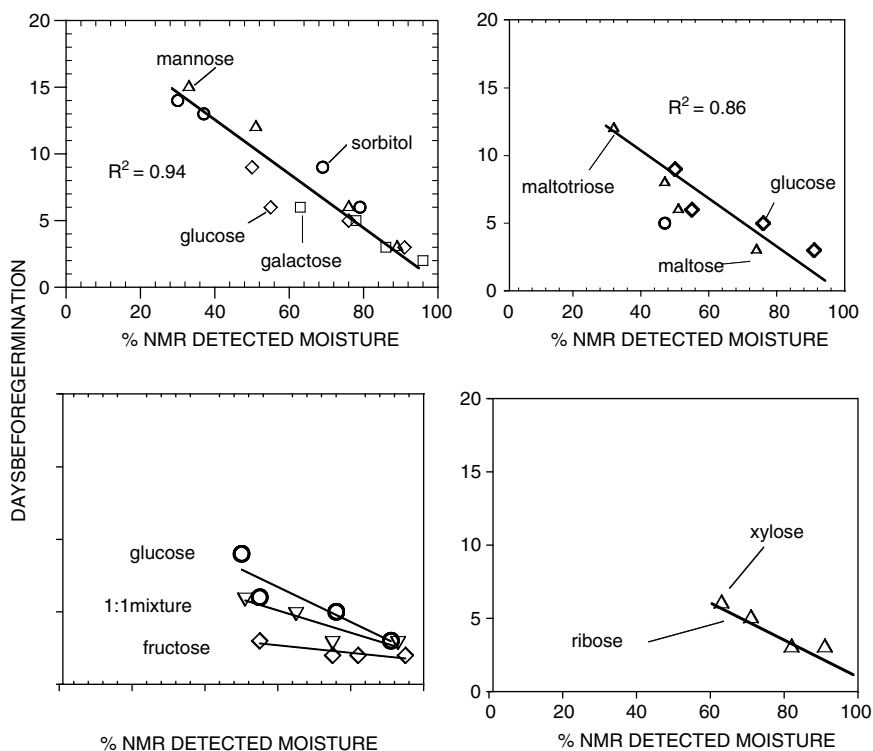
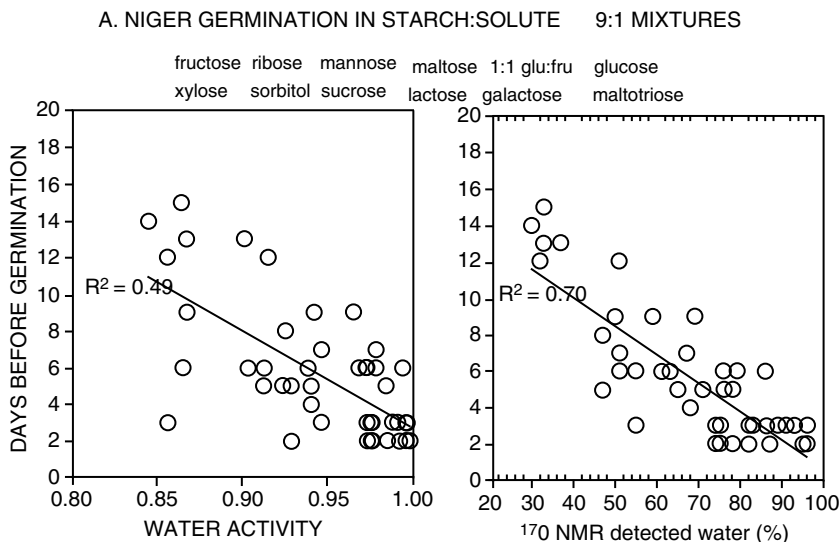


FIGURE 10.9

Aspergillus niger spore germination time as a function of a_w and ^{17}O NMR in small carbohydrates:starch (1:9 ratio) systems at various a_w . Relative intensity expressed as NMR active (detected) water.

**FIGURE 10.10**

Aspergillus niger spore germination time as a function of a_w and ^{17}O NMR signal intensity in small carbohydrates:starch (1:9 ratio) systems at various a_w . Relative intensity expressed as NMR active (detected) water.

Interestingly, the spore germination did not seem to correlate well with the ^{17}O NMR line-width, which theoretically could represent the mobility of water. Perhaps the line-widths data were subjected to some unknown contributions resulting from the complex quadrupolar interactions and the complex baseline (it was noted that in dry systems, phasing of the spectrum became more difficult because of the rolling baseline that was particularly observed in highly solid systems). It could be further explained that NMR line-width in semi-solids was affected by unknown contributions of quadrupolar interaction leading to additional line broadening. Hence, later experiments were performed to include both ^{17}O NMR as well as ^2H NMR relaxation. Deuterium NMR in this case offers a much improved signal that is less influenced by quadrupolar interaction because of its lower spin number of 1, compared with 5/2 for ^{17}O nuclei.

The second set of experiments was performed to address or separate the influence of the carbohydrate solute as the potential carbon source itself. This led to the reports on *A. nidulans* as follows.

H and ^{17}O NMR in *Aspergillus nidulans* Germination Study (Lavoie and Chinachoti, 1995; Pham et al., 1999)

In order to completely separate the physiological effect of the solute, another system was designed. A mutant strain of *A. nidulans* (biA-1 sorA-2) was selected because of its defect in L-sorbose transportation into the cells. In the wild strain, *A. nidulans* allows L-sorbose transportation. The media

contained cellulose, sorbose, and orange serum broth (OSB). The media system contained L-sorbose-cellulose mixtures (0:1, 1:2, 1:1, 2:1, and 1:0 s:c ratios) and all substrates contained an equal concentration of OSB as nutrient (4% solids basis) for the mold. Systems containing various water contents and a_w were prepared as described elsewhere (Pham, 1998; Pham et al., 1999). Germination time and hyphae growth rate were tested in two experiments. The media were tested for both ^2H and ^{17}O NMR water mobility.

When ^2H NMR was performed the media hydrated with 1:1 $\text{H}_2\text{O}:\text{D}_2\text{O}$ were packed in 10 mm NMR tubes to reach a sample height of 8 to 10 mm. A 90° pulse WALTZ sequence was used with acquisition parameters 7.45 to $780\ \mu\text{s}$ pulse width, 1500 to 20,000 Hz pulse width, 0.012 to 0.166 sec acquisition time and recycle delay $>5T_1$. Spin-spin relaxation time (T_2) was determined with a Carr-Purcell-Meiboom-Gill (CPMG) pulse sequence with interpulsed spacing (τ) ranging from 5 to 500 ms. At least eight different τ values were used for each T_2 determination.

The spin-spin relaxation times for water as obtained from ^2H (CPMG pulse sequence) and ^{17}O NMR (estimated from line-width) were found to more closely correlate with germination time and hyphae growth rate. The hyphae growth rate was obtained from tracking hyphae length of an individual germination over time and from fitted growth curves according to the Velhulst-Pearl model (Brown and Rothery, 1993) ($r^2 > 0.90$). The data supported the earlier trends found in *A. niger* in sucrose-starch media

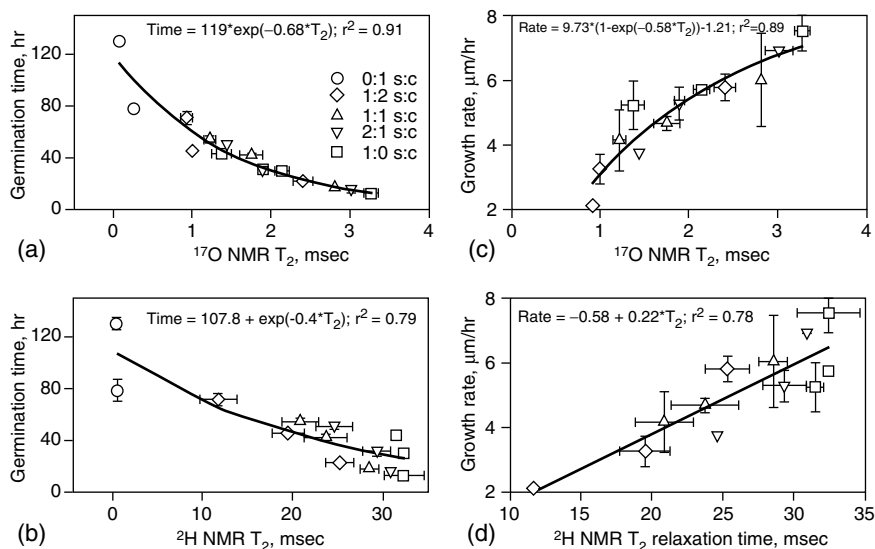


FIGURE 10.11

Aspergillus nidulans (biA-1 sorA-2) germination time and hyphae growth rate as a function of ^2H NMR and ^{17}O NMR T_2 relaxation times of cellulose (c), sorbose (s), and orange serum broth solids with different s:c ratios at 25°C . (Source: From Brown, D. and Rothery, P. *Models in Biology-Mathematics, Statistics and Computing*, Wiley, Chichester, UK, 1993. With permission.)

that the spore germination dependence on a_w was limited to composition (see Figure 10.8a). In the presence of solute (L-sorbose), the spore germination time and hyphae growth rate were highly dependent on water mobility regardless of system composition (Figure 10.11), both for the case of ^2H and ^{17}O NMR, and the experiments were repeated twice.

Figure 10.12 demonstrates that spore germination time was logarithmically correlated with ^{17}O T_2 relaxation time, whereas the hyphae growth rate was inversely proportional to ^{17}O T_2 relaxation (i.e., linearly correlated with R_2 or the spin-spin relaxation rate). The exponential dependence of germination time on ^{17}O NMR water mobility clearly indicates that the germination time (which depends highly on the spore hydration process) is governed primarily by the presence of liquid water (relatively free with T_2 in the ms range). As described earlier, the ^{17}O NMR signal in these experiments measured the amount of liquid water associated with small solutes (Figure 10.7) i.e., in this

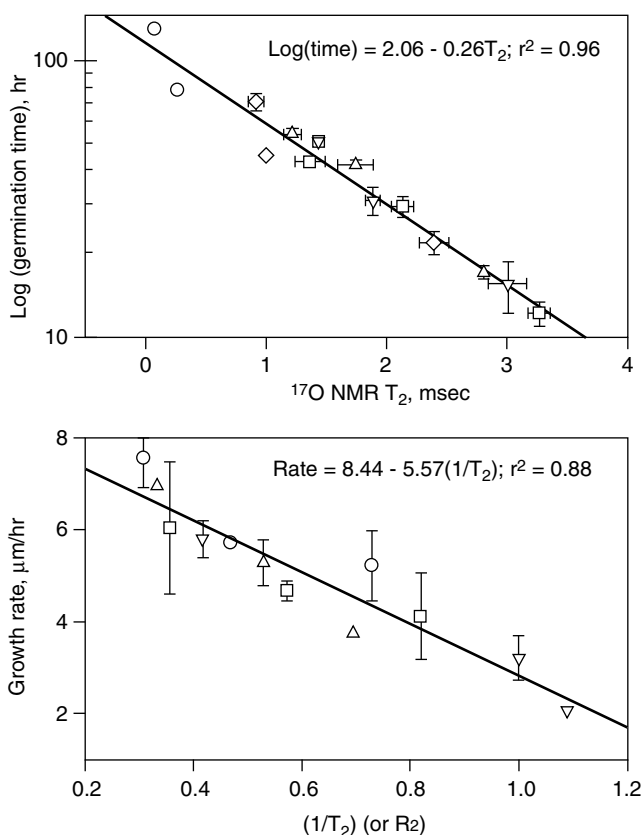


FIGURE 10.12

Aspergillus nidulans (biA-1 sorA-2) germination time and hyphae growth rate as a function of ^{17}O NMR T_2 relaxation time and rate, respectively. (Source: From Brown, D. and Rothery, P. *Models in Biology-Mathematics, Statistics and Computing*, Wiley, Chichester, UK, 1993. With permission.)

case L-sorbose. The biochemical and physiological processes of germination are complex processes involving not only spore hydration, swelling of spore walls but also gene expression triggering a series of biochemical processes. It is still unclear why the dependence is logarithmic or exponential in nature and certainly the explanation cannot be a straightforward one.

Once germinated, the growth of the hyphae is greatly dependent on the nutrients delivered to them by water mediation. In this case there is a direct relationship or trend between the growth rate and the rate of water mobility. Note that, in this case, the correlation is with the mobility of the water associated with soluble solute molecules on the outside of the starch granules, which happens to be the location where the mold spores are located. It would be important to take into consideration the microstructure and location of the microorganisms and the local water mobility surrounding the cells. In our case, ^{17}O NMR happens to be able to distinguish the water populations inside the starch granules and outside. In other cases, the NMR parameters can be predetermined in such a way that the discrimination can also exist within the experimental NMR timeframe.

For practical purposes, one can develop a curve as shown in Figure 10.12 for a specific food being processed and use NMR water mobility as a predictor parameter for potential mold spoilage.

Solid System (Survivability)

In solids (that is, $a_w < 0.6$) microorganisms do not grow and instead either die or adapt themselves to withstand the water stress by different means. The microbial survival ability generally is the highest in an extremely low moisture environment ($a_w \sim 0$). As a_w increases, the cellular survival ability decreases through complex cellular damage. Media composition has been shown to play an important role in microbial survival ability. Mugnier and Jung, (1985) reported a large number of sugars in those media in which *Rhizopus japonicum* survived. It was reported that at a given a_w , the presence of some solutes promoted or prolonged survival ability, whereas some others lead to higher susceptibility to osmotic stress and consequently to death. There are several theories describing physico-chemical and biochemical pathways by which a cell adapts to survive a drought condition (Potts, 1994).

Freeze-dried locust bean and xanthan gum mixtures containing no and 14% mannitol, respectively, were studied from water sorption, glass transition and solid-state proton (^1H) and deuteron (^2H) NMR. It has been reported previously that both systems showed highest survival rate at $\sim 0 a_w$ and as water content and a_w increased beyond about 10% moisture, the survival rate decreased. The control (no mannitol) showed a greater decrease with increasing moisture than the mannitol-containing system. Such a discrepancy has been proposed to be caused by the greater mobility manifested by the presence of mannitol (Mugnier and Jung, 1985). Thermal and

thermo-mechanical analyses were performed on these samples by DSC and DMA (Potts, 1994). Unfortunately, no evidence of a glassy–rubbery transition was observed. Solid-state ^1H and ^2H NMR spectroscopy showed distinguishable mobile and immobile fractions that slowly inter-exchanged

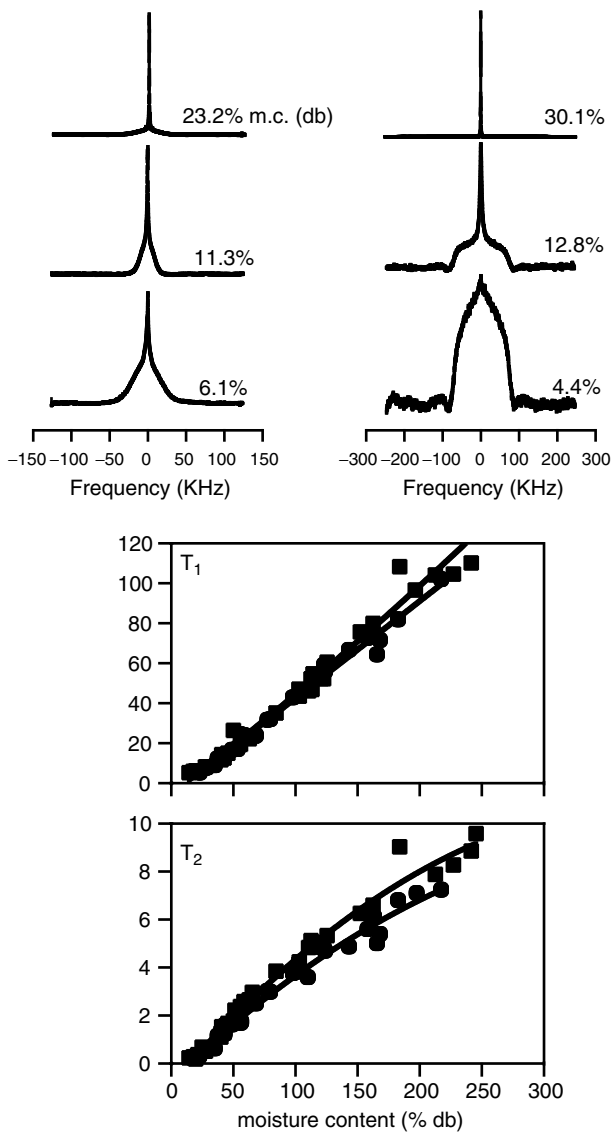


FIGURE 10.13 (Top) Solid-state proton (left) and deuterium (right) NMR spectra for freeze-dried media systems containing 14% mannitol indicating narrow (rapidly exchanging) and broad (slowly exchanging) components. (Bottom) T_1 and T_2 deuterium relaxation times for freeze-dried xanthan-locust bean gum with (solid circles) and without (solid squares) 14% mannitol.

(within the NMR timeframe). Figure 10.13 depicts signals from the mobile and immobile protons and deuterons obtained from solid-state NMR (more details can be found elsewhere (Vittadini et al., 2002). The relative signal intensities and ^2H NMR T_1 and T_2 relaxation times are plotted against water content (Figure 10.14). No differences in ^2H NMR T_1 and T_2 and the relative ^2H intensities between the two systems were observed. However, ^1H NMR intensity showed that at $>10\%$ moisture, less relative mobile fractions were

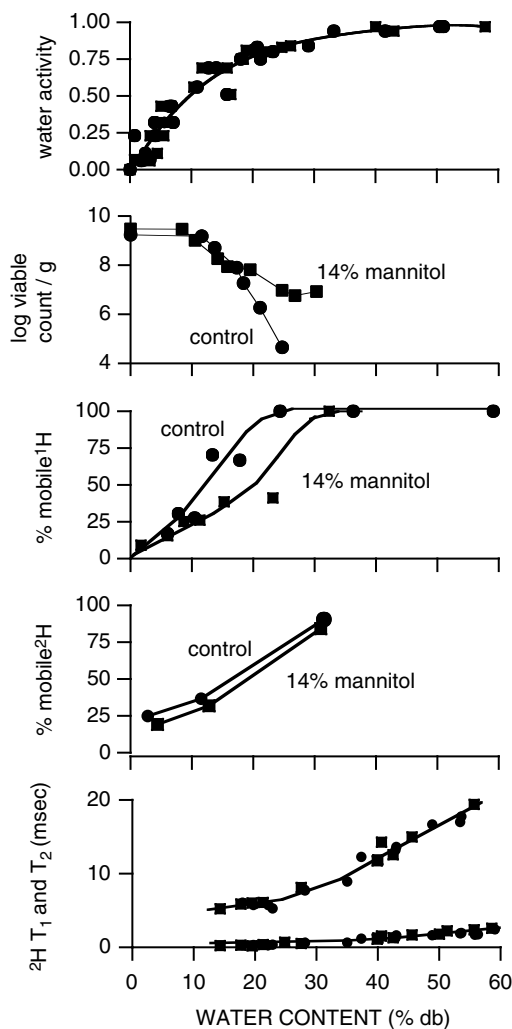


FIGURE 10.14

Water sorption, viable cell count of *Rhizopus japonicum*, relative mobile protons and deuterons and ^2H T_2 relaxation times for freeze-dried xanthan and locust bean gum gels. (Source: From Vittadini, E., Dickinson, L.C., and Chinachoti, P. NMR water mobility in xanthan and locust bean gum mixtures: possible explanation of microbial response, *Carb. Poly.*, 49, 261, 2002. With permission.)

observed in the 14% mannitol sample. This corresponded to an emergence of mobile mannitol protons (mobilization of plasticized mannitol). A possible explanation is that part of the water molecules participated in the hydration of plasticized mannitol, thus becoming less mobile. Further investigation is needed to better understand the cellular mechanism for mortality in such a situation.

Concluding Remarks

The results of this study indicated that NMR molecular mobility of water molecules is a very useful tool to describe the complex nature of the water availability to organisms in semi-solids and liquid systems. In the case of *S. aureus* in liquid media over the range 0.90 to 0.99 a_w (and T_2 in ms range), the majority of the water is liquid and freely moves (correlation time in ~ 10 ps), hence the growth parameter is less dependent on the mobility and the quantity of bound water (10 to 30% of the water was considered perturbed or bound) as described by a model derived to describe two-state, fast exchange with anisotropic, two correlation time for bound water. In this case, a_w has been consistently shown to be a describing parameter governing the bacterial activity not because of the presence of “bound” water but rather to another effect, primarily osmotic.

Perhaps one of the most meaningful findings in this work is that solvent water is the driver for mold spore germination. Water available to spore germination in semi-solids depends on the ^{17}O NMR water mobility of the population of water surrounding the spores (outside of the starch granules). Once the spores are hydrated and swollen, germinating hyphae growth rate is linearly dependent on the mobility of the water molecules (^{17}O NMR R_2), which shows a strong dependence on the water function to bring nutrients to the cells. Based on these results it is quite clear that the mechanisms related to growth and germination of mold spores are highly dependent on the mobility of water surrounding the spores. The presence of mobile water around the spores means a better hydration of the spore walls triggering the germination process and at the same time that mobile water participates in dissolving essential components that support growth. It is critical to keep in mind the paramount difference in genetic, biochemical, and physiological processes among organisms and hence discrepancies among strains and systems are expected.

In addition, water availability as discussed in terms of water mobility here may only be relevant at the local level where the microorganisms are located. If the system is so efficiently heterogeneous that water molecules cannot rapidly exchange among different domains or locations, the mobility effect is only local. NMR parameters can be manipulated to discriminate various water populations and hence the method can be made robust for studying water availability in a given heterogeneous food system. This would be

beneficial particularly in systems with microscopic scale heterogeneity. ^{17}O NMR has been shown to be rather useful in the system studied and further investigation in this area could lead to a wider use of this technique to measure water availability. For practical purposes, ^2H NMR can serve as the alternative method that is more appropriate for an industrial application because its measurement can be done in a relatively less expensive instrument.

Acknowledgments

Work was performed by Xuyen Pham, James P. Lavoie, and Elena Vittadini with generous contributions from their colleagues (Drs Leonard Charlie Dickenson, Ronald G. Labbe, and Robert E. Levin). Support from U.S. Department of Agriculture and the University of Massachusetts College of Food and Natural Resources Minority Scholarship Program (to support Xuyen Pham) are appreciated.

References

- Ballesteros, S.A., Chirife, J., and Bozzini, J.P. Specific solute effects on *Staphylococcus aureus* cells subjected to reduced water activity, *Int. J. Food Microb.*, 20, 51, 1993.
- Belton, P.S., Ring, S.G., Botham, R.L., and Hills, B.P. Multinuclear NMR studies of water in solutions of simple carbohydrates II oxygen-17 relaxation, *Mol. Phys.*, 72, 1123, 1991.
- Brown, D. and Rothery, P. *Models in Biology-Mathematics, Statistics and Computing*, Wiley, Chichester, UK, 1993.
- Buera, M.P., Jouppila, K., Roos, Y.H., and Chirife, J. Differential scanning calorimetry glass transition temperatures of white bread and mold growth in the putative glassy state, *Cereal Chem.*, 75, 64, 1998.
- Cardona, S., Schebor, C., Buera, M., Karel, M., and Chirife, J. Thermal stability of invertase in reduced-moisture amorphous matrices in relation to glassy state and trehalose crystallization, *J. Food Sci.*, 62, 105, 1997.
- Chinachoti, P. and Steinberg, M.P. Interaction of sucrose with starch during dehydration as shown by water sorption, *J. Food Sci.*, 49, 1604, 1984.
- Chinachoti, P. and Stengle, T.R. Water mobility in starch/sucrose systems: An oxygen-17 NMR study, *J. Food Sci.*, 55, 1732, 1990.
- Chirife, J. and Buera, M.P. Water activity, glass transition and microbial stability in concentrate/semi-moist food systems, *J. Food Sci.*, 59, 921, 1994.
- Chirife, J. and Buera, M.P. A critical review of some non-equilibrium situations and glass transitions in water activity values of foods in the microbiological growth range, *J. Food Engr.*, 25, 531, 1995.
- Chirife, J. and Buera, M.P. Water activity, water glass dynamics, and the control of microbiological growth in foods, *Crit. Rev. Food Sci. Nutr.*, 36, 465, 1996.

- Chirife, J., Gonzalez, H.H.L., and Resnik, S.L. On water dynamics and germination time of mold spores in concentrated sugar and polyol solution, *Food Res. Int.*, 28, 531, 1996.
- Christian, J.H.B. Specific solute effects on microbial/water relations, *Water activity-Influences on Food Quality*, L. Rockland and G. Stewart, eds., Academic Press, San Diego, pp. 825, 1981.
- Colquhoun, I.J. and Goodfellow, B.J. Nuclear magnetic resonance spectroscopy, *Spectroscopic Techniques for Food Analysis*, R.H. Wilson, ed., VCH Publisher, New York, pp. 87, 1994.
- Franks, F. Water activity: A credible measure of food safety and quality?, *Trends Food Sci. Technol.*, 68, 1991.
- Gilbert, S.G. New concepts on water activity and storage stability, *The Shelf-Life of Foods and Beverages: Proceedings of the 4th International Flavor Conference*, Elsevier, G. Charalambous, ed., pp. 791, 1986, July 1985.
- Halle, B., Carlstrom, G., Anderson, T., Wennerstrom, H., and Lindman, B. NMR of water nuclei in heterogeneous systems-relaxation theory and oxygen-17 data from aqueous solutions of proteins, polyelectrolytes and micelles, *Biophysics of Water*, F. Franks, ed., Wiley, New York, pp. 221, 1982.
- Halle, B. and Winnerstrom, H. Interpretation of magnetic resonance data from water nuclei in heterogeneous systems, *J. Phys. Chem.*, 75, 1981, 1928.
- Hills, B.P. Multinuclear NMR studies of water in solutions of simple carbohydrates I. Proton and deuterium relaxation, *Mol. Phys.*, 72, 1099, 1991.
- Kou, Y., Lavoie, J.P., and Chinachoti, P. ^{17}O , NMR for water and its correlation with microbial activity, *The Proceeding of the Food Preservation Conference*, US Army RD&E Center, Natick, MA, 1996.
- Lang, K.W., Physical, chemical and microbiological characterization of polymer and solute bound water, Ph.D. Dissertation, Department of Food Science, University of Illinois, Urbana-Champaign, 1980.
- Lavoie, J.P. Cellular response of *Staphylococcus aureus* as related to NMR detected water and system mobility, water activity and media formulation, Ph.D. dissertation, Department of Food Science, University of Massachusetts (Amherst), 1998.
- Lavoie, J.P. and Chinachoti, P. The role of water mobility in promoting *Staphylococcus aureus* and *Aspergillus niger* activities, *Magnetic Resonance in Food Science*, Belton, P., Delgadills, I., Gil, A.M. and Webb, G.A.). The Royal Society of Chemistry, Cambridge, UK, pp. 33, 1995.
- Lavoie, J., Labbe, R.G., and Chinachoti, P. Comparison of ^{17}O NMR water mobility to water activity for the determination of growth of *Staphylococcus aureus*, *J. Food Sci.*, 62, 861, 1997.
- Mugnier, J. and Jung, G. Survival of bacteria and fungi in relation to the solvent properties of water in biopolymer gels, *Appl. Env. Microb.*, 108, 1985.
- Paik, S.W. The state of water in food component related to germination of mold spores, Ph.D. Dissertation, Food Science Department, Rutgers University, New Brunswick, NJ, USA, 1985.
- Pham, X. Role of water mobility on germination and growth of *Aspergillus nidulans*, Masters Thesis, Department of Food Science, University of Massachusetts, Amherst, MA, USA, 1998.
- Pham, X., Vittadini, E., Levin, R.E., and Chinachoti, P. The role of water mobility on mold spore germination, *J. Agric. Food Chem.*, 47, 4976, 1999.
- Potts, M. Desiccation tolerance of prokaryotes, *Microbiol. Rev.*, 58, 755, 1994.

- Scott, W.J. Water relations of *Staphylococcus aureus* at 30°C, *Aust. J. Biol. Sci.*, 6, 549, 1953.
- Slade, L. and Levine, H. Non-equilibrium behavior of small carbohydrate-water systems, *Pure Appl. Chem.*, 60, 1841, 1988.
- Slade, L. and Levine, H. Beyond water activity: recent advances based on an alternative approach to the assessment of food quality and safety, *Crit. Rev. Food Sci. Nutr.*, 30, 115, 1991.
- van den Berg, C. and Bruin, S. Water activity and its estimation in food systems: theoretical aspects, *Water Activity: Influences on Food Quality*, L. Rockland and G. Stewart, eds., Academic Press, San Diego, pp. 1, 1981.
- Vittadini, E. Water mobility in heterogeneous systems as examined by ^1H , ^2H , and ^{17}O NMR, Ph.D. dissertation, Department of Food Science, University of Massachusetts, Amherst, MA, USA, 1998.
- Vittadini, E. and Chinachoti, P. Correlation of microbial response in model food systems with physico-chemical and mobility (NMR descriptors) of the media, *Int. J. Food Sci. Technol.*, 38, 841, 2003.
- Vittadini, E., Dickinson, L.C., and Chinachoti, P. NMR water mobility in xanthan and locust bean gum mixtures: possible explanation of microbial response, *Carb. Poly.*, 49, 261, 2002.
- Vittadini, E., Schmidt, S.J., and Chinachoti, P. Mobility of water in NaCl and Brain Heart Infusion (BHI) solutions as studied by ^{17}O NMR, *Mol. Phys.*, 99, 1641, 2001.

11

Water Properties and Cell Longevity

Christina Walters

CONTENTS

Background: Long-Term Preservation of Genetic Resources	191
Factors that Affect Seed Longevity	192
The Kinetics of Seed Deterioration: Driving Forces.....	195
The Kinetics of Seed Deterioration: Resistance Factors.....	198
Conclusions.....	201
References	201

Background: Long-Term Preservation of Genetic Resources

The USDA National Center for Genetic Resources Preservation (NCGRP) in Fort Collins, CO, USA is home to over 450,000 accessions of plant and animal germplasm, maintained in perpetuity so that genetic diversity of agronomically important species is available to future generations. Germplasm is collected and stored from wild populations, landraces and improved breeding stocks of over 3000 species. The USDA started genebanking in the 1890s when plants with interesting traits were introduced to the US and evaluated at Plant Introduction Stations around the country. The National Seed Storage Laboratory (NSSL) was built in 1958 to consolidate the plant collections in a single facility. The name change in 2002 to NCGRP reflected a broader mission to preserve a diverse array of plant and animal germplasm and a future goal of preserving microbes. Current preservation protocols maintain germplasm viability for several decades or centuries, and ensure that these valuable genetic resources are always replenishable and available when needed.

Most of the germplasm at NCGRP (~350,000 accessions) is stored as dried seeds. The innate desiccation tolerance of mature seeds from most agricultural crops allows them to be dried to very low water contents

without damage. At NCGRP, seeds are dried to water contents between 0.04 and 0.08 g H₂O/g dw in a relative humidity-controlled room set at 10°C and 25 to 30% RH. Once dried, seeds survive exposure to subfreezing temperatures and the bulk of the NCGRP collection is stored at −18°C (conventional storage at −18°C was instituted in 1978; previously seeds were stored at 5°C). The use of liquid nitrogen for seed storage (cryogenic storage) was introduced in 1977 and became routine by 1990. Cryogenically stored seeds are placed in the vapor phase above liquid nitrogen where temperatures range from −120 to −180°C. Viability of stored seeds is monitored on a 5 to 10 year cycle to ensure that the accession is flagged for regeneration before the seed becomes badly deteriorated.

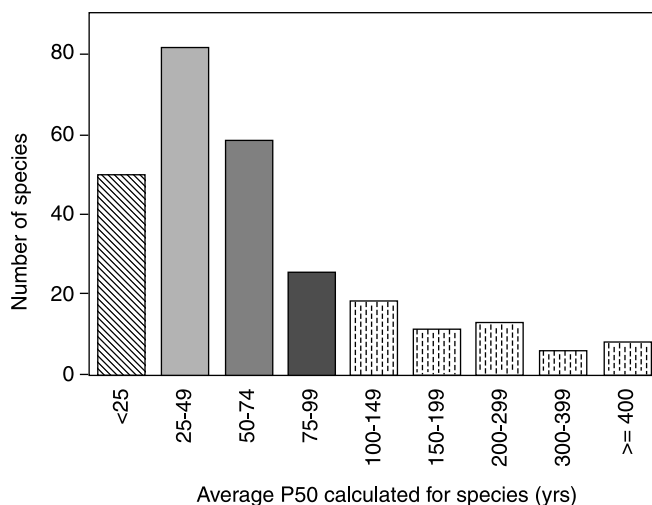
Factors that Affect Seed Longevity

Viability time courses, collected at NCGRP for a large number of samples for more than 30 years, provide a rich source of information on the nature and kinetics of seed deterioration. Time courses follow a sigmoidal pattern, where a period of minor loss in viability precedes a cataclysmic phase where severe reductions in viability are observed. Recently, Avrami kinetics, which describe cooperative reactions based on visco-elastic properties (Avrami, 1941), have been used to describe the pattern of seed aging (Walters et al., 2004; Walters et al., 2005):

$$\ln\left(\frac{N_0}{N}\right) = \left(\frac{t}{\phi}\right)^n$$

where t is storage time and N_0/N is the reciprocal of percentage germination (i.e., viability). The coefficients ϕ and n describe the shape of the sigmoidal curve, with the abruptness at which viability declines increasing as n increases above 1. When $n = 1$, the Avrami equation assumes the form of a typical first-order equation. The time coefficient, ϕ , can be treated as an Arrhenius function of temperature (Williams et al., 1993). The shelf life of the accession, also called longevity, can be quantified by the calculated time for germination to decrease to 50% (P50). In a recent survey of seeds that had been stored at NCGRP for 38 to 80 years, we found that projected P50s among species ranged from 12 to >450 years with a median value of 54 years (Figure 11.1). Initially stored at 5°C (until 1978), the seeds have spent the last 22 to 26 years at −18°C (Walters et al., 2005).

Characteristic longevity among seed species is almost anecdotal among seed scientists, but a mechanistic explanation remains elusive. As with other seed longevity surveys, we found that species such as lettuce, onion, elm, and fescue were notoriously “bad keepers” and species such as spinach, tomato, cucumber, okra, pea, and radish consistently stored well. Species such as sunflower, flax, cereal grains, and poppy exhibited typical seed storage behavior. The propensity for seeds to survive for long periods has

**FIGURE 11.1**

Projected longevity calculated for 278 species stored at NCGRP since the 1960s. The graph shows a skewed distribution with some species (e.g., onion, peanut, lettuce, pepper, fescue, and elm) having characteristically short life spans, while others (e.g., okra, chickpea, cucumber, pea, spinach, and oats) having characteristically long life spans. Species such as sunflower, flax, wheat, eggplant, sesame, and poppy have median life spans. Data are from (Walters et al., 2005).

been related to the accumulation of soluble sugars, which contribute to aqueous glass formation (Horbowicz and Obendorf, 1994; Leopold et al., 1994). However, we saw no correlation between soluble carbohydrate content, sucrose content and oligosaccharide content (Walters et al., 2005). While this observation does not rule out a role for glasses in regulating seed longevity, it is consistent with the idea that oligosaccharides do not affect mobility of intracellular glasses in seeds (Buitink et al., 2000).

Aging rates of individual accessions within a species stored at NCGRP are highly variable despite consistent handling and storage protocols. For example, percent germination of 234 accessions of beet seeds stored at NCGRP for 21 to 26 years ranged from 95 to 0% and averaged 75%. After 50 years of storage, average percent germination decreased to about 30%, but the range of germination percentages among accessions was still considerable: 85 to 0%. The range of seed aging rates most likely results from genetic or environmental factors that regulate seed maturation programs or post-harvest conditions that accelerate reactions occurring during the initial, asymptomatic stage of deterioration. Because the nature of these factors and the reactions they affect are unknown, it is difficult to predict how rapidly an accession will age once it enters the NCGRP storage vaults. Lack of predictive tools necessitates the monitoring program, which is labor-intensive and consumes valuable genetic resources.

Cryogenic storage was introduced to NCGRP in the mid 1970s to prolong seed viability indefinitely, thereby obviating the need to monitor viability and regenerate deteriorated accessions. The initiation of NCGRP's cryogenic program coincides with the heightened understanding of vitrification of aqueous systems. The new technology presented the implicit assumption that if an organism survived the stress of initial exposure to cryogenic temperatures, then it would survive almost forever because the ultra-low temperatures would virtually stop the chemical and physical reactions that cause aging. An authoritative study showed that exposure of cryopreserved mouse embryos to a dose of about 2000 years of background radiation over a 5 month period did not affect viability (Whittingham et al., 1977).

Predictions of infinite life-spans of cryogenically stored seeds are not supported by data, which show significant decreases in viability in a relatively short time (Walters et al., 2004). In one experiment initiated in 1977, 15 out of 42 species of seeds that were placed in liquid nitrogen (-196°C) showed decreased germination after 11 to 20 years of storage (Walters et al., 2004). Deterioration was progressive with time, demonstrating that the loss of viability resulted from aging stresses rather than initial exposure. Data from lettuce seed is particularly revealing because of numerous studies on deterioration kinetics initiated by Drs Louis Bass and Phil Stanwood in the 1960s and 1970s and continued by Dr Bass's protégé, Ms Patricia Conine. As expected, the level of deterioration of lettuce seeds decreased with decreasing storage temperature (though deterioration was observed at all temperatures), and the average P50 projected for lettuce seed storage at -18 , -135 (LN vapor) and -196°C was 150, 524 and >3000 years, respectively. Clearly, longevity of seeds improved under cryogenic storage; however, the benefits of low temperature storage were not as great as originally anticipated. The diminished effect of temperature is illustrated by a break in the Arrhenius plot of the time coefficients calculated for lettuce deterioration at different temperatures (ϕ from the Avrami equation) (Figure 11.2); the temperature coefficient below the break at about -12°C is shallow (data summarized in (Walters et al., 2004)). In some cases, storage at cryogenic temperatures resulted in a surprising *increase* in seed aging rates compared with counterparts stored at -18°C (unpublished data). Current models of deterioration in biological materials do not account for the disappointing and counter-intuitive observation that cryogenic storage does not maintain viability of seeds indefinitely. Frequent monitoring and regeneration cycles are still required at NCGRP because the variability of aging rates and the potential risks of faster aging at extremely low temperatures cannot be predicted or explained.

As with extremely low temperatures, excessively low water content also has a limited benefit on seed longevity. In the early 1990s, it was evident that drying seeds below a critical water content did not increase seed life spans, and in some cases, detrimental effects of over-drying seeds were reported (Vertucci and Roos, 1990; Ellis, 1991; Walters, 1998a) (Figure 11.3). Critical water contents vary among seed species and storage temperature; however,

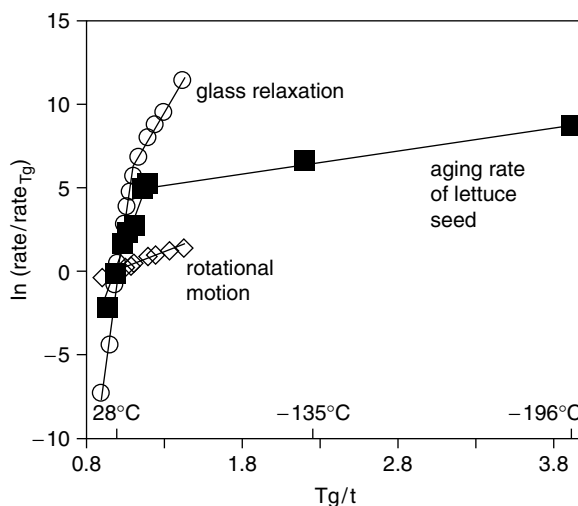


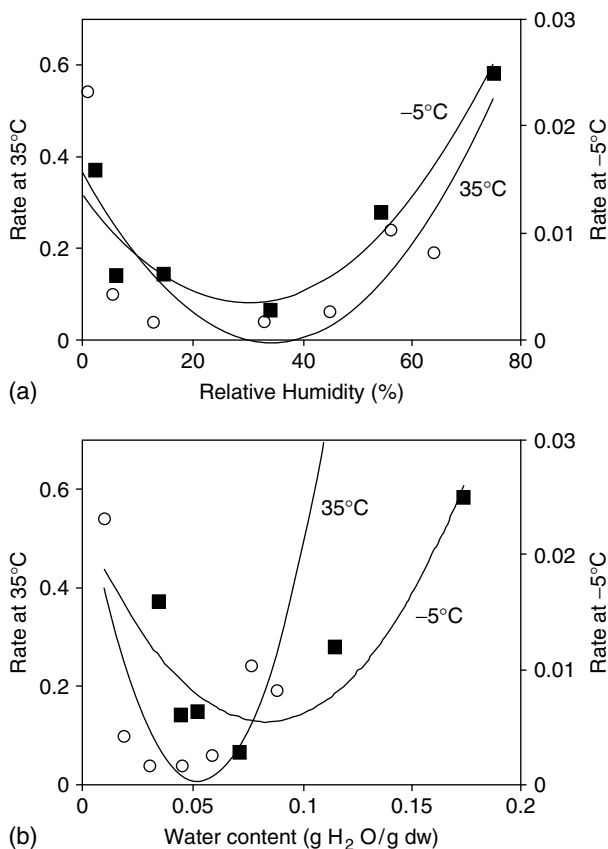
FIGURE 11.2

Arrhenius plots demonstrating the effect of temperature on lettuce seed aging rate (squares) and on molecular mobility calculated using the Adam–Gibbs model and heat capacity measurements (open circles) and from rotational motion using electron spin resonance measurements. Data are from Walters et al., (2004) (aging rate), Walters, (2004) (glass relaxation rates) and Buitink et al., (2000) (ESR measurements).

the relative humidity corresponding to these critical water contents appears to be fairly consistent. Theoretical considerations and empirical evidence point to an increasing critical water content with decreasing temperature (Figure 11.3b) (Vertucci and Roos, 1993; Buitink et al., 1998; Walters, 1998a, 1998b). This observation, in combination with the finding that longevity is either unchanged or declines at water contents less than the critical value, inevitably leads to the conclusion that progressively lower storage temperatures have increasingly limited beneficial effects on seed lifespans. In other words, the faster than expected deterioration of dried seeds stored under cryogenic conditions (described in previous paragraphs) may be explained by an interaction between water and temperature. This is a compelling reason to approach the study of seed deterioration kinetics through an examination of how the properties of water change with temperature in dry biological systems.

The Kinetics of Seed Deterioration: Driving Forces

The interaction of water, temperature and seed quality factors on seed aging kinetics can be examined through a simple model that describes kinetics of

**FIGURE 11.3**

Aging rates in soybean seeds at 35 and -5°C as a function of RH of storage (top panel) and water content of storage (bottom panel). The curves are quadratic equations fit to the data.

all reactions:

$$J = \frac{\Delta G}{R}$$

where J is the reaction rate, ΔG is free energy difference between products and reactants (the driving force of the reaction) and R represents barriers to the reactions either by limited molecular mobility or sequestration of reactants away from reaction sites. The parameter ΔG is controlled directly by the composition of aging substrates and protectants within the seed. Water content and temperature will have indirect effects by changing solubility and equilibrium coefficients. The parameter R is mostly regulated by temperature and water content since these factors affect molecular mobility; however, R may be indirectly affected by cellular constituents that modify viscosity.

The parameter ΔG is difficult to quantify because the specific reactants, products and protectants of aging reactions are not known for seeds, although they are surmised from model studies using systems of defined composition. Changing water concentration would necessarily change the concentration of reaction constituents, so even if concentrations cannot be directly quantified, they can be regulated. Application of this concept was the basis of the practice, popular in the 1960s through 1980s, of expressing food deterioration kinetics using water activity (Karel, 1980; Labuza, 1980). Though this treatment has proven controversial in the recent food quality and safety literature, it continues to be useful in seed technology. For seeds, the kinetics of different reactions increase or decrease with changing water contents, and hydration levels define the types of reactions that are likely to occur (Vertucci and Farrant, 1995). For example, oxidative phosphorylation (mitochondrial respiration) is not measured in seeds with water contents less than about 0.2 g H₂O/g dry mass and occurs at a maximum rate at water contents greater than about 0.5 g/g. Water contents for this transition vary among seed species and tissue types, but water activity and water potential are consistent (a_w ranges from about 0.90 to 0.98 corresponding to water potentials between -13 and -3 MPa). Anaerobic respiration and Maillard reactions appear to be facilitated at lower relative humidities (between 25 and 85%), and protein and membrane destabilization and free-radical induced auto-oxidation are the predominant reactions at relative humidity less than 20% (Walters, 1998b). We hypothesize that the changing physiology at different hydration levels results from changes in equilibrium constants among a suite of reactions or from differential responses of molar free energy among reaction constituents to changes in water content. Thus, changing water content can force a shift in equilibrium making different reactions more or less likely. Though not necessary to explain shifting equilibria, structural changes of water or other molecules when sorbed water is removed from surfaces can also have profound effects on the molar free energy of reaction constituents. These structural changes are implied by losses of protein activity, polar lipid phase changes (e.g., Crowe et al., 1997), or changes in heat capacity or freezing behavior of water (Vertucci, 1990; Buitink et al., 1996).

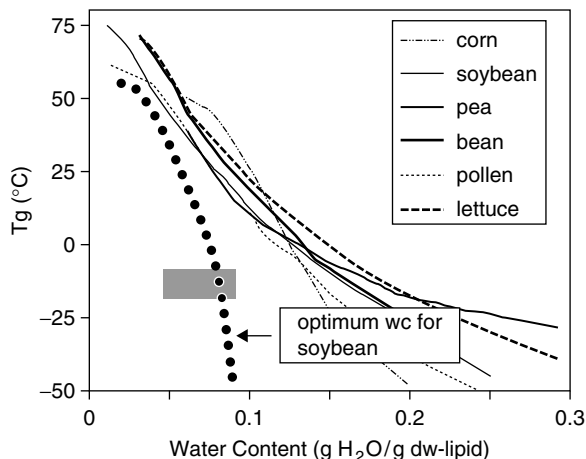
Concepts of critical hydration levels have helped to predict reduced longevity of seeds that are dried excessively. Storing seeds at relative humidities less than about 20%, at best, provides a constant, maximum shelf life (Ellis, 1991) and, at worst, reduces shelf life (Vertucci and Roos, 1990; Walters, 1998a, 1998b) (Figure 11.3). It is likely that the shift in the effect of water content on aging kinetics results from a changing propensity among different aging reactions. However, an alternative explanation, that molecular mobility increases under severely dry conditions, has also been proposed (Buitink et al., 2000). Combining the ideas that reaction kinetics shift at about 20% RH and that water content at a given RH increases when temperature is lowered, it follows that the water content providing maximum longevity will increase when the temperature is reduced

(Figure 11.3b). Studies comparing seed aging rates as a function of water content, RH and temperature have confirmed this prediction. If the optimum water content for seed storage increases with decreasing temperature and if aging rate increases at suboptimal water contents, then the risks of exacerbating the effects of over-drying increase at lower storage temperatures (Walters, 1998b).

The Kinetics of Seed Deterioration: Resistance Factors

The rate at which a reaction occurs is also regulated by resistance factors — factors that accelerate (catalysts) or slow down progress towards equilibrium, but do not directly affect the conditions defining equilibrium. Barriers to diffusion such as impermeable membranes or molecules with restricted mobility are considered resistance factors. Thus, both temperature and water content affect the R parameter for aging reactions because they affect molecular mobility within cells. The effect of temperature is most classically quantified by Arrhenius plots where the slope (temperature coefficient) provides an indication of the activation energy of the reaction. The effect of water content on molecular mobility often invokes a discussion of aqueous glasses (e.g., Slade and Levine, 1991). Glasses form in seeds as a consequence of maturation drying. The relationships between glass transition temperature (T_g , calculated as the midpoint of a baseline shift in DSC experiments) and seed water content are similar for seeds from several crop species and *Typha latifolia* pollen, and most materials enter a glassy phase once water contents decline to about 0.10 g H₂O/g (assuming drying at $\leq 25^\circ\text{C}$) (Figure 11.4). Hence, the aqueous domain of seeds is well within the glassy phase when seeds are placed under conventional storage conditions in genebanks, which prescribe storage at water contents between 0.04 and 0.07 g/g and temperatures between 5 and -18°C .

Comparisons of longevity data from the NCGRP genebank and glass transition characteristics among seeds demonstrate that glass formation per se is not sufficient for most species to survive desired durations of more than 20 years. Drying and cooling below T_g (calculated as the midpoint of a baseline shift in DSC experiments) enhances longevity and is necessary for efficient operation of genebanks. Further, T_g -water content relationships among species do not account for their characteristic longevity. For example, T_g curves for seeds (lettuce and soybean) and pollen with poor keeping quality are comparable with T_g curves for pea and bean seeds, which characteristically have exceptional longevity (compare Figures 11.1 and 11.4) (T_g was calculated as the midpoint of a baseline shift in DSC experiments and does not represent the temperature range at which the glass transition occurs, which could vary among species). These characterizations of glassy behavior also do not account for increased aging rates when seeds are dried to very low water contents. Clearly, additional factors besides

**FIGURE 11.4**

Glass transition temperatures as a function of water content in seeds and *Typha* pollen. Water content values are corrected for the lipid content. The gray rectangle represents the water content-temperature combinations used for conventional storage at NCGRP. The dotted curve to the left of the T_g curves is the projected optimum water content for storing soybean seeds, which was assumed as a water activity of 0.2 and determined from water sorption isotherms of soybean seeds constructed at a range of temperatures. Glass transition behavior was taken from Williams and Leopold (1989) and Williams and Leopold (1995) (corn, pea), Bruni and Leopold, (1992) (soybean), Leprince and Walters-Vertucci, (1995) (bean), Buitink et al., (1996) (pollen), and Walters, (2004) (lettuce) and represents the midpoint of the baseline shift in DSC heating thermograms. Optimum water content for soybean seeds is based on Vertucci and Roos, (1993) with subsequent unpublished data also considered.

T_g -water content relationships are needed to explain physiological observations. One such parameter may be molecular mobility within the glassy state.

Experimental measures of molecular mobility within glasses have proven technically difficult because of the long time spans required. General behavior is described by the Vogel–Tamman–Fulcher (VTF) Model, valid for temperatures near T_g , where viscosity increases in a double exponential relationship with decreasing temperature (Angell, 1991):

$$\frac{\tau}{\tau_{\infty}} = \exp\left(\frac{DT_0}{T - T_0}\right)$$

and τ and τ_{∞} represent viscosity at temperature T and infinite viscosity achieved at T_0 . The coefficient D is specific to the glass and is assumed constant with temperature. The Adam–Gibbs model describes structural relaxation of glasses with temperature and is valid below T_g (Adam and Gibbs, 1965; Scherer, 1984; Andronis and Zografi, 1998):

$$\frac{\tau}{\tau_{\infty}} = \exp\left(\frac{DT_0}{T\left(1 - \frac{T_0}{T_f}\right)}\right)$$

In the Adam–Gibbs model, the structure trapped within a glass when temperature is decreased (i.e., the configurational entropy) is defined by the temperature of the equilibrium super-cooled liquid with that amount of entropy (i.e., the fictive temperature, T_f) (see schematic diagram in Shamblin et al. (1999)). With further reductions of temperature to the Kauzmann temperature (T_K), the structure of the equilibrium super-cooled liquid becomes equivalent to the structure of the crystalline phase, and mobility associated with structural rearrangements becomes virtually nil (equivalent to the mobility of the crystalline phase). The difference between the actual temperature of the glass and T_f describes the residual mobility maintained by the glassy structure. If T_f equals the actual temperature of the glass, the Adam–Gibbs model takes the form of the VTF model where viscosity tends toward infinity with small changes in temperature. If T_f is constant, and likely near T_g , the Adam–Gibbs model takes the form of the Arrhenius equation, where structural rearrangements require relatively large changes in temperature. The terms “fragile” and “strong” were coined to describe the relative effects of temperature on molecular mobility and structure of glasses (fragile glasses being affected by small changes in temperature while strong glasses requiring larger temperature changes for comparable disruption of glassy structure) (Angell, 1991). Because the variables of the Adam–Gibbs model can be measured from comparisons of heat capacity (C_p describes the change of entropy with temperature), it provides an experimentally accessible method to approximate molecular mobility of glasses.

In an attempt to relate the effects of temperature on aging kinetics in seeds with temperature-mediated changes in molecular mobility, we estimated relaxation rates in aqueous glasses of seeds containing 0.07 g H₂O/g dry mass using the Adam–Gibbs Model and heat capacity measurements (Walters, 2004). At this water content, T_g was about 28°C according to the midpoint of a baseline shift in DSC continuous scanning experiments (Figure 11.4). The value of T_f changed with temperature until it was below T_g and then remained constant at 17°C with further reductions of temperature. Molecular mobility, calculated using this treatment, decreased by five orders of magnitude when temperature was reduced from 60 to 0°C (Figure 11.2). In a similar temperature range, pea aging rates decreased by about four orders of magnitude. The close correspondence between the effects of temperature on seed aging rate and molecular mobility appears to break down as temperatures decreased further (Figure 11.2). Arrhenius plots of molecular mobility show deviation from VTF towards Arrhenius behavior at temperatures less than 0°C (Walters, 2004). Lettuce seeds (for which there are analyzed data of aging rates under cryogenic temperatures) show a similar deviation, but the temperature coefficient for aging rate at cryogenic temperatures becomes small (Walters et al., 2004) (Figure 11.2). Interestingly, the slope of the Arrhenius plot for lettuce seed aging at cryogenic temperatures becomes similar to the slope of Arrhenius plots of mobility measured from rotational motion of a probe, 3-carboxy-proxyl, using electron spin resonance (Figure 11.2) (Buitink et al., 2000).

Assessment of molecular mobility using concepts of configurational entropy underscores the importance of considering molecular mobilities below the glass transition temperature. Clearly, there is sufficient molecular motion below T_g (i.e., the midpoint of the baseline shift and not the entire temperature range of the glass transition) to allow seeds to deteriorate at an unacceptable rate for germplasm preservation purposes. Mobility theoretically stops at the Kauzmann temperature, T_K , and we have calculated this parameter for seeds containing 0.07 g H_2O /g dw at about $-42^\circ C$ using equations derived by Shamblin et al., (1999). The significance of T_K may also be arbitrary, as we note that there is still sufficient mobility below this temperature to allow aging reactions to proceed. However, the effect of temperature on aging rates is different below T_K compared with above T_g and it is intriguing that the optimal storage temperature for seeds containing 0.07 g H_2O /g dw is between the fictive and Kauzmann temperatures (note 0.07 g/g is near the optimum water content between 0 and $-40^\circ C$ in Figure 11.4). Perhaps the intermediate moisture-temperature region between T_g and T_K represents a critical change in water behavior on surfaces.

Conclusions

Seed longevity is a function of the interaction of water content, storage temperature and unknown quality characteristics. To develop more predictive models of the rate that seeds deteriorate under extremely cold or dry conditions we have studied how water in these systems behave. We have discovered that there are limited benefits to both temperature and water content in prolonging seed lifespans. These critical conditions may reflect a change in how water and constituents of cells interact.

References

- Adam, G. and Gibbs, J.H. On the temperature dependence of cooperative properties in glass-forming liquids, *J. Chem. Phys.*, 43, 139, 1965.
- Andronis, V. and Zografi, G. The molecular mobility of supercooled amorphous indomethacin as a function of temperature and relative humidity, *Pharm. Res.*, 15, 835, 1998.
- Angell, C.A. Relaxation in liquids, polymers and plastic crystals — strong/fragile patterns and problems, *J. Non-Crystall. Solids*, 131, 13, 1991.
- Avrami, M. Granulation, phase change and microstructure, III. Kinetics of phase change, *J. Chem. Phys.*, 9, 177, 1941.
- Bruni, F. and Leopold, A.C. Cytoplasmic glass formation in maize embryos, *Seed Sci. Res.*, 2, 251, 1992.

- Buitink, J., Hemminga, M.A., and Hoekstra, F.A. Is there a role for oligosaccharides in seed longevity? An assessment of intracellular glass stability, *Plant Physiol.*, 122, 1217, 2000.
- Buitink, J., Leprince, O., Hemminga, M.A., and Hoekstra, F.A. Molecular mobility in the cytoplasm: an approach to describe and predict lifespan of dry germplasm, *PNAS, USA*, 97, 2385, 2000.
- Buitink, J., Walters, C., Hoekstra, F.A., and Crane, J. Storage behavior of *Typha latifolia* L. pollen at low water contents: interpretation on the basis of water activity and glass concepts, *Physiol. Plant.*, 103, 145, 1998.
- Buitink, J., Walters-Vetucci, C., Hoekstra, F.A., and Leprince, O. Calorimetric properties of dehydrating pollen, *Plant Physiol.*, 111, 235, 1996.
- Crowe, J.H., Crowe, L.M., Carpenter, J.F., Prestrelski, S.J., Hoekstra, F.A., de Araujo, P.S., and Panek, A.D. Anhydrobiosis: cellular adaptations to extreme dehydration, *Handbook of Physiology, Sec. 13, Comparative Physiology*, Vol. 2, W.H. Dantzler, ed., Oxford University Press, Oxford, pp. 1445–1477, 1997.
- Ellis, R.H. The longevity of seeds, *HortScience*, 26, 1119, 1991.
- Horbowicz, M. and Obendorf, R.L. Seed desiccation tolerance and storability: dependence on flatulence-producing oligosaccharides and cyclitols — review and survey, *Seed Sci. Res.*, 4, 385, 1994.
- Karel, M. Lipid oxidation, secondary reactions and water activity of foods, *Autoxidation in Food and Biological Systems*, M.G. Simic and M. Karel, eds., Plenum Press, New York, pp. 191–206, 1980.
- Labuza, T.P. The effect of water activity on reactions kinetics of food deterioration, *Food Technol.*, 34, 36, 1980.
- Leopold, A.C., Sun, W.Q., and Bernal-Lugo, I. The glassy state in seeds: analysis and function, *Seed Sci. Res.*, 4, 267, 1994.
- Leprince, O. and Walters-Vetucci, C. A calorimetric study of the glass transition behaviors in axes of *Phaseolus vulgaris* L. seeds with relevance to storage stability, *Plant Physiol.*, 109, 1471, 1995.
- Scherer, G.W. Use of the Adam–Gibbs equation in the analysis of structural relaxation, *J. Am. Cer. Soc.*, 67, 504, 1984.
- Shamblin, S.L., Tang, X., Chang, L., Hancock, B.C., and Pikal, M.J. Characterization of the time scales of molecular motion in pharmaceutically important glasses, *J. Phys. Chem. B*, 103, 4113, 1999.
- Slade, L. and Levine, H. Beyond water activity: recent advances based on an alternative approach to the assessment of food quality and safety, *Crit. Rev. Food Sci. Nutr.*, 30, 115, 1991.
- Vetucci, C.W. Calorimetric studies of the state of water in seed tissues, *Biophys. J.*, 58, 1463, 1990.
- Vetucci, C.W. and Farrant, J. Acquisition and loss of desiccation tolerance, *Seed Development and Germination*, J. Kigel and G. Galili, eds., Marcel Dekker, Inc, New York, pp. 237–272, 1995.
- Vetucci, C.W. and Roos, E.E. Theoretical basis of protocols for seed storage, *Plant Physiol.*, 94, 1019, 1990.
- Vetucci, C.W. and Roos, E.E. Theoretical basis of protocols for seed storage II. The influence of temperature on optimal moisture levels, *Seed Sci. Res.*, 3, 201, 1993.
- Walters, C. Ultra-dry seed storage, *Seed Sci. Res.*, 8, 1998a, supplement.
- Walters, C. Understanding the mechanisms and kinetics of seed aging, *Seed Sci. Res.*, 8, 223, 1998b.

- Walters, C. Temperature dependency of molecular mobility in preserved seeds, *Biophys. J.*, 86, 1253, 2004.
- Walters, C., Wheeler, L.M., and Grotenhuis, J.M. Longevity of seeds stored in a genebank: species characteristics, *Seed Sci. Res.*, 15, 1, 2005.
- Walters, C., Wheeler, L., and Stanwood, P.C. Longevity of cryogenically-stored seeds, *Cryobiology*, 48, 229, 2004.
- Whittingham, D.G., Lyon, M.F., and Glenister, P.H. Long-term storage of mouse embryos at -196°C , the effect of background radiation, *Gen. Res.*, 29, 171, 1977.
- Williams, R.J., Hirsh, A.G., Meryman, H.T., and Takahashi, T.A. The high-order kinetics of cytolysis in stressed red cells, *J. Therm. Anal.*, 40, 857, 1993.
- Williams, R.J. and Leopold, A.C. The glassy state in corn embryos, *Plant Physiol.*, 89, 977, 1989.
- Williams, R.J. and Leopold, A.C. Changes in glass transition temperatures in germinating pea seeds, *Seed Sci. Res.*, 5, 117, 1995.

12

Water and Biological Structures at High Pressure

Jorge Welti-Chanes, Fernanda San Martín-González,
José A. Guerrero-Beltrán, and Gustavo V. Barbosa-Cánovas

CONTENTS

Introduction	206
High Pressure and Chemical and Thermodynamic Principles.....	206
High Pressure Effects	207
Compression and Temperature Increase	207
Thermal and Physical Properties of Water.....	208
Equilibrium and Kinetics of Chemical Reactions.....	208
Effects of HP on Food Components and Their Reactions.....	211
Effects of HP on Water–Ice Transitions in Foods.....	212
Action of HP on Microorganisms and Enzymes.....	214
Mechanisms of Action on Microorganisms.....	214
Kinetics Effects of HP on Microorganisms	215
Inhibition of Enzymes	218
HP and Changes of Biological Structures of Some Particular Foods.....	220
Milk	220
Casein Micelles.....	221
Whey Proteins	222
Fat Globules	222
Effects on Cheese-Making Properties	223
Meat.....	224
Fish	224
Cereals.....	225
Vegetables.....	225
Gels.....	225
Other Products	226
Final Remarks.....	226
References	227

Introduction

High pressure (HP) is part of the new food preservation procedures that allow products to be obtained with high nutritional characteristics, sensorial quality, and that are microbiologically safe. HP can also deliver products with a long shelf life and characteristics similar to those of fresh products. When applying HP to preserve foods, microorganisms are inactivated without the use of heat and, therefore, it does not affect vitamin content, flavor or color of foods (Swientek, 1992; Palou et al., 2000) or the change is minimum. Consequently, the use of HP is considered a “cold” process (Crawford et al., 1996). Progress of research in the food and pharmaceutical industries has, during recent years, allowed the manufacture of products processed by HP. The potential uses of this technology for food processing were first suggested in the late 19th and early 20th centuries when Hite et al. (1899, 1914) demonstrated that the shelf life of milk and other foods could be extended by subjecting the products to high pressures. However, it was not until 1991 that the first commercial products became available in Japan, and consisted mainly of fruit jams and jellies. Currently, products such as avocado, oysters, rice, desserts, fruit juices, sauces and sliced ham can be found in countries such as United States, Spain, France, Mexico, and Japan (San Martín-González et al., 2004).

HP can be generated by direct or indirect compression or through heating of the pressure medium (Mertens, 1995; Palou et al., 2000). Generally, the level of pressures used in commercial systems is in the range 100– to 600 MPa (Palou et al., 2002). The pressure transmitting medium is water, usually mixed with mineral or vegetable oil to lubricate and with anticorrosive aims (Swientek, 1992; Mertens, 1995). Processing by HP offers the advantage that once the desired treatment pressure is reached, it is maintained with no further energy requirements (Farr, 1990).

Much of the increasing interest in exploiting the effects of high pressures is based on research carried out on the thermodynamic and chemical principles that support HP. In order to understand about actual and potential applications of HP on foods, a short review of those principles are presented in this contribution.

High Pressure and Chemical and Thermodynamic Principles

Pressure affects a reaction system in two ways: (1) reduction of the available molecular space, which has to do with conformation, and (2) increase of intrachain reactions (Hoover et al., 1989), which affect the dynamics and reactions of biomolecules. The effect of HP on microbial inactivation, chemical or enzymatic reactions, and structural and/or functional properties of foods is based on the principle of Le Chatelier–Braun and on the State Transition Theory.

High Pressure Effects

The principle of Le Chatelier–Braun states that any reaction or phase transition, molecular transformation or chemical reaction that is accompanied by a volume decrease of the medium will be favored by HP, while reactions that involve an increase in volume will be inhibited. On the other hand, the State Transition Theory points out that the rate constant of a reaction in a liquid phase is proportional to the quasi-equilibrium constant for the formation of active reactants (Mozhaev et al., 1994; Bordarías, 1995; López-Malo et al., 2000). To fully understand the dynamic behavior of biomolecules, the study of the combined effect of temperature and pressure is necessary. The Le Chatelier–Braun Principle states that changes in pressure and temperature cause volume and energy changes dependent on the magnitude of pressure and temperature levels and on the physicochemical properties of the system such as compressibility. “If χ is a quantity characteristic of equilibrium or rate process, then the influence of temperature (T) and pressure (P) can be written as:

$$(\delta \ln \chi / \delta T)_P = (A \text{ characteristic energy} / RT^2) \quad (12.1)$$

$$(\delta \ln \chi / \delta P)_T = (A \text{ characteristic volume} / RT) \quad (12.2)$$

These formulas summarize the basic thermodynamic and kinetic concepts for the interpretation of the effects of pressure and temperature in equilibriums as well as rate processes (Heremans, 2001)."

Compression and Temperature Increase

The effect of compression of biomaterials can be illustrated by first considering the effects in liquids. Water and hexane are of particular interest because they represent typical examples of polar and non-polar materials, respectively. If one performs the compression under adiabatic conditions, then the following equation gives the temperature increase for a given pressure increase:

$$\left(\frac{\delta T}{\delta P} \right)_s = \left(\frac{T}{Cp} \right) \left(\frac{\delta V}{\delta T} \right)_P = \frac{\alpha T}{\rho Cp} \quad (12.3)$$

In this equation, α is the thermal expansion, ρ the density and Cp the heat capacity of the system. The temperature increase depends on the maximum pressure reached as well on the temperature of the system before compression. For example, pressurization of water from atmospheric pressure up to 800 MPa with initial temperatures of 5 and 100°C results in final temperatures of 23 and 140°C, respectively (Heremans, 2001).

This increase of temperature has substantial implications for reaction kinetics during HP treatment cycles. Additionally, in real (non-adiabatic) situations, thermal equilibrium with the environment occurs, which produces a time and spatially varied temperature field. However, for hexane, a temperature increase of 40 times or more (in comparison with

water) is obtained (Denys et al., 2000). Denys et al. (2000) determined the expansivity of tomato paste and apple sauce to evaluate the temperature increase in those products. It is likely that the temperature increase of a product is determined by its water content. Although the temperature increases, because water compression is small, high pressure processes can still be considered “cold processes.”

Alternatively, the effect of pressure on the melting temperature (T_m) of compounds is given by the Clausius–Clapeyron equation:

$$\frac{dT_m}{dP} = \frac{T_m \Delta V}{\Delta H} \quad (12.4)$$

With the change in volume (ΔV) and enthalpy (ΔH) on melting are generally positive, one can expect an increase in melting temperature with increasing pressure. For many organic compounds, the change in melting temperature because of the change in pressure is approximately 15 K/100 MPa. One remarkable exception to this general rule is water and this behavior will be discussed in the water–ice transitions section of this contribution.

Thermal and Physical Properties of Water

Since water is the most abundant ingredient in many food products, understanding its behavior under pressure is very important. However, determining the properties of water under pressure poses some challenging requirements. This is an important topic to be studied, not only for water but for the foods to be treated at high pressures. In the case of water, currently official international calculations for all thermodynamic and transport properties within a broad range of temperatures and pressures are developed and maintained by the International Association for the Properties of Water and Steam (Wagner et al., 1995). This organization recently released a new international formulation for thermodynamic properties of water within the range of 0.1 to 240 MPa and for temperatures as low as -20°C (Wagner et al., 1995). However, additional information is required for higher pressures and other temperatures and their relation to food composition.

Equilibrium and Kinetics of Chemical Reactions

The driving force of a reaction is the change (negative) in free energy $\Delta G = G_{(\text{product})} - G_{(\text{reactants})}$, which depends on the concentration of initial matter and final products as well as temperature and pressure. When ΔG is negative, the reaction is spontaneous, but if ΔG is positive, the reaction is not spontaneous. The fundamental equation of Gibbs that correlates free energy with pressure, temperature, and chemical potential (μ) is:

$$dG = -SdT + VdP + \sum \mu_i dn_i \quad (12.5)$$

where S is entropy, V is volume, and n the number of moles of compound i .

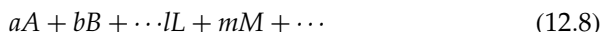
Equation 12.6 correlates the influence of pressure on G with the volume:

$$V = \left[\frac{\partial G}{\partial P} \right]_{T, n_i} \quad (12.6)$$

Pressure and temperature are used to change the equilibrium of a reaction. This change is determined by the modification of chemical potentials of the components involved. The dependence of the chemical potential μ_i of a dissolved compound i as a function of pressure is:

$$\left(\frac{\partial \mu_i}{\partial P} \right)_T = \bar{V}_i = \text{partial molar volume of compound } i \quad (12.7)$$

For a general chemical reaction in equilibrium:



it is applied that:

$$l\mu_L + m\mu_M + \cdots - a\mu_A - b\mu_B - \cdots = 0 \quad (12.9)$$

The equilibrium constant K_x of the reaction as a function of pressure is obtained by:

$$-RT \left[\frac{d \ln K_x}{dP} \right] = l\bar{V}_L + m\bar{V}_M + \cdots - (a\bar{V}_A + b\bar{V}_B + \cdots) = \Delta \bar{V} \quad (12.10)$$

where \bar{V} is the partial molar volume.

In Equation 12.10 K_x is expressed in terms of molar fractions as:

$$K_x = \frac{x_L^l x_M^m \cdots}{x_A^a x_B^b \cdots} \quad (12.11)$$

In order to describe the equilibrium state of a chemical reaction under pressure, the reaction volume ($\Delta \bar{V}$) is decisive (Tauscher, 1995).

The influence of pressure on the reaction rate should be described by the Transition State Theory: the rate constant k_x of a reaction in a liquid phase is proportional to the quasi-equilibrium constant k_x^\ddagger regarding the formation of an active complex of reactants (X^\ddagger).



It has been proven that an increase in pressure changes the rate of a chemical reaction in solution, but this effect is low when compared with that of temperature. Thus, an increase of 100 MPa is required to achieve the same effects as a 10°C temperature increase (Tauscher, 1995). The dependence of k_x as a function of the pressure can be expressed in terms of the so-called activation volume ΔV^\ddagger :

$$-RT \left[\frac{d \ln k_x}{dP} \right]_T = \Delta V^\ddagger \quad (12.13)$$

In chemical reactions, the partial molar volume of dissolved components is influenced by three factors: (1) an intrinsic part of the component that is determined by a change in the Van der Waals radius, (2) by interactions between solute and solvent, oriented to electrostriction, and (3) by interaction of the component with all other dissolved components, including itself. The third factor is negligible in diluted solutions (as most fresh and high moisture foods can be considered). The intrinsic factor is supposed to be independent of solvent and concentration. In a preliminary way, total reaction volume is the addition of two parts of volume, the intrinsic part mentioned before and that of solvation, as Equation 12.14 shows:

$$\Delta \bar{V} = \Delta \bar{V}_{\text{intr}} + \Delta \bar{V}_{\text{solv}} \quad (12.14)$$

$\Delta \bar{V}_{\text{intr}}$ could be a consequence of the nucleus of the atom of reacting component, and of changes in bonding length and angle during the formation of the products (Tauscher, 1995). $\Delta \bar{V}_{\text{solv}}$ includes any change in volume associated with changes in polarity, electrostriction, and interaction of dipoles with the solvent during the reaction (Tauscher, 1995).

The activation volume ΔV^\ddagger can be described in a similar way to the reaction volume, and in this way Equation 12.15 is obtained:

$$\Delta V^\ddagger = \Delta V_{\text{intr}}^\ddagger + \Delta V_{\text{solv}}^\ddagger \quad (12.15)$$

In a reaction without important solvation contribution ΔV^\ddagger is determined by $\Delta V_{\text{intr}}^\ddagger$. For example, it is supposed that the formation of a covalent bond between two atoms is associated with a negative intrinsic contribution $\Delta V_{\text{intr}}^\ddagger$ whereas the breakdown of a bond is characterized by a positive change in volume $\Delta V_{\text{intr}}^\ddagger$. The bond formation process is accelerated by pressure while breakdown is retarded. However, when changes occur in the transition state or in the product formation, the situation is more complex because of interactions with the cortex of the solute. In reactions with strong changes in polarity $\Delta V_{\text{solv}}^\ddagger$ should be greater than $\Delta V_{\text{intr}}^\ddagger$. It has been found that polar reactions of this type depend to a great extent on the polarity of the solvent. In general, the formation of bonds, separation of charges, concentration of equal charges, and steric crowding result in volume contraction. On the other hand, breakdown of bonds, neutralization and re-localization of charges generate volume expansion (Tauscher, 1995).

Biological processes are influenced by the application of pressure, because most biochemical reactions result in a change in volume. Reactions that are strongly affected by pressure generally include reactants and products that differ in the number of groups that can be ionized. However, when the charge number does not change, the reaction is basically independent from pressure. In aqueous systems, a decrease in volume is generally a factor when dissociation reactions yield an increase in the number of groups that can be ionized. This is generally caused by electrostriction of water near the ions. Pressure tends to dissociate electrostatic interactions in such a way that more ions are exposed to water (Hoover et al., 1989).

Effects of HP on Food Components and Their Reactions

Water in foods is found as aqueous solutions or dispersions and as suspensions of proteins, carbohydrates, and lipids among others. Pressure affects the properties of water, surface tension, density, viscosity, dipolar moment, dielectric constant, and thermal properties. Such changes and the changes in compressibility of water influence the effects of pressure on microorganisms, enzymes, and reactions present in the aqueous medium of the food. High moisture foods present a similar compressibility to water, and as a result, when treated with HP, an increase in the density of water or food is obtained (Cheftel, 1992). Low molecular weight biopolymers with covalent structure such as peptides, lipids, and sugars are not affected by pressures greater or equal to 1000–2000 MPa because of the negligible compressibility of covalent bonds. Also, the primary structure of macromolecules such as proteins, nucleic acids, and polysaccharides are not affected at the same pressures (Mozhaev et al., 1994). Bonds that help to maintain the native state of biopolymers are affected by pressure, thus affecting the spatial conformation of macromolecules.

Formation of hydrogen bonds is accompanied by a volume decrease. This type of bonding will be favored by the application of pressure. It is known that HP can promote protein denaturation; however, at moderate pressures (<101 MPa) the denaturation rate of proteins is reduced because the generation of hydrogen bonds that keep the helical structure of peptides is favored. Hydrophobic interactions are also influenced by pressure. At pressures lower than 100 MPa, the hydrophobic interactions give an increase in volume and therefore are destroyed. At pressures higher than 100 MPa, these types of interactions are associated with a volume decrease and tend to stabilize the structure. In this way, the magnitude of hydrophobicity or hydrophilicity of a protein will determine the extent of denaturation at a given pressure (Hoover et al., 1989). The structure of proteins changes under the influence of pressure. Pressure favors the dissociation of oligomeric proteins or complex macromolecular systems, as well as not unfolded protein chains. A protein in its native state is stabilized by: (a) covalent bonds including disulfide bonds, (b) electrostatic interactions (ions pairs, polar groups), (c) hydrogen bonds, and (d) hydrophilic interactions. Pressure affects the quaternary structure (through hydrophobic interactions), the tertiary structure (through reversible unfolding), and the secondary structure (irreversible unfolding) of proteins. The denaturation of simple protein chains should be considered as a two component system (native \leftrightarrow denatured). Denaturation temperature initially increases with increasing pressure, at a maximum transition temperature the sign of $\Delta\bar{V}$ changes and from this point on proteins denature at low temperatures. Figure 12.1 shows the relationship between pressure and temperature on protein denaturation. The sign of ΔS changes at the maximum transition pressure, and from this point on proteins denature at lower pressures at a given temperature. Thus, it is possible to denature proteins by the action of

pressure at low temperatures, which is very interesting in the food area. Generally, most proteins denature when exposed to pressures above 400 MPa.

When evaluating the effect of HP on enzymatic reactions, two stages should be considered: (1) enzyme linking to the substrate, yielding a substrate-enzyme complex, and (2) the catalytic stage, in which the substrate-enzyme complex is activated. Both stages should be divided into sub-processes, in which hydrophobic or polar interactions, water molecules rearrangements and changes in conformations are involved. The total volume change is the addition of all the individual volume changes and the change can be positive (activation) or negative (inhibition) because of the application of HP depending on the enzyme and the type and quantity of substrate (Tauscher, 1995).

Volume changes and their relation with chemical reactions are accompanied by the formation of interactions in biosystems. Some of the interactions important for foods have been described in detail in Tauscher (Tauscher, 1995) and Welte-Chanes et al. (San Martín-González et al., 2004).

Effects of HP on Water–Ice Transitions in Foods

The kinetics of any process that occurs within HP treatment and phase changes generally takes place during the compression (Perrier–Cornet et al., 1995). For example, HP reduces the freeze and fusion points of water to a minimum of -22°C at 207.5 MPa because pressure opposes the increase in volume that arises when type I ice crystals are formed. The homogeneous nucleation temperature of ice reduces from -40°C to a minimum of -92°C at 209 MPa. Other polymorphs of ice can be formed at HP. Type I ice is unique in having a density lower than that of water, yielding a 9% increase of volume at 0°C and 13% at 20°C . The increase of volume can cause important damage to tissues or texture of foods. The formation of other types of ice (polymorphs) generally involves a similar volume or a slight decrease

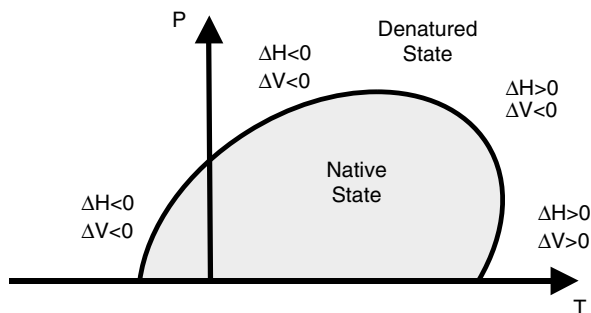


FIGURE 12.1

Relationship between pressure–temperature and protein denaturation (adapted from Heremans (2001)).

(density increase) with respect to the liquid state, and as a result, a reduction of tissue damage compared with that caused by type I ice may occur. Type II ice can be formed at room temperature at pressures about 900 MPa. This can generate an economic alternative to freeze foods without cooling them. It should be taken into account that solutes in foods (particularly those of low molecular weight) will generate a displacement in the phases diagram, particularly in the depression of the fusion point. In the case of surimi it has been found that the curve of the depressed fusion point is almost parallel to that of water in function of pressure (Kalicevsky et al., 1995).

The potential applications of pressure with respect to the phases diagram of water are: (1) the increase of freezing rates obtained employing pressure-aided freezing, the depression of the fusion point induced by pressure allows the sample to be super cooled at -20°C , yielding rapid and uniform nucleation and the growth of ice crystals once the pressure is released, (2) the increase of thawing rates, and (3) storage of unfrozen foods at sub-zero temperatures. Nucleation rate increases almost ten times per each Kelvin degree of super-cooling. The use of HP eases super-cooling and promotes uniform and rapid nucleation and ice growth once pressure is released, producing small ice crystals. This process usually involves cooling of the sample (unfrozen) under pressure (generally at $P > 200$ MPa) until -21°C or above (without freezing) before pressure is released. Higher pressures and lower temperatures can lead to the formation of other types of ice (Kalicevsky et al., 1995). Possibilities of new applications of HP in freezing, thawing and preservation processes of foods are being studied. Knorr et al. (1998) for the first time introduced the terminology used to distinguish between different processes: pressure-assisted means that the transition occurs under constant pressure, pressure-shift refers to a phase transition caused by a pressure change, and pressure-induced means a phase transition initiated with pressure change but continued at constant pressure.

As commented before, if HP processes are used for food preservation, they should be applied together with other treatment to increase effectiveness and reduce the deteriorating effects caused by excessive pressure (Hoover et al., 1989). The employment of moderate pressure combined with temperatures under zero allow the freezing of foods without forming ice, avoiding damage caused by the formation of crystals and preventing microbial deterioration (Farr, 1990). HP has been used to store beef and pork meat under temperatures from 5 to -20°C and 50 to 200 MPa, to change pressure during tofu and soy noodles freezing, and thawing of tuna fish at 150 MPa (Tauscher, 1995). The pressure-shift freezing process results in high quality products (tofu, potatoes, pork) because of the homogeneous matrix of small crystals formed—high degree of super cooling and rapid ice nucleation. In the case of thawing, the increased thawing rate associated with pressure-induced processes is mainly attributed to the larger temperature gradient between the melting product and the ambient pressure transmitting medium, resulting after compression. Faster thawing is known to reduce

the loss of liquid and can improve color and flavor preservation in food (Heremans, 2001).

Action of HP on Microorganisms and Enzymes

Mechanisms of Action on Microorganisms

The effects of pressure on microorganisms in foods are determined by the effect of pressure on water, the temperature during pressure treatment, the constituents of foods and the properties and physiologic state of microorganisms. In real situations in foods, there are two effects that always determine security and microbiological stability: the effect on food during treatment and the effect after treatment during recovery of microorganisms. It should be taken into account that the results using buffers or laboratory media cannot be directly extrapolated to real foods situations. For example, it is known that milk and cream protect the microorganisms against the action of pressure compared with the destructive action of HP on the same microorganisms in model systems (Smelt, 1998). Most of the studies carried out in the 1960s and 1970s on the effects of HP on intact cells focused on microorganisms at pressures naturally present in the biosphere, such as sea bottom pressures (Hoover et al., 1989), where there are species that can stand pressures of 20 to 30 MPa. Those capable of growing above 40 MPa are called barophiles, those that can grow between 0.1 and 50 MPa are called eurybaric, and those that can survive but cannot grow at pressures of 50 to 202 MPa are called baroduric (Barbosa-Cánovas et al., 1998).

Microbial inactivation can occur because of several factors. One of them is the permeability change of the cell membrane as well as denaturation of proteins caused by bond breakdown besides the inactivation of key enzymes. Pressures in the 101 to 303 MPa range give, as a result, a reversible denaturation, and pressures above 303 MPa cause irreversible denaturation (Hoover et al., 1989; Swientek, 1992). The use of HP affects the cell morphology in different ways: the intracellular gas vacuoles can collapse; it has been proven that there is an increase in the cell of *Escherichia coli* (from 1–2 to 10–100 μm); in mobile microorganisms (protozoa) movement can be eliminated although the phenomenon is reversible; in *Pseudomonas* the individual cells are enlarged, there is separation of the cell wall from the membrane, thinning of the cell walls, and reduction of the number of ribosomes (Hoover et al., 1989). In other microorganisms, a modification of the cell nucleus and of some organelles occurs, there is a release of intracellular material to extracellular spaces, inhibition of the ATPase, and crystallization of phospholipids in the membrane, among others (Cheftel, 1992). A marked change in cells subjected to HP is the formation of filaments, as observed in *E. coli*, *Vibrio* spp., *Bacillus mycoides*, and *Serratia marcinorubra* (Barbosa-Cánovas et al., 1998). Pérez-Delgado (Pérez-Delgado, 1996)

observed during a microscopy study that the use of HP (517 and 689 MPa) on yeast causes wrinkles on the cell wall, plasmolysis, disintegration or breakage of wall (irreversible process) and cell death, whereas lower pressures (172 and 345 MPa) cause only slight physical damage on the wall. When cells of *Saccharomyces cerevisiae* are treated with pressures from 400 to 500 MPa, the structure of the cell's nucleus and cytoplasmic organelles present deformation; also, the application of pressures greater than 400 MPa at room temperature causes the release of intracellular material (Alemán et al., 1994). In treatments at 250 MPa for 15 min applied to *S. cerevisiae* and *S. fibuligera*, a reduction of cellular volume (25%) was not completely recovered after the process was released. Ten percent of the permanent volume reduction was attributed to the mass transfer between the cell and the medium because of damage caused to the permeability of the membrane (Alemán et al., 1996). Carballa et al. (1997) observed a change in cell diameter of microorganisms' colonies present in beef patties; around 75% of non-pressurized cell populations presented a diameter of 0.5 mm, and after applying 300 MPa for 20 min, 75% of the cells presented a diameter change (being lower than 0.5 mm). Also, application of pressure modifies the conditions of the medium (pH, a_w , ionization, compressibility) creating an osmotic gradient between the cell and the medium. Perrier-Cornet (Perrier-Cornet et al., 1995) observed that cell inactivation followed a three-phase kinetics. During the first stage, when the desired pressure was achieved, there was a compression of the cell membrane; while the pressure was maintained, a transfer of intercellular material with the medium occurred; finally, during the third stage, a new compression of the membrane happened without recovering the initial volume. It has been observed that the lose of nutrients in water, peptone water or phosphate buffers prevents the recovery of cells damaged by the effect of pressure (Palou et al., 2000).

However, the nucleic acids are more resistant to HP than proteins. Because the structure of the DNA helix is basically the result of the formation of hydrogen bonds, the negative change in volume inherent to the formation of hydrogen bonds should be favored by a pressure increase. According to Hoover et al. (Hoover et al., 1989), studies made by Landau in 1967 demonstrated that the induction, transcription, and translation of *E. coli* were inhibited at 27, 68, and more than 68 MPa, respectively, but when pressure was released all processes returned to normal. For protein synthesis, the ribosome-polysome system and the bond from t-RNA to the polysomes have been suggested as the main sites sensible to pressure (Hoover et al., 1989).

Kinetics Effects of HP on Microorganisms

Inactivation, regarding thermal treatment, is based on the assumption that death of microorganisms versus time is linear in a semi logarithmic graph. Thus, inactivation by HP usually uses the kinetic concepts of thermal treatment D (decimal reduction time: time in minutes required to inactivate

90% of microorganisms or enzymes at constant pressure) and z (change in pressure required to obtain a 10-fold change in decimal reduction time, MPa), or k (value of first order inactivation rate, $k = 2.303/D$), as well as the activation volume (ΔV^\ddagger) that, according to Equation 12.10, relates the value of k (or D) with pressure. It has been demonstrated that this description has some deviations of linearity in the case of thermal treatment, and they seem to be more common in the case of HP treatment. Inactivation with pressure is frequently characterized by tailing because microbial inactivation does not follow a first order kinetics (Palou et al., 1998). Deviations from linearity can be explained as a two-step reaction that passes through an intermediate step. An adequate description of this behavior can be made by applying distribution models as those employed in toxicology.

While thermal treatment calculations are complicated because of the existence of temperature profiles within the container, in the case of HP, calculations are easier because of the isostatic principle. In the application of HP, temperature change can play an important role because of the adiabatic heating. Thus, tri-dimensional time–temperature–pressure models should be employed instead of the classic bi-dimensional time–temperature models (Smelt, 1998).

The kinetics of microbial inactivation because of HP is variable; some authors affirm that the death of microorganisms follow a first order kinetics while others state that two processes occur during treatment; inactivating in the first part some of the microbial population, leaving the more resistant cells. Also, it was observed that not all the authors take into account the CUT (come up time); this is the time needed to reach the desired pressure when some inactivation occurs, making it difficult to compare results. Some microorganisms that follow a first order kinetics regarding inactivation by HP are *Citrobacter freundii*, *E. coli*, *Pseudomonas fluorescens*, *P. aeruginosa*, *Listeria innocua*, *Staphylococcus aureus*, *Bacillus coagulans*, and *Saccharomyces bailii*. On the other hand, the microorganisms that present tailings with respect to inactivation since part of the microbial population is inactivated first in a rapid form are *E. coli*, *Salmonella* sp., *Vibrio parahaemolyticus*, *L. monocytogenes*, *S. cerevisiae*, *Rhodotorula rubra* and some molds and yeast (Cheftel, 1995).

Palou et al. (2000) found in a study made on *S. cerevisiae* and *Zygosaccharomyces bailii* that the logarithm of the survival fraction decreased linearly with respect to time; this can suggest that it follows a first order kinetics.

The inactivation kinetics followed by *L. innocua* in ewe's milk when applying pressure was first order, yielding D values of 3.12 min at 2°C and 400 MPa and 4 min at 25°C at the same pressure (Gervilla et al., 1997). *E. coli* and *B. stearothermophilus* followed an n order inactivation model (Stóforos and Taoukis, 2001).

According to the results of Hashizume et al. (1995), *S. cerevisiae* presents a first order kinetics because the number of survivors decreases linearly when plotted against pressurization time, independently of temperature. Similar results are reported for *Lactobacillus casei* and *E. coli*.

In the case of onion treated at 300 MPa and 40°C, the microbial load was reduced in five cycles with a 30 min treatment; however, the inactivation kinetics of the different microorganisms found in the tissues of this vegetable did not follow a linear tendency (Butz et al., 1994).

Inactivation of *V. parahaemolyticus* T-3765-1 in oyster juice was achieved when applying 170 MPa of pressure for 10 min, not finding viable colonies after treatment; juice did not offer protection to the cells as did the buffer used under the same conditions (Styles et al., 1991).

Two to three decimal reductions of molds and yeast in pineapple pieces were obtained with the application of 340 MPa of pressure for 15 min independently of temperature, which in this case was 4, 21, and 38°C (Alemán et al., 1994). Inactivation rates (*k*) were calculated for *Z. bailii* with different pressure and *a_w* levels. This allowed further observation of the effect of the medium’s composition. For *a_w* = 0.98 and 345 MPa the value of *k* was 2.8327 min⁻¹ while for *a_w* = 0.95 and 414 MPa the constant was 0.9019 min⁻¹ (Palou et al., 1997). For the case of *L. innocua* present in milk, the inactivation rates were obtained for different pressures, from 345 MPa (*k* = 0.44 min⁻¹) up to 448 MPa (*k* = 1.83 min⁻¹) (Correa-Balderas, 2001).

Regarding the activation volumes, a negative value means a reaction favored by pressure increase, such as microorganism inactivation, although it is difficult to give a physical meaning to activation volume. Table 12.1 shows examples of microorganisms and pressure ranges for which activation volumes have been determined.

TABLE 12.1
Activation Volume (Δ*V*[‡]) Reported for Various Microorganisms

Microorganism	Suspending Medium	Δ <i>V</i> [‡] (cm ³ /mole)	Pressure Range (MPa)	Temperature (°C)	Reference
<i>Z. bailii</i>	Sabourad-dextrose 2% broth <i>a_w</i> 0.98 <i>a_w</i> 0.95	- 65.2	345-414	25	Palou et al. (1997)
		- 25.3	345-414	25	Butz et al. (1994)
<i>L. innocua</i>	Milk	- 35.4	345-448	25	Correa-Balderas (2001)
<i>L. monocytogenes</i>	Milk	- 21.1	150-350	25	Mussa et al. (1999a,b)
	Pork meat	- 34.3	200-400	25	Mussa et al. (1999a,b)
<i>E. coli</i>	Phosphate buffer	- 50.0	200-300	30	Hinrichs et al. (1996)

In studies made on *Z. bailii*, Palou et al. (1997) obtained a value of $z = 85.5$ MPa for $a_w = 0.98$ and $z = 222.7$ MPa for $a_w = 0.95$. The former value indicates a greater dependency on pressure. Correa–Balderas (2001) obtained for *L. innocua* $z = 161$ MPa in a high a_w medium.

An alternative way to model microbial inactivation by means of HP not using the first order kinetics model is the model of Fermi. This model demonstrates that population decreases because of exposure to lethal agents such as heat, electric pulses, and radiation or ozone doses. The equation of Fermi relates the fraction of survivors $S(P)$, the pressure applied P (MPa), the critical pressure P_c at which the survivors fraction is 0.5, and the constant k that indicates the rate at which inactivation is occurring (Palou et al., 1998).

Palou et al. (1998) used the equation of Fermi to demonstrate that the critical pressure for *Z. bailii* is 297.8 MPa for cells in stationary phase and 145 MPa for the exponential phase at $a_w = 0.98$. However, this model is only used to describe and compare the inactivation parameters between microorganisms that have been subjected to the same treatment. Other models that can be applied are those commented by Alzamora et al. (2005).

Inhibition of Enzymes

The use of HP in foods can cause activation, inhibition or improvement of enzymatic activity (Hoover, 1993). During food processing, many enzymes play an important role because they can produce reactions that alter or modify the quality of the product, as in the case of fruits. A commonly used method to inactivate enzymes is food blanching; however, the use of high temperatures causes thermal damage to tissues and loss of nutrients. For these reasons, the use of HP includes also enzyme inactivation, which can be obtained by two main methods: (1) alteration of intramolecular structures, and (2) conformational changes of the active sites and/or enzyme–substrate interaction (Hoover et al., 1989; Palou et al., 2002). There are reports on trypsin and carboxypeptidase Y, whose activity decreased when HP were applied, while reactions that use thermolysin and cellulase as catalysts are favored. Regarding foods, the activity of protease in meat, pectinesterase in juice, and carboxypeptidase and phosphatases in leaver, among others have been studied. A favorable change in the quality of meat was observed (Hoover, 1993). In this case, similarly to microorganisms, pH, temperature, the concentration of substrate, and the subunits of the enzyme structure are variables that can affect the effectiveness of treatment. Different studies have been performed on catalase, phosphatase, lipase, pectinesterase, lipoxigenase, polyphenoloxidase, lactoperoxidase, and peroxidase. The last enzyme is the more stable in front of HP treatments, so it is used as a reference in this type of process (Palou et al., 2002). Another factor that has influence is a_w . HP treatments applied on pork fat with a_w between 0.40 and 0.55 exert a catalyzing effect on lipid oxidation (Cheah and Ledward, 1995).

Palou et al. (2002) reported studies on enzymatic inactivation in some foods. For example, peroxidase was completely inactivated in carrot extract

at 900 MPa for 1 min and important reductions regarding polyphenoloxidase were achieved in apple extract at different pHs.

López-Malo et al. (1998) studied the effect of HP on polyphenoloxidase in avocado purée. An important reduction of enzymatic activity as treatment time increased (up to 30 min) when applying 689 MPa at pH 4.1 was observed. However, at lower pressures (517 and 345 MPa) treatment time was not significant, while the initial pH of samples (3.9, 4.1, and 4.3) was significant with respect to enzymatic activity. Regarding the color of the puree, there were no significant changes between the color of fresh avocado and of the puree subjected to HP.

It can be observed, in the study performed by Hernández-Salgado (1999) on guacamole that after 20 min at 689 MPa the residual activity of polyphenoloxidase was 22%, although treatments with 5 or 10 min pulses reduced activity to 15%. On the other hand, to achieve a total inactivation of lipoxygenase, continuous treatments of 15 or 20 min, or treatments of 2, 3 or 4 cycles of 5 or 10 min each were required. Onion slices treated with HP presented browning with any treatment above 100 MPa. The color change rate increased as pressure increased because of the presence of polyphenoloxidase. Damage produced in cells and vacuoles in onion tissue were also observed. Some studies indicate that when applying pressures above 500 MPa, the activity of polyphenoloxidase in onion reaches a maximum of 142% (Butz et al., 1994).

In strawberry puree, pressurization above 250 MPa generated a polyphenoloxidase activity loss of 60%, while peroxidase activity decreased in 25% with pressures above 230 MPa. A combination of temperature and pressure reduced the activity of pectin methyl esterase in orange juice by up to 50% (Cano et al., 1997). As shown by Basak and Ramaswamy (1996), the inactivation of pectin methyl esterase in orange juice depends on pressure level, time of treatment, pH, and soluble solids content. In Satsuma mandarin juice, 300–400 MPa for 10 min was required to partially inactivate the pectin methyl esterase, which was reactivated neither after treatment nor during storage. This demonstrated that the greater the concentration of soluble solids in the medium the lower the inactivation of the enzyme (Ogawa et al., 1990).

Pectin methyl esterase in juices requires processing times of 10 min combined with pressures of 600 and 1000 MPa and temperatures of 57 and 20°C, respectively. These combinations prevent microbial deterioration, but must be combined with a mild blanching, refrigerated storage and addition of inhibitory enzymes to achieve a stable product with respect to pectin methyl esterase (Cheftel, 1992). Guava puree samples were treated with pressures of 400 and 600 MPa looking for pectinesterase and polyphenoloxidase inactivation. The residual activity of the former was greater than 76%, while of the latter was above 63% at the lower pressure.

The actomyosin or myosin ATPase activity in fish was reduced after subjecting the myofibrils to treatments above 300 MPa for 20 to 30 min,

besides inactivating the lipases present in muscle (Cheftel, 1992). The proteolytic activity in fish was reduced as the pressure was increased (Ashie et al., 1996). It has been demonstrated that fish enzymes are more susceptible to pressure than beef enzymes because of the different adaptation of organisms to different temperatures (Ashie and Simpson, 1996). In the case of meat, when HP treatments were applied in combination with heat, the activity of cathepsin B1 presented a baroprotective effect regarding thermal damage, while temperature on its own is a great inhibitor of activity (Kurth, 1986).

In studies made with casein, it was found that turbidity of casein solutions treated at low pressures of 148 MPa decreased while it increased when applying pressures above 297 MPa, but the reversible change observed suggests that the association state of casein depending on pressure cannot be attributed to an irreversible denaturation. This fact is important because it favors the formation of curd and cheeses (Ohmiya et al., 1989).

Oligomeric proteins subjected to HP tend to dissociate in subunits that are vulnerable to hydrolysis (Hayashi et al., 1987). However, once denatured, some oligomeric enzymes can reconstitute by means of a unimolecular step (fold) and a biomolecular step (aggregation). This is the case of the lactate dehydrogenase present in *B. stearothermophilus* treated with pressures of 280 MPa (Müller et al., 1984).

HP and Changes of Biological Structures of Some Particular Foods

Within the industrial applications of HP, besides the antimicrobial actions they present, they have been used in some countries for soy protein hydrolysis, for freezing, to soften meat, for discoloration of hemoglobin, as by-products in the meat industry, to deodorize proteins, and to make soluble or modify fish proteins (Cheftel, 1995; Palou et al., 2002; Ting and Marshall, 2002a,b). Some examples of the interaction of HP with biological structures of foods are presented in the next section with a major description on milk and its products.

Milk

It has been observed that the use of HP on milk changes the conformational structure of proteins and alters the functional properties of the system; for this reason, foaming, emulsifying, gelation and binding water capacities of proteins are affected. Therefore, this phenomenon can have a wide application field in the milk industry (Johnston et al., 1992). For this reason, HP have been used to prevent acidification of yogurts after packing without reducing the number of lactoacid bacteria or modifying texture, having the objective of increasing the shelf life of the product (Cheftel, 1992;

Bordarías, 1995). Crystallization of milk fat, coagulation and physicochemical changes of skimmed milk were produced when treated with pressures above 600 MPa. Also produced were acid gels of skimmed milk, stabilization of immunoglobulin (in bovine colostrum), inactivation of lactobacillus, *E. coli* and *Listeria*, and softening and acceleration of cheese maturity (Tauscher, 1995). HP applied as pulses have modified the microstructure of cheeses (Alemán et al., 1996). Decomposition of milk was inhibited during 12 days when treating raw milk at 700 atm. In addition, elaboration of curd was accelerated when milk was HP treated (Barbosa-Cánovas et al., 1998). In milk concentrates used for baby foods it is desirable to maintain α -lactalbumin and remove β -lactoglobulin, because it is the main cause of milk allergenicity. Studies have been carried out using thermolysin at HP (around 202 MPa) to hydrolyze β -lactoglobulin in concentrated whey, resulting in the removal of this component (Hayashi et al., 1987; Farr, 1990). Microbiological safety problems in Mexican style fresh cheese were solved by elaborating it with milk treated with HP. A greater yielding was also observed than when it was elaborated with pasteurized milk (Correa-Balderas, 2001).

Casein Micelles

HP processing of milk alters the size of casein micelles depending on the applied pressure. Gaucheron et al. (1997) observed that under HP, the average size of casein micelles, obtained from reconstituted low-heat skim milk, decreased depending on the temperature used. Mean particle sizes were determined by laser granulometry and by transmission electron microscopy (TEM) and noted that laser granulometry yielded greater mean diameters than TEM and attributed this to sample dehydration. At 250 MPa, the observed sizes were dependent on treatment temperature (160 and 185 nm at 4 and 20°C, respectively), whereas higher pressures (400 and 600 MPa) resulted in minimum sizes (≈ 100 nm) and size was independent of treatment temperature. Similar observations were made by Needs (Needs et al., 2000) with HP of skimmed milk. Mean particle diameters were determined by photon correlation spectroscopy (PCS) and by TEM. PCS yielded mean particle diameters of 180, 196, 110, and 106 nm for 0, 200, 400, and 600 MPa, respectively. They also demonstrated that gels obtained from HP treated milk consisted of dense networks of fine casein strands, whereas untreated milk samples were coarser and with large interstitial spaces. Using skimmed goat's milk, Law et al. (1998) showed that casein micelle size decreased with increasing pressure, except for a treatment temperature of 45°C and pressures between 300 and 350 MPa. This resulted in larger casein aggregates than micelles in untreated milk. Higher pressures (400 to 500 MPa) resulted in smaller sizes and were not affected by temperature. Accepted micellar models indicated that submicelles are formed by hydrophobic and electrostatic interactions. Partial dissolution of colloidal calcium phosphate (CCP) as well as structural modifications of hydrophobic

segments may explain changes in casein micelles subjected to HP treatments (Gaucheron et al., 1997; Needs et al., 2000; Huppertz et al., 2002).

Whey Proteins

Whey proteins represent about 20% of the proteins of bovine milk and are susceptible to denaturation by different agents because of their typical globular nature, with high levels of secondary and tertiary structures. Denaturation can be determined by measuring the loss of solubility in saturated NaCl at pH 4.6 and expressing the extent of denaturation relative to control samples, by differential scanning calorimetry (DSC) (Fox and McSweeney, 1998; Huppertz et al., 2002) or by proteolytic peptide profiling (Knudsen et al., 2002). β -Lactoglobulins are the most abundant whey proteins (45%) followed by α -lactalbumin (20%), proteose peptones (20%), immunoglobulins (10%) and serum albumin (5%) (Swaigood, 1996). López-Fandiño et al. (1996) observed that β -lactoglobulin was denatured by pressures over 100 MPa but α -lactalbumin and bovine serum albumin were not denatured by pressures lower than 400 MPa for 60 min at room temperature. In a later study, Fandiño and Olano (1998) reported that α -lactalbumin underwent considerable denaturation at 300 MPa when the treatment temperature was 50 to 60°C, and that at 400 MPa and 60°C, 60% denaturation took place. They also reported that up to 400 MPa, α -actalbumin undergoes reversible denaturation, whereas β -lactoglobulin experiences irreversible denaturation at pressures higher than 150 MPa. Denaturation differences among whey proteins were attributed to differences in secondary structure, number of disulfide bonds and Ca^{2+} binding sites.

Fat Globules

There are few studies on the effects of HP treatment over milk fat globules. Gervilla et al. (2001) studied the effects of HP treatment at 100 to 500 MPa for 10 and 30 min at 4, 25 and 50°C on ewe's milk. They observed that pressurization at 25 and 50°C caused a slight increase in the number of milk fat globules with a size between 1 and 2 μm and a decrease in those with a size between 2 and 10 μm , whereas at 4°C an opposite trend was observed. That effect was more noticeable at 200 and 300 MPa and suggested that at 400 and 500 MPa there could be a hardening effect on the milk fat globule membrane that did not allow coalescence or fission of the globules. In another work, Huppertz et al. (2003) reported that no significant changes on milk fat globule size were observed for treatments at 200, 400 or 600 MPa for 0 to 60 min. They also observed the formation of milk fat globules clusters in untreated milk and in milk treated at 200 MPa after storage for 4 h at 5°C; the aggregates were larger in HP treated milk. However, when the pressure treatment was 600 MPa, only a slight clustering was observed even after 24 h storage at 5°C.

Effects on Cheese-Making Properties

The changes caused by HP in individual milk components will affect their technological properties. Treatment by HP prior to cheese-making has been shown to alter enzymatic coagulation of milk as compared with raw or pasteurized milk (Desobry–Bañon et al., 1994; López-Fandiño et al., 1996; Drake et al., 1997). Rennet coagulation time has been shown to decrease by pressure treatments at 200 MPa for 30 min. However, as pressure increases rennet coagulation time becomes similar to that of untreated milk. Coagulation time was found to be dependent on the treatment temperature. At 60 and 50°C, pressures higher than 200 and 300 MPa, respectively, hindered rennet coagulation (López-Fandiño et al., 1996; López-Fandiño and Olano, 1998).

López-Fandiño et al. (1996) studied the effects of HP on primary and secondary phases of enzymatic coagulation of milk. They observed that release of casein-macropeptide was larger in 200 MPa treated or untreated milk than when milk was treated at 400 MPa or at 300 MPa and 40°C. They suggested that the decrease in casein-macropeptide release could be caused by interactions between denatured β -lactoglobulin and κ -casein that would have rendered the glycosylated κ -casein less susceptible to rennet action. In a later study, Needs et al. (2000) reported that release of glycosylated casein-macropeptide was not affected by pressure but that rates of aggregation at 200 MPa were higher than for untreated milk. However, these rates decreased with increasing pressure. They also demonstrated that free -SH groups were involved in the induced effects on rennet coagulation time as previously suggested by López-Fandiño.

Perhaps one of the applications of most interest in HP for processing milk for cheese manufacture is the capacity of increasing cheese yield. López-Fandiño et al. (1997) estimated unadjusted wet yields by centrifugation of the curd at 15,000 g for 15 min. Their results indicated that treatments at 300 and 400 MPa for 30 min caused estimated mean curd weight increases of 14 and 20%, respectively. At 200 MPa the yield increase was not significant. Yield increase was the result of whey protein retention within the casein matrix but mainly came from higher moisture retention. Holding time influenced yield at 400 MPa, with the wet yield increasing with increasing holding time during the first 20 min of treatment. Drake et al. (1997) studied the effects of HP of milk in the manufacture of Cheddar cheese. They applied a cyclic pressure treatment consisting of three 1 min cycles at 586 MPa. Wet yields were 11.3 and 10.5% for pressurized and pasteurized milk, respectively ($\approx 7.6\%$ increase). The only significant compositional difference observed between cheeses made from raw, pasteurized or pressurized milk was moisture content. Cheese yield increase has also been reported for semi-hard goat cheeses (Trujillo et al., 1999) with no detrimental effects on cheese flavor.

The effect in lipolysis of HP treatment of goat's milk for cheese-making was evaluated by Buffa et al. (2001). Applied treatment was 500 MPa for

15 min at 20°C and free fatty acids (FFA) profile analyzed by gas chromatography. FFA content was higher in cheeses made from pasteurized or raw milk as compared with pasteurized milk. Milk lipase was resistant to HP treatment, leading to increased FFA concentration. However, during sensory evaluation after ripening for 60 days, although cheeses made from pressure treated milk received higher scores for aroma and flavor, no significant differences were observed for raw, pasteurized or pressurized cheeses.

The quality of cheese will be the major factor determining the potential application of HP in cheese-making.

Meat

In the specific case of meats, pressures between 100 and 150 MPa have been employed to tenderize pre-rigor meat. This can be caused by the activation of proteolytic enzymes as cathepsins or by the destruction of connective fibers of muscle. These studies have been performed on beef, pork, chicken, and rabbit. Pressures of 250 MPa are employed to treat roast beef and bacon before smoking; to inactivate germs in minced meat and for some aspects of storage; to treat foie gras with excellent quality and extended shelf life; for stability of thiamine in re-hydrated pork meat (Hoover et al., 1989; Cheftel, 1992; Tauscher, 1995; Ting and Marshall, 2002a,b). In the case of beef, the effect of pressure on delay of shrinkage caused by cold during rigor mortis was studied. When the product was treated with 103.5 MPa at 37°C for 2 min the pH of meat lowered and several effects at the fiber level occurred that produced a tenderizing effect on tissue (Elgasim and Kennick, 1982). Other studies were carried out on cured and non-cured pork meat, looking at increasing hardness in both cases and the digestibility of non-cured meat. A slight discoloration was observed after treatment in both types of meat (Farr, 1990). Something similar occurred with beef when treated with 103.5 MPa; the digestibility of protein improved without affecting either the biological value or the net utilization of protein, contrary to what occurs with thermal treatment (Elgasim and Kennick, 1980). However, discoloration of beef was observed after 10 min at pressures higher than 150 MPa; losing the red color until reaching a gray color at 350 MPa (Carlez et al., 1993). Treatment at 800 MPa for short times (20 min) on pork meat stabilizes lipids and permits longer storage times; peroxides were sensible at 19°C combined with pressure, reducing the value of peroxide rancidity of lipids (Cheah and Ledward, 1995).

Fish

When treating fish with HP, products with a new texture and whose aroma is retained for longer times are obtained, as in the case of sardine, mackerel, carp, and tuna fish among others. HP also allows sterilization of sea urchin eggs and texturization of water soluble proteins (Tauscher, 1995).

Fish sausages, terrines, and puddings elaborated with this treatment are commercialized in the Japanese market (Cheftel, 1995). When codfish meat was treated at 202, 404 and 608 MPa during 15 to 30 min, the peroxide value of the oils extracted increased as pressure and time increased. However, when lipids extracted from fishes (sardine) and when defatted muscle is absent, the oxidation is minimum. This suggests that HP catalyzes the oxidation of lipids in fish muscles (Cheah and Ledward, 1995).

Cereals

The use of HP on cereals improves their cooking characteristics and reduces allergenicity potential, induces the formation of soy gels, modifies corn hydration and the sensorial properties of rice, sponges, cookies and rice liquor; decontaminates rice products and spaghetti (Tauscher, 1995). Treatment with HP increases the digestibility of amylase when using the minimum thermal treatment. This was observed in studies made with potato, corn and wheat starches (Farr, 1990).

Vegetables

HPs have been used for potato blanching, preservation of marinates, tomato juice and onions. It has an influence on the hardness of radishes, inactivation of bean lecithin, decontamination of pepper, and paprika pigments (Tauscher, 1995). Results of studies made on potato, carrot, and broad beans pressurized and not pressurized showed that dried not pressurized samples presented the dark color characteristic of enzymatic reactions, whereas the dried pressurized batch presented an acceptable color. This suggests that HP can be an alternative to blanching because they produce vegetables with a similar color to that of the fresh product and better than that of thermal treated samples (Eshtiaghi et al., 1994). The activity of polyphenoloxidase in peas was reduced (12% of residual activity) and the retention of ascorbic acid increased (82%) at a pressure of 900 MPa for 5 min. No important changes in texture between the fresh and pressurized product were reported. Therefore, HP may become an alternative method to vegetable blanching (Quaglia et al., 1996). HPs are used also in combination with CO₂ to inactivate microorganisms in aromatic herbs such as thyme, parsley and mint, but at levels not above 100 MPa because texture can be affected (Cheftel, 1995).

Gels

In Japan, there are various products and processes preformed with HP, for example, gels of meat (studying the influence on flavor), of soy proteins, and of egg yolk and white. Pressurization is also used for gelating surimi, sardine, tuna fish, squid, starches, and alginates. HP induces the opposite behavior in the sol-gel transition of carragenine and agarose; modifies the

properties of gels made with pectin using heat; and gives more stability to gels made with jelly (Farr, 1990; Swientek, 1992; Tauscher, 1995). It has been demonstrated that when using HP for the elaboration of gels of egg, the texture properties were different because the effect of pressure caused them to be softer and more resistant to rupture, digestibility was easier, they did not present a cooked flavor and they maintained their original color (Farr, 1990; Hoover, 1993). Based on studies such as those mentioned here, it has been demonstrated that the formation mechanisms of gels are different if they are induced by heat or by pressure, because of the breakage of different types of bonds (Farr, 1990). However, the pressure required to induce the formation of gel depends on the type and concentration of protein, the pH and the ionic strength of the solution (Cheftel, 1992).

Other Products

The fusion point of triglycerides increases with pressure; thus, lipids present in liquid state at room temperature crystallize under the effect of HP, which generate more stable and dense crystals. For this reason, HP can be used to soften chocolate (Cheftel, 1992; Bordariás, 1995).

HPs are effective for the extraction of metabolites that function as pigments or flavorings; permit the selective proteolysis of proteins that is important for the elaboration of modified milk for babies; and allow the inhibition of the Maillard reaction among others (Barbosa-Cánovas et al., 1998). However, it has been observed that the color of food can be affected by pressure. Within the more resistant pigments are the carotenoids, chlorophyll and anthocyanines, while myoglobin is more sensible (Cheftel, 1992).

Another potential use of HP refers to agglomeration of powders that can be used in the elaboration of food bars, tablets, etc. (Mozhaev et al., 1994). Also, culture of microorganisms at HP to produce gases and to prepare phenylalanine methyl ester (used in the synthesis of aspartame) in bioreactors is another use of this new technology in the food area (Mozhaev et al., 1994).

The process to elaborate tofu is to coagulate protein with CaCl_2 , CaSO_4 or MgCl_2 followed by a thermal treatment; however, when protein is subjected to 100 MPa it is coagulated with CaCl_2 and a gel is formed, presenting a great hardness when pressures above 300 MPa are employed (Kajiyama et al., 1995). Alternatively, Fuchigami et al. (2001) used HP to freeze tofu, finding that the quality of the frozen product markedly improved at levels between 200 and 600 MPa applied for 60 min; they obtained even better results when pressure was combined with trehalose.

Final Remarks

Consumer tendencies nowadays are for products that are “minimally processed” with a high nutritional value and long shelf life. The use of HP

for food preservation addresses this requirement effectively. However, even though the commercial application of this process is increasing, there are still many kinetics and thermodynamic studies on the effects of high pressures on food components to be made.

The application of HP for food preservation can also be used in combination with other technologies; heat, gases, bacteriocins (Gould, 2001) among other possibilities that are being studied and reported.

References

- Alemán, G., Farkas, D.F., Torres, J.A., Wilhelmsen, E., and McIntyre, S. Ultra-high pressure pasteurization of fresh cut pineapple, *J. Food Prot.*, 57, 931, 1994.
- Alemán, G.D., Ting, E.Y., Mordre, S.C., Hawes, A.C.O., Walker, M., Farkas, D.F., and Torres, J.A. Pulsed ultra high pressure treatments for pasteurization of pineapple juice, *J. Food Sci.*, 61, 388, 1996.
- Alzamora, S.M., Guerrero, S., Viollaz, P.E., and Welti-Chanes, J. Experimental protocols for modeling the response of microbial populations exposed to emerging technologies: some points of concern, *Novel Food Processing Technologies*, G.V. Barbosa-Cánovas, M.S. Tapia and P. Cano, eds., CRC Press, Boca Raton, Florida, pp. 591–608, 2005.
- Ashie, I.N.A. and Simpson, B.K. Application of high hydrostatic pressure to control enzyme related fresh seafood texture deterioration, *Food Res. Int.*, 29, 569, 1996.
- Ashie, I.N.A., Simpson, B.K., and Ramaswamy, H.S. Control of endogenous enzyme activity in fish muscle by inhibitors and hydrostatic pressure using RSM, *J. Food Sci.*, 61, 350, 1996.
- Barbosa-Cánovas, G.V., Pothakamury, U.R., Palou, E., and Swanson, B.G. *Nonthermal Preservation of Foods*, Marcel Dekker, New York, 1998.
- Basak, S. and Ramaswamy, H.S. Ultra high pressure treatment of orange juice: a kinetic study on inactivation of pectin methyl esterase, *Food Res. Int.*, 29, 601, 1996.
- Bordarías, A.J. Aplicación de altas presiones en la tecnología de alimentos, *Alimentación, Equipos y Tecnología.*, 109, 1995.
- Buffa, M., Guamis, B., Pavia, M., and Trujillo, A.J. Lipolysis in cheese made from raw, pasteurized or high-pressure-treated goat's milk, *Int. Dairy J.*, 11, 175, 2001.
- Butz, P., Koller, W.D., Tauscher, B., and Wolf, S. Ultra-high pressure processing of onions: chemical and sensory changes, *Lebensm Wiss u Technol.*, 27, 463, 1994.
- Cano, M.P., Hernández, A., and De Ancos, B. High pressure and temperature effects on enzyme inactivation in strawberry and orange products, *J. Food Sci.*, 62, 85, 1997.
- Carballa, J., Fernández, P., Carrascosa, A.V., Solas, M.T., and Jiménez-Colmenero, F. Characteristics of low- and high-fat beef patties: effect of high hydrostatic pressure, *J. Food Prot.*, 60, 48, 1997.

- Carlez, A., Rosec, J.P., Richard, N., and Cheftel, J.C. High pressure inactivation of *Citrobacter freundii*, *Pseudomonas fluorescens* and *Listeria innocua* in Inoculated Minced Beef Muscle, *Lebensm Wiss u Technol.*, 26, 357, 1993.
- Cheah, P.B. and Ledward, D.A. High-pressure effects on lipid oxidation, *JAOCs.*, 72, 1059, 1995.
- Cheftel, J.C. Effects of high hydrostatic pressure on food constituents: an overview, *High Pressure and Biotechnology, Colloque INSERM*, Vol. 224, C. Balny, R. Hayashi, K. Heremans and P. Masson, eds., John Libbey Eurotext Ltd., Montrouge, France, p. 195, 1992.
- Cheftel, J.C. Review: high-pressure, microbial inactivation and food preservation, *Int. Food Sci. and Technol.*, 1, 75, 1995.
- Correa-Balderas, M. Efecto de altas presiones sobre la cinética de inactivación de *Listeria innocua* y sobre la calidad de queso fresco mexicano. BS Thesis, Universidad de las Américas-Puebla. Mexico, 2001.
- Crawford, Y.J., Murano, E.A., Olson, D.G., and Shenoy, K. Use of high hydrostatic pressure and irradiation to eliminate *Clostridium sporogenes* spores in chicken breast, *J. Food Prot.*, 59, 711, 1996.
- Denys, S., van Loey, A.M., and Hendrickx, M.E. Modeling conductive heat transfer during high pressure thawing processes and determination of latent heat as function of pressure, *Biotechnol. Prog.*, 16, 447, 2000.
- Desobry-Banon, S., Richard, F., and Hardy, J. Study of acid and rennet coagulation of high pressurized milk, *J. Dairy Sci.*, 77, 3267, 1994.
- Drake, M.A., Harrison, S.L., Asplund, M., Barbosa-Cánovas, G.V., and Swanson, B.G. High pressure treatment of milk and effects on microbiological and sensory quality of cheddar cheese, *J. Food Sci.*, 62, 843, 1997.
- Elgasim, E.A. and Kennick, W.H. Effect of pressurization of pre-rigor beef muscles on protein quality, *J. Food Sci.*, 45, 1122, 1980.
- Elgasim, E.A. and Kennick, W.H. Effect of high hydrostatic pressure on meat microstructure, *Food Microstruct.*, 1, 75, 1982.
- Eshtiaghi, M.N., Stute, R., and Knorr, D. High-pressure and freezing pretreatment effects on drying, rehydration, texture and color of green beans, carrots and potatoes, *J. Food Sci.*, 59, 1168, 1994.
- Farr, D. High pressure technology in the food industry, *Trends Food Sci. Technol.*, 1, 14, 1990.
- Fox, P.F. and McSweeney, P.L.H. *Dairy Chemistry and Biochemistry*, International Thomson Publishing, Great Britain, pp. 347, 1998.
- Fuchigami, M., Ogawa, N., and Teramoto, A. The effects of high pressure and trehalose on improving both texture and structure of frozen tofu (soybean curd), *Proceedings of the 8th International Congress on Engineering and Food. ICEF 8.* Vol. II, J. Welti-Chanes, G.V. Barbosa-Cánovas and J.M. Aguilera, eds., Technomic Publishing Co. Inc., Lancaster, PA, p. 1442, 2001.
- Gaucheron, F., Famelart, M.H., Mariette, F., Raulot, K., Michel, F., and Le Graet, Y. Combined effects of temperature and high-pressure treatments on physico-chemical characteristics of skim milk, *Food Chem.*, 59, 439, 1997.
- Gervilla, R., Capellas, M., Ferragut, V., and Guamis, B. Effect of high hydrostatic pressure on *Listeria innocua*: 910 CECT inoculated into ewe's milk, *J. Food Prot.*, 60, 33, 1997.
- Gervilla, R., Ferragut, V., and Guamis, B. High hydrostatic pressure effects on color and milk-fat globule of ewe's milk, *J. Food Sci.*, 66, 880, 2001.

- Gould, G.W. *The Evolution of High Pressure Processing of Foods*, E.G. Hendrickx and D. Knorr, eds., Kluwer/Plenum Publishers, New York, 2001, chap. 1.
- Hashizume, C., Kimura, K., and Hayashi, R. Kinetic analysis of yeast inactivation by high pressure treatment at low temperatures, *Biosci. Biotech. Biochem.*, 59, 1455, 1995.
- Hayashi, R., Kawamura, Y., and Kunugi, S. Introduction of high pressure to food processing: preferential proteolysis of lactoglobulin in milk whey, *J. Food Sci.*, 52, 1107, 1987.
- Heremans, K. The effects of high pressure on biomaterials, *Ultra High Pressure Treatments of Foods*, E.G. Hendrickx and D. Knorr, eds., Kluwer/Plenum Publishers, New York, 2001, chap. 2.
- Hernández-Salgado, C.E. Estabilización de guacamol: efecto combinado del control de pH, incorporación de sal, aplicación de altas presiones hidrostáticas y almacenamiento refrigerado, Thesis to Obtain Master Degree, Universidad de las Américas Puebla, México, 1999.
- Hinrichs, J., Rademacher, B., and Kessler, H.G. Food processing of milk products with ultra high pressure, *Heat Treatments and Alternative Methods*, IDF Doc 9602, pp. 185, 1996.
- Hite, B.H. The effect of pressure in the preservation of milk, *West Virginia Agricultural Experimental Station Bulletin*, 58, 15, 1899.
- Hite, B.H., Giddings, N.J., and Weakly, C.E. The effect of pressure on certain microorganisms encountered in the preservation of fruit and vegetables, *West Virginia Agricultural Experimental Station Bulletin*, 146, 1, 1914.
- Hoover, D.G. Pressure effects on biological systems, *Food Technol.*, 47, 150, 1993.
- Hoover, D.G., Metrick, C., Papineau, A.M., Farkas, D.F., and Knorr, D. Biological effects of high hydrostatic pressure on food microorganisms, *Food Technol.*, 43, 99, 1989.
- Huppertz, T., Fox, P.F., and Kelly, A.L. High pressure-induced changes in the creaming properties of bovine mil, *Inn. Food Sci. Emerging Technol.*, 4, 349, 2003.
- Huppertz, T., Kelly, A.L., and Fox, P.F. Effects of high pressure on constituents and properties of milk, *Int. Dairy J.*, 12, 561, 2002.
- Johnston, D.E., Austin, B.A., and Murphy, R.J. Effects of high hydrostatic pressure on milk, *Milchwissenschaft*, 47, 760, 1992.
- Kajiyama, N., Isobe, S., Uemura, K., and Noguchi, A. Changes of soy protein under ultra-high hydraulic pressure, *Int. J. Food Sci. Technol.*, 30, 147, 1995.
- Kalichevsky, M.T., Knorr, D., and Lillford, P.J. Potential food applications of high-pressure effects on ice-water transitions, *Trends Food Sci. Technol.*, 6, 253, 1995.
- Knorr, D., Schlueter, O., and Heinz, V. Impact of high hydrostatic pressure on phase transitions of foods, *Food Technol.*, 52, 42, 1998.
- Knudsen, J.C., Otte, J., Olsen, K., and Skibsted, L.H. Effect of high hydrostatic pressure on the conformation of (–)lactoglobulin A as assessed by proteolytic peptide profiling, *Int. Dairy J.*, 12, 791, 2002.
- Kurth, L.B. Effect of pressure–heat treatments on cathepsin B1 activity, *J. Food Sci.*, 51, 663, 1986.
- Law, A.J.R., Leaver, J., Felipe, X., Ferragut, V., Pla, R., and Guamis, B. Comparison on the effects of high pressure and thermal treatments on the casein micelles in goat's milk, *J. Agric. Food Chem.*, 46, 2523, 1998.
- López-Fandiño, R., Carrascosa, A.V., and Olano, A. The effects of high pressure on whey protein denaturation and cheese-making properties of raw milk, *J. Dairy Sci.*, 79, 929, 1996.

- López-Fandiño, R. and Olano, A. Effects of high pressures combined with moderate temperatures on the rennet coagulations properties of milk, *Int. Dairy J.*, 8, 623, 1998.
- López-Fandiño, R., Ramos, M., and Olano, A. Rennet coagulation of milk subjected to high pressures, *J. Agric. Food Chem.*, 45, 3233, 1997.
- López-Malo, A., Palou, E., Barbosa-Cánovas, G.V., Welti-Chanes, J., and Swanson, B.G. Polyphenoloxidase activity and color changes during storage of high hydrostatic pressure treated avocado puree, *Food Res. Int.*, 31, 549, 1998.
- López-Malo, A., Palou, E., Barbosa-Cánovas, G.V., Swanson, B.G., and Welti-Chanes, J. Minimally processed foods and high hydrostatic pressure, *Advances in Food Engineering*, J. Lozano, M.C. Añón, E. Parada-Arias and G.V. Barbosa-Cánovas, eds., Technomic Publishing Co., Lancaster, PA, 2000.
- Mertens, B. Hydrostatic pressure treatment of food: equipment and processing, *New Methods of Food Preservation*, G.W. Gould, ed., Blackie Academic and Professional, Great Britain, p. 135, 1995.
- Mozhaev, V.V., Heremans, K., Frank, J., Masson, P., and Balny, C. Exploiting the effects of high hydrostatic pressure in biotechnological applications, *Trends Biotechnol.*, 12, 493, 1994.
- Müller, K., Seifert, T., and Jaenicke, R. High pressure dissociation of lactate dehydrogenase from *Bacillus stearothermophilus* and reconstitution of the enzyme after denaturation in 6 M guanidine hydrochloride, *Eur. Biophys. J.*, 11, 87, 1984.
- Mussa, D.M., Ramaswamy, H.S., and Smith, J.P. High pressure destruction kinetics of *Listeria monocytogenes* Scott A in raw milk, *Food Res. Int.*, 31, 343, 1999a.
- Mussa, D.M., Ramaswamy, H.S., and Smith, J.P. High pressure destruction kinetics of *Listeria monocytogenes* on pork, *J. Food Prot.*, 62, 40, 1999b.
- Needs, E., Stenning, R.A., Gill, A.L., Ferragut, V., and Rich, G.T. High-pressure treatment of milk: effects on casein micelle structure and on enzymic coagulation, *J. Dairy Res.*, 67, 31, 2000.
- Ogawa, H., Fukuhisa, K., Kubo, Y., and Fukumoto, H. Pressure inactivation of yeasts, molds, and pectinesterase in Satsuma mandarin juice: effects of juice concentration, pH, and organic acids, and comparison with heat sanitation, *Agric. Biol. Chem.*, 54, 1219, 1990.
- Ohmiya, K., Kajino, T., Shimizu, S., and Gekko, K. Effect of pressure on the association states of enzyme-treated caseins, *Agric. Biol. Chem.*, 53, 1, 1989.
- Palou, E., Barbosa-Cánovas, G.V., Swanson, B.G., López-Malo, A., and Welti-Chanes, J. High hydrostatic pressure inactivation kinetics of *Zygosaccharomyces bailii*, *Engineering and Food at ICEF 7 (Part I)*, S.R. Jowitt, ed., Academic Press, New York, 1997.
- Palou, E., López-Malo, A., Barbosa-Cánovas, G.V., Welti-Chanes, J., and Swanson, B.G. Kinetic analysis of *Zygosaccharomyces bailii* inactivation by high hydrostatic pressure, *Lebensm Wiss u Technol.*, 30, 703, 1997.
- Palou, E., López-Malo, A., Barbosa-Cánovas, G.V., Welti-Chanes, J., Davidson, P.M., and Swanson, B.G. High hydrostatic pressure come-up time and yeast viability, *J. Food Prot.*, 61, 1657, 1998.
- Palou, E., López-Malo, A., Barbosa-Cánovas, G.V., and Welti-Chanes, J. High hydrostatic pressure and minimal processing, *Minimally Processed Fruits and Vegetables. Fundamentals and Applications*, S.M. Alzamora, M.S. Tapia and A. López-Malo, eds., Aspen, Maryland, 2000.

- Palou, E., López-Malo, A., and Welti-Chanes, J. Innovative fruit preservation methods using high pressure, *Engineering and Food for the 21st Century*, J. Welti-Chanes, G.V. Barbosa-Cánovas and J.M. Aguilera, eds., CRC Press, Boca Raton, FL, p. 715, 2002.
- Pérez-Delgado, J. Uso de alta presión hidrostática como un obstáculo para la inhibición de *Saccharomyces cerevisiae* en sistemas modelo alimenticios de alta actividad de agua, Thesis to obtain Master Degree, Universidad de las Américas-Puebla, Mexico, 1996.
- Perrier-Cornet, J.M., Marechal, J.M., and Gervais, P. A new design intended to relate high-pressure treatment to yeast-cell mass transfer, *J. Biotechnol.*, 41, 49, 1995.
- Quaglia, G.B., Gravina, R., Paperi, R., and Paoletti, F. Effect of high pressure treatments on peroxidase activity, ascorbic acid content and texture in green peas, *Lebensm Wiss u Technol.*, 29, 552, 1996.
- San Martín-González, M.F., Welti-Chanes, J.S., and Barbosa-Cánovas, G.V. Cheese Manufacture Assisted by Ultra-High Pressure, *Proceedings of the IFT 2004 Annual Meeting, Book of Abstracts*. Institute of Food Technologists, Chicago, IL, 2004, p. 11.
- Smelt, J.P.P.M. Recent advances in the microbiology of high pressure processing, *Trends Food Sci. Technol.*, 9, 152, 1998.
- Stóforos, N.G. and Taoukis, P.S. Pressure process evaluation through kinetic modeling, *Proceedings of the 8th International Congress on Engineering and Food*. ICEF 8., Vol. II, J. Welti-Chanes, G.V. Barbosa-Cánovas and J.M. Aguilera, eds., Technomic Publishing Co, Inc., Lancaster, PA, p. 1437, 2001.
- Styles, M.F., Hoover, D.G., and Farkas, D.F. Response of *Listeria monocytogenes* and *Vibrio parahaemolyticus* to high hydrostatic pressure, *J. Food Sci.*, 56, 140, 1991.
- Swaigood, H.E. Characteristics of milk, *Food Chemistry*, O. Fennema, ed., Marcel Dekker, New York, p. 841, 1996.
- Swientek, R.J. High hydrostatic pressure for food preservation, *Food Proc.*, 90, 1992.
- Tauscher, B. Pasteurization of food by hydrostatic high pressure: chemical aspects, *Z. Lebensm Unters Forsch*, 200, 3, 1995.
- Ting, E.Y. and Marshall, R.G. Production issues related to UHP food, *Engineering and Food for the 21st Century*, J. Welti-Chanes, G.V. Barbosa-Cánovas and J.M. Aguilera, eds., CRC Press, USA, 2002a.
- Ting, E.Y. and Marshall, R.G. Production issues related to UHP food, *Engineering and Food for the 21st Century*, J. Welti-Chanes, G.V. Barbosa-Cánovas and J.M. Aguilera, eds., CRC Press, Boca Raton, FL, 2002b, p. 727.
- Trujillo, A.J., Royo, C., Guamis, B., and Ferragut, V. Influence of pressurization on goat milk and cheese composition and yield, *Milchwissenschaft*, 54, 197, 1999.
- Wagner, W. and Pruss, A. The IAPWS formulation 1995 for the thermodynamic properties of ordinary water substance for general and scientific use, *J. Phys. Chem.* Submitted. 1999.

13

Viability of Probiotic Bacteria as Affected by Drying

Barry Corcoran, Catherine Stanton, Song Miao, Gerald F. Fitzgerald, and R. Paul Ross

CONTENTS

Introduction	233
Spray Drying	235
Freeze Drying	238
Storage of Dried Probiotic Powders	240
Applications of Dried Probiotic Powder Ingredients	240
Conclusions.....	242
Acknowledgments	242
References	242

Introduction

Probiotics, described as “live microorganisms which when consumed in adequate amounts confer a health benefit on the host”(FAO/WHO, 2001), are currently receiving much research attention, both from clinical and commercial perspectives. Over the past two decades, the intake of probiotic bacteria, particularly in dairy products, has increased substantially, spawning an industry now valued at €30 billion worldwide (Saarela et al., 2000; de Vos et al., 2004). The most commonly used probiotic strains for food use belong to the genera *Lactobacillus* and *Bifidobacterium* (Stanton et al., 2003), and generally share such features as generally recognized as safe (GRAS) status of human origin and tolerance to acid and bile, in addition to demonstrated health benefits (Ouweland et al., 2002). A number of health benefits have been demonstrated in clinical trials associated with regular ingestion of probiotics, including alleviation of lactose intolerance

TABLE 13.1
Examples of Recent Documented Health Benefits of Probiotics in Human Clinical Trials

Genus and Species	Examples	Health Benefit	Reference
<i>L. casei</i>	Shirota	Immune modulation	Nagao et al. (2000)
<i>L. johnsonii</i>	La1	Reduced <i>H. pylori</i> colonization	Felley et al. (2001)
<i>L. plantarum</i>	LP0 1	Relief of IBS	Saggioro (2004)
<i>B. breve</i>	BR0		
<i>L. acidophilus</i>		Reduction of colonic infection of <i>C. difficile</i>	Plummer et al. (2004)
<i>B. bifidum</i>			
<i>L. rhamnosus</i>	GG	Shortening of diarrhoea	Guandalini et al. (2000)
		Treatment/prevention of allergy	Kalliomaki et al. (2001)
		Delay of first onset of pouchitis	Gosselink et al. (2004)
<i>L. salivarius</i>	UCC118	Reduced IBD	Mattila-Sandholm et al. (1999)
	VSL#3	Reduced symptoms associated with diarrhoea-predominant IBS	Kim et al. (2003)
<i>B. breve</i>		Reduced IBD	Brigidi et al. (2001))
<i>B. longum</i>	Bb536		
<i>B. lactis</i>	Bb12	Allergy treatment	Isolaure et al. (2001)
<i>S. boulardii</i>		Reduction of antibiotic associated diarrhoea	Erdeve et al. (2004)

(Martini et al., 1991; Jiang et al., 1996), diarrhea (Isolaure et al., 1991; Saavedra et al., 1994; Shornikova et al., 1997; Guandalini et al., 2000), atopic eczema (Isolaure et al., 1999; Kalliomaki et al., 2001), and urinary tract infections (Reid et al., 2003) (Table 13.1). While the clinical evidence for probiotics in preventing and/or treating some disorders, particularly in the gut, are well documented, there also appears to be potential for probiotics in areas such as the management of inflammatory bowel diseases, Crohn's disease, and cancer, although further investigations are required (Shanahan, 2000; Stanton et al., 2003).

From a processing perspective, probiotic bacteria should be technologically suitable for incorporation into food systems so that they retain viability and efficacy through storage and following consumption (Rogelz, 1994; Stanton et al., 1998). Candidate probiotic microorganisms must be suitable for large-scale industrial production. In this respect, the drying of live probiotic strains is a critical step in the preparation of concentrated probiotic food ingredients, with most focus on freeze drying and spray drying. Freeze drying is the method most commonly used for the preparation of dried concentrated cultures, while spray drying is also suitable in some cases (Teixeira et al., 1995a; 1995b; To and Etzel, 1997; Ross et al., 2005). While there are a number of disadvantages associated with both approaches, the harsher

processing conditions encountered during spray drying generally result in greater viability losses than freeze drying. These drying techniques expose bacteria cells to such stresses as extremes of heat and cold, oxygen, and osmotic stresses, all of which may impair survival (Fu and Etzel, 1995; Teixeira et al., 1997; To and Etzel, 1997). In this chapter, we will examine approaches that have been taken in efforts to overcome the technological challenges associated with drying of live probiotic cultures.

Spray Drying

Spray drying has long been used in the dairy industry to concentrate surplus supplies of liquid milk to a dry stable powder. Such powders have long shelf life because of low moisture content ($<4\%$), which inhibits development of microorganisms during storage. The spray-drying process involves the atomization of a concentrated feed solution into a drying chamber where the wet material is passed through a hot-air stream, resulting in moisture loss and powder formation. During spray drying, the time required for drying of particles, i.e., the residence time, is extremely short, and most of the wet particles experience only the wet bulb temperature during removal of the majority of the water. Therefore, thermal damage of most dried materials may be avoided; however, maintenance of viability during spray drying of heat-sensitive cultures is a greater challenge. Spray drying has been investigated for the preparation of culture-containing powders for both starter and probiotic applications, particularly lactic acid bacteria (LAB) (Knorr, 1998; Gardiner et al., 2000; 2002; Desmond et al., 2002; Corcoran et al., 2004). During spray drying, bacterial cultures are exposed to a number of stresses, such as dehydration, heat, and osmotic stress, etc. (Brennan et al., 1986; Teixeira et al., 1997). Loss of membrane integrity during drying has been associated with proteins and lipids damage (Brennan et al., 1986; Teixeira et al., 1997), and in particular the importance of water to their stability. Water molecules are vital components of reaction mechanisms and contribute to the stability of proteins, lipids, and DNA (Potts, 1994). When hydrogen-bonded water is removed from the head group regions of phospholipid bilayers, head group packing increases and the probability of Van der Waals interactions increases, resulting in state transition of the lipid component (Crowe et al., 1985). Upon cell rehydration, the transition reverses, revealing regions with packing defects, leading to leaky membranes (Leslie et al., 1995). It has also been proposed that water in close contact with proteins is responsible for affecting cell stability (Laroche and Gervais, 2003). Water molecules vibrate during heating, weakening disulfide and hydrogen bonds in surrounding proteins, altering three-dimensional structures, and potentially affecting function (Laroche and Gervais, 2003). In addition, ribosomes and DNA are also affected at higher temperatures (Teixeira et al., 1997).

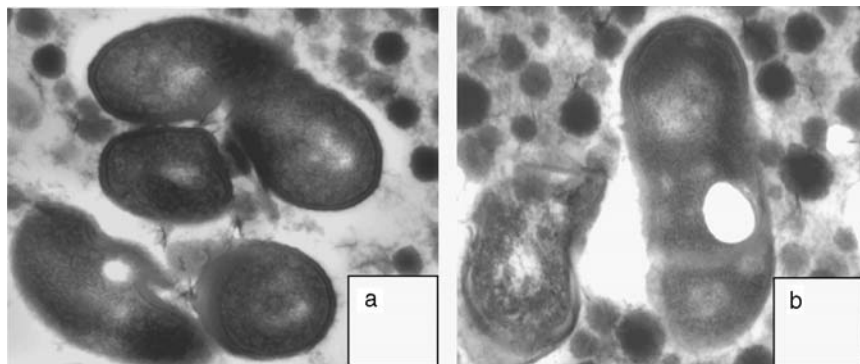
Many factors affect the survival of bacteria during spray drying, including inlet and outlet temperatures, composition of the carrier medium, use of protectants and choice of strain. It has been demonstrated that outlet temperature was inversely linearly related to survival of probiotic lactobacilli during spray drying (Gardiner et al., 2000). Inlet and outlet temperatures of 170°C and 85–90°C, respectively, resulted in good survival of some probiotic lactobacilli, such as *Lactobacillus paracasei* NFBC 338, while *Lactobacillus salivarius* UCC 118 exhibited poor survival under these conditions (Gardiner et al., 2000). Kim and Bhowmik (1990) reported that *L. bulgaricus* declined by 1 log when atomizing air pressure was increased from 98 to 188 kPa and Fu and Etzel (1995) reported that viability of *Lactococcus lactis* was affected by 14% during heating inside the atomizer. Labuza et al. (1972) reported an activation energy of 40 Kcal/mole/°C, suggesting that cell death of *Saccharomyces cerevisiae* occurred primarily in the wet state, i.e., during the first seconds the particles enter the spray dryer. Co-current spray dryers resulted in poorer survival of *L. helveticus* spray dried in 30% (w/v) condensed skim milk medium compared with counter-current spray dryers (Johnson and Etzel, 1993).

The nature and composition of the spray drying medium is known to affect survival of probiotics during spray-drying. The medium most used is milk-based, and indeed, reconstituted skim milk (RSM) appears to be a very suitable media for efficacious spray-drying of probiotic cultures (Lian et al., 2002; Corcoran et al., 2004). The solids content of the medium also affect survival during spray drying. For example, Daeman and van der Stege (1982) showed that increasing total solids increased bacterial thermoresistance to spray drying. Miller et al. (1972) reported that survival of *Salmonella* species and *Escherichia coli* increased following spray drying in milk at total solids content of 40% (w/v) compared with 20% (w/v). This was attributed to the thicker wall of particles made with higher total solids, resulting in increased thermoprotection to the bacteria during drying. Espina and Packard (1979) also reported better survival of *Lactobacillus acidophilus* at 25% (w/v) solids compared with 40% (w/v) solids. In contrast, Chopin et al. (1977) found that total solids did not have an effect on *Staphylococcus aureus* survival, while Johnson and Etzel, (1993) linked decreased survival of *L. helveticus* with increasing total solids from 20 to 34% (w/v). Spray drying with 20% (w/v) solids resulted in powders with reduced moisture content at lower outlet temperatures, and consequently more stable product (Johnson and Etzel, 1993). Therefore, feed concentrations may require tailoring to optimally accommodate the probiotic strain selected for spray drying.

Prebiotics are nondigestible food ingredients that beneficially affect the host by stimulating the growth and/or activity of one or a limited number of bacteria in the colon, thus improving host health (Cummings and Macfarlane, 2002). These substances have received interest as carriers of probiotics in food products, with the resultant products referred to as

synbiotics (O'Riordan et al., 2001). However, the application of prebiotics as sole encapsulating agents for probiotics during spray drying generally leads to poor probiotic survival rates (Lian et al., 2002; Corcoran et al., 2004). A combination of RSM and prebiotics (polydextrose or inulin) in a 1:1 ratio, however, resulted in spray dried powders harbouring numbers of *Lactobacillus rhamnosus* GG up to 10^9 CFUg⁻¹ (Corcoran et al., 2004). A combination of RSM with the prebiotic substance gum acacia (final solids content 20% w/v) also resulted in enhanced survival of lactobacilli compared to cultures spray-dried in RSM only, particularly at outlet temperatures of 100–105°C (Desmond et al., 2002). Use of starch for encapsulation of *Bifidobacterium* PL1 resulted in protection during drying (O'Riordan et al., 2001). Furthermore, the use of proteins as protectants during spray drying was also demonstrated. For example, Picot and Lacroix (2004) reported good viability (up to 25% survival) of bifidobacteria spray dried in whey protein polymers (10% w/w) at outlet temperature of 80°C.

Strain selection is another important consideration, as different strains showed different survival rate during spray-drying (Foster, 1962; Gardiner et al., 2000; Lian et al., 2002; Corcoran et al., 2004; Picot and Lacroix, 2004). Heat tolerance has been linked with survival during spray drying, although other stresses, such as dehydration and osmotic shock are also encountered during the process (LiCari and Potter, 1970; Gardiner et al., 2000; Desmond et al., 2001; Corcoran et al., 2004). Thermophilic LAB, in particular *Streptococcus thermophilus*, are reported to survive well during spray drying (Abd-El-Gawad et al., 1989; To and Etzel, 1997; Bielecka and Majkowska, 2000). While approximately 50% of *L. paracasei* NFBC 338 survived spray drying in RSM (20% w/v) at outlet temperatures of 85–90°C, survival rate of *L. salivarius* UCC 118 was only ~1% under identical conditions (Gardiner et al., 2000). In general, bifidobacteria are more labile to spray drying than lactobacilli, and furthermore, differences between species have been observed during spray drying. Lian et al. (2002) reported that *Bifidobacterium longum* survived better than *B. infantis* and suggested the difference might reflect a higher thermotolerance in *B. longum* leading to enhanced survival during spray drying. In another study, it was shown that *B. breve* was more labile than *B. longum*, exhibiting only 1.4% survival during spray drying at outlet temperature 80°C (Picot and Lacroix, 2004), compared with 25.1% survival of *B. longum* under identical conditions. In a recent study in our laboratory, the heat and oxygen tolerance of a number of *Bifidobacterium* species were compared, and performance during spray drying evaluated (Simpson et al., 2005). Considerable heterogeneity among the species tested was observed for heat and oxygen tolerance, with several of the strains tested exhibiting tolerance to both heat and oxygen. Moreover, closely related species exhibiting heat and oxygen tolerance, notably *B. animalis* ssp. *lactis* survived spray drying at ~70% or greater in RSM (20% w/v) at outlet temperature of 85–90°C (Simpson et al., 2005) (Figure 13.1).

**FIGURE 13.1**

Transmission electron micrograph (TEM) images of log phase *Lactobacillus paracasei* NFBC 338 (a), spray dried at inlet and outlet temperatures of 180°C and 95–100°C respectively, (b), freeze dried cultures with dead (a) and live intact cell (b). Both cultures were dried in RSM (20% w/v). (Magnification $\times 60,000$).

Freeze Drying

Freeze drying is a process based upon sublimation and occurs in three phases, freezing, primary and secondary drying. Freeze drying exposes cells to attenuating effects of freezing, and dehydration. While freeze-drying is more effective for preparation of stable cultures, it is less economical than spray drying. As the processing conditions are milder than spray drying, higher probiotic survival rates are typically achieved in freeze dried powders (Wang et al., 2004). However, many factors also affect probiotic survival during freeze-drying. The formation of ice crystals during the process leads to mechanical damage of membranes as well as other cellular components. The crystallization process also exacerbates solute cryo-concentration, inducing osmotic damage as the barrier for ion permeation is ruptured, leading to a collapse in membrane potential (Gomez Zavaglia et al., 2003; Monnet et al., 2003). The principle causes of cell damage and mortality during freeze drying are both the freezing and dehydration processes (Castro et al., 1997). It has been proposed that the lipid fraction of the cell membrane is the primary target area for damage, where lipid peroxidation may occur (Brennan et al., 1986; Linders et al., 1997). Similar to the effects of spray drying, bilayer properties are disturbed by temperature changes as well as water lipid ratio alterations (Gomez Zavaglia et al., 2003). Membrane proteins can also be damaged during freeze drying (Castro et al., 1997). In addition, secondary structures of RNA and DNA stabilize, reducing efficiency of DNA replication, transcription and translation (van de Guchte et al., 2002). All of these factors substantially affect the culture viability during drying.

Many approaches have been investigated for protection of microbial viability during freeze-drying. For example, the use of nitrogen has been reported to avoid compositional changes in the lipid fraction of cells (Castro et al., 1997). Furthermore, the use of cryo-protectants such as amino acids, carbohydrates, polyols, and the use of complex media such as yeast extract and skim milk can have positive effects on survival during the drying process (Hubalek, 2003). For example, glutamate has been shown to be an effective cryo-protectant of *Lactobacillus reuteri* during freeze drying (de Valdez et al., 1997). The amino acid derivative betaine, as well as sucrose/bovine serum albumin (S/BSA) and trehalose are also widely used as cryoprotectants (Cleland et al., 2004). However Ananta et al. (2004) found that the use of betaine resulted in approximately $2 \log_{10}$ CFU/ml lower survival of *L. rhamnosus* GG compared with starch. The use of trehalose-borate in bacterial concentrates greatly improved the recovery of viable cells of freeze dried *L. acidophilus* after storage at 37°C (Conrad et al., 2000). The mechanism of trehalose protection has been reported to involve water replacement of the lipid head groups, in addition to preserving the structure and function of isolated proteins during drying (Potts, 1994; Leslie et al., 1995). In addition to trehalose, other sugars such as fructose, lactose, and mannose in the drying medium have yielded positive effects on survival of LAB during drying and storage. For example, *L. bulgaricus* survived better during storage at -20°C over 10 months when cells were grown in the presence of fructose, lactose or mannose or when glucose, fructose or sorbitol were added to the drying medium (Carvalho et al., 2004). A combination of gelatine, maltodextrin and lactose provided good protection of *L. rhamnosus* E800 during freeze drying (Ananta et al., 2004).

Exploitation of the stress response mechanisms of lactobacilli is an alternative approach that has received attention for improving the survival capacity of probiotic lactobacilli during drying (Kullen and Klaenhammer, 1999; Walker et al., 1999; Desmond et al., 2002; Prasad et al., 2003). Acid-adaptation has successfully been used to exploit the acid stress response of *L. acidophilus* in order to enhance survival of the culture in normally lethal acid conditions and in yoghurt (Shah, 2000). In a study conducted in our laboratory, exposure of *L. paracasei* NFBC 338 to sub-lethal heat stress (52°C for 15 min) resulted in up to 18-fold higher survival rates following spray drying compared with unstressed cells (Desmond et al., 2001). Teixeira et al. (1995) also reported that heat shock of exponential phase *L. bulgaricus* cells prior to spray drying resulted in higher drying survival rates compared with unstressed cells. Similarly, Ananta and Knorr (2004) reported enhanced survival of *L. rhamnosus* GG by the use of pressure-treatment (100 MPa for 10 min at 37°C) of cells prior to spray drying. The application of stress is known to induce changes in the bacterial cell, such as modification of membrane permeability, variation of internal solute concentration and the synthesis of heat shock proteins (Marechal, 1999).

Storage of Dried Probiotic Powders

A number of factors have been shown to affect probiotic survival during storage, including temperature, moisture content, relative humidity (RH) and packaging conditions. Storage temperature is critical to microbial stability with many studies showing that probiotic viability is inversely related to storage temperature (Teixeira et al., 1995; Mauriello et al., 1999; Gardiner et al., 2000; Corcoran et al., 2004). Moisture content of the powder is critical for optimum bacterial survival during storage. Powder moisture content of ~3% is reported as optimum for storage stability of freeze dried bifidobacteria (Nagawa et al., 1988) and LAB (Prajapati et al., 1987). a_w represents the fraction of the total water that is available to cells for metabolism and growth (Kosanke et al., 1992). This concept has been developed to account for water interaction with other food components (Hardy et al., 2002) and is believed to play a major role in probiotic stability during storage. Optimum bacterial stability is encountered in powders with low a_w . Ishibashi (Ishibashi et al., 1985) recommended a_w values of 0.2 for maximum stability of probiotic bacteria in powders, while a value of a_w 0.1 resulted in best survival of *L. bulgaricus* during storage of spray dried powders, while lower a_w yielded poorer survival rates (Teixeira et al., 1995). RH of the storage environment can also affect the viability of LAB during storage, and storage under nitrogen has been reported to improve probiotic survival, such as *L. acidophilus* (Espina and Packard, 1979) and *S. lactis* (Foster, 1962). Media composition can also have dramatic effects on probiotic viability during storage. For example, survival of dried *L. paracasei* NFBC338 (in RSM powder containing gum acacia) was 1000-fold higher than control (dried in the presence of RSM alone) during storage at 15°C and 30°C (Desmond et al., 2002). The use of antioxidant such as ascorbic acid in the drying medium resulted in approximately 1 log₁₀ CFU/ml improved survival of *L. bulgaricus* during storage at 20°C (Teixeira et al., 1995). Incorporation of the prebiotic substances, polydextrose and inulin into the drying medium did not lead to improved survival of *L. rhamnosus* GG, *L. rhamnosus* E 800 and *L. salivarius* UCC 500, during storage, particularly at 37°C, in comparison to powders made with RSM alone (Corcoran et al., 2004). The packaging material has also been reported to affect bacterial survival during storage (Nagawa et al., 1988). Materials with high water vapor permeability resulted in poorest survival of freeze dried *Bifidobacterium* over 30 days at 35°C and 70% RH (Nagawa et al., 1988).

Applications of Dried Probiotic Powder Ingredients

Dried powders containing probiotics may be applied to downstream processes, e.g., adjuncts for Cheddar cheese manufacture (Gardiner et al., 2002), malted beverages (O'Riordan et al., 2001) and the exploitation of bacteriocin

producing cultures (Mauriello et al., 1999; Morgan et al., 2001; Silva et al., 2002). For example, Rykba and Kailasapathy (1995) used freeze drying to manufacture a yoghurt powder containing *L. acidophilus*, *B. bifidum* and *B. longum*, while a spray dried probiotic skim milk powder containing 1×10^9 CFU/g rifampicin-resistant *L. paracasei* NFBC338 strain was a suitable adjunct inoculum for Cheddar cheese manufacture, resulting in probiotic numbers of $\sim 10^8$ CFU/g throughout ripening, without adversely affecting product quality (Gardiner et al., 2002). Mc Brearty et al. (2001) also used freeze dried inocula of the probiotic strains *B. lactis* Bb-12 and *B. longum* BB536 in Cheddar cheese. *B. lactis* Bb-12 survived at high numbers ($> 10^8$ CFU/g), while *B. longum* BB536 counts declined to 10^5 CFU/g over 6 months ripening. Freeze dried *B. lactis* Bb-12 has also been included in cereal bars (at 5×10^9 CFU per bar), and successfully used to deliver the strain to the human gastrointestinal tract (Ouweland et al., 2004) (Table 13.2).

TABLE 13.2
Examples of Some Recent Drying Trials Conducted with Probiotic Bacteria

Genus and Species	Medium	Conditions ^a	CFU/g	Reference
Spray drying				
<i>L. paracasei</i> NFBC 338	RSM (20% w/v)	170, 80–85°C	3.2×10^9	Gardiner et al. (2000)
<i>L. salivarius</i> UCC 118			5.2×10^7	
<i>L. rhamnosus</i> GG	RSM (20% w/v)	170, 85–90°C	2.9×10^9	Corcoran et al. (2004)
	RSM (10% w/v) and PD (10% w/v)		1×10^9	
<i>B. animalis</i> subsp. <i>lactis</i> BB12	RSM (20% w/v)	170, 85–90°C	1.7×10^9	Simpson et al. (2005)
<i>B. longum</i> B6	Fermented soymilk	100, 60–90°C	$\sim 10^7$	Wang et al. (2004)
<i>L. acidophilus</i>	Skim milk (25% w/v)	170, 80°C	2.9×10^7	
				Espina and Packard (1979)
Freeze drying				
<i>B. longum</i> B6	Fermented soymilk	n/a	$\sim 5 \times 10^7$	Wang et al. (2004)
<i>L. rhamnosus</i> E800	General edible medium (GEM)	n/a	$> 1 \times 10^{12}$	
<i>L. acidophilus</i>	Yoghurt ^b	n/a	8.7×10^6	Rykba and Kailasapathy (1995)
<i>B. longum</i> E194b	Skim milk (20% w/v) and malt extract (20% w/v)	n/a	$\sim 10^{10}$	
				Nagawa et al. (1988)

n/a: not applicable.
^a Temperatures indicate inlet and outlet temperatures, respectively.
^b program Yoghurt also contained *L. bulgaricus*, *S. thermophilus*, *B. bifidum* and *B. longum*.

Conclusions

In the last decade there has been a dramatic increase in the number of clinical studies supporting the concept that ingestion of probiotic cultures is health-promoting. However, a prerequisite to generating probiotic food products is the ability to cost-effectively produce stable dried culture preparations. To achieve this, both freeze drying and spray drying have been used, with both approaches having advantages and disadvantages. Furthermore, stability during storage is critical to the successful development of probiotic foods, with viability invariably inversely linearly related to storage temperature. In this chapter, we have attempted to outline the main technical issues associated with retention of viability during processing of sensitive cultures, and have presented the main approaches for successful drying of live probiotics.

Acknowledgments

This work was funded by the Irish Government under the National Development Plan 2000–2006, by the European Research and Development Fund, the EU project QLK-CT-2000-30042 and Science Foundation Ireland. B. Corcoran is in receipt of a Teagasc Walsh Fellowship.

References

- Abd-El-Gawad, I.A., Metwally, M.M., El Nockrashy, S.A., and Ahmed, K.E. Spray drying of lactic acid cultures II: the effect of culture conditions and storage on microorganisms' survival, *Egypt. J. Dairy Sci.*, 17, 273, 1989.
- Ananta, E., Birkeland, S.-E., Corcoran, B., Fitzgerald, G., Hinz, S., Klijn, A., Matto, J., Mercernier, A., Nilsson, U., Nyman, M., O'Sullivan, E., Parche, S., Rautonen, N., Ross, R.P., Saarela, M., Stanton, C., Stahl, U., Soumalainen, T., Vincken, J.-P., Virkajarvi, I., Voragen, F., Wesenfeld, J., Wouters, R., and Knorr, D. Processing effects on the nutritional advancement of probiotics and prebiotics, *Microb. Ecol. Health Dis.*, 16, 114, 2004.
- Ananta, E. and Knorr, D. Evidence on the role of protein biosynthesis in the induction of heat tolerance of *Lactobacillus rhamnosus* GG by pressure pre-treatment, *Int. J. Food Microbiol.*, 96, 307, 2004.
- Bielecka, M. and Majkowska, A. Effect of spray drying temperature of yoghurt on the survival of starter cultures, moisture content and sensoric properties of yoghurt powder, *Nahrung*, 44, 257, 2000.
- Brennan, M., Wanismail, B., Johnson, M.C., and Ray, B. Cellular damage in dried *Lactobacillus acidophilus*, *J Food Prot.*, 49, 47, 1986.
- Brigidi, P., Vitali, B., Swennen, E., Bazzocchi, G., and Matteuzzi, D. Effects of probiotic administration upon the composition and enzyme activity of human faecal microbiota in patients with irritable bowel syndrome, *Res. Microbiol.*, 152, 735, 2001.

- Carvalho, A.S., Silva, J., Ho, P., Teixeira, P., Malcata, F.X., and Gibbs, P. Effects of various sugars added to growth and drying media upon thermotolerance and survival throughout storage of freeze-dried *Lactobacillus delbrueckii* ssp. *bulgaricus*, *Biotechnol. Progr.*, 20, 248, 2004.
- Castro, H.P., Teixeira, P.M., and Kirby, R. Evidence of membrane damage in *Lactobacillus bulgaricus* following freeze drying, *J. Appl. Microbiol.*, 82, 87, 1997.
- Chopin, A., Mocquot, G., and Le Graet, Y. Destruction of *Microbacterium lacticum*, *Escherichia coli* and *Staphylococcus aureus* in milk by spray drying. II. Effect of drying conditions, *Can. J. Microbiol.*, 23, 755, 1977.
- Cleland, D., Krader, P., McCree, C., Tang, J., and Emerson, D. Glycine betaine as a cryoprotectant for prokaryotes, *J. Microbiol. Methods*, 58, 31, 2004.
- Conrad, P.B., Miller, D.P., Cielenski, P.R., and de Pablo, J.J. Stabilization and preservation of *Lactobacillus acidophilus* in saccharide matrices, *Cryobiology*, 41, 17, 2000.
- Corcoran, B.M., Ross, R.P., Fitzgerald, G.F., and Stanton, C. Comparative survival of probiotic lactobacilli spray-dried in the presence of prebiotic substances, *J. Appl. Microbiol.*, 34, 1024, 2004.
- Crowe, L.M., Crowe, J.H., Rudolph, A., Womersley, C., and Appel, L. Preservation of freeze dried liposomes by trehalose, *Arch. Biochem. Biophys.*, 242, 240, 1985.
- Cummings, J.H. and Macfarlane, G.T. Gastrointestinal effects of prebiotics, *Br. J. Nutr.*, 87, S145, 2002.
- Daeman, A.L.H. and van der Stege, H.J. The destruction of enzymes and bacteria during the spray-drying of milk and whey. 2. The effect of the drying, *Neth. Milk Dairy J.*, 36, 211, 1982.
- Desmond, C., Ross, R.P., O'Callaghan, E., Fitzgerald, G., and Stanton, C. Improved survival of *Lactobacillus paracasei* NFBC 338 in spray-dried powders containing gum acacia, *J. Appl. Microbiol.*, 93, 1003, 2002.
- Desmond, C., Stanton, C., Fitzgerald, G.F., Collins, K., and Ross, R.P. Environmental adaptation of probiotic lactobacilli towards improvement of performance during spray drying, *Int. Dairy J.*, 11, 801, 2001.
- de Valdez, G.F., Martos, G., Taranto, M.P., Lorca, G.L., Oliverde, G., and Ruiz Holgado, A.P. Influence of bile on beta-galactosidase activity and cell viability of *Lactobacillus reuteri* when subjected to freeze-drying, *J. Dairy Sci.*, 80, 1955, 1997.
- de Vos, W.M., Bron, P.A., and Kleerebezem, M. Post-genomics of lactic acid bacteria and other food-grade bacteria to discover gut functionality, *Curr. Opin. Biotechnol.*, 15, 86, 2004.
- Erdeve, O., Tiras, U., and Dallar, Y. The probiotic effect of *Saccharomyces boulardii* in a pediatric age group, *J. Trop. Pediatr.*, 50, 234, 2004.
- Espina, F. and Packard, V.S. Survival of *Lactobacillus acidophilus* in a spray-drying process, *J. Food Prot.*, 42, 149, 1979.
- FAO/WHO, Evaluation of health and nutritional properties of powder milk with live lactic acid bacteria., Report from FAO/WHO expert consultation 1–4 October, 2001.
- Felley, C.P., Corthesy-Theulaz, I., Rivero, J.L., Sipponen, P., Kaufmann, M., Bauerfeind, P., Wiesel, P.H., Brassart, D., Pfeifer, A., Blum, A.L., and Michetti, P. Favourable effect of an acidified milk (LC-1) on *Helicobacter pylori* gastritis in man, *Eur. J. Gastroenterol. Hepatol.*, 13, 25, 2001.
- Foster, E.M. VI Culture preservation, *J. Dairy Sci.*, 45, 1290, 1962.

- Fu, W.-Y. and Etzel, M.R. Spray drying of *Lactococcus lactis* ssp. *lactis* C2 and cellular injury, *J. Food Sci.*, 60, 195, 1995.
- Gardiner, G.E., Bouchier, P., O'Sullivan, E., Kelly, J., Collins, J.K., Fitzgerald, G.F., Ross, R.P., and Stanton, C. A spray dried culture for probiotic Cheddar cheese manufacture, *Int. Dairy J.*, 12, 749, 2002.
- Gardiner, G.E., O'Sullivan, E., Kelly, J., Auty, M.A., Fitzgerald, G.F., Collins, J.K., Ross, R.P., and Stanton, C. Comparative survival rates of human-derived probiotic *Lactobacillus paracasei* and *L. salivarius* strains during heat treatment and spray drying, *Appl. Environ. Microbiol.*, 66, 2605, 2000.
- Gomez Zavaglia, A., Tymczyszyn, E., De Antoni, G., and Anibal Disalvo, E. Action of trehalose on the preservation of *Lactobacillus delbrueckii* ssp. *bulgaricus* by heat and osmotic dehydration, *J. Appl. Microbiol.*, 95, 1315, 2003.
- Gosselink, M.P., Schouten, W.R., van Lieshout, L.M., Hop, W.C., Laman, J.D., and Ruseler-van Embden, J.G. Delay of the first onset of pouchitis by oral intake of the probiotic strain *Lactobacillus rhamnosus* GG, *Dis. Colon Rectum*, 47, 876, 2004.
- Guandalini, S., Pensabene, L., Zikri, M.A., Dias, J.A., Casali, L.G., Hoekstra, H., Kolacek, C., Massar, K., Micetic-Turk, D., Papadopoulou, A., De Sousa, J.S., Sandhu, B., Szajewska, H., and Wieszmann, Z. *Lactobacillus* G.G. administered in oral rehydration solution to children with acute diarrhoea: a multicenter European trial, *J. Pediatr. Gastroenterol. Nutr.*, 30, 54, 2000.
- Hardy, J., Scher, J., and Banon, S. Water activity and hydration of dairy powders, *Lait*, 82, 441, 2002.
- Hubalek, Z. Protectants used in the cryopreservation of microorganisms, *Cryobiology*, 46, 205, 2003.
- Ishibashi, N., Tatematsu, T., Shimura, S., Tomita, M., and Okonogi, S., Effect of water activity on the viability of freeze-dried bifidobacteria and lactic acid bacteria, in I.I.F.-I.I.R.-Commission C1, Tokyo, Japan — 1985/1,227-32 (1985).
- Isolauri, E., Juntunen, M., Rautanen, T., Sillanauke, P., and Koivula, T. A human *Lactobacillus* strain (*Lactobacillus casei* sp. strain GG) promotes recovery from acute diarrhea in children, *Pediatrics*, 88, 90, 1991.
- Isolauri, E., Salminen, S., and Mattila-Sandholm, T. New functional foods in the treatment of food allergy, *Ann. Med.*, 31, 299, 1999.
- Isolauri, E., Sutas, Y., Kankaanpää, P., Arvilommi, H., and Salminen, S. Probiotics: effects on immunity, *Am. J. Clin. Nutr.*, 73, S444, 2001.
- Jiang, T., Mustapha, A., and Saviano, D.A. Improvement of lactose digestion by ingestion of unfermented milk containing *Bifidobacterium longum*, *J. Dairy Sci.*, 79, 750, 1996.
- Johnson, J.A.C. and Etzel, M.R. Inactivation of lactic acid bacteria during spray drying, *AIChE Symp. Ser.*, 89, 98, 1993.
- Kalliomaki, M., Salminen, S., Arvilommi, H., Kero, P., Koskinen, P., and Isolauri, E. Probiotics in primary prevention of atopic disease: a randomised placebo-controlled trial, *Lancet*, 357, 1076, 2001.
- Kim, S.S. and Bhowmik, S.R. Survival of lactic acid bacteria during spray drying of plain yoghurt, *J. Food Sci.*, 55, 1008, 1990.
- Kim, H.J., Camilleri, M., McKinzie, S., Lempke, M.B., Burton, D.D., Thomforde, G.M., and Zinsmeister, A.R. A randomized controlled trial of a probiotic VSL#3, on gut transit and symptoms in diarrhoea-predominant irritable bowel syndrome, *Aliment Pharmacol. Ther.*, 17, 895, 2003.
- Knorr, D. Technology aspects related to microorganisms in functional foods, *Trends Food Sci. Technol.*, 9, 295, 1998.

- Kosanke, J.W., Osburn, R.M., Shuppe, G.I., and Smith, R.S. Slow rehydration improves the recovery of dried bacterial populations, *Can. J. Microbiol.*, 38, 520, 1992.
- Kullen, M.J. and Klaenhammer, T.R. Identification of the pH-inducible, proton-translocating F1F0-ATPase (atpBEFHAGDC) operon of *Lactobacillus acidophilus* by differential display: gene structure, cloning and characterization, *Mol. Microbiol.*, 33, 1152, 1999.
- Labuza, T.P., Jones, K.A., Sinskey, A.J., Gomez, F., Wilson, S., and Miller, B. Effect of drying conditions on cell viability and functional properties of single cell protein, *J. Food Sci.*, 37, 103, 1972.
- Laroche, C. and Gervais, P. Unexpected thermal destruction of dried, glass bead-immobilized microorganisms as a function of water activity, *Appl. Environ. Microbiol.*, 59, 3015, 2003.
- Leslie, S.B., Israeli, E., Lighthart, B., Crowe, J.H., and Crowe, L.M. Trehalose and sucrose protect both membranes and proteins in intact bacteria during drying, *Appl. Environ. Microbiol.*, 61, 3592, 1995.
- LiCari, J.J. and Potter, N.N. *Salmonella* survival during spray drying and subsequent handling of skim milk powder. II. Effects of drying conditions, *J. Dairy Sci.*, 53, 871, 1970.
- Lian, W.C., Hsiao, H.C., and Chou, C.C. Survival of bifidobacteria after spray-drying, *Int. J. Food Microbiol.*, 74, 79, 2002.
- Linders, L.J.M., Wolkers, W.F., Hoekstra, F.A., and van't Riet, K. Effect of added carbohydrates on membrane phase behaviour and survival of dried *Lactobacillus plantarum*, *Cryobiology*, 35, 31, 1997.
- Marechal, P.A. Martinez de Marnanon, I., Poirer, I., Gervais, P., The importance of kinetics of application of physical stresses on the viability of microorganisms: significance for minimal food processing, *Trends Food Sci. Technol.*, 10, 15, 1999.
- Martini, M.C., Lerebours, E.C., Lin, W., and Harlander, S.K. Strains and species of lactic acid bacteria in fermented milks (yoghurts): effect on in vivo lactose digestion, *Am. J. Clin. Nutr.*, 54, 1041, 1991.
- Mattila-Sandholm, T., Blum, S., Collins, J.K., Crittenden, R., de Vos, W., Dunne, C., Fonden, R., Grenov, G., Isolauri, E., Kiely, B., Marteau, P., Morelli, L., Ouwehand, A., Reniero, R., Saarela, M., Salminen, S., Saxelin, M., Schriffen, E., Shanahan, F., Vaughan, E., and von Wright, A. Probiotics: towards demonstrating efficacy, *Trends Food Sci. Technol.*, 10, 393, 1999.
- Mauriello, G., Aponte, M., Andolfi, R., Moschetti, G., and Villani, F. Spray-drying of bacteriocin-producing lactic acid bacteria, *J. Food Prot.*, 62, 773, 1999.
- Mc Brearty, S., Ross, R.P., Fitzgerald, G.F., Collins, J.K., Wallace, J.M., and Stanton, C. Influence of two commercially available bifidobacteria cultures on Cheddar cheese quality, *Int. Dairy J.*, 11, 599, 2001.
- Miller, D.L., Goepfert, J.M., and Amundson, C.H. Survival of salmonellae and *Escherichia coli* during the spray drying of various food products, *J. Food Sci.*, 37, 828, 1972.
- Monnet, C., Beal, C., and Corrieu, G. Improvement of the resistance of *Lactobacillus delbrueckii* ssp. *bulgaricus* to freezing by natural selection, *J. Dairy Sci.*, 86, 3048, 2003.
- Morgan, S.M., Galvin, M., Ross, R.P., and Hill, C. Evaluation of a spray-dried lactacin 3147 powder for the control of *Listeria monocytogenes* and *Bacillus cereus* in a range of food systems, *Lett. Appl. Microbiol.*, 33, 387, 2001.

- Nagao, F., Nakayama, M., Muto, T., and Okumura, K. Effects of a fermented milk drink containing *Lactobacillus casei* strain Shirota on the immune system in healthy human subjects, *Biosci. Biotechnol. Biochem.*, 64, 2706, 2000.
- Nagawa, M., Nakabayashi, A., and Fuj, S. Preparation of the bifidus milk powder, *J. Dairy Sci.*, 71, 1777, 1988.
- O'Riordan, K., Andrews, D., Buckle, K., and Conway, P. Evaluation of microencapsulation of a Bifidobacterium strain with starch as an approach to prolonging viability during storage, *J. Appl. Microbiol.*, 91, 1059, 2001.
- Ouwehand, A.C., Kurvinen, T., and Rissanen, P. Use of a probiotic Bifidobacterium in a dry food matrix, an in vivo study, *Int. J. Food Microbiol.*, 95, 103, 2004.
- Ouwehand, A.C., Salminen, S., and Isolauri, E. Probiotics: an overview of beneficial effects, *Antonie Van Leeuwenhoek*, 82, 279, 2002.
- Picot, A. and Lacroix, C. Encapsulation of bifidobacteria in whey protein-based microcapsules and survival in simulated gastrointestinal conditions and in yoghurt, *Int. Dairy J.*, 14, 505, 2004.
- Plummer, S., Weaver, M.A., Harris, J.C., Dee, P., and Hunter, J. *Clostridium difficile* pilot study: effects of probiotic supplementation on the incidence of *C. difficile* diarrhoea, *Int. Microbiol.*, 7, 59, 2004.
- Potts, M. Desiccation tolerance of prokaryotes, *Microbiol. Rev.*, 58, 755, 1994.
- Prajapati, J.B., Shah, R.K., and Dave, J.M. Survival of *Lactobacillus acidophilus* — spray dried acidophilus preparations, *Aus. J. Dairy Technol.*, 42, 17, 1987.
- Prasad, J., McJarrow, P., and Gopal, P. Heat and osmotic stress responses of probiotic *Lactobacillus rhamnosus* HN001 (DR20) in relation to viability after drying, *Appl. Environ. Microbiol.*, 69, 917, 2003.
- Reid, G., Jass, J., Sebelsky, M.T., and McCormick, J.K. Potential uses of probiotics in clinical practice, *Clin. Microbiol. Rev.*, 16, 658, 2003.
- Rogelz, I. Lactic acid bacteria as probiotic, *Mljekarstvo*, 44, 277, 1994.
- Ross, R.P., Desmond, C., Fitzgerald, G.F., and Stanton, C. Overcoming the technological hurdles in the development of probiotic foods, *J. Appl. Microbiol.*, 98, 1410, 2005.
- Rykba, S. and Kailasapathy, K. The survival of culture bacteria in fresh and freeze dried AB yoghurts, *Aus. J. Dairy Technol.*, 50, 51, 1995.
- Saarela, M., Mogensen, G., Fonden, R., Matto, J., and Mattila-Sandholm, T. Probiotic bacteria: safety, functional and technological properties, *J. Biotechnol.*, 84, 197, 2000.
- Saavedra, J.M., Bauman, N.A., Oung, I., Perman, J.A., and Yolken, R.H. Feeding of *Bifidobacterium bifidum* and *Streptococcus thermophilus* to infants in hospital for prevention of diarrhoea and shedding of rotavirus, *Lancet*, 344, 1046, 1994.
- Saggioro, A. Probiotics in the treatment of irritable bowel syndrome, *J. Clin. Gastroenterol.*, 38, S104, 2004.
- Shah, N.P. Probiotic bacteria: selective enumeration and survival in dairy foods, *J. Dairy Sci.*, 83, 894, 2000.
- Shanahan, F. Probiotics and inflammatory bowel disease: is there a scientific rationale?, *Inflamm. Bowel Dis.*, 6, 107, 2000.
- Shornikova, A.V., Casas, I.A., Isolauri, E., Mykkanen, H., and Vesikari, T. *Lactobacillus reuteri* as a therapeutic agent in acute diarrhea in young children, *Eur. J. Clin. Nutr.*, 24, 399, 1997.
- Silva, J., Carvalho, A.S., Teixeira, P., and Gibbs, P.A. Bacteriocin production by spray-dried lactic acid bacteria, *Lett. Appl. Microbiol.*, 34, 77, 2002.

- Simpson, P.J., Stanton, C., Fitzgerald, G., and Ross, R.P. Intrinsic tolerance of *Bifidobacterium* species to heat and oxygen and survival following spray drying and storage, *J. Appl. Microbiol.*, 99, 493, 2005.
- Stanton, C., Desmond, C., Coakley, M., Collins, J.K., Fitzgerald, G.F., and Ross, R.P. Challenges facing development of probiotic-containing functional foods, *Handbook of Fermented Foods*, E.R. Farnworth, ed., CRC Press, Boca Raton, FL, pp. 27–58, 2003.
- Stanton, C., Desmond, C., Fitzgerald, G., and Ross, R.P. Probiotic health benefits — myth or reality?, *Aus. J. Dairy Technol.*, 58, 107, 2003.
- Stanton, C., Gardiner, G., Lynch, P.B., Collins, J.K., and Ross, R.P. Probiotic cheese, *Int. Dairy J.*, 8, 491, 1998.
- Teixeira, P., Castro, H., and Kirby, R. Spray drying and a method for preparing concentrated cultures of *Lactobacillus bulgaricus*, *J. Appl. Microbiol.*, 78, 456, 1995.
- Teixeira, P., Castro, H., Malcata, F.X., and Kirby, R.M. Survival of *Lactobacillus delbruekii* spp. *bulgaricus* following spray-drying, *J. Dairy Sci.*, 78, 1025, 1995.
- Teixeira, P., Castro, H., Mohacsi-Farkas, C., and Kirby, R. Identification of sites of injury in *Lactobacillus bulgaricus* during heat stress, *J. Appl. Microbiol.*, 83, 219, 1997.
- To, B.C.S. and Etzel, M.R. Spray drying, freeze drying or freezing of three different lactic acid bacteria species, *J. Food Sci.*, 62, 576, 1997.
- Walker, D.C., Girgis, H.S., and Klaenhammer, T.R. The groESL chaperone operon of *Lactobacillus johnsonii*, *Appl Environ. Microbiol.*, 65, 3033, 1999.
- Wang, Y.C., Yu, R.C., and Chou, C.C. Viability of lactic acid bacteria and bifidobacteria in fermented soymilk after drying, subsequent rehydration and storage, *Int. J. Food Microbiol.*, 93, 209, 2004.
- van de Guchte, M., Serror, P., Chervaux, C., Smokvina, T., Ehrlich, S.D., and Maguin, E. Stress responses in lactic acid bacteria, *Antonie Van Leeuwenhoek*, 82, 187, 2002.

Part 4: Water and the Structure and Stability of Microdisperse Systems

14

Proteins and Lipids Can Alter the Thermodynamic and Dynamic Characteristics of Water at Fluid Interfaces

Juan Miguel Rodríguez-Patino, María Rosario Rodríguez-Niño,
Cecilio Carrera-Sánchez, and Ana Lucero-Caro

CONTENTS

Introduction	251
Spreading and Adsorption at Equilibrium.....	254
Dynamics of Adsorption	257
Film Structural Characteristics	258
Reflectivity and Viscoelastic Properties of LMWE (Monoglycerides)	261
Long-Term Relaxation Phenomena in Protein and LMWE Monolayers..	263
Spreading and Adsorption of Protein and LMWE Mixed Films at Equilibrium.....	265
Surface Tension of Protein + Oil-Soluble LMWE.....	265
Surface Tension of Protein + Water-Soluble LMWE.....	265
Structural and Topographical Characteristics of Protein–LMWE Mixed Films	266
Long-Term Relaxation Phenomena in Protein–LMWE Mixed Films.....	267
Dilatational Characteristics of Protein–LMWE Mixed Films	267
Surface Shear Characteristics of Protein–LMWE Mixed Monolayers.....	268
Protein–LMWE Mixed Films (Orogenic Mechanism).....	270
Acknowledgments	271
References	271

Introduction

Many natural and processed foods consist of dispersions or have been in a dispersed state at some time during their formation. Most of these food

dispersions are emulsions and foams. These dispersions include traditional food formulations (such as bakery, confectionery or meat products, ice cream, dressings, etc.) or new formulations (low fat and instant foods, high- or low-alcohol food formulations, functional foods, etc.). Thus, the analysis of food colloids is of practical importance.

The manufacture of dispersion-based food products with specific quality attributes depends on the selection of the most appropriate raw materials and processing conditions (Dickinson, 1982; McClements, 1999). Food dispersions do not form spontaneously. In order to make a stable dispersion, a large amount of mechanical energy must be supplied (Walstra, 1993). The free energy required to increase the area of air- or oil–water interface is proportional to the surface or interfacial tension. The surface or interfacial tension is usually also referred to as surface free energy. The term surface free energy implies that work is required to form more surface; that is, to bring molecules from the interior of the phase to the surface region.

In thermodynamic terms, emulsification and foaming are extremely inefficient processes because only a relatively small amount of the mechanical energy is used for the surface free energy (Walstra, 1993). In fact, most of the mechanical energy is dissipated as heat. In practice, it is possible to form a dispersed systems from two immiscible phases, but the particles tend to merge when they collide with each other, and this leads to complete phase separation. This is because dispersions are energetically and thermodynamically unstable systems. However, from a practical point of view, it is possible to form dispersions that are kinetically stable (or metastable) for a reasonable period of time by including substances known as emulsifiers and/or stabilizers. In fact, to stabilize food emulsions and foams, emulsifiers must be placed at the interface forming a film around droplets or bubbles, respectively. Two types of emulsifiers are used in foods (Dickinson, 1982; Hassenhuette and Hartel, 1997; Whitaker et al., 1998; McClements, 1999): low molecular weight emulsifiers (LMWE), mainly mono- and diglycerides, phospholipids, etc., and macromolecules (proteins and certain hydrocolloids). From a thermodynamic point of view, these emulsifiers decrease the surface tension and thus the free energy of the system, and impart the desired kinetic stability to the dispersion (emulsion or foam). The increasing demand for low-fat products, convenience, instant, and functional foods has placed a greater importance upon the use of emulsifiers in foods. The formation and stability of these dispersed systems (food emulsions and foams), and their organoleptic characteristics are very dependent on the thermodynamic and dynamic characteristics of the films that these emulsifiers form at fluid interfaces (both air- and oil–water interfaces).

The adsorption of emulsifiers at fluid–fluid interfaces is considered to play an important role in the formation and stabilization of food dispersions (Dickinson, 1982). During the formation of a dispersed system, the emulsifier must be adsorbed at the interface to prevent the recoalescence of the initially formed dispersed particles (bubbles or droplets). In addition, during

emulsifier adsorption, the surface or interfacial tension of the fluid interfaces lowers, which is an important factor both to optimize the input of energy involved in the emulsification or foaming process and, finally, to achieve smaller particle size, which is an important factor for the stability of the dispersed system (Figure 14.1).

The interfacial characteristics of the adsorbed films depend on the interactions between emulsifiers at fluid interfaces (Patino and Niño, 1999; Horne and Patino, 2003; Niño et al., 2003). Thus, from a fundamental point of view, orientational phenomena and domain structure are of particular interest. In this regard the structure and topography of the monolayer are of great utility. However, real foods contain mixtures of both classes of emulsifiers that stabilize the interface and can contribute to the stability or instability of the dispersions. The interactions between both of them are also of great importance for the formation and stability of the dispersion (Figure 14.1). Thus, an understanding of these phenomena is a key factor in the development of strategies for controlling dispersion instability.

However, nonequilibrium processes occur in many systems containing emulsifiers at fluid interfaces (Figure 14.1). Thus, relaxation phenomena have great importance from a practical point of view in emulsifier films that stabilize food dispersions. The dynamic phenomena and the development of intermolecular associations at the interface lead to alterations in surface properties that have measurable rheological consequences (Murray and Dickinson, 1996; Murray, 1998, 2002; Bos and van Vliet, 2001); that is, surface

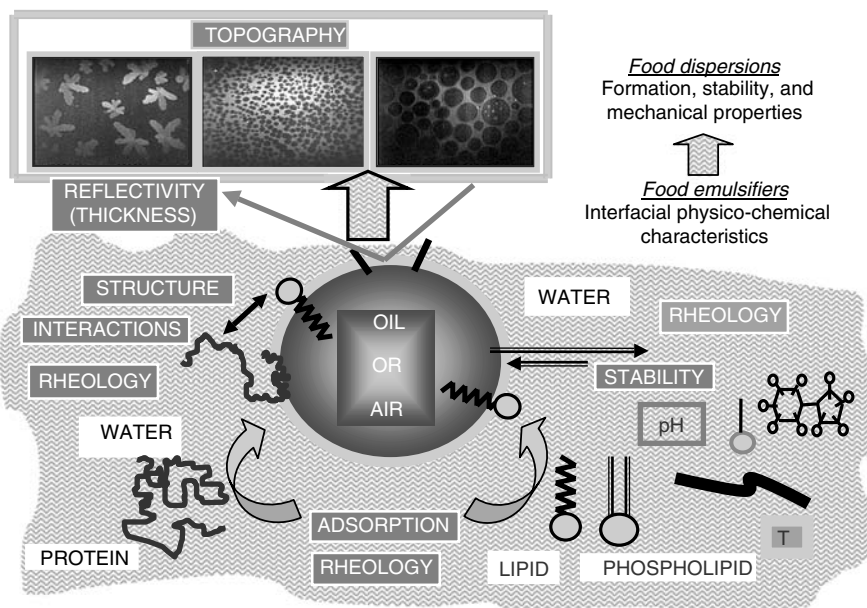


FIGURE 14.1

Interfacial physico-chemical characteristics of food emulsifiers at fluid interfaces.

rheology is very sensitive to the structural characteristics and relaxation phenomena of emulsifiers at interfaces.

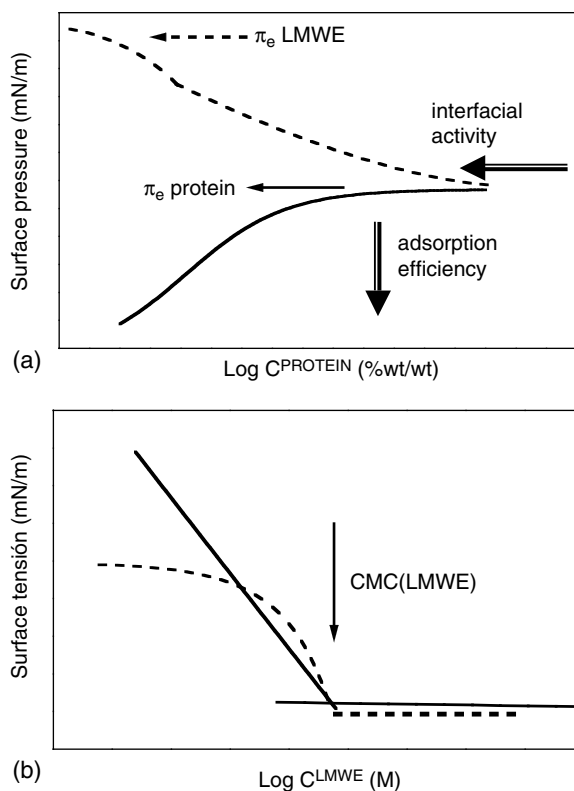
In this analysis we have also included the effect of the aqueous phase composition (pH, sugars, ethanol, hydrocolloids, salts, etc.) and the processing conditions (temperature). By incorporating solutes in the aqueous phase, we hope to approach the behavior of a simple well-defined model of complex, real food formulations.

In summary, the formation, stability, and mechanical properties of food dispersed systems depend on the way in which the constituent particles and macromolecules adsorb and interact at fluid–fluid interfaces (Figure 14.1). Thus, the optimum use of emulsifiers depends on our knowledge of their interfacial physico-chemical characteristics — such as surface activity, structure, stability, superficial viscosity, etc. — and the kinetics of film formation at fluid–fluid interfaces.

Spreading and Adsorption at Equilibrium

The protein concentration (C) dependence on surface pressure (π), that is, the surface pressure isotherm, showed sigmoidal behavior (Figure 14.2) (Niño et al., 2005). At low protein concentrations, the initial solutions caused only a small increase in π . The surface pressure increased with C and tended to a plateau. This plateau commenced at the point where π reached its maximum value over the range of protein concentrations. The behavior of adsorbed protein films can be interpreted in terms of monolayer coverage. At the lower C , as the π value is close to zero, the adsorbed protein residues may be considered as a two-dimensional ideal gas. Proteins at higher C , but lower than that of the plateau, form a monolayer of irreversibly adsorbed molecules. As the plateau is attained, the monolayer is saturated by protein that is irreversibly adsorbed. The protein concentration at which the plateau is attained is the adsorption efficiency (AE). At higher C , the protein molecules may form multilayers beneath the primary monolayer, but these structures do not contribute significantly to the surface pressure. The maximum π at the plateau is the superficial activity (SA).

Some differences exist between milk and soy proteins depending on the pH (Niño et al., 2005). The superficial activity of milk and soy proteins is almost identical at neutral pH. However, at pH 5 (close to the isoelectric point (pI) of these proteins), the superficial activity of soy proteins is lower than at neutral pH. Moreover, at pH 5 the superficial activity of soy proteins is lower than for milk proteins. The adsorption efficiency is also lower at pH 5, especially for soy globulins. The lower surface activity at pH 5 coincides with an aggregation of soy proteins at interface and in the bulk phase, a phenomenon which explains the bad foaming and emulsifying properties of soy and other vegetable proteins at the pI.

**FIGURE 14.2**

(a) The effect of spreading of an oil-soluble LMWE (discontinuous line) on a film of (solid line) protein previously adsorbed on the air–water interface. The arrows indicate the equilibrium surface pressures (π_e) for LMWE and protein. C is the concentration of protein in the bulk phase. The amount of LMWE spread on the protein film is enough to saturate the monolayer by itself. At the higher concentrations of protein in the bulk phase the surface activity (SA) of the mixed film is similar to that for pure protein. At the lower concentrations of protein in the bulk phase the SA of the mixed film is similar to the equilibrium surface pressure of the LMWE. (b) The effect of addition of a protein (discontinuous line) on a film a water-soluble LMWE (solid line) previously adsorbed on the air–water interface. The arrow indicate the critical micelar concentration (CMC) for LMWE.

Equilibrium spreading pressures (π_e) of proteins and LMWE at the air–water interface as a function of pH and temperature were also studied (Patino and Martín, 1994; Niño et al., 2001, 2005). The equilibrium spreading pressure is a measure of the surface activity of spread films at equilibrium. The magnitude of π_e was dependent on the emulsifier and on the aqueous phase composition. For example, the minimum π_e for 7 and 11 S soy globulin fractions at pH 5 as compared with π_e on aqueous solutions at pH different to pI can be explained by the fact that the protein is more difficult to convert into a monolayer at its isoelectric point. This behavior is not observed for globular milk proteins (like WPI).

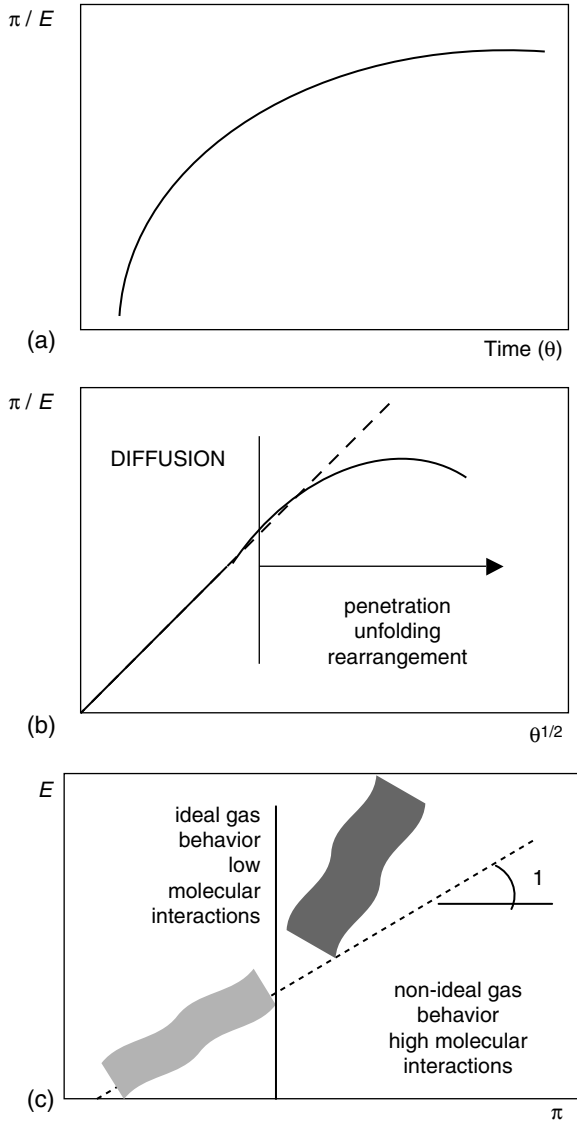


FIGURE 14.3

(a) Time dependence of surface pressure (π) and surface dilatational modulus (E), (b) application of the Ward–Tordai equation — $\pi = 2C_0KT/(D\theta/3.14)^{1/2}$, where C is the concentration in the bulk phase, K is the Boltzman constant, T is the absolute temperature and D is the diffusion coefficient — and (c) surface dilatational modulus as a function of surface pressure for emulsifier adsorbed films at fluid interfaces.

Dynamics of Adsorption

The dynamics of adsorption of emulsifiers at fluid interfaces have been determined by tensiometry and surface rheology (Figure 14.3); that is, from the time dependence of surface pressure and surface dilatational modulus (E). We found that π and E increase with time (θ), which should be associated with emulsifier adsorption (Patino and Niño, 1999; Niño et al., 2003; Carrera et al., 2005).

The adsorption kinetic of emulsifiers at short adsorption time may be quantified by the diffusion of the protein towards the interface (Walstra, 1993) in agreement with the Ward and Tordai model (Figure 14.3b). However, at long-term adsorption, a first-order kinetic model is a satisfactory mathematical description of the rheokinetic data (π vs. θ and E vs. θ) for protein adsorption and unfolding at the interface. In practice, a plot of these equations usually yields two or more linear regions. The initial slope is taken to correspond to a first-order rate constant of unfolding, while the second slope is taken to correspond to a first-order rate constant of rearrangement, occurring among a more or less constant number of adsorbed molecules (Niño et al., 2003).

Transient surface dynamic properties of emulsifier adsorbed films also depend on emulsifier concentration in the bulk phase. As a general rule it was observed that the rate of π or E change over time increases when the emulsifier concentration in the bulk phase is increased. These data should be associated with emulsifier adsorption at the interface; that is, emulsifier adsorption at the interface is facilitated at higher emulsifier concentrations in the bulk phase.

The application of the Ward and Tordai equation to monitor the kinetics of diffusion of emulsifiers at the air–water interface is shown in Figure 14.3b. We find, for all emulsifier concentrations in the bulk phase, a good fit of the experimental data in agreement with the Ward and Tordai equation, at low π (Niño and Patino, 2002; Niño et al., 2003). Thus, it can be concluded that during the initial period the kinetics of emulsifier adsorption at fluid interfaces is controlled by a diffusion mechanism. The discrepancies observed at longer adsorption time for the adsorption of proteins could be attributed to an energy barrier related to the penetration, unfolding, and rearrangement of the emulsifier at the interface after the diffusion.

To analyze the effect of emulsifier concentration and aqueous phase composition on the kinetics of diffusion (k_{diff}), the evolution of the slope of π vs. $\theta^{1/2}$ or E vs. $\theta^{1/2}$ is of great utility (Niño et al., 2003). We have observed that k_{diff} increases with the emulsifier concentration in the bulk phase according to the Ward and Tordai equation. The presence of sucrose in the aqueous phase increases the diffusion of proteins towards the interface. However, k_{diff} is lower in ethanol aqueous solutions than in water. In addition, k_{diff} decreases with increasing ethanol or at higher sucrose concentrations in the aqueous phase (Niño et al., 2003).

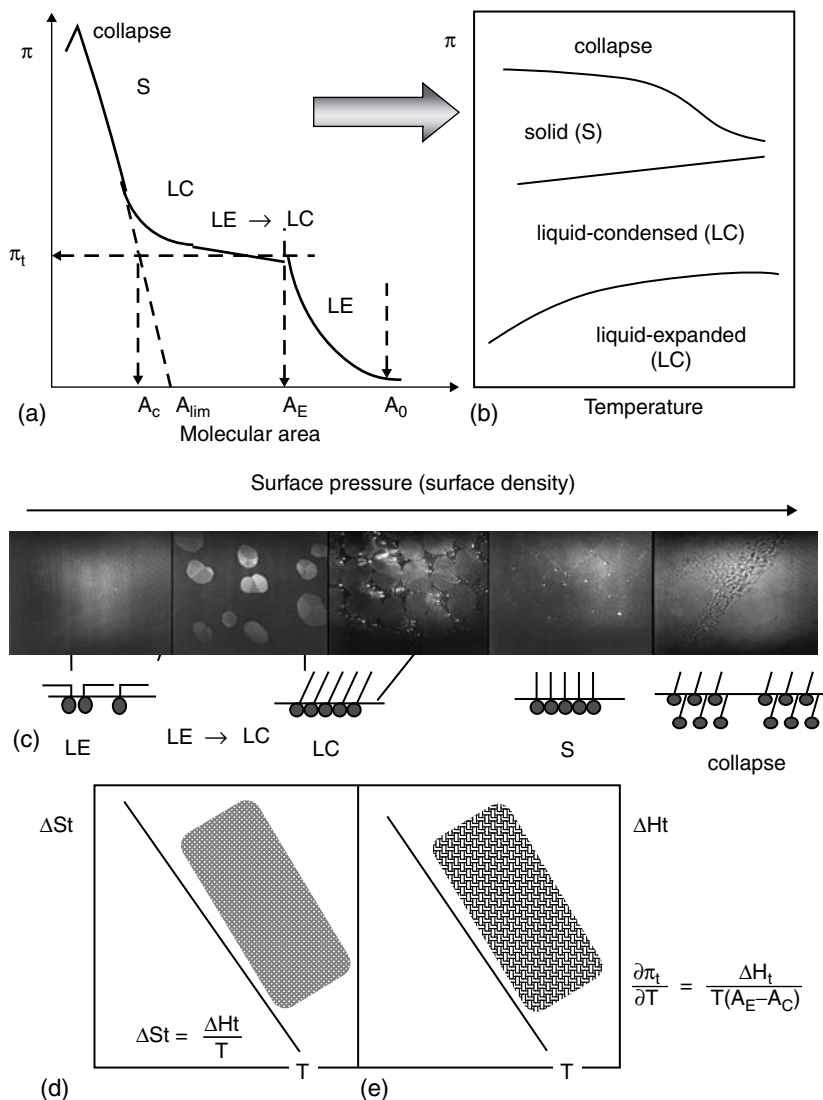
Solutes are one of the major components of foods, and they have significant effects on their adsorption at fluid interfaces. In addition, the study of the effects of ethanol and/or sucrose on protein adsorption at fluid interfaces is of practical importance in the manufacture of food dispersions. The presence of ethanol in the bulk phase apparently introduces an energy barrier for the protein diffusion towards the interface. This could be attributable to competition with previously adsorbed ethanol molecules for the penetration of the protein into the interface. However, if ethanol causes denaturation and/or aggregation of the protein in the bulk phase, the diffusion of the protein towards the interface could be diminished. The causes of the higher rate of protein diffusion from aqueous solutions of sucrose, in comparison with that observed for water, must be different in aqueous ethanol solutions. Since protein molecules are preferentially hydrated in the presence of sucrose, it is possible that sucrose limits protein unfolding in the bulk phase and reduces protein–protein interactions in the bulk phase and at the interface. Both of these phenomena may increase the rate of protein diffusion towards the interface. Clearly, the kinetics of adsorption of proteins at interfaces are highly complex, especially in the presence of typical food solutes such as ethanol and sucrose in the aqueous phase.

In Figure 14.3c a normalization in a single master curve of E vs. π data reflects the interfacial behavior of emulsifier adsorbed films for different emulsifier concentrations, at different adsorption times, and under different processing conditions (Niño and Patino, 2002; Niño et al., 2003). The plot suggests that interactions between adsorbed emulsifier molecules (residues) increase with π . In fact, at lower π values the slope of the E – π plot was close to 1, which corresponds to the behavior of an ideal gas with low emulsifier interactions. However, at higher π values the slope changes, which implies an important nonideal behavior with higher molecular interactions as the amount of emulsifier at the interface increases. These data indicate that the interfacial activity and the surface dilatational modulus of emulsifier films are mainly a result of the amount of adsorbed emulsifier.

In summary, tensiometry and surface rheology give complementary information about emulsifier adsorption and interactions at fluid interfaces as a function of emulsifier concentration, aqueous phase composition, and the scale of adsorption time.

Film Structural Characteristics

The thermodynamics of spread films at the air–water interface can be expressed by the π – A isotherm, obtained in a Langmuir- or Wilhelmy-type film balance (Figure 14.4a). From the π – A isotherm, different structures can be deduced for emulsifier monolayers as a function of emulsifier, temperature, and surface density or surface pressure. A phase diagram

**FIGURE 14.4**

(a) Surface pressure (π)-area (A) isotherm, (b) phase diagram, (c) topography and the temperature dependence of (d) entropy (ΔSt) and (e) enthalpy (ΔHt) for liquid-condensed (LC) to liquid-expanded (LE) transition in spread monolayers on water (solid line) and sugars (stripped region) evaluated from a form of the Clausius-Clapeyron equation applied to the LE to LC first-order phase transition, at temperature T .

can be drawn from the π - A isotherm (Patino and Niño, 1999; Horne and Patino, 2003; Niño et al., 2003) (Figure 14.4b).

For saturated-LMWE monolayers the liquid expanded (LE), liquid-condensed (LC), solid (S) structures and, finally, the collapse at the highest surface pressure take place as a function of surface pressure and

temperature. Brewster angle microscopy allows direct visualization of changes in topography and collapse of saturated-LMWE monolayer at the air–water interface (Figure 14.4c). These monolayers at low π show circular LC domains from the homogeneous ambient phase with a LE structure. Each LC domain does not have a uniform intensity. At the highest π , the LC domains are so closely packed that they occupy the entire field of view, the contrast vanishes, and the presence of monolayer fractures can be observed in different zones by the movement of BAM along the length of the film balance. Finally, after expansion, the monolayer undergoes a break up of the collapsed structure to a 2D-foam structure.

In contrast with saturated-LMWE, unsaturated-LMWE monolayers present only the liquid expanded structure and the collapse. BAM images corroborate that only the homogeneous LE phase is present during the compression of unsaturated-LMWE monolayers. From the observation with BAM along the film balance no fractures were visualized after the monolayer collapse. These monolayers collapse with the formation of lenses.

The structural characteristics of the monolayer also depend on the aqueous phase composition. The results suggest that there was an increase in the lipid–subphase interactions when ethanol was added to the aqueous phase. Ethanol molecules tend to be located at the interface between lipid molecules. Thus: (i) van der Waals interactions are possible, which explain the monolayer condensation observed from the isotherms and (ii) in addition, dipole–dipole interaction with the polar group produces monolayer instability by dissolution into the bulk phase.

The effect of temperature and aqueous phase composition on the structural characteristics of emulsifier spread films can be also analyzed by thermodynamic parameters of the liquid-condensed to liquid-expanded transition (Patino and Niño, 1999; Niño et al., 2003). The latent heat, ΔH_t , and the entropy, ΔS_t , of a two-dimensional first-order phase transition can be evaluated from the Clausius–Clapeyron equations applied to the isotherm (Figure 14.4d and e). The LC to LE transition requires energy ($\Delta H_t > 0$) and involves an increase in the system disorder ($\Delta S_t > 0$), which is in agreement with a process that is endothermic and increasingly disordered. The values of ΔH_t and ΔS_t also depend on the addition of solutes in the aqueous phase. In fact, the presence of glycerol, sugars, electrolytes, etc., produces higher values of entropy and enthalpy. ΔH_t and ΔS_t also increase when the concentration of the these reagents in the subphase increases. LMWE monolayers with a LE structure spread on these reagents are favorable to the existence of a large accumulation of water molecules at the interface. Thus, compression involves either the removal of intervening water molecules or a rearrangement of the polar group as the film condenses. In addition, LMWE monolayers spread on glycerol and sugars may possess greater configurational freedom than when they are spread on water due to the location of these reagents at the aqueous interface between the monolayer head groups, introducing spatial separation and disorder into the lipid head region with a consequent increase in entropy. This location can be helped by the formation

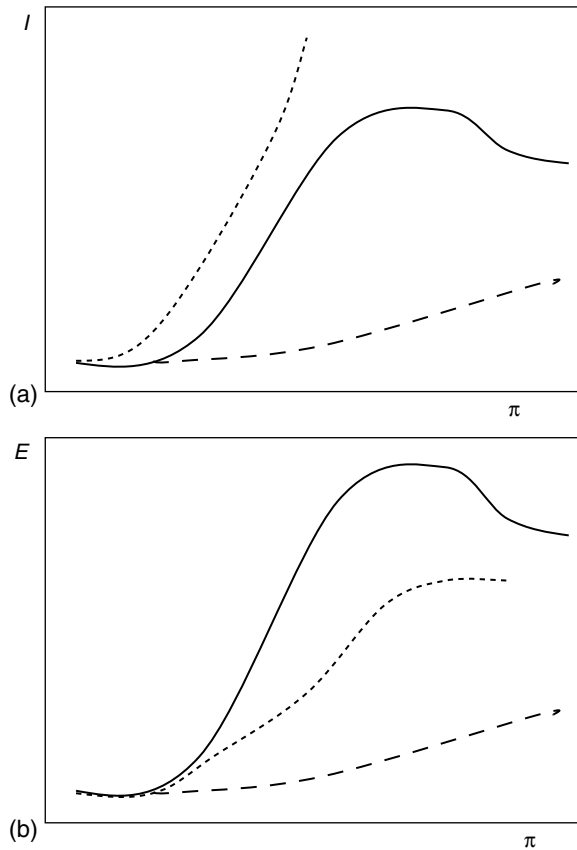
of intermolecular hydrogen-bonded complexes between the LMWE head group and sugar or glycerol molecules.

The results of π -A isotherms confirm that disordered protein (β -casein and caseinate) monolayers at the air-water interface adopt two different structures and the collapse phase (Horne and Patino, 2003; Niño et al., 2003). At low surface pressures, β -casein and caseinate molecules exist as trains with some amino-acid segments located at the interface (Structure 1). At higher surface pressures, and up to the monolayer collapse, amino-acid segments adopt the form of loops and tails (Structure 2). However, globular proteins (WPI, soy globulins, etc.) retain elements of the native structure, not fully unfolded at the interface. Thus, most amino-acid residues in globular proteins adopt a loop conformation at the air-water interface. This loop conformation becomes more condensed at higher surface pressures and is displaced towards the bulk phase at the collapse point. As expected, the reflection of the interface at the Brewster angle for protein films is no different from the background of the clean subphase. In addition, BAM images corroborate that only a homogeneous phase is present during the compression of milk proteins up to the monolayer collapse. BAM images for disordered protein monolayers with Structure 1 and with Structure 2 are practically the same as those for globular proteins. However, at the collapse point the reflectivity is high and some folds are observed along the interface with different illumination (Niño et al., 2005).

Reflectivity and Viscoelastic Properties of LMWE (Monoglycerides)

The evolution with monolayer compression of the relative reflectivity (I) of the BAM image gives complementary information about the structural characteristics of emulsifiers during monolayer compression (Figure 14.5a). For saturated-LMWE (monoglyceride or phospholipid) monolayers the LE, LC, S structures and, finally, the collapse at the higher π take place. In contrast with saturated-LMWE, unsaturated-LMWE monolayers present only the LE structure and the collapse at the highest π . Moreover, the reflectivity during unsaturated-LMWE monolayer compression, and especially at the collapse point, is lower than for saturated-LMWE (Horne and Patino, 2003; Niño et al., 2003; Carrera et al., 2005; Lucero, in press).

In Figure 14.5b we show that a common trend of the π dependence of E for LMWE monolayers is that E increased with increasing π up to the collapse point. This increase is a result of an increase in the interactions between the monolayer molecules, as deduced from monolayer reflectivity. However, for the more condensed monolayer (saturated-LMWE), this increase is higher than for the more expanded unsaturated-LMWE monolayer. In summary, I - π and E - π curves (Figure 14.5) could reflect the surface equation of state

**FIGURE 14.5**

(a) Relative reflectivity (I) and (b) surface dilatational modulus (E) as a function of surface pressure (π) for (—) saturated LMWE, (–) unsaturated LMWE, and (···) protein spread monolayers at the air–water interface.

of the spread emulsifier at the air–water interface, and are particularly sensitive for assessing phase structures in the monolayer (Niño et al., 2003).

As for unsaturated-LMWE, the domains that residues of protein molecules adopt at the air–water interface appeared to be of uniform reflectivity, suggesting homogeneity in thickness and film isotropy. I increased with π and reaches a maximum at the collapse point. At $\pi < \pi_c$, I was independent of the protein but, at the collapse point, I was higher for β -casein and caseinate than for WPI. That is, at higher π and especially at the collapse point, the thickness of β -casein or caseinate monolayer is higher than that for WPI. However, for globular protein monolayers, E increased with increasing π up to the collapse point. However, for the more disordered proteins (β -casein and caseinate) the E - π dependence is more complex. E increases to a maximum with π for Structure 1, but decreases with π and

passes to a minimum with Structure 2. Finally, E increases up to the collapse point.

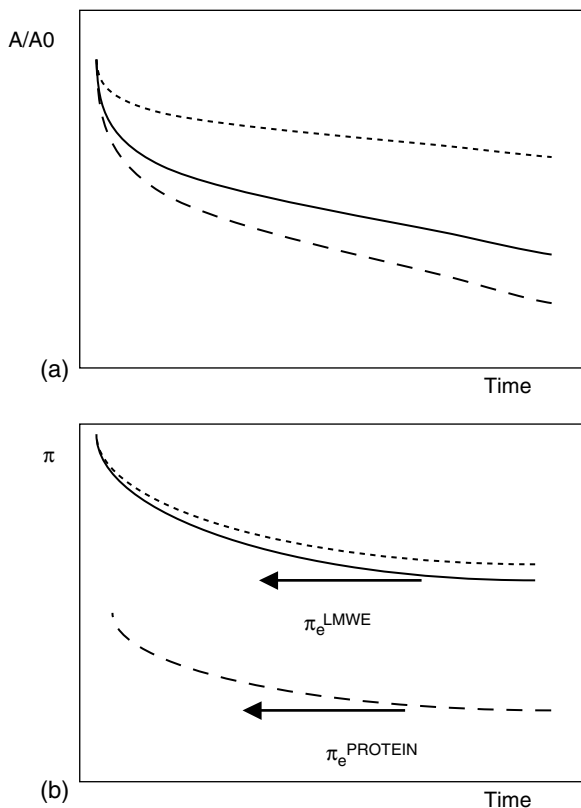
The results with biosurfactant (protein and LMWE) monolayers indicate that the dilatational modulus is not only determined by the interactions between spread biosurfactant molecules (which depend on the surface pressure or surface density), but that the structure of the spread molecule also plays an important role (Niño et al., 2003).

Long-Term Relaxation Phenomena in Protein and LMWE Monolayers

Long-term relaxation phenomena of spread emulsifiers at the air–water interface are of practical importance for different technological operations such as emulsification and foaming. Two experimental approaches can be used for the analysis of long-term relaxation phenomena in emulsifier monolayers (Figure 14.6) (Patino and Niño, 1999; Horne and Patino, 2003). In the first, the surface pressure is kept constant, and the area is measured as a function of time. The relaxation in surface area at $\pi < \pi_e$ can be modeled by the desorption of monoglyceride molecules, involving two stages: the dissolution and further diffusion into the bulk aqueous phase. The monolayer molecular loss was lower for saturated-LMWE than for unsaturated-LMWE, and increased with temperature and surface pressure. In the second approach, the area is kept constant (at the collapse) and the decrease in surface pressure is monitored as a function of time.

At $\pi > \pi_e$ the relaxation phenomena for insoluble monolayers are caused by the transformation of a homogeneous monolayer phase into a heterogeneous monolayer-collapse phase system. However, some differences exist between saturated-LMWE and unsaturated-LMWE monolayers (Figure 14.6b). Relaxation phenomena in saturated-LMWE monolayer are controlled predominantly by the collapse mechanism because the surface pressure relaxes to π_e . For these systems the monolayer collapses by nucleation and growth of critical nuclei. Unsaturated-LMWE monolayers behave differently to saturated-LMWE monolayers. As the surface pressure relaxes from the collapse value, which is close to π_e , towards values lower than π_e at longer times, the collapse competes with a desorption mechanism (Patino and Niño, 1999).

Protein monolayers behave differently from typical lipids under the same experimental conditions (Figure 14.6). For protein monolayers, fits of the experimental data at π lower than and higher than π_e require two exponential decays. The relaxation of the protein monolayer is therefore not a simple process. At $\pi < \pi_e$ the relaxation rate and the amplitude of the relaxation area depend on the surface pressure and the protein. The relaxation rate (quantified by means of the relaxation time, τ , inverse rate constant) is higher at the highest surface. Protein monolayer stability was

**FIGURE 14.6**

Relaxation phenomena of (—) LMWE, (---) proteins and (■) protein-LMWE mixed films at (a) constant surface pressure (at $\pi < \pi_e$) and (b) at constant molecular area at the collapse point. The arrows indicate the equilibrium surface pressure for LMWE (π_e^{LMWE}) and proteins (π_e^{protein}).

also tested under the most adverse conditions, at the maximum interfacial density (at constant collapse area). Under these conditions (at $\pi \geq \pi_e$), the relaxation phenomena in protein monolayers are controlled predominantly by the collapse mechanism. At higher relaxation time, the surface pressure tends to a plateau that is practically coincident with the value of π_e . The formation of multilayers of protein molecules under collapse conditions is more likely as confirmed by the significant increase in the reflectivity of the interface. In summary, the relaxation in relative molecular area at $\pi < \pi_e$ and in surface pressure at $\pi > \pi_e$ — which is mainly limited to the first 50 min (should be attributed to processes related to monolayer organization/reordering and collapse, respectively. These phenomena are a reversible process. In fact, we have not observed any hysteresis π - A isotherm during continuous compression-expansion cycles in the monolayer after the relaxation experiments (Niño et al., 2003).

Spreading and Adsorption of Protein and LMWE Mixed Films at Equilibrium

In food systems, the interfacial layer often comprises both proteins and LMWE. Proteins and LMWE typically coexist in the interfacial layer, sometimes unassociated with each other, but also in association, with specific functions in the processing and properties of the final product (Hassenhuette and Hartel, 1997; Whitaker et al., 1998; Patino et al., 2003).

Protein–LMWE interactions at the air–water interface have been studied by tensiometry (Patino et al., 2003). From these experiments it has been observed that the interfacial characteristics of mixed proteins and LMWE at air–water interfaces depend at least on the way in which these surface active compounds are adsorbed/spread to the interface (Figure 14.2).

Surface Tension of Protein + Oil-Soluble LMWE

The existence of protein–LMWE interactions depends on the interfacial composition and on the protein/LMWE ratio. In general, the surface activity of the mixed films is determined by the LMWE as the surface pressure of the mixed film is the same as the LMWE equilibrium spreading pressure, and the monolayer is not saturated by the protein. However, the protein determines the surface activity of mixed films as the protein saturates the monolayer. In the intermediate region there exists coexistence of protein and LMWE at the interface.

Surface Tension of Protein + Water-Soluble LMWE

When a soluble LMWE (like Tween 20) as well as a protein is present in water both components will form adsorbed films at the air–water interface. At low LMWE concentrations, protein reduces the surface tension to a greater extent than protein–LMWE mixed systems. However, the opposite was observed at high LMWE concentrations, above the critical micelle concentration (CMC), because the protein molecules are displaced from the interface by the LMWE. Over the intermediate region, close to the CMC, both protein and LMWE coexist at interface. However, tensiometric studies indicate that the compatibility of proteins and nonionic emulsifier at fluid interfaces is very poor, in contrast to mixtures of ionic-surface-active homologues.

However, it was observed that typical food reagents (salts, ethanol, or sugars) in the aqueous phase play a role in soluble LMWE micellisation and protein–LMWE interactions and, as a consequence, on the interfacial characteristics of the mixed films (Patino et al., 2003).

Structural and Topographical Characteristics of Protein–LMWE Mixed Films

Using a unique device that incorporates different interfacial techniques, such as surface film balance and Brewster angle microscopy (BAM), we have analyzed the structural characteristics of protein–LMWE mixed films spread on the air–water interface (Patino et al., 2003; Lucero, in press). At surface pressures lower than that for protein collapse a mixed monolayer of LMWE and protein may exist. At surface pressures higher than that for protein collapse, collapsed protein residues may be displaced from the interface by LMWE molecules; that is, the mixed film is practically dominated by LMWE molecules: the π –A isotherms of the mixed film are parallel to that of the lipid.

From a systematic study focused on the π –A isotherm of protein–LMWE mixed monolayers (including the application of the additivity rule on miscibility and the quantification of interactions between monolayer components by excess free energy (it has been concluded that, at a macroscopic level, these compounds form a practically immiscible monolayer at the air–water interface, at $\pi < \pi_e^{\text{protein}}$). At higher π the collapsed protein is displaced from the interface by LMWE (monoglycerides, phospholipids, etc.). The existence of low protein interactions in disordered proteins (β -casein and caseinate) facilitates the protein displacement by LMWE from the air–water interface. However, the lower surface activity of unsaturated-LMWE explains the fact that this lipid has a lower capacity than saturated-LMWE for protein displacement.

Results of BAM as a function of π obtained with protein–LMWE mixed monolayers clearly show at a microscopic level the same structural characteristics as those deduced from the π –A isotherm, at a macroscopic level (Patino et al., 2003; Lucero, in press). BAM images at $\pi < \pi_e^{\text{protein}}$ show (a) segregated LE–LC saturated-LMWE and protein domains, (b) homogeneous LE LMWE–protein domains, and (c) segregated LC saturated-LMWE and protein domains. At $\pi > \pi_e^{\text{protein}}$ we can distinguish (d) a region of saturated-LMWE LC domains, (e) the coexistence of saturated-LMWE and collapsed protein, and (f) the squeezing out of protein by LMWE. Finally, at the collapse point we observe (g) that a region of collapsed LMWE dominates the topography of the interface, but we also see minor regions with (h) the presence of fractures of collapsed saturated-LMWE, and (i) the coexistence of collapsed LMWE and islands of collapsed protein. However, the displacement of proteins by LMWE is reversible because the π –A isotherms are reproducible and same topography is visualized after repeated compressions of the same monolayer.

Long-Term Relaxation Phenomena in Protein–LMWE Mixed Films

The strength of interactions between protein and LMWE can also be studied by relaxation experiments (Patino et al., 2003). Long-term relaxation phenomena in protein–LMWE mixed films at the air–water interface have been analyzed according to models for desorption, collapse, and/or organization/reorganization changes. At lower surface pressures (at $\pi < \pi_e^{\text{protein}}$), the organization/reorganization change of protein molecules in the mixed film is the mechanism that controls the relaxation process. From a practical point of view it must be emphasized that under these conditions the mixed film is more stable in relation to monolayer molecular loss than that of the pure components. At the collapse point of the mixed film, the relaxation phenomena may be caused by either nucleation and growth of critical nuclei of LMWE or a complex mechanism including competition between desorption and monolayer collapse.

The reasons for these behaviors may be associated again with the immiscibility between protein and LMWE at the air–water interface and to the protein displacement by the LMWE at surface pressures higher than that for protein collapse.

Dilatational Characteristics of Protein–LMWE Mixed Films

Surface dilatational rheology is a very sensitive technique to analyze the competitive adsorption/displacement of protein and LMWE emulsifier at the air–water interface (Patino et al., 2003). A common trend is that the surface dilatational modulus increases as the monolayer is compressed and is a maximum at the highest surface pressures, at the collapse point of the mixed film, and as the content of LMWE in the mixture increases. At higher π , the collapsed protein residues displaced from the interface by LMWE molecules have important influence on the dilatational characteristics of the mixed films. The mechanical properties of the mixed films also demonstrate that, even at the highest π , the LMWE is unable to displace completely protein molecules from the air–water interface.

As for pure LMWE films, the surface dilatational modulus is higher for protein–saturated-LMWE than for protein–unsaturated-LMWE mixed films at every surface pressure. The surface dilatational properties of mixed protein–emulsifier films also depend on the presence of some food components (ethanol and sucrose) in the aqueous phase. In general, a decrease in the dilatational rheological properties on the addition of ethanol was found for protein–water–insoluble LMWE. That is, the static and

dynamic characteristics of mixed films depend on the monolayer and aqueous phase compositions and the surface pressure (Patino et al., 2003).

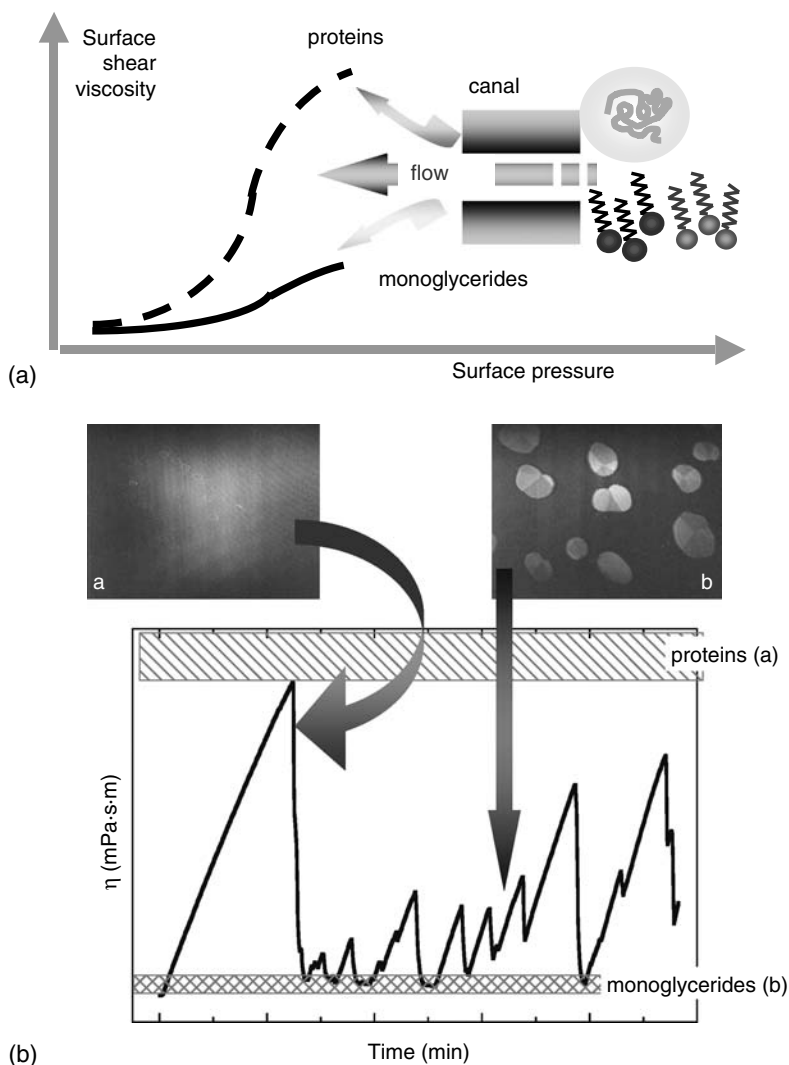
Surface Shear Characteristics of Protein–LMWE Mixed Monolayers

While dilatational rheology plays an important role in short-term stability of dispersions shear viscosity may contribute appreciably to the long-term stability (Murray and Dickinson, 1996; Murray, 1998, 2002). The shear characteristics of the interfacial film are governed by the composition and structure of the adsorbed material. In addition, surface shear viscosity is a very sensitive technique to analyze the competitive adsorption of protein and water-soluble LMWE at the air–water interface (Murray and Dickinson, 1996; Murray, 1998, 2002; Bos and van Vliet, 2001).

To study the shear characteristics of spread films a home-made canal viscometer was used (Patino and Carrera, 2004a). The experiments have demonstrated the sensitivity of the surface shear viscosity (η_s) of protein and monoglyceride films at the air–water interface, as a function of surface pressure (or surface density). We have observed that, at the same π , the η_s values were higher for proteins than for monoglycerides (monopalmitin and monoolein), with the lower η_s values for monoolein (Figure 14.7a). Therefore, differences between η_s values for various proteins are rather large and reflect differences, among others, in the protein structure and the potential for the formation of interfacial aggregates of significant sizes.

For protein–monoglyceride mixed film the η_s value varies greatly with the surface pressure (or surface density) of the mixed monolayer at the interface (Carrera and Patino, 2004a, 2004b; Patino and Carrera, 2004). In general, the greater the surface pressure (i.e., at the higher surface density), the greater were the values of η_s , as might be expected on the basis of greater intermolecular interactions. Moreover, the η_s value is also sensitive to the displacement of film forming components at the interface: (i) at surface pressures lower than that for the protein collapse the values of η_s peaks — associated with the flow of the protein through the canal — are an indication that a shear-induced segregation in the mixed films was produced. (ii) near to the collapse point the mixed film was dominated by the presence of the monoglyceride and the η_s values were practically the same as those for pure monoglyceride monolayers (monopalmitin or monoolein) (Figure 14.7b).

Comparing the data for different protein monoglyceride mixed films we conclude that the structural and topographical characteristics, the shear-induced segregation, and squeezing out phenomena of mixed films appear to be generic (Patino et al., 2003; Carrera and Patino, 2004a, 2004b; Patino and Carrera, 2004). The reasons for these behaviors must be associated with immiscibility between protein and monoglyceride at the air–water interface,

**FIGURE 14.7**

(a) The surface pressure dependence of surface shear viscosity (η_s) of proteins and LMWE during the flow through a canal shear viscometer. (b) Shear-induced molecular segregation during the flow (solid line) of protein-LMWE mixed films at the air-water interface. The surface shear viscosity for pure LMWE (checked pattern) and pure protein (checked pattern) monolayers is included as reference.

with protein displacement by the monoglyceride at $\pi > \pi_e^{\text{protein}}$, and with shear-induced segregation in the mixed films.

These phenomena have significant repercussions on surface shear properties. That is, the surface shear characteristics reflect the complex phenomena that take place in protein-monoglyceride mixed films under flow conditions.

Protein–LMWE Mixed Films (Orogenic Mechanism)

Recent works by the Norwich group (Gunning et al., 1999; Mackie et al., 1999, 2000; Wilde, 2000) have demonstrated how surfactants disrupt and displace proteins from an interface by a three-stage “orogenic” mechanism. We have adopted this mechanism to describe spread protein–LMWE mixed films (Figure 14.8) (Patino et al., 2003). The results suggest that for spread

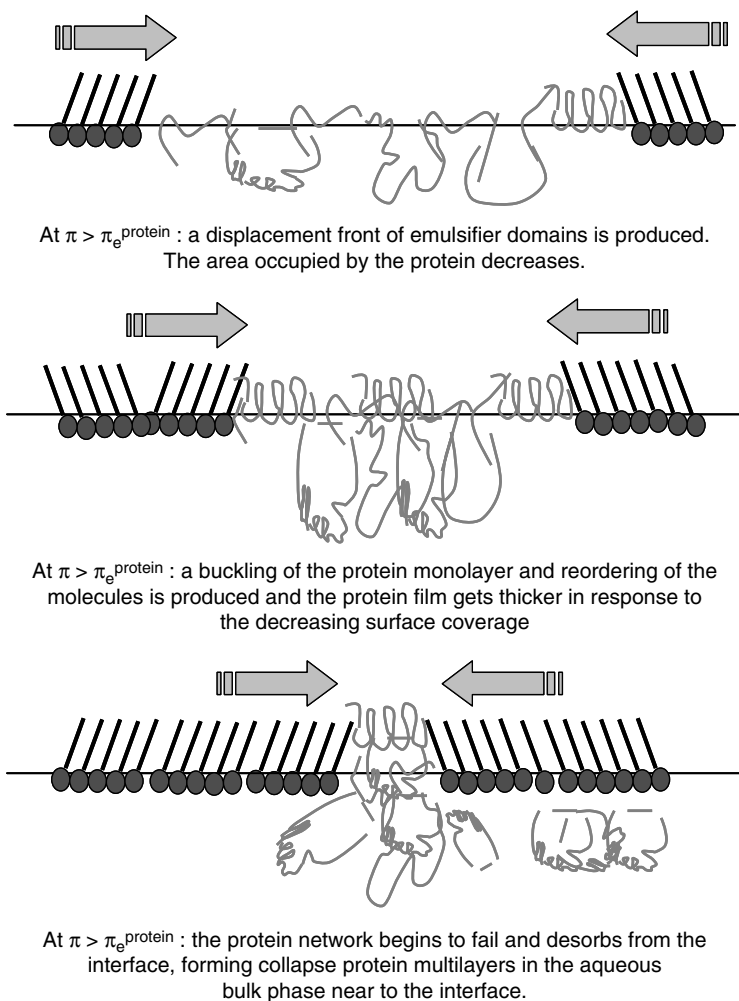


FIGURE 14.8

Three-stage “orogenic” mechanism for displacement of proteins by water-insoluble LMWE spread at the air–water interface.

water-insoluble LMWE the first stage of the orogenic mechanism, which occurs at $\pi < \pi_e^{\text{protein}}$, involves a displacement front of emulsifier domains. The second stage, which occurs at $\pi \geq \pi_e^{\text{protein}}$, involves a buckling of the monolayer and reordering of the molecules as the protein film gets thicker in response to the decreasing surface coverage. Finally, at sufficiently high π the protein network begins to fail, freeing proteins, which then desorbs from the interface. But, for spread water-insoluble LMWE monolayers, the protein displacement is not total even at the highest surface pressure, at the collapse point of the mixed film.

The orogenic displacement mechanism is a consequence of the low level of interaction between proteins and LMWE at the air–water interface. This model has been shown to work for a range of proteins with different secondary and tertiary structures and different types of LMWE (monoglycerides and phospholipids).

Acknowledgments

The authors acknowledge the support from CICYT through the grant AGL2001-3843-C02-01.

References

- Bos, M.A. and van Vliet, T. Interfacial rheological properties of adsorbed protein layers and surfactants: a review, *Adv. Colloid Interface Sci.*, 91, 437, 2001.
- Carrera, C. and Patino, J.M.R. Surface shear rheology of WPI–monoglyceride mixed films spread at the air–water interface, *Colloid Surf. B- B.*, 36, 57, 2004a.
- Carrera, C. and Patino, J.M.R. Flow-induced molecular segregation in β -casein-monglyceride mixed films spread at the air–water interface, *Langmuir*, 20, 6327, 2004b.
- Carrera, C., Niño, Ma.R.R., Lucero, A., and Patino, J.M.R. Biopolymers and emulsifiers at the air–water interface. Implications in food colloid formulations, *J. Food Eng.*, 67, 225, 2005.
- Dickinson, E. *An Introduction to Food Colloids*, Oxford University Press, Oxford, U.K., 1982.
- Gunning, A.P., Mackie, A.R., Wilde, P.J., and Morris, V.J. In-situ observation of surfactant-induced displacement of protein by atomic force microscopy, *Langmuir*, 15, 4636, 1999.
- Hassenhuetten, G.L. and Hartel, R. *Food Emulsifiers and their Applications*, Chapman & Hall, New York, 1997.
- Horne, D.S. and Patino, J.M.R. Adsorbed biopolymers: behavior in food applications, *Biopolymers at Interfaces*, 2nd Ed., M. Malmsten, ed., Marcel Dekker, New York, 2003, chap. 30.
- Lucero, A., Rodríguez Niño, Ma.R., Carrera, C., Gunning, A.P., Mackie, A.R., and Rodríguez Patino, J.M. The displacement of β -casein from the air–water

- interface by phospholipids, in *Food Colloids 2004: Interactions, Microstructure and Processing*, E. Dickinson, ed., Royal Society of Chemistry, Cambridge, pp. 160–175, 2005.
- Mackie, A.R., Gunning, A.P., Wilde, P.J., and Morris, V.J. The orogenic displacement of proteins from the air/water interface by surfactant, *J. Colloid Interface Sci.*, 210, 157, 1999.
- Mackie, A.R., Gunning, A.P., Wilde, P.J., and Morris, V.J. Competitive displacement of β -lactoglobulin from the air–water interface by sodium dodecyl sulfate, *Langmuir*, 16, 8176, 2000.
- McClements, D.J. *Food Emulsions: Principles, Practice and Techniques*, CRC Press, Boca Raton, FL, 1999.
- Murray, B.S. Interfacial rheology of mixed food protein and surfactant adsorption layers with respect to emulsion and foam stability, *Proteins at Liquid Interfaces*, D. Möbius and R. Miller, eds., Elsevier, Amsterdam, 1998.
- Murray, B.S. Interfacial rheology of food emulsifiers and proteins, *Curr. Opin. Colloid Interface Sci.*, 7, 426, 2002.
- Murray, B.S. and Dickinson, E. Interfacial rheology and the dynamic properties of adsorbed films of food proteins and surfactants, *Food Sci. Technol. Inst.*, 2, 131, 1996.
- Niño, Ma.R.R., Carrera, C., Cejudo, M., and Patino, J.M.R. Protein and lipid films at equilibrium at the air–water interface, *J. Am. Oil Chem. Soc.*, 78, 873, 2001.
- Niño, Ma.R.R., Carrera, C., Pizones, V., and Patino, J.M.R. Milk and soy protein films at the air–water interface, *Food Hydrocolloid*, 19, 417, 2005.
- Niño, Ma.R.R. and Patino, J.M.R. Effect of the aqueous phase composition on the adsorption of bovine serum albumin to the air–water interface, *Ind. Eng. Chem. Res.*, 41, 1489, 2002.
- Patino, J.M.R. and Carrera, C. Structural, topographical, and shear characteristics of milk proteins and monoglyceride monolayers spread at the air–water interface, *Langmuir*, 20, 4530, 2004a.
- Patino, J.M.R. and Carrera, C. Shear characteristics, miscibility, and topography of sodium caseinate–monoglyceride mixed films at the air–water interface, *Biomacromolecules*, 5, 2065, 2004b.
- Patino, J.M.R. and Martín, R.M. Spreading of acylglycerols on aqueous surfaces at equilibrium, *J. Colloid Interface Sci.*, 167, 150, 1994.
- Patino, J.M.R., Niño, Ma.R.R., and Carrera, C. Protein–emulsifier interactions at the air–water interface, *Curr. Opin. Colloid Interface Sci.*, 8, 387, 2003.
- Patino, J.M.R. and Niño, Ma.R.R. Interfacial characteristics of food emulsifiers (proteins and lipids) at the air–water interface, *Colloid Surf. B- B.*, 15, 235, 1999.
- Niño, Ma.R.R., Patino, J.M.R., Sánchez, C., Cejudo, M., and Navarro, J.M. Physicochemical characteristics of food lipids and proteins at fluid–fluid interfaces, *Chem. Eng. Commun.*, 190, 15, 2003.
- Walstra, P. Principles of emulsion formation, *Chem. Eng. Sci.*, 48, 333, 1993.
- Whitaker, J.R., Fereidoon, S., Munguia, A.L., Yada, R.Y., and Fuler, G. *Functional Properties of Proteins and Lipids*, American Chemical Society, Washington, DC, 1998.
- Wilde, P.J. Interfaces: their role in foam and emulsion behavior, *Curr. Opin. Colloid Interface Sci.*, 5, 176, 2000.

15

Studies on Molecular Organization at the Water Interface

Victor J. Morris

CONTENTS

Introduction	273
Microscopical Methods	274
The Atomic Force Microscope	274
The Scanning Near-Field Optical Microscope	275
Sample Preparation	276
Interfacial Structures	276
Protein–Surfactant Interactions	276
Mixed Protein Films	281
Real Systems	282
Droplet–Droplet Interactions	284
Conclusions	286
Acknowledgments	287
References	287

Introduction

Preparation of food foams and emulsions requires the creation and stabilization of air–water or oil–water interfaces. Interfaces found in food systems contain a range of surface-active molecules and the interactions between these components determine the long-term stability of the foam or emulsion. The most common species present at the interface will be proteins and various small, highly mobile molecules such as surfactants or lipids. Both proteins and surfactants (or lipids) are capable, on their own, of stabilizing interfaces, but they do so by different molecular mechanisms (Wilde et al., 2004).

Proteins are considered to adsorb at the interface, partially unfold and interact to form molecular “gel-like” networks (Wilde et al., 2004). Collapse of emulsions or foams involves the stretching of the interface and the elasticity of the protein structure is supposed to oppose this effect. For mobile surfactants or lipids stretching of the interface will lead to concentration gradients and rapid diffusion of the molecules to restore the status quo (Wilde et al., 2004). A source of instability for most foods is the presence of both proteins and small mobile molecules at the interface. The incompatibility of the two mechanisms means that mixed interfaces are less stable than interfaces containing pure protein or pure surfactant or lipid (Wilde et al., 2004). If there is sufficient surfactant or lipid present then they will eventually displace the protein. It is the structures formed during the battle for control of the interface that gives rise to instability.

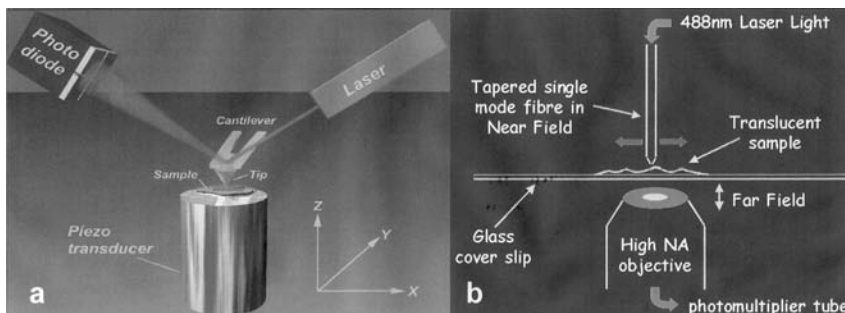
So how do small molecules competitively displace proteins? This can be answered by visualizing the structural changes that occur during displacement using probe microscopes such as the atomic force microscope (AFM). Understanding the interactions between proteins and small molecules is of importance, but is not the whole story. In food systems there will almost always be mixtures of proteins present at the interface, and we need to know what sorts of structures are formed by mixtures of proteins and how they resist displacement. We need to be able to recognize and locate individual proteins.

Mechanisms deduced from the use of AFM are based on model systems and it is necessary to establish that these conclusions apply in commercial foams and emulsions under realistic processing conditions. Molecular understanding of interfacial structures offers the prospect for rational modification or design of interfacial structure. In the case of emulsions this requires understanding how interfacial structures control droplet–droplet interactions. AFM provides a tool for monitoring interactions and relating them to interfacial structure.

Microscopical Methods

The Atomic Force Microscope

AFMs are the most widely used form of probe microscope (Figure 15.1a). They have proved particularly useful for solving previously intractable problems relating to the molecular structure of foods (Morris, 2004). They generate images by “feeling” rather than “looking” at samples. The samples are scanned beneath a sharp probe attached to a cantilever. Changes in the force between the sample and the probe cause the cantilever to deflect and these deflections are monitored using an optical lever. In the normal mode of operation the change in deflection of the cantilever at each sample point, the so-called error signal, is used via a feedback circuit, to adjust the

**FIGURE 15.1**

Schematic pictures showing the modes of operation of different probe microscopes. (a) An atomic force microscope and (b) a scanning near-field optical microscope.

sample–probe separation in order to maintain a constant, preset cantilever deflection. A three-dimensional topographic image is generated by amplifying these resultant changes in sample–tip separation. Because the probe is effectively touching the sample this imaging mode is called “contact mode imaging.” For homogeneous samples imaging at constant cantilever deflection is equivalent to imaging at constant applied force. The force changes as a result of changes in probe–sample separation during scanning and the resultant image is a true representation of surface topography. A variety of additional imaging modes are available to emphasize molecular structure, or to probe structural features such as charge or elasticity. The principle of operation allows the AFM to be operated in air or under liquids. The operating range spans that accessible to both the light and the electron microscopes, allowing molecular resolution under more natural conditions.

The AFM can also be used to measure force–distance curves. At a single sample point, the change in cantilever deflection is used to measure the force between the probe and the sample, as the probe approaches and recedes from the sample surface. The AFM can be adapted to monitor the interactions between deformable oil droplets in aqueous media as a model for interactions in oil-in-water emulsions (Gunning et al., 2004a).

The Scanning Near-Field Optical Microscope

The resolution of conventional far-field optical microscopes is limited by diffraction. In near-field optical microscopes (Figure 15.1b) the illuminating light is delivered, via a fiber optic, so close to the sample surface that diffraction cannot occur and in this case, the achievable resolution depends on the size of the illuminating aperture, rather than the wavelength of the light. At present optical probes with apertures of 50 nm are currently available. In order to obtain images it is necessary to track the sample surface in the near-field region. This can be achieved by attaching the optical probe to a tuning fork that is vibrated close to its resonant frequency. Any interactions between the probe and the sample damp this motion and can be used to

monitor and control the sample–probe separation. Piezoelectric devices developed for the AFM are used to scan the sample. SNOM is not routine and is really only suitable for imaging relatively smooth sample surfaces (Morris, 2004).

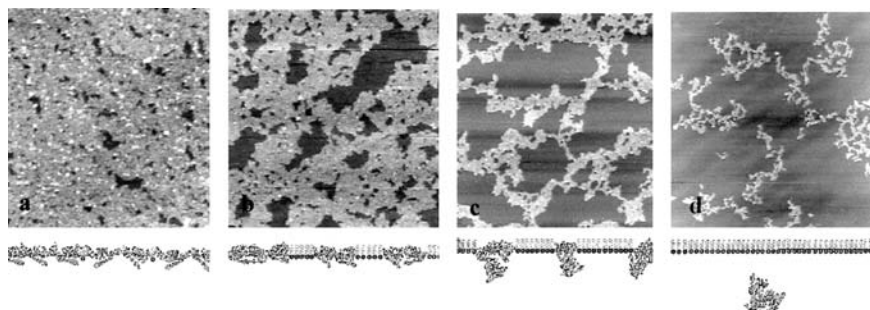
Sample Preparation

Interfacial structures present in foams and emulsions are modeled on a Langmuir trough and sampled using Langmuir–Blodgett (LB) techniques (Gunning et al., 1996; Mackie et al., 1999). Samples for AFM are deposited onto mica substrates and imaged under 1-butanol in order to facilitate control of the applied force. In the present study the samples were imaged in the dc contact mode using a minimal applied force (Gunning et al., 1996; Mackie et al., 1999). In this mode of imaging the tip is brought into contact with the sample surface and a preset applied force is applied to the sample. A feedback circuit is used to adjust the tip–sample separation in order to maintain a constant applied force during scanning. The displacements of the piezoelectric tube scanner, used to maintain the applied force constant, are amplified and displayed as the topographic image of the sample. An alternative approach would be to use the Tapping mode™ of imaging. The tip-cantilever assembly is oscillated at a high frequency and “taps” intermittently onto the sample surface. The feedback circuit senses the damping of the oscillation and the image is generated from the displacements of the piezoelectric scanner used to maintain a constant applied normal force. Tapping is often used to eliminate frictional forces that can distort or damage the sample. In the present case, for relatively flat monolayers, these frictional effects can easily be eliminated by imaging under butanol and applying minimal force. SNOM samples are deposited onto glass and imaged in air (Gunning et al., 2001). Mixed interfaces can be generated by spreading or co-adsorbing the samples. Both air–water and oil–water interfaces can be investigated using this approach (Mackie et al., 1999; Mackie et al., 2000a). Sampling the interfacial structures for spread films is comparatively simple. However, the procedures need to be modified when co-adsorbed films are prepared in order to prevent any passive adsorption of bulk protein during the LB dip obscuring the interfacial film (Mackie et al., 1999).

Interfacial Structures

Protein–Surfactant Interactions

The simplest mixed interface consists of a protein and a small molecule, such as a surfactant or lipid. We will model competitive displacement of proteins

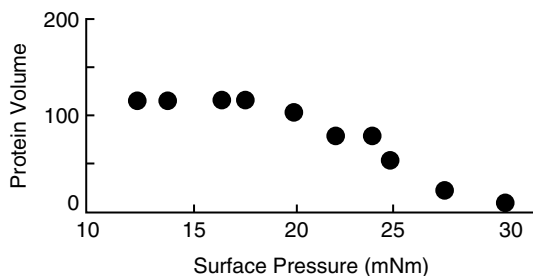
**FIGURE 15.2**

AFM images showing the displacement of a spread β -lactoglobulin protein film from an air–water interface by the progressive addition of the surfactant (polyoxyethylene sorbitan monolaurate) Tween 20. Image sizes are (a) $1.0 \times 1.0 \mu\text{m}$, (b) $1.6 \times 1.6 \mu\text{m}$, (c) $3.2 \times 3.2 \mu\text{m}$, and (d) $10.0 \times 10.0 \mu\text{m}$. A cartoon representing the displacement process is shown below the images.

using surfactants. Figure 15.2 shows displacement of a spread β -lactoglobulin film from an air–water interface by the nonionic surfactant Tween 20 (polyoxyethylene sorbitan monolaurate). Contrast in the image is determined by the height of the sample above the substrate. The bright regions represent protein and the black areas show where the surfactant has invaded the interface. The AFM images (Figure 15.2a–d) correspond to a progressive increase in surface pressure and show increased coverage of the interface with surfactant. These images directly confirm that proteins form networks at interfaces (Mackie et al., 1999). At the lowest surface pressures the surfactant appears to be randomly adsorbed onto the interface and small holes have appeared in the protein network. With increasing surface pressure these holes expand into larger domains until eventually at the highest surface pressure the protein network becomes too extended and snaps, leaving protein aggregates adrift in a sea of surfactant. A purely visual inspection of the images seems compatible with the idea that the more surface-active surfactant simply displaces individual proteins. Domains would be considered to expand by loss of protein at the boundaries of the domains.

However, it is possible to quantify the AFM images (Mackie et al., 1999). Areas occupied by either protein or surfactant can be calculated and, when combined with measurements of the thickness of the protein network, the protein volume can be determined. Figure 15.3 reveals the true nature of the displacement process. The protein volume remains constant until the network snaps, indicating that no protein is lost from the interface into the bulk until the protein network has been broken.

The molecular mechanism of displacement is illustrated schematically in Figure. Initially nucleation of surfactant domains occurs at defects in the protein network. Once these defects are full the surfactant domains expand and, as the area occupied by protein decreases, the protein layer thickens

**FIGURE 15.3**

Changes in protein volume during the displacement of a spread β -lactoglobulin from an air–water interface by the nonionic surfactant (polyoxyethylene sorbitan monolaurate) Tween 20.

keeping the total protein volume constant. This initially involves the refolding of individual proteins, and then buckling of the protein network. Eventually the network is pulled out into thin filaments that finally snap, freeing the protein and allowing it to escape into the bulk phase. Because the mechanism involves folding and buckling of the interfacial structure, it has been termed (Mackie et al., 1999) an “orogenic displacement mechanism.”

The mechanism has been shown to be generic for all proteins and surfactants studied to date (Gunning et al., 1999; Mackie et al., 1999; Gunning et al., 2001; Mackie et al., 2000a; Mackie et al., 2000b; Mackie et al., 2001a; Gunning et al., 2004b; Gunning et al., 2004c; Woodward et al., 2004). This includes water-soluble, oil-soluble, neutral, and charged surfactants. Similar results are found for spread and co-adsorbed films and for air–water, oil–water, and even solid–water interfaces. For solid–water interfaces the displacement can be studied (Gunning et al., 1999) *in situ* within the AFM and presented as a molecular video [www.ifr.bbsrc.ac.uk/spm]. Why is the mechanism generic? This is because proteins that stabilize foams or emulsions partially unfold on adsorption at the interface and link together to form networks. Once a network is formed it has to be broken before protein can be displaced into the bulk.

AFM led to the discovery of this new mechanism of displacement because it allowed visualization of the interfacial structure at the molecular scale. The heterogeneity of the interfacial structure was found to be crucial to understanding displacement. If a protein is spread at an interface and then imaged, the film is found to contain holes. This is because as proteins adsorb they partially unfold and stick together. As more proteins adsorb onto the interface the space available decreases, and the opportunity to unfold and to attach to other proteins decreases. The last proteins to arrive are probably passively adsorbed and weakly, if at all, attached to the network. These proteins are lost on sampling the interface and are the holes seen in the protein network. These are the sites that surfactant can attack allowing surfactant to invade the interface. As surfactant domains expand the boundaries are ragged. This is also a result of molecular heterogeneity.

Individual proteins unfold and interact to different extents and, as the protein network is compressed, refolding occurs more easily in certain regions, and stress can thus be redistributed around the boundary of the growing domain.

Subtle differences are seen for different proteins. The milk protein β -casein is not very effective as a foam stabilizer. On displacement with Tween 20 the domain boundaries are circular (Mackie et al., 1999), indicating uniform compression and weak inter-protein interactions. At oil–water interfaces β -casein is more difficult to displace (Mackie et al., 2000a). It is better at stabilizing emulsions. Domain boundaries are ragged and the network fails at higher surface pressures (Wilde et al., 2004).

Different surfactants also show (Mackie et al., 2000b; Gunning et al., 2004b; Gunning et al., 2004c) differences in the way they competitively displace protein. The displacement of β -lactoglobulin with different Tweens, such as Tween 20 (polyoxyethylene sorbitan monolaurate) and Tween 60 (polyoxyethylene sorbitan momostearate), shows that the surfactant concentration at which failure of the protein film occurs (Gunning et al., 2004b; Gunning et al., 2004c) depends on the nature of the side-chain of the surfactant. This must be caused by the different solubilities of the surfactants, because failure of the protein network occurs at the same surface pressure for both surfactants (Figure 15.4a). This is important because it is known that the Tweens will bind to the protein, and clearly such binding does not alter the final failure strength of the network.

Charged surfactants show detectable differences in displacement (Mackie et al., 2000b; Gunning et al., 2004b; Gunning et al., 2004c). Ionic surfactants such as cetyl-trimethyl-ammonium bromide (CTAB), sodium dodecyl sulphate (SDS), and lyso-phosphatidylcholine lauroyl (LPC-L) show slightly

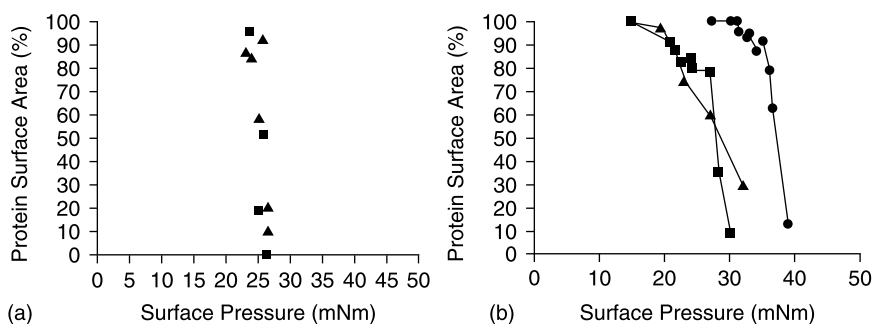


FIGURE 15.4

Competitive displacement of spread β -lactoglobulin from an air–water interface by (a) nonionic and (b) ionic surfactants. The collapse of the protein network is indicated by showing the change in area occupied by the protein at the interface as a function of surface pressure. (a) Data for \blacktriangle -Tween 20 (polyoxyethylene sorbitan monolaurate) and \blacksquare -Tween 60 (polyoxyethylene sorbitan momostearate). (b) Data for \blacktriangle -cetyl-trimethyl-ammonium bromide (CTAB), \blacksquare -lyso-phosphatidylcholine lauroyl (LPC-L), and \bullet -sodium dodecyl sulphate (SDS).

different behavior. For both spread and co-adsorbed films, SDS initially nucleates into small domains. However, with increasing surface pressure the number of nuclei increase, but the nuclei do not expand and grow into larger domains. At the highest surface pressures, coalescence of domains appears to occur just prior to the collapse point of the network (Mackie et al., 2000b). At present it is not clear whether this coalescence actually occurs on unperturbed interfaces, or is triggered by the Langmuir–Blodgett sampling procedure. For anionic, cationic, or zwitterionic surfactants the behavior is similar (Gunning et al., 2004b; Gunning et al., 2004c); displacement involves nucleation but little domain growth. Figure 15.5 shows the differences in domain sizes for the displacement of a spread β -lactoglobulin film from an air–water interface by the nonionic surfactant Tween 20 (Figure 15.5a) and the charged surfactant CTAB (Figure 15.5b). Screening the charge on the surfactant allows growth of surfactant domains (Figure 15.5c). Strong charge–charge repulsions between surfactants and localisation of counter ions would favor even dispersal of surfactant across the interface and the presence of many small domains. If the charge is screened then domain growth is restored (Gunning et al., 2004c) (Figure 15.5c). Another feature of displacement by ionic surfactants is that failure of the network occurs at different surface pressures (Figure 15.4b) for different surfactants (Gunning et al., 2004c). For CTAB, SDS, and LPC-L, the failure occurs at higher surface pressures than that seen for the Tweens (Figure 15.4a). In this case binding of surfactant to the proteins does alter the failure strength of the network. In fact it can be shown that, at low LPC-L surfactant concentrations, co-adsorption of the protein–surfactant complex actually leads to an increase in the shear modulus of the protein network (Gunning et al., 2004c). At higher surfactant concentrations the orogenic mechanism predominates and the

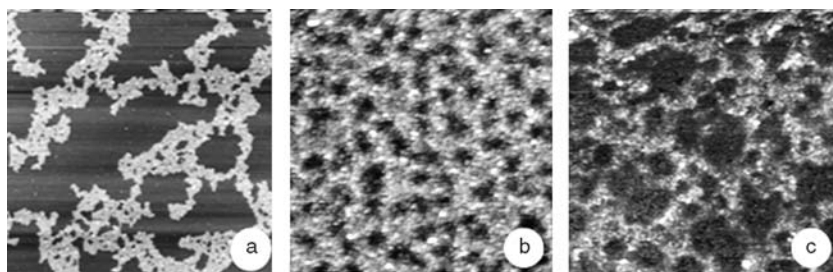


FIGURE 15.5

AFM images showing the displacement of a spread β -lactoglobulin protein film from an air–water interface by the progressive addition of surfactant. (a) Displacement with (polyoxyethylene sorbitan monolaurate) Tween 20, surface pressure $\pi = 22.5$ mN/m, image size 3.2×3.2 μm . (b) Displacement with cetyl-trimethyl-ammonium bromide (CTAB), $\pi = 22.8$ mN/m, image size 1×1 μm . (c) Displacement with CTAB in the presence of 0.2 M sodium phosphate buffer, pH — 7, $\pi = 22.8$ mN/m. scan size 1×1 μm . Data are shown at similar surface pressures in order to allow comparison of domain sizes for ionic and nonionic surfactants.

protein network weakens. However, the final failure occurs at higher surface pressures than expected (Gunning et al., 2004c).

Such intricate interactions suggest possible synergisms that could be investigated. Will small amounts of added SDS strengthen the protein network causing final displacement with a nonionic surfactant to occur at higher surface pressures? Such studies are needed to understand subtle interplays between the mixtures of surfactants encountered in commercial food samples.

Mixed Protein Films

Most interfaces encountered in food systems will contain more than one protein. Commercial materials used to stabilize emulsions or foams are complex isolates rather than purified single proteins. To describe the behavior of protein isolates it is necessary to understand the types of structures formed by mixtures of proteins at the interface, and also how such mixed structures are displaced by surfactants.

Bulk mixtures of native proteins will phase separate. Does such phase separation occur at the interface? As proteins adsorb at the interface they partially unfold and stick to one another. If the adsorption is random and the proteins collide and stick together very rapidly then the network formed would be an intimately mixed structure. Which type of interface is formed?

To determine the type of interfacial structure formed it is necessary to label and locate different proteins. Although AFM can visualize individual proteins it is actually quite difficult to distinguish one protein from another. A better approach is to tag proteins and fluorescent tags are particularly useful. It has to be established that tagging does not alter the functional properties of the proteins (Gunning et al., 2001). Once this has been shown then fluorescent tagging can be used to visualize network structure.

Ideally we would like to use different color tags in order to locate both proteins in a mixture. This requires optical microscopy below the diffraction limit and the use of near-field microscopy. SNOM can be used to visualize the displacement of tagged proteins by surfactants (Gunning et al., 2001) but, at present, the resolution achievable is only about 50 nm. This is not sufficient, at present, to visualize individual proteins in a mixture using different colored tags. Advances in SNOMs should lead to improved resolution and the imaging of mixed protein layers should become possible in the future.

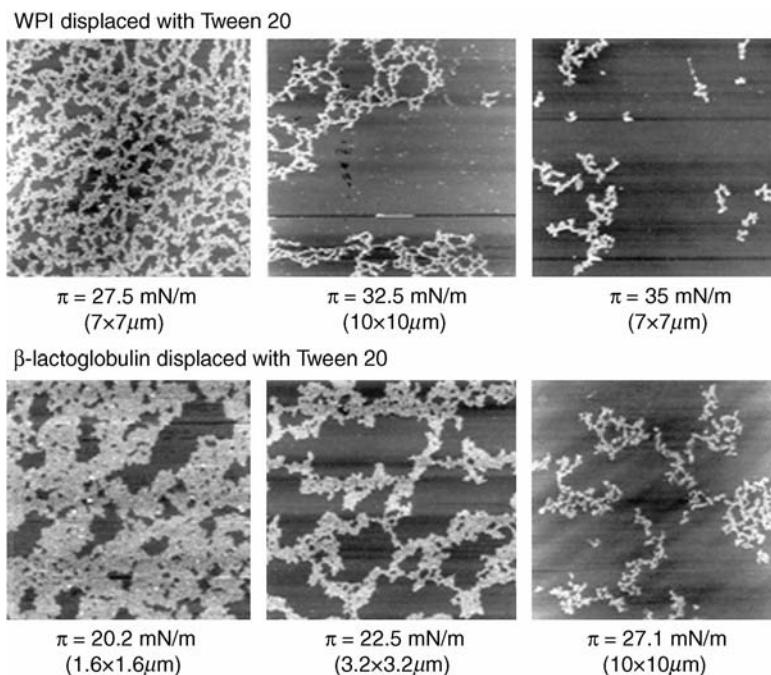
The production of samples for SNOM studies yields interfacial layers of tagged mixed protein networks deposited onto glass substrates. These can be imaged by far-field fluorescence and the images provide information on the distribution of proteins within the network. Such studies show no evidence for gross phase separation (Mackie et al., 2001a). This suggests that the interactions between proteins are rapid and kinetically trap the network as an intimately mixed structure. Displacement studies (Mackie et al., 2001a) show that, provided there are sufficient concentrations of both proteins

present at the interface, the behavior of simple binary mixtures is related to the behavior of the pure components. Final failure of the mixed network will occur at surface pressures equal to, or less than, that of the component protein which alone most resists displacement. Although more needs to be done on these mixed systems, it does appear that they are likely to behave as simple mixtures, and that synergisms between proteins may be rare.

Real Systems

The molecular models for displacement are based on probe microscopic studies of interfacial structures sampled by LB methods. The question can be asked as to whether the sampling procedure alters the surface structure. Therefore it is necessary to test whether orogenic displacement occurs at the interface in a Langmuir trough. From the AFM studies it is possible to predict the distribution of surfactant domain sizes as a function of added surfactant (Mackie et al., 2003). Therefore it is possible to predict when the domains induced by nonionic surfactant will become sufficiently large to be visible by conventional microscopy. Brewster angle microscopy (BAM) can be used to look directly at interfacial structure. Combined AFM and BAM studies have confirmed (Mackie et al., 2001b) the presence of surfactant domains directly at the interface. The in situ observations of protein displacement from a solid surface (Gunning et al., 1999) show that the structures observed by AFM cannot be attributed to drying artefacts. Finally, studies on liquid lamellae as models for foam drainage have revealed the presence of domains of different thickness when both protein and surfactant are present (Clark et al., 1990; Wilde and Clark, 1993; Wilde et al., 2004). Fluorescence recovery after photobleaching (FRAP) measurements have revealed different rates of diffusion for the molecular species present in the domains of different thickness (Clark et al., 1990; Clark et al., 1994a; Wilde et al., 2004). The thinner "surfactant" domains contain highly mobile molecules whereas the thicker "protein" domains contain immobile molecules, consistent with the idea of a protein network. It would still be useful to demonstrate that orogenic displacement also occurs on finite-sized, curved surfaces, representing the spherical oil droplets present in oil-in-water emulsions. As will be described later it is possible to use AFM to measure the deformation of oil droplets in aqueous media (Dagastine et al., 2004; Gunning et al., 2004a). Such studies are consistent with orogenic displacement of protein from the oil–water interface (Gunning et al., 2004a).

The behavior of simple mixtures provides a basis for analysing the behavior of protein isolates. Whey protein isolate (WPI) contains the milk proteins β -lactoglobulin, α -lactalbumin, and bovine serum albumen. The displacement of the individual proteins has been studied (Mackie et al., 1999; Gunning et al., 2001). The major component of WPI is β -lactoglobulin, and it might be expected that competitive displacement of WPI would resemble that of β -lactoglobulin. Displacement of WPI from air–water interfaces by Tweens occurs via an orogenic mechanism (Figure 15.6) but the surface

**FIGURE 15.6**

Comparison of the competitive displacement of spread films of whey protein isolate (WPI) and β -lactoglobulin from an air–water interface with the nonionic surfactant (polyoxyethylene sorbitan monolaurate) Tween 20. Note that the WPI network remains intact at surface pressures (π) above those at which the β -lactoglobulin network has failed. The image sizes are indicated in brackets below the images.

pressures at which network failure occurs are higher than those found for β -lactoglobulin alone (Woodward et al., 2004). These differences can be shown to be caused by the different conditions under which individual milk proteins are extracted and purified, and the isolation conditions used to prepare WPI. In unpublished studies it has been possible to identify the chemical origins of the improved stability of the WPI, and clearly this knowledge can be used to rationally manipulate the properties of WPI. Modeling of protein isolates as simple protein mixtures provides a basis for understanding and manipulating their properties.

Knowledge of the competitive displacement mechanisms allows rational modification of interfacial structure to improve functionality. Because the molecular displacement mechanism is generic these strategies can be employed for a range of food systems produced by the baking, brewing, and dairy industries. A variety of intervention strategies have been suggested or implemented. Broadly speaking, it is possible to strengthen the protein network (Clark et al., 1991; Sarker et al., 1995; Sarker et al., 1998; Saeker and Wilde, 1999) to resist failure, or to remove the mobile small

molecules (Clark et al., 1994b; Cooper et al., 2002) that break down the protein network. Lipid-binding proteins can be added to remove lipid (Clark et al., 1994b; Cooper et al., 2002). Various procedures can be used to improve the cross-linking of the protein network (Clark et al., 1991; Sarker et al., 1995; Sarker et al., 1998; Saeker and Wilde, 1999). Suggestions can be made for improving the choice of raw materials. For example, in the baking industry the foam structure of a loaf, and the loaf volume, will depend on the stabilization of the air–water interface during baking. A variety of surface-active proteins, lipids, and other materials are present in dough liquors and the air–water interface probably contains mixtures of such components (Mills et al., 2003; Li et al., 2004). The industrial solution to stabilizing such complex structures is to add DATEM esters which displace all protein and then dominate the interfacial structure. Alternatives approach might be to target wheat varieties with enhanced levels of surface-active proteins, or possibly increased levels of lipid-binding proteins that might prevent lipid reaching the interface. Such approaches are possible through improved understanding of interfacial structures.

Droplet–Droplet Interactions

Collapse of foams depends on the drainage of liquid from the thin lamellae separating air bubbles (Wilde et al., 2004). In emulsions drainage occurs in the thin aqueous layers formed between compressed faces of oil droplets, leading to droplet coalescence (Wilde et al., 2004). As two deformable particles approach each other hydrodynamic forces are considered to give rise to a dimple-shaped draining film. These films are considered to evolve into plane-parallel films. Film drainage and coalescence will depend on the tangential mobility of the structured interface. For proteins which form networks the rigidity of the interface will inhibit drainage and enhance stability to coalescence. Even with surfactant-stabilized interfaces there will never be complete tangential mobility. As the draining film attempts to drag the surfactant along the interface this displacement will be opposed by the Gibbs–Marangoni effect, enhancing stability to coalescence. The orogenic displacement model (Mackie et al., 1999) describes what happens as surfactant competes with protein for control of the interface. Disruption of the protein network reduces the elasticity of the network, weakening its ability to oppose drainage. Equally, the presence of a residual protein network hinders the mobility of surfactant, and reduces its stabilizing effect against coalescence. Thus, it might be anticipated that orogenic displacement will enhance coalescence. In addition, interfacial structures will influence the deformability of the droplets and this will also influence drainage and coalescence.

To study and control such effects it is necessary to understand how interfacial structures influence interactions between deformable particles. This can be done by directly measuring the interactions between droplets as the interfacial structure is manipulated. Recently, it has been shown

(Dagastine et al., 2004; Gunning et al., 2004a) that it is possible to attach droplets to AFM cantilevers and to compress these droplets against solid substrates or other droplets attached to surfaces. These studies can be carried out in aqueous media and the interfacial structure can be changed. They provide the most realistic studies of the interactions of oil droplets in emulsions. The force–distance curves can be measured and used to investigate either droplet deformation or droplet interactions. By compressing droplets against each other, or against solid substrates, it is possible to examine how the interfacial structure influences droplet deformation (Gunning et al., 2004a).

As two oil droplets are pressed together the repulsive interaction causes the cantilever to deflect, providing a measure of the repulsive force between the droplets. The deformation of the droplets will moderate this force, and the change in slope of the cantilever deflection, as a function of droplet separation, provides an indication of droplet deformability (Gunning et al., 2004a). Hence, we can monitor the effect of interfacial structure on droplet deformation (Gunning et al., 2004a). Such data are shown in Figure 15.7. Droplet deformation has been monitored as a function of time after adding protein to the bulk. Protein adsorbs at the interface, interacts, and forms a network which ages, strengthening the protein network as a function of time. Addition of surfactant leads to orogenic displacement and weakening of the protein network. Further addition of surfactant eventually destroys the protein network resulting in a surfactant-stabilized interface. Thus the interfacial shear modulus rises during protein adsorption and ageing, and then drops eventually to zero as protein is displaced. During this time addition of protein and then of surfactant results in a progressive decrease in interfacial tension. It is generally considered that decreases in interfacial

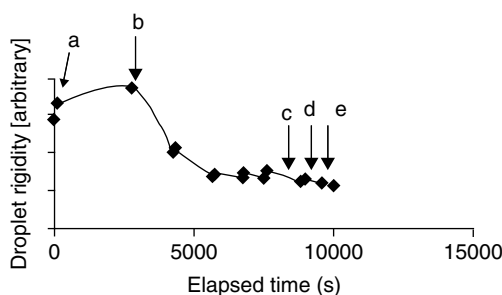


FIGURE 15.7

Changes in the deformability of tetradecane droplets caused by changes in the interfacial structure. Addition of the protein β -lactoglobulin (a) leads to an increase in the rigidity of the droplets. As the protein network ages the droplets become more rigid (a, b) with elapsed time. Addition of (polyoxyethylene sorbitan monolaurate) Tween 20 (b) leads to progressive disruption of the protein network as a function of elapsed time, and a progressive increase with time in the deformability of the oil droplets (b, c). Further additions of Tween 20 (c–e) lead to further increases in droplet deformability.

tension will lead to decreases in Laplace pressure within the droplets and increased deformability. Clearly Figure 15.7 shows that this is not true when protein networks are present at the interface (Gunning et al., 2004a). Protein adsorption will decrease interfacial tension and hence the Laplace pressure. However, droplets clearly become less deformable as protein networks form, and as they strengthen during aging. This suggests that the elastic skin, formed at the surface, opposes deformation of the droplets, making them more rigid (Gunning et al., 2004a).

Other types of interactions such as coalescence (Gunning et al., 2004a), depletion forces, or steric interactions on close approach of droplets can be studied by these methods. Thus, it is now possible to selectively modify the interfacial structure and to study the implications of such changes in terms of droplet interactions. For liquid fat droplets controlled (partial) coalescence, followed by solidification of the fat, is used to control aggregation or network formation, as a means of generating texture in whipped foods and ice creams. Partial coalescence should be particularly sensitive to the structure of mixed interfaces and the methods described above can be adapted to study this phenomenon.

Through studying droplet interactions it is possible to consider how to modify interfacial structures to control evolution of emulsion structure and stability. Droplet deformation is important as it controls the area of contact shared by droplets and hence the degree of repulsive or attractive interactions between droplets. On approach, diffusion at the interface can distort interfacial structure moderating interactions. The effects of droplet deformation or the disruption or distortion of interfacial structures on droplet–droplet interactions has not at present been studied. Understanding these effects offers the prospect for rational manipulation of interfacial structures or the designing of new interfaces by building structures layer by layer. Papers describing this type of approach are starting to appear in the food literature (Ogawa et al., 2004).

Conclusions

Through using atomic force microscopy, a tool developed to probe the nanoworld, it has been possible to visualize the structures present at air–water and oil–water interfaces that control the stability of foams and emulsions. Molecular interactions at the interface that are responsible for instability have been investigated and new molecular mechanisms discovered. A new understanding of the competitive displacement of proteins from interfaces by lipids or surfactants has been found to be generic and widely applicable to a range of food systems. New methodology has been developed to probe the interactions between deformable oil droplets in aqueous medias a model for interactions responsible for the structure and stability of emulsions. It has been shown that the interfacial structure can be

manipulated to control droplet deformation and interaction. The prospects for rational modification or design of interfacial structures has been considered and discussed.

Acknowledgments

The research described in this chapter has been funded by the BBSRC through the core strategic grant to the Institute, funding for apparatus from the BBSRC Bioimaging Initiative (D 11145) and BBSRC research grants involving collaborations with researchers at Colworth House, Unilever, UK (D 13192), and with Professor Dickinson's group at The Proctor Department of Food Science, University of Leeds, UK (D 14067). The interfacial studies carried out at IFR were performed collaboratively with P.J. Wilde and A.R. Mackie. The probe microscopy studies were made by A.P. Gunning, P.A. Gunning, A.R. Kirby, and N.C. Woodward.

References

- Clark, D.C., Coke, M., Mackie, A.R., Pinder, A.C., and Wilson, D.R. Molecular-diffusion and thickness measurements of protein-stabilized thin liquid-films, *J. Colloid Interface Sci.*, 138, 207, 1990.
- Clark, D.C., Wilde, P.J., and Wilson, D.R. The effect of pre-isomerized hop extract on the properties of model protein stabilized foams, *J. Inst. Brew.*, 97, 169, 1991.
- Clark, D.C., Mackie, A.R., Wilde, P.J., and Wilson, D.R. Differences in the structure and dynamics of the adsorbed layers in protein-stabilized model foams and emulsions, *Faraday Discuss.*, 98, 253, 1994a.
- Clark, D.C., Wilde, P.J., and Marion, D. The protection of beer foam against lipid-induced destabilization, *J. Inst. Brew.*, 100, 23, 1994b.
- Cooper, D.J., Husband, F.A., Mills, E.N.C., and Wilde, P.J. Role of beer lipid-binding proteins in preventing lipid destabilization of foam, *J. Agric. Food Chem.*, 50, 7645, 2002.
- Dagastine, R.H., Stevens, G.W., Chan, D.Y.C., and Grieser, F. Forces between two oil drops in aqueous solution measured by AFM, *J. Colloid Interface Sci.*, 273, 339, 2004.
- Gunning, A.P., Wilde, P.J., Clark, D.C., Morris, V.J., Parker, M.L., and Gunning, P.A. Atomic force microscopy of interfacial protein films, *J. Colloid Interface Sci.*, 183, 600, 1996.
- Gunning, A.P., Mackie, A.R., Wilde, P.J., and Morris, V.J. *In-situ* observation of surfactant-induced displacement of protein by atomic force microscopy, *Langmuir*, 15, 4636, 1999.
- Gunning, A.P., Mackie, A.R., Kirby, A.R., and Morris, V.J. Scanning near-field optical microscopy of phase separated regions in a mixed interfacial protein (BSA) surfactant (Tween 20) film, *Langmuir*, 17, 2013, 2001.

- Gunning, A.P., Mackie, A.R., Wilde, P.J., and Morris, V.J. Atomic force microscopy of emulsion droplets: probing droplet–droplet interactions, *Langmuir*, 20, 116, 2004a.
- Gunning, P.A., Mackie, A.R., Gunning, A.P., Wilde, P.J., Woodward, N.C., and Morris, V.J. The effect of surfactant type on protein displacement from the air–water interface, *Food Hydrocolloids*, 18, 509, 2004b.
- Gunning, P.A., Mackie, A.R., Gunning, A.P., Woodward, N.C., Wilde, P.J., and Morris, V.J. The effect of surfactant type on surfactant–protein interactions at the air–water interface, *Biomacromolecules*, 5, 984, 2004c.
- Li, W., Dobraszezyk, B.J., and Wilde, P.J. Surface properties and locations of gluten proteins and lipids revealed using confocal scanning laser microscopy in bread dough, *J. Cereal Sci.*, 39, 403, 2004.
- Mackie, A.R., Gunning, A.P., Wilde, P.J., and Morris, V.J. The orogenic displacement of protein from the air/water interface by competitive adsorption, *J Colloid Interface Sci.*, 210, 157, 1999.
- Mackie, A.R., Gunning, A.P., Wilde, P.J., and Morris, V.J. Orogenic displacement of protein from the oil–water interface, *Langmuir*, 16, 2242, 2000a.
- Mackie, A.R., Gunning, A.P., Wilde, P.J., and Morris, V.J. The competitive displacement of β -lactoglobulin from the air–water interface by SDS, *Langmuir*, 16, 8176, 2000b.
- Mackie, A.R., Gunning, A.P., Ridout, M.J., Wilde, P.J., and Morris, V.J. Orogenic displacement in mixed β -lactoglobulin/ β -casein films at the air/water interface, *Langmuir*, 17, 6593, 2001a.
- Mackie, A.R., Gunning, A.P., Ridout, M.J., Wilde, P.J., and Patino, J.R. In situ measurement of the displacement of protein films from the air/water interface by surfactant, *Biomacromolecules*, 2, 1001, 2001b.
- Mackie, A.R., Gunning, A.P., Wilde, P.J., Morris, V.J., Pugnali, L.A., and Dickinson, E. The growth of surfactant domains in protein films, *Langmuir*, 19, 6032, 2003.
- Mills, E.N.C., Wilde, P.J., Salt, L.J., and Skeggs, P. Bubble formation and stabilization in bread dough, *Food Bioprocess Process.*, 81, 189, 2003.
- Morris, V.J. Probing molecular interactions in foods, *Trends Food Sci. Technol.*, 15, 291, 2004.
- Ogawa, S., Decker, E.A., and McClements, D.J. Production and characterization of O/W emulsions containing droplets stabilized by lecithin–chitosan–pectin multilayered membranes, *J. Agric. Food Chem.*, 52, 3595, 2004.
- Saeker, D.K. and Wilde, P.J. Restoration of protein stability through electrostatic propylene glycol alginate-mediated protein–protein interactions, *Colloids Surf. B Interfaces*, 15, 203, 1999.
- Sarker, D.K., Wilde, P.J., and Clark, D.C. Control of surfactant-induced destabilization of foams through polyphenol-mediated protein–protein interactions, *J. Agric. Food Chem.*, 43, 295, 1995.
- Sarker, D.K., Wilde, P.J., and Clark, D.C. Enhancement of protein foam stability by formation of wheat arabinoxylan-protein crosslinks, *Cereal Chem.*, 493, 1998.
- Wilde, P.J. and Clark, D.C. The competitive displacement of β -lactoglobulin by Tween 20 from oil–water and air–water interfaces, *J. Colloid Interface Sci.*, 155, 48, 1993.
- Wilde, P.J., Mackie, A.R., Husband, F.A., Gunning, A.P., and Morris, V.J. Proteins and emulsifiers at liquid interfaces, *Adv. Colloid Interface Sci.*, 63, 108, 2004.
- Woodward, N.C., Wilde, P.J., Mackie, A.R., Gunning, A.P., Gunning, P.A., and Morris, V.J. The effect of processing on the displacement of whey protein; applying the orogenic model to a real system, *J. Agric. Food Chem.*, 52, 1287, 2004.

16

Stability of Cloudy Apple Juice Colloidal Particles Modeled with the Extended DLVO Theory

Diego B. Genovese and Jorge E. Lozano

CONTENTS

Introduction	289
Materials and Methods	292
Results and Discussion	292
Conclusion	298
Acknowledgments	299
References	299

Introduction

Cloudiness of turbid or opalescent apple juice is provided by particulate material that remains in suspension (Genovese et al., 1997). This cloud has been modeled to consist of negatively charged pectin wrapped around a core of positively charged protein (Yamasaki et al., 1964; Endo, 1997). Particle sizes above 0.5 μm are unstable and settle out (Beveridge, 2002). Below this range, particles are colloidal in nature and follow Brownian motion. These colloidal particles are retained in suspension as a result of their small size, mutual charge repulsion, and the protective effect of pectin (Beveridge, 1997).

Pectin acts as a protective colloid in turbid juices, retarding the coagulation and precipitation of small insoluble particles. Pectin slows aggregation by coating the particles, preventing the close-enough approach of one to another needed for the formation of hydrogen bonds or effective dipole interactions. In addition, it may give particles a large enough charge that significant electrostatic repulsion takes place between particles

(Van Buren, 1989). However, the colloidal mechanism of particle stabilization in cloudy juices is still unclear.

In general, in dispersions of fine particles in a liquid, frequent encounters between particles occur through Brownian motion. Whether such encounters result in permanent contact or whether the particles rebound and remain free is determined by the forces between them. A dispersion is colloidally stable when its particles remain permanently free. In dilute dispersions it is sufficient to consider only interactions between pairs of particles (Overbeek, 1977). This would be the case for cloudy apple juice (CAJ) where the volume fraction of particles is less than 0.5% (Genovese and Lozano, 2000).

The forces acting on a colloidal system include gravitational, diffusion, viscous, inertial, attractive Van der Waals, and electrical repulsive forces. Because most of these forces are functions of the particle size, it is important to know both particles size and size distribution. The classical Derjaguin–Landau–Verwey–Overbeek (DLVO) theory describes colloid stability on the basis of pair interaction, considering only attractive van der Waals forces and repulsive electrostatic forces (Molina-Bolívar and Ortega-Vinuesa, 1999). The total potential energy of interaction, U_{Tc} , between two particles is defined as:

$$U_{Tc} = U_A + U_E \quad (16.1)$$

where sub index c stands for “classical.” The van der Waals attraction energy, U_A , is expressed as

$$U_A = -\frac{A}{6} \left[\frac{2a^2}{H(4a+H)} + \frac{2a^2}{(2a+H)^2} + \ln \frac{H(4a+H)}{(2a+H)^2} \right] \quad (16.2)$$

where A is the Hamaker constant for particles interacting in the medium, a is the particle radius, and H is the distance between the surfaces of the particles. The value of A depends on the properties of the particles and the dispersing medium.

Electrically charged particles in aqueous media are surrounded by ions of opposite charge (counterions) and electrolyte ions, namely, the electrical double layer. The quantity U_E represents the energy of repulsion caused by the interaction of the electrical double layers. The expression for U_E depends on the ratio between the particle radius and the thickness of the electrical double layer, κ^{-1} , called the Debye length. For $\kappa a > 5$ (Quemada and Berli, 2002):

$$U_E = 2\pi\epsilon_0\epsilon_r\psi_0^2a \ln[1 + \exp(-\kappa H)] \quad (16.3)$$

where ϵ_0 is the permittivity in vacuum, ϵ_r is the relative permittivity (= dielectric constant) of the medium, and ψ_0 is the surface potential of particles. The value of ψ_0 is often unknown; however, the potential to be used in calculating the repulsion is the potential in the Stern plane (plane of closest approach of counterions to the surface), ψ_δ , rather than ψ_0 . In most cases, the nearest practical approximation to ψ_δ is the zeta-potential (ζ), and

this presupposes that the Stern plane and the slipping plane are nearly identical (Overbeek, 1977). The Debye length is given by the expression

$$\kappa^{-1} = \sqrt{\frac{\epsilon_0 \epsilon_r k_B T}{2eFI}} \quad (16.4)$$

where k_B is the Boltzman constant, T is the temperature, e is the electronic charge, F is Faraday's constant, and I is the ionic strength calculated as

$$I = \frac{1}{2} \sum c_i z_i^2 \quad (16.5)$$

where z_i and c_i are the valence and molar concentration of ions i in the bulk, respectively (Overbeek, 1977; Zhang et al., 2004). Increasing the concentration of counterions is expected to reduce the net surface charge and the thickness of the double layer, reducing the electrostatic repulsion, and vice versa. In apple juice, the dominant mobile positive ion is K , although other cations such as Ca , Mg , Cu , and Fe have also been found (Van Buren, 1989; Beveridge, 1997). A variety of organic and inorganic anions provide the mobile negative ions.

Although DLVO theory was originally developed in order to predict the adhesion behaviors between nonbiological lyphobic particles, this theory has been applied to describe adhesion in a wide range of applications, such as stability of microorganisms suspension (Chang and Chang, 2002). The classical DLVO theory (Equation 16.1) alone generally fails to predict the stabilities of very hydrophilic and very hydrophobic particle suspensions where other interaction energies exist, such as the short-range hydration forces (Molina-Bolívar and Ortega-Vinuesa, 1999). In the case of hydrophilic particles in aqueous media, like apple juice particles, the surface functional groups (such as hydrated ions or hydroxyl groups) may interact via hydrogen bonding with the water molecules, producing a restriction in their motion referred to as hydration pressure. The pressure of the water in the boundary layer increases as surfaces approach one another resulting in a repulsive interaction (Israelachvili, 1992; Grasso et al., 2002). Hydrophilic particles with low ξ potential, which would not be able to form a lasting stable suspension according to classical DLVO theory, may be predicted as stable suspension by another approaches, as the (extended) XDLVO theory (Wu et al., 1999).

Therefore, the XDLVO theory should be used to calculate the total interaction energy:

$$U_{Te} = U_A + U_E + U_H \quad (16.6)$$

where sub-index e stands for "extended." It has been shown (Chang and Chang, 2002) that the empirical Equation of repulsive hydration energy, U_H , interacting between two hydrophilic spheres can be written as

$$U_H = \pi a \kappa^{-1} C_0 \exp(-H/\lambda) \quad (16.7)$$

where λ is the decay length, usually in the range 0.2 to 1.1 nm for 1:1 electrolytes, and C_0 is a constant usually in the range 3 to 30 mJ/m².

The aim of this work was to study the effect of the ionic atmosphere surrounding the particle on the stability of a CAJ suspension, and to predict it with the classical and the extended DLVO theory.

Materials and Methods

Granny Smith apples were bought on a local market and stored at 4°C until further use. Five samples of CAJ, 10.5 ± 0.4 °Brix, $\text{pH} = 3.52 \pm 0.06$, were obtained by a method described elsewhere (Genovese et al., 1997). A strongly acid cationic exchange resin (Dowex-50W, Sigma, U.S.A.) was added to each sample until the juice reached a minimum pH of 2.41 ± 0.05 (CAJ + cationic resins (CR)). CR are insoluble polyelectrolytes with the ability to reversibly exchange cations with a liquid phase. A typical example of a cationic exchange reaction with potassium ions in aqueous solution is (Norman, 1990)



Particle-size distribution and zeta-potential measurements of CAJ and CAJ + CR were performed on a Malvern Zetasizer 3000 (Malvern Instruments Inc., London). Both CAJ and CAJ + CR were centrifuged at $4200 \times g$ during 15 min to remove unstable particles (Stahle-Hamatschek, 1989; Genovese et al., 1997). Cloud stability (S%) was calculated with the expression (Genovese and Lozano, 2001; Mensah-Wilson et al., 2002):

$$S\% = \frac{\text{Op}_C}{\text{Op}_0} \times 100 \quad (16.9)$$

where Op_0 and Op_C are the opacities before and after centrifugation, respectively. Opacity was measured in a Hunterlab Ultrascan XE Colorimeter (Hunter Assoc. Laboratory, USA) as described elsewhere (Genovese and Lozano, 2001). Particle-size distribution was measured again after centrifugation. All measurements were performed at 25°C.

Finally, another four samples of CAJ were treated with different amounts of RC (0, 6.7, 13.3, and 36.7 mg/ml, respectively). For each sample, concentration of metal ions K, Ca, Fe, Cu, and Zn were determined by atomic absorption spectroscopy in a GBC 902AA model Spectrophotometer. Since valence and concentration of anions in CAJ were unknown, ionic strength was estimated assuming a symmetric z-z electrolyte for each cation.

Results and Discussion

As shown in Table 16.1, the dominant metal ion found in CAJ was potassium (94.2% w/w), followed by calcium (5.5% w/w), while the other cations (iron,

TABLE 16.1

Effect of Cationic Resin (CR) Treatment on the pH, Ion Concentration, and Ionic Strength (*I*) of Cloudy Apple Juice (CAJ)

CR (mg/ml)	pH ^a	Ion Concentration (ppm) ^a					<i>I</i> × 10 ³ (mol/l) ^b
		K	Ca	Fe	Cu	Zn	
0	3.55	615.1	35.6	1.36	0.50	0.47	20.58
6.7	3.10	308.9	29.9	1.11	0.46	0.31	11.69
13.3	2.65	108.1	21.6	1.05	0.31	0.18	5.39
36.7	2.20	20.9	18.5	0.93	0.10	0.18	2.68

^a Experimental.

^b Calculated with Equation 16.5.

cooper, and zinc) represented less than 0.4% w/w altogether. When CAJ is treated with CR, native cations are replaced by H⁺ ions until equilibrium, as predicted by Equation 16.8. Consequently, addition of CR is expected to decrease pH and concentration of metal ions in CAJ, as observed in our experiments (Table 16.1). As a result, ionic strength (*I*) of the juice also decreased with increasing concentrations of CR. Ionic strength (mol/l) was correlated as a function of juice pH ($R^2 = 0.9997$):

$$I \times 10^3 = 32.94 - 30.58 \text{ pH} + 7.637 \text{ pH}^2 \quad (16.10)$$

Equation 16.10 was used to predict the ionic strength of CAJ and CAJ + CR.

As shown in Table 16.2, addition of CR reduced the zeta-potential (ζ) of CAJ, suggesting that H⁺ ions produced a higher shielding effect on the surface charge of the particles compared with native cations. As proposed later in this work, it seems that this shielding effect is associated with the degree of particle hydration (Figure 16.3). However, the decrease in the ionic strength produced an increase in the thickness of the electrical double layer (κ^{-1}) surrounding the particles. Both effects (decrease in ζ and increase in κ^{-1})

TABLE 16.2

Stability Parameters of Untreated and Resin-Treated Cloudy Apple Juice (CAJ and CAJ + CR, Respectively)

Sample	pH ^a	ζ (mV) ^a	<i>D</i> (nm) ^a	<i>S</i> % ^b	<i>I</i> × 10 ³ (mol/l) ^c	κ^{-1} (nm) ^d	κa
CAJ	3.52 ± 0.06	−6.62 ± 0.73	2274 ± 54	64.9	19.92	2.1	79.3
CAJ + CR	2.41 ± 0.05	−2.82 ± 0.63	2361 ± 114	63.7	3.60	5.0	33.7

^a Experimental.

^b Calculated with Equation 16.9.

^c Calculated with Equation 16.10.

^d Calculated with Equation 16.4.

are expected to affect the electrostatic repulsion energy (U_R), and consequently the stability of the system. However, the cloud stability of CAJ did not change significantly (<2% difference) after CR addition. This result will be analyzed in terms of the classical and the extended DLVO theory.

Average particle diameter (D) of noncentrifuged samples did not show a significant difference (<4%) between CAJ and CAJ + CR. These high particle sizes are attributed to the presence of big/unstable particulate material that will settle out by gravity (Genovese et al., 1997). After 15 min centrifugation at $4200 \times g$, only small/colloidal particles remain in suspension. Interaction forces between these colloidal particles will determine final cloud stability. Consequently, the a value needed for calculation of U_A and U_R (Equation 16.2 and Equation 16.3) was considered as the average particle radius of the centrifuged CAJ, $a = 167 \pm 7$ nm.

Calculated values of κa (Table 16.2) confirm the validity of Equation 16.3 to calculate the electrostatic repulsion energy of CAJ and CAJ + CR. Dielectric constant of apple juice ($\epsilon_r \approx 75$) was obtained from literature (Nelson and Bartley, 2002) and considered to be the same for both samples. Zeta-potential values were used as a valid approximation to the surface potential ($\zeta \approx \psi_0$). Electrostatic repulsion energy normalized with the Brownian thermal energy ($U_R/k_B T$) as a function of the surface-to-surface distance (H) between particles is shown in Figure 16.1 for CAJ and

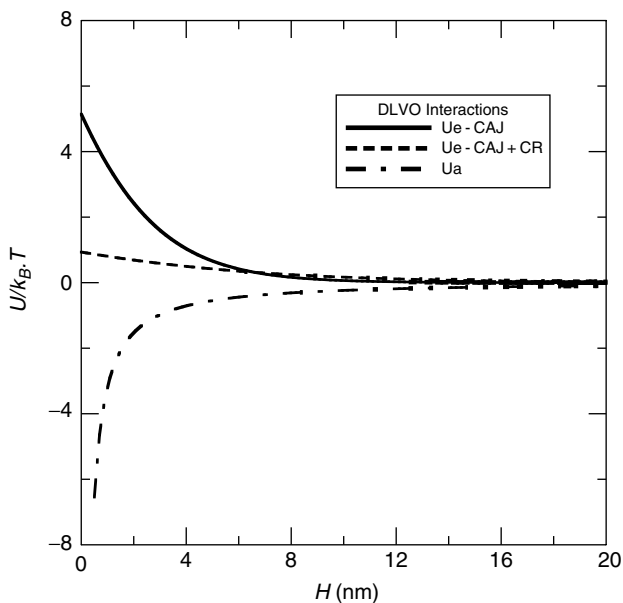


FIGURE 16.1

Electrostatic repulsion (U_r) and Van der Waals attraction (U_a) energies as function of the surface-to-surface distance (H) of cloudy apple juice particles, before and after treatment with a cationic resin (CAJ and CAJ + CR, respectively).

CAJ + CR. It can be observed that at short distances ($H < 6.2$ nm) electrostatic repulsion was higher in CAJ than in CAJ + CR as a result of the higher ζ of CAJ, while the opposite trend (CAJ + CR $>$ CAJ) was found at longer distances due to the higher κ^{-1} of CAJ + CR.

There are no reports of the Hamaker constant (A) for CAJ in the literature, and its determination will be considered in our future works. Nevertheless, it is known that CAJ particles consist of molecular aggregates and cellular debris, which in turn is made up of hydroxyproline-rich glycoproteins (Beveridge, 1997). Rodin and Izmailova (Rodin and Izmailova, 1996) reported a value of $A = 1 \times 10^{-21}$ J ($0.243 k_B T$) for a hydroxyproline-rich gelatin, which is within the experimental range (3×10^{-25} to 2×10^{-21} J) reported for glycoproteins (Jones, 1976). Consequently, that value was applied in Equation 16.2 to estimate the profile (Figure 16.1) of the normalized Van der Waals interaction energy ($U_A/k_B T$). The same value was used for CAJ and CAJ + CR, because A is considered to be an intrinsic property of the material, and consequently the electrolyte should not affect its value (Molina-Bolívar and Ortega-Vinuesa, 1999).

Normalized total interaction energy ($U_{Tc}/k_B T$) calculated with the classical DLVO theory (Equation 16.1) is represented in Figure 16.2. It can be observed that, unlike CAJ, CAJ + CR did not show an energy barrier or maximum net repulsion between particles, U_{Tmax} . Considering that cloud

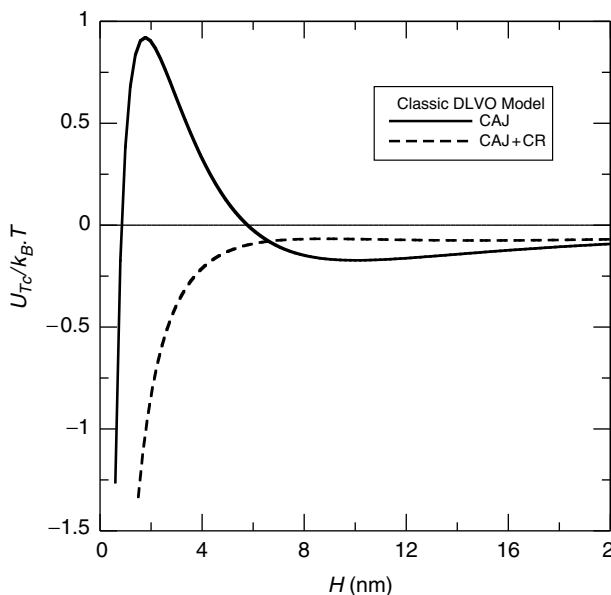
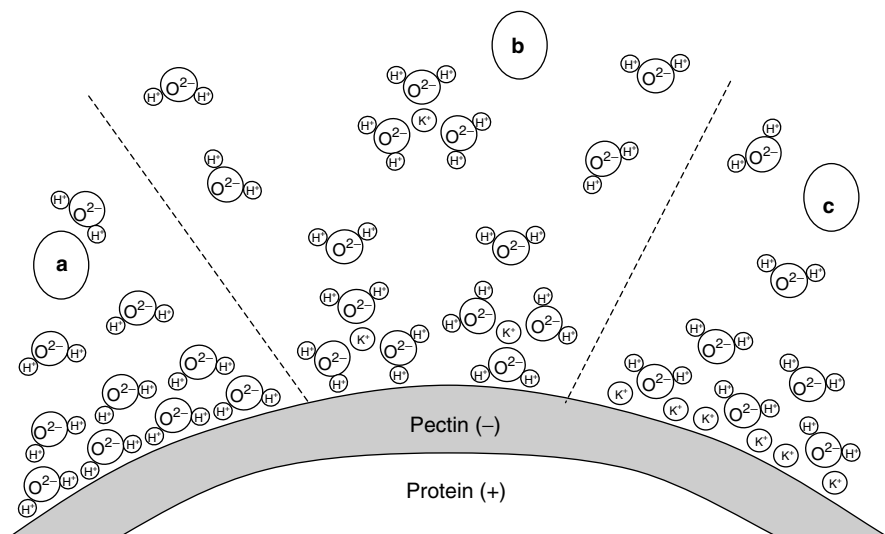


FIGURE 16.2

Classic DLVO total interaction energy (U_{Tc}) as function of the surface-to-surface distance (H) of cloudy apple juice particles, before and after treatment with a cationic resin (CAJ and CAJ + CR, respectively).

**FIGURE 16.3**

Tentative mechanisms of hydration via hydrogen-bonding, for a cloudy apple juice particle.

stability is determined by U_{Tmax} (Chang and Chang, 2002), the classical DLVO theory predicts that CAJ should be far more stable than CAJ + CR, and that CAJ + CR would flocculate spontaneously. However, that was not the behavior observed in our experiments. Therefore, it is evident that hydration forces played a significant role in the stability of these juices.

Since the water-insoluble pectin coating the particles is constituted by hydrophilic polygalacturonic acid, it is probable that water molecules formed hydrogen bonds with its negative functional groups (Figure 16.3a). The first layer of water molecules (primary hydration shell) is highly restricted in its motion, resulting in structural or hydration forces. The second layer of water molecules (secondary hydration shell) has more freedom to rotate and so on. Consequently, the effect of hydration forces decreases exponentially (Equation 16.7) from the primary hydration cell to the bulk of the solution. As two particles approach, the repulsive interaction between hydration shells is the result of hydrogen-bonding repulsion from opposing layers of orientated water molecules (Israelachvili, 1992; Grasso et al., 2002).

In apple juice, it is also possible that water molecules formed hydrogen bonds with the free cations, and some (or all) of these hydrated ions were later adsorbed on particle's surface (Figure 16.3b). Another possibility is that water molecules hydrated previously adsorbed cations (Figure 16.3c). Either of these hydration mechanisms could happen alone or in combination. Nevertheless, it is expected that the scenario depicted in the middle and/or the right side of Figure 16.3 was more frequent in CAJ, where more cations were present, while the situation on the left side was probably more frequent in CAJ + CR, with fewer cations.

So far, we are not able to predict the stability of CAJ and CAJ + CR with the extended DLVO theory (Equation 16.6), because values of λ and C_0 are not available to calculate U_H with Equation 16.7. However, we may be able to estimate U_{Te} and U_H from stability results. Since both juices (CAJ + CR and CAJ) showed the same stability, it means that both juices should have the same U_{Tmax} . Combining Equation 16.1, Equation 16.6, and Equation 16.7 this can be expressed as follows:

$$\begin{aligned} U_{Tc1}(H_1) + \pi a \kappa_1^{-1} C_{01} \exp(-H_1/\lambda_1) \\ = U_{Tc2}(H_2) + \pi a \kappa_2^{-1} C_{02} \exp(-H_2/\lambda_2) \end{aligned} \quad (16.11)$$

where sub-indexes 1 and 2 stand for CAJ and CAJ + CR, respectively. Equation 16.11 has six unknown variables: H_1 , λ_1 , C_{01} , H_2 , λ_2 , and C_{02} . The values of H_1 and H_2 can be obtained by making zero the derivatives of U_{Te1} and U_{Te2} , respectively. Also, it is known that the decay length does not vary significantly with I , and consequently $\lambda_1 \approx \lambda_2 \approx \lambda$. As a preliminary approximation, we will assume a value of $\lambda \approx 1$ nm, which was used for soy proteins in water (Berli et al., 1999). It has also been observed (Chang and Chang, 2002) that U_H decreases with increasing electrolyte concentrations. If we assume that this effect is entirely absorbed by κ^{-1} in Equation 16.7, then $C_{01} \approx C_{02} \approx C_0$ is the only unknown variable. The problem was solved

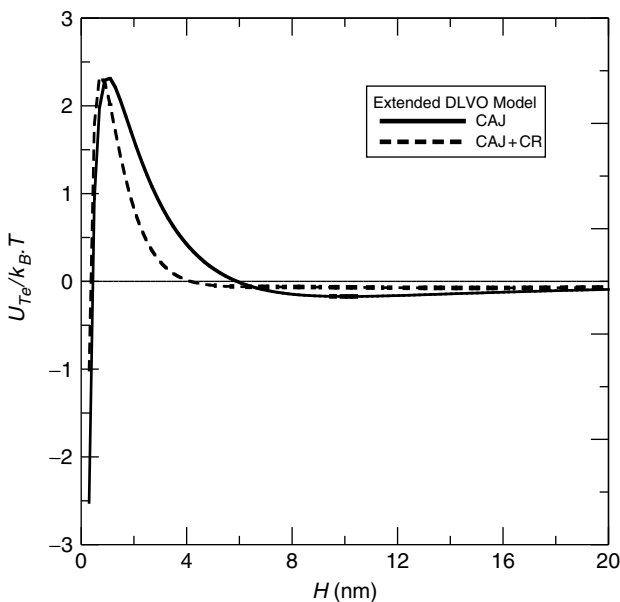
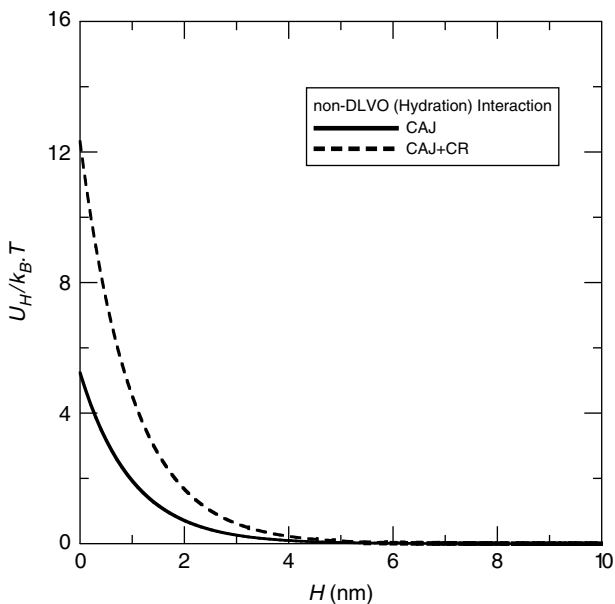


FIGURE 16.4

Extended DLVO total interaction energy (U_{Te}) as function of the surface-to-surface distance (H) of cloudy apple juice particles, before and after treatment with a cationic resin (CAJ and CAJ + CR, respectively).

**FIGURE 16.5**

Hydration repulsion energy (U_h) as function of the surface-to-surface distance (H) of cloudy apple juice particles, before and after treatment with a cationic resin (CAJ and CAJ + CR, respectively).

graphically, inputting different values of Co in Equation 16.11 until $U_{Tmax1} \approx U_{Tmax2}$ (Figure 16.4). Following this iterative method, we obtained $Co \approx 0.0195 \text{ mJ/m}^2$. This value is two orders of magnitude lower than expected. This is probably attributed to an underestimation of the value of A .

Normalized hydration repulsion energy ($U_H/k_B T$) calculated with Equation 16.1 is shown in Figure 16.5. As mentioned, it can be observed that hydration is a short-range interaction energy. As expected, hydration forces were stronger in CAJ + CR to compensate its lower electrostatic repulsion. This may be justified as follows: as the hydrated-adsorbed metal cations were exchanged by protons, it is probable that the particle's surface became more hydrophilic (Chang and Chang, 2002); therefore the repulsive hydration force increased with the addition of CR. As suggested earlier, it seems that this stronger hydration produced a shielding effect on the particle-surface charge, reducing the absolute zeta potential.

Conclusion

Experimental results showed that treatment of CAJ with a cationic resin decreased the zeta (\approx surface) potential of the particles, decreased the ionic strength, and consequently increased the thickness of the electrical double layer surrounding the particles (Debye length), but did not change cloud

stability. The classical DLVO model alone was unable to explain this behavior. It seems that non-DLVO hydration repulsion forces played a significant role in the stability of these juices.

Acknowledgments

This investigation was supported in part by a research grant from the Agencia Nacional de Promoción Científica y Tecnológica (BID 1202-OC/AR), Argentina.

References

- Berli, C.L.A., Deiber, J.A., and Añón, M.C. Connection between rheological parameters and colloidal interactions of a soy protein suspension, *Food Hydrocolloids*, 13, 507, 1999.
- Beveridge, T. Haze and cloud in apple juices, *Crit. Rev. Food Sci. Nutr.*, 37, 75, 1997.
- Beveridge, T. Opalescent and cloudy fruit juices: formation and particle stability, *Crit. Rev. Food Sci. Nutr.*, 42, 317, 2002.
- Chang, Y.I. and Chang, P.-K. The role of hydration force on the stability of the suspension of *Saccharomyces cerevisiae* — application of the extended DLVO theory, *Colloids Surfaces A*, 211, 67, 2002.
- Endo, A. Studies on the enzymatic clarification of apple juice, *Agric. Biol. Chem.*, 2, 25, 1965.
- Beveridge, T. Haze and cloud in apple juices, *Crit. Rev. Food Sci. Nutr.*, 37, 75, 1997.
- Genovese, D.B., Elustondo, M.P., and Lozano, J.E. Color and cloud stabilization in cloudy apple juice by steam heating during crushing, *J. Food Sci.*, 62, 1171, 1997.
- Genovese, D.B. and Lozano, J.E. Effect of cloud particle characteristics on the viscosity of cloudy apple juice, *J. Food Sci.*, 65, 641, 2000.
- Genovese, D.B. and Lozano, J.E. The effect of hydrocolloids on the stability and viscosity of cloudy apple juices, *Food Hydrocolloids*, 15, 1, 2001.
- Grasso, D., Subramaniam, K., Butkus, M., Strevett, K., and Bergendahl, J. A review of non-DLVO interactions in environmental colloidal systems, *Rev. Environ. Sci. Bio/Technol.*, 1, 17, 2002.
- Israelachvili, J.N. *Intermolecular and Surface Forces*, Academic Press, London, 1992.
- Jones, M.N. Hydrogen bonding in cellular cohesion, *FEBS Lett.*, 62, 21, 1976.
- Mensah-Wilson, M., Reiter, M., Bail, R., Neidhart, S., and Carle, R. Cloud stabilizing potential of pectin on pulp-containing fruit beverages, *Fruit Process.*, 2, 47, 2002.
- Molina-Bolívar, J.A. and Ortega-Vinuesa, J.L. How proteins stabilize colloidal particles by means of hydration forces, *Langmuir*, 15, 2644, 1999.
- Nelson, S.O. and Bartley, P.G. Jr. Frequency and temperature dependence of the dielectric properties of food material, *Trans. ASAE*, 45, 1223, 2002.
- Norman, S.I. Juice enhancement by ion exchange and adsorbent technologies, *Production and Packaging of Non-Carbonated Fruit Juices and Fruit Beverages*, D. Hicks, ed., Blackie-Van Nostrand Reinhold, New York, 1990.

- Overbeek, J.Th.G. Recent developments in the understanding of colloid stability, *Colloid and Interface Science*, M. Kerker, A.C. Zettlemoyer, and R.L. Rowell, eds., Academic Press Inc, New York, 1977.
- Quemada, D. and Berli, C. Energy of interaction in colloids and its implications in rheological modeling, *Adv. Colloid Interface Sci.*, 98, 51, 2002.
- Rodin, V.V. and Izmailova, V.N. NMR method in the study of the interfacial adsorption layer of gelatin, *Colloids Surfaces A*, 106, 95, 1996.
- Stahle-Hamatschek, S. Cloud composition and its effect on cloud stability in natural cloudy apple juices, *Flussiges Obst.*, 56, 543, 1989.
- Van Buren, J.P. Causes and prevention of turbidity in apple juice, *Processed Apple Products*, D.L. Downing, ed., Van Nostrand Reinhold, New York, 1989.
- Wu, W., Giese, R.I., and Van Oss, C.J. Stability vs. flocculation of particle suspension in water-correlation with the extended DLVO approach for aqueous system, compared with DLVO theory, *Colloidd Surfaces B: Biointerfaces*, 14, 47, 1999.
- Yamasaki, M., Yasui, T., and Arima, K. Pectic enzymes in the clarification of apple juice, *Agric. Biol. Chem.*, 28, 779, 1964.
- Zhang, X., Grimes, B.A., Wang, J.C., Lacki, K.M., and Liapis, A.I. Analysis and parametric sensitivity in the behavior of overshoots in the concentration of a charged adsorbate in the adsorbed phase of charged adsorbent particles: practical implications for separation of charged solutes, *J. Colloid Interface Sci.*, 273, 22, 2004.

**Part 5: Overlapping Water
Relations and Material
Sciences for the
Improvement of Quality
Products**

The Hydration Limit of Amorphous Solids and Long-Term Stability

David Lechuga-Ballesteros and Danforth P. Miller

CONTENTS

Hydration Limit and Long-Term Stability.....	303
Hydration Limit of Small Molecule Hydrophilic Glasses	304
Hydration Limit of Hydrophilic Polymer Glasses	306
Hydration Limit of Protein Glasses	307
Is the Hydration Limit Related to the Zero Mobility Temperature?.....	307
References	307

Hydration Limit and Long-Term Stability

Predicting the long-term stability of amorphous solids remains an unresolved challenge. The simplest approach, selecting a storage condition well below the glass-transition temperature, T_g , has been widely used. More recently, determination of the so-called zero mobility temperature, T_0 , the temperature at which the characteristic relaxation time exceeds pharmaceutically relevant storage times, is a frequently used predictor of the physical and chemical stability of amorphous pharmaceutical solids. The effect of residual water on stability is often estimated using the T_g of the hydrated amorphous solid, as dictated by its degree of plasticization by water. With the advent of automated water vapor sorption microbalances, rapid measurements of the moisture sorption isotherms of amorphous systems have become commonplace. Despite these advances, the combined effects of water content and storage temperature, T_s , on the stability of such amorphous systems has not been described in a straightforward fashion.

Hydration Limit of Small Molecule Hydrophilic Glasses

The water-sorption properties of amorphous solids and the deleterious impact of residual moisture on physical stability have been known for a long time (Makower and Dye, 1956). Makower and Dye studied the physical stability of amorphous sucrose during exposure to various relative humidities (25°C). By periodically measuring the masses of the samples and observing them under cross-polarized light, they found that samples remained amorphous for over 800 days when stored below 12% RH at 25°C (Table 17.1). In contrast, crystallization was observed at 200 days when stored at 16% RH; induction times for crystallization were correspondingly shorter at higher relative humidities (see Table 17.1). The corresponding T_g of the amorphous sucrose at each relative humidity is also shown in Table 17.1. If correlated to T_g , it is evident that crystallization occurs almost instantaneously when the storage temperature is about 20°C above the T_g (i.e., for the sample stored at 33.6% RH). This is not surprising because, at this $T_s - T_g > 20^\circ\text{C}$ (where T_s is the storage temperature), the viscosity of the amorphous solid is less than ca. 10^7 to 10^{10} Pa s, such that structural collapse is observed within minutes to hours (Sun, 1997). The induction time for crystallization continuously increases even when the amorphous solid is stored well below its T_g , where the viscosity is assumed to be constant (ca. 10^{12} to 10^{14} Pa s). Crystallization is observed to occur in within 42 days (24% RH) at $T_s = T_g$, within 200 days when stored 13°C below T_g and

TABLE 17.1
Amorphous Sucrose: Water Content, Estimated Glass Transition Temperature, and Induction Time for Crystallization for Samples Stored at the Indicated RH Values (25°C)

RH (%) ^a	Water Content (% w/w) ^a	T_g (°C) ^b	$T_g - T_s$ (°C) ^c	Time (days) ^a
4.6	0.98	60	35	> 800
8.6	1.56	52	27	> 800
11.8	2.14	45	20	> 800
16.2	2.8	38	13	200
24.0	4.1	24	−1	42
28.2	5.2	15	−10	12
33.6	-	6	−19	<2

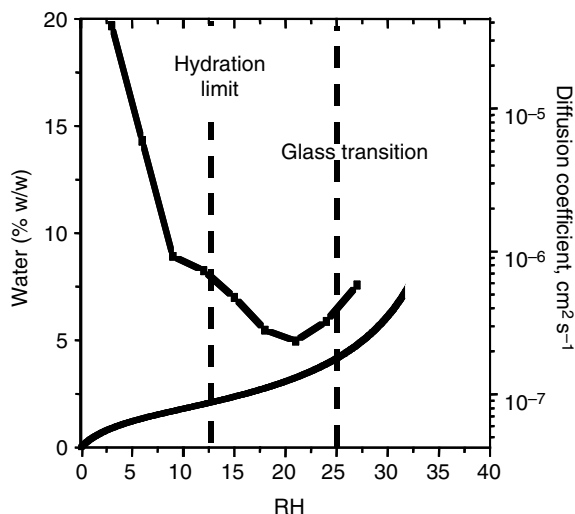
^a From Makower and Dye (1956).
^b Calculated using Gordon–Taylor equation with an intrinsic glass transition, T_g^0 of 74°C (347 K) and −139°C (135 K) for sucrose and water, respectively, and a Gordon–Taylor constant value of 0.13675.
^c The storage temperature, T_s is 25°C.

crystallization of amorphous sucrose is arrested for longer than 800 days when stored more than 20°C below the T_g .

Because of the presence of residual water in spray-dried amorphous powders, we are keenly interested in the interactions of water vapor with amorphous solids, especially how these interactions can be used to predict long-term physical stability. We developed an isothermal microcalorimetric technique (Lechuga-Ballesteros et al., 2003), RH-perfusion microcalorimetry, to measure the energetic response of an amorphous sample to a linearly increasing RH profile. Despite the vast differences in the timescales of both experiments, the results obtained from studying the so-called moisture-induced thermal activity trace (MITAT) obtained are consistent with those of Makower and Dye, (1956). RH-perfusion calorimetry has enabled rapid screening of candidate formulations and assessment of suitable storage conditions for a given formulation.

Analysis of the thermodynamic quantities of an RH-perfusion experiment provides additional insight into the effects of residual water on stability. We have determined that, beyond 15% RH, the enthalpy of interaction between amorphous sucrose and water vapor reaches a plateau of about 42 kJ mol⁻¹, a value corresponding to the enthalpy of condensation of water. Mechanistically, this can be interpreted as evidence that, at and above a certain relative humidity, water molecules in the vapor state interact with the hydrated amorphous sample as they would with liquid water (i.e., simple physisorption). The corresponding water content has been referred to as W_m , the hydration limit. We have also suggested that the hydration limit could be analogous to the solubility of water vapor in the amorphous solid because the hydration limit is similar for compounds with similar chemical composition regardless of the molecular weight (Lechuga-Ballesteros et al., 2002).

To quantify the mobility of water above and below the hydration limit, we have determined the diffusivity of water vapor in a compressed cylindrical sample of amorphous sucrose using an automated microbalance with humidity control. Preliminary results show that the hydration limit may delineate two diffusive regimes of water within the amorphous solid (Figure 17.1) (Miller et al., 2001). Further studies are being conducted in our laboratory to investigate this hypothesis. One salient observation is that the diffusivity of water within the amorphous solid increases as the material is dried below its hydration limit. Because stability is most often correlated with dryness, this suggests that the overall stability of an amorphous solid is not always correlated with the mobility of water molecules within it. We hypothesize that, under nearly dry conditions, water molecules interact with the amorphous solid structure, but readily move within the free volume fraction of the rigid amorphous structure. At higher water contents (yet still under the hydration limit), clusters of water molecules begin to form, restricting the average mobility of water molecules within the amorphous solid. We propose that, above this limit, the solid may begin to dissolve in the water to form a supersaturated solution, providing a medium for crystal

**FIGURE 17.1**

Water-sorption isotherm of amorphous sucrose at 25°C and diffusion coefficient of water at 25°C within compressed disks of amorphous sucrose as a function of relative humidity.

growth. Similar results regarding the heat of condensation and the diffusivity behavior of water within the amorphous solid have been generated for another model amorphous system (spray-dried raffinose) in our laboratory (Miller and Lechuga-Ballesteros, 2001). However, because the stable crystalline form of raffinose is a pentahydrate crystal, crystallization does not occur until the water content is well above the hydration limit.

Hydration Limit of Hydrophilic Polymer Glasses

Similar behavior has been observed for noncrystallizing polymers. For example, the diffusivity of water in poly(vinylpyrrolidone) (PVP) (Oksanen and Zografi, 1993) has been shown to increase at water contents beyond the hydration limit. Additional reports have shown that the hydration limit has physical significance for other polymer excipients. Microcrystalline cellulose and lactose for compression, for example, lose their direct compaction properties at water contents just below W_m (Huettenrauch and Jacob, 1977), and gelatin capsules become brittle as the water content is reduced below W_m (Kontny and Mulski, 1989). Recently, the chemical stability of a model peptide in PVP matrices was shown to improve when the amorphous dispersion was stored below the polymer's hydration limit (Lai et al., 1999a; Lai et al., 1999b; Lechuga-Ballesteros et al., 2002).

Hydration Limit of Protein Glasses

The effect of “residual water” on either protein stability or enzyme activity continues to be a topic of great interest. For example, several properties of lysozyme (e.g., heat capacity, diamagnetic susceptibility (Hageman, 1988), and dielectric behavior (Bone and Pethig, 1985; Bone, 1996)) show an inflection point at the hydration limit. Detailed studies on the direct current protonic conductivity of lysozyme powders at various levels of hydration have suggested that the onset of hydration-induced protonic conduction (and quite possibly for the onset of enzymatic activity) occurs at the hydration limit. It was hypothesized that this threshold corresponds to the formation of a percolation network of absorbed water molecules on the surface of the protein (Careri et al., 1988). More recently, Smith et al., (2002) have shown that, beyond the hydration limit, the heat of interaction of water with the amorphous solid approaches the heat of condensation of water, as we have shown to be the case for amorphous sugars.

Is the Hydration Limit Related to the Zero Mobility Temperature?

Though there have been significant advances in the sophistication of long-term stability predictions (i.e., beyond a simple T_g -based approach), the hydration limit continues to be an active area of research in our and others' laboratories. The hydration limit may be related to the temperature of “zero mobility” and that the use of the temperature dependence of the hydration limit has shown some promise as a quantitative approach to determine the effect of residual water on the long-term stability of amorphous solids.

References

- Bone, S. Dielectric and gravimetric studies of water binding to lysozyme, *Phys. Med. Biol.*, 41, 1265, 1996.
- Bone, S. and Pethig, R. Dielectric studies of protein hydration and hydration-induced flexibility, *J. Mol. Biol.*, 323, 1985.
- Careri, G., Giansanti, A., and Rupley, J.A. Critical exponents of protonic percolation in hydrated lysozyme powders, *Phys. Rev. A*, 37, 2703, 1988.
- Hageman, M.J. The role of moisture in protein stability, *Drug Dev. Ind. Pharm.*, 14, 2047, 1988.
- Huettenrauch, R. and Jacob, J. Über einen neuen Zusammenhang Zwischen Tablettenbildung und Feuchtigkeit der Ausgangsstoffe, *Pharmazie*, 32, 241, 1977.
- Kontny, M.J. and Mulski, C.A. Gelatin capsule brittleness as a function of relative humidity at room temperature, *Int. J. Pharm.*, 54, 79, 1989.

- Lai, M.C., Hageman, M.J., Schowen, R.L., Borchardt, R.T., Laird, B.B., and Topp, E.M. Chemical stability of peptides in polymers. 1. Effect of water on peptide deamidation in poly(vinyl alcohol) and poly(vinyl pyrrolidone) matrices, *J. Pharm. Sci.*, 88, 1073, 1999a.
- Lai, M.C., Hageman, M.J., Schowen, R.L., Borchardt, R.T., Laird, B.B., and Topp, E.M. Chemical stability of peptides in polymers. 2. Discriminating between solvent and plasticizing effects of water on peptide deamidation in polyvinylpyrrolidone, *J. Pharm. Sci.*, 88, 1081, 1999b.
- Lechuga-Ballesteros, D., Miller, D.P., and Bakri, A. Characterization of the interactions of water vapor and amorphous pharmaceutical solids, *Pharm. Res.*, 20, 308, 2003.
- Lechuga-Ballesteros, D., Miller, D.P., and Zhang, J. Residual water in amorphous solids, measurement and effects on stability, *Progress in Amorphous Food and Pharmaceutical Systems*, H. Levine, ed., The Royal Society of Chemistry, London, pp. 275–316, 2002.
- Makower, B. and Dye, W.B. Equilibrium moisture content and crystallization of amorphous sucrose and glucose, *Agric. Food Chem.*, 4, 72, 1956.
- Miller, D.P. and Lechuga-Ballesteros, D. Characterization of raffinose and its interactions with water, *AAPS Pharm. Sci.*, 3, Abstract, 2001.
- Miller, D.P., Lechuga-Ballesteros, D., and Bakri, A. Development of stability diagrams for amorphous pharmaceutical solids, *Pharmaceutical Congress of the Americas*, Orlando, Florida, 2001.
- Oksanen, C.A. and Zografi, G. Molecular mobility in mixtures of absorbed water and solid poly(vinylpyrrolidone), *Pharm. Res.*, 10, 791, 1993.
- Smith, A.L., Shirazi, H.M., and Mulligan, S.R. Water sorption isotherms and enthalpies of water sorption by lysozyme using the quartz crystal microbalance/Heat-conduction calorimeter, *Biochim. Biophys. Acta — Protein Struct. Mol. Enzymol.*, 1594, 150, 2002.
- Sun, W.Q. Temperature and viscosity for structural collapse and crystallization of carbohydrate solutions, *Cryo-Lett.*, 18, 99, 1997.

18

Physicochemical Changes in Frozen Products: Glass Transition and Rheological Behavior in Frozen Starch–Sucrose Hydrocolloid Systems

Noemí Zaritzky and Cristina Ferrero

CONTENTS

Introduction	309
Thermal Characterization of the Systems by Differential Scanning	
Calorimetry	313
Glass Transition Temperatures in Frozen Gelatinized Systems	314
Starch Systems Without Sucrose	314
Starch Systems Containing Sucrose	316
Amylopectin Retrogradation.....	317
Effect of Freezing Rate and Frozen Storage on the Dynamic	
Rheological Behavior	318
Conclusions.....	321
Acknowledgments	322
References	322

Introduction

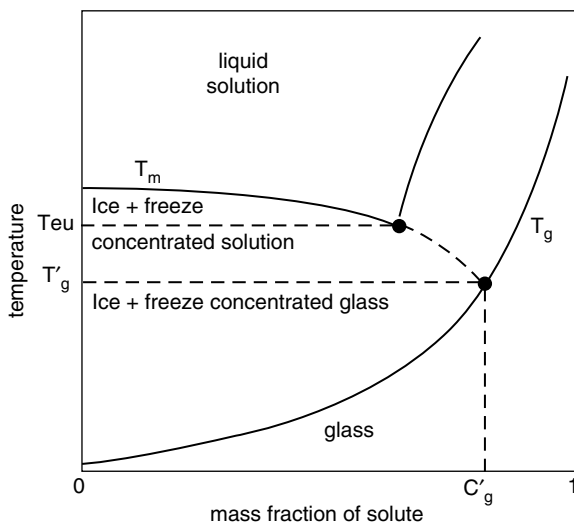
Freezing is recognized as one of the best methods of preserving food quality. Low temperatures inhibit the growth of deteriorative and pathogenic microorganisms, and retard biochemical and enzymatic reactions that would otherwise occur in unfrozen food. Although the physico-chemical reactions slow down at low temperatures, they will nevertheless continue during frozen storage conditions.

Freezing involves different factors in the conversion of water into ice: thermodynamic factors that define the position of the system under equilibrium conditions, and kinetic factors that describe the rates at which equilibrium might be approached. The freezing process includes two main stages: the formation of ice crystals (nucleation), and the subsequent increase in crystal size (growth).

An energy barrier must be surpassed before nucleation can occur. Supercooling is necessary to overcome the free energy that accompanies the formation of a new phase (an ordered solid particle) from the melted phase. Nucleation is necessary for freezing to initiate, thus the temperature can fall below 0°C without crystallization occurring.

Freezing involves the removal of heat accompanied by a phase change, converting water to ice. Meanwhile, in the remaining unfrozen portion, the concentration of dissolved substances increases and water activity of the product decreases.

During freezing of pure water, the viscosity of the liquid phase rises. If the liquid is cooled very quickly the viscosity may reach such high values that molecular rearrangements in the liquid become extremely slow, avoiding ice crystallization. The liquid is in a metastable state until it gets below the glass transition temperature (T_g) where the system is an amorphous solid or glass. A glass is defined as a nonequilibrium, metastable, amorphous, disordered solid of very high viscosity (Le Meste et al., 2002). Glass transition (or glass–liquid transition) is produced when a supercooled melt is converted into a glass during cooling or when the reverse transformation occurs upon heating. Both the supercooled melt and the glass are noncrystalline states; the glass is an out-of-equilibrium state where the liquid-like structure of the melt is maintained as a rigid solid, and the supercooled melt, observed between the glass–liquid transition and the melting point, can be a viscoelastic “rubber” in the case of a polymeric material, or a viscous liquid for low molecular weight materials. The glass–liquid transition is a kinetic and relaxation process associated with the relaxation of the material. At temperatures above the T_g , the material, if submitted to a perturbation, can recover after a characteristic relaxation time; the supercooled melt is a viscoelastic material having a relaxation time that is similar to the experimental time scale. The process of glass formation is called vitrification and the system is considered to be vitrified if its viscosity is extremely high (10^{10} to 10^{14} Pa sec) (Franks, 1985; Slade and Levine, 1995). The T_g of pure water is close to -135°C ; achieving vitrification with pure water requires very small specimens and extremely high cooling rates ($>10^7$ K sec $^{-1}$) (Wolfe and Bryant, 1999). Vitrification can also be achieved by adding solutes that impede the process of crystal growth. The schematic state diagram of Figure 18.1 is useful to analyze vitrification in aqueous solutions. The equilibrium thermodynamic freezing process can be represented by the equilibrium liquid–solid curve (Figure 18.1), which gives the melting temperature as a function of solute concentration. The curve extends from the melting temperature (T_m) of pure water (0°C) to the

**FIGURE 18.1**

Schematic state diagram at constant pressure of an aqueous binary solution showing the equilibrium freezing curve, the solubility line, and the glass transition temperatures.

eutectic temperature (T_{eu}). Along the freezing process, the solution becomes more concentrated. Cocrystallization of solute at T_{eu} , is unlikely, because of the high viscosity of the system produced by solute concentration and low temperature (Goff, 1997). Freeze concentration continues beyond T_{eu} , into a nonequilibrium state through a viscoelastic liquid/solid glass state transition as a result of the reduction in molecular motion and diffusion kinetics (Roos and Karel, 1991a; Goff, 1994). The glass transition curve extends from the glass transition temperature (T_g) of pure water (-135°C) to the T_g of pure solute. Rapidly cooled solutions exhibit less ice formation and the T_g of the unfrozen portion is usually low. At subzero temperatures, the formation of an amorphous state is time dependent since the limiting factor of the process (water removal in the form of ice) becomes more difficult as concentration increases. The marked effect of viscosity on mass transfer properties acts as the limiting factor for ice growth. In addition, under conditions where heat removal is rapid, a high level of supercooling at the interface decreases the propagation rate and freezing becomes progressively slower as ice crystallization is hindered, and consequently more time is required for crystal growth at each temperature. In aqueous solutions, as the concentration of solutes increases, the temperature T_g at which vitrification occurs also increases, and the cooling rate necessary to achieve vitrification is reduced with respect to pure water. Vitrification in solutions is then easier to be produced than in pure water, because the addition of solutes decreases the probability of ice nucleation and growth. The reasons are that solutes are incompatible with the ice structure and that the viscosity at any temperature is usually larger when solutes are present, making more difficult the motion

and reorientation of the water molecules into the ice structure; the higher viscosity hinders both nucleation and growth.

The intersection of the nonequilibrium extension of the liquid curve, beyond T_{eu} (Figure 18.1) and the glass transition curve, is given by T'_g defined as the maximally freeze concentrated T_g of the frozen system where the unfrozen water in the matrix is unable to freeze and then ice formation ceases within the time-scale of normal measurement (Franks, 1985; Levine and Slade, 1988; Levine and Slade, 1991; Roos and Karel, 1991b; Goff, 1994, 1997; Le Meste et al., 2002). Maximum ice formation is attained by slow freezing and annealing at a temperature close to the glass transition value; under such conditions, an unfrozen matrix that contains maximum solute concentration is obtained. Below T'_g the unfrozen matrix takes on solid properties because of reduced molecular motion, which is responsible for the marked reduction in translational, not rotational, mobility (Roos and Karel, 1991a; Slade and Levine, 1995). At this temperature the concentrations of solute within the glass is C'_g (Figure 18.1). If a product is stored at a temperature below T'_g it may be expected to be composed of ice and a freeze-concentrated phase in the glassy state and long-term stability may be predicted. If the storage temperature is between T'_g and T_m , the freeze-concentrated phase is not in the glassy state, it is more diluted and processes governed by diffusion are not inhibited. These processes can lead to deterioration during food storage (Fennema, 1996). In rapidly cooled systems in the glassy state, ice formation can occur during rewarming (exothermic devitrification) at a temperature above T'_g (Roos and Karel, 1991a, 1991c) and ice is produced by crystallization of the immobilized water before the onset of ice melting. Recrystallization and crystal growth may cause freezing damage in foods.

Starch is commonly used to impart suitable rheological properties to a product. Food systems based on gelatinized starch may undergo important textural changes (sponge formation and syneresis) when stored at low temperatures that may turn such products unacceptable for the consumer. These changes are related to starch retrogradation.

Starch is a polysaccharide formed by two polymers of glucose: linear amylose and branched amylopectin. The gelatinization process can be regarded as a fusion of the crystalline starch regions in the presence of enough water and heating. Starch retrogradation is a recrystallization process that is controlled by diffusion and depends on solute mobility in the system.

The formulation of complex food products frequently involves the addition of other components such as low molecular weight sugars, which play several roles: taste, reduction of water activity, and contribution to texture. The addition of these carbohydrates affects both the starch gelatinization process and the retrogradation that may occur during the frozen storage. The gelatinization temperature range for corn starch pastes ($100 \text{ g starch kg}^{-1}$) was 66.9 to 78.4°C and the enthalpy value was 11.5 J g^{-1} . Sucrose increases starch gelatinization temperatures to values ranging

between 72.9 and 83.6°C (Ferrero et al., 1996; Ferrero and Zaritzky, 2000). This increase can be attributed to different reasons: a reduction in water activity produced by sugar, which could negatively affect starch gelatinization (Derby et al., 1975), sugar–starch interactions (Hansen et al., 1989), and the less plasticizing effect of the co-solvent sucrose–water mixture (Miles et al., 1985).

Starch-based formulations are usually stabilized with low proportions of hydrocolloids as xanthan gum, sodium alginate, and guar gum, which help to minimize the negative effects of freezing and frozen storage. In previous works (Ferrero et al., 1993, 1994), the beneficial effect of using small quantities of gums in gelatinized starch–aqueous systems with high water content to minimize textural changes has been demonstrated. The addition of low hydrocolloid (guar, xanthan, or alginate) concentration (10 g kg⁻¹) did not affect significantly gelatinization temperatures or enthalpies compared with the system without hydrocolloids (Ferrero et al., 1996).

In the present chapter the effect of sucrose and hydrocolloids (xanthan gum, guar gum, and sodium alginate) on: (i) T_g of the freeze-concentrated matrix (T'_g), (ii) amylose and amylopectin retrogradation, and (iii) rheological behavior of the system, are analyzed in gelatinized water–starch formulations frozen at different rates and stored at -18°C. Besides, the importance of T'_g as a parameter related to texture quality of starch–sucrose–hydrocolloids-based foods during frozen storage is discussed.

Thermal Characterization of the Systems by Differential Scanning Calorimetry

The model systems were formulated using commercial corn starch, different hydrocolloids (xanthan gum, guar gum, and sodium alginate), and sucrose. The selected range of ingredients concentrations was based on common food product formulations such as puddings, custards, and other desserts in order to get useful technological applications. Model food systems based on starch (100 g kg⁻¹), sucrose (150 g kg⁻¹), and water (750 g kg⁻¹) with and without the addition of 10 g kg⁻¹ of hydrocolloid (xanthan gum, guar gum, or sodium alginate) were tested.

Thermal transitions (amylopectin retrogradation and glass transition) were studied by differential scanning calorimetry (DSC), using a Du Pont calorimeter with 910 cell (Du Pont Co., USA) fitted with conventional refrigeration; this equipment allows the performance of annealing at a controlled temperature. In the preparation of the starch pastes with gums, components were dry-mixed and then they were slowly added to the predetermined amount of water under constant stirring. Once a homogeneous system was obtained, the DSC hermetic aluminum pans were filled with aliquots of 10 to 15 mg for the thermal analysis runs.

Glass Transition Temperatures in Frozen Gelatinized Systems

To analyze the glass transition of the freeze-concentrated matrix containing the maximum solute concentration, freezing must be carried out slowly to allow maximum possible ice formation and then the sample has to be annealed. Considering that this thermal transition is characteristic of the matrix with maximum solute concentration regardless of the initial concentration, and that the transition had to be observed with the best possible accuracy, the concentrations were doubled for these tests. Samples in the DSC pans were gelatinized in situ and then cooled at 1.5°C min⁻¹ from 25 to -40°C, the minimum temperature reached by our DSC equipment. The samples were then heated at 1.5°C min⁻¹ and annealed at -19°C for 30 min. After this annealing period, they were again cooled to -40°C and reheated to ambient temperature at 1.5°C min⁻¹. Annealing temperature and time were selected from preliminary tests; a temperature of -19°C is just above the *T*_g' onset and 30 min annealing time was the minimum period that led to maximum ice formation. Cooling and heating procedures were carried out at the same rate (1.5°C min⁻¹) to avoid relaxation phenomena. Tests were carried out in five replicates, using an empty double pan as reference.

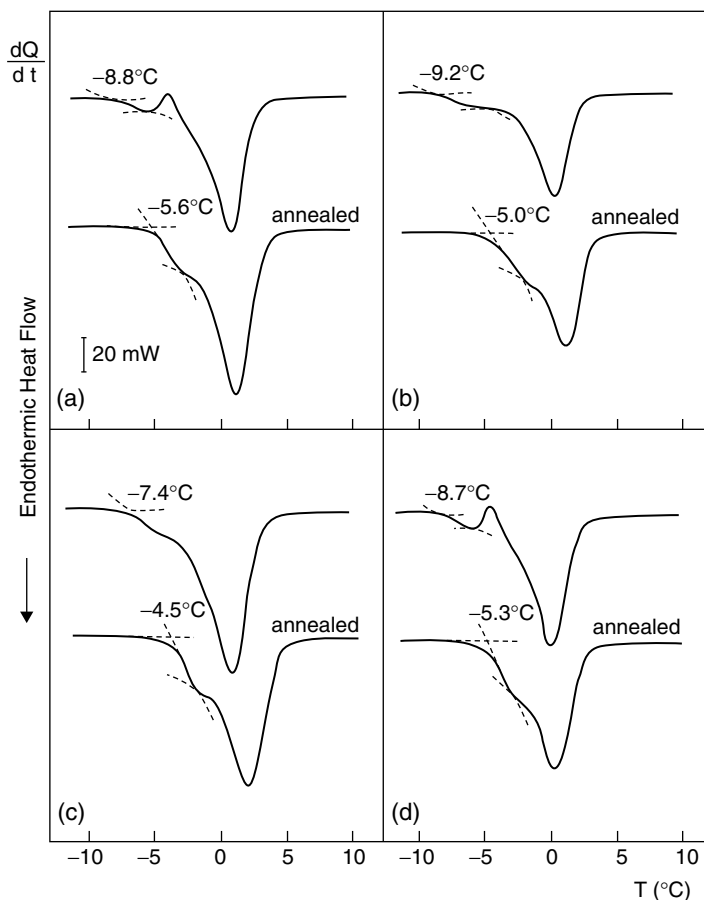
Starch Systems Without Sucrose

Figure 18.2 shows typical thermograms obtained by DSC during thawing of gelatinized starch pastes with hydrocolloids (b, c, d) and without hydrocolloids (a). These curves (corresponding to different mass samples) were obtained to determine the glass transition temperatures of annealed (*T*_g') and not annealed samples (*T*_g). Before the ice-melting peak, the characteristic change in heat capacity caused by the glass transition was observed. *T*_g' onset is located between -4.5 and -5.5°C (Table 18.1); small quantities of gums did not shift significantly the *T*_g' value. In the case of

TABLE 18.1
Onset (*T*_g^o), Medium (*T*_g^m) and Conclusion (*T*_g^c) Glass Transition Temperatures (°C) of Concentrated Aqueous Starch–Sucrose–Hydrocolloid Systems Submitted to Slow Freezing and Annealing

System Composition (g kg ⁻¹)	<i>T</i> _g ^o	<i>T</i> _g ^m	<i>T</i> _g ^c
C = 100; W = 900	-5.2(0.5)	-4.1(0.4)	-3.1(0.4)
C = 100; S = 150; W = 750	-22.9 ^a (0.3)	-20.8 ^a (0.2)	-18.7 ^a (0.2)
C = 100; S = 150; X = 10; W = 740	-22.2 ^a (0.3)	-19.2 ^a (0.4)	-16.1 ^b (0.9)
C = 100; S = 150; G = 10; W = 740	-23.0 ^a (0.7)	-20.3 ^a (0.7)	-17.5 ^{a,b} (0.6)
C = 100; S = 150; A = 10; W = 740	-22.3 ^a (0.4)	-19.6 ^a (0.4)	-17.0 ^{a,b} (0.5)

C, corn starch; W, water; S, sucrose; X, xanthan gum; G, guar gum; A, alginate. Standard error (SE) between parentheses. Assays were performed in quintuplicate. Within a column, values with different superscripts are significantly different (*P* < .05).

**FIGURE 18.2**

DSC thermograms obtained during thawing of starch pastes (sucrose not included) (a) without hydrocolloid, (b) with xanthan gum, (c) with guar gum, and (d) with sodium alginate. Upper curves: not-annealed samples; numbers indicate T_g onset. Lower curves: samples annealed at -4.5°C ; numbers indicate T_g' onset. Curves were not normalized and correspond to different mass samples.

starch pastes without gum (Figure 18.2a) and pastes with sodium alginate (Figure 18.2d), both without annealing, an exothermic peak can be observed between the ice-melting endotherm and the T_g temperature. This peak was attributed to additional ice crystallization (devitrification). This ice crystallization cannot take place in the glassy state, so when the temperature exceeds T_g , pastes move into the rubbery state of increasing molecular mobility, thus allowing additional ice formation to occur (Slade and Levine, 1991; Roos, 1995). This additional ice formation during thawing of systems stored at $T < T_g'$ is one of the main factors in food deterioration. The absence

of an exothermic devitrification peak in the systems with xanthan or guar gum without annealing (Figure 18.2b and c) may be related to the higher viscosity of the pastes with these gums, which delays the formation of additional ice, compared with the paste with sodium alginate. Maximum ice formation was obtained by annealing samples between T_g^m and T_g^o (approximately -4.5°C) at a slow cooling rate. In this case no exothermic peak was obtained.

Starch Systems Containing Sucrose

Sucrose addition caused the decrease of T_g temperatures in frozen systems either annealed or not (Table 18.1). This phenomenon was described by several authors as a plasticizing effect of low molecular weight sugars (Levine and Slade, 1989; Roos and Karel, 1991d; Slade and Levine, 1991). It has been stated that foods containing high amounts of low molecular weight sugars show considerable freezing temperature depression and contain higher amounts of unfrozen water at lower temperatures than foods based on polymeric compounds with the same solid content.

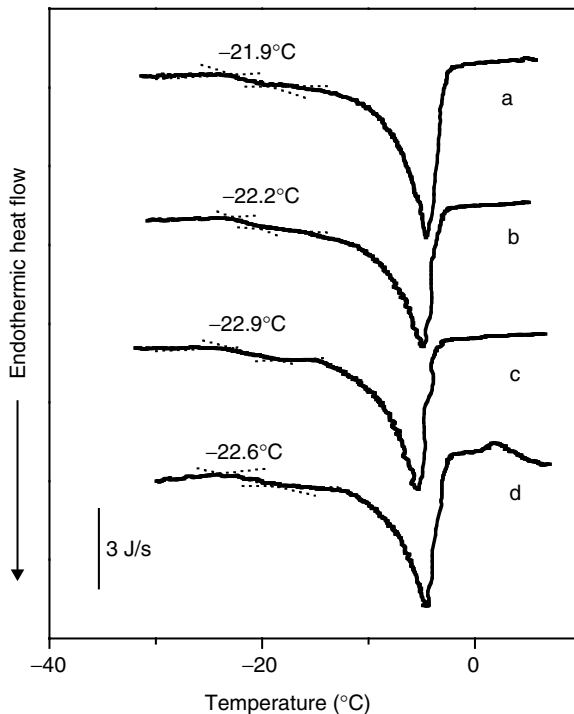


FIGURE 18.3

DSC thermograms of samples frozen and annealed (30 min) at $T = -19^\circ\text{C}$: (a) starch-sucrose-water; (b) starch-sucrose-xanthan gum-water; (c) starch-sucrose-guar gum-water; (d) starch-sucrose-alginate-water. Numbers indicate T_g onset.

Results obtained with different starch–sucrose–hydrocolloid samples are shown in Figure 18.3. A peak of additional ice formation before ice melting was not observed because the freezing process led to maximum ice formation.

Considering that the obtained T'_g value in our tested systems is below -20°C in all cases, the commonly used frozen storage conditions (approximately -18°C) would be located above the T_g temperatures; thus systems stored at this temperature would be at the rubbery state and would have more molecular mobility. In this situation, deteriorative phenomena depending on diffusion could occur. As amylopectin and amylose retrogradation are crystallization phenomena occurring in starch systems, they were studied in the present work as examples of deteriorative changes. As observed in Table 18.1, values found for the onset temperature (T_g^o) varied between -23.0 and -22.2°C for annealed samples containing sucrose with and without gums. Nonsignificant differences were observed among these systems.

Amylopectin Retrogradation

Recrystallization of amylopectin is a reversible process that can be analyzed by DSC below 100°C (Miles et al., 1985). Amylopectin retrogradation was measured in starch systems containing sucrose from DSC runs immediately after freezing and after 91 days of storage at -80 and -18°C . Aliquots of gelatinized pastes were run between 20 and 120°C at a heating rate of $10^\circ\text{C min}^{-1}$ in order to detect the presence of the amylopectin retrogradation peak.

Retrogradation of amylopectin in starch–sucrose–hydrocolloid systems was not detected in any of the just-frozen samples independently of the freezing rate used, but at the end of the frozen storage (91 days at -18°C) all the slowly frozen samples evidenced amylopectin recrystallization. Gum addition did not avoid amylopectin retrogradation and had no significant effect on temperature range or enthalpy values. DSC endotherms showed retrogradation peaks with mean temperature ranges varying between an onset temperature of 43.7°C ($\text{SE} = 0.5^\circ\text{C}$) and a final temperature of 60°C ($\text{SE} = 0.6^\circ\text{C}$). The enthalpy mean value was 3.1 J g^{-1} ($\text{SE} = 0.3 \text{ J g}^{-1}$), being similar for the different formulations, independently of the type of gum used. Control samples stored 91 days at -80°C did not show amylopectin retrogradation. The obtained results confirm that amylopectin retrogradation can occur even at a temperature near -20°C , when starch systems contain sucrose and T'_g is below this storage temperature. Amylopectin retrogradation was not observed in systems without sucrose because their T_g temperatures are close to -5°C (Ferrero et al., 1993, 1994). In starch systems, with or without sucrose, the presence of a hydrocolloid did not avoid amylopectin retrogradation during frozen storage at a temperature close to the glass transition.

Effect of Freezing Rate and Frozen Storage on the Dynamic Rheological Behavior

Gelatinization of starch systems for rheological analysis was performed by heating at 90°C for 15 min in a thermostatic bath with continuous mechanical stirring. Gelatinization was controlled through microscopy observations with polarized light (Leitz Ortholux II, Leitz, Germany), which allowed a total loss of birefringence to be verified once the given heating time had elapsed. Before freezing, each sample was divided into aliquots, placed in cylindrical containers, and wrapped to prevent dehydration during storage and exudate losses during thawing. Samples were frozen at two different rates: (a) quick freezing with a liquid nitrogen jet in a commercial freezer and (b) slow freezing in a still-air freezer at -18°C . Freezing rates were recorded by thermocouples inserted in the thermal center of control samples; the quick freezing rate was $4^{\circ}\text{C min}^{-1}$ and the slow one was $0.1^{\circ}\text{C min}^{-1}$.

Once the samples were frozen, they were placed in a temperature-controlled cold store chamber ($-18 \pm 1^{\circ}\text{C}$). During 3 months of storage, two samples from each formulation were thawed at different times; thawing was done in a temperature-controlled room at 20°C . Unfrozen samples as well as quickly frozen samples stored at -80°C were used as controls.

The rheological behavior was studied at 20°C in a Haake RV20 oscillatory rheometer (Haake, Germany) using a plate–plate sensor system with 1 mm gap between plates. Data were analyzed using the Oscillation 2.0, Haake software. Two types of rheological tests were conducted: (a) deformation sweeps at constant frequency to determine the maximum deformation attainable by a sample in the linear viscoelastic range and (b) frequency sweeps (from 0.01 to 10 Hz) at a constant deformation within the linear viscoelastic range. By this procedure, the mechanical spectra were obtained recording the variation of the G' , G'' and G^* dynamic moduli as a function of frequency. The G' value is the dynamic elastic or storage modulus, related to the material response as a solid; the G'' value is the viscous dynamic or loss modulus, related to the material response as a fluid. The complex modulus G^* is defined as $(G'^2 + G''^2)^{1/2}$ and represents the global viscoelastic response of the system. Objective rheological studies were complemented by visual observations of the samples to test spongy and sandy (grainy) appearances.

Textural changes causing deterioration in frozen starch pastes, like sponge formation, can be related to amylose retrogradation; it occurs at $T > T'_g$ because of the mobility of the molecular chains. In previous works (Ferrero et al., 1993, 1994) it was reported that in starch–water gelatinized systems, storage at -20°C had not affected the texture; this was attributed to the fact that storage temperature was below T'_g ($\approx -5^{\circ}\text{C}$). When a starch gel is submitted to freeze–thaw treatments, water is separated because of the tendency of starch molecules to reassociate forming insoluble aggregates.

Textural changes like sponge formation and weepy or grainy appearances are easily appreciated by visual analysis of the tested samples.

Rheological behavior of the tested samples containing sucrose is observed in Figure 18.4; the complex dynamic modulus (G^*) was plotted as a function of frequency at a constant deformation ($\gamma = 4\%$) within the linear viscoelastic range. The following samples were analyzed: unfrozen, control samples that were quickly frozen and stored at -80°C , slowly or quickly frozen samples (without storage), and slowly or quickly frozen samples that were stored at -18°C ; G' and G'' were also determined for the same samples. Figure 18.4a corresponds to a sample containing only starch, sucrose, and water, and Figure 18.4b shows the effect of xanthan gum addition. Similar behavior was found with the other tested gums.

Starch–sucrose–water sample and alginate added system showed a gel-like behavior (weak gel) in which the storage modulus G' (elastic response) remained constant and always above G'' (viscous response); in this case, G' almost coincided with G^* . Xanthan or guar gum addition modified this behavior; these systems showed a crossover frequency below which G'' is higher than G' whereas above that value, the behavior reverts ($G'' < G'$). The complex modulus G^* coincides with G'' below the crossover frequency and with G' above it. The results obtained indicate that the behavior of the systems with xanthan gum approaches that of a semi-concentrated entangled solution of macromolecules (Ross-Murphy, 1995). Starch systems containing guar gum have a gel-like behavior. The effect of freezing rate and frozen storage can also be analyzed in Figure 18.4. The complex dynamic modulus G^* of the just-frozen samples containing starch and sucrose without gums increased with respect to the unfrozen sample having the

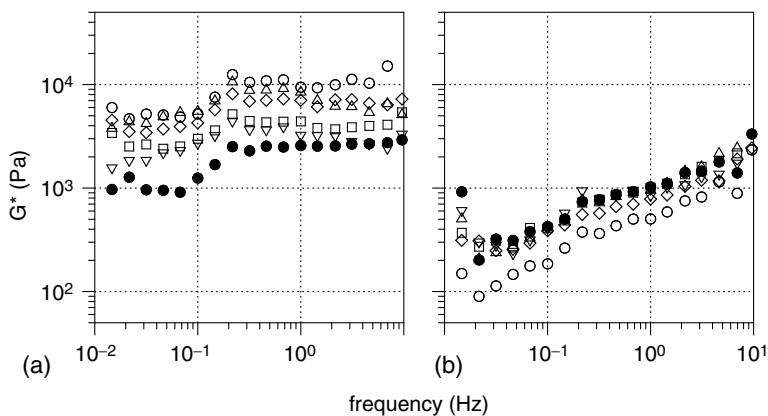


FIGURE 18.4

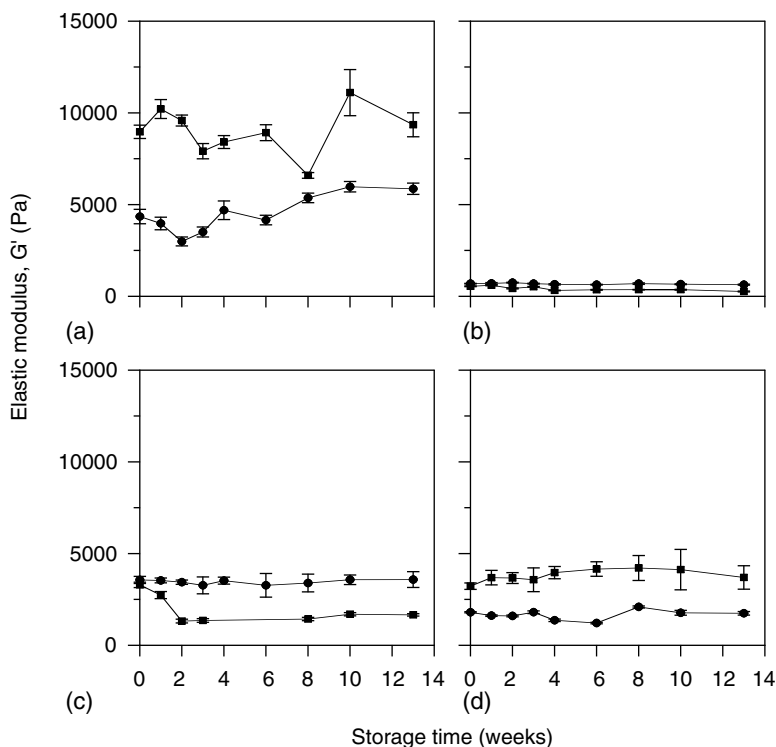
Frequency sweeps (at a constant deformation, $\gamma = 4\%$) at different times and storage temperatures for the following samples: (a) starch–sucrose–water; (b) CSXW starch–sucrose–xanthan gum–water •: unfrozen; □: quickly frozen without storage; Δ: quickly frozen and stored 91 days at -18°C ; ▽: quickly frozen and stored 91 days at -80°C ; ◇: slowly frozen without storage; ○: slowly frozen and stored 91 days at -18°C .

same composition (Figure 18.4a). This increase was significantly higher for slow freezing than for quick freezing and can be related to structural changes, particularly sponge formation caused mainly by amylose retrogradation at low freezing rates.

In systems containing gums, no spongy structure was evidenced in just slowly frozen samples; quickly frozen samples practically did not differ from the unfrozen ones. Systems with starch, sucrose, and xanthan or guar gum that were frozen at low rates showed values of G^* slightly lower than those of the unfrozen samples in all the range of tested frequencies (Figure 18.4b). Results could be attributed to structural changes related to large ice crystal formation. In alginate added systems, G^* increased with respect to the unfrozen samples only at frequencies higher than 1 Hz. The linear viscoelastic range was nonsignificantly affected by quick freezing. However, in slow freezing, the ranges of linear viscoelasticity tended to decrease, this effect being only significant for systems containing guar gum. A lower linear viscoelastic range denotes that the structure resistance to the applied deformation is reduced.

The effect of frozen storage at -18 and -80°C can be analyzed from G^* data of Figure 18.4. For each tested system, samples were thawed at different storage times to study their behavior during deformation and frequency sweeps. The dynamic complex modulus G^* increased in the quickly frozen starch–sucrose–water samples (CSW) after 91 days of storage at -18°C ; this increase can be attributed to amylose retrogradation during storage. However, this behavior was not observed in quickly frozen CSW samples stored at -80°C whose G^* values coincided practically with those of the just quickly frozen sample. In the slowly frozen CSW systems, negligible changes were observed after 91 days of storage at -18°C because sponge was mainly formed during freezing. The effect of frozen storage can also be observed in Figure 18.5 where G' values at 1 Hz were plotted as a function of storage time. Figure 18.5a corresponds to the CSW system; the initial values of G' (just-frozen samples) show the effect of freezing rate. Slow freezing produced higher G' values that can be associated with the spongy structure. Quick-frozen samples showed lower G' values that increased during storage as a result of sponge development; the addition of gums modified this behavior. The effect of freezing rate was less marked in xanthan and guar gum added systems than in alginate pastes. In alginate systems, slow freezing gives more firm gel structures than quick freezing in coincidence with samples without gums. In the case of xanthan gum or guar gum added pastes, the slowly frozen samples showed lower G' values, demonstrating that sponge structure was not formed; however, these samples showed the development of a sandy appearance during frozen storage. Frozen storage practically did not change initial G' values in systems containing gums.

In our study, systems without gums undergo a significant increase in gel firmness and thus in G' values mainly as a consequence of freezing. Hydrocolloid addition minimizes these textural changes during both freezing and storage even at slow freezing rates. Hydrocolloids should act

**FIGURE 18.5**

Elastic modulus G' as a function of frozen storage time at -18°C for samples containing (a) CSW (starch-sucrose-water); (b) CSXW (starch-sucrose-xanthan gum-water); (c) CSGW (starch-sucrose-guar gum-water); (d) CSAW (starch-sucrose-alginate-water). \bullet : quickly frozen samples; \blacksquare : slowly frozen samples. Confidence level for error bars = 95%.

by different ways: hydrocolloids-amylose interaction probably competes against amylose-amylose interactions, thus avoiding amylose retrogradation. Additionally, hydrocolloids can make systems in the rubbery state more viscous, decreasing molecular mobility and avoiding retrogradation-related to sponge formation (Ferrero et al., 1996).

Conclusions

In gelatinized starch systems T'_g onset is located between -4.5 and -5.5°C ; small quantities of hydrocolloids did not significantly shift this temperature.

The addition of sucrose shifted T'_g towards lower values (onset between -23 and -22°C , depending on the system). Thus, commercial storage temperatures ($\approx -18^{\circ}\text{C}$) lie above T'_g in starch-sucrose systems, allowing molecular mobility; this fact led to amylose and amylopectin retrogradation

and, as a consequence, to textural changes. Small quantities of gums (in the ranges used in common formulations) did not change the T'_g of the samples, but they had an important role in minimizing structural damage. This was verified by rheological viscoelastic tests where an increase of the dynamic moduli G^* and G' after slow freezing and during storage at -18°C ($T > T'_g$) was observed in starch sucrose systems related to the sponge-like structure formation due to amylose retrogradation.

From the results of the present work, it can be concluded that the storage at the usual commercial temperatures ($T = -18^\circ\text{C}$ slightly above T'_g) affects the quality of aqueous starch sucrose pastes without gums caused by amylose and amylopectin retrogradation. However, when hydrocolloids are included in the formulations, the usual storage conditions allows maintenance of acceptable textural attributes.

Acknowledgments

The authors gratefully acknowledge the financial support given by Consejo Nacional de Investigaciones Científicas y Técnicas, Agencia Nacional de Promoción Científica y Tecnológica, and the University of La Plata, Argentina.

References

- Derby, R.I., Miller, B.S., Miller, B.F., and Trimbo, H.B. Visual observation of wheat-starch gelatinization in limited water systems, *Cereal Chem.*, 52, 702, 1975.
- Fennema, O. Water and Ice, *Food Chemistry*, 3rd Ed., O. Fennema, ed., Marcel Dekker, New York, p. 17, 1996.
- Ferrero, C. and Zaritzky, N.E. Effect of freezing rate and frozen storage on starch-sucrose-hydrocolloid systems, *J. Sci. Food Agric.*, 80, 2149, 2000.
- Ferrero, C., Martino, M.N., and Zaritzky, N.E. Stability of frozen starch pastes: effect of freezing, storage and xanthan gum addition, *J. Food Process. Preserv.*, 17, 191, 1993.
- Ferrero, C., Martino, M.N., and Zaritzky, N.E. Corn starch-xanthan gum interaction and its effect on the stability during storage of frozen gelatinized suspensions, *Starch*, 46, 300, 1994.
- Ferrero, C., Martino, M.N., and Zaritzky, N.E. Effect of hydrocolloids on starch thermal transitions, as measured by DSC, *J. Thermal Anal.*, 47, 1247, 1996.
- Franks, F. *Biophysics and Biochemistry at Low Temperatures*, Cambridge University Press, Cambridge, p. 39, 1985.
- Goff, H.D. Measuring and interpreting the glass transition in frozen foods and model systems, *Food Res. Int.*, 27, 187, 1994.
- Goff, H.D. Measurement and interpretation of the glass transition in frozen foods, *Quality in Frozen Food*, M.C. Erickson and Y.C. Hung, eds., Chapman & Hall, New York, p. 29, 1997.

- Hansen, L.M., Setser, C.S., and Paukstelis, J.V. Investigations of sugar–starch interactions using carbon-13 nuclear magnetic resonance. I. Sucrose, *Cereal Chem.*, 66, 411, 1989.
- Le Meste, M., Champion, D., Roudat, G., Blond, G., and Simatos, D. Glass transition and food technology. A critical appraisal, *J. Food Sci.*, 67, 2444, 2002.
- Levine, H. and Slade, L. Principles of cryostabilization technology from structure/property relationships of carbohydrate/water systems — A review, *Cryo-Letters*, 9, 21, 1988.
- Levine, H. and Slade, L. A food polymer science approach to the practice of cryostabilization technology, *Comments Agric. Food Chem.*, 1, 315, 1989.
- Levine, H. and Slade, L., eds. *Water Relationship in Foods*, Plenum Press, New York, p. 251, 1991.
- Miles, M.J., Morris, V.J., Orford, P.D., and Ring, S.G. The roles of amylose and amylopectin in the gelation and retrogradation of starch, *Carbohydr. Res.*, 135, 271, 1985.
- Roos, Y. Characterization of food polymers using state diagrams, *J. Food Eng.*, 24, 339, 1995.
- Roos, Y. and Karel, M. Non equilibrium ice formation in carbohydrate solutions, *Cryo-Letters*, 12, 367, 1991a.
- Roos, Y. and Karel, M. Amorphous and state and delayed ice formation in sucrose solutions, *Int. J. Food Sci. Technol.*, 26, 553, 1991b.
- Roos, Y. and Karel, M. Applying state diagrams to food processing and development, *Food Technol.*, 45, 66, 1991c.
- Roos, Y. and Karel, M. Water and molecular weight effects on glass transitions in amorphous carbohydrates and carbohydrate solutions, *J. Food Sci.*, 56, 1676, 1991d.
- Ross-Murphy, S.B. Rheological characterisation of gels, *J. Texture Stud.*, 26, 391, 1995.
- Slade, L. and Levine, H. Beyond water activity: recent advances based on an alternative approach to the assessment of food quality and safety, *Crit. Rev. Food Sci. Nutr.*, 30, 115, 1991.
- Slade, L. and Levine, H. Glass transitions and water–food structure interactions, *Adv. Food Nutr. Res.*, 38, 103, 1995.
- Wolfe, J. and Bryant, G. Freezing, drying and/or vitrification of membrane–solute–water systems, *Cryobiology*, 39, 103, 1999.

19

The Mystery of Marshmallow Hardening

Miang Hoong Lim, Yin Jia, and Samuel Heenan

CONTENTS

Introduction	325
Study of Mechanism of Marshmallow Hardening	326
Method.....	326
Results.....	327
Stabilization Through Formulation.....	330
Method.....	331
Results.....	332
Effect of Replacement Sugar/Sugar Syrups on the Moisture Loss in Film	332
Effect of Replacement Sugar/Sugar Syrups on the Sugar Crystallization in Film	333
Stabilization through Process Control.....	334
Method.....	335
Results.....	335
Mean Air Cell Diameter and Total Surface Area	335
Air Cell Size Distributions	337
Stability of Marshmallow in Relation to Foam Structure	337
Conclusion	340
References	340

Introduction

Marshmallow originated in France as a medicinal paste called Pate de Guimauve. Its common name comes from the fact it was produced using the viscous juice extracted from the roots of the marsh mallow plant, *Althaea officinalis*. This extract was mixed with eggs and sugar and then beaten into a light fluffy foam (Lees and Jackson, 1973). Nowadays, marshmallow is an

aerated confectionery product with a characteristic foamy structure created when air and moisture is incorporated into a syrup mixture. The air increases the volume of the marshmallow and is responsible for its fluffy texture (Jackson, 1990). The basic ingredients in marshmallow are sucrose, glucose syrup, water, color and/or flavor, and whipping agents. A variety of whipping agents can be used either individually or in combination with other ingredients, such as egg albumen, gelatine, pectin, agar, and starch, to help produce a stable foam structure (Jackson, 1990; Kaletunc et al., 1992). In the confectionery industry, marshmallow is prepared by heating a base syrup, which evaporates water to achieve an optimal concentration. The mixture is cooled to a predetermined temperature and a whipping agent is added prior to beating. Depending on the texture required, the moisture content of marshmallow can vary between 17 and 21%, and the density can vary between 0.25 and 0.50 g/ml (Jackson, 1990).

Marshmallows have a short shelf life compared with other confections because of their unstable foamy gel structure, high moisture, and large air interfacial surface area. The degradation of marshmallow may be caused by several physicochemical changes, including moisture loss, sugar crystallization, foam collapse, or texture aging (Tiemstra, 1964; Lees and Jackson, 1973; Howling and Jackson, 1990). In this chapter, a standard marshmallow formula was analyzed in order to determine the mechanisms behind the marshmallow hardening, and then effect of ingredient replacement and process parameters on marshmallow quality and stability was evaluated.

Study of Mechanism of Marshmallow Hardening

Because of its elastic texture and tendency to harden, marshmallow was assumed to exist in a rubber state. Molecules in the rubbery state of marshmallow can be mobile and lead to sugar crystallization, loss of moisture from the matrix, cross-linking of proteins in gelatin, and collapse of foam. In order to stabilize the product, it is necessary to identify the factors limiting the shelf life of the marshmallow under a specific storage condition.

Method

A standard recipe marshmallow foam (density = 0.50 to 0.55 g/ml) was piped into dome-shaped starch moulds with a volume of 12 ml, and left to dry for 20 h before being individually packed in plastic trays and wrapped in plastic. The marshmallows were stored at 25°C and 21% RH for 21 weeks in cabinets containing saturated solutions of potassium acetate. The moisture content during storage was determined by recording the change in weights of the samples. Changes in texture, glass transition, and crystal formation during storage were measured using: an Instron UTM (Model 5564),

differential scanning calorimeter (DSC, Pyris 1, Perkin Elmer), and x-ray diffraction (XRD, PW 1130/00, Philips), respectively (Jia, 2004).

Results

The marshmallow lost most of its moisture during the initial 9 weeks of storage at 25°C and 21% RH (Figure 19.1). The rate of the moisture loss subsequently decreased, and no significant moisture loss occurred after 17 weeks of storage. The T_g of the marshmallow increased from -45 to 2°C over the 21 weeks of storage (Figure 19.1).

As the storage temperature (25°C) was significantly higher than the T_g of the marshmallow, the marshmallow was in a rubbery state and therefore there was a possibility that the sugar in marshmallow would crystallize. However, in this study, insignificant sugar crystallization was observed. Sucrose crystallization was observed to occur only in week 1, despite the fact that the marshmallow was in the rubbery state over the 21 weeks storage period (Figure 19.2). It appeared that marshmallow tended to lose moisture rather than crystallize when stored at 25°C and 21% RH. This may have been a result of the high rate of moisture loss during the first week of storage, resulting in increased viscosity of the matrix, which could have limited the

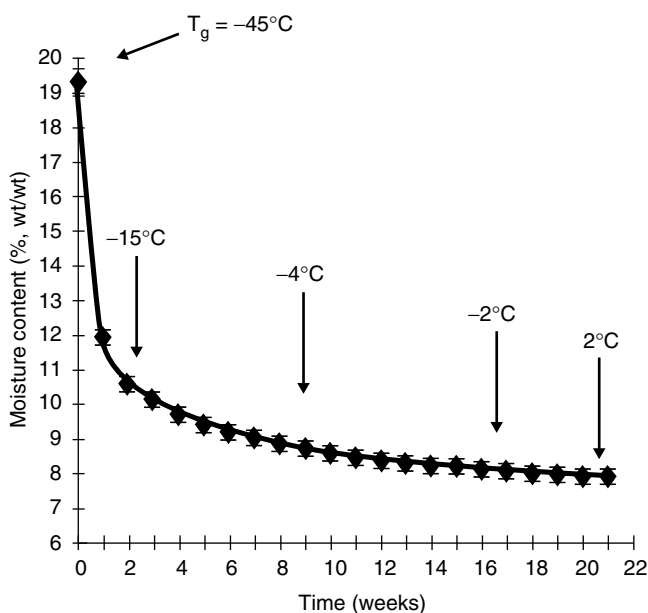


FIGURE 19.1

Moisture content and glass-transition temperatures of marshmallow during storage at 21% RH and 25°C .

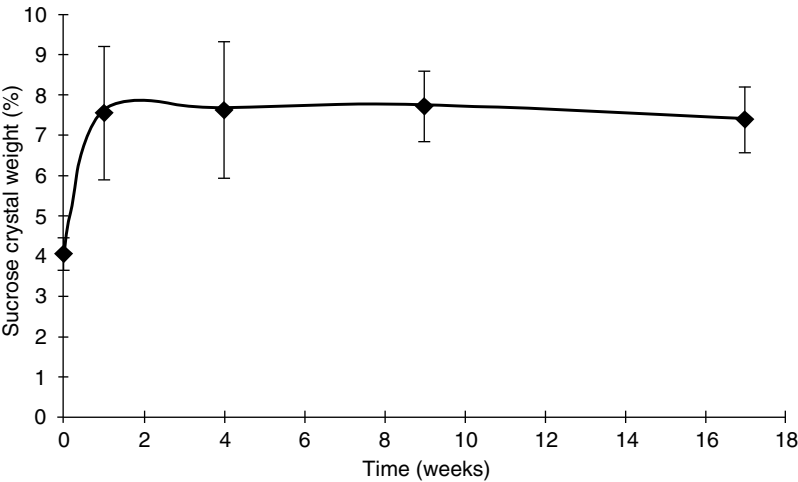


FIGURE 19.2
Amount of sucrose crystallized in marshmallow measured by x-ray diffraction over 17 weeks of storage at 21% RH and 25°C.

molecular mobility of sucrose. The presence of glucose syrup and gelatine may also have had an inhibition effect on sucrose crystallization.

The springiness or elasticity of the marshmallow was observed to decrease sharply during the first 2 weeks of storage (Figure 19.3). This corresponded to the observation of crystallization occurring in the marshmallow. It has

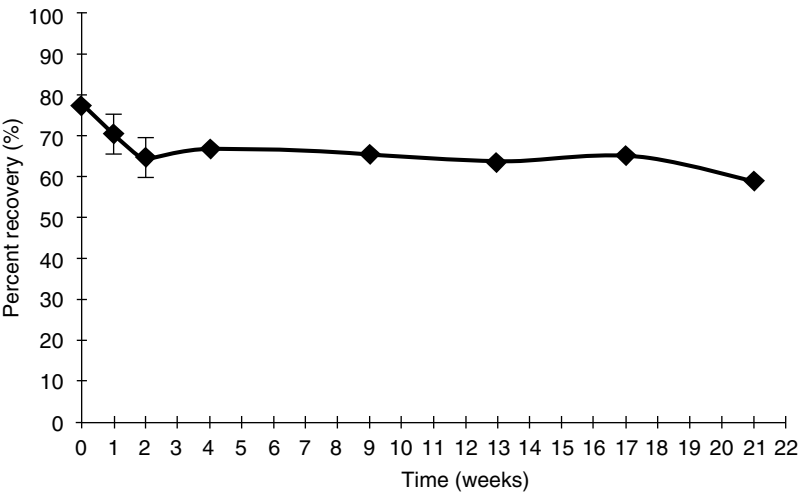


FIGURE 19.3
Change in percent recovery (springiness) in marshmallow measured using Instron texture analyzer over 17 weeks of storage at 21% RH and 25°C.

previously been shown that crystallization disrupts the elasticity of the gel matrix, which makes the marshmallow foam discontinuous (Tiemstra, 1964; Jackson, 1990). The elasticity of the marshmallow did not change much from week 2 to week 17, despite the fact that the moisture content changed continuously. This observation further proves that crystallization could be the main factor contributing to the loss of the elasticity in marshmallow during storage.

The hardness of marshmallow increased significantly throughout the storage period with week 0 to week 2 and week 17 to week 21 showing a relatively faster rate of increase (Figure 19.4) compared with week 2 to week 7. Moisture loss has been hypothesized to increase the T_g of marshmallow. Previous research has shown that when product temperature approaches the $T_{g'}$, the viscosity of the product significantly increase exponentially (Roos, 1998). The effect of moisture loss on the hardness of marshmallow is demonstrated in Figure 19.5, which shows that at a similar amount of moisture loss, a more drastic increase in marshmallow hardness at lower moisture content was observed. Since no crystallization was observed after the first week, the further increase in hardness would not have been caused by crystallization. Gelatin gel maturation has been proposed as another possible factor for contributing to the hardening of the marshmallow. Johnston-Banks (Johnston-Banks, 1990) showed that the viscosity of a gelatin gel increased in a more or less logarithmic relationship with an increase in concentration. Ledward (Ledward, 2000) demonstrated that the strength of a gelatin gel increases at temperatures over time. The effect of gelatin on marshmallow was not determined in this study.

Overall, the hardness of the marshmallow during storage at 25°C and 21% RH could be categorized into three stages (Figure 19.4): stage A (weeks 0 to 2),

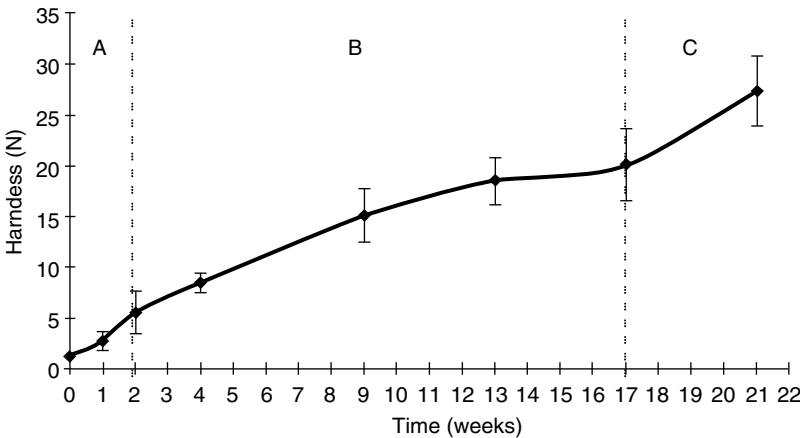
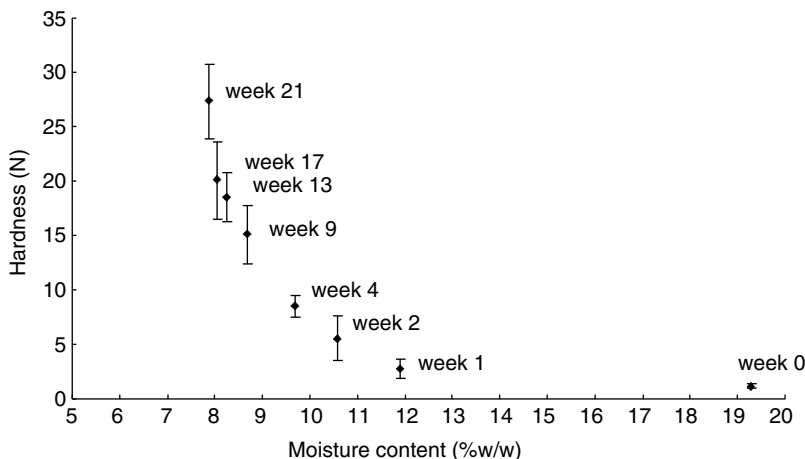


FIGURE 19.4
Change in marshmallow hardness measured using the Instron texture analyzer over 17 weeks of storage at 21% RH and 25°C.

**FIGURE 19.5**

Hardness of marshmallow as a function of moisture content during storage at 21% RH and 25°C.

where an initial increase in hardness caused by the combined effect of moisture loss, sucrose crystallization, and gelatine gel maturation; stage B (weeks 2 to 17), where a more gradual but significant increase in hardness occurred, caused mainly by viscosity increase as the marshmallow lost moisture and moved closer to the glassy state; and stage C (weeks 17 to 21), where a further significant increase in hardness occurred, caused mainly by the moisture loss as the viscosity effect is more pronounced at a moisture level closer to the glass transition and the proposed higher gelatin gel networking at low moisture content.

In a structurally stable marshmallow, moisture loss and sugar crystallization were identified as the two main factors contributing to an increase in hardness through different stages of storage. Moisture loss is likely to have played a more important role in contributing to the hardening of marshmallow through an increase in the viscosity of matrix than crystallization under the experimental condition of 25°C and 21% RH. Sugar crystallization, however, was considered to be the controlling factor for the loss of the elasticity and cohesiveness of marshmallow at the initial stage. It was likely that gelatine gel maturation also affected the hardening of marshmallow throughout the whole storage period but this was not tested during this study.

Stabilization Through Formulation

With a basic understanding of the mechanisms of hardening of marshmallow, the following approaches may be used to extend the shelf life:

- (a) Reduce loss of moisture by adding water withholding ingredients or monitoring the interfacial area of the marshmallow foam
- (b) Prevent sucrose crystallization by adding sucrose crystallization inhibiting agent or decrease the mobility of sugar molecules in the matrix by adding high T_g ingredients

However, whilst a higher T_g of a marshmallow premix may reduce molecular mobility and thus inhibit crystallization, it may also lead to a significant higher viscosity and cause hardening during storage at temperatures close to their T_g . However, a marshmallow premix with good moisture holding ability and a soft elastic texture may lead to crystallization. The effect of ingredients on moisture holding capability and crystallization inhibition on maintaining the soft texture of marshmallow was therefore investigated.

One of the ingredients targeted for replacement was sugar syrups as the viscosity of a mixture may be affected by high molecular weight glucose syrups and thus reduce the molecular mobility in the matrix. Additionally, sugars or glucose syrups may also inhibit the incorporation of crystallizing sugar molecules by absorbing onto the surface of the sugar crystal or by incorporating themselves into certain sites on the crystalline lattice (Hartel, 2001).

The foamy structure of marshmallows may have large variations in the internal surface area, which could influence the loss of moisture at different rates. Therefore, there might be large variations between the results on the rate of moisture loss if marshmallow samples were used to study the effects of ingredient replacement. For this reason, films were developed as a model system for the study of moisture loss and crystallization of the different ingredient replacements. The advantage of using a film is that the surface area is similar for each formulation stored under the various experimental conditions. A uniform surface area is also advantageous for determining the ability of replacement sugar/sugar syrups to prevent sugar crystallization in the film, as the extent of crystallization in each of the formulations can easily be compared.

Method

The preparation of the marshmallow premix for the five different formulations involved replacing the glucose syrup (42DE) from the standard formula with either a 63DE glucose syrup, 17DE glucose syrup, trehalose, or a 50:50 mix of 17DE and 63DE glucose syrup. All the replacement syrups, with the exception of trehalose, varied from each other by the level of starch hydrolysis. The higher the level of hydrolysis (high DE), the sweeter and more hygroscopic the syrup, lower DE syrups provide higher viscosity and tend to increase the T_g of the matrix.

Trehalose is a disaccharide and is known for its high T_g and low hygroscopicity (Fennema, 1996; Richards et al., 2002).

A thin layer or a film of marshmallow premix was prepared by spreading approximately 0.6 g of the premix (about 60°C) evenly across the surface of a plastic petri dish with the help of glass Pasteur pipette. The weight of the film was recorded and then the petri dishes were placed inside a desiccator that was preconditioned with a saturated salt solution in order to achieve the desired relative humidity. The moisture content of the films were determined from their weight change over time when stored at 49% RH and 20°C. A similar set of films were stored at 20°C for 5 months at 39% RH followed by 4 months at 70% RH, and the storage conditions were changed because sugar crystals were not observed after 5 months storage at 20°C and 39% RH. The presence of sugar crystals was clearly observed as white specks and the surface area covered by sugar crystals could be measured using NIH-image analysis on optical images.

Results

Effect of Replacement Sugar/Sugar Syrups on the Moisture Loss in Film

The different formulations lost most of their moisture when stored at 20°C and 49% RH over the first 24 h and then a quasi-equilibrium was established for the remaining 7 days (Figure 19.6). The 17DE formula lost the most moisture compared with the other formulations. These results were not unexpected as the 17DE syrup is known for its ability to decrease hygroscopicity in food products (Howling and Jackson, 1990;

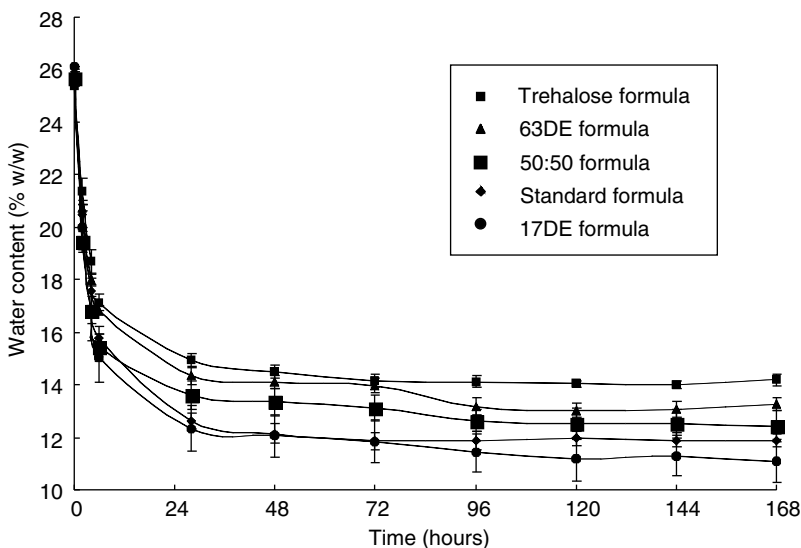


FIGURE 19.6

Moisture content of the five different formulation films during storage at 49% RH and 20°C.

Roos and Karel, 1991). A high DE sugar syrup, however, is known to have a high hygroscopicity as a result of a high degree of starch hydrolysis and thus the product remains moist and retains its texture (Howling and Jackson, 1990).

There was no significant difference between the extent of moisture loss from the trehalose formula, the 63DE formula, and the standard, which indicates that trehalose has a similar moisture-holding capacity relative to the higher DE glucose syrups which could also be helpful in preventing moisture loss from the marshmallow premix syrup. Previous studies have shown that the moisture content of crystalline trehalose is relatively stable up to 94% RH (Taylor and York, 1998; Richards et al., 2002). This indicates that trehalose does not readily absorb moisture at 94% RH and below. This current result provides a new insight into the use of trehalose for maintaining the moisture content in food.

Effect of Replacement Sugar/Sugar Syrups on the Sugar Crystallization in Film

The relative amount of sucrose crystallized at the end of the storage period is shown in Table 19.1. Theoretically, an increase in the amount of long-chain saccharides will result in an increase in the viscosity of the marshmallow premix, thus retarding the diffusion of the sugar molecules to an appropriate crystal lattice incorporation site (Gabarra and Hartel, 1998). However, the results showed that 17DE formula produced the biggest crystals of the batch and that high DE glucose syrups were more effective in inhibiting sucrose crystallization than low DE glucose syrups. This observation confirmed the conclusion reported by Tjuradi and Hartel (1995), where it was found that a high DE glucose syrup with a low molecular weight was more effective at hindering sucrose crystallization than glucose syrups with a higher molecular weight (low DE). The high DE glucose syrup contained more short-chain saccharides that would interfere with the incorporation of sucrose molecules into the lattice (Gabarra and Hartel, 1998; Hartel, 2001). Table 19.1 also shows that the film composed of the 50:50 formula had the

TABLE 19.1
Percentage of the Total Surface Area of Individual Film
Covered by Sugar Crystals

Formula	Average (%)	SD (%)
17 DE	91.3a	5.15
50:50	37.6b	6.75
Trehalose	33.2b	6.97
63 DE	15.4c	5.78
Control	14.6c	1.00
Fruitrim	12.9c	2.15

second highest percentage of crystallization, and this percentage was significantly higher than the film composed of the 63DE formula. It appears that the inclusion of the 17DE glucose syrup significantly reduced the effectiveness of the 63DE glucose syrup to inhibit glucose crystallization. There was no observable significant difference between the extent of crystallization in the standard formula and 63DE formula after 9 months storage. Therefore, the relative effectiveness of the 63DE glucose syrup over the standard formulation could not be determined within the time scale of the current study.

Hartel (Hartel, 1993; Levenson and Hartel, 2005) demonstrated that the closer T_g is to the storage temperature, the slower the rate of sucrose crystallization. However, trehalose formula had the highest T_g of all the formulations (Jia, 2004), and the trehalose formula had significantly higher crystal formation than the 63DE and the standard formula. This result supports the conclusion made by Gabarra (Gabarra and Hartel, 1998), which stated that materials with a high T_g are not necessarily the best inhibitors of sucrose crystallization, and the conclusion made by Labuza (2002) that trehalose did not inhibit sucrose crystallization.

In summary, higher DE glucose syrup (63DE) showed the second highest moisture-holding capacity and was significantly more effective in preventing sucrose crystallization compared with the other new formulations tested in this study. Despite trehalose having the highest T_g and moisture-holding capacity, it was shown to have a high tendency to crystallization and is therefore not recommended for marshmallow.

Stabilization through Process Control

The stability of the foam and the texture of marshmallow can be significantly affected by various production factors, including mechanical processing such as type of whipping process, whipping time and speed, speed of syrup feed pump, air flow rate and pressure, temperature of whipping, and the formulation, which include the amount of whipping agent used, residual moisture content, pH, and composition of ingredients (Tiemstra, 1964; Lees, 1991; Macrae et al., 1993; Groves, 1995; Hanselmann and Windhab, 1999).

The whipping process directly affects the amount of air incorporated into the matrix and therefore, variable process parameters should be selected in order to optimize foam quality and to avoid deterioration of the foam. A study by Hanselmann and Windhab (1999) showed that an increase in the rotor speed from 600 to 2000 rpm led to a decrease in bubble size and thus improved drainage stability. Lees (1991) demonstrated that at the upper limits of the beating temperature, aeration was faster and the volume of the foam increased as the temperature increased. This effect was attributed to the fact that higher temperatures lower the viscosity of the mixture and when the mixture is less viscous, more aeration is likely to occur.

In marshmallow whipping processes, large air bubbles in the foam initially become elongated and then break up into smaller bubbles through shear force. Some of the small bubbles may re-form into larger air bubbles and others will be trapped in the syrup/whipping agent matrix. The matrix later becomes solidified or semi-solidified and thus the air bubbles are entrapped (Lees, 1991). The more air incorporated in small bubbles, the more stable and smooth-textured the marshmallows. If the bubbles are too large, the syrup may flow and the bubbles may coalesce causing destabilization of the foam and a reduction in the shelf life of the product (Groves, 1995). The purpose of the following result was to investigate the interaction of whipping time and temperature on air cell characteristics and its effect on the shelf life of marshmallow.

Method

Sample treatments with respect to temperature and time of whipping were based on a 3 × 3 experimental design as shown in Table 19.2. Optical microscopic images of the foams were analyzed using Scion image (NIH). Marshmallow air cell characteristics were determined by assessing mean air cell size, total air cell surface area (assuming surface area of a sphere for each air cell) and air cell size distribution within a fixed volume (Heenan, 2004). The loss of moisture from the marshmallow was measured by weight change and texture hardening assessment using Instron Texture analysis (UTM) (Heenan, 2004).

Results

Mean Air Cell Diameter and Total Surface Area

As time of whipping increased, the mean air cell diameter decreased and the mean total surface area increased (Figure 19.7 and Figure 19.8). This observation of air cells break up into smaller air cells with an increase in

TABLE 19.2
Experimental Conditions of Marshmallow Foam Treatment

Treatments	Premix Temperature (°C)	Whipping Time (min)
1	40	3.5
2	40	4.5
3	40	6.0
4	50	3.5
5	50	4.5
6	50	6.0
7	60	3.5
8	60	4.5
9	60	6.0

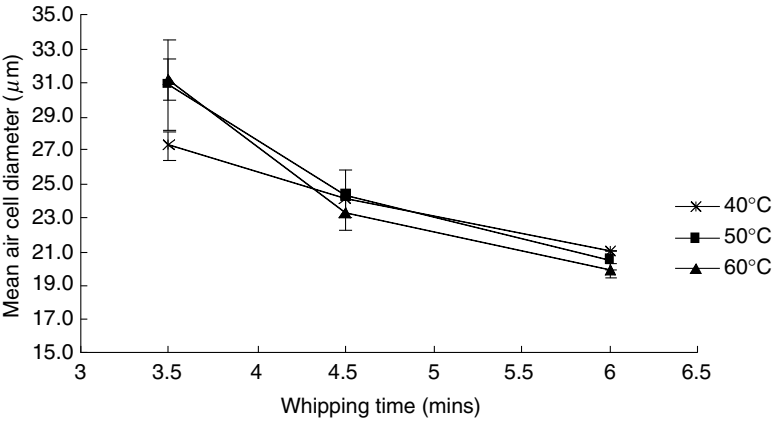


FIGURE 19.7
Effect of whipping time and temperature on air cell diameter.

whipping time is consistent with an earlier report (Massey et al., 2001). In our study, mean air cell size was greatest at the lowest whipping time of 3.5 min. When carried out at whipping temperatures of 50 and 60°C (Figure 19.7). This coincided with a decrease in marshmallow premix viscosity during whipping, and a resulting decrease in the density and in the overrun of the foam mixture (Heenan, 2004). These changes were postulated to be a result of foam collapse caused by coalescence, disproportionation, and drainage. This instability was demonstrated in an increase in the standard deviation for mean air cell diameter for samples whipped at the two higher temperatures of 50 and 60°C and lowest time of 3.5 min (Figure 19.7).

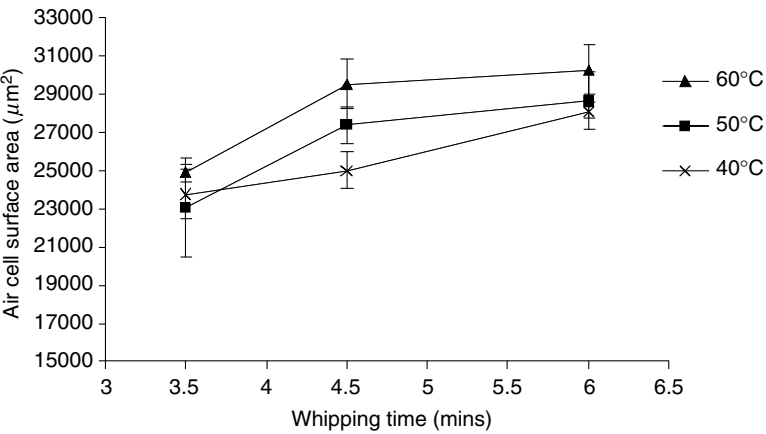


FIGURE 19.8
Effect of whipping time and temperature on air cell total surface area.

Samples whipped for 4.5 or 6.0 min had a smaller standard deviation, which indicates a more uniform distribution of air cells (Figure 19.7). Disproportionation becomes stabilized when the surface tension of the smaller air cells achieves a value low enough to compensate for the decrease in the radius of the air cell, meaning that the pressure differences remain constant throughout the marshmallow (Kinsella, 1980; Bee et al., 1987). This stability can be observed by the uniformity of air cell distribution (Campbell and Mougeot, 1999).

Air Cell Size Distributions

The distribution of air cells in marshmallow foam whipped at all the three temperatures for 6.0 min had the smallest size and narrowest at distribution range, which is indicative of evenly distributed air cells size (Figure 19.9). Temperature seemed to have a limited effect on the air cell distribution of samples whipped for 6.0 min. However, marshmallow batches whipped for 3.5 min (the lowest whipping time) at 50 and 60°C showed a dramatic increase in the spread of the air cell size distribution and increased shift in the median of the air cell size distribution (Figure 19.9). These findings are supported by Massey et al. (2001), who showed the size of the bubbles in cake batters shifted to a smaller size and a narrower spread of the air cell distributions as whipping time increased. It appears that as whipping time increases, more air cells are broken up, producing more and more air cells that collectively increase the air cell film interfacial surface area. This relationship indicates that whipping time tends to be the dominant factor in dictating the air cell distribution in marshmallow foam, mean air cell size, and total surface area.

Stability of Marshmallow in Relation to Foam Structure

The loss of moisture is expected to be indicator of quality deterioration because of its effects on texture, hardening, and induction of crystallization. It was found that the change in marshmallow moisture content of all marshmallow samples followed a general trend of moisture content significantly decreasing as the sample aged (Figure 19.11). This finding is in line with previous reports suggesting marshmallow loses moisture as it ages (Edmond, 2000; Eyres, 2001; Jia, 2004). In the current research, whipping time was the significant factor with reference to moisture loss. This significant difference is illustrated in Figure 19.10, where the highest whipping time introduced a lowest initial moisture content (at day 1), which could have contributed to the acceleration of moisture loss. This observation is in accordance with Lees et al. and Groves (Lees and Jackson, 1973; Groves, 1995), who stated that 2 to 3% of moisture may be lost during atmospheric beating. These results imply there is an inverse relationship between moisture loss and air cell size with a greater total air cell film interfacial surface, resulting in a faster rate of moisture loss.

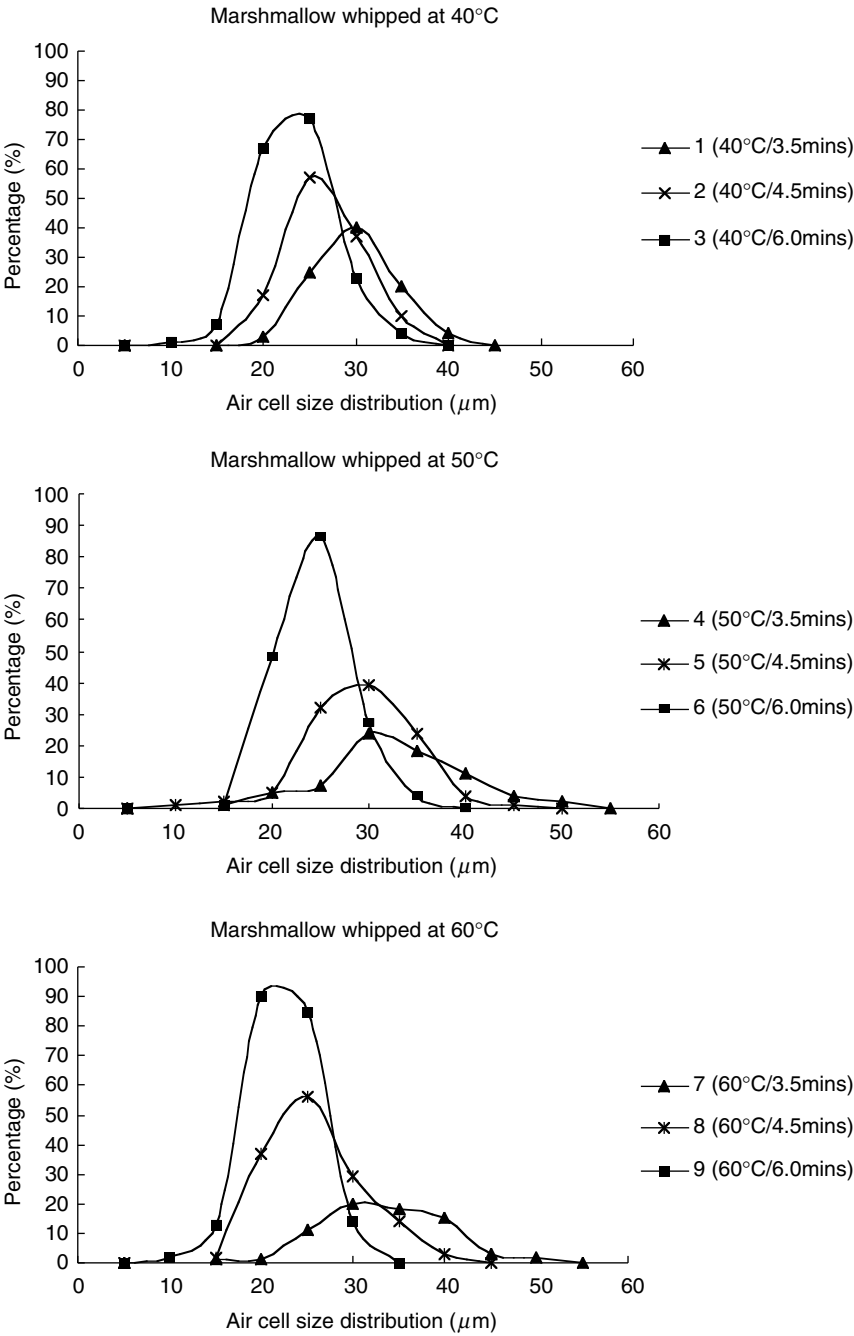


FIGURE 19.9
Air cell size distributions of marshmallow foam whipped at 40, 50, and 60°C for 3.5, 4.5, and 6.0 min.

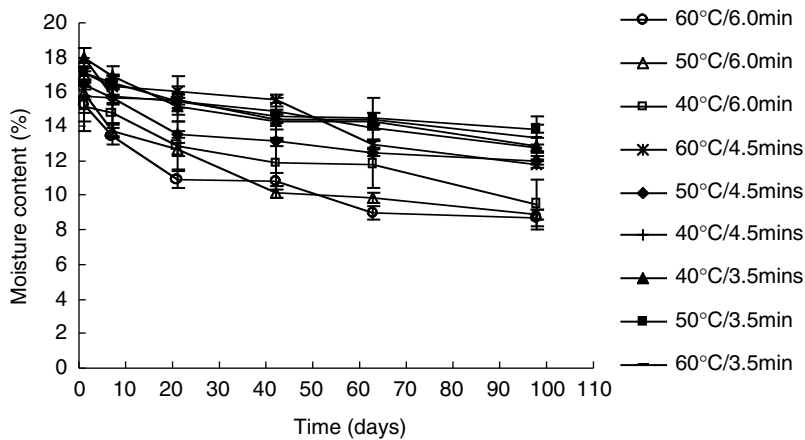


FIGURE 19.10
Marshmallow moisture content for samples stored at 75% RH and 25°C.

There was a corresponding increase in the hardness of the marshmallow as moisture content decreased (Figure 19.11). Samples whipped for 6.0 min were the hardest over the whole storage period. It has been suggested by Jia (2004) that hardening of marshmallow could be caused by moisture loss, sucrose crystallization, and gelatin gel maturation. The loss of moisture increases the sugar concentration of the marshmallow matrix and promotes sucrose crystallization and also increases the viscosity of the matrix, both factors which contribute to hardening. In this case, the longer the whip time, the greater the total surface area, and therefore as a consequence, the faster the loss of moisture from the marshmallow.

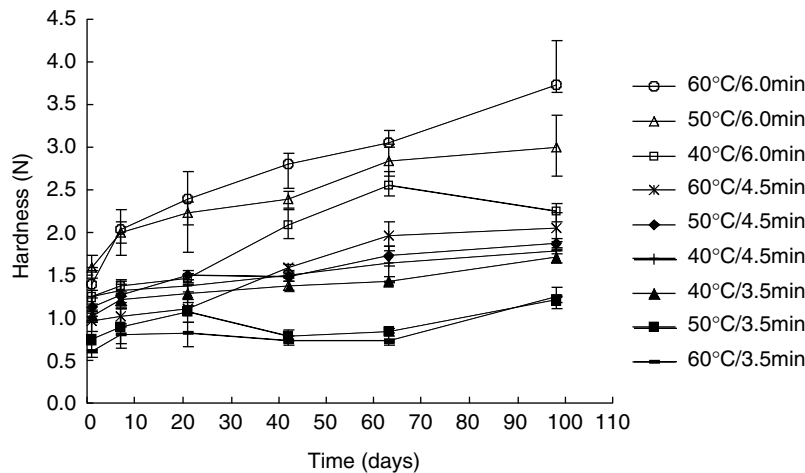


FIGURE 19.11
Marshmallow hardness for samples stored at 75% RH and 25°C.

Overall, high whip foams (6 min) produced a narrower air cell size distribution that increased foam stability against collapse, but had the most significant impact on the quality deterioration as a result of moisture loss and increasing hardness during storage. Whip temperature had no significant effect on quality deterioration (moisture loss or texture hardening) during storage. However, high whip temperature decreased the viscosity of the premix during production at a low whipping time (3.5 min) and caused foam instability. Unstable foam would produce lower overrun and therefore a much denser marshmallow and could result in the collapse of marshmallow during storage.

Conclusion

The development of hardness in the marshmallow during storage was shown to correlate with the moisture loss, sucrose crystallization, and possibly gelatin gel maturation. Although crystallization was likely to have reduced the elasticity and cohesiveness at the beginning of storage, moisture loss could be the most important factor contributing to the hardening process because it increased the viscosity of the matrix continuously through the whole storage period. Gelatin gel maturation effect on hardening is yet to be determined.

The shelf life of marshmallow could be extended by reformulation or modifying the manufacturing process to reduce moisture loss and prevent crystallization. The film model showed that high DE glucose syrups were better in extending the shelf life of the marshmallow than the low DE glucose syrups in terms of better moisture retention and retarding the growth of sucrose crystals. In the size-distribution study, time and temperature of whipping are important factors in maximizing foam quality and stability. Longer whipping produced marshmallows with narrower air cell size distribution and smaller air cell diameter, which tend to be structurally more stable but they tend to lose more water and consequently a harder product on storage. Therefore, an optimum air cell size distribution will have to be determined for each product quality and stability requirement.

References

- Bee, R., Clement, A., and Prins, A. Behaviour of an aerated food model, *Food Emulsions and Foams*, E. Dickson, ed., RSC, London, pp. 128–144, 1987.
- Campbell, G.M. and Mougeot, E. Creation and characterization of aerated food products, *Trends Food Sci. Technol.*, 10, 283, 1999.
- Edmond, J. *The Effect of Ingredients on the Glass Transition Temperature and the Shelf Life of Marshmallow*, Honours thesis, University of Otago, New Zealand, 2000.

- Eyres, G. *The Effect of Foam Air-Cell Size Distribution on the Stability of Marshmallow*, NZIFST Annual Meeting, Dunedin, New Zealand, 2001.
- Fennema, O.R. Water and ice, *Food Chemistry*, 3rd ed., O.R. Fennema, ed., Marcel Dekker, New York, pp. 17–95, 1996.
- Gabarra, P. and Hartel, R.W. Corn syrup solids and their saccharide fractions affect crystallization of amorphous sucrose, *J. Food Sci.*, 63, 523, 1998.
- Groves, R. Marshmallow production: technology and techniques, *Manuf. Confect.*, May, 99, 1995.
- Hanselmann, W. and Windhab, E. Foam generation in a continuous rotor-stator mixer, *Bubbles in Food*, G.M. Campbell, C. Webb, S.S. Pandiella and K. Niranjana, eds., Eagan Press, USA, pp. 65–73, 1999.
- Hartel, R.W. Controlling sugar crystallization in food products, *Food Technol.*, November, 99, 1993.
- Hartel, R.W. Nucleation, *Crystallization in Foods*, R.W. Hartel, ed., Aspen Publishers Inc., Maryland, pp. 145–191, 2001.
- Heenan, S. *The Effect of Processing Parameters on Marshmallow Air Cell Size Distribution, Shelf Life Stability and Quality*, Honours thesis, University of Otago, New Zealand, 2004.
- Howling, D. and Jackson, E.B. *Sugar Confectionery Manufacture*, E.B. Jackson, ed., Blackie and Son Ltd, New York, pp. 34–56, 1990.
- Jackson, E.B. Liquorice paste, cream and aerated confectionery, *Sugar Confectionery Manufacture*, E.B. Jackson, ed., Blackie and Son Ltd, New York, pp. 218–236 1990.
- Jia, Y. *The Mechanisms of Marshmallow Hardening in Model System and Commercial Marshmallow*, MS thesis, University of Otago, New Zealand, 2004.
- Johnston-Banks, F.A. Gelatine, *Food Gels*, P. Harris, ed., Elsevier, England, pp. 233–290, 1990.
- Kaletunc, G., Normand, M.D., Johnston, E.A., and Peleg, M. Instrumental determination of elasticity of marshmallow, *J. Texture Stud.*, 23, 47, 1992.
- Kinsella, J.E. Properties of proteins: possible relationships between structure and function in foams, *Food Chem.*, 7, 273, 1980.
- Labuza, T.P. *Stability of Soft Cookies*, Department of Food Science and Nutrition, University of Minnesota, USA, 2002, PDF file online, Accessed 14 October 2003.
- Ledward, D.A. Gelatine, *Handbook of Hydrocolloids*, G.O. Phillips and P.A. Williams, eds., Woodhead Publishing Limited, England, pp. 67–86, 2000.
- Lees, R. Fundamental principles in the production and characteristics of foam confectionery products, part one, *Confect. Prod.*, March, 210–211, 1991.
- Lees, R. and Jackson, E.B. Sugars and related materials, *Sugar Confectionery and Chocolate Manufacture*, Leonard Hill Books, United Kingdom, pp. 15–46, 1973.
- Levenson, D.A. and Hartel, R.W. Nucleation of amorphous sucrose-corn syrup mixture, *J. Food Eng.*, 69, 9, 2005.
- Macrae, R., Robinson, R.K., and Sadler, M.J. Sweets and candies, *Encyclopedia of Food Science, Food Technology and Nutrition*, Vol. 7, Academic Press, London, pp. 4480–4496, 1993.
- Massey, A.H., Khare, A.S., and Niranjana, N. Air inclusion into a model cake batter using a pressure whisk: development of gas hold-up and bubble size distribution, *J. Food Sci.*, 66, 1152, 2001.
- Richards, A.B., Krakowka, S., Dexter, L.B., Schmid, H., Wolterbeek, A.P.M., Waalkens-Berendsen, D.H., Arai, S., and Kurimoto, M. Trehalose: a review of properties,

- history of use and human tolerance, and results of multiple safety studies, *Food Chem. Toxicol.*, 40, 871, 2002.
- Roos, Y. Role of water in phase-transition phenomena in foods, *Phase/State Transitions in Foods*, M.A. Rao and R.W. Hartel, eds., Marcel Dekker, New York, pp. 57–86, 1998.
- Roos, Y. and Karel, M. Phase transition of mixture of amorphous polysaccharides and sugars, *Biotechnol. Prog.*, 7, 49, 1991.
- Taylor, L.S. and York, P. Characterization of the phase transition of trehalose dihydrate on heating and subsequent dehydration, *J. Pharm. Sci.*, 87, 347, 1998.
- Tiemstra, P.J. Marshmallows, *Food Technol.*, 18, 125, 1964.
- Tjuradi, P. and Hartel, R.W. Corn syrup oligosaccharide effects on sucrose crystallization, *J. Food Sci.*, 60, 1353, 1995.

20

Beyond Water Activity and Glass Transition: A Broad Perspective on the Manner by which Water Can Influence Reaction Rates in Foods

Craig P. Sherwin and Theodore P. Labuza

CONTENTS

Introduction	343
Fundamental Principles	344
Two Polarizing Food Stability Theories Have Overshadowed True Complexities.....	347
Diffusion and Reaction.....	349
Observations on Rates of Diffusion and Reaction.....	350
Observations on the Influence of Matrix Mobility on Reaction Rate	353
Correlations of T_g to Chemical and Physical Processes.....	356
The Presence of Charged Solutes.....	364
Conclusions.....	365
References	368

Introduction

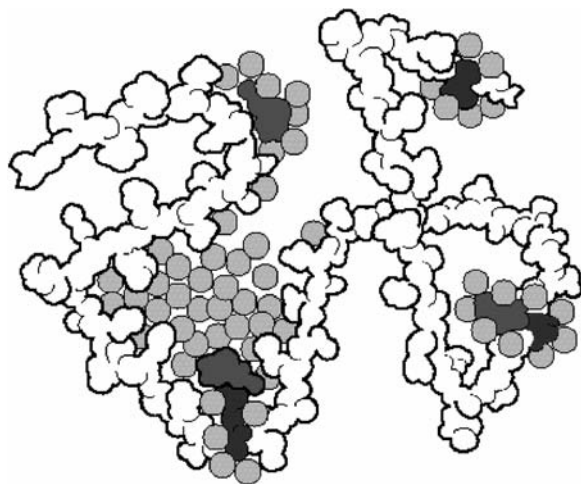
Water is highly important in foods as both an environmental variable and an ingredient. Changes in the water content of foods can be accompanied by drastic changes in the nature of food texture, microbial growth, flavor, color, and other properties. This dynamic nature of food systems can be modeled just as any chemical reaction by the principles of thermodynamics and reaction kinetics. Today, this field within food science is struggling with the increasing complexity that predictive models are developing. Food physical chemists once thought that the simple concept of water activity (a_w) would provide all of the predictive power one would need to ensure food quality. However, the anomalies of a_w -based shelf-life predictions that were

discovered in laboratories revealed the shortcomings of this theory (Labuza et al., 1977; Saltmarch and Labuza, 1980). Elegant as empirical relationships at first seemed, there was no actual theoretical link between the thermodynamic measure of a_w and chemical reaction kinetics. When the glass transition (T_g) was recognized to occur in food polymers, the reasons for kinetic limitations became more complete and provided a molecular mechanism for the role of moisture. However, there were few experiments done to challenge the mechanism and isolate the competing effects of moisture. Regarding the role of moisture in governing food stability, food scientists are caught in the uphill struggle of "the more we learn, the more we discover how much we do not know."

This review will first highlight fundamental concepts in chemistry that are important for the evaluation of kinetic data and the influence of moisture. Secondly, we will posit several key considerations to bear in mind while predicting reaction rates when moisture is a variable, comprised of unanswered questions, common assumptions that deserve challenge, or hypotheses that deserve more focus by researchers. Foremost, we will highlight previous key research regarding the role moisture plays in the stability of low and intermediate moisture foods. It is at these moisture levels that many of the theoretical shortcomings regarding the links among a_w , moisture content, and reaction rates are revealed. We will see that for any given food, there are a number of perspectives one must consider before making predictions. There is not a sufficiently consistent body of data to show a causation between chemical reaction rates and any single parameter such as a_w or T_g for every food system and every reaction. Most reliably, it is the mobility of reactants that is the foremost predictor for reaction rate, yet this is not an easily measured parameter. We will see that the role of moisture and temperature in governing reactant mobility is in fact complex and may or may not encompass the influence of moisture and temperature on both long- and short-range motions by reactant molecules, concurrent changes in the mobility of polymer molecules, or all of the above.

Fundamental Principles

It is a well-documented fact that changes in reaction rate correlates well to changes in a_w , with references too numerous to include. Because reactions alter their behavior as a function of a_w , researchers often mistakenly redefine a_w either as: (1) a measure of the ability of water to participate in reactions, (2) a ratio of the amount of water that participates in chemical reactions and microbial growth to water that cannot participate, or (3) a ratio of "free" to "bound" water. The actual role of a_w in food reactions, microbial growth, and moisture transfer has been extensively documented and reviewed but not completely understood (Labuza, 1980; Rockland and Nishi, 1980; Chirife and Buera, 1994).

**FIGURE 20.1**

Heterogeneous distribution of water molecules about a polymer chain. Reactive species are shaded as an illustration of the hydration state of chemical reactants. *Illustration by Cynthia Gresham.*

For the purposes of discussion, it is important to agree on a physical picture of the distribution of water in a semi-moist food (Figure 20.1). Consider the hydration states of a completely dry ideal food exposed to humidity. The most energetically restricted water will theoretically interact with hydrophilic and polar regions of the polymers and solutes until one molecule of water has bonded to each hydrophilic group. This water content is known as the *theoretical monolayer moisture value* (m_0). In reality, such a continuous single aqueous phase covering the entire molecular surface does not actually exist in a food, but rather it is heterogeneously composed of clusters of water about polar sites. However, the behavior of the system at this moisture content mimics what would occur if such a homogeneous monolayer actually existed. Since the concept was initially developed for super-cooled gases and not for moisture at room temperature (Brunauer et al., 1938), purists question its applicability. For example, Harry Levine states in the preface to his recent book *Amorphous Food and Pharmaceutical Systems* that “even today the myths of water activity and bound water are hard to kill” (Levine, 2002), and so-called “bound water” was a topic of discussion at the ISOPW VIII meeting in Israel (http://faculty.che.umn.edu/fscn/Ted_Labuza/PDF_files/papers/ISOPW8_WaterInFood_Panel.pdf). Yet research has shown that m_0 can have great relevance to predicting both moisture adsorption in foods and food stability (Labuza et al., 1969; Labuza, 1980), even if not a fully accurate description of the molecular distribution of water.

Continuing with the adsorption process, further hydration results in highly ordered layers of water molecules hydrogen-bonded to each

water molecule. The next level of hydration is a more disordered liquid phase hydrogen-bonded to these ordered layers. At a higher level, water can exist in a condensed phase within capillary spaces (Labuza et al., 1969; Zografi, 1988). These classifications of water constitute what is mistakenly defined as “bound water” when a_w is used to predict the availability of water for reactions. Although this term is commonly used, it is an imperfect and vague description of the decreased availability of water to participate in reactions at lower a_w , as noted in the quote above from Levine. More accurately, the forces encountered by water in these states of hydration contribute to a lowering of vapor pressure and a lowering of the chemical potential driving force for change. Any additional water that is adsorbed will not be affiliated with the surrounding solid matrix, but rather the water already present within the system. This moisture will behave as solvent water, and it freely exchanges with adsorbed water (Bryant and Shirley, 1980). It will in fact cause a decrease in the concentration of any existing reactants that have gone beyond their solubility point. Lechuga-Ballesteros and others (Lechuga-Ballesteros et al., 2003) studied protein-based pharmaceutical systems and found that the lower limit of reaction is the hydration limit of the protein, which they term W_m , and that the moisture value at which the excess enthalpy of condensation of water (Q_s) approaches zero is just above the BET monolayer (BET theory states that above the monolayer $Q_s = 0$). The GAB equation, which is less frequently used, shows that the mobility point may be slightly above the BET m_0 . Lechuga-Ballesteros (Lechuga-Ballesteros et al., 2003) discusses this in much more depth.

Importantly, Labuza and others (Labuza, 1968) showed in a review of reaction rates in foods as a function of a_w , that at some value above the monolayer for amorphous phase food systems, the rate of reaction increases exponentially to some maximum at an intermediate a_w (0.6 to 0.8) and then decreases again. If reactions were based on the lack of boundness (i.e., free water) and a_w was a measure of freeness, then rates should continue to rise as a function of a_w . This has been found to be the case for some reactants in pure glycerol–water systems (unpublished work in our lab) but is not found in foods or drugs with a solid phase. This decrease in rate above a critical a_w in an amorphous solid–liquid matrix could be caused by a variety of factors including changes in dielectric constant and thereby solubility, as well as changes in viscosity, ionic strength, and pH as a function of solute moles to solvent volume. Lechuga-Ballesteros and others (Lechuga-Ballesteros et al., 2002) in a review of the pharmaceutical stability area (mostly protein functional loss) also show a similar behavior of a rate maximum at intermediate moisture content in amorphous drug systems. For example, the work of Lui and others (Liu et al., 1991) at MIT on the stability of bovine serum albumin demonstrated a rate minimum at about 5% moisture (db), a maximum at 28%, and a decrease at higher moisture contents.

To make things even more complex, solvent water and/or solutions such as polyols in water can also act as a plasticizer, increasing the mobility of the polymer molecular chains and theoretically, reactant molecules within

clustered regions of polymer molecular strands. The *glass transition* is a physical state change that occurs as temperature increases and amorphous polymer strands undergo a significant increase in their chain mobility or molecular vibrational space, or as a change in moisture content increases at constant temperature. The mechanism by which T_g changes with moisture content is *plasticization*. Water associates via hydrogen bonding with hydrophilic molecular regions in food polymers, causing a more fluid-like structure around local regions of the polymer molecule. In this plasticized state where polymers are more fluid-like, the energy required for polymer chain mobility is greatly reduced and T_g decreases. Thus, at a given storage temperature, the T_g can be sufficiently lowered with moisture adsorption such that the food will transform into a highly viscoelastic material, sometimes called “rubbery” material when referring to some bakery and confectionery goods. Water is a ubiquitous substance in foods and thus is considered to be a primary contributor to plasticization in food matrices. However, any solute molecule or other added component that does not demonstrate a phase separation with other components can provide significant changes in the free volume of the polymer and thereby could affect the T_g (Slade and Levine, 1991).

Two Polarizing Food Stability Theories Have Overshadowed True Complexities

The original molecular-based theory for food stability was centered on the monolayer moisture value (m_0), which can be understood as a point defining mobility. The theory predicts that a threshold for molecular mobility is witnessed at or slightly above m_0 and increases at higher moisture contents. Since dissolution of reactants is a requirement for reactivity, reactions could only begin to occur at or near m_0 where there is enough solvent phase to dissolve the reactants. Mobility would increase with higher a_w according to some mobility-based mechanism. The relationship between a_w and m_0 via the BET and GAB models suggested an applicability of a_w towards predicting chemical reaction rates. Even with the widespread acceptance and success of this application of a_w towards improving food stability, the role of moisture in food systems from a physical chemical standpoint was never clear. The definition of the moisture monolayer and subsequent research linked a minimum moisture content to a a_w at which there was enough mobility such that reactions could begin (Labuza, 1968), e.g., either chemical reactions like nonenzymatic browning or physical state changes like the collapse and crystallization of sucrose in cotton candy (Labuza and Labuza, 2004). Since the monolayer moisture indicates a point of minimum reactant mobility (Duckworth, 1962), the increased reaction rate witnessed for higher moisture contents was assumed by some to be a result of increased

dissolution of reactants. However, reaction rate and mobility as such have never been directly linked in a single comprehensive study.

By the late 1980s, a second theory had developed that assigned a new point for the threshold of moisture content that marks the onset of reaction as well as a new mechanism for increased reactivity as moisture content increases (Slade and Levine, 1988; Slade and Levine, 1991). According to the original form of this theory, only at moisture contents at or above the T_g would any reaction begin to occur. The rate was stated to be dependent on $T - T_g$ at constant moisture (or plasticizer), although subsequent experiments considered constant T and variable moisture content (variable T_g). Therefore, this second theory for food stability asserted that the T_g of the polymer matrix (or more precisely, the moisture content corresponding to a T_g that equals the storage temperature) is the key point at which reactants can undergo sufficient mobility for reactions to occur. This theory was quickly embraced because unlike the monolayer value prediction, it provided a clear molecular explanation as to why at higher moisture contents there is an increased rate of chemical reaction. According to glass-transition theory, it is the increase in free volume or reaction space that governs reaction rate in correspondence to a reduced local viscosity and increased mobility of the reactants (Slade and Levine, 1991). Increased moisture provides increased free volume, reduced local viscosity, and increased reaction rate. This mechanism for reaction rate changes with changes in temperature is described by the Williams–Landel–Ferry equation (WLF) or variations thereof such as the VLF equation (Vogel–Tammann–Fulcher), the use of which has been previously reviewed (Peleg, 1992; Nelson and Labuza, 1994; Shriraldi, 2002). Several publications called into question the fundamental assertion that the limiting moisture for reaction was defined by the T_g , as will be reviewed below. It was found by Nelson and Labuza (1994) that ascorbic acid degradation occurred well below the moisture content values at any T_g . More recently in pharmaceuticals, Pikal (2002) studied the stability of human growth hormone and found significant reaction well below T_g ($T - T_g = -60^\circ\text{C}$), as did Shamblin and Zografis (1998) for a study on sucrose relaxation based on the VLF equation. Lechuga-Ballesteros et al. (2002) in a review of food science literature and from their own studies argued that (1) the moisture at T_g is not the limiting moisture for reaction; (2) the Kauzmann temperature projected using VLF may be the absolute limit of no mobility or reaction although as we note those times are much longer than the shelf life of foods or drugs and (3) that for proteins, the calculated BET W_m is a practical limit point giving maximum stability.

Thus the basic requirements for a chemical reaction in which water might play a role for food stability are four-fold (lipid oxidation is a notable exception to these requirements). First, there must be enough solvent present to allow the reactants sufficient mobility to encounter each other. Second, the reactants dissolved in water need sufficient mobility to diffuse and encounter one another. Third, there must be sufficient mobility provided by the surrounding polymer system to allow the entire reactant solution

phase to move within the solid amorphous phase. Similarly, reaction will be limited when there is not mobility for products to diffuse away from the reaction site, and thereby the reaction is limited by a “local” equilibrium. Diffusion is dependent on both the properties of the polymer-restricted pores as well as the size of the diffusing molecule. Lastly, many food reactions require water as part of the chemical equation, such as in hydrolysis reactions.

Diffusion and Reaction

At very low moisture contents and water activities, the rate of diffusion within the solid matrix is theorized to be the rate-limiting step for many reactions that require a liquid-like phase. Whether the rate of diffusion is specifically related to a parameter such as monolayer moisture value, a_w , temperature above the glass transition ($T - T_g$), or perhaps more generally the degree of mobility or dissolution of reactants is at the heart of the current discussion. According to the monolayer model, diffusion of reactants is limited by the degree to which they are dissolved. However, reactions involving small gaseous molecules such as oxygen are probably not diffusion-limited because significant rates of diffusion occur in the gaseous pore spaces of many foods. Similarly, lipid oxidation can increase in rate below the monolayer or T_g by processes unhindered by mobility and instead promoted via basic chemical principles of catalysis and concentration (Labuza, 1971).

One effect of diffusivity on the reaction rate constant of a bimolecular reaction has been proposed by Atkins (Equation 20.1) (Atkins, 1982). The Stokes–Einstein equation (Equation 20.2) (Edward, 1970) relates molecular size and local liquid phase viscosity to diffusion on very small scales. For the purposes of this review, we will refer to this type of diffusion as local translational diffusion.

$$k_d = 4\pi d^* D_r A^0 \quad (20.1)$$

k_d = rate constant ($\text{m}^3/\text{mol}\cdot\text{s}$)

d^* = collision diameter (m)

D_r = diffusion coefficient (m^2/s)

A^0 = Avogadro's constant (particles/mol)

$$D_{\text{eff}} = \frac{RT}{6\pi r\eta} (\text{m}^2/\text{s}) \quad (20.2)$$

R = universal gas constant ($\text{J}/\text{mol}\cdot\text{K}$)

T = absolute temperature (K)

r = radius of diffusing molecule (m)

η = viscosity of the medium (Pa·s)

The Stokes–Einstein D_{eff} is proportional to temperature both directly and through its effect on η . Yet on an absolute scale, temperature increases are relatively small for deteriorative reactions in foods. For example, when increasing temperature from 20°C (293 K) to 45°C (318 K), the theoretical diffusivity by Stokes–Einstein increases only 8%. Since deteriorative food reactions typically increase by 200 to 1000% per 10°C increase ($Q_{10} = 2$ to 5), a simple local translational diffusion model would be insufficient.

It is important to note that diffusion is not a universally defined term. In foods, the processes of self-diffusion of the polymer matrix molecules, self-diffusion of solutes, translational diffusion of solutes, and diffusion of moisture and other liquids have not been well discerned among theorists. All of these diffusion or mobility-based processes may occur in foods and pharmaceuticals. Yet recent theories do not clearly and consistently address which of these processes are of significance to chemical reactions, and how changes in water content or a_w as well as T or T_g affect each of these types of diffusion.

Translational diffusion would be expected to be important only when molecules are located at significant distances from one another. Using a tri-layered model system of xylose, lysine, and PVP, Buera and Karel (Buera and Karel, 1994) found that the rate of Maillard browning throughout the system was proportional to the thickness of a 100% PVP layer sandwiched between a layer of xylose dispersed within PVP and a layer of lysine dispersed within PVP. In this experiment, molecules were artificially separated in order to illustrate the significance of diffusion for reaction rate. However, for most homogeneously distributed food systems, reactants would only be expected to diffuse on the order of nanometers prior to encountering a second reactant species. It is unknown whether the Stokes–Einstein or a Fickian model for bulk diffusion would best model diffusion on this scale. For still other chemical systems, perhaps rotational mobility is the key mobility process that limits the ability of closely-packed reactants to orient with each other. Yet even under these conditions, translational diffusion of reactant products away from the reaction site may be a rate-limiting step for some reactions. Once more clarification of these mobility processes is established for various reactions in foods, it will then be possible to determine to what extent these models can be included into a more inclusive and realistic model.

Observations on Rates of Diffusion and Reaction

In an important early study that linked a_w and the monolayer value directly to diffusion, Duckworth (1962) found that browning in vegetable strips

during dehydration was affected by the distribution of applied sulfite (a browning inhibitor) and reactant concentration. In further experiments, he applied a radioactive tracer to one end of dry carrot strips and potato strips and equilibrated them to various humidities. The movement of radio-labeled glucose in the samples was nonquantitatively observed by autoradiography, whereby the expansion of a band on the developed film signified a positive test for diffusion. The sample stored below the monolayer value was the only sample to show no diffusion in the time studied (Table 20.1). The authors claimed similar results when using tracer counting coupled with autoradiography, for ^{14}C -glucose, ^{45}Ca -chloride and ^{35}S -sulphate in potato and fish tissue, although these data were never published (Duckworth and Smith, 1963).

This study was done before the importance of T_g of foods was proposed. The coincidence of the monolayer with a slow diffusion seemed to support the monolayer theory. Below the m_0 , it was theorized that water molecules are tightly bound to hydrophilic groups and supposedly cannot influence the diffusion of solutes, or that clusters are spread so far apart that diffusion of a solute would have to take place in the solid phase without any hydration by water. Systems above the monolayer value contain sufficient water to act as a solvent for water-soluble reactants. Yet there may yet have been a T_g significance demonstrated in these systems but not measured at the time.

While several researchers have studied reactions in the glassy state that were assumed to be diffusion-dependent, few researchers have directly correlated rate of diffusion to physical state. The reason for this may be the difficulty in obtaining accurate diffusion coefficients when it is such a very slow process. Slow processes are typically not thought of as being significant in the lifetime of a food. However, since WLF kinetics and the glass-transition theory for food stability are both based on diffusion limitation, then a thorough study of diffusion and mobility below T_g at low moisture is the key to understanding reaction rates. The work of Karel and Saguy (1991), Pikal (2002), Lechuga-Ballesteros et al. (2002), as well as the numerous papers out of the Simatos group at Dijon (Le Meste et al., 1991; Le Meste et al., 1995) suggest that this mobility is significant as a controlling factor in reactions. In fact, a much earlier paper by Makower and Dye (1956) showed crystallization of sucrose taking place in a freeze dried matrix only after over 200 days of storage at 16% RH and 35°C. This corresponds to a moisture content of less than 2 g/100 g sucrose or ~ 1 molecule of water to 2 or 3 molecules of sucrose. Thus, mobility in the amorphous solid state becomes extremely important at low moistures, a question not generally addressed. Does the reaction take place in the solid amorphous phase or does the solute actually dissolve in the water? Perhaps it will be found that bulk diffusion measurements might be used to estimate the motions of molecules over nanometer scales, but most likely other techniques such as magic angle spinning NMR are needed, as we will suggest below.

TABLE 20.1
Diffusion in Vegetable Samples as Affected by Moisture Content. (+) Denotes Detectable Movement of the Radioactive Tracer, and (–) Denotes No Detectable Movement

Air-Dried Potato Glucose Diffusion		Air-Dried Carrot Glucose Diffusion		Freeze-Dried Potato Glucose Diffusion		Scalded Potato Tissue Sulfate Diffusion	
Moisture Content	Diffusion	Moisture Content	Diffusion	Moisture Content	Diffusion	Moisture Content	Diffusion
6.7	—	5.9	—	2.3	—	5.7	—
7.2	N/A	7.9	N/A	9.6	N/A	6.2	—
Monolayer		Monolayer		Monolayer			
	+	8.1	+	10	+	7.5	+
	+	10.2	+	10.7	+	7.8	+
	+	13.9	+	12.6	+	9	+
11.9	+						
14.7	+	18.1	+	15.9	+	9.2	+
16.3	+	21.7	+	18.5	+	10.4	+
23.4	+	26.3	+	24.2	+	11.6	+
						13.8	+

Observations on the Influence of Matrix Mobility on Reaction Rate

Can moisture changes in low to intermediate foods be modeled simply by an increase in the total solvent phase available to dissolve reactants? What other properties in a food or amorphous solid pharmaceutical change with moisture gain or loss, and can these be part of the mechanism that governs reaction rate? The first question is sometimes overlooked today, but remains the simplest explanation for the role of moisture in governing reaction rate. The original theory for food stability, as described above, does in fact encompass this view but simplifies the measurement of the solvent phase into a single theoretical parameter derivable from models, the monolayer value or the hydration limit as proposed by Lechuga-Ballesteros et al. (2002). The second question of whether other properties that change with moisture content led to the exploration of the T_g as a useful parameter. Yet this view as well may have been oversimplified into the narrow view of the mobility of the polymer matrix, without considering other forces that can affect the mobility of reactants. It is clear that mobility or diffusion, in some sense, is the mechanism linking moisture changes to reaction rates in foods. Viscosity is a property of the solvent phase that governs the mobility of solutes and polymer segments and may be a significant contributor to their reactivity. But in what manner is the solvent phase distributed in a low to intermediate moisture food, and is local viscosity more limiting than this distribution of a concentrated reactant solution phase? In addition, the mobility of the polymer matrix and the ability of water to plasticize are other frequently cited influences on reactivity. However, overall, there is a significant gap in our knowledge of the various roles that moisture plays in governing the rates of chemical reactions in foods, functioning as a solvent containing reactive solutes and influenced by temperature dependent viscosity changes (note the inverse effect on mobility of viscosity from the Stokes–Einstein equation) as well as a plasticizer within a polymer matrix.

There are numerous references that show a correlation between matrix properties and reaction rates (Labuza et al., 1977; Roos, 1993; Bell and Hageman, 1994; Buera and Karel, 1994; Bell, 1996), but arguably not to the exclusivity of solvent-based effects, and never with a direct link to the mobility of the reactant itself rather than the polymer. Yet there are a handful of studies that come very close to showing a direct link between reactant mobility and polymer mobility.

Simatos et al. (1981) measured the mobility of a spin-label probe, TEMPO, a stable free radical commonly used for electron paramagnetic resonance (EPR) spectroscopy. She found that the probe showed no mobility below a critical a_w that correlated to m_0 . A critical a_w also existed at which the probe demonstrated a partitioning into a dissolved and a solid-like state. This critical a_w could represent the moisture content correlating to T_g , though this concept had not been introduced in foods at that time. The partitioning of a

solute into a dissolved and more solid-like state demonstrates the inherent heterogeneity of food systems. There is no true equilibrium within the lifetime of foods. Studies that measure bulk properties of food systems must address the issue of heterogeneity of the physical state and mobility of solute reactants prior to drawing conclusions as to a molecular mechanism for a property change. Local heterogeneity of reactant species can be an important factor in predicting net chemical reactivity. Also of significance in the study is the direct measure of changes in the mobility of small solute-like molecules such as TEMPO with changes in moisture content.

In a similar study using another spin-label probe, TEMPOL, in frozen 20% sucrose–water mixtures, Roozen and Hemminga (1990) showed that a significant increase in probe rotational correlation time occurs as one increases the temperature above T_g at constant moisture content. Figure 20.2 shows this shift in the temperature dependence of the rotational correlation time. According to the authors, characterizing T_g of the frozen system could enable better control of ice crystal growth. Thus, the authors set out to examine the glass-transition theory for food stability, stating that T'_g theoretically controls the mobility of water molecules in a rapidly frozen solution and warming a frozen solution to $T > T'_g$ would allow ice crystal growth and a loss of quality. Roozen and colleagues have also performed similar TEMPOL mobility studies in maltodextrin systems, also using values for T_g previously published in the literature (Roozen et al., 1991). The researchers assumed an Arrhenius relationship for probe mobility over a small temperature range in the glassy state in order to calculate activation energy for probe mobility. Nelson and Labuza (1994) showed such an assumption to be appropriate. If a spin-label probe can be assumed to exhibit

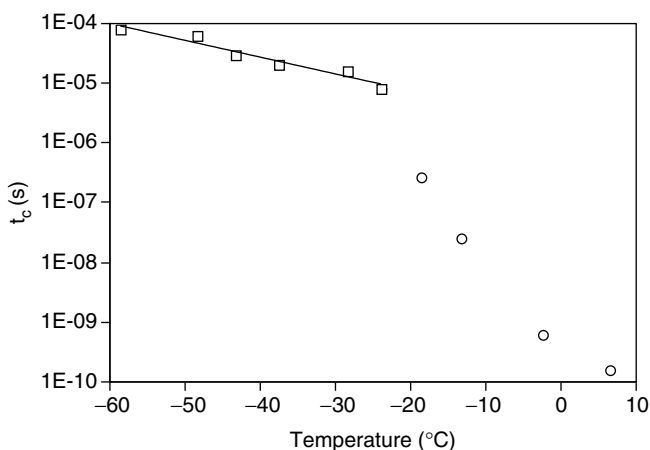


FIGURE 20.2

Rotational correlation time (τ_c) of TEMPOL as a function of temperature in a 20% maltotriose solution (Roozen and Hemminga, 1990).

a similar relative mobility to small solute reactants, then the measured coincidence of the T_g and probe correlation time in these studies was an important initial step in confirming any significance of polymer mobility for governing the mobility of embedded reactant molecules.

Researchers who reference the aforementioned EPR studies stressed some significance of the coincidence of the T_g and mobility of a solute, and hence the studies fostered much interest in the location of T_g as a predictor for food quality. Yet subsequent research has tended to isolate the effects of temperature, moisture, and mobility either on reaction rate or on mobility and has never linked the two processes.

In our research group, a CP/MAS NMR technique was developed to study glucose rotational mobility in the solid state over a range of a_w and in matrices with different T_g (Sherwin et al., 2002). One notable difference from previous NMR work in foods was that the data analysis stressed the significance of separating molecular mobility (in terms of rotational correlation time) from relaxation time (T_1 or T_2). Summarized in Figure 20.3, results showed that in a caseinate matrix, over the entire range of a_w and moisture contents, adding glycerol yielded the highest glucose mobility and sorbitol the second highest, compared to a control with no plasticizer other than water. This correlated well with the T_g curves of the three plasticized systems, where adding glycerol also increased caseinate mobility the most, followed by sorbitol and then the control. Consequently, plasticization either by moisture or these humectants increased the mobility of the reactant solute molecules of glucose, which reacts with the caseinate through Maillard browning.

These results support the assertion that plasticization will affect the mobility of small solute molecules embedded within. However, there is a significant caveat in using these results to confirm that plasticization may also be linked to the reactivity of small solutes embedded within the matrix. As shown by Simatos et al. (1981), one would expect the increased

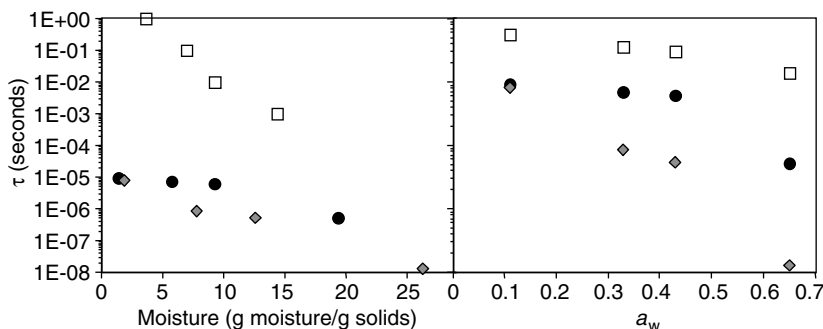


FIGURE 20.3

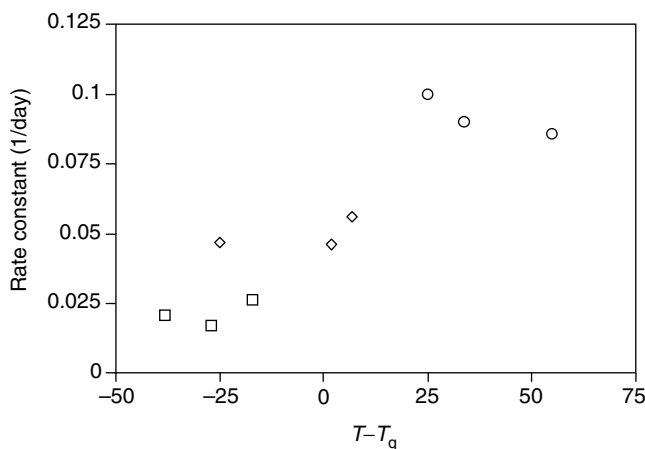
Semi-log plot of the effect of moisture content and a_w on rotational correlation time of the (\square) control formulation, (\blacklozenge) glycerol formulation, and (\bullet) sorbitol formulation (Sherwin et al., 2002).

adsorption of moisture to dissolve and render more mobile a greater proportion of glucose molecules in the aqueous phase. The technique of CP/MAS yields the net mobility of those glucose molecules that exhibit longer time-frame motions. This can be thought of as the glucose that is partitioned into the undissolved or solid state. Whether there is sufficient mobility of these undissolved glucose molecules to allow reactivity has not been shown. Instead, it may be that only the more mobile dissolved partition of glucose would be able to participate in chemical reactions. This caveat was born out in subsequent experiments that measured rate of NEB in these plasticized model systems, where glycerol showed a much higher reaction rate than the control while the sorbitol was equal to the control (Sherwin and Labuza, 2003). To further examine the role of increased moisture as both a plasticizer and as a solvent, additional experiments are needed that would explore the effect of plasticization of the caseinate matrix on the mobility of the *dissolved* or more highly mobile glucose molecules, in contrast to the above experiments on *undissolved* or solid-state glucose.

Correlations of T_g to Chemical and Physical Processes

Reactions do occur in the glassy state for many systems, even when mobility of reactants is limited as noted earlier, and for ones that have not, it is the time frame for studying the reaction that needs to be expanded. Note that Makower and Dye (1956) carried out their observations for 700 days. Nonenzymatic browning (Karmas et al., 1992; Karmas and Karel, 1995; Bell, 1996; Lievenon et al., 1998), aspartame degradation (Bell and Hageman, 1994), and ascorbic acid degradation (Nelson and Labuza, 1993; Nelson and Labuza, 1994) have all shown significant rates of reaction in the glassy state. As an example, Bell and Hageman (1994) examined aspartame degradation in a polyvinylpyrrolidone (PVP) system of differing molecular weights to distinguish the effects of a_w and T_g on the reaction rate. Three PVP fractions with molecular weights of <3500, 10,000, and 40,000 were found to have identical moisture sorption isotherms but give an increasing T_g with increasing molecular weight. Therefore, the researchers could control T_g either by plasticization with water (variable a_w) or by altering molecular weight of the PVP at constant a_w . As a result, they could differentiate a_w effects from T_g effects. Using this approach, aspartame degradation showed a clear effect by changes in a_w but no predictable effect with changes in T_g (Figure 20.4).

In this and similar studies, reaction occurred at moisture contents greater than the monolayer, but below the glass transition. Therefore it is clearly not the case that reactions cease below the T_g , as the theory was originally formulated. More recently, the T_g theory has been restructured to allow that the T_g serves as an inflection point above which reactions occur much more significantly. Yet this approach carries certain pitfalls regarding the

**FIGURE 20.4**

Rate constants for aspartame degradation as a function of distance from T_g : (\square) $a_w = 0.33$, (\diamond) $a_w = 0.54$, and (\circ) $a_w = 0.76$ (Bell and Hageman, 1994).

application of kinetic models. There have been a number of other studies investigating the coincidence of the T_g and an increase in reaction rate or some other property of a food-related system (Slade and Levine, 1991; Karmas et al., 1992; Aguilera et al., 1993; Nelson and Labuza, 1993; Roos, 1993; Bell and Hageman, 1994; Chuy and Labuza, 1994; Karmas and Karel, 1995; Bell, 1996; Formi et al., 1997; Tsimidou and Biliaderis, 1997; Lievonon et al., 1998; Netto et al., 1998; Gunning et al., 1999; Lai et al., 1999; Burin et al., 2000). Yet these experiments were not designed to control other moisture-mediated properties in foods, such as total solvent phase.

Some of the evidence for a T_g dependence relies on successful application of the WLF model to reaction rate data, using T_g as the reference temperature. There are several reasons for discrepancies among the theoretical WLF dependency of reactions that have been outlined by Le Meste et al. (1995) for frozen food systems. Of particular relevance, is the assertion that WLF kinetics predicts an overly strong temperature-dependence for the diffusion of reactants. This is because diffusion is not only affected by temperature, but also by solvent, diffusant size, and the fact that one or more reactants may not be diffusion-limited while others are.

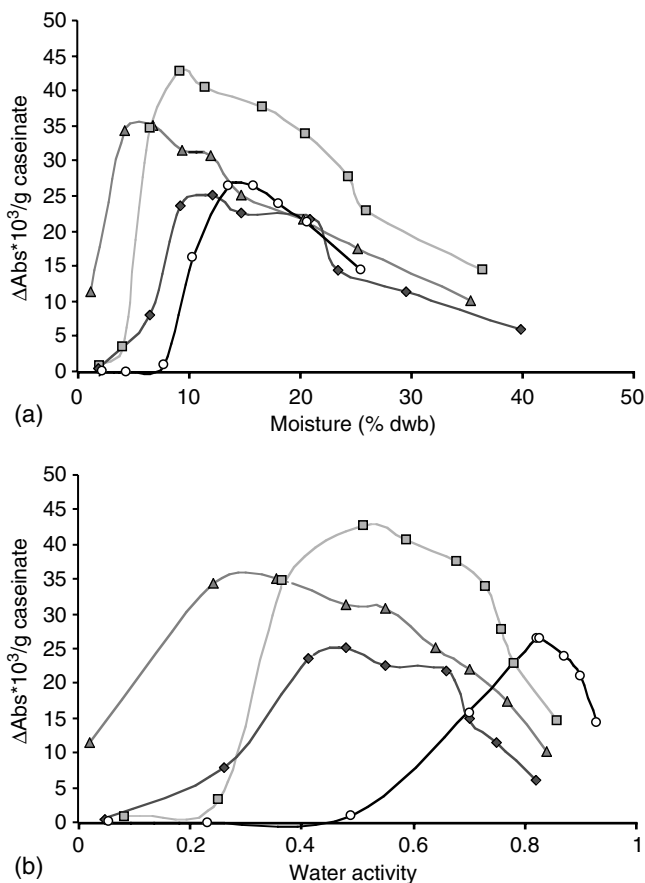
In studying a WLF-controlled kinetic reaction, there are three ways one might vary the $T - T_g$ experimentally. A system with a known T_g could be studied at a single moisture content and multiple temperatures, thus maintaining a constant T_g and altering T . By this means, the concentration of constituents remains the same and only the structure or energies may vary. This is the foundation for the derivation of the WLF model (Williams et al., 1955). Secondly, one can vary the T_g by replacing the polymer with an equivalent lower molecular weight species, such as PVP of shorter chain

lengths, and then measure the reaction at a single temperature (Lievonon et al., 1998). Here, applying the WLF model would be akin to fitting the kinetics of ascorbic acid loss in dry potatoes and in dry cereal on the same line. Lastly, one could vary the T_g by studying the reaction at multiple moisture contents, which would cause a plasticization of the polymer, at a constant T . Both of the latter designs introduce the potential error, or the competing effects of other mechanisms, that we have targeted for this review. Altering moisture content may have affects beyond that of plasticization of the polymer, and we cannot necessarily compare systems at different moisture contents as having reaction rate differences that are only dependent on T_g (or $T - T_g$). Therefore, the WLF model should only be applied to systems where the moisture content is held constant (constant T_g and variable temperature) and not over a set of systems with different compositions (variable T_g). This same caveat is applicable to wrongly applying the Arrhenius equation for reaction temperature-dependence while using data for the correlation from different moisture contents.

In fact, we have found that in the literature the most common way that researchers test the applicability of the WLF model is to measure reaction rates at one temperature while lowering the T_g . T_g is lowered either by raising the moisture content or sometimes by decreasing the molecular weight of the solid matrix (Bell and Labuza, 1994; Bell, 1996; Lievonon et al., 1998). In effect, the researchers are treating $T - T_g$ as the variable in the WLF model rather than T as the variable and T_g as a constant. This is not the basis upon which the WLF model was developed (Williams et al., 1955) and such a treatment does not allow us to isolate the other physical and chemical changes that increasing moisture content or decreasing molecular weight of the matrix might have on reaction rate.

Although there are several studies reporting either a coincidence of T_g and a shift in reaction rate or a rate that changes with changes in T_g , or changes in $T - T_g$, we believe that an unmistakable correlation has yet to be shown. This is because alternative explanations for the shifts have not been ruled out, and in some studies there is no T_g dependence demonstrated at all. Combined with the lack of extensive data on actual food ingredients at a broad range of moisture contents and temperatures there remains some skepticism over the significance of the T_g as a universal critical moisture-temperature combination for food stability, particularly for chemical reactions such as NEB.

If one could conclusively show that there is an effect of plasticizers on reaction rate that is independent of moisture content or a_w , then this would demonstrate the significance of matrix properties for governing reaction rate. Labuza et al. (1977) studied the Maillard reaction and measured the effects of several parameters. These included temperature, a_w , reactant concentration, pH, buffers, and the addition of humectants. The formulation consisted of glucose and casein as reactants within a carrier matrix of microcrystalline cellulose and an inert lipid. Reaction rate was measured both as glucose loss, lysine loss, and pigment production (A_{420}).

**FIGURE 20.5**

NEB reaction rate in three plasticizer-containing matrices against moisture content (a) and water activity (b). (Δ) propylene glycol, (\blacksquare) 1,3-butane diol, (\blacklozenge) glycerol, (\circ) (Labuza et al., 1977).

Of particular interest was the effect of adding the humectants propylene glycol, glycerol and 1,3-butane diol. These results are shown in Figure 20.5, as a function of both moisture content and a_w .

NEB and almost all chemical reactions in foods are thought to cease in systems that are below a a_w of 0.23 to 0.43, the typical range of the moisture monolayer value (Labuza et al., 1969; Rockland and Nishi, 1980). In Figure 20.5b, this trend appeared as expected for the control formulation, which contained no humectant. However, upon the addition of hydrophilic glycols as humectants (which were liquids at the test temperature and thus miscible in water), the a_w at which the maximum reaction rate occurred shifted to a much lower value. Propylene glycol showed a maximum rate at a a_w of about 0.2, with a rate equal to the maximum rate of the control at a a_w of 0.8.

Similar results were found for glycerol, which showed a maximum rate at 0.5 a_w , and 1,3-butane diol with a maximum at 0.55 a_w . A food processor who uses the general rule of 0.43 as a safe a_w for food stability and who achieves this with the addition of glycols would find the product to have a very poor shelf life. The trend with added glycol humectants cannot be explained simply by differences in moisture content because a similar trend appears when rate constants are expressed against moisture content (Figure 20.5a). The authors theorized that the liquid glycols acted as a solvent phase for the reactants in place of moisture at low a_w and moisture contents. However, as shown in Figure 20.6, when sorbitol was added, a pure solid at room temperature but still very soluble in water, a very slow reaction rate occurred at all a_w . Solutions of sorbitol are very viscous, and a similar viscosity within the nano-scale of adsorbed moisture within the matrix could be expected to influence the mobility of reactants in a sorbitol-containing semi-moist food.

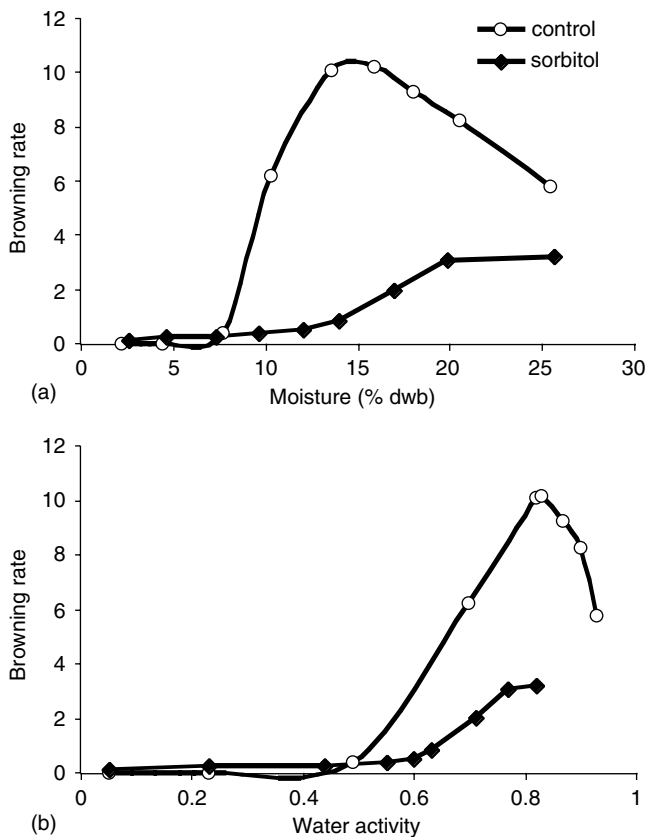


FIGURE 20.6

NEB reaction rate model system containing sorbitol or no added plasticizer. Rate against moisture (a) and water activity (b) (Labuza et al., 1977).

With today's knowledge of glass-transition theory, one might attempt to explain these results in terms of plasticization. All of the studied humectants would be expected to have some plasticization effect on the MCC matrix. Once again, there are two reasonable explanations for the effect of added glycols from each of the two main theories for food stability. These theories were explored further by our research group, as outlined below (Sherwin and Labuza, 2003).

Regardless of the mechanism, the results most clearly illustrate that a_w alone does not provide an adequate mechanism to explain the role of moisture in governing food stability. Model systems are perfect for studying the complexities of reactant mobility as a determinant for reaction rate. What is lacking is a study that examines multiple aspects of mobility in correlation to the rate of a chemical reaction. Changes in moisture content and a_w affect matrix plasticity and thus mobility, solute solvency, rotational mobility, and translational mobility. Each of these aspects of mobility may or may not each have an effect on reaction rate, depending on the reaction and the chemical constituents within the system.

In conjunction with the CP-MAS studies referenced above for glucose mobility (Sherwin et al., 2002), we measured the glass-transition curves (polymer mobility) and NEB reaction rates in plasticized systems to comprehensively link these two types of molecular mobility to a reaction rate (Sherwin and Labuza, 2003). The work of Labuza et al. (1977) on glycols in an MCC matrix was replicated, with changes in the model system formulation. Since MCC was prone to fall out of solution, the new matrix was a freeze-dried solution of caseinate, glucose, and sorbic acid (a preservative) plasticized with either glycerol, sorbitol, or no added humectant, and equilibrated to a range of a_w from 0.11 to 0.75. T_g curves (Figure 20.7) showed that plasticization increased in the order control < added sorbitol < added glycerol, the latter providing the highest polymer

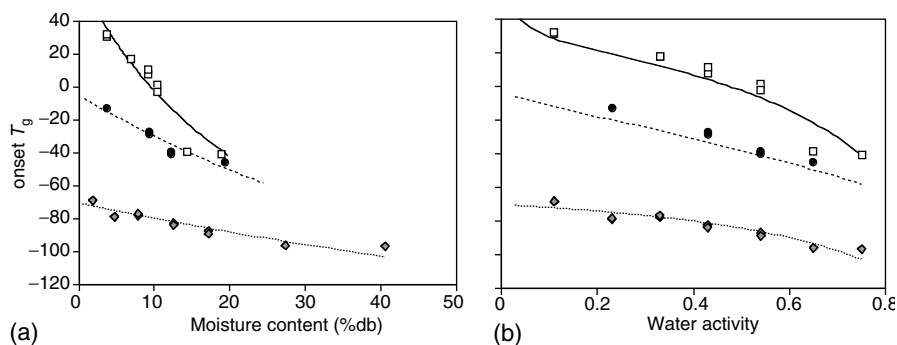
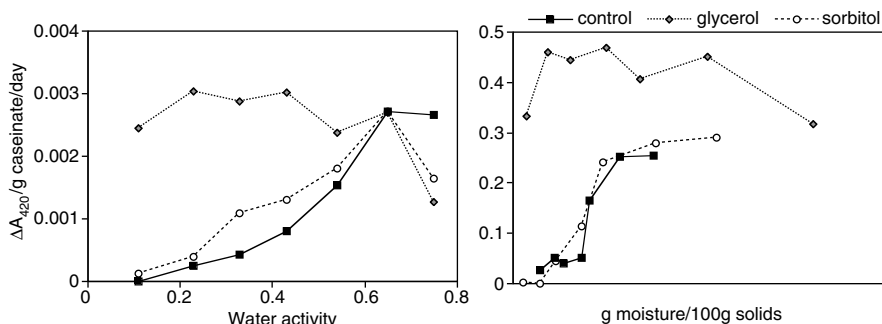


FIGURE 20.7

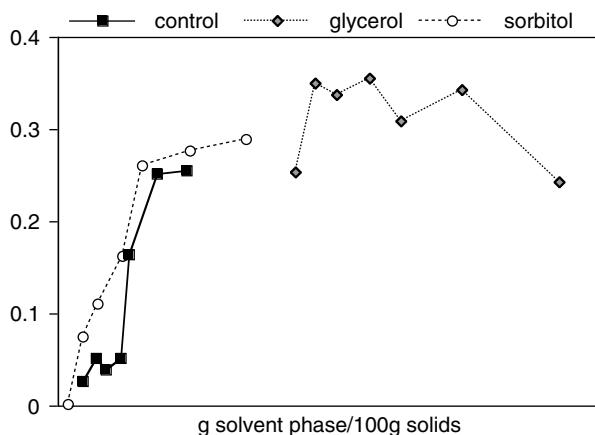
Glass-transition curve of three model system formulations (\square control, \circ sorbitol, \blacklozenge glycerol) expressed vs. (a) water activity or (b) moisture content. Lines indicate the predicted values according to the Gordon-Taylor model (Sherwin and Labuza, 2003).

**FIGURE 20.8**

Browning of the three humectant formulations (\blacksquare control, \circ sorbitol, \blacklozenge glycerol) over seven a_w and moisture contents (Sherwin and Labuza, 2003).

mobility and lowest T_g curve. Confirming the earlier study, the maximum rate of NEB with glycerol occurred at the surprisingly low $a_w = 0.25$ and was 1.5 times higher than the control at $a_w = 0.65$ (Figure 20.8). As an alternate control formulation, no measurable NEB occurred in glycerol or sorbitol containing matrices with no added glucose, and therefore the polyols were not directly participating in NEB. Unlike the earlier MCC matrix where added sorbitol inhibited NEB, the sorbitol samples showed rates identical to the control. Since sorbitol showed a significantly lower T_g than the control (Figure 20.7), yet an identical reaction rate at equal moisture contents (Figure 20.8), it is not possible that the degree of plasticization, $T - T_g$, or matrix mobility was a mechanism governing reaction rate. Instead, we proposed that glucose mobility within the available solvent phase was the most plausible mechanism. With sorbitol unable to dissolve the glucose, reaction rates were identical to the control at equal moisture contents, and slightly lower in the sorbitol system at equal a_w . When glycerol was added, the glucose was highly mobile over all a_w and moisture contents because the glycerol served as a solvent phase in the absence of, or in conjunction with water. To illustrate the concept of total solvent phase for reaction as a viable mechanism governing reaction rate, Figure 20.9 shows reaction rate vs. total solvent phase, and the familiar ascending/descending relationship for reaction rate appears over the range of water activities. As explained earlier, although plasticization by sorbitol and glycerol did increase the mobility of glucose as measured by CP/MAS NMR (Sherwin et al., 2002), it was only the population of dissolved glucose molecules that participated in NEB and this population was not measured by CP/MAS NMR.

The best documented example of a T_g -dependent phenomenon is the crystallization of sugars (Hartel and Sastry, 1991; Roos and Karel, 1991; Roos, 1993; Joupilla et al., 1997), but this is not a chemical reaction, rather it is a physical state change and may have only diffusion limitations, with no protons or electrons exchanged. Other important phenomena more closely

**FIGURE 20.9**

Browning of three humectant formulations (■ control, ○ sorbitol, ◆ glycerol) expressed against total solvent phase mass (Sherwin and Labuza, 2003).

linked to T_g include the diffusion of water, stickiness of powders, crystallization, and collapse. In fact, some of these processes are interrelated. But for chemical reactions in foods, the evidence for a T_g dependence does not exist. We propose that for many food systems, as a_w decreases, that more solute material will dissociate from the liquid phase and crystallize or adsorb to the solid phase and become less mobile and less available for reaction. Mobility can be defined strictly in terms of the solute and for many food systems, there may be no need to model the effect of moisture on matrix mobility as well. Consequently, the influence of a_w on reaction rate so often seen may be explained by a degree of dissolution of the reactants. Less dissolution results in lower mobility and less reactivity. If it is the immediate solvent environment of the reactant that is the most critical factor governing reaction rates in foods, then an understanding of local solvent properties is needed.

Based on the basic principles of chemistry and thermodynamics, an observed reaction rate must in some way be affected by the chemical process of the reaction, the properties of the surrounding polymer medium (that is, starches, gums, and proteins) and the properties of the adsorbed solvent phase. The chemical process of the reaction (that is, electron, proton, and molecular exchange) is the most basic and the most highly studied in dilute solutions. Yet there are few other applied sciences for which moisture changes in low to intermediate moisture viscoelastic systems are of interest. Dry and intermediate moisture foods including the storage of dry seeds and amorphous pharmaceutical products are uniquely sensitive to this process, and there are few other disciplines from which to borrow data and theories. We propose that it is always the chemical process of reaction, including order of reaction and equilibrium kinetics that should be the starting point for any

consideration of reaction rate modeling. However, this point is beyond the scope of this review. However, if we are to consider the immediate reaction space surrounding the reactants as a concentrated solution, then there are certain chemical and solvent-mediated effects that are important to consider with moisture adsorption.

The Presence of Charged Solutes

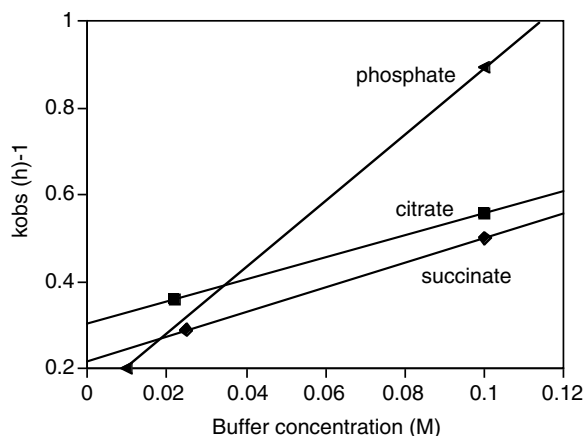
Changes in moisture content affect charged species in foods that are not part of the chemical equation, but that may impart their own effects upon reaction rate. Reactions that involve proton and electron transport, which include hydrolysis, Maillard browning, oxidation, and almost every critical shelf-life-limiting reaction in foods, will be affected by the presence of ions. This is part of the theory behind the Debye–Hückel equation. This model describes the effect of ionic strength on the reaction rate constant in dilute solutions:

$$\ln k = \ln k_0 + 1.02(z^+)(z^-) \left[\frac{\sqrt{\epsilon}}{1 + \sqrt{\epsilon}} \right] \quad (20.3)$$

where ϵ = ionic strength, z = charge, and k_0 = rate constant when $\epsilon = 0$.

Thus, any changes in moisture content with relative humidity must also be examined from the standpoint of the effect of moisture on ionic strength. By Debye–Hückel, a 10-fold increase in ionic strength would yield a 30% increase in reaction rate. For electron transport reactions, the presence of charged particles in solution theoretically promotes a more rapid transport of charge. Is this equation useful for intermediate to low moisture foods? As an example, Stamp (1990) found that a 10-fold increase in buffer concentration yielded a 4.5-, 1.5-, and 1.67-fold observed rate increase for phosphate, citrate and succinate buffers, respectively (Figure 20.10). These rate increases are much greater than the 30% increase predicted by Debye–Hückel. If we consider that protein conformation and solubility are highly dependent on ionic strength, then reactions of proteins might be expected to deviate quite far from ideality, possibly even showing inhibition with increasing ionic strength. The model does not predict salting-out effects and protein conformational changes in the presence of ions. As a whole, the model serves as a starting point for simple reactions in dilute solutions, in that it predicts that there is a rate increase with ionic strength. As with many other food reactions, modifications to this ideal system model would take on increasing complexity.

Researchers who use the very complex Maillard browning reaction to study the significance of moisture, T_g and a_w should be familiar with the complicated pathways, feedback inhibitions, and intermediates that are inherent to the reaction (Hodge, 1953) before validating kinetic data and drawing conclusions as to the mechanism for the influence of moisture on the reaction. Other than the aforementioned considerations, such as matrix

**FIGURE 20.10**

Observed rate of aspartame loss at 80°C against buffer concentration for aqueous model systems containing phosphate, citrate, or succinate buffer (Stamp, 1990).

mobility, chemical factors that are more obvious include the production of reaction inhibitors and promoters, an influence of catalysts, changes in pH that may occur as a reaction proceeds, and other basic chemical considerations such as ionic strength and buffer capacity.

Solubility is a function of both the dielectric properties (ϵ) and the hydrogen bonding ability of both the solvent and solute phases. The low moisture systems with which we are interested will behave far from the ideal dielectric-governed solvency. Given the nature of the moisture monolayer, water molecules may be highly ordered about polar groups of the matrix materials or with other water molecules. Beyond the bulk property defined by ϵ , the immediate physical environments of water molecules determine its ability to serve as a solvent. In a low to intermediate moisture food system the ability of moisture to participate in hydrogen bonding with solutes is greatly affected by the substance to which water is adsorbed. While a_w is defined by fugacity, both fugacity and solvency are affected by many of the same forces. One may theorize that in foods, a key to chemical reaction rate is the amount of reactants that are truly dissolved under a given set of temperature and relative humidity conditions in a given plasticizer/water phase (solvent) with a specific local viscosity, H^+ activity, dielectric strength, and ionic strength.

Conclusions

Increased moisture can allow greater solubility of amorphous food components. In an intermediate moisture food, it is very likely that some

of the solid components are exposed to sufficient water that they can become fully dissolved and not merely affiliated with water molecules through hydrogen bonding. In this state the reactant component is freely mobile and can interact with other components in the food. However, if the pocket of adsorbed water in which the component is dissolved is itself immobile, for instance close to a macromolecular surface, then only limited reaction can occur within that reaction space without the diffusion of the moisture phase throughout the matrix. If the adsorbed water itself gains mobility with further hydration, then all components dissolved within it will also gain mobility over larger distances. Diffusion within the matrix begins to occur and reactions proceed at a greater rate. At some level of hydration, it is expected that the solutes are completely in solution and further addition of water only dilutes this adsorbed moisture phase in which reaction is occurring. First- and second-order reactions (or pathways within a complex scheme such as NEB) that are dependent on reactant concentration will begin to show lower rates. This is a dilution effect caused by the increase of solvent water upon adsorption. At lower water activities there is no dilution of reactants since the adsorbed water continually dissolves more and more solutes within the system. The reactants hover near a state of saturation in the aqueous phase.

Increased moisture can plasticize a polymer matrix. Water acts not only as a solvent for small solutes but as an agent that increases the free volume of polymer molecules and their degree of segmental motion (i.e., water is differentially solvated and mobilizes parts of the heterologous structure of protein and polysaccharide polymers). When polymers, or segments within them, are given more freedom of movement, then other diffusion-based phenomena might occur more readily. Chemical reactions should not necessarily be expected to be affected by increased free volume of the polymer, and a review of the literature yields little support for this theory for most chemical reactions. Instead, some of the increased reaction rates that have been attributed to plasticization are instead the result of increased solvation.

Increased moisture content can alter pH. It is very difficult to control pH in a semi-moist food system; nor is there an adequate method for measuring pH in a semi-solid food matrix, much less in the local reaction environment in a food with heterogeneously distributed pockets of water. It is also unpredictable whether increasing moisture will increase or decrease pH for a given food system. As a result, pH effects are always overlooked when considering water activity and thus moisture content changes. There is much evidence linking various aspects of mobility to various food reactions. The pH of a food may play a role in determining reaction rate. However, changes in moisture content in foods with changes water activity are not likely to change pH nearly as greatly as the solubility and mobility effects, though this deserves further study. Regardless, local pH in particular should never be completely ignored as it may play a role in any mathematical model or in interpreting pathways of NEB.

Moisture content versus water activity. Certain theories proposed above, for example that water governs reaction rate by dissolving reactants, suggest that a_w may not be a useful measure in this area of molecular modeling of moisture and reaction rates. a_w is indeed a very useful measure to describe the adsorption process that occurs when a food is exposed to different humidity environments. a_w defines the moisture equilibrium state of a food in response to the equilibrium relative humidity of the food's environment. It should be remembered that a_w , while not defined as amount of solvent water, has been experimentally linked to the amount of water available to act as a solvent (Duckworth, 1962; Duckworth and Smith, 1963). Therefore, changes in a_w will result in changes in amount of solvent water. The ability to condense almost all food systems and food reactions a plot showing reaction rate against a_w , most likely is caused by the fact that a_w as a measure essentially normalizes reaction rate data for systems with different moisture sorption isotherms and for chemical reactions with different solvency and mobility requirements. The relationship between reaction rate and a_w is very real and continues to serve as a useful guide, particularly for microbial growth. Yet the anomaly first demonstrated by Labuza et al. (1977) with added glycols points to the importance of the mass of the total solvent phase as a governing factor for any individual food and any individual system. Based on many of the conclusions in the above review, it is the properties that moisture content changes which affect reaction rates, and a_w merely serves as the equilibrium definition that governs the process of adsorption or migration.

Is there a simple unifying food stability theory? In the end, it is highly unlikely that there is, and it has been a futile attempt to pin either glass transition, monolayer, and a_w theory or any single parameter as a prime indicator of food stability across the spectrum of foods and conditions. We know that in order for molecules to react they must collide and be oriented properly. But food systems are far too complex and variable to discount any of the myriad interactions, reactions, and physical changes occurring in the system during storage. However, there is some evidence to suggest that a food scientist may have the best success in predicting food stability if he or she can predict how a change in an environmental variable will affect the concentration of reactant in the total solvent phase.

It is the goal of food science physical chemical researcher to determine molecular information about substances by observing physical phenomena and to use this information to develop models that will enable us to control these processes. Ideally, by understanding the molecular mechanism by which moisture governs reaction rates, new preservation techniques and precise physical control of these processes can be developed. As we learn how to measure and control the solubility of reactants and moisture migration throughout a food system (possibly by inhibiting physical changes such as crystallization), we can optimize the shelf life of foods. Only through the combination of measurements of chemical phenomena (for example, rate of browning), physical phenomena (physical state changes

and diffusion), and molecular-level phenomena (relaxation rates and mobilities of constituents) can such mechanisms ever be deciphered.

References

- Aguilera, J.M., Levi, G., and Karel, M. Effect of water content on the glass transition and caking of fish protein hydrolysates, *Biotechnology*, 9, 651, 1993.
- Atkins, P.W. *Chimie Physique 2. Paris*, La. Vuibert, ed., pp. 1131–1168, 1982.
- Bell, L.N. Kinetics of non-enzymatic browning in amorphous solid systems: distinguishing the effects of water activity and glass transition, *Food Res. Int.*, 28, 591, 1996.
- Bell, L.N. and Hageman, M.J. Differentiating between the effects of water activity and glass transition dependent mobility on a solid-state chemical reaction: aspartame degradation, *J. Agric. Food Chem.*, 42, 2398, 1994.
- Bell, L. and Labuza, T.P. The influence of pH on reactions in the reduced moisture state, *J. Food Eng.*, 22, 281, 1994.
- Brunauer, S., Emmet, P.H., and Teller, E. Adsorption of gases in multimolecular layers, *J. Am. Chem. Soc.*, 60, 309, 1938.
- Bryant, R. and Shirley, W. Dynamical deductions from NMR resonance relaxation at the water protein interface, *Biophys. J.*, 14, 3, 1980.
- Buera, M.P. and Karel, M. Effect of physical changes on the rates of nonenzymic browning and related reactions, *Food Chem.*, 52, 167, 1994.
- Burin, L., Joupilla, K., Roos, Y., Kansikas, J., and Buera, M.P. Color formation in dehydrated modified whey powder systems as affected by compression and T_g , *J. Agric. Food Chem.*, 48, 5263, 2000.
- Chirife, J. and Buera, M.D.P. A critical review: water activity, glass transition and microbial stability in concentrated/semimoist food systems, *J. Food Sci.*, 59, 921, 1994.
- Chuy, L.E. and Labuza, T.P. Caking and stickiness of dairy-based food powders as related to glass transition, *J. Food Sci.*, 59, 43, 1994.
- Duckworth, R.B. Diffusion of solutes in dehydrated vegetables, *Recent Adv. Food Sci.*, J. Hawthorn and M. Leitch, eds., Butterworths, London, pp. 46–49, 1962.
- Duckworth, R.B. and Smith, G.M. Diffusion of solutes at low moisture levels, *Recent Adv. Food Sci.*, M. Leitch and D.N. Rhodes, eds., Butterworths, London, pp. 230–238, 1963.
- Edward, J.T. Molecular volumes and the Stokes–Einstein equation, *J. Chem. Educ.*, 47, 261, 1970.
- Formi, E., Sormani, A., Scalise, S., and Torregiani, D. The influence of sugar composition on the colour stability of osmodehydrofrozen intermediate moisture apricots, *Food Res. Int.*, 30, 87, 1997.
- Gunning, Y.M., Gunning, P.A., Kemsley, E.K., Parker, R., Ring, S.G., Wilson, R.H., and Blake, A. Factors affecting the release of flavor encapsulated in carbohydrate matrixes, *J. Agric. Food Chem.*, 47, 5198, 1999.
- Hartel, R. and Sastry, A.V. Sugar crystallization in food products, *Crit. Rev. Food Sci. Nutr.*, 30, 49, 1991.
- Hodge, J.E. Dehydrated foods: chemistry of browning reactions in model systems, *J. Agric. Food Chem.*, 1, 928, 1953.

- Joupilla, K., Kansikas, J., and Roos, Y.H. Glass transition, water plasticization and lactose crystallization in skim milk powder, *J. Dairy Sci.*, 80, 3152, 1997.
- Karel, M. and Saguy, I. *Water Relations in Foods*, H. Levine and L. Slade, eds., Plenum Press, New York, pp. 123–138, 1991.
- Karmas, R., Buera, M.P., and Karel, M. Effect of glass transition on rates of nonenzymatic browning in food systems, *J. Agric. Food Chem.*, 40, 873, 1992.
- Karmas, R. and Karel, M. Modeling Maillard browning in dehydrated food systems as a function of temperature, moisture content, and glass transition temperature, *Flavor Technology: Physical Chemistry, Modification, and Process*, American Chemical Society, Washington D.C., pp. 64–73, 1995.
- Labuza, T.P. Sorption phenomena in foods, *Food Technol.*, 22, 263, 1968.
- Labuza, T.P. Kinetics of lipid oxidation in foods, *Crit. Rev. Food Technol.*, 2, 355, 1971.
- Labuza, T.P. The effect of water activity on reaction kinetics of food deterioration, *Food Technol.*, 34, 36, 1980.
- Labuza, P.S. and Labuza, T.P. Cotton candy shelf life, *J. Food Proc. Presv.*, 28, 274, 2004.
- Labuza, T.P., Tannenbaum, S.R., and Karel, M. Water content and stability of low and intermediate moisture foods, *Food Technol.*, 24, 35, 1969.
- Labuza, T.P., Warren, R., and Warmbier, H.C. The physical aspects with respect to water and non-enzymatic browning, *Nutritional, Biochemical and Chemical Consequences of Protein Cross-linking*, M. Friedman, ed., Plenum Press, New York, pp. 379–418, 1977.
- Lai, M.C., Hageman, M.J., Schowen, R.L., Borchardt, R.T., Laird, B.B., and Topp, E.M. Chemical stability of peptides in polymers. 2. Discriminating between solvent and plasticizing effects of water on peptide deamidation in poly(vinylpyrrolidone), *J. Pharm. Sci.*, 88, 1081, 1999.
- Lechuga-Ballesteros, D., Bakri, A., and Miller, D.P. Microcalorimetric measurements of the interactions of water vapor and amorphous pharmaceutical solids, *Pharm. Res.*, 308, 2003.
- Lechuga-Ballesteros, D., Miller, D.P., and Zhang, J. Residual water in amorphous solids: measurement and effects on stability, *Amorphous Food and Pharmaceutical Systems*, H. Levine, ed., Royal Soc. of Chemistry, London, pp. 275–316, 2002.
- Le Meste, M., Simatos, D., and Gervais, P. Interaction of water with food components, *Ingredient Interactions: Effects on Food Quality*, A.G. Gaonkar, ed., Marcel Dekker, New York, pp. 85–129, 1995.
- Le Meste, M., Voilley, A., and Colas, B. Influence of water on the mobility of small molecules dispersed in a polymeric system, *Water Relations in Foods*, H. Levine and L. Slade, eds., Plenum Press, New York, pp. 123–128, 1991.
- Levine, H. *Preface in Amorphous Food and Pharmaceutical Systems*, H. Levine, ed., Royal Soc. of Chemistry, London, pp. 7, 2002.
- Lievonen, S.M., Laaksonen, T.J., and Roos, Y.H. Glass transition and reaction rates: nonenzymatic browning in glassy and liquid systems, *J. Agric. Food Chem.*, 46, 2778, 1998.
- Liu, W.R., Langer, R., and Klibanov, A. Stabilization of bovine serum albumin, *Biotech. Bioeng.*, 37, 177, 1991.
- Makower, B. and Dye, W.B. Equilibrium moisture content and crystallization of amorphous sucrose and glucose, *J. Agric. Food Chem.*, 4, 72, 1956.
- Nelson, K.A. and Labuza, T.P. Glass transition theory and the texture of cereal foods, *The Glassy State in Food*, J.M.V. Blanshard and P.J. Lilleford, eds., Nottingham University Press, Loughborough, England, pp. 513–517, 1993.

- Nelson, K.A. and Labuza, T.P. Water activity and food polymer science: implications of state on Arrhenius and WLF models in predicting shelf-life, *J. Food Eng.*, 22, 271, 1994.
- Netto, F.M., Desobry, S.A., and Labuza, T.P. Effect of water content on the glass transition, caking and stickiness of protein hydrolysates, *Int. J. Food Prop.*, 1, 141, 1998.
- Peleg, M. On the use of the WLF model in polymers and foods, *Crit. Rev. Food Sci. Nutr.*, 32, 59, 1992.
- Pikal, M. Chemistry in solid state amorphous matrices: implication for biostabilization, *Amorphous Food and Pharmaceutical Systems*, H. Levine, ed., Royal Soc. of Chemistry, London, pp. 252–272, 2002.
- Rockland, L.B. and Nishi, S.K. Influence of water activity on food product quality and stability, *Food Technol.*, 34, 42, 1980.
- Roos, Y. Water activity and physical state effects on amorphous food stability, *J. Food Proc. Pres.*, 16, 433, 1993.
- Roos, Y. and Karel, M. Plasticizing effect of water on thermal behavior and crystallization of amorphous food models, *J. Food Sci.*, 56, 38, 1991.
- Roozen, M.J.G.W. and Hemminga, M.A. Molecular motion in sucrose-water mixtures in the liquid and glassy state as studied by spin probe ESR, *J. Phys. Chem.*, 94, 7326, 1990.
- Roozen, M.J.G.W., Hemminga, M.A., and Walstra, P. Molecular motion in glassy water-malto-oligosaccharide (maltodextrin) mixtures as studied by conventional and saturation-transfer spin-probe ESR spectroscopy, *Carbohydr. Res.*, 215, 229, 1991.
- Saltmarsh, M. and Labuza, T.P. Influence of relative humidity on the physicochemical state of lactose in spray-dried sweet whey powders, *J. Food Sci.*, 45, 1231, 1980.
- Shamblin, S.L. and Zografi, G. *Pharm. Res.*, 16, 1186, 1998.
- Sherwin, C. and Labuza, T. Role of moisture in Maillard browning reaction rate in intermediate moisture foods: comparing solvent phase and matrix properties, *J. Food Sci.*, 68, 588, 2003.
- Sherwin, C., Labuza, T., McCormick, A., and Chen, B. Cross-polarization/magic angle spinning NMR to study glucose mobility in a model intermediate moisture food system, *J. Agric. Food Chem.*, 50, 7677, 2002.
- Shiraldi, A. Comparison between WLF and VTF expressions and related physical meaning, *Amorphous Food and Pharmaceutical Systems*, H. Levine, ed., Royal Soc. of Chemistry, London, pp. 131–136, 2002.
- Simatos, D., LeMeste, M., Petroff, D., and Halphen, B. Use of electron spin resonance for the study of solute mobility in relation to moisture content in model food systems, *Water Activity: Influences on Food Quality*, L. Rockland and G.F. Stewart, eds., Academic Press, New York, pp. 319–346, 1981.
- Slade, L. and Levine, H. Non-equilibrium melting of native granular starch: Part I. Temperature location of the glass transition associated with gelatinization of A-type starches, *Carbohydr. Polym.*, 8, 183, 1988.
- Slade, L. and Levine, H. Beyond water activity: recent advances based on an alternative approach to the assessment of food quality and safety, *Crit. Rev. Food Sci. Nutr.*, 30, 115, 1991.
- Stamp, J.A. Kinetics and analysis of aspartame decomposition mechanisms in aqueous solutions using multiresponse methods, Ph.D. Thesis, St. Paul, MN: University of Minnesota, 432, 1990.

- Tsimidou, M. and Biliaderis, C.G. Kinetic studies of saffron (*Crocus sativus* L.) quality deterioration, *J. Agric. Food Chem.*, 45, 2890, 1997.
- Williams, M.L., Landel, R.F., and Ferry, J.D. The temperature dependence of relaxation mechanisms in amorphous polymers and other glass-forming liquids, *J. Am. Chem. Soc.*, 77, 3701, 1955.
- Zografi, G. States of water associated with solids, *Drug Dev. Indust. Pharm.*, 14, 1905, 1988.

SECTION 2

Oral and Poster Presentations

Part 6: Functional and Mechanical Properties of Biomolecules

21

Glass-Transition Temperature and Self-Detaching of Maltodextrin Films: Effect of Molecular Weight and Sucrose Addition

Fernanda P. Collares, José R.D. Finzer, and Theo G. Kieckbusch

CONTENTS

Introduction	377
Material and Methods.....	379
Aqueous Food Pastes Composition	379
Determination of Mean Molecular Weight.....	379
Solid Support Surfaces	379
Detachment Tests	379
Glass-Transition Temperatures	380
Results and Discussion	381
Effect of Molecular Weight on Self-Detachment.....	381
Effect of Composition on Self-Detachment.....	382
Conclusions.....	385
Acknowledgments	385
References	385

Introduction

During water removal by evaporation, many substances, including proteins and sugars, can be converted to an amorphous state. The temperature at which this transformation takes place is called the glass-transition temperature (T_g), which involves the transition of a liquid-like structured material from an “elastic” or “rubbery” state to a solid “vitreous” one (Roos and Karel, 1991; Roos, 1995). The main consequence of glass transition is an exponential decrease in molecular mobility and free volume as well as

changes in the mechanical and electrical properties below T_g (Roos and Karel, 1991; Roos, 1993). The free volume, which corresponds to the volume not occupied by material, represents the space available for the free movement of molecules. Below T_g , molecular mobility reduces diffusion, affecting the reaction rates and food deterioration (Roos, 1995).

T_g is not a clearly located point, but defines the center of a range of about 20°C or larger where the transformation occurs (Roos, 1995). T_g is different for each material and is affected mainly by three factors: the plasticizer, the molecular weight, and the mixture composition.

Plasticization at a molecular level leads to an increase in intermolecular space or free volume, decreasing the viscosity and, at the same time, increasing mobility (Ferry, 1980). In food polymers, water is the most prominent plasticizer. Its presence affects the T_g of completely amorphous polymers, and the T_g and T_m (melting temperature) of partially crystalline polymers (Slade et al., 1993). It is considered a "mobility intensifier" (Levine and Slade, 1992). The larger the amount of water present the greater the solute mobility, making it increasingly more difficult to attain the glassy or rubbery state. Consequently a lower temperature is required for the ingredients (including water) to be transformed into the amorphous states.

In 1950, Fox and Flory (1950) observed that the T_g of homopolymers such as glucose polymers was related to their molecular weight (M). The value for T_g was reported to decrease linearly with the increase in M .

The fundamental relationship most widely used to evaluate the effect of composition on T_g is based on the condition of continuity of the entropy at T_g (Couchman and Karasz, 1978). For a multi-component system as demonstrated by Arvanitoyannis et al. (1993) for the glucose–fructose–water ternary system and by Kalichevsky and Blanshard (1993) for the water–fructose–amylpectin ternary system, the following expression can be used:

$$T_g = \sum_{i=1}^n \frac{w_i \Delta C_{pi} T_{gi}}{w_i \Delta C_{pi}} \quad (21.1)$$

where ΔC_{pi} is the change in heat capacity; T_g is the glass-transition temperature; and the subscripts i refer to the components of the system.

T_g has been related to changes in physical properties occurring during processing or storage of dehydrated products such as: (i) the collapse of a food during freeze drying; (ii) the sticking of a product to the walls of a spray dryer during the dehydration process; (iii) the caking and agglomeration of powders during processing and handling; (iv) poor behavior in the fluidization of sticky products; (v) cracking of rice grains during storage; and (vi) clumping of dried fruits (Cnossen et al., 2001; Ozmen and Langrish, 2002; Labuza et al., 2004).

Collares et al. (2004), studying the drying of gum Arabic and maltodextrin (DE 10) on a glass surface, observed that self-detachment occurred when the moisture content of the film reached values related to the glass-transition

curve (T_g). The present work extends the investigation to different food paste compositions with a wider range of T_g (aqueous solutions of maltodextrins with different molecular weights, with or without sucrose addition) in order to validate the assumption of the glass-transition control over the self-detachment of the dried films.

Material and Methods

Aqueous Food Pastes Composition

- (i) Experimental maltodextrin, code RD-111 (hydrolyzed cassava starch product from Corn Products, Brazil) at concentration of 52.6%;
- (ii) Commercial maltodextrins MOR-REX[®] 1910 and 1914 (hydrolyzed corn starch products from Corn Products, Brazil), at concentration of 61.5%;
- (iii) Mixtures of MOR-REX[®] 1910 maltodextrins and analytical grade sucrose (Synth, Brazil).
 - (a) 58.5% maltodextrin and 3.0% sucrose;
 - (b) 55.3% maltodextrin and 6.1% sucrose;
 - (c) 52.3% maltodextrin and 9.2% sucrose.

Determination of Mean Molecular Weight

The determination of the numerical mean molecular weight (M_n) of the maltodextrins RD-111 and MOR-REX[®] 1914 was carried out by gel permeation chromatography (GPC) using the procedure described by Collares et al. (2004) for MOR-REX[®] 1910. The values found were: 4759, 1021, and 957.5 g/mol for RD-111, MOR-REX[®] 1910, and MOR-REX[®] 1914, respectively.

Solid Support Surfaces

Microscope glass slides (Perfecta, Brazil) were used as the solid support for the drying of the films of pasty material, having the following dimensions: 48.5 mm long, 24.5 mm wide, and 1.0 mm thick.

Detachment Tests

The description of the system used in the detachment runs can be found in Collares et al. (2004). The pre-heating of the sample container, the spreading of the food paste over the inert solid surface, and finally, the drying of the film were all carried out inside a small chamber (200 mm wide, 200 mm long, and 160 mm high) placed in a controlled air temperature and relative

humidity room. The dry bulb temperature inside the chamber was controlled during the detachment tests and ranged from 40 to 75°C. The paste was spread over the glass plate using a stainless steel blade with adjustable gap, coating the surface with a pre-determined thickness of 0.10 mm. The moment of self-detachment of the dried film of the paste from the solid surface was determined visually and all the dried material was immediately placed inside a weighing bottle and its moisture content determined gravimetrically. All weighing was carried out using an OHAUS analytical balance model AP210 (legibility and reproducibility of 0.1 mg).

Glass-Transition Temperatures

The glass-transition temperature curve of the maltodextrin RD-111, MOR-REX[®] 1910, and MOR-REX[®] 1914 were obtained using the Gordon-Taylor equations for binary systems, according to the procedure described by Collares et al. (2004).

The T_g curves for the water–maltodextrin–sucrose system was plotted using the expanded Gordon-Taylor model (Equation 21.1) for ternary systems, considering the variation in heat capacity for water (ΔC_{p1}) equal to 1.94 J/g °C (Kalicevsky and Blanshard, 1993) and for sucrose (ΔC_{p2}) equals to 0.60 J/g °C (Roos, 1993). The value for ΔC_{p3} of 0.24 J/g °C used here for maltodextrin MOR-REX[®] 1910 was estimated from considering the value for k (the ratio of changes in the water and solid heat capacities at T_g) to be equal to 8.055. Table 21.1 shows the parameters used to determine the glass-transition curves for the maltodextrins, with and without additives (sucrose).

TABLE 21.1
Parameters Used to Determine the Glass-Transition Curves
According to the Gordon-Taylor Model

Material	T_g (°C)	k
Amorphous water	– 135 ^a	—
Maltodextrin RD-111	171.1 ^b	8.623 ^c
Maltodextrin MOR-REX [®] 1910	151.7 ^b	8.055 ^c
Maltodextrin MOR-REX [®] 1914	150.1 ^b	8.007 ^c
Sucrose	62 ^a	—

^a Source: From Roos, Y., *Carbohydr. Res.*, 238, 39–48, 1993. With permission.

^b Calculated from the expression: $T_g = -1.4(\text{DE}) + 176.4$ (Busin et al., 1996).

^c Values obtained from the equation: $k = 0.0293T_g + 3.61$ (Roos, 1993).

Results and Discussion

Effect of Molecular Weight on Self-Detachment

The influence of molecular weight on the self-detachment of maltodextrin films from the surface of a glass slide can be appreciated from the experimental points located in Figure 21.1. The smaller the molecular weight, the drier the film needed to be for the detachment to occur. The glass-transition temperatures are also related to the molecular weight of the material (Fox and Flory, 1950). As observed by Mitsuiki et al. (1999) for various commercial agar–agars, T_g increased with the increase in molecular weight in agreement with the transition curves for the maltodextrins RD-111 (Figure 21.2a) and MOR-REX[®] 1914 (Figure 21.2b). As observed by Roos and Karel (1991), the values for T_g of the maltodextrins increased with an increase in M , as occurred for the conditions necessary for self-detachment.

The results obtained for the detachment of the maltodextrins RD-111 (Figure 21.4a) and MOR-REX[®] 1914 (Figure 21.5b) confirmed the behavior found by Collares et al. (2004) for maltodextrin MOR-REX[®] 1910. The conditions for the self-detachment of maltodextrins with different M followed the same pattern as the glass-transition curve of the corresponding material. The experimental points, however, are located underneath the curve, probably due to an overdrying during the sample collection procedures. For the maltodextrins RD-111 and MOR-REX[®] 1910, self-detachment occurred in the temperature range of 15°C below the T_g curve, and for the maltodextrin MOR-REX[®] 1914, the limits of temperature was 20°C.

In the paste drying practice, films made with low molecular weight materials will take longer to detach and become available for removal from

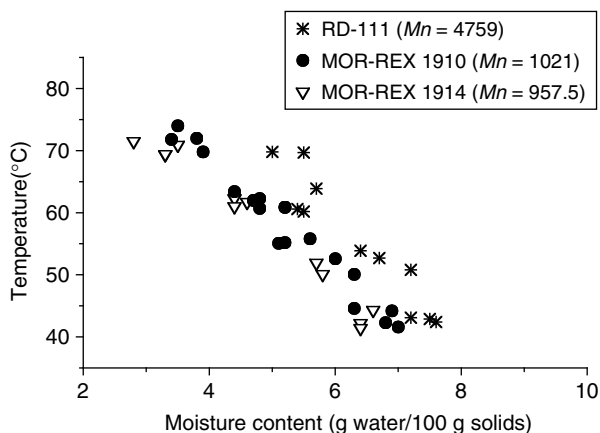
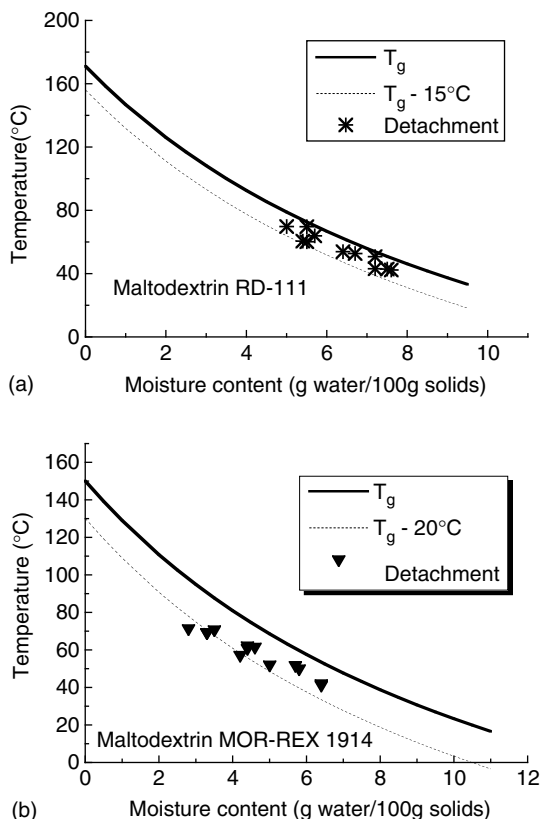


FIGURE 21.1

Temperatures and moisture contents of dried films of maltodextrin at the moment of self-detachment from an inert solid (ordinary glass slide).

**FIGURE 21.2**

Glass-transition curves for maltodextrins with different molecular weights: (a) 4759 g/mol, $DE = 04$ and (b) 957.5 g/mol, $DE = 19$, and experimental points at the moment of self-detachment of the film from a solid surface.

the surface. In other words, at the same drying temperature, products with higher glass-transition temperatures will detach at higher moisture content than products with lower glass-transition temperatures.

Effect of Composition on Self-Detachment

The effect of mixtures on the detachment conditions was also evaluated by drying pastes made by a mixture of maltodextrin MOR-REX 1910 and sucrose, with a total solid content of 61.5%, but with increasing amount of sucrose (5, 10, and 15% sucrose, dry weight basis (dwb)). Results in Figure 21.3 indicate that for a defined drying temperature, the moisture content at the moment of self-detachment of the dried film decreased with the increase in sucrose addition. Thus the addition of sucrose made the detachment of dried films of maltodextrin from an inert solid surface during the drying process more difficult. The larger the amount of sucrose added,

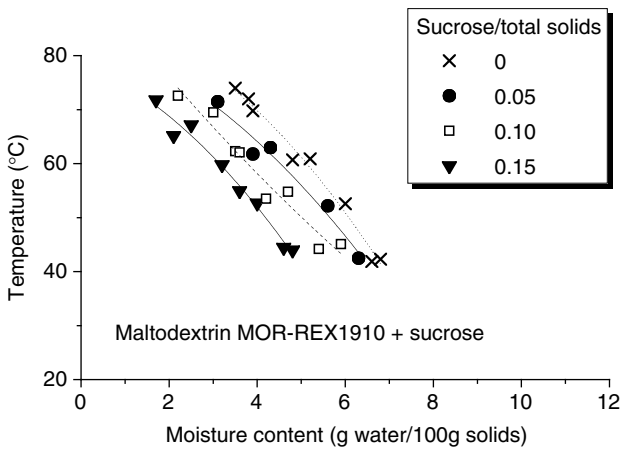


FIGURE 21.3
Detachment conditions of mixtures of maltodextrin MOR-REX 1910 and sucrose dried film from the glass plate surface.

the drier the material has to be in order to be able to detach from the inert surface for a given temperature.

The composition of the mixture influences the glass-transition phenomenon in a similar way. Figure 21.4 shows the glass-transition curves calculated for aqueous solutions of MOR-REX[®] 1910 and sucrose. The proportion of sucrose was: 5, 10, and 15% with respect to the solids content. The curves show the decrease in T_g with an increase in sucrose concentration, a behavior

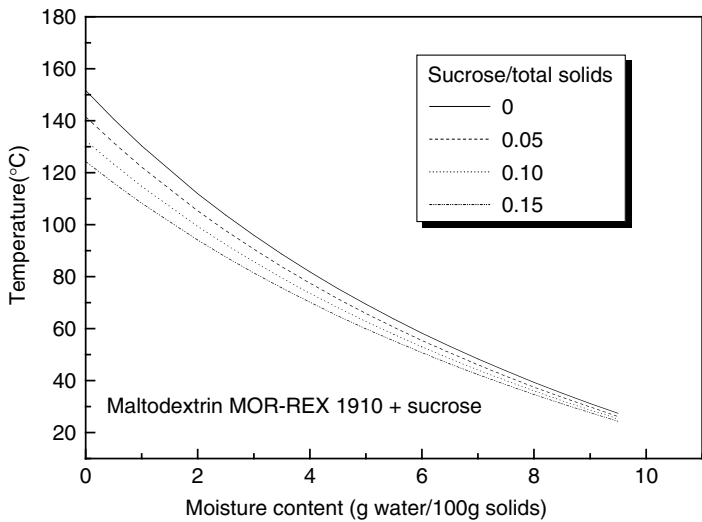


FIGURE 21.4
Glass-transition curves (Gordon-Taylor model) for maltodextrin MOR-REX[®] 1910 and sucrose.

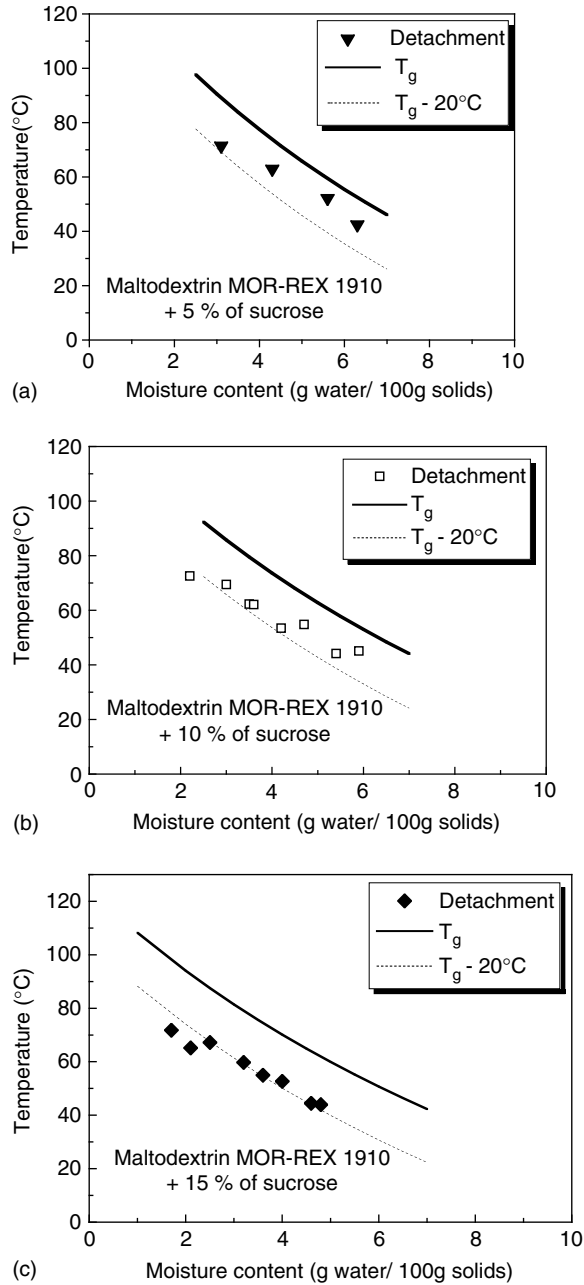


FIGURE 21.5
Glass-transition curves and self-detachment conditions for aqueous solutions of maltodextrin MOR-REX[®] 1910: (a) maltodextrin + 5% sucrose, (b) maltodextrin + 10% sucrose, and (c) maltodextrin + 15% sucrose.

observed by Torreggiani et al. (1999) in strawberry juices with 20% added carbohydrates (maltose, sorbitol, and a glucose–fructose–sucrose mixture).

In Figure 21.5, the self-detachment conditions for aqueous solutions of the maltodextrin MOR-REX[®] 1910 and sucrose at 5, 10, and 15% (dwb) are compared with the glass-transition curves calculated using the expanded Gordon-Taylor model (Roos, 1993). The self-detachment of the dried films of aqueous solutions of the maltodextrin MOR-REX[®] 1910 and sucrose followed the same pattern of decreasing moisture content of the material with an increase in temperature as observed with the glass-transition data. This process occurred in a temperature range of 20°C below T_g , for 5, 10, and 15% sucrose concentrations, as was observed by Collares et al. (2004) for maltodextrin MOR-REX[®] 1910 without the addition of sucrose.

Conclusions

For detachment of dried food materials from a glass surface to occur naturally without external aid, the moisture content of the film must reach values corresponding to those of the glass transition at the operating temperature. As a consequence (i) the higher the drying temperature, the lower the moisture content necessary for detachment to occur; (ii) at the same drying temperature, products with higher glass-transition temperatures (maltodextrin RD-111) detach with higher moisture contents than products with lower glass-transition temperatures (maltodextrin MOR-REX[®] 1914); (iii) the addition of products with lower glass-transition temperatures makes the detachment of the dry film more difficult (maltodextrin + sucrose mixture); (iv) process–glass transition relationships constitute a solid basis to optimise both existing and novel dehydration methods.

Acknowledgments

The authors thank Corn Products Brazil for providing the maltodextrin samples. Fernanda Paula Collares was supported by a scholarship of *Coordenação de Aperfeiçoamento de Pessoal de Nível Superior* (CAPES, Brazil).

References

- Arvanitoyannis, I., Blanshard, J.M.V., Ablett, S., Izzard, M.J., and Lillford, P.J. Calorimetric study of the glass transition occurring in aqueous glucose:fructose solutions, *J. Sci. Food Agric.*, 63, 177, 1993.

- Busin, L., Buisson, P., and Bimbenet, J.J. Notion de transition vitreuse appliquée au séchage par pulvérisation de solutions glucidiques, *Sci. Aliments*, 16, 443, 1996.
- Cnossen, A.G., Siebenmorgen, T., Yang, W., Bautista, R. An application of glass transition temperature to explain rice kernel fissure occurrence during the drying process, *Drying Technol.*, 19, 1661, 2001.
- Collares, F.P., Finzer, J.R.D., and Kieckbusch, T.G. Glass transition control of the detachment of food pastes dried over glass plates, *J. Food Eng.*, 61, 261, 2004.
- Couchman, P.R. and Karasz, F.E. A classical thermodynamic discussion of the effect of composition on glass transition temperatures, *Macromolecules*, 11, 117, 1978.
- Ferry, J.D. *Viscoelastic Properties of Polymers*, 3rd ed., Wiley, New York, 1980.
- Fox, T.G. Jr. and Flory, P.J. Second-order transition temperatures and related properties of polystyrene. I. Influence of molecular weight, *J. Appl. Phys.*, 21, 581, 1950.
- Kalichevsky, M.T. and Blanshard, J.M.V. The effect of fructose and water on the glass transition of amylopectin, *Carbohydr. Polym.*, 20, 107, 1993.
- Labuza, T., Roe, K., Payne, C., Panda, F., Labuza, T.J., Labuza, P.S., and Krusch, L. Storage stability of dry food systems: Influence of state changes during drying and storage, *Proceedings of the 14th International Drying Symposium (IDS 2004)*, São Paulo, Brasil, 22–25 August 2004, pp. A48–68.
- Levine, H. and Slade, L. Glass transitions in foods, *Physical Chemistry of Foods*, H.G. Schwartzberg and R.W. Hartel, eds., Marcel Dekker, New York, pp. 83–221, 1992.
- Mitsuiki, M., Mizuno, A., and Motoki, M. Determination of molecular weight of agars and effect of molecular weight on the glass transition, *J. Agric. Food. Chem.*, 47, 473, 1999.
- Ozmen, L. and Langrish, T.A.G. Comparison of glass transition temperature and sticky point temperature for skim milk powder, *Drying Technol.*, 20, 1177, 2002.
- Roos, Y. Melting and transitions of low molecular weight carbohydrates, *Carbohydr. Res.*, 238, 39, 1993a.
- Roos, Y.H. Water activity and physical state effects on amorphous food stability, *J. Food Process. Preserv.*, 16, 433, 1993b.
- Roos, Y. Characterization of food polymers using state diagrams, *J. Food Eng.*, 24, 339, 1995.
- Roos, Y. and Karel, M. Applying state diagrams to food processing and development, *Food Technol.*, 45, 66, 1991a.
- Roos, Y. and Karel, M. Plasticizing effect of water on thermal behavior and crystallization of amorphous food models, *J. Food Sci.*, 56, 38, 1991b.
- Slade, L., Levine, H., Levelella, J., and Wang, M. The glassy state phenomenon in applications for the food industry: application of the food polymer science approach to structure-function relationships of sucrose in cookie and cracker systems, *J. Sci. Food Agric.*, 63, 133, 1993.
- Torreggiani, D., Forni, E., Guercilena, I., Maestrelli, A., Bertolo, G., Archer, G.P., Kennedy, C.J., Bone, S., Blond, G., Contreras-Lopez, E., and Champion, D. Modification of glass transition temperature through carbohydrates additions: effect upon colour and anthocyanin pigment stability in frozen strawberry juices, *Food Res. Int.*, 32, 441, 1999.

The Polyproline II Conformation: How Protein Hydration Influences Conformation in Solution

Patricio A. Carvajal and Tyre C. Lanier

CONTENTS

Introduction	387
Collagen.....	388
Collagen Hydration	388
Collagen and the Polyproline II Conformation	390
PPII in Globular Proteins and Host–Guest Experiments	392
Protein Unfolding and the PPII Conformation.....	393
Protein Folding.....	395
Conclusions.....	396
Acknowledgments	397
References	397

Introduction

During the past 10 years, tremendous advances have occurred in protein science that are due, in large part, to combining experimental studies with sophisticated computer simulations. In particular, these techniques have revealed the critical role that water plays in the function and structural stability of proteins, an aspect largely ignored in the past (Ghosh et al., 2003).

Most studies on protein folding have centered on the stability of the folded state. The unfolded state has essentially been neglected because of its reputation of being devoid of biological function, difficult to study, and not well defined (Plaxco and Gross, 2001). Recently, the importance of unfolded segments as part of the secondary structure of globular proteins and their role in the performance of biological functions has become apparent

(Dunker et al., 2002). We also are beginning to realize that there may be a surprising simplicity to what previously appeared to be a heterogeneous mess: that the unfolded state can be characterized, in part, as the same conformation as that adopted by a single polypeptide chain of the collagen molecule. And the unfolded state is stabilized by the interaction of the peptide backbone with surrounding water molecules.

This overview article compiles recent significant findings that recognize the important role of water on the unfolded state and in protein folding.

Collagen

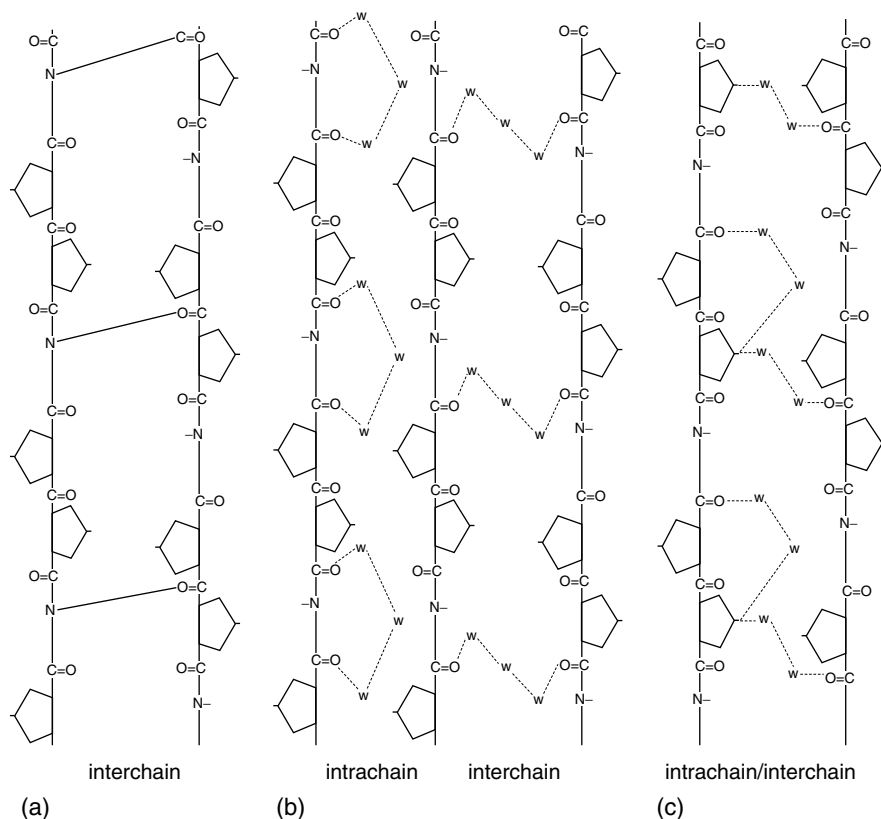
Collagens are characterized by the assembly of three polypeptides chains (α chains) arranged in a triple helical conformation. Individual triple helices of collagen are organized into fibrils of great tensile strength and flexibility. All members are distinguished as containing domains with repetitions of proline-rich tripeptides $(\text{Gly-X-Y})_n$, where X and Y are frequently proline (Pro) and hydroxyproline (Hyp), respectively.

A major stabilizing feature of α -helical and β -sheet conformations in proteins is the participation of each residue in hydrogen bonding between backbone carbonyl (CO) and amide groups (NH). Hydrogen bonding in collagen, however, occurs only every third residue and always between chains, mainly between the backbone NH of glycine and the backbone CO of the residue in the X position of the adjacent chain (Figure 22.1a) (Brodsky and Ramshaw, 1997). The remaining two backbone CO groups in each tripeptide, as well as any backbone NH groups of nonproline X and Y residues, are not involved in either intra or interchain hydrogen bonds with other groups. In addition, the hydroxyl groups of the hydroxyproline residues point outward from the triple helix and therefore cannot directly hydrogen bond to any other groups within the molecule (Brodsky and Ramshaw, 1997).

This model exhibits the basic characteristics of that previously proposed for collagen by Rich and Crick (1961), and for several years the unsatisfied potential for more hydrogen bonding was not understood.

Collagen Hydration

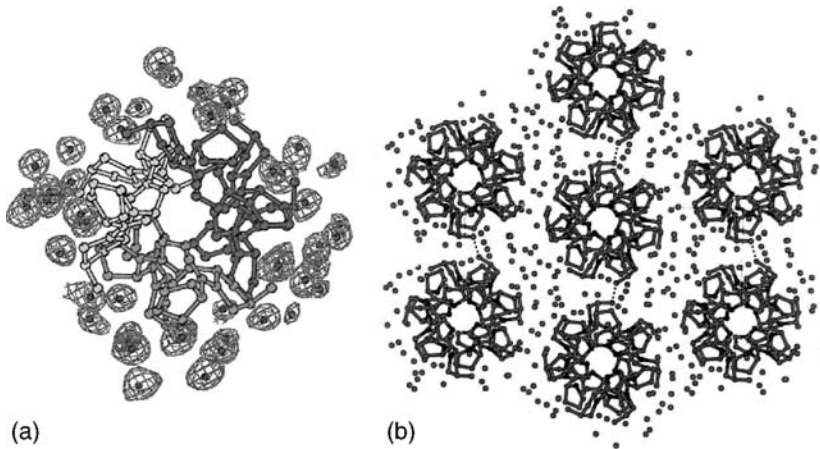
The manner by which the hydrogen bonding potential of this conformation is satisfied was later revealed by the determination of the structure of the triple-helical collagen-like molecule $(\text{GlyProHyp})_{10}$ by x-ray crystallography (Bella et al., 1994, 1995). This first high-resolution structure of a collagen-type triple helix revealed an ordered and thick cylinder of hydration surrounding the triple helix (Figure 22.2a). Also surprisingly, the lateral molecular

**FIGURE 22.1**

A schematic drawing illustrating the types of hydrogen bonding patterns found in the triple helix: (a) direct peptide group hydrogen bonding; (b) water mediated hydrogen linking carbonyl groups; and (c) water mediated hydrogen bonding linking hydroxyproline OH group and carbonyl groups (Bella et al., 1995; Brodsky and Ramshaw, 1997).

packing of these collagen molecules shows little or not direct contact between neighboring triple helices (Figure 22.2b). Rather, the distance among them is maintained by water molecules of its hydration shell (Kramer, 1998; Berisio et al., 2000). This finding supported the idea that water molecules could play a major role in the stabilization of the triple helix (Ramachandran et al., 1973).

These water molecules mediate hydrogen bonds between the hydroxyl groups of hydroxyproline and the peptide backbone CO and NH (if available) groups both within each chain and between different chains (Figure 22.1b and c). The number of water molecules involved in bridging two groups appears to vary along the molecule, such that two, three, four, or even five water molecules may form a chain linking the two groups (Bella et al., 1995). Additionally, all side chains, as well as the backbone CO group

**FIGURE 22.2**

(a) Overall view of the hydration layer surrounding collagen molecule and the electron density map of the water molecules (Berisio et al., 2001). (b) Molecular packing of the triple helices looking down the helical axis of (GlyProHyp). Dots represent water (Kramer, 1998; Berisio et al., 2001).

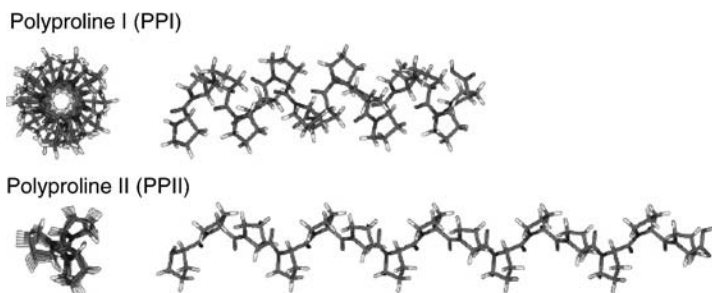
of the glycine in all three chains, are found on the outside of the triple helix molecule and in contact with water molecules.

Nuclear magnetic resonance (NMR) spectroscopy has also been used to probe the structure of the collagen triple helix in solution as well as to measure its dynamics and folding kinetics. In general, the structural data obtained by NMR spectroscopy and x-ray diffraction analyses are in gratifying agreement (Melacini et al., 2000; Reichert et al., 2004). Additionally, high-resolution structures of these collagen-like polypeptides, obtained using synchrotron radiation, have demonstrated that the triple helices are highly hydrated (Berisio et al., 2000, 2001).

Collagen and the Polyproline II Conformation

The unique conformation of every polypeptide chain in the collagen molecule is, in part, due to the high percentage of proline residues. Proline is unique among the 20 amino acids in having a cyclic side chain that includes its backbone nitrogen atom. This restricts the torsion angle for the N–C α bond (ϕ torsion angle), allowing only a limited number of conformations (Reiersen and Rees, 2001). Furthermore, the lack of a hydrogen substituent on its imide nitrogen prevents backbone residues from engaging in the usual hydrogen bonding observed in α -helices or β -sheets.

As a consequence, peptide sequences of the collagen molecule tend to form a different helical structure. In aqueous solution, there is a strong

**FIGURE 22.3**

Representation of structures for a 15-residue poly-L-proline. The PPI helix contains all *cis*-residues; PPII contains all *trans*-residues (Counterman and Clemmer, 2004).

preference for a left-handed, all *trans*, extended helix, termed the *polyproline II* (PPII) conformation since it is the same structure adopted by a polyproline peptide of three or more proline residues in water (Schweitzer-Stenner et al., 2003) (Figure 22.3). In the PPII conformation, the peptide bonds adopt average backbone dihedral angles of $(\phi, \psi) = (-78^\circ + 149^\circ)$, corresponding to a region of the Ramachandran map slightly to the right of the β region. This conformation is stabilized by hydrogen bonding to the surrounding water, and is so stable that temperatures as high as 90°C (Kelly et al., 2001) and ionic interactions (pH and salt effects) (Rucker et al., 2002) cannot disrupt it to any great extent (Rucker et al., 2002). In a nonaqueous environment, however, polyproline assumes a more compact right-handed, all *cis* helix with backbone dihedral angles of $(\phi, \psi) = (-83^\circ + 158^\circ)$ (Schweitzer-Stenner et al., 2003). This conformation is properly called the *polyproline I* (PPI) conformation (Figure 22.3). It is stabilized by van der Waals forces on the interior of the helix (Counterman and Clemmer, 2004).

The important role of water in the stabilization of PPII conformation is demonstrated by its mutarotation depending upon the polarity of its solvent. When polyproline in the PPI configuration is introduced into water it will mutarotate to the PPII configuration. Likewise polyproline in the PPII conformation will mutarotate to PPI if introduced into propanol (Dukor and Keiderling, 1996).

Additionally, a recent study on the gas-phase conformations of varying lengths of polyproline ions demonstrated that while PPI conformation is maintained in the gas phase, PPII conformation is not. The authors sustain that as the aqueous phase was removed from the PPII-structured polyproline during an electrospray process, the loss of water destabilized the PPII helix. Although it was not clear what conformations were formed from PPII polyproline in the gas phase, a mixture of *cis*- and *trans*-proline was evident (Counterman and Clemmer, 2004). This study also clearly demonstrated the critical importance of water in stabilizing the PPII helix.

PPII in Globular Proteins and Host–Guest Experiments

Although originally defined for the conformation adopted by polymers of proline, the PPII helical conformation can be adopted by amino acid sequences other than those based on proline. This was noticed during several statistical surveys of structures in the Protein Data Base (PDB), which estimated that up to 10% of residues that are not assigned to a regular secondary structure have PPII dihedral angles but contain little proline (Sreerama and Woody, 1994).

Typical PPII segments are observed in globular proteins. They appear at the beginning of helices, at the edges of sheets, or more frequently within loop or turn regions (Bochicchio et al., 2002; Tompa, 2002). The sequence of these short, extended peptides in globular proteins have been characterized by amino acid compositional bias, being substantially enriched in Glu, Lys, Arg, Gln, Ser, Ala, Pro, and Gly (Dunker et al., 2001). Additionally, these short segments are always located close to the protein surface, where they can maximize interaction with water.

The extended nature of the PPII helix, with the backbone CO and NH groups pointed out from the helical axis into the solvent in a strategic manner, favors interaction with water molecules. Alanine and residues with long, flexible side chains (such as Glu, Lys, Arg, and Gln) seem not to occlude the backbone from water access, or do so to a limited extent, and are therefore favored in this conformation. However, bulky branched or aromatic residues, such as Leu, Ile, Val, Trp, Phe, Tyr, and Trp, seem to occlude peptide backbone access to solvent (Persikov et al., 2000; Creamer and Campbell, 2002) (Figure 22.4).

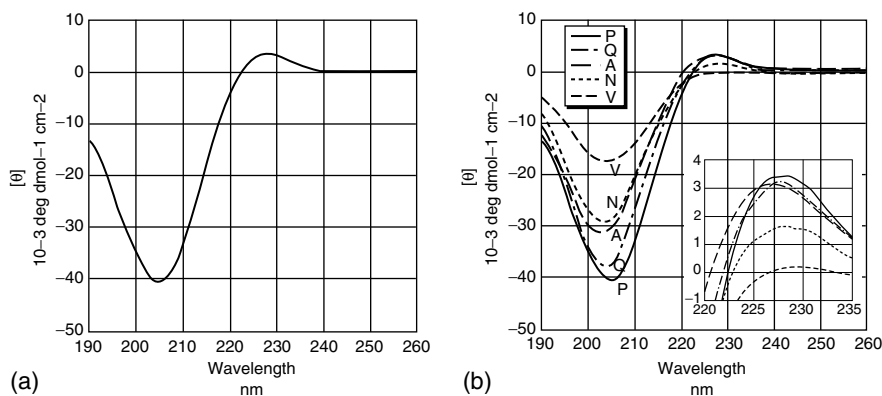
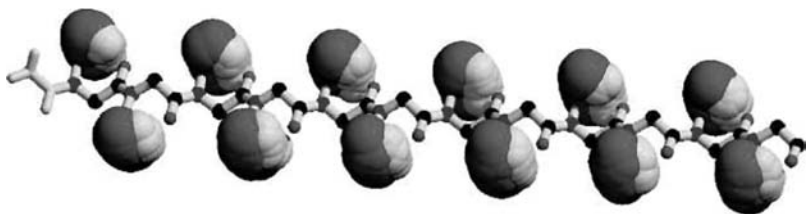


FIGURE 22.4

CD spectra of $(\text{Pro})\text{X}(\text{Pro})$ at 5°C . (a) $(\text{Pro})_7$ peptide (b) $(\text{Pro})_7$ peptide (solid line) with Gln (long- and short-dashed line), Ala (long-dashed line), Asn (short-dashed line), and Val (Medium-dashed line) single guest residue peptides. Inset shows maxima (Chellgren and Creamer, 2004).

**FIGURE 22.5**

A strand (little ball-and-stick, backbone only) on which 911 clustering waters (big balls; gray, oxygen; white, hydrogen) from multiple simulation have been superimposed. Some proximate water molecules are not hydrogen bonded to the peptide (Mezei et al., 2004).

The tendency of each amino acid to form the PPII conformation has been quantified using a host–guest model system in several studies (Persikov et al., 2000; Creamer and Campbell, 2002; Rucker et al., 2003; Chellgren and Creamer, 2004). Such experiments consist of introducing guest residues into the center of a polyproline-based peptide. The PPII conformation can then be determined by circular dichroism (CD) spectroscopy. In particular, PPII-typical CD spectra are characterized by a negative band near 200 nm and by a weaker positive band at about 220 nm (Figure 22.5a) (Chellgren and Creamer, 2004).

Figure 22.5b illustrates the effect of adding Glu (Q), Asn (N), Ala (A), and Val (V) to a host system P_3XP_3 . It is observed that alanine does not significantly disrupt the PPII conformation, while valine strongly disfavors it (Chellgren and Creamer, 2004).

Such host–guest experiments have demonstrated that each residue possesses its own propensity to induce the PPII conformation, with proline being the most stabilizing in this respect. Charged residues (Glu, Lys, Arg, and Asp) were among the most stabilizing of this conformation after proline, with Ala and Gln also falling into this category. Note that this list is very similar to the list of amino acids typically found in PPII conformations on the surface of globular gloteins. The next lower in stability was a group including the nonpolar residues Leu, Phe, Ile, Val, and Met, along with Asn, Ser, His, Thr, and Cys (Rucker et al., 2003; Persikov et al., 2000). Tyr and Trp residues seemed highly destabilizing (Persikov et al., 2000).

This finding seems correlated to the thermal stability of host–guest triple helical peptides in collagen and the observed frequency of its amino acid residues (see Table 1 in Persikov et al. (2000)).

Protein Unfolding and the PPII Conformation

The conventional view of the unfolded state is that denatured proteins are featureless, random coil polymers, with a negligible preference for any

particular conformation. This view reflects the predictions of the random-coil model of Brant and Flory (1965), who treated an unfolded polypeptide like a synthetic flexible polymer. However, two recent lines of evidence suggest that denatured protein chains may be far from random in their conformation.

First, it is now becoming more evident that when a protein unfolds, not all of its secondary structure is lost. Moreover, it has been shown that a residual structure could exist even under the most severe denaturing conditions, such as high concentrations of strong denaturants. In reduced (without S–S bonds), unfolded hen lysozyme, for instance, six hydrophobic clusters are detected forming a network connected by cooperative interactions (Klein-Seetharaman et al., 2002).

Second, combined evidence from theoretical computer modeling studies of short peptides (too short to form any detectable α -helix or β -sheet) in aqueous solution and a variety of spectroscopic studies, including ultraviolet CD (Rucker et al., 2002), nuclear magnetic resonance (NMR) (Poon et al., 2000), two-dimensional vibrational spectroscopy (Woutersen and Hamm, 2001), vibrational circular dichroism (VCD) (Keiderling et al., 1999), and vibrational Raman spectroscopy (Blanch et al., 2000), reveal that the PPII helix is the dominant conformation in a variety of these short peptides.

For example, using NMR and CD spectroscopy, Shi et al. (2002) recently demonstrated that a seven-residue alanine peptide is predominantly in the PPII conformation in aqueous solution. Following up on this result, Eker et al. (2004) showed, using a variety of spectroscopic techniques, that the acidic and basic tripeptides, triglutamate, triaspartate, and trilyserine, adopted a distorted PPII conformation. Interestingly, a comparison of structures obtained from the spectra measured at acid, neutral, and alkaline pH strongly suggested that the structural preference of all these peptides does not depend on the protonation states of the residues. Earlier, Rucker and Creamer, (2002) showed similar results for a seven-residue lysine peptide which retained PPII helical CD signals over a range of pH levels. They concluded that PPII helices must be preferred conformations for the polypeptide backbone and that electrostatic repulsion is not a driving force for PPII helix formation (Rucker et al., 2002; Eker et al., 2004). In contrast, tripeptides such as trivaline and triserine only adopt an extended β -sheet conformation (Eker et al., 2002, 2003).

Much larger alanine peptides have also been studied. For instance, Asher et al. (2004), using UV Raman spectroscopy, examined the melting of a 21-residue, mainly alanine peptide (containing three arginines to confer solubility). The peptide was mainly in an α -helix conformation at 0°C and melted to a PPII conformation as the temperature increased. Above room temperature the peptide existed mainly as a PPII helix. The authors did not observe evidence of any other significantly populated intermediates.

The recent reports by several laboratories that PPII is the major backbone conformation present in short alanine peptides has motivated an interest in

finding the cause of this preference. There is general agreement that solvation is probably an important factor. For instance, the unsolvated PPII conformation in polyalanine is not stable in the gas phase, but it is stable in water (Richrads et al., 2002; Drozdov et al., 2004).

Experiments in water have also shown that alanine peptides fluctuate between a PPII and an extended β -strand conformation (Eker et al., 2002; Shi et al., 2002; Schweitzer-Stenner et al., 2004), while valine and proline peptides exist only as β -strand and PPII conformations, respectively. At low temperatures, and as the number of alanine residues in the peptide increases, the PPII fraction substantially increases. This last observation has been interpreted as indicating that the addition of an alanine residue changes the hydration shell of the peptide in a way that stabilizes the peptide-solvent interaction and its PPII conformation (Schweitzer-Stenner et al., 2004). Using a molecular dynamic approach, Garcia supported this hypothesis, establishing that a peptide segment comprising four alanine residues is needed for the formation of a strongly hydrated groove around the peptide backbone that stabilizes the PPII conformation (Garcia, 2004).

A recent Monte Carlo simulation of the interaction between water and a 12-residue alanine peptide has complemented this later finding (Mezei et al., 2004). The simulation included water molecules (explicit), and it was possible to examine the hydrogen bonding interactions made between water and the alanine peptide as an α -helix, β -strands, or PPII conformation. This study found that the apparent enthalpic interaction between water and the alanine peptide is significantly stronger in the PPII conformation than in the extended β -conformation or α -helix. This suggests that β -strands induce formation of entropically disfavored (ordered) water, reminiscent of the hydrophobic effect (Figure 22.5).

Thus, the PPII structure fully utilizes the hydrogen bonding capacity of the CO and NH groups, maximizes peptide-water cooperativity, and leaves the first solvation layer of hydration able to participate in further hydrogen bonding with the next solvation shell (Figure 22.2a). PPII helices produce a less disruptive effect on surrounding water organization as compared with β -strands (Kentsis et al., 2004; Mezei et al., 2004). These studies strongly suggest that water plays a major role in determining the conformational preference of proteins in the unfolded state.

Protein Folding

The essential features of the folded state of globular proteins is the formation of a densely anhydrous core in which the hydrophobic side chains come together, dragging their CO and NH peptide backbone into the interior. These latter groups then form hydrogen bonds one with another.

The interaction of hydrophobic side chains is believed to be the main driving force that stabilizes the native structure of globular proteins

(Dill, 1985). However, there are important properties of water that are not considered in this model. Recent theoretical and experimental studies have demonstrated a depletion (drying) of water at the hydrophobic surface–water interface (Ball, 2003). This depleted zone extends 2 to 5 nm from the hydrophobic surface. The water molecules in this zone are 85 to 90% less dense than that of the bulk water zone (Schwendel et al., 2003; Steitz et al., 2003). It follows that when two strongly hydrophobic surfaces are brought together to a separation that allows more than one layer of water to occupy space between them, the water is expelled spontaneously (Zhou et al., 2004). The number of the water layers that are expelled depends on the geometry of the surfaces, pressure, and temperature (Mamatkulov and Khabibullaev, 2004).

Thus, hydrophobic collapse and CO–NH hydrogen bonding occurs simultaneously rather than as two independent sequential processes (Uversky and Fink, 2002; Rhee et al., 2004). Therefore, these hydrogen bonds will form intramolecularly only if the majority of such bonds are adequately dehydrated (Fernandez et al., 2003). This desolvation requires that hydrophobic groups cluster around the amide–carbonyl hydrogen bonds, expelling the surrounding water and thus stabilizing the folded structure.

Corroborating results came from Fernandez and Scott (2003), who examined the microenvironments of backbone hydrogen bonds in globular protein structures in the PDB. In 95% of the stable soluble proteins they examined, at least 92% of the backbone hydrogen bonds were dry through being encompassed by hydrophobic clusters. They concluded that hydrophobic clustering of the side chains is inevitably bound to backbone burial, and the latter process would be too thermodynamically costly and kinetically unfeasible without amide–carbonyl hydrogen bond formation (Fernandez et al., 2002).

Conclusions

Recent studies have shown a radically different picture of the unfolded state. In this new view, unfolded proteins have a more limited range of conformations than was formerly appreciated. This provides a basis for understanding not only the nature of the unfolded state but also the earliest events that occur during folding.

The critical role of water has also emerged as a factor to condition protein conformation. In this new model, the optimal bridging of water with the peptide backbone groups (carbonyl and amide) determines a well-known conformation termed polyproline II. The specific role of the side chains is to modulate conformations by interfering to a certain degree with the solvation of the peptide backbone. Interestingly, the folded state is stabilized by

avoiding backbone hydrogen bond contact with water. This factor is resolved by the number and hydrophobic character of close side chains.

This new understanding has potentially broad-reaching implications, particularly with respect to modeling the unfolded state and understanding the determinants of protein stability.

Acknowledgments

The authors thank Penny Amato and Brad Wright for editing, comments, and enlightening discussions. This research was supported by a grant from USDA/NRIGP Project 2002-0891.

References

- Asher, S.A., Mikhonin, A.V., and Bykov, S. UV Raman demonstrates that alpha-helical polyalanine peptides melt to polyproline II conformations, *J. Am. Chem. Soc.*, 126, 8433, 2004.
- Ball, P. How to keep dry in water, *Nature*, 423, 25, 2003.
- Bella, J., Brodsky, B., and Berman, H.M. Hydration structure of a collagen peptide, *Structure*, 3, 893, 1995.
- Bella, J., Eaton, M., Brodsky, B., and Berman, H.M. Crystal-structure and molecular-structure of a collagen-like peptide at 1.9-Angstrom resolution, *Science*, 266, 75, 1994.
- Berisio, R., Vitagliano, L., Sorrentino, G., Carotenuto, L., Piccolo, C., Mazzarella, L., and Zagari, A. Effects of microgravity on the crystal quality of a collagen-like polypeptide, *Acta Crystallogr. D*, 56, 55, 2000.
- Berisio, R., Vitagliano, L., Mazzarella, L., and Zagari, A. Crystal structure of a collagen-like polypeptide with repeating sequence Pro-Hyp-Gly at 1.4 Å resolution: implications for collagen hydration, *Biopolymers*, 56, 8, 2001.
- Blanch, E.W., Morozova-Roche, L.A., Cochran, D.A., Doig, A.J., Hecht, L., and Barron, L.D. Is polyproline II helix the killer conformation? A Raman optical activity study of the amyloidogenic prefibrillar intermediate of human lysozyme, *J. Mol. Biol.*, 301, 553, 2000.
- Bochicchio, B. and Tamburro, A.M. Polyproline II structure in proteins: identification by chiroptical spectroscopies, stability, and functions, *Chirality*, 14, 782, 2002.
- Brant, D.A. and Flory, P.A. Configuration of random polypeptide chains .2. Theory, *J. Am. Chem. Soc.*, 87, 2791, 1965.
- Brodsky, B. and Ramshaw, J.A.M. The collagen triple-helix structure, *Matrix Biol.*, 15, 545, 1997.
- Chellgren, B.W. and Creamer, T.P. Short sequences of non-proline residues can adopt the polyproline II helical conformation, *Biochemistry*, 43, 5864, 2004.
- Counterman, A.E. and Clemmer, D.E. Anhydrous polyproline helices and globules, *J. Phys. Chem. B*, 108, 4885, 2004.

- Creamer, T.P. and Campbell, M.N. Determinants of the polyproline II helix from modeling studies, unfolded proteins, *Adv. Protein Chem.*, 62, 263, 2002.
- Dill, K.A. Theory for the folding and stability of globular proteins, *Biochemistry*, 24, 1502, 1985.
- Drozdo, A.N., Grossfield, A., and Pappu, R.V. Role of solvent in determining conformational preferences of alanine dipeptide in water, *J. Am. Chem. Soc.*, 126, 2574, 2004.
- Dukor, R.K. and Keiderling, T.A. Mutarotation studies of poly-L-proline using FTIR, electronic and vibrational circular dichroism, *Biospectroscopy*, 2, 83, 1996.
- Dunker, A.K., Lawson, J.D., Brown, C.J., Williams, R.M., Romero, P., et al. Intrinsically disordered protein, *J. Mol. Graphics Modell.*, 19, 26, 2001.
- Dunker, A.K., Brown, C.J., Lawson, J.D., Lakoucheva, L.M., and Obradovic, Z. Intrinsic disorder and protein function, *Biochemistry*, 41, 6573, 2002.
- Eker, F., Cao, X., Nafie, L.A., and Schweitzer-Stenner, R. Tripeptides adopt stable structures in water. A combined polarized visible Raman, FTIR, and VCD spectroscopy study, *J. Am. Chem. Soc.*, 124, 14330, 2002.
- Eker, F., Griebenow, K., and Schweitzer-Stenner, R. Stable conformations of tripeptides in aqueous solution studied by UV circular dichroism spectroscopy, *J. Am. Chem. Soc.*, 125, 8178, 2003.
- Eker, F., Griebenow R., Cao X., Nafie L.A., and Schweitzer-Stenner, R. Tripeptides with ionizable side chains adopt a perturbed polyproline II structure in water, *Biochemistry*, 43, 613, 2004.
- Fernandez, A., Kardos, J., and Goto, Y. Protein folding: could hydrophobic collapse be coupled with hydrogen-bond formation?, *FEBS Lett.*, 536, 187, 2003a.
- Fernandez, A. and Scott, R. Dehydron: a structural encoded signal for protein interaction, *Biophys. J.*, 85, 1914, 2003b.
- Fernandez, A., Sosnick, T.R., and Colubri, Y. Dynamic of hydrogen bond desolvation in protein folding, *J. Mol. Biol.*, 321, 659, 2002.
- Garcia, A.E. Characterization of non-alpha helical conformations in Ala peptides, *Polymer*, 45, 669, 2004.
- Ghosh, T., Garde, S., and Garcia, A.E. Role of backbone hydration and salt-bridge formation in stability of α -helix solution, *Biophys. J.*, 85, 3187, 2003.
- Keiderling, T.A., Silva, R.A., Yoder, G., and Dukor, R.K. Vibrational circular dichroism spectroscopy of selected oligopeptide conformations, *Bioorg. Med. Chem.*, 7, 133, 1999.
- Kelly, M.A., Chellgren, B.W., Rucker, A.L., and Troutman, J.M., Fried, M.G. Host-guest study of left-handed polyproline II helix formation, *Biochemistry*, 40, 14376, 2001.
- Kentsis, A., Mezei, M., Gindin, T., and Osman, R. Unfolded state of polyalanine is a segmented polyproline II helix, *Prot. Struct. Funct. Biol.*, 55, 493, 2004.
- Klein-Seetharaman, J.M., Oikawa, S.B., Grimshaw, J., Wirmer, J., Duchardt, E., et al. Long-range interactions within a nonnative protein, *Science*, 295, 1719, 2002.
- Kramer, R.Z., Vitagliano, L., Bella, J., Berisio, R., Mazzarella, L., Brodsky, B., Zagari, A., and Berman, H.M. X-ray crystallographic determination of a collagen-like peptide with the repeating sequence (Pro-Pro-Gly), *J. Mol. Biol.*, 280, 623, 1998.
- Mamatkulov, S.I. and Khabibullaev, P.K. Water at hydrophobic substrates: curvature, pressure, and temperature, *Langmuir*, 20, 4756, 2004.
- Melacini, G., Bonvin, A.M.J.J., Goodman, M., Boelens R., and Kaptein, R. Hydration dynamics of the collagen triple helix by NMR, *J. Mol. Biol.*, 300, 1041, 2000.

- Mezei, M., Fleming, P.J., Srinivasan, R., and Rose, G.D. Polyproline II helix is the preferred conformation for unfolded polyalanine in water, *Prot. Struct. Funct. Biol.*, 55, 502, 2004.
- Persikov, A.V., Ramshaw, J.A.M., Kirkpatrick, A., and Broadsky, B. Amino acid propensities for the collagen triple-helix, *Biochemistry*, 39, 14960, 2000.
- Plaxco, K.W. and Gross, M. Unfolded, yes, but random? Never!, *Nat. Struct. Biol.*, 8, 659, 2001.
- Poon, C.D., Samulski, E.T., Weise, C.F., and Weisshaar, J.C. Do bridging water molecules dictate the structure of a model dipeptide in aqueous solution?, *J. Am. Chem. Soc.*, 122, 5642, 2000.
- Ramachandran, G.N., Bansal, M., and Bhatnaga, R.S. Hypothesis on role of hydroxyproline in stabilizing collagen structure, *Biochim. Biophys. Acta*, 322, 166, 1973.
- Reichert, D., Pascui, O., deAzevedo, E.R., Bonagamba, T.J., Arnold, K., and Huster, D. A solid-state NMR study of the fast and slow dynamics of collagen fibrils at varying hydration levels, *Magn. Reson. Chem.*, 42, 276, 2004.
- Reiersen, H. and Rees, A.R. The hunchback and its neighbours: proline as an environmental modulator, *Trends Biochem. Sci.*, 26, 679, 2001.
- Rhee, Y.M., Sorin, E.J., Jayachandran, G., Lindahl, E., and Pande, V.S. Simulations of the role of water in the protein-folding mechanism, *Proc. Natl Acad. Sci. USA*, 101, 6456, 2004.
- Rich, A. and Crick, F.H.C. Molecular structure of collagen, *J. Mol. Biol.*, 3, 483, 1961.
- Richards, F.M., Eisenberg D.S., and Kuriyan J., eds. Unfolded proteins, *Adv. Protein Chem.*, 62, 2002.
- Rucker, A.L. and Creamer, T.P. Polyproline II helical structure in protein unfolded states: lysine peptides revisited, *Protein Sci.*, 11, 980, 2002.
- Rucker, A.L., Pager C.T., Campbell, M.N., Qualls, J.E., and Creamer, T.P. Host-guest scale of left handed polyproline II helix formation, *Protein. Struct. Funct. Genet.*, 53, 68, 2003.
- Schweitzer-Stenner, R., Eker, F., Perez, A., Griebenow, K., Cao, X., and Nafie, L.A. The structure of tri-proline in water probed by polarized Raman, fourier transform infrared, vibrational circular dichroism, and electric ultraviolet circular dichroism spectroscopy, *Biopolymers*, 71, 558, 2003.
- Schweitzer-Stenner, R., Eker, F., Griebenow, K., Cao, X., and Nafie, L. The conformation of tetra-alanine in water determined by polarized Raman, FT-IR and VCD spectroscopy, *J. Am. Chem. Soc.*, 126, 2768, 2004.
- Schwendel, D., Hayashi, T., Dahint, R., Pertsin, A., Grunze, M., Steitz, R., and Schreiber, F. Interaction of water with self-assembled monolayers: neutron reflectivity measurements of the water density in the interface region, *Langmuir*, 19, 2284, 2003.
- Shi, Z.S., Olson, C.A., Rose, G.D., Baldwin, R.L., and Kallenbach, N.R. Polyproline II structure in a sequence of seven alanine residues, *Proc. Natl Acad. Sci. USA*, 99, 9190, 2002.
- Sreerama, D. and Woody, R.W. Poly(pro) II helices in globular-proteins — identification and circular dichroic analysis, *Biochemistry*, 33, 10022, 1994.
- Steitz, R., Gutberlet, T., Hauss, T., Klosgen B., Krastev, R., Schemmel, S., Simonsen, A.C., and Findenegg, G.H. Nanobubbles and their precursor layer at the interface of water against a hydrophobic substrate, *Langmuir*, 19, 2409, 2003.
- Tompa, P. Intrinsically unstructured proteins, *Trends Biochem. Sci.*, 27, 527, 2002.

- Uversky, V.N. and Fink, A.L. The chicken egg scenario of protein folding revisited, *FEBS Lett.*, 515, 79, 2002.
- Woutersen, S. and Hamm, P. Isotope-edited two-dimensional vibrational spectroscopy of trialanine in aqueous solution, *J. Chem. Phys.*, 114, 2727, 2001.
- Zhou, R.H., Huang, X.H., Margulis, C.J., Margulis, C.J., and Berne, B.J. Hydrophobic collapse in multidomain protein folding, *Science*, 305, 1605, 2004.

*Rheology and Microstructure of Interfaces
Stabilized by Mixed Proteins and Surfactants:
A Computer Simulation Study*

Luis A. Pagnaloni, Rammile Ettelaie, and Eric Dickinson

CONTENTS

Introduction	401
The Model	402
Brownian Dynamics Simulation.....	403
One-Component Monolayers.....	405
Two-Component Monolayers	407
Conclusions.....	410
Acknowledgments	411
References	411

Introduction

The adsorption of proteins and small-molecule surfactants at air–water and oil–water interfaces is crucial to the formation and stabilization of emulsions and foams. Complex interfaces that consist of mixtures of adsorbing species are of particular relevance in food systems (Dickinson and McClements, 1995). Proteins and low-molecular-weight (LMW) surfactants have very different individual adsorption behavior and, most interestingly, they present complex interfacial structures when adsorbed from mixed bulk solutions (Pagnaloni et al., 2004a). In particular, it has been shown by atomic force microscopy (AFM) (Mackie et al., 1999) and Brewster angle microscopy (Rodríguez Patino et al., 1999) that competitive adsorption of protein plus surfactant mixtures occurs in a heterogeneous fashion, with the surfactant forming segregated domains in a quasi-two-dimensional protein matrix, at least over periods of time of a few days.

The large-deformation mechanical properties of these types of adsorbed films can be directly measured by using new apparatus such as interfacial tensiometers (Jones and Middelberg, 2002). Stress–strain curves can be obtained during a large compression (expansion) of the interfacial film. The mechanical properties of the adsorbed film determine its ability to support the stress to which it is subjected during droplet (bubble) deformation or shrinkage (disproportionation). Moreover, the adsorbed films are subjected to large deformations during processing (stirring, whipping, etc.) of food products. Therefore, a better understanding of the response of these interfaces to large deformations is crucial to the development of the engineering multi-phase systems in the food industry.

In this chapter, we present a few examples of the increased understanding achieved by the computer simulation of adsorbing binary mixtures subjected to large interfacial deformation (Pugnaloni et al., 2005a). A more extensive report can be found elsewhere (Pugnaloni et al., 2005b). The species are modeled as spherical particles that adsorb at a planar interface by virtue of a steep external attracting force. The protein-like particles can form elastic bonds with each other; the idealized surfactant-like particles do not bind to other particles. The simulation is carried out using a Brownian dynamics (BD) algorithm. A strong justification for the adopted approach is that the simulated structure of complex mixed adsorbed films has been shown (Pugnaloni et al., 2004a) to compare very well with experimental AFM images of adsorbed mixtures of globular protein plus nonionic surfactant.

Here, we investigate the stress response to large uniaxial deformations of model single-protein films and protein plus surfactant mixed films. We show that the general structure of a compressed (expanded) protein film is very sensitive to the breakability of the protein–protein bonds. We then study the structural changes and mechanical response of a protein plus surfactant mixed film to large compression (expansion). We show that the nature of the protein–protein bond parameters also affects the overall displacement behavior of the coadsorbed surfactant during compression.

The Model

In order to study the structural implications of adsorption of surface-active components, a simple simulation approach was developed by Wijmans and Dickinson (1999a, 1999b). A detailed description of this model can be found in a recent review (Pugnaloni et al., 2004a). The model consists in essence of spherical particles interacting through a steeply repulsive spherical core potential. To mimic the preference of the molecules to adsorb at the interface, each particle interacts with an external potential, acting in the z -direction. This potential has the shape of a well with one infinite wall and one finite wall. The infinite wall prevents particles from escaping to the phase in which

they cannot diffuse — typically air or oil in the case of proteins. Conversely, the finite wall allows for interchange of particles between the interface and the phase where they can diffuse — typically an aqueous solution. A particle is said to be *directly* adsorbed if it is within the interfacial potential well.

To account for the intermolecular cross-linking behavior of some proteins, the adsorbing particles can also interact through flexible bonds. Nodes are created on the nominal surface of the spherical particles. The bond interaction acts along the straight line that joins the corresponding nodes, and it depends on the node-to-node distance b_{ij} only. As these forces do not need to operate in purely radial directions, they can give rise to torques acting on each particle. The interparticle bonds are created whenever two particles approach within a distance b_1 . Initially, nodes are created on the line that joins the particle centres. After bond formation, the nodes that define the ends of the bond are fixed within the corresponding particle reference system. That is, the nodes remain fixed at the initial position on the surface of each particle. If the particle moves such that the length of a bond exceeds b_{\max} , the bond is deemed to be broken. By setting $b_{\max} = \infty$, permanent (unbreakable) bonds can be simulated. Through this chapter we use bonds with an elastic constant of $200 k_B T \sigma^{-2}$. Here, σ is the diameter of the particles, k_B is the Boltzmann constant, and T is the absolute temperature.

Particles cannot escape in the negative z -direction as they are trapped by the infinite wall of the interface, but they can move away (and become “lost”) in the positive z -direction. In order to avoid this happening, an additional “wall” has to be added at a given z -position, z_w .

The properties of the present model could, in principle, be studied by means of molecular dynamics, Monte Carlo, or BD simulation. However, the first two techniques would require the introduction of an extra component in the system to account for the solvent. Therefore, BD simulations are normally more efficient as they introduce the solvent effect by just assuming a bulk solvent viscosity, η . The time is conventionally normalized with respect to the average time τ taken for a particle to diffuse a distance equal to its radius in an infinitely diluted system, i.e.,

$$\tau = \frac{(\sigma/2)^2}{6D_0} = \frac{\pi\sigma^3\eta}{8k_B T} \quad (23.1)$$

where $D_0 = k_B T / (3\pi\eta\sigma)$ is the diffusion coefficient at infinite dilution.

Brownian Dynamics Simulation

The simulation is carried out using the BD technique to represent solvent effects. The dynamics of the particles are assumed to be over-damped. Therefore, inertial terms are negligible and the velocity of each particle is directly proportional to the applied force on that particle. Consequently, we update only the positions of the particles throughout the simulation.

The diffusion coefficient at infinite dilution is set to $D_0 = 2.21 \times 10^{-4} \sigma(k_B T/m)^{1/2}$, where m is the mass of the particles. In addition to the particle–particle and particle–interface interactions, a drag force and a random force consistent with D_0 are applied to each particle. The position update algorithm is

$$\mathbf{r}_i(t + \Delta t) = \mathbf{r}_i(t) + \mathbf{F}_i(t) \frac{\Delta t}{\xi} + \mathbf{R}_i(t, \Delta t) \quad (23.2)$$

where $\xi = k_B T/D_0$ is the Stokes friction coefficient, and $\mathbf{R}_i(t, \Delta t)$ is a Gaussian random displacement of zero mean and variance $\langle \mathbf{R}_i^2(t, \Delta t) \rangle = 2D_0 \Delta t$ (Allen and Tildesley, 1987). Because of the torque applied by the bonds to the particles, there is an analogous rotational update algorithm (Whittle and Dickinson, 1997).

Particles are normally allowed to spread at random at the interface ($z = 0$) and then the system is allowed to equilibrate. The equilibration time depends on the particular set of parameters chosen; in some cases involving aggregation, coarsening, and/or desorption, the simulation may require a long equilibration time.

The system is simulated within a cubic box of side length L . Periodic boundary conditions are applied in the x - and y -directions only. The area fraction Γ is defined as the area occupied by the adsorbed particles divided by the total area A of the interface in the simulation, i.e., $\Gamma = \pi N^{\text{ads}}/(4A)$, where N^{ads} is the number of adsorbed particles.

The response of the interface to an external perturbation is analyzed using the interfacial stress tensor \mathbf{S} . For a pairwise-additive interaction, \mathbf{S} is given by the Kirkwood formula (Doi and Edwards, 1986; Wijmans and Dickinson, 1999a)

$$\mathbf{S}_{\alpha\beta} = \frac{N}{A} k_B T \delta_{\alpha\beta} - \frac{1}{A} \sum_{j>i}^N \sum_{i=1}^{N-1} \mathbf{r}_{\alpha ij} \mathbf{F}_{\beta ij} \quad (23.3)$$

Here, α and β indicate the different Cartesian components of the interfacial stress tensor \mathbf{S} , the interparticle distance \mathbf{r}_{ij} , and the interparticle force \mathbf{F}_{ij} , respectively. We assume that the contribution to the stress tensor due to particles that are completely desorbed from the interface is negligible, and therefore we sum over all particles in the system.

The dilatational rheology of a system can be extracted by subjecting the system to changes in the interfacial area (Wijmans and Dickinson, 1999a). We compress (expand) the interface in the x -direction at constant velocity, thereby simulating the type of experiments typically carried out in a Langmuir trough. The variable length of the interface is then given by

$$L_x(t) = L_{x,0} \pm v_x t \quad (23.4)$$

where $L_{x,0}$ is the initial length and v_x is the velocity of the imaginary mobile barrier. The positive and negative symbols in Equation 23.4 correspond to expansion and compression, respectively. In order to maintain a constant

volume for the entire system, the simulation box has to be simultaneously expanded (compressed) in the z -direction according to

$$L_z(t) = L_{z,0} \mp \frac{L_{z,0}v_x t}{L_{x,0} \pm v_x t} \quad (23.5)$$

Since we consider only uniaxial deformation in the x -direction, the normal component \mathbf{S}_{xx} of the interfacial stress is the most affected. Therefore, we only report this component of \mathbf{S} . It is worth noticing that a positive value of \mathbf{S}_{xx} means that the adsorbed film pulls in from the imaginary moving barrier, whereas a negative value implies that the film pushes out the barrier.

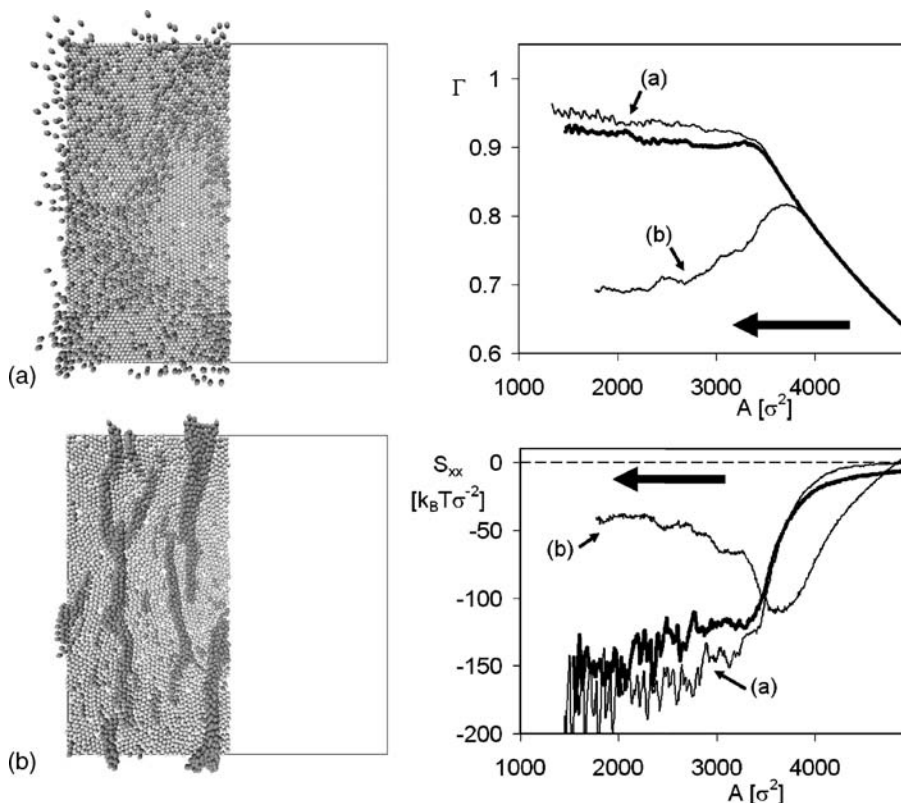
One-Component Monolayers

Monolayers consisting of a single component have been subjected to uniaxial compression (expansion). Particles were initially spread at random at the interface and equilibrated over 10^6 time steps. Then, the monolayers were compressed (expanded) in the x -direction. The velocity of compression (expansion) has been set at $v_x = 0.132\sigma\tau^{-1}$.

The microstructure of the compressed interface can be observed on the left in Figure 23.1. The stress response curves for the different monolayers $\mathbf{S}_{xx}(A)$ and the area fraction $\Gamma(A)$ are shown on the right in Figure 23.1. As we can see from image (a), the presence of highly breakable bonds ($b_{\max} = 0.3$) allows the desorption and diffusion of isolated particles into the bulk phase. However, desorption does not occur completely at random as we find for nonbond-forming particles (data not shown). The film tends to form two-dimensional crystalline domains at the interface as the collapse point is approached. The defect boundaries that separate these microcrystalline domains are the critical regions where the particles tend to desorb upon collapse. The evolving area fraction during compression shows that systems with very breakable bonds (curve (a)) can accommodate particles more efficiently at the interface and take more stress than an equivalent nonbond-forming system (thick curve). This is because of the formation of crystalline domains which are capable of a higher degree of compaction before failure. We have observed (Pugnaloni et al., 2004b) this same behavior for particles interacting through spherical short-range attractions.

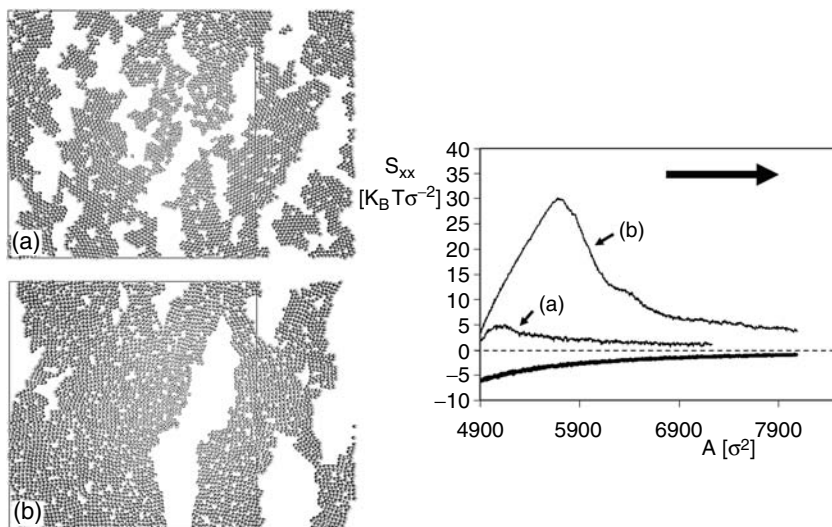
For systems whose particle–particle bonds are permanent (image (b) in Figure 23.1), the film tends to form a secondary layer of wrinkles. The displaced particles do not completely remove themselves from the interface, but remain connected to the cross-linked network. Contrary to what happens with very breakable bonds, part of the interfacial stress is released — and the area fraction decreases significantly — once the collapse point is passed (see curve (b)).

The responses of two different transient-bond systems to uniaxial expansion are shown in Figure 23.2. We have found that no desorption

**FIGURE 23.1**

Uniaxial compression of a model protein layer: (a) transient bonds ($b_{\max} = 0.3$), and (b) permanent bonds ($b_{\max} = \infty$). The snapshots of the system on the left correspond to 50% compression. Dark spheres represent particles not directly adsorbed at the interface. The area fraction Γ as a function of the interfacial area A and the corresponding interfacial stress S_{xx} in the direction of compression are shown on the right. The thick lines correspond to a system of particles that do not form bonds at all. The arrows indicate the direction of compression.

takes place during expansion. For bonds that are relatively easy to break ($b_{\max} = 0.4$), the system presents numerous small cracks (see Figure 23.2a) that grow during expansion. When the bonds are somewhat longer lasting ($b_{\max} = 0.7$), the cracks are less numerous but larger in size (see Figure 23.2b). This fracture-type behavior has been seen experimentally (Hotrum et al., 2003), for example, in films of the globular protein β -lactoglobulin. The stress response, shown on the right hand part of Figure 23.2, clearly indicates the fracture point. For the case of less breakable bonds (curve (b)), the interfacial stress grows initially through bond stretching, but then it reaches a maximum and decays as some bonds are broken during expansion. This mechanical behavior has also been observed experimentally when β -lactoglobulin films are expanded (Jones and Middelberg, 2002).

**FIGURE 23.2**

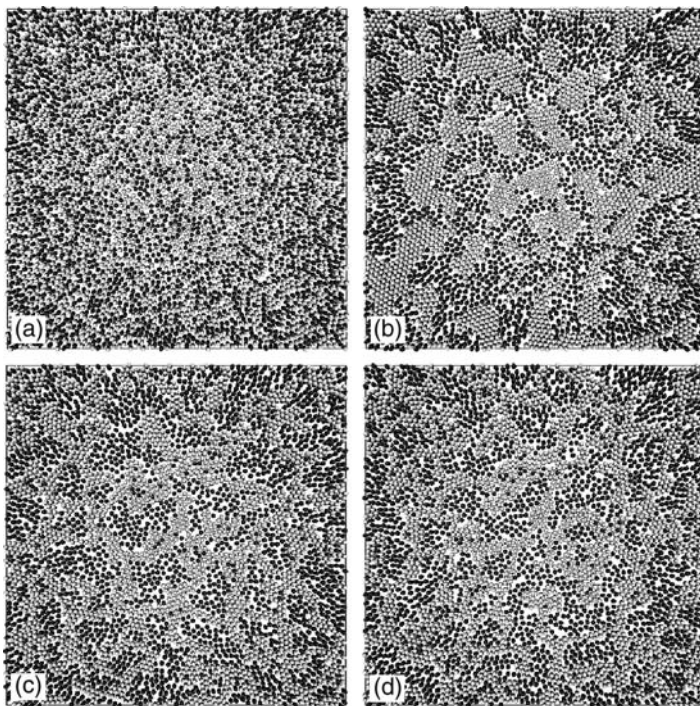
Uniaxial expansion of a model protein layer: (a) transient bonds ($b_{\max} = 0.4$), and (b) transient bonds ($b_{\max} = 0.7$). The snapshots of the system correspond to 40% expansion. The interfacial stress S_{xx} in the direction of compression is shown as a function of the interfacial area A . The thick line corresponds to a system of particles that do not form bonds.

If the bonds are somewhat easier to break (curve (a)), the collapse point is reached sooner, and the stress at rupture is significantly lower. For comparison, we have included the response of a system with no bonds at all (thick curve). In this case, the stress relaxes continuously from a negative value (i.e., the film pushes the imaginary mobile barrier).

Two-Component Monolayers

In order to assess the effect of compression (expansion) on more complex mixed layers (protein + protein or protein + surfactant), we have simulated four different binary systems. The mixtures are composed of two species of the same spherical size in a 1:1 molar ratio. In all cases, one of the species (Type 1) interacts solely through the repulsive core potential both with particles of its same type and with particles of Type 2. The Type 2 particles, however, are able to form bonds with particles of their own type. The four different cases correspond to different classes of bonding between the particles of Type 2: (a) no bonds, (b) very-easy-to-break bonds ($b_{\max} = 0.3$), (c) breakable bonds ($b_{\max} = 0.5$), and (d) permanent bonds ($b_{\max} = \infty$).

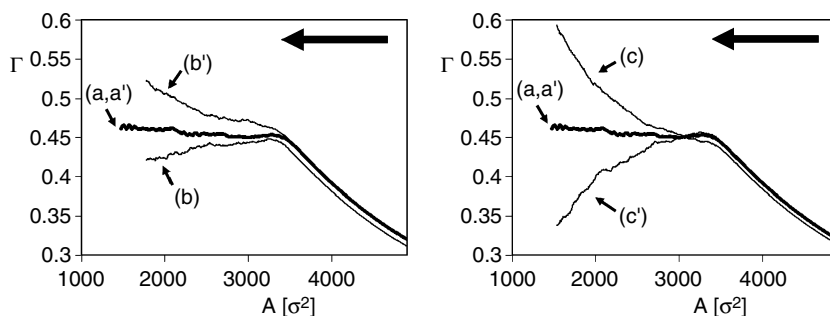
The structures of the four different systems after 6×10^6 equilibration time steps are shown in Figure 23.3. Case (a) represents a perfect mixture since

**FIGURE 23.3**

Interfacial structure of complex mixed interfaces. In (a) two identical non-bond-forming species form a perfect mixture. Mixtures with one species (Type 1) that does not form bonds (dark spheres) and another species (Type 2) that forms transient bonds (light spheres) are shown for different degrees of breakability: (b) $b_{\max} = 0.3$, (c) $b_{\max} = 0.5$, and (d) $b_{\max} = \infty$. The system in case (b) is phase separating, but with a very slow dynamics.

there is no asymmetry in the interactions of the two species. In case (b) a process of phase separation takes place through the aggregation of Type 2 particles, with bonds being created and destroyed during the rearrangement of the clusters. The system is not fully equilibrated at this stage. In cases (c) and (d), the Type 2 particles develop a cross-linked network, i.e., a two-dimensional gel. Particles of Type 1 sit in the gaps of this network. The main difference between cases (c) and (d) is the fact that in case (c) the particles of Type 2 are able to rearrange the particle network by breaking and reforming bonds so as gradually to reduce the system free energy by coarsening. However, this process is so slow that it is not generally observed within the simulation timescale. The structure of this type of monolayer has been reported previously (Pugnaroni et al., 2003); we focus here on its mechanical properties.

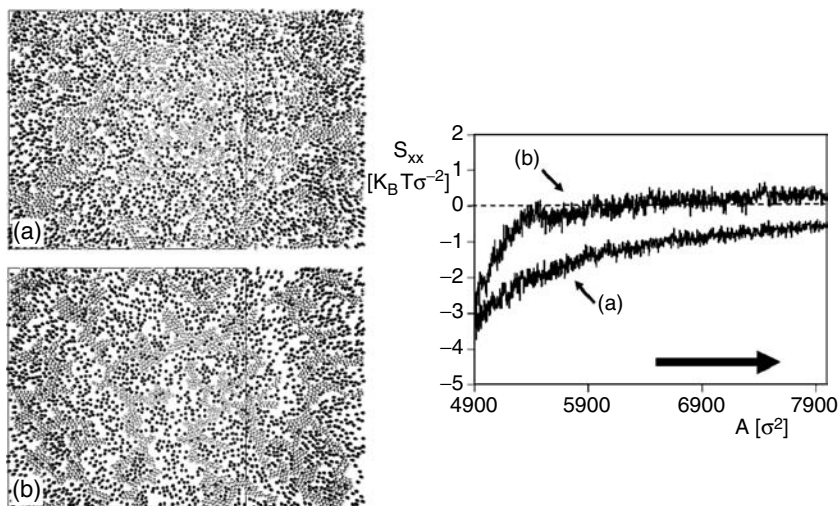
The response of cases (a), (b), and (c) to uniaxial compression ($v_x = 0.132\sigma\tau^{-1}$) is presented in Figure 23.4. The partial area fraction, Γ_α , of each species ($\alpha = 1$ or 2) and the interfacial stress, S_{xx} , in the direction of

**FIGURE 23.4**

Area fraction Γ as a function of the interfacial area A during uniaxial compression of a mixed adsorbed monolayer. The curves (a), (b) and (c) correspond to the partial area fraction of the non-bond-forming species (Type 1) in the systems shown in Figure 23.3(a)–(c). The curves (a'), (b') and (c') correspond to the bond-forming species (Type 2).

compression are shown. We have seen that the stress response is not sensitive to the bond breakability (Pugnaroni et al., 2005a). The desorption of the competing species upon compression does depend on the nature of the bonds formed by the particles of Type 2. Figure 23.4 shows that, in comparison with the symmetric case (a), the desorption beyond the collapse point in the case (b) of very-easy-to-break bonds is mainly caused by the nonbond-forming particles of Type 1. In case (c), however, the bond-forming particles of Type 2 are desorbed preferentially. In this last case, the Type 2 particles tend to remain adsorbed in a secondary layer after displacement by virtue of the bonds that connect them to the Type 2 particles still remaining at the interface. The reason for this change in “competitive desorption” behavior lies in the balance of two effects. On the one hand, particle–particle bonding diminishes the ability of a particle to desorb since it will tend to be attracted to the interface not only by its individual adsorption energy but also by its connected neighbors. On the other hand, once a particle has been displaced from the interface, it will tend to drag its connected neighbors into the bulk solution enhancing the desorption of other particles of its own species. By varying the bond breakability, one is therefore able to change the balance between these two competing effects since very breakable bonds are not able to contribute efficiently to the “drag effect.”

Expansion of complex mixed monolayers does not lead to such large differences. In Figure 23.5(a) we can see the system presented in Figure 23.3(b) after 50% expansion. Figure 23.5(b) corresponds to the expansion of the system in Figure 23.3(c). For very breakable bonds (image (a)), the clusters of particles of Type 2 dissociate upon expansion and the system tends to become more miscible. However, for long-lasting bonds (image (b)), the overall microstructure of the interface seems to remain unchanged except for the reduction in area fraction. The stress response during expansion of the two mixed monolayers is shown on the right hand part of

**FIGURE 23.5**

Snapshots of a mixed interface after 50% uniaxial expansion. Dark spheres represent particles that do not form bonds (Type 1). Light spheres represent bond-forming particles (Type 2). The degree of bond breakability of the Type 2 is (a) $b_{\max} = 0.3$, and (b) $b_{\max} = 0.5$. The interfacial stress S_{xx} as a function of the interfacial area A is shown on the right.

Figure 23.5. In both cases, the stress prior to expansion is negative since the volume exclusion outweighs the positive contribution to the stress from the elastic bonds. During expansion, the system with very-easy-to-break bonds (curve (a)) relaxes slowly. In this case, the set of isolated clusters of particles of Type 2 prevents the elastic bonds from pulling-in from the imaginary moving barrier. The system with long-lasting bonds (curve (b)) seems to relax more rapidly initially. This is due to the initial stretching of the bonds of the percolated network of particles of Type 2, which adds an increasingly positive contribution to the stress. Since the bonds eventually break, the rapid increase in stress is halted at the point at which the percolated network breaks into two disconnected parts.

Conclusions

We have found that the microstructural changes and stress response of our model protein monolayer to uniaxial compression is very sensitive to the nature of the particle–particle interactions. The structural differences of the same systems at equilibrium are much less obvious. These findings suggest that the validation of simulation models by comparing their qualitative behavior under large-deformation compression (expansion) with the experimental results is likely to be more powerful than the comparison of just the equilibrium properties of the adsorbed films.

When particles interact through relatively permanent bonds, the displacement induced by compression leads to wrinkles that line up perpendicular to the direction of compression. This feature has been observed experimentally, for example, for proteins found in lung surfactants (Lipp et al., 1998), and the various desorption mechanisms induced by compression have been identified, for example, in 2-hydroxytetracosanoic acid monolayers (Ybert et al., 2002). Furthermore, we believe that the same type of behavior might also be found for adsorbed milk proteins, especially heat-treated whey proteins. The expansion of films formed by particles that crosslink through transient bonds leads to fracture of the films, a mechanism also seen with globular milk proteins (Hotrum et al., 2003).

Finally, we have shown that the stress response to compression of a mixed system (protein + protein or protein + surfactant) is not significantly affected by the nature of the bonding mechanism of the bond-forming species. In contrast, the “competitive desorption” induced by compression favors the displacement of one or other of the species depending on the extent of breakability of the bonds. This phenomenon seems to arise as a consequence of the delicate balance between a “bond-enhanced adsorption effect” and a “drag-desorption mechanism.”

Acknowledgments

This research was supported by BBSRC (U.K.). Computing was carried out on the Leeds Grid Node 1 facility, funded under the 2001 HEFCE Science Research Investment Fund initiative, at the University of Leeds, a partner in the White Rose Grid project.

References

- Allen, M.P. and Tildesley, D.J. *Computer Simulation of Liquids*, Clarendon Press, Oxford, 1987, chap. 9.
- Dickinson, E. and McClements, D.J. *Advances in Food Colloids*, Blackie, Glasgow, 1995.
- Doi, M. and Edwards, S.F. *The Theory of Polymer Dynamics*, Oxford University Press, New York, 1986, chap. 3.
- Hotrum, N.E., Cohen Stuart, M.A., van Vliet, T., and van Aken, G.A. Flow and fracture phenomena in adsorbed protein layers at the air/water interface in connection with spreading oil droplets, *Langmuir*, 19, 10210, 2003.
- Jones, D.B. and Middelberg, A.P.J. Micromechanical testing of interfacial protein networks demonstrates ensemble behavior characteristic of a nanostructured biomaterial, *Langmuir*, 18, 5585, 2002.
- Lipp, M.M., Lee, K.Y.C., Takamoto, D.Y., Zasadzinski, J.A., and Waring, A.J. Coexistence of buckled and flat monolayers, *Phys. Rev. Lett.*, 81, 1650, 1998.

- Mackie, A.R., Gunning, A.P., Wilde, P.J., and Morris, V.J. Orogenic displacement of protein from the air/water interface by competitive adsorption, *J. Colloid Interface Sci.*, 210, 157, 1999.
- Pugnaloni, L.A., Ettelaie, R., and Dickinson, E. Do mixtures of proteins phase separate at interfaces?, *Langmuir*, 19, 1923, 2003.
- Pugnaloni, L.A., Dickinson, E., Ettelaie, R., Mackie, A.R., and Wilde, P.J. Competitive adsorption of proteins and low-molecular-weight surfactants: computer simulation and microscopic imaging, *Adv. Colloid Interface Sci.*, 107, 27, 2004a.
- Pugnaloni, L.A., Ettelaie, R., and Dickinson, E. Computer simulation of the microstructure of a nanoparticle monolayer formed under interfacial compression, *Langmuir*, 20, 6096, 2004b.
- Pugnaloni, L.A., Ettelaie, R., and Dickinson, E. Computer simulation of interfacial structure and large-deformation rheology during competitive adsorption of proteins and surfactants, *Food Colloids: Interactions, Microstructure and Processing*, E. Dickinson, ed., Royal Society of Chemistry, Cambridge, U.K., 2005a, p. 131.
- Pugnaloni, L.A., Ettelaie, R., and Dickinson, E. Brownian dynamics simulation of adsorbed layers of interacting particles subjected to large extensional deformation, *J. Colloid Interface Sci.*, 287, 401, 2005b.
- Rodríguez Patino, J.M., Carrera Sánchez, C., and Rodríguez Niño, M.R. Analysis of β -casein-monopalmitin mixed films at the air–water interface, *J. Agric. Food Chem.*, 47, 4998, 1999.
- Whittle, M. and Dickinson, E. Brownian dynamics simulation of gelation in soft spheres systems with irreversible bond formation, *Mol. Phys.*, 90, 739, 1997.
- Wijmans, C.M. and Dickinson, E. Brownian dynamics simulation of a bonded network of reversibly adsorbed particles: towards a model of protein adsorbed layers, *Phys. Chem. Chem. Phys.*, 1, 2141, 1999a.
- Wijmans, C.M. and Dickinson, E. Brownian dynamics simulation of the displacement of a protein monolayer by competitive adsorption, *Langmuir*, 15, 8344, 1999b.
- Ybert, C., Lu, W., Möller, G., and Knobler, C.M. Collapse of a monolayer by three mechanisms, *J. Phys. Chem. B*, 106, 2004, 2002.

Effects of Content and Type of Binary Polyol Mixtures on Physical and Mechanical Properties of Starch-Based Edible Films

Riku A. Talja, Harry Helén, Yrjö H. Roos, and Kirsi Jouppila

CONTENTS

Introduction	413
Materials and Methods	414
Results and Discussion	415
Conclusions	418
Acknowledgments	418
References	419

Introduction

Biomaterial films can be used to prevent water sorption by low moisture foods or pharmaceutical solids and, thus, to maintain product quality, and to improve shelf life and storage stability. For many biomaterials water acts as a plasticizer and therefore affects stability and quality (Roos and Karel, 1990, 1991). Hence, it is important to control water sorption properties of low moisture foods or pharmaceutical products. Edible films can be used as barriers or retarders of water sorption of low moisture products.

Before edible films can be applied to foods or pharmaceutical products, it is necessary to obtain knowledge of water sorption, permeability, as well as mechanical properties of edible films. Films with good water vapor barrier properties (low or no water permeation and diffusion through film) should not change or change very little with relative humidity (Lawton, 1996). Films should last under mechanical strain and stress to such an extent that they do not break easily under a reasonable mechanical force. Film-forming techniques and composition of films affect such properties of biomaterial

films as water sorption, water vapor permeability, gas permeability, crystallization of plasticizers, glass-transition temperature, as well as mechanical properties. Materials containing starch can be plasticized, e.g., by water or polyols (Stading et al., 2001; Mathew and Dufresne, 2002).

Crystallization of a polyol, e.g., xylitol or sorbitol, when used singly as a plasticizer at high concentrations, has been observed to occur in starch-based edible films (Krogars et al., 2003; Talja et al., 2003, 2004). Crystallization of plasticizers affects the mechanical properties of starch-based edible films (Talja et al., 2003). The amount of plasticizing polyol (amorphous state) decreases if crystallization of polyol occurs. Thus, Young's modulus and the tensile strength of the film may increase with the concurrent decrease of elongation as a result of crystallization.

In this study, we investigated effects of binary mixtures (1:1) of glycerol, xylitol, and sorbitol on physical and mechanical properties of potato starch-based edible films stored at various relative humidities.

Materials and Methods

Materials used for the edible film preparation were potato starch with amylose content of 14.2% (Evijärven Peruna Ltd., Evijärvi, Finland), glycerol (Dow, Stade, Germany), xylitol (Xyrofin, Kotka, Finland), and sorbitol (Cerestar, Krefeld, Germany). Edible films were prepared using suspensions of binary polyol mixtures (1:1), potato starch, and distilled water. Starch concentration (50 to 80% of solids) was 5% (w/w) of overall water content independently of the content of binary polyol mixtures (20 to 50% of solids). Potato starch-based edible films without plasticizer were also prepared. The suspensions obtained were heated up to 90 to 100°C to gelatinize starch. Starch-based films were obtained then by spreading the warm gel on a Teflon-coated plate using a spreader with a gap of 0.8 mm. Excess water was evaporated in an oven at 35°C.

Water-sorption properties of various films were determined gravimetrically after storage of freeze-dried samples in vacuum desiccators at a relative humidity ranging from 11 to 86% at 25°C. Water-sorption behavior was modeled with the Guggenheim–Anderson–de Boer (GAB) Equation 24.1 in which water content is m , monolayer moisture content is m_m , water activity is a_w , and K and C are constants.

$$\frac{m}{m_m} = \frac{KCa_w}{(1 - Ca_w)[1 + (K - 1)Ca_w]} \quad (24.1)$$

Water vapor permeability (WVP) was determined gravimetrically at 25°C at the relative humidity of 33, 54, and 76% according to ASTM (American Society for Testing Materials) E 96 (ASTM E 96, 2001). Anhydrous CaCl_2 of about 50 g (Baker, J.T., Deventer, The Netherlands), was used as a desiccant. WVP was calculated with Equation 24.2 where mass of water is $m_{\text{H}_2\text{O}}$,

thickness of film is L , permeation area is A , time is t , and difference of water vapor pressure between the inside atmosphere of a cup with a desiccant covered by film and vapor pressure in the desiccator is Δp .

$$WVP = \frac{m_{H_2O}L}{At\Delta p} \quad (24.2)$$

An Instron Universal Testing Machine (model 4465) was used to measure the mechanical properties of the starch-based films. Samples prepared had a width of 10 mm with initial length (grip separation) of 100 mm. A crosshead speed of 100 mm min^{-1} was used. Films were stored at a relative humidity of 33, 54, and 76% for 7 days before measurements.

Results and Discussion

Elastic and flexible potato starch-based films could be prepared fairly well using binary polyol mixtures as plasticizers but brittle films were obtained without plasticizer. Potato starch-based films plasticized with glycerol–polyol used and xylitol–sorbitol mixtures with content up to 40 and 50%, respectively, were easy to handle. Potato starch-based films were sticky with the glycerol–polyol content of 50% and thus difficult to handle. The thickness obtained for starch-based films was in the range of 33 to $74 \mu\text{m}$.

The amount of sorbed water of the films increased with increasing relative humidity. Water contents in steady state were reached within 48 h of storage. At water activities below ~ 0.6 films without plasticizer had higher water contents than films with plasticizer (Figure 24.1). Similar results were obtained by Talja et al. (2003) for films plasticized with a single polyol and by Saravacos and Stinchfield (1965) for a freeze-dried gelatinized starch and glucose mixture. With increasing plasticizer content of starch-based films the water content increased and the extent of the increase was more pronounced at high relative humidity (Figure 24.1). At a constant starch–plasticizer ratio with a plasticizer content of 30%, the films plasticized with glycerol–xylitol

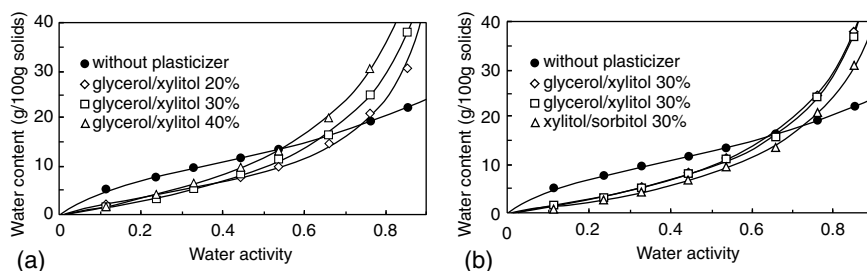


FIGURE 24.1

Water sorption isotherms for starch-based edible films plasticized with different contents (a) and types (b) of binary polyol mixtures at 25°C .

and glycerol–sorbitol mixtures gained approximately the same water content but films plasticized with xylitol–sorbitol mixtures gained lower water content (Figure 24.1). Talja et al. (2003) also found that at constant starch–plasticizer ratio films plasticized with a single lower molecular weight polyol had lower water content than films containing a higher molecular weight plasticizer. Moisture content corresponding to the monolayer covering for films without plasticizer and with a plasticizer content of 20% was reached at water activities of 0.39 and 0.34, respectively, independently of the kind of the plasticizer. At higher plasticizer contents (30 and 40%) moisture contents for monolayer covering were reached at a water activity around 0.5. Films without plasticizer and with any plasticizer at 20% showed sigmoidal and slightly sigmoidal sorption isotherms, respectively (Figure 24.1).

The effect of relative humidity on water vapor permeability of films was similar to the water sorption results. Water vapor permeability of potato starch-based films without plasticizer was generally higher than that of starch-based films plasticized with different binary polyol mixtures independent of relative humidity (Figure 24.2). One exception for this was films plasticized with 50% glycerol–xylitol and glycerol–sorbitol mixtures at the relative humidity of 33%. Water vapor permeability increased with increasing plasticizer content. Films plasticized with glycerol–xylitol and xylitol–sorbitol mixtures had the highest and lowest water vapor permeability at fixed plasticizer content. Talja et al. (2004) reported that water vapor permeability of starch-based films increased with decreasing glass transition temperature of the binary polyol plasticizer and with increasing relative humidity. Talja et al. (2004) reported glass transition temperatures of -61 , -57 , and -15°C for binary polyol mixtures of glycerol–xylitol, glycerol–sorbitol, and xylitol–sorbitol, respectively. Moreover, glass-transition temperatures of starch-based films with a plasticizer content of 40% decreased as a result of plasticization by binary polyol mixtures and with increasing water content (Talja et al., 2004).

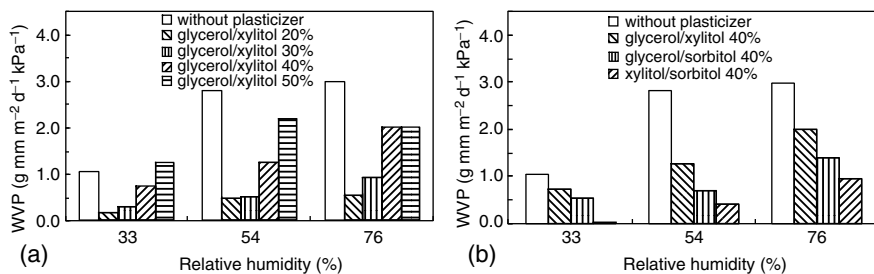


FIGURE 24.2

Water vapor permeability (WVP) for starch-based films plasticized with different contents (a) and types (b) of binary polyol mixtures at various relative humidities at 25°C .

Values of tensile strength at breaking point for films plasticized with binary polyol mixtures decreased with increasing plasticizer content and storage relative humidity (Figure 24.3). Values of Young's modulus changed concurrently with tensile strength. Effects of any binary polyol plasticizer with 20% content on elongation at breaking point were similar at the storage relative humidity of 33 and 54%. At these relative humidities, approximately 5% elongation was observed for all films with plasticizer content of 20% whereas elongation was 33 to 40% at a relative humidity of 76%. For films with binary polyol content of 30%, elongations of 6 to 9%, 46 to 75%, and 46 to 60% were observed at relative humidities of 33, 54, and 76%, respectively. Elongation of 76 to 110% was observed as plasticizer content increased from 30 to 40% at storage relative humidity of 33%, whereas elongation was 30 to 48% at relative humidities of 54 and 76%. Elongation of starch-based films with a plasticizer content of 20 and 30% increased with increasing storage relative humidity. Effects of binary polyol plasticizers on elongation at breaking point were largest for glycerol–xylitol and smallest for xylitol–sorbitol mixtures at a fixed starch–plasticizer ratio at any relative humidity. However, elongation decreased at the 40% plasticizer content as the storage relative humidity increased from 33% to 54 and 76%, as shown in Figure 24.3. Similar elongation behavior was observed for films with xylitol–sorbitol content of 50%.

Young's moduli reported by Talja et al. (2003) for films plasticized with a single polyol decreased with decreasing molecular weight of the polyol coinciding with an increase in elongation. An exception to this was films plasticized by xylitol in which crystallization of xylitol was observed to result in a concurrent increase in Young's modulus and a decrease in elongation at a relative humidity of 54 and 76% (Talja et al., 2003). Polyol crystallization was not observed when binary polyol mixtures were used as plasticizers in starch-based edible films. Krogars et al. (2003) reported that crystallization of sorbitol in maize starch-based films was not observed during 9 months of storage at 25°C and relative humidity of 60% using a binary polyol mixture of glycerol–sorbitol (1:1) as a plasticizer at a content of 33 and 50% (w/w, solids).

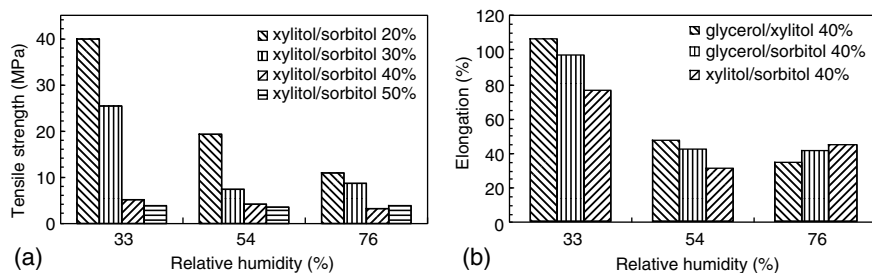


FIGURE 24.3

Mechanical properties for starch-based edible films plasticized with different contents (a) and types (b) of binary polyol mixtures and stored at various relative humidities.

Overall, the best properties for potato starch-based films studied in this work were observed in xylitol–sorbitol plasticized films. Such films were easy to handle and they were not sticky like glycerol–polyol plasticized films at a high plasticizer content and high relative humidity. Water sorption and water vapor permeability were lower for the films plasticized with xylitol–sorbitol mixture compared with the films plasticized with glycerol–xylitol and glycerol–sorbitol mixtures at constant plasticizer contents. The glass-transition temperature of xylitol–sorbitol mixture was higher than glycerol–sorbitol and glycerol–xylitol mixtures (Talja et al., 2004). Generally, water vapor permeability and elongation of potato starch-based films decreased as the glass-transition temperature of the plasticizing polyol mixture increased.

Consideration of functional properties of starch-based films is important if they are used to increase the quality and shelf life of foods and pharmaceutical products. The main function of film could be to prevent mass transfer of water or other compounds, such as oxygen, carbon dioxide, oil, and aroma compounds, between the product and the surroundings or between different layers of a product. The function of film could also be to act as a carrier of an antimicrobial substance, aroma compounds, or coloring agents or to improve the mechanical handling of foods or pharmaceutical products.

Conclusions

Elastic and flexible potato starch-based films plasticized with different binary polyol mixtures could be prepared successfully. The water sorption and water vapor permeability of potato starch-based edible films increased as a result of plasticization by binary polyol mixtures. Generally, the Young's modulus and tensile strength at breaking point decreased and elongation at breaking point increased with the increasing plasticization effect of the binary polyol mixture. Crystallization of polyol was not observed when binary polyol mixtures were used as plasticizers. These basic data on the effects of water and plasticizer contents on the physical and mechanical properties of starch-based edible films are important in assessing the applicability of starch-based edible films in the food and pharmaceutical industries. Films studied in the present work are suggested to be suitable for low moisture foods and pharmaceutical products.

Acknowledgments

Funding from Tekes (National Technology Agency of Finland) and ABS (The Finnish Graduate School on Applied Bioscience: Bioengineering, Food & Nutrition, Environment), Plastiroll Ltd. and Evijärven Peruna Ltd.

References

- ASTM E 96, Standard methods of test for water vapor transmission of materials in sheet forms, *Annual Book of ASTM Standards*, American Society for Testing and Materials, Philadelphia, 2001.
- Krogars, K., Heinämäki, J., Karjalainen, M., Niskanen, A., Leskelä, M., and Yliruusi, J. Enhanced stability of rubbery amylose-rich maize starch films plasticized with a composition of sorbitol and glycerol, *Int. J. Pharm.*, 251, 205, 2003.
- Lawton, J.W. Effect of starch type on the properties of starch containing films, *Carbohydr. Polym.*, 29, 203, 1996.
- Mathew, A.P. and Dufresne, A. Plasticized waxy maize starch: effect of polyols and relative humidity on material properties, *Biomacromolecules*, 3, 1101, 2002.
- Roos, Y. and Karel, M. Differential scanning calorimetry study of phase transitions affecting the quality of dehydrated materials, *Biotechnol. Prog.*, 6, 159, 1990.
- Roos, Y. and Karel, M. Plasticizing effect of water on thermal behavior and crystallization of amorphous food models, *J. Food Sci.*, 56, 38, 1991.
- Saravacos, G.D. and Stinchfield, R.M. Effect of temperature and pressure on the sorption of water vapor by freeze-dried food materials, *J. Food Sci.*, 30, 779, 1965.
- Stading, M., Rindlav-Westling, Å., and Gatenholm, P. Humidity-induced structural transitions in amylose and amylopectin films, *Carbohydr. Polym.*, 45, 209, 2001.
- Talja, R.A., Helén, H., Roos, Y.H., and Jouppila, K., Physical properties of starch-based edible films plasticized with binary polyol mixtures, *The Ninth International Congress on Engineering and Food (ICEF9)*, Montpellier, France, March 7–11, 2004, Extended abstract #918.
- Talja, R.A., Jouppila, K., Helén, H., and Roos, Y.H., Physical properties of starch-based edible films, *The IFT Annual Meeting*, Chicago IL, USA, July 12–16, 2003. Abstract #60A-26.

The Dynamics of Formation and Structure of the Air–Water Interface in the Presence of Protein–Polysaccharide Mixtures

Rosa Baeza, Cecilio Carrera-Sánchez, Juan Miguel Rodríguez-Patino, and Ana M.R. Pilosof

CONTENTS

Introduction	421
Materials and Methods	422
Preparation of Solutions	422
Automatic Drop Tensiometer	423
Results	423
Dynamics of Adsorption	423
Adsorption Kinetics	425
Viscoelastic Characteristics of Air–Water Interface	427
Conclusions	428
Acknowledgments	428
References	429

Introduction

Proteins and polysaccharides (PS) are present in many kinds of foods. The main role of proteins in foamed products is to stabilize the air–water interface through their capacity to lower the surface tension of water (Damodaran and Paraf, 1997). β -Lactoglobulin (β -lg), the most abundant protein in whey, is a globular protein of molecular mass 18.3 kDa being stabilized by two internal disulfide cross-linkings, and exhibits good foaming properties.

The structural and dynamic properties of β -lg at the air–water interface have been extensively studied in past years (Patino et al., 2001a; Horne and

Patino, 2003). PS are widely used for stabilization of food emulsions and foams (Renard et al., 2002). Most high-molecular-weight PS, being hydrophilic, do not have much of a tendency to adsorb at the air–water interface, but they can strongly enhance the stability of protein foams by acting as thickening or gelling agents (Dickinson, 2003). Recently, we have described the characteristics of β -lg/polysaccharides spread monolayers through static measurements performed in a film-type balance (Baeza et al., 2004a). Polysaccharides with or without interfacial activity have considerable effects on the surface pressure evolution and rheological properties of the air–water interface.

In the present work we have studied the dynamics of formation and structure of the air–water interface in the presence of β -lg + PS at 20°C and at pH 7 in a drop tensiometer. As PS with interfacial activity we have used propylene glycol alginates (PGA). To evaluate the effect of the degree of PGA esterification and viscosity, different commercial samples were studied. Xanthan gum (X) and λ -carrageenan (λ -c) were studied as nonsurface active polysaccharides.

Materials and Methods

Preparation of Solutions

β -Lg was supplied by Danisco Ingredients (Denmark). The powder contained 92% of protein, being β -lg >95% and α -lactalbumin <5%. The polysaccharides λ -c and X were provided by BIOTEC (Argentina) and PGA were from ISP Alginates. The PGA used were Kelcoloid O (KO), Kelcoloid LVF (KLVF), and Manucol ester (MAN). The degree of esterification and viscosity of these PGA are shown in Table 25.1.

The powder samples were dissolved in Milli-Q ultrapure water at room temperature and pH was adjusted to 7 by a commercial buffer solution (Sigma >99.5%) called *trizma* ($((\text{CH}_2\text{OH})_3\text{CNH}_2)/(\text{CH}_2\text{OH})_3\text{CNH}_3\text{Cl}$). The ionic

TABLE 25.1
Degree of Esterification and Viscosity of Propylene Glycol
Alginates

PGA	Degree of Esterification	Viscosity ^a
Manucol ester (MAN)	High	High (11.8 cP)
Kelcoloid LVF (KLVF)	Medium	High (13.9 cP)
Kelcoloid O (KO)	High	Low (4.7 cP)

^a Viscosity (at a shear rate of 60 sec⁻¹) of 0.5 wt% solution.

strength was 0.05 M in all the experiments. The concentration of protein alone or in the mixed systems was 0.1 wt% and polysaccharide concentration varied between 0.1 and 0.5 wt%.

Automatic Drop Tensiometer

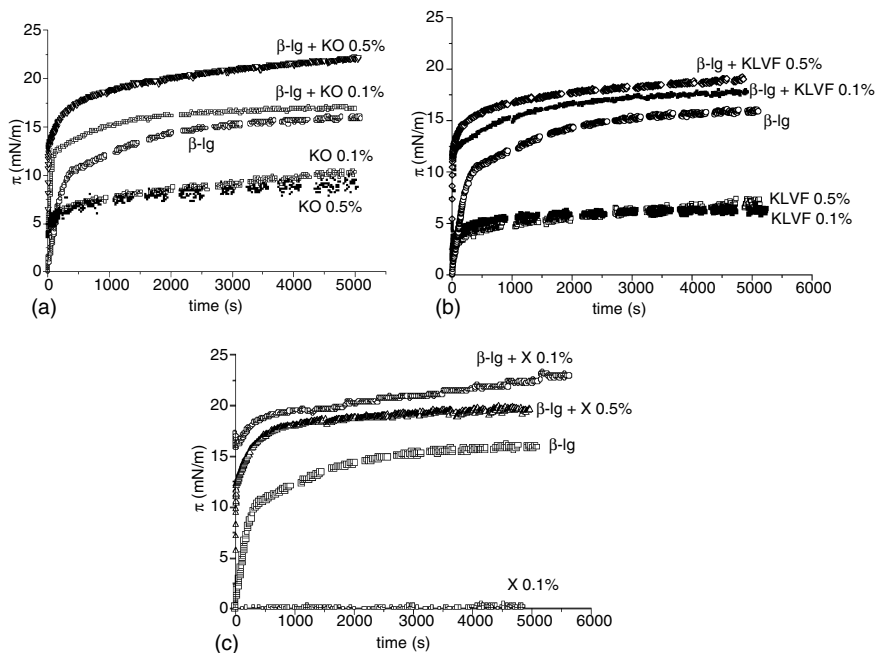
The existence of β -lg–PS interactions at the air–water interface was evaluated by monitoring the dynamics of surface pressure (π) evolution of single components and mixed systems. Time-dependent surface pressure and dilatational modulus (Ed) measurements of adsorbed β -lg, PS and β -lg/PS mixed films at the air–water interface were performed by an automatic drop tensiometer (IT-Concept, France) as described elsewhere (Niño and Patino, 2002). Protein and/or polysaccharide solutions were prepared freshly by weighing proper amounts of protein and/or polysaccharide and buffer solution in order to attain the desired protein concentration in solution, and then stirred for 30 min. The protein and/or polysaccharide solution was placed in a 15 μ l glass Hamilton syringe equipped with a stainless steel needle and then in a rectangular glass cuvette (5 ml) covered by a compartment, which was maintained at constant temperature ($20 \pm 0.2^\circ\text{C}$) by circulating water from a thermostat and allowed to stand for 30 min to reach constant temperature and humidity in the compartment. Then a drop of protein and/or polysaccharide solution (5 to 8 μ l) was delivered and allowed to stand at the tip of the needle for about 100 min to achieve the adsorption equilibrium at the air–water interface. The image of the drop was continuously taken by a CCD camera and digitalized. The surface tension (σ) was calculated through analyzing the profile of the drop (Niño and Patino, 2002). The surface pressure is $\pi = \sigma^0 - \sigma$, where σ^0 is the surface tension of pure water in the absence of any surface-active component.

The average accuracy of the surface tension is roughly 0.1 mN/m. However, the reproducibility of the results (for at least two measurements) was better than 1%.

Results

Dynamics of Adsorption

The transient surface pressure (π) of adsorbed β -lg, PS and mixed β -lg/PS systems was determined. Figure 25.1 shows π –time curves for the systems with KO, KLVE, and X. The increase in the surface pressure with time observed for β -lg should be associated with protein adsorption at the air–water interface (Graham and Phillips, 1979; Damodaran and Song, 1988). The value of surface pressure after long adsorption time of 5000 sec, $r(\pi_{5000})$ for 0.1 wt% protein concentration was 14 mN/m, a value close to that

**FIGURE 25.1**

Time dependent surface pressure (π) for β -lg, PS and mixed β -lg/PS adsorbed films at the air–water interface. β -lg concentration in the bulk phase 0.1 wt%, Temperature 20°C, pH 7 Ionic strength, 0.05 M. β -Lg/PS sytems: (a) β -lg + KO, (b) β -lg + KLVF, (c) β -lg + X.

reported for the transition from a monolayer with a more expanded structure towards a monolayer in which the protein forms a more condensed structure (Graham and Phillips, 1979; Horne and Patino, 2003). In a previous study we have shown that a higher surface pressure (23 mN/m) is achieved at higher β -lg concentration in the bulk phase (2 wt%) (Baeza et al., 2004a, 2005a), which indicates that at the concentration used in this study the interface is not saturated. However, the shapes of the π – t curves for β -lg/mixed systems in Figure 25.1 indicate that even at low concentrations, the protein determines the interfacial behavior of the mixed systems.

In the case of single PGA films (Figure 25.1a and b), the surface pressure reached lower values (up to 10 mN/m), and an increase in polysaccharide concentration (0.5 wt%) did not produce a significant additional increase in surface pressure, indicating that the interface would be saturated at 0.1 wt% (Baeza et al., 2004b). The surface pressure after long term showed the following order: KO > MAN > KLVF (not shown). The highest surface activity of KO is consistent with the high degree of esterification and low viscosity (i.e., the lower molecular weight) of this PGA (Table 25.1).

X and λ -c, being highly hydrophilic PS, are not considered to be surface-active agents. In fact, X did not cause an increase in surface pressure

(Figure 25.1c), which was consistent with previous reports (Carp et al., 2001). However, λ -c caused a linear increase of surface pressure as a result of adsorption after 1000 sec that may be caused by small amounts of surface-active contaminants present in the λ -c preparation (i.e., proteins) (Huang et al., 2001).

When β -lg adsorbs at the air–water interface in the presence of PS three phenomena can occur: (i) the polysaccharide adsorbs at the interface on its own in competition with the protein for the interface (competitive adsorption) (ii) the polysaccharide complexes with the adsorbed protein mainly by electrostatic interactions or hydrogen bonding (Dickinson, 2003), and (iii) because of a limited thermodynamic compatibility between the protein and polysaccharide, the polysaccharide concentrates the adsorbed protein. In a previous work we have shown that the existence of competitive or cooperative adsorption between the β -lg and the PS could be deduced from the comparison of π –time curves for the single biopolymers and for the mixtures (Baeza et al., 2005b).

The π values of β -lg/PGA films (0.1 wt% PGA in the bulk phase) showed an antagonistic behavior when compared to the π of single β -lg and PGA films, which should be attributed to their high degree of esterification (higher hydrophobicity) that allows them to rapidly adsorb at the interface. However, in the presence of KO at 0.5% (Figure 25.1a), the system showed a more cooperative adsorption. Similarly, KLVF at 0.5% increased π of the mixed system. The increased cooperativity as PGA increased from 0.1 to 0.5% may be ascribed to an increase of segregation phenomena in the bulk solution.

The existence of a limited thermodynamic incompatibility between protein and polysaccharide may improve the amount of adsorbed protein (Burova et al., 1992; Dickinson, 2003). As X did not increase the surface pressure (Figure 25.1), the significant increase in π of the mixed system indicated a strong synergism between those biopolymers. Because of the high molecular weight and anionic character, X would promote at pH 7 segregation phenomena in the bulk solution (Sanchez et al., 1997; Baeza and Pilosof, 2001). It has been demonstrated that X addition to soy protein solutions at neutral pH had an effect similar to that observed by increasing protein concentration, arising mainly from excluded volume effects (Carp et al., 1999).

In the presence of X and λ -c (nonsurface-active PS with high viscosity), a higher concentration of PS in the bulk phase led to a decrease in surface pressure of mixed films. It may indicate that a higher viscosity would interfere in the adsorption of β -lg at the interface.

Adsorption Kinetics

The kinetics of adsorption at the air–water interface can be monitored by measuring changes in surface pressure (π) with time. During the first step, at relatively low surface pressures when diffusion is the rate-determining step,

a modified form of the Ward and Today equation (Ward and Today, 1946) can be used to correlate the change in the surface pressure with time:

$$\pi = 2C_0KT(Dt/3.14)^{1/2} \quad (25.1)$$

where C_0 is the concentration in the bulk phase, K is the Boltzmann constant, T is the absolute temperature, and D is the diffusion coefficient. If the diffusion at the interface controls the adsorption process, a plot of π against $t^{1/2}$ will then be linear (Mc Ritchie, 1978; De Feijter and Benjamins, 1987) and the slope of this plot will be the diffusion rate (k_{diff}).

The rate of penetration and rearrangements of adsorbed protein molecules have been analyzed by a first-order reaction (Tornberg, 1978; Graham and Phillips, 1979; Suttiprasit et al., 1992):

$$\text{Ln}(\pi_f - \pi_t)/(\pi_f - \pi_0) = -k_i t \quad (25.2)$$

where π_f , π_0 , and π_t are the surface pressures at the final adsorption time of each step, t_f , at the initial time t_0 and at time t , respectively, and k_i is the first-order rate constant. In practice, a plot of Equation 25.2 usually yields two or more linear regions. The initial slope is taken to correspond to a first-order rate constant of penetration (k_p), while the second slope corresponds to a rate constant of protein rearrangement (k_R) (Patino et al., 1999). The application of Equation 25.1 and Equation 25.2 to the adsorption kinetics of a milk and soy protein to evaluate the rates of diffusion, penetration, and rearrangement of protein at the air–water interface has been discussed by Horne and Rodríguez Patino, and Rodríguez Niño and Rodríguez Patino (Niño and Patino, 2002; Horne and Patino, 2003).

Figure 25.2 shows the diffusion rate for β -lg (0.1%) and β -lg (0.1 wt%)/PS (0.1 to 0.5%) adsorption at the air–water interface. In the case of surface-active KLVE (Figure 25.2a), its diffusion rate is included.

The presence of PGA and λ -c increased the diffusion rate, and the effect became more evident at higher PS concentrations. Xanthan promoted a

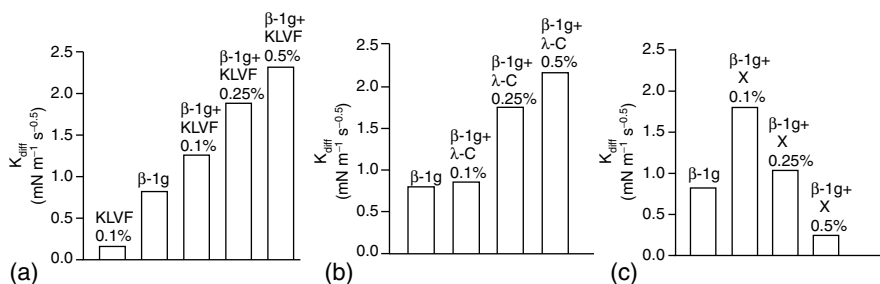


FIGURE 25.2

Diffusion rate for adsorption of β -lg, PS or mixed β -lg/PS systems at the air–water interface at 20°C and pH 7. β -Lg concentration in the bulk phase 0.1 wt%. (a) β -Lg + KLVE, (b) β -Lg + λ -c, (c) β -Lg + X.

faster diffusion of β -lg only at lower concentrations as a result of increased viscosity effects with the concentration increase.

An increase in diffusion rates occurs as a consequence of increasing protein bulk concentration (Patino et al., 1999; Horne and Patino, 2003; Baeza et al., 2004a). Excluded volume effects can have an effect similar to increasing protein concentration because of the increased thermodynamic activity of the protein in the bulk solution — that would perform as a more concentrated one (Carp et al., 1999) — and can lead to an enhancement of protein adsorption at fluid interfaces (Tsapkina et al., 1992).

The long-term adsorption kinetics for β -lg is controlled by the unfolding and further rearrangement of adsorbed molecules (Patino et al., 2001b). The presence of PS decreased the rearrangement rate of β -lg molecules at the interface from $1.16 \times 10^{-3} \text{ min}^{-1}$ for β -lg film to an average of $4 \times 10^{-4} \text{ min}^{-1}$ for the mixed systems. The implication of some protein patches in electrostatic interactions with X or λ -c or the penetration of PGA into the interface would interfere with the interactions between β -lg molecules resulting in a decrease in the rates of rearrangement of the adsorbed protein.

Viscoelastic Characteristics of Air–Water Interface

The surface dilatational modulus of β -lg (0.1 wt%), PS (0.1 and 0.5 wt%) and β -lg/PS (0.1 to 0.5 wt%) mixed films as a function of time are shown in Figure 25.3.

The protein film showed a higher E_d than PS films, which reveals the ability of protein to form a structured film with solid characteristics, even at relatively low β -lg concentrations in the bulk phase. For PGA films, the surface dilatational modulus increased in the order of KO > MAN > KLVF, reaching values from 5 to 17 mN/m. These results indicate the formation of a film with high viscoelasticity that may be caused by the association of PGA molecules at the interface. This association would involve interactions between the esterified hydrophobic regions in PGA molecules giving a gel-like film (Baeza et al., 2004b). Figure 25.3a and b also shows that the dilatational modulus for KO and KLVF was decreased at 0.5% in the bulk phase compared with 0.1%. This behavior could be related to the collapse of the films.

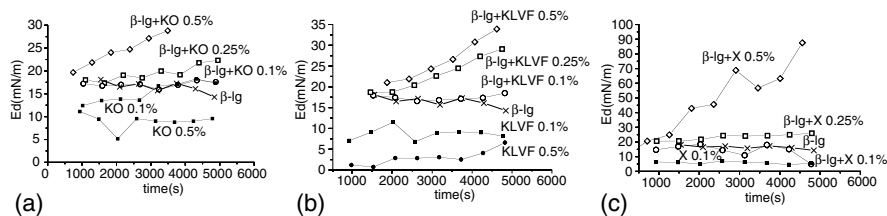


FIGURE 25.3

Time-dependent surface dilatational modulus (E_d) for β -lg, PS and β -lg/PS adsorbed films at the air–water interface at 20°C and pH 7. (a) β -Lg + KO, (b) β -lg + KLVF, (c) β -lg + X.

As X is not surface active, the low values of E_d (Figure 25.3c) may be attributed to the structurization ability of the molecules in the proximity of the air–water interface.

In the mixed systems, the behavior was similar to that observed for surface pressure. In the presence of surface-active PGA (Figure 25.3a and b) at low concentrations in the bulk phase (0.1 wt%), competition between the biopolymers at the interface results in a lower E_d than that expected from the observation of the single components. However, at higher concentrations of PS and long adsorption times, a cooperative adsorption can be deduced. This result could be explained by a concentration of β -lg at the interface caused by the incompatibility with different biopolymers (that is more evident at higher concentrations). These phenomena would lead to an increase in the protein association in the film with the resultant increase in viscoelasticity.

One possible interpretation of the increased viscoelasticity obtained in the presence of nonsurface-active X (Figure 25.3c) and λ -c is that they adsorb onto the protein film, forming a combined structure with a primary protein layer predominantly in contact with the air phase (Baeza et al., 2005b).

Conclusions

The results revealed a significant effect of surface-active and nonsurface active polysaccharides on the properties of adsorbed protein films at the air–water interface. To explain the observed effects on the dynamics of adsorption, the rates of diffusion and rearrangement and the surface dilatational modulus were taken into account: (i) the competitive adsorption, (ii) the complexation, and (iii) the existence of a limited thermodynamic compatibility between protein and polysaccharide at the air–water interface and in the aqueous bulk phase.

Nonsurface-active PS as X strongly increase the surface pressure and the elastic character of the interfacial film. This unexpected behavior would arise from incompatibility with the aqueous bulk phase and possible complexation onto the adsorbed protein.

Surface-active PGA compete with the protein for the interface. Depending on the concentration and molecular structure they can show they can behave in a competitive manner or additive. Among the different PGA, KO (highest degree of esterification and lowest viscosity) would perform most cooperatively in the presence of β -lg.

Acknowledgments

This research was supported by CYTED through project XI.17 and CICYT through grant AGL2001-3843-C02-01. The authors also acknowledge the

support from Universidad de Buenos Aires, Agencia Nacional de Promoción Científica y Tecnológica and Consejo Nacional de Investigaciones Científicas y Técnicas de la República Argentina.

References

- Baeza, R. and Pilosof, A.M.R. Mixed biopolymer gel systems of β -lactoglobulin and non gelling gums, *Food Colloids 2000: Fundamentals and Formulation*, E. Dickinson and R. Miller, eds., The Royal Society of Chemistry, Cambridge, pp. 392, 2001.
- Baeza, R., Carrera, C., Pilosof, A.M.R., and Patino, J.M.R. Interactions of polysaccharides with β -lactoglobulin spread monolayers at the air–water interface, *Food Hydrocolloids*, 18, 959, 2004a.
- Baeza, R., Carrera, C., Pilosof, A.M.R., and Patino, J.M.R. Interfacial and foaming properties of propylenglycol alginates. Effect of degree of esterification and molecular weight, *Colloids Surf. B: Biointerfaces*, 36, 139, 2004b.
- Baeza, R., Carrera, C., Pilosof, A.M.R., and Patino, J.M.R. Interactions of polysaccharides with β -lactoglobulin adsorbed films at the air–water interface, *Food Hydrocolloids*, 19, 239, 2005a.
- Baeza, R., Carrera, C., Pilosof, A.M.R., and Patino, J.M.R. Interactions between β -lactoglobulin and polysaccharides at the air–water interface and the influence of foaming properties, *Food Colloids 2004: Interactions, Microstructure and Processing*, E. Dickinson, ed., Royal Society of Chemistry, Cambridge, pp. 301, 2005b.
- Burova, T., Grinberg, N., Grinberg, V.Ya., Leontiev, A.L., and Tolstoguzov, V.B. Effects of polysaccharides upon the functional properties of 11S globulin of broad beans, *Carbohydr. Polym.*, 18, 101, 1992.
- Carp, D.J., Bartholomai, G.B., and Pilosof, A.M.R. Electrophoresis studies for determining soy proteins–xanthan gum interactions in foams, *Colloids Surf. B: Biointerfaces*, 12, 309, 1999.
- Carp, D.J., Bartholomai, G.B., Relkin, P., and Pilosof, A.M.R. Effects of denaturation on soy protein–xanthan interactions: comparison of a whipping-rheological and a bubbling method, *Colloids Surf. B: Biointerfaces*, 21, 163, 2001.
- Damodaran, S. and Paraf, A. *Food Proteins and Their Applications*, Marcel Dekker, New York, 1997.
- Damodaran, S. and Song, K.B. Kinetics of adsorption of protein at interfaces: role of protein conformation in diffusional adsorption, *Biochim. Biophys. Acta*, 954, 253, 1988.
- De Feijter, J. and Benjamins, J. Adsorption kinetics of proteins at the air–water interface, *Food Emulsions and Foams*, E. Dickinson, ed., The Royal Society of Chemistry, London, pp. 72, 1987.
- Dickinson, E. Hydrocolloids at interfaces and the influence on the properties of dispersed systems, *Food Hydrocolloids*, 17, 25, 2003.
- Graham, D.E. and Phillips, M.C. Proteins at liquid interfaces III. Molecular structures of adsorbed films, *J. Colloid Interface Sci.*, 70, 427, 1979.
- Horne, D.S. and Patino, J.M.R. Adsorbed biopolymers: behavior in food applications, *Biopolymers at Interfaces*, M. Malmsten, ed., Marcel Dekker, New York, pp. 857, 2003.

- Huang, X., Kakuda, Y., and Cui, W. Hydrocolloids in emulsions: particle size distribution and the interfacial activity, *Food Hydrocolloids*, 15, 533, 2001.
- McRitchie, F. Protein at interfaces, *Adv. Protein Chem.*, 32, 283, 1978.
- Niño, M.R.R. and Patino, J.M.R. Effect of the aqueous phase composition on the adsorption of bovine serum albumin to the air–water interface, *Ind. Eng. Chem. Res.*, 41, 1489, 2002.
- Patino, J.M.R., Niño, M.R.R., and Sánchez, C.C. Adsorption of whey protein isolate at the oil–water interface as a function of processing conditions: a rheokinetic study, *J. Agric. Food Chem.*, 47, 3640, 1999.
- Patino, J.M.R., Carrera, C., Niño, M.R.R., and Cejudo, M. Structural and dynamic properties of milk proteins spread at the air–water interface, *J. Colloid Interface Sci.*, 242, 141, 2001a.
- Patino, J.M.R., García, J.M.N., and Niño, M.R.R. Protein–lipid interactions at the oil–water interface, *Colloid Surf. B: Biointerfaces*, 21, 207, 2001b.
- Renard, D., Della Valle, G., and Popineau, Y. *Plant biopolymer science, Food and Non Food Applications*. The Royal Society of Chemistry, Cambridge, 2002.
- Sanchez, C., Schmitt, C., Babak, V.G., and Hardy, J. Rheology of whey protein isolate xanthan mixed solutions and gels. Effect of pH and xanthan concentration, *Nahrung*, 41, 336, 1997.
- Suttiprasit, F., Krisdahasima, V., and McGuire, J. The surface activity of α -lactalbumin, β -lactoglobulin and BSA I, *J. Colloid Interface Sci.*, 154, 316, 1992.
- Tornberg, E. The application of the drop volume technique to measurements of the adsorption of proteins at interfaces, *J. Colloid Interface Sci.*, 154, 316, 1978.
- Tsapkina, E.N., Semenova, M.B., Pavlovskaya, G.E., and Tolstoguzov, V.B. The influence of incompatibility on the formation of adsorbing layers and dispersions of n-decane emulsion droplets in aqueous solution containing a mixture of 11S globulin from *Vicia faba* and dextran, *Food Hydrocolloids*, 6, 237, 1992.
- Ward, A. and Todai, L. Time dependence of boundary tensions of solutions I. The role of diffusion in time effects, *J. Chem. Phys.*, 14, 353, 1946.

Mechanical and Water Vapor Properties of Gelatin-Based Films as Function of Relative Humidity, Temperature, and Film Thickness

Rosemary A. Carvalho, Paulo José do Amaral Sobral, and
Florença C. Menegalli

CONTENTS

Introduction	431
Material and Methods.....	432
Material.....	432
Production of Films	432
Mechanical Properties	432
Water Vapor Permeability.....	433
Results and Discussion	433
Mechanical Properties	433
Water Vapor Permeability.....	435
Conclusions.....	436
References	436

Introduction

The gelatin is a biopolymer with good functional properties, produced abundantly at relatively low cost, and thus very interesting to edible films technology. Edible films based on hygroscopic biopolymers and plasticizers are strongly affected by intrinsic and extrinsic factors. The intrinsic factors are related to the macromolecule chemical nature. The macromolecule structure and configuration influence the polymeric matrix interactions involved during dehydration in film formation (Miller and Krochta, 1997). However, the intensity of the protein–protein and protein–solvent interactions can be manipulated by controlling the film formation conditions and the plasticizers (Sánchez et al., 1998).

In general, water has a strong plasticizer effect in hygroscopic biopolymers like gelatin (Sobral and Habitate, 2001). These macromolecules contain hydrophilic groups capable of absorbing water molecules by hydrogen bonds. This absorbed moisture can provoke disruption of intermolecular interactions affecting the films properties (McHugh and Krochta, 1994).

Thus, the relative humidity and the room temperature are important extrinsic factors concerning the functional properties of edible films (Gennadios et al., 1993). Beyond these factors, the film properties can also be influenced by the film thickness (Sobral, 1999). Thus, the objective of this work was to study the effect of the relative humidity during conditioning and of the film thickness on the mechanical properties, and the effect of the temperature and film thickness on the water vapor permeability (WVP) of gelatin-based films plasticized by glycerol.

Material and Methods

Material

Type B gelatin (Leiner Davis Brasil, Bloom = 252 g, moisture content = 10.5%), glycerol (MERCK), sodium hydroxide (MERCK), magnesium chloride (SYNTH), sodium nitrate (SYNTH), sodium chloride (SYNTH), and sodium sulphate (SYNTH) were used in this study.

Production of Films

The films were prepared according to the following steps: gelatin hydration (15 g/100 g of film forming solution) in distilled water (room temperature, 20 min), solubilization (55°C, 30 min) in thermostatic bath (Tecnal, TEO39), and plasticizer addition (45 g glycerol/100 g of gelatin) along constant agitation. The filmogenic solution was poured in acrylic plates (9.5 × 19.0 cm) and dried (35°C, 24 h) in a forced ventilation oven (Tecnal, MA037). The film thickness was determined using a micrometer (resolution 0.01 mm, TESA) corresponding to the arithmetic mean value of 20 random measures over the film area. The film forming solutions were applied using different grammage values (mass/area) to provide films with different thicknesses between 0.13 and 0.32 mm.

Mechanical Properties

The films used for the mechanical tests were previously conditioned for 48 h at 20°C (climatized room) inside desiccators containing saturated saline solutions of MgCl₂, NaOH, NaCl, KCl, and CuSO₄ which provided relative humidity of 33.2, 65.5, 75.5, 85.5, and 97.3%, respectively. The mechanical properties (puncture force and puncture deformation) were determined,

always in three replicates, using a texturometer TA.XT2i (TA instruments) by puncture test using a cylindrical probe of 3.0 mm of diameter and rate of 1.0 mm/s (Gontard et al., 1993). The puncture force (N) corresponded to the maximum point of the curve force versus the probe displacement, and the puncture deformation ($\Delta l/l_0$) was calculated according to Equation 26.1 (Sobral et al., 2001):

$$\frac{\Delta l}{l_0} = \frac{\sqrt{D^2 + l_0^2} - l_0}{l_0} 100 \quad (26.1)$$

where l_0 is the initial length of the film (26.3 mm) and D is the probe displacement.

Water Vapor Permeability

The WVP was determined gravimetrically (Gontard et al., 1993) at 15, 25, and 35°C and relative humidity gradient of 100% (silica gel inside and pure water outside the permeation cell). The WVP was calculated with Equation 26.2 (Gontard et al., 1993):

$$P_{va} = \frac{gx}{tA\Delta p} \quad (26.2)$$

where g/t is the slope of the cell weight gain calculated by linear regression, x is the average thickness of the films, A is the area ($9.08 \times 10^{-8} \text{ m}^2$) and p is the vapor pressure difference at 15 (1.705 Pa), 25 (3.167 Pa) and 35°C (5.623 Pa). These permeation tests were run during 6 days.

Results and Discussion

Mechanical Properties

The effect of relative humidity in the domain between 30 and 98% and of the film thickness from 0.13 to 0.32 mm on the puncture force and deformation can be observed in Figure 26.1. It can be seen that the increment of the relative humidity of conditioning provoked the reduction of the puncture force and the increase of puncture deformation following an exponential behavior, according to Equation 26.3:

$$MP = a e^{bRH} \quad (26.3)$$

where MP is the mechanical property (puncture force in N, or deformation in %), RH is the relative humidity, and a and b are constants of the model calculated by nonlinear regression (Table 26.1).

The effect of the relative humidity of conditioning on the puncture force and deformation can be related to the increase of the matrix hydration considering that gelatin and glycerol are both hydrophilic. The consequent

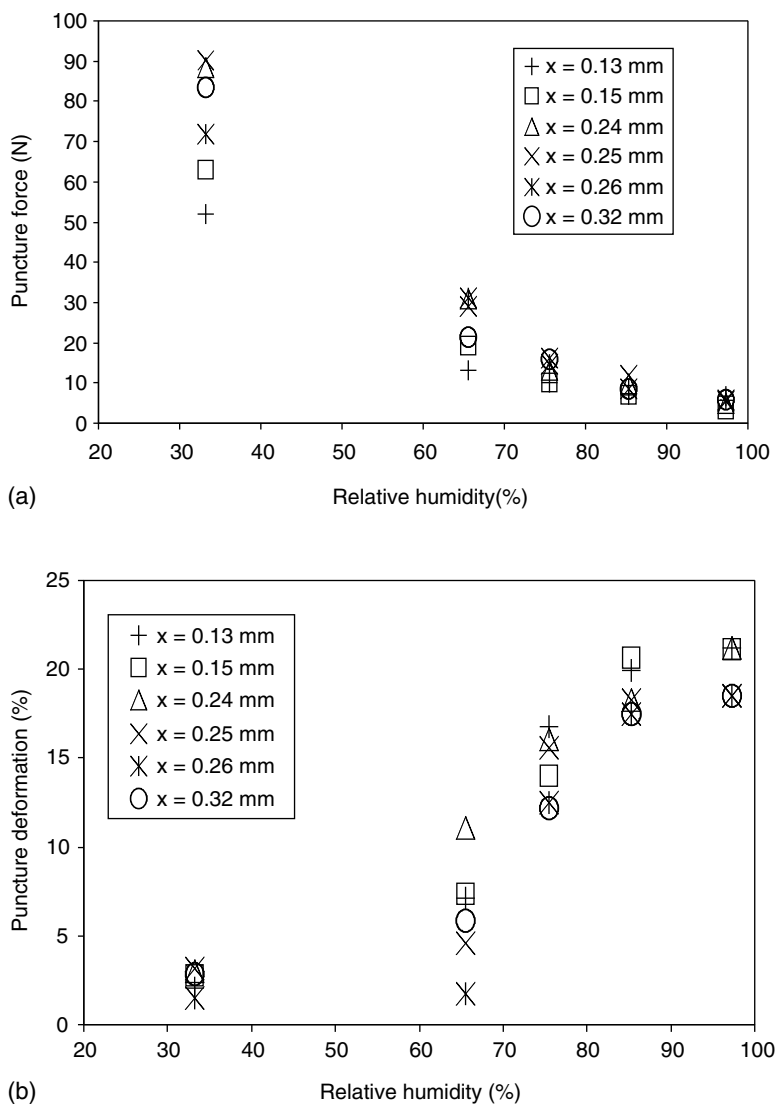


FIGURE 26.1
Puncture force (a) and puncture deformation (b) as function of the relative humidity of conditioning and film thickness in gelatin-based films.

increase of the film humidity caused an augmentation of the polymeric chains mobility (Donhowe and Fennema, 1992), reducing the hydrogen bond interactions between them, and thus provoking an increase of the deformation capacity and a reduction of the film resistance. This behavior confirms the plasticizer effect of water, similar to the additives used as plasticizers (Sobral et al., 2001).

TABLE 26.1

Parameters of Equation 26.3 Calculated by Nonlinear Regression of the Puncture Force (PF) and Puncture Deformation (PD) Data as Function of the Relative Humidity (RH) for Different Thicknesses (X)

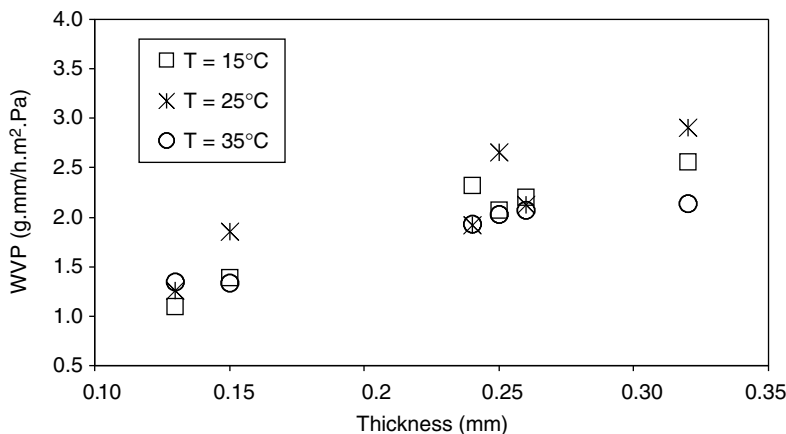
X (mm)	PF (N)			PD (%)		
	a	b	R	a	b	R
0.13	140.2	-0.039	0.959	0.599	0.039	0.939
0.15	315.2	-0.042	0.985	0.884	0.035	0.985
0.24	440.5	-0.045	0.975	1.227	0.031	0.950
0.25	413.2	-0.042	0.984	0.992	0.032	0.821
0.26	320.8	-0.041	0.961	0.247	0.046	0.760
0.32	344.5	-0.042	0.995	0.937	0.032	0.993

However, it was observed that, in general, the increment of the film thickness provoked an increase of its mechanical resistance, that is, increased the puncture force, and at the same time implied a reduction of the deformation capacity. However, these effects are dependent on the relative humidity of conditioning, certainly as a function of the possible structural alterations within the polymeric matrix.

The increase of the puncture force with the augmentation of the film thickness may be related to the increase of gelatin concentration by area unit, enhancing the intermolecular interactions (Cuq et al., 1996) and leading to the formation of a polymeric matrix with high cohesion. Sobral (Sobral, 1999) also observed an increase of the puncture force from 2.5 to 30 N with the thickness increment from 0.020 to 0.140 mm for gelatin-based films. Similar behaviors were also observed by others authors working with myofibrillar proteins-based films with thickness between 0.010 and 0.055 (Cuq et al., 1996) and for hydroxypropil-cellulose-based films with thickness between 0.025 and 0.125 mm (Park and Chinnan, 1995).

Water Vapor Permeability

In general, WVP increased linearly with film thickness (x), for 15 (WVP = $0.181 + 8.894x$, $R = 0.933$), 25 (WVP = $0.084 + 11.577x$, $R = 0.874$) and 35°C (WVP = $0.617 + 5.536x$, $R = 0.879$) (Figure 26.2). These results agree with other studies about the influence of thickness on the WVP of corn zein and wheat gluten-based films (Sobral and Habitante, 2001), where the increment of thickness from 0.1 to 0.5 mm provoked the increase of the WVP from 0.1 to 0.2 (mg m/m² s Pa) and from 0.4 to 0.7 (mg m/m² s Pa), respectively. The explanation of this behavior is very difficult, but it has been observed also by other authors working with myofibrillar proteins (Cuq et al., 1996) and gelatin-based films (Sobral, 1999).

**FIGURE 26.2**

Water vapor permeability (WVP) as function of the thickness (x) of gelatin-based films at 15°C (\square), 25°C (\diamond) and 35°C (\circ).

Unfortunately, the influence of temperature on the WVP was not clear, probably because of the dispersion of data. It was verified that for practically all film thicknesses (>0.13 mm), the lower WVP was obtained at 35°C, which can be considered as unexpected. However, Menegalli et al., (1999), working on drying of gelatin films, also observed an unusual behavior: decreasing drying kinetics with increasing air temperature when the film temperature during the drying process nears the melting temperature of the film. These behaviors can be related to structural changes around the sol–gel transition of this system, which is about 45°C (Sobral et al., 2001).

Conclusions

The properties of gelatin-based films are strongly influenced by the film thickness and the conditioning conditions. It was verified that an increment of the relative humidity provokes a reduction of the puncture force and an increase of the puncture deformation. The temperature also affects the water vapor permeability of the films, but this effect depends on the film thickness.

References

- Cuq, B., Gontard, N., Cuq, J.L., and Guilbert, S. Functional properties of myofibrillar protein based biopackaging as affect by film thickness, *J. Food Sci.*, 61, 580, 1996.
- Donhowe, I.G. and Fennema, O. The effect of relative humidity on water vapor permeance of lipid–hydrocolloid bilayer films, *JOACS*, 69, 1081, 1992.

- Gennadios, A., Park, H.J., and Weller, C.L. Relative humidity and temperature effects on tensile strength of edible protein and cellulose ether films, *Trans. ASE*, 36, 1867, 1993.
- Gontard, N., Guilbert, S., and Cuq, J.L. Water and glycerol as plasticizers affect water vapor barrier properties of an edible wheat gluten film, *J. Food Sci.*, 58, 206, 1993.
- McHugh, T.A. and Krochta, J.M. Sorbitol vs. glycerol-plasticized whey protein edible films: integrated oxygen permeability and tensile property evaluation, *J. Agric. Food Chem.*, 42, 841, 1994.
- Menegalli, F.C., Sobral, P.J.A., Roques, M.A., and Laurent, S. Characteristics of gelatin biofilms in relation to drying process conditions near melting, *Drying Tech. J.*, 17, 1697, 1999.
- Miller, K.S. and Krochta, J.M. Oxygen and aroma barrier properties of edible films: a review, *Trends Food Sci. Technol.*, 8, 228, 1997.
- Park, H.J. and Chinnan, M.S. Gas and water vapor barrier properties of edible films from protein and cellulosic materials, *J. Food Eng.*, 25, 497, 1995.
- Sánchez, A.C., Popineau, Y., Mangavel, C., Larré, C., and Guéguen, J. Effect of different plasticizers on the mechanical and surface properties of wheat gliadin films, *J. Agric. Food Chem.*, 46, 4539, 1998.
- Sobral, P.J.A. Propriedades funcionais de biofilmes de gelatina em função da espessura, *Ciência engenharia*, 8, 60, 1999.
- Sobral, P.J.A. and Habitante, A.M.Q.B. Phase transitions of pigskin gelatin, *Food Hydrocolloids*, 15, 423, 2001.
- Sobral, P.J.A., Menegalli, F.C., Hubinguer, M.D., and Roques, M.A. Mechanical, water vapor barrier and thermal properties of gelatin based edible films, *Food Hydrocolloids*, 15, 423, 2001.

Thermal Analysis and Textural Properties of Frozen French Bread Dough with Different Quantities of Ascorbic Acid

Tatiana G. Matuda, Clarissa C. Romeu, Denise T. Tavares, Duclerc
Fernandes Parra, Ademar Benévolo Lugão, and Carmen Cecília Tadini

CONTENTS

Introduction	439
Materials and Methods	440
Water Content Determination	441
Thermal Analysis	441
Textural Analyses	442
Statistical Analysis	442
Results and Discussion	442
Acknowledgments	444
References	444

Introduction

A typical French bread in Brazil should be 12.5 cm long, 5.5 cm diameter, and 50 g of final weight, with a brown and glossy crust, white and soft crumb and with a unique cut, largely following the length of the dough piece, and made before baking (Carr and Tadini, 2003). French bread production represents 85% of the total amount of bread produced in Brazil (Nutrinews, 1999).

The rise in popularity of frozen breads has been driven mainly by the economic attraction of centralized manufacturing and distribution and the practicality of consumption (Best, 1995). Nevertheless, frozen doughs still have presented problems such as dough weakening and loss of yeast viability and consequently decrease in CO₂ retention during proofing and reduction of loaf volume (Casey and Foy, 1995; Ribotta et al., 2003). These problems could make the frozen product less acceptable than fresh bread.

Ascorbic acid is used in food processing and preservation as an anti-oxidant or oxidizing agent depending on its use. The rheological properties of dough and its three-dimensional network are dependent on the interaction of sulfhydryl ($-S-H$) groups and disulfide ($-S-S-$) bonds of the protein. Ascorbic acid in bread acts as an oxidizing agent on ($-S-H$) groups of protein molecules forming inter- and intra-molecular ($-S-S-$) improving the dough (Nakamura and Kurata, 1997).

Wolt and d'Appolonia (1984) studied the influence of dough additives on frozen dough stability. Sodium stearoyl lactylate (SSL) and diacetyl tartaric acid decreased the effects of frozen storage on rheological properties, but they were not effective in reducing the dough proofing time. Kenny et al. (1999) verified that frozen dough with SSL, diacetyl-tartaric acid ester of monoclycerides (DATEM), and ascorbic acid after frozen storage presented higher resistance to extension. The authors verified a decrease in resistance to extension as caused by freezing.

Water separates out as ice during the freezing and the solute concentration of the unfrozen phase in contact with it increases when temperature decreases. After a certain concentration of the unfrozen phase, no more ice separates. This is the maximum freeze-concentration of the unfrozen phase and it becomes so viscous that it turns into a glass. Glass transition is a time-dependent change in physical state from glassy to rubbery, and it occurs in a temperature range (Laaksonen, 2001) that can be determined by differential scanning calorimetry (DSC). Unfrozen water content is the water present in the unfrozen phase.

Matuda et al. (2004) studied the influence of vegetable shortening, CSL, and PS80 on unfrozen water content and storage time on textural properties of frozen French dough. The value of unfrozen water content was 0.30 to 0.34 g H_2O /g solids and was not influenced by these additives; however, the frozen dough textural properties were significantly affected by storage up to 56 days.

Materials and Methods

Four formulations were used to produce French bread dough with different ascorbic acid quantities, as listed in Table 27.1. AACC 54-21 (AACC, 1995), a commercial bakers' flour (Moinho Pacifico, Brazil) with a water content of 13.60% and farinograph water absorption of 65.60%, was used for all formulations.

All ingredients except the salt were blended in a mixer for complete water absorption at low speed. After that, salt was added and the dough was mixed at high speed until its complete development. The final temperature of the dough was monitored. Yeast was not added because the goal of this study was to determine only the influence of ascorbic acid on dough. The fresh dough was divided into 60-g pieces and molded. Fresh dough samples

TABLE 27.1
Ingredients Used to Produce Frozen French Bread Dough
from Four Different Formulations

Ingredients	Formulations (g)			
	0	100	200	300
Wheat flour	2500.0	2500.0	2500.0	2500.0
Water	1500.0	1500.0	1500.0	1500.0
Salt	50.0	50.0	50.0	50.0
VS	25.0	25.0	25.0	25.0
PS80	7.5	7.5	7.5	7.5
DATEM	5.0	5.0	5.0	5.0
Ascorbic acid	0	0.25	0.50	0.75

VS, vegetable shortening; PS80, polysorbate 80; DATEM, diacetyl-tartaric acid ester of monoclycerides.

were also collected for water content, DSC, and textural analyses. The dough pieces were packed with PVC film without vapor space, frozen in a climatic chamber at -30°C and freezing rate of $-1.6^{\circ}\text{C}/\text{min}$, and stored at -18°C up to 13 days. After 1, 4, 7, 10, and 13 days of frozen storage, samples were removed from the freezer, thawed in a controlled environment at 30°C , and textural analyses were conducted.

Water Content Determination

The water content of the French bread dough was determined according to AACC 44-15A in five replicates (AACC, 1995). This analysis provided the total amount of water of the dough (w_{tot}).

Thermal Analysis

Ice melting curves were obtained using a DSC. The fresh dough samples were frozen up to -40°C at a freezing rate of $-3^{\circ}\text{C}/\text{min}$ and then heated at a rate of $3^{\circ}\text{C}/\text{min}$ from -40 to 20°C in a medium pressure pan ($120\ \mu\text{l}$) (DSC 822^e Module Mettler Toledo, Switzerland). The DSC apparatus was calibrated with Indio metal (m.p. 156.61°C ; $\Delta H = 28.54\ \text{J/g}$) and Mercury (m.p. -38.8°C ; $\Delta H = 11.4\ \text{J/g}$). An empty pan was used as reference.

Unfrozen water content, UFW (g $\text{H}_2\text{O}/\text{g}$ solids), was obtained from the relationship between latent heat of ice melting (ΔH_{m} , J/g solids) and total water content (g/g solids) using Equation 27.1 (Laaksonen and Ross, 2000):

$$\text{UFW} = \frac{w_{\text{tot}} - \frac{\Delta H_{\text{tot}}}{\Delta H_{\text{mw}}}}{C_{\text{tot}}} \quad (27.1)$$

where w_{tot} is total amount of water (g), ΔH_{tot} is the total heat of melting of ice (J), ΔH_{mw} is the latent heat of ice melting (334 J/g), and C_{tot} is the total amount of solids (g). $\Delta H_{\text{tot}}/\Delta H_{\text{mw}}$ is the amount of ice (g) in the sample.

Textural Analyses

A texture analyzer TA-XT2i (SMS, England) equipped with A/KIE dough and gluten extensibility rig accessory was used to measure the extensibility and resistance to extension of fresh and frozen dough. Pieces of frozen dough were removed from the freezer and thawed at a controlled temperature of 30°C. The analyses were carried out according to the *Extensibility of dough and measure of gluten quality* method (SMS, 1995). The thawed dough was placed into a Teflon-coated block, and cut into dough strips using the appropriate mold. For each run, ten replicates were conducted, totalizing 240 measurements. The test was conducted under the following conditions: pre-test speed: 2 mm/sec, test speed: 3.3 mm/sec, post-test speed: 10 mm/sec, distance 75 mm and trigger type auto 5 g.

Statistical Analysis

Analysis of variance (ANOVA) was applied within a 95% confidence interval to the results obtained for water content, resistance to extension, extensibility, and unfrozen water content.

Results and Discussion

The results obtained for water content, fusion enthalpy, T_{onset} and T_{peak} , are presented in Table 27.2. Water content varied from 44.17 to 44.27% and

TABLE 27.2
Values of Water Content (w_{tot}), Enthalpy, T_{onset} , T_{peak} and Unfrozen Water Content (UFW) from Ice Melting Curves, After Freeze Cycle on DSC, of Dough According to Formulation

	Ascorbic Acid (ppm)				Tukey HSD 5%
	0	100	200	300	
W_{tot} (g H ₂ O/100 g sample)	44.27 ^a	44.18 ^a	44.17 ^a	44.19 ^a	0.15
Enthalpy (J/g)	−89.32 ^a	−87.33 ^a	−87.44 ^a	−86.07 ^a	4.53
T_{onset} (°C)	−6.97 ^a	−6.94 ^a	−7.12 ^a	−7.08 ^a	1.02
T_{peak} (°C)	0.38 ^a	0.28 ^a	0.32 ^a	0.06 ^a	1.28
UFW (g H ₂ O/g solids)	0.315 ^a	0.323 ^a	0.321 ^a	0.330 ^a	0.024

^a Averages with same letter, in the same row, are not significantly different at a 95% confidence interval.

unfrozen water content varied from 0.315 to 0.330 g H₂O/g solids. However, the values obtained for unfrozen water content are comparative because of the variation of ice melting enthalpy with temperature. These results were not influenced by ascorbic acid addition. Usually ascorbic acid is used in the baking process as an oxidant to improve crosslinks ($-S-S-$) in the gluten matrix and it could modify dough structure during freezing.

Textural properties of frozen dough stored up to 13 days were significantly affected by ascorbic acid and by storage time. Resistance to extension increased (from 0.32 to 0.55 N) while extensibility decreased (from 26.46 to 14.27 mm) with ascorbic acid addition, as expected, because ascorbic acid is an oxidizing agent that strengthens the gluten network. However, increasing frozen storage time caused a decline in resistance to extension (from 0.48 to 0.39 N) and an increase in extensibility (from 18.33 to 21.52 mm) for all formulations (Figure 27.1). This event could indicate that frozen storage of the dough changed the amount of freezable water. Water migration, which occurs during the freezing process and continues during frozen storage, could affect inter- and intramolecular protein bonds, which might change the gluten structure irreversibly according to Lu and Grant (1999). For a better understanding of this phenomenon, unfrozen water content analysis should be carried out throughout frozen storage and not only for fresh dough.

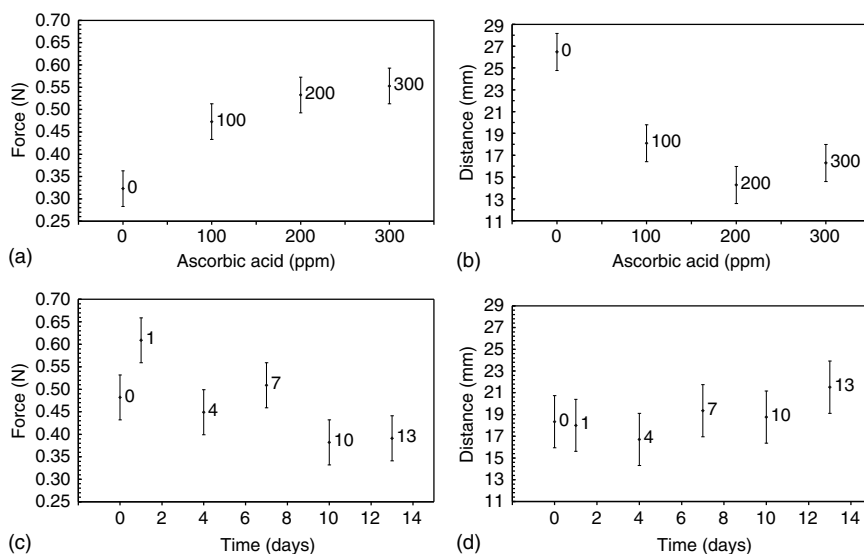


FIGURE 27.1

Resistance to extension (force in N) and extensibility (distance in mm) of French bread dough according to ascorbic acid quantities for all periods [a, b] and to frozen storage for all formulations up to 13 days [c, d].

Acknowledgments

The authors acknowledge the financial support of Fapesp (The State of São Paulo Research Foundation), Capes (Brazilian committee for postgraduate courses in scholarship education) and CNPq (The National Council for Scientific and Technological Development).

References

- AACC, American Association of Cereal Chemists. *Approved Methods of the American Association of Cereal Chemists*, 9th ed., Saint Paul, 1995.
- Best, D. Economic potential of frozen and refrigerated doughs and batters, *Frozen and Refrigerated Doughs and Batters*, K. Kulp, K. Lorenz, and J. Brümmer, eds., AACC, Minnesota, pp. 1–18, 1995.
- Carr, L.G. and Tadini, C.C. Influence of yeast and vegetable shortening on physical and textural parameters of frozen part baked French bread, *Lebensm. Wiss. Technol.*, 36, 609, 2003.
- Casey, G.P. and Foy, J.J. Yeast performance in frozen doughs and strategies for improvement, *Frozen and Refrigerated Doughs and Batters*, K. Kulp, K. Lorenz, and J. Brümmer, eds., AACC, Minnesota, pp. 19–52, 1995.
- Kenny, S., Wehrle, K., Dennehy, T., and Arendt, E.K. Correlations between empirical and fundamental rheology measurements and baking performance of frozen bread dough, *AACC, Cereal Chem.*, 76, 421, 1999.
- Laaksonen, T.J. Effects of ingredients on phase and state transition of frozen doughs. Academic dissertation, University of Helsinki, 2001.
- Laaksonen, T.J. and Ross, Y.H. Thermal, dynamic-mechanical, and dielectric analysis of phase and state transitions of frozen wheat dough, *J. Cereal Sci.*, 32, 281, 2000.
- Lu, W. and Grant, L.A. Effects of prolonged storage at freezing temperatures on starch and baking quality of frozen doughs, *Cereal Chem.*, 76, 656, 1999.
- Matuda, T.G., Parra, D.F., Lugão, A.B., and Tadini, C.C. Influence of vegetable shortening and emulsifiers on the unfrozen water content and textural properties of frozen French bread dough, *Lebensm. Wiss. Technol.*, 38, 275, 2004.
- Nakamura, M. and Kurata, T. Effects of L-ascorbic acid on the rheological properties of wheat flour dough, *Cereal Chem.*, 74, 647, 1997.
- Nutrinews, Semi assados, a nova era da panificação, 1999. Available in <http://www.nutrinews.com.br/edicoes/9905/mat01.html>, captured in January 2002.
- Ribotta, P.D., León, A.E., and Añón, M.C. Effect of freezing and frozen storage on the gelatinization and retrogradation of amylopectin in dough baked in a differential scanning calorimeter, *Food Res. Int.*, 36, 357, 2003.
- SMS, Stable Micro Systems, TA-XT2 Application study, Extensibility of dough and measure of gluten quality. Texture expert guide contents, 1995.
- Wolt, M.J. and d'Appolonia, B.L. Factors involved in the stability of frozen dough II. The effects of yeast type, flour type, and dough additives on frozen-dough stability, *Cereal Chem.*, 61, 213, 1984.

Effect of Nutraceuticals on Physico-Chemical Properties of Sodium Caseinate Films Plasticized with Glycerol

Elizabeth Lima-Lima, Susana Altamirano-Romo, Rocío Rivas-Araiza, Gabriel Luna-Bárceñas, and Cristina Pérez-Pérez

CONTENTS

Introduction	445
Materials and Methods	447
Materials	447
Preparation of Film-Forming Solutions.....	447
Film Formation	447
Measurement of Film Thickness and Physical Properties	448
Water Vapor Permeability.....	448
Mechanical Properties	448
Differential Scanning Calorimetry (DSC).....	448
Statistical Analysis	449
Results and Discussion	449
Water Vapor Permeability.....	449
Mechanical Properties	450
Differential Scanning Calorimetry (DSC).....	450
Conclusions.....	452
References	453

Introduction

There has been a resurgence of interest in recent years in the development of edible films for food (Debeaufort et al., 1998). Several studies have indicated the potential of milk proteins for use in edible films. For instance, caseinates easily form films from aqueous solutions because of their random-coil

nature and ability to form extensive intermolecular hydrogen, electrostatic, and hydrophobic bonds, resulting in an increase of the interchain cohesion (McHugh and Krochta, 1994).

Moreover, edible films based on milk proteins were reported to be flavorless, tasteless, and flexible, and depending on the formulation, they varied from transparent to translucent (Chen, 1995). Hydrophilic polymers, such as proteins that contain polar groups that provide hydrogen bonding, will absorb water from the surrounding air or from the food product they contain. Glycerol, a polyol, is well known for its plasticizing effects and its use in food technology. Glycerol was mixed at different concentrations to sodium caseinate solutions, generating films with good properties.

Among the films investigated, edible films based on proteins showed the best mechanical properties. However, their barrier properties are variable (Kester and Fennema, 1986). The increase of cohesion between protein polypeptide chains was thought to be effective toward the improvement of the barrier properties of the films. For instance, the presence of calcium was reported to decrease the water permeability of caseinate-based film (Avena-Bustillos and Krochta, 1993).

The milk proteins as edible and/or biodegradable films could be interesting because of their favorable functional properties as well as their food nutritional value. Sodium caseinate (SC) has the capability to carry nutraceuticals (Gontard et al., 1992; McHugh et al., 1993).

The concepts of incorporating nutraceuticals into edible films to enhance the nutritional value of foods have been discussed, but few studies have been reported.

Nutraceuticals are chemicals found as natural components of foods or other ingestible forms that have been determined to be beneficial to the human body in preventing or treating one or more diseases or improving physiological performance (Alvídrez-Morales et al., 2002). Calcium and vitamin C are important nutraceuticals as they play significant roles in the human body to prevent certain diseases (Elliot, 1998; Pszezola, 1998). The film properties depend strongly on film composition, its formation, and the methods of its application to the products (Arvanitoyannis and Biliaderis, 1998; Debeaufort et al., 1998). When calcium is added to protein-based films, the calcium ions may induce static cross-linking and the level of ionic strength may affect protein microstructure and interactions, which would in turn impact the mechanical and barrier properties (Kester and Fennema, 1986; Avena-Bustillos and Krochta, 1993; Mezgheni et al., 1998). Calcium has been one of the most difficult minerals to add to foods because of its high DRI value, its low solubility at neutral pH, and the bitter taste of some calcium salts. Mei and Zhao (2002) identified that Gluconal Cal (GC; Glucona America Inc., Janesville, WI, USA), a mixture of calcium lactate and calcium gluconate, has high nutritional value, good bioavailability and water solubility, and neutral taste and successfully incorporated it into edible coatings. However, few studies (Mei and Zhao, 2002; Mei and Zhao, 2003; Park and Zhao, 2004)

have been reported. The performance of vitamin C in edible films has not been evaluated.

Our objectives in this study were to formulate SC film solutions that can carry high concentrations of calcium and vitamin C, and to investigate the impacts of calcium and vitamin C on the physico-chemical properties of the films.

Materials and Methods

Materials

The materials used for film formation include SC (Sigma C-8654, St. Louis, MO, USA) containing approx. 96% protein, and 4% ashes (dry basis); glycerol plasticizer (G: Sigma G-6279, St. Louis, MO, USA), serving as plasticizer in all film-forming solutions, GC (Glucona America Inc.), a mixture of calcium lactate and calcium gluconate with water solubility up to 40 g/100 ml and neutral taste, and ascorbic acid (VC; Fermont. Productos Quimicos Monterrey, Mty, N.L., Mexico). All chemicals used were of reagent grade.

Preparation of Film-Forming Solutions

Aqueous solutions of 10% (w/w) SC were made with addition of 0 to 30% (w/w SC) G in the mixture. The addition nutraceuticals were 5 and 10% (w/w SC) GC, and 0.01% (w/w SC) VC in the mixture.

SC and glycerol were mixed in distilled water. Solutions were heated to $60 \pm 2^\circ\text{C}$ approximately for 1 h while being stirred continuously. The samples containing nutraceuticals required the most time to obtain complete dissolution of the substances. The solutions were placed in a shaking water bath with a magnetic stirrer. Finally the solutions were dried over PVC plates at room temperature.

Film Formation

Different sizes of films were formed. The samples were cut to measure film properties and to establish a film thickness control equation. The small-diameter films were used for the water vapor permeability (WVP) and puncture strength (PS); large ones for tensile strength and elongation at break (%) measurement. The volume of solution was added over PVC plates at volume constant using a thin layer chromatography spreader. The plates were placed on a leveled surface to achieve uniform films and dried at room condition ($25 \pm 2^\circ\text{C}$ and $58 \pm 3\%$ HR) for 24 to 48 h. Films used for each property measurement were manufactured and stored under the same temperature but at different relative humidity conditions.

Measurement of Film Thickness and Physical Properties

The thickness of the film was measured using a micrometer (Foil Dial Thickness Gauge F 1101/30). Films samples were cut according to the standard methods for the measurement of functional properties. For each film sample, five thickness measurements were randomly taken at different locations. The average value was taken to calculate the water barrier and mechanical properties.

Films density was calculated by dividing the film weight by the film volume, where the film volume was calculated by multiplying the film area by the thickness.

Water Vapor Permeability

Films used for WVP measurement were first conditioned at 58% RH at room temperature ($25 \pm 0.5^\circ\text{C}$) for >48 h. A modification of the ASTM E96-80 (ASTM, 1989) gravimetric method was used to measure the WVP of the films. Three replicates of each film type were tested, and the result was reported as the mean value in $\text{mol m/m}^2 \text{ sec Pa}$.

Mechanical Properties

The mechanical properties of the films were determined with a texture analyzer TA-XT2i (Microstable System, Godalming, England). Prior to the measurements, film samples were conditioned in the same environment at 25°C and 58% RH for at least 2 days. All properties measurements were performed immediately after removing film specimens from the chamber to minimize moisture variances of these natural hydrophilic films.

The ASTM D882-83 method (ASTM, 1983) was used for measuring tensile strength (TS) and percent elongation at the break (EL). The TS value was reported as measured maximum load (N) divided by film cross-sectional area (mm^2) with units of Pa. El values were obtained by recording elongation at the break divided by the initial length of the specimen and multiplying by 100.

The puncture test was realized as described previously by Gontard et al. (1992). To avoid any thickness variation, the puncture strength values were divided by the thickness of the film. Three replicates of each film type were tested.

Differential Scanning Calorimetry (DSC)

The measurements were performed on a DSC Mettler Toledo (DSC822e/400). About 10 mg of each film-forming component or film conditioned at 25°C and 58% RH for 2 days previously was sealed in a standard aluminum pan. The first scan, from 20 to 150°C was applied to remove any thermal history effects. This first scan was stopped before the material melted, and samples

were then cooled down quickly to -60°C . The second scan from -40 to 260°C was performed to establish the glass-transition temperature (T_g). The DSC curve was obtained in a temperature range of -40 to 260°C at a heating rate of $5^{\circ}\text{C}/\text{min}$. The T_g values quoted correspond to the “midpoint” of the transition.

Statistical Analysis

All experiments were replicated three times in a randomized complete block experiment. Each analysis was done in duplicate. Statistical analysis was conducted using STATGRAPHIC PLUS (Statistical Graphics Corp.).

Results and Discussion

Water Vapor Permeability

WVP of SC-based films incorporated with nutraceuticals is shown in Figure 28.1. The film thickness was controlled in the range of 70 to $90\ \mu\text{m}$ for all the films. The water vapor property of the films was significantly improved by incorporation of mineral or vitamin C in the film matrix ($P < 0.05$). By adding a high concentration of mineral salts into the film matrix, counterion interactions increase among adjacent molecular structures and small mineral ions act as fillers, thus resulting in a decrease in diffusivity of water vapor through a film matrix and a decrease in hydrophilic tendency of SC (Park and Zhao, 2004). Ionic calcium is known

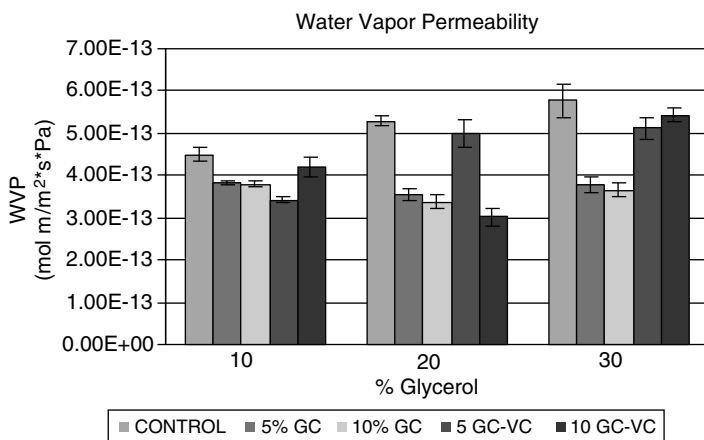


FIGURE 28.1

Water vapor permeability (WVP) of sodium caseinate films with nutraceutical substances. Film thickness was controlled in a range of 70 to $90\ \mu\text{m}$ for all films tested.

to form strong molecular crosslinking in caseinate films, which would improve protein network formation and stability (Park et al., 2001), reducing the moisture diffusion rate. Ionic calcium crosslinking also reduced protein solubility in water and led to decreased WVP through the protein matrix (Avena-Bustillos and Krochta, 1993). Park et al. (Park et al., 2001) indicated that calcium sulfate improved water barrier properties of soy protein isolate (SPI) film by reacting with protein constituents to yield insoluble proteinates and altered film consistency. From this study associated with a high concentration of calcium incorporation into film-forming solution, it might be concluded that calcium improves the WVP of SC films through its capacity to promote aggregation, thus reducing the solubility of protein.

Incorporating a high concentration of glycerol increase the WVP of the SC films significantly ($P > 0.05$). McHugh et al. (1993) suggested that as film thickness increased, the film provided an increased resistance to mass transfer across it, but in this study, film thickness varied among the films used for WVP determination (data not shown) and this might affect the accuracy of WVP calculation. Future research must have better control of film thickness to fully understand the WVP of films.

Mechanical Properties

The tensile strength of SC film was significantly affected by the addition of glycerol and nutraceuticals substances ($P > 0.05$). At increased concentration of glycerol in the film matrix, the tensile strength is lowered, but adding VC increased the value markedly. The percent elongation of the films decreased with increasing GC concentration (Table 28.1). The puncture strength was significantly decreased with the incorporation of glycerol and decreased by adding GC and VC (Figure 28.2). The thickness for the test specimen was also important. Tensile strength is the measurement of maximum strength a film can withstand against applied tensile stress, and percent elongation represents the ability of films to stretch. While the puncture strength is the measurement of hardness of a film under the stress applied at right angles to its surface that generates multidirectional forces. Puncture deformation is the measurement of film elasticity under vertically loaded stress. Both tensile and puncture strength values can be used as a measurement of hardness of films. The Young's modulus is the measurement of the elastic properties of the materials, and can be regarded as a measurement of the rigidity. (Table 28.1) The addition of glycerol was significantly in this study ($P > 0.05$). Park and Zhao (2004) showed a similar effect with chitosan-based films.

Differential Scanning Calorimetry (DSC)

The T_g values of SC films are shown in Figure 28.3. Increasing plasticizer concentration led to a significant reduction in T_g values in all SC films, the addition of GC decreased the T_g and the VC increased lightly the T_g .

TABLE 28.1
Mechanical Properties of Sodium Caseinate Films with Glycerol^a

Treatments	Tensile Strength (Pa)		% Elongation		Young's Module (Pa)	
	Average	SD	Average	SD	Average	SD
10G	277545.80	83158.46	2.99	0.37	1273.11	434.74
20G	158520.00	16577.86	7.31	1.01	492.57	47.67
30G	76456.83	5297.73	52.69	3.58	33.99	10.74
5GC10G	182484.23	47533.72	4.33911765	1.82	1178.34	629.50
5GC20G	128406.1967	10917.01	5.64	1.31	488.95	88.18
5GC30G	100342.4201	17224.34	14.6935294	2.70	130.75	16.11
10GC10G	230261.9197	29165.21	5.60156863	0.07	644.95	17.03
10GC20G	145909.8158	24964.26	6.49735294	2.21	906.95	314.90
10GC30G	96900.9394	11827.92	15.0313725	3.12	151.68	28.13
5GC10GV	821465.02	54390.07	3.40568627	0.31	936.39	130.93
5GC20GV	671683.1505	35887.36	8.42164706	1.84	272.56	54.26
5GC30GV	711665.3339	2510.47	48.3591176	5.56	16.50	1.76
10GC10GV	725000.00	5349.21	2.95	0.07	104.52	11.34
10GC20GV	663294.8142	11130.02	8.16729412	1.87	321.66	76.19
10GC30GV	628574.8432	35251.11	44.4615126	1.34	29.00	19.18

^a Means of five measurements.

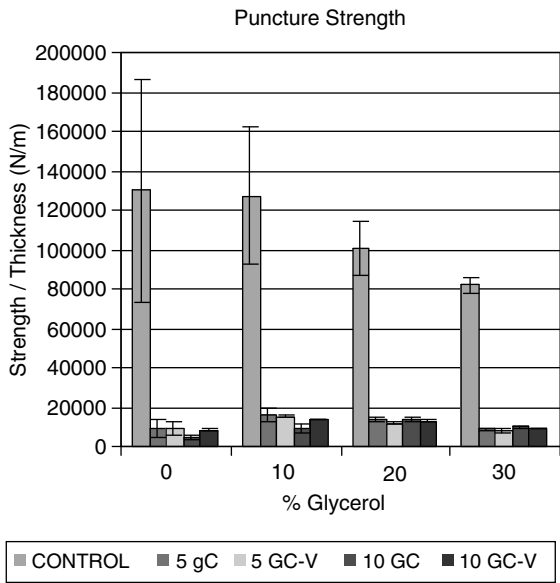
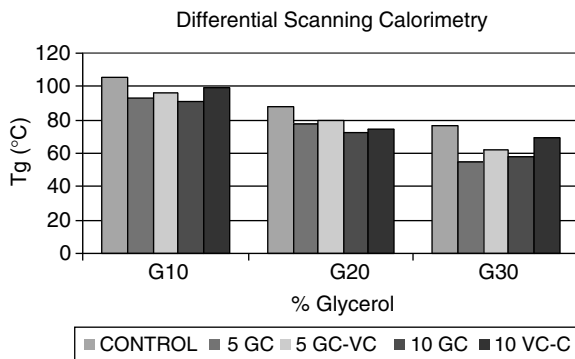


FIGURE 28.2
Effect puncture strength in sodium caseinate films. The puncture strength was calculated considering the thickness.

**FIGURE 28.3**

T_g values of sodium caseinate films incorporated with mineral and vitamin C.

Changes in the thermal properties of SC films were correlated with effects on the mechanical properties of film, i.e., reduced film strength and increased film elongation. Plasticizations disrupt intermolecular interactions between polymer molecules with the effect of decreasing brittleness and increasing film flexibility (Sears and Darby, 1982). Lillie and Gosline (1993) pointed out that the T_g of proteins, especially at a low water content, may occur over a wide temperature range. However, few T_g data are available for proteins (Roos, 1995).

Conclusions

This study quantified the properties of SC films containing different types and concentrations of mineral or vitamin. The intended use of the coating or films would dictate the requirements for water barrier and mechanical properties. The GC and VC affect the evaluation of film functionality. The mechanical properties of the films were influenced by the glycerol concentration and nutraceuticals substances; the addition of plasticizers to the film formulations generally decreased the puncture strength values. The WVP was influenced by the addition of GC in the film matrix. Moisture content of the films correlated well with glass-transition temperatures. The specific formulation of such films depends strongly on their intended applications, in which the concentration of mineral or vitamin C incorporated into the films needs to be carefully selected to meet the required water barrier, mechanical, and thermal properties of the films. The feasibility and stability of these coatings applied to fresh fruits for enhancing storability and nutritional values are under evaluation now. To understand their effects fully, future research must study the gas

permeability and microstructure of the films at different levels of glycerol incorporation.

References

- ASTM, Standard test method for tensile properties of thin plastic sheeting. D-882-83, *Annual Book of ASTM Standards*. American Society for Testing and Material, Philadelphia, PA, 1983.
- ASTM, *Annual Book of ASTM Standards*, American Society for Testing and Material, Philadelphia, PA, 1989.
- Alvídrez-Morales, A., González-Martínez, B.E., and Jiménez-Salas, Z. Tendencias en la producción de alimentos: Alimentos Funcionales, *Respyn*. Revista de la Facultad de Salud Pública y Nutrición. Universidad Autónoma de Nuevo León (México). Vol. 3, No. 3. Julio-Septiembre; <http://www.uanl.mx/publicaciones/respyn/iii/3/index.html>.
- Arvanitoyannis, I. and Biliaderis, C. Physical properties of polyol-plasticized edible films made from sodium caseinate and soluble starch blends, *Food Chem.*, 62, 333, 1998.
- Avena-Bustillos, R.J. and Krochta, J.M. Water vapor permeability of caseinate-based films as affected by pH, calcium cross-linking and lipid contents, *J. Food Sci.*, 58, 904, 1993.
- Chen, H. Functional properties and applications of edible films made of milk proteins, *J. Dairy Sci.*, 78, 2563, 1995.
- Debeaufort, F., Quezada-Gallo, J.A., and Voilley, A. Edible films and coatings: Tomorrow's packagings: A review, *Crit. Rev. Food Sci.*, 38, 299, 1998.
- Elliot, J.G. Application of antioxidant vitamins in foods and beverages, *Food Technol.*, 53, 46, 1998.
- Gontard, N., Guilbert, S., and Cuq, J.L. Edible wheat gluten films: influence of the main process variables on film properties using response surface methodology, *J. Food Sci.*, 57, 190, 1992, see also p. 199.
- Kester, J.J. and Fennema, O. Edible films and coatings: A review, *Food Technol.*, 47, 1986, December.
- Lillie, M.A. and Gosline, J.M. The effects of swellings solvents on the glass transition in elastin and other proteins, *The Glassy State in Foods*, J.M.V. Blanshard and P.J. Lillford, eds., Nottingham University Press, Loughborough, UK, pp. 281-301. 1993, Chapter 17.
- McHugh, T.H., Avena-Bustillos, R., and Krochta, J.M. Hydrophilic edible films; modified procedure for water vapor permeability and explanation of thickness effects, *J. Food Sci.*, 58, 899, 1993.
- McHugh, T.H. and Krochta, J.M. Milk-protein-based edible films and coatings, *Food Technol.*, 97, 1994, January.
- Mei, Y. and Zhao, Y. Using edible coating to enhance nutritional and sensory qualities of baby carrots, *J. Food Sci.*, 65, 1964, 2002.
- Mei, Y. and Zhao, Y. Barrier and mechanical properties of milk protein-based edible films containing nutraceuticals, *J. Agric. Food Chem.*, 51, 1914, 2003.
- Mezgheni, E., D'Aprano, G., and Lacroix, M. Formation of sterilized edible films based on caseinates: effects of calcium and plasticizers, *J. Agric. Food Chem.*, 46, 318, 1998.

- Park, S.K., Rhee, C.O., Bae, D.H., and Hettiarachchy, N.S. Mechanical properties and water-vapor permeability of soy-protein films affected by calcium salts and glucono- δ -lactone, *J. Agric. Food Chem.*, 49, 2308, 2001.
- Park, S. and Zhao, Y. Incorporation of a high concentration of mineral or vitamin into chitosan-based films, *J. Agric. Food Chem.*, 52, 1933, 2004.
- Pszezola, D.E. The ABCs of nutraceutical ingredients, *Food Technol.*, 52, 30, 1998.
- Roos, Y.H. *Phase Transitions in Foods*, Academic Press, London, pp. 360, 1995.
- Sears, J.K. and Darby, J.R. *The Technology of Plasticizers*, Wiley, New York, 1982.

29

Behavior of Hydroxypropylmethylcelluloses of Different Molecular Structure and Water Affinity at the Air–Water Interface

Oscar E. Pérez, Cecilio Carrera-Sánchez, Juan Miguel Rodríguez-Patino, and Ana M.R. Pilosof

CONTENTS

Introduction	455
Materials and Methods	456
Equilibrium Surface Pressure	456
Surface Film Balance	457
Automatic Drop Tensiometer	457
Results	457
Conclusions	460
Acknowledgments	460
References	461

Introduction

Hydroxypropylmethylcellulose (HPMC) is a water-soluble nonionic macromolecule derived from cellulose (Yoguchi et al., 1995) that is able to gel upon heating. It has interesting applications in food, pharmaceutical, and cosmetic areas, mainly for controlled release (Fyfe and Blazek, 1997; Avranas and Tasapoulus, 2000). The surface properties of HPMC solutions depend on the length and distribution of trains, loops, and tails. This can be explained in terms of the structure of the polymer, which is a consequence of the manufacturing process that involves heterogeneous reactions. The presence of crystalline and amorphous regions in the solid-state form of cellulose results in a nonuniform distribution of substituents along the backbone of the cellulose molecule (Nahringbauer, 1995). As a result there may exist

regions of the cellulose backbone that are hydrophobic in nature, regions rich in methoxyl groups, and others which are hydrophilic, being rich in hydroxypropyl groups. Thus, once adsorbed, the hydrophobic regions that would correspond to the so-called trains would be located at the air–water interface and the hydrophilic groups, the loops and tails, would be immersed in the subphase. HPMCs exhibit different surface activity depending on their varying methoxyl/hydroxypropyl ratio.

The ability of polymeric materials to act at interfaces depends on the manner in which they respond to mechanical stress through their surface viscoelasticity (Gau et al., 1993). In addition, the dynamics of adsorption provides information concerning the processes that occur during surface adsorption.

The objective of the present work was to evaluate the impact of the degree and type of substitution and the water affinity of different HPMCs on the structure and dynamics of structure formation of the air–water film.

Materials and Methods

Methocell E4M, E50LV, and F4M (food grade) from The Dow Chemical Company were kindly supplied by Colorcon-Argentina and used without purification. Table 29.1 shows some characteristic properties, namely, the methyl/hydroxypropyl ratio and the viscosity (25°C) of 1% wt solutions.

Equilibrium Surface Pressure

Equilibrium surface pressure (π_e) values were calculated as $\pi_e = \sigma_0 - \sigma_e$; where (σ_e) is the equilibrium surface tension and σ_0 is the solvent surface tension. They were measured by the Wilhelmy plate method, using a platinum plate attached to a Sigma digital tensiometer. The range of concentrations studied were 5×10^{-7} to 2% wt.

TABLE 29.1
Properties of HPMCS Used in this Work

HPMC	% Methyl	% Hydroxypropyl	Methyl/Hydroxypropyl Ratio	Viscosity (N s/m ²)
E4M	25	10	2.8	0.126
E50LV	25	10	2.8	6×10^{-3}
F4M	29.2	6	4.86	2×10^{-2}

Surface Film Balance

The surface pressure (π) measurements vs. trough area (A) were performed on fully automated Wilhelmy-type balance (KSV 3000, Finland) as described elsewhere (Rodríguez Patino et al., 2001). HPMC powders were dissolved in a commercial buffer solution called Trizma and Milli-Q ultrapure water: pH and ionic strength in all the experiments were 7 and 0.05 M, respectively. The final concentration of HPMC gums in the sub-phase was $1 \times 10^{-7}\%$ wt. The reproducibility of the surface pressure results was better than ± 0.4 mN/m.

The film elasticity was derived from π - A isotherms as $E = -A (d\pi/dA)$. The surface dilatational modulus (E) of films with its elastic and viscous components (E_d and E_v) and loss angle tangent ($\tan \delta$) were obtained by sinusoidal periodic compressions and expansions.

Automatic Drop Tensiometer

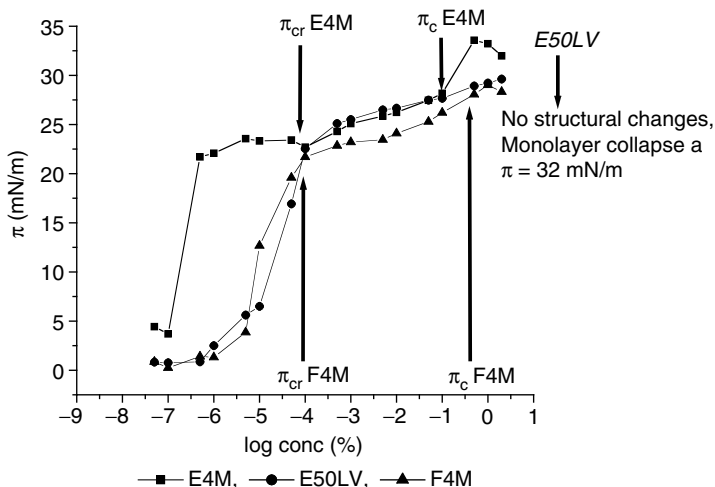
The dynamics of adsorption and the development of film structure were monitored simultaneously using an automatic drop tensiometer, as described elsewhere (Rodríguez, 1999).

Results

Figure 29.1 shows the variation of equilibrium surface pressure of E4M, E50LV, and F4M with polymer concentration. The surface pressure increased with HPMC concentration tending to a pseudo-equilibrium in the case of E4M and F4M, whereas for E50LV the surface pressure continuously grew within the range of concentrations studied.

At low bulk concentrations ($<10^{-4}\%$), E4M showed the highest surface activity. However, E50LV and F4M had similar surface pressure values, e.g., surface activity, but both were lower than E4M. When the bulk concentration was higher than $10^{-4}\%$, E4M and E50LV displayed similar surface activity increasing the surface pressure to a greater extent than F4M, which became less surface-active. It is also remarkable to note the further increase of surface pressure of E4M and F4M at concentrations higher than 0.1% and then the final decrease of around 0.5%. E4M caused a strong increase in surface pressure as a result of the saturation of the interface at very low concentrations in the bulk phase ($5 \times 10^{-6}\%$).

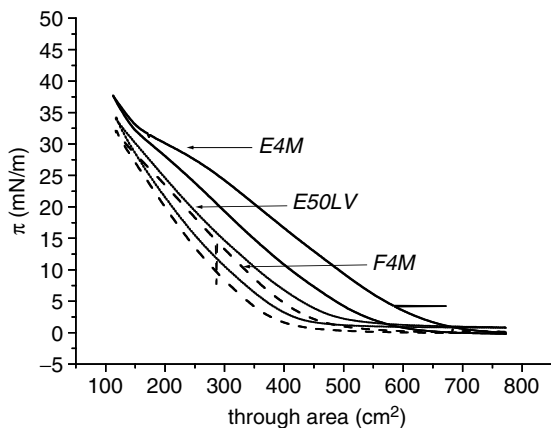
π - A isotherms after a compression and expansion cycle for the three celluloses derivatives are shown in Figure 29.2. E4M showed the highest surface activity in comparison to E50LV and F4M, even during expansion. E50LV registered highest π -values than F4M. The structural changes in the monolayers could be determined by changes in the slope of the 24-h isotherms. These changes represent the transition from a more expanded monolayer (Structure I) to a more condensed monolayer (Structure II) and

**FIGURE 29.1**

Adsorption isotherms at equilibrium for E4M, E50LV, and F4M monolayers. Temperature: 20°C, pH 7 and $I = 0.05$ M. π_{cr} indicates pressure corresponding to the transition from *Structure I* to *Structure II* and π_c that of *Collapse*.

the monolayer collapse, occurring at π_{cr} and π_c , respectively, as are indicated in Figure 29.1.

A remarkable hysteresis between the compression and expansion cycles is apparent for the cellulose derivatives, with E4M the cellulose that showed the highest area within the compression and expansion cycles. This behavior is associated with the rearrangement and reorganization of the polymer

**FIGURE 29.2**

π - A isotherms (compression and expansion cycle) for E4M, E50LV, and F4M monolayers. 24 h of aging. 20°C, pH 7 and $I = 0.05$ M.

molecules at the interface as the expansion occurs. The polymer segments situated at the subphase can interact generating networks amongst the molecules; as a consequence, the rapid recovery of the initial structure is hindered. Film compression would raise the film thickness that would then be higher than the initial value.

Measurement of the elasticity of a film is a way to quantify the film resistance to the area changes and this can be directly calculated from the slope of π -A isotherm at equilibrium (Lucassen and van den Temple, 1972). The study of the elasticity of E4M, E50LV, and F4M as a function of π was similar for the three HPMCs displaying strong dependence on surface pressure. The elasticity shows a sharp increase, followed by a less pronounced decrease, and then finally rises again (data not shown).

The overall adsorption process could be divided into three stages, diffusion, unfolding, and rearrangement. Table 29.2 shows the rates of these processes as measured by an automatic drop tensiometer. It can be observed that E4M could diffuse an order of magnitude faster than E50LV and F4M. Even though E4M was the most viscous it should have a more appropriate molecular structure for faster surface adsorption. The diffusion rate of E4M and F4M above $10^{-2}\%$ wt, and of E50LV over the whole concentration range, decreased as the concentration increased, which would indicate that the viscous effect is controlling the process.

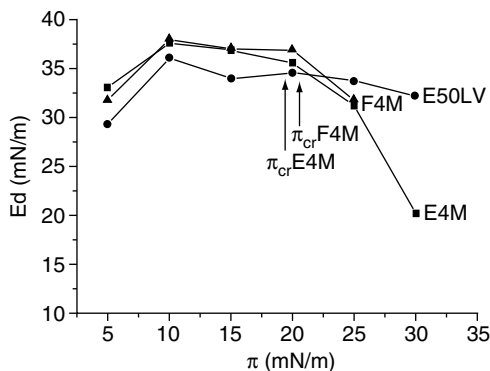
During unfolding, E4M displayed the higher unfolding rate when it is present at $10^{-4}\%$. This would suggest the ease at which E4M is able to penetrate and unfold at the interface.

A noticeable result during the rearrangement period was the low rate of rearrangement for E4M at high concentrations.

TABLE 29.2
Characteristic Parameters for the Adsorption of HPMCs
at the Air–Water Interface

HPMC	Concentration (% wt)	Diffusion Rate [(mN/m) s ^{1/2}] (<i>R</i> ²) ^a	Unfolding Rate, <i>k</i> ₁ [(mN/m) s ^{1/2}] (<i>R</i> ²) ^a	Rearrangement Rate, <i>k</i> ₂ [(mN/m) s ^{1/2}] (<i>R</i> ²) ^a
E4M	1	2.61 (0.95)	0.0043 (0.94)	5.1 E-4(0.99)
	1E-2	6.92 (0.99)	0.0060 (0.96)	3.5 E-5(0.98)
	1E-4	3.66 (0.98)	1.6 (0.97)	1.8 E-4 (0.99)
E50LV	1	0.13 (0.96)	0.0069 (0.93)	3.0 E-4 (0.95)
	1E-2	0.48 (0.98)	0.011 (0.95)	1.7 E-4 (0.92)
	1E-4	0.99 (0.95)	0.010 (0.99)	3.4 E-4(0.97)
F4M	1	0.47 (0.95)	0.008 (0.94)	2.8 E-4 (0.95)
	1E-2	0.62 (0.95)	0.009 (0.95)	4.1 E-4 (0.91)
	1E-4	0.254 (0.83)	0.001 (0.90)	2.5 E-4 (0.96)

^a Linear regression coefficient.

**FIGURE 29.3**

Elastic component of the surface dilatational modulus as a function of surface pressure for E4M, E50LV and F4M at a frequency of 20 mHz, 20°C, pH 7 and $I = 0.05M$. π_{cr} indicates pressure corresponding to the transition from *Structure I* to *Structure II*.

Figure 29.3 exhibits the surface elastic moduli of E4M, E50LV, and F4M films (frequency 20 mHz) as a function of surface pressure. F4M formed the most elastic film whilst E50LV was found to be the less elastic below π_{cr} .

Conclusions

The cellulose derivatives E4M, E50LV, and F4M have shown different behavior at the air–water interface. E4M displayed the highest adsorption efficiency and surface activity, as could be determined from tensiometry and π -A isotherms. E4M was found to adsorb fastest at the interface. The high hysteresis shown by E4M implies that it forms monolayers where molecules can be more compacted after compression and yet keep the acquired spatial conformation.

HPMCs were all able to generate viscoelastic films after adsorption. F4M formed the most elastic films, because of a higher content of methyl groups in the molecule which favor the formation of hydrophobic bonds at the interface.

Acknowledgments

This research was supported by CYTED through project XI.17, and by CICYT through the grant AGL 2001-3843-C02-01. The authors also acknowledge support from the Universidad de Buenos Aires, Consejo Nacional de

Investigaciones Científicas y Técnicas, and Agencia Nacional de Promoción Científica y Tecnológica de la República Argentina.

References

- Avranas, A. and Tasapoulus, V. Aqueous solutions of sodium deoxycholate and hydroxypropylmethylcellulose: dynamic surface tension measurements, *J. Colloid Interface Sci.*, 221, 223, 2000.
- Fyfe, C.A. and Blazek, A.I. Investigation of hydrogel formation from hydroxypropylmethylcellulose (HPMC) by NMR spectroscopy and NMR imaging techniques, *Macromolecules*, 30, 6230, 1997.
- Gau, C.S., Yu, H., and Zografi, G. Surface viscoelasticity of hydroxypropylmethylcellulose and hydroxyethylcellulose monolayers at the air–water interface, *Macromolecules*, 26, 2524, 1993.
- Lucassen, J. and van den Temple, M. Dynamic measurements of dilatational properties of a liquid interface, *Chem. Eng. Sci.*, 27, 1283, 1972.
- Nahringbauer, I. Dynamic surface tension of aqueous polymer solutions, I: Ethyl(hydroxyethyl)cellulose (BERMOCOLL cst-103), *J. Colloid Interface Sci.*, 176, 328, 1995.
- Rodríguez Patino, J.M., Rodríguez Niño, M.R., and Carrera, C. Adsorption of whey protein isolate at the oil/water interface as a function of processing conditions: a rheokinetic study, *J. Agric. Food Chem.*, 47, 2241, 1999.
- Rodríguez Patino, J.M., Carrera-Sánchez, C., Rodríguez-Niño, M.R., and Cejudo-Fernández, M. Structural and dynamic properties of milk proteins spread at the air–water interface, *J. Colloid and Interface Sci.*, 242, 141, 2001.
- Yoguchi, Y., Urakawa, H., Kitamura, S., Ohno, S., and Kajiwarra, K. Gelation mechanism of methylhydroxypropylcellulose in aqueous solution, *Food Hydrocolloids*, 9, 173, 1995.

30

Drying of Lactobacillus bulgaricus Grown at High Osmolarity in the Presence of Disaccharides

Emma Tymczyszyn and E. Aníbal Disalvo

CONTENTS

Introduction	463
Materials and Methods	464
Dehydration Procedure	464
Results	465
Effect of Growth at Low Water Activities in the Presence of Sugars	465
Growth at Low Water Activities in the Absence of Sugars	466
Conclusion	467
References	468

Introduction

The cell membrane is the main target for damage during stress processes (i.e., freeze–thawing and lyophilization) (Texeira et al., 1997). Cytoplasmic membrane (together with nucleic acid and ribosomes) has been considered as the cellular thermosensor. Preservation procedures imply a stress for the cell. Therefore, the recovery of biological properties after these procedures is one of the issues in preservation. Freeze–thaw and lyophilization are widely used to preserve *starter* cultures in the dairy industry, but these techniques imply a high cost. These reasons encouraged us to investigate the use of dehydration as an alternative method to preserve lactic acid bacteria. From the biotechnological point of view, the spray drying process may be highly convenient and economical when large volumes of cultures are dehydrated. Spray drying is a methodology that implies a thermal dehydration (Teixeira et al., 1994, 1995a). However, starter cultures of lactic acid bacteria prepared

by spray drying cannot be used for direct inoculation of milk for dairy fermentation due to the increase in the *lag* phase before growth onset. Injured cells have extended lag periods before they start to grow. This means that injured cells will take longer to start their desirable activities in food fermentations (Busta, 1976; Texeira et al., 1997).

Therefore, the procedures used to preserve starter cultures have to improve the recovery of cells and also to maintain the lag time of the preserved strain as short as in the original strain.

Lactobacillus delbrueckii subsp. *bulgaricus* is particularly sensitive toward any kind of stresses (Teixeira et al., 1995). In previous work, we have demonstrated that trehalose is a good protectant against dehydration. The action of trehalose to protect cells during drying appears to be dependent on the hydration level of the cell to be preserved (Gomez Zavaglia et al., 2003). Trehalose is also a protectant agent against osmotic shock (Gomez Zavaglia et al., 2003). Cells washed with water or 250 mM trehalose were shocked with PEG 25% w/v for 3, 6, and 9 h. In this way the effect of heat was ruled out.

After the PEG treatment, the cells previously washed with water displayed the longest lag times depending on the shock time. This indicates that lag time is not reduced immediately after the restoration of the isotonic conditions. However, this restoration reduces significantly the lag time in the presence of trehalose. This suggests that trehalose is able to buffer the stress suffered by cells in its recovery from a hypertonic stress.

For this reason, the purpose of this work is to determine the action of other sugars in addition to trehalose on bacteria grown in high osmolarity by which they are subjected to dehydration stress. With this aim, we have studied the recovery of lactic bacteria after applying different strategies of dehydration to improve the recovery of *L. bulgaricus* after dehydration.

Materials and Methods

Bacterial strains and growth conditions. *L. delbrueckii* subsp. *bulgaricus* CIDCA 333 was isolated from a fermented product (Gomez Zavaglia et al., 1998). The strain was maintained frozen at -80°C in 120 g/l nonfat milk solids. Cultures were grown in the following media: MRS and MRS plus: polyethyleneglycol PM 10,000 (Sigma), or sucrose (Merck, Darmstadt).

Dehydration Procedure

Cultures in the stationary phase were harvested by centrifugation at 10,000 g for 10 min. Aliquots of 1.2 ml were washed with different concentrations of sucrose and trehalose. After this, they were dehydrated for 30 min in a vacuum centrifuge (Integrated Speed Back System ISS 100 (Savant Knowledge Storm, Inc. 2520 Northwinds Parkway Suite 300 Alpharetta, GA 30004) at 70°C . Then they were immediately resuspended in distilled

water and the number of viable cells before and immediately after dehydration–rehydration was determined by means of the most probable number method (Bibiloni, 2001).

Results

The effect of trehalose, maltose, and sucrose on the recovery of *L. bulgaricus* after dehydration was evaluated. Figure 30.1 shows the viability of cells after drying in the presence of different concentrations of sugars. Maltose shows a low effectiveness in comparison with trehalose and sucrose. While the optimal trehalose concentration was 250 mM, sucrose and maltose did not show such behavior.

Effect of Growth at Low Water Activities in the Presence of Sugars

In order to improve the recovery of cells after dehydration, we added polyethyleneglycol (PEG) and sucrose to MRS broth in order to promote an osmotic stress. After growing and harvesting, cells were dried in 250 mM trehalose or in 250 mM sucrose. Figure 30.2 shows that the recovery of *L. bulgaricus* dried in trehalose was higher when cells were grown in MRS–sucrose and in MRS–PEG. However, the recovery of cells dried in sucrose

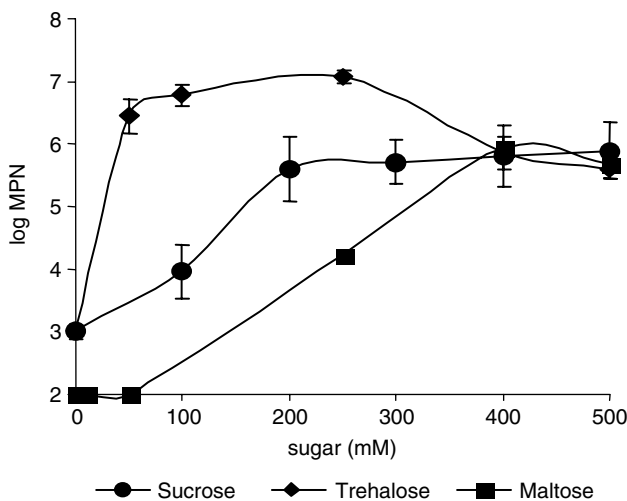
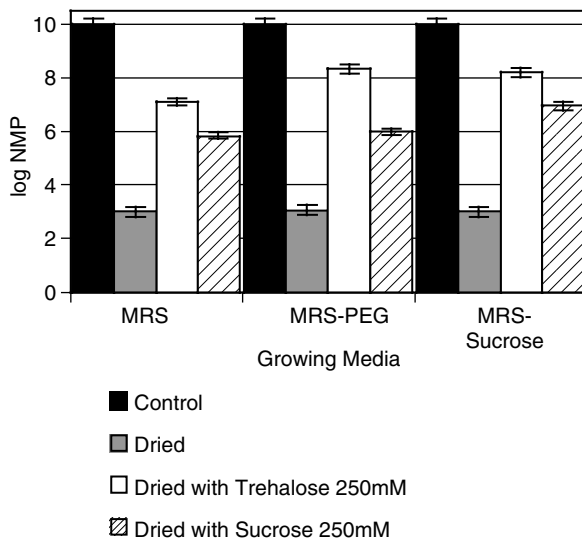


FIGURE 30.1

Viability of cells (expressed as the most probable number, MPN) after drying in the presence of different sugars.

**FIGURE 30.2**

Viability of *L. bulgaricus* dried in 250 mM trehalose or sucrose.

was enhanced when cells were grown at low water activities in a medium composed by sucrose.

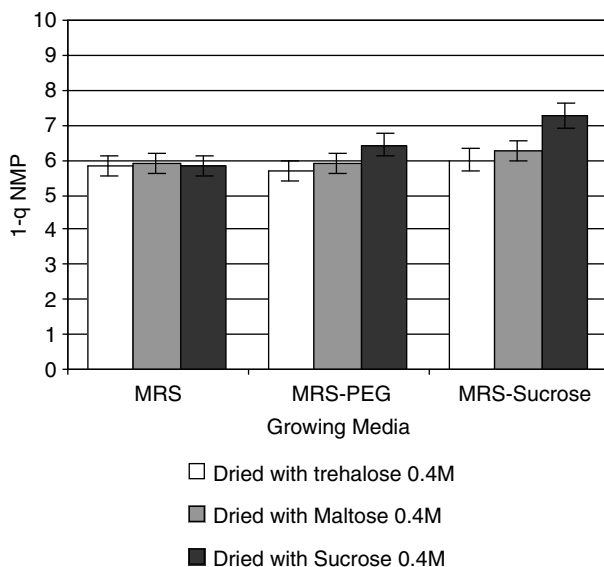
Figure 30.3 shows the viable cells (most probable number) of strain CIDCA 333 grown in MRS–PEG and MRS–sucrose and dried in the presence of 400 mM trehalose, 400 mM sucrose, and 400 mM maltose. At this concentration, the recovery was higher in cells grown in sucrose 33 mosm and dried in 400 mM sucrose.

Growth at Low Water Activities in the Absence of Sugars

It has been reported that bacterial protection against heat may be achieved by the accumulation of osmolytes that may enhance protein stability and protect enzymes against heat activation (Abee and Wonters, 1999).

The growth at osmolalities larger than 33 mosm does not enhance the recovery of bacteria dried in absence of sugar (data not shown). Thus, it is unlikely that *L. bulgaricus* can accumulate osmolites to face hydric stress in the culture, or that its accumulation is insufficient to protect the bacteria from the stress produced by drying at high temperatures.

According to our results, the presence of an osmolyte in the growth medium and a disaccharide in the dehydration step was a preferred combination. When only the osmolytes were added to the growth medium and no thermoprotectant was used to dehydrate, the recovery was weakly improved (only one order of magnitude).

**FIGURE 30.3**

Viability of *L. bulgaricus* dried in 400 mM trehalose, maltose, or sucrose.

Cultures supplied with sucrose or polyethyleneglycol enhanced only slightly the recovery of dried bacteria in the presence of 250 mM sucrose (Figure 30.2). Although the trehalose is the most effective at 250 mM in cells grown in nonsupplemented MRS or in MRS/PEGF or MRS sucrose, the recovery is also efficient when *L. bulgaricus* is grown in MRS broth supplied with sucrose 33 mosm and dehydrated in the presence of 400 mM sucrose.

Conclusion

- Dehydration factors may affect cells by different mechanisms. However, in all of them it is possible to adapt cells to the hydric stress by growing them in media of high osmolality. In the case of *L. bulgaricus*, it cannot accumulate osmolites. Hence, the presence of protectant compounds in the dehydration process is vital to preserve the structure of protein and membranes.
- Sucrose is as effective as trehalose at 400 mM. This is an important result for the milk industry to obtain culture starters since sucrose is less expensive than trehalose.
- The recovery in the presence of this sugar is higher when cells are grown in high osmolality. This may be due to a favorable interaction between sugar and membrane when the water activity is low.

References

- Abee, T. and Wonters, J. Microbial stress response in minimal processing, *Int. J. Food Microbiol.*, 50, 65, 1999.
- Bibiloni, R., Gómez Zavaglia, A., and De Antoni, G. Enzyme-based most probable number method for the enumeration of *Bifidobacterium* in dairy products, *J. Food Prot.*, 64, 2001, 2001.
- Busta, F.F. Practical implications of injured microorganisms in food, *J. Milk Food Technol.*, 39, 138, 1976.
- Gomez Zavaglia, A., Kociubinski, G., Perez, P., and De Antoni, G. Isolation and characterization of *Bifidobacterium* strains for probiotic formulation, *J. Food Prot.*, 61, 865, 1998.
- Gomez Zavaglia, A., Tymczyszyn, E.E., De Antoni, G., and Disalvo, E.A. Action of trehalose on the preservation of *Lactobacillus delbrueckii* ssp. *bulgaricus* by heat and osmotic dehydration, *J. Appl. Microbiol.*, 95, 1315, 2003.
- Teixeira, P., Castro, H., and Kirby, R. Inducible thermotolerance in *Lactobacillus bulgaricus*, *Lett. Appl. Microbiol.*, 18, 218, 1994.
- Teixeira, P., Castro, H., and Kirby, R. Spray drying as a method for preparing concentrated cultures of *Lactobacillus bulgaricus*, *J. Appl. Bacteriol.*, 78, 456, 1995.
- Teixeira, P., Castro, H., Malcata, P., and Kirby, R. Survival of *Lactobacillus delbrueckii* ssp. *bulgaricus* following spray-drying, *J. Dairy Sci.*, 78, 1025, 1995.
- Teixeira, P., Castro, H., Mohácsi-Farkas, C., and Kirby, R. Identification of sites of injury in *Lactobacillus bulgaricus* during heat stress, *J. Appl. Microbiol.*, 83, 219, 1997.

**Part 7: Structure,
Microstructure, and the
Stability of Biomolecules and
Biological Systems**

The Effect of High Pressure and Temperature on the Macroscopic, Microscopic, Structural, and Molecular Properties of Tapioca Starch Gels

Elena Vittadini, Eleonora Carini, and Davide Barbanti

CONTENTS

Introduction	471
Materials and Methods	472
Preparation of Starch Gels	472
Characterization of Starch Gels	473
Macroscopic Characterization	473
Structural Characterization	473
Microscopic Characterization	473
Molecular Characterization	474
Statistical Analysis	474
Results	474
Macroscopic Properties	474
Structural Properties	476
Microscopic Properties	478
Molecular Properties	481
Conclusions	481
Acknowledgments	481
References	481

Introduction

High pressure processing (HPP) is becoming a popular tool in food industry not only to reduce microbial load but also to induce physical changes in the

constituents of food products. Starch gelatinization can be induced by HPP at pressure >300 MPa (depending on starch type and HPP time). HPP-induced gels were reported to maintain a somewhat intact granular structure and present a lower degree of retrogradation and of freezable water (Ezaki and Hayashi, 1992; Stolt et al., 2001; Baik et al., 2003). Gels produced by HPP are expected to develop different physico-chemical properties that might account for the greater stability of these gels.

The objective of this work was to characterize the physico-chemical properties and the stability of HP-induced tapioca starch gels as compared with thermally induced ones. The references listed in this paper can provide additional background information.

Materials and Methods

Tapioca starch was obtained from a local supermarket and it was used to produce tapioca starch gels. The dry matter of the product was 91.8%.

Preparation of Starch Gels

Samples were prepared using a method where the bulk native starch is suspended in a pregelatinized starch dispersion in order to reduce the sedimentation of starch during the gelatinization processes (Roulet et al., 1988). A 2% starch/water solution was therefore prepared, brought to boiling temperature, held at this temperature for 5 min to obtain a completely clear solution, and then cooled to room temperature. Dry starch was then suspended into this pregelatinized starch solution at 5, 10, 15, 20, 25, 30, and 50% starch/pregelatinized starch solution levels (% s/w), stirred and mixed with a hand mixer for 5 min. Some (125 to 130 g) of the slurry was then poured into PE-EVOH-PE containers and hermetically sealed.

The packaged starch suspensions were then gelatinized using the following procedures:

- *Temperature*: in a water bath thermostated at 90°C for 20 min \rightarrow *gel-T*
- *High pressure*: in a Quintus[®] Food Press 35L-600 Hydrostatic Press at 32°C for 10 min \rightarrow *gel-HP*
- *High pressure and temperature*: in the same Hydrostatic Press at 83°C for 10 min \rightarrow *gel-HP-T*

The gelatinized starch in the sealed containers were cooled to room temperature and then stored at 4°C . Samples were analyzed after production (within 24 h) and after 14 and 28 days of storage. At least three sets of gels were produced for each gelatinization treatment.

Characterization of Starch Gels

Macroscopic Characterization

Water activity (a_w) determination: a_w was measured at 25°C with an Aqualab TE8255 water activity meter (Decagon Devices, Inc. Washington, USA).

Moisture content (mc) determination: moisture content of starch gels was determined by vacuum oven drying (AOAC, 2002) at 60°C for 24 h. At least duplicate moisture content analyses were carried out for each gel.

Texture determination: textural properties of starch gels were determined using a TA-XT2 texture analyzer (Stable Micro Systems, Scarsdale, NY, USA). A textural profile analysis (TPA) test was performed using a 0.50 S sphere (0.5 in. diameter) probe on gels equilibrated to room temperature to measure hardness and adhesiveness. Only the samples with starch concentration of 10% (% s/w) could be analyzed because they had a texture that fell within the detectability limit of the instrument. At least ten replicates were run for each gel.

Structural Characterization

Differential scanning calorimetry: Samples of gels (8 to 11 mg) were placed in hermetically sealed stainless steel pans and analyzed with a DSC Q100 (TA Instruments, New Castle, DE, USA). An empty pan was used as reference. Samples were heated at 10°C/min from -40 to 120°C. At least triplicate samples were analyzed for each gel. The endothermic melting peak around 0°C was taken as an evidence of ice melting. Endothermic peaks in the 50 to 70°C range were taken as evidence of starch retrogradation (stored samples).

Rheology: Rheological measurements were performed at 25°C with an ARES 2 KFRT controlled strain rheometer (Rheometric Scientific). For the measurements parallel plates of 50 mm diameter were used. The gels were loaded between the plates (2-mm gap) and allowed to rest for 3 min. A strain sweep (0.1 to 100%) was performed at 1 Hz frequency to determine the range of viscoelasticity for each sample and a 2% strain was selected for all samples. A frequency sweep test (0.1 to 16 Hz) was then performed. Samples of 30 and 50% s/w concentration could not be analyzed because of the difficulty in obtaining samples of proper and constant geometry.

Microscopic Characterization

Light microscopy: Microscopic images (10 ×) of the gels were taken with a video camera mounted on a Dialux 20EB (Leitz Italiana) microscope and interfaced with a personal computer equipped with an Image Pro Plus (4.5.1.29) software. Samples were prepared either by cutting thin sections of the gels (5 μm thick) using a cryo-microtome Benchtop Cryostat MTC (Slee Technik GmbH) or by re-suspension of a small amount of the gelatinized gel in water (1 gel: 100 water; 5 min stirring). The thin sections of the gels were placed over a microscopy slide and stained by placing a drop of congo red solution on the thin section for 5 min. The stain was then washed out with

water and approximately ten images were taken for each sample. One drop of re-suspended gel solution was placed on a microscopy slide, 15 to 20 images were taken for each sample and analyzed with Image Pro Plus software to measure the area of the granules present in the samples.

Molecular Characterization

¹H NMR molecular mobility: Relaxation times (¹H NMR T_1 and T_2) determination was carried out with a Bruker Avance 300 Spectrometer (Bruker Instruments, Billerica, MA, USA). Samples were packed into 5-mm diameter NMR tubes. T_1 was measured using an inversion recovery (Derome, 1987) and T_2 with a Carr Purcell Meiboom Gill (CPMG; Carr and Purcell, 1954; Meiboom and Gill, 1958) pulse sequences. All data were best fit with mono-exponential relaxation with $R^2 > 0.99$ in all samples.

Statistical Analysis

Means and standard deviations (SD) were calculated with SPSS (Version 11.5.1, SPSS Inc., Chicago, IL, USA) statistical software. SPSS was used to verify significant differences between treatments by one-way analysis of variance (ANOVA) followed by least significant difference test (LSD) at $p \leq 0.05$ to identify differences among groups.

Results

Macroscopic Properties

Characterization of the macroscopic water properties of the gels considered in this study did not show significant difference among the processes used to induce gelation of tapioca starch gels. Water activity was found to be > 0.97 at 25°C for all samples and moisture content was not significantly different among samples with the same solid concentration (and gelatinized with different technological processes). Moisture contents measured by using vacuum oven were not significantly different from the theoretical ones (calculated from formulation) and did not change with time (data not shown).

Hardness and adhesiveness were measured for all the samples with concentration $\geq 10\%$ s/w and the results are reported in Table 31.1 and Figure 31.1. Hardness (g, Table 31.1) of all samples increased with increasing starch content, as expected. Gel-HP of concentrations ranging from 10 to 30% s/w was significantly harder than gel HP-T while gel-T was significantly softer than both HP treated samples at time 0. This finding is in contrast with the work of Douzals et al. (1998), who reported significantly higher Young's modulus for thermally induced than HP-induced (600 MPa, 25°C, 15 min) wheat starch gels. Hardness increased also during storage at 4°C in

TABLE 31.1
Hardness (g) of Tapioca Starch Gels Obtained by Temperature (T), High Pressure at 32°C (HP) and High Pressure at 83°C (HP-T) Processing, at Time 0, 14, and 28 Days of Storage at 4°C. The Results of the Statistical Analysis Carried out among Samples of Same Concentration but Different Technological Treatment for Gelatinization Are also Shown. Samples with Same Letter Indicate no Significant Difference in Hardness

		Time 0 Days			Time 14 Days			Time 28 Days		
		% s/w	Average	SD		Average	SD		Average	SD
T	10		10	1	C	13	1	C	79	2
	15		13	3	C	19	6	C	47	20
	20		19	1	C	99	33	C	253	96
	25		21	2	C	441	89	B	815	83
	30		59	3	B	725	155	B	1461	214
	50		1086	81	A	6181	554	A	6934	718
HP	10		44	4	A	71	15	A	108	2
	15		61	10	A	152	31	A	238	82
	20		98	10	A	407	21	A	761	125
	25		173	30	A	1252	533	A	1792	479
	30		169	56	A	977	45	A	1301	147
	50		1073	172	A	2808	191	C	3685	143
HP-T	10		29	4	B	29	4	B	33	4
	15		39	6	B	47	9	B	102	36
	20		67	6	B	170	15	B	301	35
	25		83	6	B	565	52	B	1080	122
	30		88	24	B	638	182	B	2799	1829
	50		1029	590	A	4217	1089	B	5962	1979

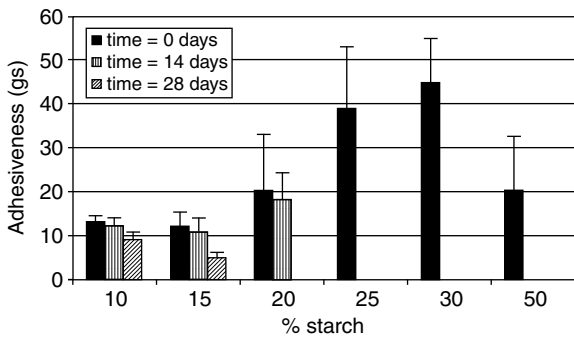


FIGURE 31.1
Adhesiveness of tapioca starch gels obtained by thermal treatment (T) at time 0, 14, and 28 days of storage at 4°C.

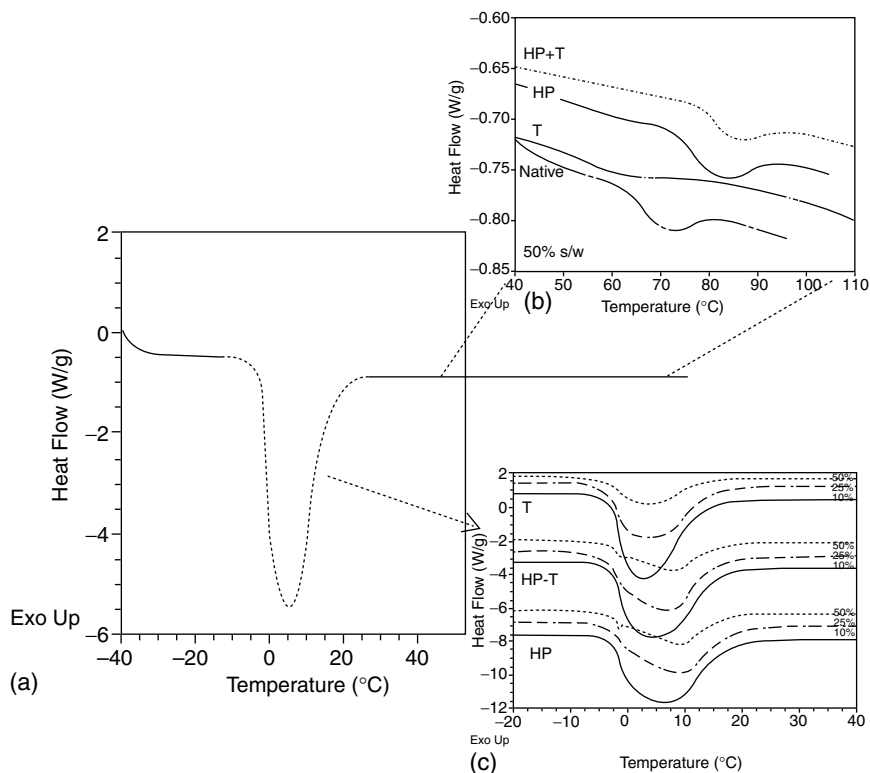
all samples. Gels-HP of 10 to 25% starch/water were significantly harder than the other samples of same concentration. On the other hand, gel-T and gel-HP-T (10 to 20% s/w samples) were significantly different from each other up to 14 days of storage but such a difference was no longer evident among all the samples at 1 month of storage. The high temperature applied during the gelatinization process induced the formation of a softer gel that was maintained also during the storage at 4°C. A very different trend was observed for the 50% s/w gels when compared with the samples of lower solid content. The hardness of all the 50% gel types was comparable immediately after production but gel-T became harder than gel-HP after storage at 4°C (Table 31.1).

Adhesiveness was found only in gel-T samples while both gel-HP and gel-HP-T did not show any evidence of such property (Figure 31.1). Adhesiveness decreased with increasing storage time, and more quickly in more concentrated gels (Figure 31.1). Detection of adhesiveness only with the gel-T samples might be explained by the only partial disintegration of the granules with the gels produced by the HP technology and/or the presence of more intimate interaction between the water and the starch molecules in gel-HP samples (Douzals et al., 1996). A role for the absence of adhesiveness might have also been played by a reduced amount of leached amylose during the HP treatment as previously suggested (Stute et al., 1996; Stolt et al., 2001), and/or by a possible closer structure of the starch molecules developed during the HP processing that might result in a lower tendency of starch molecules to separate and create sticky interactive surfaces.

Structural Properties

Structural properties of tapioca starch gels considered were their rheological and thermal (DSC) behaviors. Rheological analysis was carried out with the gels of concentration of 5 to 25% s/w and indicated that all the gels considered were weak gels. A predominance of the elastic (G') over the viscous (G'') component was found in all cases (data not shown). The different technological processes considered to induce starch gelatinization resulted in different rheological behavior with the gel-HP having both G' and G'' significantly higher than gel-T both in the fresh [as previously reported also by Stolt et al. (1999)] and aged samples. G' and G'' of the gel-HP-T sample were not significantly different from gel-HP in the fresh sample, while at a time of 14 and 28 days storage it was significantly different from gel-HP but undistinguishable from gel-T.

Differential scanning calorimetry analysis indicated the presence of a major endothermic peak around 0°C during heating (Figure 31.2a) in all the samples analyzed. Such a peak was primarily attributed to ice melting in the sample. The shape of the 0°C peak was quite symmetrical with the samples of low starch content (up to 10% s/w) produced by HP, T, or HP-T. At higher starch concentrations the 0°C endothermic peak maintained a symmetrical shape (although not Lorentian) with the gel-T while with the gel-HP and

**FIGURE 31.2**

(a) Typical DSC thermograms of tapioca starch gel (fresh gel HP, 20% s/w); (b) typical DSC thermograms (−20 to 40°C range) of fresh tapioca starch gels of 10, 25, and 50% s/w concentration, produced with different technological processes; (c) typical DSC thermograms (40 to 110°C range) of fresh tapioca starch gels of 50% s/w concentration, produced with different technological processes. The characteristic thermogram of native tapioca starch is also shown.

gel-HP-T samples it became asymmetrical and more skewed towards higher temperatures (Figure 31.2b), and at 50% s/w an additional small peak centered at $\sim -2^{\circ}\text{C}$ was found. The shape of each peak was maintained throughout storage (data not shown). The different shape of the endothermic peak at around 0°C might lead to speculation on the presence of different types of interaction between water molecules and the macromolecular matrix that results in a retarded melting transition and/or the existence of a possible second overlapping transition. Even though the temperature of the observed events should not be taken as “absolute” since the high heating rate used in the experiment ($10^{\circ}\text{C}/\text{min}$) may have artificially shifted the observation of events to higher temperatures, the discussed differences observed among samples are still valid.

Additional endothermic peaks were observed in the fresh samples of 50% s/w content (Figure 31.2c) in the 50 to 70°C range (referred to as “peak-60”) for gel-T and in the 72 to 94°C range (referred to as “peak-80”) for gel-HP and gel-HP-T. Peak-60 was attributed to the melting of recrystallized amylopectin and it was observable only in the 50% s/w gel-T sample at time 0. At longer storage time the peak attributed to amylopectin appeared also in samples of lower starch concentrations and the melting enthalpy increased with storage time for all gel types. The degree of amylopectin recrystallization was higher in the gel-T as compared with the gel-HP and gel-HP-T samples. For example, at 28 days of storage the enthalpy for the peak-60 of 50% s/w gel-T was 3.2 ± 0.9 J/g (wet basis) while it was 1.3 ± 0.3 and 1.6 ± 0.1 J/g for gel-HP and gel-HP-T (50% s/w), respectively. A similar trend (gel-T > gel-HP-T > gel-HP) of the peak-60 was found for all the sample concentrations after 28 days of storage (data not shown). The lower extent of amylopectin retrogradation observed with HP-induced gels as compared with T-induced gels was reported also by other authors (Ezaki and Hayashi, 1992; Douzals et al., 1998; Baik et al., 2003) but there are reports for barley starch that disagree with the results (Stolt et al., 2001).

Peak-80 was observed only with the 50% gel-HP and gel-HP-T samples and the transition enthalpy for the peak was constant over time (Figure 31.2c). Although a shifting to higher temperatures of the endothermic peak above 40°C as a consequence of HP processing was previously reported for wheat starch (Douzals et al., 1996), the increase in temperature was not as significant as that observed for tapioca starch in this work. It might be speculated that this peak represents a melting of starch that has been somewhat modified during the HP treatment. The presence of a more intimate interaction among starch molecules or starch–water molecules that results in an endothermic transition at higher temperatures might be hypothesized. The possible formation of amylose–lipid complexes melting at around 80°C should also be verified.

Microscopic Properties

Thin sections of the gels could be obtained only for samples of concentration $\geq 15\%$ (% s/w; gel-HP and gel-HP-T) and $\geq 25\%$ (% s/w; gel-T). Samples of lower starch content were too soft or sticky to allow for sectioning with the cryomicrotome used in this study. Characteristic images of the 50% starch/water gel samples gelatinized by the different processes are shown in Figure 31.3.

The images indicate the predominance of an amorphous matrix in all samples and the presence of some residual granular structures. The residual granular structures were quite scarce in the gel-T sample and more numerous in both gel-HP and gel-HP-T samples. Moreover, the residual granules observable in the gel-T sample appeared to have maintained a crystalline/para-crystalline structure (as observable under polarized light conditions) while the granules in the both gel-HP and gel-HP-T samples

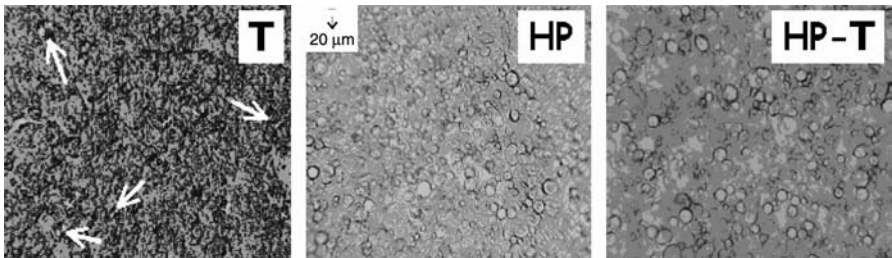


FIGURE 31.3
Characteristic images (10 ×) of thin slices of 50% starch/water gels obtained by thermal (T), high pressure at 32°C (HP) and high pressure at 83°C (HP-T) processing.

appeared to be somewhat swollen and to have lost their ordered structure due to penetration of water in the granules (Figure 31.3), as reported also by Hibi et al. (1993) and Douzals et al. (1996).

To better characterize the residual granules in the gel-HP and gel-HP-T samples, the gels were resuspended into water and observed under an

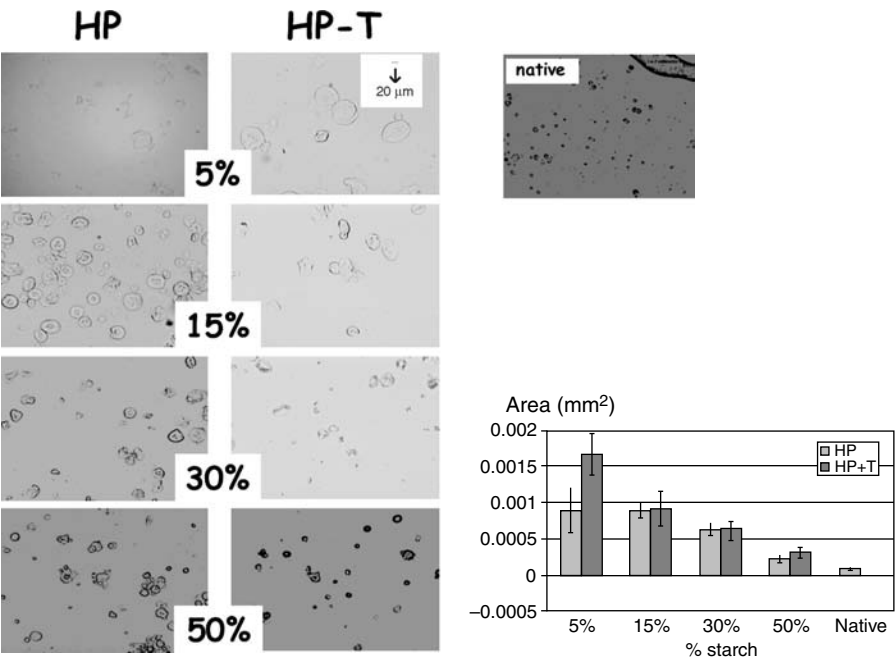


FIGURE 31.4
Characteristic images (10 ×) of resuspended tapioca starch gels (5 to 50% starch/water) obtained by high pressure at 32°C (HP) and high pressure at 83°C (HP-T) processing. An image characteristic of native starch is also shown. The graph on the bottom of the right side shows the area of the granules measured with image analysis techniques.

optical microscope. Images characteristic for some selected concentrations are reported in Figure 31.4. The granules were in all samples larger and swollen when compared with the resuspended native tapioca starch powder. Granules maintained a well defined and sharp borders especially with gels of higher starch concentration while, at lower concentrations (5 to 15% s/w), the structure of the granules was less clear, especially with the gel-HP-T samples. The degree of swelling decreased with the increase in the starch concentration where gels of lower starch content have larger and more swollen granules, suggesting penetration of water molecules in the granules. The area of the granules was measured using image analysis and the results are also shown in Figure 31.4. The average size of the native granule was found to be about $0.10 \pm 0.01 (\times 10^{-3}) \text{ mm}^2$ while it was increased by two, six, and nine times for the 50, 30, and 15% s/w gels of both samples, respectively. The 5% s/w samples were, on the contrary, significantly different with the granules of the gel-HP-T larger ($1.66 \pm 0.28 \times 10^3 \text{ mm}^2$) than the gel-HP ones ($0.90 \pm 0.30 \times 10^3 \text{ mm}^2$). The less defined and the more

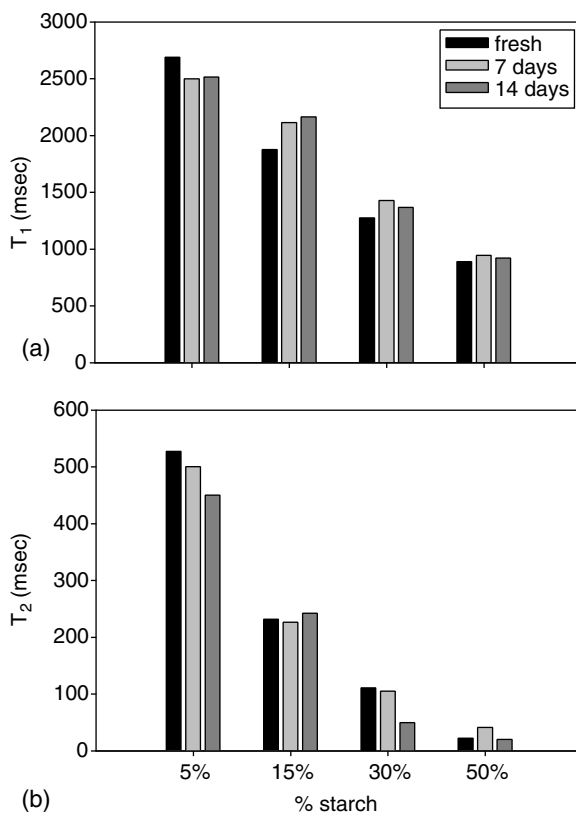


FIGURE 31.5

T_1 (a) and T_2 (b) relaxation times for gel-T samples at time 0, 7, and 14 days of storage at 4°C.

extensive swelling of the granules in the gel-HP-T may suggest an important role of the higher temperature during the HP treatment that might have enhanced the process towards granule disintegration generally associated to temperature induced starch gelatinization.

Molecular Properties

Molecular mobility of the gel systems was obtained using ^1H NMR T_1 and T_2 relaxation times. T_1 and T_2 relaxation times were not significantly different among the three sample types (T, HP and HP-T). T_1 and T_2 relaxation times for the gel-T sample are shown in Figure 31.5 as an example. A single ^1H population was detected with all samples since relaxations for both T_1 and T_2 indicated a monoexponential decay. The T_1 and T_2 values measured were, therefore, the weighted average of the contribution of all the multiple ^1H populations likely present in the starch gels. The T_1 values were significantly higher than the T_2 values, indicating that the ^1H was not in the extreme narrowing limit suggesting that the motion of water molecules was strongly retarded by the presence of solids. Both T_1 and T_2 did not change during storage for all samples.

Conclusions

High-pressure processing was shown to induce the formation of tapioca starch gels with different physico-chemical properties from temperature-induced gels. These differences might result in a different performance in starch-containing food products.

Acknowledgments

Special thanks to Elena Curti and Nicola Ceci Neva for collecting part of the data. This research was funded by the Italian Ministry for University and Research, Program "Rientro dei Cervelli", D.M. n.96, 23.04.2001.

References

- AOAC, *Official Methods of Analysis*, 16th ed., Method 925.09, Washington, DC, 2002.
- Baik, M.Y., Feeherry, F.E., and Doona, C.E. *NMR and DSC Analysis of Physical Changes to Model Food Systems Using High Pressure Processing*, IFT Annual Meeting, Chicago, IL, USA, July 2003.
- Carr, H.Y. and Purcell, E.M. Effects of diffusion on free precession in nuclear magnetic resonance experiments, *Phys. Rev.*, 94, 630, 1954.

- Derome, A.E. *Modern NMR Techniques for Chemistry Research*, Pergamon Press, New York, 1987.
- Douzals, J.P., Perrier Cornet, J.M., Gervais, P., and Coquille, J.C. Microscopic study of starch gelatinization under high hydrostatic pressure, *J. Agric. Food Chem.*, **44**, 1403, 1996.
- Douzals, J.P., Marechal, P.A., Coquille, J.C., and Gervais, P. High pressure gelatinization of wheat starch and properties of pressure induced gels, *J. Agric. Food Chem.*, **46**, 4824, 1998.
- Ezaki, S. and Hayashi, R. High pressure effects on starch: structural change and retrogradation, *High Press. Biotechnol.*, **224**, 163, 1992.
- Hibi, Y., Matsumoto, T., and Hagiwara, S. Effect of high pressure on the crystalline structure of various starch granules, *Cereal Chem.*, **70**, 671, 1993.
- Meiboom, S. and Gill, D. Modified spin-echo method for measuring nuclear relaxation times, *Rev. Sci. Instrum.*, **29**, 688, 1958.
- Roulet, P., Macinnes, W.M., Gumy, D., and Wursch, P. A comparative study of the retrogradation kinetics of gelatinized wheat starch in gel and powder from using x-rays differential scanning calorimetry and dynamic mechanical analysis, *Food Hydrocolloids*, **2**, 381, 1988.
- Stolt, M., Stoforos, N.G., Taoukis, P.S., and Autio, K. Evaluation and modeling of rheological properties of high pressure treated waxy maize starch, *J. Food Eng.*, **40**, 293, 1999.
- Stolt, M., Oinonen, S., and Autio, K. Effect of high pressure on the physical properties of barley starch, *Innovative Food Sci. Emerg. Technol.*, **1**, 167, 2001.
- Stute, R., Klingler, R.W., Boguslawski, S., Eshtiaghi, M.N., and Knorr, D. Effect of high pressure treatment on starches, *Starch*, **48**, 399, 1996.

Characterization of Food Product Surfaces during Drying Using Fractal Geometry

Gustavo F. Gutiérrez-López, José Jorge Chanona-Pérez, Liliana Alamilla-Beltrán, Roberto Campos-Mendiola, and Reynold Ramón Farrera-Rebollo

CONTENTS

Introduction	483
Materials and Methods	484
Results and Discussion	486
Descriptive Model for Drying of Agar–Maltodextrin Slabs	490
References	492

Introduction

During drying, moisture and temperature profiles as well as morphology of materials follow a nonlinear behavior. Variability of drying conditions and heterogeneity of materials contribute to this phenomenon. It is also known that microstructure of the material influences diffusion (Gekas and Lamberg, 1991; Cronin and Kearney, 1998; Aguilera and Stanley, 1999). Tensions within structural networks and formation of crusts of different permeability to water transport cause fractures associated to drying. The presence of tensions in the structural networks of materials and the formation of partially impermeable crusts on the exterior layers may cause fractures associated to shrinkage and the presence of tension forces within the material (Brinker and Sherer, 1990). An alternative to describe the complexity of drying may be the use of the fractal theory (Doulia et al., 2000). Some authors have proposed equations to describe molecular and convective transport through fractal structures, and have also applied them to chemical kinetics and media transport in more than two phases (Giona et al., 1996a, 1996b).

However, analysis of the surfaces of biological products and the application of fractal geometry may provide useful information to find relationships with processing variables. Fractal geometry leads a numeric description of structural changes that biological products undergo when processed. In the drying operation it may be interesting to correlate transport parameters as well as operating conditions with fractal dimension of the material, and this is the main objective of the present work.

Materials and Methods

A squared section model slab-shaped food, 0.02 m length and 0.006 m thick, was prepared by mixing agar-agar solutions (Ragar, food-grade, Mexico) and maltodextrin (20% DE, Amidex, food-grade, Mexico). The final amounts of agar and maltodextrin in the model food were 0.8% w/w and 31.2% w/w, respectively. The resulting solution after mixing the ingredients with water was warmed up to 90°C, poured into an acrylic tray, and left to stand at room temperature. The model food was dehydrated in an experimental tunnel dryer with air flow parallel to the sample (Figure 32.1). Apple and potato slices 3 mm thickness and 4 cm diameter were dehydrated in the same manner. For each material, a 3² factorial design was proposed; air flow rates

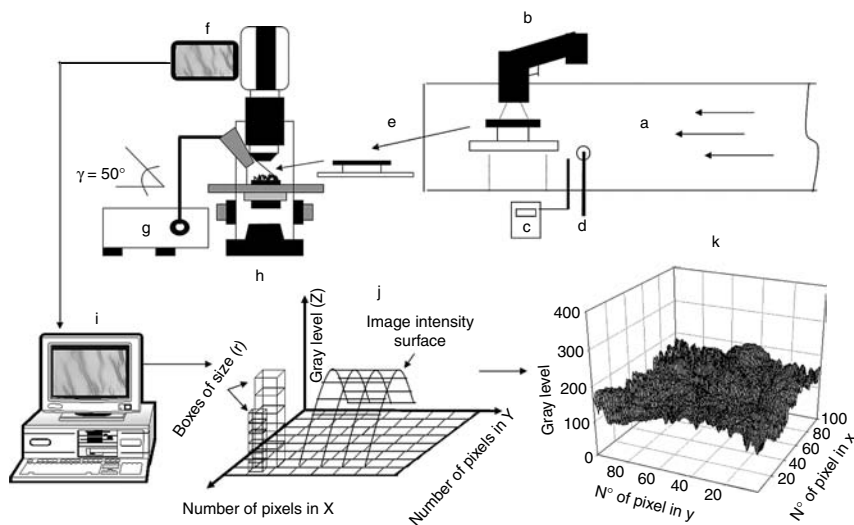


FIGURE 32.1

Diagram of the simplified procedure for drying experiments and characterization of microstructure of a food model: (a) test section for drying slabs, (b) infrared thermometer, (c) hot wire thermoanemometer, (d) thermometer of wet bulb, (e) slab, (f) video-camera, (g) source of light, (h) light microscope, (i) computer with image acquisition card, (j) representation of box counting-method in images, and (k) example of grey level intensity plot.

used were 1, 2, and 3 m/sec and the dry bulb temperatures (T_b s) were 45, 55, and 65°C. The procedure used in the determination of drying kinetics has been described by Chanona et al. (2003); sample weight was measured using an analytical balance (Ohaus Analytical Plus, USA). The surface temperature (ST) of the material was measured with an infrared thermometer (Raytek Raynger ST, USA). For every drying experiment, air flow rate and dry bulb temperatures were evaluated with a digital thermoanemometer (TSI Inc., 8330-M, USA). Initial moisture content of the samples was calculated from the formulation, taking into account initial moisture of agar and maltodextrin. Moisture contents of apple and potato were measured using a thermobalance (Ohaus Corporation, MB200, USA) and AOAC method 32.1.03 was used to validate moisture measurements (AOAC, 1995). Effective diffusion coefficients (D_{eff}) of water through the samples along the drying process were calculated using Fick's second law for slabs (Crank, 1975; Saravacos, 1995). To evaluate the changes in microstructure of the model food surface during drying, images of the surface at the center of the slab were taken at different times and processing conditions. A tri-ocular light microscope (National Optical & Scientific Instrument Inc., 163-SD, USA) coupled to a video camera (Sony Digital 8, USA) was used to obtain the images. Observations were made under a light source (Karl Storz, 482 B, Germany) with an illumination angle of 50°C (Figure 32.1). The objects under observation were magnified 100 times; exploration area was 0.005×0.006 m. Images were acquired by connecting the video camera to a personal computer with imaging software (ATI version 6.2, Multimedia Center, USA). The images were stored as bit maps in a grey scale of 0 to 255 and a resolution of 200×200 pixels for further processing. Fractal dimension of the surface (FD_{BCM}) of the images was calculated by means of the Box-Counting Method (BCM) proposed by Sarkar and Chaudhuri (1994) using MatLab version 6.0 software (Mathworks, 2000, USA). The principle used to calculate the FD_{BCM} from the BCM is shown in Figure 32.1. This figure also shows how the software interprets digital images as three-dimensional Cartesian maps, where X and Y (in pixels) represent the areas of the images, and every coordinated pair represents a position in the map. The Z axis appears in a grey scale of 0 to 255 and can be considered as the height of the Cartesian map. FD_{BCM} can be obtained by means of Equation 32.1, using the coefficient of the logarithm of the number of intercepted boxes (Nr) as a function of the logarithm of the inverse size of the box ($1/r$)

$$FD_{BCM} = \frac{\log(Nr)}{\log(1/r)} \quad (32.1)$$

Values of global shrinkage of the agar-maltodextrin slabs were digitally determined taking the difference between initial and final dimensions of sample (width length and thickness) at both the beginning and the end of the process (Arnosti et al., 2000). D_{eff} , FD_{BCM} , and percentage of shrinkage were taken as dependent variables, while temperature and air flow rate were

considered independent. A multiple regression analysis was carried out to evaluate the effect of independent variables over dependent ones.

Results and Discussion

Figure 32.2 shows the changes that took place in the microstructure of the samples through the drying process, presenting moisture loss as a function of the apparent fractal dimension of the surface of agar–maltodextrin slabs. An increase in roughness associated to an increase in FD_{BCM} and therefore a higher complexity of the surface as drying takes place is observed in Figure 32.2, in which a selection of images depicting the microstructure of the surfaces as a function of time is presented.

Regarding apple and potato samples, microstructural changes of slices were similar to the ones observed for agar–maltodextrin slabs. Absence of constant rate period of drying was also observed (Figure 32.3a–c), and confirmed by means of the ST evaluation at the center of the samples, which was always superior to the wet bulb temperature of the drying air. This suggests that the predominating transport mechanism that takes place in the drying of these vegetables is the diffusion of water through the solid matrix. Such behavior has been thoroughly documented in the literature for different biological materials (Sano and Keey, 1982; Rovedo et al., 1995; Rovedo et al., 1997; Gogus and Maskan, 1998; Hernández et al., 2000).

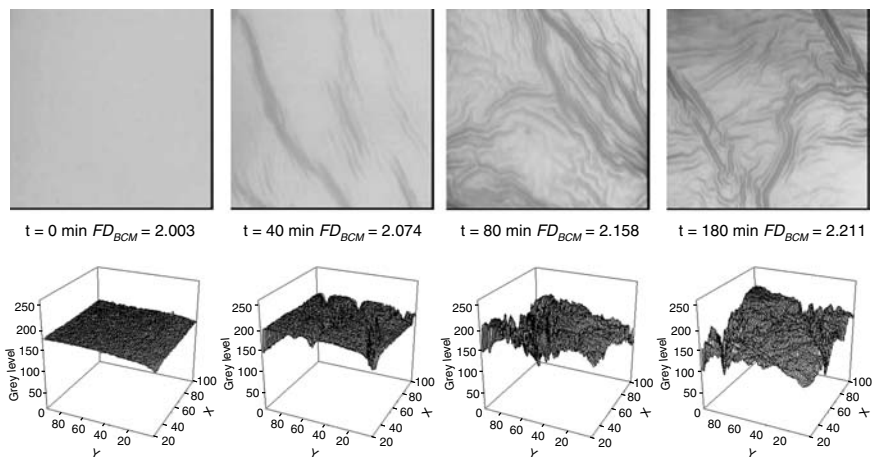


FIGURE 32.2

Light microscopy images (100 ×) of agar–maltodextrin slabs during drying at several times and fractal dimension of images using the box-counting method. The corresponding grey level intensity plots. X, Y are spatial position coordinates. Drying conditions: 55°C, 1 m/sec.

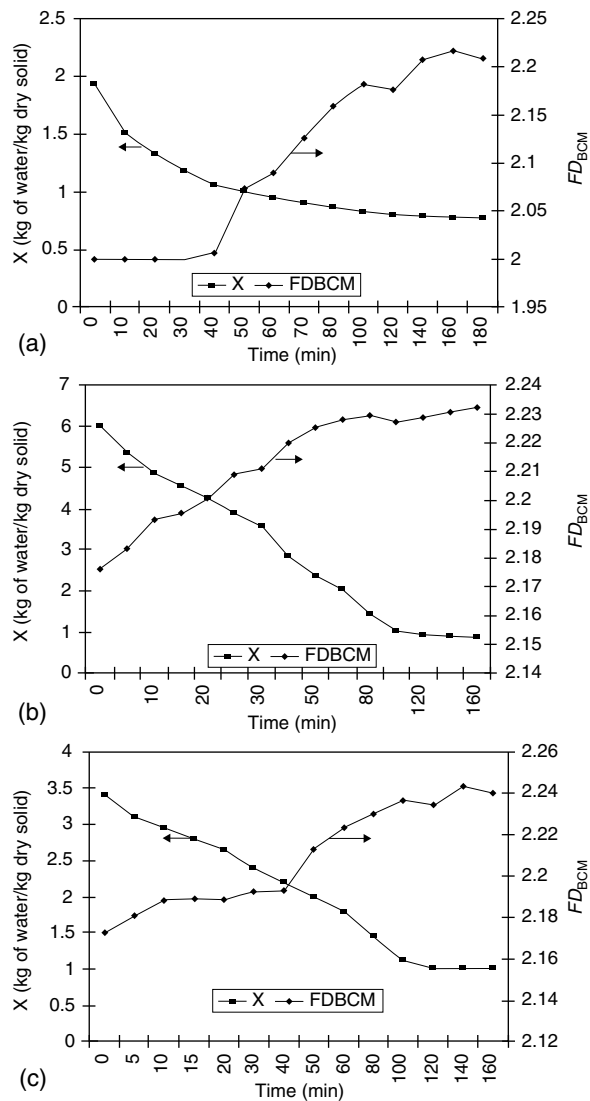


FIGURE 32.3 Drying kinetics and changes of FD_{BCM} during drying of: (a) maltodextrin-agar slabs at 55°C and 1 m/sec, (b) apple slices at 55°C and 1 m/sec and (c) potato slices at 45°C, 1 m/sec.

Agar-maltodextrin slabs were taken as models to evaluate the influence of the processing conditions over drying velocity (D_{eff}), microstructure generation of the surface in terms of FD_{BCM} and shrinkage. Empirical equations and their coefficients (Table 32.1) corresponding to the fitting polynomial (Equation 32.2 to Equation 32.4) were determined to carry out

TABLE 32.1
Coefficients for D_{eff} , FD_{BCM} , % of Shrinkage and Values of R^2 for Agar–Maltodextrin Slabs. Coefficients with a Value of $P < 0.05$

Coefficients of Polynomial and R_2	Polynomial Coefficients for D_{eff}	Polynomial Coefficients for FD_{BCM}	Polynomial Coefficients for Shrinkage%
A	1.820	1.389	17.979
B	0.065	0.018	0.467
C	−0.396	0.250	16.103
D	—	−0.0001	—
E	0.221	−0.066	−4.2
R_2	0.978	0.992	0.955

this evaluation, according to the methodology described above:

$$D_{\text{eff}} = a + bT + cV + eV^2 \tag{32.2}$$

$$FD_{\text{BCM}} = a + bT + cV + dT^2 + eV^2 \tag{32.3}$$

$$\% \text{ Shrinkage} = a + bT + cV + eV^2 \tag{32.4}$$

Table 32.1 shows that D_{eff} is dependent on both temperature and drying rate, given the magnitude of the values of the polynomial coefficient, and keeps a linear correspondence to temperature and a quadratic one to air flow rate (Equation 32.2). Figure 32.4 presents the dependence of D_{eff} values to the drying conditions.

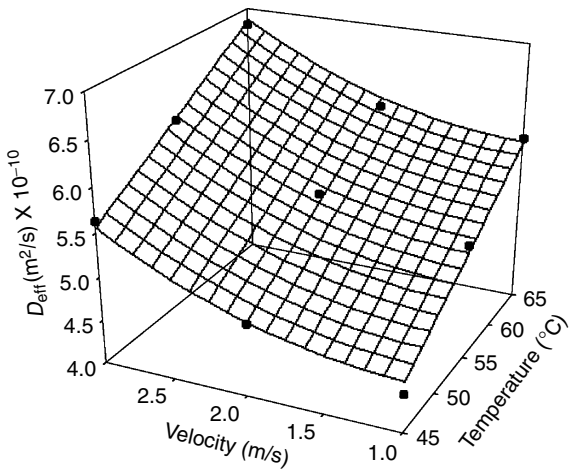


FIGURE 32.4
Graphic behavior of the experimental values of D_{eff} (•) as a function of the processing conditions, and estimated values obtained with Equation 32.2 for agar–maltodextrin slabs.

Analyzing the variation of the FD_{BCM} as a function of processing conditions, an increase in the temperature of the dry air produces a proportional increase in the values of FD_{BCM} (Figure 32.5). Increase in airflow does not produce increase over the values of FD_{BCM} , as seen in Figure 32.5. To analyze the influence of the independent variables (T and V) over the FD_{BCM} , a determined polynomial (Equation 32.5) and its coefficients (Table 32.1) can be used. In this case, FD_{BCM} is dependent on both temperature and air rate. Figure 32.5 illustrates the graphic behavior of the polynomial (Equation 32.5) and its experimental values as a function of processing conditions.

The influence of temperature and dry air rate on the microstructure indicates that the processing conditions that give high (Figure 32.4) and low drying rates are associated with low values of FD_{BCM} (Figure 32.5). This results in development of smoother surfaces, while intermediate drying rates are associated to more irregular surfaces and high values of FD_{BCM} . Microstructural characteristics related to drying conditions has not been extensively described in the literature. Some studies report quantitative data using fractal geometry (Pedreschi and Aguilera, 2001; López, 2002; Quevedo et al., 2002a, 2002b), such as those analyzed the behavior of textural changes of a model paint film (Takase et al., 1994), and reported that the increase in temperature and dry air rate promoted a decrease in surface roughness and an increase of the porosity of the film. Additionally, authors included a descriptive model for the development of texture, establishing that at low drying rates, texture first adopted horizontal orientation. As drying proceeded, structures packed, increasing roughness and possibly decreasing

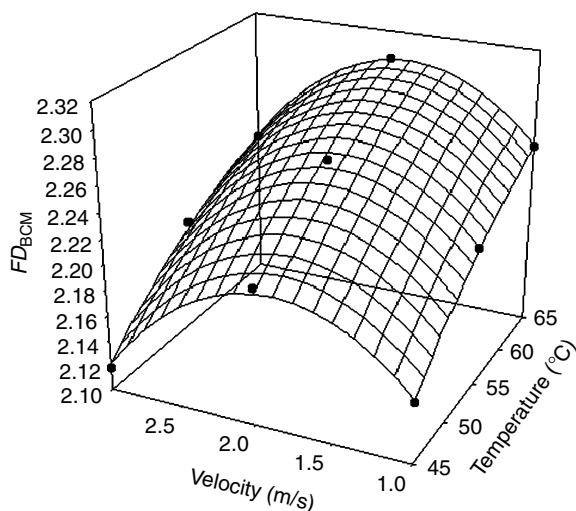


FIGURE 32.5

Experimental values of FD_{BCM} (•) as a function of processing conditions and estimated values obtained with Equation 32.3 for agar–maltodextrin slabs.

porosity. For high drying rates, the paint solvent evaporated rapidly, producing a formation of a pigment crust with a lower roughness and a higher porosity of the film. The results obtained for dehydrated slabs in our work are in agreement with this report.

Given the above, it can be said that the phenomenon of roughness change during drying is not linearly dependent on air rate nor on air temperature. Another factor that has an important effect over microstructure and dry rate is shrinkage. In our study, shrinkage was a relevant factor since its values ranged from 50.42% to 63.5% for every experiment with agar–maltodextrin slabs. Regarding shrinkage, the corresponding polynomial and its coefficients are shown in Table 32.1 and Equation 32.6. From these results, it can be seen that shrinkage depends on both temperature and drying rate, where the quadratic term of the dry air rate is also relevant. This agrees with studies by Ratti (1994), who pointed out that in the case of apple and potato slices, dry air rate is an important factor that affects shrinkage.

Mathematical behavior of shrinkage is similar to that of FD_{BCM} (Figure 32.4), which agrees with the development of microstructure since roughness tends to increase at higher shrinkage values. A possible explanation for the increase in roughness and shrinkage at intermediate drying rates (2 m/sec) can be inferred when considering that a higher air-drying rates (3 m/sec), a crust with a smooth microstructure is formed and shrinkage is limited. This causes D_{eff} to increase in spite of a higher resistance to the transfer of mass caused by the formation of the crust. However, when airflow is low (< 1.5 m/sec), the dehydration velocity may be limited, possibly because of the external resistance (Ferrao et al., 1998). This causes a slower drying which results in lower shrinkage and roughness. When using 2 m/sec, the formation of the crust may be slower since the maximum roughness of the samples is achieved at longer times as compared with the maximum roughness observed at 1 and 3 m/sec. The effect of dry air temperature over D_{eff} , shrinkage, and FD_{BCM} closely resembles a linear relationship, which agrees with other reports that point out that drying rate is dependent on temperature (Ferrao et al., 1998; Johnson et al., 1998; Hernández et al., 2000).

Descriptive Model for Drying of Agar–Maltodextrin Slabs

From results described above, a descriptive model for the drying process of biological slabs or slices is proposed. The model is based on the drying periods described in the classic theory, and requires establishing relationships between drying kinetics and evolution of FD_{BCM} values. Figure 32.6 is a selected example that illustrates drying kinetics with evolution of fractal dimension.

The initial drying stage, known as period of adjustment of the drying conditions in the classic theory, is usually short. Its characterization is

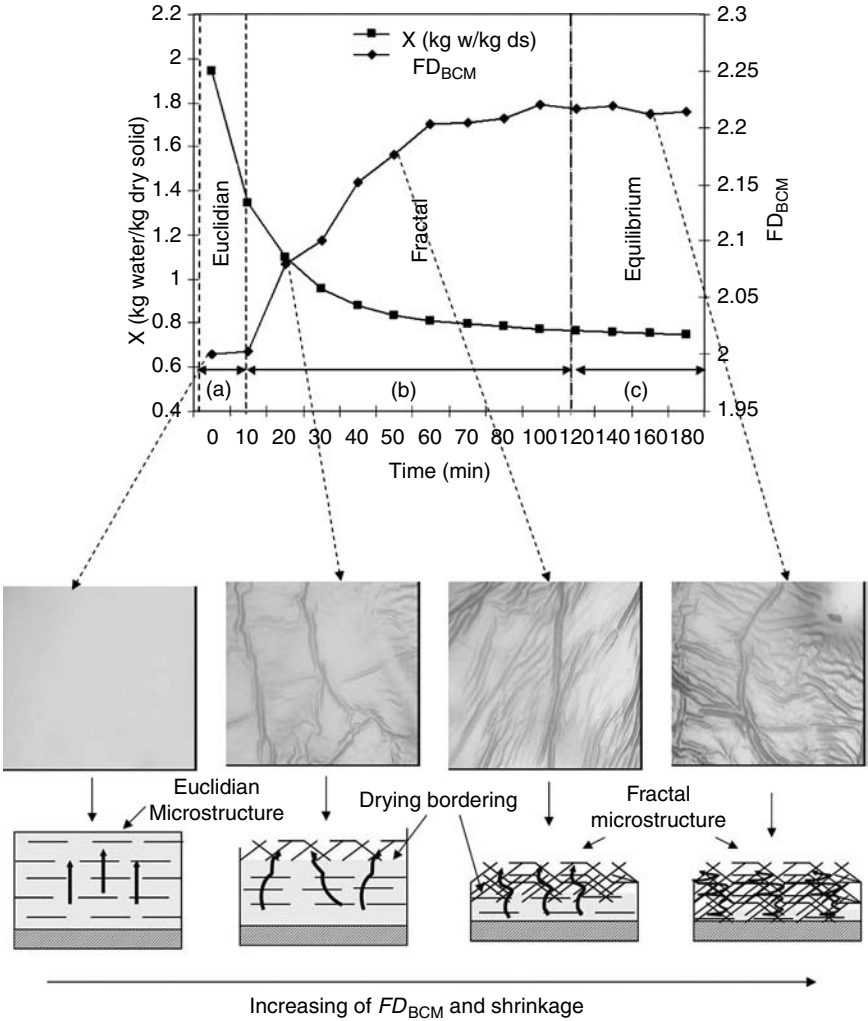


FIGURE 32.6

Graphic representation of the conformation of a surface with fractal microstructure during drying of agar–maltodextrin slabs at 65°C and 3 m/sec. (a) It may delimit the initial period of adjustment of the process and the constant dry rate period, (b) delimits the decreasing rate period; the change in microstructure and shrinkage may modify the resistance to mass transfer, (c) delimits the equilibrium period, where drying is completed and a surface with a fractal microstructure is formed.

important for the phenomenological study of drying. Previous reports (Gutiérrez et al., 2002; Chanona et al., 2003) on convective drying of a model food (agar–glucose syrup) showed that at this initial period the superficial temperatures showed a chaotic behavior which may be a result of the heterogeneity of surface moisture distribution fluctuations that take place as

the sample adjusts itself to the drying conditions (Gutiérrez et al., 2002; Chanona et al., 2003). For the case of agar–maltodextrin slabs, this stage could not be seen at the conditions under study. When, dried zones appear on the surface of the samples, distribution and fluctuation of superficial temperatures may be of a fractal nature (Gutiérrez et al., 2002; Chanona et al., 2003). This can be described with the use of potency laws. Also, during the first minutes of this stage, the surface of the material presents some textural changes (Figure 32.6).

As the moisture continues to evaporate, changes in microstructure may be observed. The surface of the sample acquires fractal geometry and the drying front is in the interior of the material. At 2 m/sec, fractal structures (higher FD_{BCM}) are associated with a drop in D_{eff} . This implies that diffusion of water does not follow Euclidian paths but takes place through a solid matrix with fractal characteristics, and diffusion may not be considered constant as defined by Fick's second law. Evidence on transport through fractal media has already been published for phenomena other than drying (Sapoval et al., 1989; Giona et al., 1996a, 1996b). The complexity of the medium is higher towards the end of the drying process where at low moisture contents, water is located in the interior of the sample and the moisture has to move through a dense net that is irregular and of fractal characteristics (Figure 32.6).

Finally, it is possible to point out that fractal surfaces and drying fronts are generated during drying. Temperature and airflow have a strong influence towards the level of irregularity of the structure. Diffusion is partially controlled by these fractal structures and, therefore, drying rate strongly influences the fractal behavior of the materials subjected to dehydration.

References

- AOAC, *Official Methods of Analysis*, 16th ed, Arlington Virginia: Association of Official Analytical Chemists International, 1995.
- Aguilera, J.M. and Stanley, D.W. *Microstructural principles of food processing and engineering*, 2nd ed., Aspen Publishing Inc., Maryland, USA, pp. 373–411, 1999.
- Arnosti, S., Freire, J.T., and Sartori, D.J.M. Analysis of shrinkage phenomenon in *Brachiaria brizantha* seeds, *Drying Technol.*, 18, 1339, 2000.
- Brinker, C.J. and Sherer, W.G. *Sol–Gel Science The Physics and Chemistry of Gel Processing*, Academic Press, London, pp. 507–508, 1990.
- Chanona, P.J., Alamilla, B.L., Farrera, R., Quevedo, R., Aguilera, J.M., and Gutiérrez, L.G. Description of convective air-drying of a food model by means of the fractal theory, *Food Sci. Technol. Int.*, 9, 207, 2003.
- Crank, J. *The Mathematics of Diffusion*, Oxford University Press, Oxford, 1975.
- Cronin, K. and Kearney, S. Monte Carlo modelling of vegetable tray dryer, *J. Food Eng.*, 35, 233, 1998.

- Doulia, D., Tzia, K., and Gekas, V. A knowledge base for the apparent mass diffusion coefficient (D_{EFF}) of foods, *Int. J. Food Prop.*, 3, 1, 2000.
- Ferrao, P., Figueiredo, A., and Freire, F. Experimental analysis of drying kinetics of food product, *Drying Technol.*, 16, 1687, 1998.
- Gekas, V. and Lamberg, I. Determination of diffusion coefficients in volume-changing systems-application in case of potato drying, *J. Food Eng.*, 14, 317, 1991.
- Giona, M., Schwalm, W.A., Schawalm, M.K., and Adrover, A. Exact solution of linear transport equations in fractal media. Renormalization analysis and general theory, *Chem. Eng. Sci.*, 51, 4717, 1996a.
- Giona, M., Schwalm, W.A., Schawalm, M.K., and Adrover, A. Exact solution of linear transport equations in fractal media. Diffusion and convection, *Chem. Eng. Sci.*, 51, 4731, 1996b.
- Gogus, F. and Maskan, M. Water transfer in potato during air drying, *Drying Technol.*, 16, 1715, 1998.
- Gutiérrez, L.G.F., Chanona, P.J., Alamilla, B.L., Hernández, P.A., Jiménez, A.A., Farrera, R.R., and Ondorica, V.C. A proposal of análisis the drying phenomena by means of fractal theory, *Engineering and food for the 21st century*, J. Welti-Chanes, G.V. Barbosa-Cánovas and J.M.C.R. Aguilera, eds., CRC Press, Boca Raton, pp. 269–287, 2002.
- Hernández, J.A., Pavón, G., and García, M.A. Analytical solution of mass transfer equation considering shrinkage for modeling food-drying kinetics, *J. Food Eng.*, 45, 1, 2000.
- Johnson, P.N.T., Brennan, J.G., and Addo-Yobo, F.Y. Air-drying characteristics of plantain (Musa AAB), *J. Food Eng.*, 37, 233, 1998.
- López, G.C. *Interpretación microestructural del transporte de agua en tejido de papa durante el proceso de fritura por inmersión en aceite*, Tesis de Doctorado. Instituto Politécnico Nacional-ENCB, México, D.F., 2002.
- Pedreschi, F. and Aguilera, J.M. Quantitative characterization of potato product surfaces using scale-sensitive analysis, *Proceedings of the 8th International Congress on Engineering and Food (ICEF8)*. Puebla México, pp. 88–93, 2001.
- Quevedo, R., Aguilera, J.M., and Pedreschi, F. Characterization of food surfaces (Roughness) using the different box counting method, *Proceedings of the 8th International Congress on Engineering and Food (ICEF 8)*. Puebla México, pp. 189–193, 2002a.
- Quevedo, R., López, G.R., Aguilera, J.M., and Cadoche, L. Description of food surfaces and microstructural changes using fractal image texture analysis, *J. Food Eng.*, 53, 361, 2002b.
- Ratti, C. Shrinkage during drying of foodstuffs, *J. Food Eng.*, 23, 91, 1994.
- Rovedo, C.O., Suárez, C., and Viollaz, P.E. Drying of foods: Evaluation of drying model, *J. Food Eng.*, 26, 1, 1995.
- Rovedo, C.O., Suárez, C., and Viollaz, P.E. Kinetics of forced convective air drying of potato and squash slabs, *Food Sci. Technol. Int.*, 3, 251, 1997.
- Sano, Y. and Keey, R.B. The drying of spherical particle containing colloidal material into a hollow sphere, *Chem. Eng. Sci.*, 27, 881, 1982.
- Sapoval, B., Ross, M., and Gouyet, J.F. Fractal interfaces in diffusion, invasion a corrosion, *The Fractal Approach to Heterogeneous Chemistry. Surfaces, Colloids, Polymers*, D. Avnir, ed., Wiley, London, pp. 227–245, 1989.
- Saravacos, G.D. Mass transfer properties of foods, *Engineering Properties of Foods*, 2nd Ed., M.A. Rao and S.S.H Rizvi, eds., Marcel Dekker, New York, pp. 169–221, 1995.

- Sarkar, N. and Chaudhuri, B.B. An efficient differential box-counting approach to compute fractal dimension image, *IEEE Trans. Systems, Man Cybernetics*, 24, 115, 1994.
- Takase, K., Miura, H., Tamon, H., and Okazaki, M. Structure formation of coated films with dispersed pigments during drying, *Drying Technol.*, 12, 1279, 1994.

33

Effect of Vacuum Impregnation and Microwave Application on Structural Changes during Air Drying of Apple

Carolina Contreras, María Eugenia Martín,
Nuria Martínez-Navarrete, and Amparo Chiralt

CONTENTS

Introduction	495
Materials and Methods	496
Materials	496
Drying Treatments	496
Moisture Equilibration	497
Analytical Determinations	497
Statistical Analysis	498
Results and Discussion	498
Changes in Pectic Composition as a Result of Drying Treatment	498
Calorimetric Analysis	499
Mechanical Properties	500
Conclusions	501
Acknowledgments	502
References	502

Introduction

Drying of fruits promotes water loss and changes in product phases and components. In a simplified way, fruits can be considered as being made up of two phases: the insoluble cellular matrix and the liquid phase containing the water-soluble compounds inside cells or intercellular spaces. Water distribution among phases changes during the drying process, depending on the process conditions. Changes in soluble components and the insoluble

matrix can also occur. These phenomena affect molecular interactions in each phase and so the final properties and structure of the product also. Mechanical properties of dehydrated products are closely related to the physical state (glassy or rubbery) of the phases (Roos et al., 1998) and to the structure developed as a result of induced deformations in cells and intercellular spaces and of ruptures in cell bonding. Previous studies showed that the drying process induces changes in the pectic substances because of the structural modification of the cell wall, which is also related to textural changes in dehydrated products (Forni et al., 1986; Torreggiani et al., 1998). Analysis of mechanical behavior related to product texture, glass-transition temperatures, and changes in pectic fractions during fruit drying may help understand the structural and quality changes that take place during dehydration as a function of process conditions. The aim of this work was to analyze the effect of drying conditions (vacuum impregnation pretreatment, MW application, and air temperature) on structural changes that took place in apple. In this sense, the analysis of changes that occurred in the structural polymers (pectic fractions), mechanical properties of dried products, and glass-transition temperature of the soluble solid fraction of the fruit was carried out as a function of moisture content.

Materials and Methods

Materials

Apples (var. Granny Smith) were purchased in a local market. All apples were characterized as to water content (x_w): 0.87 ± 0.01 g water/g sample, 11.5° Brix ± 0.4 , pH 3.4 ± 0.1 and water activity (a_w) 0.985 ± 0.004 . Slices 7 mm thick were cut perpendicularly to the fruit axis. Only the three central slices of each apple were used. These were not peeled but the core was taken out with a 20-mm diameter cylindrical core borer.

Drying experiments were carried out using fresh and vacuum-impregnated samples. Apple slices were impregnated with a commercial and isotonic apple juice (same a_w as fresh apple, 12° Brix, pH 3.6 ± 0.2) by applying vacuum pressure (50 mbar) for 5 min and then restoring the atmospheric pressure, and keeping the samples immersed for 10 min more. The weight of samples was controlled before and after vacuum impregnation.

Drying Treatments

Vacuum-impregnated (VI) and nonvacuum-impregnated (NVI) apple slices were dried by air drying (AD) and by combined air-microwave technique (MWD) using a modified household microwave oven, where air temperature and velocity and MW power may be controlled

(Martín et al., 1999; Martín et al., 2003). For the experiments, air rate was 2.5 m/sec, air temperature 30 and 50°C and microwave incident power 80 W (corresponding to 0.5 W/g). Sample VI in MWD was only processed at 30°C air temperature because at 50°C notable thermal damage was observed in samples. Thus, seven drying treatments were considered. All samples were dried to 10 g water/100 g sample by the continuous control of sample mass in a specially designed MW-air drying oven coupled to a balance and connected to a computer (Martín et al., 2003), taking into account the initial moisture content. Each drying treatment was carried out on six slices from two apples and it was repeated five times. Six apple slices were used to analyze pectin fractions as described in the next subsection. The rest of the dried slices were conditioned at different moisture contents to determine their mechanical properties and glass-transition temperature.

Moisture Equilibration

Dried slices with 10 g water/100 g sample were further equilibrated at different moisture contents in chambers at 20°C with controlled relative humidity, using saturated salt solutions: P_2O_5 $a_w = 0$, LiCl $a_w = 0.11$ and CH_3COOK $a_w = 0.22$ (Katz and Labuza, 1981).

Analytical Determinations

Moisture content was determined by drying in a vacuum oven at 60°C until constant weight was reached (AOAC, 1980). Analysis of pectic fractions was carried out through the quantification of galacturonic acid in the fractions: water-soluble pectin (WSP), oxalate-soluble pectin (OSP), and total pectin (TP). These fractions were obtained by selective extraction of homogenized samples according to the method described by Yu et al. (1996). Galacturonic acid (GalA) content in the different fractions was determined colorimetrically at 520 nm (in triplicate for each extract), as described by Kinter and Van Buren (1982), by using the *m*-hydroxydiphenyl method. Results were expressed as g GalA/100 g of initial fresh sample (even in the dried samples). The difference between TP and the sum of WSP and OSP was taken into account to estimate the amount of nonextractable pectin (NXP), which was the protopectin fraction. Glass-transition temperature (T_g) was measured in samples with different water contents by using differential scanning calorimetry (DSC 5200Co, Seiko Instruments). The heating rate of samples in the calorimeter was 5°C/min and the analysis was carried out between -20 and 80°C, depending on the moisture content. The midpoint of the observed transition was considered. Mechanical properties of dried samples with different water contents were analyzed at 25°C by using a puncture test with a Universal Texture Analyzer (TA.XT2, Stable Micro Systems). A cylindrical 2-mm diameter punch was used at a penetration rate of 1.5 mm/sec until total sample penetration.

Statistical Analysis

Analyses of variance (ANOVA) were carried out to study the effects of process conditions on the sample measured properties by using Statgraphics Plus vers. 5.1.

Results and Discussion

Changes in Pectic Composition as a Result of Drying Treatment

Table 33.1 shows the ratio of the different pectic fractions in samples submitted to the different treatments as compared with the values obtained in fresh samples, all of which are expressed as galacturonic acid (GalA) content per 100 g of initial fresh sample. Content in the different pectin fractions was heavily dependent on drying conditions. A multifactor analysis of variance (ANOVA) in both NVI and VI samples revealed a significant influence of air temperature and MW applications on the levels of WSP and protopectin. When air temperature increased or when microwaves were applied, WSP content increased and protopectin fraction decreased, this effect being more marked when samples were submitted to vacuum impregnation. Sample heating during drying by air or MW promotes pectin solubilization. This effect was especially important when sample inter-cellular spaces were full of an aqueous phase (VI samples) in contact with the middle lamellae. Pectin solubilization affects both the average molecular weight of solutes in the fruit liquid phase and the cell bonding forces supporting the cellular structure. These two factors will have a great impact on the sample texture of dried samples.

TABLE 33.1
Galacturonic Acid Content (g GalA/100 g of Initial Fresh Sample) Analyzed in the Different Pectic Fractions of Fresh and Dried Apple

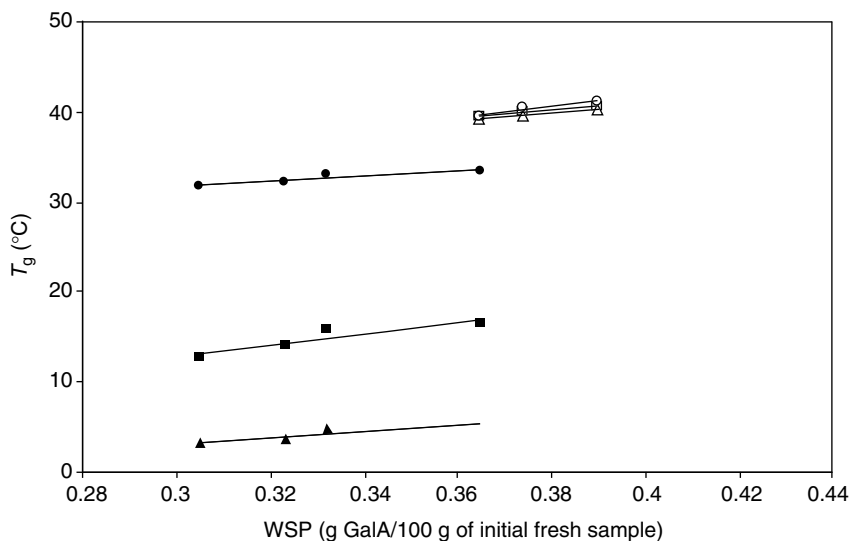
	WSP	OSP	NXP	TP
Sample	g GalA/100 g of Initial Fresh Sample			
Fresh	0.313 ± 0.001	0.063 ± 0.003	0.468 ± 0.001	0.844 ± 0.001
VI-AD-30°C	0.365 ± 0.001	0.018 ± 0.001	0.255 ± 0.002	0.638 ± 0.001
VI-AD-50°C	0.374 ± 0.003	0.019 ± 0.002	0.229 ± 0.001	0.621 ± 0.001
VI-AD-MWD-30°C	0.390 ± 0.002	0.012 ± 0.001	0.214 ± 0.003	0.616 ± 0.002
NVI-AD-30°C	0.305 ± 0.001	0.058 ± 0.002	0.446 ± 0.001	0.810 ± 0.001
NVI-AD-50°C	0.323 ± 0.001	0.059 ± 0.001	0.410 ± 0.003	0.791 ± 0.001
NVI-AD-MWD-30°C	0.332 ± 0.003	0.035 ± 0.001	0.395 ± 0.001	0.762 ± 0.001
NVI-AD-MWD-50°C	0.365 ± 0.002	0.023 ± 0.001	0.237 ± 0.002	0.626 ± 0.002

Calorimetric Analysis

Mean T_g values for samples from different treatments are shown in Table 33.2. T_g values were affected by the kind of drying treatment. VI samples showed higher values and no influence of MW application and air temperature was observed. In NVI samples an increase in T_g was observed when MWs were applied and when air temperature increased. These results are in agreement with the increase in the average molecular weight of solutes provoked by pectin degradation and solubilization in the aqueous phase. Lineal relationships (Figure 33.1) were observed between T_g and soluble pectin content at the different a_w levels. Different behavior for VI and NVI samples was observed, which could be associated to the fact that other compounds with higher molecular weight could contribute to the higher T_g of the aqueous phase in VI samples, which are not notably plasticized in the a_w range considered in the study.

TABLE 33.2
Equilibrium Moisture Content (x_{we}) and Glass Transition
Temperature (T_g) for Vacuum Impregnated and Nonvacuum
Impregnated Samples Dried at Different Conditions,
as a Function of Water Activity (a_w)

Sample	a_w	x_{we} (g_{water}/g_{sample})	T_g (°C)
VI-AD-30°C	0	0.000 ± 0.002	39.5 ± 0.5
	0.11	0.044 ± 0.002	39.6 ± 0.3
	0.22	0.079 ± 0.001	39.3 ± 0.4
VI-AD-50°C	0	0.000 ± 0.001	40.6 ± 0.4
	0.11	0.044 ± 0.002	40.3 ± 0.1
	0.22	0.079 ± 0.002	39.5 ± 0.3
VI-AD-MWD-30°C	0	0.000 ± 0.001	41.2 ± 0.3
	0.11	0.043 ± 0.001	40.7 ± 0.3
	0.22	0.079 ± 0.002	40.3 ± 0.3
NVI-AD-30°C	0	0.000 ± 0.003	31.7 ± 0.4
	0.11	0.038 ± 0.001	12.6 ± 0.3
	0.22	0.065 ± 0.003	3.1 ± 0.1
NVI-AD-50°C	0	0.000 ± 0.001	32.2 ± 0.6
	0.11	0.038 ± 0.002	13.9 ± 0.2
	0.22	0.065 ± 0.001	3.4 ± 0.1
NVI-AD-MWD-30°C	0	0.000 ± 0.003	33.0 ± 0.1
	0.11	0.037 ± 0.002	15.7 ± 0.1
	0.22	0.064 ± 0.002	4.5 ± 0.1
NVI-AD-MWD-50°C	0	0.000 ± 0.001	33.4 ± 0.5
	0.11	0.038 ± 0.003	16.2 ± 0.1
	0.22	0.064 ± 0.002	4.9 ± 0.1

**FIGURE 33.1**

Relationships between glass-transition temperature (T_g) and water-soluble pectin content (WSP) for VI and NVI samples: (○) VI a_w 0, (◻) VI a_w 0.1, (△) VI a_w 0.2, (●) NVI a_w 0, (■) NVI a_w 0.1, (▲) NVI a_w 0.2.

Mechanical Properties

Parameters obtained from the force–deformation curves were: the maximum force required to break the sample, the deformation at this point, the initial slope of the curves, and the ratio at the break point. The peak of maximum force and the ratio force–deformation are related to the product resistance to fracture or sample firmness (Prothon et al., 2001) and the initial slope of the force–deformation curves is related to the elasticity modulus or sample resistance to deformation. Figure 33.2 shows the obtained average values for the force–distance ratio at the maximum point (F_{\max}/d), as a function of the sample water activity. For the same drying treatment, significant differences were found as a function of a_w for NVI samples. However, this factor did not significantly affect the mechanical response of the VI samples. The increase of a_w in dried NVI samples provokes a decrease in the slope of the curves, and the ratio F_{\max}/d , whereas deformation at break increases. This behavior indicates a reduction in the resistance to deformation as product water content increases, in agreement with the water plastizicer effect. In general, the slope and F_{\max}/d were higher when microwaves were applied and no notable effect of air temperature was appreciated. None of these effects was evident in VI samples.

No clear correlations between T_g values and mechanical parameters of the samples were observed. Properties of the cellular matrix and its water binding capacity, not reflected in T_g values (characteristic of the water

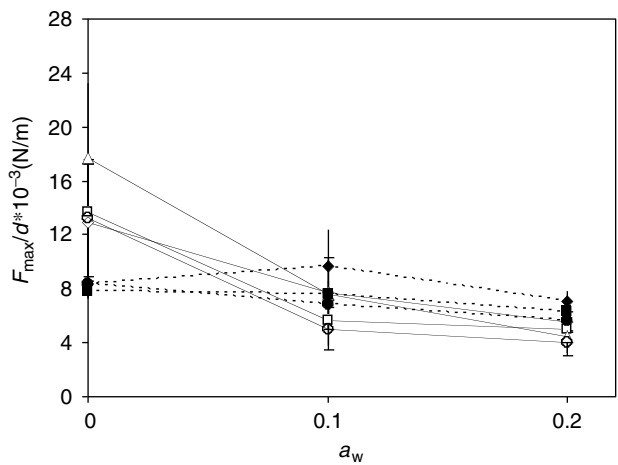


FIGURE 33.2
Ratio force–deformation (F_{\max}/d) of dried apple as a function of water activity (a_w): (■) VI-AD-30°C, (●) VI-AD-50°C, (◆) VI-AD-MWD-30°C, (□) NVI-AD-30°C, (○) NVI-AD-50°C, (◇) NVI-AD-MWD-30°C, (△) NVI-AD-MWD-50°C.

soluble phase), play an important role in the dried sample texture. Pectin solubilization, commented on above, implies cell debonding and an increase in the average molecular weight of solutes present in the aqueous phase. In dried products where cells are collapsed, the force of cellular bonds can be less relevant to product texture appreciation than the pectin content in the aqueous phase that affects its consistency. Thus, the treatments where pectin solubilization occurs to a greater extent will lead to more rigid, less deformable structures. In VI samples, the greater pectin solubilization and the exchange of internal gas in the pores for an external liquid can contribute to the increase in cellular compactness and the homogeneity in mechanical behavior.

Conclusions

MW application during air drying and vacuum-impregnation pretreatment with isotonic solution greatly affect the structural changes in apple slices. Different changes in product phases explain the different mechanical behavior of dried samples. Dried samples become harder when pectin solubilization increases. Different process conditions will be recommended depending on the required properties of the final product: To obtain brittle products, MW application in nonimpregnated samples is recommended. However, VI pretreatment gives rise to tougher, nonbrittle products of low sensitivity to plasticization.

Acknowledgments

The authors thank the Ministerio de Ciencia y Tecnología and the Fondo Europeo de Desarrollo Regional (FEDER) for their financial support throughout the projects AGL2001-3025 and AGL2002-01793.

References

- AOAC, *Official Methods of Analysis*, 13th Ed., Association of official analytical chemists, Washington, DC, 1980.
- Forni, E., Torreggiani, D., Battiston, P., and Polesello, A. Research into changes of pectic substances in apricots and peaches processed by osmotic dehydration, *Carbohydr. Polym.*, 6, 379, 1986.
- Katz, E.E. and Labuza, T.P. Effect of water activity on the sensory crispness and mechanical deformation of snack food products, *J. Food Sci.*, 46, 403, 1981.
- Kinter, P.K. and Van Buren, J.P. Carbohydrate interference and its correction in pectin analysis using the *m*-hydroxydiphenyl method, *J. Food Sci.*, 47, 756, 1982.
- Martín, M.E., Fito, P., Martínez-Navarrete, N., and Chiralt, A. Combined air-microwave drying of fruit as affected by vacuum impregnation treatments, *Proceedings of the 6th Conference of Food Engineering*, 1999.
- Martín, M.E., Martínez-Navarrete, N., Chiralt, A., and Fito, P. Diseño y construcción de una instalación experimental para el estudio de la cinética de secado combinado por aire caliente y microondas, *Alimentación. Equipos Tecnol.*, 181, 101, 2003.
- Prothon, F., Ahrné, L., Funebo, T., Kidman, S., Langton, M., and Sjöholm, I. Effects of combined osmotic and microwave dehydration of apple on texture, microstructure and rehydration characteristics, *Lebensm. Wiss. Technol.*, 34, 95, 2001.
- Roos, Y.H., Roininen, K., Jouppila, K., and Tuorila, H. Glass transition and water plasticization effects on crispness of a snack food extrudate, *Int. J. Food Prop.*, 1, 163, 1998.
- Torreggiani, D., Forni, D., Maestrelli, A., and Quadri, F. Influence of osmotic dehydration on texture and pectic composition of kiwifruit slices. *Proceedings of the 11th International Drying Symposium (IDS'98)*, vol. A, 930, 1998.
- Yu, L., Reitmeier, C.A., and Love, M.H. Strawberry texture and pectin content as affected by electron beam irradiation, *J. Food Sci.*, 61, 844, 1996.

Modulation of the Hydration of Lipid Membrane Phosphates by Choline, Glycerol, and Ethanolamine Groups

Fabiana Lairion, Florencia Martíni, Sonia Díaz, Silvia Brandan, Aída Ben Altabef, and E. Aníbal Disalvo

CONTENTS

Introduction	503
Results.....	505
Discussion	508
References	509

Introduction

Water is crucial to maintain the integrity and the permeability of biological membranes. Therefore, the preservation processes by which water is extracted from cells and tissues, such as dehydration, lyophilization, or desiccation, need careful analysis with regard to the interaction of water with membrane groups and the interfacial properties derived from it.

Dehydration may produce a change in the relative areas of the polar head groups with respect to the acyl chain region affecting the topological conformation of the lipid arrangements. Thus, lipids that in normal conditions are stabilized in a bilayer may abandon this conformation to adopt a hexagonal phase, destroying the permeability barrier of the membrane and its ability to separate electrical charges (Epand, 1997).

Calorimetric measurements have shown phosphatidylcholine hydrates with five to seven water molecules in the gel state and 18 to 20 in the liquid crystalline state (Jendrasiak and Hasty, 1974; Hauser et al., 1981). According to small angle x-ray spectrometry (SAXS) of phosphatidylcholines, these water molecules are distributed in the polar head group region, composed

by the water/glycerol interface, the phosphates, and several kinds of groups esterified to it (choline, ethanolamine, glycerol, inositol, etc.) (White and Wiener, 1995). In addition, a small penetration towards the carbonyl groups is also found (Simon and McIntosh, 1986).

Part of this water is polarized, that is, the dipole moment is partly oriented around an angle normal to the membrane surface, contributing to the surface potential. In the bilayer conformation, the low dielectric permittivity of the hydrocarbon core ($\epsilon = 2$) makes the membrane an electrical insulator (Montal and Mueller, 1972). The orientation of the water dipole with respect to the plane of the membrane contributes to the dipole potential (Brockman, 1994).

Phosphate is a common chemical group in all the phospholipids composing natural membranes. It is linked to the acyl glycerol backbone and esterified to choline, ethanolamines, and glycerol among others. Phosphates are the primary regions of hydration in lipid membranes. The mobility of phosphates increases as hydration increases, reaching a constant value at around six water molecules per lipid. Thus, these water molecules constitute the first hydration layer bound to the oxygen phosphates and ester bonds. Hydrogen-bonding compounds, such as trehalose and phloretin, bind to these same regions displacing water.

The hydration state of the membrane structure determines a water-restricted media in its surroundings since phospholipids impose different degrees of orientation and freedom to water molecules hydrating the polar head groups (Diaz et al., 1999). The different hydration levels of the polar head groups determine different values of the surface potential and the dipole potential (Diaz et al., 2001). This potential modulates the penetration of peptides to the membrane phase, the permeability of hydrophobic anions, the permeation of water (Flewelling and Hubbell, 1986; Gawrisch et al., 1992; Simon et al., 1992; Cafiso, 1995), and opposes the membrane–membrane contact during adhesion processes.

The dipole potential of a lipid membrane is manifested between the hydrocarbon core of the membranes and the first few water molecules adjacent to the lipid head groups (Brockman, 1994). This potential is caused by the uniform orientation of the phosphocholine moiety, the carbonyl groups of the ester union, and, to some extent, by the presence of polarizable groups in the membrane hydrocarbon phase (Voglino et al., 1998; McIntosh, 2002). Therefore, in addition to steric hindrance and electrostatic forces, the hydration of the phospholipids plays a significant role in protein–membrane interactions as a participant in the short-range repulsive forces (McIntosh, 2002).

In this context, it is worthwhile to take into account that the catalytic activity of water-soluble enzymes is affected by the environment. Proteases show considerable changes in its enzymatic activity when trapped in water-restricted media such as reverse micelles (Peng and Luisi, 1990). Based on data obtained with Fourier transform infrared (FTIR) spectrometry and dipole surface potential in monolayers, we demonstrate that the hydration of

the phosphate groups in lipid membranes depends on the chemical group esterified to the phosphate. Thus, the interaction of an aqueous soluble enzyme, such as an aspartyl protease from *Mucor miehe*, and its activity may be modulated by the groups anchored to the phosphate bias of their hydration level. To test this hypothesis we measured the interaction of proteases with monolayers composed by dimyristoylphosphatidylcholine (DMPC), dimyristoylphosphatidylethanolamine (DMPE), and dioleoylphosphatidyl choline plus phloretin (DOPC:Phlo) (1:1). The changes in the activity of aqueous-soluble enzymes in the presence of membranes of different lipid composition was measured in correlation with the exposure of the phosphate of those compounds to the water phase.

FTIR spectrometry is a powerful tool to explore the degree of hydration for different polar groups of the lipid membrane (Bush et al., 1980; Hübner and Blume, 1998).

It has been shown that the asymmetric vibration mode of the PO_2 group is very sensitive to the hydration state of the bilayer. Thus, the hydration of the phosphate can be followed by the frequency shift of the $\text{P}=\text{O}$ asymmetrical mode. In addition, as water in the phosphate determines the dipole potential, its variation is indicative of the participation of this group in the membrane process.

Results

Dehydration of lipids by heat drying and by osmotic stress promotes a shift of the $\text{P}=\text{O}$ frequency mode of vibration to higher values, denoting the displacement of water molecules (Table 34.1).

In a dehydrated state, the frequency corresponding to the PO_2 group asymmetric mode of vibration is 1237 nm. Upon full hydration (18 to 20 water molecules per lipid) the frequency decreases to 1211 nm because of the formation of hydrogen bonds with the water molecules. When fully hydrated lipids are subjected to a hypertonic shock by the addition of polyethylene glycol (PEG), the frequency increases in 6 nm, indicating a small but significant water displacement from the phosphate regions.

In addition, hydrogen-bonding compounds that may compete with water binding to carbonyl or to phosphate displace the frequency to lower values.

The shifts of the frequency mode of vibration for phosphates are correlated with the amount of water displaced by each of these compounds from the lipid membrane and with the dipole potential (Table 34.2).

As shown in Figure 34.1, phloretin only affects the asymmetric mode of vibration of the phosphate groups.

A way to analyze different distributions of dipoles at the membrane interface is by studying the behavior of the surface potential as a function of the group esterified to the phosphate (Diaz et al., 2001; Disalvo et al., 2002).

TABLE 34.1
Effect of Dehydration and Osmotic Stress on the Symmetric and Asymmetric Vibration Modes of Phosphate Groups of Phosphatidylcholines

	DMPC Dehydrated	DMPC Hydrated	DMPC Hydrated + PEG	Δ Dehydrated	Δ Osmotic Shock
ν_{as} PO ₂ (nm)	1237	1211.14	1216.6	- 26	+5.45
ν_{sym} PO ₂ (nm)	1091	1086	1090.5	- 5	+4.34

Δ dehydrated: difference of frequencies between the frequencies corresponding to dehydrated DMPC and hydrates DMPC;
 Δ osmotic shock: difference between the frequencies corresponding to hydrated DMPC and hydrated PC in the presence of PEG.

TABLE 34.2
Effect of Trehalose and Phloretin on the Hydration and Dipole Potential of Lipid Membranes

Compound	Water Activity	Hydration Number	Hydrated Groups	Dipole Potential Change (mV)
DMPC	0.4803	18–20	All	0
DMPC in SUCROSE	0.4612	17	All	+5
DMPC + phloretin (1:1)	0.3170	11	C=O, PO ₂	- 120
DMPC + trehalose 0.15 M	0.265	6–7	PO ₂	-40

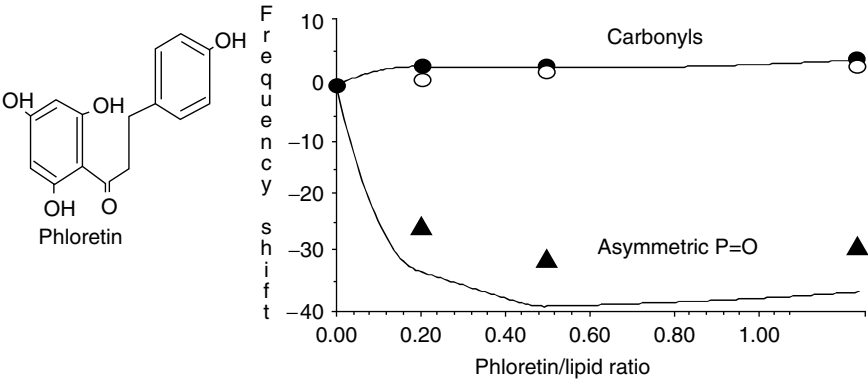
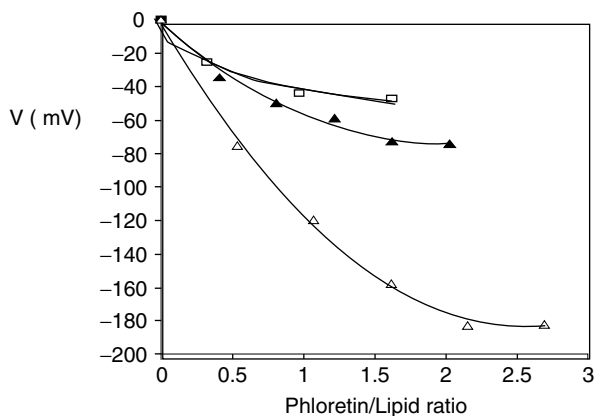


FIGURE 34.1
Effect of phloretin on the vibrational asymmetric modes of phosphates and the two populations of carbonyls in phosphatidylcholines. The frequency shift is obtained from the subtraction from the frequency value at each concentration the corresponding to DMPC without additives.

**FIGURE 34.2**

Decrease of the dipole potential of phosphatidylcholine (Δ), phosphatidylethanolamine (\blacktriangle), and phosphatidylglycerol (\square) monolayers by the addition of phloretin. Values are differences between the potential obtained at each concentration and that corresponding to monolayers of DMPC without phloretin (modified from Lairion and Disalvo (2004)).

It is of interest to correlate the phloretin action with the exposure of phosphate groups to the aqueous solution. In this regard, the head group arrangement of phospholipids, such as phosphatidylcholine (PC), phosphatidylethanolamine (PE), and phosphatidylglycerol (PG) is different, probably because of the space requirement to orient the P–N dipoles.

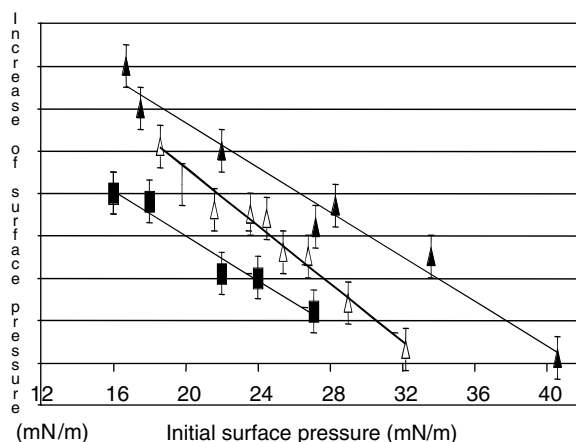
The effect of phloretin on the potential of different monolayers composed of PC, PE, and PG is shown in Figure 34.2.

The effectiveness of phloretin to decrease the dipole potential of monolayers in the fluid state is lessened by the moieties esterified to the phosphate group in the sequence choline > ethanolamine > glycerol.

The decrease in the dipole potential is correlated with the amount of water per lipid displaced by phloretin molecules (Table 34.2). As shown in Figure 34.2, a 20% phloretin decreases by 180 mV the dipole potential in phosphatidylcholine monolayers, with the displacement of around 40% of the water hydrating the phospholipids. As phloretin does not interact with the carbonyls (Figure 34.1), the decrease of dipole potential may be ascribed to the elimination of polarized water from the P=O group (Diaz et al., 2001). This action is not observed in DMPE monolayers, whose phosphate group is hydrogen bonded to the amine group (Lairion and Disalvo, 2004).

The effect of phloretin on the dipole potential of lipids with different head groups suggests that the surface properties may be modulated by the group esterified to the phospho acyl glycerol moiety.

It is of interest now to find out whether these changes may affect the interaction of water-soluble enzymes with the lipids. With this purpose, the changes in the surface pressure at constant temperature was measured at different initial surface pressure of DMPC, DMPE, and DMPC plus phloretin

**FIGURE 34.3**

Changes induced by the injection of similar concentrations of proteases on the surface pressure of DMPC (▲), DMPE (■), and DMPC with phloretin (△) monolayers at different initial surface pressures.

1:1 monolayers. The penetration of an aspartylprotease into DMPC monolayers depends on the initial lateral pressure (Figure 34.3). At low lateral pressures major changes were induced on DOPC and DMPC monolayers in the fluid state. However, at the same lateral pressure, the effects were much lower when the monolayer was composed by DMPE. The interaction of the protein with PC monolayers is notably reduced in the presence of phloretin.

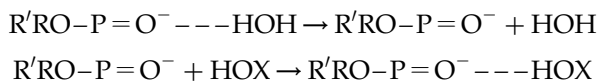
Discussion

According to the FTIR measurements showed above, there is no effect of phloretin on the ester carbonyl vibration modes parallel to a significant shift of the asymmetric mode of the phosphate. Thus, the decrease in dipole potential produced by phloretin on ester lipids, shown in Table 34.2, can be ascribed to the formation of hydrogen bonds between the OH groups of phloretin and the P=O. This interaction decreases the hydration of the lipids.

In PCs, the phosphate groups are linked to infinite zig-zag ribbons by water molecules of hydration. In this case, the choline end of the $-P-O-N^+(CH_3)_3$ group is lying toward the hydrocarbon phase because of the hydrophobic character of the methyl groups (Seelig et al., 1987). In contrast, the ammonium groups in PE link together with unesterified phosphate oxygen by very short bonds (Hauser et al., 1981; Wieslander and Karlsson, 1997). The ethanolamine groups form linkage between adjacent phosphates producing a very compact, rigid head group network at the bilayer surface. The $-N^+$ end of phosphatidylethanolamines (PE) seems to be oriented

toward the water phase, forming hydrogen bonds between the phosphates and the amines of neighboring molecules and promoting a membrane packing. In phosphatidylglycerol (PG), the glycerol moiety appears to mimic the phosphate hydration (Zhang et al., 1997).

Taking into account that the interaction of H bonding compounds from the aqueous solution with the P=O groups may follow a sequence such as



it is reasonable to think that the dehydration step may have a relevant role.

The inclusion of the groups esterified to the phosphates results in a surface on which water can offer several profiles of hydration. In a region rich in PE, phosphate and amino groups would form a compact layer above the carbonyl hindering the mobility of phosphates, its hydration, and its interaction with OH of molecules such as phloretin. This region is hydrated with fewer than four water molecules. In these regions, protease would find a low water activity environment, giving place to an increase in the activity, although much lower, as observed in reversed micelles (Peng and Luisi, 1990).

In regions rich in PC, the hydrophobicity of the choline group will pull it towards the membrane phase. This orientation would make the phosphate group, and hence its charge, exposed to the water phase. This region has 18 to 20 water molecules per lipid, and OH groups from solutes such as phloretin have access both to phosphates and carbonyls.

The exposure of phosphates to water may be blocked by the glycerol moiety. In this case, the OH groups of the glycerol would mimic the water of hydration, thus decreasing the access of phloretin to the phosphate.

In correspondence with the adsorption pattern and the penetration behavior on PCs, the proteolytic activity remains unchanged. However, in PE or DOPC/phloretin membranes, activity is enhanced. The activity changes are congruent with the level of hydration of the interface. Fully hydrated phosphocholines give activities similar to that found with the enzyme in bulk water. When the hydration is reduced, as it is in the case of DMPE and DMPC + phloretin, the activity is increased (Martini, 2003). These changes in hydration appear centered in the phosphate group of the phospholipids. That is, interfaces with low water activity may increase the enzyme activity, congruent with the results reported in reversed micelles (Peng and Luisi, 1990).

References

- Brockman, H. Dipole potential of lipid membranes, *Chem. Phys. Lipids*, 73, 57, 1994.
 Bush, F.S., Adams, R.G., and Levin, I.W. Structural reorganizations in lipid bilayer systems: effect of hydration and sterol addition on Raman spectra of dipalmitoylphosphatidylcholine multilayers, *Biochemistry*, 19, 4429, 1980.

- Cafiso, D. *Permeability and Stability of Bilayers*, E.A. Disalvo and S.A. Simon, eds., CRC Press, Boca Raton, FL, pp. 179–195, 1995, chap. 9.
- Diaz, S.B., Amalfa, F., Biondi de Lopez, A.C., and Disalvo, E.A. Effect of water polarized at the carbonyl groups of phosphatidylcholines on the dipole potential of lipid bilayers, *Langmuir*, 15, 5179, 1999.
- Diaz, S., Lairi3n, F., Arroyo, J., Biondi de Lopez, A.C., and Disalvo, E.A. Contribution of phosphate groups to the dipole potential of dimiristoyl phosphatidylcholine monolayers, *Langmuir*, 17, 852, 2001.
- Disalvo, E.A., Lairion, F., Diaz, S., and Arroyo, J. *Recent Research Developments in Biophysical Chemistry*, C.A. Condat and A. Baruzzi, eds., Research Signpost, India, pp. 181–197, 2002.
- Epand, R.M. *Lipid Polymorphism and Membrane Properties*, R. Epand, ed., Academic Press, San Diego, CA, pp. 237–252, 1997.
- Flewelling, R.F. and Hubbell, W.L. The membrane dipole potential in a total membrane potential model. Applications to hydrophobic ion interactions with membranes, *Biophys. J.*, 49, 541, 1986.
- Gawrisch, K., Ruston, D., Zimmerberg, J., Parsegian, V.A., Rand, R.P., and Fuller, N. Membrane dipole potentials, hydration forces, and the ordering of water at membrane surfaces, *Biophys. J.*, 61, 1213, 1992.
- Hauser, R., Pascher, I., Pearson, R.H., and Sundell, S. Preferred conformation and molecular packing of phosphatidylethanolamine and phosphatidylcholine, *Biochim. Biophys. Acta*, 650, 21, 1981.
- Hübner, W. and Blume, A. Interactions at the lipid–water interface, *Chem. Phys. Lipids*, 96, 99, 1998.
- Jendrasiak, G.L. and Hast, J.H. The hydration of phospholipids, *Biochim. Biophys. Acta*, 337, 79, 1974.
- Lairion, F. and Disalvo, E.A. Effect of phloretin on the dipole potential of phosphatidylcholine, phosphatidylethanolamine and phosphatidylglycerol monolayers, *Langmuir*, 20, 9151, 2004.
- Martini, M.F. and Disalvo, M.F. Effect of polar head groups on the activity of aspartyl protease adsorbed to lipid membranes, *Chem. Phys. Lipids*, 122, 177, 2003.
- McIntosh, T., Vidal, A., and Simon, S.A. The energetics of peptide–lipid interactions: modulation by interfacial dipoles and cholesterol, *Peptide–Lipid Interactions*, S.A. Simon and T. McIntosh, eds., pp. 310–338, 2002, chap. 11.
- Montal, M. and Mueller, P. Formation of bimolecular membranes from lipid monolayers and a study of their electrical properties, *Proc. Natl Acad. Sci. USA*, 69, 3561, 1972.
- Peng, B. and Luisi, P.L.J. The behavior of proteases in lecithin reverse micelles, *Biochemistry*, 188, 471, 1990.
- Seelig, J., MacDonald, P.M., and Scherer, P.G. Phospholipid head groups as sensors of electric charge in membranes, *Biochemistry*, 26, 7535, 1987.
- Simon, S.A. and McIntosh, T.J. Depth of water penetration into lipid bilayers, *Methods Enzymol.*, 127, 511, 1986.
- Simon, S.A., McIntosh, T.J., Magid, A.D., and Needham, D. Modulation of the interbilayer hydration pressure by the addition of dipoles at the hydrocarbon/water interface, *Biophys. J.*, 61, 786, 1992.
- Voglino, L., McIntosh, T.J., and Simon, S.A. Modulation of the binding of signal peptides to lipid bilayers by dipoles near the hydrocarbon–water interface, *Biochemistry*, 37, 12241, 1998.

- White, S.H. and Wiener, M.C. *Permeability and Stability of Lipid Bilayers*, E.A. Disalvo and S.A. Simon, eds., CRC Press, Boca Raton, FL, pp. 1–20, 1995.
- Wieslander, A. and Karlsson, O.P. *Lipid Polymorphism and Membrane Properties*, R.M. Epand, ed., Academic Press, San Diego, CA, pp. 517–540, 1997.
- Zhang, Y.P., Lewis, R.N., and McElhaney, R.N. Calorimetric and spectroscopic studies of the thermotropic phase behavior of the *n*-saturated 1,2-diacylphosphatidylglycerols, *Biophys. J.*, 72, 779, 1997.

Morphology and Size of Particles during Spray Drying

Liliana Alamilla-Beltrán, José Jorge Chanona-Pérez, Antonio R. Jiménez-Aparicio, and Gustavo F. Gutiérrez-López

CONTENTS

Introduction	513
Materials and Methods	514
Results and Discussion	514
Conclusions	517
Acknowledgments	517
References	517

Introduction

In spray drying, inadequate drying conditions can produce a powder with nondesirable characteristics. The size distribution of the droplets is the variable that influences most the properties of final products. Droplet diameter or particle size is a very important parameter but difficult to evaluate given the many variables influencing it (Furuta et al., 1994; Kieviet and Kerhof, 1997; Aguilera and Stanley, 1999; Chanona et al., 2003). At the same time, phenomena associated with evaporation such as shrinkage, deformation, expansion, formation of crust, and breakage arise (Liang and King, 1991; Oakley, 1997; Walton, 2000). The thickness of the crust will depend on drying velocity. High drying rates tend to produce large particles with a thin crust and low density, whereas low drying velocity produces small particles with a thick crust and high density (Masters, 1985; Oakley, 1997). Also, depending on the temperature of the particles, the liquid caught inside may vaporize and generate pressure. If a portion of the crust is broken, water vapor will be displaced and hollow spheres or fragments of spheres will be produced, which may improve rehydration. If the crust is

flexible, particles may expand or collapse depending on drying conditions (Oakley, 1997; Walton, 2000).

Microscopy is one of the most appropriate techniques for characterizing the structure of foods (Kaláb et al., 1995; Aguilera and Stanley, 1999), and morphology and size development of particles along drying could be analyzed by digital image analysis (Aguilera and Stanley, 1999; Chanona et al., 2003; Alamilla-Beltrán et al., 2005). In this work, morphological development of particles and their moisture content reduction during an actual spray-drying operation are reported.

Materials and Methods

A two-fluid nozzle laboratory co-current spray drier was used in this work. It was equipped with a peristaltic pump and a cyclone for powder collection. The dimensions of the drying chamber were 0.38 m diameter and 0.60 m height with a cone of 0.40 m height (Alamilla-Beltrán et al., 2001). The experimental material was, in all cases, a 40% TS Maltodextrin solution (20 ED) supplied by Arancia Corn Products S.A. (Mexico). The dryer was operated at inlet/outlet air temperatures of 200/173°C (condition A) and 170/145°C (condition B). For all the experiments, volumetric airflow and feed rate were 75 m³/h and 1.2 l/h, respectively. Powder sampling during drying at different distances from the atomizer and from the final product was performed for both drying conditions. Sampling of material inside the drying chamber and into the atomized cone was performed by means of a bayonet-type sampler which was introduced to the drier through six specially constructed tapped devices separated 0.10 m from each other (Figure 35.1). The moisture content of material withdrawn from inside the chamber from the final product was evaluated following AOAC 32.1.03 method (A.O.A.C., 1995). Particles obtained during drying experiments were observed using light microscopy. The microscope (Zeiss Axiophot 1) was fitted with a 20X objective and a blue filter (total magnifications of 100 and 200X were used depending on the drying experiment). KS400 ver. 3.01 software was used to process images and to determine the diameter of individual particles; 110 particles were measured in each of the 20 microscopy fields considered per observation. The mean diameter of the particles was evaluated for material sampled at the center of the spray cone and at different heights of the drying chamber and were reported as the corresponding average value of material collected.

Results and Discussion

For both drying conditions, an initial droplet diameter (D_{vs}) of 16.9 μm was found (on axial point A). For drying condition A, at a distance of 0.10 m from

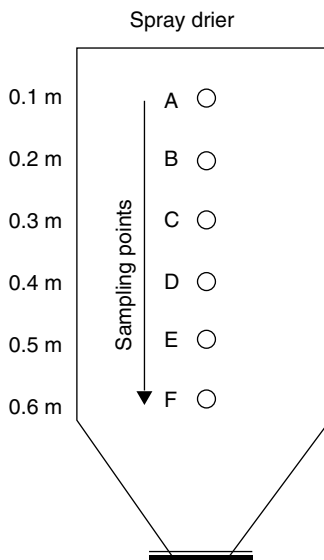
**FIGURE 35.1**

Diagram of the drying chamber showing sampling points.

the nozzle (corresponding to axial point B), the material was a sticky paste having a decrease in moisture content of 46%, but no particle observation could be carried out.

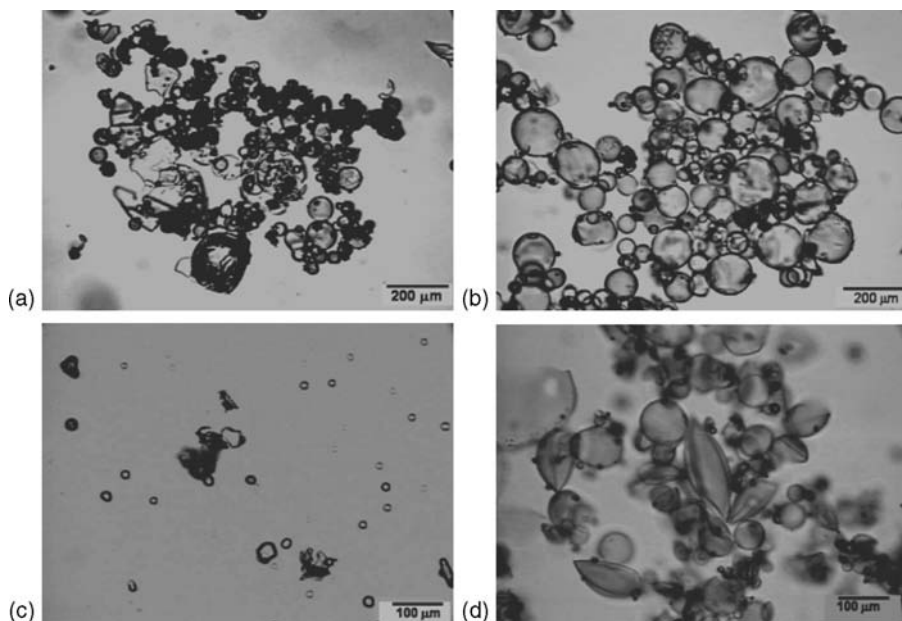
At axial point C, the presence of dry material was observed. The average particle size was $19.5\ \mu\text{m}$. Figure 35.2a shows an image of these particles. The particles had a spherical form and some of them had a compact appearance, while others were hollow with a thin crust. The presence of broken particles and fragments were also observed. An incipient expansion of the particle was observed during drying, along with a decrease of 93% in the moisture content of the material.

At axial point E, an increase of 39% in particle size in relation to the atomized droplet was observed. The average size evaluated was $23.5\ \mu\text{m}$, while no further change was observed in the moisture content of the material. These particles presented a spherical form and a thin crust.

At axial point F, the particle size was $32\ \mu\text{m}$ (Figure 35.2b), which represents an increase in particle size of 89%.

At distances greater than 0.3 m from the atomizer, the change in moisture content was small (approximately 2%). However, the residual water is probably important with respect to the expansion process. Particles dried at this condition developed a total expansion of 89%. This material presented in spherical form with a thin crust, no appreciable fracture, and the possible presence of micro-pores on the surface of the particles.

For drying condition B, only liquid was collected at a distance of 0.10 m from the nozzle. At axial point C the particle size was $13.9\ \mu\text{m}$ (Figure 35.2c)

**FIGURE 35.2**

Particles observed at air-drying condition of 170/145°C (a) 0.3 m from the nozzle and (b) at 0.6 m; particles observed at 200/173°C (c) 0.3 m from the nozzle and (d) at 0.6 m.

representing a decrease of 18% with respect to the initial diameter of the droplet. This was accompanied by an important loss in moisture content of 97%. Up to this point, a linear relationship was maintained between the particle volume and the mass of evaporated water, which was of about 80%. Therefore, the linearity of water removal and shrinkage of the material for this extent of evaporation coincided with reports by Masters (1985).

At axial point D, particles presented diameters of 15.8 μm . From this point, an increment in average size particle was observed and the moisture content of the material decreased by 98%. The increment in size (D_{vs}) reached 118% relative to the initial diameter of the droplet. Particles were hollow and spherical. Broken spheres and fragments of material were also present. These observations coincided with those described by Kieviet and Kerhof (1997) and Oakley (1997) when drying individual particles who pointed out that at the beginning of the drying process, the drop presents a liquid surface that forms a crust when evaporating; the particles increase their temperature and the liquid caught in the interior evaporates, causing expansion in the material and in some cases a fracture of the crust. These particles are shown in Figure 35.2d. This kind of material presents a low bulk density and better rehydration characteristics (Oakley, 1997). Conditions leading to the production of this sort of particles are not desirable for encapsulated materials (Ré, 1998).

Conclusions

Particles change in size and shape during drying. These changes are related to the moisture content of the material and operating drying conditions. At 170/145°C and 200/173°C, particles with mean diameters of 32 and 37 μm were obtained corresponding to 89 and 118% inflation, respectively, relative to the initial atomized droplet. It was possible to explore the relation of morphology and moisture content of particles with drying temperature during the actual drying operation, especially those related to breakage, inflation, and collapse. Formation of thick, compact, and irregular crust was more evident for 170/145°C. At 200/173°C, smooth and regular surfaces of complete and broken material were observed. Shrinkage as well as inflation arises during dehydration and may indicate the presence of spray-drying stages similar to those proposed by other authors when drying individual droplets.

Acknowledgments

The authors wish to thank National Polytechnic Institute (IPN-Mexico), COTEPABE, and Iberoamerican Program of Science and Technology for Development (CYTED Project XI.13)

References

- Aguilera, J.M. and Stanley, D.W. *Microstructural Principles of Food Processing and Engineering*, 2nd Ed., Aspen Publisher Co., Gaithersburg, 1999.
- Alamilla-Beltrán, L., Chanona-Pérez, J.J., Jiménez-Aparicio, A.R., and Gutiérrez-López, G.F. Description of morphological changes of particles along spray drying, *J. Food Eng.*, 67, 179, 2005.
- Alamilla-Beltrán, L., Hernández-Parada, A., Chanona-Pérez, J., Jiménez-Aparicio, A., Suárez-Fernández, O., Santiago-Pineda, T., and Gutierrez-Lopez, G.F. Design and performance of a spray drier for food processing, *Proceedings of the 8th International Conference on Engineering and Food. ICEF 8*, J. Weltri Chanes, G.V. Barbosa-Cánovas and J.M. Aguilera, eds., Technomic Publishing Co., U.S.A, pp. 1151–1155, 2001.
- A.O.A.C., *Official Methods of Analysis*, 16th Ed., Association of Official Analytical Chemists International, Arlington Virginia, 1995.
- Chanona, P.J.J., Alamilla, B.L., Farrera, R.R.R., Quevedo, J.M., Aguilera, J.M., and Gutiérrez, L.G.F. Description of the convective air-drying of a food model by means of the fractal theory, *Food Sci. Technol. Int.*, 10, 207, 2003.
- Furuta, T., Hayashi, H., and Ohashis, T. Some criteria of spray drying design for food liquid, *Drying Technol.*, 12, 151, 1994.

- Kaláb, M., Allan-Wojtas, P., and Miller, S.S. Microscopy and other imaging techniques in food structure analysis, *Trends Food Sci. Technol.*, 6, 177, 1995.
- Kieviet, F.G. and Kerhof, P.J.A.M. Air flow, temperature and humidity patterns in a co-current spray dryer: modelling and measurement, *Drying Technol.*, 15, 1763, 1997.
- Liang, B. and King, J. Factors influencing flow patterns, temperature fields and consequent drying rates in spray drying, *Drying Technol.*, 9, 1, 1991.
- Masters, K. *Spray Drying*, Leonard Hill, London, 1985.
- Oakley, D.E. Produce uniform particles by spray drying, *Chem. Eng. Prog.*, 10, 48, 1997.
- Ré, M.I. Microencapsulation by spray drying, *Drying Technol.*, 16, 1195, 1998.
- Walton, D.E. The morphology of spray-dried particles a qualitative view, *Drying Technol.*, 18, 1943, 2000.

36

Evaluation of Morphological and Microstructural Changes during Air Drying of Spheres Using Fractal Analysis and Relationships with Spray Drying

José Jorge Chanona-Pérez, Liliana Alamilla-Beltrán, Reynold Ramón Farrera-Rebollo, and Gustavo F. Gutiérrez-López

CONTENTS

Introduction	519
Materials and Methods	520
Results and Discussion	521
Conclusions	523
Acknowledgments	523
References	523

Introduction

Fractal analysis could be an alternative tool for describing the shape and microstructure of dehydrated products and for evaluating structural changes during drying processes (Belloutio et al., 1997; Pedreschi and Aguilera, 2001; Quevedo et al., 2002; Chanona-Pérez et al., 2003; Alamilla-Beltrán et al., 2005). The microstructural changes of materials with drying conditions can be correlated to fractal analysis parameters, and may help to improve the product quality in the manufacture and processing of foods. Aspects related to moisture transport in biological models could be explained by fractal analysis, thus allowing the finding of a descriptive model for the drying of spheres and powders based on the different correlations observed between morphology evolution and apparent fractal dimension. The objective of this work was to study morphology and

microstructure development, including evaluation of particle size and parameters related to transport phenomena such as drying kinetics and effective diffusion coefficients during the air drying of spheres and the spray drying of particles.

Materials and Methods

Testing materials were 0.9-mm jellified spherical maltodextrin solutions using agar solution as jellifying agent. Experiments were carried out in an experimental drying tunnel (Figure 36.1) that allowed air to pass the spheres at 0.5, 2, 7, and 12 m/sec and 50, 60, 70, and 80°C. Additionally an experiment was conducted in still air conditions and at the same above-mentioned temperatures. Three identical spheres were used for each experimental run: one was used to follow shrinkage, morphological changes, and surface temperature. The second one was used to track the weight of sample by means of an analytical balance (Ohaus, Analytical Plus) and the last one was used for microstructure evaluation. Shrinkage and morphological changes were monitored by a video camera (Sony Digital 8, DRC-TRV-120) with magnifying lenses (+2, +3, +3). Images were transferred to a PC by using appropriate software (ATI versión 6.2, Multimedia Center). Surface temperature was registered by means of an infrared thermometer (Raytek, Raynger ST) fitted in the tunnel at 3 cm from the sample (Figure 36.1). Microstructure was evaluated by using a light microscope (National Optical & Scientific Instrument, 163-SD) with a total

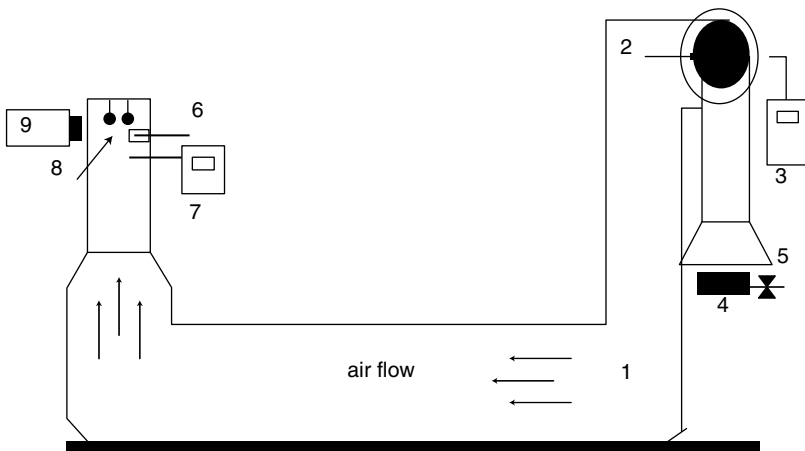


FIGURE 36.1

Diagram of experimental drying tunnel (1) test section, (2) fan, (3) controller air flow, (4) heating element, (5) valve controller of gas, (6) thermometer of wet bulb, (7) thermoanemometer, (8) spheres, (9) video camera.

magnification of 100X to which the video camera was coupled. Images were stored as bitmaps. The effective diffusion coefficient for each run was evaluated by means of Fick's second law, and the fractal dimension of spheres contours (FD_c) was evaluated by using different resolution levels (Belloutio et al., 1997). This step was carried out by means of Corel photo paint version 9.337 software (Corel Corporation Limited). Perimeter (P) and Feret diameter (D_{Feret}) were evaluated and log-log plots of (P) vs. magnification level (λ) were constructed and the slope (α) of the lines so obtained were used to obtain FD_c . Fractal dimension of surface (FD_s) was measured by means of the box counting method (BCM) according to Sarkar and Chaudhuri (1994) and Quevedo et al. (2002)

Results and Discussion

In Figure 36.2a and b, changes in the form and texture of samples during drying can be observed. Shrinkage, texture, and morphology of contours

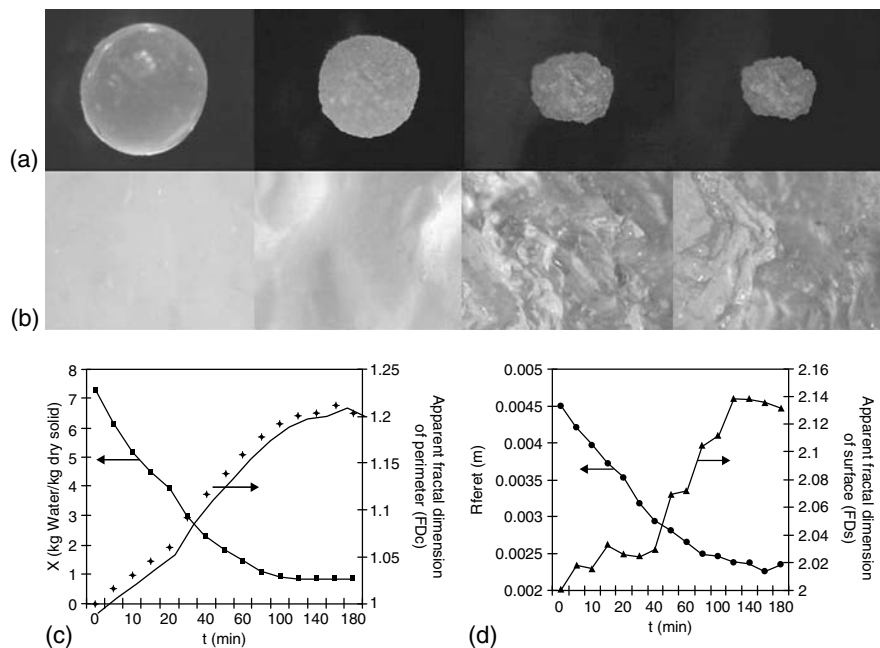


FIGURE 36.2

(a) Evolution form and microstructure, (b) images in light microscopy (100X) of maltodextrin-agar spheres at several times of drying, 0, 30, 100, and 180 min, (c) drying kinetics (■) and changes in FD_c values (◆), and (d) shrinkage, R_{Feret} (●) and changes in FD_s values (▲) during drying at 70°C and 0.5 m/sec.

were related with drying time. This is shown in Figure 36.2c and d. FD_c and FD_s increased with drying time while X and yR_{Feret} decreased with time.

Values of FD_c and FD_s ($\cong 1$ and 2 , respectively) suggested Euclidian behavior. As dehydration progressed, irregularity in materials causes increments of FD_c and FD_s values. Towards the end of drying, these parameters reached a constant value. A summary of results from the different drying experiments is presented in Table 36.1.

It is possible to observe that under intermediate thermal drying conditions (i.e., 60°C) and 7 m/sec , values of D_{eff} are lower than when 0.5 and 2 m/sec were applied. This is associated with a higher shrinkage extent expressed as R_{Feret} . Also, values of FD_c and FD_s are indicative of higher irregularity of contours and surface texture. These findings may be associated to an early evolution of irregularity and increased density of particles. This may be partially responsible for increased water transport resistances, which will be characteristic of a solid that has developed a fractal structure, thus making paths for water migration intricate and complex. Mild thermal drying conditions such as 50°C for all the studied airflows give place to materials whose shape and microstructure are less irregular than those obtained at the

TABLE 36.1
Drying Conditions for Agar-Maltodextrin Spheres and Effective Diffusion Coefficient $D_{\text{eff}} \times 10^9$ (m^2/sec), $R_{\text{Feret}} \times 10^3$ (m), FD_c and FD_s

Drying Conditions	$D_{\text{eff}} \times 10^9$ (m^2/sec)	$R_{\text{Feret}} \times 10^3$ (m)	FD_c	FD_s
50°C , 0 m/sec	0.722	2.39	1.226	2.124
60°C , 0 m/sec	0.896	2.36	1.206	2.120
70°C , 0 m/sec	1.655	2.88	1.181	2.131
80°C , 0 m/sec	1.696	2.58	1.173	2.081
50°C , 0.5 m/sec	0.923	2.26	1.216	2.131
60°C , 0.5 m/sec	1.511	2.02	1.252	2.130
70°C , 0.5 m/sec	1.741	2.33	1.205	2.136
80°C , 0.5 m/sec	1.882	2.87	1.131	2.097
50°C , 2 m/sec	0.988	2.23	1.217	2.124
60°C , 2 m/sec	1.590	2.27	1.231	2.164
70°C , 2 m/sec	1.532	2.43	1.185	2.143
80°C , 2 m/sec	2.606	2.69	1.156	2.089
50°C , 7 m/sec	1.050	2.58	1.158	2.076
60°C , 7 m/sec	1.207	2.26	1.215	2.117
70°C , 7 m/sec	2.729	2.94	1.120	2.110
80°C , 7 m/sec	1.798	3.04	1.111	2.092
50°C , 12 m/sec	1.274	2.44	1.204	2.110
60°C , 12 m/sec	1.460	2.69	1.174	2.103
70°C , 12 m/sec	1.851	2.69	1.162	2.094
80°C , 12 m/sec	1.846	2.63	1.144	2.075

mild drying conditions reported above. FD_c and FD_s are also lower than for intermediate conditions, which may be associated with less dense and less complex crusts, and so lower D_{eff} values. For the high range of thermal drying conditions (70 and 80°C), materials showed low values of FD_c and FD_s , which indicates an intermediate irregularity and a smooth microstructure. Most probably an early formation of rather impermeable thin crusts occurs. It is worth mentioning that the behavior of the apparent fractal dimension of the contour of spheres for drastic drying conditions was similar to that observed for FD_c values found in works in which spray-dried particles were evaluated for fractal dimension (Alamilla-Beltrán et al., 2005). This may indicate that shrinkage and deformation phenomena associated with water migration may be somehow analogous for drying suspended particles and droplets in spray drying. This possibility has been reported by our research group elsewhere (Alamilla-Beltrán et al., 2005).

Conclusions

Use of fractal dimension to evaluate irregularity associated with drying phenomena may be a useful tool when assessing shrinkage, crust formation, and water transport. High water fluxes and drastic drying conditions may lead to fractal structures smoother than those obtained at mild and intermediate drying thermal conditions. Intermediate drying conditions are associated to low water fluxes caused by high values of fractal dimension.

Acknowledgments

This work was sponsored by: CGPI-IPN 2003-1044 and CONACYT 27583-B projects, COTEPABE-IPN and Project XI.13 CYTED. Authors Chanona Jorge and Alamilla Beltrán L. thank CONACYT for their study grant.

References

- Alamilla-Beltrán, L., Chanona-Pérez, J.J., Jiménez-Aparicio, A.R., and Gutiérrez-López, G.F. Description of morphological changes of particles along spray drying, *J. Food Eng.*, 67, 179, 2005.
- Belloutio, M., Alves, M.M., Novais, J.M., and Mota, M. Floccs vs. granules: differentiation by fractal dimension, *Water Res.*, 31, 1227, 1997.
- Chanona-Pérez, J.J., Alamilla-Beltrán, L., Farrera, R.R.R., Quevedo, R., Aguilera, J.M., and Gutiérrez-López, G.F. Description of the convective air drying of a food model by means of the fractal theory, *Food Sci. Technol. Int.*, 9, 207, 2003.

- Pedreschi, F., Aguilera, J.M. Quantitative characterization of potato product surfaces using scale-sensitive analysis. *Proceedings of the 8th International Congress on Engineering and Food (ICEF'8)*, 88, 2001.
- Quevedo, R., López, G.R., Aguilera, J.M., and Cadoche, L. Description of food surfaces and microstructural changes using fractal image texture analysis, *J. Food Eng.*, 53, 361, 2002.
- Sarkar, N. and Chaudhuri, B.B. An efficient differential box-counting approach to compute fractal dimension image, *IEEE Trans. Syst. Man Cybernet.*, 24, 115, 1994.

Heat Transfer Units and Morphology of Particles in Spray Drying

Liliana Alamilla-Beltrán, José Jorge Chanona-Pérez, Antonio R. Jiménez-Aparicio, and Gustavo F. Gutiérrez-López

CONTENTS

Introduction	525
Methodology	526
Results and Discussion	526
Conclusion	529
Acknowledgments	529
References	529

Introduction

The complexity of the spray-drying process makes experimental study of mass transfer in a real spray dryer impractical (Masters, 1985). Authors have studied changes in moisture content of the material during the process by suspending a drop of the liquid to be dried in a fixed position under an air stream (Ferrari et al., 1989; Adhikari et al., 2000; Dolinsky, 2001). Droplet diameter or particle size is a parameter of interest, but it is difficult to estimate during drying given the many variables having an influence in the spray–air contact stage. At the same time, phenomena related to evaporation such as shrinkage, deformation, size increase, formation of crust, and crush start to arise and will, in turn, influence actual heat and mass transfer (McCormick, 1962; Chawla, 1994; Oakley, 1997). In spray-drying processes, drying stages can be related to moisture evaporation and morphology development of the particle (Kieviet and Kerhof, 1997; Oakley, 1997). Drying zones inside the chamber and change of moisture content during dehydration may help to establish links between drier design and

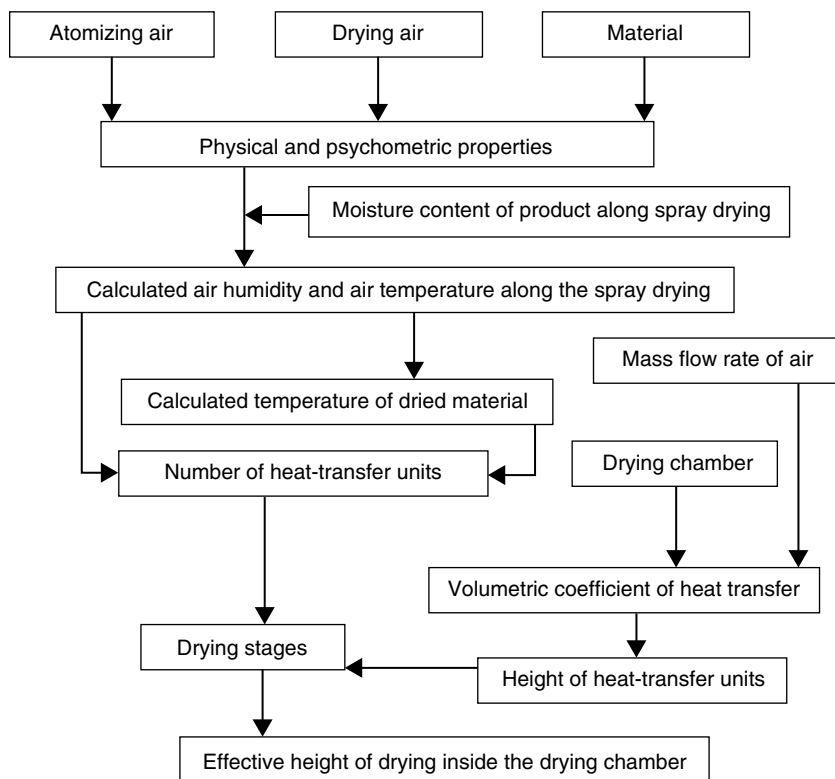
product quality. An interesting option that would allow evaluation of the height of drying stages inside the spray chamber is the application of the concept of the heat transfer unit, which would represent an option and a contribution to spray-drier design and operation. This method considers that the longitude of the path that one of the fluids travels through the dryer is formed by the number of transfer units (NtOG), which is a dimensionless relationship between the difference of the temperature of the drying air and the heat driving force. The height of the transfer unit (HtOG) is a function of the airflow, overall heat transfer coefficient, and the heat capacity of drying air. The product of the height of the heat transfer unit times the number of transfer units is equal to the total height of the effective drying stages (Masters, 1985).

Methodology

A two-fluid nozzle laboratory co-current spray drier was used in this work. The dimensions of the drying chamber were 0.38 m diameter and 0.60 m height, with a cone of 0.40 m height (Alamilla-Beltrán et al., 2001). The testing material was a 40% TS Maltodextrin solution (20 ED) supplied by Arancia Corn Products S.A. (Mexico). The inlet/outlet air temperatures were 200/173 and 170/145°C. Volumetric airflow was 75 m³/h and feed rate was 1.2 l/h for each experiment. The sampling of material inside the drier during drying and from the final product was performed for both drying conditions. The sampling of material inside the chamber was carried out by means of a bayonet-type sampler, which was introduced to the drier through each of the six tapped devices separated 0.10 m from each other fitted to the wall of the drier (Alamilla-Beltrán et al., 2005). The moisture content of the material taken from inside the chamber during drying and the final product was evaluated following AOAC 32.1.03 method (Official methods of analysis of AOAC International, 1995) for the different heights of the chamber of the equipment. The addition of each stage can be considered as the minimum or effective drying height; in Figure 37.1, a diagram of the applied methodology is shown. Morphological characteristics of materials collected from the different heights of the drying chamber were reported elsewhere (Alamilla-Beltrán et al., 2005) and helped to correlate effective drying stages with structural properties of material during spray drying.

Results and Discussion

By applying the heat transfer unit concept in spray drying, it is possible to describe the different stages of elimination of moisture content along the drier (named first to third in this work). Consequently, for drying conditions,

**FIGURE 37.1**

Flow diagram for applying heat transfer unit concept.

it was possible to detect three different stages with defined characteristics. These drying stages present a certain similarity with the five drying stages reported by Dolinsky (2001). For inlet/outlet air drying temperature 170/145°C and in the first stage, the material temperature was close to the adiabatic saturation temperature of drying air; the loss of moisture content of the product was approximately 46% of the initial value, and no presence of dry material was detected. In this stage, the number of transfer units was 0.16, the height of the transfer unit was 0.85 m, and the height of the stage was 0.14 m. Observations in this first spray-drying stage coincide with the description of stages I and II given by Dolinsky (2001) (named I to V in this work) for the drying of individual spherical particles 1.6 mm in diameter subjected to drying at 160°C. In stages I and II, the temperature of the particle moved to the wet bulb temperature and a decrease in particle size was reported.

In the present work, the second drying stage presented a considerable increase of feed temperature. The number of heat transfer units for this stage was 0.30, the height of the unit was 0.85 m and the drying stage of 0.26 m.

In this stage, the moisture content of the material was reduced to approximately 47% and the presence of dry material was observed. This stage coincides with stage III reported by Dolinsky (2001), in which the temperature of the particle subjected to drying increased from the wet bulb temperature to nearly the boiling point of water, and particle crusts started to appear. This is similar to observations made in this work regarding crust formation in the second drying stage.

At the third stage of drying, an expansion process was observed and the material reached its final size. Loss of moisture content of material was of only 4% with respect to the last stage; the material reached its maximum temperature and the drying air its minimum temperature. Further changes in moisture content of material, drying air, and material temperatures were not observed. For this stage, the number of heat transfer units was 0.05 and height of the heat transfer unit was 0.85 m, giving a total height of this stage equal to 0.04 m. This stage coincides with stages IV and V reported by Dolinsky (2001), where an increment in the particle size and in its temperature were observed.

The calculated total height corresponded to the effective height of drying, comprising two drying stages and a third (expansion) stage, of 0.44 m. This may be compared with the experimental height of 0.5 m, suggesting that it is possible to apply the heat transfer unit concept to evaluation of the effective height of drying.

For inlet/outlet air drying temperature 200/173°C, the first evaluated stage presented a calculated material temperature near to the adiabatic saturation temperature of drying air; the loss in moisture content of the material was 44% relative to the initial water content, but without the presence of dry material. In this stage, the number of transfer units was of 0.13, the height of the transfer unit was of 0.84 for a total height of 0.11 m. This stage coincides with the description of stages I and II by Dolinsky (2001). The second drying stage presented a considerable change of material temperature inside the drying chamber. This temperature increased from the adiabatic saturation temperature of drying air up to a calculated temperature above the boiling temperature of water. Also, a decrease of approximately 22°C was observed in the drying air temperature. The number of heat transfer units for this stage was of 0.25 and the height of transfer unit was 0.84, for a total height of 0.25 m. In this stage, the moisture content of material eliminated approximately 53% relative to the first stage, and dry material was detected. This second stage coincides with stage III reported by Dolinsky (2001). Finally, in the third stage an expansion process was detected, particle size reached its final magnitude, and loss in moisture content was only 1%. Also, in this stage the material reached its maximum temperature and the drying air its minimum. Starting from this stage, there were no changes in moisture content of material or drying air and material temperatures. For this stage the number of transfer units was 0.01 and its height was 0.84, for a total height of 0.01 m. Reported observations for this stage coincide with stages IV and V reported by Dolinsky (2001). Calculated

total height corresponding to the effective height of drying, which comprises the two drying stages and the third expansion stage, was 0.34 m. This compares with the experimental height of 0.3 m and may suggest that it is possible to apply the heat transfer unit concept for the evaluation of the effective height of drying and relationships with morphological development of the atomized material.

For both drying conditions, differences between calculated individual lengths for each stage and the real ones are caused by the fact that for each zone, different amounts of water are evaporated, and so the number of transfer units is also different. However, for both cases, total drying length coincided with those determined experimentally.

Conclusion

The heat transfer unit concept can be applied in spray drying and allows three stages to be identified. Two of them describe the drying process and the third is mainly related to expansion of material and incipient drying. In the first drying stage, the material temperature stays constant and near to the adiabatic saturation temperature of the drying air. In the second stage, the material temperature was increased in the presence of dry powder. In the third stage, an increment in the size particle was observed. The first and the second drying stages represent an effective drying height inside the spraying chamber. The application of the heat transfer unit concept could be a useful tool in the calculation of the effective drying height; therefore, it represents an important alternative for the study of spray drying.

Acknowledgments

The authors thank National Polytechnic Institute (IPN-Mexico), COTEPABE-IPN, and Iberoamerican Program of Science and Technology for Development (CYTED-Project XI.13).

References

- Adhikari, B., Howes, T., Bhandari, B.R., and Truong, V. Experimental studies and kinetics of single drop drying and their relevant in drying of sugar-rich foods: a review, *Int. J. Food Prop.*, 3, 323, 2000.
- Alamilla-Beltrán, L., Chanona-Pérez, J.J., Jiménez-Aparicio, A.R., Gutiérrez-López, G.F. Description of morphological changes of particles along spray drying, *J. Food Eng.*, 67, 179, 2005.

- Alamilla-Beltrán, L., Hernández-Parada, A., Chanona-Pérez, J., Jiménez-Aparicio, A., Suárez-Fernández, O., Santiago-Pineda, T., Gutierrez-Lopez, G.F. Design and performance of a spray drier for food processing. J. Welte Chanes, G.V. Barbosa-Cánovas and J.M. Aguilera, eds., *Proceedings of the 8th International Conference on Engineering and Food*, ICEF 8 Technomic Pub. Co., Lancaster, PA, USA, pp. 1151–1155, 2001.
- AOAC, *Official Methods of Analysis of AOAC International*, 16th Ed., AOAC International, Gaithersburg, MD, pp. 31–32, 1995.
- Chawla, J.M. Effect of the droplet agglomeration on the design of spray dryer towers, *Drying Technol.*, 12, 1357, 1994.
- Dolinsky, A.A. High-temperature spray drying, *Drying Technol.*, 19, 785, 2001.
- Ferrari, G., Meeerdink, G., and Walstra, P. Drying kinetics for a single droplet of skim milk, *J. Food Eng.*, 10, 215, 1989.
- Kieviet, F.G. and Kerhof, P.J.A.M. Air flow, temperature and humidity patterns in a co-current spray dryer: modelling and measurement, *Drying Technol.*, 15, 1763, 1997.
- Masters, K. *Spray Drying*, Leonard Hill, London, 1985.
- McCormick, P.Y. Gas velocity effects on heat transfer in direct heat rotary dryers, *Chem. Eng. Prog.*, 58, 57, 1962.
- Oakley, D.E. Produce uniform particles by spray drying, *Chem. Eng. Prog.*, 10, 48, 1997.

Convective Drying with Tempering of Mushrooms (Pleurotus ostreatus) and Color Changes of Final Product

Santiago S. Ocegüera, José Jorge Chanona-Pérez, Liliana Alamilla-Beltrán, Jorge Mendoza-Pérez, Ramón Arana-Erasquín, and Gustavo F. Gutiérrez-López

CONTENTS

Introduction	531
Materials and Methods	532
Results and Discussion	532
Conclusions.....	534
Acknowledgments	535
References	535

Introduction

Production of mushrooms is commercially and economically important and *P. ostreatus* is one of the most widely produced mushrooms (Chang, 1991). However, there are few drying studies that report parameters such as the effective coefficient diffusion and mass transfer coefficients for convective drying of this material. There is also little information about drying periods, which may be of importance in the design and operation of drying equipments. The quality aspects of the products have been studied independently of the drying engineering operation (Chua et al., 2000). However, drying with tempering cycles represents an alternative that may have certain advantages over conventional convective drying. Some of these advantages are: less energy consumption, less thermal damage to the product, and improved quality properties including homogeneity of the product. The objectives of this work were to compare conventional air

drying and drying with tempering and to evaluate quality by means of color comparison of the products.

Materials and Methods

P. ostreatus were bought in a local market in Mexico City, were cut into small pieces and placed in 8×8 cm trays, and dehydrated in an experimental drying tunnel with an air flow parallel to the sample. A number of drying conditions were tested following a 3^3 factorial design (40, 50, and 60°C and 1, 2, and 3 m/sec). Two drying kinetics were carried out for each drying condition. One used conventional drying and the other used a tempering cycle (60 min). This cycle consists of removing the sample from the drier after a certain time (90 min) and placing it at ambient temperature, thus producing a redistribution of the water through the solid (Tolaba et al., 1999; Chua et al., 2000). Surface temperatures throughout drying were obtained by means of an infrared thermometer (Raytek, model RAYST6LXE) and were used to determine the duration of the drying periods. The effective diffusion coefficients of *P. ostreatus* were determined using Fick's second law. The color of the samples was evaluated by means of a reflectance spectrophotometer (Color-dull HDS, Milton Roy USES).

Results and Discussion

The drying kinetics and thermal history of the sample surface were used for delimiting drying periods and for evaluating effective diffusion coefficients. A constant rate-drying period with a duration varying from 50 min (40°C and 1 m/sec) down to 4 min (to 60°C and 3 m/sec) for both types of drying was followed by a falling rate period of drying. For both types of drying at 40°C , it was possible to observe that the drying rate increased with the airflow (Figure 38.1a) this effect is less marked at 60°C (Figure 38.1b).

When comparing drying kinetics for both types of drying processes, final moisture contents were very similar for drying at 40 and 60°C , while at 50°C the final moisture content when cycle tempering was applied was lower than in traditional drying (Figure 38.2). This could be caused by morphological differences between products dried under different thermal regimes. Redistribution of moisture caused by tempering may affect these findings. Drying with tempering may be associated with softening of the crusts, giving rise to a decreased resistance to water diffusion. Drying of corn with tempering cycles has been associated with the redistribution of moisture within the solid matrix, which increased drying rates (Tolaba et al., 1999). The application of drying with tempering cycles may represent several advantages over traditional drying, such as lower moisture contents, improved energy savings, and decreased damage to the product. Similar

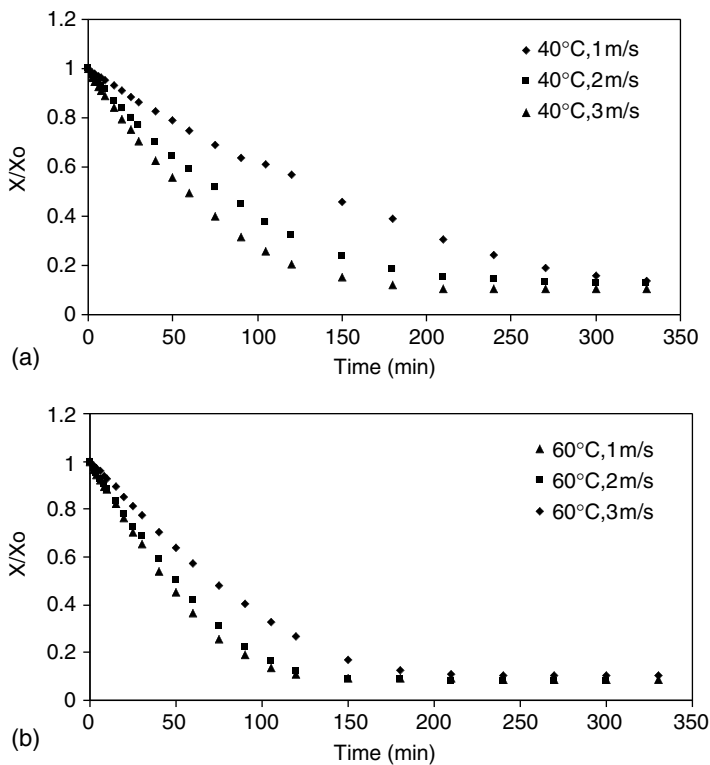


FIGURE 38.1
(a) shows the effect of the air flow on the drying rate of *P. ostreatus*, with drying conditions at 40°C and 1, 2, 3 m/sec; (b) shows drying kinetics at 60°C and 1, 2, and 3 m/sec, where the effect of the air flow is not significant.

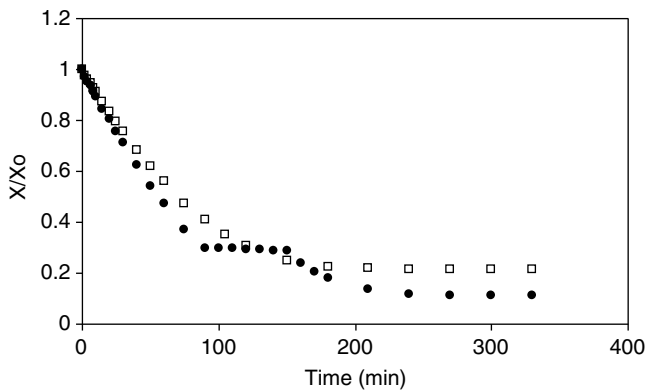
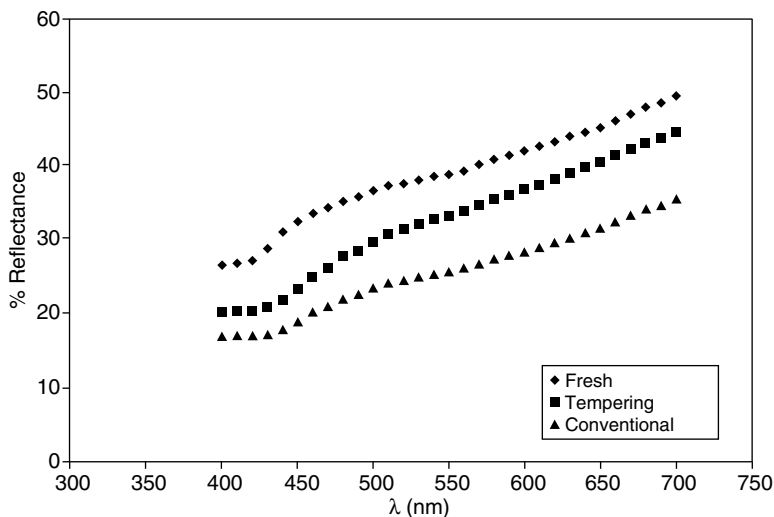


FIGURE 38.2
Kinetics of (□) conventional drying and (●) drying with tempering cycles of slabs of *P. ostreatus* at 50°C and 3 m/sec.

**FIGURE 38.3**

Reflectance of slabs of *P. ostreatus* fresh and dried with and without tempering cycle at 50°C and 3 m/sec air flow.

findings have been reported for drying of banana, guava, and potato pieces (Chua et al., 2000).

As far as the evaluation of color is concerned, samples dried with and without tempering at 40°C and 2 m/sec presented no significant differences among them. However, when operating at 60°C and 2 m/sec, samples subjected to drying with tempering cycles were darker than those obtained by conventional drying. This can be a result of a higher surface concentration of solids and longer thermal treatment times. In the case of drying at 50°C and 3 m/sec, the product reflectance obtained when drying with tempering is similar to reflectance of the fresh sample (Figure 38.3). Also, it is important to point out that under these drying conditions (applying drying with tempering cycles) slabs of *P. ostreatus* showed lower moisture content than samples obtained by means of conventional drying. These results may indicate that the application of cycles with mild drying conditions could improve the quality of the products, producing not only a redistribution of moisture gradients but also a number of favorable structural changes of the processed materials.

Conclusions

The drying of slabs of *P. ostreatus* using cycles of tempering may present an alternative for obtaining good quality products and represents a potentially

novel methodology for food drying in which the development of structures may induce technological improvements to conventional air drying. Further investigations should include microscopy and the evaluation of the complexity of structures and the product–quality relationships.

Acknowledgments

This work was sponsored by: CGPI-IPN 2003-1044 and CONACYT 27583-B projects, COTEPABE-IPN and Project XI.13 CYTED. Authors Chanona-Jorge and Alamilla-Beltrán L. thank CONACYT for their study grant.

References

- Chang, S.T. Mushroom biology and mushroom production, *Mush. J. Tropics*, 11, 117, 1991.
- Chua, K.J., Mujumdar, A.S., Chou, S.K., Hawlader, M.N.A., and Ho, J.C. Convective drying of banana, guava, and potato pieces: effect of cyclical variations of air temperature on drying kinetics and color changes, *Drying Technol.*, 18, 907, 2000.
- Tolaba, M., Aguerre, R., and Suárez, C. Drying simulation of corn with tempering, *Drying Technol.*, 17, 1081, 1999.

Modeling of Structural and Quality Changes during Drying of Vegetables: Application to Red Sweet Pepper (Capsicum annuum L.)

Karina C. di Scala, Sara I. Roura, and Guillermo H. Crapiste

CONTENTS

Introduction 537

Mathematical Models and Simulation 538

Results and Discussion 539

 Batch Drying 539

 Continuous Drying 540

Conclusions 540

Notation 541

Acknowledgments 542

References 542

Introduction

During recent years an important improvement in the knowledge of the dehydration process has occurred. Simulation programs of the mathematical models that represent heat and mass transfer during drying have allowed contemporary researchers to substitute expensive experimental work for faster and accurate results as well as to predict the effect of relevant process variables on the performance of the process itself.

The efficiency of the process and the quality of the final product depend upon the physical and chemical properties of the raw material, dryer design, and operating conditions.

Because vegetables are highly heat sensitive, drying of these products at high temperatures implies structural, organoleptic, and nutritional changes during dehydration.

In a previous work, Di Scala and Crapiste (2005) studied the effect of temperature on some of the most important quality characteristics of individual pieces of red sweet pepper (*Capsicum annuum*. L) during drying. Color and antioxidant content are among the main quality attributes of these vegetables besides textural and flavor attributes. Both carotenoids (provitamin A) pigments and ascorbic acid contents are related to pepper variety (Roura et al., 2001) and technological factors.

There are different mathematical models describing unsteady simultaneous one-dimensional heat and mass transfer during drying of foodstuffs (Ratti, 1991; Stakic, 2002) but the information about pepper dehydration is rather scarce. Lee and Park (1989) studied the optimal drying conditions for an on-farm red pepper dryer. However, no data of shrinkage of the product during the process were reported.

The purpose of this work was to model and simulate the dehydration of vegetables, particularly red pepper, in batch and continuous dryers. The models used for the simulation took into account the shrinkage of particles during drying as well as the moisture and temperature-dependent properties of the product. Effects of several parameters such as temperature and velocity of air, bed thickness, and recycle ratio on drying time, process efficiency, and final product quality were studied.

Mathematical Models and Simulation

Batch and continuous packed bed dryers were simulated in cross-flow mode.

Mathematical models were developed from the governing differential equations that represent mass and energy transfer in the dryers.

Drying kinetics was represented by a diffusive model. The models were completed with water sorption equilibrium equation, expressions for product and moist air properties, correlations for convective heat and mass transfer coefficients, and the kinetics of drying and of the selected quality changes in the product as functions of water content and temperature (Di Scala and Crapiste, 2005). Experimental data were obtained from Di Scala and Crapiste (2005) and Roura et al. (2001).

A moving coordinate accounting for the movement of shrinking particles was used to handle the problem of structural changes during drying (Ratti, 1991).

The resulting models with the corresponding initial and boundary conditions were integrated along the bed with respect to time (t) in batch drying or position (z) in continuous drying by using finite difference techniques and the MATLAB program (MathWorks Inc., v. 7.0).

The model for batch drying is shown in Table 39.1 (continuous drying model not shown).

TABLE 39.1
Batch Drying Model

$$\left[\frac{\partial X}{\partial t} \right]_{\lambda} = \frac{-n_w * a_v * (1 + X)}{\rho_s}$$

$$\left[\frac{\partial Y}{\partial t} \right]_{\lambda} = \frac{n_w * a_v * (1 - \varepsilon) * (1 + Y)}{\varepsilon \rho_a} - \frac{G_a}{(AL_0) * \varepsilon * \rho_a} \frac{\rho_s (1 - \varepsilon)}{\rho_{s,0} (1 - \varepsilon)} \frac{\partial Y}{\partial \lambda}$$

$$\left[\frac{\partial T_s}{\partial t} \right]_{\lambda} = \frac{a_v}{\rho_s * C_{psh}} [-n_w \Delta H_s + h_g * (T_a - T_s)]$$

$$\left[\frac{\partial T_a}{\partial t} \right]_{\lambda} = - \frac{G_a}{(AL_0) * \varepsilon * \rho_a} \frac{\rho_s (1 - \varepsilon)}{\rho_{s,0} (1 - \varepsilon)} \frac{\partial T_a}{\partial \lambda} - \frac{h_g * (T_a - T_s) * a_v * (1 - \varepsilon)}{\rho_a * \varepsilon * C_{pah}}$$

Initial and Boundary Conditions

Results and Discussion

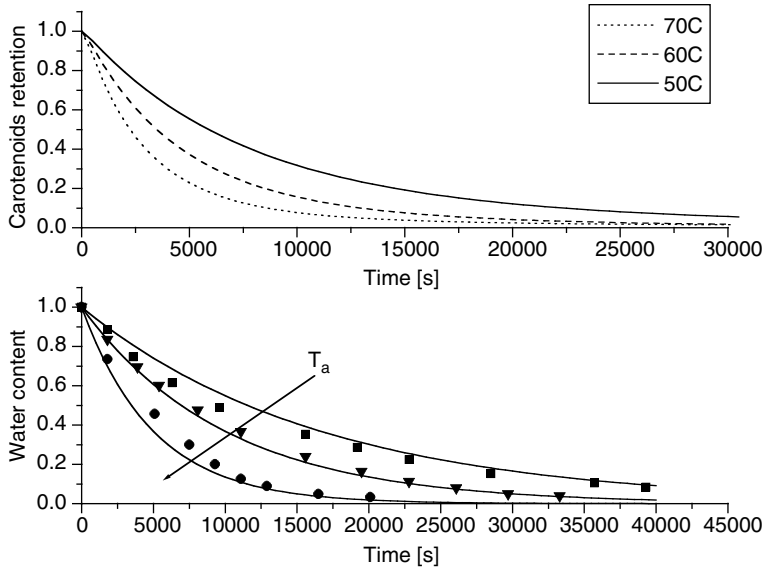
Batch Drying

The effects of drying temperature, bed thickness, and recycle ratio on water content and ascorbic acid/carotenoids retention were studied. Energy consumption per mass of water evaporated was evaluated considering only the energy used for heating ambient air to the inlet temperature.

Comparison of the model with experimental data was done successfully (Figure 39.1). Profiles of water content and carotenoids retention as functions of air temperature (50 to 70°C) are shown in Figure 39.1 for a bed thickness of 0.1 m and a circulation velocity of 1.5 m/sec. As can be observed, drying temperature drastically affects the carotenoids retention of the product in the range of temperature analyzed. Retentions of both carotenoids and vitamin C were less than 10% ($X_f = 0.1$). Similar results were reported by other authors in relation to ascorbic acid retention in green peppers during drying (Sigge et al., 1999).

In addition, the drying time needed to reach the required final moisture content decreased with inlet air temperature and increased with bed thickness and recycle ratio (data not shown). Therefore, drying of red peppers requires relatively low air temperatures and longer drying times to preserve product quality.

Recirculation of a proportion of exhaust air improved the process efficiency in terms of energy; however, product quality is negatively affected because of the higher drying times (data not shown). These results are in agreement with those reported by Lee and Park (1989).

**FIGURE 39.1**

Change in dimensionless water content and carotenoids retention as a function of air temperature in batch drying ($X_0 = 9.67$ kg/kg, HR = 14–30%, $v_a = 1.5$ m/sec, $L_0 = 0.1$ m, $r = 0$)

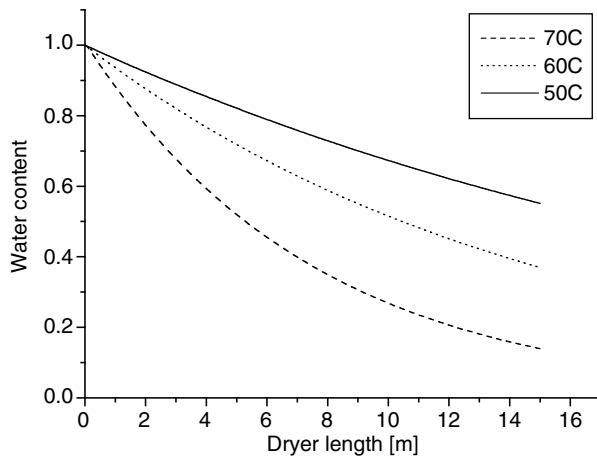
Continuous Drying

The minimum air-flow rate was calculated by assuming that the leaving streams were in thermal equilibrium. The dependency of water content on the most important drying variables (air temperature and air flow rate) was studied. Dimensionless water content as a function of drying temperature is shown in Figure 39.2 for a bed thickness of 0.1 m and a circulation velocity of 1 m/sec.

Drying temperature and air-flow rate decreased the dryer length needed to achieve the required final water content of the product. As a result of shorter residence times at high temperatures, quality retention represented by color and ascorbic acid is relatively high in the range of temperatures and flow rates analyzed (retention > 98%). Therefore, continuous drying allows the use of higher drying temperatures than batch drying.

Conclusions

Numerical simulation results of batch and continuous drying models for slices of peppers in packed beds were presented in this work. The reported models were based on differential mass and energy balances in the dryer along with kinetic equations describing transport phenomena in individual particles and product quality deterioration. The shrinkage problem was

**FIGURE 39.2**

Change in dimensionless water content as a function of air temperature in continuous drying. ($X_0 = 9.67$ kg/kg, $v_a = 1$ m/sec, $L_0 = 0.1$ m)

solved by taking into account changes in volume particles during the process.

The results showed that the developed models can be used to optimize the process from a quality standpoint in order to increase process efficiency as well as to obtain high-quality dry products in a highly demanding market.

Notation

Symbol	Quantity	Symbol	Quantity
A	transversal area of the dryer section, m^2	T_a, T_s	air and product temperature, K
a_v	area per unit volume, m^2/m^3	v_s	belt velocity, m/sec
$C_{p_{ah}}, C_{p_{sh}}$	specific heat of air and product on wet bases, J/kg K	v_a	air circulation velocity, m/sec
G_a	dry air mass flow rate, kg/sec	X	product water content, kg/kg
h_g	heat transfer coefficient, J/ m^2 sec K	Y	air moisture content, kg/kg
L_0	bed depth, m	z, x	coordinate, m
n_w	drying rate, kg/ m^2 sec	ΔH_s	heat of sorption, J/kg K
r	recycle ratio	ε	bed porosity
t	time, sec	ρ_a, ρ_s	air and product density, kg/ m^3
		λ	dimensionless moving coordinate

Acknowledgments

The authors wish to acknowledge that this work was partially realized under the financial support given by the CONICET (Consejo Nacional de Investigaciones Científicas y Técnicas) from Argentina.

References

- Di Scala, K.C. and Crapiste, G.H. Sorptional equilibrium, drying kinetics and quality changes during drying of red pepper (*Capsicum annuum* L.). *J. Food Eng.* 2005 (Submitted).
- Lee, D. and Park, M. Quality optimization in red pepper drying, *Kor. J. Food Sci. Technol.*, 21, 655, 1989.
- Ratti, C. Diseño de Secadores de Productos Frutihortícolas. PhD Thesis. Universidad Nacional del Sur., 1991.
- Roura, S.I. et al. Biochemical characterization of two pepper varieties in the green and red ripening stages, *Ital. J. Food Sci.*, 4, 13, 2001.
- Sigge, G.O., Hansman, C.F., and Joubert, E. Optimizing the dehydration conditions of green bell peppers (*Capsicum Annuum* L.): quality criteria, *J. Food Qual.*, 22, 439, 1999.
- Stakic, M.B. Numerical Study on Hygroscopic Capillary-Porous Material Drying in Packed Bed. EFCE-WPD Technical Meeting, 2002.

The Role of Residual Water for the Stability of Protein Freeze-Dried with Trehalose

Kiyoshi Kawai, Tomoaki Hagiwara, Rikuo Takai, and Toru Suzuki

CONTENTS

Introduction	543
Materials and Methods	544
Preparation of Freeze-Dried LDH Sample, Assay of the LDH Activity, and DSC Measurement	544
Preparation of Freeze-Dried Lysozyme Sample and FT-IR Study	545
Results	546
The Loss of LDH Activity Caused by Freeze-Drying and Long-Term Storage	546
The Effect of Trehalose and Residual Water on the Degree of the Hydration Structure of Freeze-Dried Lysozyme	547
Discussion	548
Acknowledgments	549
References	549

Introduction

Freeze-drying has been commonly used in both the food and pharmaceutical industries as a long-term stabilizing method for unstable proteins. However, since proteins are damaged by numerous stresses involved in the freeze-drying process, it is necessary to add an agent such as trehalose to protect the proteins from these stresses (Crowe, 2002). The protein protection mechanism of trehalose upon freeze-drying has been primarily explained by two effects: a water-replacement effect in which amorphous trehalose plays the role of the water substitution forming a hydrogen bond with the protein (Carpenter and Crowe, 1989; Suzuki et al., 1998; Wolkers et al., 1998;

Allison et al., 1999; Crowe, 2002); and the glass-transition effect in which a glassy matrix formed by amorphous trehalose controls the molecular mobility of the protein (Suzuki et al., 1998; Wolkers et al., 1998; Allison et al., 1999; Crowe, 2002). Although these concepts are commonly acknowledged as the stabilizing mechanisms for proteins by amorphous trehalose, the influence of the residual water on the stabilizing effect remains unclear. It is well known that residual water not only behaves as a reactant in the chemical reactions such as deamidation (Hsu et al., 1991), but also sharply lowers the glass-transition temperature (T_g) of glassy matrix by the plasticizing effect (Crowe, 2002). These effects of residual water promote the whole reactivity in the system and, therefore, the concept "the drier the better" has been commonly accepted (Hsu et al., 1991). However, from the viewpoint of maintaining protein structure, over-drying may not necessarily be a suitable method, even in the case in which amorphous trehalose functions to maintain the protein structure by water substitution. This is thought to be because trehalose is larger than water and is unable fit into all the hydration sites in the protein because of steric hindrance. Thus, residual water may be able to fill the remaining hydration sites. In order to evaluate the validity of this proposal, the following two experiments were carried out. First, the enzymatic activity of lactate dehydrogenase (LDH) was investigated in order to determine the influence of amorphous trehalose and residual water on the loss of LDH activity caused by freeze-drying and long-term storage. The T_g of amorphous trehalose affects the long-term storage stability of LDH; therefore, the T_g of each sample was also examined using DSC. Second, the effect of amorphous trehalose and residual water on the maintenance of the hydrated state of freeze-dried lysozyme was investigated using FT-IR. The results of these investigations are discussed herein.

Materials and Methods

Preparation of Freeze-Dried LDH Sample, Assay of the LDH Activity, and DSC Measurement

LDH suspension from rabbit muscle (Wako Pure Chem. Ind., Ltd., Japan) was dialyzed against 50 mM sodium phosphate buffer (pH 7.5) at 5°C for 24 h. The LDH concentration was determined by absorbance at 280 nm using an extinction coefficient of $0.6481 \text{ cm}^{-1} \text{ g}^{-1}$ (Hitachi U-3200, Japan). A mixture containing 100 μg LDH and 100 mg trehalose (99.3% purity, Hayashibara Biochemical Lab., Inc., Japan) per 1 ml was prepared, and the 1-ml solution was aliquoted into 2-ml polyethylene tubes. The solution was frozen by immersion in liquid nitrogen for at least 1 min and transferred to a pre-cooled freeze-drier. The freeze-drying was performed by increasing the temperature from -40 to 20°C at 3.0×10^{-2} Torr over a 2-day period. In order to prepare the fully dried LDH sample (dry LDH/TRE), the residual

water was removed over P_2O_5 in a vacuumed desiccator for 1 week at room temperature. In addition, a LDH sample containing a low amount of moisture (moist LDH/TRE) was prepared over saturated CH_3COOK (RH 22%) in a desiccator for 1 week at room temperature. As a control, freeze-dried LDH without trehalose (dry LDH) was also prepared.

The LDH activity was assayed according to the method described by Suzuki et al. (1998) at the three stages: before freeze-drying, after preparation of the freeze-dried sample, and after storage for several days at either 60 or 40°C. The remaining LDH activity was expressed as activity relative to that determined before freeze-drying.

The T_g of each sample was examined by DSC (Shimadzu DSC-50, Japan). Indium (Wako) and distilled water were used to calibrate the temperature and heat capacity for the DSC measurements. α -Alumina powder (Shimadzu) was used as a reference material. Approximately 10 mg sample was weighed and sealed into an aluminum DSC pan. Each sample was scanned from 0 to 140°C at a heating rate 5°C/min.

Preparation of Freeze-Dried Lysozyme Sample and FT-IR Study

Lysozyme from chicken egg white (Wako) was used without further purification. In the experiment evaluating the influence of the IR spectra of lysozyme, all solutions or moisture were prepared in D_2O . A quantity of 20 mg of lysozyme and 100 mg of trehalose was dissolved in 1 ml D_2O . The freeze-drying sequence and adjustment of residual water was carried out according to the method described above. The following four samples were prepared: 200 mg/ml lysozyme D_2O solution (hydrate LYS), fully freeze-dried lysozyme containing trehalose (dry LYS/TRE), freeze-dried lysozyme containing trehalose and 5.5% residual water (moist LYS/TRE), and fully freeze-dried lysozyme without trehalose (dry LYS).

FT-IR spectra between 1500 and 1700 cm^{-1} (amide band region) were taken using a FT-IR spectrophotometer (Shimadzu IR Prestige-21, Japan). Three primary bands could be observed in the spectra: amide I, carboxylate, and amide II at around 1650, 1580, and 1540 cm^{-1} , respectively. When the demand to form a hydrogen bond in a protein is not filled, these bands change significantly. The amide I and amide II bands shift to higher and lower wavenumbers, respectively, as a result of the dehydration of the protein (Carpenter and Crowe, 1989; Suzuki et al., 1998). The intensity or the area of the carboxylate band at 1580 cm^{-1} , which indicates the extent of the hydrogen bonding to the protein carboxyl groups, becomes lower as a result of the dehydration of the protein (Carpenter and Crowe, 1989; Allison et al., 1999). Thus, the hydration degree of the protein structure can be evaluated based on these assignments (Carpenter and Crowe, 1989; Suzuki et al., 1998; Wolkers et al., 1998; Allison et al., 1999). The freeze-dried sample was placed directly on the diamond prism of a circle 2 mm in diameter and clamped at a constant pressure. For each spectrum a 256-scan interferogram was collected in single beam mode with a 2 cm^{-1} resolution at room temperature.

The intensity in the obtained FT-IR spectrum was described as an absorbance per gram of lysozyme.

Results

The Loss of LDH Activity Caused by Freeze-Drying and Long-Term Storage

The moisture content immediately after freeze-drying was determined by Karl–Fisher assays to be approximately 5.0% (w/w). By a subsequent moisture-control treatment, the final moisture content of a fully dried and a slightly moist sample were reduced below 0.5 and 5.5%, respectively.

The obtained T_g values for a dry LDH/TRE sample and moist LDH/TRE sample were 92.8 and 42.4°C, respectively (DSC thermograms are not shown). The T_g s were lower than the $T_g = 115^\circ\text{C}$ of trehalose alone reported in the literature (Crowe, 2002) because of the plasticizing effect of the buffer and water.

The remaining LDH activity after freeze-drying is shown in Figure 40.1. Although the dry LDH sample lost almost all activity upon freeze-drying, LDH maintained high activity in the presence of amorphous trehalose. Furthermore, LDH activity of the moist LDH/TRE sample was higher than that of the dry LDH/TRE sample. The storage stability at 60 or 40°C for each sample was also examined. Dry LDH sample was observed to lose all activity within 30 days during storage at 60 and 40°C. In storage at 40°C, however, both the dry LDH/TRE sample and the moist LDH/TRE sample

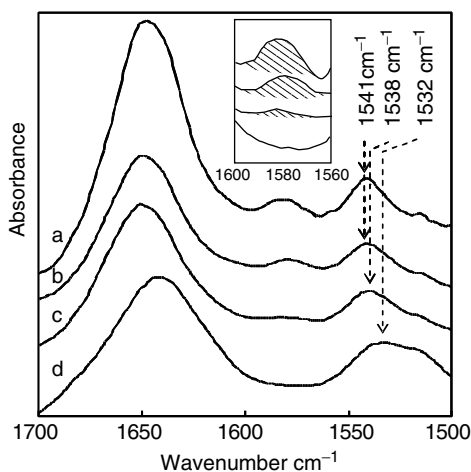


FIGURE 40.1

FT-IR spectra of amide band region of lysozyme: (a) hydrate LYS; (b) moist LYS/TRE; (c) dry LYS/TRE; (d) dry LYS. The carboxylate band region was expanded in the insert.

maintained activity for 90 days. Similarly, upon storage at 60°C, the dry LDH/TRE sample maintained adequate activity for 90 days. However, the moist LDH/TRE sample lost all activity within 30 days. This was thought to be because the sample was in the rubbery state since the storage temperature of 60°C was higher than the T_g of the moist LDH/TRE sample.

The Effect of Trehalose and Residual Water on the Degree of the Hydration Structure of Freeze-Dried Lysozyme

FT-IR spectra in the amide band region of each sample are shown in Figure 40.2. The amide II band of the hydrate LYS sample located at 1541 cm^{-1} , whereas the dry LYS sample reduced the amide II band up to 1532 cm^{-1} . However, the amide II band change of the dry LYS/TRE sample was small, and the band position of moist LYS/TRE sample was in good agreement with that of the hydrated LYS sample. The carboxylate band peak area (insert, Figure 40.2) indicated a remarkable response upon dehydration of lysozyme. Although a large carboxylate band peak for the hydrated LYS sample disappeared completely in the spectra of the dry LYS sample, both the dry LYS/TRE sample and the moist LYS/TRE sample prevented the disappearance of the peak. The peak area of the moist LYS/TRE sample was significantly larger than that of the dry LYS/TRE sample. These two assignments indicate that the degree of hydration of the structure formed during freeze-drying of lysozyme with amorphous trehalose was improved by the presence of the residual water. However, although a clear response in the amide I band caused by dehydration (shift to higher wavenumber) was

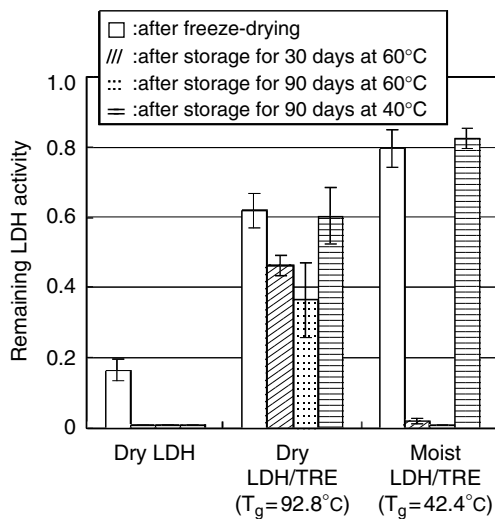
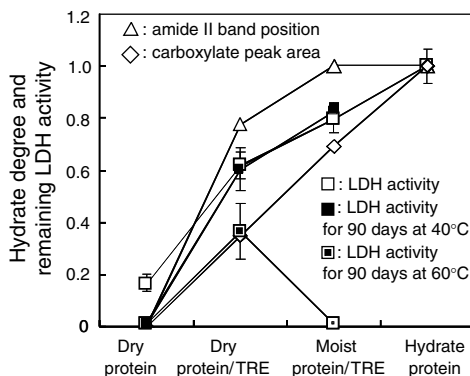


FIGURE 40.2

Remaining LDH activity in each sample.

**FIGURE 40.3**

Effect of residual water on the hydrate degree and the remaining enzymatic activity of freeze-dried LDH.

not observed, the amide I band peak of the dry LYS sample was confirmed to be wider than that of the other bands. Protein secondary structure (α -helix and random coil) (Wolkers et al., 1998) contributes to the amide I band; therefore, the broadening of the peak for amide I of the dry LYS sample was thought to be the result of the loss of the secondary structure of lysozyme.

In order to evaluate the degree of hydration of freeze-dried LYS/TRE based on these results, the amide II peak position (Carpenter and Crowe, 1989; Suzuki et al., 1998) and the carboxylate peak area (Allison et al., 1999) were analyzed using the following equation:

$$\text{Hydration degree} = (X - X_0)/(X_\infty - X_0) \quad (40.1)$$

where X_∞ , X_0 , and X represent the band position in amide II or the peak area in the carboxylate band of the hydrate LYS sample (maximum value), the dry LYS sample (minimum value), and the dry or moist LYS/TRE sample (between X_0 and X_∞), respectively. The obtained degree of hydration of LYS/TRE and the result of LDH activity research are represented as shown in Figure 40.3.

Discussion

The results presented in Figures 40.2 and 40.3 suggest that amorphous trehalose partially satisfied the hydrogen bond requirement of the exposed polar group on freeze-dried protein and the residual water supplemented the remaining hydrogen bond requirement. Amorphous trehalose has been believed to efficiently serve freeze-dried protein as a substitute for water (Carpenter and Crowe, 1989; Allison et al., 1999; Crowe, 2002). However, as mentioned above, trehalose, which is larger than water, is not able to cover

fully the hydration sites in the protein as a result of steric hindrance. Although the possibility of the lack of a hydrogen bond within the protein through steric hindrance has been pointed out for amorphous polymers (Allison et al., 1999), amorphous trehalose is also thought to have steric hindrance. Considering this steric hindrance, the possibility of maintaining better hydration structures for freeze-dried proteins is of great interest.

In contrast, the results presented in Figure 40.2 revealed that the remaining LDH activity of the moist LDH/TRE sample after freeze-drying was higher than that of the dry LDH/TRE sample. Damage to the protein structure, including the hydration shell, would result in the loss of enzymatic activity (Carpenter and Crowe, 1989). Therefore, these results are thought to be related to the supplementary effect of maintaining the hydrate structure by the residual water observed in the LYS/TRE sample, as shown in Figure 40.3. In order to prepare freeze-dried proteins with higher activity, both amorphous trehalose and residual water are necessary additives. However, residual water decreased the T_g of the glassy trehalose matrix sharply, and the moist LDH/TRE sample stored at temperatures above the T_g lost all activity within 30 days. Therefore, for long-term preservation a freeze-dried protein must contain some residual water to satisfy the degree of hydration. This investigation concludes that the residual water of freeze-dried proteins should be controlled based on water replacement and the glass-transition temperature.

Acknowledgments

The authors gratefully acknowledge the financial support from a Grant-in-Aid for JSPS Fellows provided by The Ministry of Education, Culture, Sports, Science and Technology of Japan. The authors thank Prof. M. Tanaka and Dr. S. Ishizaki (Tokyo University of Marine Science and Technology) for the use of the UV-spectrometer, and Dr. H. Chaen (Hayashibara Biochemical Lab. Inc., Japan) for providing trehalose dihydrate reagent.

References

- Allison, S.D., Chang, B., Randolph, T.W., and Carpenter, J.F. Hydrogen bonding between sugar and protein is responsible for inhibition of dehydration-induced protein unfolding, *Arch. Biochem. Biophys.*, 365, 289, 1999.
- Carpenter, J.F. and Crowe, J.H. An infrared spectroscopic study of the interactions of carbohydrates with dried proteins, *Biochemistry*, 28, 3916, 1989.
- Crowe, L.M. Lessons from nature: the role of sugars in anhydrobiosis, *Comp. Biochem. Phys. A*, 131, 505, 2002.

- Hsu, C.C., Ward, C.A., Pearlman, R., Nguyer, H.M., Yeung, D.A., and Curley, J.G. Determining the optimum residual water in lyophilized protein pharmaceuticals, *Dev. Biol. Stand.*, 74, 255, 1991.
- Suzuki, T., Imamura, K., Fujimoto, H., and Okazaki, M. Relation between thermal stabilizing effect of sucrose on LDH and sucrose-LDH hydrogen bond, *J. Chem. Eng. Jpn.*, 31, 565, 1998.
- Wolkers, W.F., van Kilsdonk, M.G., and Hoekstra, F.A. Dehydration-induced conformational changes of poly-L-lysine as influenced by drying rate and carbohydrates, *Biochim. Biophys. Acta*, 1425, 127, 1998.

Effects of Trehalose on the Stability and Phase Transition Behavior of Freeze-Dried Liposomes Containing Cholesterol

Satoshi Ohtake, Carolina Schebor, Sean P. Palecek, and Juan J. de Pablo

CONTENTS

Introduction	551
Materials and Methods	552
Sample Preparation	552
Differential Scanning Calorimetry.....	552
Water Content Analysis	552
Calcein Retention Analysis.....	552
Results.....	553
References	556

Introduction

The desiccation of lipid vesicles has been studied in efforts to understand the behavior of biological membranes under low water content conditions (Crowe and Crowe, 1988) and to enhance the stability of liposomes used for drug-delivery applications (Van Winden et al., 1998). Upon the addition of sugars, phospholipid liposomes can be protected against the stresses caused by dehydration through the formation of a glassy matrix (Levine and Slade, 1992). The desiccation of phospholipid liposomes increases their phase transition temperature (T_m) (Crowe and Crowe, 1988; Koster et al., 1994). In the presence of sugars, however, the transition temperature can be depressed (Crowe and Crowe, 1993). This T_m depression has been ascribed to hydrogen-bond formation between the sugar molecules and the phospholipid headgroups (Crowe and Crowe, 1993; Sum et al., 2003). With regard to cholesterol, the majority of previous studies have focused on the physical

properties of cholesterol-containing membranes in aqueous dispersions. It has been shown that cholesterol incorporation to phospholipid bilayers modulates the physical properties of the membrane (McMullen et al., 1993). Given that one of our objectives is to better understand how cell membranes respond to desiccation, in this study we examine in detail the effects of membrane composition on the phase transitions and stability of freeze-dried DPPC- and DPPE-cholesterol liposomes in the presence of trehalose.

Materials and Methods

Sample Preparation

Phospholipids and cholesterol (Avanti Polar Lipids, Alabaster, AL) were mixed at 0 to 70 mol% cholesterol. Chloroform was evaporated under a stream of N₂, and the sample was further dried under vacuum at 50°C. The lipids were resuspended (50 mg/ml) at 50°C in a 3.11% (w/v) calcein solution containing trehalose (Pfanstiehl Laboratories, Waukegan, IL) to give a 1:1 sugar/lipid weight ratio. After 5 heating-cooling cycles, the samples were extruded (at 50°C) 19 times using an extruder (Avanti Polar Lipids, Alabaster, AL) with 100-nm pore diameter membranes. Calcein outside the liposomes was removed by passage through a Sephadex C-16 column (Amersham Biosciences, Uppsala, Sweden). Then 10% (w/v) trehalose was added to the liposome suspension. The extruded solutions were frozen at -20°C and quenched with liquid N₂ prior to freeze-drying for 48 h in a Virtis Genesis 12EL (New York) freeze-drier.

Differential Scanning Calorimetry

DSC was used to determine the phase-transition temperature (T_m) of the phospholipids. T_m represents the peak temperature of the endotherm for the lipid gel-to-liquid crystalline phase transition recorded during the heating scan. The instrument used was a TA Q100 DSC (New Castle, DE). All measurements were made at 10°C/min, using sealed aluminum pans, and an empty pan was used as a reference.

Water Content Analysis

Karl Fisher Coulometer Metrohm, Model 737 (Herisau, Switzerland) was employed to measure the water content of the samples.

Calcein Retention Analysis

The fluorescence spectrum was scanned at an excitation range of 488 to 496 nm, at an emission wavelength of 520 nm using a Jobin Yvon

Fluoromax-3 spectrofluorometer (Edison, NJ). The total calcein content of the vesicles was determined after lysis of the membranes with Triton X-100 (1% (v/v)). Calcein retention of vesicles was estimated from the fluorescence before and after the addition of Triton X-100. Prior to calcein retention analysis, the freeze-dried samples were rehydrated at room temperature.

Results

Figure 41.1 shows the gel-to-liquid crystalline phase transition temperatures (T_m) of DPPC-cholesterol mixtures as a function of the cholesterol-lipid molar ratio. The T_m of fully hydrated DPPC is 42°C (Crowe and Crowe, 1988; Vist and Davis, 1990; McMullen et al., 1993; Ohtake et al., 2004). Upon the addition of cholesterol, the transition enthalpy decreases continuously until it is no longer observable at 50 mol% cholesterol. The disappearance of the melting transition has been attributed to strong interactions between cholesterol and DPPC (McConnell, 2003). Upon dehydration, the T_m for DPPC increases from 42 to 105°C (Crowe and Crowe, 1988; Ohtake et al., 2004). This T_m increase is caused by the reduction in the spacing between the phospholipids, which allows for increased van der Waals interactions between the lipid hydrocarbon chains (Koster et al., 1994). Between 10 and 70 mol% cholesterol, two endothermic transitions are observed, both lower than the T_m of the pure phospholipid (Figure 41.1). High-sensitivity DSC studies on fully hydrated DPPC-cholesterol systems reported endotherms consisting of two components, suggesting the existence of domains enriched/depleted in cholesterol (Vist and Davis, 1990; McMullen et al., 1993). The two peaks present in our freeze-dried systems also suggest the

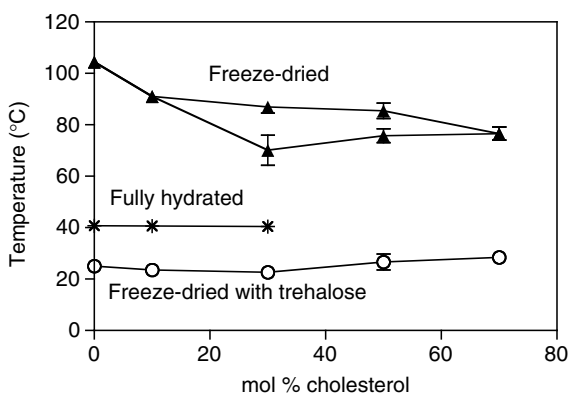
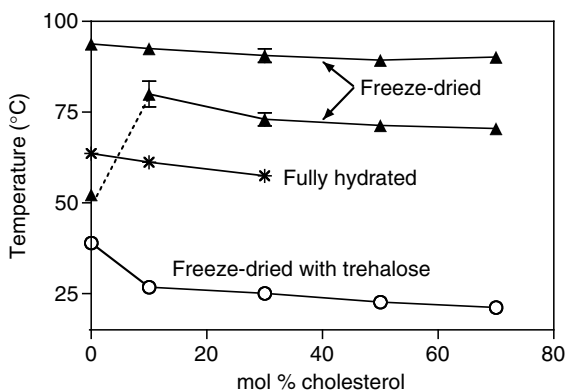


FIGURE 41.1

Phase-transition temperature-composition diagram for the fully hydrated and freeze-dried DPPC-cholesterol liposomes.

presence of two well-defined domains. The removal of water hence not only increases the transition temperatures, but also enhances the segregation of the lipid components. In the presence of trehalose, however, only one transition is observed for the freeze-dried DPPC–cholesterol liposomes; the T_m is depressed to approximately 25°C and varies only slightly ($\pm 4^\circ\text{C}$) with cholesterol proportion (Figure 41.1). The presence of a single peak (independent of the cholesterol proportion) indicates that trehalose is preventing the extensive phase separation caused by dehydration; however, the transitions are broad, which suggests the heterogeneity of the sample. Figure 41.2 presents the transition-temperature data for DPPE–cholesterol mixtures (0 to 70 mol% cholesterol). The T_m of fully hydrated DPPE is 63°C (McMullen et al., 1999). Upon the addition of cholesterol, both the transition temperature and enthalpy decrease continuously until the transition is no longer observable at 50 mol% cholesterol. Dehydrated DPPE shows two transitions: the gel-to-liquid crystalline phase transition at 52°C and the crystal-to-liquid crystalline phase transition at 93°C (Handa et al., 1985). Freeze-dried DPPE–cholesterol liposomes also exhibit two transitions at all cholesterol proportions studied. Lyophilization with trehalose allows the membrane to remain in a more fluid state, hindering the formation of the crystalline phase. The gel-to-liquid crystalline phase transition, centered at 39°C, decreases both in temperature and enthalpy with increasing cholesterol proportion. As is observed for DPPC–cholesterol liposomes, trehalose addition reduces the number of transitions and also the temperature of the transition. The T_m depression upon the addition of trehalose, however, is lower for DPPE compared with DPPC. This can be accounted for by the stronger PE–PE interactions that reduce the ability of trehalose to hydrogen bond with DPPE molecules.

**FIGURE 41.2**

Phase-transition temperature–composition diagram for the fully hydrated and freeze-dried DPPE–cholesterol liposomes.

In order to analyze the stability of cholesterol containing liposomes upon freeze-drying, we studied the leakage of intravesicular contents, which is the most frequently used measure of liposome damage. Figure 41.3 shows the percentage of calcein retention for DPPC-cholesterol liposomes freeze-dried in the absence and presence of trehalose. Cholesterol proportion has no significant effect on leakage; all the liposomes examined exhibit less than 40% calcein retention, which, upon the addition of trehalose, is increased above 80%. The liposome composition has no effect on the leakage, and thus we cannot attribute the loss of calcein to the presence of defects at the boundaries of the membrane domains. In the absence of trehalose, fusion can account for the observed leakage, as previously reported (Koster et al., 1994). Fusion, however, can be prevented for liposomes that are freeze-dried with trehalose through the formation of a glassy matrix (Koster et al., 1994). Leakage has also been linked to the passage of the phospholipid membrane through a phase transition (Crowe et al., 1986), and this can account for the 15 to 20% leakage observed for the liposomes freeze-dried with trehalose as the rehydration temperature (20°C) is within the width of the transition peak (width at half peak $\geq 7^\circ\text{C}$).

In this work, we have analyzed the phase behavior of various freeze-dried mixtures of DPPE, DPPC, and cholesterol and have examined the effects of trehalose addition to these liposomes. Generally, dehydration leads to increase in transition temperature of the phospholipids and also to phase separation. Addition of trehalose, however, can prevent the increase in transition temperature and phase separation; freeze-dried DPPC-cholesterol liposomes exhibit only one transition and their retention capability increases by more than 40%. Further studies on the phase separation and stability of multicomponent model membranes will be required to understand better its relation to the survival of cells to freeze-drying procedures.

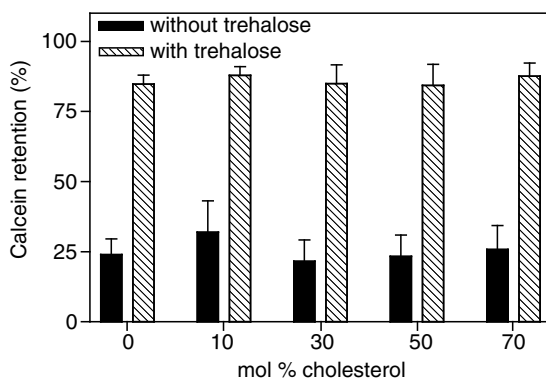


FIGURE 41.3

Effect of cholesterol addition on the retention of calcein by DPPC-cholesterol liposomes.

References

- Crowe, L. and Crowe, J. Trehalose and dry dipalmitoylphosphatidylcholine revisited, *Biochim. Biophys. Acta*, 946, 193, 1988.
- Crowe, J. and Crowe, L. Preservation of liposomes by freeze-drying, *Liposome Technology*, G. Gregoriadis, ed., CRC Press, Boca Raton, FL, pp. 229–252, 1993.
- Crowe, L.M., Womersley, C., Crowe, J.H., Reid, D., Appel, L., and Rudolph, A. Prevention of fusion and leakage in freeze-dried liposomes by carbohydrates, *Biochim. Biophys. Acta*, 861, 131, 1986.
- Handa, T., Ichihashi, C., and Nakagaki, M. Polymorphic phase transition and monomolecular spreading of synthetic phospholipids, *Progress Colloid Polym. Sci.*, 71, 26, 1985.
- Koster, K., Webb, M., Bryant, G., and Lynch, D. Interaction between soluble sugars and POPC (1-palmitoyl-2-oleoylphosphatidylcholine) during dehydration: Vitrification of sugars alters the phase behavior, *Biochim. Biophys. Acta*, 1193, 143, 1994.
- Levine, H. and Slade, L. Another view of trehalose for drying and stabilizing biological materials, *BioPharm*, 5, 36, 1992.
- McConnell, H.M. and Radhakrishnan, A. Condensed complexes of cholesterol and phospholipids, *Biochim. Biophys. Acta*, 1610, 159, 2003.
- McMullen, T., Lewis, R., and McElhaney, H.R. Differential scanning calorimetric study of the effect of cholesterol on the thermotropic phase behavior of a homologous series of linear saturated phosphatidylcholines, *Biochemistry*, 32, 516, 1993.
- McMullen, T., Lewis, R., and McElhaney, R. Calorimetric and spectroscopic studies of the effects of cholesterol on the thermotropic phase behavior and organization of a homologous series of linear saturated phosphatidylethanolamine bilayers, *Biochim. Biophys. Acta*, 1416, 119, 1999.
- Ohtake, S., Schebor, C., Palecek, S., and de Pablo, J. Effect of sugar-phosphate mixtures on the stability of DPPC membranes in dehydrated systems, *Cryobiology*, 48, 81, 2004.
- Sum, A., Faller, R., and de Pablo, J.J. Molecular simulation study of phospholipid bilayers and insights of the interaction, *Biophys. J.*, 85, 2830, 2003.
- Van Winden, E., Zuidam, N., and Crommelin, D. Strategies for large scale production and optimised stability of pharmaceutical liposomes developed for parenteral use, *Medical Applications of Liposomes*, D.D. Lasic and D.P. Papahadjopoulos, eds., Elsevier, Amsterdam, pp. 567–604, 1998.
- Vist, M. and Davis, J. Phase equilibria of cholesterol/dipalmitoylphosphatidylcholine mixtures: 2H nuclear magnetic resonance and differential scanning calorimetry, *Biochemistry*, 29, 451, 1990.

Storage Changes and Subcellular Freezing Injuries in Recalcitrant Araucaria angustifolia Embryos

Víctor H. Panza, Verónica R. Láinez, Sara B. Maldonado,
Horacio L. Maroder, and María del Pilar Buera

CONTENTS

Introduction	557
Materials	558
Water Content Analysis	558
Freezing Treatments	558
Calorimetric Analysis.....	559
Germination Test.....	560
Light and Transmission Electron Microscopy (LM and TEM)	560
Results and Discussion	560
Acknowledgments	562
References	563

Introduction

Orthodox seeds undergo a programmed desiccation at the termination of their development. In these seeds, desiccation tolerance is acquired during development and is lost after germination. In contrast, recalcitrant seeds do not tolerate a reduction in water below a relatively high level without loss of viability (Roberts, 1973). Conventional storage techniques are thus not applicable to these seeds and cryopreservation is the only feasible alternative for their long-term storage. However, their high freezable water content promotes injuries, and their low-temperature conservation represent a challenge (Kermode, 1997). In order to improve cryopreservation techniques, recalcitrant seeds are good models to analyze the impact of

freezing rate, storage time, and temperature on the degree of injury. Previous studies have demonstrated that only minor damage occurs if plant tissues are submitted to rapid cooling (-196°C) (Wolfe and Bryant, 2001). Those seeds with lower freezable water would be more easily cryopreserved.

Araucaria angustifolia (Bert.) O. Kuntze is a threatened species native to South America with high forestall and nutritional values. Its seed has been assumed to be recalcitrant (Tompsett, 1984; Panza et al., 2002). A previous TEM study revealed that embryo tissues have a very high water content, which mainly corresponds to vacuolar water (Panza et al., 2002). As vacuoles are scarce in cells of shoot and root apical meristems, we suggested that these cells could have more resistance to freezing than the rest of the embryo tissues. The present study has been addressed to examine the change of water content during storage at 5°C and evaluate subcellular freezing injuries of *A. angustifolia* embryo tissues, specifically the apical meristems, using slow (-20°C) and rapid (-196°C) cooling.

Materials

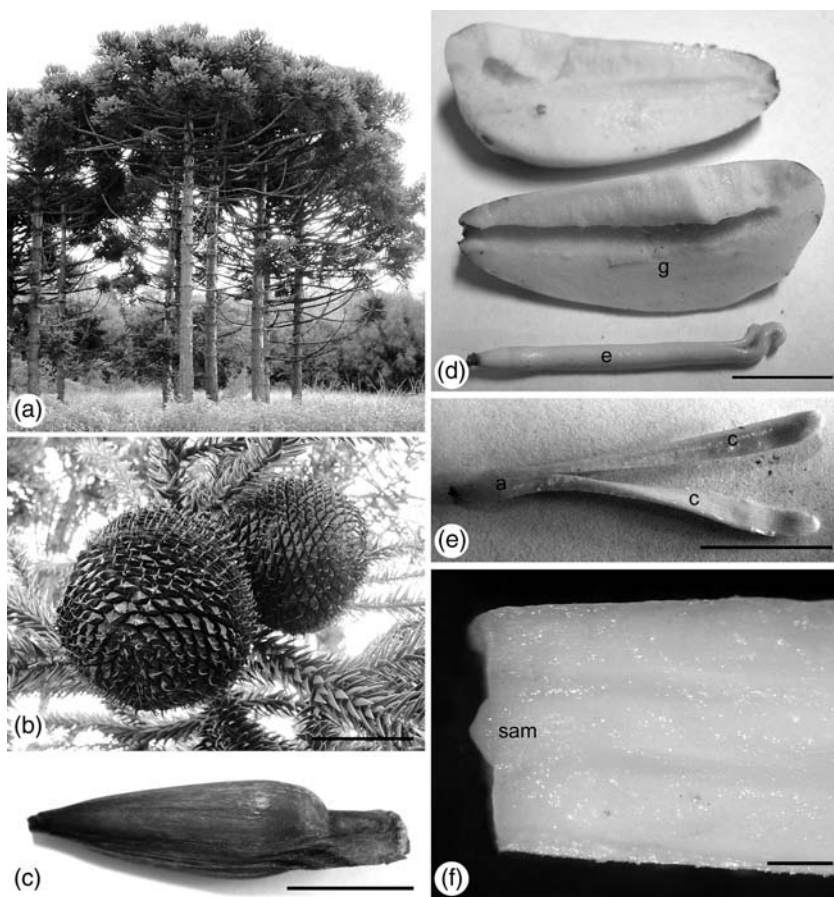
A. angustifolia (Bert) O. Kuntze seeds from the Botanical Garden of INTA-Castelar, Buenos Aires, Argentina (Figure 42.1a–c), were collected every year over six years. For conservation, seeds were placed in $30\text{-}\mu\text{m}$ thick polyethylene bags and stored at $5^{\circ}\text{C} \pm 2^{\circ}\text{C}$ in the darkness. Bags were opened for 10 min, at 30-day intervals to aerate the seeds until they were analyzed. Embryos and axes were excised from the seeds by a scalpel immediately before the freezing experiments. Studies on freezing injuries were carried out in the apical meristems of the mature frozen axes 6 months after collection.

Water Content Analysis

Water content of isolated embryos (Figure 42.1d–e) was determined by the oven method at $103 \pm 2^{\circ}\text{C}$ for 17 h (International Seed Testing Association, 2005). The results were expressed as the mean content obtained from three replicates.

Freezing Treatments

For each replicate, ten axes (Figure 42.1e–f) were placed at -20°C for slow freezing, and another ten at -196°C , by immersion in liquid nitrogen, for rapid freezing.

**FIGURE 42.1**

Araucaria angustifolia (Bert) O. Kuntze: (a) Cluster of trees from de Botanical Garden of INTA, Castelar, Argentina; (b) cones; (c) bract and megasporophyll containing the seed; (d) median longitudinal section of seed showing embryo (e) and gametophyte (g); (e) embryo showing cotyledons (c) and the hypocotyl–radicle axis (a); (f) section of the embryo axis (after the cotyledons have been excised) showing the shoot apical meristem (sam). Bars: b, 9 cm; c, 1.7 cm; d and e, 1 cm; f, 0.6 mm.

Calorimetric Analysis

For thermal analysis, shoot and root meristems were analyzed using a differential scanning calorimeter (DSC) Mettler TA 4000. Samples were rapidly cooled to -100°C and then warmed in the DSC from -100 to 100°C at $10^{\circ}\text{C min}^{-1}$. The data were analyzed using TCII TA Processor and Graph Ware TA 72 software. The ratio of unfrozen water was calculated from the

area of the melting peak of water (melted during rewarming) related to the total amount of water.

Germination Test

Germination was performed at 25°C with a photoperiod of 16/8 h light/darkness at 100% relative humidity. Germination criterion was defined as the emergence of a 5-mm radicle in sets of ten seeds in three replicates.

Light and Transmission Electron Microscopy (LM and TEM)

For LM and TEM, the treated apical meristems were fixed frozen in 2.5% glutaraldehyde in 0.1 M phosphate buffer pH 7.2 at 4°C overnight. Control unfrozen samples were also fixed in the same way. For TEM, tissues were postfixed in 1% OsO₄ in water for 2 h, dehydrated in a graded ethanol–acetone series and embedded in low-viscosity Spurr's resin. Sections were stained with uranyl acetate followed by lead citrate and examined in a Zeiss EM109T transmission electron microscope. For LM, sections were stained with Sudan Black B (Sigma S 2380 CI 26150) and Toluidine blue O (Sigma T 3260 CI 52040).

Results and Discussion

Figure 42.2 shows the water content and percent of freezable water in the apical meristems of seeds as a function of storage time at 5°C. The water content of embryos varied from 60 to 69% (Figure 42.2) on increasing storage time at 5°C. It can also be observed that the amount of freezable water increased on increasing storage time from 65 to 80% in axes with less than 1 and 6 years, respectively. Since starch concentration decreased (data not shown), the increase of freezable water was attributed to the consumption of soluble components and reserves during storage, which is supposed to promote a negative impact on embryo conservation.

Calorimetric studies on embryos by DSC showed an endothermic event attributable to a glass transition between –60 and –65°C. Thus, at storage conditions (5°C), the systems were well above the glass-transition temperature, with most of their solutes in solution or in supercooled liquid state. At such a high proportion of water, metabolic activity and deteriorative reactions involved in the short life span of this seed are not precluded by mobility restrictions. The nonstored seeds presented the relative lowest values of freezable water and they were selected for the studies on cryoconservation.

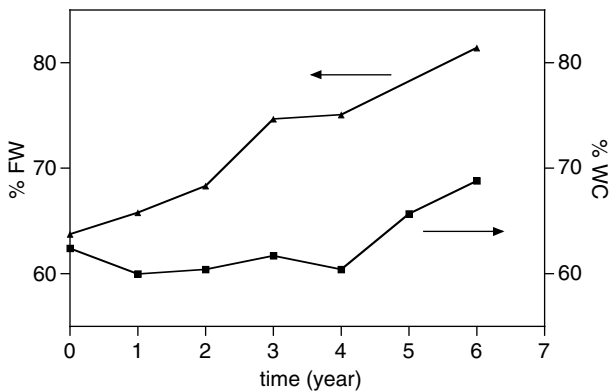


FIGURE 42.2
Water content (WC) and freezable water (FW) in the apical meristems of *Araucaria angustifolia* seeds as a function of storage time at 5°C.

As 64% of the total water in the apical meristems of embryos in recently collected seeds was freezable, freezing injuries are able to occur, the extent of damage being cooling-rate dependent. In fact, both LM and TEM revealed different degrees of cellular injuries in the apical meristems of frozen embryos (Figures 42.3 and 42.4).

Cells from the control (embryos not exposed to freezing conditions) displayed features typically found in hydrated and metabolically active cells: numerous mitochondria nuclei exhibiting fairly disperse chromatin and plastids with highly dense stroma could be seen (Figure 42.3a and Figure 42.4a and b). Starch, lipids, and proteins were the reserves present in plastids, lipid bodies, and vacuoles, respectively.

Rapid freezing (at -196°C) was the treatment that better preserved the cellular and subcellular structures. In fact, plasmalemma retained its integrity and membranes of organelles remained distinguishable. However,

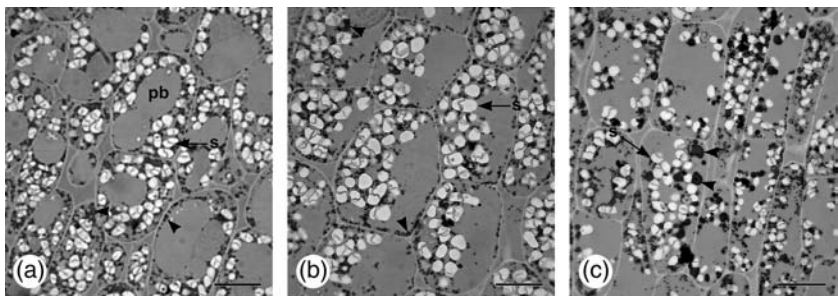
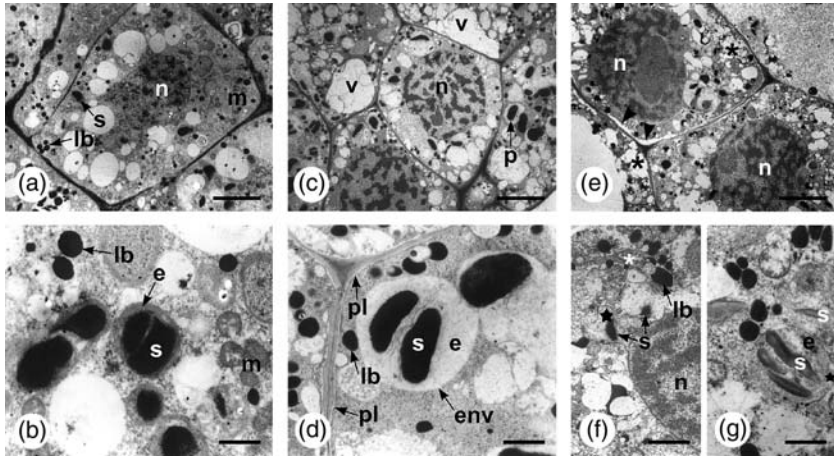


FIGURE 42.3
LM of sections of the axis showing the cortical parenchyma after staining with Sudan Black B. (a) Control; (b) rapid cooling; (c) slow cooling. Coalescence of lipid bodies can be observed (arrowheads). Abbreviations: Protein vacuole (pv); starch (s). Bar = 20 μm .

**FIGURE 42.4**

TEM of the shoot apical meristem (sam). (a, b) Control; (c, d) rapid cooling; (e–g) slow cooling. Abbreviation: stroma (s); envelope (env); lipid bodies (lb); mitochondrion (m); nucleus (n); plastid (p) plasmalemma (pl); starch (s); plastids became disorganized leading to the disintegration of the envelope (star), high degree of vacuolation (v). Symbols: Arrowheads indicate withdrawal of plasmalemma from the cell wall. Black and white asterisks indicate fragments and accumulation of membranes. Bars: a, c, e = 6 μm ; b, d, g = 1 μm ; f = 2 μm .

some injuries were evident: nuclear chromatin condensed; stroma from mitochondria and plastids became electronically translucent; plastids were swollen and distorted; and numerous vacuoles next to cell wall were formed (Figures 42.3b and 42.4c and d).

Slow frozen systems exhibited higher injuries than rapidly cooled systems: plasmalemma appeared severely damaged and retracted from the cell wall; membranes in general disrupted and fragments of membranes were frequent in the cytoplasm; nuclear chromatin condensed into clumps; organelles collapsed; vacuole number increased and cisternae of endoplasmic reticulum distended; and coalescence of lipid droplets was also observed (Figures 42.3c and 42.4e–g). Similar organelles injuries induced by freezing, especially mitochondria, have been reported in sensitive plant tissues from different species (McKersie, 1996).

These results represent the first approach to relate thermophysical properties, cooling rates, and subcellular injuries in recalcitrant seeds, and they indicated that embryo cryoconservation will be improved by employing rapid cooling and using nonpreviously stored seeds.

Acknowledgments

This work was supported by grants from Agencia de Promoción Científica y Tecnológica (ANPCyT) (Argentina) BID 1201/OC-ARPICT 08-04536.

References

- International Seed Testing Association, International rules for seed testing. Chapter 9, pp. 1–8, 2005.
- Kermode, A.R. Approaches to elucidate the basis of desiccation-tolerance in seeds, *Seed Sci. Res.*, 7, 75, 1997.
- McKersie, B.D. Freezing stress, Department of Crop Science, University of Guelph (<http://cropsoil.psu.edu/courses/AGRO518/freezing.htm>), 1996.
- Panza, V., Láinez, V., Maroder, H., Prego, I., and Maldonado, S. Storage reserves and cellular water in mature seeds of *Araucaria angustifolia*, *Bot. J. Linn. Soc.*, 140, 273, 2002.
- Roberts, E.H. Predicting the storage life of seeds, *Seed Sci. Tech.*, 1, 499, 1973.
- Tompsett, P.B. Desiccation studies in relation to the storage of *Araucaria* seed, *Ann. Appl. Biol.*, 105, 581, 1984.
- Wolfe, J. and Bryant, G. Cellular cryobiology: thermodynamic and mechanical effects, *Int. J. Refrig.*, 24, 438, 2001.

Thermal Transitions of Quinoa Embryos and Seeds as Affected by Water Content

Silvia B. Matiacevich, Martina L. Castellión, Sara B. Maldonado, and
María del Pilar Buera

CONTENTS

Introduction	565
Materials and Methods	566
Results.....	567
Discussion and Conclusions	569
Acknowledgments	570
References	570

Introduction

Quinoa (*Chenopodium quinoa* Willd) is an ancestral crop from the South American Andes. Quinoa seeds have high nutritional value and energetic content, and are consequently very suitable as food. It has a protein content of 14 to 20% and is particularly rich in essential aminoacids such as lysine and methionine, which are rare in most cereals (Sigstad and Prado, 1999).

Seeds are orthodox and deteriorative processes during storage are reported as dependent on their physical state and on solid/water interactions (Walters, 1998).

Under long-term storage conditions, i.e., cool storage environment and low seed water content, seeds are likely to be in the glassy state. The extremely high viscosity and low molecular mobility in glassy systems would prevent or inhibit many deleterious processes (Williams and Leopold, 1989; Buitink et al., 1998). In orthodox seeds, transitions of seed cytoplasm components may affect seed viability and their vitrification is proposed to be advantageous for germplasm stability (Vertucci and Roos, 1990). As storage

temperature or water content increases, the seed will undergo the glass-to-liquid transition (at the glass-transition temperature, T_g), resulting in an increase in molecular mobility. T_g is a function of water content, and whether the seed is in glassy state or not will depend on seed water content and on storage temperature (Buitink et al., 1998; Murthy et al., 2003).

Different genotypes of quinoa have different storage stability. In this work we analyzed three genotypes, two of them, Ollagüe and Sajama, belonging to the altiplano-genotypic group (Tapia et al., 1979), are native of the Chilean-Bolivian Altiplano, i.e., a remarkably dry area where precipitations are very scarce. The third genotype, Baer II, belongs to the sea-level genotypic group (Tapia et al., 1979), which is an improved line obtained from Baer, an ecotype original from wet areas of Southern Chile (where precipitations reach up to 1000 mm/year).

The purpose of this work was to analyze thermal transitions in embryos and whole seeds as a part of a comprehensive study on seed conservation.

Materials and Methods

Quinoa seeds of three different genotypes (Ollagüe, Baer II, and Sajama) were grown in the experimental greenhouse of the University of Buenos Aires, Buenos Aires, Argentina. In all experiments, seeds were manually pre-sorted, discarding excessively small, large, and damaged seeds. Embryos (with protein and lipid storage reserves) and perisperm (with starch) were separately processed employing tweezers under a stereoscope. Grounded seeds, embryos, and perisperm were placed in 1-cm diameter glass vials and stored over saturated salt solutions in the relative humidity (RH) range 11 to 98% into dessicator jars for 7 days at $6 \pm 1^\circ\text{C}$ to achieve different water contents. After equilibration, samples of approximately 15 mg of embryos and seeds were weighed on a Mettler Toledo balance with a precision of ± 0.01 mg, sealed into aluminium pans (40- μl capacity) and loaded into the differential scanning calorimeter (DSC Mettler Toledo 822). All experiments were performed in triplicate following the same protocol.

Lipid extraction from grounded seeds was achieved by 2 h soaking in a mixture 2:1 of chloroform:methanol (3 ml/g of seed) (Williams and Leopold, 1989).

The thermograms were obtained by warming from -125 to 100°C at a scanning rate of $10^\circ\text{C}/\text{min}$ during both cooling and warming. Water content was determined after the DSC scans. The pans were punctured and dried in an oven at 100°C for 10 days.

Starch gelatinization was analyzed in suspensions of perisperm with water (1 mg of perisperm:2 μl of water), prepared 24 h before analysis (Calzetta Resio et al., 1999).

Results

Table 43.1 shows the water content of the seeds and embryos after equilibrium at the different RH. Even though seeds and embryos have different composition, their water contents at a given RH are similar. Water content values of the different quinoa varieties are also in the same range, and comparable with those obtained by Tolaba et al. (2004).

Embryos and seeds showed thermograms with exothermic and endothermic transitions. Freezable water was detected in embryos at or above RH 88%. Figure 43.1 shows that: (i) Ollagüe and Sajama embryos have freezable water at RH 88%; (ii) no Baer embryos nor any of the seeds showed water fusion despite their high water content (Table 43.1); (iii) in the three genotypes, embryo thermograms equilibrated at 98% RH, for which ice melting occurred with onset at -30°C . Seeds equilibrated at this relative humidity have freezable water at the same onset (data not shown).

Endothermic peaks were observed between 70 and 90°C , but they were not evident after re-scans. This result could be a result of protein denaturation. The area of the endothermic transitions (related ΔH of protein denaturation) increased with water content. The temperature of protein denaturation diminished at RH 98%, which was coincident with a high amount of freezable water, as shown in Figure 43.1. At low RH values, the temperatures of the endothermic transitions were similar for the different genotypes. Above 88% RH, the protein denaturation temperature for Ollagüe was lower than those for the other varieties.

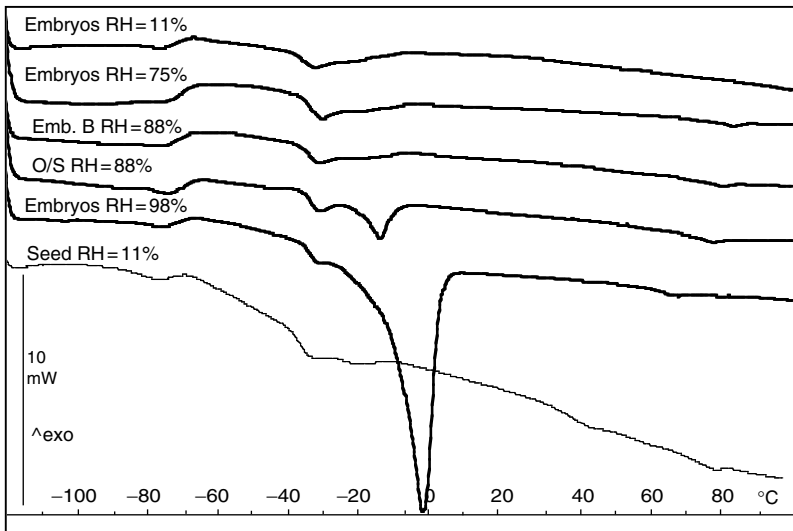
Thermal transitions of quinoa starch were analyzed using the perisperm samples. Starch gelatinization did not occur below 100°C in the samples equilibrated up to 98% RH. Their water content was not enough to allow gelatinization. In fully hydrated suspensions, gelatinization was observed at $61 \pm 2^{\circ}\text{C}$. There were no differences in gelatinization temperatures among genotypes (data not shown).

TABLE 43.1

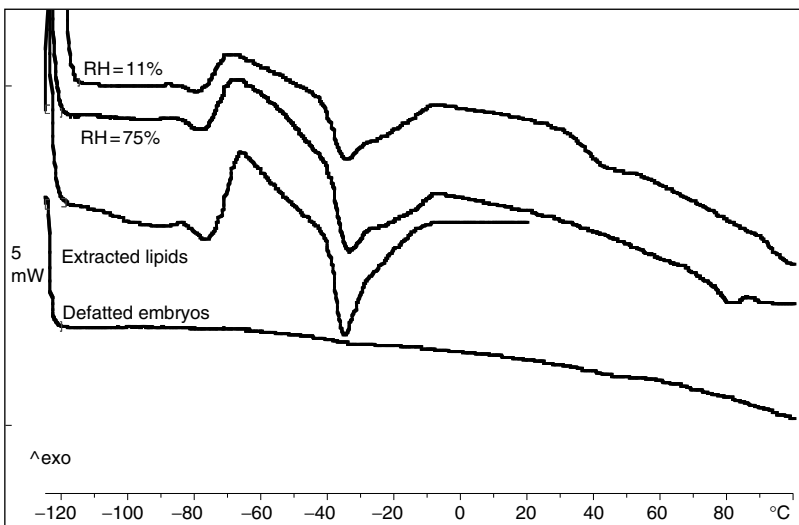
Water Content of Embryos and Seeds of Three Genotypes Equilibrated at Various Relative Humidities (RH)

RH, %	Baer		Ollagüe		Sajama	
	Embryos	Seeds	Embryos	Seeds	Embryos	Seeds
11	7.8 ± 0.9	6.1 ± 0.8	5.1 ± 0.4	7.2 ± 0.2	4.7 ± 0.8	7 ± 2
75	18 ± 1	18 ± 1	17.18 ± 0.05	16 ± 1	17.2 ± 0.8	17 ± 1
88	20 ± 2	21.4 ± 0.5	23 ± 4^a	18.6 ± 0.3	22 ± 2^a	19.4 ± 0.5
98	35 ± 10^a	30 ± 1^a	39 ± 12^a	33.8 ± 0.8^a	35 ± 9^a	37 ± 4^a

^a Freezable water was detected by DSC.

**FIGURE 43.1**

DSC Thermograms of embryos and seeds equilibrated at various relative humidities (RH). Scanned from -125°C to 100°C at $10^{\circ}\text{C}/\text{min}$. Ice melting transitions were observed as endothermic peaks close to 0°C indicating the presence of freezable water. Differences in freezable-water content were observed at 88% RH between genotypes. B: Baer II; O: Ollagüe; S: Sajama.

**FIGURE 43.2**

DSC thermograms of embryos, defatted embryos and extracted lipids from embryos. Scanned from -125°C to 100°C at $10^{\circ}\text{C}/\text{min}$. Peaks in the range -90°C to 10°C correspond to lipid transitions. These peaks were independent of relative humidity (RH). This pattern was observed in the three analysed genotypes.

An endothermic peak (shown as head arrows in Figure 43.1 and Figure 43.2) was observed at $48 \pm 3^\circ\text{C}$ in samples up to 75% RH. The enthalpy of this transition diminished with increasing RH and was not seen in the re-scans. This transition may be because of a crystalline component that melts, denatures, or dissolves in water at high RH, or it is only present at low water contents as a result of metabolic responses to dehydration. These transitions require further investigation.

Other transitions observed in the samples were independent of water content. Figure 43.2 shows thermograms of embryos where endotherms were centered at -79 ± 2 and $-35 \pm 1^\circ\text{C}$ and exotherms at $-68 \pm 2^\circ\text{C}$. As these thermal events could be related to the lipidic components, a lipid extraction with chloroform:methanol was performed on grounded seeds. DSC thermograms showed diminished signals for defatted seeds (Figure 43.1, defatted line) while for the lipidic fraction dried at 25°C , DSC thermograms (Figure 43.1, lipids line) resemble those of embryos and whole seeds. These results indicate that the signals recorded in Figure 43.1 were mainly attributable to the lipidic component of the embryos. Therefore, the endothermic and exothermic peaks correspond to fusion and crystallization of lipids, respectively. Regarding thermal transitions produced by lipid components, there were no significant differences among genotypes or water activity.

Discussion and Conclusions

Although embryos and seeds are complex systems, the thermal transitions of their main components can be analyzed by DSC. The peaks generated by the melting of freezable water (shown in Figure 43.1) interfered with the observation of lipid transitions. Therefore, the extraction of lipidic components resulted from an interesting approach to analyze these complex systems, as it allows identification of the transitions of the different components occurring at similar temperatures.

Molecular mobility above T_g appears to be a key factor influencing the storage stability of biological tissues because it controls the rate of detrimental reactions that reduce storage life (Buitink et al., 1998; Murthy et al., 2003). Although the change in water content could help in the identification of glass transitions, these events were difficult to observe and were overlapped with other thermal phenomena.

The inhibition of molecular mobility at low water content was better reflected in the restrictions for protein denaturation, starch gelatinization, and water crystallization. Starch gelatinization was only observed in fully hydrated systems. The increase in water content was also reflected on the increased extent of protein denaturation and the decrease of the temperatures at which this transition occurred. Freezable water was detected in samples of

water content above 20%. For the particular systems studied the RH of 88% seems to be a limit to define the conditions for developing accelerated aging or freezing in these seeds. The occurrence of freezable water or protein denaturation would indicate that deteriorative reactions are not restricted.

Even though the three varieties had a similar thermal behavior, Baer showed some different values from the other two varieties (Ollagüe and Sajama), the most significant of which was the lower freezable water content in Baer. Given the fact that Baer is native of a wet area and has a lower free and freezable water seed content, we suggest that this difference would represent an advantage for the lifespan of this genotype in a wet seed bank.

From the results of the present work, we propose the degree of freezable water and of protein denaturation as better indicators than T_g to predict the susceptibility of seeds during storage.

Acknowledgments

The authors acknowledge financial support from CONICET, ANPCYT, Universidad de Buenos Aires, and Fundación Antorchas. Special thanks to Drs. Daniel Bertero and Fabio Causin for providing the seeds.

References

- Buitink, J., Claessens, M.M.A.E., Hemminga, M.A., and Hoekstra, F.A. Influence of water content and temperature on molecular mobility and intracellular glasses in seeds and pollen, *Plant Physiol.*, 118, 531, 1998.
- Calzetta Resio, A.N., Tolaba, M.P., and Suarez, C. Some physical and thermal characteristics of amaranth starch, *Food Sci. Technol. Int.*, 6, 371, 1999.
- Murthy, U.M.N., Kumar, P.P., and Sun, W.Q. Mechanisms of seed ageing under different storage conditions for *Vigna radiate* (L.) Wilczek: lipid peroxidation, sugar hydrolysis, Maillard reactions and their relationship to glass state transition, *J. Exp. Bot.*, 54, 1057, 2003.
- Sigstad, E.E. and Prado, F.E. A microcalorimetric study of *Chenopodium quinoa* Willd. seed germination, *Thermochim. Acta*, 326, 159, 1999.
- Tapia, M., Alandia, S., Cardozo, A., Gandarillas, H., Mujica, A., Ortiz, R., Otazu, V., Rea, J., and Zanabria, E. Quinoa y Canihua, *Cultivos andinos, Serie libros y materiales educativos* 49, M. Tapia, ed., IICA, Bogotá, Colombia, 1979.
- Tolaba, P.P., Peltzer, M., Enriquez, N., and Pollio, M.L. Grain sorption equilibria of quinoa grains, *J. Food Eng.*, 61, 365, 2004.
- Vertucci, C.W. and Roos, E.E. Theoretical basis of protocols for seeds storage, *Plant Physiol.*, 64, 1019, 1990.
- Walters, C. Understanding the mechanisms and kinetics of seed aging, *Seed Sci. Res.*, 8, 223, 1998.
- Williams, R.J. and Leopold, A.C. The glassy state in corn embryos, *Plant Physiol.*, 89, 977, 1989.

Part 8: Molecular Mobility, State Diagrams, and Chemical Reactions

Physical Structure, Water Plasticization, and Crystallization of Spray-Dried and Freeze-Dried Lactose

Md. Kamrul Haque and Yrjö H. Roos

CONTENTS

Introduction	573
Materials and Methods	574
Materials	574
Methods	575
Spray Drying	575
Freeze Drying	575
Scanning Electron Micrographs	575
Differential Scanning Calorimetry	575
Water Sorption and Time-Dependent Crystallization	576
Results and Discussion	576
Physical Structure	576
Glass-Transition Temperature	576
Instant Crystallization Temperature	578
Time-Dependent Lactose Crystallization	579
Conclusions	580
Acknowledgments	581
References	581

Introduction

Lactose, the characteristic milk sugar, is present in dairy-based products. Its physical state is important for the stabilization of products during processing and storage (Roos and Karel, 1991a; Slade and Levine, 1991). Lactose in foods is often in an amorphous state, which is very hygroscopic.

Amorphous materials can be produced from a solution by rapid cooling or removal of solvent water, e.g., by freeze drying, and spray drying. Different drying methods produce amorphous materials with different physical properties, e.g., in terms of particle size and structure (Saito, 1985) and their thermal behavior may differ. Spray-dried lactose and milk powders are widely used in the food industries. The physical and chemical changes of lactose can be affected or controlled by the glass transition (Roos and Karel, 1990; Slade and Levine, 1991). Above the glass transition, increasing molecular mobility and free volume result in endothermic changes in heat capacity, which can be detected by differential scanning calorimetry (DSC) (Roos and Karel, 1990; 1991a; 1991b). Lactose crystallization in dairy products is controlled by glass transition and water content causing rapid product deterioration.

Crystallization is a phase transition occurring in amorphous lactose or other crystallizing carbohydrates. Crystallization occurs time-dependently when water content or temperature exceed a critical value (Roos, 1993). Jouppila and Roos (1994a) observed that freeze-dried lactose and lactose in milk powders crystallized at RH > 40% at 24°C. Other researchers (Roetman, 1979; Saltmarch and Labuza, 1980; Saito, 1985) also observed the appearance of lactose crystals in dairy powders by scanning electron microscope (SEM). Roetman (1979) observed the structural change in skim milk powder by SEM and found that tomahawk-like crystals were formed in precrystallized (crystal formed before spray drying) products and needle-like crystals formed in postcrystallized (crystal formed after spray drying) products. Saito (1985) reported that α -lactose monohydrate crystals were formed in both spray-dried whole and instant skim milk powders as a result of water sorption. The sensitivity of the amorphous materials to changes in temperature and water content requires knowledge of temperature and water content that can lead to crystallization of lactose. The objectives of the present study were to compare changes in physical structure resulting from water sorption and thermal transitions, such as glass transition and crystallization, and to observe differences in time-dependent crystallization in spray-dried and freeze-dried lactose.

Materials and Methods

Materials

α -Lactose monohydrate (Dairygold, Mitchlestown, Cork, Ireland) was used to prepare spray-dried and freeze-dried amorphous lactose to study physical structure, thermal transitions, and time-dependent lactose crystallization.

Methods

Spray Drying

Aqueous solution (15% w/w) of α -lactose monohydrate was spray dried using a Niro Atomizer spray drier (Copenhagen, Denmark) with inlet temperature of 185 to 190°C and outlet temperature 85 to 90°C. Spray-dried powder was kept immediately in vacuum desiccators over P_2O_5 at room temperature (22 to 23°C).

Freeze Drying

α -Lactose monohydrate solution (15% w/w) was frozen at -20°C for 12 h, subsequently stored at -80°C for 24 h and then dried using a freeze drier (Lyovac GT2 freeze-dryer; Amsco Finn-Aqua GmbH, Hürth, Germany) for 60 to 70 h ($T_{\text{em}} < -40^\circ\text{C}$; $p < 0.1$ mbar). Solution was dried in glass vials (3 ml in each) for determination of water sorption and time-dependent crystallization, and in petri dishes for measuring thermal transitions. Dried samples were kept in vacuum desiccators over P_2O_5 , samples from petri dishes were ground using mortar and pestle, and powdered samples were stored in evacuated desiccators over P_2O_5 until analyses were carried out.

Scanning Electron Micrographs

The physical structures of spray-dried and freeze-dried amorphous and crystalline (humidified over 54.5, 65.6 and 76.1% RVP for 144 h for spray-dried and 72 h for freeze-dried) lactose were viewed by SEM (JSM-840, Tokyo, Japan). Small amounts of samples were mounted on SEM specimen stubs by using double-sided adhesive tape. The mounted samples were then coated with gold in a sputter coater (Edwards sputter coater, Sussex, UK) under high vacuum. The coated samples were viewed with SEM at 20 KV in the secondary electron mode. The samples were systematically viewed at 500 to 10,000 \times magnifications.

Differential Scanning Calorimetry

Dried lactose was transferred in preweighed DSC aluminum pans (40 μL ; Mettler Toledo-27331, Schwerzenbach, Switzerland) and stored in open pans for 144 h for spray-dried and 72 for freeze-dried materials to equilibrate at room temperature in evacuated desiccators over P_2O_5 and different saturated salt solutions, i.e., LiCl, CH_3COOK , MgCl_2 , and K_2CO_3 (Sigma Chemical Co., St. Louis, MO, USA) with respective relative water vapor pressure (RVP) of 11.4, 23.1, 33.2, and 44.1 giving an a_w of $0.01 \times$ percentage of RVP at equilibrium. The pans were hermitically sealed after equilibration. Triplicate samples of each material were analyzed. An empty pan was used as a reference. The DSC was calibrated for temperature and heat flow as reported by Haque and Roos (2004). The samples were scanned first over the glass-transition temperature region at $5^\circ\text{C}/\text{min}$, then cooled at $10^\circ\text{C}/\text{min}$ to

below glass transition, and a second heating scan at 5°C/min was run to well above the crystallization temperature. Anhydrous samples were scanned using pans with punctured lids to allow evaporation of any residual water during the measurement. Samples with various water contents were scanned in hermetically sealed pans. Glass transition (T_g , onset) and instant crystallization temperature (T_{cr} , onset) were analyzed using STAR^e thermal analysis software, version 6.0 (Mettler Toledo Schwerzenbach, Switzerland)

Water Sorption and Time-Dependent Crystallization

Water sorption for triplicate samples of each material were studied for 192 h at room temperature (22 to 23°C) in evacuated desiccators over saturated solutions of LiCl, CH₃COOK, MgCl₂, K₂CO₃, Mg(NO₃)₂, NaNO₂, and NaCl at RVP of 11.4, 23.1, 33.2, 44.1, 54.5, 65.6, and 76.1%, respectively. We use RVP for storage and a_w of $0.01 \times$ percentage of RVP for equilibrated materials. The samples were weighed at 3, 6, 9, 21, and 24 h, and then at 24-h intervals for 11.4 to 44.1% RVP at 2, 4, 6, 8, 10, 21, and 24 h and then at 24-h intervals for 54.5% RVP, and every hour up to 6 h then at 8, 10, 21, 24 h, and then at 24-h intervals for 65.6 and 76.1% RVP. All vials were kept closed with caps after the vacuum was released in the desiccators prior to weighing (Jouppila and Roos, 1994b). The water content of each material was measured as a function of time and the mean weight of triplicate samples was calculated.

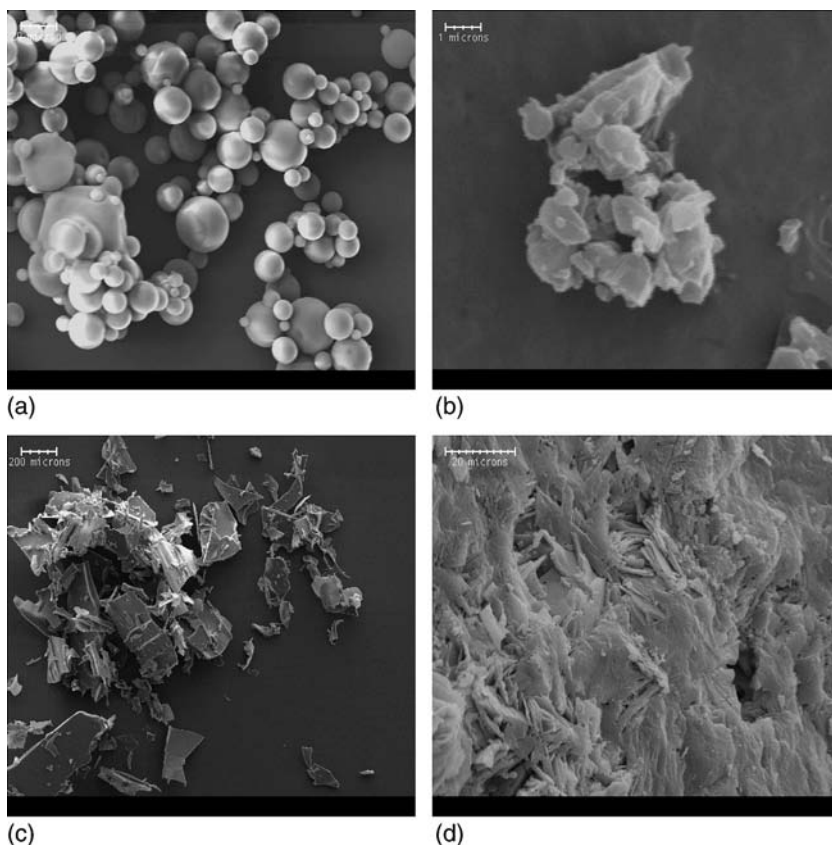
Results and Discussion

Physical Structure

The amorphous and humidified samples of spray-dried and freeze-dried lactose over 76.1% RVP are shown in Figure 44.1. Spray-dried amorphous lactose particles were spherical-shaped with a smooth surface as reported by Roetman (1979) and Saltmarch and Labuza (1980). However, freeze-dried lactose resembled broken glass or had a flake-like structure. Tomahawk-like crystals (lactose monohydrate) were observed in spray-dried lactose after 144 h of storage and needle-like or rod-like structures in freeze-dried lactose after 72 h of storage at RVP 76.1% (Figure 44.1). Millqvist-Fureby et al. (1999) showed that flake-like morphology was obtained in freeze-dried amorphous lactose and long rod-like structure in crystalline lactose. These observations agreed well with the present study. Our observations suggested that different drying methods give different microstructures for both the amorphous and crystalline state.

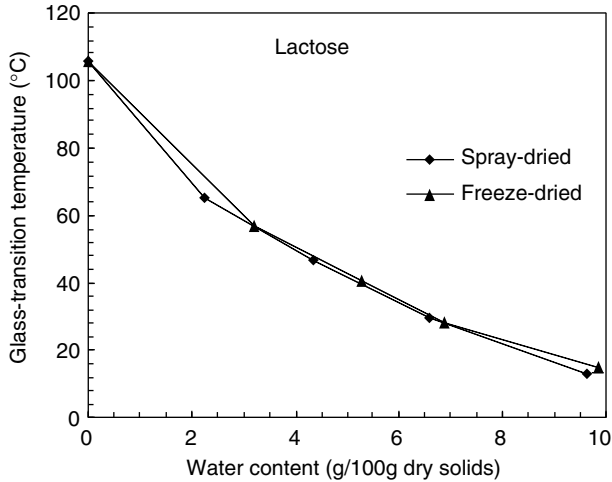
Glass-Transition Temperature

The T_g (onset) values for spray-dried and freeze-dried lactose are shown in Figure 44.2 with corresponding water contents. T_g decreased with increasing

**FIGURE 44.1**

Scanning electron micrographs of amorphous spray-dried lactose (a), crystalline spray-dried lactose (b), humidified over 76.1% RVP for 144 h, amorphous freeze-dried lactose (c), and crystalline freeze-dried lactose (d) by humidified over 76.1% RVP for 72 h.

water content, which was in accordance with the findings of other researchers (Roos and Karel, 1991a; 1991b; Roos, 1993; Jouppila and Roos, 1994b; Fernández et al., 2003). T_g of anhydrous spray-dried and freeze-dried lactose was the same, being 105.4°C. This value was slightly higher than that reported by Roos and Karel (1990, 1991a, 1991b) (101°C) for freeze-dried amorphous lactose. Jouppila and Roos (1994b) and Fernández et al. (2003) also found slightly lower T_g value for freeze-dried milk powder than that of lactose in the present study. Slightly higher T_g in our present study resulted from the use of punctured pans in the DSC analysis, which allowed evaporation of residual water. However, the T_g of freeze-dried lactose was slightly higher than the T_g of spray-dried lactose at corresponding water contents (Figure 44.2). T_g of freeze-dried lactose was lower than those of spray-dried lactose at corresponding water activities up to 0.332 a_w .

**FIGURE 44.2**

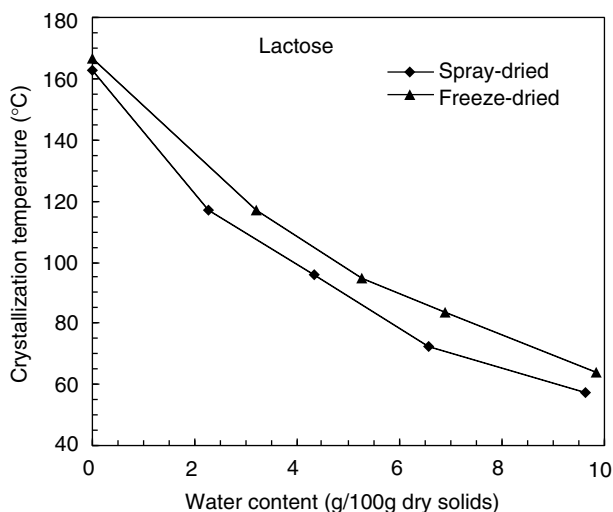
Glass-transition temperature (onset) for spray-dried and freeze-dried lactose as a function of water content, determined using DSC during heating at 5°C/min.

At higher a_w levels, the T_g of freeze-dried materials were slightly higher than those of spray-dried materials. Differences in T_g were explained by differences in water contents and water activities. Freeze-dried materials sorbed more water than spray-dried materials at corresponding water activities.

An endothermic relaxation peak was associated with glass transition in spray-dried and freeze-dried lactose, even in immediate rescanning during DSC analysis. The lower molecular weight lactose molecules may be more mobile in the vicinity of the glass transition and relax more rapidly to a lower energy state, which could explain the observed endothermic relaxation behavior. This result suggested that plasticizing effect of water on T_g was also different in differently dehydrated materials.

Instant Crystallization Temperature

The T_{cr} (onset) of spray-dried and freeze-dried materials obtained from dynamic DSC analysis are shown in Figure 44.3 with respective water contents. The T_{cr} decreased with increasing water activities and water contents showing a similar behavior as T_g . T_{cr} of freeze-dried lactose was higher than T_{cr} of spray-dried lactose in the anhydrous state and at all corresponding water contents (Figure 44.3). T_{cr} for freeze-dried lactose was nearly the same as reported by Roos and Karel (1990) for freeze-dried anhydrous and humidified lactose over various RVP. Crystallization of lactose also occurred differently from differently dehydrated materials.

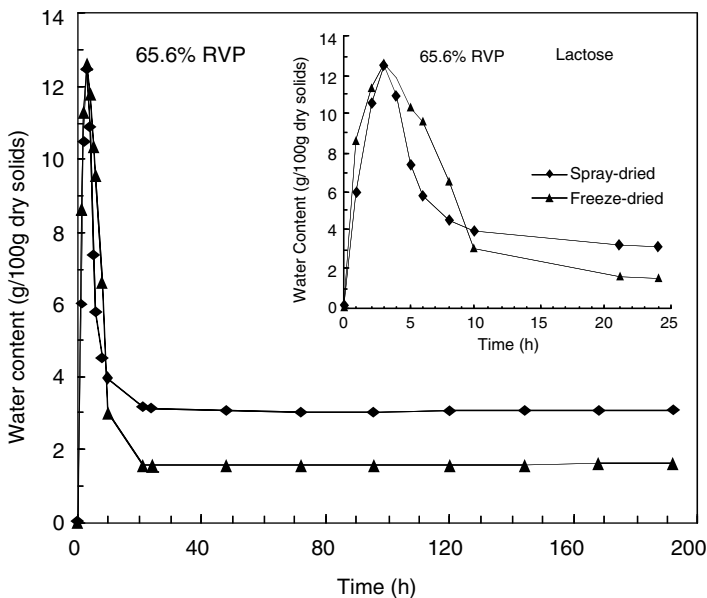
**FIGURE 44.3**

Instant crystallization temperature (onset) for spray-dried and freeze-dried lactose as a function of water content, determined using DSC during heating at 5°C/min.

Time-Dependent Lactose Crystallization

Crystallization of lactose was observed to be time-dependent from the loss of sorbed water (Vuataz, 1988; Jouppila and Roos, 1994a). Lactose crystallization occurred in spray-dried and freeze-dried materials at RVP $\geq 44.1\%$. Freeze-dried lactose sorbed higher amounts of water than spray-dried lactose at all corresponding RVP (11.4 to 76.1). Freeze-dried lactose sorbed more water even at higher RVP before crystallization. Loss of sorbed water in spray-dried and freeze-dried lactose was observed after the same period of time (< 4 h) at RVP $\geq 65.6\%$ (Figure 44.4). At 54.5% RVP loss of sorbed water in freeze-dried lactose was more delayed than in spray-dried lactose. These results suggested that lactose crystallization was different in the instant and slow crystallization, and different in differently dehydrated materials. Time-dependent lactose crystallization observed in the present study agreed with the results of Jouppila and Roos (1994a) for freeze-dried lactose, and of Berlin et al. (1968) for lactose crystallization in spray-dried and freeze-dried skim milk powders. Vuataz (1988) found that lactose in skim milk powder crystallized at 39.1% RH at 25°C after 200 h of storage. Bronlund and Peterson (2004) also observed that a decrease of sorbed water occurred in partially amorphous lactose because of lactose crystallization at RH $> 40\%$ at 20°C, which was similar to our results. Slight differences with our present studies and previous other studies might be a result of differences in material composition, drying, and experimental conditions.

Water sorption of freeze-dried and spray-dried materials leveled off with various amounts of water contents, depending on RVP, and drying methods.

**FIGURE 44.4**

Water contents for spray-dried and freeze-dried lactose as a function of storage time under RVP of 65.6% at room temperature. Inset shows water sorbed at 65.6 RVP within 24 h of storage.

Water contents in freeze-dried lactose leveled off at lower amounts of water than spray-dried lactose at the higher RVP ($\geq 65.6\%$) (Figure 44.4) and leveled off water contents occurred earlier in freeze-dried materials (72 h) than in spray-dried materials (144 h). Water contents in freeze-dried pure lactose after crystallization were $< 2\%$ but in spray-dried lactose around 3% , suggesting that lactose probably crystallized in a mixture of α -lactose monohydrate and various anhydrous forms of α/β -lactose crystals (Jouppila and Roos, 1994a; 1994b; Haque and Roos, 2004). The percentage of anhydrous crystals was probably higher in freeze-dried lactose than in spray-dried lactose. However, we assume that different crystal forms may form, depending on the method used for powder production and storage conditions.

Conclusions

The present study has shown that spray-dried and freeze-dried lactose have different physical structures, thermal transitions, and time-dependent lactose crystallization behavior. Spray-dried lactose had round-shaped particles but freeze-dried lactose resembled broken glass or had a flake-like structure. T_g and T_{cr} of freeze-dried lactose were higher than those of

spray-dried lactose. Lactose crystallization occurred slightly more slowly in freeze-dried lactose than in spray-dried lactose.

Acknowledgments

The study was carried out with the financial support of PRTL Cycle 3 of the Higher Education Authority of Ireland. We are grateful to Professor B.K. Hodnett and Ahmad Shawqi for their assistance in SEM image analysis of the materials in the Materials and Surface Science Institute at the University of Limerick.

References

- Berlin, E., Anderson, B.A., and Pallansch, M.J. Comparison of water vapor sorption by milk power components, *J. Dairy Sci.*, 51, 1912, 1968.
- Bronlund, J. and Paterson, T. Moisture sorption isotherms for crystalline, amorphous and predominantly crystalline lactose powders, *Int. Dairy J.*, 14, 247, 2004.
- Fernández, E., Schebor, C., and Chirife, J. Glass transition temperature of regular and lactose hydrolysed milk powders, *Lebensm.-Wiss. U. Technol.*, 36, 547, 2003.
- Haque, M.K. and Roos, Y.H. Water plasticization and crystallization of lactose in spray-dried lactose/protein mixtures, *J. Food Sci.*, 69, 23, 2004.
- Jouppila, K. and Roos, Y.H. Water sorption and time-dependent phenomena of milk powders, *J. Dairy Sci.*, 77, 1798, 1994a.
- Jouppila, K. and Roos, Y.H. Glass transition and crystallization in milk powders, *J. Dairy Sci.*, 77, 2907, 1994b.
- Millqvist-Fureby, A., Malmsten, M., and Bergenståhl, B. Surface characterisation of freeze-dried protein/carbohydrate mixtures, *Int. J. Pharm.*, 191, 103, 1999.
- Roetman, K. Crystalline lactose and the structure of spray-dried milk products as observed by scanning electron microscopy, *Neth. Milk Dairy J.*, 33, 1, 1979.
- Roos, Y.H. Water activity and physical state effect effects on amorphous food stability, *J. Food Process. Preserv.*, 16, 433, 1993.
- Roos, Y.H. and Karel, M. Differential scanning calorimetry study of phase transitions affecting the quality of dehydrated materials, *Biotechnol. Prog.*, 6, 159, 1990.
- Roos, Y.H. and Karel, M. Applying state diagrams to food processing and development, *Food Technol.*, 45, 66, 1991a.
- Roos, Y.H. and Karel, M. Plasticizing effect of water on thermal behaviour and crystallization of amorphous food models, *J. Food Sci.*, 56, 38, 1991b.
- Saito, Z. Particle structure in spray-dried whole milk and in instant skim milk powder as related to lactose crystallization, *Food Microstruct.*, 4, 333, 1985.
- Saltmarch, M. and Labuza, T.P. SEM investigation of the effect of lactose crystallization on the storage properties of spray-dried whey, *Scan. Electron Microsc.*, 3, 659, 1980.

- Slade, L. and Levine, H. Beyond water activity: recent advances based on an alternative approach to the assessment of food quality and safety, *Crit. Rev. Food Sci. Nutr.*, 30, 115, 1991.
- Vuataz, G. Preservation of skim milk powders: role of water activity and temperature in lactose crystallization and lysine loss, *Food Preservation by Moisture Control*, C.C. Seow, ed., Elsevier Applied Science publishers, London, pp. 73, 1988.

FT-IR Study of the Hydration of Caffeine, Sucrose, and Their Mixtures in Water

Barbara Rogé, Vincent Aroulmoji, and Mohamed Mathlouthi

CONTENTS

Introduction	583
Materials and Methods	584
Results and Discussion	585
Conclusion	590
References	591

Introduction

In taste studies, sucrose is usually taken as a reference standard in the sensory evaluation of sweetness and caffeine is generally used as the reference material for bitterness. However, sour and salty tastants modulate taste-receptor function by direct effect on specific ion channels in the membrane, while sweet and bitter tasting compounds seem to bind to closely located receptors which are coupled to a guanine-nucleotide binding protein (G-protein). The perception of their tastes proceeds through a transduction mechanism involving G-protein and a second messenger system (Kinnamon, 1988).

It is also well known that sweet and bitter tastes interact. It is the case for the inhibition of sucrose sweet taste by inhibitors like lactisol or methyl-4, 6-dichloro-4,6-dideoxy-galactopyranoside which was attributed to their hydrophobic character and their bitterness (Mathlouthi et al., 1993). Bitter taste was found to be suppressed by sweeteners such as sucrose (Bartoshuk, 1975). The masking of unpleasant taste by pleasant (sweet) stimuli is greatly sought after in pharmaceuticals. For example, cyclodextrins were described to have the ability of masking the bitterness of drugs like propantheline

bromide (Funasaki et al., 1996) or oxyphenonium bromide (Funasaki et al., 1999), and this effect was explained by the change in surface properties of the solution when the carbohydrate and the drug were mixed in water.

One of the approaches found most suitable to explain the sensorial properties of sweet, bitter, and sweet-bitter substances proves to be the physico-chemical approach especially as concerns hydration and surface properties (DeSimone and Heck, 1980; Funasaki et al., 1996; Funasaki et al., 1999; Mathlouthi and Hutteau, 1999). Thus, solution properties of sweet and bitter molecules were found informative on their type of hydration (hydrophobic or hydrophilic) and on the extent of the hydration layer (Hutteau et al., 2003). Physico-chemical properties (intrinsic viscosity, apparent specific volume, and surface tension) and NMR relaxation rates of the aqueous solutions of sucrose, caffeine, and sucrose-caffeine mixtures were used in the interpretation of the taste modalities of these molecules and to explain the inhibition of caffeine bitterness by sucrose (Aroulmoji et al., 2001). Caffeine molecules were found to form an adsorption layer whereas sucrose induces a desorption layer at the air/water interface. The adsorption of caffeine gradually increases with concentration and is delayed when sucrose is added in the caffeine solution (Aroulmoji et al., 2004).

As a general rule, sweeteners are rather hydrophilic and bitter molecules have a predominantly hydrophobic character. Because of the close relationships of sweet and bitter tastes (Shallenberger and Acree, 1971) and the already demonstrated (Mathlouthi et al., 1973) role of water in sweet taste chemo-reception, it was decided to record the FT-IR spectra of caffeine, sucrose, and their mixtures in water and to analyze these spectra with the aim of interpreting the taste modalities of these molecules and the inhibition of caffeine bitterness by sucrose on a structural basis.

Materials and Methods

Caffeine was obtained from Sigma Aldrich France (Saint Quentin Fallavier) as a reagent grade chemical (purity >99%). It was recrystallized twice in absolute ethanol to reach a higher purity. Commercial sucrose was also recrystallized in a pilot crystallizer in the laboratory to reach a surface tension above 73 mN/m, which is the evidence of the absence of traces of impurities, especially the surface active ones. Doubly distilled deionized water (HPLC grade) was used to prepare the aqueous solutions.

Concentrations of caffeine in water were varied from 0.01 to 0.1 mol/l. Sucrose concentration in aqueous solution ranged from 0 to 30% at 25°C. The effect of increasing sucrose concentration on a fixed amount of caffeine (0.04 or 0.08 mol/l) in the ternary mixture was studied using ATR-FT-IR spectra.

A Nicolet Impact 410 spectrometer was used with a Thunderdome ATR accessory (Spectra Tech). Two hundred scans were recorded and averaged

with a spectral resolution of 2 cm^{-1} . No baseline corrections or smoothing was applied to data.

Two regions of the spectra were analyzed: the carbonyl ($\text{C}=\text{O}$) stretching region (1630 to 1710 cm^{-1}) and the OH stretching region (2800 to 3800 cm^{-1}). Data were normalized in the carbonyl stretching region by calculating the ratio of the peak absorbance (peak height referenced to two-point baseline). Data processing was performed using OMNIC software. The deconvolution of the broad band assigned to OH stretching in water (2800 to 3800 cm^{-1}) was made by fitting the experimental band to four calculated Gaussian components using LC software from Bomem Grams. Interpretation of the four calculated components in terms of H-bonded water clusters was based on the analysis of Raman spectra of pure water by Luu et al. (1982) and Starzak and Mathlouthi (2003).

Results and Discussion

The caffeine FT-IR spectrum in the carbonyl stretching region (Figure 45.1) contains two major absorption bands: band 1 with maximum intensity at a frequency around 1700 cm^{-1} is assigned to the isolated carbonyl group and band 2 between 1641 and 1647 cm^{-1} is attributed to the conjugated $\text{C}=\text{O}$ group vibration (Falk et al., 1990). Variation of the intensity ratio for these two bands (I_{1646}/I_{1770}) as a function of caffeine concentration is reported in Figure 45.2. The ratio of intensities is constant up to a caffeine concentration

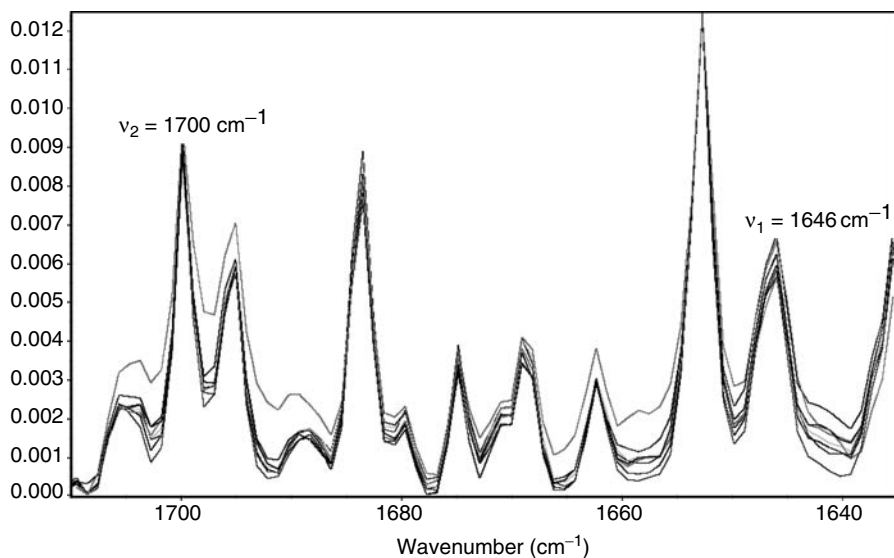


FIGURE 45.1

FT-IR spectra of caffeine with increasing concentrations in water in the $\text{C}=\text{O}$ stretching region.

of 0.05 mol/l. After this concentration a gradual increase is observed which is attributed to self-association of caffeine molecules in water and a probable stacking of caffeine dimers (Falk et al., 1998). The intensity of IR absorption of isolated carbonyls at 1700 cm^{-1} remains constant, while the intensity of the band assigned to conjugated carbonyls (1646 cm^{-1}) increases as a result of rearrangement of caffeine molecules at high concentration (above 0.05 mol/l).

The effect of adding 5 to 25% sucrose on the ratio of intensities (I_{1646}/I_{1770}) of caffeine carbonyls is reported in Figure 45.3. A slight increase in intensity of IR bands assigned to conjugated carbonyls corresponding to caffeine molecules stacking is observed when 5 or 10% (w/w) sucrose is added to 0.04 or 0.08 mol/l of caffeine in water. As sucrose concentration is increased, the intensity ratio decreases which means that caffeine molecules are no more stacked with 15% sucrose in 0.04 mol/l of aqueous caffeine or more 20% sucrose for 0.08 mol/l of caffeine (see Figure 45.3). Molecular interactions between water sucrose and caffeine are very likely at the origin of caffeine stacking removal. As water molecules may be inserted between associated caffeine monomers as is the case for caffeine–cation adducts (Nasifi et al., 2004), it seems important to study the effect of each of the sapid solutes and their mixtures on water structure.

The region of the FT-IR spectrum of aqueous solutions allowing such an investigation is that of water OH stretching (2800 to 3800 cm^{-1}). Figure 45.4 shows the FT-IR spectrum of water deconvoluted into four Gaussian components. The calculated frequencies and proportions (% total area) of the four species of water species are reported in Table 45.1. These components are respectively assigned to quasi-crystalline clusters (1), solid-like

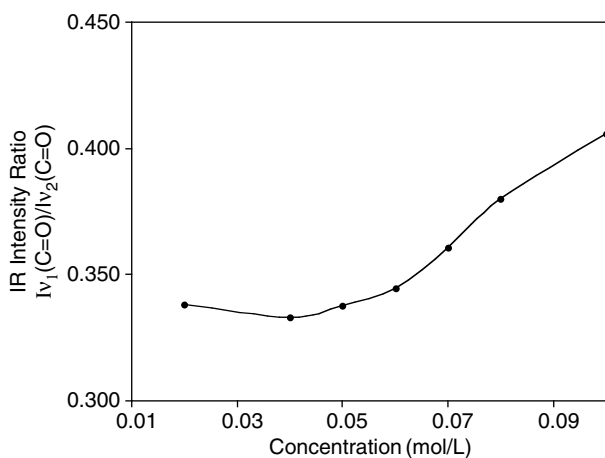
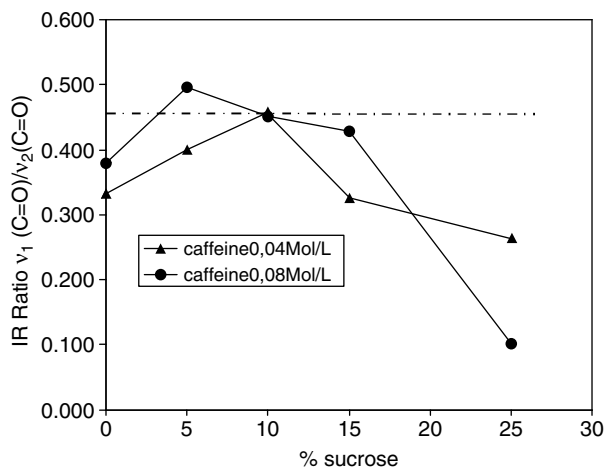


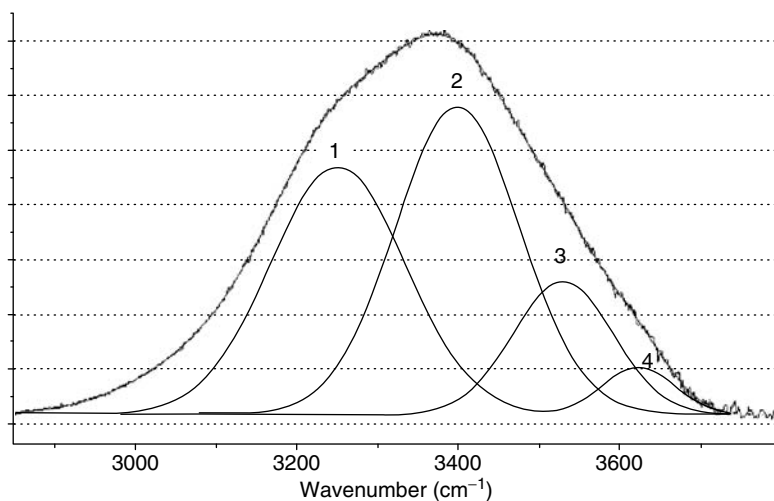
FIGURE 45.2

Variation of the ratio of intensities of the two carbonyl IR absorptions $I(1641\text{ cm}^{-1})/I(1700\text{ cm}^{-1})$ in function of caffeine concentration.

**FIGURE 45.3**

Ratio of intensities of the two carbonyl IR absorptions $I(1641\text{ cm}^{-1})/I(1700\text{ cm}^{-1})$ for 0.04 and 0.08 M caffeine as a function of added sucrose concentration.

amorphous (2), liquid-like amorphous (3), and nonassociated water molecules (4) in agreement with the analysis of pure water Raman spectra of water (Luu et al., 1982). The binding of water is less and less rigid when we go from component 1 to component 4. This model of water structure is taken as a basis of comparison to follow the effect of sapid solutes, caffeine, and sucrose on the molecular association of the aqueous solvent.

**FIGURE 45.4**

Deconvolution of the FT-IR spectrum of water into four Gaussian components.

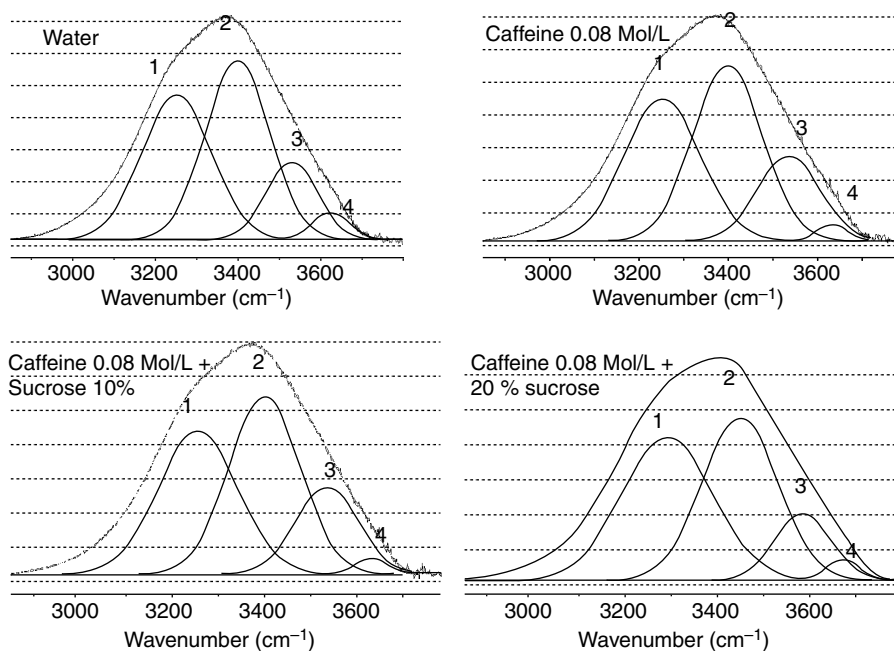
TABLE 45.1
Calculated Components of the IR Absorption Band for Water in the Region 2800 to 3800 cm⁻¹

Component	Frequency ν (cm ⁻¹)	Intensity (% area)	Assignment (after Luu et al., 1982)
1	3250	37.83	Quasi-crystalline water
2	3400	43.43	Solid-like amorphous cluster
3	3530	14.98	Liquid-like amorphous cluster
4	3624	3.78	Unassociated water

Comparison of frequencies and integrated intensities (band area) of 0.04 mol/l of caffeine, 10% sucrose, and the mixture (0.04 mol/l caffeine + 10% sucrose) with that of pure water is given in Table 45.2. The shifts in frequency provoked by the presence of sucrose in water fall within experimental accuracy, i.e., water structure is not perturbed by 10% sucrose. The presence of 0.04 mol caffeine per liter of water yields an increase of the frequencies of vibration of the less organized water species. This in agreement with Nemethy and Scheraga (1962), who characterized the apolar groups influence on liquid water H-bonding by an increase in the energy of binding of the less organized species, whereas tetrahedric water clusters are stabilized (lower energy). When 10% of sucrose is mixed with 0.04 mol/l caffeine in water, there is a preponderance of caffeine hydrophobic effect. This is comparable with what was previously observed in the region of carbonyl stretching. A concentration of 10% sucrose does not prevent caffeine stacking (see Figure 45.3). Caffeine molecules behave in 10% sucrose aqueous solution as in pure water. Water molecules are mobile enough to be inserted between self-associated caffeine molecules. This is the reason why adding 10% sucrose in 0.04 mol/l of caffeine aqueous solution does not affect the stacking of caffeine.

TABLE 45.2
Shifts in Frequencies ($\Delta\nu$ cm⁻¹) and Change in Intensity (Δ area%) of Water Components in Presence of 10% Sucrose, 0.04 mol/l Caffeine, and the Mixture (10% sucrose + 0.04 mol/l Caffeine)

Component	10% Sucrose		0.04 mol/l Caffeine		(Sucrose + 0.04 M Caffeine)	
	$\Delta\nu$ cm ⁻¹	Δ area%	$\Delta\nu$ cm ⁻¹	Δ area%	$\Delta\nu$ cm ⁻¹	Δ area%
1	+4.0	-0.08	-0.1	+1.3	+5.0	+0.8
2	+1.8	0.0	+2.5	-0.3	+3.6	+2.1
3	-3.4	-0.3	+7.4	+0.1	+10.3	+2.1
4	-4.5	+0.8	+6.0	-1.1	+10.7	-2.2

**FIGURE 45.5**

Deconvolution into four components of water IR band in the region 2800 to 3800 cm^{-1} of caffeine and caffeine–sucrose mixtures.

The deconvoluted IR bands for water, 20% sucrose, 0.08 M caffeine, and the mixture (0.08 M caffeine + 20% sucrose) in water are shown in Figure 45.5. The values of frequency shifts ($\Delta\nu \text{ cm}^{-1}$) and intensity changes ($\Delta\text{area}\%$) of water components in the presence of solutes are compared with that of pure water in Table 45.3. From these results, it appears that shifts in

TABLE 45.3

Shifts in Frequencies ($\Delta\nu \text{ cm}^{-1}$) and Change in Intensity ($\Delta\text{area}\%$) of Water Components in Presence of 20% Sucrose, 0.08 mol/l Caffeine, and the Mixture (20% Sucrose + 0.08 mol/l Caffeine)

Component	20% Sucrose		0.08 mol/l Caffeine		(Sucrose + 0.08 M Caffeine)	
	$\Delta\nu \text{ cm}^{-1}$	$\Delta\text{area}\%$	$\Delta\nu \text{ cm}^{-1}$	$\Delta\text{area}\%$	$\Delta\nu \text{ cm}^{-1}$	$\Delta\text{area}\%$
1	+7.2	+4.6	+1.6	−0.2	+10.6	+4.8
2	+8.3	−3.4	−0.8	−1.1	+9.4	−3.4
3	+1.8	−1.4	+6.4	+3.4	+2.3	−1.4
4	−0.7	+0.1	+9.5	−2.1	+1.0	+0.1

frequencies that account for the effect of solute on water structure are comparable for sucrose (20%) and the mixture (0.08 M caffeine + 20% sucrose). Whereas no noticeable change in water H-bonding was observed in presence of 10% sucrose, an increase in the energy (frequency) of the binding of the most organized species (components 1 and 2) is obtained with 20% sucrose as a result of the well-known structure-maker effect of this carbohydrate while the less organized species show negligible decrease in frequency. This effect remains preponderant in the presence of caffeine, which is very likely at the origin of caffeine dimers unstacking provoked by increased proportions of sucrose (above 15%) (see Figure 45.3).

Conclusion

FT-IR spectra of the aqueous solutions of caffeine, sucrose, and their mixtures were analyzed in two regions of the spectra: the carbonyl region (1630 to 1720 cm^{-1}) and the OH stretching region (2800 to 3800 cm^{-1}). In the C=O vibration region, the ratio intensities (I_{1646}/I_{1700}) of the IR absorptions, respectively, assigned to conjugated and free carbonyls allowed observation of a change in caffeine structure around a concentration of 0.05 mol/l, very likely because of the stacking of caffeine dimers. The effect of sucrose on caffeine association in ternary sucrose–caffeine–water solutions shows a decrease in intensities ratio (I_{1646}/I_{1700}) above 15 to 20% sucrose concentration in presence of 0.04 and 0.08 mol/l of caffeine. This result is related to the possible unstacking of caffeine molecules and attributed to the specific influence of each of the two solutes on water structure.

In the OH stretching region, the deconvolution of the experimental IR absorption band of water into four components attributed to four species of water hydrogen-bonded clusters permitted a mean of comparison of the effects of sucrose and caffeine on water structure. Sucrose (10%) did not perturb the hydrogen bonding of water clusters. Caffeine manifested a hydrophobic effect as expected, which resulted in shifts of frequencies of the less tightly bound water clusters towards higher frequencies, i.e., higher energies. The effect of sucrose (10%) on 0.04 or 0.08 mol/l of caffeine did not change either the structuring of water under the hydrophobic influence of caffeine or the stacking of caffeine dimers revealed by analysis of C=O stretching intensity ratio variation. Adding 20% sucrose to 0.08 M caffeine solution induces destacking of caffeine dimers and shows a similarity of water structure between pure sucrose solution and the mixture (20% sucrose + 0.08 mol/l caffeine).

Analysis of the effect of sweet and bitter solutes on water components after deconvolution of the IR absorption bands may be used in the interpretation of their taste modalities, especially as concerns the inhibition of caffeine bitterness by sucrose.

References

- Aroulmoji, V., Hutteau, F., Mathlouthi, M., and Rutledge, D.N. Hydration properties and the role of water in taste modalities of sucrose, caffeine, and sucrose-caffeine mixtures, *J. Agric. Food Chem.*, 49, 4039, 2001.
- Aroulmoji, V., Aguié-Beguín, V., Mathlouthi, M., and Douillard, R. Effect of sucrose on the properties of caffeine adsorption layers at the air solution interface, *J. Colloid Interface Sci.*, 276, 269, 2004.
- Bartoshuk, L.M. Taste mixtures: is mixture suppression related to compression?, *Physiol. Behav.*, 14, 643, 1975.
- DeSimone, J.A. and Heck, G.L. Surface active taste modifiers: a comparison of the physical and psychophysical properties of gymnemic acid and sodium lauryl sulfate, *Chem. Senses*, 5, 317, 1980.
- Falk, M., Gil, M., and Iza, N. Self-association of caffeine in aqueous solution: an FT-IR study, *Can. J. Chem.*, 68, 1293, 1990.
- Falk, M., Chew, W., Walter, J.A., Kwiatkowski, W., Barclay, K.D., and Klassen, G.A. Molecular modelling and NMR studies of caffeine dimer, *Can. J. Chem.*, 76, 48, 1998.
- Funasaki, N., Uemura, Y., Hada, S., and Neya, S. Reduction of the bitter taste intensity of propantheline bromide by cyclodextrins as predicted by surface tension measurements, *J. Phys. Chem.*, 100, 16298, 1996.
- Funasaki, N., Kawaguchi, R., Ishikawa, S., Hada, S., Neya, S., and Katsu, T. Quantitative estimation of the bitter taste intensity oxyphenonium bromide reduced by cyclodextrins from electromotive measurements, *Anal. Chem.*, 71, 1733, 1999.
- Hutteau, F., Mathlouthi, M., and Birch, G.G. Rôle de l'eau dans la perception des saveurs, *L'eau dans les aliments*, M. LeMeste, D. Lorient and D. Simatos, eds., Lavoisier Tech & Doc, Paris, pp. 285–311, 2003.
- Kinnamon, S.C. Taste transduction: a diversity of mechanisms, *Trends Neurosci.*, 11, 491, 1988.
- Luu, C., Luu, D.V., Rull, F., and Sopron, F. Raman effect study of structural perturbation of liquid water by foreign substances, *J. Mol. Struct.*, 81, 1, 1982.
- Mathlouthi, M. and Hutteau, F. Sweet-bitter interactions and the solution properties of chlorinated sugars, *Food Chem.*, 64, 77, 1999.
- Mathlouthi, M., Bressan, C., Portmann, M.O., and Serghat, S. Role of water structure in sweet taste chemoreception, *Sweet Taste Chemoreception*, M. Mathlouthi, J.A. Kanter and G.G. Birch, eds., Elsevier Applied Science, London, pp. 141–171, 1993.
- Mathlouthi, M. Maciejewski, C., Serghat, S., Hooft, R.W., Kanter, J.A., and Kroon, J. Structural studies on sweet taste inhibitors: methyl-4,6-dichloro-4,6-dideoxy-galactopyranoside, *J. Mol. Struct.*, 291, 173, 1993.
- Nasifi, S., Monajemi, M., and Ebrahimi, S. The effect of mono- and divalent cations on the solution structure of caffeine and theophylline, *J. Mol. Struct.*, 705, 35, 2004.
- Nemethy, G. and Scheraga, H.A. Structure of water and hydrophobic bonding in proteins. I. A model for the thermodynamic properties of water, *J. Phys. Chem.*, 36, 3382, 1962.

- Shallenberger, R.S. and Acree, T.E. Chemical structure of compounds and their sweet and bitter taste, *Handbook of Sensory Physiology. IV: Chemical Senses, 2: Taste*, L.M. Beidler, ed., Springer, Berlin, pp. 221–277, 1971.
- Starzak, M. and Mathlouthi, M. Cluster composition of liquid water derived from laser-Raman spectra and molecular simulation data, *Food Chem.*, 82, 3, 2003.

46

Solute Diffusion in Biopolymers as a Function of Water Activity Using a Modified Free Volume Theory

Mustafa E. Yildiz and Jozef L. Kokini

CONTENTS

Introduction	593
Free Volume Theory	594
Modification to Account for the Effect of Water Activity	595
Materials and Methods	597
Mechanical Spectrometry Experiments	597
Stress Relaxation Experiments and Time–Temperature Superposition Principle	597
Diffusion Experiments	598
Results and Discussion	598
References	600

Introduction

Many food processes, which affect food quality and stability, are diffusion controlled (Karel et al., 1994; Roos, 1995). Transport of key penetrants such as water into or out of a polymeric food matrix can play a critical role in food quality and stability. Water is one of the major components and a very good plasticizer in foods. The quality and stability of dehydrated products, multi-domain foods, and the performance of biofilms and encapsulation and controlled release technologies are affected by moisture transport. The rates of molecular mobility and diffusion-limited reactions strongly depend on the factors surrounding the food. Temperature and water activity (a_w) play significant roles in penetrant diffusion. The physical state of the carrier matrix, chemistry, size, and structure of diffusing molecule and specific

interactions between the matrix and penetrant also affect diffusivity. Therefore, it is necessary to quantitatively predict the effects of temperature, water activity, physical properties, and phase/state transitions of biopolymers and physical/chemical interactions on the diffusion of solutes in biological polymers.

This research is focused on developing quantitative predictive strategies to estimate diffusion coefficients based on the changes in free volume in the food biopolymers. The free volume theory is modified to utilize the physical properties of moisturized soy flour (Vrentas and Duda, 1978; Vrentas and Vrentas, 1994). The modification is based on treating the moisturized soy flour as a single system and determining the WLF constants as a function of a_w (and moisture content). This modification is necessary because of the difficulty of determining the WLF constants of biopolymers at zero moisture content. Since the WLF constants are related to free volume parameters, we can quantify the free volume as a function of a_w in soy flour/moisture system. The WLF constants of moisturized soy flour are obtained using the stress relaxation experiments and the time-temperature principle. Proposed model captures the effect of T_g on solute diffusion and shown to be suitable for biopolymers.

Free Volume Theory

From the free volume theory (Vrentas and Vrentas, 1994), the following expression for concentration and temperature dependence of a solute diffusion coefficient in a concentrated polymer solution has been proposed:

$$D_1 = D_0 \exp\left(\frac{-E}{RT}\right) \exp\left(\frac{-\gamma(\omega_1 \hat{V}_1^* + \omega_2 \xi \hat{V}_2^*)}{\hat{V}_{FH}}\right) \quad (46.1)$$

where D_0 is a constant pre-exponential factor, E is the activation energy per mole for a molecule to overcome attractive forces holding it to its neighbors, R is the ideal gas constant, T is the absolute temperature, γ is an overlap factor introduced to correct for overlap free volume, ω_i is the mass fraction of component i (for solvent $i = 1$ and polymer $i = 2$), \hat{V}_i^* is the specific critical hole free volume of component i required for a diffusive jump, and ξ is the ratio of polymer and solvent jumping units (Zielinski and Duda, 1992):

$$\xi = \frac{M_{j1} \hat{V}_1^*}{M_{j2} \hat{V}_2^*} \quad (46.2)$$

where M_{ji} is the molecular weight of a jumping unit of component i . In Equation 46.1, \hat{V}_{FH} is the specific hole free volume of the polymer/solvent mixture, given by:

$$\hat{V}_{FH} = \omega_1 K_{11}(K_{21} - T_{g1} + T) + \omega_2 K_{12}(K_{22} - T_{g2} + T) \quad (46.3)$$

where K_{1i} and K_{2i} are free volume parameters of component i , and T_{gi} is the glass transition temperature of component i . Then Equation 46.1 becomes

$$D_1 = D_0 \exp\left(\frac{-E}{RT}\right) \exp\left[-\frac{\gamma(\omega_1 \hat{V}_1^* + \omega_2 \xi \hat{V}_2^*)}{\omega_1 K_{11}(K_{21} + T - T_{g1}) + \omega_2 K_{12}(K_{22} + T - T_{g2})}\right] \quad (46.4)$$

In the limit of low penetrant concentration, it reduces to the following form (Vrentas and Duda, 1978):

$$D_1 = D_{01} \exp\left[-\frac{\gamma \xi \hat{V}_2^*}{K_{12}(K_{22} - T_{g2} + T)}\right] \quad (46.5)$$

where $D_{01} = D_0 \exp(-E/RT)$. Free volume parameters are related to the WLF constants, C_1 and C_2 for the polymer through the following relationships:

$$K_{2m} = C_{2m} \quad (46.6)$$

$$\gamma \frac{\hat{V}_2^*}{K_{1m}} = 2.303 C_{1m} C_{2m} \quad (46.7)$$

Modification to Account for the Effect of Water Activity

In the free volume theory (Williams et al., 1955), a binary system is characterized using the properties of pure components. In the present work a simple modification is introduced. It is based on the determination of concentration dependence of hole free volume using properties of the mixed system, rather than individual components. This modification is used to account for the effect of a_w on the free volume in the moisturized soy flour matrix.

Firstly the effect of a_w on T_g of a food polymer is considered. To establish moisture content and a_w relationship, the sorption isotherm for water/soy flour system is developed. Information of this kind is readily available in the literature for various systems (Labuza and Hyman, 1998). The Gordon–Taylor equation (Gordon and Taylor, 1952) is used to predict the effect of a_w (using moisture content vs. a_w relationship obtained from MSI) on T_g . The Gordon–Taylor equation has been used to predict the T_g of several binary mixtures (Roos, 1995; Morales-Diaz and Kokini, 1998). In general for most food polymers with a distribution of hydrophilic groups an increase in a_w results in a decrease in T_g (Slade and Levine, 1995). The T_g predicted with the Gordon–Taylor equation is used as a first part of our modification.

The Gordon–Taylor equation is written as:

$$T_{gm} = \frac{\omega_1 T_{g1} + k \omega_2 T_{g2}}{\omega_1 + k \omega_2} \quad (46.8)$$

where T_{gm} is the glass transition temperature of a polymer–water mixture, T_{gi} is the T_g value of component i , either water or polymer, respectively, ω_i is the weight fraction of component i , and k is a constant.

Additionally, it is known that the values of the WLF constants are sensitive to plasticizer content. Therefore, further modification is needed to introduce the relationship between the WLF constants and a_w into free volume theory, in order to be able to account for the effect of a_w on diffusion coefficients. We previously determined the WLF constants for soy flour at different water activities (Yildiz and Kokini, 2001). Then we developed relationships between the WLF constants and a_w dependent $T_g (= T_{gm})$, which could be used to determine C_{1m} and C_{2m} as a function of T_{gm} at a given moisture content and a_w .

$$C_{2m} = C_2 + T_g - T_{gm} \quad (46.9)$$

$$C_{1m} = \frac{C_1 C_2}{C_2 + T_g - T_{gm}} \quad (46.10)$$

These relationships allowed us to approximate the properties and behavior of soy flour at different water activities. Therefore, new parameters, C_{1m} and C_{2m} were calculated for a new $T_g (> T_{gm})$ using C_1 and C_2 . Thus, the following general equations were proposed to determine C_{1m} and C_{2m} as a function of T_{gm} for soy flour at different moisture contents:

$$C_{2m} = 430 - T_{gm} \quad (46.11)$$

$$C_{1m} = \frac{2761}{430 - T_{gm}} \quad (46.12)$$

To verify the proposed relationships in Equation 46.11 and Equation 46.12, the shift factors for soy flour samples were predicted using these equations and compared with the experimental data. Predicted values were close to the experimental ones for all water activities, suggesting that the proposed relationships represent a useful tool to approximate the molecular behavior of soy flour at the water activity value of interest (Yildiz and Kokini, 2001).

These modifications combined with free volume parameters (in relation to the WLF constants) resulted in the following equation:

$$\ln D_1 = \ln D_{01} - (2.303 C_{1m} C_{2m}) \left[\frac{1}{(C_{2m} + \lambda(T - T_{gm}))} \right] \quad (46.13)$$

where λ is equal to 1 above T_g , and below T_g it accounts for the difficulty in volumetric contractions of polymer (Vrentas and Duda, 1978). C_{1m} , C_{2m} and T_{gm} are physical properties dependent on a_w as described above.

Materials and Methods

The food polymer system of biological origin used as the main matrix in this study is soy flour (S9633 lot# 103H0820 Sigma Chem.). The protein, moisture, and fat contents of the flour are 52% (85 + % dispersible), 13%, and 1%, respectively.

Soy flour is brought to approximately 40% (w/w) moisture content with distilled water. The dough obtained is kneaded, rolled flat, and then pressed between glass plates to give it the shape of a film. It is then left overnight in a refrigerator at 4 to 5°C. The dough that becomes easily workable is then cut into small disks with a cork borer for diffusion experiments.

Mechanical Spectrometry Experiments

An advanced rheometric expansion system (ARES) is used to determine T_g of samples. Strain sweep experiments from 0.01 to 1% strain are conducted to ensure that experiments are carried out in the linear viscoelastic region. All experiments are done at a frequency of 1Hz and a strain level of 0.05%, which is in the linear region. Temperature sweeps are conducted at a heating rate of 5°C/min over a temperature range which covers the glassy and rubbery regions of the soy flour samples at different water activities. The temperature at which the loss modulus (G'') was at a maximum is used to estimate the T_g .

Stress Relaxation Experiments and Time–Temperature Superposition Principle

The transient step–strain mode of the torsion rectangular geometry of the ARES is used to obtain the stress–relaxation profile of soy flour. The temperature ranges were selected to cover regions both above and below T_g . Samples are brought to the initial experimental temperature and the ARES was programmed to hold at that temperature for 5 min to equilibrate. Relaxation modulus $G(t)$ vs. time curves were obtained for each starting temperature. The construction of a $G(t)$ master curve requires the use of a suitable shift factor (a_T) at each temperature. To shift the stress–relaxation curves and obtain the master curve, the first step is the selection of a reference temperature, T_r . Reference temperature was chosen to be as close as possible to T_g of the sample. The ARES software was used to shift the relaxation modulus data to smoothly superimpose each curve, using an appropriate shift factor (a_T), and create a master curve. The WLF constants

are obtained using the ARES software that fits the a_T vs. temperature data with the WLF equation.

Diffusion Experiments

The kinetics of moisture sorption/desorption in the soy flour films was studied using a gravimetric sorption apparatus. It contains a Cahn 2000 electrobalance to monitor the weight change, flow and temperature controllers and a chart recorder. Moisture sorption/desorption was studied at $32.6 \pm 0.3^\circ\text{C}$ as a function of relative humidity. Desired relative humidity was created by mixing a fully saturated airflow with a completely dry air at a proper mixing ratio at a desired temperature. Airflows were controlled using flowmeters. Relative humidity in the chamber was monitored using three sensors (Humicap Vaisala hygrometer HMI-32 with HMP-31 probes, Vaisala Inc., MA) located at the bottom of the hangdown tube.

To obtain diffusion coefficients, the following equation can be applied to the linear portion of the normalized sorption/desorption data assuming Fickian behavior with constant diffusion coefficient (Crank, 1975):

$$\frac{M_t}{M_f} = 4 \left(\frac{Dt}{\pi L^2} \right)^{1/2} \quad (46.14)$$

Results and Discussion

Water acts as a plasticizer for soy flour (Yildiz and Kokini, 2001). Therefore, increase in water content will plasticize the matrix causing an increase in available free volume for molecular transport. Moisture diffusion as a result will be effected from the water activity of the system. The relationship between moisture content and a_w can be established using the moisture sorption isotherm (MSI) of soy flour. The glass transition temperature is a very important concept in the diffusion process. At the vicinity of the glass-transition temperature the diffusion process increases at a higher rate. Figure 46.1 shows the plasticization effect of moisture on soy flour and Gordon–Taylor prediction of T_g vs. moisture content (Yildiz and Kokini, 2001).

The sorption/desorption experiments were carried out as a function of a_w both above and below the T_g of the matrix. The data obtained from both experiments closely resembled Fickian diffusion. Below $0.55a_w$ (between $0 < M_t$ and $M_f < 0.5$) and above $0.55a_w$ (between $0.08 < M_t$ and $M_f < 0.75$) initial slope of M_t/M_f vs. $t^{1/2}$ curves were linear with respect to abscissa ($R^2 \geq 0.98$). Diffusion coefficients were obtained using the linear portion of the normalized moisture sorption (M_t/M_∞ vs. $t^{1/2}$) curves from Equation 46.14. Moisture diffusion coefficients as a function of moisture content in soy flour are shown in Figure 46.2. There is a change in the rate of decrease of diffusion coefficient as the material undergoes glass transition.

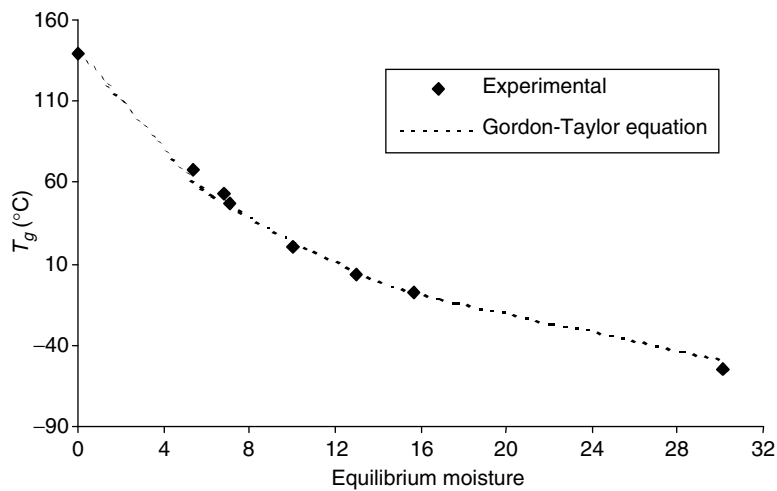


FIGURE 46.1 Experimental T_g values as a function of moisture content predicted well with the Gordon–Taylor equation.

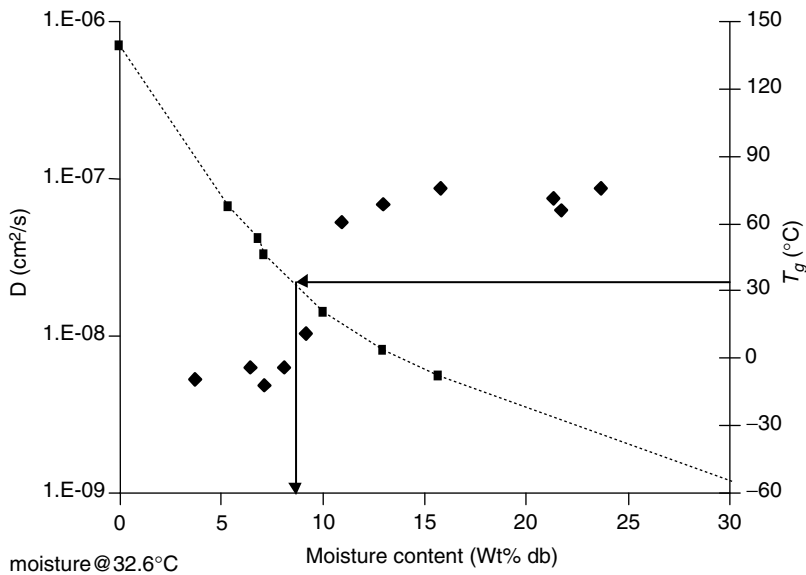
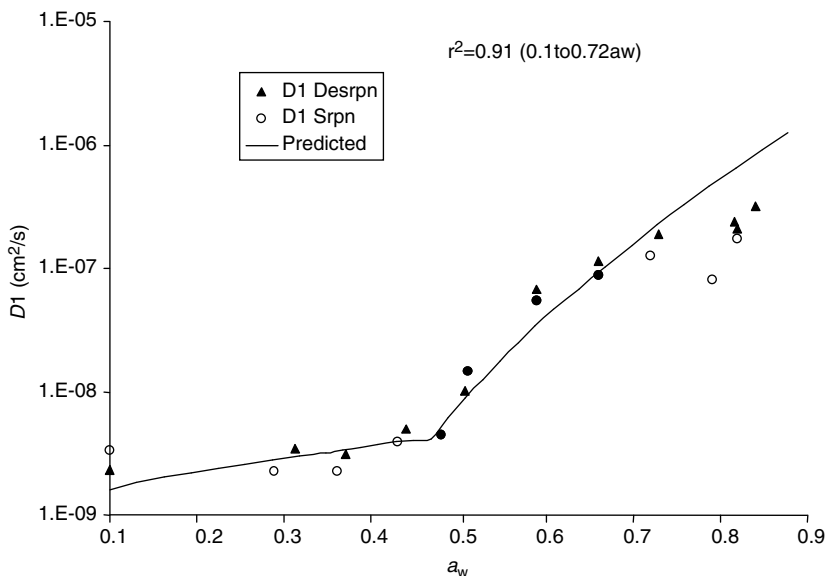


FIGURE 46.2 The effect of glass-transition temperature on moisture diffusivity. Diamonds represent moisture diffusivity data while squares represent T_g as a function of a_w . Once the matrix undergoes glass transition, diffusion rates increases dramatically.

Using the adjustable parameters and the suggested model, we compared the experimental diffusion data both below and above T_g with the predictions of the model. Our results are shown in Figure 46.3. Values estimated with free volume analysis are in good agreement with the experimental data. In the

**FIGURE 46.3**

Comparison between experimental diffusion data from the sorption (circles) and desorption (triangles) and predicted (solid lines) diffusion coefficients for water.

glassy state, diffusion coefficients increase very slowly as the T_g is approached. However, once material undergoes a transition from glassy solid to rubbery liquid, diffusion rates increase dramatically. This indicates that mobility mechanisms above and below T_g are different. Limited molecular mobility below T_g is caused by the limited free volume in the system. Data suggest that free volume below T_g remains more or less constant. Rapid increase above T_g is caused by increased free volume in the matrix upon plasticization by water.

Based on FVT analysis, clearly these results reduce the uncertainty that would surround a new field of research in food-based biological polymers. Clearly FVT is a useful tool that will generate the capability to systematically predict the temperature and water activity dependence of diffusion of small molecules near the glassy state.

References

- Crank, J. *The Mathematics of Diffusion*, 2nd Ed., Clarendon Press, Oxford, 1975.
- Gordon, M. and Taylor, J.S. Ideal copolymers and second order transitions in synthetic rubbers. I. Non-crystalline polymers, *J. Appl. Chem.*, 2, 493, 1952.
- Karel, M., Anglea, S., Buera, M.P., Karmas, R., Levi, G., Roos, Y. et al. *Stability related transitions of amorphous foods*, 246. pp. 249, 1994.

- Labuza, T.P. and Hyman, C.R. Moisture migration and control in multi-domain foods, *Trends Food Sci. Technol.*, 9, 47, 1998.
- Morales-Diaz, A. and Kokini, J.L. Understanding phase transitions and chemical complexing reactions in 7S and 11S soy protein fractions, *Phase State Transitions in Foods*, M.A. Rao and R.W. Hartel, eds., Marcel Dekker Inc., New York, pp. 273, 1998.
- Roos, Y.H. Glass-transition related physicochemical changes in foods, *Food Technol.*, 10, 97, 1995.
- Slade, L.H. and Levine, H. Glass transition and water–food structure interactions, *Adv. Food Nutr. Res.*, 38, 103, 1995.
- Vrentas, J.S. and Duda, J.L. A free volume interpretation of the influence of the glass transition on diffusion in amorphous polymers, *J. Appl. Polym. Sci.*, 22, 2325, 1978.
- Vrentas, J.S. and Vrentas, C.M. Solvent self diffusion in rubbery polymer-solvent systems, *Macromolecules*, 27, 4684, 1994.
- Williams, M.L., Landel, R.F., and Ferry, J.D. Temperature dependence of relaxation mechanisms in amorphous polymers and other glass forming liquids, *J. Am. Chem. Soc.*, 77, 3701, 1955.
- Yildiz, M.E. and Kokini, J.L. Determination of Williams–Landel–Ferry constants for a food polymer system; effect of water activity and moisture content, *J. Rheol.*, 45, 903, 2001.
- Zielinski, J.M. and Duda, J.L. Predicting polymer/solvent diffusion coefficients using free-volume theory, *AIChE J.*, 38, 405, 1992.

Molecular Mobility in Glassy Starch: Influence of Hydration and Sucrose

**Fabienne Poirier, Marie Tanguy, Dominique Champion, and
Gaëlle Roudaut**

CONTENTS

Materials and Methods	604
Materials	604
Samples Preparation	604
Compression of Powders	605
DSC Measurements	605
DMTA Measurements	605
Statistical Significance	605
Results and Discussion	606
Mobility around the Glass Transition	606
Mobility within the Glass	606
Conclusion	610
References	610

Low moisture biopolymer-based systems are commonly encountered in food (e.g., cereal products) or nonfood applications (e.g., packaging films, pharmaceutical excipients). Obviously, understanding the physical basis of their quality or performance over time or as a function of their composition (water or other added solutes) is of primary importance. For several years, a polymer science approach based on physical state, phase transitions, and molecular mobility has been applied to investigate these aspects. Contrary to the data generally found in literature, in recent years several quality or property changes of biopolymer-based materials (Attenburrow et al., 1992; Nicholls et al., 1995; Roudaut et al., 1999b; Grattard et al., 2002;) have been observed while the samples were still in the glassy state. As an example, baked or extruded cereal products that are mostly amorphous as a result of their hydrothermal process exhibit, following moisture pickup, texture

changes (Valles Pamies et al., 2000) below their glass-transition temperature (T_g). Structural relaxation (evolution of the material towards thermodynamic equilibrium) and secondary relaxations of the material (localized motions of the polymer chains) are signs of possible evolutions within the glass.

Whether food or nonfood, the materials are often complex in their formulation, being composed not only of biopolymers but also of smaller molecular weight solutes interacting with their homologs or the other components. The presence of water in biopolymer-based materials is known to have a pronounced influence on their quality and stability (Ablett et al., 1986; Le Meste, 1995). Indeed, changing the water content of a complex material would be expected to cause important changes in the interactions (mainly H-bonds) between the different components, interactions that are, to a great extent, responsible for the properties of the material. Many works have investigated the role of water, sugars, or polyols in glass-transition-related processes (Kalichevsky et al., 1992; Kalichevsky et al., 1993), but many fewer have focused on sub- T_g processes. As an example, mechanical properties of starch–sucrose extrudates were shown to exhibit different water sensitivity depending on the sucrose level (0 or 20%) (Valles Pamies et al., 2000), but the origin of such phenomena has not been clearly identified. Faced with the scarcity of data on vitreous biopolymers, one often has to rely on hypotheses or models developed for synthetic polymers that may not always be applicable to biological materials.

The aim of this study was to better understand the origin of glassy stability and more particularly to determine the role of both hydration and sucrose on residual molecular mobility in low moisture glasses.

Molecular mobility of gelatinized starch was considered through the effect of water and sucrose contents on structural relaxation and viscoelastic behavior.

Materials and Methods

Materials

Pregelatinized waxy maize starch (PregeFlow CH 20: adipic acid-reticulated, acetic anhydride-stabilized and drum drying-gelatinized) was supplied by Roquette Freres (Lestrem, France) and crystalline sucrose by Merck.

Samples Preparation

Starch was added to a sucrose solution in the amount needed for a final dry matter of 5.6% in the prepared solution, and sucrose starch proportions

corresponding to 0, 5, 10, and 20% sucrose (g sucrose/100 g dry matter). This preparation was thoroughly mixed and freeze-dried.

The water content of the samples was then adjusted in air-tight containers via water vapor phase conditioning over P_2O_5 or various concentrations of glycerol–water solutions according to UNIQUAC-LARSEN model (Larsen et al., 1987). An X-ray diffraction analysis performed on the equilibrated samples confirmed the amorphous state of all prepared samples.

Compression of Powders

Faced with a lack of sensitivity of differential scanning calorimetry (DSC) for detecting a clear event assignable to the glass transition in low-density material, the powders were compressed for 5 min at 25°C into disk-shaped tabletted samples. For further DSC analysis, the tabletted samples were crushed into a coarse powder. For dynamical mechanical thermal analysis (DMTA), the disks were cut into parallelepiped shape ($10 \times 7 \times 2$ mm). Prior to their analysis, the samples were returned to the humidity-controlled atmospheres.

DSC Measurements

The measurements were performed on a Perkin Elmer DSC7 calorimeter, calibrated for temperature and energy with azobenzol and indium. For the physical aging study, prior to storage, 30 to 40 mg of compressed samples were placed in DSC pans, and their thermal history erased by a thermal treatment to temperature slightly above their T_g (characterized by the ΔC_p jump). They were subsequently placed at $[T_g - T] = 15^\circ\text{C}$ for 24, 48, 72, and 668 h. After the storage period, the samples were scanned twice between 10 and 170°C at $10^\circ\text{C min}^{-1}$. The amount of enthalpy relaxed during aging was evaluated by the difference between the thermograms of aged and unaged samples.

DMTA Measurements

The measurements of the viscoelastic properties were performed on a viscoanalyzer Metravib (R.D.S., Limonest, France) operating between 5 and 40 Hz, and between -50 and 180°C at a heating rate of 1°C min^{-1} . Samples were coated with silicon lubricant and submitted to a deformation rate of 0.1%.

Statistical Significance

The different measurements were repeated several times per sample, the data are calculated averages of at least three repetitions, and the errors bars represent the confidence intervals.

Results and Discussion

Mobility around the Glass Transition

T_α as expected decreased with increasing water as a result of its plasticizing effect (Slade and Levine, 1991; Lourdin et al., 1997; Gaudin et al., 1999; Matveev et al., 2000; Benczédi, 2001). This primary cooperative relaxation is generally associated to the glass transition and related to large amplitude movements of the main chain.

T_α also decreased with increasing sucrose content. Figure 47.1 shows the T_g for samples with a water content between 4.6 and 6% (wb) and with sucrose content between 20 and 0%, respectively. Although the samples differed by 1.4% of water, the T_g difference (40.5°C) can be mainly attributed to the sucrose content difference (0 to 20% db). Indeed, the T_g difference induced by the addition of 1.6% water to dry starch would be equal to 23°C.

No significant effect of either water or sucrose content was observed on the activation energy of the relaxation ($E_a \sim 480$ kJ/mol) in the concentration range studied. This could be due to the actual merging of sub- T_g processes, dehydration artifacts, and α relaxation features, which caused some difficulties in the accurate determination of the peak maximum at different frequencies.

Mobility within the Glass

As previously mentioned, relaxation peaks were observed on loss modulus–temperature plots of the samples. As they immediately preceded in

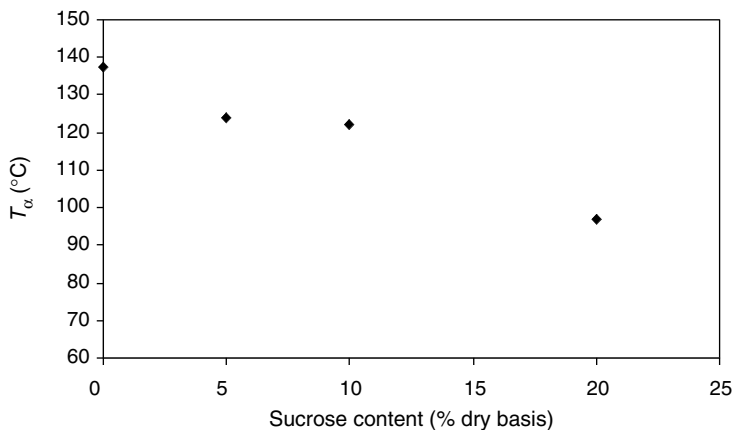


FIGURE 47.1

Evolution of T_α (filled symbols) determined at E'' maximum with sucrose content for gelatinized starch at a water content between 4.6 and 6% (wb).

temperature the α relaxation, and because of their low activation energy (~ 50 kJ/mol), they were attributed to β relaxation processes. This type of motion has been observed for several carbohydrates (Lourdin et al., 1998; Montes et al., 1998; Montes and Cavaille, 1999). β -Relaxation temperature (T_β) measured at the maximum of E'' (T) at 5 Hz for gelatinized starch were higher than the values found in literature (Roudaut et al., 1999a; Einfeldt et al., 2001a; Einfeldt et al., 2001b). Such a difference could be because of the physical and chemical treatments to which the starch used was submitted by the suppliers. Moreover, Figure 47.2a shows that T_β decreased with hydration and increased with sucrose content. Water seemed to “facilitate” β -relaxations; in contrast, sucrose could hinder β -relaxations, shifting them to higher temperatures. This is in agreement with Lourdin et al. (1998), who studied the temperature behavior of amylose–glycerol–water and maltose–glycerol–water and observed T_β both increasing with glycerol content and decreasing with water content. Such results were attributed by these authors to a possible coupling of the β -motions of the “polymer” (maltose or amylose) with the α relaxation of the pure solute (glycerol).

Prior to controlled aging, the samples as they were exhibited an endothermic peak on the first scan only, and a thermal feature assignable to a glass transition was clearly visible on the subsequent heating. The endotherm reappeared on the thermograms of the aged samples (inset Figure 47.3). It was attributed to an enthalpic or structural relaxation

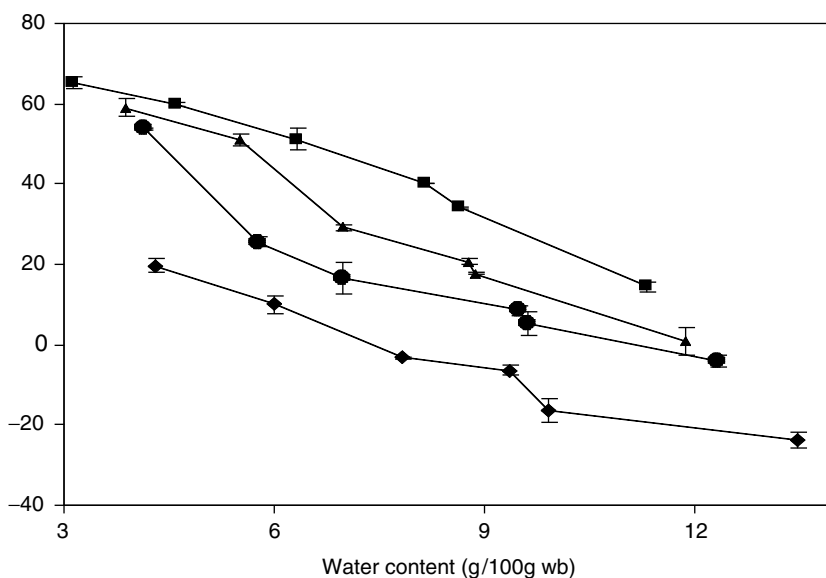
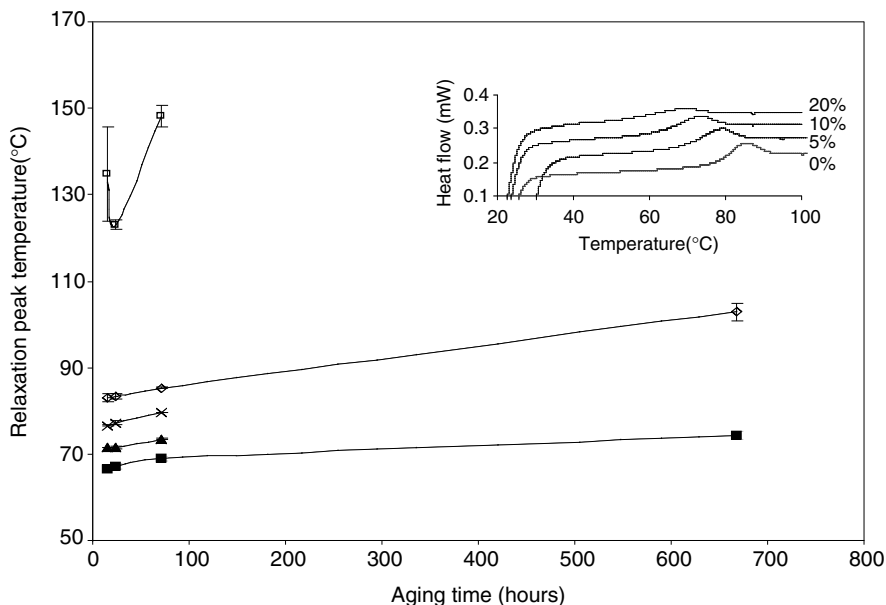


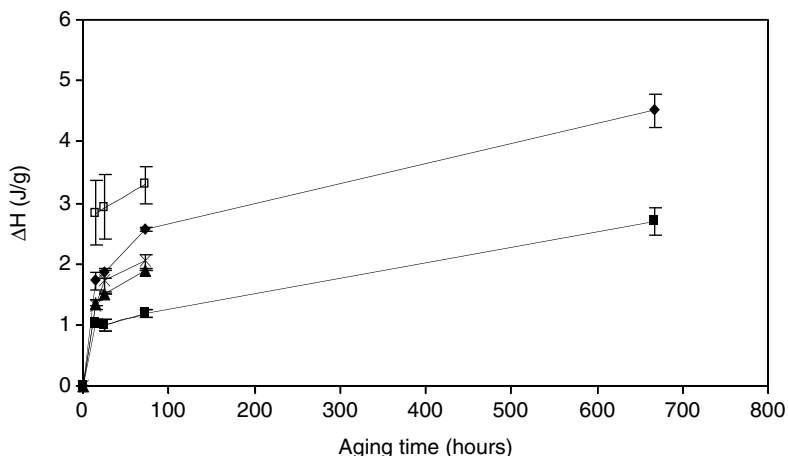
FIGURE 47.2

Evolution of T_β (determined at 5 Hz and at E'' maximum) with water content for gelatinized starch at different sucrose contents: 0% (◆), 5% (●), 10% (▲), and 20% (■) (error bars are confidence intervals).

**FIGURE 47.3**

Effect of aging time on the relaxation peak temperatures for gelatinized starch at different sucrose contents: 0% (◆), 5% (●), 10% (▲), and 20% (■) equilibrated at $a_w = 0.66$ and for comparison for starch 20% sucrose (□) equilibrated over P_2O_5 (error bars are confidence intervals). Inset: corresponding DSC traces for the samples equilibrated at $a_w = 0.66$.

similar to that previously observed in many aged biopolymers (Shogren, 1992; Borde et al., 2002). The structural relaxation is known to be controlled by the aging conditions, i.e., temperature and time (Hodge, 1994; Hutchinson, 1995; Hutchinson et al., 1996; Thiewes and Steeneken, 1997; Shamblin and Zografi, 1998). In the present work, the aging temperature (T_a) was chosen 15°C below T_g . Indeed, when the sample is aged at lower temperature ($T_a < T_g - 15^\circ\text{C}$), the temperature and magnitude of the peak are not significantly affected by the aging time. 0 and 20% sucrose–starch blends, equilibrated at $a_w = 0.66$, were aged at $T_g - T = 15^\circ\text{C}$ for 24, 48, 72, and 668 h. Figure 47.3 shows the evolution of the peak temperature increasing with time, the more markedly for the longest time. As expected from the plasticizing effect of both water and sucrose, the temperature of the endothermic peak decreased with increasing sucrose or water content. It is noticeable that between 24 and 668 h, the increase of the peak temperature was slightly greater in pure starch than in the sample with 20% sucrose. The relaxation enthalpy (Figure 47.4) increased with aging time, but even after 668 h the enthalpy had not leveled off, suggesting that equilibrium had not yet been reached, i.e., there could be remaining extra free volume allowing further structural relaxation (if the relaxation kinetics of enthalpy and specific volume are similar). The enthalpy relaxation decreased, on

**FIGURE 47.4**

Effect of aging time on the relaxation enthalpy for gelatinized starch at different sucrose contents: 0% (◆), 5% (●), 10% (▲), and 20% (■) at $a_w = 0.660$ and for comparison for starch 20% sucrose (□) equilibrated over P_2O_5 (error bars are confidence intervals).

the one hand, at a given humidity level with increasing sucrose content, and on the other hand, with increasing humidity when the sucrose content was kept constant.

Structural relaxation is generally mainly governed by molecular mobility (Struik, 1976), its manifestation through enthalpy recovery (after aging) reflecting the “distance” of the sample from thermodynamic equilibrium. The vitrification kinetics are expected to control this parameter (Moynihan et al., 1976) but the composition of the material and particularly its content in small molecules may also affect the distance to equilibrium. Lourdin et al. (2003) studied the volume of starch–sorbitol–water mixtures in relation to structural relaxation, and showed that adding sorbitol to a starch–water mixture induced negative excess volume of mixing. Thus, if prior to aging, the excess volume is already lower than in pure starch, the extent of structural relaxation could be expected to be lower in the presence of sucrose.

In the free volume theory (Vrentas, 1977), adding small molecules such as sucrose or water is generally associated with an increase of free volume responsible for the plasticizing effect (i.e., decrease of T_g). Nevertheless, in the present study, increasing the small molecules content induced a lower structural relaxation, thus suggesting a higher stability or lower mobility of the glass. The expected enhancing effect of small molecules on residual molecular mobility is thus questionable. Two hypotheses can be suggested: (1) the sucrose and water molecules modified the initial molecular arrangement, i.e., denser packing and thus restricted structural relaxation; (2) the structural relaxation may be not only controlled by the distance

between the aging temperature T_a and T_g , but also by the distance between T_a and T_β . In the present work, in the aging study, whereas the distance ($T_g - T_a$) was kept constant for all samples, the distance to T_β changed with the water and sucrose content. Moreover, since the distance to T_g is kept constant, the distance to T_β can be considered through the distance [$T_g - T_\beta$]. As shown in Figure 47.1, when either water or sucrose content increases, the distance $T_g - T_\beta$ decreases. Above T_β , movements associated with cooperative, or not, localized motions of small units of the molecule, ascribed to rotations of lateral groups or to motions of the main chain segments (Heijboer, 1976; Ferry, 1980) become possible. Thus, the lower structural relaxation observed with increasing sucrose or water content could result from the lower mobility induced by the shorter distance to T_β .

Conclusion

Through this work, the complex role of diluents (water, sugar, or polyols) in the mobility of amorphous biopolymers was highlighted. The results pointing towards a lower structural relaxation in the presence of water or sucrose suggests quite a novel view in glass studies and science, for it contradicts the free volume theory. Future works will include a study of free volume in ternary systems (starch–sucrose–water) to validate or deny the hypotheses suggested in this paper. Moreover, the T_β lowering effect of sucrose also comes as a step forward in the knowledge of the glassy state. Indeed, if the physical state of the pure solute (above or below its T_g) may have an impact on the effect of the solute on T_β , in the scarce previous studies considering the effects of solutes on the secondary relaxation temperatures of biopolymers (Lourdin et al., 1998), the temperature range of the relaxations is always above the solute's T_g whereas in the hydration range considered in the present work, the β relaxations observed occurred mostly below the T_g of sucrose.

Finally, in the future, the fracture properties of the materials studied here will be investigated to evaluate the impact of the formulation combined to the storage conditions on the material mechanical properties at large deformations.

References

- Ablett, S., Attenburrow, G.E., and Lillford, P.J. The significance of water in the baking process, *Chemistry and Physics of Baking: Material, Process and Products*, J.M.V. Blanshard, P.J. Frazier and T. Galliard, eds., Royal Society of Chemistry, London, p. 30, 1986.

- Attenburrow, G.E., Davies, A.P., Goodband, R.M., and Ingham, S.J. The fracture behaviour of starch and gluten in the glassy state, *J. Cereal Sci.*, 16, 1, 1992.
- Benczédi, D. Plasticization and antiplasticization of starch glasses by water, *Water Science For Food, Health, Agriculture and Environment*, Z. Berk, Technomic Publishing Company, Inc, Lancaster, pp. 273, 2001.
- Borde, B., Bizot, H., Vigier, G., and Buleon, A. Calorimetric analysis of the structural relaxation in partially hydrated amorphous polysaccharides. II. Phenomenological study of physical ageing, *Carbohydr. Polym.*, 48, 111, 2002.
- Einfeldt, J., Meißner, D., and Kwasniewski, A. Polymer dynamics of cellulose and other polysaccharides in solid state-secondary dielectric relaxation processes, *Prog. Polym. Sci.*, 26, 1419, 2001a.
- Einfeldt, J., Meißner, D., Kwasniewski, A., and Einfeldt, L. Dielectric spectroscopic analysis of wet and well dried starches in comparison with other polysaccharides, *Polymer*, 42, 7049, 2001b.
- Ferry, J.D. *Viscoelastic Properties of Polymers*, Wiley, New York, 1980.
- Gaudin, S., Lourdin, D., Le Botlan, D., Ilari, J.L., and Colonna, P. Plasticisation and mobility in starch-sorbitol films, *J. Cereal Sci.*, 29, 273, 1999.
- Grattard, N., Salaün, F., Champion, D., Roudaut, G., and Le Meste, M. Influence of physical state and molecular mobility of freeze-dried maltodextrin matrices on the oxidation rate of encapsulated lipids, *J. Food Sci.*, 67, 3002, 2002.
- Heijboer, J. Molecular origin of relaxations in polymers, *Ann. N.Y. Acad. Sci. Part II*, 104, 1976.
- Hodge, I.M. Enthalpy relaxation and recovery in amorphous materials, *J. Non-Crys. Solids*, 169, 211, 1994.
- Hutchinson, J.M. Physical aging of polymers, *Prog. Polym. Sci.*, 20, 703, 1995.
- Hutchinson, J.M., McCarthy, D., Montserrat, S., and Cortés, P. Enthalpy relaxation in a partially cured epoxy resin, *J. Polym. Sci. Part B: Polym. Phys.*, 34, 229, 1996.
- Kalichevsky, M.T., Jaroszkiewicz, E.M., and Blanshard, J.M.V. Glass transition of gluten. 1: gluten and gluten-sugar mixtures, *Int. J. Biol. Macromol.*, 14, 257, 1992.
- Kalichevsky, M.T., Jaroszkiewicz, E.M., and Blanshard, J.M.V. A study of the glass transition of amylopectin-sugar mixtures, *Polymer*, 34, 346, 1993.
- Larsen, B.L., Rasmussen, P., and Fredenslund, A. A modified UNIFAC group-contribution model for prediction of phase equilibria and heats of mixing, *Ind. Eng. Chem. Res.*, 26, 2274, 1987.
- Le Meste, M. Mobility of small molecules in low and intermediate moisture foods, *Food Preservation by Moisture Control Fundamentals and Applications*, G.V. Barbosa Canovas and J. Welti-Chanes, eds., Technomic, Lancaster, pp. 209, 1995.
- Lourdin, D., Coignard, L., Bizot, H., and Colonna, P. Influence of equilibrium relative humidity and plasticizer concentration on the water content and glass transition of starch materials, *Polymer*, 38, 5401, 1997.
- Lourdin, D., Ring, S.G., and Colonna, P. Study of plasticizer-oligomer and plasticizer-polymer interactions by dielectric analysis: maltose-glycerol and amylose-glycerol-water systems, *Carbohydr. Res.*, 306, 551, 1998.
- Lourdin, D., Colonna, P., and Ring, S.G. Volumetric behaviour of maltose-water, maltose-glycerol and starch-sorbitol-water systems mixtures in relation to structural relaxation, *Carbohydr. Res.*, 338, 2883, 2003.
- Matveev, Y.I., Grinberg, V.Y., and Tolstoguzov, V.B. The plasticizing effect of water on proteins, polysaccharides and their mixtures. Glassy state of biopolymers, foods and seeds, *Food Hydrocol.*, 14, 425, 2000.

- Montes, H. and Cavaille, J.Y. Secondary dielectric relaxations in dried amorphous cellulose and dextran, *Polymer*, 40, 2649, 1999.
- Montes, H., Mazeau, K., and Cavaille, J.Y. The mechanical β relaxation in amorphous cellulose, *J. Non-Cryst. Solids*, 235, 416, 1998.
- Moynihan, C.T., Macedo, P.B., Montrose, C.J., Gupta, P.K., Debolt, M.A., Dill, J.F., Dom, B.E., Drake, P.W., Eastal, A.J., Elterman, P.B., Moeller, R.P., Sasabe, H., and Wilder, J.A. Structural relaxation in vitreous materials, *Ann. N.Y. Acad. Sci.*, 279, 15, 1976.
- Nicholls, R.J., Appelqvist, I.A.M., Davies, A.P., Ingman, S.J., and Lillford, P.J. Glass transitions and fracture behaviour of gluten and starches within the glassy state, *J. Cereal Sci.*, 21, 25, 1995.
- Roudaut, G., Maglione, M., and Le Meste, M. Sub-Tg relaxations in cereal-based systems, *Cereal Chem.*, 76, 78, 1999a.
- Roudaut, G., Maglione, M., Van Duschotten, D., and Le Meste, M. Molecular mobility in glassy bread: a multi spectroscopic approach, *Cereal Chem.*, 76, 70, 1999b.
- Shamblin, S.L. and Zografi, G. Enthalpy relaxation in binary amorphous mixtures containing sucrose, *Pharm. Res.*, 15, 1828, 1998.
- Shogren, R.L. Effect of moisture content on the melting and subsequent physical aging of corn starch, *Carbohydr. Polym.*, 19, 83, 1992.
- Slade, L. and Levine, H. A food polymer science approach to structure-property relationships in aqueous food systems: non-equilibrium behavior of carbohydrate-water systems, *Water Relationships in Foods*, H. Levine and L. Slade, eds., Plenum Publisher Company, New York, pp. 29, 1991.
- Struik, L.C.E. Physical aging in amorphous glassy polymers, *Ann. N.Y. Acad. Sci. Part II*, 279, 78, 1976.
- Thiewes, H.J. and Steeneken, P.A.M. The glass transition and the sub-Tg endotherm of amorphous and native potato starch at low moisture content, *Carbohydr. Polym.*, 32, 123, 1997.
- Valles Pamies, B., Roudaut, G., Dacremont, C., Le Meste, M., and Mitchell, J.R. Understanding the texture of low moisture cereal products: mechanical and sensory measurements of crispness, *J. Sci. Food Agric.*, 80, 1679, 2000.
- Vrentas, J.S. Solvent and temperature effects on diffusion in polymer-solvent systems, *J. Appl. Polym. Sci.*, 21, 1715, 1977.

High-Speed Observations of the Nucleation of Ice by Power Ultrasound

Rachel C. Chow, Derek Atkins, Scott Singleton, Robert Mettin,
Bernhard Lindinger, Thomas Kurz, Werner Lauterborn, Malcolm Povey,
and Robert Chivers

CONTENTS

Introduction	613
Ultrasonic Horn Studies	614
Single-Bubble Cavitation Studies	616
Laser-Induced Cavitation Studies	619
Ultrasonic Cold-Stage Studies	621
Conclusions	621
Acknowledgments	622
References	622

Introduction

The crystallization of water to produce ice crystals is important for a wide range of foods ranging from ice cream to frozen foods. The control of the crystallization process is one of the major factors affecting the stability and sensory characteristics of these products. Crystallization can be divided into two main stages: nucleation and growth. Nucleation can be difficult to control as under ambient pressure conditions, nucleation can occur at any temperature between 0 and -41°C . This temperature range is called the supercooling temperature and in this region water exists in a metastable state.

There are several methods that can be used to promote the nucleation of ice (Kennedy, 1998). One promising technique is the application of power ultrasound. In the presence of an acoustic wave, ice crystallization can be

initiated at a higher nucleation temperature than under control conditions. It is also thought that smaller crystals that are evenly distributed throughout a material can be obtained. There is a limited body of literature on the nucleation of ice by power ultrasound. The results from theoretical studies have indicated that the cavitation bubbles produced by the ultrasonic wave are responsible for the nucleation process (Hickling, 1965, 1994). The exact mechanism is still under debate (Hickling, 1965; Hunt and Jackson, 1966; Hickling, 1994) although it is thought that the high pressure emitted from a transient cavitation bubble is responsible. One of the main problems in the experimental validation has been that the processes involved occur on a microscopic level and take place over very short timescales, making them difficult to be observed.

In our studies, we have utilized high-speed optical photography to investigate the nucleation of ice in relation to the cavitation bubbles produced by power ultrasound. A variety of different ultrasonic systems were used. First, a commercial ultrasonic probe was used to study the nucleation and population density of ice crystals produced by a multicavitation system. The nucleation of ice was studied in more detail by examining the dynamics of a single oscillating bubble. The single bubble was levitated in a fixed location by using a standing wave system. The nucleation of ice was also studied using a laser-induced bubble system. The laser-induced bubble underwent a single cycle of growth and collapse. Lastly, an ultrasonic cold stage device was constructed to observe the fragmentation of preexisting ice dendrites and the production of more crystal nuclei. Details of all these studies can be found in Chow-McGarva (2004).

Ultrasonic Horn Studies

The first measurements were performed using a standard commercial 20 kHz ultrasonic horn (450L, Branson Ultrasonics). A quantitative study of the nucleation temperature in both pure water and a 15 wt% sucrose solution showed that the ice was always stimulated at a higher temperature and required less supercooling in the presence of ultrasound (Chow et al., 2003a, 2003b, 2005).

Figure 48.1(a) compares the evolution of the multibubble cloud produced at power output level 7 both above and below the equilibrium freezing point in pure water. These images were obtained by using a high-speed camera (Phantom V, Photsonics Ltd) to film a single 0.1-sec pulse of ultrasound (3700 frames per second and a 61 μ sec shutter time). The probe tip (12.7 mm diameter) can be seen at the top of each image. The dense "clouds" observed at -2.8°C and the presence of the dendritic ice crystals after the end of the ultrasonic pulse strongly suggest that the crystals are nucleated only within

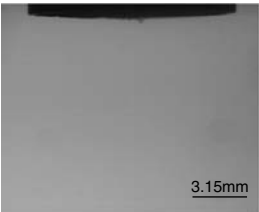
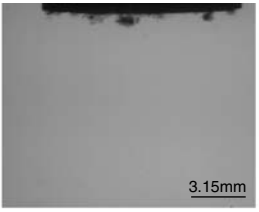





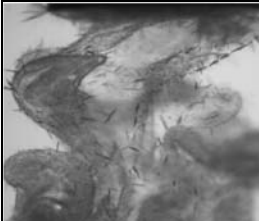
Time (seconds)	Temperature above equilibrium freezing point (1.0°C)	Temperature below equilibrium freezing point (−2.8°C)
$t=0$	First bubbles observed 	First bubbles observed 
$t=0.025$	Bubble cloud and density increase 	Bubble cloud and density increase Denser cloud suggests presence of ice crystals 
$t=0.050$	Bubble cloud and density increase 	Bubble cloud and density increase Denser cloud suggests presence of ice crystals 
$t=0.938$	No bubbles observed 	Ice nuclei only observed 

FIGURE 48.1 (a)

High-speed observations of the ice crystals produced by an ultrasonic horn: (a) comparison of the bubble cloud (1.0°C) and bubble cloud containing ice crystals (−2.8°C) in pure water at ultrasonic power output 7 (0.1-sec pulse); (b) density population of ice crystals observed in a 15 wt% sucrose solution (−3.8°C) at increasing ultrasonic output levels (0.1-sec pulse) ($t = 0.41$ sec).

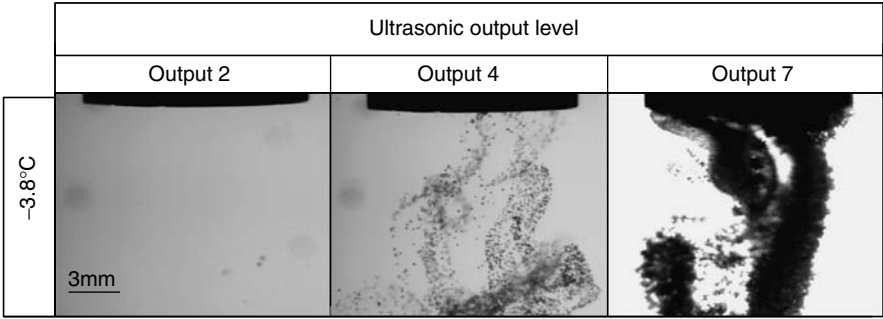


FIGURE 48.1 (b)

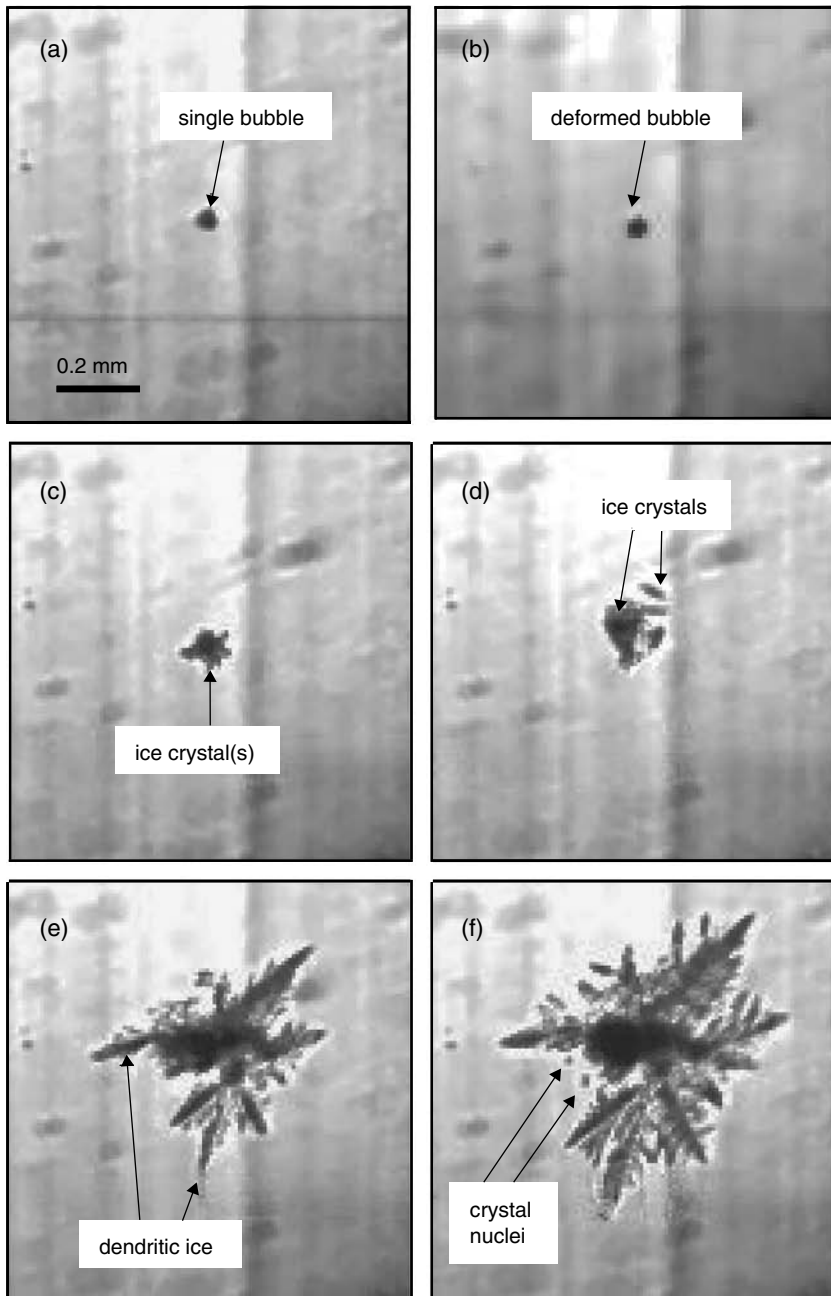
the body of the cloud, thus confirming the requirement of cavitation bubbles for the nucleation process.

Figure 48.1(b) shows the population density of crystals filmed under increasing ultrasonic power output levels. A single 0.1-sec pulse of ultrasound was applied at -3.8°C in a 15 wt% sucrose solution. The growing crystals are shown 0.40 sec later. These results highlight that a commercial ultrasonic horn can be used to control the nucleation and the size distribution of ice crystals produced within the supercooled liquid. Further results by the first author have shown that as the power output level is increased, the level of transient cavitation increases (Chow-McGarva, 2004). This increase in transient cavitation could be correlated to an increase in the primary nucleation events and thus explain the increase in the observed number of crystals.

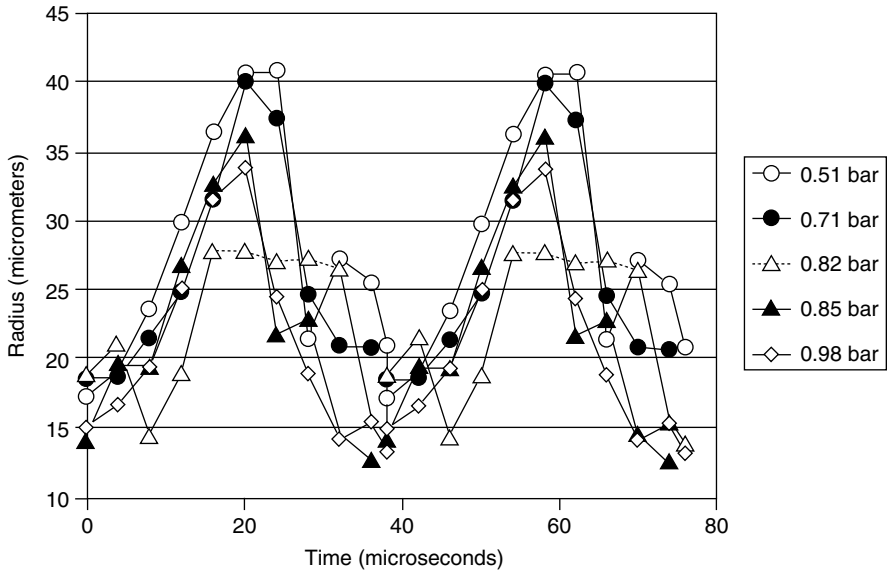
Single-Bubble Cavitation Studies

In order to study the mechanism by which a cavitation bubble may stimulate ice crystallization, a standing wave system was used to levitate a single bubble in a fixed location within pure water. It was found that the nucleation of ice could only be stimulated at a higher nucleation temperature in the presence of the oscillating cavitation bubble (Chow et al., 2004).

Figure 48.2 shows the nucleation of ice which was filmed (HiSIS 2000) using 1120 frames per second ($444\text{ }\mu\text{sec}$ shutter time). Prior to the nucleation event, the bubble appeared deformed, or “dancing,” and sometimes microbubble ($<5\text{ }\mu\text{m}$) ejections were observed within one frame. As the temperature was decreased, the acoustic pressure had to be adjusted to maintain a stable bubble. In this example, the pressure was increased from

**FIGURE 48.2**

High-speed photography of the nucleation of ice from a single acoustic bubble at -3.26°C . Prior to nucleation the pressure was increased from 0.69 to 0.98 bar (27.34 kHz): (a) $t = 0$ sec, (b) $t = 0.023$ sec, (c) $t = 0.050$ sec, (d) $t = 0.100$ sec, (e) $t = 0.235$ sec, (f) $t = 0.300$ sec.

**FIGURE 48.3**

Observed radius time curve for a single oscillating bubble in pure water using the single bubble levitation system at 26.73 kHz (temperatures between -0.5 and 1.1°C).

0.69 to 0.98 bar. When the pressure was increased, several ice crystals were observed in the immediate vicinity of the bubble. Further repetitions of the experiment showed that ice could only be stimulated with a minimum acoustic pressure of 0.60 bar.

The dynamics of the single bubble were investigated. Figure 48.3 shows the bubble radius–time curves measured for a range of different acoustic pressures using a synchronous flash illumination ($\sim 5 \mu\text{sec}$). There were several interesting observations. First, the bubble responded in phase with the ultrasonic field. Second, it exhibited a radius maximum to minimum compression value of $\sim 3:1$. These observations were both characteristics of a “stable” cavitation bubble. In contrast to “transient” cavitation, this type of cavitation bubble does not undergo the rapid collapse, nor emit the pressure shock wave that is thought to be responsible for the sonocrystallization of ice. Other characteristics of a nontransient cavitation bubble, which were noted, included no bubble luminescence and the unstable dancing motion. The mechanism currently accepted relating to the nucleation process is based upon the theoretical calculations of a symmetrically collapsing “transient” cavitation bubble (Hickling, 1965, 1994). These findings suggest that the nucleation of ice by power ultrasound may occur by another mechanism. This could be related to the flow field established by the cavitation bubble (Zhang et al., 2003), or the presence of the asymmetrical bubble.

Laser-Induced Cavitation Studies

Optical laser-induced cavitation is a technique which utilizes a laser to produce a single cycle of the nucleation, growth, and collapse of a single cavitation bubble (Lauterborn et al., 1999). A Q-switched Nd-YAG laser (Lumonics HY750) was focused into supercooled samples of water and dilute sucrose solutions, and an ultra high-speed camera (Imacon 468, Hadland Phototonics) capable of frame rates of up to 100 million frames per second was used to film the nucleation event in the sample after a single laser shot (8 nsec pulse width, up to 20 mJ energy).

Figure 48.4 shows the nucleation of an ice crystal from a single laser-induced bubble in a 15 wt% sucrose solution. Figure 48.4(a) shows the single plasma produced by the laser. Figure 48.4(b) and (c) shows the growth and then collapse of a symmetrical bubble. At 250 μ sec after the appearance of the plasma (Figure 48.4(d)), the bubble seemed to split into some smaller bubbles. The fragments remained in Figure 48.4(e) and (f). After 60,000 μ sec (Figure 48.4(g) and (h)), an ice crystal could be observed. The ice crystal was produced in the immediate vicinity of one bubble fragment.

Further experiments showed that the laser bubble did not always induce ice. The probability of ice nucleation in a 15 wt% sucrose solution supercooled to $-4.74 \pm 1.75^\circ\text{C}$ was 91.7%. The probability of nucleation was increased if the bubble became asymmetric or fragmented.

These results were in contrast to the previous experiments described above, where nucleation was always observed. It is thought that as nucleation is a stochastic process, a single oscillation of a laser-induced bubble may not always lead to the nucleation. The probability of nucleation is increased by the continuously oscillating bubble produced by the standing wave system, and it is increased further by the multicavitation events produced by the ultrasonic horn.

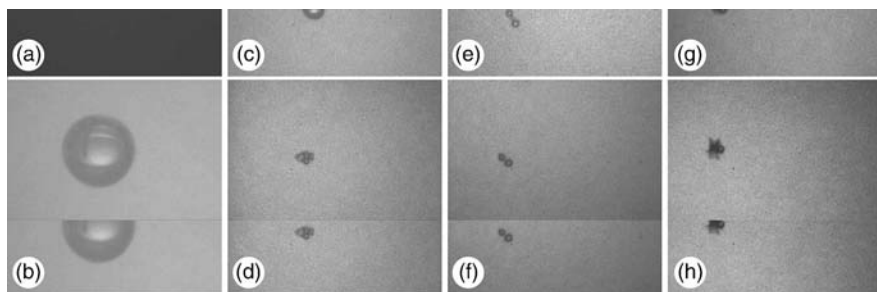


FIGURE 48.4

Ultra high-speed photography of the nucleation of an ice crystal (-4.2°C) from a single laser induced bubble in a 15 wt% sucrose solution (each image width = 3.5 mm): (a) 200–202 μ sec, (b) 230–280 μ sec, (c) 350–352 μ sec, (d) 450–452 μ sec, (e) 3000–3005 μ sec, (f) 20,000–20,800 μ sec, (g) 100,000–101,000 μ sec.

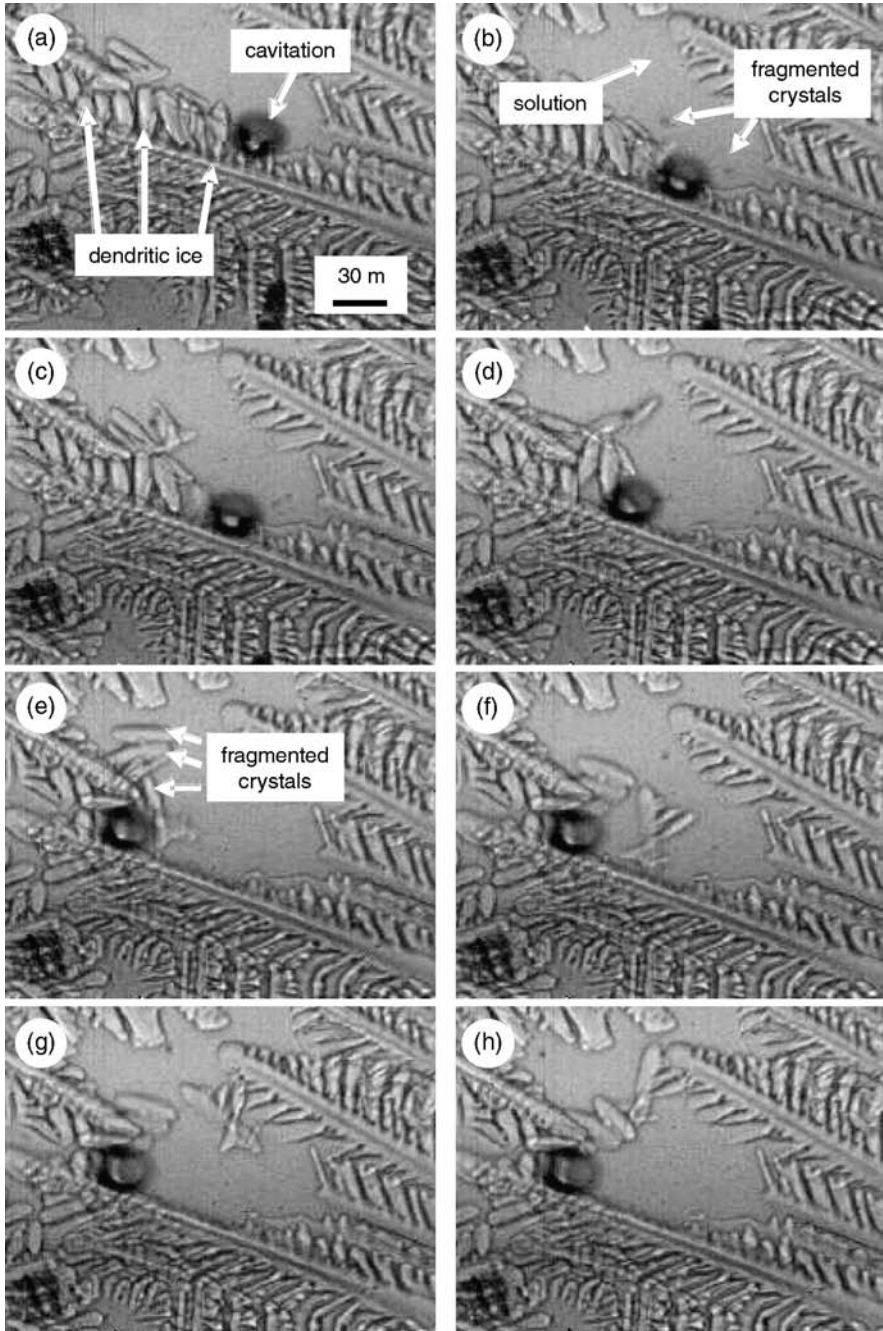


FIGURE 48.5

The microscopic effect of a cavitation bubble on the fragmentation of ice in a 15 wt% sucrose solution at -3.0°C : (a) $t = 0$ sec, (b) $t = 2$ sec, (c) $t = 2.2$ sec, (d) $t = 2.8$ sec, (e) $t = 3.0$ sec, (f) $t = 3.2$ sec, (g) $t = 3.4$ sec, (h) $t = 3.6$ sec.

Ultrasonic Cold-Stage Studies

In these studies a unique ultrasonic cold stage was used to examine the effect of ultrasound on ice crystallization. The experimental system was composed of three principal components: (1) an ultrasonic cold stage, (2) a temperature control system, and (3) a microscope and imaging setup. The ultrasonic cold stage allowed a thin sample of liquid to be subjected to an alternating acoustic pressure.

Initial studies have shown that an alternating pressure can lead to the fragmentation of preexisting ice crystals (Chow et al., 2003a, 2003b, 2004). This was shown to occur by either the production of a crack around the base of the dendritic structure, or by the melting caused by a cavitation. In the present work, a high-speed camera (Phantom V, Photsonics Ltd) was used to study the process of the effect of cavitation in a 15 wt% sucrose solution in more detail.

Figure 48.5 shows the effect of a cavitation bubble on the fragmentation of preexisting ice dendrites. These were filmed at 100 frames per second (shutter time $22 \mu\text{sec}$) at 66 kHz ($30 V_{\text{rms}}$). A cavitation bubble can be seen to move along the primary dendrite, breaking off the dendritic structures to produce fragmented crystals. This process occurred very quickly and the solution contained many small fragments after a couple of seconds of sonication. These results suggest that the population density of crystals observed in Figure 48.1 was produced by a secondary nucleation (fragmentation) process.

Conclusions

A detailed study of the nucleation of ice by power ultrasound has been performed using a variety of high-speed photography systems with a particular focus on the influence of cavitation. The nucleation of ice has been shown to occur predominantly within the bubble cloud produced by a commercial ultrasonic horn. An investigation of a single oscillating bubble has confirmed that ice crystals are nucleated in the immediate vicinity of the bubble.

It is widely thought that the high pressure emitted from a “transient” cavitation bubble is responsible for the nucleation process (Hickling, 1994); however, experiments utilizing a single oscillating bubble have shown that ice can be initiated by a “stable” cavitation bubble. The mechanism of nucleation may be related to the asymmetric bubble shape, the flow field associated with the cavitation bubble, or the production of microbubbles.

The nucleation of ice was also shown to not always occur after a single cycle of a cavitation bubble. It is thought that the probability of ice nucleation

is increased by a continuously oscillating single bubble, and further increased by the multi-bubble cavitation system.

The number of ice crystals produced at increasing ultrasonic output levels of the ultrasonic horn was observed to increase as the power output level was increased. Microscopic studies using a unique ultrasonic cold-stage device have shown that this may occur by the fragmentation of preexisting ice dendrites by cavitation bubbles.

Acknowledgments

The primary author would like to thank the Royal Commission for the Exhibition of 1851 for their Industrial Fellowship award, and funding provided by Unilever R&D.

References

- Chow, R.C.Y., Blindt, R.A., Chivers, R.C., and Povey, M.J. The sonocrystallization of ice in sucrose solutions: primary and secondary nucleation, *Ultrasonics*, 41, 595, 2003a.
- Chow, R.C.Y., Blindt, R.A., Kamp, A., Grocutt, P., and Chivers, R.C. Stimulation of ice crystallization with ultrasonic cavitation—microscopic studies, *Ind. J. Phys.*, 77A, 315, 2003b.
- Chow, R.C.Y., Blindt, R.A., Kamp, A., Grocutt, P., and Chivers, R.C. The microscopic visualisation of the sonocrystallisation of ice using a novel ultrasonic cold stage, *Ultrasonics Sonochem.*, 11, 245, 2004.
- Chow, R.C.Y., Blindt, R.A., Chivers, R.C., and Povey, M.J.W. A study on the primary and secondary nucleation of ice by power ultrasound, *Ultrasonics*, 43, 227, 2005.
- Chow-McGarva, R.C.Y. A study on the sonocrystallisation of ice. Ph.D., submitted to the University of Leeds, 2004.
- Hickling, R. Nucleation of freezing by cavity collapse and its relation to cavitation damage, *Nature*, 206, 915, May, 1965.
- Hickling, R. Transient high pressure solidification associated with cavitation in water, *Phys. Rev. Lett.*, 73, 2853, 1994.
- Hunt, J.D. and Jackson, K.A. Nucleation of solid in an undercooled liquid by cavitation, *J. Appl. Phys.*, 37, 254, 1966.
- Kennedy, C.J. Formation of ice in frozen foods and its control by physical stimulus, *The Properties of Water in Foods ISOPOW 6*, 1st ed., D.S. Reid, ed., Blackie Academic & Professional, Glasgow, pp. 329–365, 1998.
- Lauterborn, W., Kurz, T., Mettin, R., and Ohl, C.D. Experimental and theoretical bubble dynamics, *Adv. Chem. Phys.*, 110, 295, 1999.
- Zhang, X., Inada, T., and Tezuka, A. Ultrasonic-induced nucleation of ice in water containing air bubbles, *Ultrasonics Sonochem.*, 10, 71, 2003.

Relationships between the Maximum Rate of Nonenzymatic Browning, Relative Humidity, and Structural Changes

Nuria Acevedo, Carolina Schebor, and María del Pilar Buera

CONTENTS

Introduction	623
Materials and Methods	624
Model Systems	624
Determination of Water Content	625
Heat Treatment	625
Determination of Browning Degree	625
Calorimetric Measurement	625
Results and Discussion	625
Acknowledgments	629
References	629

Introduction

Nonenzymatic browning (NEB) results from a series of reactions starting with an amino-carbonyl condensation. It represents an important cause of quality loss in foods, and has also been reported as a cause of damage of pharmaceutical products (Kumar and Banker, 1994). Its mechanism and kinetics have been extensively studied in real foods and in model systems. These studies have shown that the rate of the NEB reaction is strongly dependent on the material composition, temperature, water content, water activity, and pH (Hodge, 1953; Labuza et al., 1970; Labuza and Baisier, 1992).

In solid systems, the NEB rate is expected to show a maximum value at intermediate relative humidities (RH) around 60 to 80% RH. At higher RH values, the rate of the reaction decreases as a result of both dilution of the

water-soluble reactants and inhibition of the reaction by water (which is one of the final products of the reaction). At low RH values, the reaction rate may be controlled by diffusion of the reactants and the NEB rate is relatively slow (Labuza et al., 1970). It has been shown that in liquid systems the NEB rate continuously diminishes while RH increases (Eichner and Karel, 1972). Several authors have studied NEB as a diffusion-controlled chemical reaction related to the glass transition. There are many reports on browning development in glassy systems (Karmas et al., 1992; Schebor et al., 1999). However, the structural changes that take place above the glass-transition temperature may affect the kinetics of NEB (Buera et al., 1992; Karmas and Karel, 1994; Buera and Karel, 1995).

The purpose of the present work is to analyze the relationship between the RH range at which NEB rate is maximum and the structural properties of the systems. The knowledge of the combined factors involved in NEB reactions can offer the opportunity to develop strategies for controlling the kinetics of this deteriorative reaction.

Materials and Methods

Model Systems

Samples were prepared by freeze drying aqueous solutions of the corresponding matrices in phosphate buffer pH 6, 0.175 M containing the browning reactants glycine and glucose, both 0.5% on solid basis. Systems containing lactose did not contain glucose. Glycine and glucose were analytical grade (obtained from Merck Darmstadt, Germany and Anedra San Fernando, Argentina, respectively). These compounds were chosen because of their high reactivity in NEB, and they were employed at very low concentrations so that diffusional effects could be expected.

The following matrices were employed: polyvinylpyrrolidone (PVP) of molecular weight 34,000 obtained from ISP Technologies, Inc. (Wayne, NJ); a mixture (2:1 (w/w)) of PVP:gelatinized wheat starch; a mixture (2:1 (w/w)) of PVP:native wheat starch; a mixture (3:1 (w/w)) of lactose obtained from Mallinckrodt Chemical Works (St Louis, MO):gelatinized wheat starch; and gelatinized wheat starch and lactose.

Wheat starch was previously gelatinized by heating an aqueous suspension for 15 min at 80°C. Gelatinization was confirmed by observation under polarized light microscopy.

Aliquots of 1 ml of each model solution were placed in 3-ml glass vials, frozen at -20°C, and quenched with liquid nitrogen before freeze drying. The freeze-drying process lasted 48 h. A Heto-Holten A/S, cooling trap model CT110 freeze drier (Heto Lab Equipment, Denmark) was used, operated at -110°C with a chamber pressure of 4×10^{-4} mbar. After freeze

drying, the model systems were equilibrated over saturated salt solutions in vacuum desiccators for 15 days to obtain the desired water contents (Labuza et al., 1985).

Determination of Water Content

The water content was determined (in duplicate samples) by difference in weight before and after drying in a vacuum oven for 48 h over magnesium perchlorate, at 94°C for polymeric systems or 70°C for lactose-containing systems.

Heat Treatment

After equilibration, vials were hermetically sealed with a cap and an aluminum strap, and placed in forced air ovens operated at constant temperature (70 and 55°C). At suitable intervals samples were removed from the oven and kept at 4°C until the browning analysis was carried out.

Determination of Browning Degree

The heated model systems were reconstituted with distilled water to their original volume. Photographs were taken before and after samples reconstitution in order to record their macroscopic structure, degree of collapse, and color. Browning was determined spectrophotometrically by measuring absorbance at 445 nm. The rate of browning was expressed as absorbance (per gram of sample)/storage time. Some samples with water-insoluble constituents were centrifuged after dilution and the supernatant used to determine color.

The browning analysis was performed in duplicate and an average value was reported.

Calorimetric Measurement

Glass-transition temperatures were determined by differential scanning calorimetry (DSC; onset values) using a DSC 822^e Mettler Toledo calorimeter (Schwerzenbach, Switzerland). The instrument was calibrated with indium (156.6°C), lead (327.5°C), and zinc (419.6°C). All measurements were performed at a heating rate of 10°C/min. Hermetically sealed 40- μ l medium pressure pans were used (an empty pan served as reference). Thermograms were evaluated using Mettler Star^e program. An average value of two replicates was reported.

Results and Discussion

The NEB rate was analyzed in model systems with different structural characteristics such as their tendency to crystallize or collapse. PVP was

chosen because it collapses readily above the glass-transition temperature and it does not crystallize. Lactose was chosen as a crystallizable matrix, since it readily crystallizes at relative humidities higher than 33% at room temperature (Buera et al., 2003). Starch forms a high glass-transition matrix which, when mixed with PVP or lactose, delays collapse and/or crystallization of the matrix. As systems of different composition and reactants concentrations were analyzed, absolute values of the NEB rate were not compared. The analysis was thus focused on the shape of the curves on the RH scale and the location of its maximum.

Figure 49.1 shows the rate of NEB at 70°C versus relative humidity for different polymeric matrices: PVP and gelatinized starch (Figure 49.1a); mixtures of PVP–starch (native or gelatinized) (2:1) (Figure 49.1b). The maximum NEB rate was observed at 33% RH for the PVP system, where the

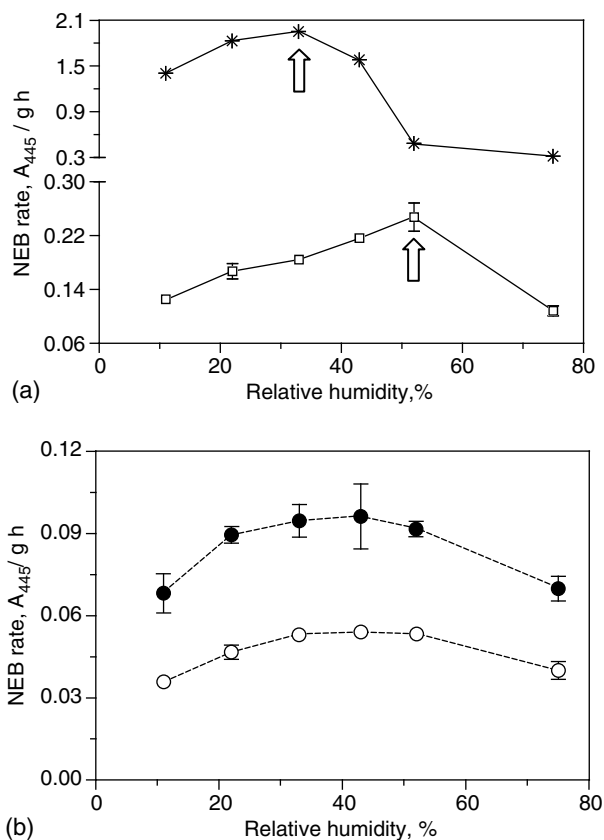


FIGURE 49.1

(a) NEB rate versus RH for PVP (*) and gelatinized starch (□) systems stored at 70°C. The arrow indicates the RH for the maximum NEB rate. (b) NEB rate versus RH for PVP–native starch (●) system (partially crystallized matrix); and PVP–gelatinized starch (○) (amorphous matrix) system, stored at 70°C.

glass-transition temperature (64°C) is slightly below the storage temperature. Buera and Karel (Buera and Karel, 1995) and Bell (Bell, 1996) analyzed the kinetics of NEB in PVP systems (molecular weight: 24,500 at 59°C and 40,000 at 25°C, respectively), and they also observed the maximum NEB rate at 33% RH in the glassy state. The gelatinized starch system showed a maximum NEB rate at 52% RH, while for mixtures of PVP and starch the maximum rates occurred in a broad range between 33 and 52% RH. The PVP–gelatinized starch system showed a very low browning rate compared with those observed for the individual matrix components, suggesting that the mixture offers a system in which the browning reaction is possibly delayed because of mobility restrictions. At 52% RH, the NEB rate markedly decreased in the PVP system, in which the degree of collapse was high and the system was semifluid.

The addition of starch to the PVP matrix reduced the degree of collapse. Although a certain degree of collapse occurred upon storage above T_g , the PVP–starch samples were never fluid or semifluid systems as in the PVP system.

To examine the effect of the degree of crystallinity on NEB rate, the browning rates were compared in a PVP–native starch matrix (representing a partially crystalline system), and in a PVP–gelatinized starch (representing an amorphous system) (Figure 49.1b). The NEB rate was twice as high for the partially crystalline system, probably as a result of the exclusion and concentration of reactants in the non-crystallized regions. Similar results were reported by Schebor et al. (Schebor et al., 2001) for native starch and other starchy matrices.

Table 49.1 shows the glass-transition and water-content values as a function of relative humidity for all systems which are in agreement to those reported in previous papers (Buera et al., 1992; Roos and Himberg, 1994; Buera and Karel, 1995; Mazzobre et al., 2001; Biliaderis et al., 2002; Fernández et al., 2003).

Figure 49.2 shows the rate of NEB as a function of RH for lactose and lactose–gelatinized starch (3:1) systems incubated at 70°C. Since lactose is a reducing sugar, NEB rate values were higher in the lactose systems than in the lactose–starch ones as a result of a dilution effect of the reactants. As previously indicated the purpose was to compare the shape of the curves and the location of the maximum in the RH scale. The maximum NEB rate for the lactose system was observed at 43% RH, in which the sample was completely crystalline. The kinetics of lactose crystallization was delayed by the incorporation of starch. However, the RH value at which crystallization started was the same as the lactose system, and the rate of NEB decreased only slightly above 52% RH (Figure 49.2). Several other studies have also indicated that the addition of a polymer to an amorphous matrix delayed the crystallization of the sugar (Roos and Karel, 1991; O'Brien, 1996; Gabarra and Hartel, 1998; Mazzobre et al., 2001; Biliaderis et al., 2002). At higher RH, the NEB rate dramatically decreased for lactose, which was completely crystalline and where water had an inhibitory effect on the reaction. In the

TABLE 49.1
Water Content and Glass-Transition Temperatures for Model Systems at Various Relative Humidities

System	PVP		Gel. St.		PVP–Nat. St.		PV–P–Gel. St.		Lact.		Lact.–Gel. St.	
RH	W.C.	T _g	W.C.	T _g	W.C.	T _g	W.C.	T _g	W.C.	T _g	W.C.	T _g
11	3.1	95.8	2.8	104.0	3.5	92.1	4.4	95.1	3.5	47.6	2.9	50.0
22	5.9	79.7	5.5	ND	7.3	72.2	6.3	84.2	5.1	36.9	5.0	32.0
33	9.7	64.0	9.1	58.0	10.8	62.5	10.1	67.1	6.9	22.4	6.4	14.0
43	13.6	47.0	15.1	44.0	14.6	41.1	13.7	41.1	3.2	CR	7.9	6.0
52	16.5	41.6	36.9	42.0	20.1	26.6	17.6	35.5	3.6	CR	5.8	—
75	31.6	–6.7	27.6	–3.1	38.9	–19.12	35.9	–10.7	14.8	CR	12.8	—

RH: relative humidity (%), Gel. St.: gelatinized starch, W.C.: water content (% dry basis), Nat. St.: native starch, T_g: glass transition temperature (°C), Lact.: lactose.

starch–lactose system, the starchy matrix could adsorb part of the water and thus its inhibitory effect was not evident.

The maximum for the NEB rate in solid systems is generally expected at a range of RH between 60 and 80% (Labuza and Baisier, 1992). However, as observed in Figure 49.1 and Figure 49.2, the RH values for maximum NEB rates were located at a different RH according to the structural characteristics of the systems.

The location of the maximum rate of NEB with respect to RH depends on the storage conditions (temperature, RH), on the thermo-physical properties

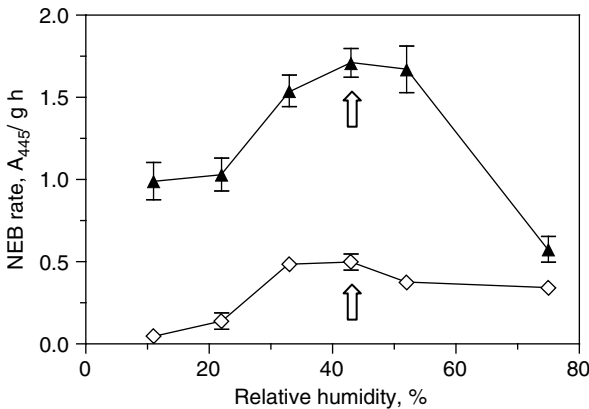


FIGURE 49.2
NEB rate versus RH for lactose (▲) and lactose–gelatinized starch (3:1) (◇) systems, incubated at 70°C. The arrow indicates the RH for the maximum NEB rate.

of the matrix media, and on their thermal history, which determine structural changes during storage.

In the polymeric collapsing systems the maximum NEB rate was located at temperatures close to T_g and before the collapse of the sample. In these systems the point at which the rates decreased was located above T_g and may be related to the point at which the systems became supercooled liquids and their behavior across the water-content scale resembled that observed in liquid systems (Eichner and Karel, 1972).

In the lactose systems the rate increased when the sugar crystallized, probably as a result of the increase of reactants concentration in the noncrystallized parts of the matrix.

Acknowledgments

The authors acknowledge financial support from CONICET (PIP 2734), UBACYT EX 226.

References

- Bell, L. Kinetics of non-enzymatic browning in amorphous solid systems: distinguishing the effects of water activity and the glass transition, *Food Res. Int.*, 28, 591, 1996.
- Biliaderis, C.G., Lazaridou, A., Mavropoulos, A., and Barbayiannis, N. Water plasticization effects on crystallization behavior of lactose in a co-lyophilized amorphous polysaccharide matrix and its relevance to the glass transition, *Int. J. Food Prop.*, 5, 463, 2002.
- Buera, M. and Karel, M. Effect of physical changes on the rates of nonenzymic browning and related reactions, *Food Chem.*, 52, 167, 1995.
- Buera, M., Levi, G., and Karel, M. Glass transition in poly(vinyl)pyrrolidone: effect of molecular weight and diluents, *Biotechnol. Prog.*, 8, 144, 1992.
- Buera, M., Schebor, C., and Elizalde, B. Carbohydrate crystallisation phenomena in dehydrated food and ingredient formulation. Involved factors, consequences and prevention, *J. Food Eng.*, 10, 2003.
- Eichner, K. and Karel, M. The influence of water content and water activity on the sugar-amino browning reaction in model systems under various conditions, *J. Agric. Food Chem.*, 20, 218, 1972.
- Fernández, E., Schebor, C., and Chirife, J. Glass transition temperature of regular and lactose hydrolyzed milk powder, *Lebensm. Wiss. u. Technol.*, 36, 547, 2003.
- Gabarra, P. and Hartel, W. Corn syrup solids and their saccharide fractions affect crystallization of amorphous sucrose, *J. Food Sci.*, 63, 523, 1998.
- Hodge, J. Chemistry of Browning Reactions in Model Systems, *J. Agric. Food Chem.*, 1, 928, 1953.

- Karmas, R. and Karel, M. The effect of glass transition on Maillard browning in food models, *Maillard Reactions in Chemistry, Food, and Health*, T.P. Labuza, G.A. Reineccius, V.M. Monnier, J. O'Brien and J.W. Baynes, eds., The Royal Society of Chemistry, Cambridge, U.K., pp. 182–187, 1994.
- Karmas, R., Buera, M., and Karel, M. Effect of glass transition on rates of non-enzymatic browning in food systems, *J. Agric. Food Chem.*, 40, 873, 1992.
- Kumar, V. and Banker, G., Maillard reactions in chemistry, food and health, *Maillard Reactions in Chemistry, Food, and Health*, T.P. Labuza, G.A. Reineccius, V.M. Monnier, J. O'Brien and J.W. Baynes, eds., The Royal Society of Chemistry, Cambridge, U.K., pp. 20–27, 1994.
- Labuza, T. and Baisier, W.M. The kinetics of nonenzymatic browning, *Physical Chemistry of Foods*, H. Schwartzberg and R. Hartel, eds., Dekker, M., New York, pp. 595–649. 1992.
- Labuza, T., Tannenbaum, S., and Karel, M. Water content and stability of low-moisture and intermediate moisture foods, *Food Technol.*, 24, 543, 1970.
- Labuza, T., Kaanane, A., and Chen, J.Y. Effect of temperature on the moisture sorption isotherms and water activity shift of two dehydrated foods, *J. Food Sci.*, 50, 385, 1985.
- Mazzobre, M.F., Soto, G., Aguilera, J.M., and Buera, M. Crystallization kinetics of Lactose in systems co-lyophilized with trehalose. Analysis by differential scanning calorimetry, *Food Res. Int.*, 34, 903, 2001.
- O'Brien, J. Stability of trehalosa, sucrose and glucose to nonenzymatic browning in model systems, *J. Food Sci.*, 61, 679, 1996.
- Roos, Y. and Himberg, M.J. Non-enzymatic browning behaviour, as related to glass transition of a food model at chilling temperatures, *J. Agric. Food Chem.*, 42, 893, 1994.
- Roos, Y. and Karel, M. Amorphous state and delayed ice formation in sucrose solutions, *Int. J. Food Sci. Technol.*, 26, 553, 1991.
- Schebor, C., Buera, M., Karel, M., and Chirife, J. Color formation due to non-enzymatic browning in amorphous, glassy, anhydrous, model systems, *Food Chem.*, 65, 427, 1999.
- Schebor, C., Chirife, J., and Buera, M. Non-Enzymatic Browning in dehydrated potato and Starch Model Systems in relation to physical state, *International Congress on Engineering and Food*, J. Welti-Chanes, G.V. Barbosa-Cánovas and J.M. Aguilera, eds., Technomic Publishing Company, Inc., USA, pp. 309–313, 2001.

Water Determination in Dried Milk Products: Is the International Standard Method Reasonable?

Heinz-Dieter Isengard, Andrea Felgner, Renate Kling,
and Christoph T. Reh

CONTENTS

Introduction 631

Background 632

Methods 633

 Oven Drying 633

 Reference Drying..... 633

 Karl Fischer Titration..... 633

Procedure 634

Samples..... 634

Results and Discussion 634

Summary of Conclusions 636

References 637

Introduction

Water content of foodstuffs is important for several reasons including technological, nutritional, logistic, economic, and legal aspects. A correct determination of water content is also particularly important in the context of reference materials with respect to the guaranteed values for which they are certified (Rückold et al., 2001). Water content also affects — via water activity — enzymatic and microbiological stability and thus shelf life. Water activity indicates the degree of “freedom” of the water and the availability for enzymatic and microbiological activities.

In many cases drying methods are applied to determine what is believed to be the water content. It is also often believed that by drying only the free water fraction is detected (de Knecht and van den Brink, 1998).

Different drying techniques are in use, ranging from the classical drying oven to rapid methods like infrared, so-called halogen and microwave drying. All of these methods analyze a mass loss caused by drying and not principally the water content. The results depend on the parameters applied. The mass loss is caused by evaporation of all volatile matter in the sample, not only by water. This comprises compounds that are originally present in the sample but also those that are formed during the drying process itself by chemical reactions, particularly by decomposition reactions at higher temperatures. This leads to results that are too high. Strongly bound water, however, may be retained and escape detection. This effect causes results that are too low. If the true water content for a given sort of product can be determined by a selective method that then serves as a calibration method, the parameters of a drying technique can be chosen in such a way that the two contradictory errors compensate each other (Isengard, 1995). The result of drying methods should not be called "water content." The best term would be "mass loss on drying" (with indication of the parameters). A compromise that seems to be widely accepted is "moisture content."

The Karl Fischer Titration (KFT) is based on a selective reaction of water (Scholz, 1984). Various measures can be taken to bring the water of the sample into contact with the reagents (Isengard, 1995) and the result of these analyzes is indeed the water content of the sample.

A particular problem exists with dried milk products. They contain more or less high amounts of lactose. In the α -form it contains 1 mol water per mole corresponding to 5.0 g/100 g in the pure crystallized form. This crystallized water can only be separated with a high-energy input (Rüegg and Moor, 1987; Rückold et al., 2003), which brings about the risk of destroying the molecule itself. These reactions may lead to the formation of further volatile material.

Background

The water content of dried milk was so far determined in a drying oven according to a standard of the International Dairy Federation (IDF, 1993). Recently, a special oven was designed by the Centraal Orgaan voor Kwaliteitsaangelegenheden in de Zuivel (COKZ) (de Knecht and van den Brink, 1998) to determine moisture content in milk powder. The proposed method was approved by IDF and is now a reference method (ISO/FDIS, 2004). This type of dryer is therefore referred to as the "reference dryer" in the following.

In a previous interlaboratory study it could already be shown that only a part of the crystallized water of α -lactose is detected by this method

(Rückold et al., 2000). This leads to greater or smaller discrepancies between the “official” results for moisture and the water content, depending essentially on the lactose content of the product. For the typical spray-dried milk such as full cream or skimmed milk powder these discrepancies are normally small as the lactose is in most cases amorphous.

In this investigation several dried dairy products with various compositions were analyzed by drying and by KFT.

Methods

Oven Drying

The drying oven FD 115 from Binder, Tuttlingen, Germany was used. According to IDF (1993), 1 to 3 g of the sample — for this investigation approximately 2 g were used — are dried at $102 \pm 2^\circ\text{C}$ in a ventilated drying oven. The mass loss is measured by weighing before and after 2 h drying and cooling in a desiccator. According to the method the sample is then to be dried for another hour or more until the difference between consecutive measurements is less than 0.5 mg. In this investigation the samples were analyzed after different drying times to follow the drying process more closely (see below). The result after 2 h was, however, used to compare the results with each other.

Reference Drying

For “reference drying” (RD) according to (ISO/FDIS, 2004), the Referenz-trockner RD 8 from Funke-Dr. N. Gerber Labortechnik, Berlin, Germany was used. The samples (5.0 ± 0.3 g) are placed in containers of 20 mm diameter and 90 mm height (plastic syringes without needle) between polyethylene filters and dried (up to eight in parallel per analysis) in a heating block at $87 \pm 1^\circ\text{C}$ for 5 h. An airflow (dry pressed air) with a rate of 33 ml/min is passed through the containers with the samples. The mass loss determined by weighing the sample and the containers before and after the drying process (after cooling in a desiccator) is defined as moisture content. It is not controlled if a constant mass has been reached.

Karl Fischer Titration

The KF Titrino 701 from Metrohm, Herisau, Switzerland with titration stand 703 and titration cell with thermostatic jacket was used. The two-component technique was applied with Hydranal-Titrant 2 as titrating solution and Hydranal-Solvent as working medium. All chemicals were from Sigma-Aldrich, Seelze, Germany. The end point was detected using the voltametric technique with a polarizing current of 20 μA and a stop voltage of 100 mV,

the stop criterion being the drift ($5 \mu\text{l}/\text{min}$ above the drift measured before analysis). The minimal titration volume increment was set to $0.5 \mu\text{l}$ and the maximal titration rate to $5 \text{ ml}/\text{min}$. In order to obtain a more rapid dissolution or dispersion of the samples in the working medium and, consequently, shorter titration times, the analyses were carried out at 50°C .

Procedure

The different samples were analyzed on the same day by the three methods. Five KFTs were carried out for every sample. The RD was started with eight portions of each sample; two each were analyzed as duplicates after 3, 4, 5, and 6 h (the official drying time being 5 h). Twelve portions of each sample were put in the drying oven. Two each were analyzed in parallel after 60, 80, 100, 120, 150, and 180 min (the official drying time being 120 min).

Samples

Five dried milk products with various compositions, all provided by Nestlé, Vers-chez-les-Blanc, Lausanne, Switzerland, and α -lactose were analyzed:

- Sample 1: Lactose
 - Sample 2: Skimmed milk powder
 - Sample 3: Full cream milk powder
 - Sample 4: Whey powder
 - Sample 5: Calcium caseinate
-

Results and Discussion

Table 50.1 gives a juxtaposition of the results obtained by KFT by conventional oven drying (OD) according to the former standard method (IDF, 1993) and by the new standard method (RD) (ISO/FDIS, 2004). The OD results are — for better comparison — those obtained after 2 h and the RD results are the values after the official time of 5 h. Values for other drying times both for OD and for RD are given below.

The shape of the KFT curves indicated a complete and correct determination of water for all the samples. The results for samples 2 and 3 are very close to each other. The KFT and the RD results are not significantly different. The OD results (obtained after 2 h drying time) come closer to the KFT results when the drying times are longer: $(3.90 \pm 0.01) \text{ g}/100 \text{ g}$ after 2.5 h for sample 2

TABLE 50.1

Results for Water Content by Karl Fischer Titration (KFT) and for Mass Loss by Oven Drying (OD) after 2 h and by “Reference Drying” (RD)

Sample	Water Content by KFT (<i>n</i> = 5) (g/100 g)	Mass Loss by OD (<i>n</i> = 2) (g/100 g)	Mass Loss by RD (<i>n</i> = 2) (g/100 g)
Lactose	4.45 ± 0.19	2.45 ± 0.13	1.04 ± 0.03
Skimmed milk powder	3.92 ± 0.07	3.85 ± 0.00	3.94 ± 0.13
Full cream milk powder	2.65 ± 0.05	2.46 ± 0.02	2.72 ± 0.14
Whey powder	4.46 ± 0.05	2.12 ± 0.01	2.24 ± 0.07
Calcium caseinate	6.19 ± 0.11	5.62 ± 0.03	5.73 ± 0.02

n = Number of Replicates.

and (2.58 ± 0.01) g/100 g after 3 h for sample 3 (see below). In the other cases the results for water content and mass loss differ more or less.

The drying times were varied for the two drying methods to receive information on the evolution of the results in the course of time. The results of these experiments are shown in Table 50.2.

TABLE 50.2

Mass Loss by Oven Drying and by “Reference Drying” after Different Drying Times (*n* = 2 each) and — for Comparison and Reference — Water Content by Karl Fischer Titration (*n* = 5)

Drying Time	Lactose	Skimmed Milk Powder	Full Cream Milk Powder	Whey Powder	Calcium Caseinate
	Water Content by Karl Fischer Titration in g/100 g				
	4.45 ± 0.19	3.92 ± 0.07	2.65 ± 0.05	4.46 ± 0.05	6.19 ± 0.11
	Mass Loss by Oven Drying in g/100 g after Different Drying Times				
60 min	1.56 ± 0.01	3.86 ± 0.02	2.43 ± 0.01	1.89 ± 0.01	5.59 ± 0.01
80 min	1.85 ± 0.13	3.93 ± 0.07	2.46 ± 0.05	1.96 ± 0.02	5.54 ± 0.02
100 min	2.12 ± 0.08	3.88 ± 0.00	2.47 ± 0.02	2.18 ± 0.13	5.78 ± 0.06
120 min	2.45 ± 0.13	3.85 ± 0.00	2.46 ± 0.02	2.12 ± 0.01	5.62 ± 0.03
150 min	2.51 ± 0.10	3.90 ± 0.01	2.46 ± 0.01	2.10 ± 0.07	5.72 ± 0.13
180 min	2.73 ± 0.08	3.84 ± 0.03	2.58 ± 0.01	2.09 ± 0.04	5.72 ± 0.09
	Mass Loss by Reference Drying in g/100 g after Different Drying Times				
3 h	0.88 ± 0.17	3.60 ± 0.06	2.71 ± 0.17	2.18 ± 0.04	5.29 ± 0.03
4 h	1.02 ± 0.20	3.64 ± 0.15	2.70 ± 0.02	2.07 ± 0.17	5.62 ± 0.12
5 h	1.04 ± 0.03	3.94 ± 0.13	2.72 ± 0.14	2.24 ± 0.07	5.73 ± 0.02
6 h	1.31 ± 0.07	4.14 ± 0.01	3.39 ± 0.35	2.25 ± 0.04	6.06 ± 0.01

The lactose sample was a technical product and obviously contains not only α -lactose but also anhydrous modifications. The water content found by KFT is therefore slightly below 5 g/100 g. This value is far above that reached by the drying techniques because the water of crystallization is very strongly bound.

For the two milk powder samples, the mass loss by drying corresponds approximately to the water content determined by KFT, the values of OD being slightly lower. This may be because of the content of α -lactose in the product or other components that hold water strongly (see sodium caseinate below). This "lack" can be compensated by the determination of volatile substances formed by decomposition at higher temperatures. This is obvious from the results by RD, which rise to numbers above the KFT results when the drying process is longer than the official 5 h. The value for both milk powders after 5 h is, however, in very good consistency with the water content.

The whey powder contains approximately 85% lactose. A part of it is crystallized. Consequently, the mass loss by drying does not reach the water content. Other components with high water-binding capacity may contribute to this effect.

The calcium caseinate sample does not contain lactose. The reason for the too low drying results may therefore be a slow diffusion of the water from the core of the particles to the surface. The airflow in the RD is obviously advantageous for the drying process as it keeps the partial pressure of water above the sample extremely low.

Summary of Conclusions

Results obtained for mass loss by drying and for water content after KFT differ in many cases. With increasing α -lactose content the difference increases and is extreme for pure lactose. The drying techniques determine neither the total water nor the free water fraction alone.

The results of the RD depend very strongly on the drying time and also other parameters (Isengard et al., 2006). Only for ordinary milk powders are they close to the KFT results. For products with other compositions, other product-specific parameters must be found. This makes the method very limited.

The KFT method detects the total water content selectively and is independent from the lactose content. The precision of the KFT results is very good, even though the sample sizes are much smaller than those of the drying techniques.

These drying techniques are more time consuming than the KFT method. Conventional drying takes several hours and real mass constancy is only rarely reached. Experience shows that it is recommendable to terminate the measurement after a fixed time of 2 h. This makes results more comparable

as in many cases additional mass loss may be a result of decomposition processes. The RD is very time consuming (practically one day for a set of eight samples). The KFT method is by far the most rapid method for a sample (a couple of minutes). A disadvantage of the KFT technique is the use of chemicals.

These and other (Isengard et al., 2006) investigations have shown that the RD method is correct only for ordinary milk powders but not for other dried dairy products. KFT, on the contrary, can generally be applied on these products and would be a more reasonable reference method.

References

- de Knegt, R.J. and van den Brink, H. Improvement of the drying oven method for the determination of the moisture content of milk powder, *Int. Dairy J.*, 8, 733, 1998.
- IDF Standard. Dried milk and dried cream, Determination of Water Content, 26A, 1993.
- International Organization for Standardization (ISO) and International Dairy Federation (IDF), ISO 5537/IDF 26: Dried Milk — Determination of Moisture Content (Reference method), 2004.
- Isengard, H.-D. Rapid water determination in foodstuffs, *Trends Food Sci. Technol.*, 6, 155, 1995.
- Isengard, H.-D., Kling, R., and Reh, C.T. Proposal of a new reference method to determine the water content of dried dairy products, *Food Chem.*, 2006, (in press).
- Rückold, S., Grobecker, K.H., and Isengard, H.-D. Determination of the contents of water and moisture in milk powder, *Fresenius J. Anal. Chem.*, 368, 522, 2000.
- Rückold, S., Grobecker, K.H., and Isengard, H.-D. Water as a source of errors in reference materials, *Fresenius J. Anal. Chem.*, 370, 189, 2001.
- Rückold, S., Isengard, H.-D., Hanss, J., and Grobecker, K.H. The energy of interaction between water and surfaces of biological reference materials, *Food Chem.*, 82, 51, 2003.
- Rüegg, M. and Moor, U. Die Bestimmung des Wassergehaltes in Milch und Milchprodukten mit der Karl-Fischer-Methode, V. Die Wasserbestimmung von getrockneten Milchprodukten, *Mitt. Gebiete Lebensm. Hyg.*, 78, 309, 1987.
- Scholz, E. *Karl Fischer Titration*, Springer, Berlin, 1984.

51

The Impact of Water Adsorption on the Energetics of Surface Interactions of Powders of Different Crystal Forms

M. Teresa Carvajal

CONTENTS

Introduction	639
Materials and Methods	640
Water-Uptake Measurements	641
Isothermal Microcalorimetry	641
Results and Discussion	642
Conclusions	645
Acknowledgments	645
References	645

Introduction

Water adsorbed on the surface of pharmaceutical or food powders, even at low levels, has a significant impact on the behavior of such powders during processing, and ultimately on the quality and performance of the final product. Bakri (1993) reported the application of heat conduction microcalorimetry to study the adsorption of water vapor onto solid pharmaceuticals. The high sensitivity of the calorimeter permits detection, even at low humidities, of heat flow as a result of interaction of solvent vapor with the solid. The heat flow (P_{μ}) can be described by:

$$P_{\mu} = \frac{dQ_{\text{ads}}}{dt} = \Delta H_{\text{ads}} \frac{dn}{dt} \quad (51.1)$$

where dQ_{ads}/dt and ΔH_{ads} are the rate and enthalpy of adsorption, respectively, and n denotes the number of moles adsorbed. This equation

is related to two aspects of the process having place during interactions, a thermodynamic aspect (what interactions will occur, extent of adsorption) and kinetic aspect (how fast, rate of adsorption). For a given polymorphic drug quantity, Q_{ads} , is given by Bakri (1993)

$$Q_{\text{ads}} = \Delta H_{\text{ads}} n \quad (51.2)$$

where ΔH_{ads} is the adsorption enthalpy of the organic probe vapor on the polymorphic drug, and n is the quantity of sorbed water. ΔH_{ads} can be obtained directly from the calorimetric data. Physical adsorption is considered a reversible process. The physical adsorption and magnitude of adhesion of drug particles on excipient particles in a powder blend are likely to be affected by the interactive forces. Physical adsorption and adhesion phenomena are in turn likely to influence physical and mechanical properties of powders including blend stability, flowability, dispersibility, compressibility, and dissolution characteristics. The physical properties of powders are also affected by the crystalline form of an active ingredient or excipient entity. Staniforth et al. (1981) investigated the use of excipients, including lactose, prepared with different crystal habits. His experiments resulted in various nonsegregated and de-agglomerated system behavior. Powder behavior in terms of mixing and the physical stability of powder blends is very much dependent on the energetics of the interaction between powder particles. Since the components in a powder blend interact with each other at the level of their particles' surfaces, the surface properties of powders are a determining factor in their mixing behavior.

This study focuses on the effect of water on the variations of surface characteristics of the drug substance and how these surfaces manifest themselves in terms of measurable physico-chemical quantities. Water plays a central role in many pharmaceutical and food situations, not only because of its unique interactive properties and behavior, but also because its importance, ubiquitous nature, and common use in pharmaceutical and food processing. In this study, the working hypothesis is that the surface energetics of the two polymorphs can be distinguished through the study of their interactions with a common probe, water, and that such differences can, in turn, be related to differences in the corresponding powder properties.

In the present investigation, microcalorimetry and water-sorption measurements are used in combination for studying the differences in surface energetics between two crystal modifications of the same drug.

Materials and Methods

The investigational drug, active ingredient (API) is a leukotriene D_4 antagonist (Hoffmann-La Roche, Nutley, NJ) with a MW of 412, and was chosen in the present study. It is very hydrophobic, practically insoluble in water (equilibrium solubility $< 2 \mu\text{g/ml}$) and a buffer at physiological pH;

the $\log P_{o/w}$ is 4.14. The API exists as two well characterized crystal forms, A and B. The two polymorphs, of which form B is the thermodynamically stable phase, are monotropically related. However, the metastable form, A, is kinetically stable and can exist indefinitely without undergoing physical transformation.

The two crystal forms of the API were milled to the give the same particle size distribution and similar specific surface area. For the micronization process, the bulk drug was first screened through 6- and 12-mesh sieves. The screened material was then placed in the mill's feeder, and passed through a fluid energy mill (4-in. Sturtevant Microniser) where the micronization took place.

Water-Uptake Measurements

The water-sorption experiments were carried out in a dynamic flow vapor sorption apparatus (Model SGA 100, VTI Corporation, Hialeah, FL). Samples of the two polymorphs were placed in the instrument's sample chamber and their moisture uptake as a function of relative humidity (RH) was measured. Water-sorption isotherms for both polymorphs were carried out under the temperature conditions of 20, 25, 35, and 45°C. The amount of sample used for an analysis depends on the sample's tendency to pick up water. If the sample is highly hygroscopic, about 2–5 mg is sufficient for the test, but if the sample is nonhygroscopic, a larger mass is needed, about 25 mg or more. For this study, water-sorption isotherms for both polymorphs were carried out using the flow system and a sample size of about 50 mg.

Isothermal Microcalorimetry

The heat of adsorption of water vapor onto the surface of both polymorphs of the drug was measured under different RH conditions using an isothermal heat conduction microcalorimeter (Thermal Activity Monitor, TAM, Thermometric AB, Sweden). The integral heats of adsorption were measured using a TAM instrument fitted with a Thermometric RH perfusion ampoule (accessory Model 2255) adapted with Kalrez O-rings. The RH above the solid samples was controlled as originally described by Bakri (1993)

For the sorption experiments, an accurately weighed sample of approximately 30 mg of the powder was placed in a 4-ml stainless steel sealed ampoule. Prior to calorimetric analysis, the sample was dried overnight under dry nitrogen flow ($\sim 0\%$ RH) until a signal of zero heat flow was attained. With every run, a blank experiment was conducted under identical conditions using an empty ampoule. The calorimetric adsorption

experiments were conducted at four temperatures, 20, 25, 35, and 45°C. The incoming relative vapor pressure of water was set to increase in 10% increments up to 100%. With every increase in RH, a positive response was recorded until equilibrium was re-established, i.e., zero heat flow ($P_\mu = 0$). The time integral of the recorded heat flow (P_μ) gives the heat evolved for the process under study. The area under the curve of each adsorption peak was calculated using Origin™ version 5.0 software (Microcal, MA).

Results and Discussion

The water uptake data are presented in Figure 51.1, which shows that polymorph A adsorbs greater quantities of water vapor than polymorph B under all conditions of temperature and RH investigated. In general, sorption isotherms of form A also exhibit more pronounced hysteresis than form B. A notable exception is the 45°C isotherm, where the two crystal forms show similar and quite pronounced hysteresis. In fact, the profiles obtained at 45°C are suggestive of condensation taking place at that temperature.

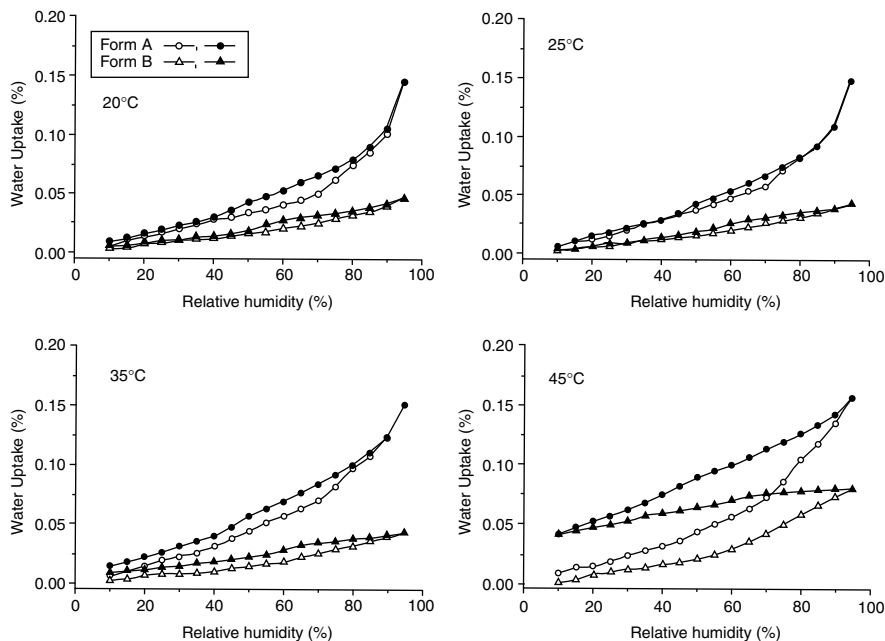
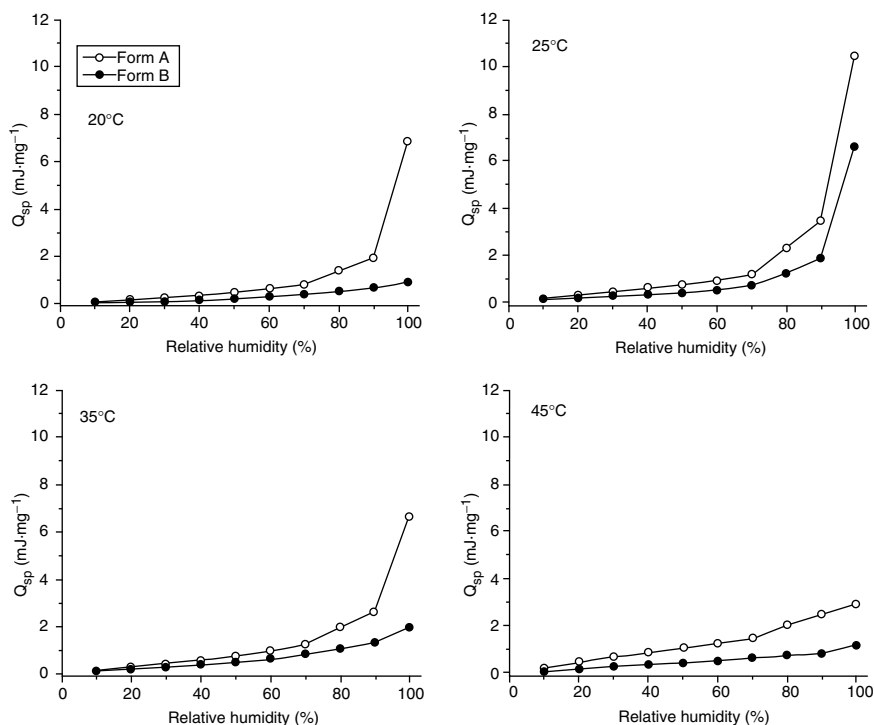


FIGURE 51.1

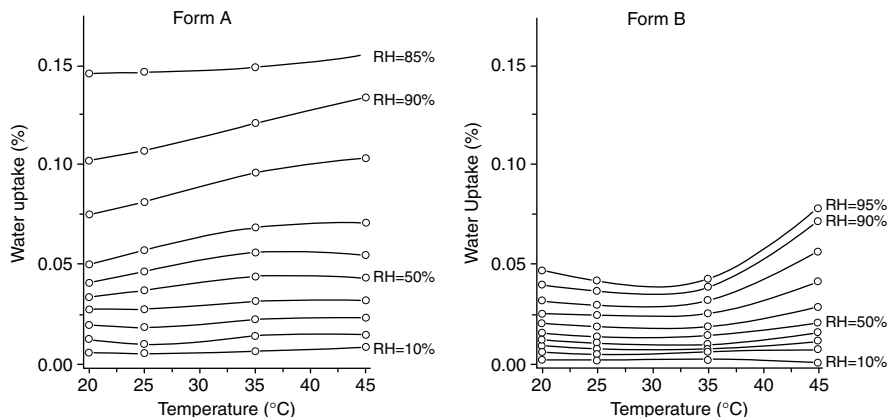
Water uptake isotherms for the two crystal forms at different temperatures. Open symbols represent adsorption curves, closed symbols represent desorption.

**FIGURE 51.2**

Integral heat of adsorption (Q_{sp}) for water onto the two crystal forms as a function of relative humidity at different temperatures.

Results for water sorption obtained by isothermal microcalorimetry at various temperatures and RH values are shown in Figure 51.2, which shows that the metastable form, A, exhibits greater heat of adsorption than form B under all conditions of temperature and RH investigated. At the three lower temperatures (20, 25, and 35°C), form A shows a sharp increase in heat of adsorption as function of RH at RH values above the 70–80% range. Form B also shows a similar sharp increase, but in this case the sharp raise is only observed only at 25°C. Figure 51.3 also shows that for each of the two polymorphs, the heat of adsorption reaches the highest values at 25°C in comparison with the other temperatures.

Figure 51.1 and Figure 51.2 clearly show that the two polymorphic surfaces are measurably different in their ability to interact with water. The metastable form, A, shows greater adsorption capacity in terms of water uptake and a corresponding higher heat of adsorption under all temperature and RH conditions investigated. The results presented in Figure 51.1 and Figure 51.2 are consistent with a situation in which the crystal form with higher free energy in its core exhibits also greater free energy at its surface; a less stable crystal is expected to have a greater number of energetic (active)

**FIGURE 51.3**

Water uptake data presented as relative isobars for the two crystalline forms.

sites that favor water sorption (Zografi and Tam, 1976). However, in order to facilitate more detailed comparisons between the two crystal surfaces, an alternative fashion for data presentation would be helpful. All the information relative to the uptake of water and the corresponding heat evolved upon water adsorption by each of the two selected crystal forms, is contained in Figure 51.1 and Figure 51.2, respectively. Data presentation as isotherms, however, may not be the optimal format for purposes of comparison. The use of isobars offers an alternative, more convenient means of presenting the same data for purposes of comparison. Presentation of adsorption data in the form of isobars is very useful because it makes it visually simple to separate the effects of temperature from those of RH when comparing the adsorptive properties of different surfaces.

Figure 51.2 shows the sorption data of Figure 51.1 but in the form of isobars, specifically as *relative* isobars, i.e., as lines of constant RH. Each line in Figure 51.3 corresponds to a constant level of RH; the lines are termed relative isobars because each line corresponds to a constant value of water vapor pressure relative to the water-saturation pressure at the same temperature (i.e., constant water activity). The relative isobars presented in Figure 51.2 correspond to RH ranging from 10% (bottom) to 95% (top), with 10% increments between 10 and 90% RH. Thus, moving upward in Figure 51.3 (constant temperature) corresponds to a *linear* increase in the water activity, which also corresponds to a directly proportional increase in the water concentration of the vapor phase. This means, for example, that a change from the 20% isobar to the 40% RH line at the same temperature corresponds to a doubling of the water activity resulting from a doubling in the concentration of water molecules in the vapor phase. In addition to being linear, such an isothermal increase in the vapor-phase activity of water also represents

a degree of freedom in terms of the Gibbs phase rule since it is controlled directly by the experimenter.

Conclusions

Water-adsorption experiments were conducted to probe the surface properties of two polymorphs of a drug. The surfaces of the two polymorphs of the present study are energetically different to sufficient degree as to allow direct and reliable measurements in terms of their interaction with a common probe such as water. The two polymorphs showed measurable differences in terms of the extent of water sorption as well as in the level of heterogeneity of their surfaces. The combined use of vapor-sorption measurements and microcalorimetry proved to be a powerful tool capable of revealing critical differences in the interactive properties of the two surfaces investigated. The combination of techniques provides details about the two surfaces that clearly differentiate them. Form A exhibits a greater number of weaker active sites for water on its surface compared with form B. Conversely, the surface of form B has a composite nature that exhibits stronger binding sites for water, but these are more limited in number. The type of adsorptive behavior shown by form A was analogized to (energetic) surface fuzziness.

This research resulted in a substantial gain in the understanding of powders at the molecular level and the way in which the surface properties of powders affect their behavior at the bulk level for not only small molecules obtained from chemical synthesis "as is" but can be extended to the engineered particles like the spherical-shaped crystalline particles obtained by novel methods such as supercritical fluids, electro-hydrodynamic spraying, and sono-crystallization.

Acknowledgments

The authors acknowledge VTI Corporation and Hoffmann-LaRoche.

References

- Bakri, A., *Thermometric Application Note 22021*, Thermometric AB, Jarfalla, Sweden, 1993.
- Staniforth, J.N., Rees, J.F., Kayes, J.B., Priest, R.C., and Cotterill, N.J. *Drug Dev. Ind. Pharm.*, 7, 179, 1981.
- Zografi, G. and Tam, S. J. *Pharm. Sci.*, 65, 1145, 1976.

Water-Sorption Behavior of Glycinebetaine and the State Diagram of Its Aqueous System

Kenta Komai and Norio Murase

CONTENTS

Introduction	647
Materials and Methods	648
Results and Discussion	648
Conclusions	654
Acknowledgments	654
References	654

Introduction

Some organisms including bacteria, plants, and animals respond to drought, salt, or low-temperature stress by increasing the concentration of compatible solutes (Brown, 1976; Yancy et al., 1982; Booth, 1998). Compatible solutes, such as sucrose, trehalose, glycinebetaine (GB), and proline have common characteristics of high solubility in water and nontoxicity to organisms at high concentrations. The mechanism of protection against water stress by these compounds, however, is subject to debate and various hypotheses have been proposed. Compatible solutes of sugars and polyols are assumed to protect membrane lipids or protein molecules by direct interaction (Rudolph et al., 1986). As another possibility for their protective function, high glass-transition temperatures of these aqueous systems being ready to turn into a glassy state when dehydrated or freeze-concentrated might contribute to the stabilization of native structures of membranes or protein molecules (Crowe et al., 1998). In the case of GB and proline, they are electrically neutral as a whole molecule but exist as a zwitterion with positive and negative charges at physiological

pH, which is different from the case for sugars and polyols. Then, the protection mechanism against water stress indicated by them might also be different from that shown by sugars and polyols (Pollard, 1979). It was indicated that the protective function of GB against osmotic stress can be explained by the colligativity of solutions (Carley and Record, 2003). However, scant information is available about the concentration range where the aqueous zwitterion solutions hold the colligativity, while the concentration of GB in the cytoplasm is known to become 1 M or so when it functions as an osmoprotectant (Booth, 1998). What is the remarkable difference between aqueous solutions of electrolytes and zwitterions? In this connection, there are many kinds of zwitterion molecules in biological systems including amino acids and phospholipids, and they might play a crucial role in the life process. The reason why they are introduced into the life process and function variously, for example, as compatible solutes is unclear and worth further attention. Then we investigated in this study the characteristics of hydration properties of GB by obtaining the water-sorption isotherm and freezing behavior of the aqueous solution by the use of differential scanning calorimetry (DSC).

Materials and Methods

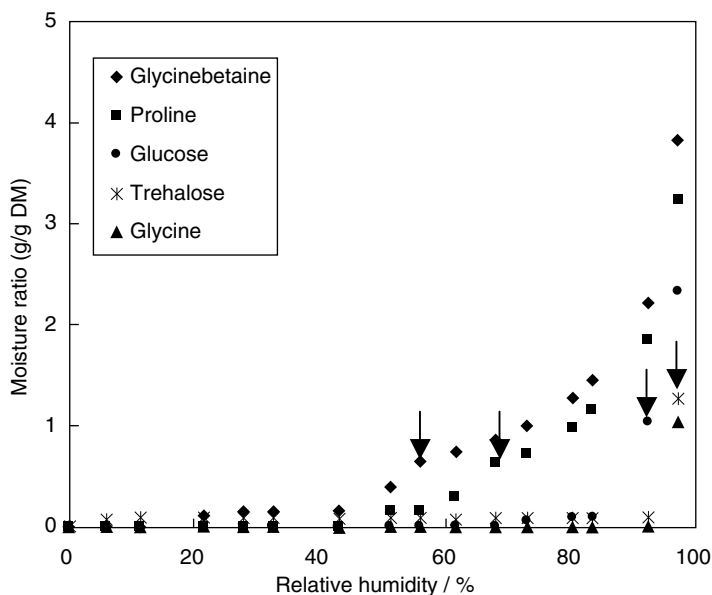
GB (anhydrous, purity: >98%), L-proline, glycine, glucose, and trehalose (dihydrate) were purchased from Wako Pure Chemical Industry, Ltd (Osaka, Japan), and used without further purification.

Water-sorption isotherms were obtained at 30°C by keeping the samples in desiccators under the controlled relative humidity (RH) prepared with saturated inorganic salt solutions. The weight increase of the samples was measured after 3 weeks.

DSC measurements were carried out using a Perkin Elmer Pyris 1 instrument equipped with subambient accessories. A solution (1 μ l) was transferred into an aluminum pan and the pan was sealed hermetically. Samples were cooled mostly at a rate of 10 K min⁻¹ to -150°C and the heating rate was 5 K min⁻¹. Rapid cooling by dipping the sample pans into liquid nitrogen was also conducted to vitrify the solutions and to obtain T_g values. For the determination of freezing points, a heating rate of 1 K min⁻¹ was used. The concentration of GB employed was in the range of 0–100 wt%.

Results and Discussion

Water-sorption isotherms obtained are shown in Figure 52.1. GB is very hygroscopic and deliquesced at around 50% RH. Proline is also hygroscopic and deliquesced at around 60% RH. Although glycine is a zwitterion

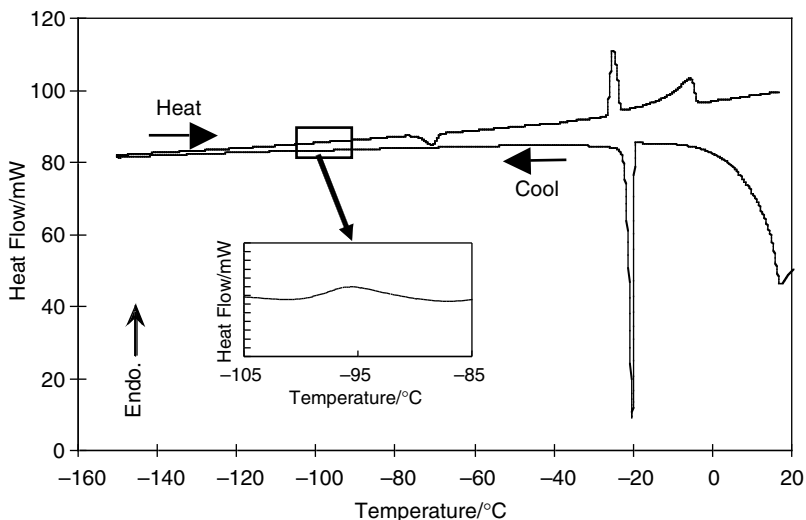
**FIGURE 52.1**

Water-sorption isotherms of various salts at 30°C. Arrows indicate the points of deliquescence.

molecule as well as GB and proline, it hardly adsorbed water even at 90% RH. Water adsorption and/or absorption ability of glycine was lower than glucose and trehalose with no charge in the molecules.

DSC cooling and heating scans obtained for a 2.0 M GB aqueous solution are shown in Figure 52.2. The cooling scan indicated a single exotherm due to ice crystallization. During the subsequent heating, however, a DSC scan indicated an endotherm at -26°C following a small exotherm at around -70°C besides an ice melting endotherm at around 0°C . The small exotherm is probably a result of eutectic separation composed of ice and $\text{GB}\cdot\text{H}_2\text{O}$, and the endotherm at -26°C is because its melting as the temperature of the endotherm was independent of the GB concentration. When the cooling was stopped at -70°C or above, eutectic separation did not occur during rewarming. These results suggest that the nucleation of the eutectic initiates below the temperature, and that the nucleation occurred during cooling does not always lead to crystal growth. Glass-transition behavior during rewarming is shown in the inserted figure. The T_g value estimated from the midpoint of the change in C_p was -98°C .

The solid-liquid state diagram of the GB-water system shown in Figure 52.3 was constructed from data obtained in the present study supplemented by the existing ones (Landolt-Börnstein, 1962). As the DSC heating scans obtained with the system in the concentration above 60 wt% were complicated, there remained ambiguity in the diagram about the existence of crystal hydrates other than monohydrate. Although eutectic

**FIGURE 52.2**

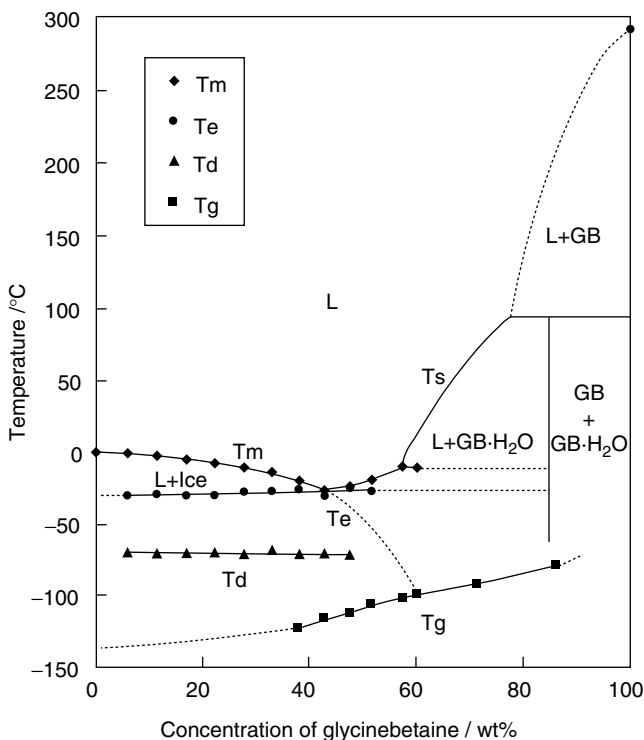
DSC cooling and heating scans obtained with a 2.0 M aqueous glycinebetaine solution. An inserted figure indicates glass-transition behavior.

temperature is ca. -26°C , freeze-concentrated GB solutions were super-saturated when they were cooled further and turned into a glassy state. By extrapolating the freezing point curve, T'_g , i.e., T_g for the most freeze-concentrated system, was estimated from the intersection point with the T_g curve. The temperature of -98°C was the same as T_g obtained for the 2.0 M solution. C'_g , the concentration corresponding to T'_g , was 58 wt%.

In Figure 52.4, the freezing point depression of aqueous GB solutions against molality is shown, together with data of aqueous NaCl and glucose solutions (Lide, 2003). While the concentration of GB was low, freezing points of the solution were depressed following the behavior of the ideal solution like that of glucose. With increasing molality of the GB solution higher than 1 mol/kg water, however, deviation from the linear relationship against the concentration became remarkable. Therefore, the colligativity was found to be inapplicable when the GB concentration is above 1 mol/kg water.

Values of T'_g against C'_g are plotted in Figure 52.5. Compared with these values for trehalose, reported to be -35°C and 81.6 wt%, respectively (Roos, 1993), the corresponding values for GB are very low. The values for proline obtained in this study, -67°C and 61 wt%, and for glucose reported (Roos, 1993) are also plotted in Figure 52.5.

For aqueous electrolyte solutions, both electrostatic interaction between dissociated ions and ionic hydration induce the deviation of freezing-point depression from that of the ideal solution at high concentrations. In the case of aqueous zwitterion solutions where each ion within a molecule cannot

**FIGURE 52.3**

Solid-liquid state diagram of glycinebetaine-water system. Solubility curve (T_s) was supplemented by the data in Landolt-Börnstein, Lösungsgewichte von Festen und Flüssigen Stoffen in Flüssigkeiten, 6th Ed., Vol. II/2b, 3-446, Springer, Berlin, 1962. With permission. ---,: expected or extrapolated lines, respectively. T_m : melting temperature, T_e : eutectic temperature, T_d : devitrification temperature, T_g : glass transition temperature.

dissociate, dipole-dipole interaction is to be considered between molecules instead of ionic interaction. Then, remarkable deviation from the linearity observed with the GB solutions, different from the NaCl solution, can be explained by the hydration effect as well as the restricted dipole-dipole arrangement. Hydration structures of negative and positive ions in adjacent molecules of GB are incompatible with each other as hydration of a trimethylammonium cation is hydrophobic and that of a carboxyl anion is hydrophilic. Because of the incompatibility of hydration structures together with the presence of bulky trimethylammonium groups, these counter-charge ions in the adjacent molecules might be inaccessible to each other. Further hydration is, then, necessary for the stabilization of the GB aqueous system and more water is absorbed to cause deliquescence. Although the GB-water system becomes stabilized mediated by the hydration water, the water structure in the system is broken. Substantial depression of freezing points of the aqueous system is caused consequently.

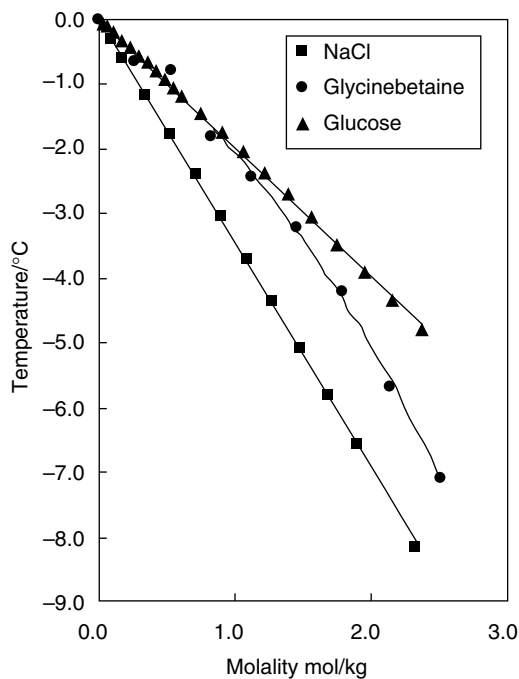


FIGURE 52.4 Freezing-temperature depression of aqueous systems. (Source: Data for NaCl and glucose were taken from Lide, D.R. *Handbook of Chemistry and Physics*, 84th Ed., CRC Press, Boca Raton, FL, 2003–2004. With permission.)

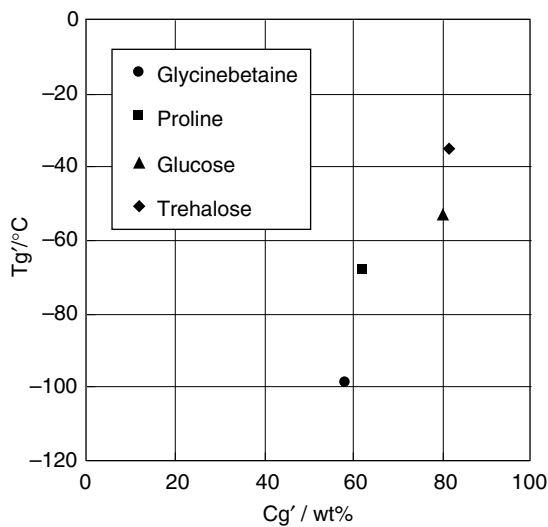


FIGURE 52.5 T_g' vs. C_g' . (Source: Data for glucose and trehalose were taken from Roos, Y. *Carbohydr. Res.*, 238, 1993, With permission.)

In this connection, glycine with an ammonium ion and a carboxyl ion in a molecule is ready to form a eutectic as a result of freeze-concentration, where eutectic temperature was reported to be ca. -4°C (Suzuki and Franks, 1993). It is probably because ammonium ions, instead of trimethylammonium ions for GB, and carboxyl ions are accessible to each other, easily dehydrated, and are stabilized by the formation of hydrogen bonds as well as by ionic contacts. The finding of low water-sorption ability of glycine is in accordance with the interpretation. These considerations are also supported by the crystal structures of phosphatidylethanolamine (PE) and phosphatidylcholine (PC), which are also zwitterion molecules (Pascher et al., 1992). The structural relationship of the polar groups in these two phospholipids is similar to that of glycine and GB; PE has an ammonium ion and PC has a trimethylammonium ion in a molecule linked with a phosphate ion. The crystal structure of PE indicates the presence of direct interaction because of hydrogen bonds between an ammonium ion and a phosphate ion in the neighboring molecules, and that of PC indicates the presence of water molecules hydrogen-bonded to phosphate ions in the molecules (Pascher et al., 1992). Therefore, substantial freezing-point depression observed with GB can be explained by the hydration effect. Moreover, hydration and solution properties of zwitterions are certainly different from those of electrolytes and sugars.

The value of T'_g for the freeze-concentrated GB system was very low compared with that of the trehalose and other sugar systems. Although the GB solution was vitrified at lower temperatures, the amount of unfrozen water estimated from the C'_g (42 wt%) was more than the aqueous trehalose system (18.4 wt%). Then, the mechanism of protection against water stress by GB and other zwitterions is considered to be different from that by trehalose and other sugars. Trehalose is ready to turn into a glassy state with a least amount of hydration water, which might stabilize the native structures of membranes or protein molecules, and can protect from deleterious effects from water stress eventually, or direct interaction of trehalose molecules with membrane structures or protein molecules by substituting them for water molecules might contribute to the avoidance of serious damages. In the case of GB and proline, they are reluctant to be dehydrated, as is comprehensible from the T'_g and C'_g values, and the existence of the molecules might contribute to the sustenance of the native hydrated structures of membranes and proteins. However, there is a possibility that zwitterion molecules also interact directly with membranes and proteins.

The values of T'_g , C'_g , and their combination can be important indices for understanding hydration properties of various solutes including compatible solutes (Levine and Slade, 1992), and to comprehend characteristics of these molecules in aqueous systems is a prerequisite for understanding the protection mechanism against water stress indicated by them and for understanding the biological meaning of their existence in various organisms as well.

Conclusions

GB is very hygroscopic and shows remarkable freezing-point depression at high concentrations compared with other compatible solutes. T'_g value for the freeze-concentrated GB system was very low and the amount of unfrozen water is large. These characteristics of GB, ascribed to those of zwitterions with trimethylammonium ions, might contribute to the protective function against drought, salt, or low-temperature stress.

Acknowledgments

The authors thank T. Kanno, Nippon Beet Sugar Manufacturing Co. Ltd, for giving useful information of the properties of GB and Dr. H. Takahashi, Gunma University, for helpful discussions.

References

- Booth, I.R. Bacterial responses to osmotic stress: diverse mechanisms to achieve a common goal, *The properties of water in foods, ISOPOW 6*, D.S. Reid, ed., Blackie Academic & Professional, London, pp. 456, 1998.
- Brown, A.D. Microbial water stress, *Bacteriol. Rev.*, 40, 803, 1976.
- Carley, S. and Record, M.T.J. Compatible solutes in *E. coli* can be explained by colligative properties, *Biochemistry*, 42, 12596, 2003.
- Crowe, J.H., Carpenter, J.F., and Crowe, L.M. The role of vitrification in anhydrobiosis, *Annu. Rev. Physiol.*, 60, 73, 1998.
- Landolt-Börnstein, Lösungsgewichte von Festen und Flüssigen Stoffen in Flüssigkeiten, 6th Ed., Vol. II/2b, 3-446, Springer, Berlin, 1962.
- Levine, H. and Slade, L. Another view of trehalose for drying and stabilizing biological materials, *Biopharmaceutics*, 5, 36, 1992.
- D.R. Lide, ed., *Handbook of Chemistry and Physics*, 84th Ed., CRC Press, Boca Raton, FL, 2003–2004.
- Pascher, I., Lundmark, M., Nyholm, P.-G., and Sundell, S. Crystal structures of membrane lipids, *Biochim. Biophys. Acta*, 1113, 339, 1992.
- Pollard, A. and Wyn Jones, W.R.G. Enzyme activities in concentrated solutions of glycinebetaine and other solutes, *Planta*, 144, 291, 1979.
- Roos, Y. Melting and glass transitions of low molecular weight carbohydrates, *Carbohydr. Res.*, 238, 39, 1993.
- Rudolph, A.S., Crowe, J.H., and Crowe, L.M. Effects of three stabilizing agents — proline, betaine, and trehalose — on membrane phospholipids, *Arch. Biochem. Biophys.*, 245, 134, 1986.
- Suzuki, T. and Franks, F. Solid–liquid phase transitions and amorphous states in ternary sucrose–glycine–water systems, *J. Chem. Soc. Faraday Trans.*, 89, 3283, 1993.
- Yancy P.H., Clark, M.E., Hand, S.C., Bowlus, R.D., and Somero, G.N. Living with water stress: evolution of osmolyte systems, *Science*, 217, 1214, 1982.

*Effects of Sugar Crystallization
on Nonenzymatic Browning Kinetics
in Low-Moisture Food Systems*

Song Miao and Yrjö H. Roos

CONTENTS

Introduction	655
Materials and Methods	656
Results and Discussion	656
Water Sorption.....	656
Glass-Transition Temperature.....	659
Nonenzymatic Browning.....	659
Conclusions	661
References	661

Introduction

Maillard reaction can cause deterioration of dehydrated foods (Friedman, 1996). Stability of food and other biological systems containing sugars and /or polymers is often related to their physical state (O'Brien, 1996). Studies of NEB kinetics have considered temperature, moisture content, water activity, pH, concentration of reactants, etc., as controlling factors, and recently related to crystallization and viscosity (Labuza and Braisier, 1992; Buera and Karel, 1995). The glass transition together with viscosity, material composition, water activity, temperature, and other factors affect the rate of the reaction through changes in molecular mobility. Crystallization of component sugars may enhance the rate of an enzymatic reaction as a result of release of sorbed water during the crystallization process (Cardona et al., 1997; Kouassi and Roos, 2000). The crystallization of amorphous lactose in dehydrated milk products has also been observed to result in acceleration of nonenzymatic

browning reactions, loss of lysine, as well as other deteriorative changes and caking (Roos, 2001). The rate of crystallization depends on the composition of food materials. Crystallization of lactose has been reported to be delayed by trehalose (Mazzobre et al., 2001). The objective of the present work was to study the nonenzymatic browning kinetics in lactose, trehalose, and lactose/trehalose matrices, and to evaluate the effects of matrix composition and component crystallization on NEB kinetics.

Materials and Methods

Three amorphous food model systems consisting of lactose, trehalose, and lactose/trehalose (1:1) as matrix materials, and L-lysine and D-xylose (1:1, 5% w/w) as reactants were prepared by freeze-drying. Aliquots (1 g) of the powdered freeze-dried model materials were transferred into 20-ml glass vials, which were stored in desiccators over four relative vapor pressures (RVP) of 33.2, 44.1, 54.5, and 65.6%. Triplicate samples were removed at 10- to 24-h intervals depending on the RVP, and the extent of browning was determined spectrophotometrically at 280 and 420 nm.

Sorption isotherms of model systems were determined gravimetrically and data were modeled using the Brunauer–Emmett–Teller (BET) and Guggenheim–Anderson–deBoer (GAB) models.

Differential scanning calorimetry (DSC) was used to measure the glass transition (T_g) of samples humidified over saturated solutions of LiCl, CH₃COOK, MgCl₂, and K₂CO₃. The Gordon–Taylor equation was fitted to the glass-transition data.

Results and Discussion

Water Sorption

The three model systems were very hygroscopic. Water contents at different RVPs $\leq 44.1\%$ generally leveled off within 24 h. When exposed to RVP $\geq 54.5\%$, the three model systems showed different sorption behaviors (Figure 53.1). Loss of sorbed water indicated time-dependent crystallization. Compared with the lactose/reactant and trehalose/reactant systems, crystallization of component sugars in the lactose/trehalose/reactant system occurred more slowly. At RVP 65.6 and 76.1%, loss of sorbed water in lactose/reactant system was observed after 21 and 8 h of storage, and in trehalose/reactant system after 5 and 3 h, respectively, while in lactose/trehalose/reactant system, after 79 and 33 h, respectively. Three model systems sorbed different amounts of water before showing the loss of water. The higher water content in the lactose/trehalose/reactant system

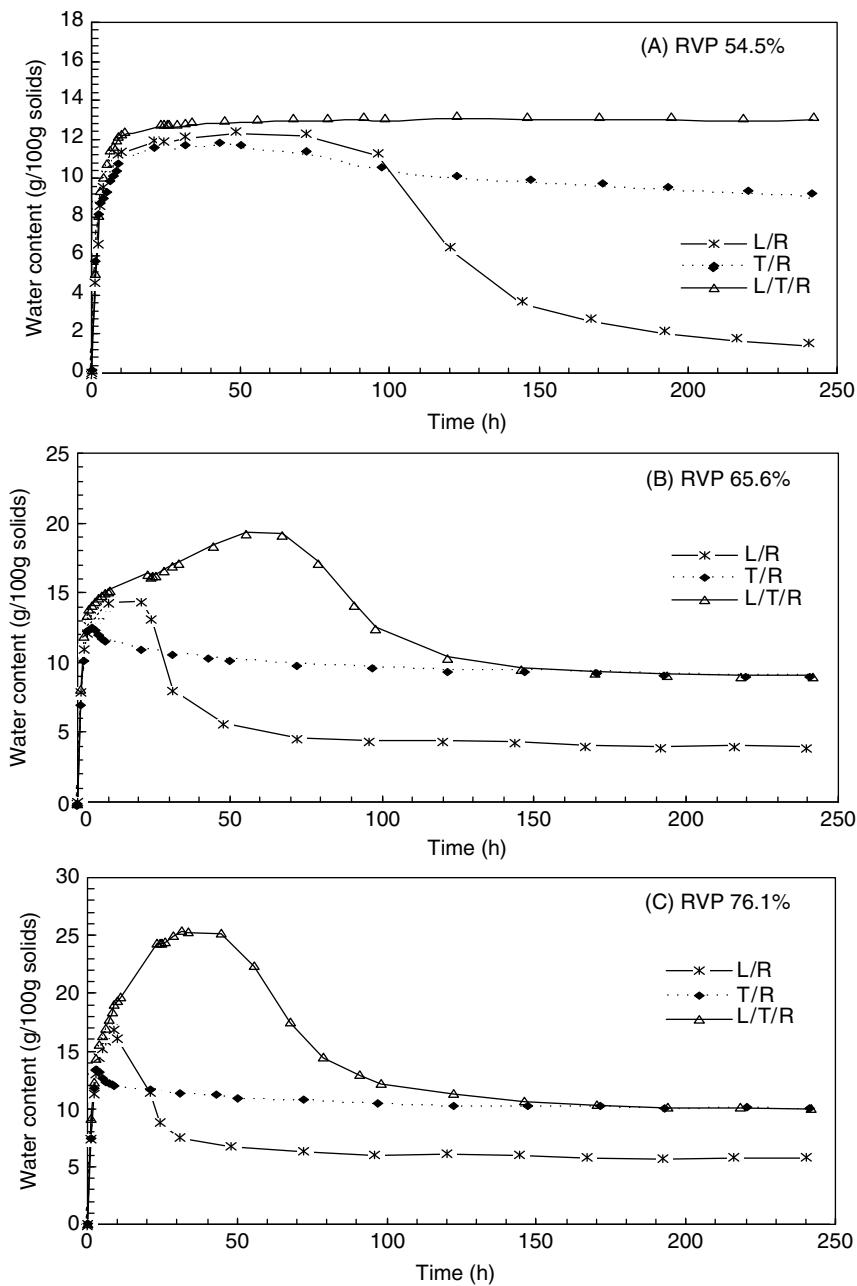


FIGURE 53.1
Water content of model systems over various RVP (54.5, 65.6, and 76.1%) at room temperature during storage.

probably related to the interaction between lactose and trehalose in the mix. In fact, the lactose/trehalose/reactant system also took a longer time to release sorbed water during crystallization. At $RVP \geq 65.6\%$, loss of water after initial crystallization in the three model systems leveled off after 150 h of storage (Figure 53.1b and c) and crystallization of component sugars in the model systems was considered to proceed only to a given extent. Experimental sorption data for the three model systems over the a_w range 0.114 to 0.441 were successfully modeled with the BET and GAB models, as shown in Figure 53.2. The GAB monolayer values were 5.2, 4.0,

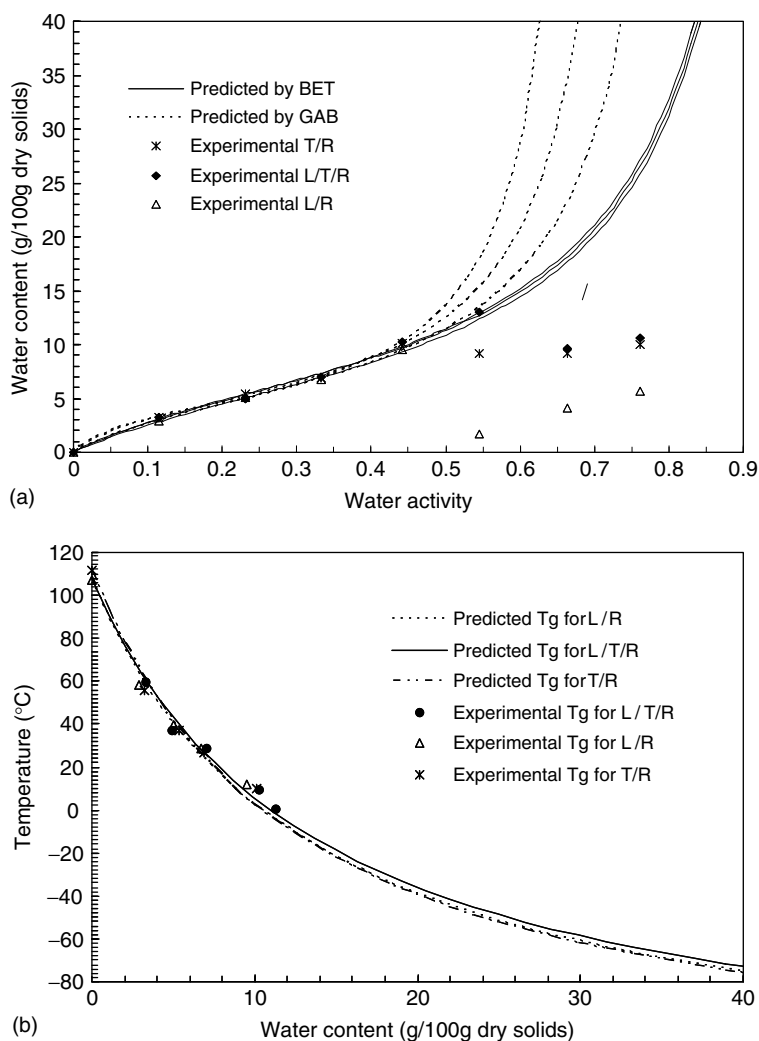


FIGURE 53.2

Water sorption isotherms (a) and water plasticization (b) of model systems. The Gordon–Taylor equation was applied for predicting T_g .

and 4.6 g/100 g solids for lactose/reactant, lactose/trehalose/reactant, and trehalose/reactant systems, respectively.

Glass-Transition Temperature

Water plasticized the food models and caused a substantial decrease of the glass-transition temperature. The Gordon–Taylor equation was successfully fitted to experimental glass transition temperatures of the three model systems, as shown in Figure 53.2b. The constant, k , for the Gordon–Taylor equation was found to be 7.6 ± 0.8 for lactose/reactant systems, 7.2 ± 0.7 for lactose/trehalose/reactant systems, and 7.9 ± 0.9 for trehalose/reactant systems. The three model systems had corresponding glass-transition behaviors, which were typical of lactose-based dairy products. The critical water contents at 23°C obtained from T_g data for lactose/reactant, lactose/trehalose/reactant, and trehalose/reactant systems were 7.0, 7.4, and 7.1 g/100 g of dry solids, respectively.

Nonenzymatic Browning

Nonenzymatic browning occurred in the three model systems at all RVP environments studied during storage. A plot of optical density (OD) at 280 nm against storage time is shown in Figure 53.3. The browning kinetics

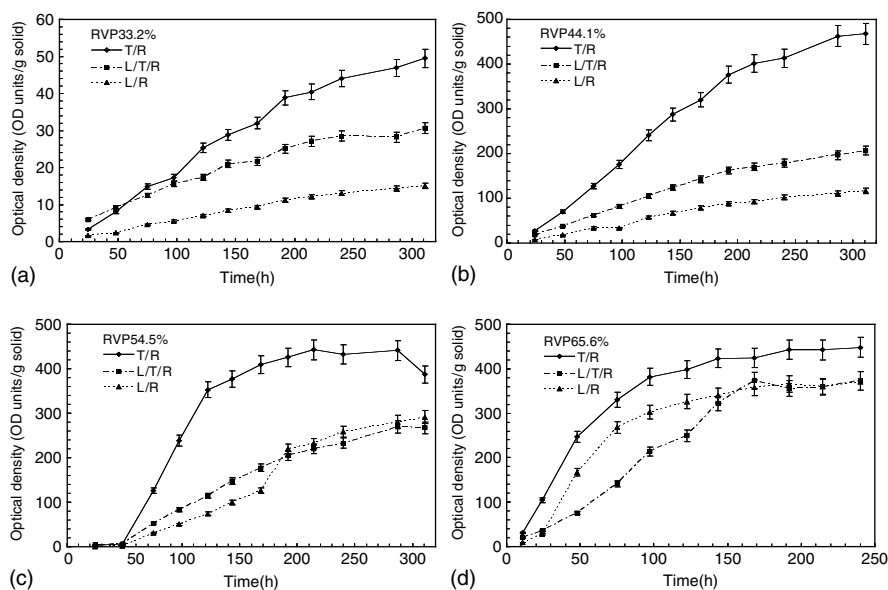


FIGURE 53.3

Optical density development of the model systems at 280 nm as a function of storage time at room temperature (22 to 23°C). Error bars represent standard deviation ($n = 3$).

observed from OD at 280 and 420 nm (data not shown) were very similar. The three model systems showed different NEB kinetics during storage at different RVPs. At RVP 33.2 and 44.1% (Figure 53.3a and b), optical densities for the three food models increased linearly, indicating apparent zero-order kinetics, but leveled at a plateau as the reaction proceeded.

The NEB extent in the trehalose model is highest at 33.2 and 44.1% RVP probably because of local heterogeneities. In fact, during preparation of the freeze-dried samples in Petri dishes, we found that the trehalose model showed different extents of browning between the top and bottom of the sample. Of course, the uptake of water at 33.2 and 44.1% RVP environments enhanced the NEB reaction. NEB was observed at a temperature lower than the glass-transition temperature in the present study, which might be related to the heterogeneities and porosity of the matrix structure.

When samples were stored at 54.5% RVP (Figure 53.3c), OD development was observed to occur in three stages. In the first stage, browning developed at a low rate, corresponding to the water sorption in Figure 53.1a, and loss of water contents was not observed, indicating no crystallization of component sugars at this stage. The optical density increased rapidly and linearly in the second stage, which was followed by the third plateau stage. Meanwhile, crystallization of the component sugars in the model systems was observed from the loss of water (Figure 53.1) occurring during this second stage. Crystallization of the component sugars in the model systems seemed to increase the browning rate. When component sugars crystallized, they formed a separated phase, resulting in phase separation in the systems and reactant molecules were assumed to be repelled or released from the crystal structure. In this case, it was also assumed that the concentration of the reactants increased in the remaining noncrystalline matrix during the crystallization period. Meanwhile, during crystallization, sorbed water was released, which also accelerated the molecular mobility in the matrix. All these factors accelerated the nonenzymatic browning in the model systems. In fact, during our experiments, different extents of browning in one sample at different locations were observed, which confirmed the local heterogeneous and uneven redistribution of the reactants after crystallization.

When the model samples were stored in a 65.6% RVP environment, OD of the three systems was observed at 11-, 24-, and then at 24-h intervals up to 240 h, as shown in Figure 53.3d. OD in the trehalose/reactant system increased linearly from 11 h, which was followed by a leveled-off plateau. In lactose/reactant systems, from 11 to 24 h, rate constant was low, then started to increase linearly and rapidly because of the crystallization of lactose, and finally ended at the plateau stage. In agreement with the water-sorption results for the model systems at 65.6% RVP (Figure 53.1), crystallization of component sugars was observed from the loss of sorbed water at 5, 21, and 56 h for trehalose/reactant, lactose/reactant, and lactose/trehalose/reactant systems, respectively. The rapid linearly increasing region of OD in the trehalose/reactant and lactose/reactant systems seemed to be directly

related to the crystallization of the component sugars in the systems. The slow loss of sorbed water in the lactose/trehalose/reactant system probably explained the continuous and linear increase in OD before the optical density leveled off. It should be mentioned that the rate constant (data not shown) in the trehalose/reactant system at 65.6% RVP was close to that in lactose/reactant system at 65.6% RVP, and also only slightly higher than that at 54.5% RVP. Typically, the maximum NEB rates in foods and model systems occur over a RVP range of 50–75% depending on the composition of the systems. The rate constant in the trehalose/reactant system at 65.6% RVP seemed to approach its maximum value.

Conclusions

The results of the present study have shown that the three model systems had similar glass-transition behaviors but different crystallization properties. Mixtures of lactose and trehalose showed delayed crystallization of component sugars. Addition of trehalose in lactose-based dairy products may delay crystallization during storage. The NEB rate was accelerated by crystallization and affected by the matrix composition. In the trehalose/reactant system, the NEB rate was higher than in lactose/trehalose/reactant and lactose/reactant systems. As a nonreducing sugar, trehalose has been suggested to be used as a new ingredient in food industry to prevent nonenzymatic browning, especially in the dairy industry. We found that the NEB rate was highest in the trehalose/reactant system and the reaction was accelerated by crystallization during storage. These results indicated that NEB was related to the composition of the matrix. When trehalose is used in dairy products, especially those containing proteins and reducing sugars that might cause browning, much attention should be paid in controlling the NEB reaction during storage and processing.

References

- Buera, M.P. and Karel, M. Effect of physical changes on the rates of nonenzymatic browning and related reaction, *Food Chem.*, 52, 167, 1995.
- Cardona, S., Schebor, C., Buera, M.P., Karel, M., and Chirife, C. Thermal stability of invertase in reduced-moisture amorphous matrices in relation to glassy state and trehalose crystallization, *J. Food Sci.*, 62, 105, 1997.
- Friedman, M. Food browning and its prevention: an overview, *J. Agric. Food Chem.*, 44, 631, 1996.
- Kouassi, K. and Roos, Y.H. Glass transition and water effects on sucrose inversion by invertase in a lactose-sucrose system, *J. Agric. Food Chem.*, 48, 2461, 2000.
- Labuza, T.P. and Braisier, W.M. The kinetics of nonenzymatic browning, *Physical Chemistry of Foods*, H.G. Schwartzberg and R.W. Hartel, eds., Marcel Dekker Inc, New York, pp. 595–649, 1992.

- Mazzobre, M.F., Soto, G., Aguilera, J.M., and Buera, M.P. Crystallization kinetics of lactose in systems co-lyophilized with trehalose: analysis by differential scanning calorimetry, *Food Res. Int.*, 34, 903, 2001.
- O'Brien, J. Stability of trehalose, sucrose and glucose to nonenzymatic browning in model systems, *J. Food Sci.*, 61, 679, 1996.
- Roos, Y.H. Water activity and plasticization, *Food Shelf Life Stability*, N.A.M. Eskin and D.S. Robinson, eds., CRC Press LLC, NewYork, pp. 3–36, 2001.

Chemical and Physical Stability of Disaccharides as Affected by the Presence of $MgCl_2$

Patricio Román Santagapita and María del Pilar Buera

CONTENTS

Introduction	663
Materials and Methods	664
Preparation of Model Systems	664
Methods	664
Results and Discussion	665
Acknowledgments	668
References	668

Introduction

It is well known that carbohydrates, particularly disaccharides, can provide significant protection to labile biomolecules during dehydration and their later storage and they are widely employed in biological, pharmaceutical, and food science (Leslie et al., 1995; Crowe et al., 1998). The action of the protective effect can be ascribed to both kinetic and specific effects. At the kinetic level, dehydroprotectants promote the formation of amorphous, glassy systems, inhibit crystallization, and influence the kinetics of deteriorative reactions upon storage. At the specific interaction level, protectants are believed to interact (mainly by hydrogen bonding) with biological structures and stabilize them, although by different mechanisms (Carpenter and Crowe, 1988; Crowe et al., 1996). Salts modify important properties of sugar systems, affecting their efficiency as protein stabilization agents (Carpenter et al., 1987; Mazzobre and Buera, 1999; Mazzobre et al., 2001) and their effect is of special interest because of their universal presence

in foods and in biological systems. Sugar-metal complexes can be formed in solution (Angyal, 1973; Morel-Desrosier et al., 1991) and it has been reported that salts affect the kinetics of sugar crystallization, Maillard reaction, and sugar hydrolysis. However, the several possible effects of salts on the kinetics of those important interrelated phenomena has not been analyzed simultaneously. The purpose of the present work was to analyze the effect of MgCl_2 on chemical and physical properties of two nonreducing disaccharides. Glass-transition temperatures and the kinetics of sugar hydrolysis, Maillard reaction, and crystallization were compared for sucrose and trehalose.

Materials and Methods

Preparation of Model Systems

Solid systems consisted of freeze-dried solutions containing 20% D(+)-sucrose or D(+)-trehalose and 1% L-glycine (Gly). The systems were prepared in phosphate buffer 0.07 M at pH 5.0. MgCl_2 was added in a 5:1 sugar:salt molar ratio; controls without MgCl_2 and without glycine were also prepared. Aliquots of 2.5 ml of each model were placed in 5-ml vials, frozen at -26°C for 24 h and immersed in liquid nitrogen immediately before freeze drying (which was performed in a Heto Holten A/S, cooling trap model CT 110 freeze-dryer, Heto Lab Equipment, Denmark, operating at a condenser plate temperature of -111°C and a chamber pressure of 4×10^{-4} mbar). After freeze-drying the systems were transferred to vacuum desiccators and exposed to water activity of 0.43 at $25^\circ\text{C} \pm 1^\circ\text{C}$ for 2 weeks.

Liquid systems were prepared with 40% of D(+)-glucose or D(+)-fructose and 1% L-glycine with and without MgCl_2 , in a 5:1 sugar:salt molar ratio. Aliquots of 2.5 ml of each model were placed in 5-ml vials. The systems were prepared in phosphate buffer 0.07 M, at pH 5.0. All reactants were analytical grade.

After humidification, the samples into vials were hermetically sealed and stored at $70^\circ\text{C} \pm 1^\circ\text{C}$ in a forced air-convection oven.

Methods

Water content was determined by difference in weight before and after humidification in vacuum ovens at $96^\circ\text{C} \pm 2^\circ\text{C}$ for trehalose systems and $62^\circ\text{C} \pm 3^\circ\text{C}$ for sucrose systems for 48 h. Sugar hydrolysis was analyzed by measuring the amount of glucose released during the incubation time by means of an enzymatic method. The progress of nonenzymatic browning (NEB) was followed by a browning index (BI) defined as absorbance readings at 445 nm multiplied by the dilution factor. Thermal transitions (glass-transition temperature (T_g), crystallization and melting)

were determined by dynamic differential scanning calorimetry (DSC) in the temperature range from -100 to 120°C , by means of a Mettler Toledo 822 equipment at a heating rate of $10^{\circ}\text{C}/\text{min}$. Direct observation of samples was performed with polarized light microscopy at $160\times$. All experiments were performed in duplicate.

Results and Discussion

After humidification, all the samples containing MgCl_2 had a higher water content and consequently lower T_g than those without salt (Table 54.1). This effect on water retention was more marked in sucrose systems than in trehalose systems. Sucrose and trehalose (without salt) crystallized during humidification at a_w 0.43, as indicated by the absence of glass transitions in the DSC thermograms and confirmed by microscopic observations with polarized light. As expected, while water release occurred during sucrose crystallization at 25°C , trehalose crystals retained 10% water (Table 54.1). A delay/inhibition of sugar crystallization was observed in the samples containing MgCl_2 and the corresponding glass transitions could be observed in the DSC thermograms (as indicated in Table 54.1).

Sugar hydrolysis and browning occurred during heat treatment at 70°C , and developed faster in sucrose samples containing MgCl_2 (Figure 54.1 and Figure 54.2). It is well known that trehalose is very stable to hydrolysis, and sucrose hydrolysis occurs much faster because of its molecular structure

TABLE 54.1
Water Content and Glass-Transition Temperature (T_g , Onset) Values
after Humidification ($t = 0$ h), and After 100 h of Storage at 70°C
($t = 100$ h) for $a_w = 0.43$

System ^a	W. C ^b (%) at $t = 0$ h	T_g ($^{\circ}\text{C}$) at $t = 0$ h	T_g ($^{\circ}\text{C}$) at $t = 100$ h
T	10.1	*	*
T-M	16.3	21.9	-35.3
T-G	10.4	*	*
T-M-G	15.4	-4.5	-28.3
S	1.9	*	-47.5
S-M	19.8	-55.3	-30.9
S-G	1.4	*	-29.6
S-M-G	20.5	-65.2	-30.2

* Highly crystalline sugar.

^a T, Trehalose; TM, Trehalose- MgCl_2 ; TG, Trehalose-Gly; TMG, Trehalose- MgCl_2 -Gly; S, Sucrose; SM, Sucrose- MgCl_2 ; SG, Sucrose-Gly; SMG, Sucrose- MgCl_2 -Gly.

^b W.C, water content.

and conformation (Schebor et al., 1999). Figure 54.1 shows that in the absence of salt, trehalose hydrolysis was almost negligible at the studied conditions while more than 1.5% sucrose had been hydrolyzed. However, the rate of hydrolysis of both sugars increased in the presence of salt (75% sucrose and 1% trehalose had been hydrolyzed in the MgCl_2 -containing samples, as shown in Figure 54.1).

It should be noted that sucrose samples without MgCl_2 , which were crystalline before heat treatment at 70°C , became highly plasticized on heating. This was visually observed and confirmed by their very low T_g values (Table 54.1). The decreased T_g can be explained by the combined effects of the hydrolysis products and of the water released during the Maillard reaction, which contributed to crystal solubilization and sample plasticization. However, sucrose samples with MgCl_2 were partially crystalline before heat treatment and became soluble at 70°C . Thus, their T_g values increased through sugar solubilization. Trehalose samples without salt remained crystalline after heat treatment because of their low degree of hydrolysis and of NEB. In the presence of MgCl_2 the samples were only partially crystalline either before or after heat treatment, but were also plasticized after heat treatment at 70°C . Because of the low rates of the concurrent reactions (NEB and hydrolysis) in trehalose systems, the influence of their products was not expected to affect dramatically the plasticization or crystallinity of the systems. In trehalose samples, water redistribution from the dihydrate crystals could have occurred at 70°C , promoting a decrease of the T_g values of the amorphous regions.

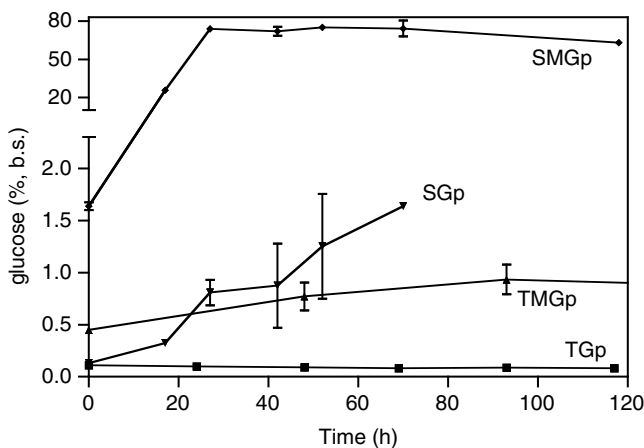
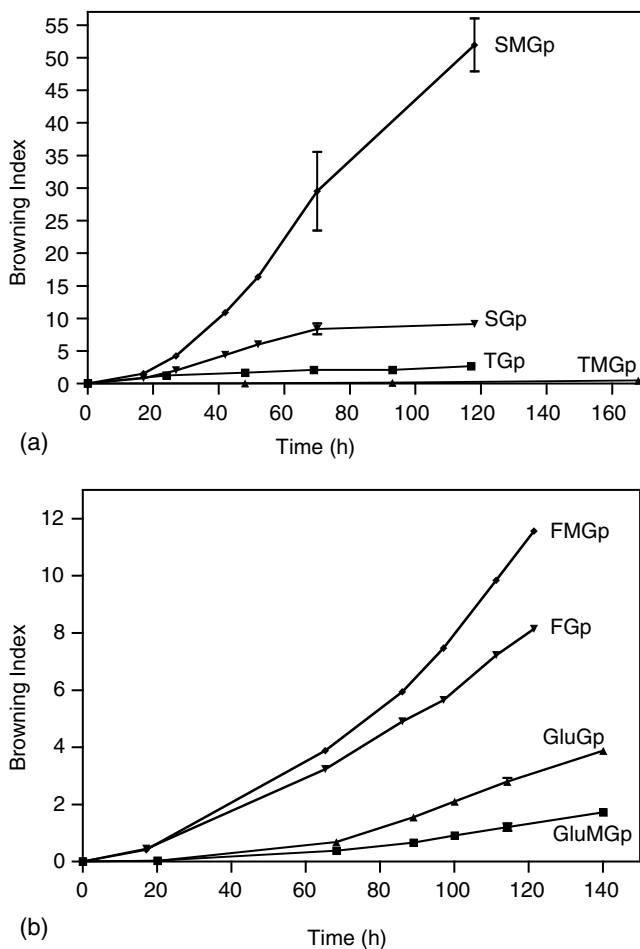


FIGURE 54.1

Percent of free glucose as a function of storage time at 70°C ($a_w = 0.43$). SMG: Sucrose- MgCl_2 -Gly; SG: Sucrose-Gly; TMG: Trehalose- MgCl_2 -Gly; TG: Trehalose-Gly. Bars represent the confidence intervals.

**FIGURE 54.2**

Nonenzymatic browning development as a function of storage time. Browning Index is defined as absorbance at 445 nm multiplied by the dilution factor. (a) $a_w = 0.43$; (b) liquid systems. SMG: Sucrose- MgCl_2 -Gly; FMG: Fructose- MgCl_2 -Gly; SG: Sucrose-Gly; FG: Fructose-Gly; GG: Glucose-Gly; TG: Trehalose-Gly; GMG: Glucose- MgCl_2 -Gly; TMG: Trehalose- MgCl_2 -Gly. Bars represent the confidence intervals.

While the effects of MgCl_2 on physical stability and on sugar hydrolysis were of similar qualitative influence for both disaccharides, nonenzymatic browning was accelerated in sucrose systems containing salt, while an inhibition of this reaction was observed in the presence of MgCl_2 in trehalose systems (Figure 54.2). The effect of MgCl_2 on browning rates was analyzed in systems containing glucose or fructose, the products of hydrolysis of the disaccharides. In systems of fructose as carbonyl source, the kinetics of the hydrolysis and NEB displayed the same behavior as sucrose systems.

Systems that contained only glucose as carbonyl source showed a kinetic behavior similar to trehalose systems (Figure 54.2). The interaction between glucose and the salt seems to be responsible for the inhibitory effect on browning. The formation of sugar–cation complexes has been previously reported and depends on the tautomeric forms and spatial position of hydroxyl groups of the sugar (Angyal, 1973). MgCl_2 may thus interact with glucose (product of trehalose hydrolysis) to a higher extent than with fructose (product of sucrose hydrolysis). Thus, in trehalose systems the inhibitory effect of the salt on NEB prevailed over the effect of increasing the concentration of reducing sugar caused by disaccharide hydrolysis, and the overall rate of NEB decreased. As well as effects at a supramolecular level, specific sugar–salt interactions at a molecular level affect physico-chemical stability of sugar products.

Acknowledgments

This work was supported by Agencia Nacional de Promoción Científica y Tecnológica (PICT 06-5066), CONICET (PIP 02734), and Universidad de Buenos Aires (X226).

References

- Angyal, S.J. Complex formation between sugars and metal ions, *Pure Appl. Chem.*, **35**, 131, 1973.
- Carpenter, J.F. and Crowe, J.H. The mechanism of cryoprotection of proteins by solutes, *Cryobiology*, **25**, 459, 1988.
- Carpenter, J.F., Crowe, L.M., and Crowe, J.H. Stabilization of phosphofructokinase with sugars during freeze-drying: characterization of enhanced protection in the presence of divalent cations, *Biochim. Biophys. Acta*, **923**, 109, 1987.
- Crowe, J.H., Carpenter, J.F., and Crowe, L.M. The role of vitrification in anhydrobiosis, *Ann. Rev. Physiol.*, **60**, 73, 1998.
- Crowe, L.M., Reid, D.S., and Crowe, J.H. Is trehalose special for preserving dry biomaterials?, *Biophys. J.*, **71**, 2087, 1996.
- Leslie, S.B., Israeli, E., Lighthart, B., Crowe, J.H., and Crowe, L.M. Trehalose and sucrose protect both membranes and proteins in intact bacteria during drying, *Appl. Environ. Microbiol.*, **61**, 3592, 1995.
- Mazzobre, M.F. and Buera, M.P. Combined effects of trehalose and cations on the thermal resistance of β -galactosidase in freeze-dried systems, *Biochim. Biophys. Acta*, **1473**, 337, 1999.
- Mazzobre, M.F., Longinotti, M.P., Corti, H.R., and Buera, M.P. Effect of the salts on the properties of aqueous sugar systems, in relation to biomaterial stabilization. 1. Water sorption behaviour and ice crystallisation/melting, *Cryobiology*, **43**, 199, 2001.

- Morel-Desrosier, N., Lhermet, C., and Morel, J.P. Interaction between cations and sugars. Part 6. Calorimetric method for simultaneous determination of the stability constant and enthalpy change for weak complexation, *J. Chem. Soc. Faraday Trans.*, 87, 2173, 1991.
- Schebor, C., Burin, L., Buera, M.P., and Chirife, J. Stability to hydrolysis and browning of trehalose, sucrose and raffinose in low-moisture systems in relation to their use as protectants of dry biomaterials, *Lebensm.-Wiss. Technol.*, 32, 481, 1999.

Evolution of Some Physical Properties of “Aceto Balsamico Tradizionale Di Reggio Emilia” during Long-Term Aging

Paola Pittia, Dino Mastrocola, and Enrico Maltini

CONTENTS

Introduction	671
Materials and Methods	672
Samples	672
DSC Analysis	672
Rheological Measurements	673
Analytical Determinations	673
Results and Discussion	673
References	676

Introduction

Balsamic vinegar, a typical product from the area of Modena and Reggio Emilia in the north center of Italy dates back to the X to XI century. According to Italian laws, traditional balsamic vinegar (Aceto Balsamico tradizionale di Reggio Emilia, Italy), is obtained from natural sugar alcoholic fermentation and acetic oxidation of unfermented, cooked, and concentrated crushed grape (*must*) ($\geq 30^\circ\text{Bx}$, according to Italian regulations) of the cv. Trebbiano, Spergola, Lambrusco, and other local grape-wine varieties. This takes place during long-term aging carried out in a series of small casks (*vaselli*) made of different kinds of wood (mulberry, cherry, juniper) and with progressively lower capacities. Every year the last and smallest cask of the sequence provides a few liters of the final product, which are compensated for by the product coming from the preceding barrel, and so backward until the biggest ones where an amount of fresh must is added.

Generally, evaporation accounts for about 10% loss in volume per year; an average of about 15 l of *Traditionale* can be obtained from 100 l of fresh must. The traditional balsamic vinegar must be aged for at least 12 years but it is possible to find some series of casks up to 100 to 200 years old. During the process, microbial metabolism and natural evaporation induce a marked increase in the concentration of derivatives of acetic fermentation, oxidation, and Maillard reaction, which impart the typical sensorial characteristics to the final product. Meanwhile, a change in some physical properties, including density and viscosity, takes place (Mascolo, 1990; Giudici et al., 1994; Meglioli et al., 1994; Anklam et al., 1998; Chiavaro et al., 1998; Del Signore, 1998; Del Signore et al., 2000; Calabrese et al., 2002; Cocchi et al., 2002; Zeppa et al., 2002).

The high added value of the traditional vinegar causes problems regarding its characterization with respect to common vinegar and “imitative” commercial products that are commonly called “balsamic vinegar”.

The aim of this paper is to evaluate the evolution of some thermal and rheological properties of the traditional balsamic vinegar during the aging process in order to obtain physical indices useful to differentiate the traditional product from the commercial imitative ones.

Materials and Methods

Samples

Six samples taken from the same acetification battery of six casks (1–6; 6: younger; 1: older) of “Aceto Balsamico Tradizionale di Reggio Emilia” aged between 3 and 25 years, provided by a local producer, were analyzed. Two balsamic vinegars (C), representative of the commercial, nontraditional, products were purchased in a local market.

DSC Analysis

Phase transitions were analyzed using a DSC (Mettler TA4000, Mettler, Greifensee, Switzerland), equipped with a TC11 TA processor and a DSC30 cell. The instrument was calibrated for temperature with *n*-hexane, water, and indium and for heat flow using indium (heat of fusion 28.45 J/g). Thermograms were analyzed for (a) the glass-transition temperatures (onset) in nonannealed states (T_g); (b) the glass-transition temperature of the maximally freeze concentrated amorphous solution (T'_g) after annealing; (c) the onset temperature of ice melting (T'_m); (d) the onset temperature of ice recrystallization in nonannealed states referred to as “irruptive recrystallization” (T_R). Total ice melting (ΔH_m) was obtained by integration.

Rheological Measurements

Flow curves were evaluated using a stress-controlled Reologica Stresstech rheometer equipped with a bob-and-cup geometry at 20°C. A power law model was used for curve fitting over a shear rate range of 0.1 to 159 sec⁻¹. Data reported are the average of three replications.

Analytical Determinations

pH was measured using a AMEL 334-B pH meter. Acidity (% acetic acid) was determined according to official Italian methods (Meglioli et al., 1994). Total soluble matter content was evaluated with a refractometer and reported as °Bx. Total sugar content was determined according to Fehling method.

Results and Discussion

Chemical characteristics of the differently aged traditional balsamic vinegar and of commercial balsamic product are reported in Table 55.1. In the former, from an initial total soluble matter of 35.7°Bx of the larger cask (sample 6), long-term aging and refining led to values of about 70°Bx in the product of the last, small capacity cask (sample 1). This is the consequence of water evaporation through the wooden casks that acts as a selective membrane during aging. Both biological and chemical processes taking place during aging are responsible for the changes in pH and acidity.

Long-term aging influenced markedly the thermal behavior of vinegar as evidenced by DSC analyses (Figure 55.1, Table 55.2). In the samples from the first two larger casks (6 and 5), freezing occurs after cooling and aging is mainly associated with a decrease in the freezable water (Table 55.2). At increasing aging time, freezing of water occurred only upon rewarming

TABLE 55.1

Chemical Properties of Samples of Balsamic Vinegar during Aging and of the Two Commercial Products

Sample	°Bx	Sugar Concentration (g/l)	pH	Acidity (% acetic acid) (g/l)
6	35.5	180.0	2.49	58.0
5	39.0	301.1	2.51	60.0
4	44.5	452.3	2.56	62.2
3	57.0	551.2	2.61	64.1
2	60.0	604.0	2.69	65.3
1	70.0	680.2	2.81	68.2
C	28.0	167.0	3.05	59.1

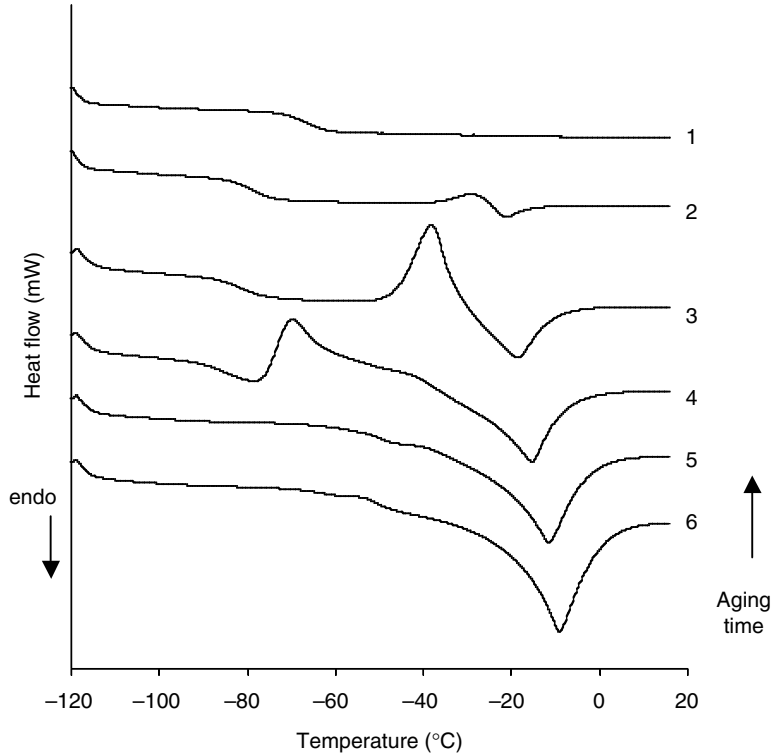
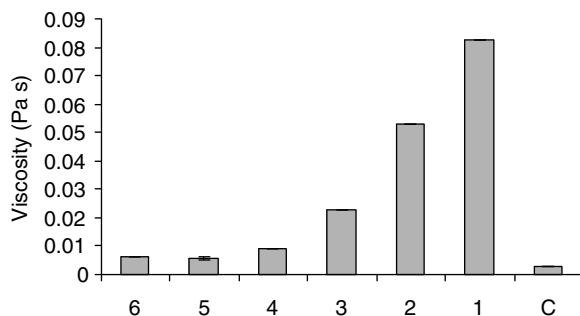


FIGURE 55.1
Thermograms of traditional balsamic vinegar during aging.

TABLE 55.2
 T_g , T'_g , T'_m , T_R and Melting Enthalpy of Water (ΔH_m) of Traditional Balsamic Vinegars Differently Aged and of Commercial Balsamic Vinegar

Sample	T_g	T'_g	T'_m	T_R	ΔH_m J/g
6	—	—	−52.0 ^a	—	92.6 ^e
5	—	—	−50.3 ^a	—	76.8 ^d
4	−92.0 ^d	−68.0 ^a	−50.0 ^a	−76.0	68.1 ^c
3	−88.0 ^c	−65.3 ^a	—	−50.0	36.6 ^b
2	−85.0 ^b	—	—	−37.0	4.1 ^a
1	−75.0 ^a	—	—	—	—
C	—	−75.6 ^b	−49.5 ^a	—	142.6 ^f

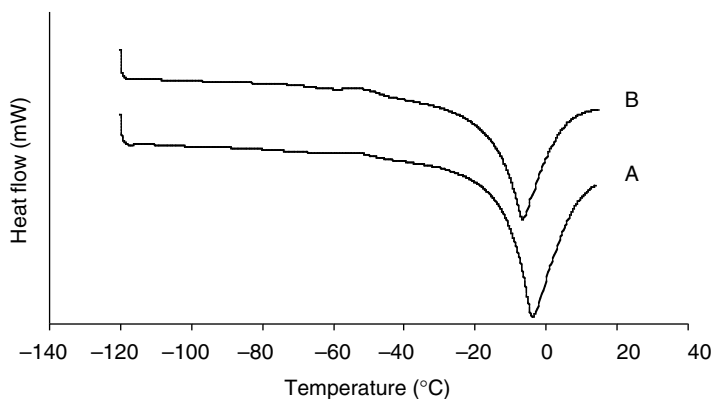
^{a–f} Different letters in the same column indicate statistical difference ($p < .05$) according to Student t -test.

**FIGURE 55.2**

Viscosity of differently aged traditional balsamic vinegar (samples 1–6) and of commercial balsamic products (C, average of two samples).

(samples 4, 3, and 2); after annealing, the glass-transition temperature of the maximally freeze-concentrated phase (T'_g) was around 66°C (data not shown). In the oldest sample (25 years old, sample 1) only a glass transition was detected. It can be noticed that at increasing concentration and T_g of the progressively aged vinegar, an increase of the temperature at which ice crystallization occurs (T_R) was associated. It was also observed that in nonannealed states, recrystallization occurred at an increasing $(T - T_g)$ (i.e., at a decreasing viscosity) as the initial solutes concentration increased. In particular, for samples 2, 3, and 4, $(T - T_g)$ was equal to 48, 38, and 16°C , respectively.

Viscosity values of traditional balsamic vinegar at different aging times and of commercial products are shown in Figure 55.2. Power law modeling of flow curves indicated that all samples exhibit Newtonian behavior, with viscosity ranging from 6.0×10^{-3} to 8.3×10^{-3} Pa sec, reflecting the increase of solids concentration. The longer the aging, the higher the viscosity of the traditional

**FIGURE 55.3**

Thermograms of two commercial balsamic vinegars.

balsamic product which, in the older ones, looks like a viscous, highly concentrated sugar syrup. It should be stressed that viscosity is among the main factors that impart the typical sensorial properties to the product.

As regards the commercial products, thermograms showed a marked endothermal melting peak whose enthalpy was significantly higher than that observed in all the traditional products (Figure 55.3, Table 55.2). Viscosity was extremely reduced and significantly lower with respect to the traditional product. Actually, physical properties of the commercial vinegars derive from a different formulation and production process, as also indicated by their chemical properties (Table 55.1).

On the basis of the results it could be evidenced that traditional balsamic vinegar is markedly different as compared to the balsamic commercial products. Moreover, changes in composition taking place during aging induce significant modification in both thermal and rheological properties, which could contribute to characterization of both the production process and typical properties of the traditional balsamic vinegar manufactured according to Italian regulations.

References

- Anklam, E., Lipp, M., Radovic, B., Chiavaro, E., and Palla, G. Characterisation of Italian vinegar by pyrolysis-mass spectrometry and a sensor technique, *Food Chem.*, 61, 243, 1998.
- Calabrese, M., Stancher, B., and Del Signore, A. Proline isomerisation in traditional balsamic vinegar from Modena as a function of ageing period, *Ital. Food Beverage Technol.*, 27, 11, 2002.
- Chiavaro, E., Caligiani, A., and Palla, G. Chiral indicators of ageing in balsamic vinegars of Modena, *Ital. J. Food Sci.*, 10, 329, 1998.
- Cocchi, M., Lambertini, P., Mancini, D., Marchetti, A., and Ulrici, A. Determination of carboxylic acids in vinegars and in Aceto Balsamico Tradizionale di Modena by HPLC and GC methods, *J. Agric. Food Chem.*, 50, 5255, 2002.
- Del Signore, A. Differentiation of balsamic vinegars using physical indexes, *J. Commodity Sci.*, 37, 51, 1998.
- Del Signore, A., Stancher, B., and Calabrese, M. Characterisation of Balsamic vinegars by aminoacid content using a multivariate statistical approach, *Ital. J. Food Sci.*, 12, 317, 2000.
- Giudici, P., Barbagallo, R.N., Altieri, C., and Masini, G. Origine ed evoluzione degli acidi organici durante l'invecchiamento dell'aceto balsamico tradizionale, *Ind. Bevande*, 23, 569, 1994.
- Mascolo, A. L'aceto Balsamico di Modena, *Quadr. Vitic. Enol.*, 14, 101, 1990.
- Meglioli, G., Parigini, G., Tedeschi, M., and Pesenti, G. L'aceto balsamico tradizionale di Reggio Emilia. Studio delle caratteristiche chimiche, chimico-fisiche, *Ind. Bevande*, 26, 41, 1994.
- Zeppa, G., Giordano, M., Gerbi, V., and Maglioli, G. Characterisation of volatile compounds in three acetification batteries used for production of "Aceto Balsamico Tradizionale di Reggio Emilia", *Ital. J. Food Sci.*, 14, 247, 2002.

56

Incorporation of Solute in the Ice Phase during Freezing

Julia Telford and Peter Lillford

CONTENTS

Introduction	677
Experimental.....	678
Computational Modeling	679
Results.....	679
Computational Modeling	679
Experimental.....	682
Discussion	682
References	682

Introduction

During a freezing process, ice crystallizes out of solution at a rate largely dependent on the rate of removal of the heat of crystallization. If this rate is faster than the diffusion of solutes away from the growing ice front, then the ice may entrap areas of concentrated solution. If the solute interacts with/adsorbs to the growing ice front, it may partition itself between the solution and the grain boundaries of the ice.

A technique has been developed that investigates the effect of the growth rate of a polycrystalline ice hemisphere from solution on the incorporation levels of solutes into the ice phase. The technique uses an adaptation of apparatus designed by Charles Knight to determine ice-binding sites for peptides (Knight, 1991).

Experimental

Materials: Sucrose and sodium chloride (NaCl) were purchased from Fisher Scientific (Loughborough, UK). Bovine serum albumin (BSA), locust bean gum (LBG), and xanthan gum were purchased from Sigma-Aldrich (Poole, UK). Polyvinyl alcohols (PVA), with average molecular weight ranges of 9–10, 16–23, 31–50, 50–85, and 85–146 K, were purchased from Aldrich Chemicals (Gillingham, UK). A type III fish antifreeze peptide from ocean pout, average molecular weight 6.5 kda (AFP III), was purchased from A/F Proteins (Waltham, MA). A 5-mg/ml solution of each solute was prepared by dissolving the material in deionized water with stirring and heating as appropriate.

Methods: The cold finger apparatus for continuous freezing is shown in Figure 56.1. The equipment consisted of a brass cold finger connected to a circulating cooling bath set to the desired experimental temperature. The cold finger was placed in a small beaker of distilled water cooled to 5°C, and a thin film of ice was allowed to form on the cold finger before it was removed from the water. The test solution was placed in a 250-cm³ insulated dish, and the cold finger was placed in the test solution. The initial temperature of the test solution was 5°C. Ice grew onto the cold finger and formed a hemisphere. At the end of the experiment, the ice hemisphere was

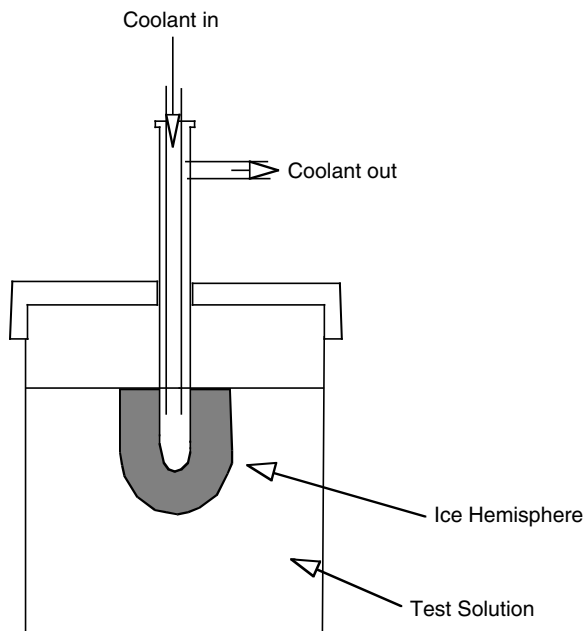
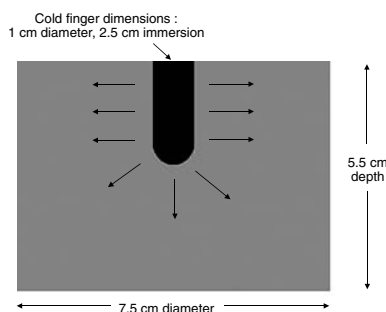


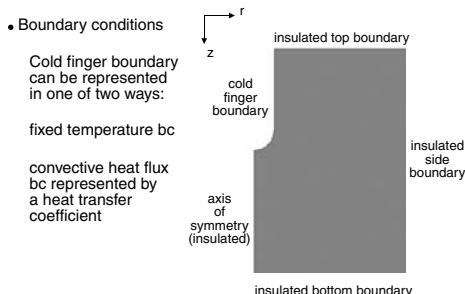
FIGURE 56.1

Cold finger apparatus for ice-crystal growth.

Geometry of Cold Finger Freezing Experiments



Cold Finger Freezing Experiment Simulation Model

**FIGURE 56.2**

Computational thermal model.

removed from the solution and melted off the cold finger by raising the cold finger temperature to 5°C. The ice hemisphere was dried with a tissue to remove any solution from its surface. The amount of solute in each phase was measured by freeze-drying the separated phases and weighing the amounts of solid remaining. The results are quoted as apparent partition coefficients, which were calculated as follows:

$$\text{Partition Coefficient}_{\text{ICE PHASE}} = \frac{\text{Solute Concentration}_{\text{ICE PHASE}}}{\text{Solute Concentration}_{\text{ORIGINAL SOLUTION}}}$$

Computational Modeling

A computational thermal model was developed (Figure 56.2) to simulate the growth of the ice hemisphere for different cold finger coolant temperatures. Thermally, heat is removed from the test solution at the surface of the cold finger by the coolant circulating through the cold finger, and consequently, the resulting heat transfer is not expected to be one-dimensional in character. This ruled out the use of relatively simple one-dimensional heat transfer models, and it was decided to develop the thermal model in the MARC finite element package (MSC Software Corporation, Palo Alto, CA).

Results

Computational Modeling

An example of the results of modeling compared with experimental results for pure water is shown in Figure 56.3 for a cold finger temperature of -20°C. The growth data generated by the model show good agreement with

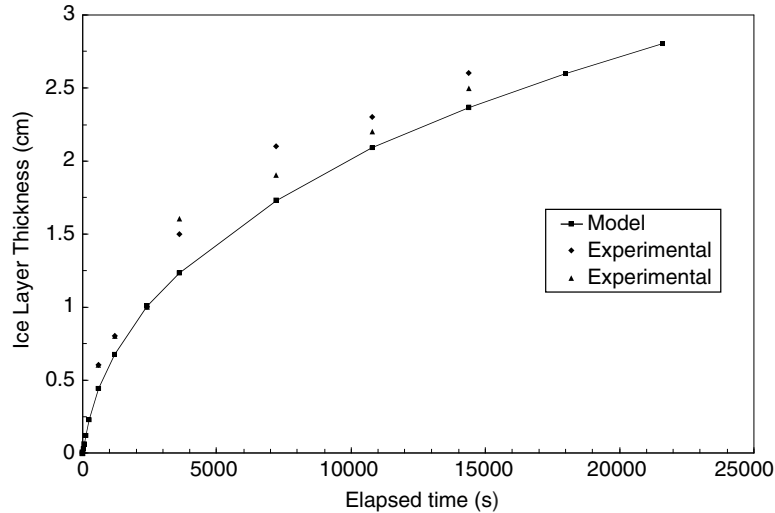


FIGURE 56.3
Comparison of results from model with experimental measurements for ice growth in pure water using a cold finger temperature of -20°C .

experimental data for pure water. The ice-layer thickness is measured from the cold finger to the outer edge of the top of the ice hemisphere in several places, and an average value is calculated. From the model data, average rates of growth were calculated for the following radial growth

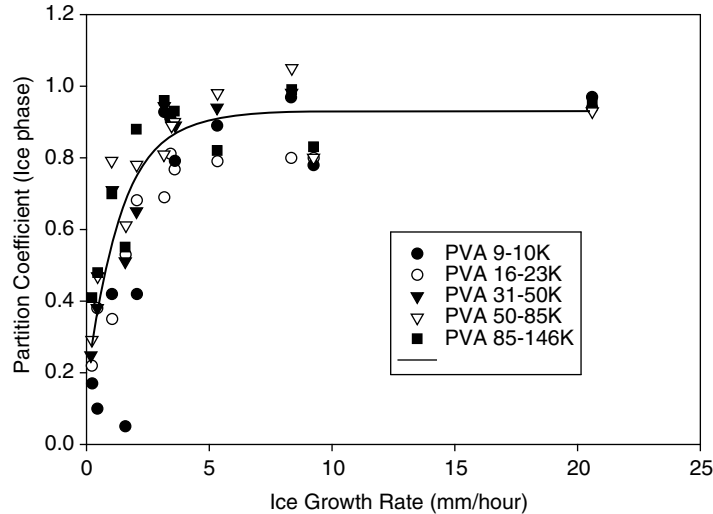
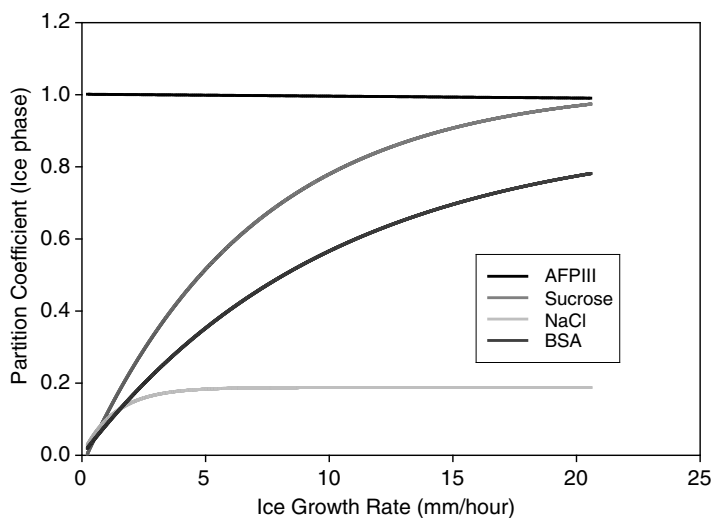
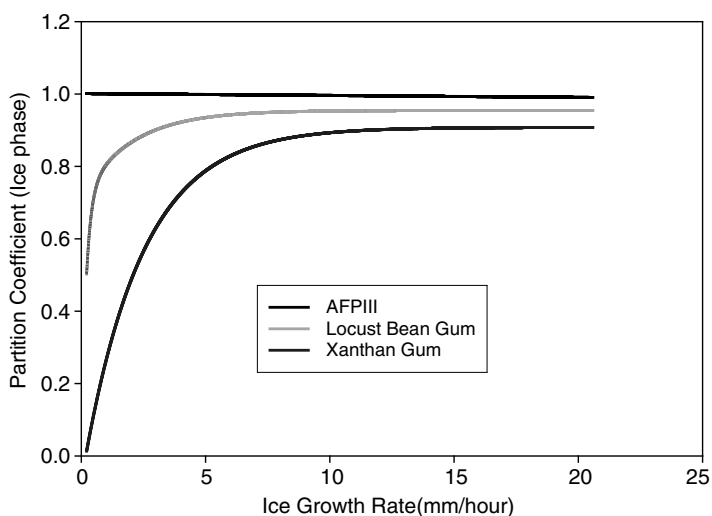


FIGURE 56.4
Possible nonkinetic effects with PVAs.

**FIGURE 56.5**

Adsorption vs kinetic trapping.

distances: 0–5, 5–10, 10–15, and 15–20 mm. The growth rate was calculated by determining the gradient of the growth curve over the relevant growth period. Different cold finger temperatures were used to give a range of growth rates.

**FIGURE 56.6**

Examples of results for large molecules.

Experimental

Typical results for freezing of PVA polymers of varying molecular weight are shown in Figure 56.4. All show some kinetic trapping at fast growth rates (>5 mm/h), but the polymer is excluded from ice at the slowest growth rates. The polymer exclusion is not dependent on the molecular weight of the polymer, which may suggest some nonkinetic effects.

The results for food polymers and small molecules are shown schematically in Figure 56.5 and Figure 56.6. These two graphs show possible kinetic and nonkinetic solute partitioning.

Discussion

The development of the computational model allows positions in the growing ice to be equated directly with ice-growth rates, allowing a complete range of growth rates to be sampled in a single experiment. Likewise, the partition coefficients of molecules can be measured in the same experiment by sampling the unfrozen material and comparing its concentration with the original composition of the unfrozen material. Furthermore, it is possible to examine differential partitioning from a complex mixture of solutes in the same experiment.

Conspicuously, different from all other polymers is the antifreeze, which at *all* freezing rates partitioned equally between ice and the unfrozen solution; i.e., it appears to be equally “soluble” in ice and water. This result confirms that the molecule can interact with the ice phase over a kinetically long period of time. It is not known from these results whether the mechanism is a permanent adsorption; this would require supporting evidence from other physical measurement techniques. All the other solutes show a rate-dependent mechanism of partitioning, presumably dominated by the diffusion rates of the molecules. LBG and PVA may exhibit some nonkinetic partitioning properties, but this has not been conclusively proven.

The results have implications for the structures in products. For example, for quiescently frozen products, the data produced here can be used to identify possible separation of solute components as freezing progresses. This implies that the frozen phase will change in composition and properties, dependent on the distance from and temperature of the cold sink.

References

Knight, C.A., Cheng, C.C., and DeVries, A.L. Adsorption of alpha-helical antifreeze peptides on specific ice crystal surface planes. *Biophys. J.*, 59, 409, 1991.

Enthalpy Relaxation in Freeze-Concentrated Sucrose–Water Glasses

Chiharu Inoue and Toru Suzuki

CONTENTS

Introduction	683
Materials and Methods	684
Results and Discussion	685
Conclusion	687
References	687

Introduction

The glassy state is regularly observed in food (Blanshard and Lillford, 1993, Simatos et al., 1994). Food is generally assumed to be stable in the glassy state over a practical time scale. Recently, enthalpy relaxation of the glassy state has been reported on food materials such as starch (Kim et al., 2003) and sugars (Kawai et al., 2004). Kim et al. (2003) evaluated the water vapor permeability of the thin layer of glassy starch after various aging times of the film and showed that it decreased with increase in the aging time (Kim et al., 2003). This suggests that quality change can happen in food even when it is stored at temperatures below the T_g . Although the enthalpy relaxation has been widely referred in the field of polymer science in relation to the stability of glassy state, there is much less data on the enthalpy relaxation of glassy food materials.

The enthalpy relaxation of glassy pure sugars (glucose, sucrose, maltose, and trehalose) has been reported and analyzed by the theories proposed in the field of polymer science (Kawai et al., 2004). The activation energy was shown to be a useful index comparing the stability of various glassy sugars, which may be considered as a model for food systems. These studies showed

that glucose glass had the smallest activation energy of the enthalpy relaxation and trehalose had the largest, with sucrose and maltose being intermediate. It was proposed that the stability of these glassy sugars could depend on molecular size and structure, which in turn could influence their ability as stabilizers. The results from the studies suggest that various glassy food systems are worthwhile investigating in terms of the enthalpy relaxation to evaluate their stability.

In many frozen foods, glass transition takes place at maximally freeze concentrated concentration (C_g') at a temperature T_g' , which can be considerably lower than the freezing point of water (Levine and Slade, 1990, Inoue and Ishikawa, 1997). Thus, it has been generally assumed that it is possible to minimize the degradation of frozen food during storage by maintaining it below T_g' . Enthalpy relaxation of freeze-concentrated glass has been observed by DSC on galactose–water (Blond, 1989) and trehalose–water (Pyne et al., 2003). However, there is not sufficient data to be able to calculate the activation energy of the relaxation in order to consider the stability of the glassy state.

The objective of the present study is to investigate enthalpy relaxation of a very common model food system, sucrose–water, by using DSC. In accordance with the previous study, the Kohlraush–William–Watts (KWW) equation is applied to calculate the relaxation time and the activation energy of the enthalpy relaxation.

Materials and Methods

Sucrose (food ingredient grade) and distilled water were weighed and mixed to give 40 wt% sucrose. The mixture was heated and completely dissolved. Any water that evaporated during this process was determined by weighing and added back to the solution.

A Perkin Elmer DSC7 was used to make measurements. A sample of the solution (20 μ l) was sealed in an aluminum pan and this was then cooled from 10 to -35°C , held at this temperature for 30 min before being further cooled from -35 to -70°C , then aged at a temperature (-70 , -65 , -60 , or -55°C) for 24 to 144 h, cooled back to -70°C , and heated to 10°C . The rates of cooling and heating were all $3^\circ\text{C}/\text{min}$.

Analysis of the enthalpy relaxation: the enthalpy relaxation time and the activation energy were calculated by KWW in accordance with the previous work (Kawai et al., 2004). The KWW theory was originally proposed in dielectric relaxation study by Williams and Watts (1970), then applied in the form of nonexponential function such as the enthalpy relaxation. In KWW theory, the enthalpy relaxation, ΔH_{relax} , which corresponds to the peak area given from the enthalpy relaxation is expressed by the equation

$$\Delta H_{\text{relax}} = \Delta H_{\infty} [1 - \exp[-(t/\tau^{\text{KWW}})\beta]] \quad (57.1)$$

where: t , τ^{KWW} and β are the aging time, characteristic enthalpy relaxation time, and the nonexponential parameter, respectively. The ΔH_{∞} is the maximum enthalpy recovery at the given temperature and calculated from the following equation:

$$\Delta H_{\infty} = \Delta C_p(T_g - T) \quad (57.2)$$

where: ΔC_p is the specific heat change at T_g obtained from the DSC measurements. T is the aging temperature in Kelvin.

Results and Discussion

Typical DSC heating curves of 40 wt% sucrose are shown in Figure 57.1. The curve (without aging) shows three main features in the heat flow; an endothermic step-wise change identified as glass to rubber transition of the freeze-concentrated matrix, a small endothermic peak caused by the onset of ice melting, and a large endothermic peak identified to be melting of the majority of the ice (Figure 57.1). The T_g^{onset} and ΔC_p were detected to be -47°C and $0.433 \text{ J}/(\text{g sample K})$, respectively. These features are similar to previously reported results for a sucrose solution (Izzard et al., 1991). The DSC curve of the aged 40 wt% sucrose solution has an endothermic peak overlapping with the glass transition. The curve of repeated scan without aging (data not shown) did not show the peak and gave a similar trace to that of the nonaged glass. These results suggest that this peak appeared during

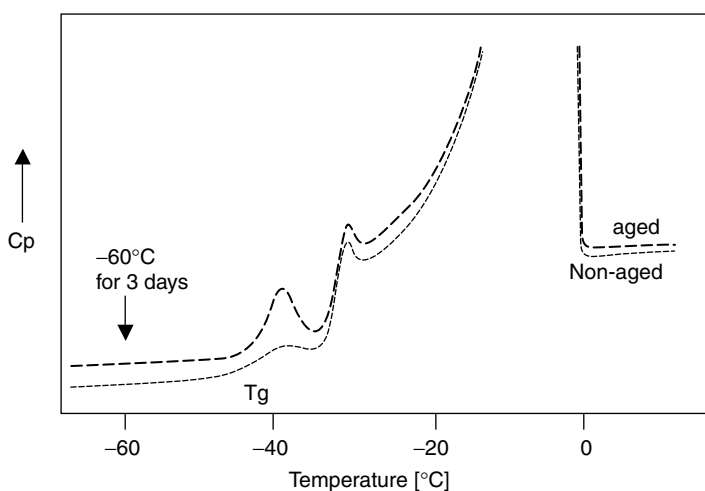


FIGURE 57.1

DSC heating curves of 40 wt% sucrose.

the aging process in the glassy state, and may be the same enthalpy relaxation commonly observed with synthetic polymers.

In the previous studies (Kawai et al., 2004), a series of analyses was made to relate molecular mobility to the enthalpy relaxation of freeze-concentrated sucrose–water glass. Also in the previous study (Liesebach et al., 2003), the concentration of the freeze-concentrated glassy state was suggested to be about 80% sucrose, and thus ΔC_p can be expressed to be 0.833 J/(g 80% sucrose K). The peak area of the enthalpy relaxation, ΔH_{relax} in J/g 80% sucrose was plotted vs. time (Figure 57.2), where the peak area was calculated from the differential curve given by subtracting the nonaged curve from the aged one. The enthalpy relaxation increases with aging time and is greater for higher aging temperatures (Figure 57.2). This result is similar to that reported for pure sugar glasses (Kawai et al., 2004) and polymer glasses (Cowie and Ferguson, 1989). The data for an aging temperature of -70°C showed large scattering under the conditions used in the experiments and thus were not analyzed further (data not shown).

The KWW parameters of τ^{KWW} and β were calculated from Equation 57.1. By using these values, the enthalpy relaxation, ΔH_{relax} , was also calculated from Equation and plotted in Figure 57.2 as dashed lines, which shows a good fit. From the Arrhenius plot of τ^{KWW} for the 40% sucrose solution, the activation energy, ΔE^{KWW} , is calculated to be 125.2 kJ/mol and considerably smaller than that reported for pure sucrose of 214.5 kJ/mol (Kawai et al., 2004). This suggests that the molecular arrangement in the sucrose–water glass might be different from that in a pure sucrose glass, at least in the nonaged state, because it may have more molecular motion and less stability

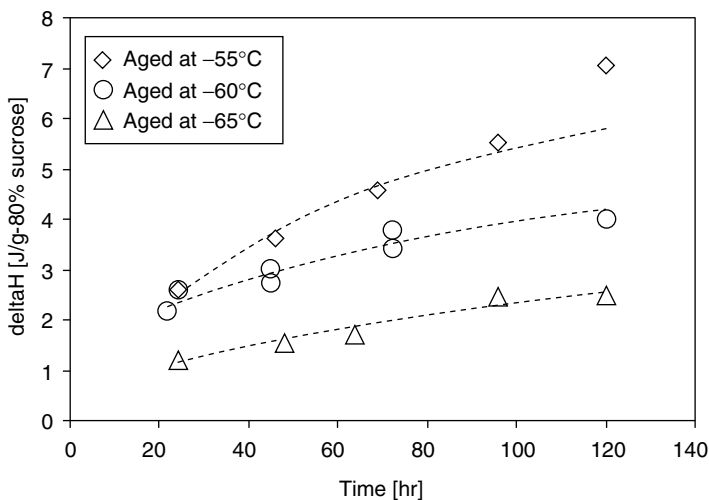


FIGURE 57.2

The enthalpy relaxation, ΔH (J/g 80% sucrose), and aging time. Dashed lines were obtained by fitting of the KWW equation.

than pure sucrose. The β parameter was calculated to be 0.97, 0.41, and 0.62 for -55 , -60 , and -65°C , respectively, which is similar to that reported for pure sucrose glass, 0.53 to 0.62 (Kawai et al., 2004).

Conclusion

Enthalpy relaxation of freeze-concentrated sucrose–water glass was regularly observed under the condition and investigated by DSC. The data have been successfully analyzed by KWW theory. The freeze-concentrated glass has a smaller activation energy than pure sucrose glass, which suggests it to be less stable than pure sucrose glass.

References

- Blanshard, J.M.V. and Lillford, P.J. *The Glassy State in Foods*, 1993.
- Blond, G. Water-galactose system: supplements state diagram and unfrozen water, *Cryo-Letters*, 10, 299, 1989.
- Cowie, J.M.G. and Ferguson, R. Physical aging studies in poly (vinyl methyl ether). 1. Enthalpy relaxation as a function of aging temperature, *Macromolecules*, 22, 2307, 1989.
- Inoue, C. and Ishikawa, M. Glass transition of tuna flesh at low temperature and effect of salt and moisture, *J. Food Sci.*, 62, 496, 1997.
- Izzard, M.J., Ablett, S., and Lillford, P.J. Calorimetric study of the glass transition occurring in sucrose solutions, *Food Polymers, Gels and Colloids*, E. Dickenson, ed., The Royal Society of Chemistry, Cambridge, pp. 289, 1991.
- Kawai, K., Hagiwara, T., Takai, R., and Suzuki, T. Comparative investigation by two analytical approaches of enthalpy relaxation for glassy glucose, sucrose, maltose and trehalose, *Pharm. Res.*, 2004, in press.
- Kim, Y.J., Hagiwara, T., Kawai, K., Suzuki, T., and Takai, R. Kinetic process of enthalpy relaxation of glassy starch and effect of physical aging upon its water vapor permeability property, *Carbohydr. Polym.*, 53, 289, 2003.
- Levine, H. and Slade, L. Cryostabilization technology; thermoanalytical evaluation of food ingredients and systems, *Thermal Analysis of Foods*, p. 221, 1990.
- Liesebach, J., Rades, T., and Lim, M. A new method for the determination of the unfrozen matrix concentration and the maximal freeze-concentration, *Thermochim. Acta*, 401, 159, 2003.
- Pyne, A., Surana, R., and Suryanarayanan, R. Enthalpis relaxation in frozen aqueous trehalose solutions, *Thermochim. Acta*, 405, 225, 2003.
- Simatos, D., Blond, G., and Martin, F. Influence of macromolecules on the glass transition in frozen systems, *Food Macromolecules and Colloids*, p. 519, 1994.
- Williams, G. and Watts, D.C. *Trans. Faraday Soc.*, 66, 80, 1970.

State Diagram for Freeze-Dried Plum and Glass Transitions of Plum Skin and Pulp

Vânia Regina Nicoletti Telis, Paulo José do Amaral Sobral,
and Javier Telis-Romero

CONTENTS

Introduction	689
Materials and Methods	690
Results and Discussion	691
Conclusions	693
Acknowledgments	694
References	694

Introduction

The physical state of foods, including sugars and biopolymers, has received increasing attention because of its importance to food processing and storage (Roos and Karel, 1991a). In Food Polymer Science, one of the most important events used to characterize the physical state is the glass transition, which involves transition from a “glassy” solid to a “rubbery” liquid-like state (Roos and Karel, 1991a; Slade and Levine, 1991). This change occurs within a temperature range characteristic for each material and the mid-point temperature of such change is taken as the glass-transition temperature (T_g). Because there is a great increase on molecular mobility across T_g , it is hypothesized to be an important parameter for storage stability and quality of dried or frozen products (Zeleznek and Hosene, 1987; Inoue and Ishikawa, 1997). For frozen food, another important property is the T_g of the maximally freeze-concentrated matrix (T'_g). The minimal moisture content at which T'_g is visible corresponds to the unfreezable water content (X'_g). When submitted to slow freezing, the system will consist of ice crystals embedded

in an amorphous glass matrix with a characteristic glass/rubber transition temperature, $T'_{g'}$, above which it begins to lose quality (Slade and Levine, 1991). The breakdown of structure above a "collapse" temperature (related to T_g) during freeze-drying is considered a major contributor to product quality deterioration (Anglea et al., 1993).

The T_g plotted versus the product moisture content gives the glass-transition curve. If the melting temperature is also added to this plot, a state diagram is obtained. Complete state diagrams for some natural foods have been published, but they are still limited in number, being found only for onion, grape, and strawberry (Roos, 1987; Sá and Sereno, 1994), apple (Sá et al., 1999; Bai et al., 2001), pineapple (Telis and Sobral, 2001), persimmon (Sobral et al., 2001), and tomato (Telis and Sobral, 2002).

The plum is a worldwide-distributed fruit and can be consumed either fresh or dried, and also as an ingredient of many prepared foods. Studies on drying kinetics (Sabarez et al., 1997; Gabas et al., 2002) and sorption isotherms (Gabas et al., 2000) of plums may be found in literature, but no works were found concerning freezing or freeze-drying processes.

The objective of this work was to study the state transitions of freeze-dried plum and to draw the corresponding state diagram for this material. Glass transitions of separated plum skin and pulp were also investigated, aiming to clarify the effect of each of these fractions on the behavior of the whole fruit.

Materials and Methods

Black Diamond plums (*Prunus domestica*) were obtained at the local market. Analysis of the fruits resulted in 16.65 ± 0.89 g of total sugars/100 g moist sample, including 5.20 ± 0.24 g of reducing sugars/100 g moist sample, and 6.21 ± 0.44 g of pectin/100 g dry matter. The fruits had their stone removed and were cut in small pieces, being immediately frozen by immersion in liquid nitrogen and freeze-dried in a Heto HD1 (Heto Lab Equipment). The separated skin and pulp of some fruits were also frozen and freeze-dried.

Freeze-dried samples (1.0 to 1.6 g) were equilibrated over saturated salt solutions (LiCl, MgCl_2 , K_2CO_3 , $\text{Mg}(\text{NO}_3)_2$, NaNO_2 , NaCl, $(\text{NH}_4)_2\text{SO}_4$, KCl, BaCl_2) to give water activities (a_w) between 0.11 and 0.90 at 25°C (Spiess and Wolf, 1983). Samples of $a_w > 0.90$ were obtained by mixing freeze-dried samples with distilled water in order to give 54 to 80% moisture content (wet basis). These samples were equilibrated at 4°C for 24 h before DSC analysis (Sobral et al., 2001; Telis and Sobral, 2001). In addition, a_w was measured at 25°C in an AquaLab CX2 (Decagon Devices, Inc.), whereas equilibrium moisture contents were determined in a vacuum oven at 70°C for 48 h.

For DSC analysis, samples of about 10 mg conditioned in hermetic TA aluminum pans were heated at 10°C/min, between -120 and 100°C , in inert atmosphere (45 ml/min of N_2) in a DSC TA2010 controlled by a TA5000 module (TA Instruments, New Castle, DE). The reference was an empty

aluminum pan. Liquid N_2 was used for sample cooling before the run. When a devitrification peak occurred, the sample was annealed at the devitrification peak temperature for 30 min before second scan. T_g was calculated as the point of inflexion in the DSC curve base line. The exotherm peak temperature was taken as the devitrification temperature (T_d) and the endotherm onset temperature was taken as an approximate ice melting temperature (T_m). These properties were calculated using the Universal Analysis V1.7F software (TA Instruments). Analyses were made in triplicate and all weighing (± 0.01 mg) was accomplished on analytical balance (Analytical Plus, Ohaus).

Results and Discussion

The results of DSC analyses of freeze-dried plum (skin and pulp at the natural proportion) presented different behaviors for each a_w domain. At $a_w \leq 0.75$, two glass transitions (T_g) were visible (Figure 58.1a) as a deviation in base line and shifted toward lower temperatures with increasing moisture content and a_w caused by the plasticizing effect of water (Slade and Levine, 1991). The first one, clearly visible at lower temperatures, was attributed to the glass transition of a matrix formed by sugars and water. The second one, less visible and less plasticized by water, was probably caused by macromolecules of the fruit pulp. Two T_g are normally visible in systems formed by blends of polymers (Verghoogt et al., 1994) and in edible films (Sobral et al., 2002) caused by phase separation between polymers and between proteins and plasticizers, respectively. However, Sobral et al. (2001) and Telis and Sobral (2002) also observed two T_g for persimmon and tomato, respectively, at low a_w domain.

At a_w of 0.80 and 0.84 (Figure 58.1b), a clearly visible devitrification peak appeared after T_g and before T_m . This occurred because rapid cooling

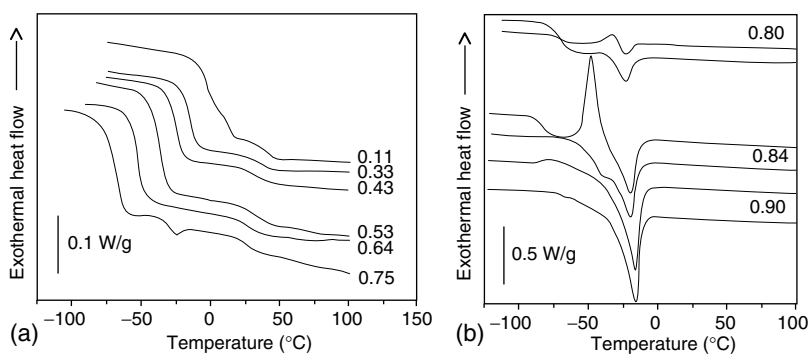


FIGURE 58.1

DSC traces of freeze-dried plum (skin/pulp at the natural proportion) at $0.11 \leq a_w \leq 0.90$.

resulted only in partial freeze-concentration of the solution. During reheating, the increase of water mobility caused crystallization of trapped amorphous water (Roos and Karel, 1991a; Slade and Levine, 1991). Sá et al. (1999) for apple, Sobral et al. (2001) for persimmon, and Telis and Sobral (2002) for tomato obtained similar results in this range of a_w . Thirty minutes of isothermal annealing at T_d were sufficient to eliminate the devitrification peak and, as expected, T_g of annealed samples were higher than that of the nonannealed ones as a result of the greater fraction of ice formed and consequent concentration of the amorphous glassy matrix (Sá and Sereno, 1994; Sobral et al., 2001; Telis and Sobral, 2001; Telis and Sobral, 2002). For $a_w \geq 0.90$, the melting of ice crystals surrounding the maximally freeze-concentrated solution (T'_m) appeared subtly as observed by Roos and Karel (1991b).

DSC traces for the separated fractions of plum, as well as a trace for the mixture of skin and pulp at the natural proportion, freeze-dried and without subsequent conditioning, are shown in Figure 58.2. The thermogram of pure skin presented only an endothermic peak, without second-order transitions. However, thermograms of pure pulp showed the two glass transitions already observed in samples of pulp and skin at the natural proportion. These results eliminated the possibility that the second glass transition observed at higher temperatures in samples of whole fruit could be caused by components of plum skin.

Values of T_g of nonannealed samples and onset T_m plotted against moisture content generated the state diagram of plum (Figure 58.3). At $a_w \leq 0.9$, the plasticizing effect of water is evident, with a great reduction of T_g caused by

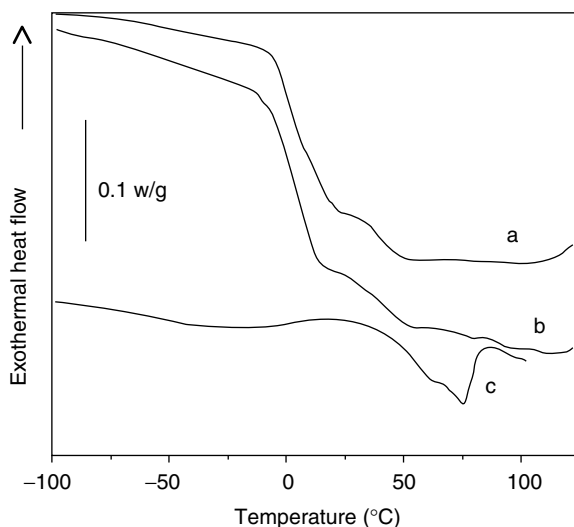


FIGURE 58.2

DSC traces of freeze-dried pulp/skin at the natural proportion (a), pure pulp (b), and pure skin (c).

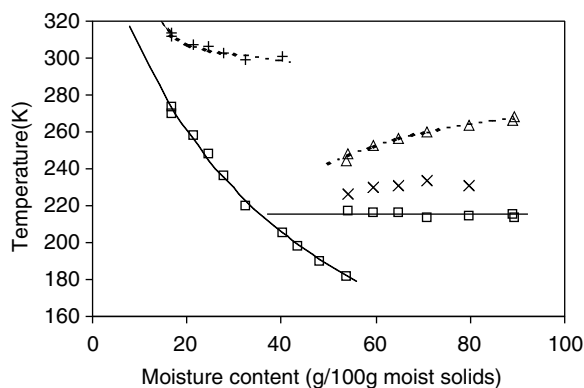


FIGURE 58.3

State diagram of freeze-dried plum (skin/pulp at the natural proportion): (\square , First T_g ; Δ , T_m ; \times , T'_m ; $+$, Second T_g).

increasing moisture content and molecular mobility. At $a_w > 0.90$, the glass-transition curve exhibited a discontinuity, with a sudden increase of T_g that approached a constant value corresponding to the glass transition of the maximally freeze-concentrated amorphous matrix ($T'_g = 216.1 \pm 1.3$ K). Roos and Karel (1991b), studying diluted sucrose solutions, Telis and Sobral (2001, 2002) working with freeze-dried pineapple and tomato, respectively, and Sobral et al. (2001) with persimmon, obtained similar glass-transition curves.

The Gordon–Taylor model (Equation 58.1) for binary systems could well represent the glass-transition curve of the sugar matrix at $a_w \leq 0.90$. The following parameters were calculated by nonlinear regression: $k = 3.76$ and $T_{gs} = 375.7$ K, with $r^2 = 0.996$, using $T_{gw} = 138$ K (Inoue and Ishikawa, 1997). In Equation 58.1, X_s is the dry solids fraction and X_w is the water fraction of the material:

$$T_g = \frac{X_s T_{gs} + k X_w T_{gw}}{X_s + k X_w} \quad (58.1)$$

As expected, the melting temperature decreased with decreasing water content. The intersection of the extrapolated ice melting and glass-transition curves would be expected to occur at T'_g (Slade and Levine, 1991). Other authors (Karel et al., 1994) consider that this intersection would occur at T'_m , which corresponds to the lowest equilibrium melting point within the unfrozen matrix. Values of T'_m were also included in Figure 58.3.

Conclusions

A state diagram for freeze-dried plum was obtained and the Gordon–Taylor model could adequately represent the sugar matrix glass-transition curve.

A second, higher T_g was observed in low moisture samples, and was attributed to the presence of natural macromolecules behaving like a separated phase. Thermograms of separated plum skin and pulp showed that glass transitions appeared only in the pulp. At a_w of 0.80 and 0.84, devitrification peaks were observed, which disappeared after annealing of 30 min. In the high moisture range, samples exhibited a constant glass-transition value of -57.1°C , which corresponds to T'_g . Also, T'_m was observed in these samples.

Acknowledgments

The authors acknowledge FAPESP (Fundação de Amparo à Pesquisa do Estado de São Paulo).

References

- Anglea, S.A., Karathanos, V., and Karel, M. Low-temperature transitions in fresh and osmotically dehydrated plant materials, *Biotechnol. Prog.*, 9, 204, 1993.
- Bai, Y., Shafiur Rahman, M., Perera, C.O., Smith, B., and Melton, L.D. State diagram of apple slices: glass transition and freezing curves, *Food Res. Int.*, 34, 89, 2001.
- Gabas, A.L., Menegalli, F.C., and Telis-Romero, J. Water sorption enthalpy-entropy compensation based on isotherms of plum skin and pulp, *J. Food Sci.*, 65, 680, 2000.
- Gabas, A.L., Telis-Romero, J., and Menegalli, F.C. Determination of concentration dependent effective moisture diffusivity of plums based on shrinkage kinetics, *Transport Phenomena in Food Processing*, J. Welti-Chanes, J.F. Vélaz-Ruiz and G.V. Barbosa-Cánovas, eds., CRC Press, Boca Raton, FL, pp. 153, 2002.
- Inoue, C. and Ishikawa, M. Glass transition of tuna flesh at low temperature and effects of salt and moisture, *J. Food Sci.*, 62, 496, 1997.
- Karel, M., Anglea, S., Buera, P., Karmas, R., Levi, G., and Roos, Y. Stability related transitions of amorphous foods, *Thermochim. Acta*, 246, 249, 1994.
- Roos, Y. Effect of moisture on the thermal behavior of strawberries studied using differential scanning calorimetry, *J. Food Sci.*, 52, 146, 1987.
- Roos, Y. and Karel, M.J. Plasticizing effect of water on thermal behavior and crystallization of amorphous food models, *J. Food Sci.*, 56, 38, 1991a.
- Roos, Y. and Karel, M. Phase transitions of amorphous sucrose and frozen sucrose solutions, *J. Food Sci.*, 56, 266, 1991b.
- Sá, M.M., Figueiredo, A.M., and Sereno, A.M. Glass transitions and state diagrams for fresh and processed apple, *Thermochim. Acta*, 329, 31, 1999.
- Sá, M.M. and Sereno, A.M. Glass transitions and state diagrams for typical natural fruits and vegetables, *Thermochim. Acta*, 246, 285, 1994.
- Sabarez, H., Price, W.E., Back, P.J., and Woolf, L.A. Modelling the kinetics of drying of d'Agen plums (*Prunus domestica*), *Food Chem.*, 60, 371, 1997.

- Slade, L. and Levine, H. Beyond water activity: recent advances based on an alternative approach to the assessment of food quality and safety, *Crit. Rev. Food Sci. Nutr.*, 30, 115, 1991.
- Sobral, P.J.A., Monterrey-Quintero, E.S., and Habitante, A.M.Q.B. Glass transition of Nile tilapia myofibrillar protein films plasticized by glycerin and water, *J. Thermal Anal. Calorim.*, 67, 499, 2002.
- Sobral, P.J.A., Telis, V.R.N., Habitante, A.M.Q.B., and Sereno, A. Phase diagram of freeze-dried persimmon, *Thermochim. Acta*, 376, 83, 2001.
- Spiess, W.E.L. and Wolf, W.R. The results of the COST 90 project on water activity, *Physical Properties of Foods*, F. Escher, B. Hallstrom, H.S. Meffert, W.E.L. Spiess and G. Voss, eds., Applied Science Publishers, New York, pp. 65, 1983.
- Telis, V.R.N. and Sobral, P.J.A. Glass transitions and state diagram for freeze-dried pineapple, *Lebensm.-Wiss. Technol.*, 34, 199, 2001.
- Telis, V.R.N. and Sobral, P.J.A. Glass transitions for freeze-dried and air-dried tomato, *Food Res. Int.*, 35, 435, 2002.
- Verghoogt, H., Ramsay, B.A., and Favis, B.D. Polymer blends containing poly (3-hydroxyalkanoate)s, *Polym. Rev.*, 35, 5155, 1994.
- Zelezna, K.J. and Hoseney, R.C. The glass transition in starch, *Cereal Chem.*, 64, 121, 1987.

Effect of Type of Amorphous Sugar Excipients on the Preservation of Lactate Dehydrogenase Activity as a Function of Storage Conditions

Kazuhito Kajiware and Tomoko Imai

CONTENTS

Introduction	697
Experimental Procedures.....	698
Reagents.....	698
Sugar Crystallinity	698
X-ray Diffraction.....	698
Glassy Preservation	699
Enzyme Assay	699
Results and Discussion	700
Crystallinity Changes as a Function of RH	700
LDH Preservation	701
Conclusion	701
References	701

Introduction

Freeze-drying is the conventional way to stabilize labile biological products, such as proteins and enzymes (Franks et al., 1991). Freeze-dried products usually contain sugars, polyols, or amino acids as excipients. For example, trehalose and other glass-forming solutes have been used as excipients for enzyme *Eco* RI stabilization (Rossi et al., 1992). Excipients with the ability to turn into the glassy state during the freeze-drying process help preserve the physical and chemical integrity of biological products (Fox, 1995). Solute crystallization from amorphous mixtures is considered to be of importance, usually undesirable, for many applications of concentrated aqueous

carbohydrate systems; examples include food processing and preservation of biological activity in freeze-dried pharmaceutical preparations. Recently, however, it has been proposed that sugar crystallization may, in the case of the formation of a stable crystalline hydrate, be of benefit in the enhancement of chemical and physical stability in humid environments. Thus, if a sugar can crystallize in the form of a hydrate in real time, then depending on the hydrate stoichiometry, its crystallization from the amorphous state will prevent the dilution of the remaining amorphous solution phase. If the residual (noncrystalline) solution phase then becomes sufficiently concentrated, its glass-transition temperature will be raised (Kajiwara and Franks, 1997). In this study, raffinose and trehalose, which at ambient conditions exist as a crystalline pentahydrate and dehydrate, respectively, were used as amorphous excipients and its ability to stabilize LDH in various humid conditions was tested.

Experimental Procedures

Reagents

Lactate dehydrogenase (from rabbit muscle, EC 1.1.1.27) was purchased from Oriental Yeast Co. Raffinose and trehalose were purchased from Sigma Co. All other chemicals used in this study were reagent grade and were purchased from Wako Pure Chemical Co. Deionized distilled water was used in the experiments.

Sugar Crystallinity

Aqueous raffinose and trehalose solutions (400 mmol dm^{-3}) were dropped separately on x-ray sample holders. These samples were precooled at -85° for 30 min and then freeze-dried for 20 h in the condition of below 1.33 Pa. After freeze-drying, the samples were determined by a microbalance and an x-ray diffractometer. Then the samples were stored in desiccators at 35° containing saturated salt solutions with different relative humidities (RHs). After a certain interval storage at each of two humid conditions, the samples were determined by a microbalance and an x-ray diffractometer. RHs of saturated $\text{Mg}(\text{NO}_3)_2$ and NaCl solutions at 35° are 52 and 76%, respectively.

X-ray Diffraction

X-ray diffraction of freeze-dried products was determined to observe sample crystallinity. The determinations were carried out with the aid of a JEOL Model JDX-8030 x-ray diffractometer.

Glassy Preservation

LDH was diluted 1/1000 with 50 mmol dm⁻³ sodium phosphate buffer (pH 7.4). LDH (5000 U ml⁻¹) solution (100 ml) and the same quantity of an excipient solution were mixed well in the microtubes. The final concentration of each excipient was 200 mmol dm⁻³. The mixtures were precooled at -85° for 30 min and then freeze-dried for 20 h in the condition of below 1.33 Pa. After freeze-drying, mixtures were stored at 35° in three controlled humidities (relative humidity (RH): 6% (saturated NaOH solution), 52% and 76%) sample bottles without saturated salt solutions for 2 days (Figure 59.1). After the sorptions the microtubes were covered with the lid, then mixtures were stored at the ambient temperature for 1 month.

Enzyme Assay

The freeze-dried products were added 100 µl of deionized distilled water, then diluted with 200 µl of 50 mmol dm⁻³ phosphate buffer solution to determine the residual activity of LDH (Lin and Thomahow, 1992). Residual activities of LDH were assayed at 35° using NADH as a substrate. An enzyme solution (50 µl) was added to 2 ml of the substrate solution (0.18 mmol dm⁻³ NADH in a mixture solution of phosphate buffer (50 mmol dm⁻³, pH 7.5) and 0.62 mmol dm⁻³ lithium pyruvate). The absorbance at 340 nm was observed by a Beckman DU-65 spectrometer.

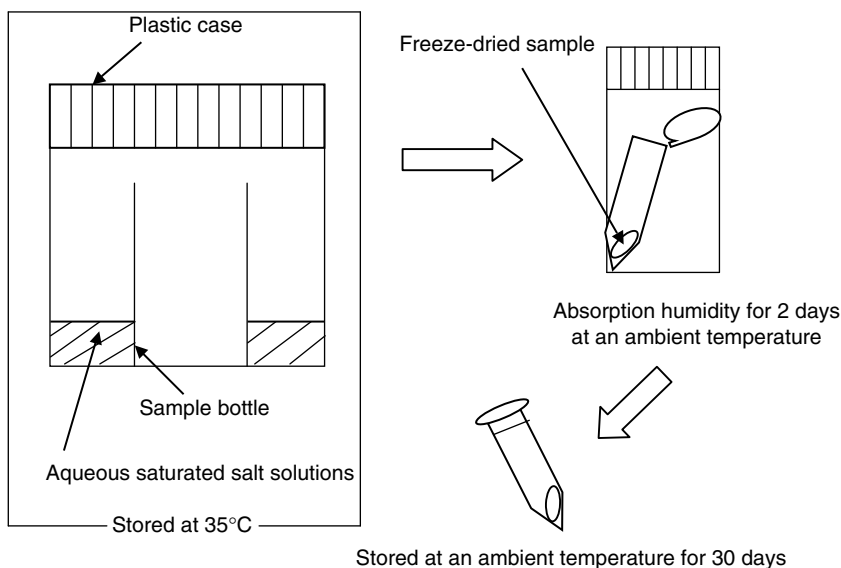


FIGURE 59.1

Diagram of the absorbing humidity method of freeze-dried lactate dehydrogenase samples.

Results and Discussion

Crystallinity Changes as a Function of RH

The crystallinity of freeze-dried samples of either raffinose or trehalose were measured by XRPD immediately after freeze-drying. No signs of crystallinity were found on any of the samples. Then the samples were stored in desiccators at 35° containing the saturated $\text{Mg}(\text{NO}_3)_2$ solution (52% RH at 25°). After a certain interval storage, the samples were weighed in a microbalance and analyzed by XRPD. Raffinose crystallization was observed after 49 h and it crystallized completely after 304 h. Trehalose crystallized almost completely under the same conditions after 3 h. Figure 59.2 shows the weight change of freeze-dried raffinose and trehalose during 400 h after freeze-drying. Raffinose absorbed about 11% w/w of water (i.e., 11 g of water/100 g of dry sample) immediately. Thereafter, the amount of absorbed water increased gradually and reached a constant value (ca 14% w/w) after 300 h. Trehalose absorbed about 12% water and reached constant value (ca 9.2% water) after 3 h. Raffinose pentahydrate contains about 18% water. Samples of either raffinose or trehalose that were stored in desiccators containing saturated NaCl solution (76% RH at 25°) crystallized completely after 20 min. Crystallizing rates of two amorphous sugars were almost same in the condition of such a high RH.

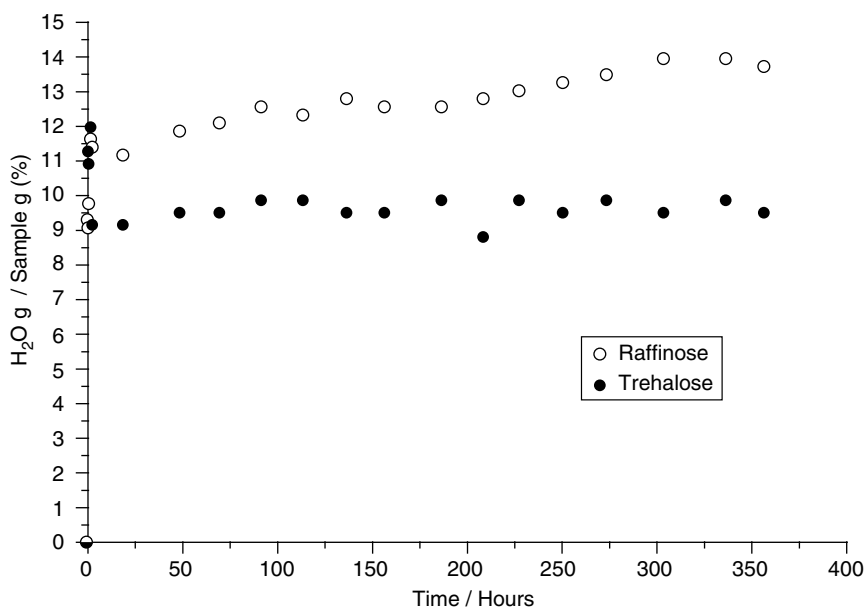
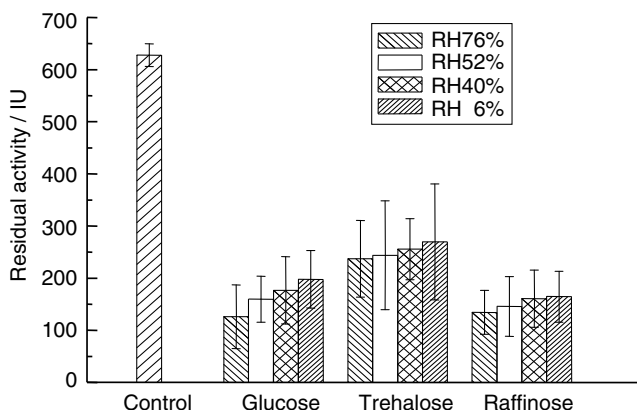


FIGURE 59.2

The weight change of freeze-dried sugars during 400 h after freeze-drying in the condition of 52% relative humidity.

**FIGURE 59.3**

Residual activity of lactate dehydrogenase after 30 days storage.

LDH Preservation

The enzymatic activity of freeze-dried LDH samples containing raffinose or trehalose as excipients were examined as a function of humidity. The samples were stored in desiccators containing saturated $\text{Mg}(\text{NO}_3)_2$ solution (53% RH at 25°) for 2 days. All samples crystallized and had no LDH activity. LDH activity is shown in Figure 59.3. LDH activity decreased with increasing relative humidity. After storage at 76% RH, LDH has 22% activity in a glucose system compared with the initial one, 24% in a raffinose system and 42% in a trehalose system. After storage at 6% RH, LDH has a 36% activity in a glucose system, 30% in a raffinose system, and 48% in a trehalose system. LDH presented no enzymatic activity after excipient crystallization.

Conclusion

Even though raffinose resistance to moisture-induced crystallization was better than that of trehalose, the enzymatic activity was higher in the trehalose than in the raffinose system. Therefore, given the results of this study it is not clear that the ability to remove water from the amorphous solution during *in situ* crystallization will promote improved biostabilization.

References

- Fox, K.C. Putting proteins under glass, *Science*, 267, 1922, 1995.
Franks, F., Hatley, R.H., and Mathias, S.F. Materials science and the production of shelf-stable biologicals, *Pharm. Technol. Int.*, 3, 38, 1991.

- Kajiwara, K. and Franks, F. Crystalline and amorphous phases in the binary system water–raffinose, *J. Chem. Soc., Faraday Trans.*, 93, 1779, 1997.
- Lin, C. and Thomahow, M.F. A cold-regulated *Arabidopsis* gene encodes A polypeptide having potent cryoprotective activity, *Biochem. Biophys. Res. Commun.*, 183, 1103, 1992.
- Rossi, S., Buera, M.P., Moreno, S., and Chirife, J. Stabilization of the restriction enzyme *Eco*RI dried with trehalose and other selected glass-forming solutes, *Biotechnol. Prog.*, 13, 609, 1992.

*The Water Content Effect on
the Glass-Transition Temperature
of Low Calory Candy Formulations*

Adelina G. Celeghin and Amelia C. Rubiolo

CONTENTS

Introduction	703
Materials and Methods	704
Results and Discussion	705
References	708

Introduction

Most carbohydrate systems are able to form glasses below the solid melting equilibrium temperature, which is defined as an amorphous solid (noncrystalline) state. An amorphous material undergoes a change from a glassy mechanical solid to a rubbery viscous liquid at the glass-transition temperature (T_g) (Roos and Karel, 1991b). T_g is operationally defined as a kinetically controlled transition during which a discontinuity in the heat capacity change (ΔC_p) occurs over a temperature range of 10 to 20°C and it can be determined using differential scanning calorimeter (DSC) (Serenó, 2000).

While T_g values decrease with increasing water content (Roos and Karel, 1991a; Khalloufi et al., 2000), oligosaccharides or polysaccharides in monosaccharide blends increase T_g and improve the storage stability. Although T_g values are not always adequate to determine the experimental behavior of certain food systems or components, they are useful in high-sugar systems (Peleg, 1993).

Hard candy is one of the most versatile products in the confectionary industry (Chung et al., 1999). It becomes sticky and has the tendency to

adhere to a similar or different surface. Product stability is reached varying the relationship between the components or by the addition of other carbohydrates to obtain an amorphous solid state and to achieve $(T - T_g) < 0$ during processing and storage.

Candy basic components (De La Canal, 1982) are sucrose and corn syrup, which are obtained by partial hydrolysis of corn starch. These components provide the sweet flavor, bulk, conservation properties and, jointly with water, the texture and optical properties of hard candies. Sugar alcohols are used as sugar replacers because of their lower hygroscopicity, less stickiness, and noncariogenicity, and they keep plasticizer properties required in sugar-free confectionary.

The objective of this study was to analyze the effect of the water content on the glass-forming properties and stability of mixtures of isomalt and maltitol syrup, with and without maltodextrins in candy-like formulations.

Materials and Methods

Maltitol syrup (MS) 75% (P/P), Isomalt (I) 99.5% of commercial use (ARCOR, Arroyito, Córdoba, Argentina), maltodextrin 15% conversion (MD), (Maltrina 15, Glutal S.A., Esperanza, Santa Fe, Argentina) were dissolved in distilled water as 20% solutions.

Composition of mixtures (dry basis (db)) was: Mixture 1: 11.69% MS, 88.31% I; Mixture 2: 11.69% MS, 64.93% I, 23.38% MD and Mixture 3: 5.87% MS, 88.31% I, 5.82% MD.

Components were mixed at room temperature, cooked at 130°C for 10 to 12 min until the systems became clear brownish and cooled. When the mixtures reached 100°C, they were spread on an aluminum paper and cooled to room temperature. These solid melt systems were powdered in a mortar.

Duplicate solutions of the pure components and of the powdered mixtures were quickly cooled in liquid air, followed by freeze-drying in a HETO, FD 2.5 for 72 h at 0.07 mbar pressure, at room temperature, and -40°C condenser temperature to obtain an amorphous state.

Freeze-dried samples were equilibrated in desiccators over CaSO_4 Drierite^{MT} (W.A. Hammond Drierite Company Ltd., USA) and over saturated salt solutions (KCH_3COO , K_2CO_3 , and NaBr) for 0, 0.22, 0.43, and 0.57 water activities (a_w), respectively, for 20 days at 25°C (298 K) and 35°C (308 K). The water content of samples was determined by weight change after equilibration (20 days). T_g of the amorphous samples was determined by differential scanning calorimetry using DSC 821e equipment (Mettler Toledo, Greifensee, Switzerland). To avoid condensation of water the samples were purged with a flow of dry nitrogen (20 ml/min). Weighted samples were placed in 40- μl DSC pans and hermetically sealed. An empty aluminum pan was used as reference in all measurements. Scan rates were

10°C/min from -50 to 120°C . Results from duplicate samples were obtained.

The Brunauer–Emmett–Teller (BET) and Guggenheim–Anderson–deBoer (GAB) sorption isotherm models were used to obtain experimental steady-state moisture contents in dry basis by linear regression analysis according to Kouassi and Roos (2002). These equations provide the value of monolayer water content, which is an important parameter in food deterioration studies.

Results and Discussion

Figure 60.1 shows the DSC thermograms of maltitol syrup and of Mixture 2 at 298 and 308 K at different a_w . T_g of the mixture components decreased with the increase of a_w at the same storage conditions and this plasticizing effect of water is observed in Table 60.1.

Addition of maltodextrin increased the T_g of the samples. Thus, the partial substitution of isomalt and maltitol syrup by maltodextrin was expected to improve the stability of the sample, delaying crystallization, and decreasing hygroscopicity of dried materials. The stabilizing effect of oligomeric or polymeric additives in carbohydrate systems depends on the proportion and characteristics of the substituted component.

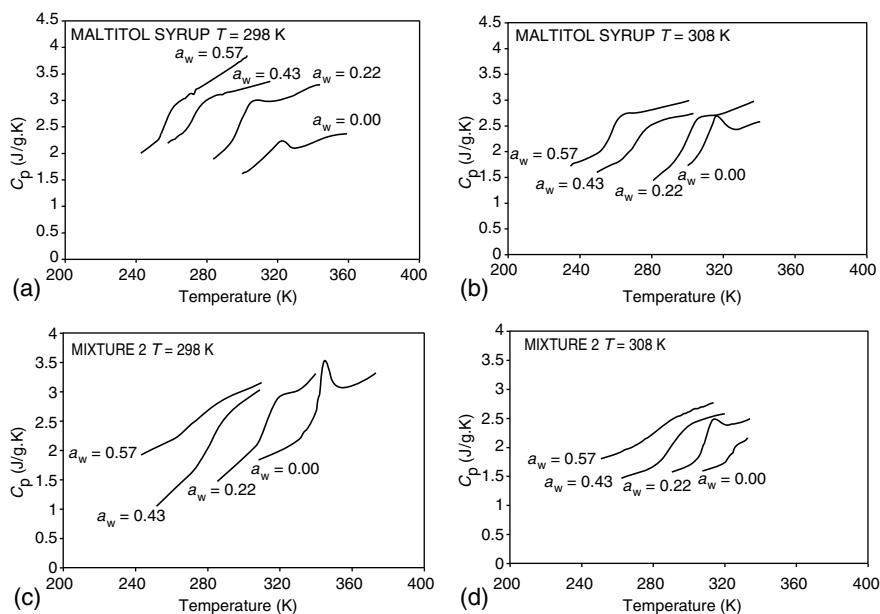


FIGURE 60.1

DSC thermograms of samples equilibrated at different water activities and temperatures.

TABLE 60.1
Water Content m (g H₂O/100 g db) and T_g (K) Values of Samples
Equilibrated at Different Water Activities and Temperatures

Sample	Storage Temperature (K)	$a_w = 0$		$a_w = 0.22$		$a_w = 0.43$		$a_w = 0.57$	
		m (%db)	T_g (K)	m (%db)	T_g (K)	m (%db)	T_g (K)	m (%db)	T_g (K)
Isomalt	298	0.88	326	2.86	299	7.00	287	6.97	N.D.
	308	0.47	316	1.46	300	4.65	N.D.	6.04	N.D.
Maltitol Syrup	298	0.78	322	3.90	295	6.73	273	12.40	255
	308	0.64	308	4.64	296	5.93	267	10.17	252
Mixture 1	298	0.18	313	2.39	310	10.16	258	16.51	240
	308	0.39	303	0.94	294	10.70	256	14.74	242
Mixture 2	298	0.20	338	1.49	307	8.21	278	9.31	267
	308	0.75	340	2.28	306	6.53	284	9.09	273
Mixture 3	298	0.16	335	1.68	300	7.98	272	9.33	N.D.
	308	0.75	316	1.65	304	8.57	266	8.97	257

Note: N.D. = No detected transition (they were in rubbery state).

Figure 60.2(a–d) shows the sorption isotherms for isomalt, maltitol syrup, and for the carbohydrate mixtures. The water content of isomalt increased with increasing a_w and water adsorption decreased with increasing temperature at the same a_w .

The samples with higher isomalt content showed a discontinuity in the water-sorption isotherm indicating isomalt crystallization, which is the most important defect during storage of hard candies. It is observed in Figure 60.2 that isomalt crystallization decreased in the samples containing maltitol and isomalt (Mixture 1), but not by the addition of maltodextrin at 298 K (Mixtures 2 and 3). In Mixture 2, containing 23.38% maltodextrin, isomalt crystallization was inhibited at 298 K but not at 308 K. At 308 K, the dissolution of sugar may have occurred and the T_g of the mixture decreased. This process is known to be endothermic, more sugar being dissolved and thus more water being held in the food products at higher temperatures. Hence, the change of the amorphous state may be accelerated. Addition of maltodextrin decreased the access of water to mixtures and the T_g values showed a smaller decline (Table 60.1). According to studies carried out by Raudonus et al. (2000), samples containing 10% polymeric additive in isomalt systems, showed a dry crystal layer similar to pure isomalt. An increase in the amount of additives to 30% led to crystallization on the surface, which remained damp during room storage. Thus, the addition of high molecular weight materials does not always inhibit crystallization and they could even accelerate crystal growth of isomalt.

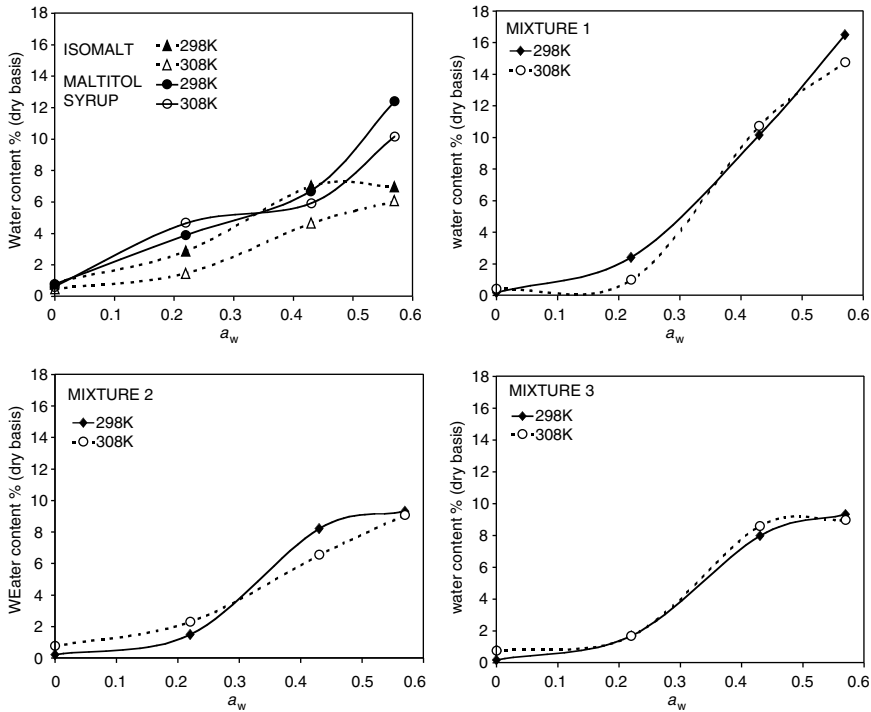


FIGURE 60.2
Water sorption isotherms isomalt, maltitol syrup and mixtures 1, 2, and 3 at 298 and 308 K.

The maltitol syrup and carbohydrate mixtures sorption isotherms cross at the two different temperatures in the a_w region between 0.3 and 0.4. Above this region, the water content was smaller at 308 K than at 298 K. A crossing of isotherms at two different temperatures was also observed by Ayranci et al. (1990) in dried apricot, fig, and raisin. Analysis of variance showed that except for isomalt, the equilibrium water contents of the different products did not differ ($p > 0.05$) for each product at different temperatures.

The monolayer values (m_m) calculated by BET and GAB equations (shown in Table 60.2) were different (Statgraphics Plus 3.0). The difference was because the BET equation allows the use of linear regression in model fitting and isotherms have nonlinear behavior even in a low water activity region.

The results showed that isomalt crystallization could be prevented in formulations MS/I 11:88 at both analyzed temperatures or in MS/I/MD 11:65:23 stored at 308 K. The knowledge of pure component T_g values at different a_w and temperature–time range can be used to formulate mixtures having desired physical properties required in food processing and storage.

TABLE 60.2
Monolayer Water Content (m_m) g H₂O/100 g
Dry Basis

Samples	Storage Temperature (K)	GAB	BET
Isomalt	298	2.77	3.27
	308	1.27	2.67
Maltitol Syrup	298	2.75	4.81
	308	3.10	4.02
Mixture 1	298	2.01	6.91
	308	0.85	6.27
Mixture 2	298	1.35	3.27
	308	1.91	3.92
Mixture 3	298	1.52	4.13
	308	1.54	2.52

References

- Ayranci, E., Ayranci, G., and Dogantan, Z. Moisture sorption isotherms of dried apricot, fig and raisin at 20°C and 36°C, *J. Food Sci.*, 55, 1591, 1990.
- Chung, M., Ruan, R.R., Chen, P.L., and Wang, X. Physical and chemical properties of caramel systems, *Lebensm.-Wiss. Technol.*, 32, 162, 1999.
- De La Canal, J.J., ed., *Codigo Alimentario Argentino: Productos de Confitería*, Art. 789, p. 125, 1982.
- Khalloufi, S., El-Maslouhi, Y., and Ratti, C. Mathematical model for prediction of glass transition temperature of fruit powders, *J. Food Sci.*, 65, 842, 2000.
- Kouassi, K. and Roos, Y.H. Glass transition, water and glycerol effects on sucrose inversion in pullulan-sucrose systems, *J. Food Sci.*, 67, 3402, 2002.
- Peleg, M. Glass transitions and physical stability of food powders, *The Glassy State in Foods*, J.M. Blanshard and P. Lillford, eds., Nottingham University Press, Nottingham, 1993.
- Raudonus, J., Bernard, J., Janben, H., Kowalczyk, J., and Carle, R. Effect of oligomeric or polymeric additives on glass transition, viscosity and crystallization of amorphous isomalt, *Food Res. Int.*, 33, 41, 2000.
- Roos, Y. and Karel, M. Water and molecular weight effects on glass transitions in amorphous carbohydrates and carbohydrate solutions, *J. Food Sci.*, 56, 1676, 1991a.
- Roos, Y. and Karel, M., Sugars (Paper 7^a. AIChE. Summer Meeting. San Diego. CA, August 19–22, 1990) American Chemical Society and American Institute of Chemical Engineers, p. 49, 1991b.
- Sereno, A.M. Thermal properties and state diagrams of fruits and vegetables by DSC, *Trends Food Eng.*, 77, 2000, chap. 7.

Release of Encapsulated Aroma Compounds from Amorphous Maltodextrin Matrices

Kirsi Jouppila, Susanna Sundberg, Sanna-Maija Miettinen,
and Lea Hyvönen

CONTENTS

Introduction	709
Materials and Methods	709
Results and Discussion	711
Conclusions	713
Acknowledgments	713
References	713

Introduction

Encapsulation of aroma compounds in amorphous carbohydrate matrices can be carried out, for example, by freeze- or spray-drying (Levine et al., 1991; Roos, 1995). Aroma compounds often remain encapsulated in glassy carbohydrate matrices stored at temperatures below their glass transition. Release of encapsulated aroma compounds may occur when amorphous carbohydrate matrices are stored at temperatures above their glass transition, allowing sufficient molecular mobility and diffusion.

The aim of the present study was to investigate the effect of the physical state of the matrix on the release of encapsulated aroma compounds from amorphous maltodextrin matrices.

Materials and Methods

Amorphous maltodextrin matrices were produced by freeze-drying maltodextrin–water solutions (15% solids, w/w) containing benzaldehyde

(0.023%, w/w) or ethyl acetate (0.08%, w/w). Maltodextrins used were Maltrin M100 (DE 11.5) and M180 (DE 18.1) (Grain Processing Corporation, USA).

Water sorption properties of maltodextrin matrices were determined in terms of weight gain, after storage of freeze-dried samples in vacuum desiccators at relative humidities ranging from 11 to 76% at 25°C (Labuza et al., 1985). Water sorption was modeled using the Guggenheim–Anderson–de Boer (GAB) equation. Onset temperatures of glass transition (T_g) for amorphous maltodextrin matrices were determined using differential scanning calorimetry (DSC). The T_g curves were predicted using the Gordon–Taylor equation.

Freeze-dried M100 and M180 samples were rehumidified by storing them for at least 1 week in vacuum desiccators at relative humidities of 66 and 54%, respectively, at 25°C. The rehumidified samples were stored at 45, 50, and 60°C in order to study the release of aroma compounds as a function of storage time. The release of benzaldehyde and ethyl acetate was analyzed using static headspace gas chromatography (HS 40 XC, Perkin Elmer, USA) and an electronic nose (Gas Detector MGD-1, Environics Ltd, Finland).

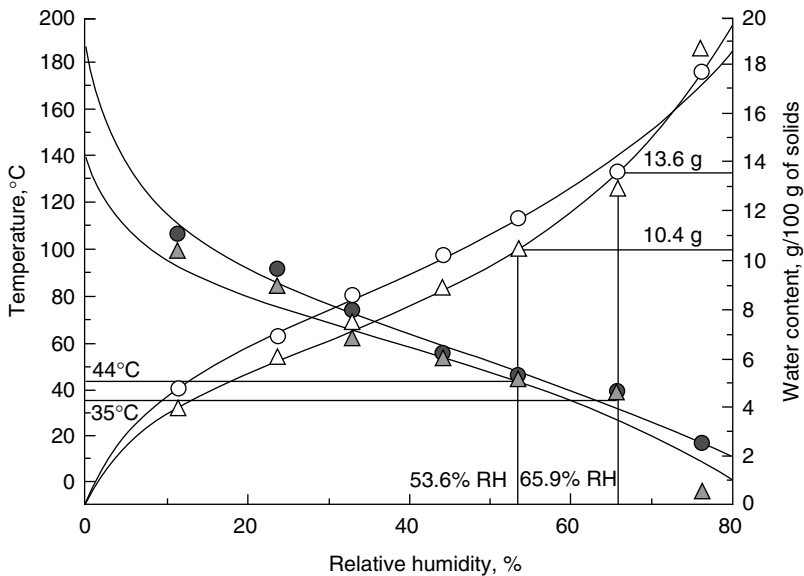


FIGURE 61.1

Experimental glass-transition temperature (onset) values (closed symbols) and water contents (open symbols) for amorphous maltodextrin M100 (circles) and M180 (triangles) matrices as a function of storage relative humidity at 25°C. The glass-transition temperatures and water contents for maltodextrin M100 and M180 matrices stored at relative humidities of 66 and 54%, respectively, are shown by straight lines.

Results and Discussion

Water-sorption behavior and T_g of freeze-dried maltodextrin M100 and M180 matrices are shown in Figure 61.1. Water contents and T_g were observed to be higher for the higher molecular weight maltodextrin M100. Slade (Levine and Slade, 1986) and Roos and Karel (1991) showed that glass transition temperatures for maltodextrins decrease with decreasing molecular weight. Maltodextrin M100 and M180 samples were stored, prior to aroma release study, at relative humidities of 66 and 54%, respectively, because then the T_g of the two matrices were quite close to each other (35 and 44°C, respectively) and a little higher than room temperature. Thus, the release of aroma compounds during rehumidification at room temperature was not likely.

The rehumidified M100 and M180 samples were stored at various temperatures (45, 50, and 60°C) above their T_g , resulting in the time-dependent collapse of matrix structure and simultaneous release of aroma compounds. Figure 61.2 shows that release of benzaldehyde occurred more rapidly when the storage temperature increased. Both static headspace-GC

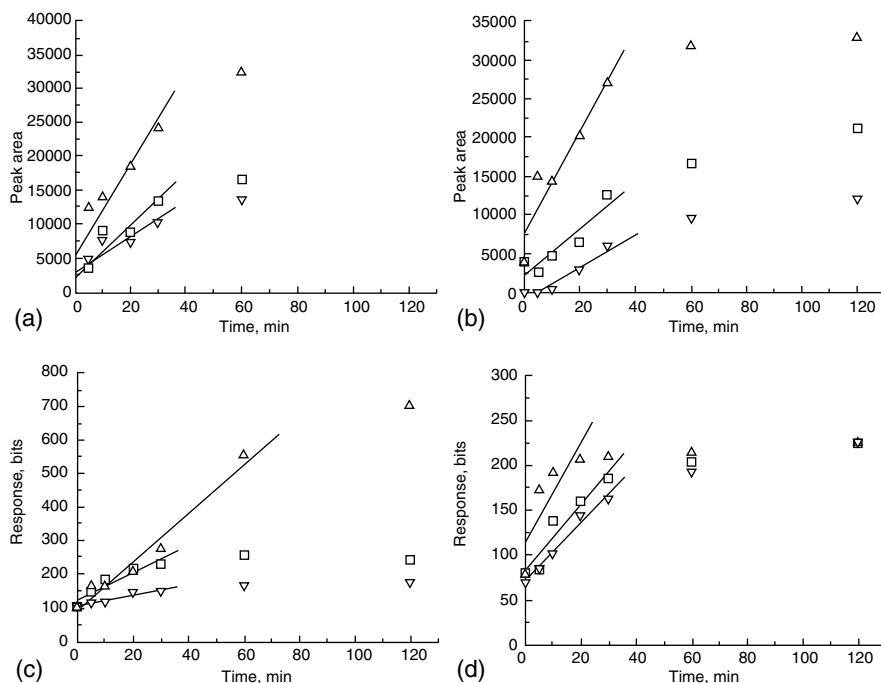


FIGURE 61.2

Release of benzaldehyde from maltodextrin M100 (a, c) and M180 matrices (b, d), during storage at 45 (▽), 50 (□), and 60°C (△) analyzed using static headspace-GC (a, b) and an electronic nose (c, d).

and an electronic nose gave similar results, although the variation of results was higher for those obtained using an electronic nose. Similar behavior was observed for release of ethyl acetate from M180 matrices and also from M100 matrices when analyses were carried out using static headspace-GC.

The rate constants for release of benzaldehyde from both matrices and of ethyl acetate from M180 matrices were found to increase when the storage temperature (T) and the temperature difference between storage temperature and glass-transition temperature ($T - T_g$) increased (Figure 61.3). Release of ethyl acetate from M100 matrix was found to occur more slowly, and the amount of released ethyl acetate was smaller than from M180 matrix, as detected using headspace-GC. This may have resulted from increased ethyl acetate entrapment in M100 matrix. Similarly, Bangs and Reineccius (1981) found that the retention of volatile compounds increased with increasing molecular weight (and decreasing DE value) of maltodextrin, probably because of decreased diffusivity of volatile compounds in such matrices. However, similar behavior was not found for the release of benzaldehyde from our maltodextrin matrices. This difference in release behavior may have been caused by differences in hydrophobicity of the aroma compounds used in the present study.

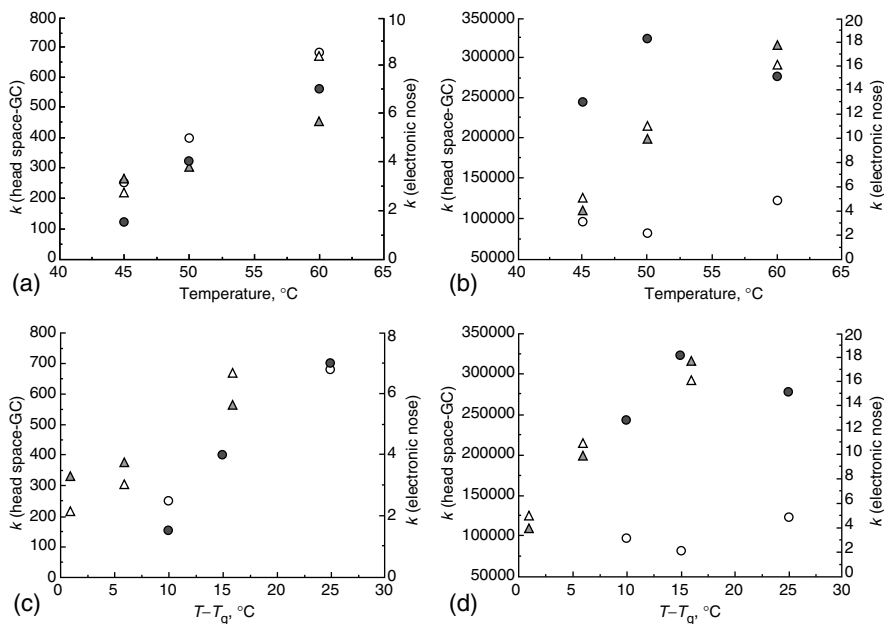


FIGURE 61.3

Rate constants for the release of benzaldehyde (a, c) and ethyl acetate (b, d) from M100 (circles) and M180 (triangles) matrices determined using headspace-GC (open symbols) and an electronic nose (closed symbols) as a function of storage temperature (a, b) and $T - T_g$ (c, d).

Conclusions

The physical state of the matrix was found to affect the rate of release of aroma compounds from amorphous maltodextrin matrices; the rate increased with increasing storage temperature and $T - T_g$. The results obtained can be used for evaluation of proper storage conditions for amorphous maltodextrin matrices containing encapsulated aroma compounds, as well as for evaluation of the usefulness of various analyzing techniques for aroma release in such studies.

Acknowledgments

The authors acknowledge funding from University of Helsinki Research Funds.

References

- Bangs, W.E. and Reineccius, G.A. Influence of dryer infeed matrices on the retention of volatile flavor compounds during spray drying, *J. Food Sci.*, 47, 254, 1981.
- Labuza, T.P., Kaanane, A., and Chen, J.Y. Effect of temperature on the moisture sorption isotherms and water activity shift of two dehydrated foods, *J. Food Sci.*, 50, 385, 1985.
- Levine, H. and Slade, L. A polymer physico-chemical approach to the study of commercial starch hydrolysis products (SHPs), *Carbohydr. Polym.*, 6, 213, 1986.
- Levine, H., Slade, L., Van Lengerich, B., and Pickup, J.G. Glassy matrices containing volatile and/or labile components, and processes for preparation and use thereof, U.S. Patent, 5,009,900, 1991.
- Roos, Y.H. *Phase Transitions in Foods*, Academic Press, San Diego, CA, 1995.
- Roos, Y. and Karel, M. Water and molecular weight effects on glass transitions in amorphous carbohydrates and carbohydrate solutions, *J. Food Sci.*, 56, 1676, 1991.

*Relationship between Glass-Transition Curves
and Sorption Isotherms for the Evaluation of
Storage Conditions of Freeze-Dried
Camu-Camu (Myrciaria dubia (Hbk)
Mcvaugh) Pulp with and without
Maltodextrin Addition*

Mariana Altenhofen da Silva, Paulo José do Amaral Sobral,
and Theo G. Kieckbusch

CONTENTS

Introduction	715
Materials and Methods	716
Results and Discussion	717
References	720

Introduction

Camu-camu (*Myrciaria dubia* (HBK) McVaugh) is a native fruit of the Amazon region with increasing marketing potential because of its high ascorbic acid content (up to 3000 mg/100 g) (Zapata and Dufour, 1993). In Brazil its commercialization is limited to fresh fruits, but many researches in course seek processed goods that can be easily transported and stored.

The amorphous state of food materials is a nonequilibrium state that affects material behavior during processing and storage. Food materials may be considered as stable in their solid "glassy" state, which is characterized by an extremely high viscosity (10^{12} Pa s). However, glasses are transformed to a more liquid-like "rubbery" state in the vicinity of the temperature known as glass transition (T_g) (Slade and Levine, 1991; Roos, 1995). Prediction of the

physical state of food materials is often based on modeling the plasticization effect of water, i.e., glass-transition temperature (T_g) depression with increasing moisture content or water activity (Roos, 1993; 1995). Food products that contain low molecular weight compounds, such as sugars and acids, are usually difficult to dehydrate and they often exhibit poor stability in the dehydrated state when stored above T_g . Most of these products are hygroscopic and excessively plasticized by water, leading to low T_g values, which even at fairly low water contents fall below typical storage temperatures (Slade and Levine, 1991; Roos, 1995).

Sorption isotherms are needed for the description of changes in the physical state that may occur during storage of low and intermediate moisture foods. From this point of view, diagrams combining water plasticization and water adsorption can be useful tools in process optimization, food formulation, and defining package/storage conditions (Moraga et al., 2004). The objective of the present work was to determine critical stability requirements of water activity (a_{wc}) and moisture content (X_{wc}), considered as the conditions that provide a T_g of 25°C, for freeze-dried camu-camu pulp with and without maltodextrin addition.

Materials and Methods

Camu-camu used in this work was cultivated in southeast Brazil and purchased at CEAGESP (São Paulo, Brazil). After washing and selection, blanching was performed in whole fruits (98°C/2 min). The pulp was obtained using a domestic centrifuge (screen openings 1 mm). Half of the lot received 30% (w/w) maltodextrin DE 20 as a drying aid. Both natural pulp (without additive) and the formulation with maltodextrin were immediately frozen at -18°C for 24 h and then fed into a bench freeze-drier operating at -50°C and 100 mTorr for 48 h (EZ-DRY, FTS Systems, USA). Representative samples of the natural pulp (before freeze-drying) were used to determine moisture content (vacuum oven, 95°C, 100 mm Hg, 48 h), ascorbic acid content by iodine titration (Instituto Adolfo Lutz, 1985), titrable acidity (Association of Official Analytical Chemistry (AOAC), 1995), total soluble solids by refractometry (ABBE, Atago 3T, Japan), reducing and nonreducing sugars by Fehling's method (Association of Official Analytical Chemistry (AOAC), 1995), and pH by direct reading with a pHmeter.

Samples (1.0 to 1.5 g) of the freeze-dried product were equilibrated over saturated salt solutions at 25°C, in order to achieve water activities between 0.11 and 0.90 (Spiess and Wolf, 1983). After equilibration (about 2 to 3 weeks), small samples were taken for DSC analyses and the remaining material was used to determine equilibrium moisture content. Phase transitions were determined by differential scanning calorimetry using a DSC TA2010 controlled by a TA5000 module (TA Instruments, Newcastle, USA). Samples of about 10 mg (± 0.01), conditioned in TA aluminum pans

were heated at $10^{\circ}\text{C min}^{-1}$, between -120 and 120°C , under inert atmosphere (45 ml min^{-1} of N_2). An empty pan was used as reference. Liquid nitrogen was used for sample cooling before the runs. All measurements were made in triplicate.

Results and Discussion

Table 62.1 presents the chemical characterization of natural (without additives) camu-camu pulp. Except for ascorbic acid, the values were similar to those found by other authors (Zapata and Dufour, 1993). As can be observed, no sucrose was present and the reducing sugars content was low, distinguishing it from other acid fruits.

The retention of vitamin C during freeze-drying process were 99% for the samples with additive and 98% for natural camu-camu pulp.

Guggenheim–Andersen–De Boer (GAB) model (Equation 62.1) was used to adjust the sorption data for freeze-dried camu-camu pulp and pulp with 30% (w/w) maltodextrin DE 20 and showed good correlation over all the water activity range studied (Spiess and Wolf, 1983). In Equation 62.1, X_w is the moisture content (dry basis), a_w is the water activity, X_m is the monolayer moisture content and C_{GAB} and k_{GAB} are constants related to the monolayer and multilayer enthalpies (Telis and Sobral, 2001). The model parameters for both sorption isotherms estimated by nonlinear regression are showed in Table 62.2. Both curves exhibit sigmoidal-shaped (Type II) isotherms, following the Brunauer classification (Figure 62.1 and Figure 62.2) which is typically found for foodstuff and biological materials (Roos, 1993).

$$X_w = \frac{C_{\text{GAB}}k_{\text{GAB}}X_m a_w}{(1 - k_{\text{GAB}}a_w)(1 - k_{\text{GAB}}a_w + C_{\text{GAB}}k_{\text{GAB}}a_w)} \quad (62.1)$$

TABLE 62.1
Chemical Characterization of Natural Camu-Camu Pulp

Component	Values ^a
Moisture content (%)	93.35 ± 0.04
Total soluble solids (°Brix)	6.0 ± 0.1
Reducing sugars (g glucose/100 g)	3.25 ± 0.03
Nonreducing sugars (g sucrose/100 g)	ND ^b
Titrate acidity (g citric acid/100 g)	2.30 ± 0.03
pH	2.63 ± 0.02
Ascorbic acid (mg AA/100 g)	1721.65 ± 15.93
Brix/acidity ratio	2.60

Average \pm standard deviation of three experimental determinations.

^a Wet basis.

^b Nondetectable.

TABLE 62.2
Parameters Estimated for GAB Model for Freeze-Dried Camu-Camu Pulp

Freeze-Dried Camu-Camu Pulp	Parameter			
	X_m (gH ₂ O/g dry solids)	C_{GAB}	k_{GAB}	r^2
Natural (without additive)	0.158	27.364	0.924	0.996
With 30% (w/w) maltodextrin DE 20	0.064	10.163	0.948	0.992

The monolayer moisture content (X_m) for freeze-dried natural camu-camu pulp can be compared with the values found for other freeze-dried fruits, such as persimmon ($X_m = 0.131$) (Telis and Sobral, 2001), pineapple ($X_m = 0.072$) (Sobral et al., 2001), grape, fig, and apricot ($X_m = 0.125, 0.117$, and 0.151) (Maroulis et al., 1988) at 25°C. The monolayer moisture content obtained for freeze-dried camu-camu pulp with 30% maltodextrin DE 20 was close to the value found by Roos (1993) for pure maltodextrin DE 20.

The glass-transition experimental data obtained with the DSC showed a great reduction in T_g with the increase in moisture content. In the water activity domain studied ($0.11 < a_w < 0.90$), Gordon–Taylor model (Equation 62.2) was adequate to adjust the experimental data. In Equation 62.2, W_s and W_w are the mass fraction of solids and water, k is a constant derived experimentally for the solid component, and T_{gm} , T_{gs} , and T_{gw} are the glass-transition temperatures for the mixture, the bone-dry solid components, and pure water (−135°C), respectively. The model parameters, estimated by nonlinear regression for freeze-dried camu-camu natural pulp

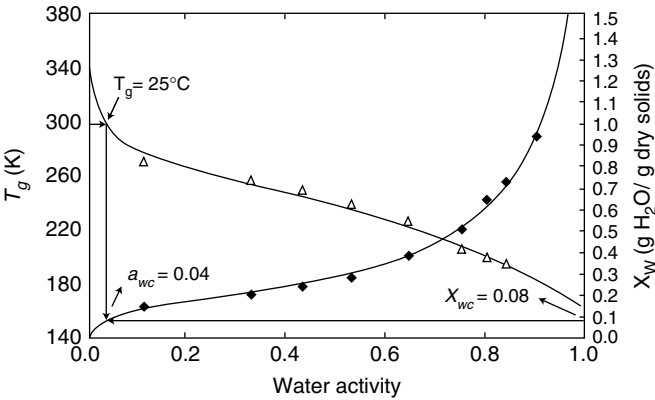


FIGURE 62.1
Water activity, glass-transition temperature, and equilibrium moisture content for freeze-dried camu-camu pulp: (♦) sorption isotherm, adjusted by GAB model, (Δ) glass-transition temperature adjusted by Equation 62.3.

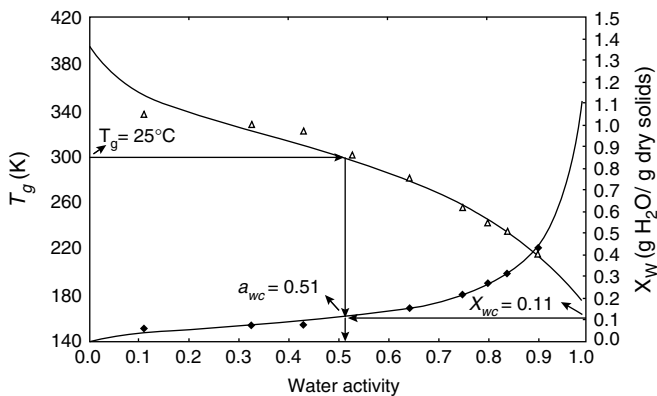


FIGURE 62.2
Water activity, glass-transition temperature, and equilibrium moisture content for freeze-dried camu-camu pulp with 30% maltodextrin DE 20: (◆) sorption isotherm, adjusted by GAB model, (Δ) glass-transition temperature adjusted by Equation 62.3.

and pulp with 30% maltodextrin DE 20 are shown in Table 62.3.

$$T_{gm} = \frac{W_s T_{gs} + kW_w T_{gw}}{W_s + kW_w}$$

(62.2)

Food products are considered stable when stored above T_g . Roos (1993) suggested to combine sorption models with the Gordon–Taylor Equation and to use the relationship to fit experimental data of T_g and water sorption in a single plot. The correlation between T_g and a_w at a constant temperature provides a simple method for the prediction of the effects of relative humidity during storage at T_g (Roos, 1995). This information is useful in locating critical values for water activity and moisture content, defined as those that provide a T_g of 25°C (ambient temperature). Since water activity is related to equilibrium relative humidity (ERH) and both T_g and a_w are functions of moisture content (X_w), the interrelationships among a_w , X_w , ERH, and T_g are

TABLE 62.3
Parameters Estimated for Gordon–Taylor Model for Freeze-Dried Camu-Camu pulp

Freeze-Dried Camu-Camu Pulp	Parameter		
	T_{gs} (°C)	k	r^2
Natural (without additive)	74.59	3.92	0.995
With 30% maltodextrin DE 20	120.45	5.52	0.997

valuable in controlling food processability and shelf life (Slade and Levine, 1991).

The GAB model (Equation 62.1) and Gordon–Taylor model (Equation 62.2) were combined to adjust the values of T_g as a function of water activity, resulting in Equation 62.3 proposed by Khalloufi et al. (2000):

$$T_g = \left(\frac{-A \cdot a_w^2 + B \cdot a_w + C}{\alpha \cdot a_w^2 + \beta \cdot a_w + 1} \right) \quad (62.3)$$

where $A = T_{gs} k_{GAB}^2 (1 - C_{GAB})$, $B = k_{GAB} [T_{gs} (C_{GAB} - 2) + C_{GAB} X_m T_{gw} k]$, $C = T_{gs}$, $\alpha = k_{GAB}^2 (1 - C_{GAB})$ and $\beta = k_{GAB} [(C_{GAB} - 2) + C_{GAB} X_m k]$.

Figure 62.1 and Figure 62.2 show the relationship between a_w , T_g , and equilibrium moisture content for freeze-dried camu-camu pulp and pulp with 30% maltodextrin DE 20, respectively. The values of critical moisture content (X_{wc}) and critical water activity (a_{wc}), for both products were estimated through the graphs on Figure. 62.1 and Figure 62.2 (indicated by arrows). For freeze-dried camu-camu pulp with 30% maltodextrin DE 20, the monolayer moisture content ($X_m = 0.064$ g H₂O/g dry solids) was lower than the critical moisture content ($X_{wc} = 0.11$ g H₂O/g dry solids). However, for freeze-dried natural camu-camu pulp, the monolayer moisture content ($X_m = 0.158$ g H₂O/g dry solids) was higher than the critical value ($X_{wc} = 0.08$ g H₂O/g dry solids). Roos (1993) observed this same trend for different DE values maltodextrins and for strawberries and horseradish roots. He determined $a_{wc} = 0.55$ and $X_{wc} = 0.09$ g H₂O/g dry solids for maltodextrin DE 20, and $a_{wc} = 0.07$ and $X_{wc} = 0.01$ g H₂O/g dry solids for strawberries. The critical water activity found for freeze-dried natural camu-camu pulp ($a_{wc} = 0.04$) was considerably lower than for camu-camu pulp with 30% maltodextrin DE 20 ($a_{wc} = 0.51$). This observation accounts for higher stability of camu-camu freeze-dried with maltodextrin. As observed during the course of the experiments, when both products were exposed to ambient conditions (approximately 25°C and 50% RH) the freeze-dried natural camu-camu pulp immediately became “sticky” and agglomerated, which is typical of this kind of material (Table 62.1) while the pulp with 30% maltodextrin remained very stable, maintaining its free flowability. This information can be very useful in designing efficient processes, since one would be able to predict and establish relative humidity limits for low moisture food products at various processing and storage conditions.

References

- Association of Official Analytical Chemistry (AOAC), *Official Methods of Analysis*, Washington, p. 1141, 1995.
- Instituto Adolfo Lutz, *Normas Analíticas do Instituto Adolfo Lutz, Métodos Químicos e Físicos Para Análises De Alimentos*, Vol. 1, 3rd Ed., Instituto Adolfo Lutz, São Paulo, 1985.

- Khalloufi, S., El Maslohi, Y., and Ratti, C. Mathematical model for prediction of glass transition temperature of fruit powders, *J. Food Sci.*, 65, 842, 2000.
- Maroulis, Z.B., Tsami, E., Marinou-Kouris, D., and Saravacos, G.D. Application of the GAB model to the moisture sorption isotherms for dried fruits, *J. Food Eng.*, 7, 63, 1988.
- Moraga, G., Martínez-Navarrete, N., and Chiralt, A. Water sorption isotherms and glass transition in strawberries: influence of pretreatment, *J. Food Eng.*, 62, 315, 2004.
- Roos, Y.H. Water activity and physical state effects on amorphous food stability, *J. Food Process. Preserv.*, 16, 433, 1993.
- Roos, Y.H. *Phase Transitions in Foods*, 1st Ed., Academic Press Inc., California, p. 360, 1995.
- Slade, L. and Levine, H. Beyond water activity: recent advances based on an alternative approach to the assessment of food quality and safety, *Crit. Rev. Food Sci. Nutr.*, 30, 115, 1991.
- Sobral, P.J.A., Telis, V.R.N., Habitante, A.M.Q.B., and Sereno, A. Phase diagram for freeze-dried persimmon, *Thermochim. Acta*, 376, 83, 2001.
- Spiess, W.E.L. and Wolf, W.R. The results of the COST 90 project on water activity, *Physical Properties of Foods*, F. Escher, B. Hallstrom, M.S. Meffert, W.E.L. Spiess and G. Voss, eds., Applied Science Publishers, New York, pp. 65–87, 1983.
- Telis, V.R.N. and Sobral, P.J.A. Glass transitions and state diagram for freeze-dried pineapple, *Lebensm.-Wiss. u- Technol.*, 34, 199, 2001.
- Zapata, S.M. and Dufour, J.P. Camu-camu (*Myrciaria dubia* (HBK) McVaugh): chemical composition of fruit, *J. Sci. Food Agric.*, 61, 349, 1993.

*Water-Sorption Isotherms and
Water-Plasticization Effect in Dried Pear*

King Xue, Consuelo González-Martínez, M. Teresa Cháfer
and Amparo Chiralt

CONTENTS

Introduction 723

Materials and Methods 724

 Raw Material and Preparation of the Samples 724

 Physicochemical Analysis..... 724

Results..... 724

Conclusion 728

References 728

Introduction

In Spain, pear var. Blanquilla has reached a production of 252,000 tons in the year 2001. As crop production mainly concentrates on the summer period (from August to September), one of the problems of its commercialization is the relatively high seasonal availability. Water-content reduction may be an interesting alternative to extend the shelf life of the product, such as occurs in other fruits (Crapiste, 2000).

State diagrams showing the relationship between product water content and its physical state as a function of the temperature together with sorption isotherms are useful tools in process optimization and food formulation in establishing processing requirements and designing package/storage conditions.

The objective of this work was to analyze the a_w -moisture content- T_g -mechanical properties relationship for pear in the range of low-intermediate moisture levels. To this end, water adsorption and desorption experiments, DSC, and mechanical analysis were carried out.

Materials and Methods

Raw Material and Preparation of the Samples

Pears var. Blanquilla purchased at a local market in Valencia (Spain) were selected according to their size uniformity and similar ripeness degree.

For adsorption isotherms, pear cubes (10 mm × 10 mm) were frozen at -40°C and freeze-dried (Telstar Lioalfa-6 lyophiliser) at 10^{-2} Pa. Afterwards, samples were placed in chambers with controlled relative humidity (RH) up to equilibrium was reached. Desorption isotherms were obtained in pear slices with skin (with approximately 8 cm diameter and 10 mm thickness), partially dehydrated in a conventional dryer at 45°C for different times to ensure different final water contents in the samples. After the drying treatment, samples were kept in plastic bags under refrigeration to ensure the internal moisture equilibration and then their water activity was measured. Experiments were carried out in triplicate for each sample.

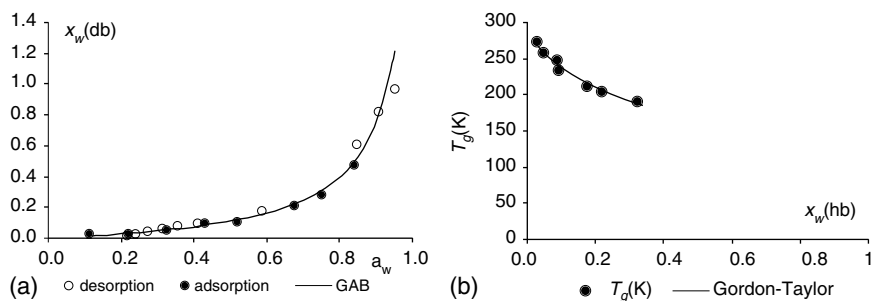
Physicochemical Analysis

Moisture content was determined by drying them under vacuum to constant weight at 60°C (AOAC, 1980). Water activity was measured at 25°C by using a Decagon Cx-3 (Aqualab) hygrometer. Mechanical properties of dried samples with different water content were analyzed at 30°C by using a puncture test with a Universal Texture Analyser (TA.XT2, Stable Micro Systems). A cylindrical 2.0 mm diameter punch was used at a penetration rate of 1.5 mm/sec until total sample penetration. Determinations were made in five different samples with the same water content.

In parallel, a small quantity of lyophilized samples placed into DSC pans was also equilibrated in each chamber at controlled RH to be submitted to DSC analysis. At equilibrium, the pans were sealed and analyzed. Glass-transition temperature was analyzed in a DSC 5200 (Seiko Instruments Inc., Chiba, Japan). Heating rate was $5^{\circ}\text{C}/\text{min}$ and temperature range varied between -20 and 80°C . The midpoint of the glass transition was considered as the characteristic temperature of the transition. Determinations were carried out in triplicate.

Results

Figure 63.1a shows the equilibrium moisture content (dry basis) at the different a_w for the desorption experiments (obtained from samples dried by hot air) and also for the adsorption experiments (obtained from the freeze-dried samples). Both isotherms are very similar and no hysteresis phenomenon was observed. Hysteresis is justified by assuming that during

**FIGURE 63.1**

(a), Water-sorption isotherms of pear at 30°C. Experimental points and fitted GAB model. (b), Relationship between T_g and moisture content of pear. Experimental points and fitted Gordon-Taylor model.

the desorption process a greater water content than the corresponding to the equilibrium is retained in the irregular porous structure because of a steric impediment to water vapor out-flow. The low porosity of this fruit, around 5% (Camañes, 2000), could explain the absence of this phenomenon presented in other fruits as mulberries, figs, raisins, prunes, and apricots (Tsami et al., 1990; Mascan and Göğüs, 1998).

As no important differences between both groups of data (absorption and desorption) were found, GAB model (Equation 63.1) was fitted to all the sorption experimental data for $a_w \leq 0.95$, where w_0 is the monolayer moisture content (g water/100 g of dry solids), C is the Guggenheim constant related to monolayer sorption heat and K is a constant related to multilayer sorption heat:

$$\frac{a_w}{w_e} = \frac{1}{w_0 \cdot C \cdot K} + \frac{C - 2}{w_0 \cdot C} a_w + \frac{K(1 - C)}{w_0 \cdot C} a_w^2 \quad (63.1)$$

GAB parameters were taken as $w_0 = 12.35\%$ g water/100 g dry solids, $C = 0.958$ and $K = 0.955$. According to Brunauer's classification (Brunauer et al., 1940), the obtained sorption isotherm may be classified as type III ($C < 2$), in agreement with that found for other fruits as blackberries, grapes, and blueberries (Roos, 1993; Vazquez et al., 1999), although type II curves were observed for other fruits as apple and strawberry (Roos, 1993; Mascan and Göğüs, 1998; Moraga et al., 2004). The typical behavior of high sugar content products was observed: a low increase in the equilibrium moisture content in the low a_w range and a sharp increase to intermediate a_w values (≈ 0.5) caused by the prevailing effect of solute-solvent interactions associated to sugar dissolution, as it has been found in other high sugar content products (Saravacos et al., 1986; Hubinger et al., 1992). Figure 63.1a shows experimental and the predicted curve, where the close fitting of the model can be observed.

All the thermograms obtained by DSC analysis of equilibrated samples showed a glass transition associated with the amorphous soluble compounds dampened to different levels. Water-soluble compounds are the main components in solid fraction of the fruits; the ratio of soluble to insoluble components being of the order of 10 to 1. The linearized equation of the Gordon–Taylor model (Equation 63.2) was fitted to experimental T_g (midpoint)-moisture data (g water/g product), considering 138 K to be T_g value of pure water ($T_{g(w)}$), $T_{g(as)}$, glass transition of anhydrous solids, and k , a constant. The obtained values for Gordon–Taylor parameters were 281.9 K and 3.91, respectively, being $R^2 = 0.819$:

$$T_g = T_{g(as)} + k \cdot \frac{w \cdot (T_{g(w)} - T_g)}{(1 - w)} \quad (63.2)$$

The experimental relationship between T_g and the moisture product content with the predicted curve is shown in Figure 63.1b, where the goodness of fitting can be observed. The plasticizing effect of the water is especially intense in the lower water content range. The T_{gas} and K obtained values were similar to those reported for fruits by other authors (Roos, 1993; Moraga et al., 2004). When T_g data were plotted as a function of a_w (Figure 63.2) a typical linear relationship in the considered a_w range was observed. Equation 63.3 shows the linear relationship between both parameters ($R^2 = 0.998$), such as has been described for other products in the intermediate a_w range (Prothon et al., 2001; Moraga et al., 2004):

$$T_g = -131.5 \cdot a_w + 302.2 \quad (63.3)$$

The obtained relationships will allow us to know the critical water content (CWC) and the critical water activity (CWA) at which the glass transition in the water-soluble phase occurs at a determined storage temperature of the product. Above these values, this phase in dried pear become sticky and rubber, and the crystallization of the amorphous compounds could take place. At 30°C (temperature at which the isotherms were obtained),

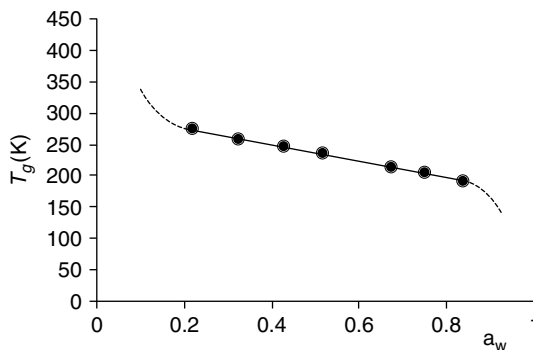


FIGURE 63.2

T_g – a_w relationship for pear samples. Experimental data and linear model.

CWC was of 3% (g water/100 g product) and CWA was of 0.22. If the CWC is compared with the monolayer moisture content ($w_0 = 12.35\%$), the greater value of the last one is observed, such as has been reported by other authors (Roos, 1993; Moraga et al., 2004). According to Roos (1993), the rates of the quality changes increase notably after plasticization promoted by temperature or water, even below the monolayer value.

Throughout a puncture test, mechanical properties of samples with different moisture content were analyzed. Parameters obtained from these curves were the maximum force required to break the sample (F_{\max}), distance at this point (d) and the ratio force–distance at the break point. The ratio force–distance at the break point (F_{\max}/d) is related to the product resistance to fracture or sample firmness (Prothon et al., 2001). The ratio F_{\max}/d has been represented vs. the moisture content in Figure 63.3, showing a sigmoid relationship, also typical in crispy products (Peleg, 1994). This behavior indicates a decrease from the resistance to deformation with the increment in moisture product content, as a consequence of the plasticizing effect of water. The ratio F_{\max}/d was adjusted to the Fermi’s model (Equation 63.4), where $Y(X_w)$ and Y_s are the firmness of samples with a moisture content X_w and in the dry state (zero moisture) respectively, X_{wc} the location of the inflection point of $Y(X_w)$, i.e., the moisture content where 50% of the firmness loss occurs and b is a measure of the steepness of the decrease in the firmness parameter over moisture range. Fitting of the model was carried out using a nonlinear regression through the program Systat (v.9.0). Obtained parameters were $Y_s = 10.66$ N/mm, $X_{wc} = 0.12$ g water/g dried product, and $b = 0.089$, being $R^2 = 0.984$. According to this model, samples have lost about 50% of its firmness when its moisture content is

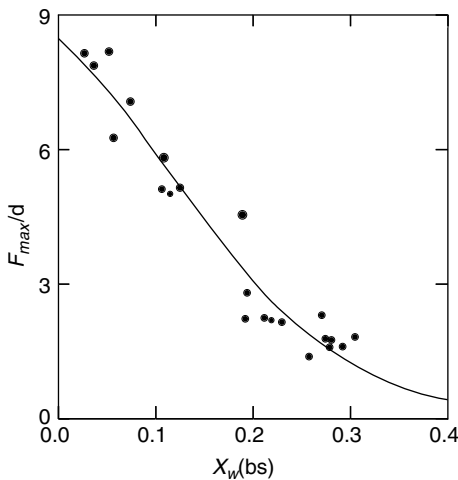


FIGURE 63.3
The ratio F_{\max}/d and water-content relationship for pear. Experimental data and fitted Fermi model.

12%, which is similar to that found for the monolayer moisture content. In Figure 63.3, the experimental data and the predicted curve are plotted, where the close fitting can be observed.

$$Y(x_w) = \frac{Y_s}{1 + \exp[(x_w - x_{wc})/b]} \quad (63.4)$$

Conclusion

Obtained results show that different phases of fruit (water-soluble compounds and insoluble product matrix) contribute to different extent to the quality preservation of dried fruit as a function of moisture content. At moisture levels higher than 3%, plasticization of the water-soluble phase can promote crystallization or deteriorative processes. Nevertheless, no relevant changes in product texture (mechanical response) occur until the moisture level reaches 12%. This observation is in agreement with the great contribution of the insoluble product matrix phase (less water-plasticizable) to the mechanical properties.

References

- AOAC, *Association of official Analytical Chemist Official Methods of Analysis*, 20.013. Washington, DC, 1980.
- Brunauer, S., Deming, L.S., Deming, W.E., and Teller, E. On a theory of the Van der Waals adsorption of gases, *J. Am. Chem. Soc.*, 62, 129, 1940.
- Camañes, B. Estudio de la deshidratación osmótica en pera var. Blanquilla, Influencia del escaldado, Thesis, Universidad Politécnica de Valencia, 2000.
- Crapiste, G.H. Simulation of drying rates and quality changes during the dehydration of foodstuffs, *Food Preservation Technology Series, Trends in Food Engineering*, J.E. Lozano, C. Añón, E. Parada-Arias and Y. Barbosa-Canovas, eds., Technomic Publishing Company, Inc., Lancaster, pp. 135–148, 2000.
- Hubinger, M., Menegalli, F.C., Aguerre, R.J., and Suarez, C. Water vapour adsorption isotherms of guava, mango and pineapple, *J. Food Sci.*, 57, 1405, 1992.
- Mascan, M. and Göğüs, F. Sorption isotherms and drying characteristics of mulberry (*Morus alba*), *J. Food Eng.*, 37, 437, 1998.
- Moraga, G., Martinez-Navarrete, N., and Chiralt, A. Water isotherms and glass transition in strawberries: influence of pretreatment, *J. Food Eng.*, 62, 315, 2004.
- Peleg, M. A mathematical model of crunchiness/crispness loss in breakfast cereals, *J. Texture Stud.*, 25, 403, 1994.
- Prothon, F., Ahrne, M., Funebo, T., Kidman, S., Langton, M., and Sjöholm, I. Effects of combined osmotic and microwave dehydration of apple on texture, microstructure and rehydration characteristics, *Lebens-Wiss Technol.*, 34, 95, 2001.
- Roos, Y. Water activity and physical state effects on amorphous food stability, *J. Food Process. Pres.*, 16, 433, 1993.

- Saravacos, G.G., Tsiourvas, D.A., and Tsami, E. Effect of temperature on the water adsorption isotherms of sultana raisins, *J. Food Sci.*, 51, 381, 1986.
- Tsami, E., Kouris, M.D., and Maroulis, Z.B. Water sorption isotherms of raisins, currants, figs, prunes and apricots, *J. Food Sci.*, 55, 1594, 1990.
- Vazquez, G., Chenlo, F., Moreira, L., and Carballo, L. Desorption isotherms of muscatel and aledo grapes and the influence of pre-treatment on muscatel isotherms, *J. Food Eng.*, 39, 409, 1999.

Index

A

Aceto Balsamico tradizionale di Reggio Emilia 671–676

acoustic bubble cavitation 613–618

acoustics 129–130, 613–618

activation activity 218–220

activation energy 683–687

activation volumes 210, 217–218

Adam–Gibbs model 199–200

adhesiveness 474–476

adsorption

air–water interface activity 423–427

at equilibrium 254–257, 265

dried pears 723–728

emulsifiers 252–254, 257–258, 265

fluid interfaces 252–258

hydroxypropylmethycelluloses 457–459

low molecular weight emulsifiers 265

propylene glycol alginates 423–425

proteins at equilibrium 265

reaction rates in foods 345–346

solute incorporation in ice phases 681–682

surface interaction energetics 639–645

water–fluid interfaces 252–258

AFM *see* atomic force microscopy

agar solutions 484–492, 520–523

agar–agar solutions 484–492

agar–maltodextrin slabs 484–492

agar–maltodextrin solutions 520–523

aging, balsamic vinegar 671–676

air cell size distribution 335–337, 338

air drying

apples 495–502

low moisture foods 120, 127–129

particle morphology 515–516

size distributions 515–516

spheres 519–523

air temperature effects 495–502

air velocity 538–542

air–water interfaces

cellulose derivative behavior 455–461

hydroxypropylmethycelluloses 455–461

protein–polysaccharide mixtures 421–429

protein–surfactant interactions 277–280

proteins and lipids 255, 261–263

rheology and microstructure 401–411

Althaea officinalis 325

altiplano quinoa genotype 566–570

amino acid residues 16–18, 26–27

amino–carbonyl condensation 623

amorphous aqueous solutions 59–75

amorphous carbohydrate matrices 709–713

amorphous maltodextrin matrices 709–713

amorphous polymer–water vapor

interactions 102–107

amorphous sugars 102, 107–112, 697–701

amorphous systems

hydration limit 303–307

long-term stability 303–307

molecular mobility 603–610

stability 303–307

water–solid interactions 101–112

amorphous trehalose 544–549

amorphous water 5–8

amylopectin retrogradation 313–317

amylose 414–419

anionic micelles 12–36

apical meristems 558–563

apples

apple juice 289–299

drying 486–487, 495–502

aqueous food pastes 379

aqueous glycinebetaine 647–654

aqueous micellar solutions 18–19, 20–22, 25

aqueous phase composition 260–261

aqueous protein solutions 16–18, 19–20, 22–25

aqueous solutions 16–25, 59–75

Araucaria angustifolia embryos 557–563

aroma compound encapsulation 709–713

Arrhenius plots/behavior 200–201

ascorbic acid 439–444, 715–720

Aspergillus nidulans 181–184

Aspergillus niger 177–184

asymmetric vibration 505–506

atomic force microscopy (AFM) 274–275, 277–279, 281, 401–402

atomistic molecular dynamics (MD) 12–36
 attraction energy 290, 294–295
 auditory sensations 129–130

B

bacteria water mobility 167–188
 bacteria water stress 167–188
 Baer II altiliano quinoa genotype 566–570
 balsamic vinegar 671–676
 BAM *see* Brewster angle microscopy
 batch drying 539–540
 BCM *see* Box-Counting method
 BD *see* Brownian dynamics
 beans 144–149
 juices 148–149
 solid residues 148–149
 bed thickness 538–542
 benzaldehyde release 711–712
 BET *see* Brunauer–Emmett–Teller
 BHI *see* brain heart infusion
Bifidobacterium 233
 binary aqueous systems 61–63
 binary polyol mixture effects 413–419
 binary water–carbohydrate mixtures 40–56
 biological activity 12–36
 biopolymer solute diffusion 593–600
 bitterness 583–591
 blanched beans 146–148
 bonding 12, 402–411, 461
 bound water 13–15, 29–33, 168
 boundary location 59–75
 bovine serum albumin (BSA) 678–682
 Box-Counting method (BCM) 485–492
 brain heart infusion (BHI) 170–177
 Brazilian French bread dough 439–444
 bread dough 439–444
 Brewster angle microscopy (BAM) 266–267, 282, 401
 brine solutions 147–148
 brittle-to-ductile transitions 126–127
 brittleness 122–130
 bromine 12–36
 Brownian dynamics (BD) 402, 403–405
 browning 364–365
 see also nonenzymatic browning
 browning index (BI) 664–668
 Brunauer–Emmett–Teller (BET) model 656–661, 705–708
 BSA *see* bovine serum albumin
 bubbles, ice nucleation 613–622
 bulk sodium chloride–water solutions 140–143
 bulk water 13, 29–33, 133–150

C

caffeine hydration 583–591
 calcein retention 552–556
 calcium 447–453
 calcium caseinate 634–637
 calorimetry 499, 503–504, 640–645
 see also differential scanning calorimetry
 camu-camu pulp 715–720
 candy 703–708
Capsicum annuum L. 537–542
 carbohydrates
 Aspergillus niger 170, 177–181
 encapsulated aroma compound release 709–713
 glass transition temperature 703–708
 magnesium chloride 663–668
 water content effect 703–708
 water diffusivity 39–56
 carbon dioxide retention 439
 carbonyl IR absorption intensity 585–587
 carbonyl peak positions 103–107
 κ-carrageenan 90–92
 λ-carrageenan 422–429
 casein micelles 221–222
 caseinates 445–453, 634–637
 catalytic activity 504–505, 507–508
 cationic micelles 12–36
 cationic resins 292–299
 cavitation bubbles 613–622
 cell cryopreservation 155–158
 cell longevity 191–201
 cell lyophilization 151–161
 cell preservation 155–158
 cellulose derivative behavior 455–461
 cellulose–sorbitol systems 170, 181–184
 cereals 123–130, 225
 cesium perfluorooctanoate anionic micelles 12–36
 charged solutes 364–365
 cheese-making properties 223–224
 chemical characterization 717
 chemical principles at high pressures 206–214
 chemical reaction equilibrium/kinetics 208–210
 chemical stability of disaccharides 663–668
 chicken egg lysozyme 545–546
 chicken meat media (CMM) 170–177
 chicken villin headpiece sub-domain 12–36
 cholesterol 156–161, 551–556
 choline 503–509
 chromatography 709–713
 Clausius–Clapeyron equation 208
 cloudy apple juice colloidal particles 289–299
 CMM *see* chicken meat media

coalescence 286
 coarse grain simulations 40–56
 cold finger apparatus 678–682
 collagens 388–397
 colloidal particles 289–299
 see also hydrocolloids
 color changes 531–535
 see also browning; nonenzymatic browning
 commercial balsamic vinegar 671–676
 compression 207–208, 212, 402–411,
 457–459, 605
 computational modeling/simulations
 401–411, 679–682
 confections 325–340, 703–708
 confocal scanning laser microscopy (CSLM)
 frozen French bread dough 440
 low moisture foods 118–119
 microstructure effect on diffusion 82–83,
 90–91, 94–96
 connectivity 81
 continuous drying 540
 convective drying 531–535
 copolymers 103–107
 corn starch 704–708
 corn syrup 704–708
 CP/MAS NMR 355–356, 361–362
 crispness 122–130
 critical water activity 726–728
 critical water content 726–728
 cryogenic storage 194–195
 cryomicroscopy 138–139
 cryopreservation
 cells 155–158
 proteins 153
 seed longevity 194–195
 tissue 155–158
 cryoprotectants 151–161
 crystal growth 133–134
 crystal hydrates 102, 107–112
 crystal packing diagrams 110–112
 crystal powders 639–645
 crystalline dehydrates 698–701
 crystalline pentahydrates 698–701
 crystalline sucrose 604–610
 crystalline-water interactions 101–112
 crystallinity of lactate dehydrogenase
 698–701
 crystallization
 amorphous aqueous solutions 61–65
 balsamic vinegar 672–676
 disaccharide stability 663–668
 freeze-dried lactose 573–581
 hydrophilic glasses 304–306
 marshmallow hardening 327–340
 nonenzymatic browning kinetics 655–661

 solute incorporation in ice phases 677–682
 spray-dried lactose 573–581
 temperatures 664–668, 672–676
 CSLM *see* confocal scanning laser microscopy
 cyclodextrin–water interactions 108

D

Debye length 290–291, 298–299
 Debye–Hückel equation 364–365
 decyl trimethyl ammonium bromide (DTAB)
 cationic micelles 12–36
 deformability/deformations 123–124,
 128–129, 284–286, 402–411,
 433–435
 degrees of freedom 52–53
 dehydration
 air drying spheres 519–523
 Lactobacillus bulgaricus 464
 lipid dehydration modulation 503–509
 red sweet peppers 537–542
 DEM *see* dynamic exchange model
 Derjaguin–Landau–Verwey–Overbeek
 (DLVO) theory 290–299
 desiccation 503–509, 557–563
 deuterium exchange 102, 107–112
 deuteron NMR 184–188
 diacetyl tartaric acid 440–444
 diacetyl tartaric acid ester of monoglycerides
 (DATEM) 440–444
 dielectric properties 73–74, 365
 dielectric relaxation (DR) 19–22
 N,N-diethyl-2-[4-(Phenylmethyl) phenoxy]
 ethanamine (DPPE) 552–556
 differential scanning calorimetry (DSC)
 amorphous aqueous solutions 66, 67–71
 bacteria and molds 170, 185
 balsamic vinegar 672–676
 camu-camu 718–720
 disaccharide stability 665–668
 dried pears 723–728
 freeze-concentrated sucrose–water
 glasses 684–687
 freeze-dried lactose 574, 575–579
 freeze-dried liposomes 552
 frozen French bread dough 440–444
 glassy starch molecular mobility 605
 glycinebetaine water sorption/desorption
 648–654
 ice nucleation 134, 137–149
 low calory candy 705–708
 low moisture foods 129
 nonenzymatic browning 625

- physicochemical changes in frozen foods 313–317
- plums 690–694
- protein freeze-dried with trehalose 544–545
- quinoa embryos and seeds 566–570
- recalcitrant *Araucaria angustifolia* 559–561
- relative humidity 625
- sodium caseinate films 448–449, 450–452
- spray-dried lactose 574, 575–579
- tapioca starch cells 473, 476–478
- water-solid interactions 105–106
- diffusion
 - air–water interface activity 426–427
 - amorphous sugars 102, 107–112
 - carbohydrates 39–56
 - coefficients
 - air drying spheres 522–523
 - convective drying of mushrooms 531–535
 - solute diffusion 594–595
 - water dynamics 30, 32–33
 - crystal hydrates 102, 107–112
 - heterogeneous materials 87–90
 - hydrated crystallines 102, 107–112
 - microstructure based modeling 92–96
 - microstructure effects 81, 85–98
 - protein–polysaccharide mixtures 426–427
 - reaction rates in foods 349–352
 - solutes 79–98, 593–600
 - solvents 79–98
 - soy flour 594–600
 - sugars 39–56
 - supramolecular microstructures 85
- dihydrates 108–112
- dilatational characteristics 267–268
 - see also* surface dilatational modulus
- diluents 610
- dimyristoylphosphatidylcholine (DMPC) 505–509
- dimyristoylphosphatidylethanolamine (DMPE) 505–509
- dioleoylphosphatidyl choline plus phloretin (DOPC:Phlo) 505–509
- dipalmitoylphosphocholine (DPPC) 156–161, 552–556
- dipolar time correlation functions 22–25
- dipole potentials 503–509
- dipole vector reorientation 22–25
- disaccharides 151–161, 463–467, 663–668
- dispersed systems 133–150, 251–271
- DMA *see* dynamic mechanical analysis
- DMPC *see* dimyristoylphosphatidylcholine
- DMPE *see* dimyristoylphosphatidylethanolamine
- DMTA *see* dynamical mechanical thermal analysis
- DOPC:Phlo *see* dioleoylphosphatidyl choline plus phloretin
- dough 439–444
- DPPC *see* dipalmitoylphosphocholine
- DPPE *see* N,N–diethyl-2-[4-(phenylmethyl)phenoxy] ethanamine
- dried products
 - milk 631–637
 - pears 723–728
 - see also* freeze-dried
- driving forces 195–198, 208–210
- drop tensiometers 422–429
- droplet size distributions 89–90, 513–517
- droplet-droplet interaction 284–286
- dry air rates 489–492
- drying
 - air drying apples 495–502
 - air drying spheres 520–523
 - fractal geometry 483–492
 - Lactobacillus bulgaricus* 463–467
 - low moisture foods 127–129
 - mushrooms 531–535
 - particle morphology 515–516
 - probiotic bacteria viability 233–242
 - size distributions 515–516
 - velocity 487–492
 - see also* freeze-dried; spray drying
- DSC *see* differential scanning calorimetry
- DTAB *see* decyl trimethyl ammonium bromide
- DVLO *see* Derjaguin–Landau–Verwey–Overbeek
- dynamic exchange model (DEM) 11–36
- dynamic mechanical analysis (DMA) 170, 185
- dynamical mechanical thermal analysis (DMTA) 605
- dynamics
 - hydrated proteins 28
 - protein–glass transition 28–33
 - protein–water systems 11–36
 - water-fluid interfaces 251–271

E

- echo 87–90, 93, 95–96, 97
- edible films 413–419, 445–453
- EDVLO *see* extended Derjaguin–Landau–Verwey–Overbeek

effective diffusion coefficients 522–523,
 531–535
 elastic modulus 320–321
 elasticity 459
 electrical double layers 290–291, 298–299
 electrical measurements 73–74
 electrolyte solutions 650–654
 electrostatic interactions 210, 290–291,
 294–295, 650–654
 electrostatic repulsion 290–291, 294–295
 electrostriction 210
 emulsifiers 251–271
 emulsions 81–85, 90–96, 273–287
 encapsulated aroma compound release
 709–713
 energy
 activation 683–687
 free energy 196–197, 208–210
 Gibbs free energy 208–210
 hydration 291–292, 296, 299
 ice nucleation 134–137
 interaction energy 290–292, 295–299
 repulsion 290–291, 294–295
 Van der Waals 290, 294–295
 enterotoxin 12–36
 enthalpy 605, 672–676, 683–687
 entropy 201, 209
 environmental scanning electron microscopy
 (ESEM) 118–119
 enzymatic activity 218–220, 504–505,
 507–509, 544–549, 701
 enzymatic reactions 212
 enzyme assays 699
 equilibrium
 adsorption 254–257, 265
 chemical reactions 208–210
 moisture content 499–500, 718–720,
 724–728
 relative humidity 719–720
 spreading 254–257
 surface pressure 456, 457
 thermodynamics 60
Escherichia coli 34–35, 216, 217
 ESEM *see* environmental scanning electron
 microscopy
 esterification 422–429
 ethanolamines 503–509
 ethyl acetate release 712
 expansion 402–411, 457–459
 extended Derjaguin–Landau–Verwey–
 Overbeek (EDLVO) theory
 290–299
 extension resistance 443
 extracted juices 148–149

F

fat globules 222
 FEMLAB 94–95
 Fermi model 218
 films
 edible 413–419, 445–453
 gelatin-based 431–436
 glycerol 414–419, 432–436, 445–453
 β -lactoglobulin protein 277–280
 maltodextrin 377–385
 mixed protein 281–282
 potato starch-based 414–419
 protein films 266–269, 270–271, 401–411,
 445–453
 sodium caseinate 445–453
 starch-based 413–419
 structural characteristics 258–261
 thickness 431–436, 448
 finite element methods 81, 88
 fish 224–225
 see also meat
 fluid interfaces
 food emulsifiers 251–271
 lipids 251–271
 protein–LMWE interactions 265–271
 proteins 251–271
 rheology and microstructure 401–411
 spread film thermodynamics 258–261
 surface pressure 257–258
 foams 252–254, 273–287, 337–340
 folding 387–388, 393–397
 forces
 cloudy apple juice 290
 driving 195–198, 208–210
 force–deformation curves 123–124,
 128–129
 maximum force at breakage 128–129
 puncture force 433–435
 formation dynamics 421–429
 Fourier transform infrared (FT-IR) 504–509,
 544, 545–546, 583–591
 Fourier Transform Raman spectroscopy
 102–107
 fractal geometry drying 483–492, 519–523
 fracture 126–127
 free diffusion 87–90
 free energy 196–197, 208–210
 free volume (FV) theory
 glassy starches 609–610
 maltodextrin films 377–378
 solute diffusion 593–600
 water–carbohydrate diffusion 49, 55–56
 free water 13–15, 29–33, 168

freeze-concentrated sucrose–water glasses 683–687

freeze-dried products

- amorphous sugar excipients 697–701
- camu-camu 715–720
- disaccharide matrices 151–161
- lactate dehydrogenase activity 697–701
- lactose 573–581
- lipid bilayers 151–161
- locust bean 170, 184–188
- low moisture foods 127–129
- lysozyme 544–549
- plums 689–694
- probiotic bacteria viability 238–239

freezing

- ice nucleation 133–150
- lipid bilayers in disaccharide matrices 151–161
- points 212–214, 648–654
- rate effects 318–321
- recalcitrant *Araucaria angustifolia* 557–563
- solute incorporation 677–682
- temperatures 134–137

French bread dough 439–444

frequency dependent dielectric functions 21–22

frozen food physicochemical changes 309–322

frozen French bread dough 439–444

frozen gelatinized systems 314

frozen plant products 133–150

frozen starch–sucrose hydrocolloids 309–322

frozen storage effects 318–321

fruits

- apple juice particles 289–299
- apples 289–299, 486–487, 495–502
- camu-camu pulp 715–720
- dried pears 723–728
- plum skin and pulp 689–694

FT-IR *see* Fourier transform infrared

full cream milk powder 634–637

fusion 212–214, 442–443

FV *see* free volume

G

GAB *see* Guggenheim–Anderson–deBoer

galacturonic acid content 498

gas chromatography 709–713

gas-phase conformations 391

GB *see* glycinebetaine

gelatin-based films 431–436

gelatinization 314, 318–321, 475

gelatinized starch 624–629

gels 81–85, 90–92, 97, 225–226

genetic resources 191–201

genotypes, quinoa 566–570

germination 170, 177–184, 560

Gibbs free energy 208–210

glass transition

- amorphous aqueous solutions 59–75
- bacteria and molds 168–169, 177
- freeze-dried lactose 573–581
- frozen starch–sucrose hydrocolloids 309–322
- lipid bilayers in disaccharide matrices 153
- maltodextrin matrices 709–713
- plum skin and pulp 689–694
- protein–water system dynamics 28–33
- reaction rates in foods 343–368
- spray-dried lactose 573–581

glass transition temperatures

- air drying apples 499–500
- amorphous solids stability 303–307
- amorphous trehalose 544–549
- balsamic vinegar 672–676
- camu-camu 715–720
- disaccharide stability 663–668
- freeze dried camu-camu 715–720
- freeze-concentrated sucrose–water glasses 684–687
- frozen gelatinized systems 314
- glassy starch molecular mobility 606–610
- glycinebetaine water sorption/desorption 647–654
- hydrophilic glasses 304–306
- low calory candy 703–708
- low moisture foods 124–127
- maltodextrin films 377–385
- nonenzymatic browning 627–629, 656–661
- protein freeze-dried with trehalose 543–549
- relative humidity 627–629
- seed deterioration kinetics 198–201
- sodium caseinate films 450–452
- solute diffusion 595–600
- water-solid interactions 105–106

glassy carbohydrates 39–56

glassy preservation 699

glassy stability 603–610

glassy starch 603–610

glassy sugars 683–687

glassy water 5–8

globular proteins 392–393, 395–396

glucose

- enthalpy relaxation 683–687
- glycinebetaine water sorption/desorption 647–654

- marshmallow hardening 326–340
- nonenzymatic browning 624–629
- rotation 39–56
- glycerol
 - lipid membrane phosphate hydration modulation 503–509
 - plasticized films 432–436, 445–453
 - Staphylococcus aureus* growth 170–177
 - starch-based edible films 414–419
- glycine 624–629, 647–654
- glycinebetaine (GB) 647–654
- Gordon–Taylor model
 - camu-camu 718–720
 - dried pear water content 726–728
 - freeze-dried plum state diagrams 693–694
 - maltodextrin films 380, 383, 385
 - nonenzymatic browning 656–661
 - solute diffusion 596
 - sugar crystallization effects 656–661
- green beans 144–149
- guar gum 313–317, 319–321
- Gugenheim–Anderson–deBoer (GAB) model
 - camu-camu 717–720
 - dried pear 725–728
 - low calory candy 705–708
 - maltodextrin matrices 709–713
 - nonenzymatic browning kinetics 656–661
- gum Arabic 378–379
- gums 170, 184–188, 313–321, 378–379, 422–429, 678–682

H

- Hamaker constant 295
- hardening 122, 325–340
- hardness 122–130, 474–476
- health benefits of probiotics 233–242
- heat capacity 200–201, 526–529
- heat of crystallization 677–682
- heat flow 139–149, 639–640
- heat generation 137–138
- heat transfer units 525–529
- heterogeneity 79–98, 170, 177–184
- hibernation 156–161
- high osmolarity 463–467
- high pressure
 - biological structure changes 205–227
 - casein micelles 221–222
 - cereals 225
 - cheese-making properties 223–224
 - chemical principles 206–214

- enzymatic activity 218–220
- fat globules 222
- fish 224–225
- gels 225–226
- living organisms 205–227
- meat 224
- microorganisms 214–218
- milk 220–224
- tapioca starch cells 471–481
- thermodynamic principles 206–214
- vegetables 225
- water stress 205–227
- whey proteins 222
- high-speed optical photography 613–622
- historical overviews 168–169
- host-guest experiments 392–393
- HPMC *see* hydroxypropylmethycelluloses
- hydrated crystallines 102, 107–112
- hydrated states 544–549
- hydration
 - amorphous solids 303–307
 - bonding 388–390, 395–396
 - energy 291–292, 296, 299
 - freeze-dried lysozyme 544–549
 - glassy starch molecular mobility 603–610
 - hydrophilic polymer glasses 306
 - layer dynamics 12–36
 - lipid membrane phosphate 503–509
 - polymer glasses 306
 - protein glasses 307
 - reaction rates in foods 345–346
 - residual water effects 548
 - seed deterioration kinetics 197–198
 - shell water molecules 12–36
 - small molecule hydrophilic glasses 304–306
 - water diffusion 102, 107–112
 - zero mobility temperature 307
- hydrocolloids 309–322
- hydrogen bonding
 - cloudy apple juice particles 296
 - high pressure 211–212
 - lifetime dynamics 25–28
 - protein freeze-dried with trehalose 543–549
 - reaction rates in foods 365
 - water with amorphous polymers 102–107, 112
- hydrogen exchange 102, 107–112
- hydrogen NMR 181–188, 474
- hydrophilic amorphous polymer–water vapor interactions 102–107
- hydrophilic glasses 304–306
- hydrophilic glycols 359

hydrophilic polymer glasses 306
 hydrophobic bonds 461
 hydrophobic collapse 396
 hydroxypropylmethycelluloses (HPMC)
 455–461
 hygroscopicity 103–107
 hyphae growth rate 182–184

I

ice

 binding sites 677
 crystal growth 678–682
 dendrite fragmentation 614, 621
 melting curves 441–443
 nucleation 133–150, 613–622
 phase during freezing 677–682
 separation 61–65

ideal phase diagrams 61–63

ideal state diagrams 61–63

IDF *see* International Dairy Federation

image analysis 85

IMF *see* intermediate moisture foods

immersion contact chilling 147–148

inactivation kinetics 214–218

ingredient applications 240–241

inhibition enzymatic activity 218–220

instant crystallization temperature 47–49

interaction energy 290–292, 295–299

interfaces

 adsorbed films 253–254
 air–water 255, 261–263, 277–280,
 401–411, 421–429, 455–461
 fluid 251–271, 277–280, 401–411, 421–429,
 455–461
 lengths 404
 mixed protein films 281–282
 molecular organization 273–287
 oil–water 401–411
 physico-chemical characteristics 252–254
 proteins 251–271, 276–281, 401–411
 rheology and microstructure 401–411
 surfactants 276–281, 401–411
 water–fluid 251–271, 276–286

intermediate moisture foods (IMF) 168,
 171–172

International Dairy Federation (IDF) standard
 632–637

International Standard Method 631–637

ion concentration 292–293

ionic strength 291, 292–293, 298

isomalt 704–708

isothermal microcalorimetry 640–645

J

jellified maltodextrin solutions 520–523

juices 148–149, 289–299

jumps 51–52

K

Karl Fischer Titration (KFT) 632–637

kinetic trapping 681–682

kinetics

 amorphous aqueous solutions 65
 chemical reactions 208–210
 diffusion 85
 high pressure effects 208–210, 215–218
 microstructure effects 85
 seed deterioration 195–201
 state diagram utility 60

Kohlraush–William–Watts (KWW) equation
 684–687

L

lactate dehydrogenase (LDH) 544–549,
 697–701

lactic bacteria recovery 464–467

Lactobacillus spp. 233, 236

L. acidophilus 155–158

L. bulgaricus 463–467

β -lactoglobulin 84–85, 90–92, 277–280,
 421–429

lactose

 crystallized water 632–637
 freeze-dried 573–581
 gelatinized starch 627–629
 monohydrate 573–581
 nonenzymatic browning 624–629,
 656–661
 relative humidity 624–629
 spray-dried 573–581
 trehalose matrices 656–661

α -lactose crystallized water 632–637

α -lactose monohydrate 573–581

lag times 171–173, 176–177, 464

Larmor frequency 93

laser-induced bubbles 614, 619–620

LBG *see* locust bean gum

LDH *see* lactate dehydrogenase

Le Chatelier–Braun principle 206–207

legume hardening 122

length scales 79–98

 emulsions 81–85, 90–96

 gels 81–85, 90–92, 97

lettuce seeds 200–201
 leukotriene antagonists 640–645
 light microscopy 82, 473–474, 560, 665–668
 lipids
 bilayers in disaccharide matrices 151–161
 dehydration modulation 503–509
 membrane phosphate hydration 503–509
 molecular organization 276–281
 vesicles desiccation 551–556
 water-fluid interfaces 251–271
 liquid water 170, 177–181
 liquid–liquid phase transitions 6–7
Listeria spp., *innocua* 216, 217, 218
monocytogenes 216, 217
 live probiotic bacteria 233–242
 living organisms
 probiotic bacteria viability 233–242
 water stress 167–188, 191–201, 205–227
 LMF *see* low moisture foods
 LMWE *see* low molecular weight emulsifiers
 local degrees of freedom 52–53
 locust bean 170, 184–188
 locust bean gum (LBG) 678–682
 long-term aging 671–676
 long-term preservation of genetic resources
 191–201
 long-term stability of amorphous solids
 303–307
 low calory candy 703–708
 low moisture foods (LMF) 115–130, 655–661
 low moisture glasses 603–610
 low molecular weight emulsifiers (LMWE)
 251–271
 adsorption 265
 reflectivity 261–263
 relaxation phenomena 263–264
 spreading 265
 viscoelastic properties 261–263
 low-fat spreads 89–90
 lyophilization 151–161
 cells 155–158
 preserving tissue 155–158
 proteins 154–155
 tissue 155–158
 lyoprotectants 151–161
 lysozyme 544–549

M

macroscopic characterization/properties 82,
 471–472, 473, 474–476
 magnesium chloride 663–668
 magnetic fields 93
 magnetic resonance imaging (MRI) 118–119

Maillard reaction 364–365, 655–661, 664
 maize starch 604–610
 maltitol syrup 704–708
 malto-oligomer glucose 40
 malto-oligosaccharides 40
 maltodextrin
 air drying spheres 520–523
 camu-camu 715–720
 encapsulated aroma compound release
 709–713
 films 377–385
 fractal geometry drying 484–492
 low calory candy 704–708
 wheat flour 126–127
 maltose 683–687
 mannitol 184–188
 margarines 89–90
 marshmallow hardening 325–340
 mass loss 635–636
 mass transfer 525–529, 531–535
 mass transport 81, 85–98
 mathematical modeling 85
 matrices
 amorphous maltodextrin 709–713
 disaccharide 151–161
 glass transition 693–694
 mobility influence 353–356
 trehalose 656–661
 maximum force at breakage (MFB) 128–129
 maximum freeze concentration 65
 MCT *see* mode coupling theory
 MD *see* molecular dynamics
 mean air cell sizes 335–336
 mean molecular weight 379
 mean square displacement (MSD) 30–33,
 42–43
 measurement limitations 66–67
 measurement-phase relationships 66–74
 meat 170–177, 224
 see also fish
 mechanical measurements 66, 71–73
 mechanical properties
 air drying apples 500–501
 dried pears 723–728
 gelatin-based films 431–436
 low moisture foods 122–130
 starch-based edible films 413–419
 mechanical spectrometry 597–600
 medicinal pastes 325
 melting temperatures 134–137, 664–668,
 672–676
 melting transition 158
 membranes
 cholesterol containing 551–556
 composition 552–556

- phase transitions 156–161
 - phosphate hydration modulation 503–509
 - metabolites extraction 226
 - MFB *see* maximum force at breakage
 - micelles 11–36
 - aqueous solutions 18–19, 20–22, 25
 - casein micelles 221–222
 - microbial growth 167–188
 - microbial inactivation 214–218
 - microcalorimetry 640–645
 - microdispersion 251–271, 273–287, 289–299
 - microheterogeneity 118
 - microlength scales 79–98
 - microorganisms 214–218
 - microscopic characterization/properties
 - 471–472, 473–474, 478–481
 - microscopic nature 11–36
 - microscopy
 - diffusion 81, 82–83, 85–98
 - ice nucleation 134, 138–139, 140–144, 145–146
 - light 82, 473–474, 560, 665–668
 - low moisture foods 118–119
 - microstructure effect 81, 82–83, 85–98
 - molecular organization 274–276
 - spray drying 514
 - microstructure
 - air drying spheres 519–523
 - fractal geometry drying 486
 - interface stabilization 401–411
 - length scales 81
 - low moisture foods 118–130
 - probe diffusion 96–98
 - solute diffusion 79–98
 - solvent diffusion 79–98
 - water diffusion 92–96
 - microwave applications 495–502
 - milk 220–224, 445–453, 631–637
 - milk powders 631–637
 - milk proteins 445–453
 - mineral oil-water solutions 143–144
 - mixed protein films 281–282
 - mobility 307
 - see also* molecular mobility;
 - water mobility
 - mode coupling theory (MCT) 30
 - modified free volume theory 593–600
 - modulated DSC 66, 70
 - modulation 503–509
 - moisture content
 - air drying apples 497–502
 - camu-camu 716–720
 - dried pears 723–728
 - low moisture foods 115–130
 - marshmallow hardening 326–340
 - moisturized soy flour 594–600
 - particle morphology 526–529
 - particles during spray drying 513–517
 - reaction rates in foods 343–368
 - tapioca starch cells 473–481
 - moisture diffusivity 120, 594–600
 - moisture equilibration 497
 - moisture sorption/desorption 594–600
 - moisturized soy flour 594–600
 - molds 167–188
 - spore germination 170, 177–184
 - molecular characterization/properties
 - 151–161, 471–472, 474, 480–481
 - molecular dynamics (MD) 12–36, 39–56
 - molecular mobility
 - amorphous aqueous solutions 59–75
 - glassy starch 603–610
 - maltodextrin films 377–378
 - quinoa embryos and seeds 569–570
 - reaction rates in foods 343–368
 - seed deterioration kinetics 199–201
 - tapioca starch cells 474
 - molecular organization 273–287
 - molecular structure 455–461
 - molecular theory 347–348
 - molecular weight 377–385
 - monoglycerides 261–263, 268–269
 - monolayers
 - interfaces 259–260, 261–263, 405–410
 - low calory candy 707–708
 - moisture value 345, 347–348
 - surface shear 268–269
 - Monte Carlo methods 88
 - morphology 513–517, 519–523, 525–529
 - MRI *see* magnetic resonance imaging
 - MRS, *Lactobacillus bulgaricus* 464–467
 - MSD *see* mean square displacement
 - multiexponential fitting parameters 24
 - Myrciaria dubia* pulp 715–720
- ## N
- nanolength scales 79–98
 - National Center for Genetic Resources
 - Preservation (NCGRP) 191–201
 - National Seed Storage Laboratory (NSSL)
 - 191
 - NCGRP *see* National Center for Genetic Resources Preservation
 - near-field optical microscopes (NOM)
 - 275–276, 281–282
 - NEB *see* nonenzymatic browning
 - NMR *see* nuclear magnetic resonance
 - NOM *see* near-field optical microscopes

nonenzymatic browning (NEB)
 disaccharide stability 664–668
 reaction rates in foods 358–362, 366
 relative humidity 623–629
 sugar crystallization effects 655–661
nonreducing disaccharide stability 663–668
nonvacuum impregnation 496–502
normalized total interaction energy 295–298
NSSL *see* National Seed Storage Laboratory
nuclear magnetic resonance (NMR)
 bacteria and molds 167–188
 diffusion 81, 85–98
 microstructure effects 81, 85–98
 polyproline II conformation 394–395
 reaction rates in foods 355–356
 Staphylococcus aureus growth 170–177
 tapioca starch cells 474
nucleation of ice 133–150, 613–622
nutraceuticals 445–453

O

oil-soluble LMWE 254–255, 265
oil–water interfaces 401–411
Ollagüe quinoa genotype 566–570
opalescent apple juice colloidal particles
 289–299
optical laser-induced cavitation bubbles
 619–620
organism survival 170, 184–188
orogenic mechanism 270–271, 284
osmolarity 463–467
osmotic stress 505–506, 648
oven drying 633–637
overlapping water relations
 glass transition 343–368
 hydration limit of amorphous solids
 303–307
 marshmallow hardening 325–340
 physicochemical changes in frozen foods
 309–322
 reaction rates in foods 343–368
 stability of amorphous solids 303–307
 water activity 343–368
oxygen-17 NMR 170–184

P

particle morphology 513–517, 525–529
particle size issues 513–517
particle-particle interactions 402–411
particulate gels 83

partition coefficients 679
Pate de Guimauve 325
pectic composition 498–502
pectin 289–290
PEG *see* polyethyleneglycol
penetration rates 426
pentahydrates 108–112
peptides 677
perfluorooctanoate 12–36
PGA *see* propylene glycol alginates
pH 292–293, 366, 673
phase diagrams 60–75, 212–214
phase transitions 6–7, 60–75, 551–556
Phaseolus vulgaris 144–149
phloretin 503–509
phosphate hydration modulation 503–509
phosphatidylcholine hydrate modulation
 503–509
phospholipid bilayers 158–159, 552–556
phospholipid liposome desiccation 551–556
physical properties
 balsamic vinegar 671–676
 disaccharides 663–668
 freeze-dried lactose 576, 577
 spray-dried lactose 576, 577
 starch-based edible films 413–419
physicochemical analysis 309–322, 472–481,
 724–728
plasticization
 dried pears 723–728
 maltodextrin films 378–379
 reaction rates in foods 346–347, 355–360,
 366
 starch-based edible films 414–419
plasticized gelatin-based films 432–436
plasticized sodium caseinate films 445–453
Pleurotus ostreatus 531–535
plum skin and pulp glass transitions 689–694
plums 689–694
polar solvent dipoles 15–19
polarization response 19–22
polarized light microscopy 665–668
polycrystalline ice hemisphere growth rates
 677–682
polyethyleneglycol (PEG) 464–467, 505
polymer fracture 126–127
polymer hydration limit 306
polymer probe diffusion 97–98
polymorphic drugs 640–645
polyol crystallization 414–419
polypeptide chain conformation 390–397
polyproline II conformation 387–397
polysorbate 80 440–441
poly(vinyl acetate) (PVAc) 103–107
polyvinyl alcohols (PVA) 678–682

poly(vinylpyrrolidone) (PVP) 103–107,
624–629

poly(vinylpyrrolidone-co-vinyl acetate)
(PVP/VA) 103–107

potatoes 127–129, 414–419, 486–487

powdered probiotics 240–241

powders

- agglomeration 226
- characteristics 513–517
- compression 605
- surface interaction 639–645
- water adsorption 639–645

power ultrasound 613–622

preferential-exclusion principle 154

pregelatinized waxy maize starch 604–610

preservation

- cells 155–158
- high pressure 205–227
- proteins 153, 154–155
- tissue 155–158

principle components analysis 106–107, 108

probe diffusion 96–98

probing water-solid interactions 101–112

probiotic bacteria viability 233–242

product functionality 119–122

proline 647–654

propagators 93

propylene glycol alginates (PGA) 422–429

protectant formulations 151–161

protein-based edible films 445–453

protein films 266–271, 401–411, 445–453

protein folding 387–388, 393–397

protein freeze-dried with trehalose 543–549

protein glasses 307

protein-glass transition 28–33

protein-LMWE films 266–271

protein-LMWE interactions 265–271

protein-LMWE mixed monolayers 268–269

protein-polysaccharide mixtures 421–429

protein-protein films 401–411

protein surface water dynamics 11–36

protein-surfactant interactions 276–281

protein-surfactant mixed films 401–411

protein unfolding 393–395, 396

protein-water hydrogen bonds 26–28

protein-water system dynamics 11–36

proteins

- at equilibrium 265
- concentrations 254–257
- hydration 387–397
- preservation 153, 154–155
- relaxation phenomena 263–264
- water-fluid interfaces 251–271

Prunus domestica 689–694

pulped camu-camu 715–720

puncture deformation 433–435

puncture force 433–435

puncture strength 450, 452

puncture tests 727–728

PVA *see* polyvinyl alcohols

PVAc *see* poly(vinyl acetate)

PVP *see* poly(vinylpyrrolidone)

PVP/VA *see* poly(vinylpyrrolidone-co-vinyl acetate)

Q

quality changes 537–542

quinoa embryos and seeds 565–570

R

rabbit muscle lactate dehydrogenase 544–545,
698–701

radioactive tracer movement 350–352

raffinose 170–177, 698–701

raffinose pentahydrate 108–112

Raman spectroscopy 102–107, 108–110,
394–395

raw beans 144–146

reaction rates in foods 343–368

recalcitrant *Araucaria angustifolia* embryos
557–563

recycle ratio 538–542

red sweet peppers 537–542

reference drying 633–637

reflectance 534

reflectivity 261–263

relative humidity

- air drying apples 497–502
- camu-camu 719–720
- gelatin-based films 431–436
- hydrophilic glasses 304, 305–306
- lactate dehydrogenase activity 700–701
- nonenzymatic browning 623–629
- quinoa embryos and seeds 567–570
- starch-based edible films 413–419

relaxation

- emulsifiers 253–254, 263–264, 267
- freeze-concentrated sucrose–water
glasses 683–687
- glassy starch molecular mobility 604,
605, 609
- low molecular weight emulsifiers
263–264, 267
- malto-oligomer glucose 40
- protein-LMWE mixed films 267

protein–water systems 13–15
 proteins 263–264
 spread emulsifiers 263–264
Staphylococcus aureus growth 172–174
 supercooled glucose 40
 tapioca starch cells 480–481
 water–carbohydrate diffusion 39–56
 relaxational spectroscopy 74
 relaxometry 74, 170, 172–174
 repulsion energy 290–291, 294–295
 residual molecular mobility 603–610
 residual water 543–549
 resins 292–299
 resistance factors 198–201
 restricted diffusion 87–90
 rheology
 balsamic vinegar 672–676
 frozen starch–sucrose hydrocolloids
 309–322
 interface stabilization 401–411
 solute diffusion 597–600
 tapioca starch cells 473, 476–478
Rhizopus japonicum survival 184–187

S

saccharides 40, 53–54, 151–161, 463–467,
 663–668
 Sajama quinoa genotype 566–570
 saturated-LMWE monolayers 259–260,
 261–263
 scanning electron microscopy (SEM) 118–119,
 574–577
 scanning near-field optical microscopes
 (SNOM) 275–276, 281–282
 seeds
 deterioration kinetics 195–201
 longevity 191–201
 quinoa embryos and seeds 565–570
 recalcitrant *Araucaria angustifolia* 557–563
 self-correlation functions 43–45, 50–53, 55
 self-detachment 377–385
 self-diffusion 88–89
 SEM *see* scanning electron microscopy
 semi-moist foods 345
 semi-solid heterogeneous systems 170,
 177–184
 sepharose gel 83–84
 SGP *see* short-gradient-pulse approximation
 shape issues 81
 short-gradient-pulse approximation (SGP)
 93, 95–96
 shrinkage 485–486, 487–492
 single bubble cavitation 614, 616–618
 single oscillating bubbles 614, 616–618
 single water molecule reorientational
 dynamics 22–25
 singularity-free interpretation 7
 skimmed milk powder 634–637
 small molecule hydrophilic glasses 304–306
 SNOM *see* scanning near-field optical
 microscopes
 sodium alginates 313–317, 319–321
 sodium caseinate films 445–453
 sodium chloride 140–143, 170–177, 678–682
 sodium stearyl lactylate (SSL) 440
 solid residues 148–149
 solid system microbial survival 184–188
 solubility 365
 solutes
 diffusion 79–98, 593–600
 incorporation 677–682
 reaction rates in foods 364–365
 solvation dynamics 15–19
 solvent diffusion 79–98
 solvents 346–347, 353–356
 sorbitol 360–363, 414–419
 sorbose systems 181–184
 sorption
 camu-camu 715–720
 dried pears 723–728
 low calory candy 705–708
 nonenzymatic browning kinetics
 656–661
 soy flour 594–600
 sugar crystallization effects 656–661
 see also water sorption/desorption
 sound 129–130
 soy flour 594–600
 spectrometry 597–600
 spectroscopy
 Fourier Transform Raman 102–107
 Raman 102–107, 108–110, 394–395
 relaxational 74
 vibrational 101–112
 spin-label probes 353–355
 spore germination 170, 177–184
 spray drying
 air drying spheres 519–523
 Lactobacillus bulgaricus 463–464
 morphology of particles 513–517, 525–529
 particle morphology 513–517, 525–529
 probiotic bacteria viability 235–238
 spray-dried lactose 573–581
 spread β -lactoglobulin protein films 277–280
 spreading
 low molecular weight emulsifiers 265
 proteins at equilibrium 265
 water-fluid interfaces 254–257, 258–261

- stability
 - amorphous solids 303–307
 - cloudy apple juice particles 289–299
 - disaccharides 663–668
 - freeze-dried liposomes with trehalose 551–556
 - limit conjecture 6
 - marshmallow hardening 326–340
 - polyproline II conformation 391
 - protein freeze-dried with trehalose 543–549
 - reaction rates in foods 343–368
- standing waves 614, 616–618
- Staphylococcus aureus* growth 168, 170–177
- starches
 - Aspergillus niger* 170, 177–181
 - gelatinization 318–321
 - molecular mobility 603–610
 - starch gels 471–481
 - starch-based edible films 413–419
 - starch–sucrose hydrocolloids 309–322
 - starch–sugars 170, 177–181
 - structure–property relationships 127–129
- state diagrams
 - boundary location 59–75
 - dried pears 723–728
 - freeze-dried plums 689–694
 - glycinebetaine aqueous systems 647–654
 - physicochemical changes in frozen foods 310–312
- State Transition Theory 206, 209–210
- stepwise DSC 66, 69–70
- stiffness 122–130
- Stokes–Einstein equation 349–350
- storage
 - amorphous sugar excipients 697–701
 - camu-camu 715–720
 - disaccharide stability 667–668
 - dried milk products, water content 631–637
 - lactate dehydrogenase 544–549, 697–701
 - lipid bilayers in disaccharide matrices 151–161
 - marshmallow hardening 327–340
 - probiotic bacteria viability 234–242
 - protein freeze-dried with trehalose 544–549
 - quinoa embryos and seeds 565–570
 - recalcitrant *Araucaria angustifolia* embryos 557–563
 - starch–sucrose hydrocolloids 318–321
- strain selection 237–238
- stress
 - glycinebetaine water sorption/desorption 648
- probiotic bacteria viability 239
- relaxation 597–598
- tensors 404
- uniaxial deformations 402–411
- structure
 - air drying apples 495–502
 - air–water interfaces 421–429
 - drying of vegetables 537–542
 - high pressure effects 205–227
 - low moisture foods 116–119
 - low moisture products 115–130
 - nonenzymatic browning 623–629
 - protein–LMWE mixed films 266–267
 - protein–polysaccharide mixtures 421–429
 - related diffusion properties 80
 - relative humidity 623–629
 - tapioca starch cells 471–472, 473, 476–478
 - see also microstructure
- subcellular freezing injuries 557–563
- sublimation 238–239
- substitution effects 456
- sucrose
 - Aspergillus niger* 170, 177–181
 - caffeine bitterness inhibition 583–591
 - enthalpy relaxation 683–687
 - glass transition 313–317
 - glassy starch molecular mobility 603–610
 - hydration 159, 583–591
 - hydration limit 304–306
 - Lactobacillus bulgaricus* 465–467
 - low calory candy 704–708
 - maltodextrin films 377–385
 - marshmallow hardening 327–340
 - rheological behavior 313–317
 - solute incorporation in ice phases 678–682
 - stability in presence of magnesium chloride 663–668
 - sucrose–starch system 170, 177–181
 - sucrose–water glasses 683–687
 - water–solid interactions 108
- sugars
 - crystallization 655–661, 663–668, 698–701
 - hydrolysis kinetics 663–668
 - lactate dehydrogenase activity 698–701
 - Lactobacillus bulgaricus* 463–467
 - matrix glass transition curves 693–694
 - nonenzymatic browning kinetics 655–661
 - reaction rates 362–363
 - sugar/sugar syrups 332–340
 - water diffusion 39–56
- superabsorbent gel 83–84, 90–92
- supercooled carbohydrates 39–56
- supercooled glucose 40
- supercooled water 5–8
- superposition principle 597–598

supramolecular microstructures 85
 surface area 333, 335–337
 surface characterization 483–492
 surface dilatational modulus
 fluid interfaces 257–258, 261–263,
 267–268, 427–428
 hydroxypropylmethycelluloses 461
 protein–LMWE mixed films 267–268
 protein–polysaccharide mixtures
 427–428
 surface elastic moduli 461
 surface film balance 457
 surface interaction energetics 639–645
 surface pressure 254–259, 261–263, 423–427,
 457–458
 surface properties,
 hydroxypropylmethycelluloses
 455–461
 surface shear films 268–269
 surface tension 265
 surface-to-surface distances 295–298
 surfactants 276–281, 401–411
 survival of organisms 170, 184–188
 sweetness 583–591
 symmetric vibration 505–506

T

tapioca starch cells 471–481
 taste masking 583–591
 TCF *see* time correlation functions
 temperature factors
 air drying apples 495–502
 emulsifier spread films 260–261
 fractal geometry drying 489–492
 frozen French bread dough 442–443
 gelatin-based films 431–436
 high pressure 207–208, 209
 ice nucleation 134–137, 139–149
 low moisture foods 121, 124–129
 protein–glass transition 29–33
 seed longevity 194–201
 tapioca starch cells 471–481
 vegetable dehydration 538–542
 see also glass transition temperature
 tempering cycles 531–535
 tensile strength 417
 texture
 dried pears 724
 frozen French bread dough 439–444
 low moisture foods 121–130
 starch–sucrose hydrocolloids 318–321
 tapioca starch cells 473
 thermal analysis 439–444

thermal characterization 313–317
 thermal properties 208, 672–676
 thermal transitions 565–570, 573–581,
 664–668
 thermal treatments 215–218
 thermodynamics
 amorphous water 5–8
 equilibrium parameters 60
 glassy water 5–8
 high pressure 206–214
 ice nucleation 135–138
 principles at high pressure 206–214
 spread films 258–261
 state diagram utility 60
 supercooled water 5–8
 water–fluid interfaces 251–271
 thermograms 139–149, 566–570
 thickness factors 431–436, 448, 538–542
 three-point bending assays 123–124, 128–129
 time correlation functions (TCF) 15–28, 33
 dielectric relaxation 20–21
 hydrogen bond lifetime dynamics 26–28
 solvation dynamics 15–19
 time-dependent lactose crystallization
 573–581
 time scales
 hydration layer dynamics 12, 14–15
 microstructure effect on diffusion 92
 water–carbohydrate diffusion 43–46,
 52–53
 time–temperature superposition principle
 597–598
 tissue preservation 155–158
 tofu 226
 topographical characteristics 266–267
 torsion measurements 71–73
 total moment–moment time correlation
 function 20–22
 toughness 123
 toxic domain of enterotoxin 12–36
 traditional balsamic vinegar 671–676
 Transition State theory 206, 209–210
 transition temperatures 551–556
 translation diffusion 349–350
 translational relaxation 46–48
 transmission electron microscopy 560
 transparent gels 83
 transport phenomena 520–523
 transverse relaxation rates 174
 trehalose
 dihydrates 108–112
 enthalpy relaxation 683–687
 freeze-dried liposomes stability 551–556
 glycinebetaine water sorption/desorption
 647–654

hydration 155–158, 159
 lactate dehydrogenase activity 698–701
Lactobacillus bulgaricus 464–468
 lipid membrane phosphate hydration
 506–509
 magnesium chloride 663–668
 marshmallow hardening 332–333
 nonenzymatic browning kinetics 656–661
 protein freeze-dried stability 543–549
 stability 543–549, 551–556, 663–668

triglycerides 226

trimethylammonium ions 654

turbid apple juice particles 289–299

U

UFW *see* unfrozen water content

ultrasonic cold stage devices 614, 621

ultrasonic horns 614–616

ultrasound 613–622

unfolding 459–460

unfrozen water content (UFW) 441–444

uniaxial deformations 402–411

unsaturated-LMWE monolayers 260, 261–263

USDA National Center for Genetic Resources
 Preservation 191–201

V

vacuum impregnation 495–502

Van der Waals attraction energy 290, 294–295

van Hove self-correlation function (VHSCF)
 43–45, 50–53, 55

VCD *see* vibrational circular dichroism

vegetable shortening 440

vegetables

 dehydration 537–542

 green beans 144–149

 high pressure effects 225

 ice nucleation 133–150

 lettuce seeds 200–201

 potatoes 127–129, 414–419, 486–487

 red sweet peppers 537–542

 strip browning 350–352

VHSCF *see* van Hove self-correlation function

vibration modes 505–506

vibrational circular dichroism (VCD) 394–395

vibrational spectroscopy 101–112

Vibrio parahaemolyticus 216, 217

villin 12–36

viscoelasticity

 air–water interfaces 427–428

 glassy starch molecular mobility 604, 605

hydroxypropylmethycelluloses 461

low molecular weight emulsifiers 261–263

protein–polysaccharide mixtures
 427–428

viscosity 422–429, 675–676

vitamin C 447–453, 715–720

Vogel–Tamman–Fulcher (VTF) Model
 199–200

W

Ward–Tordai equation 257–258

water

 activity

 air drying apples 499–500

 camu-camu 716–720

 dried milk products 631–637

 dried pears 723–728

Lactobacillus bulgaricus 465–467

 microbial growth 167–188

 reaction rates in foods 343–368

 solute diffusion 593–600

 tapioca starch cells 473–481

 affinity 455–461

 amorphous polymers 102–107, 112

 availability 167–188

 water–caffeine solutions 583–591

 cell longevity 191–201

 content

 bacteria and molds 167–188

 camu-camu 716–720

 disaccharide stability 663–668

 dried milk products 631–637

 dried pears 723–728

 freeze-dried lactose 573–581

 freeze-dried liposomes 552–556

 frozen French bread dough 441–444

 glassy starch molecular mobility
 604–610

 hydrophilic glasses 304–306

 low calory candy 703–708

 nonenzymatic browning 625, 627–629

 quinoa embryos and seeds 565–570

 recalcitrant *Araucaria angustifolia*
 558–563

 spray-dried lactose 573–581

 diffusion 39–56, 92–96, 102, 107–112

 dynamics

 micelle surfaces 11–36

 protein–glass transition 28–33

 protein surfaces 11–36

 water-soluble enzymes 504–505,
 507–509

 water-fluid interfaces 251–271

- glucose solutions 40–56
 - water–ice transitions 212–214
 - interfaces 251–271, 273–287
 - water-soluble LMWE 265
 - marshmallow hardening 326–340
 - water–mineral oil solutions 143–144
 - mobility
 - bacteria and molds 167–188
 - coupling 40, 42
 - hydrophilic glasses 304–306
 - molds 167–188
 - plasticization 573–581, 658–661, 723–728
 - reorientation 22–25
 - water-solid interactions 101–112
 - water-soluble enzymes 504–505, 507–509
 - water-soluble LMWE 265
 - sorption/desorption
 - dried pears 723–728
 - freeze-dried lactose 573–581
 - glycinebetaine 647–654
 - maltodextrin matrices 709–713
 - spray-dried lactose 573–581
 - starch-based edible films 414, 415
 - sugar crystallization 656–661
 - surface interaction energetics 640–645
 - stress 167–188, 191–201, 205–227, 233–242
 - thermal properties 208
 - translation diffusion 39–56
 - transport kinetics 80–81
 - uptake 641–645
 - vapor permeability 414–419, 431–436, 448, 449–450
 - vapor properties 431–436
 - water–caffeine solutions 583–591
 - water–fluid interfaces 251–271
 - water–ice transitions 212–214
 - water–mineral oil solutions 143–144
 - water–solid interactions 101–112
 - water-soluble enzymes 504–505, 507–509
 - water-soluble LMWE 265
 - waxy maize starch 604–610
 - wheat flour 126–127
 - wheat starch 624–629
 - whew powder 634–637
 - whew protein isolate (WPI) 282–283
 - whew proteins 222, 282–283
 - whipping agents/time 326–340
 - Williams–Landel–Ferry (WLF) constants 594, 596–600
 - Williams–Landel–Ferry (WLF) equation 348, 357–358
- ## X
- X-ray diffraction 698
 - xanthan gum
 - air–water interface activity 422–429
 - glass transition 313–317, 319–321
 - organism survival 170, 184–188
 - rheological behavior 313–317, 319–321
 - solute incorporation in ice phases 678–682
 - xylitol 414–419
- ## Y
- yeast viability 439
 - Young’s modulus 417
- ## Z
- zero mobility temperature 307
 - zeta-potential 290–298
 - zwitterions 647–654
 - zygosaccharomyces bailii* 216, 217, 218

